PROCEEDINGS

FIFTY-FIRST ANNUAL MEETING

MICROSCOPY SOCIETY OF AMERICA

CINCINNATI, OHIO

1-6 August 1993

Editors
G. W. BAILEY
and
C. L. Rieder

PUBLISHER'S NOTICE

Back Volumes

• San Francisco Press is offering all MSA, AEM, and MAS proceedings published before 1990 at a special low price of **$10 each**, while they last. The following volumes are available:

    MSA: 1983, 1987, 1988, 1989 at $10 each

    AEM: 1981, 1984, 1987 at $10 each [Note: XII ICEM vol. 2 (see below) serves as the 1990 AEM]

    MAS: 1976, 1977, 1979, 1980, 1981, 1982, 1986, 1987, 1988, 1989 at $10 each

• Proceedings published in 1990, 1991, and 1992 are offered at half price, as follows:

    MSA 1990 (XII ICEM), four volumes, also available individually: (1) imaging sciences, (2) analytical sciences, (3) biological sciences, (4) materials sciences, $32.50 each, $130 the set

    MSA 1991, $32.50

    MSA 1992, two parts (also contains MAS 1992 papers), $65 the set

    MAS 1990, 1991 at $32.50 each

Add postage and handling of $3 for first book, $2 for each additional book (foreign orders, $6 and $4); Californians add sales tax. (No credit cards.)

Also available from San Francisco Press:

    Electron Microscopy Safety Handbook (Barber & Clayton, Eds.), $15

    Electron Microscopy and Alzheimer's Disease (J. Metuzals, Ed.), $10

    Electricity and Medicine: History of Their Interaction (Rowbottom & Susskind), $30

Send orders to:

    San Francisco Press, Inc., Box 426800, San Francisco, CA 94142-6800, USA

MICROSCOPY SOCIETY OF AMERICA

Established 1942

OFFICERS 1993

Executive Council

1993 MSA PROGRAM COMMITTEE

MSA SUSTAINING MEMBERS

MICROSCOPY SOCIETY OF AMERICA

1993 DISTINGUISHED SCIENTIST AWARDS

JEAN-PAUL REVEL

KEN SMITH
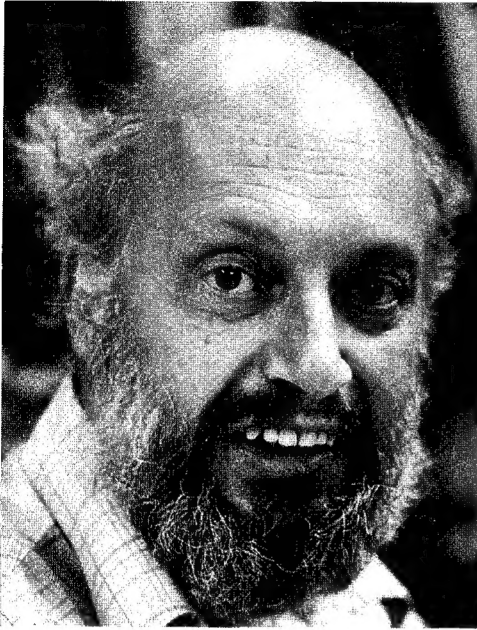
Jean-Paul Revel received the Ph.D. in Biochemistry at Harvard, where he eventually became a member of the Department of Anatomy headed by Don W. Fawcett. In 1971 he moved to the California Institute of Technology, where he is now the A. B. Ruddock Professor of Biology. In the early days of EM autoradiography, Revel studied chromatin and the synthesis/secretion of extracellular matrix proteins with E. D. Hay. He worked with S. Ito on model membranes, and with Fawcett on the structure of fast acting muscles. With M. J. Karnovsky he devised a technique to delineate gap junctions in both excitable and nonexcitable cells. He has continued his interest in that structure since, first with D. Goodenough and then with others, using a combination of biochemical, molecular, structural, and microscopy approaches. At present he is applying atomic-force microscopy to the study of these membrane channels. Revel is a past president of the American Society for Cell Biology, and of EMSA, and has recently served as Chair of the Biology Section of the American Association for the Advancement of Science.
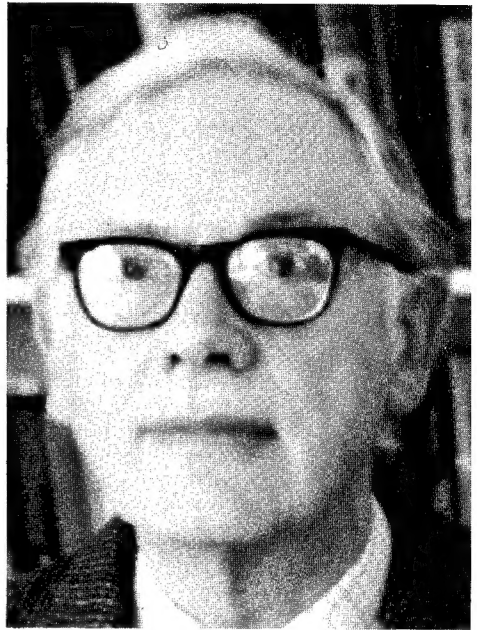
Ken Smith began his career in 1941 with an apprenticeship at the British Thomson-Houston Co. He then attended Coventry Technical College and Cambridge University, obtaining the Ph.D. in 1956 under Sir Charles Oatley. Postdoctoral work on the design and construction of a new SEM for the Pulp and Paper Research Institute of Canada was followed by his return to the Cambridge Cavendish EM Group in 1960 to lead a team in designing and constructing the Cavendish 750-kV EM, work for which he shared the Duddell Medal of the Institute of Physics with V. E. Cosslett. From the mid-1960s, in the Cambridge University Engineering Department, his main research was concerned with the application of real-time computer techniques to SEM and CTEM. He was a consultant to Cambridge Instrument Co. on the first Stereoscan and to AEI on the development of the 1-MV EM. He was made an Honorary Fellow of the Royal Microscopical Society in 1984.
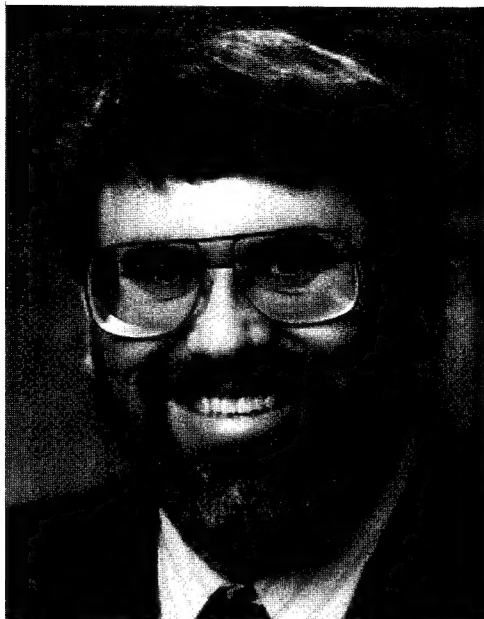
JOSEPH A. N. ZASADZINSKI

Joseph A. N. Zasadzinski received the B.S. with honors in Chemical Engineering from the California Institute of Technology in 1980, and the Ph.D. in Chemical Engineering from the University of Minnesota in 1985. He was a postdoctoral Member of the Technical Staff at AT&T Bell Laboratories from 1984 to 1986 under Dr. Saul Meiboom and Dr. Ron Pindak. He then joined the faculty of the University of California at Santa Barbara, where he is now professor of Chemical Engineering and Materials. His research interests span modern microscopy techniques and applications, with special emphasis on the applications of high-resolution electron and scanning-probe microscopy to complex fluid characterization. Three of his students have been named MSA Presidential Scholars over the past five years. Dr. Zasadzinski's other honors include being named a Presidential Young Investigator by the National Science Foundation.

E. LAURENCE THURSTON

BEN O. SPURLOCK

Larry Thurston received the M.S. and Ph.D. degrees at Iowa State University. After a post-doctoral stint in the Department of Botany at the University of Texas at Austin, he joined the Botany faculty at Texas A&M University, where he taught plant anatomy and botany. Later he became director of the Electron Microscopy Facility and a moving force in the Texas Society of Electron Microscopy. In addition, he developed training programs in electron micros-copy for JEOL. He also served as the editor of the *EMSA Bulletin* during its formative years in the later 1970s.
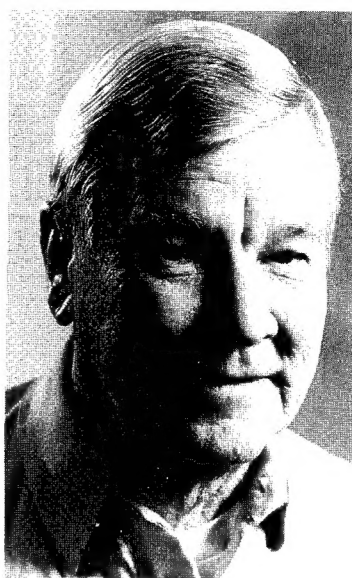
Ben O. Spurlock received the B.A. degree in science from Tulane Unviersity in 1962. He began his career as an electron-microscopy technician at Louisiana State University School of Medicine in 1960. He has held positions at Emory University School of Medi-cine, Tulane Univerisity School of Medicine, and the University of Georgia, and he is at present Director of Electron Microscopy and Associate Professor in the Department of Pathology at the Medical College of Georgia. During the past 30 years Ben has contri-buted to the training of numerous technicians in elec-tron microscopy and has served as mentor to both undergraduate and graduate students. He has pub-lished numerous scientific articles on EM techniques and on ultrastructural studies in pathobiology. He has served on the MSA Council and he is a member of the MSA Certification Committee.

DISTINGUISHED SCIENTIST AWARDS

Biological Sciences

1975	Keith Porter
1976	L. L. Marton
1977	Robley Williams
1978	Thomas Anderson
1979	Daniel Pease
1980	George Palade
1981	Sanford Palay
1982	Richard Eakin
1983	Hans Ris
1984	Cecil Hall
1985	Gaston Dupouy
1986	F. O. Schmitt
1987	Marilyn Farquhar
1988	Morris Karnovsky
1989	Don W. Fawcett
1990	Audrey M. Glauert
1991	Hugh E. Huxley
1992	Fritiof Sjöstrand

Physical Sciences

1975	Robert Heidenreich
1976	Albert Crewe
1977	James Hillier
1978	V. E. Cosslett
1979	John Cowley
1980	Gareth Thomas
1981	Vladimir Zworykin
1982	Benjamin M. Siegel
1983	Otto Scherzer
1984	Sir Charles Oatley
1985	Ernst Ruska
1986	Peter Hirsch
1987	Jan LePoole
1988	Hatsujiro Hashimoto
1989	Elmar Zeitler
1990	Gertrude F. Rempfer
1991	Archie Howie
1992	Oliver Wells

BURTON MEDALISTS

1975	James Lake
1976	Michael Isaacson
1977	Robert Sinclair
1978	David Joy
1979	Norton B. Gilula
1980	John Spence
1981	Barbara Panessa-Warren
1982	Nestor Zaluzec
1983	Ronald Gronsky
1984	David B. Williams
1985	Richard Leapman
1986	J. Murray Gibson
1987	Ronald Milligan
1988	A. D. Romig Jr.
1989	Laurence D. Marks
1990	W. Mason Skiff
1991	Joseph R. Michael
1992	Kannan Krishnan

DISTINGUISHED SERVICE AWARDS

1992

Ronald Anderson
G. W. "Bill" Bailey
Frances Ball
Blair Bowers
Deborah Clayton
Joseph Harb
Kenneth Lawless
Morton Maser
Caroline Schooley
John H. L. Watson

PAST PRESIDENTS

1942	G. L. Clark[1]	1970	Russell Steere
1943	R. Bowling Barnes[2]	1971	Robert M. Fisher
1944	R. Bowling Barnes	1972	Daniel C. Pease
1945	James Hillier	1973	Benjamin Siegel
1946	David Harker	1974	Russell J. Barrnett
1947	William G. Kinsinger	1975	Gareth Thomas
1948	Perry C. Smith	1976	Etienne de Harven
1949	F. O. Schmitt	1977	T. E. Everhart
1950	Ralph W. G. Wyckoff	1978	Myron Ledbetter
1951	Robley C. Williams	1979	John Silcox
1952	R. D. Heidenreich	1980	Michael Beer
1953	Cecil E. Hall	1981	John Hren
1954	Robert G. Picard	1982	Lee Peachey
1955	Thomas F. Anderson	1983	David Wittry
1956	William L. Grube	1984	J. David Robertson
1957	John H. L. Watson	1985	Dale Johnson
1958	Max Swerdlow	1986	Robert Glaeser
1959	John H. Reisner	1987	Linn W. Hobbs
1960	D. Gordon Sharp	1988	Jean-Paul Revel
1961	D. Maxwell Teague	1989	Ray Carpenter
1962	Keith R. Porter	1990	Keith R. Porter
1963	Charles Schwartz	1991	Charles Lyman
1964	Sidney S. Breese	1992	Patricia Calarco
1965	Virgil G. Peck		
1966	Walter Frajola		
1967	Joseph J. Comer		
1968	John H. Luft		
1969	W. C. Bigelow		

[1] Chair of committee to arrange first meeting.

[2] Temporary (pre-constitution).

Michael S. Isaacson
MSA President

Ruth V. W. Dimlich
Local Arrangements Chair

Cynthia C. Daugherty
Local Arrangements Secretary

Steven Boyce
Local Arrangements Treasurer
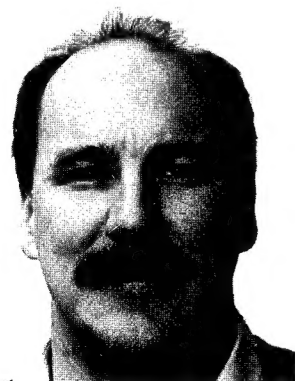
Conly L. Rieder
Program Chair

Anthony J. Garratt-Reed
Program Vice Chair

1993 MSA PRESIDENTIAL SCHOLARS

Hakan Ancin
Rensselaer Polytechnic Institute

Gregory J. Czarnota
University of Toronto

Bong-Gyoon Han
University of California—Berkeley

Jun Jiao
University of Arizona

Roger H. Johnson
University of Washington

Jorge Perdigao
University of Iowa

Kerry E. Robinson
Clemson University

Ravi Viswanathan
University of California—Santa Barbara

Kerri Winter
Duke University

Kaikee Wong
Cornell University

PREFACE

Our fifty-first annual meeting in Cincinnati represents a new beginning of our fifty-years-old Society—now the Microscopy Society of America. One of the primary objectives of the name change was to broaden the scope of the Society to include other areas of microscopy. The fact that this Proceedings contains papers from all disciplines of microscopy indicates that this objective is being met. Congratulations to the Program Chair and Vice Chair and their committee.

The production of this Proceedings, the program, and the entire meeting is the result of a combined effort by many volunteers. The Program Chair again serves as Proceedings Co-Editor, in recognition of that person's special contribution and participation in the preparation of the Proceedings. It is a pleasure to welcome Conly Rieder, 1993 MSA Program Chair, as Co-Editor. Conly and his Vice Chair Tony Garratt-Reed, and the entire Program Committee, have all done an excellent job in assembling a quality program for this year's meeting. Thanks also go to Mort Maser for his efficient handling of all papers received and for his assistance in the organization of this Proceedings. Special thanks also go to members of the Local Arrangements Committee, who have assisted in so many ways during the preparation of this Proceedings.

G. W. BAILEY

FOREWORD

MICHAEL S. ISAACSON
President, Microscopy Society of America

This is the first volume of the Proceedings of the annual meeting of the Microscopy Society of America (MSA) since the name of the Society was changed from Electron Microscopy Society of America (EMSA). It contains over 600 papers covering a wide selection of topics in all areas of microscopy and microscopic analysis. The papers range from the microscopy of ceramics and polymers to semiconductors and superconductors, and cover new results in confocal light microscopic imaging, x-ray microscopy, atomic-resolution imaging, and scanned-tip microscopies, as well as other microscopies and traditional electron microscopic imaging and analysis.

The excellence of the scientific program is due in no small part to the hard work of the Program Committee. I should particularly like to acknowledge the contributions and organizational skills of Program Chair Conly Rieder and his Co-Chair Tony Garratt-Reed. They rode herd on the Program Committee (myself included) to insure a quality mix of invited and contributed papers, and made sure that everything came together on time.

I should also like to congratulate our award recipients. They are the winners of the first MSA awards: Ken Smith, Distinguished Scientist in the Physical Sciences; Jean-Paul Revel, Distinguished Scientist in the Biological Sciences; Joe Zasadzinski, Burton Award winner; and Larry Thurston, winner of the Distinguished Service Award. This first year of the MSA is also the first year that the Outstanding Technologist Award is being given, to Ben Spurlock. In addition to these winners, MSA is making ten Presidential Student Awards. My congratulations to all these winners for their efforts in advancing microscopy.

Acknowledgments and thanks are also due to the many volunteers who contributed to the success of this year's meeting. In particular, thanks go to the Microscopy Society of the Ohio River Valley and to Ruth Dimlich, the MSA Local Arrangements Committee Chair, and her committee for their careful planning to insure the success of this meeting. Few scientific societies can boast so many volunteer workers who come together to guarantee the success of their meeting.

Finally, my warmest thanks go to Bill Bailey, who through careful supervision, prodding, and editing insures that these Proceedings stay on schedule so as to be available at the Annual Meeting.

The MSA extends an invitation to all to enjoy the exciting scientific program, as recorded in this 1993 Proceedings.

Ithaca, New York
August 1993

TITLES AND ORDER OF SESSIONS

PRESIDENTIAL SYMPOSIUM
300 YEARS AFTER HOOKE AND LEEUWENHOEK: THE REVOLUTION IN MICROSCOPY

PATHOLOGY

MOLECULAR ORGANIZATION AND DISTRIBUTION OF CELL SURFACE PROTEINS

NEW DIRECTIONS AND NEW IMAGING TECHNOLOGIES FOR FREEZE FRACTURE: A SPECIAL SYMPOSIUM IN MEMORY OF RUSSELL STEERE

CHROMOSOMES: HOW THEY FOLD AND HOW THEY MOVE IN MITOSIS

ADVANCES IN OPTICAL MICROSCOPY: APPLICATIONS FOR BIOLOGY

STRUCTURAL APPROACHES TO NEUROBIOLOGY

CRYOTECHNIQUES AND THEIR APPLICATIONS IN BIOLOGICAL MICROSCOPY

PLANT CELL STRUCTURE: RECENT ADVANCES

3-D LIGHT MICROSCOPY: IMAGING AND IMAGE RECONSTRUCTION

LIGHT AND ELECTRON MICROSCOPY OF EGG SYSTEMS

ORGANELLES

IMAGE ANALYSIS IN MICROSCOPY

SCANNING-PROBE MICROSCOPY FOR PHYSICAL AND BIOLOGICAL SCIENCES

SPECIMEN-PREPARATION METHODS: BIOLOGICAL

INSTRUMENTAL DEVELOPMENTS FOR PHYSICAL AND LIFE SCIENCES: COMMERCIAL CONTRIBUTIONS

LASER AND CONFOCAL IMAGING

CRYOTECHNIQUES AND THEIR APPLICATIONS IN BIOLOGICAL MICROSCOPY

IMMUNOCYTOCHEMISTRY

CELL ORGANELLES

CELL SURFACE AND EXTRA-CELLULAR MATRIX

PATHOLOGY AND TISSUE ORGANIZATION

BIOLOGICAL AND MATERIALS MICROANALYTICAL MICROSCOPY

DEVELOPMENTS IN INSTRUMENTATION AND TECHNIQUES FOR PHYSICAL AND LIFE SCIENCES

SCANNING ELECTRON MICROSCOPY: PAST, PRESENT, AND FUTURE

TECHNOLOGISTS' FORUM

Special Topic Presentation

Quantification in the Microscopy Laboratory

TUTORIALS

Biological Sciences

Biological and Physical Sciences

Physical Sciences

SCANNING-PROBE MICROSCOPY FOR PHYSICAL AND BIOLOGICAL SCIENCES

IMAGE ANALYSIS IN MICROSCOPY

BIOLOGICAL AND MATERIALS MICROANALYTICAL MICROSCOPY

INSTRUMENTAL DEVELOPMENTS FOR PHYSICAL AND LIFE SCIENCES

X-RAY MICROSCOPY AND RELATED TECHNIQUES

QUANTITATIVE ELECTRON CRYSTALLOGRAPHY

SPECIMEN PREPARATION METHODS: PHYSICAL

EMERGING TECHNOLOGIES IN PARTICLE CHARACTERIZATION

SCANNING ELECTRON MICROSCOPY: PAST, PRESENT, AND FUTURE

SEMICONDUCTOR HETEROSTRUCTURES

NANOMETER-SCALE SEMICONDUCTOR PROPERTIES

ADVANCES IN THE MICROSCOPY OF COATINGS AND
INTERFACES OF MATERIALS

ASPECTS OF IMAGING IN POLYMER SCIENCE

MICROSCOPY OF CERAMICS

ATOMIC-RESOLUTION MICROSCOPY

SURFACE ELECTRON MICROSCOPIES

MAGNETIC MATERIALS AND MAGNETIC IMAGING

COHERENT-BEAM IMAGING AND DIFFRACTION

AMORPHIZATION AND AMORPHOUS STRUCTURES

SEMICONDUCTOR HETEROSTRUCTURES

ADVANCES IN THE MICROSCOPY OF COATINGS
AND INTERFACES OF MATERIALS

EMERGING TECHNOLOGIES IN PARTICLE AND SURFACE CHARACTERIZATION

MICROSCOPY OF CERAMICS

APPLICATIONS OF ELECTRON MICROSCOPY TO MATERIALS

QUANTITATIVE ELECTRON CRYSTALLOGRAPHY

COHERENT-BEAM IMAGING AND DIFFRACTION

ELECTRON MICROSCOPE OF THE 21ST CENTURY

A.V. Crewe

The Enrico Fermi Institute and the Department of Physics, The University of Chicago,
5640 S. Ellis, Chicago, Il. 60637

I have been asked to talk about the future of the electron microscope by the Chairman and cannot refuse because he was one of my students. On the other hand, I do not feel comfortable with the position because there is a very poor history in science on the matter of making predictions; they are always wrong.

After giving it some thought, it would seem that the best thing that I can do is to discuss some of the problems that I can see with the instruments and suggest that the solutions to these problems will slide into the next century. That puts me on safe ground and perhaps may allow me to suggest some solutions myself.

To start with, one can say that the business shows every sign of being, or becoming, a mature industry. The instruments become more and more expensive every year. They become generally larger, and there is more attention given to appearances. This is very similar to the automobile industry and is at gross variance with the computer industry where the functionality increases and the cost decreases every year. In the present climate of financial support (or the lack of it), this means that fewer instruments are sold every year, and this increases the price of those that *are* sold.

With regard to the functionality of these microscopes, this seems to have reached a limit, as it must do. We all are aware of the Scherzer Theorem and its implications. The lenses that we all use are subject to aberrations, and there is no way to design a lens without aberrations. Furthermore, since thousands of man hours or even man years have been dedicated to the improvement of these lenses, it would be a brave person indeed who decided that they could be significantly improved.

The resolution of our instruments is stuck, and it is stuck in very uncomfortable ways. Except for very special circumstances and very special specimens, the resolution of the best high voltage instruments is around 1.5 Å, a limit which is due to spherical aberrations. This is to be compared with inter-atomic distances which are a factor of two or so lower. We cannot get there. With regard to the lower voltage instruments such as the SEM, the resolution is also uncomfortably low. One would very much like to have an SEM of, say 1kv with a resolution of a few Å (preferably 1 or 2), but we are stuck far above this level de to the effects of chromatic aberration.

So here we are. The microscopes are too expensive and they do not perform nearly as well as we would like. What to do ?

First of all, let me suggest that our microscopes are much too large. A 1 kv microscope need not be larger than a few cm, or even mm. That is all it takes to withstand that voltage. Why then are they about a meter high and weigh more than we can carry? There is no real answer other than they look more impressive when they are large. I will personally eat my hat if I cannot design a 1 kv microscope

that is less than 1 foot long. While size is not in itself an important feature, it certainly contributes to the cost. In this respect, it is interesting to note that one of my colleagues, who has technology for a "microscope on a chip", cannot get funding. Apparently, our federal funding agencies would rather provide money to purchase very expensive instruments than fund the development of ones that are infinitely cheaper.

Similarly with higher voltage instruments. Why are the lenses so large and expensive? The only answer that I have ever been able to find is that the more expensive the instrument is, the larger it must be in order to impress the buyer. The fact of the matter is that much smaller lenses can be designed, which would reduce the cost of the whole instrument by a considerable factor.

The electronic component of our instruments is getting better but not very rapidly. The computer business has evolved so rapidly that the mature industries in all areas of the economy have not kept up, and microscopy is no exception. It is now possible to buy and use a whole array of accessories for the PC that can be used effectively in the fabrication of a microscope, but we see little evidence of that. It would be desirable if the operators of all microscopes used the same type of PC based electronics, just as they all use the same type of vacuum system. It is good to see the growing use of Windows-based software, but much more needs to be done.

Finally, with regard to the real problem in electron microscopy. This is no less than the eradication of lens aberrations, which can only be done by using correction devices. This problem has existed for some 56 years and has not yet been solved. There are some possible solutions, and a few of them have been attempted. None have yet succeeded. There are some new ideas in this area, and they need to be tried. We hope to be among those who try and succeed, but I for one would be very happy if *anyone* succeeded. It is a goal to shoot for and one that may set us on a new journey into the future.

CHARACTERIZATION OF MAGNETIC MICROSTRUCTURE AT HIGH SPATIAL RESOLUTION

M.R. Scheinfein

Department of Physics and Astronomy, Arizona State University, Tempe, AZ 85287-1504

Advances in metal epitaxial growth techniques have produced renewed interest in magnetic materials through the unique properties of novel atomically engineered structures [1]. Ultrathin layered and nanocrystalline, textured composites possess unique magnetic properties which are intimately connected to the physical microstructure on both the atomic and nanometer length scales. The length scales present in magnetic interactions span several orders of magnitude from the atomic length scales of the exchange interaction, to the mesoscopic length scales important in anti-ferromagnetic RKKY coupling between thin ferromagnetic films [2] and small particles [3], to the macroscopic length scales determined by the long range magnetostatic interactions which are responsible for the formation of magnetic domains [4].

Special characterization and computation techniques are required to analyze the micromagnetic and microstructural properties of these novel, low dimensional systems. In order to correlate the structure with the magnetic properties of any system, in-situ growth, structural, chemical and magnetic characterization is desirable.

Most methods used for the observation of micromagnetic structure rely on a contrast mechanism derived from the magnetic fields present in ferromagnetic systems. We have implemented the conventional Fresnel, and less conventional Differential Phase Contrast modes of imaging magnetic microstructure in an HB5 STEM [5]. While this is not a UHV system for in-situ film growth studies, the salient features of this system are 5 nm spatial resolution and 30 ms temporal resolution, important for the study of mesoscopic magnetic correlations [6]. Transmission electron energy loss spectroscopy, nano-diffraction and high-angle annular dark field image measurements can be acquired simultaneously. The magnetic microstructure in thin Co-films and nano-textured composites will be shown as examples.

However, Lorentz contrast at high spatial resolution is only achievable for thin, electron-transparent samples. In order to image bulk samples, a unique magnetic force microscope (MFM) utilizing an ultra-sensitive vertical cantilever design [7] has been implemented in our laboratory with sub 100 nm spatial resolution. The vertical cantilever design leads to extremely high sensitivity to stray magnetic fields at sub-micron spatial resolution together with a unique capability for imaging the vector surface fields (magnetization). The salient features of this instrument include the ability to assess sub-surface magnetization configurations of semi-infinite samples. Experimental results acquired with this novel MFM for the micromagnetic structure of surface Neel walls in single crystals of Fe, and domain images of bits written in longitudinal recording media, will be compared to those derived from scanning electron microscopy with polarization analysis (SEMPA) [8].

We have pursued two separate paths towards simultaneously characterizing the real space, magnetic, chemical and physical microstructure of low dimensional magnetic systems. One system utilizes a dedicated UHV-STEM with ambient pressures of 5 x 10^{-11} mbar and extensive specimen preparation facilities. The specimen chamber is equipped with ion sputtering, Auger spectroscopy, RHEED, electron beam and knudsen cell evaporators, and a polarized light scattering station for in-situ magnetic measurements using the surface magneto-optic Kerr effect. The UHV-STEM SEM and Auger electron image resolution is in the nanometer range. Examples of recent results extracted from measurements correlating magnetic and physical/chemical structure in fcc Fe/Cu(100) and bcc Fe/Ag(100) systems will be given.

The second system for correlating physical and magnetic microstructure at surfaces employs UHV low energy scanning electron microscopy [9] using single atom terminated field emitters. This reflection instrument, still under construction, will form small probes (~ 5 nm at 2 keV and 3 mm working distance) with electrostatic mini-lenses. Probe diameters will degrade at 50 eV beam energies. A quadranted channel plate detector is used for backscattered and SEM imaging, and an electrostatic energy analyzer will be used for reflection EELS and Auger spectroscopy. This simple system will employ a two-level piezo-electrically scanned stage and STM data acquisition electronics. The system will also be equipped with an STM for atomic length scale characterization. Prospects for implementing a negative electron affinity GaAs field-enhanced photocathode will be discussed in the context of obtaining micromagnetic information within the same instrument.

References:
1. L.M. Falicov, D.T. Pierce, S.D. Bader, R. Gronsky, K.B. Hathaway, H.J. Hopster, D.N. Lambeth, S.S.P. Parkin, G. Prinz, M. Salamon, I.K. Schuller, R.H. Victora, J. Mater. Res. **5**(6), 1299 (1990).
2. R.F.C. Farrow, C.H. Lee, S.S.P. Parkin, IBM J. Res. Dev. **34**(61), 903 (1990).
3. Y.Yoshizawa, K. Yamaguchi, J. Appl. Phys. **54**(10), 6044 (1988), R.V. Chamberlin, M.R. Scheinfein, Science, in press (1993).
4. C. Kittel, Rev. Mod. Phys. **21**(4), 441 (1949) .
5. J.N. Chapman, J. Phys. **D17**, 623 (1984); M. Mankos, J.M. Cowley, R.V. Chamberlin, M.R. Scheinfein (these proceedings, 1993).
6. R.V. Chamberlin, M.R. Scheinfein, Ultramicr. **47**, 408 (1992).
7. A. DiCarlo, M.R. Scheinfein, R.V. Chamberlin, Appl. Phys. Lett. **61**(17), 2108 (1992).
8. M.R. Scheinfein, J. Unguris, M.H. Kelley, D.T. Pierce, R.J. Celotta, Rev. Sci. Instrum. **61**(10), 2501 (1990); M.R. Scheinfein, J. Unguris, J.L Bluue, K.J. Coakley, D.T. Pierce, R.J. Celotta, P.J. Ryan, Phys. Rev. **B43**(4), 3395 (1991).
9. W. Qian, M.R. Scheinfein, J.C.H. Spence, Appl. Phys. Lett. **62**(3), 315 (1993).; M.R. Scheinfein, W. Qian, J.C.H. Spence, J. Appl. Phys. **73**(5), in press (1993).

MOLECULAR MICROSCOPY:
THEORETICAL POSSIBILITIES AND EXPERIMENTAL REALITIES

John A. Sidles

Department of Orthopaedics, University of Washington, Seattle WA 98195, USA
[email: sidles@u.washington.edu]

It is interesting to imagine a world in which microscopy had never been invented. What techniques would scientists use to study cell structure? Lack of microscopy would not prevent research.... instead scientists would study cells using indirect means; e.g. by homogenizing, filtering, and centrifuging cells. After much work, they would be able to demonstrate that cells are surrounded by membranes, and contain nuclei carrying genetic information. All aspects of cell structure could be studied in this indirect way.

Biomedical researchers would not feel particularly handicapped by the lack of microscopy. Rather they would compete for access to the newest and most ingenious filtering devices. In this hypothetical world, it would not be readily apparent that instrument technology was a crucial medical/scientific issue.

It is arguably the case that we live in a similar world, and that (from a clinical perspective) we need a microscope technology that can image 3D biomolecular structure with the subangstrom spatial resolution that is required for the rational design of drugs and vaccines.

The highest-resolution techniques for determining 3D molecular structure are x-ray crystallography and mutidimensional NMR analysis. However, neither of these techniques can properly be called "microscopy". True imaging of atomic-scale structure is possible using scanning tunneling microscopy (STM) and atomic force microscopy (AFM). These techniques respond mainly to the topmost layer of atoms, and thus cannot easily determine the interior structure of complex molecules. Another problem is that they give limited information about chemical composition of the sample being imaged.

An ideal technique for imaging molecular structure would be nondestructive, three dimensional, and would achieve subangstrom spatial resolution while imaging single molecules *in situ*. Recently, researchers have begun to think seriously about achieving these goals.[1-4] With the caveat that the required microscale engineering technology is not yet in place, here is one way in which single-copy molecular imaging might work.

Suppose a cell biologist is interested in transmembrane receptors, for example the CD4 receptor for the HIV-1 protein gp120. The cell biologist begins by freeze-fracturing a cell membrane containing the CD4 receptor, as though preparing it for electron microscopy. The fractured surface is then placed on the cryogenic stage of a sensitive force microscope. The microscope consists of a high-Q vibrating cantilever tipped with a small magnetic field source. The cantilever does not contact the surface, but scans a few angstroms above it.

Now consider what happens as the oscillator approaches a given nucleus of (for example) ^{13}C. When the nucleus is far from the oscillator, it is in a weak magnetic field, and the ^{13}C nucleus precesses too slowly to resonate with the oscillator. When the nucleus is too near to the oscillator, the field is too strong, so that the nucleus precesses too fast. But at a certain critical distance, the nuclear precession is resonant with the cantilever oscillations, and this

generates a vibratory signal in the cantilever. Only nuclei within a sensitive "slice" generate a signal, and this slice can be as thin as a few tenths of an Ångstrom under the proper circumstances. With computer assistance, a tomographic reconstruction of the molecular structure can in principle be obtained.[1]

A structural scan of a single cell membrane would generate substantial quantities of information. Scanning $(0.1\ \mu m)^2$ of membrane, to a depth of a hundred Ångstroms, would generate $\sim 10^8$ atomic coordinates. Such a scan would require several hours to complete. All the different receptors present in the membrane would show up in the scan, in three-dimensional detail, with their associated ligands, and so the scan would contain much information of scientific interest.

Imaging by magnetic resonance force microscopy (MRFM) has three main advantages:

Fig. 1 A molecular imaging device.

1. The imaging is noncontact and nondestructive.
2. The imaging field is three-dimensional, and reaches below the scanned surface. This is necessary for imaging the 3D structure of subsurface molecules.
3. Most important, the theory of magnetic resonance interactions is sufficiently well developed and validated that it provides a reasonably reliable basis for the design and operation of imaging devices.

Our expectation is that the next generation of molecular biologists will routinely, quickly, and easily obtain images showing the full three-dimensional structure of the molecules they are studying, *in situ*, with all their ligands, cross-links, and glycosylation in place. Our hope is that this will substantially accelerate the development of effective treatments for presently intractable disorders.

Single-copy molecular imaging is an active area of scientific research. There is a substantial gap between the sensitivity that has been achieved experimentally,[4] and what is required theoretically.[1-3] We and other researchers are working to close this gap. Even if the approaches we have described prove impractical in the long run, we are nonetheless confident that our work will encourage other, more ingenious, researchers to do better.

1. J.A. Sidles, J.L. Garbini, and G.P. Drobny: *The theory of oscillator-coupled magnetic resonance with potential applications to molecular imaging.* Rev. Sci. Instr. 63, 3881-3899 (1992).
2. J.A. Sidles: *Noninductive detection of single-proton magnetic resonance.* Applied Physics Letters 58(24), 2854 (1991).
3. J.A. Sidles, *Folded Stern-Gerlach experiment as a means of detecting magnetic resonance in individual nuclei.* Phys. Rev. Lett. 68, 1124 (1992).
4. D. Rugar, C.S. Yannoni, and J.A. Sidles: *Mechanical detection of magnetic resonance.* Nature 360, 563-566 (1992).
5. This work was supported in part by the NIH under 1 R03 RR07891-01, and by the University of Washington Department of Orthopaedics.
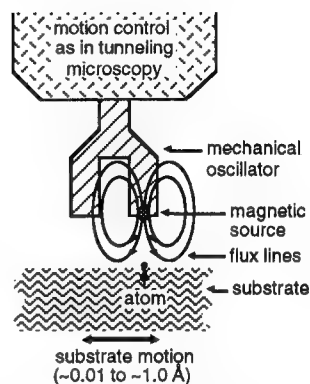
OPTICAL MICROSCOPY BEYOND THE DIFFRACTION LIMIT

Eric Betzig

AT&T Bell Laboratories, 600 Mountain Avenue, Murray Hill, NJ 07974-0636

The near-field optical interaction between a sharp probe and a sample of interest can be exploited to image, spectroscopically probe, or modify surfaces at a resolution (currently down to ~12 nm with visible light) well beyond the diffraction limited response of traditional far-field systems.[1] The resulting technique, near-field scanning optical microscopy (NSOM), still retains many of the attractive features of conventional optics, including non-invasiveness, low cost, reliability, and ease of use. Most importantly, NSOM takes advantage of the numerous and powerful contrast mechanisms and associated sample preparation procedures developed for optical microscopy over the last three centuries.[2]

Several applications have been investigated to demonstrate the versatility arising from these contrast mechanisms. For example, polarization contrast has been coupled with near-field surface modification capabilities to image and record domains in thin-film magneto-optic materials (Fig. 1).[3] This might form the basis for a new method of ultra-high density optical data storage, or could be used in a study of domain wall energetics in magnetic systems.

In the biological arena, NSOM has been used to image fluorescently labeled cytoskeletal actin in fixed mouse fibroblast cells (Fig. 2), and applied in a study of the actin organization within wound healing protrusions.[4] The resulting images were also compared to topographic data arising from the shear force mechanism which regulates the probe-to-sample separation.[5] Although many technical hurdles remain, the application of NSOM to the non-invasive dynamic imaging of living cells continues to be an exciting possibility.

Other applications which have been investigated include superresolution optical lithography, near-field optical spectroscopy, and the inspection of semiconductor lasers. Even more applications will hopefully arise as more researchers consider the possibilities of a microscope which combines the power of photons with nanometric spatial resolution.

References

1. E. Betzig et al., Science 251 (1991) 1468.

2. E. Betzig and J.K. Trautman, Science 257 (1992) 189.

3. E. Betzig et al. Appl. Phys. Lett. 61 (1992) 142.

4. E. Betzig et al., to be submitted

5. E. Betzig et al., Appl. Phys. Lett. 60 (1992) 2484.

1 μm

A

B

2 μm
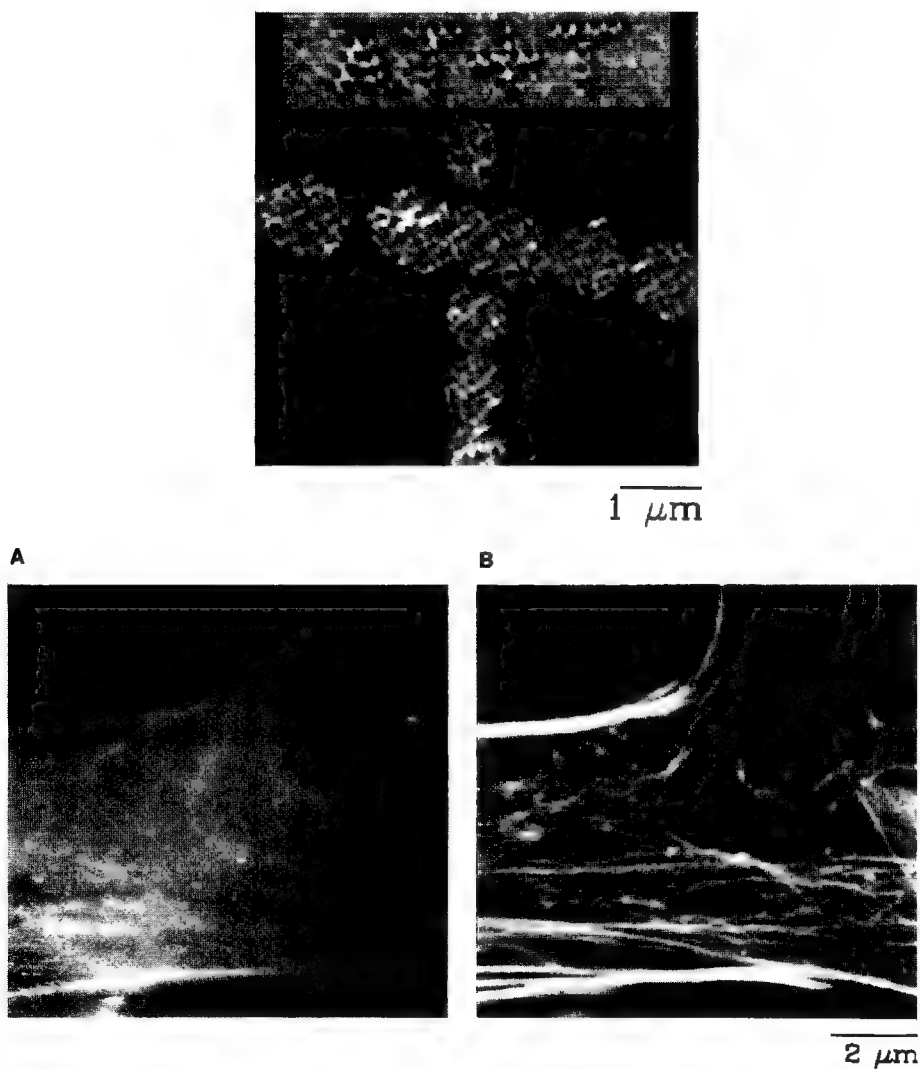
FIG. 1. Comparison of bit sizes in a magneto-optic film recorded by conventional optics (large circles, bottom) and near-field optics (small dots, top).

FIG. 2. (A) Shear force topography and (B) near-field fluorescence images of a lamellipodium from a Swiss mouse 3T3 fibroblast cell.

9

CORNEAL WOUND HEALING FOLLOWING   EXCIMER LASER ABLATION

Tammy A. Gelber,* Kathleen Waltz,* Corine R. Ghosn,* Michael E. Stern,* Beatrice Cochener,**
Lih-Huei L. Liaw,** Michael W. Berns **

Allergan Pharmaceuticals, Irvine, CA * Beckman Laser Institute, Irvine, CA**

The excimer laser is currently being investigated in ophthalmology for refractive correction, including myopia, hyperopia and astigmatism. Laser photo ablation offers a consistent, precisely controllable method of tissue removal that potentially gives the surgeon more accurate control of surgical results than do conventional methods of corneal reshaping (i.e., diamond knives for radial keratotomy).   In addition, there is interest in using laser photo ablation to smooth irregular corneal surfaces and to remove corneal stromal opacities. Early clinical studies have elucidated two problems common to refractive surgery. First, the cornea tends to develop a subepithelial haze approximately two weeks post-op in the ablation zone. In most cases this subsides during the ensuing six months. Second, the initial level of refractive correction reverses during the process of healing. This problem tends to be exaggerated in patients whose correction is greater than five diopters requiring a deeper ablation. Depending on the depth of the ablation, the epithelium, Bowman's layer and the anterior stroma will be removed. The reparative process includes reepithelialization and the restoration of the stroma through the migration of keratocytes to the wound area. This is followed by the secretion of collagenases as well as new collagen and extracellular matrix (GAGs).

The Dutch - Cross rabbit has been selected as the model for this study because it has a pigmented eye which provides a reproduction of human corneal laser surgical considerations (i.e., light absorption by iris).   The animals were anesthetized with a subcutaneous injection of Ketamine (50 mg/kg) and Rompun (5 mg/kg) mixed in a single syringe and one drop of Proparacaine (topical cornea anesthesia) in each eye.

In this study we investigated corneal wound healing after corneal laser ablation in Dutch-Cross rabbits to depths of 80 μm, group 1 (4 diopters) and 160 μm, group 2 (8 diopters). The surgery was performed with a Taunton Excimer Laser Surgical System using the following parameters: Ablation diameter - 6.00 mm; Peak Fluence - 125.0 mJ/cm**2 ; Total energy @ eye - 25.0 mJ ; Duration of surgery - 1 min. 15 sec. Each group was timed sacrificed for histology at two days and two months. The animals were evaluated using slit lamp biomicroscopy and photography at designated intervals. After sacrifice, the corneas were fixed in 2.6% gluteraldehyde, osmicated, uranyl acetate stained *en bloc*, serially dehydrated in ethanol, embedded in epon and sectioned at 60 nm on a diamond knife. The sections were placed on formvar coated copper (1X2) grids, post stained in lead citrate and examined under the Phillips 300 electron microscope at 80 KV.

As shown in Figure 1, migrating epithelium fills in the ablated area of the 160 μm laser ablated two day cornea. Adhesion plaques are evident along the epi-stromal border. Overall, there is an increased amount of ribosomes both on the endoplasmic reticulum and the in the cytoplasm indicating increased cell activity and protein synthesis. Activated keratocytes with increased amounts of rough endoplasmioc reticulum, condensed mitochondria and vacuolization are prevalent under the wound bed.   The epi-stromal border of the 80 μm laser ablated two day cornea, (Figure 2) reveals a definite basement membrane, pericellular space and irregularly spaced hemidesmosomes. The basal cells are less active than in Figure 1, fibrin aggregates are seen across the epi-stromal border under the wound bed and the collagen fibrils are more organized. The activated keratocytes under the epi-stromal border straighten out as they approach the endothelium.   At two months, the 160 μm laser ablated corneas have a definite basement membrane with semi-consistent hemidesmosomes and activated keratocytes (Figure 3).

Fibrin is evident in the epi-stromal area under the wound bed, mid-stromal keratocytes are less active than seen in the two day 160 μm laser ablated cornea and the keratocytes above the endothelium are relatively inactive. The basal epithelium of the two month 80 μm laser ablated cornea (Figure 4) is more settled than the two month 160 μm laser ablated cornea (Figure 3). A distinct basement membrane is prominent with well-established hemidesmosomes. Few keratocytes are found in the epi-stromal area, however more posterior in the stroma, straight elongated keratocytes are found. These results are indicative of a good control model to study corneal wound healing following Excimer laser ablation surgery. The reparative process of these laser ablated corneas displayed normal reepithlialization and stromal restoration in both the 80 μm and 160 μm surgeries.
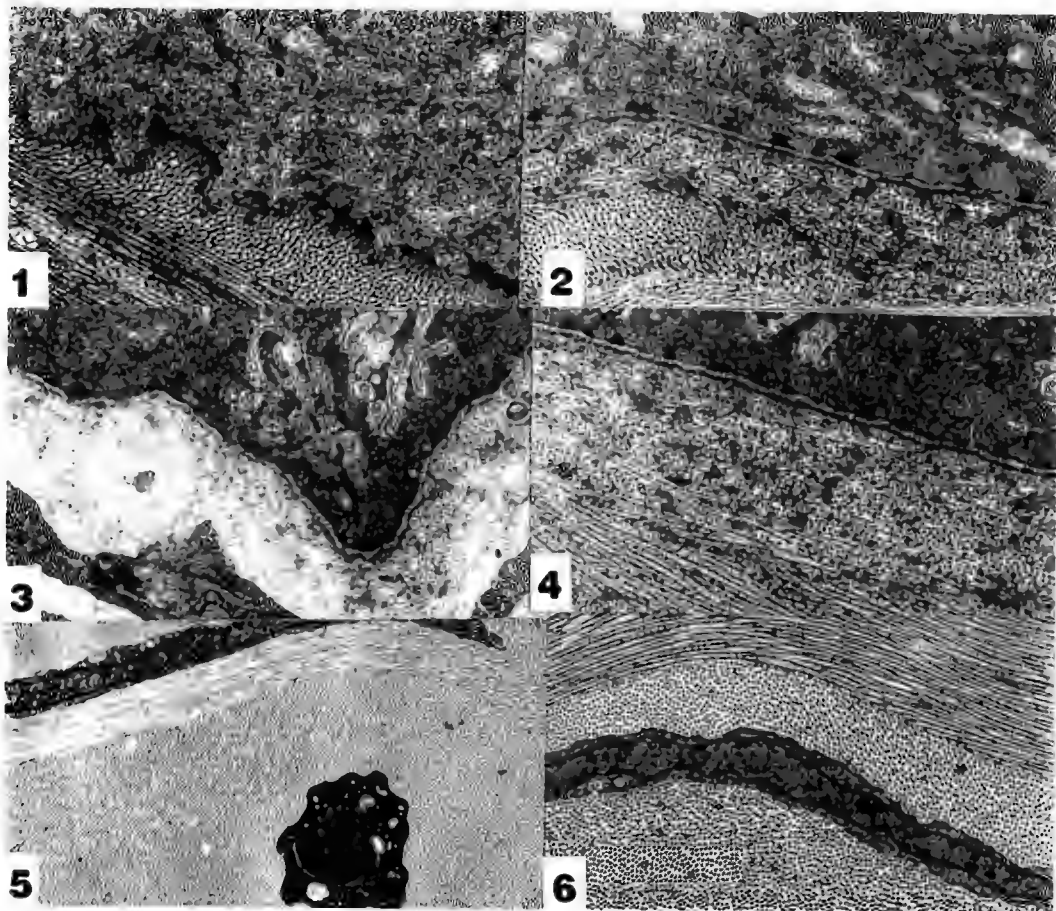
Figure 1: Two day, 160 μm laser ablated rabbit cornea epi-stromal wound area (mag. 14,727 X).
Figure 2: Two day, 80 μm laser ablated rabbit cornea epi-stromal wound area (mag. 14,727 X).
Figure 3: Two month, 160 μm laser ablated rabbit cornea epi-stromal wound area (mag. 14,727 X).
Figure 4: Two month, 80 μm laser ablated rabbit cornea epi-stromal wound area (mag. 14,727 X).
Figure 5: Polymorphonuclear cell in mid-stroma of two day 160 μm laser ablated cornea. Notice the normal keratocyte and arrayed collagen fibrils (mag. 6,700 X).
Figure 6: Representative keratocyte in mid-stromal area showing elongated body and nucleus (mag. 6,700 X).

11

ALTERED RENAL PROXIMAL TUBULE CELL ION HOMEOSTASIS DURING DIABETES

Craig C. Freudenrich,* Daniel Hockett,* Benjamin Kirk,* Kurt Gilliland,* Brian Scherer,* Kerri Winter,* Peter Ingram,** and Ann LeFurgey*

* Division of Physiology, Department of Cell Biology, Box 3709, Duke University Medical Center, Durham, NC 27710; ** Research Triangle Institute, Research Triangle Park, NC 27709

A major characteristic of human and experimental diabetes mellitus is enhanced urinary excretion of electrolytes (e.g. Na, K, Mg, Ca).[1,2,3] The increased urinary electrolyte excretion can lead to low serum electrolyte concentrations (e.g. hypomagnesemia, hyponatremia, hypocalcemia, hypokalemia), although this issue remains controversial. Ultimately, elevated urinary electrolyte excretion can result in mineral deficiencies which have important consequences such as retinopathies, convulsions, osteoporosis, arrhythmias, and sudden death ischemia. The increased urinary electrolyte excretion could be due to osmotic diuresis and/or altered renal tubule cell ion homeostasis; however, few studies have addressed whether diabetes alters specific tubule cell ion homeostasis. In this study, we used electron probe x-ray microanalysis (EPXMA) to obtain quantitative microchemical images of proximal tubule cells from diabetic rats so that we could define how subcellular ion homeostasis is altered during diabetes.

Adult male Sprague-Dawley rats were housed in individual metabolic cages and urine output was measured daily; peri-orbital plasma samples were collected every 3 days. Urine and plasma ion concentrations (Na, K, Ca, Mg) were assayed by atomic absorption spectroscopy, blood glucose was measured with a commercial glucometer, and urine glucose and ketones were detected with commercial strips. After 5 days, rats were injected with either streptozotocin (65 mg/kg, ip) to induce diabetes or citrate buffer (control); urine and plasma sampling continued as described above. After 14 days, kidneys of control and diabetic rats were cryopreserved *in situ* and processed for EPXMA imaging and individual organelle analysis as described previously.[4,5]

Streptozotocin-diabetic rats exhibited many characteristics of human diabetics such as weight loss, elevated blood glucose, increased urine output, glucosuria, and ketonuria (Table 1). Also, urinary electrolyte excretion was significantly elevated in diabetic rats, but plasma ion concentrations remained unchanged (Table 1); these data support previous findings with respect to urinary ion excretion.[1,2,3] Proximal tubule cells from streptozotocin-diabetic rats had several changes in intracellular ionic distributions: (1) Na content was significantly elevated in all subcellular compartments analyzed, while K content was significantly reduced only in mitochondria (Fig. 1A); (2) Ca content was increased significantly in cytoplasm, mitochondria, and lysosomes (Fig. 1B), while Cl content was significantly reduced in these compartments (Fig. 1C); (3) Mg was significantly elevated in mitochondria only (Fig. 1B); (4) S and P contents were significantly elevated in both cytoplasm and mitochondria (Fig. 1D). These results suggest that basic mechanisms for ion transport in renal tubule cells are changed during diabetes and are consistent with the hypothesis that glucose-stimulated increases in Na levels alter the distribution of other ions via putative Na-dependent co-transport and counter-transport mechanisms across proximal tubule plasma and organelle membranes.

1. S. G. Massry and M. S. Seelig, Clin. Nephrol. (1977) 7, 147.
2. A. B. Anwana and H. O. Garland, Acta Endocrinol (1990) 122, 479.
3. S. L. Carney et al., J. Lab. Clin. Med. (1979) 93, 950.
4. C. C. Freudenrich et al., Proc. Ann. EMSA Meeting (1992) 50, 742.
5. A. LeFurgey et al., J. Microscopy (1992) 165, 191.

TABLE 1. PLASMA AND URINE DATA FROM CONTROL AND DIABETIC RATS (DAY 14)

Parameter	Control			Diabetic		
	($n = 8$)			($n = 11$)		
Body Weight (g)	322	±	11	240	±	10*
Blood Glucose (mM)	6.1	±	0.3	20.2	±	3.8*
Urine:						
Output (ml/100g BW/24h)	6.0	±	0.9	62.7	±	5.2*
Excretion:						
Glucose (g/100g BW/24h)	Not Detected			1.1	±	0.1*
Ketones (mg/100g BW/24h)	Not Detected			43	±	12*
Ions (μmol/100 g BW/24 h)						
Na	1340	±	195	2126	±	220*
K	2188	±	246	3309	±	295*
Mg	31.5	±	9	248	±	35*
Ca	15.0	±	3.3	319	±	38*
Plasma Ions (mM)						
Na	135	±	3	122	±	9
K	4.7	±	0.4	4.1	±	0.5
Mg	0.62	±	0.03	0.65	±	0.05
Ca	2.3	±	0.2	2.3	±	0.1

Data are mean ±SE; * Significantly different from control ($p < 0.05$) as assessed by t-test.
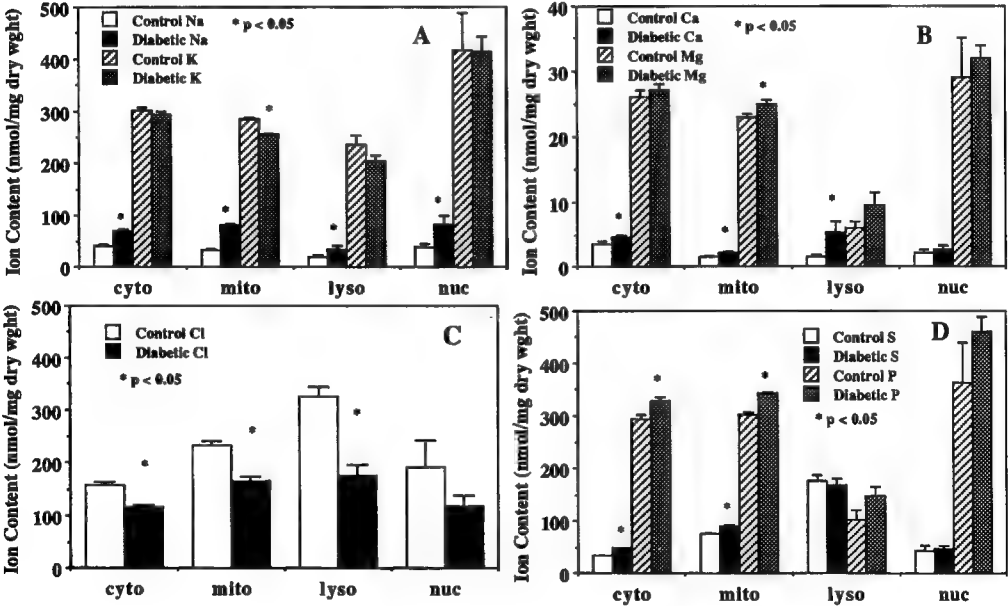
Figure 1. Subcellular ionic distributions in proximal tubule cells from control and streptozotocin-diabetic rats as measured by EPXMA imaging. Data are mean ± SE. The n numbers from controls (7 cells from 5 animals) for cytoplasm, mitochondria, lysosomes, and nucleus were 138, 142, 29, and 5, respectively. The corresponding n numbers for diabetics (12 cells from 9 animals) were 184, 228, 21, and 8, respectively. * significantly different ($p < 0.05$) from control as assessed by Games-Howell multiple comparisons test.

CHARACTERIZATION OF A HUMAN ENDOTHELIAL CELL LINE FROM A HEPATIC ANGIOSARCOMA

John M. Hoffpauir*, Marie L. Hoover**, Václav Větvička**, and Carlo H. Tamburro***

Departments of *Anatomical Sciences and Neurobiology, **Microbiology and Immunology,and ***Medicine, University of Louisville, Louisville, Kentucky, 40292

Angiosarcoma of the liver is extremely rare, but there is an increased incidence in Louisville, Kentucky due to worker exposure to gaseous vinyl chloride. The tumor is endothelial in origin as it possess factor VIII, a coagulation factor and known endothelial cell marker. The malignant cells have been described as pleomorphic malignant endothelial cells, malignant spherical and spindle cells or enlarged spindle-shaped endothelial cells. The lack of a cell line derived from a hepatic angiosarcoma has significantly limited studies of this rare lethal malignancy. This study describes the characterization of a human endothelial cell line from a liver biopsy of a hepatic angiosarcoma patient who had been previously exposed to gaseous vinyl chloride. This cell line denoted, HAEND, does not require growth factors such as endothelial cell growth factor for cultivation. Also, this line can be cultivated on untreated plastic surfaces and does not require gelatin or fibronectin coated surfaces. The cell line expresses factor VIII related antigen, an endothelial cell marker, as well as HLA class I molecules, tissue factor, and ICAM-1.

Scanning electronmicroscopy was performed on cells grown on 25 mm plastic tissue culture cover slides (Lab-Tek) were fixed for 1 hour in 3% glutaraldehyde, 0.1 M cacodylate buffer at room temperature. The cover slips were rinsed in 0.1 M cacodylate buffer and postfixed in 1% osmium tetroxide in 0.1 M cacodylate buffer. The samples were dehydrated in a graded ethanol series prior to critical point drying, coated with gold and examined with a Philips 501B scanning electron microscope. For transmission electron-microscopy and immunogold analysis, cells were grown in 6 well tissue culture plates to near confluency and fixed for 1 hour with 3% glutaraldehyde in 0.1 M cacodylate buffer at 4°C. Cells were rinsed in 0.1 M cacodylate buffer, postfixed in 1% osmium tetroxide in 0.1 M cacodylate buffer for 1 hour and dehydrated in a graded ethanol series then embedded in LX-112. *En face* sections were stained with uranyl acetate and lead citrate then photographed with a Philips CM-10 electron microscope.

This microvascular endothelial line displays a spindle-like configuration with overlapping cell borders in tissue culture. The cells have a large nucleus with a prominent nucleolus and by scanning electron-microscopy appear as flattened cells with numerous filapodia. Electron microscopy reveals that the angiosarcoma cell line, HAEND, possess similar morphology and structures as normal microvascular endothelial cells, HMVEC. The HAEND cells differ as they contain few if any Weibel-Palade bodies which are numerous in the HMVEC cells. The HAEND cells also possess numerous bundles of intermediate filaments and numerous endocytotic versicles. This cell line from a hepatic angiosarcoma due to gaseous vinyl chloride exposure should provide an opportunity to gain a better understanding of this rare malignancy.
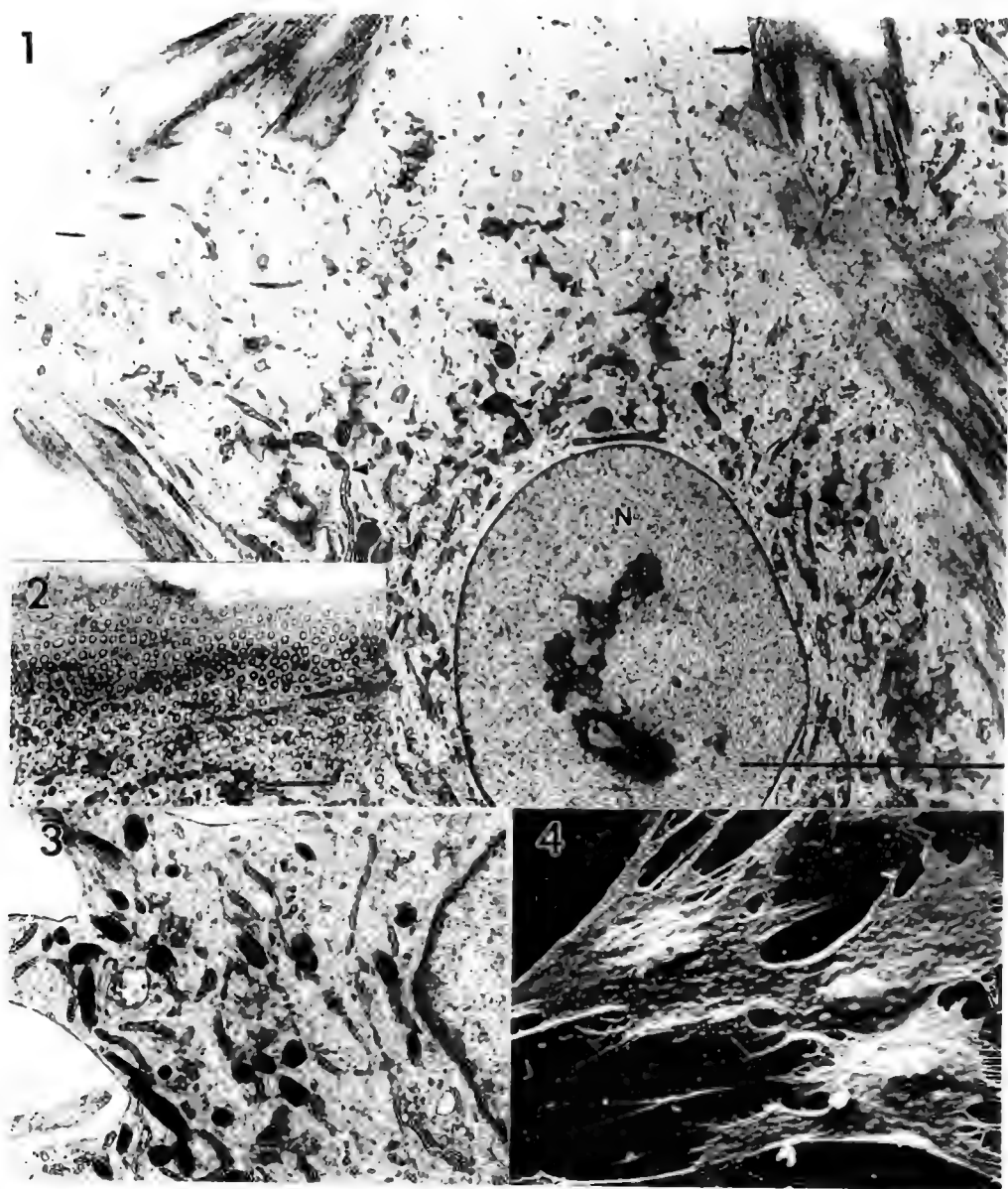
FIG 1.--TEM of malignant angiosarcoma cell, HAEND. Mitochondria (arrow heads), nucleus (N) and bundles of parallel intermediate filaments (arrows) were observed. Bar = 10 μm.

FIG 2.--Numerous endocytotic vesicles were observed. Bar = 0.5 μm.

FIG 3.--TEM of normal microvascular endothelial cell, HMVEC, with numerous Weibel-Palade bodies.

FIG 4.--SEM of malignant angiosarcoma, HAEND, exhibiting a loss of contact inhibition and numerous filapodia which contain extensive stress fibers.

15

ULTRASTRUCTURAL EFFECTS OF MANGANESE IN CULTURED HEART CELLS

Kerri Winter

Division of Physiology, Department of Cell Biology, Box 3709, Duke University Medical Center, Durham, NC 27710

Manganese (e.g. Mn^{2+}, Mn gluconate, Mn-DPDP) has been used as a contrast reagent for magnetic resonance imaging of liver and myocardial perfusion.[1,2] In addition, Mn has been used to block the voltage-dependent calcium channel,[3] interfere with excitation-contraction coupling,[4] and inhibit Na/Ca exchange.[5,6] Although Mn has proved useful in both clinical and research settings, little information is available about its effects on cell structure. Therefore, we examined the effects of Mn on ultrastructure in a model system of cultured embryonic chicken heart cells.

Free-floating cardiac myocyte aggregates were cultured from 11 day-old chick embryos.[7] Aggregates were incubated with a HEPES/TRIS-buffered salt solution containing various concentrations of $MnCl_2$ (0, 1, 20 mM) for 5 min at 37°C. Following incubation, buffer solution was removed, aggregates were chemically fixed in glutaraldehyde and processed for routine electron microscopic analysis.[7] Parallel studies on confluent myocytes were conducted to assess the Mn uptake by atomic absorption spectroscopy.

Intracellular Mn concentration was appreciably augmented from its undetectable physiological level to 16 and 49 nmol/mg protein after cells were exposed to 1 and 20 mM $MnCl_2$ solutions, respectively. Routine transmission electron microscopy revealed no evident morphological anomalies in cardiac myocytes at either Mn concentration (Fig. 1). Although minor swelling of mitochondria was noted within random myocytes, such changes were neither marked nor prevalent (Fig. 2). In contrast, fibroblasts displayed swollen mitochondria and dense-staining inclusions when exposed to 20 mM $MnCl_2$ (Fig. 1,3). These dense inclusions appear to resemble those described by Shelburne et al. in $MnCl_2$-treated macrophages.[8] However, static probe x-ray microanalysis failed to detect Mn in these dense regions, perhaps due to the chemical processing of cells prior to probing and/or the soluble nature of Mn. Severe damage of several fibroblasts was evident by dissipation of cell nucleoplasm and cytoplasm suggesting autophagocytosis. No ultrastructure changes are evident at Mn concentrations which effectively impair cardiac cell function; this raises questions as to structure-function relationships in Mn toxicity. Finally, the differential effects of Mn on heart cells and fibroblasts may be relevant to Mn toxicity in whole animals.[9]

1. S. W. Young et al., Magn. Res. Med. (1989) 10, 1.
2. S. Schaefer et al., J. Am. Coll. Cardiol. (1989) 14, 472.
3. S. Hagiwara and L. Byerly, Ann. Rev. Neurosci. (1981) 4, 69.
4. J. F. Delahayes, Circ. Res. (1975) 36, 713.
5. T. J. A. Allen, Biophys. Biochim. Acta (1990) 1030, 101.
6. R. Jacob et al., J. Physiol. (1987) 387, 567.
7. A. LeFurgey et al., Cell Calcium (1988) 9, 219.
8. J. D. Shelburne et al., SEM (1977) II, 137.
9. M. Aschner and J. L. Aschner, NeuroSci. Biobehav. Rev. (1991) 16,333.
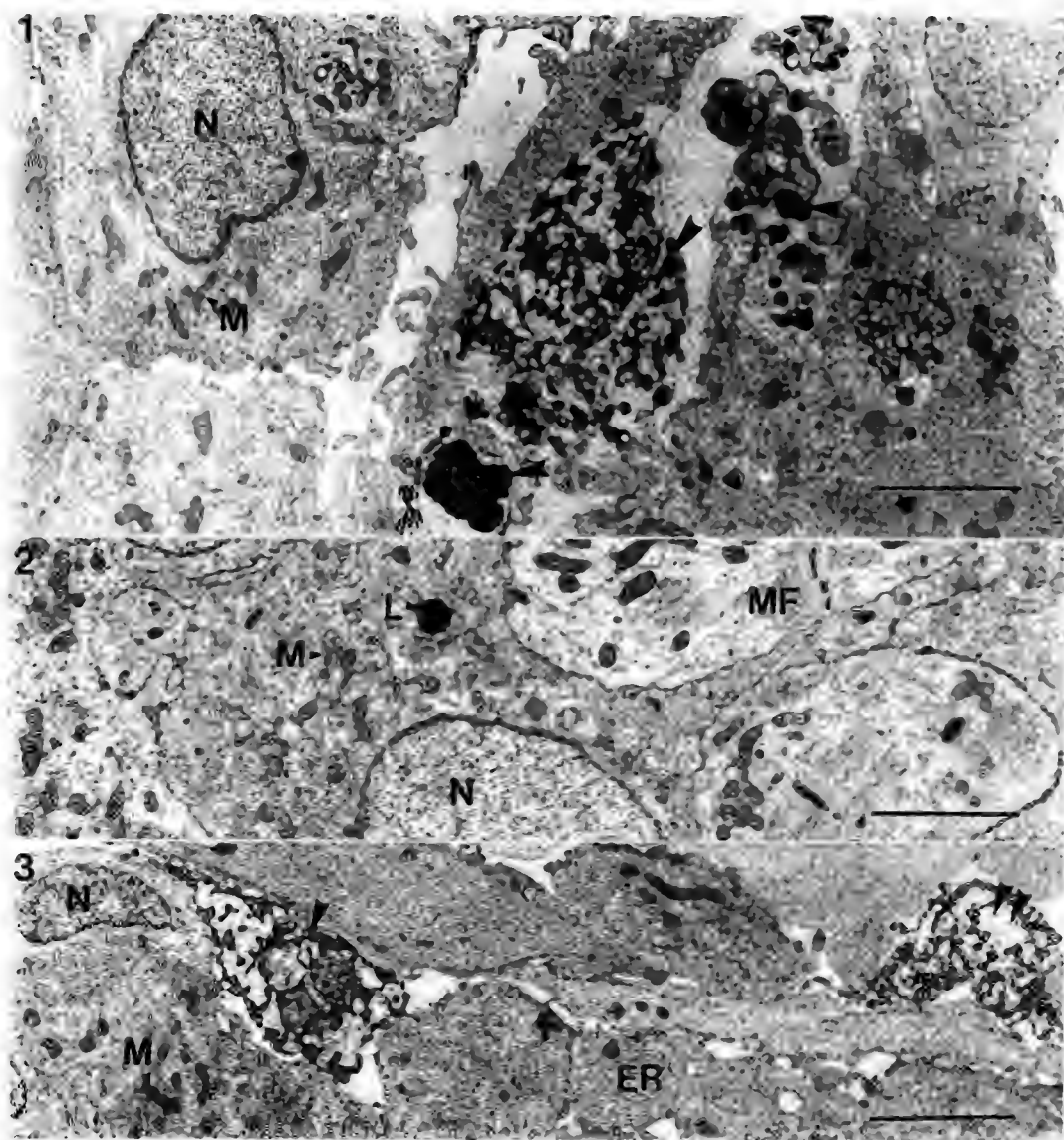
Fig. 1 -- Transmission electron micrograph (TEM) of cardiac myocyte (left) and damaged fibroblast (right). N = nucleus, M = mitochondria, arrows = dense inclusions, bar = 3 μm, 8280x.
Fig. 2 -- TEM of myocytes. L = lipofuscin granule, MF = myofibrils with visible Z-line. N, M, bar as indicated in Fig. 1. 9360x.
Fig. 3 -- TEM of fibroblasts. ER = rough endoplasmic reticulum, double arrows indicate degenerated cell. Single arrows, N, M, bar as indicated in Fig. 1. 9360x.

EFFECT OF BREFELDIN A (BFA) ON THE UNIQUE SURFACE COAT OF PULMONARY INTRAVASCULAR MACROPHAGES (PIMs) OF SHEEP: ULTRASTRUCTURAL AND CYTOCHEMICAL STUDY

Baljit Singh

Department of Biomedical Sciences, University of Guelph, Guelph, ON N1G 2W1 CANADA

The PIM of sheep, calf, goat and horse has a characteristic ultrastructural feature in the form of a unique, heparin sensitive, globular surface coat present around the plasma membrane with an intervening electron lucent space of 32-40 nm. We previously showed the active involvement of this surface coat in the phagocytosis of tracer material like monastral blue[1] and cationized ferritin[2]. The surface coat is capable of reconstitution *in vivo* following disruption with heparin[3]. The present study was aimed to investigate whether PIM is the source of surface coat or not. In the recent years the BFA has been extensively used to understand the secretory pathways in the cells because of its ability to cause a rapid and reversible block to the anterograde transport of proteins from the endoplasmic reticulum to the Golgi[4].

Sheep (n=6) were weighed, their plasma volume was calculated indirectly and based on which a sufficient single intravenous dose of BFA was given so as to reach a concentration of 4-5 microgram/ml of plasma. Sheep were euthenised at 10 min, 45 min and 120 min after the injection. Lungs were fixed intratracheally with 2.5% glutaraldehyde and 2% paraformaldehyde in 0.1M Na-cacodylate for 30 min. Lung tissue was processed for TEM including treatment with tannic acid and acid phosphatase cytochemistry.

In the control sheep the PIMs had globular surface coat and were attached to the pulmonary capillary endothelium. Ten min after the treatment most of the surface coat was internalized through an extensive network of endocytotic channels. There was slight accumulation of the secretory vesicles around a tubular Golgi in the perinuclear region indicating a block to the anterograde movement of proteins. However at 45 min, microtubules had become very prominent and most of the secretory vesicles, both coated and smooth were aligned with them. In majority of the specimens centrioles could be observed. Acid phosphatase reaction was present in some of the Golgi cisternae. After two hrs Golgi could be demonstrated cytochemically with some coated vesicles present in the vicinity. Some Golgi like structures could be seen in the proximity of the nucleus carrying globular material in their dilated ends. Acid phosphatase positive, big spherical structures were observed in the cytoplasm indicating break down of the internalized surface coat after the BFA treatment. Based on this data our tentative hypothesis is that the Golgi could be the central organelle in the metabolism (production or enzymatic break down) of surface coat. This would provide the PIM with its own lipids to produce vasoactive chemicals to modify the course of pulmonary pathology in the species having these cells.(Funded by NSERC Canada).

References
1. O.S. Atwal et al., Anat. Rec. 234 (1992) 223-239.
2. O.S. Atwal and K.J. Minhas., J. Anat. 181 (1992) 313-325.
3. B. Singh et al., FASEB J. 6 (1992) A1615.
4. R.D. Klausner et al., J. Cell Biol. 116 (1992) 1071-80.
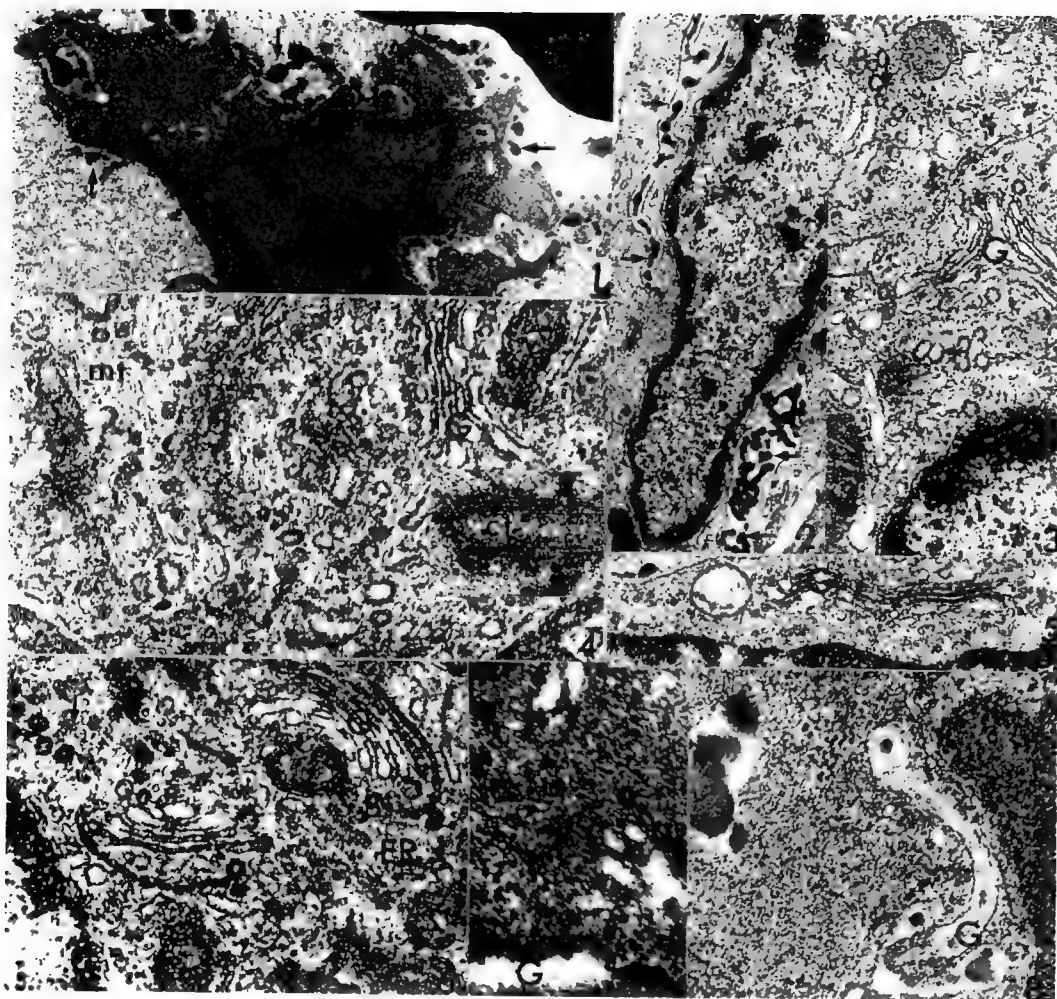
Fig. 1. A PIM from a control sheep with globular surface coat (arrows). Bar=0.62 micrometer

Fig. 2. Surface coat present in the endocytotic channels (arrows) within 10 min of BFA treatment. Bar=0.40 micrometer

Fig. 3. Slight accumulation of secretory vesicles (arrows) around tubular Golgi (G) after 10 min of BFA treatment. Bar=0.26 micrometer

Fig. 4. After 45 min of BFA injection prominent microtubules (mt) with coated and smooth vesicles around the Golgi (G). Inset a centriole. Bar=0.16 micrometer

Fig. 5. Acid phosphatase in the Golgi after 45 min of BFA treatment. Bar=0.26 micrometer

Fig. 6. A PIM at 120 min of BFA injection. Golgi (G), secretory vesicles (arrow), endoplasmic reticulum (ER). Bar=0.16 micrometer

Fig. 7. Acid phosphatase in the Golgi (G) after 120 min of BFA injection. Bar=0.16 micrometer

Fig. 8. Golgi (G) like structures having globules in their dilated ends. Bar=0.20 micrometer

FIXATION ARTIFACTS IN PERCUTANEOUS NEEDLE BIOPSIES OF LIVER

Januszewski, T.C., Harb, J.M., and Komorowski, R.A.

Department of Pathology, Medical College of Wisconsin, 8700 West
Wisconsin Ave., Milwaukee, WI 53226

Percutaneous needle biopsy is a standard procedure for obtaining liver
tissues for pathologic studies by light and electron microscopy.
Tissues obtained by this procedure usually measure 1mm to 1.5 mm in
diameter, and can be placed immediately at the bedside into a standard
glutaraldehyde fixative for processing by the electron microscopy
laboratory. Although the biopsy thickness is within the penetration
range of glutaraldehyde, we have noted a significant loss of
preservation in the center of most liver biopsies. The loss is
apparent at light and electron microscopic levels. The purpose of this
paper is to illustrate the artifact and to discuss the importance of
avoiding the artifact when selecting areas of the specimen for electron
microscopic studies.

Secimens studied were routine liver biopsies submitted to the electron
microscopy laboratory after an initial fixation of one hour in 2.5%
glutaraldehyde in O.1M cacodylate buffer. To illustrate the artifact,
one-micron thick sections of the entire block face were stained with
toluidine blue for light microscopic study (Figure 1). Biopsy
morphology was significantly different at the center versus the
periphery of the biopsy core. Central hepatocytes showed significant
shrinkage with loss of nuclear matrix and clumping of chromatin.
Hepatocyte shrinkage resulted in very prominent sinusoids in the center
of the biopsy core. Thin sections that included the area of the block
continuous from the outer edge through the center of the specimen were
cut on an ultramicrotome, mounted on 75x300 mesh grids and examined in
the electron microscope (EM). This allowed mapping of the specimen in
the EM and assured accurate correlation between sections taken from the
same block for light and electron microscopy.

Figure 2, from the outer surface of the block, shows well-preserved
nucleoplasm and mitochondrial matrix, lamellar endoplasmic
reticulum (ER), and microbodies. An area between the outer and center
areas is shown in Figure 3. Some of the nucleoplasm and mitochondrial
matrix has been lost, the ER is fragmented, and microbodies are
degranulated. Figure 4 is taken from the area most central in the
specimen. In this area the nuclei are condensed, most of the
mitochondrial matrix has been lost and the mitochondria are swollen,
and ER reticulum and microbodies are not recognizable.

This series shows that the degree of fixation varies significantly from
the outer surface to the center of the biopsy core, showing that it is
important to know where in the block the specimen is sampled for EM
studies. It is advisable to exclude sampling from the center of the
biopsy to avoid fixation artifacts which can lead to misinterpretation
of the morphology, and give a false impression of the underlying
disease process.
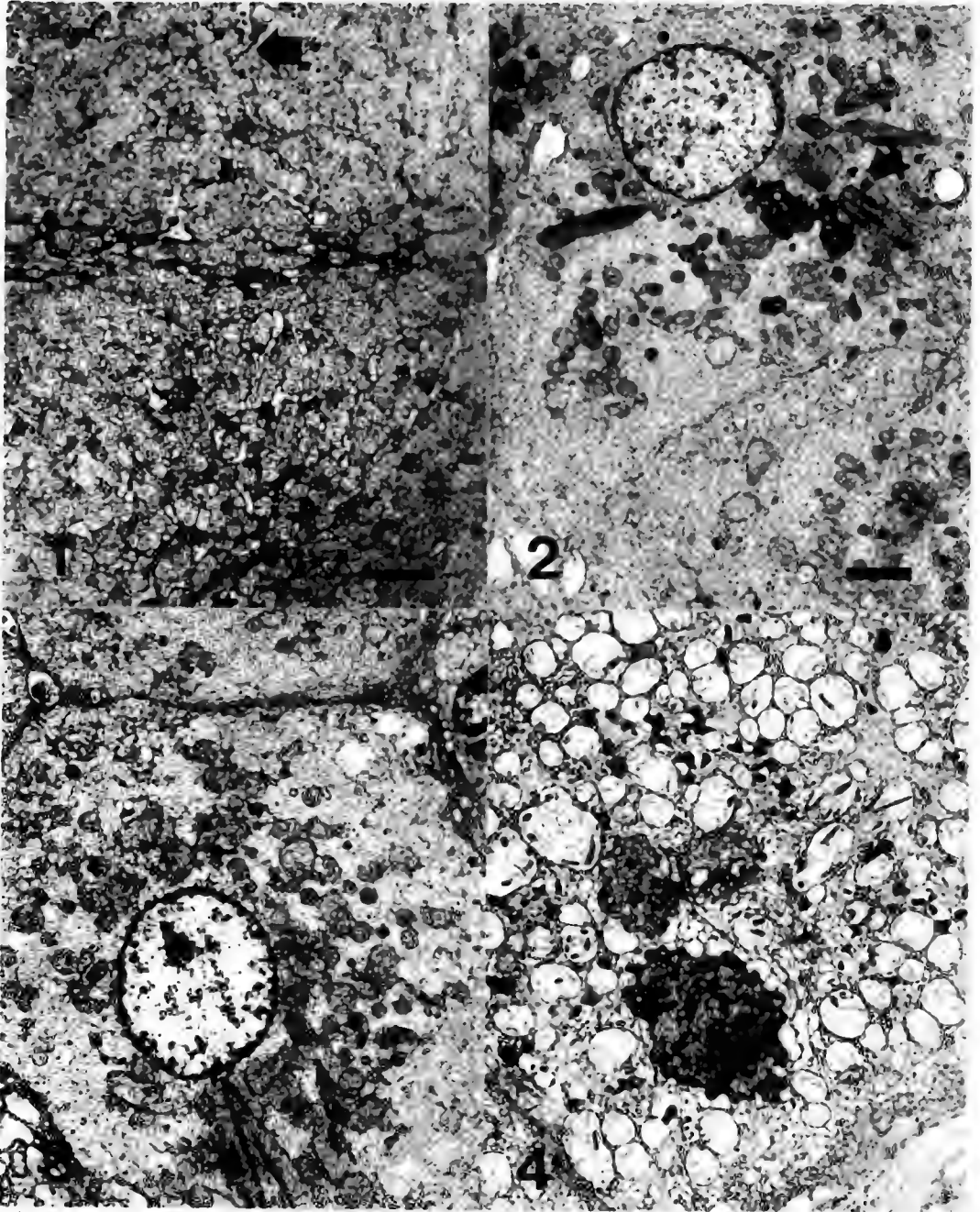
Figure 1. One-micron thick section of biopsy showing change in morphology from periphery (arrow) to core. X = 840. Bar = 10µm. Figures 2-4. X = 5,700, Bar = 2µm. 2. EM of periphery. 3. EM of transition area. 4. EM of core area.

21

ULTRASTRUCTURAL DIAGNOSIS OF A THYROTROPH CELL ADENOMA OF THE PITUITARY

Shirley Siew, Willys F. Mueller, Jr., Jonathan D. Fratkin

Michigan State University, East Lansing, MI 48824
Hurley Medical Center, One Hurley Plaza, Flint, MI 48503

Thyrotroph cell adenoma is an extremely rare neoplasm, comprising less than 1% of pituitary tumors.

We report a case of a 42 year old woman, who had presented first at the age of 33 with the chief complaint of blurred vision in the left half of her visual field. Examination showed the presence of bitemporal homonymous hemianopsia and optic atrophy in the left eye. CT scan, skull x-ray and tomograms showed expansion of the sella turcica with an intrasellar and suprasellar mass. Pancerebral angiogram showed vascular displacement secondary to an avascular sellar and suprasellar mass. There was also a history of secondary amenorrhoea. The follicle stimulating and luteinizing hormone levels were low. Thyroid function tests were within normal limits. A transsphenoidal radical excision of a pituitary adenoma was performed and the pathological diagnosis was a chromophobe adenoma. The patient was followed with periodic CT scans. The present admission followed the finding of a large recurrent pituitary adenoma with recurrence of loss of visual fields. The serum prolactin was normal, T_4 was low and TSH was normal.

A pituitary adenoma was removed. Histologic examination showed replacement of normal architecture by comparatively dense aggregates of polygonal cells with round to oval nuclei and abundant pale staining cytoplasm. No pleomorphism nor mitotic activity was noted. The tissue was interspersed with vascular fibrous septa. Transmission electron microscopy confirmed and presence of polygonal cells in close apposition. Occasional desmosomes were observed. There were some clusters of cells around small blood vessels (Fig. 1). Nuclear morphology varied from ovoid to bilobed with peripheral nucleoli. There was a fine dispersal of euchromatin with aggregates of heterochromatin, mostly on the nuclear membrane. Mitochondria were abundant in some of the cells. There was irregular vacuolation of the cytoplasm. This was quite prominent in some instances. Membrane bound electron dense granules measuring 140 nm were scattered throughout the cytoplasm but tended to be concentrated along the cell membrane (Fig. 2). However, there was no misplaced exocytosis. Endoplasmic reticulum was sparse. Cytoplasmic filaments and some fibrous bodies were present. The ultrastructural diagnosis of the granulated cells was that of thyrotrophs. Immunocytochemistry gave an abundant reaction product in cells labeled with antibody to TSH. Negative results were obtained in tests for prolactin, growth hormone and ACTH.

The post-operative course was uneventful except for a transient severe pain in her neck and numbness of her left upper extremity which cleared. The patient received radiotherapy on an outpatient basis and has continued to do well.
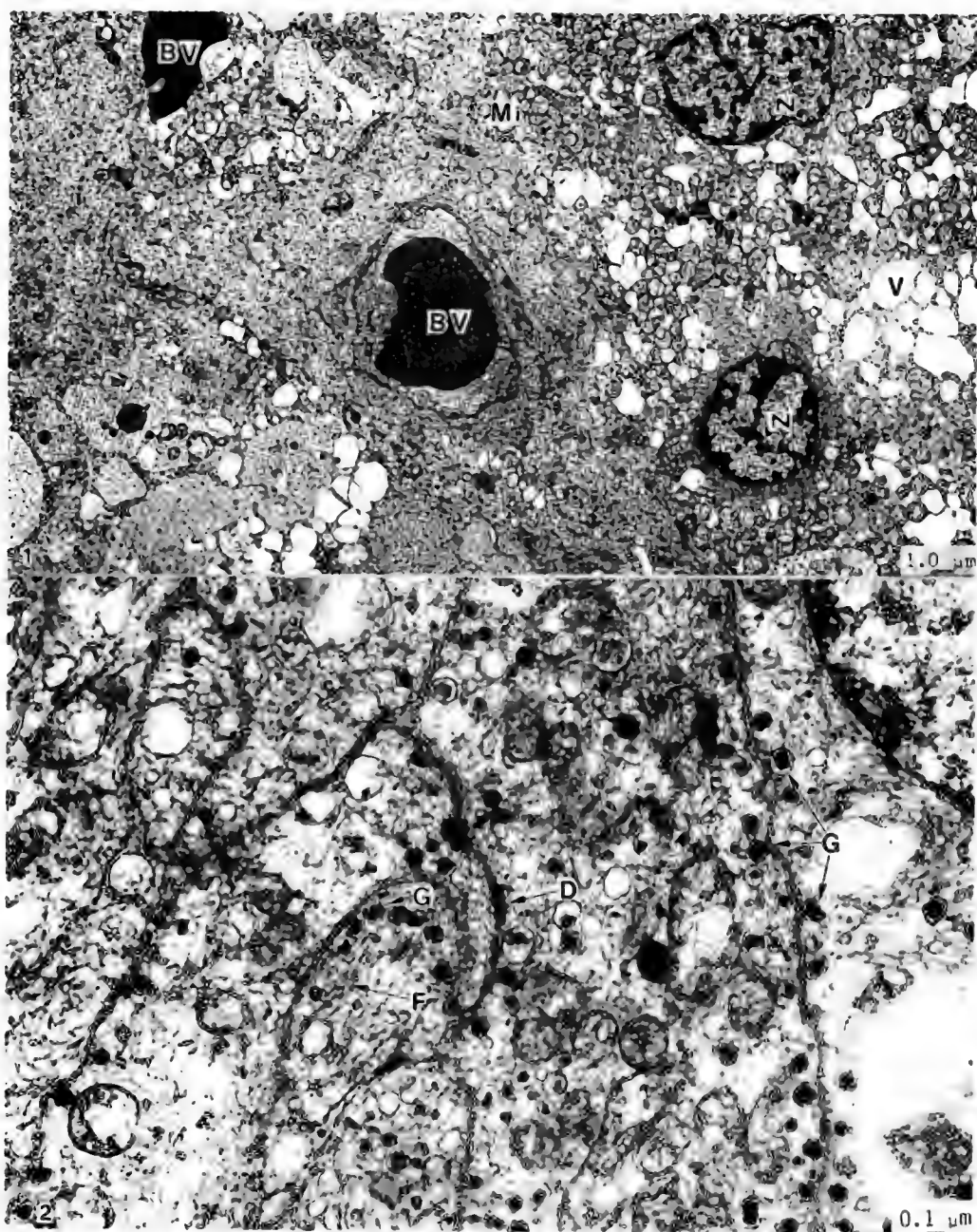
FIG. 1 -- Polygonal cells clustered around blood vessels (BV). N - Nucleus, Mi - Mitochondria, V - Vacuoles
FIG. 2 -- Closely apposed cells containing membrane bound electron dense granules (G). D - Desmosome, F - Cytoplasmic filaments.

23

ULTRASTRUCTURE AND IMMUNOCYTOCHEMISTRY OF INTERSTITIAL CELLS OF THE DEEP MUSCULAR PLEXUS IN THE CANINE SMALL INTESTINE

Shigeko Torihashi, William T. Gerthoffer and Kenton M. Sanders

Department of Physiology, University of Nevada School of Medicine, Reno, Nevada 89557-0046

In the canine small intestine one of the pacemaker regions that generates electrical activity is located in the deep muscular plexus. Within this region special cells, known as interstitial cells (IC-DMP), are distributed.[2] The ultrastructure and immuno-cytochemistry of IC-DMP were studied to clarify their identification and relationship to smooth muscle cells.

Segments of the ileum were perfused through mesenteric arteries with a physiological buffer solution (pH5.0) for 3 min followed by a fixative (2.5% glutaraldehyde, 1.25mM Ca Cl_2 and 3% sucrose in 0.05M cacodylate buffer; pH 7.4), postfixed in 1% OsO_4 and embedded in Epon 812 for transmission electron microscopy (TEM). For immunoelectron microscopy, segments were perfused with a fixative solution (0.25% glutaraldehyde, 4% paraformaldehyde, 0.2% picric acid, 0.1% Triton X-100 and 0.1M phosphate buffer pH7.4), dehydrated and embedded in glycol methacrylate (GMA).[5] Sections were stained with monoclonal antibody B4 to smooth muscle actin (ICN 1:200), anti-myosin light chain antibody[4] (1:25), anti desmin- antibody[3](1:200), and anti-vimentin antibody[3] (1:500) respectively. Immunoreactivities were detected by IgG gold (10nm, 6nm).

Interstitial cells of the deep muscular plexus (IC-DMP) were rich in mitochondria, dense bodies, caveolae, and gap junctions that formed connections with other IC-DMP and with smooth muscle cells of the outer circular muscle layer. IC-DMP were also closely associated with nerve fibers (Figs. 1,2). Several features of these cells were similar to nearby smooth muscle cells. IC-DMP were rich in myofilaments, such as primarily actin filaments, that were immunoreactive with anti-smooth muscle actin antibodies (Fig. 3). Myosin thick filaments were also identified and anti-myosin light chain antibodies labeled these filaments (Figs. 2,4). IC-DMP had also many bundles of intermediate filaments, but smooth muscle cells featured desmin immunoreactivity (Fig. 5), and IC-DMP had intermediate filaments that featured vimentin immunoreactivity (Fig. 6).

Although others have noted similarities between IC-DMP and smooth muscle cells[1,6], our study suggests that these cells may be more similar than previously recognized. We would conclude that IC-DMP are a specialized type of smooth muscle cell based on the identification of myosin thick filaments and a smooth muscle isoform of actin. Differences in intermediate filaments proteins are interesting and may be useful in distinguishing IC-DMP from smooth muscle cells. Gap junctions between smooth muscle cells and close association with nerve fibers are consistent with a role for IC-DMP as pacemakers and as mediators of neurotransmission. (Supported by DK 41315)

1. Daniel E.E. in Books F.P. and Evers P.W. eds., in Nerves and the Gut,NY: Slack (1977) 154
2. Hara Y. et al. J. Physiol. (1986) 372, 501.
3. Takehana K et al. Acta Anat.(1992)143, 294.
4. Torihashi et al. Am. J. Physiol. (submitted)
5. Uchida T. Jap. J. Oral Biol.(1985) 27, 132.
6. Yamamoto M. Arch. histol.Jap. (1977) 40,171.
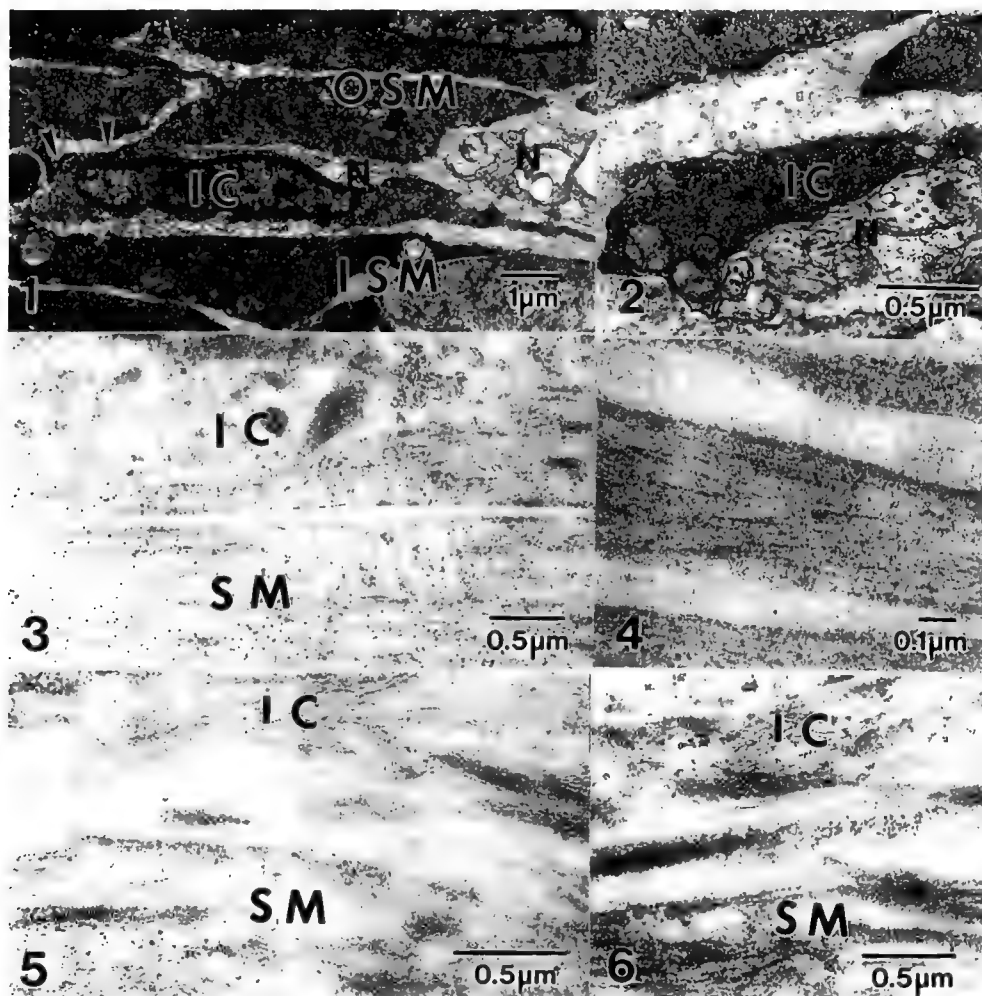
Fig. 1. - -TEM of IC-DMP (IC) located between the inner (ISM) and the outer (OSM) circular smooth muscle layer. IC-DMP is closely apposed to nerve fibers (N) and makes gap junctions (arrowheads) between outer circular smooth muscle cells.

Fig. 2. - -TEM of the cell process of IC-DMP (IC) located close to nerve fibers (N). IC-DMP is abundant in mitochondria, dense bodies and in myofilaments including both of thick filaments and thin filaments.

Fig. 3. - -Immunoelectron micrograph showing smooth muscle specific actin immunoreactivity. Both IC-DMP (IC) and smooth muscle cell (SM) have immunoreactivity.

Fig. 4. - -Immunoelectron micrograph showing myosin light chain immunoreactivity of IC-DMP. Gold particles are distributed around thick filaments.

Fig. 5. - -Immunoelectron micrograph showing desmin immunoreactivity. Smooth muscle (SM) is desmin immunopositive, however, intermediate filaments of IC-DMP (IC) are scarcely stained.

Fig. 6. - -Immunoelectron micrograph showing vimentin immunoreactivity. Intermediate filaments of IC-DMP (IC) are vimentin immunopositive. Smooth muscle (SM) has little immunoreactivity.

IDENTIFICATION OF CYTOPLASMIC TUBULAR STRUCTURES IN *PNEUMOCYSTIS CARINII*

Michael P. Goheen, Marilyn S. Bartlett and James W. Smith

Department of Pathology, Indiana University School of Medicine, Indianapolis, Indiana 46202

Pneumocystis carinii (PC) is an extracellular organism which frequently causes pneumonia in immunocompromised patients. In the United States more than 60% of patients with acquired immunodeficiency syndrome (AIDS) have at least one episode of PC pneumonia.[1] The earliest published ultrastructural study of PC was undertaken by Dickmann et al. in 1954.[2] A few articles which studied the ultrastructure of PC continued to appear in the German medical literature in the late 1950's and early 1960's. With the development of immunosuppressive chemotherapy for cancer patients and in later years the onslaught of the AIDS epidemic, the ultrastuctural literature concerned with PC has expanded. The internal morphology of PC has proved to be difficult to preserve and although extensively examined questions remain concerning the intracellular contents of PC. In this study we report the presence of cytoplasmic tubular structures (CTS) in PC. These structures have been identified in hepatocytes of Chimpanzees infected with non-A,non-B hepatitis and in the lymphocytes of humans with adult T-cell leukemia or AIDS.[3,4,5]

PC were obtained in vivo from the lungs of either transtracheally inoculated immunosupressed virus free mice or rats, or patients suspected of having AIDS. Additionaly, rat PC were obtained in vitro from spinner flask cultures. Specimens were fixed for 24 hours with Karnovsky's fixative, rinsed in buffer, postfixed with a mixture of potassium ferrocyanide and osmium tetroxide, dehydrated through a graded series of ethanol and embedded in Polybed 812 embedding media. Following sectioning, the specimens were stained with lead citrate and uranyl acetate and examined using a Philips CM 10 transmission electon microscope operated at 60 kV.

CTS were found in PC from all the aforementioned sources (Fig.1). The organelle seen in longitudinal section appeared tubular and was contained within the endoplasmic reticular system (Fig.2). The walls of the CTS most often appeared parallel and rigid. The diameter of the stuctures averaged 190 nm. The longest CTS measured 2.0 u. In cross section the CTS often demonstrated a circular pattern and sometimes appeared to arise from the nuclear envelope (Fig.3). The core region of the CTS was usually composed of cytoplasm which contained numerous glycogen particles (Fig.4).

The presence of CTS in hepatocytes of non-A, non-B infected chimpanzees is hypothesized to be associated with the active replication of the presumed viral agent. It has also been speculated that these structures are proliferations of the smooth endoplasmic reticulum in response to the NANB agent.[6] The presence of CTS in the lymphocytes of patients with Adult T-cell leukemia or AIDS further supports the hypothesis that a viral agent may somehow be responsible for the presence of CTS in mammalian cells. There is no known evidence linking a viral agent to PC itself. CTS may represent a specialization of the reticular system of PC, but their significance will require further study.

References

1. G. Lipschik & H. Mazur, Proj. Clin. Parasitol 2 (1990) 27.
2. H. Dickmann et al., Beitr. Path. Anat. 114 (1954) 48.
3. S. Watanabe et al., Hepatology 4 (1984) 628.
4. M. Shamoto et al., Cancer 47 (1981) 1804.
5. G. Sidhu et al., Lancet ii (1983) 990.
6. F. Bonino et al., Eur. J. Clin. Micro. & Infec. Dis. 7 (1988) 327.
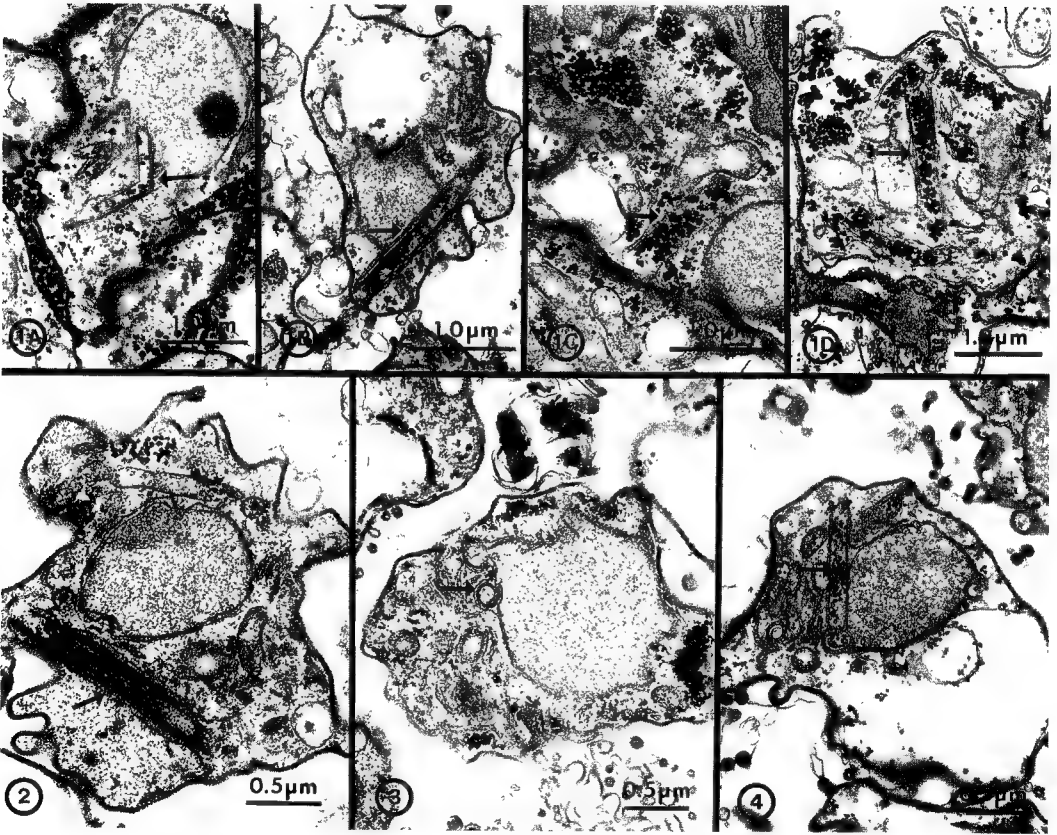
Figure 1. Trophozoites of PC illustrating the CTS (→). (A) Mouse; (B) Rat; (C) Rat,in vitro; (D) Human.
Figure 2. CTS (→) from PC trophozoite cut longitudinally. Organelle appears contained within the endoplasmic reticulum.
Figure 3. CTS (→) shown in cross section is closly associated with the nuclear envelope.
Figure 4. Central region of the CTS (→) often contains an abundant amount of glycogen.

27

ULTRASTRUCTURAL STUDIES OF THE DIGESTIVE SYSTEM OF THE LEAFHOPPER
EUSCELIDIUS VARIEGATUS INFECTED WITH BEV BACTERIA

W.W.K. Cheung
Biology Department, Chinese University of Hong Kong, Hong Kong

The leafhopper *Euscelidius variegatus* Kirshbaum transmits plant diseases
such as aster yellows and X-disease. It also harbours a BEV bacterium as
a result of congenital infection [1,2]. Since the bacterium can reduce the
fecundity of the insect it has the potential of being used as a
controlling agent for *E. variegatus*. Presently, little is known about
the cytopathology of the host infected with BEV. This study aims to
understand the damage done by the bacterium to the digestive system of
E. variegatus and the defense reaction of the host to the bacterium.

Digestive systems of BEV infected and non-infected adult females of *E.
variegatus* were dissected in buffered insect saline and fixed in 2.5%
glutaraldehyde in 0.1M sodium cacodylate (pH 7.2) for 1 hr. Tissues were
post-fixed in 1% osmium tetroxide (pH 7.2) and dehydrated in
alcohol/acetone series. These were blocked in Spurr resin and cut with
a Reichart ultrotome. Thin sections were stained with uranyl acetate and
lead citrate and were observed in a Zeiss EM 9S-2 electron microscope.

BEV infected digestive systems show dystrophy in gross morphology. Under
an electron microscope numerous bacteria were seen in midgut sections.
Principal cells of the conical segment were particularly vulnerable to
BEV invasion (Figs. 1,2). BEV bacteria were 4μ in length and 0.5μ in
width. An host cell nucleus show dispersion of chromatin materials and
the nuclear membrane was irregular in outline. The nucleolus, however,
was much enlarged. Numerous lysosomes for digestion of the invading
bacteria were found (Figs. 1,3). Sometimes when the bacteria could
overcome this lysosomal digestion, an entire host cell might be filled
with bacteria. The host cell might then drop off from the midgut
epithelium by an eruption process (Fig. 4). This could allow the
bacteria to be discharged through the egesta of the host and the healthy
cells to be less susceptible to BEV attack. By the above defence
mechanisms the host could apparently tolerate rather high numbers of BEV
in its body[3].

References
1. A.H. Purcell *et al.*, 1986, J. Invert. Pathol. 48:66-73.
2. A.H. Purcell & K.C. Suslow,1987, J. Invert. Pathol.50:285-290.
3. I thank Prof. A.H. Purcell, Entomology Department, University of
California, Berkeley, for providing me with insect specimens.

Fig. 1--LS of principal cells of midgut conical segment of leafhopper,
showing microvilli (mv), nucleus (n), lysosomes (ly) and BEV bacteria
(b). Bar=2μ.
Fig. 2--As above, showing BEV bacteria (b), mitochondria (m), lysosomes
(ly) and rough endoplasmic reticulum (rer). Bar=0.5μ.
Fig. 3--As above, showing BEV bacteria (b) and lysosomes (ly) containing
partially digested bacteria. Bar=0.5μ.
Fig. 4--As above, showing BEV bacteria (b) in a damaged cell with cell
ready to burst and release contents to gut the lumen. Bar=2μ.
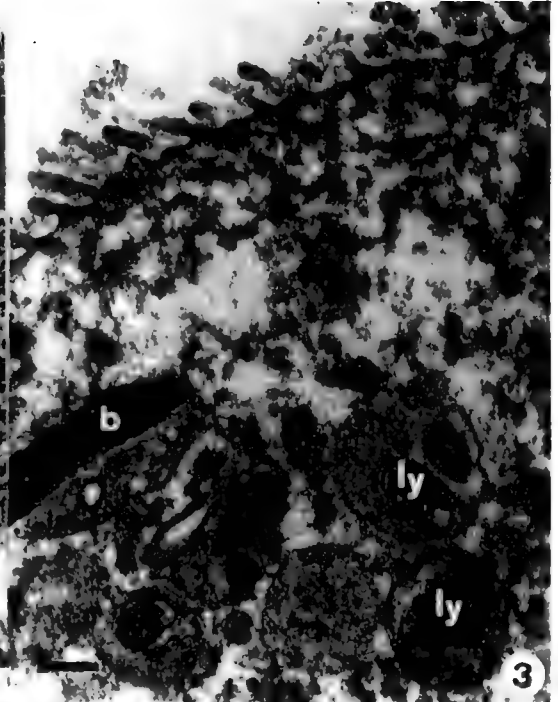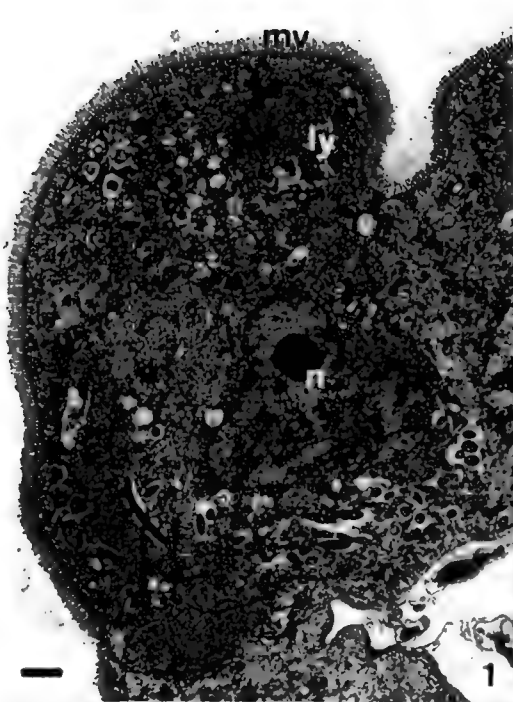
THE PRESENCE OF ACTIVE, MATURE GOBLET CELLS IN THE SMALL INTESTINE OF NEWBORN MINIATURE PIGLETS

László G. Kömüves

Microscopy Laboratory, USDA/ARS Children's Nutrition Research Center,
Department of Pediatrics, Baylor College of Medicine, Houston, Texas 77030-2600

Goblet cells in the intestine produce intestinal mucus, which acts as a protective barrier. Histochemical studies in 1-wk-old piglets have shown that goblet cells were fully mature, and contained both neutral and acidic mucopolysaccharides.[1] There is no information, however, about the secretory activity of goblet cells in newborn piglets. We present evidence that goblet cells in newborn, nonsuckled miniature piglets actively synthesize and secrete glycoproteins, as detected by wheat germ agglutinin-gold conjugates (WGA-Au$_{15}$) in LR White-embedded tissues.[4] Details of the surgical procedures, tissue collection, fixation and tissue processing have been reported.[2,3] Nonspecific binding of WGA-Au$_{15}$ to the sections was prevented by incubating the grids on drop of 10 mM Trizma buffer, pH=7.4, containing 0.1% Tween 20, and 500 mM NaCl, for 30 min. This buffer was used to dilute WGA-Au$_{15}$. The grids were then incubated with WGA-Au$_{15}$, for 60 min, followed by extensive washing. Inclusion of free WGA or 1 mM N-acetyl-glucosamine in the buffer abolished the labelling by WGA-Au$_{15}$. After the labeling, the sections were contrasted with 2% OsO$_4$, and lead citrate, and examined in a Philips CM12 electron microscope at 60 kV, using a LaB$_6$ filament.

Fully differentiated goblet cells were frequently found in the villous epithelium both in the jejunum and ileum in newborn, nonsuckled piglets. The goblet cells displayed a highly polarized ultrastructure, due to the vectorial secretion of glycoproteins (Fig.1).[5,6] The supranuclear area contained the Golgi apparatus beneath the mucous granules, which were densely packed in the apical part of the cell. Both the membranes on the *trans*-face of the Golgi apparatus and the granules were labelled with WGA-Au$_{15}$ (Figs. 1-3). In the Golgi apparatus the label was confined to the membranes (Fig. 2), whereas in the granules the secretory material was densely labeled (Figs. 2, 3). The mucous granules displayed some heterogeneity in labeling intensity, more intense labeling was seen in granules on the periphery than in those in the center (Fig. 1). The sequential exocytotic release of the secretory granules resulted in a cavitation of the apical cell surface. The formation of the mucin layer over the brush border was seen (Fig. 3).[5,6] This observation showed that in porcine neonates the goblet cells are fully differentiated, and they are capable of mucin secretion, providing a barrier over the small intestinal mucosa.[1,5,6] Further studies are needed to analyze the role of the intestinal mucin secretion in the uptake of maternal immunoglobulins from the colostrum.[2,3]

References

1. *B. R. Dunsford, W. E. Haensly & D. A. Knabe, Biol. Neonate (1990) 57, 194.*
2. *L. G. Kömüves & J. P. Heath, J. Histochem. Cytochem. (1992) 40, 1637.*
3. *L. G. Kömüves et al., Histochem. J. (1993) 25, 19.*
4. *J. Roth, J. Electron Microsc. Tech. (1991) 17, 121.*
5. *M. G. Oliver & R. D. Specian, Anat. Rec. (1991) 230, 513.*
6. *R. D. Specian & M. R. Neutra, J. Cell Biol. (1980) 85, 626.*
7. *Funded by USDA/ARS under Cooperative Agreement #58-6250-1-003.*
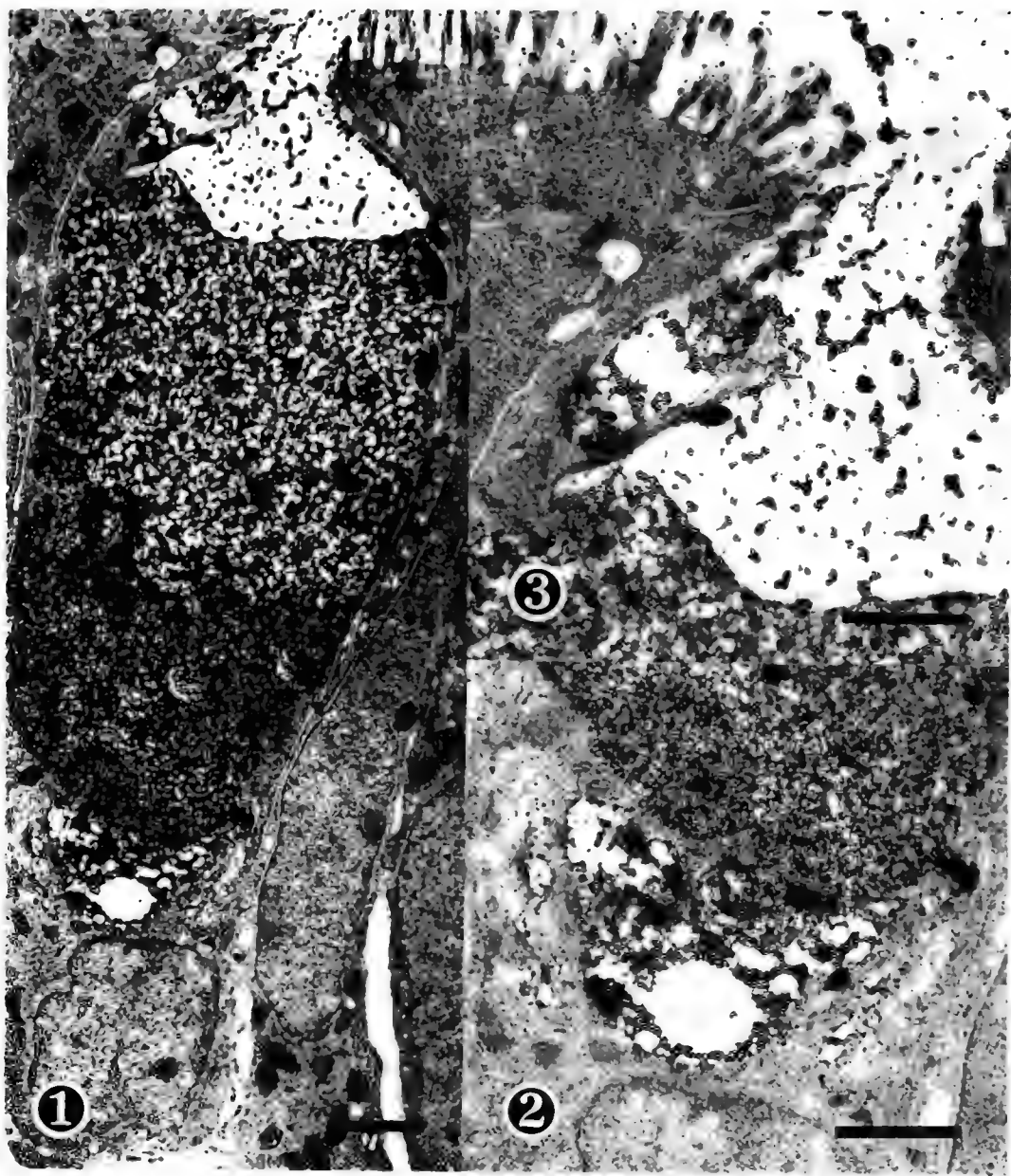
Figure 1. Goblet cell in jejunum of newborn, nonsuckled miniature piglet. Original magnification
         x12,700, bar= 1 μm.
Figure 2. Supranuclear area, including Golgi apparatus, of goblet cell in jejunum of newborn,
         nonsuckled miniature piglet. Original magnification x22,000, bar= 1 μm.
Figure 3. Apical area of goblet cell in jejunum of newborn, nonsuckled miniature piglet. Original
         magnification x22,000, bar= 1 μm.

AN IMPROVED METHOD FOR ULTRASTRUCTURAL EXAMINATION OF PARAFFIN-EMBEDDED TISSUES FOR DIAGNOSTIC PURPOSES

Tamara A. Howard, Donna N. Ziesmer*, Ardith L. Ries* and Michael J. Becich

Department of Pathology, Division of Cellular and Molecular Pathology, University of Pittsburgh School of Medicine; Diagnostic Electron Microscopy Laboratory*, University of Pittsburgh Medical Center, Pittsburgh, PA 15261

Small cell tumors, liver and skin biopsies for metabolic disorders, soft tissue tumors and kidney biopsies are the paraffin embedded tissues most frequently requested for ultrastructural examination. Preservation of cell membranes, glycogen, mucopolysaccharides, glycoproteins, glycolipids and other soluble components is problematic in these cases. Causes of cellular extraction when processing paraffin embedded tissue are:
- a) inadequate fixation of carbohydrates, mucopolysaccharides, glycoproteins and glycolipids
- b) extraction of lipids and cell membranes by polar solvents
- c) temperature effects
- d) extraction of sugars and glycoproteins due to pH and non-buffered, hypo-osmolar solutions.

A methodology which improves preservation is described below:

Enhanced deparaffinization technique *(and rationale for the modifications):*
1) Tissue samples are cut from paraffin blocks and deparaffinized in 2 changes of xylene at 4°C for 2-4 h *(low temperature decreases extraction in solvent)*.
2) The samples are then rehydrated through a decreasing series of acetone concentrations (5-10 min each) at 4°C to 2, 5-10 min changes of 0.1 M cacodylate buffer containing 14.4 mM sucrose and 3.5 mM $CaCl_2$, pH 7.8 *(less polar solvent -- acetone vs. ethanol -- should decrease lipid extraction thereby enhancing membrane preservation)*.
3) *Samples not containing glycogen* are fixed in 2.5% glutaraldehyde/2% paraformaldehyde in cacodylate buffer for 30 min at 4°C, followed by three cacodylate buffer rinses of 5 min each *(multiple fixatives enhance preservation of membranes, glycolipids and mucopolysaccharides)*.
4) Tissues are post-fixed for 1 h at 4°C in buffered 1% OsO_4, and rinsed in 3, 5 min changes of 10 mM maleate buffer containing 3.5% sucrose, pH 6.5 at 4°C.
5) *For enhanced glycogen preservation* in liver biopsies, metabolic disorders, renal/clear tumors and small cell tumors, osmium potassium ferrocyanide (OPF) alone is employed for 20 minutes at 4°C in the dark *(OPF is preferred and refixation with glutaraldehyde and paraformaldeyhde is not recommended)*.
6) *En bloc* staining is with 2% uranyl acetate containing 3.5% sucrose in maleate buffer, pH 5.0 for 2 h in the dark at 4°C *(buffered hyperosmolar solutions decrease carbohydrate extraction)*.
7) Dehydration takes place at 4°C, through a graded series of acetone changes (5-10 min each, *see #2 above*) to propylene oxide. Resin infiltration and polymerisation follow standard protocols.

The method results in improved preservation of cell membranes (Panel A), inclusion bodies, glycogen (Panel B), glycolipids, mucopolysaccharides, and other cellular components. The ability to preserve these cellular components with this technique has helped us to analyze a variety of samples from paraffin embedded tissues that would have otherwise been excluded from ultrastructural examination. This method has prevented the need for second biopsies in patients when fresh tissue for EM has not been requested by the clinician but would aid in diagnosis.
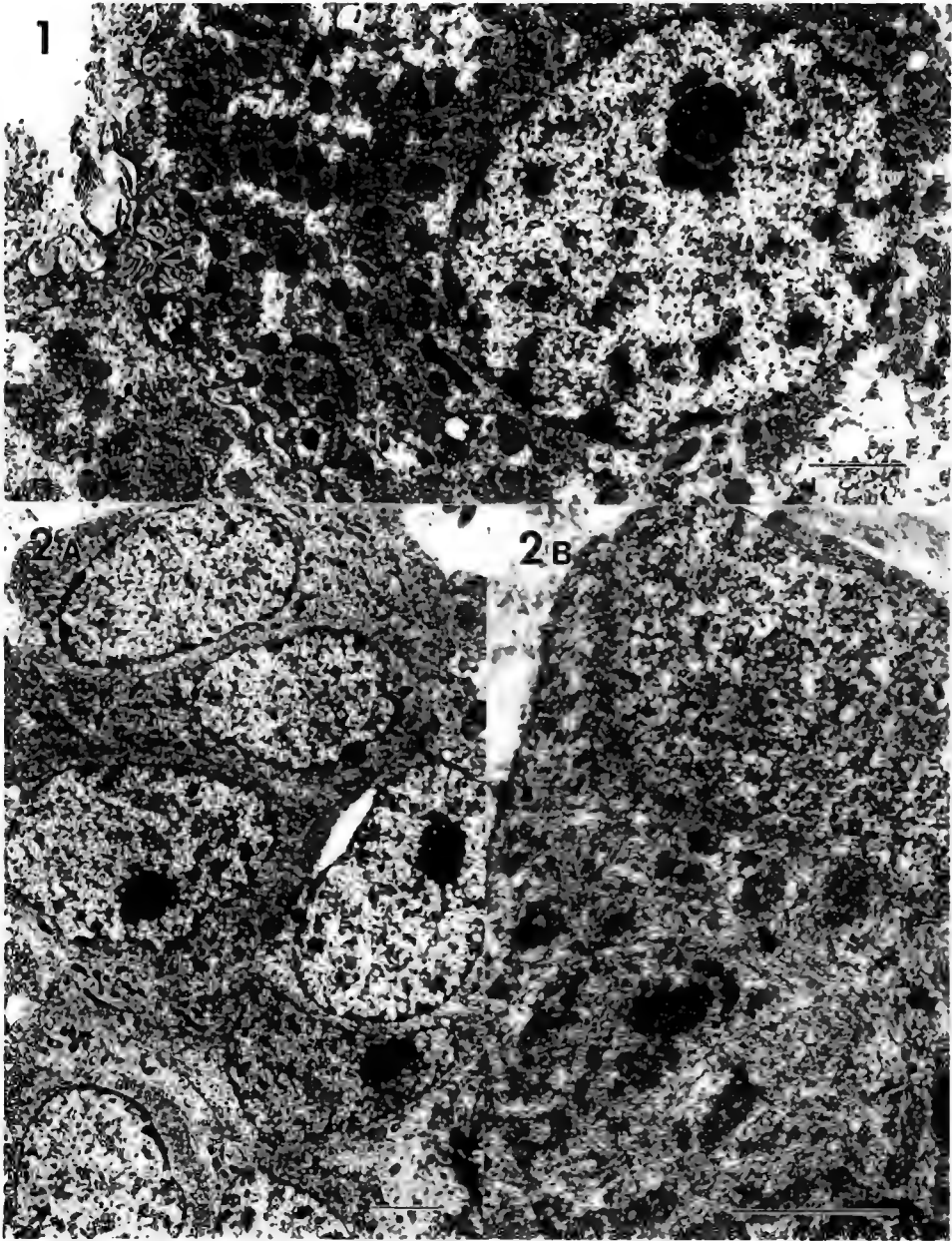
Figure 1: Hepatocyte showing increased membrane preservation in nuclear and cytoplasmic structures. Note bile canaliculus (arrow) and well-preserved cytoplasmic organelles (Enhanced technique for samples free of glycogen). Bar = 2μm

Figure 2: A & B: Small cell osteosarcoma showing preservation of glycogen (Enhanced technique for samples containing glycogen). A: Bar = 2μm; B: Bar = 1μm

DISTRUBUTION AND MODULATION OF ION CHANNEL AND RECEPTOR TOPOGRAPHY ON NERVE CELL SURFACES

Kimon J. Angelides and Barry Hicks

Department of Cell Biology, Baylor College of Medicine, Houston, TX 77030

The distribution of ion channels and receptors over the neuronal surface is important for the receipt of incoming synaptic inputs and for the integration of these inputs. Most voltage-gated and ligand-gated ion channels have non-homogeneous distributions in the neuronal membrane, many being restricted to either dendritic, axonal or somatic domains and further localized within these domains to regions such as dendritic spines, nodes of Ranvier or synaptic junctions (1-3). For example voltage-dependent calcium channels are localized and immobilized on dendrites (4), while voltage-dependent sodium channel are localized on axon hillocks (5) and nodes of Ranvier. Determining where and how ion channels are distributed and maintained is important for a variety of reasons. Ion channels in growth cones have a role in neurite outgrowth mechanisms (6), they are obligatory for synaptic transmission and they are required for amplification of neurotransmitter signals in the post synaptic membrane (7). Changes in ion channel distributions are an important aspect in development and plasticity (8,9). Finally, several neurological disorders including multiple sclerosis, are characterized by a change in ion channel distribution that is partially responsible for the clinical manifestations of the disease (10). A restricted distribution of ion channels can be initiated and maintained by a variety of mechanisms including interactions with components of the extracellular matrix (11,12), indirect or direct interactions with elements of the cytoskeleton (8,13), and by formation of tight junctions (14).

We have employed light microscopic fluorescence techniques to study ion channel and receptor distributions and dynamics. Fluorescence microscopy has extremely high sensitivity, the lower limit being the ability to detect a single fluorophore under the optimal conditions (15).

Specifically I will discuss at how neurons express, target, and segregate ion channels and receptors to specific domains on the neuronal cell surface during development, the implications of this organization for the integrative and network properties of neurons, and how modulation of their distribution during development leads to the generation of neuronal diversity and to the specification of synaptic connections in the developing brain.

Specifically, we have examined the cellular signals and elements, both intrinsic or via interactions with other neurons or with glial cells, that target and maintain calcium channels to dendrites, GABA receptors to cell somas and to specialized sites on dendrites, and that sequester sodium channels to nodes of Ranvier in myelinated nerve (9). One approach is charting the patterns of channel distribution by video microscopy in living neurons in culture and in brain slices with channel and receptor selective probes. Using such an approach, recently we have made good progress towards a long-standing question in neurobiology on how nodes of Ranvier develop in myelinated nerve. By following the dynamic distribution of labeled sodium channels on axons of living neurons in the presence of myelinating Schwann cells, videos and imaging demonstrate that the spatial segreation of sodium channels depends on specific signals transduced by Schwann cells (9).

The problem of targeting is somewhat more complicated because there are multiple genes encoding channel and receptor subtypes. For example, for the inhibiting GABA receptor while the expression of multiple genes may expand the neuron's ability to finely tune GABAergic responses, we have found a novel function for the multiple genes (16). By expressing cDNAs encoding defined subunit combinations we have found that sorting and localization of the $GABA_A$ receptor complex to specific domains is dependent upon the subunits which form the complex: depending on the subunit composition the complex can be routed to cell bodies or dendrites. Such a mechanism endows the

combinations may be regulated during differentiation and by the excitatory synaptic drive. This up and down-regulation of the expression of different subunits could be an important factor in determining the delicate balance between excitatory and inhibitory inputs in neuronal circuits. While sodium channels are targetted to axons and voltage-dependent calcium channels to dendrites, there are specific mechanisms which maintain this distribution. Biochemical and cell biological experiments have identified association of ankyrin with voltage dependent sodium channels an association which contributes to channel lateral immobilization (13). Supported by the NIH and the Multiple Sclerosis Society.

References

1.   Poo, M., and Young, S. (1985) *Ann. Rev. Neurosci.* 8, 369-406.
2.   Augustin, G. J., Charlton, M. P. and Smith, S. S. (1987) *Ann. Rev. Neurosci.* 10, 633-693.
3.   Black, J. A., Kocsis, J. D. and Waxman, S. G. (1990) *TINS* 13, 48-54.
4.   Jones, O.T., Kunze, D.L., and Angelides, K.J. (1989) *Science* 244:1189-1193.
5.   Angelides, K.J., Elmer, L.W., Loftus, D., and Elson, E.L. (1988) *J. Cell Biol.* 106:1911-1925.
6.   Saffell, J. L., Walsh, F. S. and Doherty, P. (1992) *J. Cell Biol.* 118, 663-669.
7.   Beam, K. G., J. H. and Campbell, J. T. (1985) *Nature* 313, 588-590.
8.   Stya, M. and Axelrod, D. A. (1983) *Proc. Natl. Acad. Sci.* U.S.A. 80, 449-453.
9.   Joe, E.-h. and Angelides, K. (1991) *Nature* 356, 333-335.
10.   Black, J. A., Felts, P., Smith, K. J., Kocsis, J. D. and Waxman, S. G. (1991) *Brain Res.* 544, 59-70.
11.   Koppel, D. E., Sheetz, M. P. and Schindler, M. (1981) Proc. Natl. Acad. Sci. U.S.A. 78, 3576-3580.
12.   McCloskey, M. and Poo, M. (1984) *Int. Rev. Cytol.* 87, 19-81.
13.   Srinivasan, Y., Elmer, L., Davis, J., Bennett, V., and Angelides, K. (1988) *Nature* 333, 177-180.
14.   Diamond, J. M., (1977) *Physiologist* 20, 10-18.
15.   Mathies, R. and Stryer, L. (1986) In Applications of fluorescence in the Biomedical sciences. (Taylor D. L., Waggoner, A., Murphy, R., Lanni, F. and Birdge, R., eds.), pp. 129-140.
16.   Velazquez, J.L. and Angelides, K.J. (1993) *Nature* 36:457-460.

APPLICATION OF HIGH-RESOLUTION FIELD-EMISSION LVSEM, BACKSCATTER IMAGING, IMMUNOGOLD STAINING TO DEFINITION OF THE SPATIAL DISTRIBUTIONS OF TWO HUMAN NEUTROPHIL ADHERENCE RECEPTORS, L-SELECTIN (LECAM-1) AND THE ß$_2$ INTEGRIN, Mac-1 (CD11b/CD18)

Robert D. Nelson, Sharon R. Hasslen, and Stanley L. Erlandsen

Departments of Dermatology, Laboratory Medicine and Pathology, and Cell Biology and Neuroanatomy, University of Minnesota School of Medicine, Minneapolis, MN 55455

Receptors are commonly defined in terms of number per cell, affinity for ligand, chemical structure, mode of attachment to the cell surface, and mechanism of signal transduction. We propose to show that knowledge of spatial distribution of receptors on the cell surface can provide additional clues to their function and components of functional control.

L-selectin and Mac-1 denote two receptor populations on the neutrophil surface that mediate neutrophil-endothelial cell adherence interactions and provide for targeting of neutrophil recruitment to sites of inflammation. We have studied the spatial distributions of these receptors using LVSEM and backscatter imaging of isolated human neutrophils stained with mouse anti-receptor (primary) antibody and goat anti-mouse (secondary) antibody conjugated to 12 nm colloidal gold.[1,2,7] This combination of techniques provides for three-dimensional analysis of the expression of these receptors on different surface membrane domains of the neutrophil: the ruffles and microvilli that project from the cell surface, and the cell body between these projecting structures.

When isolated, unstimulated neutrophils were stained for L-selectin, we noted that the gold particles appeared primarily as clusters on the tips of ruffles and microvilli. When the cells were stained for Mac-1, we saw that the gold particles occurred singly or in small clusters on the cell body. Viewing these photos as stereopairs confirmed that L-selectin and Mac-1 adherence receptors are restricted to these different domains of the cell membrane. Considering the proposed sequential roles of these receptors in neutrophil recruitment,[3,4,6,8-10] we find a clear correlation between receptor distribution and function. Further, new questions arise about mechanisms controlling receptor function.

L-selectin at the tips of surface projections appears optimally placed to mediate rolling and initial stopping of neutrophil on surface of the post-capillary venule; Mac-1 appears initially out of position to engage ligands on the venular surface. Next, neutrophil activation by locally accumulating stimuli increases the strength of L-selectin-mediated adherence and activates the binding function of Mac-1. Subsequently, L-selectin is shed and Mac-1 mediates the adherence contacts essential for cell migration through the vessel wall and into extravascular tissues. [5] The latter phenomena lead to questions regarding the role of capping in L-selectin function and shedding, and the nature of the event that brings Mac-1 into contact with the venular surface. We speculate that stimulated swelling of the cell resolves the membrane ruffles and microvilli to facilitate capping and shedding of L-selectin, and bring Mac-1 into contact with the endothelial cell surface.

Other applications of these techniques include direct identification of the receptor-ligand pairs involved in such cell-cell interactions, and the structural components of receptors and membranes that direct different receptors to different surface membrane domains.

36

1. E. de Harven, EMSA Bull. (1992)22, 45.
2. S.L. Erlandsen, W.J. Bemrick, D.E. Schupp, J.M. Shields, E.L. Jarroll, J.F. Sauch and J.B. Pawley, J. Histochem. Cytochem. (1990)38, 625.
3. M.A. Jutila, E.L. Berg, T.K. Kishimoto, L.J. Picker, R.F. Bargatze, D.K. Bishop, C.G. Oroz, N.W. Uw and E.C. Butcher, Transplantation (1989)48, 427.
4. T.K. Kishimoto, J. NIH Res. (1991)3, 75.
5. T.K. Kishimoto, M.A. Jutila, E.L. Berg and E.C. Burcher, Science (1989)245, 1238.
6. K. Ley, P. Gaehtgens, M.S. Fennie, M.S. Singer, L.A. Lasky and S.D. Rosen, Blood (1991)77, 2553.
7. J.B. Pawley and S.L. Erlandsen, (in) The Science of Biological Specimen Preparation for Microscopy and Microanalysis, R.M. Albrecht and R.M. Orenberg, eds., Chicago. (1989), 163.
8. L.J. Picker, R.A. Warnock, A.R. Burns, C.M. Coerschuk, E.L. Berg and E.C. Butcher, Cell (1991)66, 921.
9. U.H. von Adrian, J.D. Chambers, L.M. McEvoy, R.F. Bargatze, K.E. Arfors and E.C. Butcher, Proc. Natl. Acad. Sci. USA (1991)88, 7538.
10. Supported in part by NIH grant AI-22374 and the Minnesota Medical Foundation.
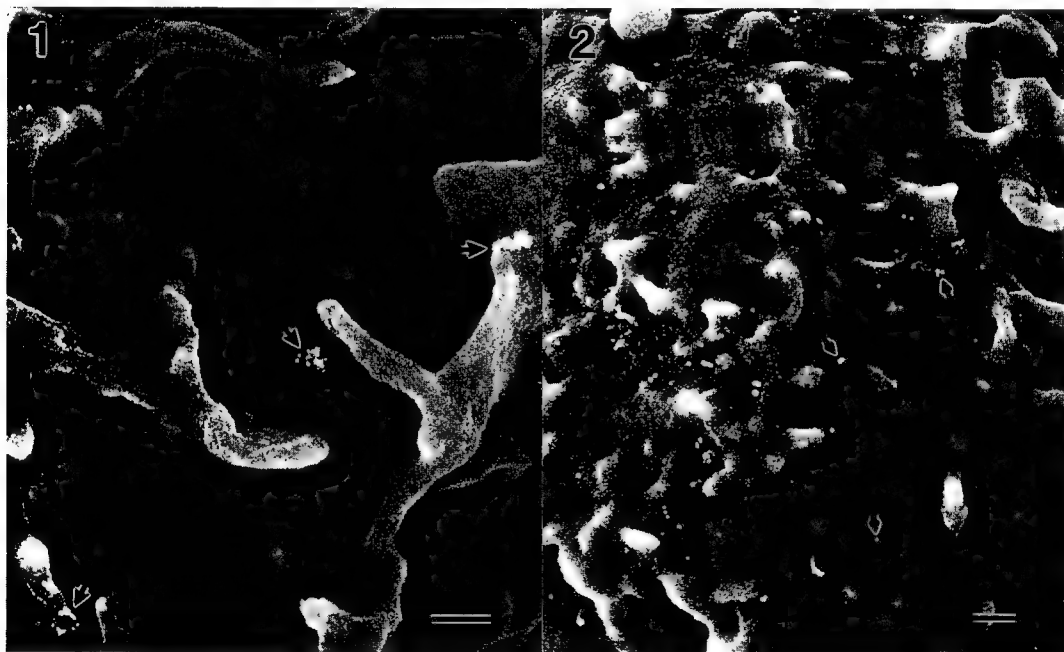
FIG. 1.--LVSEM backscatter electron image demonstrating the distribution of immunogold stained L-selectin on unstimulated human neutrophils. Note the clusters of gold particles on the tips of ruffles and microvilli (arrowheads). Bar, 200nm.

FIG. 2.--LVSEM backscatter electron image demonstrating the distribution of immunogold stained β_2-integrin on unstimulated human neutrophils. Note the single and clustered gold particles seen on the cell body but only rarely on cell surface projections (arrowheads). Bar, 200nm.

ROLE OF THE EXOSPORIAL MEMBRANE IN ATTACHMENT AND GERMINATION OF C. SPOROGENES

B.J.Panessa-Warren,*G.T.Tortora and**J.B.Warren

Dept. of Allied Health Resources,Health Sciences Ctr, State University of New York, Stony Brook,N.Y.11794,* Dept. of Medical Technology, SUNY and the Clinical Microbiology Laboratory at University Hospital, Stony Brook, N.Y.,** Division of Instrumentation,Brookhaven National Laboratory, Upton, N.Y. 11973

Some bacteria are capable of forming highly resistant spores when environmental conditions are not adequate for growth. Depending on the genus and species of the bacterium, these endospores are resistant in varying degrees to heat, cold, pressure, enzymatic degradation, ionizing radiation, chemical sterilants,physical trauma and organic solvents.[1] The genus Clostridium, responsible for botulism poisoning, tetanus, gas gangrene and diarrhea in man, produces endospores which are highly resistant. Although some sporocides can kill Clostridial spores, the spores require extended contact with a sporocidal agent to achieve spore death. In most clinical situations, this extended period of treatment is not possible nor practical. This investigation examines Clostridium sporogenes endospores by light, transmission and scanning electron microscopy under various dormant and growth conditions, cataloging each stage in the germination and outgrowth process, and analyzing the role played by the exosporial membrane in the attachment and germination of the spore. The exosporial membrane, which was formerly believed to have no known function [2], is shown here to clearly play a primary role in spore attachment and the germination process. Therefore to understand how to erradicate this spore to prevent disease, it is necessary to understand how the structures and components of the endospore function to achieve maximal attachment and growth, and resist sporocidal attack.

Methods: C. sporogenes ATCC 3584 were grown in cooked meat media and sporulation was monitored by light microscopy using a malachite green-safranin stain. After maximal sporulation, the spores were harvested in deionized water and heated to 80°C for 20 min to kill remaining vegetative cells. The spores were then washed (3X) and stored at 2-8°C until needed.

For SEM examination, spores were either grown anerobically on trypticase soy agar with 0.5% glucose, or aliquots of the stored stock solution were resuspended in distilled water and gently centrifuged to form a loose pellet. For spores growing on agar, stained smears were made for light microscopy at timed intervals to determine the germination sequence. Resuspended spores treated with EDTA, colchicine or cytochalasin B were placed on a specimen stub and fixed in an equal volume of 3% glutaraldehyde for 30 min. For spores grown on agar, a cleaned specimen stub was touched to the agar surface and fixed in 3% glutaraldehyde for 30 min, after which the stub was placed in a glass vial filled with fresh, cold 3% glutaraldehyde and stored for 5 hrs in the cold. All SEM samples were dehydrated in acetone, dried by the critical point method, sputter coated with 5-15nm AuPd and examined at 15 KV in an AMRay 1000A SEM with a LaB6 gun. Transmission electron microscopy was done on pelleted spores encased in warm agar and fixed in 3% glutaraldehyde in 0.1M cacodylate buffer (pH 7.2), post fixed in 1% aqueous osmium tetroxide (1hr), dehydrated in acetone, embedded in Epon 812,thin sectioned and examined on a Philips 300 TEM at 80KV. Spores were fixed in 1.5% glutaraldehyde in 0.05M cacodylate buffer with 2% or 4% tannic acid, and prepared as previously stated. Thin sections were examined unstained or stained with uranyl acetate-lead citrate.

Results: The endospores were angular and small   (0.5-0.7um diam) following sporulation, and when maximally dehydrated. In the presence of water the dehydrated spore became somewhat larger and had a smooth exosporial membrane.

Once germination had begun, the spores elongated, developing a tail and apical region and the exosporial membrane began to form small (25nm high X 50-60nm diam.) membranous projections. These projections elongated in the presence of calcium to form firm attachments to the substrate as well as attachments to other spores. The tail region of the spore further developed and formed a stalk which anchored firmly to the substrate.   At this time the exosporial projections detached from the substrate and regressed to short rounded bumps on the membrane. Following stalk formation, an opening of the exosporial membrane in the tail region permitted the newly formed vegetative cell to exit the endospore(see diagram below).

References

1. C. Philips, Bacteriol. Reviews 16(1952):135-138.
2. B.Davis, Bacterial Architecture, in <u>Microbiology</u>, B.Davis, R. Dulbecco, H.Eisen, and H.Ginsberg,New Yok: J.B.Lippincott Co.(1990)46.
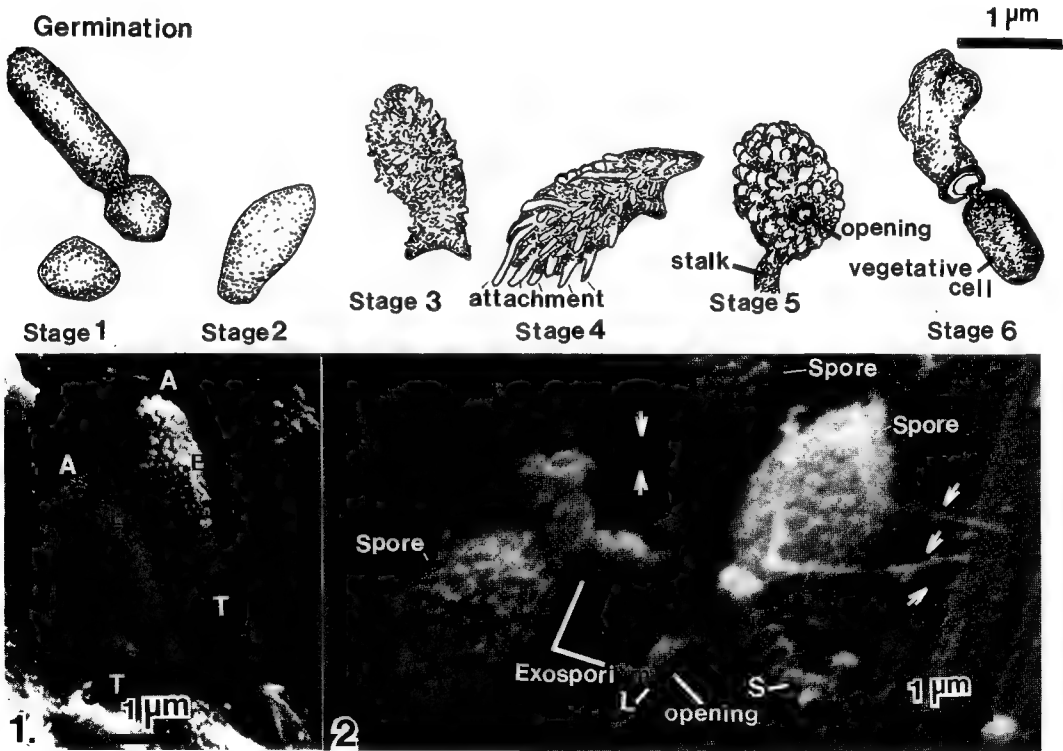
Fig.1. Endospores (E) showing apical (A) and tail (T)polarity as well as exosporial membrane projections (white bumps covering the surface of the spores).
Fig. 2. Endospore showing attachment to the aluminum substrate (white arrow), and the formation of the tail stalk (S). The opening and lip (L) of an empty exosporium following outgrowth of the vegetative cell.

FATE OF SPERM MEMBRANE IN FERTILIZED OVA

Frank J. Longo

Department of Anatomy, University of Iowa, Iowa City, IA 52242

Measurement of the egg's electrical activity, the fertilization potential or the activation current (in voltage clamped eggs), provides a means of detecting the earliest perceivable response of the egg to the fertilizing sperm. By using the electrical physiological record as a "real time" indicator of the instant of electrical continuity between the gametes, eggs can be inseminated with sperm at lower, more physiological densities, thereby assuring that only one sperm interacts with the egg. Integrating techniques of intracellular electrophysiological recording, video-imaging, and electron microscopy, we are able to identify the fertilizing sperm precisely and correlate the status of gamete organelles with the first indication (fertilization potential/activation current) of the egg's response to the attached sperm. Hence, this integrated system provides improved temporal and spatial resolution of morphological changes at the site of gamete interaction, under a variety of experimental conditions. Using these integrated techniques, we have investigated when sperm-egg plasma membrane fusion occurs in sea urchins with respect to the onset of the egg's change in electrical activity.[1,2] In specimens observed within 5 sec of the change in conductance, the sperm acrosomal process projected through the vitelline layer and abutted the egg plasma membrane (Fig. 1). Bindin surrounded the acrosomal process and connected the sperm to the egg vitelline layer; little of this material, however, was apparent along the region where the gamete plasma membranes were juxtaposed. In specimens fixed within 4 sec following the change in conductance, the area of contact between the gamete plasma membranes possessed a trilaminar structure that separated the egg's and sperm's cytoplasms. The morphology of this area of contact was consistent with previously proposed intermediates of membrane fusion.[3] Five to six sec after the change in conductance, gamete membrane fusion was completed and the sperm was connected to the egg via a narrow cytoplasmic bridge that consisted of the former acrosomal process and a projection of the egg cortex, the fertilization cone. The contents of the sperm moved through the developing fertilization cone and came to rest within the egg cortex. During early stages of sperm incorporation, the fertilization cone was relatively small; gradually it enlarged through the accumulation of cytoplasm rich in actin microfilaments, and in some cases became an extremely large projection of the egg cortex, measuring 25 μm (l) x 10 μm (d). Following sperm incorporation, the fertilization cone gradually regressed and was reabsorbed.

As a consequence of their fusion at the site of gamete contact, the egg and sperm plasma membranes become continuous with one another. Through the use of probes that bind charged groups (e.g., cationized ferritin), lectins and antibodies specific to egg or sperm plasma membrane proteins, we have shown that there is a rapid intermixing of sperm and egg plasma membrane components following gamete membrane fusion.[4-6] Utilizing antibodies recognizing 30 and 33 kDa proteins that are specific to the sperm plasma membrane, incorporation and intermixing of these proteins with egg plasma membrane components have been examined (Fig. 2). Results of such studies have established that the diffusion of sperm-specific plasma membrane proteins within the egg plasma membrane is comparable to protein diffusion in plasma membranes of somatic cells and are consistent with investigations demonstrating that the egg plasma membrane is a fluid environment permitting the lateral diffusion of lipids and proteins. Measurements of the distribution of antibody-labeled proteins along the surface of fertilized eggs examined at different intervals post-insemination indicate that the diffusion coefficient of the 30/33 kDa sperm plasma membrane protein is $0.7-2.4 \times 10^{-9}$ cm^2/sec.

Concomitant with the integration of the sperm plasma membrane components into the egg plasma membrane, studies utilizing lectins and charged probes demonstrate that a principal source of membrane to the expanding fertilization cone is from microvilli of the egg, i.e., microvilli are retracted to accommodate fertilization cone expansion. The membrane delimiting the fertilization cone has a much lower affinity for agents that bind negatively charged and carbohydrate groups compared to

other regions of the egg surface. Taken together, these observations indicate that significant rearrangements occur in the egg and sperm plasma membranes following gamete fusion. Components of both the egg and sperm plasma membranes are redistributed within the bilayer delimiting the fertilization cone and give rise to transient asymmetries in membrane topography. Whether or not and how such rearrangements in membrane components are related to later processes of fertilization and embryogenesis have yet to be determined.

References

1. F.J. Longo, D.H., McCulloh, P.I. Ivonnet and E.L. Chambers, J. Electr. Microsc. Tech. (1991) 20, 298.
2. F.J. Longo, J. Electr. Microsc. Tech. (1991) 17, 246.
3. J.R. Monck and J.M. Fernandez, J. Cell Biol. (1992) 119, 1395.
4. F.J. Longo, Dev. Biol. (1986) 116, 143.
5. F.J. Longo, Gamete Res. (1986) 15, 137.
6. F.J. Longo, Dev. Biol. (1989) 131, 37.
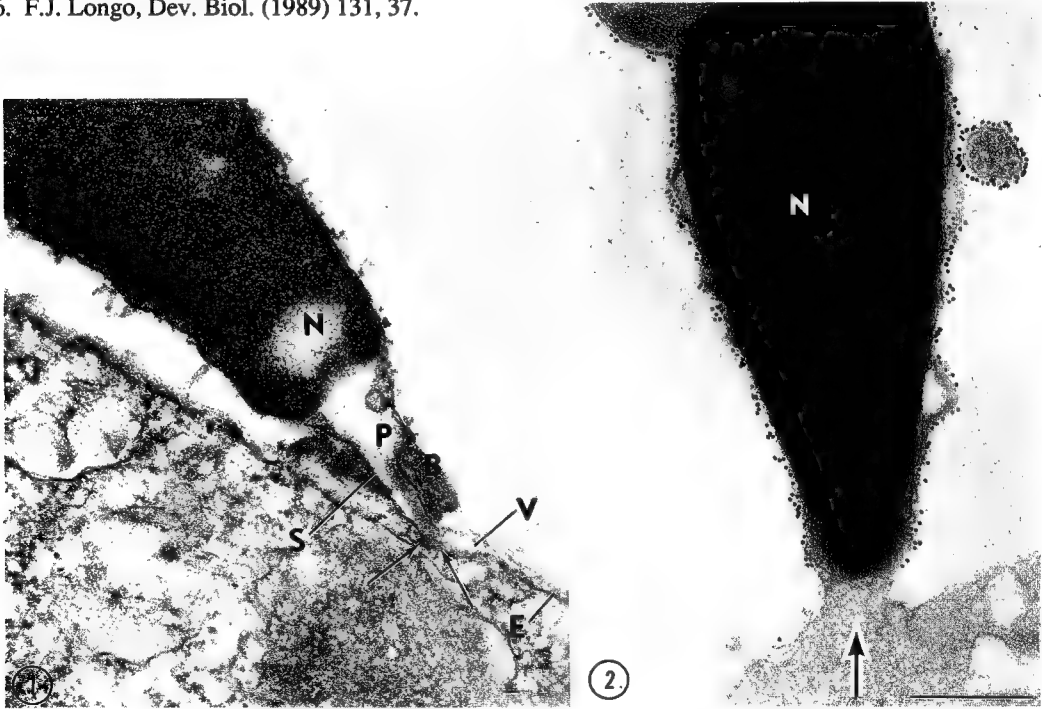
FIG. 1. -- Association of the acrosomal process (P) with the egg surface of a specimen fixed 4 sec after the onset of the activation potential. The acrosomal process has projected through the vitelline layer (V); its tip is on the egg surface and defines the area of gamete contact (arrows). Membrane fusion is not completed at the site of gamete contact. Bindin (B) is present as a plate-like structure that is in contact with the vitelline layer and not the egg plasma membrane (E). S, sperm plasma membrane; N, sperm nucleus. Bar = 0.1 μm.
FIG. 2. -- Fused sperm and egg, fixed 30 sec postinsemination. The site of gamete membrane fusion and the pore that is formed through which the sperm nucleus (N), mitochondria and axonemal complex move into the egg cortical cytoplasm is indicated by the arrow. The entire sperm surface is labeled with antibody to sperm specific 30/30 kDa protein followed by secondary antibody conjugated to colloidal gold. A gold particle is located to one side of the site of fusion on membrane that is likely to be of material origin. Bar = 0.5 μm.

IMMUNOCYTOCHEMICAL LOCALIZATION OF A BRUSH BORDER HYDROLASE, LACTASE, IN NEWBORN SUCKLING RAT JEJUNUM

László G. Kömüves, Mary A. Dudley, and Buford L. Nichols

Children's Nutrition Research Center, Department of Pediatrics,
Baylor College of Medicine, Houston, Texas 77030-2600

Lactase-phlorizin hydrolase (LPH, EC 3.2.1.23), an integral membrane glycoprotein of the small intestinal brush border, converts lactose, the main carbohydrate in milk, to its monosaccharide components.[3] Although the activity of LPH is high in suckling rats, little is known about its distribution within the intracellular compartments of the secretory pathway and brush border.[1,2] We present the first description of the ultrastructural localization of LPH in the neonatal jejunum of suckling rat pups.

Pieces of jejunum from 12- to 14-d-old suckling rat pups from three litters of Sprague-Dawley rats were fixed with 4% freshly prepared paraformaldehyde in 100 mM phosphate buffer, pH=7.40, for 4 h, and stored in 1% paraformaldehyde, at 4°C, until further processing. The samples were sectioned after cryoprotection in 2.3 M sucrose in an RMC MT-7 ultramicrotome equipped with CR21 cryoattachment. Ultrathin cryosections were collected on Formvar-coated, carbon-evaporated nickel grids. The nonspecific binding sites were blocked by 1% heat-inactivated newborn calf serum in 10 mM Trizma buffer, pH=7.60, containing 500 mM NaCl, 0.05% NaN_3 and 20 mM glycine (buffer A). The sections were incubated with an anti-rat LPH monoclonal antibody (5 µg/ml) in buffer A.[3] The sections were then washed with 5% heat-inactivated fetal calf serum in 10 mM Trizma buffer, pH=7.60, containing 500 mM NaCl, 0.05% NaN_3 and 20 mM glycine (buffer B) and incubated with affinity-purified rabbit anti-mouse IgG (4 µg/ml) in buffer B, followed by protein A-Au_{10} in the same buffer. The sections were stained with uranyl acetate in methyl cellulose, and observed in a Philips CM12 electron microscope.

The brush border (BB) was intensely labeled in the enterocytes on the villi of the jejunum (Fig 1). No labeling was seen along the baso-lateral plasma membrane (asterisk). The endoplasmic reticulum (arrowheads) was not labeled for LPH, whereas vesicles at the trans-face of the Golgi complex and in the apical cytoplasm (arrows) contained a low, but significant level of LPH immunoreactivity. No LPH was detected in the apical tubulo-vesicular membrane system (open arrows). These observations suggest that the vectorial targeting of LPH from the Golgi to the brush border is very efficient in suckling rats.

References

1. H. A. Büller et al., J. Biol. Chem. (1990) 265, 6978.
2. M. A. Dudley et al., J. Pediatr. Gastroenterol. Nutr. (1992) 15, 260.
3. D. Louvard, M. Kedinger, and H. P. Hauri, Ann. Rev. Cell Biol. (1992) 8, 157.
4. A. Quaroni, and K. J. Isselbacher, Dev. Biol. (1985) 111, 267.
5. The monoclonal antibody (FBB 3/4) used in this study was kindly provided by Dr. A. Quaroni, Cornell University, Ithaca, New York.
6. Funded by USDA/ARS under Cooperative Agreement #58-6250-1-003.

Figure 1.   *Immunolocalization of lactase on ultrathin cryosection of jejunum in 12-d-old suckling rat pup. Original magnification x47,000, bar= 0.5 µm.*

BB

①
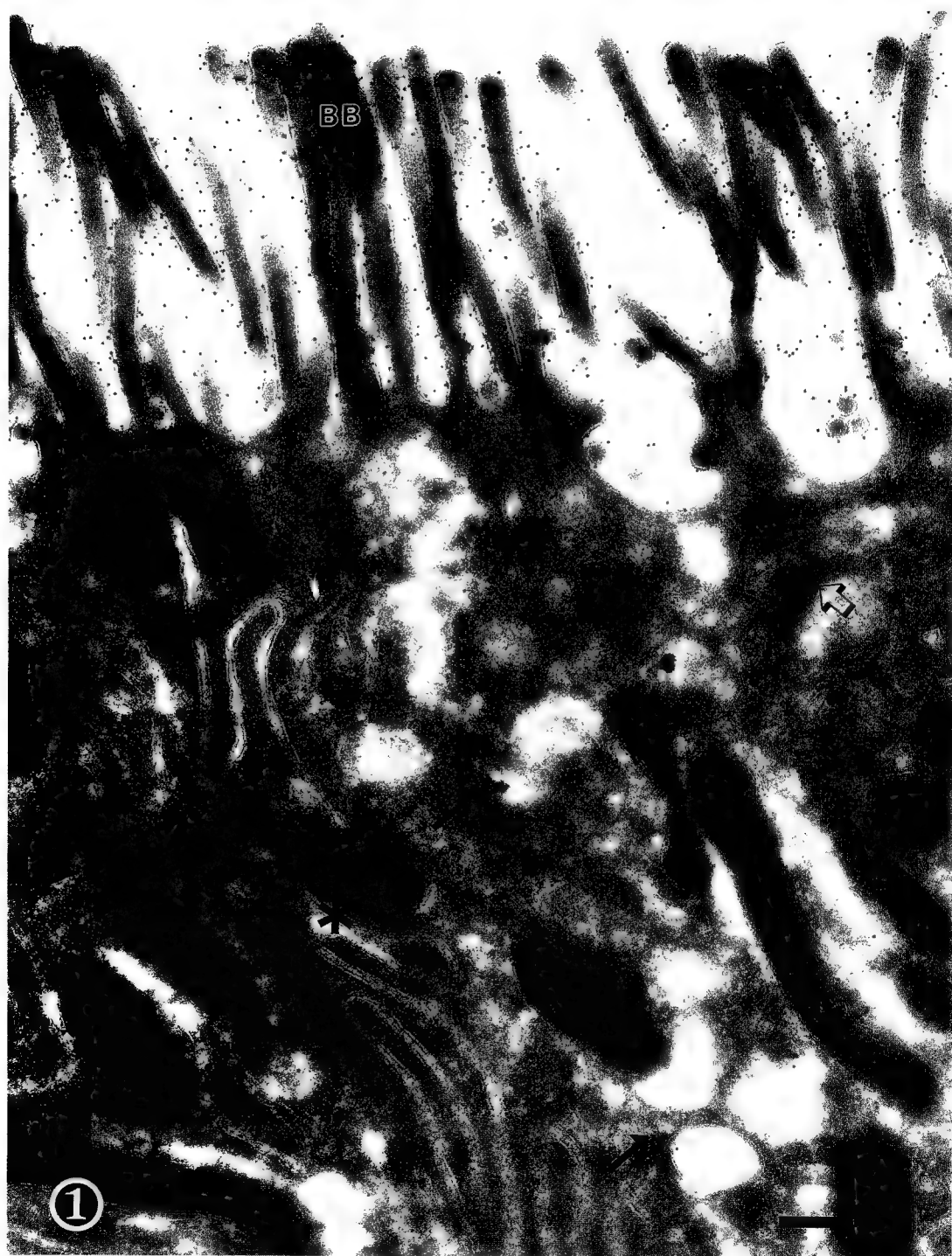
A MICROBIAL MODEL FOR VISUALIZATION OF SURFACE PROTEINS USING CRYOIMMOBILIZATION AND HIGH-RESOLUTION CRYOSEM

Stanley L. Erlandsen[1], Stephen Olmsted[2], Paul Walther[3], Ya Chen[3], Jim Pawley[3], Gary Dunny[4], and Carol L. Wells[2]

Departments of Cell Biology and Neuroanatomy[1], Laboratory Medicine and Pathology[2], Institute for the Advanced Studies in Biological Process Technology and Department of Microbiology[4], University of Minnesota, Minneapolis, MN 55455; Integrated Microscopy Resource[3], University of Wisconsin, Madison, WI 53706

Numerous studies on high resolution visualization of surface membrane proteins have utilized colloidal gold markers in conjunction with SEM, TEM, and by freeze-fracture cytochemistry using conventional or fracture flip methods[1,2,3,4,5], but in each case only information on the distribution of the marker complex, and not the actual structure of individual surface protein(s) was obtained.

To investigate the detection of individual surface proteins, we have used a microbial model to examine surface proteins involved in conjugation or the transfer of DNA in *Enterococcus faecalis*[7]. Two surface proteins encoded by the pCF10 plasmid, aggregation substance (Asc10; globular shape) and surface exclusion protein (Sec10; helical shape), mediate the aggregation of donor and recipient cells and prevent aggregation of like donor cells, respectively. Isogenic strains of *E. faecalis* that constitutively express neither Asc10 or Sec10 (pWM401) or both (pINY1801) were processed by 1) conventional chemical fixation, dehydration, critical point drying with CO_2, ion beam sputtering with a discontinuous platinum film (<1 nm), and examination in a Hitachi S-900 FESEM operated at low voltage (<3 keV), or 2) cryoimmobilization of cells by high pressure freezing (Balzers HPM 010), mounting in a Gatan cryoholder followed by etching for 60 minutes at -100°C, cryocoating by planar magnetron sputtering (Balzers MED 010), and examination at -100°C in the S-900 FESEM.

Chemical fixation and critical point drying of the isogenic strains of *E. faecalis* produced an overall shrinkage of the cells, giving them a "wrinkled or gyriform" appearance (Figs. 1 & 2). Strain pWM401 (expresses neither protein) possessed a smooth or bare appearance while strain pINY1801 had a roughened surface characterized by small "knob-like" projections. Cryoimmobilization of these isogenic strains yielded dramatically different results which were superior to that of chemical fixation. The surface of strain pWM401 appeared to lack any surface projections, but the surface had a fine felt-like appearance and shrinkage of the cell was minimized (Fig. 3). Examination of strain pINY1801, constitutively expressing both Asc10 and Sec10, revealed numerous protrusions on the cell surface, some of which had a globular appearance (arrowheads) while others possessed a helical shape (arrows).

References

1. E. De Harven, D. Soligo, and H. Christensen, Histochem. J. (1990) 22: 18.
2. S.L. Erlandsen, S.R. Hasslen, and R.D. Nelson, J. Histochem. Cytochem. (1993) 41: 327.
3. N. Severs, J. Elect. Micros. Tech. (1989) 13: 175.
4. C. Andersson Forsman and P. Pinto Da Silva, J. Cell Sci. (1988) 90: 531.
5. S. B. Olmsted, S. Kao, L.J. van Putte, J.C. Gallo, and G.M. Dunny, J. Bact. (1991) 173: 7665.
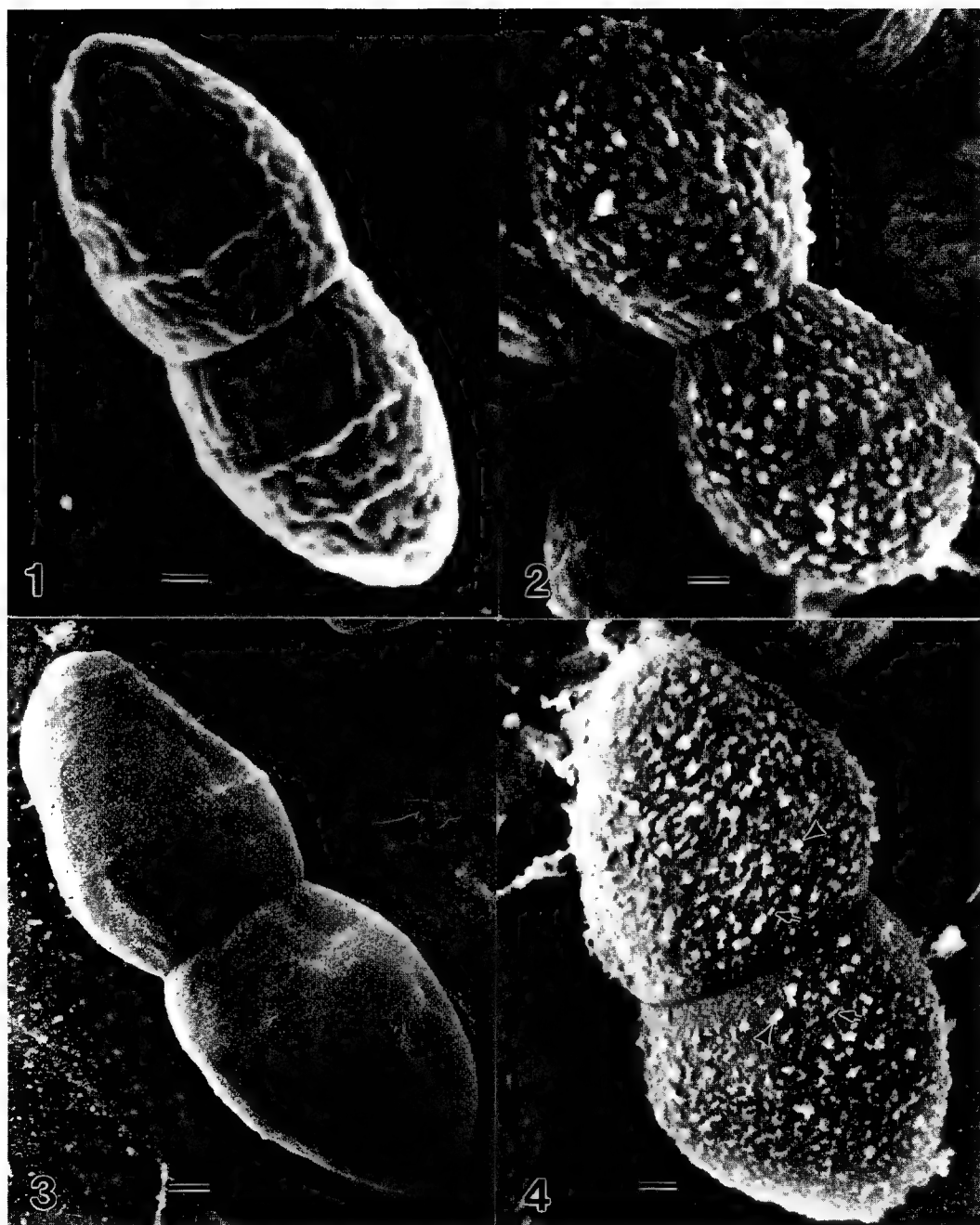
Figure 1. Conventional SEM preparation, *E. faecalis* strain pWM401 (lacks Asc10 & Sec10).
Figure 2. Conventional SEM preparation, *E. faecalis* strain pINY1801 (has Asc10 & Sec10).
Figure 3. Cryopreparation, *E. faecalis* strain pWM401.
Figure 4. Cryopreparation, *E. faecalis* strain pINY1801. Bar, 100 nm (same for all figures).

REFLECTIONS ON THE LIFE AND SCIENCE OF RUSSELL L. STEERE

Eric F. Erbe and William P. Wergin

Electron Microscopy Laboratory; ARS-BARC; Beltsville, MD 20705-2350

During the early years of electron microscopy a variety of techniques were developed to visualize biological samples. Nearly forty years ago Dr. Russell L. Steere conceived and developed a method, which became widely known as "freeze-etching", that could be used to image virus crystals.[1] Since this technique was first demonstrated, further refinements, developments and applications have advanced our knowledge of biological ultrastructure to the macromolecular level.[2,3,4,5] Until recently, use of freeze-etching was confined to TEM observations; however, today variations of the technique are being combined with the use of cryostages on SEMs to observe replicas or coating films on the surface of frozen hydrated specimens. Scanning probe microscopies are also utilizing the freeze-etch replicas to image ultrastructural detail. Not only is freeze-etching an effective preparative technique for the various forms of microscopy that are currently pushing the limits of resolution but it provides an excellent tool for advancements in the future as well.

In addition to his distinguished research career, Dr. Steere was a research administrator who strongly believed in granting individual scientific freedom to the research staff that he supervised. The effectiveness of this management style was probably learned from Robley C. Williams who was his mentor at Berkeley during the early years of his career. Dr. Steere attributed his success in developing the freeze-etch technique to the freedom he had to explore scientific ideas. In subsequent years freedom granted to scientists working under his supervision led to the discovery of new classes of pathogens such as the viroids, spiroplasmas and satellite viruses. His advice for all research administrators would be to provide a research environment where investigators are free to pursue their ideas.

This year MSA has replaced EMSA; the many fields of freeze-etching can similarly reunite in the spirit of discovery and the memory of Dr. Russell L. Steere.

References:
1. R.L. Steere, J. Biophs. Biochem. Cytol. 3(1957)45.
2. R.L. Steere, Cryobiol. 5(1969)306.
3. R.L. Steere, Freeze-Etching Techniques and Applications, Paris: Soc. Fr. Microsc. Electr. (1973)233.
4. R.L. Steere, Current Trends in Morphological Techniques, Boca Raton: CRC Press 2(1981)132.
5. R.L. Steere, J. Electr. Microsc. 13(1989)159.

Fig. 1. Assembled and exploded views of first freeze-etch apparatus (1956).
Fig. 2. Light micrograph of polio virus crystal (1958). X110.
Fig. 3. Early freeze-etch preparation of polio virus crystal (1958). Bar = 1μm.
Fig. 4. Materials Research Corporation prototype freeze-etch unit (1965).
Fig. 5. Dr. Russell L. Steere operating prototype Denton freeze-etch unit (1968).
Fig. 6. Picture and diagram of 24K gold complementary specimen holder and cap (1970).
Fig. 7. First fully successful complementary replica. Cross-fracture of myelinated nerve of mouse brain (1969). Bar = 1μm.

2 |—100µm

47
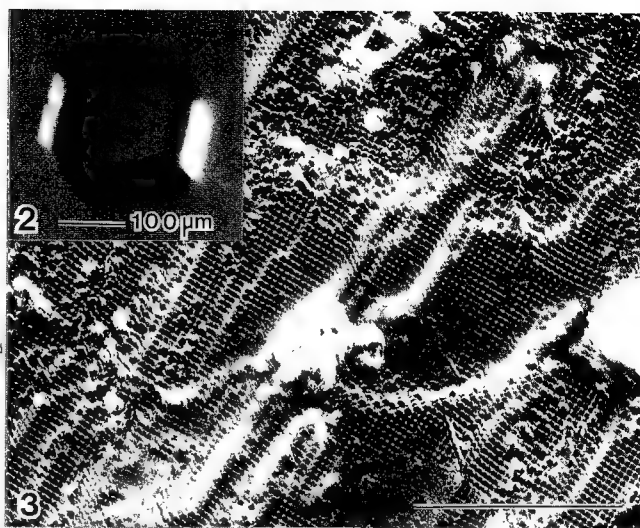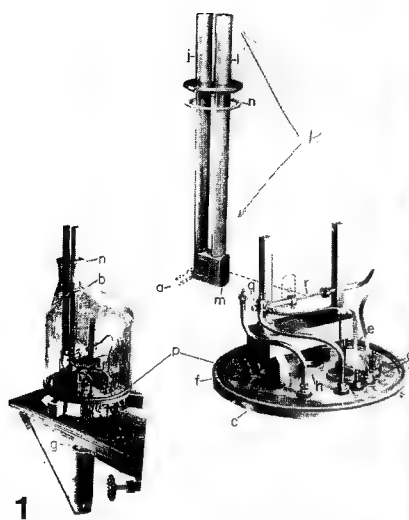
WHERE'S THE FAT? FREEZE-FRACTURE ANALYSIS OF INGREDIENT INTERACTIONS IN FOOD SYSTEMS

Jean Fincher

Kraft General Foods, 801 Waukegan Road, Glenview, IL 60030 U.S.A.

An important trend in the food industry today is reduction in the amount of fat in manufactured foods. Often fat reduction is accomplished by replacing part of the natural fat with carbohydrates which serve to bind water and increase viscosity. It is in understanding the roles of these two major components of food, fats and carbohydrates, that freeze-fracture is so important. It is well known that conventional fixation procedures are inadequate for many food products, in particular, foods with carbohydrates as a predominant structural feature.[1] For some food science applications the advantages of freeze-fracture preparation procedures include not only the avoidance of chemical fixatives, but also the opportunity to control the temperature of the sample just prior to rapid freezing.

In conventional foods freeze-fracture has been used most successfully in analysis of milk and milk products.[2,3] Milk gels depend on interactions between lipid droplets and proteins. Whipped emulsions, either whipped cream or ice cream, involve complex interactions between lipid, protein, air cell surfaces, and added emulsifiers. By combining the techniques of freeze-fracture replication and cryo-scanning electron microscopy it is possible to study microstructure of a frozen product, and gain insights into the effects of ingredients, processing variables, and storage conditions on product attributes. This knowledge is important in developing new frozen desserts, incorporating less fat, yet still possessing the characteristics of ice cream expected by consumers. Fig. 1 illustrates casein micelles and lipids in frozen ice cream, and Fig. 2 illustrates an accumulation of lipid around air cell surfaces in frozen ice cream. At freezer temperatures emulsified milk fat is present in rounded droplets with concentric layers. Several casein micelles are in contact with the surface of a lipid droplet. The surface coating of proteins or emulsifiers plays a role in determining fat destabilization, which in turn affects air cell formation and stability.[4]

Freeze-fracture has been valuable in studies of other emulsions.[5] Mayonnaise consists of tightly packed oil droplets (Fig. 3). The morphology and packing characteristics of this emulsion were not preserved by other methods. Often lamellae were present in the oil droplets, with 3 to 10 layers frequently present on the surface. These lamellae and internal patterns were related to freezing rate. However, some of the surface structures may be induced or stabilized by emulsifiers. Details of emulsion structure, as seen for different samples of mayonnaise and salad dressings, are aiding interpretations of rheological behavior.

1. J.F. Chabot Scanning Electron Microscopy (1979) III, 279
2. I. Heertje, J. Visser, P. Smits. Food Microstructure (1985) 4, 267.
3. B.E. Brooker, Food Structure (1990) 9, 223.
4. W.Buchheim, Keiler Milchwirtschaftliche Forschungsberichte (1991) 43, 247.
5. S. H. Humphreys, Journal of Electron Microscopy Technique (1989) 13, 300.
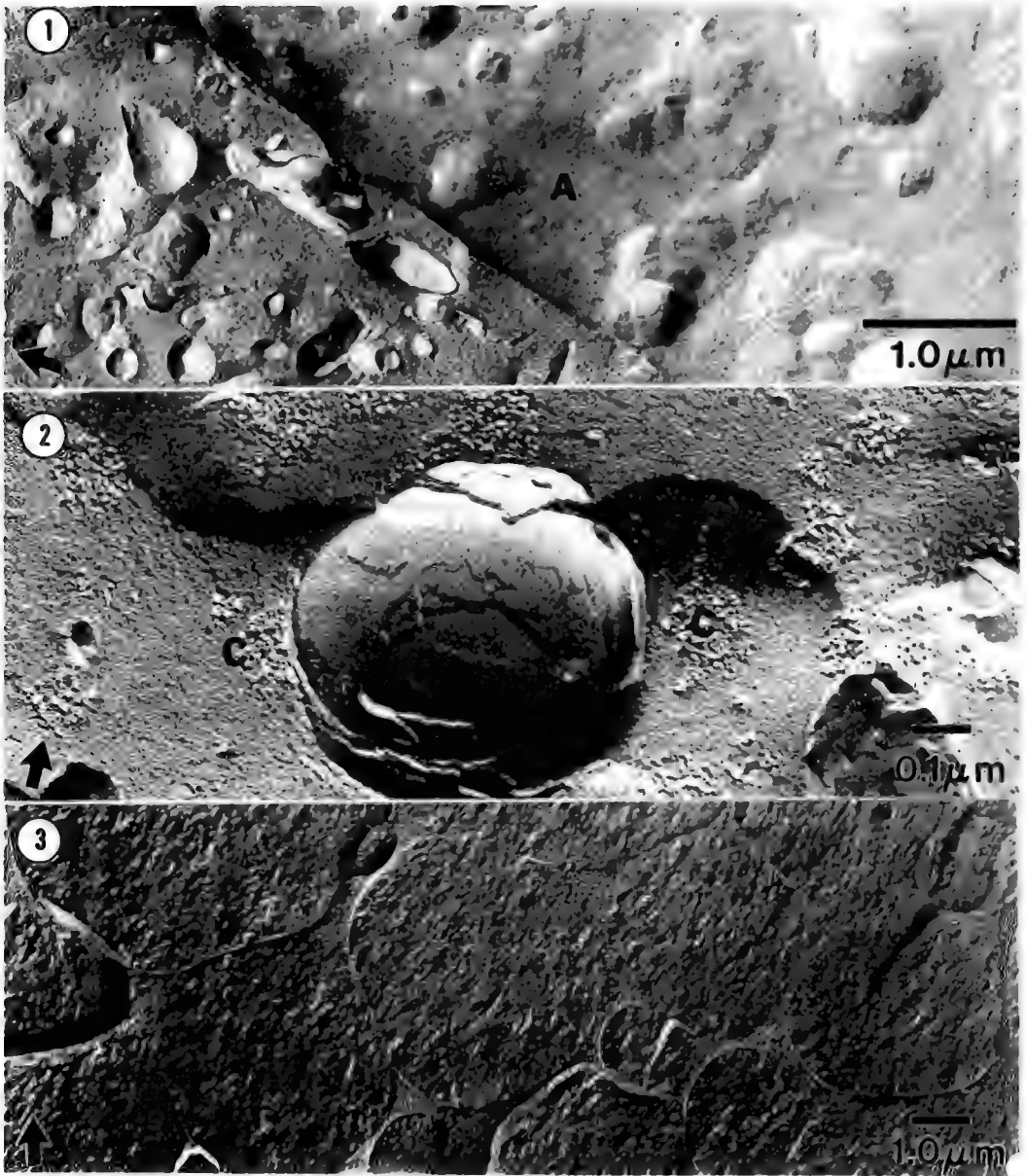
Fig. 1. Air cell surface (A) in frozen ice milk has impressions of underlying lipid droplets.
Fig. 2. Casein micelles (C) are present in the serum and some are attached to the lipid, which is seen as concentric lamellae in frozen ice cream.
Fig. 3. Mayonnaise, an oil in water emulsion, consists of very tightly packed soybean oil droplets with long contact zones.

FREEZE-FRACTURE TRANSMISSION ELECTRON MICROSCOPY (FF/TEM) STUDIES OF SYSTEMS CONTAINING SELF-ASSOCIATED STRUCTURES

Janet L. Burns, Matthew H. Chestnut and Richard J. Spontak[†]

Corporate Research Division, The Procter & Gamble Company, Cincinnati, OH 45239
[†]Present address: Department of Materials Science & Engineering, North Carolina State University, Raleigh, NC 27695

Freeze-fracture transmission electron microscopy (FF/TEM) is a well-established and highly-valued technique, often employed in the study of biological systems which are extremely sensitive to structural alteration (e.g., membranes and tissues). The technique relies on rapid specimen cooling to immobilize detailed microstructure, usually in a hydrated environment, prior to fracture and subsequent surface replication. As Zasadzinski and Bailey[1] point out, though, the principle governing this technique is general and can be applied with equal success to the study of "microstructured" or "complex" fluids, i.e., fluids consisting of self-organized supramolecular structures. In this vein, FF/TEM constitutes a powerful means of characterizing the structural attributes of dispersions, emulsions, gels, and liquid crystalline assemblies at relatively high spatial resolution. Such morphological information can prove valuable in the development of the structure-viscosity relationships needed in processing. Here, we demonstrate the utility of FF/TEM in elucidating the role of self-associated structures in three different systems: a chemical reaction environment, a high-internal-phase emulsion, and a nonaqueous gel.

Preparation of microstructured fluids for FF/TEM is by far the most crucial aspect of the technique, since freezing artifacts may preclude accurate structural interpretation. In the present work, a small portion of each specimen was either sandwiched between 3 mm gold-alloy planchets or placed into a copper well, depending on specimen fluidity, and then immersed in liquid ethane cooled by liquid nitrogen. The specimens were subsequently transferred in liquid nitrogen to a JEOL JFD-9000C freeze-fracture/etch unit, maintained at about $-170°$ C and 10^{-7} torr during fracture and replication. Unless otherwise indicated, replicas were produced by shadowing Pt/C at $45°$ and C at $90°$. In the case of the gel presented here, the specimens were etched at $-100°$ C for 4 h after fracture, and Pt/C was shadowed at $90°$ to improve resolution.[2] The resultant replicas were cleaned in appropriate solvents and imaged with a Zeiss EM902 transmission electron microscope, operated at 80 keV in zero-loss mode.

Figure 1 consists of two replicas obtained from an identical mixture of triglycerides, hexane, 2-butanol, and buffer containing 1,3-specific lipase. Prior to agitation, layered triglyceride-rich droplets[3] (Fig. 1a) are clearly differentiated from the aqueous matrix. Upon agitation, the lipase hydrolyzes the triglyceride at the oil/water interface. Although one of the reaction intermediates, 2-monoglycerides, readily isomerizes in a polar environment to 1-monoglycerides (which can be further hydrolyzed to glycerol), negligible quantities of glycerol are detected upon reaction completion. Spherical structures 30-50 nm in diameter, observed in replicas produced shortly after cessation of agitation (Fig. 1b), are interpreted[4] as "micelles" which develop in the presence of 2-monoglycerides (a nonionic surfactant) and 2-butanol (a cosurfactant) and shield the 2-monoglycerides from the aqueous environment. Thus, FF/TEM reveals that enzymatic hydrolysis is controlled, in part, by the formation of amphiphilic association structures from reaction intermediates. Figures 2 and 3 are replicas from two high-internal-phase emulsions, in which water accounts for >90% of the system but appears as the dispersed phase. Solans et al.[5] have identified, with FF/TEM, a liquid crystalline phase between the oil and water phases in such emulsions. The micrographs shown in Figs. 2 and 3 are obtained from two emulsions differing only in surfactant. A multilamellar phase is apparent from the fracture surface in Fig. 2, whereas a cubic texture possessing a mean periodicity of ca. 100 nm is visible in Fig. 3. The fibrillar network of a nonaqueous gel is evident from the micrograph in Fig. 4. The average thickness of these fibrils is 50 nm. Upon close examination of the enlargement provided in the inset, the fibrils are seen to possess periodic "bumps," which are presumed to correspond to the pitch (ca. 150 nm) of the helical molecules comprising the fibrils. A positive morphology-rheology correlation has been observed in these gels.

References

1. J.A.N. Zasadzinski and S.M. Bailey, J. Electr. Microsc. Tech. (1989)13, 309.
2. G.C. Ruben, J. Electr. Microsc. Tech. (1989)13, 335.
3. M.W. Rigler et al., J. Amer. Oil Chem. Soc. (1983)60, 1291.
4. A.W. Mazur et al., J. Phys. Chem. (submitted).
5. C. Solans et al., Colloid Polym. Sci. (1988)266, 570.
6. We acknowledge A.W. Mazur, S.A. Goldman, and C.B. Motley for their assistance in these studies.
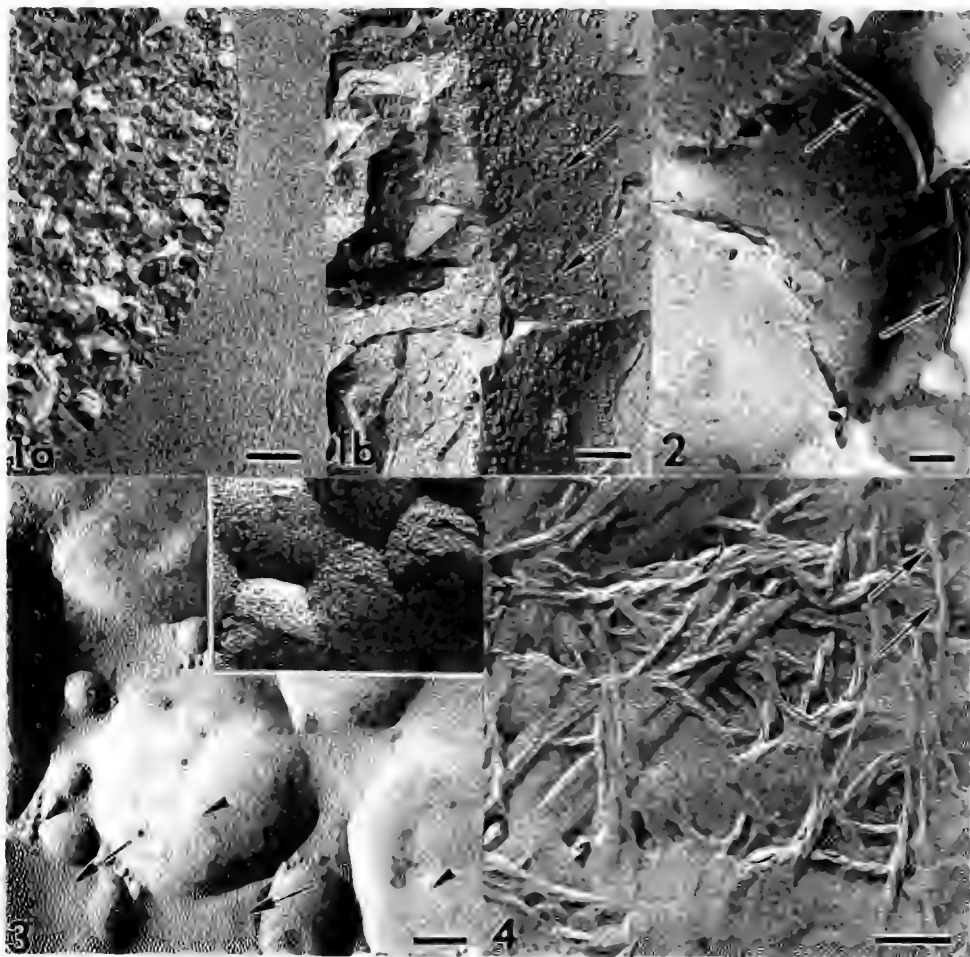
FIG. 1.—FF/TEM replicas obtained from enzymatic hydrolysis of triglycerides before (a) and after (b) addition of 1,3-specific lipase. Note formation of dispersed micelles (arrows) in (b). Bar = 250 nm.
FIG. 2.—Fracture surface of high-internal-phase emulsion showing multilamellar liquid crystalline phase (arrows) at oil/water interface. Bar = 500 nm.
FIG. 3.—Replica of oil/water interface in another high-internal-phase emulsion (with different surfactant). Cubic liquid crystalline phase (arrows) and discrete dispersions (arrowheads) are evident. Inset is 20X enlargement of cubic texture illustrating transition from texture to oil phase. Bar = 1000 nm.
FIG. 4.—FF/TEM replica of etched nonaqueous gel displaying fibrillar network and revealing pitch (arrows) of helical molecules comprising fibrils. Bar = 200 nm.

FREEZE ETCH REPLICATION OF EXTRACELLULAR BACTERIAL POLYMERS ADSORBED ONTO KAOLINITE

William W. Barker * and Vernon J. Hurst**

* Department of Geology and Geophysics, The University of Wisconsin-Madison 53706
Barker@ice.geology.wisc.edu
** Department of Geology, The University of Georgia-Athens 30602

Freeze etch replication of experimental mixtures of euhedral kaolinite and pure cultures of polysaccharide and protein-producing bacteria reveals that surface textures formed by adsorption of extracellular bacterial polymers onto kaolinite surfaces resemble structures observed in natural estuarine clay rich sediments, where anhedral 0.1 micrometer clay surfaces are covered by anhedral masses and fibrous elements of organic material.[1]

All samples, were cryofixed in a Balzers QFD101 propane jet and replicated in a Balzers 360M freeze etch device. Etching occurred at -100°C for 45 sec. and replicas were created with 15 nm Pt @ 45 °, 15 sec. C @ 90°. Following 24 h digestion in conc. HF, replicas were mounted on Formvar-coated 100 mesh Cu grids, carbon-coated for thermal stability, and examined in a Philips STEM 400.

Anionic mucopolysaccharide produced by pure cultures of encapsulated *Klebsiella pneumoniae* (ATCC 8044) readily adsorbed to both the basal (negative charge) and edge (positive charge) surfaces of kaolinite (Fig. 1). The small radius of the individual polymeric strand allows it to evade electrostatic repulsion and adsorb to either surface, irrespective of charge.[2] Tangentially-oriented kaolinite platelets cover the outer capsule surface, forming a "cutan" (Fig. 2). Clay cutans have been described from soils and sediments [3], and are sufficiently durable to survive phagocytosis and digestion by benthic foraminifera .[4] At a 50% solids level (wt/wt), each encapsulated bacterium can immobilize in excess of 250 crystallites. Masses of polysaccharide/kaolinite mixtures detached from bacteria were also seen.

F-type sex pili produced by *Escherichia coli* readily adsorb to the basal surface of kaolinite to form bridges between bacteria and clay, as well as betweeen kaolinite crystals. The larger radius of pili precludes evasion of kaolinite's surface charge and no interaction between pili and kaolinite edge surfaces was seen. As the weight/length of F-type sex pilus (3000 daltons/Å) is known [5], the amount of protein adsorbed can be measured directly. A 0.1 micrometer kaolinite crystal adsorbed 15×10^6 daltons (Fig. 3). Identical structures occur commonly on natural estuarine clay surfaces (Figs. 4, 5).

In both species, interactions between kaolinite and the bacterial cell wall result in radially oriented clay platelets (Fig. 6). This reflects a combination of electrostatic attraction and repulsion between the anionic cell membrane and the positively charged kaolinite edges and negatively charged basal surfaces.

Bacteria exist in large numbers (8.36-10.9×10^9) in salt marsh sediments [6], where high salinity and daily fluctuation in water levels combine to create ideal conditions for adsorption of large amounts of organic material onto clay minerals. Understanding this sytem is crucial to aspects of microbial ecology and the genesis of petroleum deposits.

1. W. W. Barker et al., 40th EMSA Proc., (1982)576.
2. K. C. Marshall, in D. C. Savage and M. Fletcher, eds., Bacterial Adhesion:
Mechanisms and Physiological Significance, New York, Plenum Press (1985)133.
3. P. Smart and N. K. Tovey, Electron Microscopy of Soils and Sediments: Examples,
Oxford, Clarendon Press, (1981)178 pgs.
4. S. T. Goldstein and W. W. Barker, J. Protozool. 37(1990)20.
5. W. Folkhard et al., J. Mol. Biol. 130(1979)145.
6. P. Rublee and B. E. Dornseif, Estuaries 1(1978)188.

Fig. 1. Anionic mucopolysaccharide (P) adsorbed onto kaolinite (K) basal surface.
Fig. 2. Kaolinite (arrows) delineates the outer surface of *K. pneumoniae* (B) capsule.
Fig. 3. F-type sex pili bridging *E. coli* (B) and kaolinite basal surface (K).
Fig. 4. Pilus-like structure adsorbed onto anhedral estuarine clay mineral (C).
Fig. 5. Pilus-like structures adsorbed onto anhedral estuarine clay mineral (C).
Fig. 6. Radially oriented kaolinite (K) arranged around *E. coli* cell surface (B).

FREEZE-FRACTURE VIEWS OF MEMBRANE MOTORS OF BACTERIA

Shahid Khan
Department of Physiology & Biophysics, Albert Einstein Medical School

The locomotory organelles of many bacteria are long, helical filaments called flagella. Bacterial flagella rotate. Flagellar rotation is driven by a molecular motor that is part of the membrane embedded flagellar base and fueled by electrochemical proton (or sodium) gradients. Rapid-freeze electron microscopy has revealed that rings of intramembrane particles found clustered around flagellar bases are a key structural module of this motor.

The morphology of the ring particles provides clues to their function. The particles are located in the cytoplasmic membrane across which the electrochemical gradients that energize flagellar rotation are maintained. In *Escherichia coli*, in addition to proteins needed for assembly of the flagellum, two proteins, MotA and MotB, are required for motility. MotA conducts protons across membranes and interacts with MotB, a protein with a large periplasmic domain. In non-motile mutants lacking MotA and MotB, flagellar bases lack the particle rings. Plasmid based expression of both MotA and MotB is necessary for restoration of motility and the ring structures. These findings are consistent with the view that the ring particles are proton transporting MotA-MotB channel complexes. The bacterial cell wall functions as a rigid exoskeleton against which force may be generated. Stereo-views reveal that the ring particles are unusually tall. They may function, in addition, to link the stator components of the flagellar motor to the cell wall. These stator components may reside in the cytoplasm. Molecular shadowed images of flagella, isolated avoiding extremes of pH and ionic strength, have contributed to evidence establishing the presence of a large, bell-shaped, multi-modular, cytoplasmically-located component of the flagellar motor. Consistent with the performance of these key functions, flagellar particle rings have been found in all bacteria examined thus far by rapid-freezing, including bacteria with sodium powered flagella. Currently, the dynamics of assembly of the particle rings brought about by inducible expression of the Mot proteins or by rapid change of metabolic parameters are being studied. These studies should test the idea that each particle behaves as an independent element for force-generation.

REFERENCE:

Khan, S. 1993. Gene to Ultrastructure: The Case of the Flagellar Basal Body. *J. Bacteriol* (april issue).
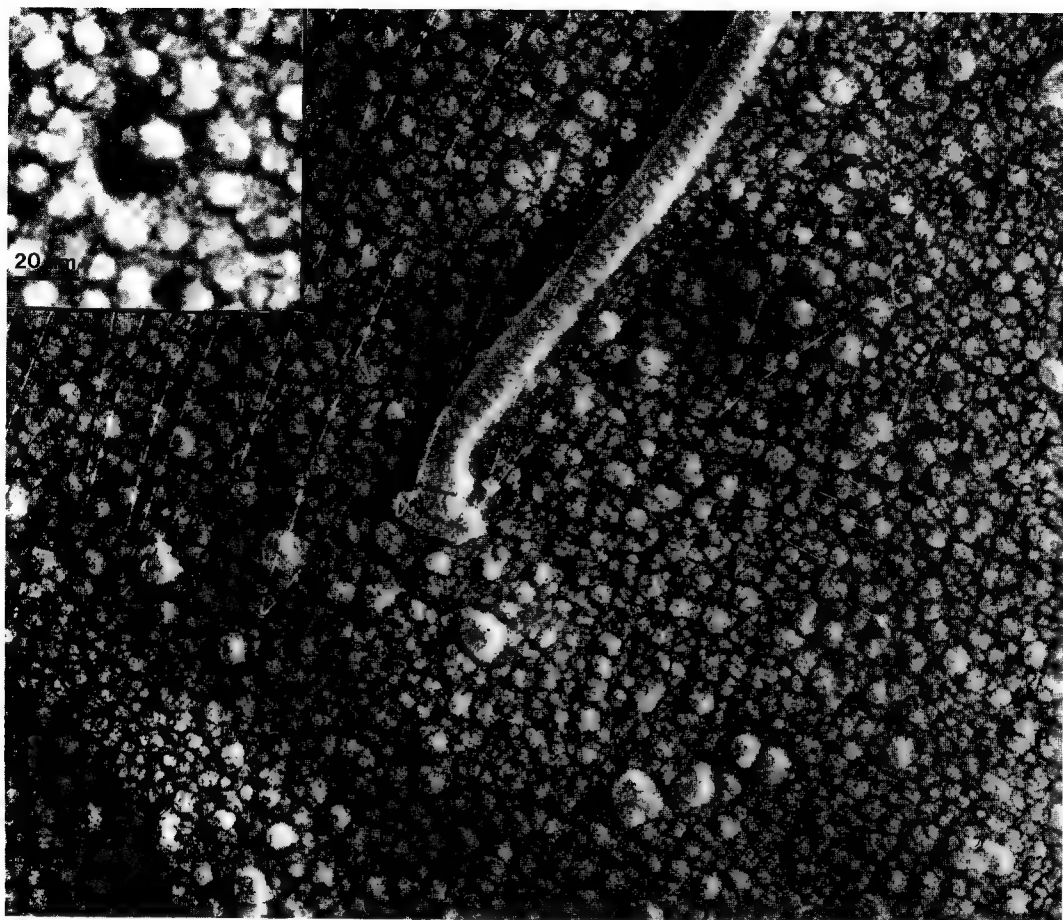
Figure Legend: Molecular shadowed *Escherichia coli* flagellum with bell-shaped cytoplasmic basal structure. **Inset:** *Escherichia coli* flagellar particle ring.

VISUALIZING REPLICAS OF MOLECULES MADE IN A FULLY AUTOMATED FREEZE-FRACTURE MACHINE

Daniel Branton

Department of Cellular and Developmental Biology, Harvard University, Cambridge, MA 01238, USA

We have designed and constructed an automated, computer driven freeze-etch apparatus that optimizes all of the standard operating procedures through which biological samples are normally processed to create a replica suitable for electron microscopy. Although designed for automated freeze-etching, manual intervention is possible at any step and the apparatus may be used to facilitate any or several sequences of computer driven or manual steps (Figure 1) that render a high resolution replica of a frozen or dried biological specimen.

The gradual evolution and improvement of scientific apparatus are commonplace, but there are some specific reasons why we sought to automate the freeze-etch process:
1) Many are dissuaded from using standard freeze-etch machines because operator training is time-consuming and using the apparatus is laborious;
2) Reproducible results are difficult to obtain and require conscientious attention to a mire of trivial details that are easily remembered by computers;
3) Numerous sub processes, e.g. the speed of fracturing, have not been systematically optimized because formidable record keeping is required to encompass the many subtle variations of conditions sustained by the specimens in a single freeze-etch run;
4) Humans are easily distracted; a single, seemingly trivial, error during the complex succession of steps in a freeze-etch run can easily ruin the entire process, with the consequent loss of specimen and waste of material and time.

We have used our automated freeze-etch apparatus to investigate both technological questions, such as avoidance of contamination and the utility of very low (less than 20°C) temperatures, as well as biological problems, such as the contours and modes of interaction of cytoskeletal proteins and the shape of cells. Results from these investigations will be presented.

PRESSURE 1×10^{-7} mB	STAGE TEMP 262.9° K	KNIFE TEMP 95.2° K	ADVANCE 0 µm/cut	POSITION 1238 µm

| | STANDBY: | Program **04** | RCP **1** | Gun angle **35.0°** |

A01　PREFIRE:　　　When P **3 x 10^{-5}** mB　　Gun 1 **048** mA　　　　Gun 2 **068** mA

A02　LOAD TEMP:　Stage **100.0°** K　Knife **290.0°** K　Wait **01** min to equilibrate

A03　LOAD:　　　　Preloaded? **Y**　Wait until pressure less than **3 x 10^{-5}** mB

M04　ROUGH CUT:　Advance **040** µm/cut at **06** mm/sec to **0600** µm

A05　WORK TEMP:　Stage **163.0°** K　Knife **095.0°** K　Wait **03** min to equilibrate

☛A06　FINAL CUT:　When P **3 x 10^{-6}** mB, advance **015** µm/cut at **04** mm/sec to **1200** µm

A07　ETCHING:　　Stage **163.0°**K　Knife **095.0°** K　Cover? **Y**　Time **0060** sec

A08　REPLICATE:　Gun 1 (Pt) **00.80** nm at **0.060** nm/sec at **3** rev/sec
　　　　　　　　　Gun 2 (C) **06.00** nm at **0.250** nm/sec at **0** rev/sec

A09　UNLOAD:　　Preloaded? **Y**　Wait until pressure less than **3 x 10^{-3}** mB

A10　WARM:　　　Maxima: Time **020** min　　　Stage **330°** K　　　Knife **330°** K

Figure 1. The central program page presented on the video monitor of our automated freeze-etch machine. Bold face designates parameters that may be entered by the user. The user enters his experiment identification number on the top line where time and date are shown; the boxed area displays important, continuously changing conditions such as vacuum, temperature, and knife position. Entering a program number in the line just below the box (here, program 4) brings up the complete program sequence with all parameters, including a set of rarely changed parameters, filled in. The user may use the program as is or may alter any of the parameters shown in bold face using an editing cursor (not shown). Each line of the program presents steps that are achieved Automatically or Manually depending on whether the user selects A or M (in this example, the user has elected to perform rough cuts manually but have the computer perform all other steps without intervention). The work cursor (☛) indicates the step that is currently being performed (here, the final cuts). The work cursor advances automatically as specified by the program requirements, but may be moved manually by depressing a "forward" or "backward" key. During replication (here, step 08) the monitor switches automatically to display a graphical, continuously updated representation (not shown) of measured replica thickness vs. time. The order of steps may be altered by changing their number in the sequence, or individual steps may be deleted entirely. Changing any step number or parameter creates a new program that may be used immediately or stored for future use. As the program (or user, if in manual mode) proceeds through each step, all of the continuously changing conditions (including the graphical display of the replication process) are stored in memory so that a report showing parameters selected and actual conditions achieved may be printed out at the end of each freeze-etch run.

SCANNING TUNNELING MICROSCOPY AND LOW-TEMPERATURE FORCE MICROSCOPY OF FREEZE-FRACTURED SAMPLES

K. A. Fisher,[*] M. B. Shattuck,[**] M. G. L. Gustafsson,[***] and J. Clarke[***]

[*]   Depts. Anatomy, Biochemistry & Biophysics, and Francis I. Proctor Foundation,
       Univ. of Calif., San Francisco, CA 94143-0944
[**]   Dept. Bioengineering, Univ. of Calif., San Francisco, CA 94143-0650
[***] Dept. Physics, Univ of Calif. & Center for Advanced Materials, Lawrence Berkeley
       Laboratory, Berkeley, CA 94720

INTRODUCTION: Monolayer freeze-fracture combined with scanned probe microscopy (SPM) offers unique advantages for studies of biological structure.[1] The freeze-fracture methodology incorporates rapid freezing approaches for sample preservation and stabilization, and the scanned probe microscopies, especially scanning tunneling microscopy (STM) and atomic force microscopy (AFM), allow high resolution examination of surface features including digital mapping, quantification, and display. In routine biological STM a sharp conductive probe is positioned with piezoelectric transducers close to a conductive surface. When electron tunneling begins, the probe is scanned while electronic feedback maintains constant current. Because the tunneling current is logarithmically sensitive to separation between the tip and the sample, the feedback signal can be calibrated to indicate height with sub-Angstrom sensitivity and precision. In routine biological AFM, the sample is scanned while the force between the tip and the sample is kept constant.

STM STUDIES: There are two fundamental problems in STM examinations of biological systems. First, biological samples are soft and are often perturbed by the scanning probe; and second, they are not electrically conductive. Coating samples with metal replicas simultaneously circumvents both these difficulties, conferring sample stability and electrical conductivity. The STM can be used to measure sample heights quite accurately, and has been used to measure the thickness and changes in thickness of metal-coated purple membrane[2,3] and the depth of surface features of freeze-fracture replicas of synthetic phospholipids.[4] For quantitative studies, freeze-fractured replicas require mechanical support and careful calibration of scanned probe displacements. Otherwise, the sample preparation techniques are the same as those for conventional freeze-fracture.

AFM STUDIES: The advantage of AFM in biological studies is that samples need not be electrically conductive.[5] However, a limitation to obtaining high-resolution information is inherent in sample softness and deformability. Low temperature force microscopy (LTFM) has been touted as a possible solution to this dilemma.[6,7] Freezing the sample could provide both increased reproducibility and stability. We have built an LTFM for operation at 143 K.[8] The microscope operates immersed in liquid isopentane, cooled to near its freezing point with liquid nitrogen, and kept in a dry nitrogen gas atmosphere. We have examined freeze-dried and nitrogen-dried samples including nucleic acids, globular and fibrillar proteins, and membrane surfaces. Recently we tested the feasibility of freeze-fracturing a test sample immersed in isopentane and used the LTFM to produce images of fractured ice (Fig 1).
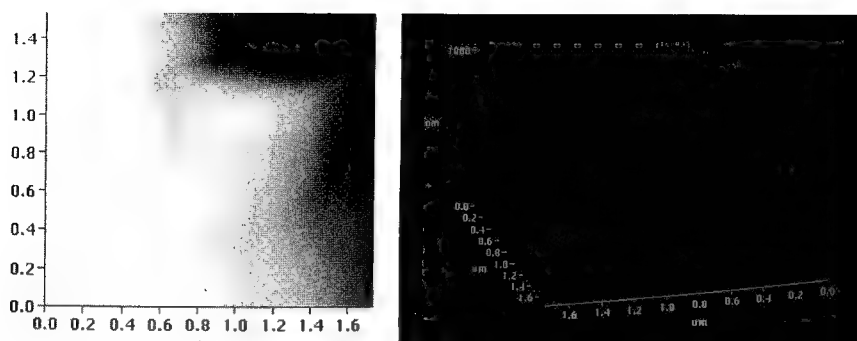
Fig. 1. Low-temperature force microscope image of freeze-fractured ice at 143 K. (A, left) Top view, gray scale. (B, right) 3-D representation of A.

The planar freeze-fracture approach[1] should be uniquely suited to LTFM. Its clear advantages include improved instrument stability, improved structural preservation by rapid freezing, improved sample stability, and the opportunity to examine freeze-fractured surfaces of frozen molecules that have not been coated with metal.

FUTURE: Stabilization of especially fragile biological samples by replication of frozen surfaces is readily compatible with conventional STM and AFM methodology. STM studies of freeze-fractured replicas can provide unique quantitative information as well as digital processing and display. A possible new direction for SPM would be in the choice of materials for replica formation. Whereas STM requires conductive replicas, AFM does not, and thus pure carbon or polymer replicas may be especially suitable for high resolution studies. For LTAFM, the future is in the direct examination of frozen and freeze-fractured unreplicated surfaces, not only their structural features but also their physical properties including elasticity and plasticity. In addition, *in-situ* freeze-fracture could provide new information about molecular interactions from an entirely unique perspective.

References

1. K. A. Fisher, *J. Elect. Microsc. Tech.* (1989) **13**, 355.
2. K.A. Fisher et al., *Biochim. Biophys. Acta* (1990) **1023**, 325.
3. K.A. Fisher et al., *Ultramicroscopy* (1990) **33**, 117.
4. J.A.N. Zasadzinski et al., *Science* (1988) **239**, 1013.
5. G. Binnig et al., *Phys. Rev. Lett.* (1986) **12**, 930.
6. C. Prater et al, *J. Vac. Sci. Technol. B.* (1991) **9**, 989.
7. K.A. Fisher et al., *Proc. Roy. Microsc. Soc.* (1990) **25**, S3.
8. K.A. Fisher et al., *Proc. Ann. EMSA Meet.* (1991) **49**, 54.
9. Supported by NIDA Grant No. DA05043 (K.A.F.), NEI Grant No. EY02162 (K.A.F.), and by the Director, Office of Energy Research, Office of Basic Energy Science, Materials Science Division of the U.S. Department of Energy, under Contract No. DE-AC03-7600098 (J.C. and M.G.L.G.).

FREEZE-FRACTURE CYTOCHEMISTRY: A GOAL SET BY RUSSELL STEERE IN 1957

Nicholas J Severs

Dept Cardiac Medicine, National Heart & Lung Institute, Dovehouse St, London SW3 6LY, ENGLAND

In his pioneering demonstration of the potential of freeze-etching in biological systems, Russell Steere assessed the future promise and limitations of the technique with remarkable foresight.[1] Item 2 in his list of inherent difficulties as they then stood stated "The chemical nature of the objects seen in the replica cannot be determined". This defined a major goal for practitioners of freeze-fracture which, for more than a decade, seemed unattainable. It was not until the introduction of the label-fracture-etch technique in the early 1970s that the mould was broken, and not until the following decade that the full scope of modern freeze-fracture cytochemistry took shape.[2-5] The culmination of these developments in the 1990s now equips the researcher with a set of effective techniques for routine application in cell and membrane biology.

Freeze-fracture cytochemical techniques are all designed to provide information on the chemical nature of structural components revealed by freeze-fracture, but differ in *how* this is achieved, in precisely *what* type of information is obtained, and in *which* types of specimen can be studied. A summary of the principal techniques that have been developed and tried is given in the table. The standard method of cleaning replicas (acids or hypochlorite) to remove biological material (including any label) stood as an initial conceptual obstacle to progress.[4] The first practical solution to this problem came with the sectioned replica technique, in which the replica is viewed *en face*, together with undigested labelled biological material, from within a section.[4] Perturbation of membrane structure before freezing using specific lipid binding agents offered another solution; here the structural alterations, rather than the cytochemical agent itself, act as the marker.[6] This approach enjoyed a spell of popularity in the 1980s but has since fallen out of favor.

The most significant breakthroughs came with the introduction of colloidal gold cytochemistry in electron microscopy in the early 1980s. Gold particles, because of their high electron density and small size, are an ideal marker to use with replicas; new ways of retaining label for viewing with the replica were thus devised. The simplest of these is to replicate a gold-labeled specimen and use cleaning conditions that leave the markers embedded in the replica. By this and other means, gold labeling can be integrated into the standard freeze-fracture procedure at the following stages; (i) before the specimen has been frozen, (ii) after fracturing and thawing, (iii) after platinum shadowing, or (iv) after completion of the full replication sequence. Included in category (i) are the modern descendants of the deep-etch technique; (ii) is represented by the technique of fracture-label[2] (visualization by replica or section); (iii) is represented by shadow-label (visualization directly by replica or using sectioned replica).[4]

An elegant method for retaining gold marker for viewing with the replica came with the introduction of the label-fracture technique.[7] The essential principle of this technique is to retain, attached to and stabilized by the replica, fractured half-membrane leaflets that would normally be digested away during replica cleaning. If the cell is gold labeled before freezing, label attached to the plasma membrane surface can be viewed superimposed upon a standard freeze-fracture replica of the membrane interior. The concept of stabilizing fractured membrane leaflets with replica underpinned a further phase of development. First, a series of techniques were developed in which labeling of fractured membrane or cell fragments attached to the replica is done after the replica has been made (category iv).[8-10] Second, a further manipulation became possible — turning the replicated specimen over during processing to provide additional structural information. This principle is exploited in fracture flip[11] (to give extended replica views of labeled membrane surfaces), and dual replica techniques (simulcast[12] and composite replica[13]) where surface label is combined with replicas of both the surface and the membrane fracture face.

References

1. R. L. Steere, J. Biophys. Biochem. Cytol. (1957)3, 45.
2. P. Pinto da Silva et al, in J. K. Koehler,Ed., Adv. Tech. Biol EM vol 3, New York: Springer (1986) 201.
3. P. Pinto da Silva, in K. R. Miller,Ed., Advances in Cell Biology. volume 1, London: Jai (1987) 157.
4. J. E. Rash et al, in S. W. Hui,Ed., Freeze-fracture Studies of Membranes, Boca Raton: CRC (1989) 41.
5. N. J. Severs, J. Electr. Microsc. Tech. (1989)13, 175; J. Microsc. (1991)161, 109.
6. N. J. Severs and H. Robenek, Biochim. Biophys. Acta (Reviews on Biomembranes) (1983)737, 373.
7. P. Pinto da Silva and F. W. K. Kan, J. Cell Biol. (1984)99, 1156.
8. C. Andersson Forsman and P. Pinto da Silva, J. Histochem. Cytochem. (1988)36, 1413;   M. Baetscher
et al, J. Cell Biol. (1986)103, 369;   W. T. M. Gruijters et al, J. Cell Biol. (1987)104, 565.
9. J. E. Dinchuk et al, J. Electr. Microsc. Tech. (1987)7, 1.
10. A. E. Semper and D. M. Shotton, in EUREM 88: Volume 3, Bristol & Philadelphia: IOP (1988) 3.
11. C. Andersson Forsman and P. Pinto da Silva, J. Cell Sci. (1988)90, 531.
12. S. Ru-Long and P. Pinto da Silva, Eur. J. Cell Biol. (1990)53, 122.
13. R. A. Coleman and J. B. Wade, J. Electr. Microsc. Tech. (1989)13, 216.

TECHNIQUE	TYPE OF SAMPLE	WHAT YOU SEE
Deep-etching— classical[3]	cell or membrane suspensions	labeled membrane surface adjacent to fracture face
Deep-etching — modern derivatives	cell cultures/suspensions	labeled surfaces (of membranes/other structures)
Label-fracture-section (Development of sectioned replica technique)[4]	isolated membranes	labeled membrane surfaces with replica of fracture face (in section)
Membrane perturbation by lipid binding agents[6]	cells, tissues	deformations in membrane structure serve as markers
Fracture-label[2]	tissues, cells	labeled (reorganized) membrane halves, cytoplasm, matrix (in replica or section)
Shadow-label[4]	cells, tissues	label on "protected" side of particle (as replica or in "sectioned replica")
Label-fracture[3,7]	cell suspensions	labeled membrane surface superimposed on replica of fracture face
LABELING AFTER REPLICATION (replica-stabilized membranes/cells)		
Replica-staining label-fracture, replica-label-whole mount, post-release fracture-labeling, FRIL.[8,4]	cell, membrane suspensions; cultured cells; whole tissue	labeled membrane surface superimposed on fracture face
Replica-label-section[9]	cell suspensions	labeled membrane surface superimposed on replica of fracture face (in section)
Cryosectioned replica[10]	whole tissue (muscle)	labeled cytoplasm + replica of fracture face (in cryosection)
TURNING OVER REPLICA-STABILIZED MEMBRANES/CELLS		
Fracture-flip[11]	cell suspension	label + replica of membrane surface
Composite replica[13]	whole tissue, luminal membrane	label & rotary replica of E-surface of membrane superimposed on standard E-face replica
Simulcast[12]	cell suspensions	labeled E-surface of membrane with side-by-side replicas of surface and fracture face

IMMUNOLOCALIZATION OF PHOSPHOLIPIDS USING FREEZE-FRACTURE CYTOCHEMISTRY

Frederick W.K. Kan[1] and Joyce Rauch[2]

[1]Department of Anatomy, University of Montreal, C.P.6128, Succ.A, Montreal, Quebec, Canada H3C 3J7 and [2]The Division of Rheumatology, The Montreal General Hospital Research Institute, McGill University, Montreal, Quebec, Canada H3G 1A4

Phospholipids are found ubiquitously in all mammalian cell membranes. The fracture-label technique offers the opportunity to localize phospholipids in tissues and cells.[1] This technique has recently been used in combination with colloidal-gold-conjugated phospholipase A_2 to demonstrate the presence of phospholipids in epithelial tight junctional strands.[2] In the present study, we show the localization of specific phospholipids in the plasma and intracellular membranes in the rat exocrine pancreatic cells using murine monoclonal anti-cardiolipin (CL) antibodies that are reactive with phosphatidylethanolamine (PE) and have lupus anticoagulant activity. These antibodies were produced from BALB/c mice immunized with either ADP-activated murine platelets or CL mixed with apolipoprotein H.[3]

Pancreatic tissue was excised from adult male Sprague-Dawley rats under light ether anesthesia and fixed by immersion with 1% glutaraldehde in 0.1 M cacodylate buffer. The tissue was trimmed into 1-mm cubes which were then embedded in 30% bovine serum albumin in 0.01 M PBS, and cross-linked with a final concentration of 1% glutaraldehyde to form a hardened gel. The gels containing the tissue were sliced into blocks of approximately 1x2x2 mm, infiltrated overnight with 30% glycerol in PBS, and then frozen in Freon 22 cooled by liquid nitrogen. For immunolabeling, the frozen gels, after freeze-fracture and thawing,[2] were incubated for 2 hr at room temperature in 250 μl of monoclonal anti-CL antibody followed by incubation in goat anti-mouse IgG+IgM at 1:80 dilution for 1 hr at room temperature. After labeling, the gels were dried by the Peldri II sublimation method.[4] Peldri II-sublimated samples were mounted on double-adhesive tape with the fracture-face up, on a Balzers-type specimen table and shadowed with platinum, followed by coating with carbon in a Balzers freeze-fracture unit. The replicated samples, upon digestion in sodium hypochlorite solution to remove tissue debris, were washed, mounted on Parlodion-coated grids and examined with a Philips 300 transmission electron microscope operated at 80 kV.

Fracture-label preparations reveal preferential labeling of the protoplasmic fracture-face of the apical and basolateral plasma membranes by the monoclonal antibody, the labeling appearing as discrete patches of gold particles on these freeze-fractured membrane halves (not shown). Similar patches of gold particles are also observed over freeze-fractured nuclear envelope membranes (Fig.1). While a majority of the freeze-fractured zymogen granule membrane halves are not labeled, the exoplasmic and protoplasmic membrane halves of some zymogen granules display patches of gold particles (Fig.1). The content of the granules and the acinar lumen are also labeled strongly with gold particles. In addition, a high concentration of gold particles is also found associated with mitochondria (Fig.2) and the euchromatin of the nucleus (Fig.1). Since the monoclonal antibodies used in this study react with hexagonal$_{II}$-phase PE, these preliminary results suggest that our induced monoclonal antibodies, when used in combination with the fracture-label technique, will be excellent probes for the localization of hexagonal$_{II}$-phase phospholipids in cell membranes.[5]

References

1. P.A. Coulombe, F.W.K. Kan and M. Bendayan, Eur. J. Cell Biol. (1988)46,564.
2. F.W.K. Kan, J. Histochem. Cytochem. (1993) In press.
3. J. Rauch, A.S. Janoff, J. Rheumatol. (1992)19,1782.
4. F.W.K. Kan, J. Electron Microsc. Tech. (1990)14,21.
5. This work was supported by grants from the Medical Research Council of Canada.
   Drs. F.W.K. Kan and Joyce Rauch are chercheur-Boursiers from the Fonds de la recherche en santé du Québec.
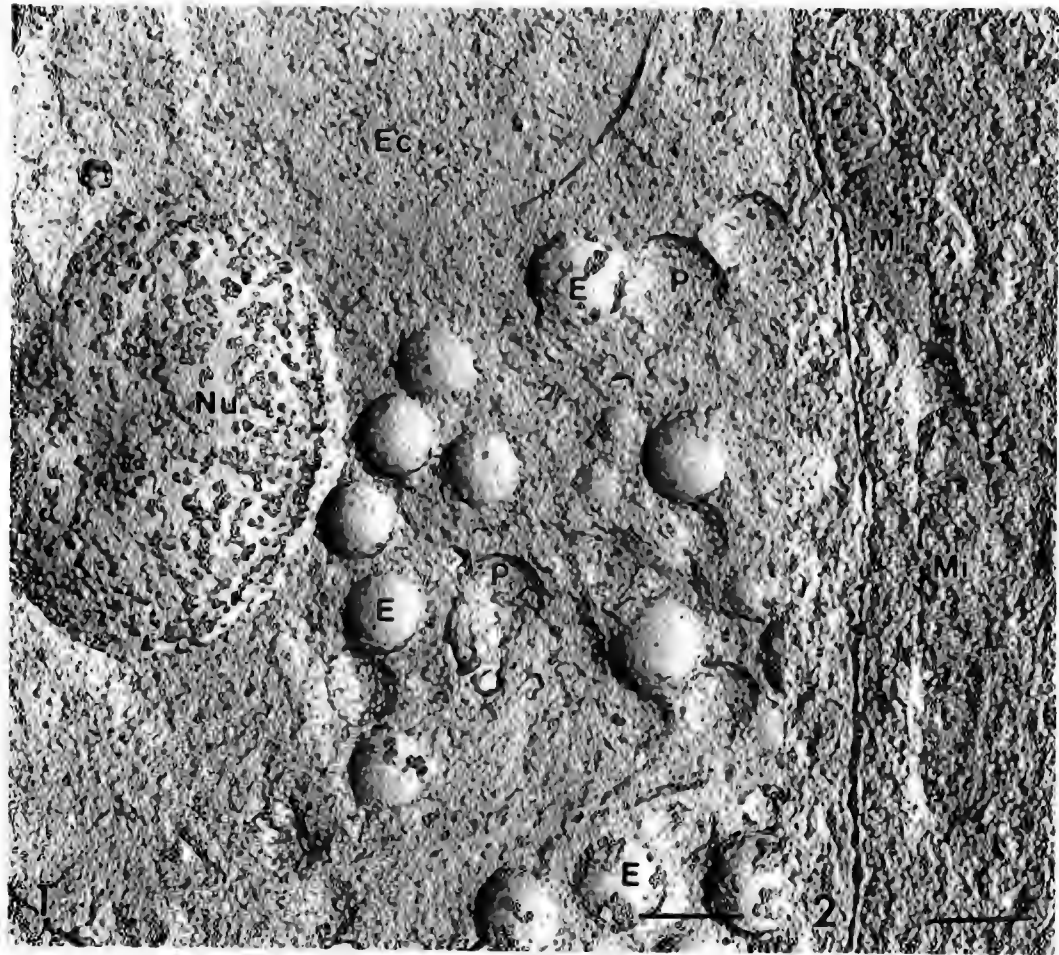
FIG. 1.--Fracture-label replica showing immunolabeling of an exocrine pancreatic cell by a monoclonal anti-cardiolipin antibody. Nu, protoplasmic fracture-face of the inner nuclear envelope membrane; Ec, euchromatin; E and P, exoplasmic (E) and protoplasmic (P) fracture-face of the zymogen granule membrane. Bar = 1μm.

FIG. 2.--High magnification of a cross-fractured mitochondrion (Mi) showing immunolabeling of the cristae by gold particles. Bar = 0.5μm.

"GRID-MAPPED" FREEZE-FRACTURE: THREE-DIMENSIONAL CONFOCAL LASER SCANNING MICROSCOPY FOR DIRECTED FRACTURING AND HISTOLOGICAL MAPPING OF NEURONS IN SPINAL CORD AND BRAIN

J. E. Rash, L. R. Whalen, P. B. Guthrie, M. Morita, R. Dillman, and D. Fay-Guthrie

Department of Anatomy and Neurobiology, Colorado State University, Fort Collins, CO 80523

A new correlative microscopic technique, "grid-mapped" freeze fracture, is introduced. This technique allows individual cells in histological slices to be freeze fractured, and their ultrastructural details to be correlated with conventional histological and gross anatomical features. Adult male rats were anesthetized, the sciatic nerve was exposed and crushed, and rhodamine-filled latex microspheres (Lumafluor, Inc) were injected at the crush site to label motor neurons. After 3-7 days, rats were fixed by whole-body perfusion. The brains and spinal cords were removed, embedded in 5% gelatin, and 50 or 100 μm thick slices were cut with a Vibratome. Slices were mapped in three-dimensions (**Figs. 1-2** and **3-4**) using a Molecular Dynamics Multiport 2001 confocal microscope, and the depths of selected cells were measured ($\pm 2\mu$m) from the cut surfaces. After freezing on gold specimen supports, the fracture plane was directed through selected neurons using the precise planar microtome of the JEOL JFD-9000-CR freeze-fracture machine. After replication, frozen samples were transferred to a -100°C cold chamber containing dry nitrogen gas. Gold "London Finder Grids" were dipped in 1-3% Lexan dissolved in ethylene dichloride and placed on the frozen specimens.[1] After the Lexan/solvent was frozen, the tissue/replica/Lexan/Finder-grid "sandwiches" were placed in a -30°C freezer for three hours to allow the solvent to melt and evaporate without infiltrating the frozen (aqueous) samples. Samples were then thawed and re-mapped by confocal microscopy (**Figs. 3-5**). Portions of some labeled neurons were confirmed to have been removed by freeze fracturing. (For example, compare the shapes of neurons in **Fig. 2** [arrowheads] with their remnants in **Fig. 4**). The grid/Lexan/replica "sandwiches" were cleaned using conventional bleach and chrome/sulfuric acid cleaning solutions. (Copper grids would not survive standard replica cleaning procedures.) The clean replica surfaces were re-coated with 6-10 nm of carbon (to bridge cracks in the replica films) before the Lexan support films were removed. To avoid displacing the replicas, the edge of the Lexan/replica/grid "sandwich" was briefly brought three times into contact with the surface of a pool of ethylene dichloride. Grids were air dried between each step, then inverted and immersed for 2-5 minutes in fresh ethylene dichloride. After removal of the Lexan support film, unfragmented, undisplaced replicas as large as 2 x 2 mm remained, each easily correlated by light and electron microscopies (compare **Figs. 5** and **6**). These "grid-mapped" freeze-fracture replicas allow unambiguous histological localization of freeze-fractured neurons, as well as the histological mapping of their neuritic processes. Spinal cord neurons linked by gap junctions (**Fig. 7**) were identified as unlabeled neurons among the motor neurons contributing to the sciatic nerve. Gap junctions were also found linking neurons and interneurons in Laminae VI and VII. (Arrowheads in **Fig. 8** designate positions of neurons found to be linked by gap junctions). "Grid-mapped" freeze fracture is useful for identifying neuron types that are localized in discrete layers, as in the dentate gyrus of the hippocampus (**Fig. 9**). It would be equally useful in other tissues where mixed cell populations prevent easy identification of cells by "conventional" freeze-fracture methods.

1. R.L. Steere and E.F. Erbe. *Proc. Ann. EMSA Meeting 41* (1983):618.
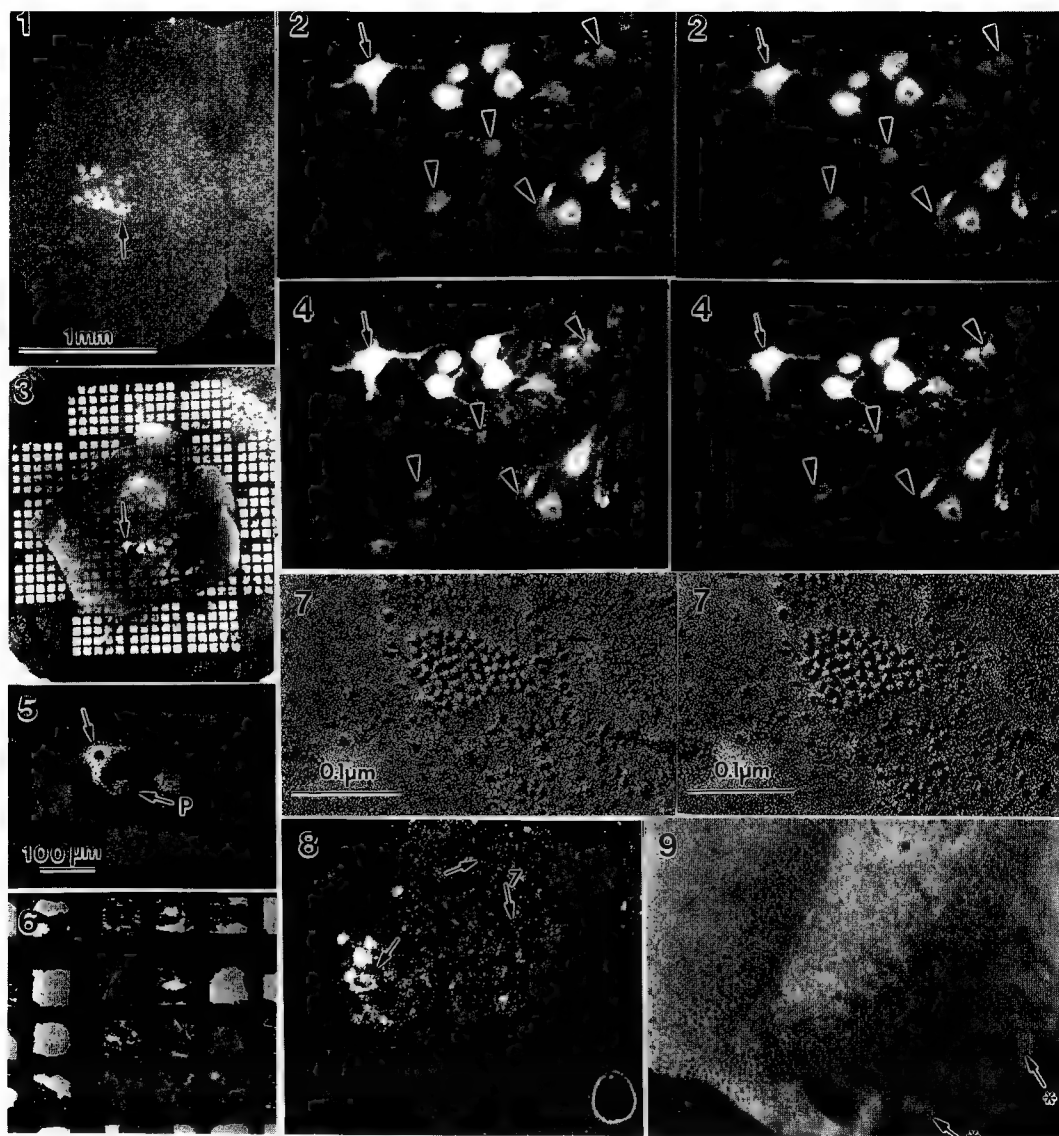
Fig. 1. Cross section of spinal cord from region L5. For orientation in subsequent micrographs, the area with labeled neurons is rotated 180°. **Fig. 2.** Stereoscopic confocal images obtained <u>before</u> freeze fracture. Cells indicated by arrowheads were cleaved and replicated, and portions of each are confirmed to be missing in Fig. 4. **Fig. 3.** The same spinal cord slice after freeze-fracture replication and mounting on a gold "London Finder" grid. Lettered grid openings permit exact correlation of confocal and freeze-fracture images (compare Figs. 5 and 6). **Fig. 4.** Arrowheads indicate cells that were cross-fractured and delineate the approximate fracture plane. **Figs. 5-6.** Finder Grid letter "P" is faintly discernable in the confocal micrograph, but is well resolved in the TEM image, and serves as a useful fiducial mark. **Fig. 7.** At moderately high magnification, a single small gap junction is seen on the neuron P-face. **Fig. 8.** Composite locations of gap junctions (arrows) mapped onto single confocal image of ventral horn. **Fig. 9.** "Grid-mapped" replica of dentate gyrus. Arrows point to faintly-resolved grid bars.

65

COMPARISON OF IVEM AND QUICK-FREEZE, DEEP-ETCH, ROTARY SHADOW IMAGES OF THE CELL CYTOPLASM

Carolyn A. Larabell

West Coast Facility for Intermediate Voltage Electron Microscopy, Lawrence Berkeley Laboratory, University of California, Berkeley 94270

The techniques of freeze-fracture and quick-freeze, deep-etch, rotary-shadow electron microscopy have provided information about cellular structures that cannot be obtained from thin section electron microscopy. Freeze-fracture replicas provide extensive views of membranes and the arrangement of integral membrane proteins, but filamentous structures such as the cytoskeleton and extracellular matrix are not visualized because they are embedded in ice. In order to visualize such fine structures, it is necessary to deeply etch (or freeze-dry) cells that have been rapidly frozen, thus revealing about 0.1 to 0.3 μm of three-dimensional structure. Replicas of cells prepared in this fashion provide excellent high magnification views of the individual filaments and their interactions with the plasma membrane as well as with membrane-bounded organelles. Another excellent method for visualization of cytoskeletal structures is whole mount electron microscopy. In this paper, I describe views of the egg cytoskeleton obtained from visualization of the isolated egg cortex prepared as a whole mount at 400 kV and compare these results with those obtained from replicas of cells that have been rapidly frozen then fractured and deeply etched. These data point out the advantages of using a combination of these two techniques to provide a comprehensive examination of cellular ultrastructure.

The egg cortex is a unique region of the cell with a specialized structure and function. We recently devised a technique for isolation of the cortex of the large *Xenopus laevis* egg for viewing as a whole mount in the IVEM. The resulting images demonstrate excellent three-dimensional views of the cortical cytoskeleton (Figure 1). The cortex of this egg is between 3-5 μm thick, and stereo micrographs reveal three-dimensional views of cytoskeletal filaments that are in focus throughout the depth of this preparation. These images demonstrate the presence of a meshwork of filaments subjacent to the plasma membrane and also demonstrate a complex interaction of filaments that interconnect cortical organelles and secure them to the submembranous cytoskeleton (Figure 1). These whole mounts facilitate visualization of the entire cortical region of one-half of this large egg (which is approximately 1.2 mm in diameter) on a single grid, and provides an excellent system for electron microscopical analyses of the modifications that occur during development. These specimens are, however, very sensitive to beam damage and must be visualized at relatively low magnifications. To obtain high magnification images of the individual filaments within the cortex, as well as the components of the granules, we analyzed replicas of eggs prepared using quick-freeze, deep-etch, rotary shadow electron microscopy (Figure 2). These images provide excellent views of the individual filaments and their interactions with the cortical granule and plasma membranes. They also provide views of the arrangement of proteins within the secretory granules. A combination of these two techniques provides the global views of the cytoskeletal network as well as high magnification views of the individual cytoskeletal filaments.
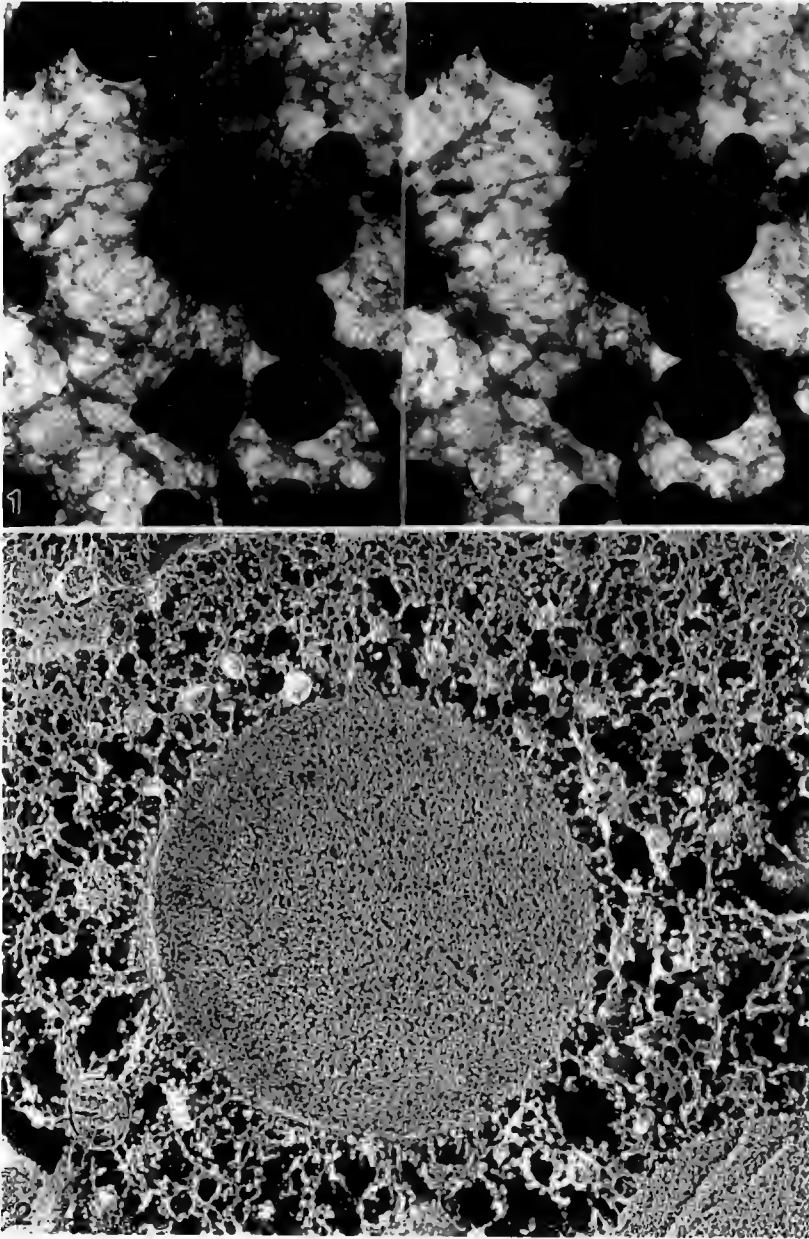
FIG. 1. Stereo micrographs of the isolated *Xenopus* egg cortex viewed as a whole mount at 400 kV. A dense meshwork of fibers can be seen subjacent to the plasma membrane. In addition, individual fibers are seen interconnecting the cortical organelles and securing them to the submembranous cytoskeleton. x 20,000.

FIG. 2. Quick-freeze, deep-etch, rotary-shadow replica of the *Xenopus* egg cortex showing interactions between a cortical granule and cytosplasmic proteins. x 50,000.

STM OF FREEZE-FRACTURE REPLICAS: PROBLEMS AND PROMISES

J. T. Woodward and J. A. N. Zasadzinski

Departments of Physics and Chemical Engineering, University of California, Santa Barbara, CA 93106

The Scanning Tunneling Microscope (STM) offers exciting new ways of imaging surfaces of biological or organic materials with resolution to the sub-molecular scale. Rigid, conductive surfaces can readily be imaged with the STM with atomic resolution. Unfortunately, organic surfaces are neither sufficiently conductive or rigid enough to be examined directly with the STM. At present, non-conductive surfaces can be examined in two ways: 1) Using the AFM, which measures the deflection of a weak spring as it is dragged across the surface, or 2) coating or replicating non-conductive surfaces with metal layers so as to make them conductive, then imaging with the STM. However, we have found that the conventional freeze-fracture technique, while extremely useful for imaging bulk organic materials with STM, must be modified considerably for optimal use in the STM.

In principle, the STM operates by measuring the tunneling current between a conductive tip and a conductive sample across a vacuum gap. However, unless the measurement is carried out in high vacuum environments, there is a liquid film of contamination that physically connects the STM tip with the sample. This mechanical coupling can lead to STM images with exaggerated height measurements. Simple modifications to TEM freeze-fracture replicas including a 0.1 micron backing layer of silver and mounting the replicas on a fine-mesh silver filters eliminate much of the height amplification.[1] If we then image the sample in a controlled environment, we can obtain reliable measures of feature heights.

STM imaging was done using a Nanoscope II STM enclosed in a sealed belljar. The belljar was evacuated with a rotary pump and a cold trap to approximately .1 torr before backfilling with dry nitrogen. To test whether eliminating the condensed contamination layer would also eliminate surface amplifications we examined Langmuir-Blodgett films of cadmium arachidate (CdA) with well-known step heights. The majority of the islands are a bilayer different in height from the surrounding area. The height of the bilayer is known from X-ray and AFM measurements to be 5.5 nm.[2] Platinum carbon replicas of the reorganized surfaces of CdA were made as described previously.[1] Ten images taken with three different tips gave 28 bilayer height measurements. The mean bilayer height was 5.1 ± 0.4 nm, in good agreement with the expected bilayer thickness (See Fig. 1a). Seventy percent of the measurements fell within eight percent of the mean, which is similar to the errors in measuring the films directly with the AFM.[2] There was no difference in heights measured with different tips. The chamber was then opened to air and several more images were taken. We then began flushing the system with dry nitrogen while taking more images. Fig. 1b shows the effect of just four minutes exposure to air. The height difference between the background and the bilayer 'hole' increased by 17% and several of the small features on the background show a significant increase in apparent height. The difference between the highest and lowest points (z-range) in the image has increased from 18.6 nm in Fig. 1a to 40.0 nm in Fig. 1b. Fig. 1c was taken after a few minutes of flushing the belljar with nitrogen. The step height has lowered to only 8.5% greater than its original value and the z-range was 26.4 nm. After about 30 minutes of flushing with dry nitrogen, the image heights returned to their original values.

This revised STM-replica technique provides us with simple, repeatable measures of surface feature heights, providing that precautions are taken to avoid feature distortions due to contamination. The cadmium arachidate multilayers provide a well characterized calibration for the 5 nm range that will be useful for our continuing investigations of bilayer structure and topology.[3]

1. J. T. Woodward, J. A. Zasadzinski, and P. K. Hansma, *J. Vac. Sci. Technol. B*, **9**, 1231 (1991)
2. D.K. Schwartz, R. Viswanathan, and J.A.N. Zasadzinski, *J. Phys. Chem.*, **96**, 10444 (1992).
3. This work was supported by ONR grant #N00014-90-J-1551 and NSF grant #CTS-9212790.
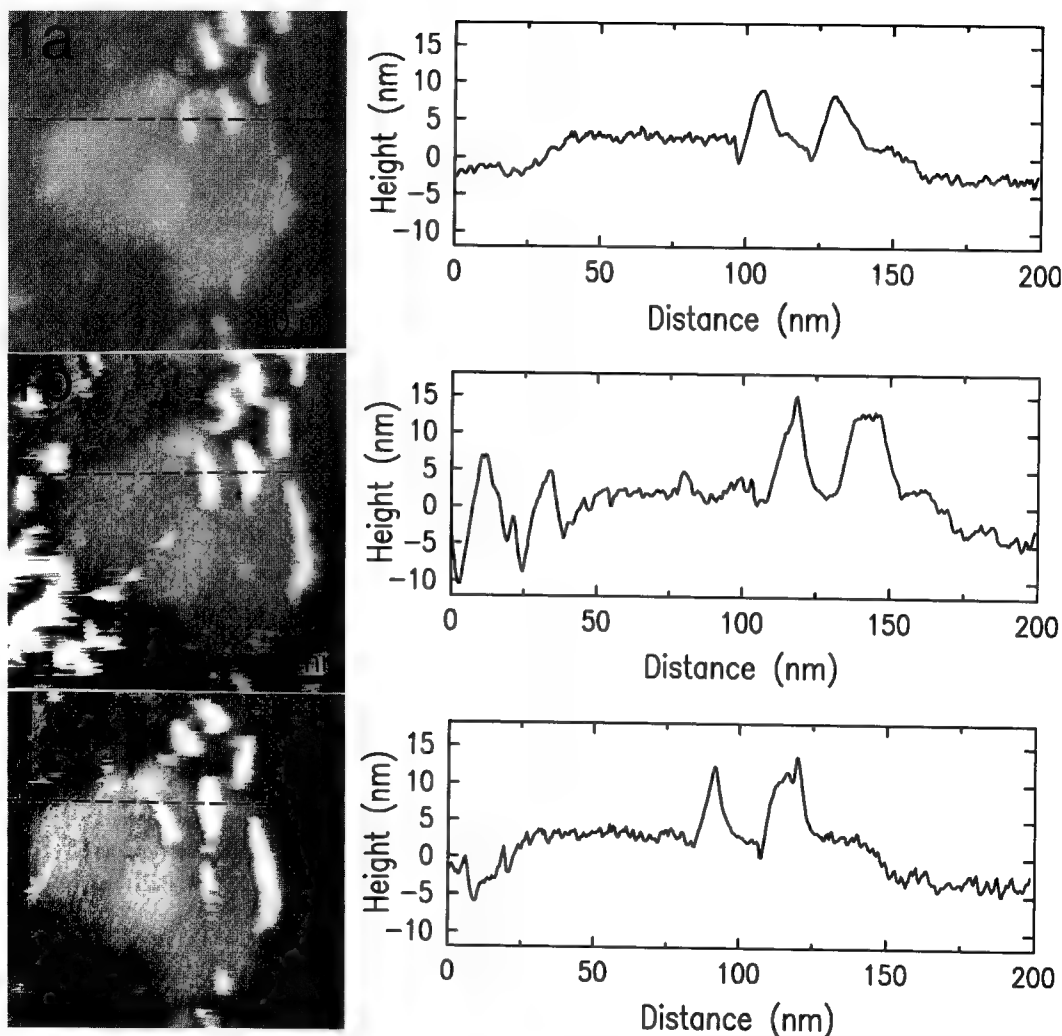
FIG. 1a. STM image of freeze-fracture replica of reorganized cadmium arachidate (CdA) multilayer film.[2] The film consists of discrete bilayer islands with a well defined bilayer steps between layers. This replica was imaged after the belljar surrounding the STM was evacuated to 0.1 torr for 1 hour and backfilled with dry nitrogen. The measured step heights were 5.1 ± 0.4 nm, in good agreement with AFM and X-ray results and the step heights were independent of tip and stable for hours.

Fig. 1b. STM image of same area as Fig. 1a except that the belljar was open to lab air for 4 minutes before imaging. The surface feature heights are amplified and several "new" features have appeared.

Fig. 1c. STM image of the same area as Figs. 1a and 1b, after the belljar was flushed with dry nitrogen for 30 minutes. The feature heights and general sample topography have returned to those in Fig. 1a.

PLATINUM SHADOWING, COMPLEMENTARY IMAGING AND STEREO ANALYSIS: TECHNIQUES DEVELOPED FOR TEM CAN NOW BE USED TO INCREASE THE RESOLUTION OF FROZEN HYDRATED SPECIMENS IN A SEM

William P. Wergin and Eric F. Erbe

Electron Microscopy Laboratory; ARS-BARC; Beltsville, MD 20705-2350

In 1957, Steere froze virus crystals, fractured and transferred them to a vacuum evaporator where they were etched, shadowed and coated.[1] The coating, which was then removed from the tissue and mounted on a grid, represented a replica that could be observed in the transmission electron microscope (TEM). This accomplishment is regarded as the first successful biological application of the freeze-etching technique in electron microscopy.[2] This technique was further advanced by describing procedures whereby the replicas from both surfaces of a frozen, fractured sample could be recovered.[3] This pair of replicas provided additional surface information by allowing one to view and compare the two opposing surfaces, or the complementary images, of a freeze-fractured biological specimen. Using a goniometer stage the replicas were also photographed, tilted and rephotographed to produce stereo pairs that could be used to analyze three-dimensionally the surface characteristics of the replica.[4] Until recently these TEM techniques have been the principle procedures utilized by biologists to gain high resolution structural details about virus crystals, biological membranes and a wide range of other material.

The first commercial scanning electron microscopes (SEM) were introduced in 1965 but the resolution of these early instruments did not rival that from the TEM replica techniques. However in 1989, a new generation of field emission (FE) SEMs, which had resolution of less than 1 nm, provided biologists with an instrument that had the potential resolution to challenge the TEM replica techniques. Our initial use of this type of instrument enabled us to view platinum/carbon (Pt/C) replicas and resolve particles on the P-face of the plasma membrane of yeast.[5,6,7] To determine whether this type of resolution could be attained on hydrated samples, a Hitachi S-4000 FE SEM was equipped with an Oxford CT 1500 Cryotrans System. This combination of instrumentation allowed us to freeze, fracture, coat and observe frozen, hydrated biological samples. The initial results appeared to be limited by the standard sputter coating procedure that was employed in the cryosystem, however they encouraged us to return to the high vacuum evaporator for Pt/C coating to evaluate the resolution of hydrated freeze-etched specimens. This combination of techniques was used to examine the freeze-etched membranes of a fractured, frozen, hydrated yeast suspension where resolution was sufficient to observe intramembrane particles similar to those that had been earlier observed on the replicas that were examined at ambient temperature.[8,9] Use of high vacuum evaporation of Pt/C in conjunction with low temperature FESEM provided useful resolution up to 100,000X. An additional advantage of this approach was that after these specimens were observed in the low temperature FESEM, their coatings, which consisted of Pt/C replicas, could be recovered from the frozen tissues and subsequently observed in the TEM. Comparison of these two electron imaging techniques allowed one to ascertain the distortion that occurs when a replica was recovered from the three-dimensional surface of a fractured specimen and was then mounted and dried onto a grid for TEM observations. For example, some membrane invaginations that followed the contour of the fractured cell in the frozen, low temperature FESEM image appeared up to 30% shorter than the same structures that occurred in the dried and flattened replica.[10]

By modifying specimen holders, both halves of a fractured sample could be retained for FESEM observation. Furthermore, the complementary images of frozen, fractured, fully hydrated cells could be observed in the low temperature FESEM and then compared to the complementary images of the identical cells that were present in the replicas that were recovered from the frozen specimens and subsequently observed in the TEM.[10] Being able to evaluate, compare and contrast data from these two different EM imaging techniques as well as from complementary surfaces, further helped to assess the resolution of coating films, the presence of contaminants and the three-dimensional distortion in replicas.

The gold holders that were used to retain both halves of fractured samples for SEM examination also had other advantages. Opening these hinged holders to fracture the specimen was superior to utilizing the knife or pick that is normally used for this purpose in low temperature SEM. The gold holders, provided a clean fractured surface that appeared to be relatively free from pre-fractures, multiple fractures, scrapes, scratches and fracture debris. For these reasons use of the hinged holders was considered advantageous even when complementary pairs were not desired. The low temperature FESEM technique was faster and simpler than the procedures that were required to produce and view replicas in the TEM where complementary imaging was more difficult and tedious. TEM replicas frequently inverted, rotated, fragmented and/or folded so that systematically recovering large replicas of complementary areas on a grid was not possible for many materials. Complementary imaging in the low temperature FESEM also allowed one to view and assess more accurately vast areas of fractured specimens that exhibited considerable surface topography due to the nature of the fracture or the composition of the tissue. The complementary areas that could be compared on TEM replicas were limited to the size of the replica that could be recovered rather than on the size of the specimen that was fractured. Extensive water and/or air spaces that were present in specimens from food, insects or plants contributed considerably to the topography of the fractured tissue; however they did not interfere with observation of the frozen complements in the SEM. Alternatively, extensive air spaces that were present in the fractured specimens frequently interfered with complete shadowing and coating of the surface; consequently holes and other discontinuities hindered the recovery and observation of the intact replicas for TEM observation. Finally, the gold holders permitted tilting the specimens for observing, recording and analyzing the specimens in three dimensions.

In conclusion, Pt shadowing, complementary imaging and stereo observation - the high resolution techniques that Dr. Russell L. Steere and others had developed nearly 35 years ago for TEM - are now being successfully applied to the SEM in an effort to further increase our knowledge and understanding of biological ultrastructure.

References:

1.   R. L. Steere, J. Biophys. Biochem. Cytol. 3(1957)45.
2.   C. Stolinski and A. S. Breathnach, Freeze-fracture replication of biological tissues, New York: Academic Press, (1975)173.
3.   R. L. Steere and J. M. Moseley, Proc. Ann. EMSA Meeting 27(1969)202.
4.   R. L. Steere, Proc. Ann. EMSA Meeting 29(1971)242.
5.   W. P. Wergin and E. F. Erbe, Proc. Roy. Microscopical Soc. 24(1989)S40.
6.   W. P. Wergin and E. F. Erbe, Inst. Phys. Conf. Ser. 98(1990)715.
7.   W. P. Wergin and E. F. Erbe, Scanning 12(1990)I69.
8.   W. P. Wergin and E. F. Erbe, Proc. Ann. EMSA Meeting 49(1991)514.
9.   W. P. Wergin and E. F. Erbe, Scanning Microsc. 5(1991)927.
10.   W. P. Wergin and E. F. Erbe, Scanning 14(1992)17.

MOLECULAR FEATURES OF HETEROCHROMATIN CONDENSATION

B.A. Hamkalo,[*] K. Lundgren,[**] M.H. Parseghian,[*] M.Z. Radic,[***] and M. Saghbini[****]

[*] Department of Molecular Biology & Biochemistry, University of California, Irvine, CA 92717
[**] Cold Spring Harbor Laboratory, Cold Spring Harbor, NY 11724
[***] Department of Microbiology & Immunology, Medical College of Pennsylvania, Philadelphia, PA 19129
[****] Department of Biology, University of California, San Diego, La Jolla, CA 92093

Eukaryotic chromosomes are nonuniformly condensed in both interphase and metaphase. This difference is most apparent in mitotic chromosomes in which centromeric heterochromatin is distinguishable from euchromatic arms because of a higher degree of condensation. This difference prevails in interphase and has led to the designation of this type of heterochromatin as "constitutive". Differences in condensation presumably are a consequence of differential stability of higher order chromatin structure. Since higher order structure is likely to be due to distinctive DNA-protein and protein-protein interactions, our goal is to identify components of such interactions as a first step in understanding the molecular basis for differential chromatin condensation.

Analysis of the structure of the mouse major centromeric satellite DNA revealed the presence of stable DNA curvature which could be reversed if certain small ligands which recognize a sequence motif common to this highly repeated DNA were bound to the DNA. In addition, growth of cells in the presence of these ligands prevented complete condensation of centromere regions of metaphase chromosomes (Fig.1).[1] Based on these results, we hypothesized that ligand-DNA interactions inhibited or reduced the binding of one or more chromosomal proteins that were involved in condensation. One conserved nonhistone chromosomal protein that exhibits the properties predicted to be required for competition binding is a member of the high mobility group of proteins named HMG-I. We showed that pure HMG-I binds to mouse satellite at sites which overlap those recognized by the small chemical ligands and that the ligands could compete for binding to the satellite *in vitro*.[2]

A second conserved chromosomal protein known to be involved in chromatin condensation is histone H1. Since this protein exists in 4-5 distinct isoforms in each cell, it is possible that each isoform possesses a distinct and differential ability to condense chromatin. In fact, a heterochromatin-preferred isoform has been identified in the midge, Chironomous.[3] In order to evaluate the possible functional differences among H1 subtypes in vertebrates we have developed a large-scale preparative scheme for the purification of each of the 4 human subtypes and generated a series of antibodies, each of which recognizes only one subtype. Whole
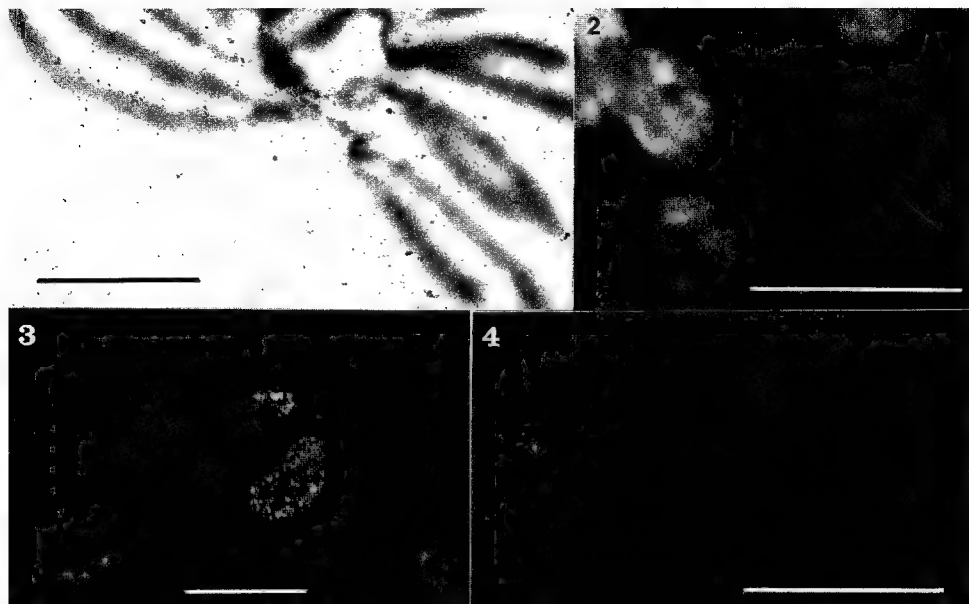
Fig. 1.   EM of Hoechst-treated mouse chromosomes. Bar = 5um.
Figs. 2-4.   Immunofluorescent localization of human histone H1 in
nuclei: total H1 (2); H1-2 (3); H1-3 (4). Bars = 25um.

----

cell immunofluorescence has been used to determine the distribution
of subtypes.   Figures 2-4 show some of these results.   Figure 2 is
the   distribution   of   total   H1   which   corresponds   with   the
distribution of DNA whereas Figures 3 and 4 show staining with 2 of
the antibodies that give distinct and non-uniform patterns.   Work
is   currently   in   progress   to   immunoselect   chromatin   fragments
containing each subtype to determine the types of DNA sequences
associated with each.

References

1. M.Z. Radic, K. Lundgren and B.A. Hamkalo Cell (1987)50,1101.
2. M.Z. Radic, M. Saghbini, T.S. Elton, R.Reeves and B.A. Hamkalo
Chromosoma (1992)101,602.
3. E. Mohr, L. Trieschmann and U. Grossbach PNAS (1989)86,9308.

THE IN VIVO DISTRIBUTION AND DYNAMICS OF DNA TOPOISOMERASE II IN DROSOPHILA EMBRYONIC NUCLEI AND CHROMOSOMES

Jason R. Swedlow*, Neil Osheroff#, Tim Karr@, John W. Sedat*, David A. Agard*

#Dept. of Biochemistry, Vanderbilt University, Nashville, TN, 37232-0146. @Dept. of Biochemistry, University of Illinois, Urbana, IL, 61801. *Graduate Group in Biophysics, Howard Hughes Medical Institute, Dept. of Biochemistry and Biophysics, University of California, San Francisco, San Francisco, CA 94143-0448

DNA topoisomerase II is an ATP-dependent double-stranded DNA strand-passing enzyme that is necessary for full condensation of chromosomes and for complete segregation of sister chromatids at mitosis *in vivo* and *in vitro*.[1-4] Biochemical characterization of chromosomes or nuclei after extraction with high-salt or detergents and DNAse treatment showed that topoisomerase II was a major component of this remnant, termed the chromosome scaffold.[5, 6] The scaffold has been hypothesized to be the structural backbone of the chromosome, so the localization of topoisomerase II to the scaffold suggested that the enzyme might play a structural role in the chromosome. However, topoisomerase II has not been studied in nuclei or chromosomes *in vivo*. We have monitored the chromosomal distribution of topoisomerase II *in vivo* during mitosis in the *Drosophila* embryo. This embryo forms a multi-nucleated syncytial blastoderm early in its developmental cycle. During this time, the embryonic nuclei synchronously progress through 13 mitotic cycles, so this is an ideal system to follow nuclear and chromosomal dynamics.

Fluorophore-conjugated topoisomerase II or anti-topoisomerase II monoclonal antibody was used to follow the *in vivo* distribution of topoisomerase II by fluorescence microscopy. Rhodamine-topoisomerase II was prepared as described.[7] Monoclonal antibody P2G3, an antibody which specifically recognizes *Drosophila* topoisomerase II and does not inhibit the activity of the enzyme *in vitro*, was used for these studies. Tetramethylrhodamine or Texas Red labeled antibody was prepared by standard methods.[8] *Drosophila* embryos were microinjected with labeled antibody during nuclear cycle 9-10. For the data shown in Figure 1, embryos were simultaneously injected with BODIPY-conjugated calf thymus histones H2A and H2B prepared as described.[9] The labeled proteins were allowed to incorporate into nuclei for one mitotic cycle (~10 minutes). Time-lapse three-dimensional images of the distribution of labeled antibody and histones were then recorded using a charge-coupled device (CCD) -based wide field optical sectioning microscope. Imaging was done in two modes: at high resolution, or 12 256 x 256 pixel optical sections, each with a 100 ms exposure, separated by 0.5 μm in focus, and imaged with an Olympus 60x/NA1.4 lens; or low resolution, or 6 256 x 256 optical sections binned 4x4 on the CCD, each with a 100 ms exposure, separated by 1.0 μm in focus, and imaged with an Olympus 40x/NA1.3 lens. Low resolution images were deblurred using a two-dimensional deconvolution of projections of each three-dimensional data set.[10] High resolution images were deblurred by full three-dimensional deconvolution of each data set.[7] Both methods used empirical point-spread functions. For the dual wavelength imaging shown in Figure 1, two images were sequentially taken at each focal plane by switching bandpass fluorophore excitation and emission filters mounted on computer-driven motorized wheels.[11]

Labeled anti-topoisomerase II is a component of nuclei and chromosomes throughout the cell cycle (Fig. 1). However, whereas the intensity of histone staining increases as the nuclei enter metaphase, the intensity of chromosomal anti-topoisomerase II staining decreases during the transition from prophase into metaphase (Fig. 1D). Simultaneously, the cytoplasmic anti-topoisomerase II intensity increases, indicating that topoisomerase II leaves the chromosomes and diffuses into the cytoplasm. Another loss of anti-topoisomerase II concentration is observed after mitosis during anaphase (Fig. 1F). These losses occur after the completion of two important functions of topoisomerase II:

chromosome condensation and segregation. Similar results were obtained using rhodamine labeled topoisomerase II.[7] Therefore it appears that there are at least two populations of topoisomerase II in the chromosome which may function separately in chromosome condensation and segregation. Interestingly, a third pool exists which remains associated with the chromosome throughout the mitotic cycle. This pool may be the topoisomerase II detected in scaffold preps and therefore might be enzyme which serves to organize the chromosome. Nonetheless, quantification of the chromosomal loss of topoisomerase II during mitosis shows that approximately 70% of topoisomerase II present in the prophase chromosome is lost during mitosis.[7] Thus the majority of the enzyme is not required for the structural integrity of the chromosome.

References

1. T. Uemura et al., Cell (1987)50, 917.
2. C. Holm et al., Cell (1985)41, 553.
3. Y. Adachi et al., Cell (1991)64, 137.
4. E. Wood and W. C. Earnshaw, J. Cell Biol. (1990)111, 2839.
5. W. C. Earnshaw et al., J. Cell Biol. (1985)100, 1706.
6. S. M. Gasser et al., J. Mol. Biol. (1986)188, 613.
7. J. R. Swedlow et al., Cell (1993)in press.
8. E. Harlow and D. P. Lane, Antibodies: a laboratory manual, Cold Spring Harbor: Cold Spring Harbor Laboratory (1988).
9. J. S. Minden et al., J. Cell Biol. (1989)109, 505.
10. Y. Hiraoka et al., Nature (1989)342, 293.
11. Y. Hiraoka et al., Semin. Cell Biol. (1991)2, 153.
12. This work was supported by the Howard Hughes Medical Institute (J. W. S. and D. A. A.) and by grants from the National Institutes of Health to J. W. Sedat (GM-25101) and D. A. Agard (GM-31627). We are grateful to Dr. Michael Paddy for providing BODIPY-histones.
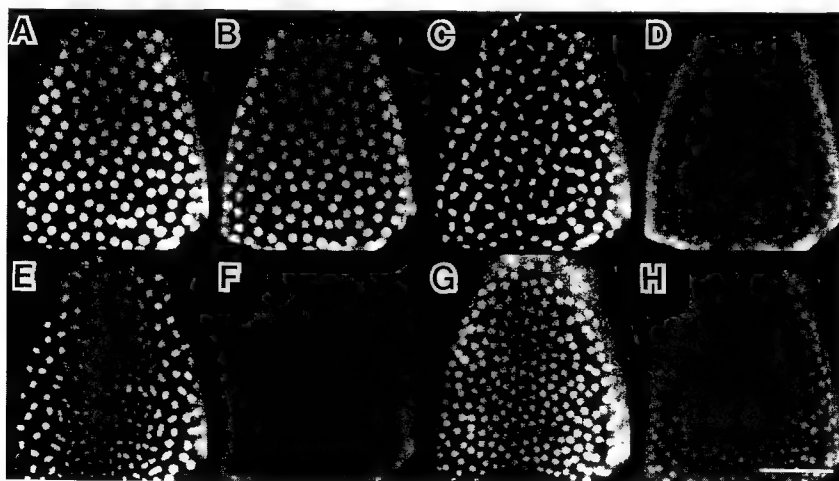
Figure 1. Low resolution dual-wavelength time lapse movie of histones and anti-topoisomerase II in a Drosophila embryo. Projections of 6 optical sections are shown. (A, C, E, G) BODIPY-histones H2A/H2B. (B, D, F, H) Texas Red-anti-topoisomerase II. (A, B) Interphase nuclear cycle 12. (C, D) Metaphase. (E, F) Anaphase. (G, H) Interphase nuclear cycle 13. Scale bar = 50 μm.

MICROTUBULE MOTORS ASSOCIATED WITH KINETOCHORES IN MITOTIC CELLS

Linda Wordeman

Department of Pharmacology, University of California, San Francisco, CA 94143

Chromosomes in dividing tissue culture cells exhibit three types of movement along mitotic spindle microtubules: 1)Fast minus-end directed movement (prometaphase), 2)Plus-end directed movement, and 3) Slow minus-end directed movement (anaphase) [1,2]. In all cases these movements are mediated by the kinetochore region of the centromere of mitotic chromosomes. This region consists of three domains based on both immunocytochemistry and electron microscopy. The outermost or kinetochore domain is composed of the distal fibrous corona and trilamminar plate. The central and pairing domains are located in the chromatin beneath the kinetochore.[3] Both plus-[4] and minus-end directed[5,6] microtubule motors have been localized to the kinetochore region of mitotic CHO chromosomes. I have used double-label immunocytochemistry to map the location of these motors within the centromere region at the level of the light microscope. Furthermore, I have cloned and expressed a number of novel kinesin-related motors, two of which (Clone 26 and Clone 14) are localized to kinetochores and kinetochore microtubules, respectively. I will discuss the interplay of these kinetochore-associated motors with respect to the movements of mitotic chromosomes in vivo.

Cytoplasmic dynein is a minus-end directed microtubule motor that has been localized to the corona region of the mammalian kinetochore.[7] I cloned several kinesin-related proteins from CHO cells in order to identify plus-end directed kinetochore-associated microtubule motors. One of these clones is associated with mitotic, but not interphase, kinetochores throughout mitosis (Figure 1). Another kinesin-related protein in which the motor domain is located at the COOH-terminal end of the protein (Clone 14) is found on kinetochore microtubules of the mitotic spindle (Figure 2). The COOH-terminal location of the motor domain of Clone 14 suggests that it may be a minus-end directed kinesin like the Drosophila homolog ncd[8]. Clone 14 is not found, however, on kinetochores or anywhere within the centromere on isolated chromosomes.

In contrast, Clone 26 is located, surprisingly, in the central and pairing region of the centromere, beneath the kinetochore plate (Figure 3). The labelling seen with anti-Clone 26 is similar to the pattern of tubulin monomers bound to isolated chromosomes (Figure 4). Clone 26 is more internally located, within the centromere, relative to cytoplasmic dynein (Figure 5). Perhaps Clone 26, which is a putative plus-end directed kinesin homolog located within the centromere, opposes the minus-end directed movement of kinetochore-associated cytoplasmic dynein. The activity of a plus-end directed motor may impose a drag on the minus-end directed velocity of dynein. This could explain the 10-fold slower rate of minus-end directed movement seen in anaphase, at which time many microtubules are firmly imbedded in the kinetochore plate.

References
1. C.L. Rieder and S.P. Alexander. J. Cell Biol. (1990) 110, 81.
2. T.J. Mitchison and E.D. Salmon. J. Cell Biol. (1992) 119, 569.
3. A.F. Pluta, C.A. Cooke and W.C. Earnshaw.TIBS (1990) 15, 181.
4. T.J. Yen, G. Li, B.T. Schaar, I. Szilak and D.W. Cleveland. Nature (1992) 359, 536.
5. C.M. Pfarr, M. Coue, P.M. Grissom, T.S. Hays, M.E. Porter and J.R. McIntosh. Nature (1990), 345, 263.
6. E. R. Steurer, L. Wordeman, T.A. Schroer, and M.P. Sheetz. Nature (1990) 345, 266.
7. L. Wordeman, E.R. Steurer, M.P. Sheetz and T.J. Mitchison. J. Cell Biol. (1991) 114, 285.
8. H.B. McDonald, R.J. Stewart and L.S. Goldstein. Cell (1990) 63, 1159.
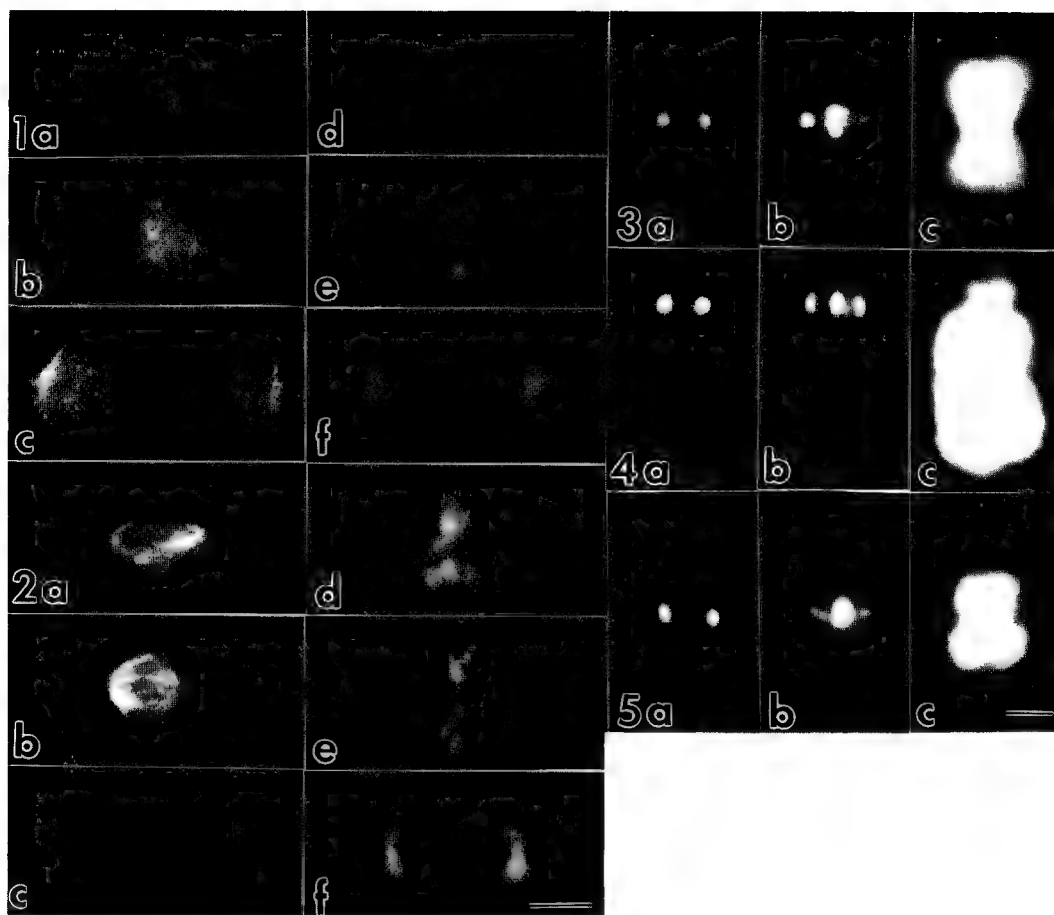
FIG. 1. --Indirect Immunofluorescence of mitotic CHO cells labeled with anti-Clone 26. a-c,
Clone 26; d-f Hoechst label of DNA. a,d, prophase; b,e, metaphase; c,f, telophase.
FIG. 2. --Indirect Immunofluorescence of CHO cells labeled with anti-Clone 14. a-c, Clone 14;
d-f Hoechst. a,d, prometaphase; b,e, metaphase; c,f, late anaphase. Bar = 6 microns.
FIG.3. --Isolated CHO chromosome double-labeled with CREST(a), Clone 26(b) and Hoechst(c).
FIG.4. --Isolated CHO chromosome, previously incubated in 0.5mg/ml tubulin, fixed then
double-labeled with CREST(a), Anti-tubulin(b) and Hoechst (c).
FIG.5. --Isolated CHO chromosome double-labeled with anti-dynein(a), Clone 26(b) and
Hoechst(c).

THE INCENPS: CHROMOSOMAL PROTEINS WITH AN ESSENTIAL CYTOSKELETAL ROLE DURING MITOSIS

Alastair M. Mackay, Calvin Chue, D. Mark Eckley, & William C. Earnshaw

Dept. of Cell Biology & Anatomy, Johns Hopkins University, Baltimore, USA

The INCENPs (INner CENtromere Proteins - M_r 133 and 145 kDa) are tightly bound to chromatin until early metaphase, and arrive at the metaphase spindle plate as integral components of the chromosomes (Cooke et al., 1987; Earnshaw & Cooke, 1991). It is thus surprising that the INCENPs leave the chromosomes during the latter part of metaphase to become associated with fibrous structures traversing the metaphase plate (presumably the overlapping polar microtubules of the spindle). Following the onset of anaphase, the INCENPs remain closely associated with the stem body material in the central spindle and also become associated with the inner surface of the cell membrane at the position where the cleavage furrow subsequently forms.

By combining library screening with reverse-transcriptase PCR, we have recovered cDNA clones that contain the complete open reading frames (ORFs) of the two chicken INCENPs. Class 1 INCENP cDNA contains an ORF of 839 codons, which includes a predicted central coiled-coil domain of about 200 residues. Class 2 differs primarily in having a 20 aa extension of the coiled coil domain. Both ORFs are hydrophilic and very basic along their lengths. The primary sequence of the INCENPs is completely distinct from those of other known proteins. To probe INCENP function in vivo, we placed the two classes of INCENP cDNAs into an expression vector that was transiently transfected into HeLa and LLCPK cells. The distribution of the full-length INCENPs in these cells recapitulated that of wild-type INCENPs in chicken cells. Further analysis revealed that the amino-terminal 41 residues direct INCENP targeting to the spindle midzone. In addition, the coiled-coil region appears to be required for the INCENPs to bind cytoplasmic microtubules. Thus, more than simple microtubule-binding activity appears to be required for INCENP movement to the spindle during metaphase. Certain INCENP expression constructs induced dominant negative phenotypes in recipient cells. Full-length wild-type Class 2 INCENP could prevent the progression of cells past telophase. In such cells, mitosis resulted in a single binucleate daughter cell. Deletion of the 57 carboxy-terminal residues also interfered with cell division, producing a range of negative phenotypes. In some cases, newly divided cells rejoined to form binucleate cells, while other daughters underwent lysis shortly after mitosis. These phenotypes implicate the INCENPs in the process of cytokinesis.

These results lend support to the notion that INCENPs and other members of the class of *chromosome passenger proteins* (Earnshaw & Bernat, 1990) may be brought by chromosomes to the metaphase plate so that they are correctly positioned to perform essential cytoskeletal functions later in mitosis.

COOKE, C. A., HECK, M. M. S. & EARNSHAW, W. C. 1987. *J. Cell Biol.* **105**, 2053-2067.
EARNSHAW, W. C. & BERNAT, R. L. 1990. *Chromosoma (Berl.)* **100**, 139-146.
EARNSHAW, W. C. & COOKE, C. A. 1991. *J. Cell Sci.* **98**, 443-461.
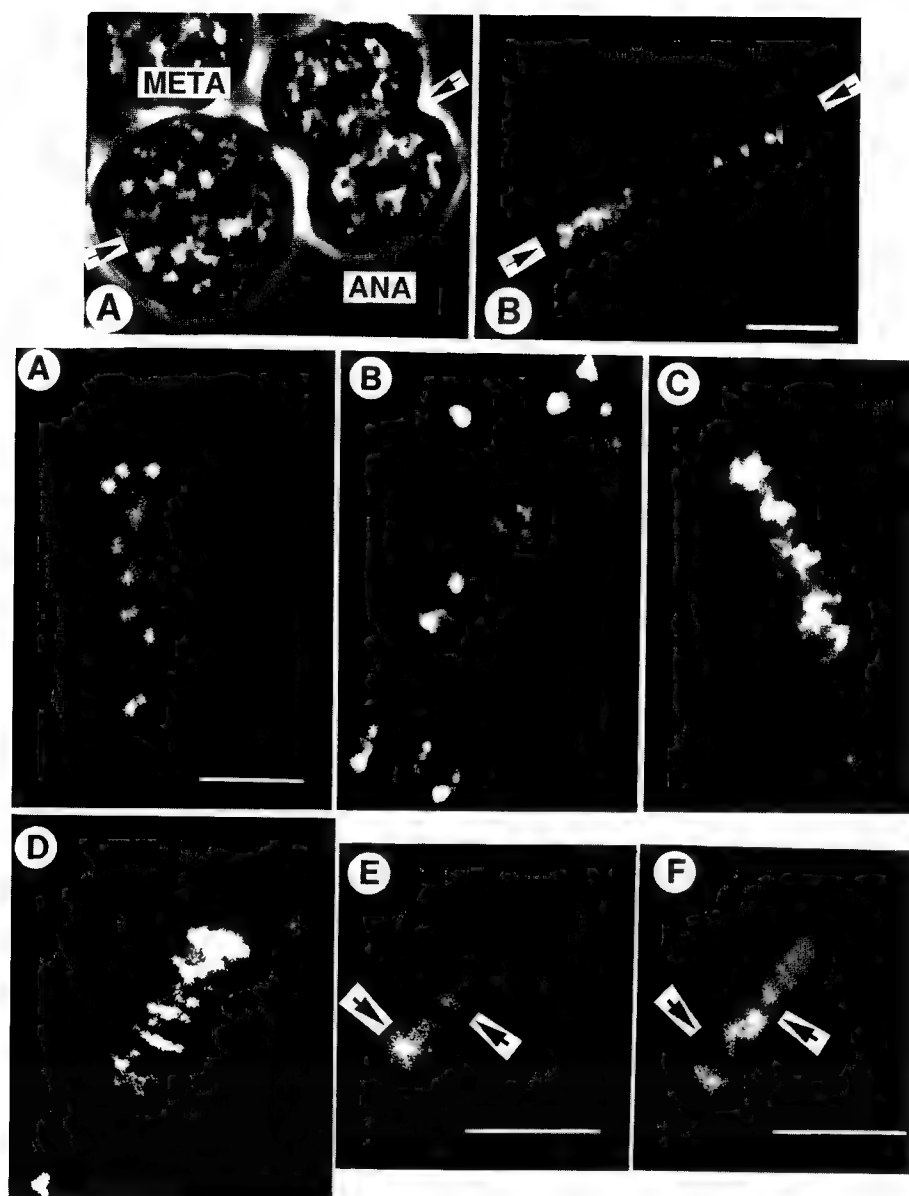
FIG. 1 (top) The INCENPs are associated with the mitotic chromosomes during metaphase and the central spindle during anaphase. Panel A - phase contrast. Panel B - indirect immunofluorescence with monoclonal anti-INCENP. Confocal micrograph. Bar - 5 microns.

Fig. 2 (bottom) The INCENPs are released from the mitotic chromosomes during metaphase. Panels A - E - indirect immunofluorescence with monoclonal anti-INCENP. Panel D - propidium iodide staining of chromosomal DNA (corresponds to panel E). Panels A, B - early metaphase, Panel C - mid metaphase, Panels D, E - late metaphase. Bar in panels A - D, E & F - 5 microns.

VIDEO-LIGHT MICROSCOPIC ANALYSES OF CENTROSOME SEPARATION *IN VIVO* DURING MITOSIS IN VERTEBRATE CELLS

Conly L. Rieder, Jennifer Waters and Richard W. Cole

Wadsworth Center for Laboratories and Research, New York State Dept. of Health, P.O. Box 509, Albany, New York

The major microtubule (MT) organizing center of the vertebrate interphase cell is the centrosome. After replication near DNA synthesis it functions as a single unit until mitosis. At the onset of mitosis the cytoplasmic MT complex is resorbed and the replicated centrosomes separate to form the spindle poles. During this time each nucleates a radial array of dynamically unstable MTs known as an aster. After spindle formation the centrosomes separate again during anaphase B to elongate the spindle. The mechanism(s) by which the centrosomes separate during these two mitotic stages remain unknown. The most popular hypothesis is that interacting MTs of opposite polarity, derived from opposing asters, elongate and slide relative to one another through the action of MT plus-end directed motor proteins.[1,4] Unfortunately, this hypothesis does not explain why centrosomes continue to separate in vertebrate cells when their MT arrays no longer overlap, as in anaphase-like prometaphase (ALP).[2]

Both centrosomes are clearly visible *in vivo* during mitosis in newt lung cells. The goal of our study was to compare, with high spatial and temporal resolution, the behavior of centrosomes as they separate when their MT arrays overlap during prophase (Fig. 1) and anaphase B (Fig. 3), with when they no longer overlap during ALP (Fig. 2). For this study we recorded centrosome separation as previously described[3]. Briefly, cells were followed with a Nikon Microphot FX light microscope equipped with a 60X (1.4 NA) DIC objective and a Hamamatsu video camera. The camera output was routed through an Image-1 video processor prior to storage on optical memory disks. Our framing rates were every 4 seconds. The particle tracking program within Image 1 was then used to determine pixel changes in centrosome position between consecutive images. From these pixel changes, an the appropriate formulae, we could determine the values for a number of characteristics that describe centrosome behavior during the separation process. These parameters included total displacement; the vector rate of motion towards and away from the other centrosome; the frequency of towards and away motion as well as that not contributing to the separation process; and the rate contributed by each centrosome to the separation process.

We found that the centrosomes, during all stages of separation, possessed a considerable degree of independence. Indeed, the direction of migration exhibited by one centrosome, and its vector magnitude, did not impart a predictable behavior to the other centrosome. Moreover, both centrosomes exhibited frequent and rapid (4-5 μm/min) displacements towards random points within the cell--often towards the other centrosome. Statistically there was no difference in the kinetic behavior of separating prophase and ALP centrosomes, over all of the parameters we examined, regardless of whether their MT arrays overlapped. By contrast, when compared to prophase\ALP centrosomes, anaphase B centrosomes separated at significantly faster rates (P = .005) even though the average vectorial rate of motion away from the other centrosome was the same as in prophase\ALP (P = .31). The difference in
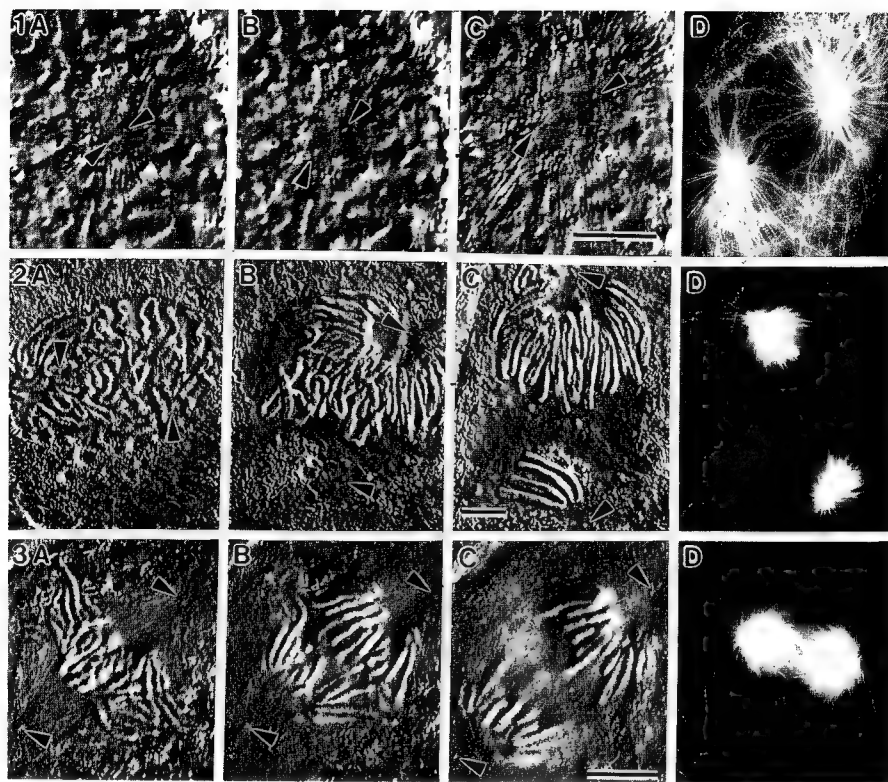
Figs. 1-3. A-C) Video micrographs of centrosomes (arrows) separating in prophase (1), ALP (2) and anaphase (3) newt lung cells. D) MT distribution in similar cells as determined by anti-tubulin immunofluorescent staining. Bar = 10 μm.

anaphase B and prophase/ALP separation rates was due to the fact that, when compared to prophase/ALP centrosomes, anaphase B centrosomes exhibited a lower frequency of towards motions (P = .03) with a significantly slower vector rate (P = .0001). From our data we conclude that the force for centrosome separation during vertebrate spindle formation is not produced by MT-MT interactions between opposing asters, i.e., the mechanism is intrinsic to each aster. Our data also suggest that this mechanism contributes to anaphase B, but that it is modified by interactions between opposing astral MTs in the interzone. For example, our data imply that the overlapping interzonal MT arrays that indirectly connect the centrosomes during anaphase B act as a rachet that allow the centrosomes to separate while impeding motion towards one another. Such a rachet mechanism may be mediated by recently-described proteins that bind to antiparallel MTs in the midzone of anaphase PtK cells[4] .

References

1) W.Z. Cande and C.J. Hogan. Bioessays (1989)11,5.
2) C.L. Rieder and S.P. Alexander. J. Cell Biol. (1990)110,81.
3) S.P. Alexander and C.L. Rieder. J. Cell Biol. (1991)113,805.
4) C. Nislow, V. Lombillo, R. Kuriyama and J.R. McIntosh. Nature (1992)359,543.

NEW POLARIZED-LIGHT MICROSCOPE FOR FAST AND ORIENTATION-INDEPENDENT MEASUREMENT OF BIREFRINGENT FINE STRUCTURE

Rudolf Oldenbourg

Marine Biological Laboratory, Woods Hole MA 02543, USA

The polarized light microscope has the unique potential to measure submicroscopic molecular arrangements dynamically and non-destructively in living cells and other specimens. With the traditional pol-scope, however, single images display only those anisotropic structures that have a limited range of orientations with respect to the polarization axes of the microscope. Furthermore, rapid measurements are restricted to a single image point or single area that exhibits uniform birefringence or other form of optical anisotropy, while measurements comparing several image points take an inordinately long time.

We are developing a new kind of polarized light microscope which combines speed and high resolution in its measurement of the specimen anisotropy, irrespective of its orientation. The design of the new pol-scope is based on the traditional polarized light microscope with two essential modifications: circular polarizers replace linear polarizers and two electro-optical modulators replace the traditional compensator. A video camera and computer assisted image analysis provide measurements of specimen anisotropy in rapid succession for all points of the image comprising the field of view. The measurement process results in particularly clear images free of shading and background light over the entire viewing field. The images and measurements document fine structural and molecular organization within a thin optical section of the specimen. The high spatial and temporal resolution of the new pol-scope together with its ease of use for obtaining quantitative specimen records, concurrently for the whole field of view, will allow new investigations into the dynamics of macromolecular organization of living cells and other systems.

The new instrument has the ability to display sequentially the spatial distribution, and rapidly measure the temporal changes in: birefringence due to intra-molecular anisotropy or fine-structural form; and (with some modification to the basic scheme) polarized fluorescence in molecular moiety selectively labeled with reporter dyes, and dichroism exhibited by naturally occurring chromophores.

Applications of the new instrument are expected to develop in many fields including biology, physics, and material science. Biological mechanisms and macromolecular phenomena that should be explored taking advantage of these unique capabilities of the new microscope include:

*   Regulated assembly and disassembly of microtubules, actin filaments, and other cytoskeletal elements and their role in organelle transport, cell division, cell differentiation, etc..

*   Functional role and organization of DNA tertiary structure as displayed in decondensing sperm head, polytene chromosomes and chromatin of lower eukaryotes.

*   Conformational and micro-environmental changes associated with motility and transport functions in myosin, dynein, membrane proteins, etc..

*   Turnover and functional changes of stacked membrane structures such as in retinal rods and cones, chloroplasts, Golgi bodies.

*   Spontaneous and induced generation of ordered domains in liquid crystals, polymer solutions and lipid layers, and their Brownian, cyclic, and propagated fluctuations.

LASER-FEEDBACK MICROSCOPY: FUNDAMENTAL PRINCIPLES AND APPLICATION TO HIGH-RESOLUTION BIOLOGICAL IMAGING

Alan Bearden, Terrence L. Wong, Morgan W. Mitchell,
Leslie C. Osborne, and Michael P. O'Neill

Laser Feedback Microscopy Research Group, Div. of Neurobiology,
Dept. of Molecular and Cell Biology, and Graduate Group in Biophysics,
University of California, Berkeley, California 94720

As discovered by Abbé,[1] a fundamental limit to the lateral resolution of a conventional optical microscope is produced by ''far-field'' aperture diffraction at the objective lens. This limitation can be expressed in terms of the Airy disc which relates the obtainable resolution to the wavelength of light used and the objective's numerical aperture (NA). In scanning confocal microscopy[2] with a laser-produced Gaussian profile illumination beam, the lateral resolution is given by $1.22\lambda/NA$. The axial resolution in this design is improved by the use of a pinhole aperture to pass light only from the objective's focal plane. Typical best values for lateral (x,y) and axial (z) resolution for visible wavelength scanning confocal microscopy are ~200nm and ~300nm with a NA=1.4 oil immersion objective.

Although optical microscopy displays limited resolution when compared to some forms of electron and scanning-probe microscopies (STM, AFM), the convenience of sample preparation and its ease in performing *in vivo* studies has given rise to new methods of increased resolution (e.g., ''near-field'' techniques, photon-tunneling, phase interference contrast). Interference techniques routinely measure phase-path differences of $\lambda/1000$ and have been incorporated into practical, widely-used microscopes. The conversion of phase information to intensity differences (i.e., phase contrast) furnishes resolution advantages but relies on indirect, non-quantitative phase-to-amplitude conversions.[3,4] Similarly, scanning differential contrast methods[5,6] have demonstrated improved visualization of both physical and biological detail.

Laser-feedback interferometry (LFI), in which coherent back-reflected light reentering the laser resonant cavity modulates the laser intensity as a function of phase-path difference,[7] is utilized in a new type of interference microscope (i.e., the laser-feedback microscope (LFM) shown schematically in Fig. 1.)[8,9] Displacement of a target surface along the axis of the microscope produces a sinusoidal variation of the laser intensity; vibration of the target surface induces a Bessel function dependence of that intensity.[9] A simple analysis considers the mirrors M2 and M3 as components of a Fabry-Perot etalon with the change in spacing producing a reflectance change for the mirror pair which, in turn, modulates the energy balance in the laser resonant cavity. The signal-to-noise ratio is sufficient to respond to target reflectances over a broad range ($\sim 10^{-6}$ to 1), allowing phase-differences to be measured from small index-of-refraction changes in biological materials.

One model of a scanning confocal LFM uses a 1mW linearly-polarized He-Ne laser (632.8nm, TEM_{00}), either a 100× 0.95NA air, or a 100× 1.25NA oil, objective (Nikon), and a linear piezoelectric transducer(PZT)-driven $x,y,$ scanning-stage (≤200μm × ≤200μm). Biological sample cells are held by vacuum to a tubular PZT providing z-axis modulation at 25kHz; this modulation is used by an electronic feedback control circuit to maintain the sample at a fixed optical path-length from the laser output mirror (M2).

84

Scanned images are digitized and computer-imaged as shown; no signal processing other than anti-alias filtering has been applied to the data. Image acquisition times are ~ 2-4 minutes.

Fig. 1. Schematic diagram of a laser-feedback microscope.

Fig. 2. Laser-feedback micrograph of neural growth cones and associated nerve cells from cell-cultured chick spinal ganglia nerve cells. Field of view: 20μm×20μm.

Fig. 3. Three-dimensional projection view of a silicon resolution standard: The dots are 800nm d., spaced 800nm apart and are 40nm high. Field of view: 25μm×25μm.
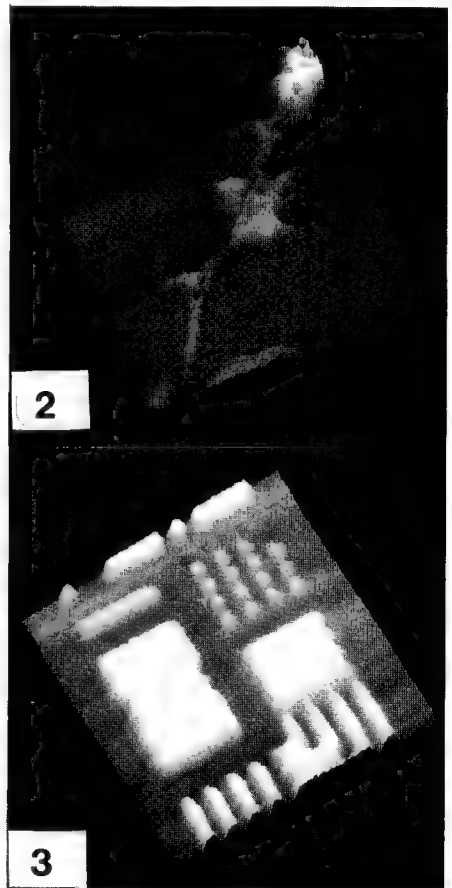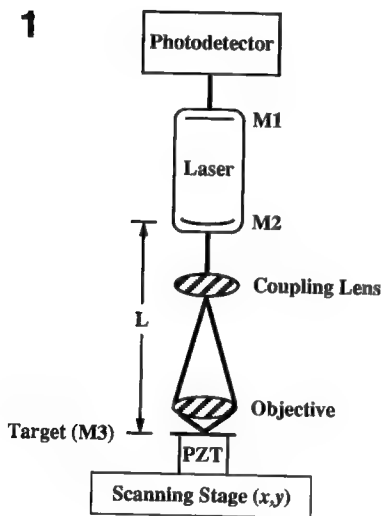
References

1. E. Abbé, Shultzes Archiv. für mikr. Anat. 9(1873),413. 2. M. Minsky, US Patent 3,013,467 (Dec. 19, 1961). 3. G. Nomarski, Revue d'hematologie 12(1957)439. 4. F. Zernike, Science 121(1955)345. 5. T. R. Corle and G. S. Kino, Appl. Opt. 29(1990)3769. 6. C. J. Cogswell and C. J. R. Sheppard, J. Microsc. (Oxford)165(1992)81. 7. P. G. R. King and G. J. Steward, US Patent 3,409,370 (Nov. 5, 1968). 8. A. J. Bearden and M. P. O'Neill, US Patent 5,029,023 (July 2, 1991). 9. A. Bearden, M. P. O'Neill, L. C. Osborne, and T. L. Wong, Opt, Lett. 18(1993)238. 10. This research is supported by the NSF (BIR). We are indebted to Dr. M. J. Ignatius for providing the nerve cell samples and to J.-P. Weber, J. Richard, S. Sabato, and C. Pietrzyk for technical assistance.

DIRECT MECHANICAL MEASUREMENT OF SINGLE DNA MOLECULES THROUGH AN OPTICAL MICROSCOPE

Carlos Bustamante and Steven B. Smith

Institute of Molecular Biology and Department of Chemistry, University of Oregon, Eugene, Oregon 97403

Understanding the mechanical properties of DNA such as their bending and torsional rigidity can provide a great deal of insight about the factors that determine the folding of DNA during the cell cycle. These quantities have been obtained from bulk experiments using light scattering, equilibrium sedimentation, DNA cyclization, etc.[1] Determination of the elastic properties of DNA with these methods is indirect, via a theoretical framework relating the observable quantities to the elastic parameters of the molecules. Moreover, the results represent an ensemble average over all accessible configurations of the molecule, with small contribution from stretched un-likely states.

We have carried a systematic study of the elastic properties of single DNA molecules.[2] Single DNA molecules were chemically attached by one end to a glass surface and by their other end to a magnetic bead. Equilibrium positions of the beads are observed in an optical microscope while the beads are acted on by known magnetic and hydrodynamic forces. Extension versus force curves are obtained for individual DNA molecules at three different salt concentrations with forces between 10^{-14} Newtons and 10^{-11} Newtons. These experiments have permitted to carry out, for the first time, a detailed investigation of the elastic properties of DNA molecules over the whole range of molecular extensions.

Significant deviations from the force curves predicted by the freely-jointed chain model have been observed suggesting that DNA has a local curvature in solution which require additional energy to straighten. Ethidium bromide and DAPI have little effect on the elastic response of the molecules but their extent of intercalation was directly measured. Conversely, the effect of bend-inducing *cis*-diammine dichloro platinum (II) (DDP) is large and supports the hypothesis of natural curvature in DNA. Similar studies are being carried out on chromatin.

Experiments are being designed now to underwind or overwind individual DNA molecules by means of their tethered beads to determine their coefficient of torsional rigidity as a function of the ionic strength.

References

1. P.J. Hagerman, Annu. Rev. Biophys. Biophys. Chem. (1988) 17, 265
2. S. B. Smith, L. Finzi, and C. Bustamante, Science (1992) 258, 1122
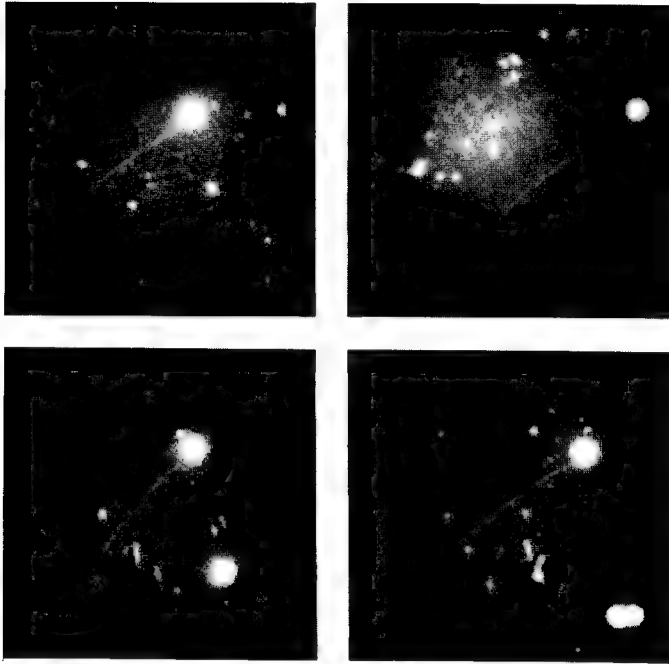
FIG. 1.-- Four magnetic beads tethered by single DNA molecules stained with ethidium bromide and imaged in epi fluorescence using an ultra-low light level camera. During the recording of these scenes, the beads were forced upward by flow and pulled to the right by a magnet. In these conditions, the DNA molecules incline at an angle corresponding to the resultant of the two perpendicular forces.

ENHANCED AXIAL RESOLUTION OF THE CYTOSKELETON IN FLUORESCENCE MICROSCOPY BY STANDING-WAVE EXCITATION

Frederick Lanni, Brent Bailey, Daniel L. Farkas, and D. Lansing Taylor

Center for Light Microscope Imaging and Biotechnology, Department of Biological Sciences, and Department of Physics, Carnegie Mellon University, 4400 Fifth Avenue, Pittsburgh, Pennsylvania 15213 USA

When the depth-of-field of a microscope is less than the axial dimension of the specimen, 3d information can be derived from a set of images recorded as the specimen is stepped through the object focal plane of the microscope. This procedure, known as optical sectioning microscopy (OSM), is the same in direct imaging and confocal scanning. For both of these cases in fluorescence microscopy, axial (depth) resolution is more limited than transverse resolution, for fundamental reasons. Our research aim has been to enhance axial resolution in fluorescence OSM (FOSM) while retaining the high-speed information transfer characteristics of direct imaging that are necessary for 3d studies of living cells in culture.

Standing-wave fluorescence microscopy (SWFM) is a direct imaging method in which the object is illuminated by a three-dimensional field of planar interference fringes (standing waves) oriented parallel to the focal plane of the microscope [1,2]. This field is produced in the specimen by crossing two coherent, collimated, s-polarized beams of equal amplitude directed through the specimen at complementary angles (θ, $\pi - \theta$) relative to the axis of the microscope. The nodal plane spacing in the field is $\lambda/(2n \cos \theta)$, and the position of the nodes in the specimen can be shifted by controlling the phase of one of the beams. This procedure can resolve stratified structures that are obscured under uniform excitation.

Two standing-wave fluorescence microscopes have recently been constructed and used in our laboratory. In the simplest, a nearly-collimated beam from a laser exits the objective, passes through the specimen, and is back-reflected by a closely-apposed mirror. Interference of the beam and its reflection set up the planar pattern of nodes and antinodes through the specimen. Movement of the mirror via a piezoelectric drive causes a matching shift of the nodal planes in the object. In our second instrument, the laser beam is split and sent into the specimen from both sides through a pair of objectives. The dual-beam system has the advantages of better wavefront flatness and better control of beam crossing angle. The phase of one beam is controlled by piezoelectric movement of an external mirror. In both instruments, high-NA immersion lenses are used for high resolution and efficiency. At present, these instruments are being used with the beams counterpropagating on-axis ($\theta = 0$ deg), giving a node spacing of $\lambda/2n$, or 0.18 μm.

In thin specimens, from which no 3d information can be derived by standard methods, SWFM provides a means for *optical subsectioning*. This is particularly noticeable in specimens that are sharply in focus, and thinner than half the node spacing, $\lambda/4n$. Controlled movement of the single node or antinode in the specimen then alternately illuminates overlapping structures; For example, the stratified order of crossed stress fibers can be determined. A field shift equal to one-quarter of the node spacing ($\lambda/8n$) was found to be readily distinguished, so that the axial resolution is in the range 0.04–0.05 μm, an order-of-magnitude enhancement over FOSM. As test cases, we have been studying the 3d distribution of F-actin in the lamellae of fixed 3T3 fibroblasts, and of myosin II in the lamellae of living 3T3 fibroblasts.

In the more general case, the specimen will be thicker than $\lambda/4n$. Standing-wave images are then recorded at a set of equi-spaced object planes, as in FOSM. We are also developing a system

for *excitation field synthesis* (EFS), of which SWFM is the simplest case. In EFS, a series of standing-wave fields of different node spacing, but all with an antinode at the focal plane, are superposed or time-multiplexed during image acquisition. The net result is an average excitation field that is peaked at the in-focus plane, but is also non-periodic. Our analysis of the EFS system shows that a fivefold improvement in axial resolution can be expected.

The most difficult problem in SWFM, or any method depending on mutual coherence, is the effect of refractive index mismatch between the specimen and the mounting medium, or within the object itself. Mismatch causes distortion of the nodal planes, approaching speckle-pattern characteristics when severe. We observe the effect of index heterogeneity mainly as a decrease in interference fringe contrast. In the relatively thin specimens examined so far, this has not been a limiting factor, but we are investigating several approaches to compensate for this effect in the data.

References:

1. Lanni, F. Standing Wave Fluorescence Microscopy, *in* Applications of Fluorescence in the Biomedical Sciences, D. L. Taylor, *et al*, eds., Alan R. Liss, Inc., New York, 1986.

2. Lanni, F., A. S. Waggoner, and D. L. Taylor. Standing-Wave Luminescence Microscopy. U.S. Patent No. 4,621,911 (1986).

BIOLOGICAL APPLICATIONS OF MICROSCOPIC MAGNETIC RESONANCE IMAGING

Russell E. Jacobs and S. Earl Fraser
Beckman Institute, California Institute of Technology, M/C 139-74, Pasadena, CA 91125

The ability of MRI to provide three dimensional images of thick opaque samples in a noninvasive manner has made it an extremely important clinical tool. In addition, the large number of types of contrast mechanisms in a MR experiment offer the clinician and research scientist the possibility of adapting the image contrast to fit the problem of interest. While typical resolutions employed clinically are on the order of a millimeter, the notion of using MRI at microscopic resolutions arose early in the development of this technique [1]. Spatial information is encoded in both the frequency and phase of the nuclear magnetic resonance signal by selective application of magnetic field gradients [2, 3]. Spatial resolution in biological samples is typically limited by a number of physical effects [4, 5, 6] as well as signal-to-noise ratio (S/N) considerations. Estimate of the *theoretical* limits of resolution in the MR image arising from these phenomena range from 2 to 0.5μm. The *practical* spatial resolution is currently determined by the S/N which is often limited by the amount of time available to actually acquire the image (*i.e.* the temporal resolution). For example, a reasonable S/N clinical MR image can be obtained in about 5 minutes with a voxel (volume element) size of $(1mm)^3$. We are interested in voxels down to ~1μm on a side. Because most of the proton MR signal arises from water in biological samples and water concentration is roughly constant, the S/N change in the image will be proportional to the volume change: a factor of 10^{-9}. Of course, this is true only if all experimental parameters are the same. The challenge in MRI microscopy is to optimize the experimental setup (hardware and software) to overcome the poor intrinsic S/N in order to obtain a respectable image in a reasonable amount of time.

Magnetic Resonance Imaging studies on a number of biological systems are being carried out at the Biological Imaging Center of the Beckman Institute. These studies rely on both the intrinsic contrast available within the sample and the use of MR contrast agents [7]. Figures 1 and 2 illustrate the types of anatomical information available from a relatively low resolution MR image obtained without the use of contrast agents. We show two slice extracted from a three dimensional data image of a newborn dwarf lemur. The data set size is 256x128x128 voxels of 140μm on a side. The two slices through the data set shown in Figure 3 show a wealth of anatomical features, ranging from the lamination of cells in the developing cortical plate to the distinct morphology of the dentate gyrus of the hippocampus. When viewed at full scale, fine structures such as the basilar membrane are clearly rendered. Blood oxygenation level-dependent (BOLD) contrast MR imaging is an exciting new functional imaging technique which promises to be able to provide information about regional cerebral activity accompanying sensory stimulation [8, 9]. We are currently implementing this technique on our MR microscopic system where the combination of high magnetic field strength (12 Tesla) and restricted sample volume present special opportunities.

Neuronal tracing and cell lineage analysis require that a particular subset of cells be uniquely identifiable. In cell lineage analysis experiments the descendants of individual precursors in the intact embryo are labeled by microinjection of a stable, nontoxic, membrane impermeable MRI lineage tracer. Because the complete time-series of high-resolution three-dimensional MR images can be analyzed forward or backward in time, one can fully reconstruct the cell divisions and cell movements responsible for any particular descendant(s). Unlike previous methods, where labeled cells are identified at the termination of the experiment, this technique allows the full kinship relationships of a clone to be determined as the clone expands. Figure 3 show a slice through the head of a four day frog embryo which had been labeled at the 16 cell stage. High intensity regions correspond to progeny of the originally labeled cell (*i.e.* right eye). Similar studies aimed at tracing

optic neurons as they grow out of the retina and towards the contra-lateral tectum utilize a lipophylic contrast agent applied to the retina of one eye which is incorporated into the emerging neuron.

References
1. Lauterbur, P. C. Nature. **242**: 190, 1973.
2. Mansfield, P. and P. G. Morris. <u>NMR Imaging in Biomedicine.</u> 1982 Academic Press. New York.
3. Talagala, S. L. and I. J. Lowe. Concepts in Magnetic Resonance. **3**: 145-159, 1991.
4. Blumich, B. and W. Kuhn. <u>Magnetic Resonance Microscopy.</u> 604, 1992.
5. Cho, Z. H., C. B. Ahn, S. C. Juh, H. K. Lee, R. E. Jacobs, S. Lee, J. H. Yi and J. M. Jo. Med Phys. **15**(6): 815-824, 1988.
6. Kuhn, W. Angew. Chem. Int. Engl. **29**(1): 1-112, 1990.
7. Lauffer, R. B. Chem. Rev. **87**: 901-927, 1987.
8. Belliveau, J. W., D. N. Kennedy, R. C. McKinstry, B. R. Buchbinder, R. M. Weisskoff, M. S. Cohen, J. M. Vevea, T. J. Brady and B. R. Rosen. Science. **254**: 716-719, 1991.
9. Ogawa, S., D. W. Tank, R. Menon, J. M. Ellermann, S. G. Kim, H. Merkle and U. K. Proc. Natl. Acad. Sci. USA. **89**: 5951-5955, 1992.

Figure 1

Figure 2

Figure 3

mesencephalon

eye

diencephalon

100 μm
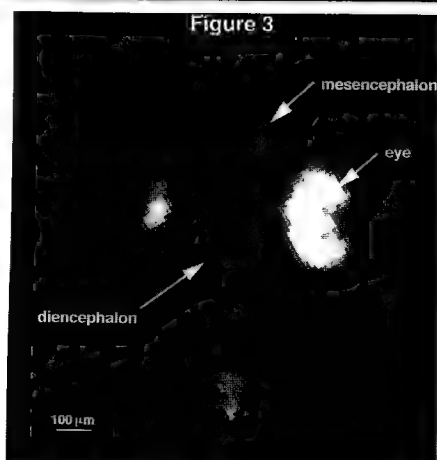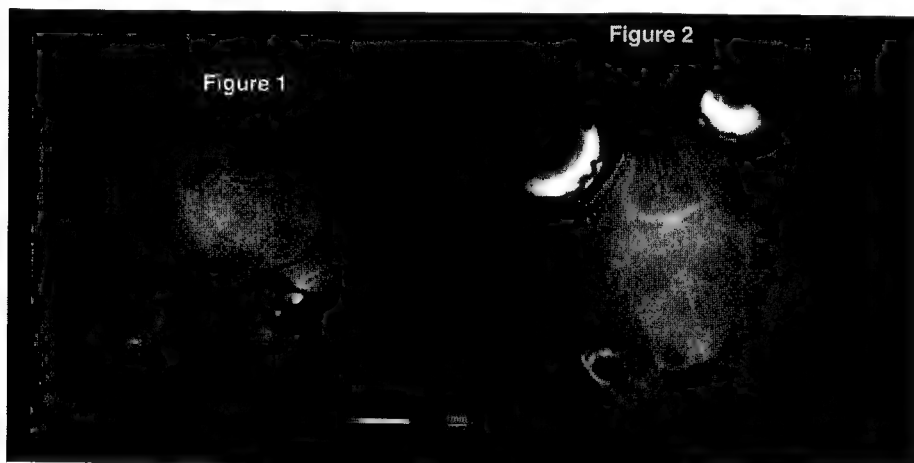
THREE-DIMENSIONAL STRUCTURE OF DENDRITIC SPINES, NEURONAL SPECIALIZATIONS THAT IMPART BOTH STABILITY AND FLEXIBILITY TO SYNAPTIC FUNCTION

Kristen M. Harris

Department of Neurology, The Children's Hospital and Harvard Medical School, 260 Enders, 300 Longwood Avenue, Boston, Massachusetts 02115

Dendritic spines are the tiny protrusions that stud the surface of many neurons and they are the location of over 90% of all excitatory synapses that occur in the central nervous system. Their small size and variable shapes has in large part made detailed study of their structure refractory to conventional light microscopy and single section electron microscopy (EM). Yet their widespread occurrence and likely involvement in learning and memory has motivated extensive efforts to obtain quantitative descriptions of spines in both steady state and dynamic conditions. Since the seminal mathematical analyses of D'Arcy Thompson,[1] the power of establishing quantitatively key parameters of structure has become recognized as a foundation of successful biological inquiry. For dendritic spines highly precise determinations of structure and its variation are proving themselves as the kingpin for establishing a valid concept of function. The recent conjunction of high quality information about the structure, function, and theoretical implications of dendritic spines has produced a flurry of new considerations of their role in synaptic transmission.[2] A powerful working hypothesis is that the structure of dendritic spines sets the boundaries within which synaptic function can be modulated. Theory defines the limits of what can happen within these boundaries and experimental manipulation defines what actually happens to spine morphology. As measurements of spine dimensions and organelle and molecular composition have become more precise, so too have the theoretical models of spine function improved.[2]

At this symposium we will summarize how differences in the three-dimensional structure and subcellular composition of dendritic spines from three brain regions (hippocampal areas CA1 and CA3, and cerebellum) could contribute to their specific biological properties. Then we will describe the series sample method, an approach to EM analysis that combines unbiased sampling of the neuropil with 3 dimensional reconstruction to determine how spine and synaptic structure (or for that matter any structure viewed in the TEM) changes during development or with experimental manipulation. In the most general application of the series sample method, every structure transected by a reference section, i.e. a single section in the middle of a series, is viewed through adjacent serial sections to obtain an unambiguous identification. The frequencies of the different structures are then computed per unit area of neuropil and adjusted to account for differences in the probability of viewing them on the reference section, based on the number of serial sections they traverse. Even this simple classification can be time consuming. To minimize the number of samples required to achieve robust findings, variability from sample to sample is reduced by subtracting from the sample areas the sectioned areas of structures that occur nonuniformly across the neuropil. Once all of the structures in a series sample are classified,

subpopulations of structures with specific characteristics are randomly selected for complete reconstruction and measurement in three dimensions.

This strategy was used to assess whether changes in the structure of hippocampal CA1 spines may contribute to the enhanced synaptic transmission and the greater endurance of longterm potentiation (LTP) that occur during maturation.[4] The results show a near doubling in synapse density between postnatal day (pnd)15 and young adults that does not occur uniformly across all spine and synapse morphologies. Spines with constricted necks increased by about four fold in density between pnd15 and young adult ages. These included spines of the thin, mushroom containing perforated postsynaptic densities (PSDs) and spine apparatuses, and branched categories. Stubby spines decreased by more than half and no change occurred in mushroom spines with macular PSDs or in dendritic shaft synapses. Only a few of the spine necks at either age were found through biophysical simulation to be constricted or long enough to reduce charge transfer from the synapses, therefore the overall doubling in synaptic density should mediate an enhanced synaptic transmission at older CA1 neurons.

There are at least four ways that the formation of dendritic spines with constricted necks could facilitate the maturation of synaptic efficacy and plasticity. First, the formation of dendritic spines allows for more synapses to interdigitate within a given volume of the brain. Second, a constricted spine neck enhances the potential that can be achieved (transiently) in the spine head thereby facilitating the opening of voltage-dependent channels. Third, the spine necks are sufficiently short and wide such that the potential achieved at one spine head can ultimately be shared amongst neighboring spines, facilitating co-activation of synaptic input. Fourth, spine necks may serve to isolate the spine synapses biochemically from the parent dendrite thereby allowing the concentration of activity-dependent molecules to be higher in the spine heads near to the synapses, thereby facilitating the specificity and possibly the endurance of synaptic plasticity.[5]

References:

1. D.W. Thompson, 1992 On Growth and Form, The Complete Revised Edition, Dover Publications, New York.
2. For review see: Koch C and Zador A. J. Neuroscience (1993) 13:413-422.
3. K.M. Harris and S.B. Kater Annual Rev. of Neuroscience, 1993 (in press).
4. Harris et al., J. Neuroscience (1992) 12:2685-2705.
5. Supported by NIH-#NS21184, The Alfred P. Sloan Foundation and MR Center Grant #P30-HD18655.

SUBCORTICAL EXCITATORY INPUTS TO NIGRAL DOPAMINERGIC AND NON-DOPAMINERGIC NEURONS: A LIGHT AND ELECTRON MICROSCOPIC STUDY

Meri Damlama and James M. Tepper

Rutgers University, Center for Molecular and Behavioral Neuroscience, Newark, NJ 07102

Midbrain dopaminergic neurons are involved in the symptomotology of motor disorders such as Parkinsonism as well as psychiatric disorders such as schizophrenia. The normal functioning of substantia nigra (SN) dopaminergic neurons is greatly influenced by their afferent inputs as evidenced by significant differences in the physiological characteristics of *in vivo* vs. *in vitro* preparations. Although the sources and neurotransmitters of many afferents to the SN are known, because dopaminergic and non-dopaminergic dendrites co-mingle in pars reticulata, the precise postsynaptic targets, particularly those of the presumed excitatory inputs, remain to be determined. In the present study inputs from the subthalamic (STN) and the pedunculopontine (PPN) nuclei (both presumed excitatory) to the SN were investigated by combined anterograde tracing and tyrosine hydroxylase (TH) immunocytochemistry at the light and electron microscopic levels.

The anterograde tracers biocytin or PHA-L were iontophoretically injected into either the STN or the PPN. Following appropriate survival times the animals were perfused transcardially with a mixture of 4% paraformaldehyde and 0.2% glutaraldehyde. Cryoprotected, free-floating brain sections were freeze-thawed and immediately processed for the visualization of the tracer with standard Vector ABC reagents and 3,3'-diaminobenzidine (DAB) or nickel-enhanced DAB. Sections containing the SN were incubated in TH antibody (Eugene Tech.), followed by sequential incubations in a bridging antibody and peroxidase anti-peroxidase solutions. The reaction product was visualized with DAB or benzidine dihydrochloride. Alternate sections were examined at the light microscopic level and the remainder were further processed for electron microscopic evaluation. Sections were post-fixed in 1% osmium tetroxide, dehydrated in an ascending series of ethanols (with 1% uranyl acetate in 70% ethanol), and propylene oxide, and embedded in resin (Durcupan ACM) between liquid release-coated glass slides and cover slips. After curing at 60° C, slides were examined and photographed in the light microscope, the slides and cover slips removed, and areas of interest trimmed out. Ultrathin sections were collected on formvar coated grids, counterstained with 0.3% lead citrate, and examined on a Phillips CM-10 electron microscope. All measurements were done with the aid of MacMeasure (NIH) and a MacTablet (Summagraphics) digitizing pad .

In the light microscope, both the PPN and STN were seen to give rise to numerous fine varicose axons in the SN. The PPN input appeared densest in the pars compacta while the STN input was densest in the pars reticulata. Many of the axonal varicosities seemed to be associated with TH positive (TH+) dendrites and perikarya (Fig. 1, 4). At the electron microscopic level, the terminal boutons of PPN and STN origin had an average area of 0.53 ± 0.07 μm^2 (SEM) and 0.43 ± 0.06 μm^2, respectively. Both terminals contained small round vesicles, and 1-3 mitochondria, and formed asymmetric synapses mostly onto small dendrites approximately 1 μm in diameter. Most of the terminals contained one active zone, but occasionally PPN terminals synapsed with more than one element. Although terminals of PPN and STN origin were quantitatively similar, PPN terminals were less tightly packed with vesicles than STN terminals, and unlike the latter, they contained some large dense core vesicles in addition to the more numerous small round vesicles. PPN terminals were observed to form synapses with both TH+ (Fig. 2) and TH- dendrites (Fig. 3), consistent with the light microscopy. In contrast, even though at the level of the light microscope some STN inputs seem to be in close apposition to TH+ dendrites, electron microscopy revealed that the overwhelming majority of these same terminals formed synaptic contacts with TH- dendrites (Fig. 5) immediately adjacent to the TH+ dendrites (Fig. 6). These data suggest that the PPN exerts a monosynaptic excitatory influence on dopaminergic neurons, whereas the STN influences on dopaminergic neurons are largely polysynaptic.
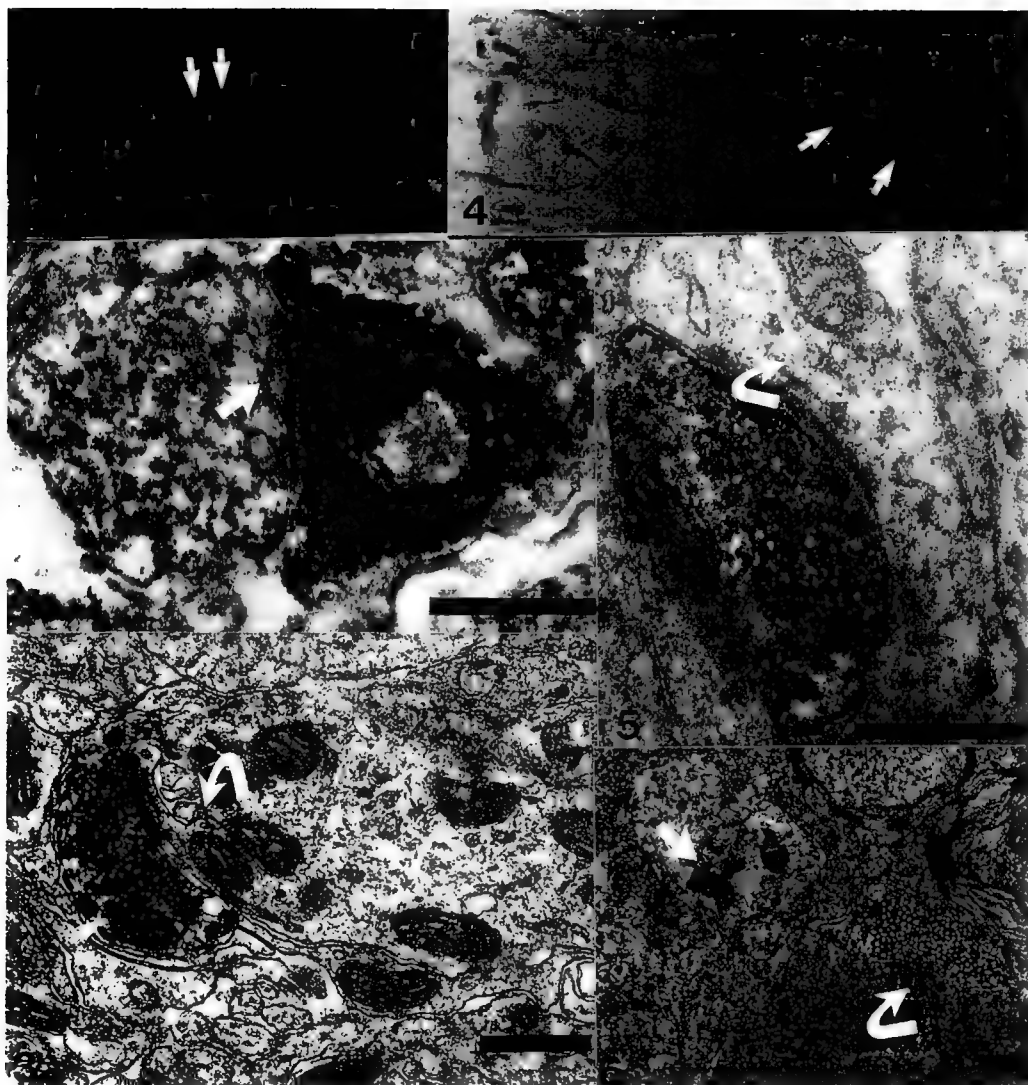
Fig. 1. PHA-L labeled afferents from PPN (light brown) form two varicosities (arrows) that appose a TH+ dendrite (dark blue) in pars reticulata. Bar = 20 μm.

Fig. 2. PHA-L labeled bouton from PPN contains small round vesicles and contacts a TH+ dendrite (arrow) in pars compacta. Bar = 0.5 μm.

Fig. 3. Biocytin-labeled bouton containing small round vesicles and a large dense-cored vesicle (small arrow) forming asymmetric synapse on TH- dendrite (curved arrow) in pars reticulata. Bar = 0.5 μm.

Fig. 4. Biocytin-labeled afferents from STN (dark blue) form two varicosities (arrows) that appose a TH+ dendrite (light brown) in pars reticulata. Bar = 20 μm.

Fig. 5. Biocytin-labeled bouton from STN contains small round vesicles and forms asymmetric synapse on TH- dendrite (arrow) in pars reticulata. Bar = 0.5 μm.

Fig. 6. Biocytin-labeled bouton from STN forms asymmetric synapse on TH- dendrite (curved arrow) but not nearby TH+ dendrite (straight arrow). Bar = 0.5 μm.

TOMOGRAPHIC METHODS FOR DETAILED EXAMINATION OF LARGE STRUCTURES IN THE NERVOUS SYSTEM

Gabriel E. Soto, Stephen J. Young, Maryann E. Martone, Thomas J. Deerinck, Stephan Lamont, Bridget O. Carragher and Mark H. Ellisman

San Diego Microscopy and Imaging Resource, University of California San Diego, La Jolla, CA 92093-0608

One of the limitations of electron microscopy has been the requirement for very thin samples to allow penetration of the electron beam. It is often the case that structures of interest are not contained within a single thin section. In these cases, serial sectioning techniques are required to reconstruct the object in its entirety. The use of higher voltage electron microscopes has allowed researchers to examine specimens up to fifty times thicker than those suitable for a conventional TEM. However, images from thick sections are often difficult to interpret as the electron micrograph is essentially a projection of the overlapping material within the section. The method of computerized axial tilt electron microscopic tomography offers the potential to visualize and analyze information contained in a thick section by deriving a three dimensional volume from a series of projections acquired by collecting images of the specimen at successive tilt increments about the Y axis. Unfortunately there are practical limitations to the resolution that can be obtained using this technique with very thick sections. Resolution of the tomogram increases with finer tilt sampling and an increased range of tilts but decreases with section thickness. Typically, the number of tilt images it is practical to obtain is limited, and the range of tilts which can be achieved with most specimens and standard specimen holders is restricted to +/- 60 degrees. One way to overcome these limitations is to use thinner sections for the reconstruction. Ironically, this can lead back to the situation where the structure of interest may not be contained in a single section thin enough to give the desired resolution. To overcome this problem, we have been developing a technique in which the serial section and electron tomography methods can be combined[1]. A series of thick sections are cut through the structure of interest and a three-dimensional volume is derived for each section using axial tilt tomography. The resulting serial volumes are then aligned and linked to form a single volume which may be visualized and analyzed using image analysis and volume rendering techniques. Since the constraint on resolution set by the specimen thickness does not apply to the lateral (X & Y) dimensions of the specimen, it is possible to obtain reconstructions of volumes with large extents in all dimensions using this serial tomographic procedure.

This technique has been used to reconstruct large extents of selectively stained neuronal material such as the *cis* face of the Golgi apparatus in bullfrog dorsal root ganglion neurons, and in gold-toned Golgi impregnated spiny dendrites in the rat neostriatum. The use of serial tomography has allowed us to track structures of interest over many microns in all dimensions at sufficient resolution to discern important ultrastructural detail. We have been experimenting with various test specimens to assess the accuracy of both our serial and single tomograms. Figure 1 shows a test for the alignment of the serial volumes. We have reconstructed a red blood cell over a thickness of seven microns using seven, serial one micron-thick sections. The tilt series for each tomogram was digitized under computer control using a high resolution slow scan CCD camera coupled to the microscope. The registration of the volumes appears to be accurate within the limits of resolution of the individual reconstructions. We have also been using specimens containing structures of known geometry to assess the accuracy of these methods.

Figure 2 presents a reconstruction based on three serial two micron sections of the Golgi apparatus stained by osmium impregnation in a neuron from frog spinal ganglia. The resolution of this six micron reconstruction is equal to that of one based on a single two micron section. We anticipate that this technique will allow us to track long thin anastomosing structures such as those associated with the Golgi apparatus[2]. Additionally, the capability of deriving tomograms with large extent has proven useful for examining relatively long segments of dendrites of spiny neurons from the rat neostriatum for purposes of quantitatively characterizing the morphology of the spines and dendrites[3].

To complement these new procedures for tomography, we are exploring methods that will facilitate registration of the serial tomograms and improving methods for automating acquisition and alignment of images in each tilt series.

References
1. G.E. Soto et al., EMSA Proceedings (1992) 704.
2. J.D. Lindsey and M.H. Ellisman, J. Neurosci. (1985) 12, 3111.
3. C. J. Wilson et al., NeuroImage (1992) 1, 11.
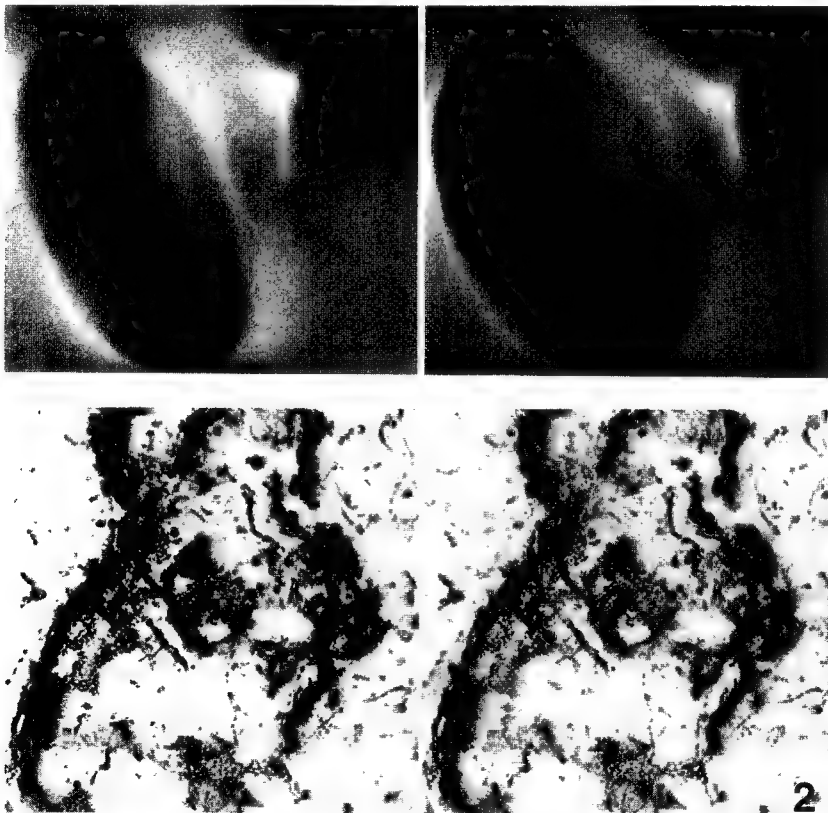
STRUCTURE AND FUNCTION OF THE NEURONAL ENDOMEMBRANE SYSTEM

Maryann E. Martone, Victoria M. Simpliciano, Ying Zhang, Thomas J. Deerinck and Mark H. Ellisman

Microscopy and Imaging Resource, University of California San Diego, La Jolla CA 92093-0608

Components of the endomembrane system in a variety of cell types appear to function in the storage and release of calcium similar to the muscle sarcoplasmic reticulum. Many proteins involved in intracellular calcium regulation in skeletal or smooth muscle, e.g. Ca^{++}ATPase, calsequestrin, the inositol 1,4,5,trisphosphate (IP3) receptor and the ryanodine binding protein, are found in the nervous system where they are particularly abundant within the smooth endoplasmic reticulum (SER) of cerebellar Purkinje neurons.[1-4] Immunolocalization studies suggest, however, that calcium regulatory proteins are not uniformly distributed within the SER but are concentrated in or excluded from certain domains.[3-4] For example, the IP3 and ryanodine receptors, two distinct calcium channels which mediate calcium release by different ligands, are found associated with the SER in cell bodies and dendrites of chick cerebellum but only the IP3 receptor is found within dendritic spines. [3] These results are consistent with evidence that cells may possess multiple intracellular calcium stores that are pharmacologically, spatially and perhaps physically distinct. [6] Elucidating the organization of these stores presents a major challenge to structural neurobiologists.

We have been investigating the 3-dimensional structure of the smooth endoplasmic reticulum within chicken Purkinje neurons in order to gain insight into the organization of calcium regulatory processes within this organelle. We were interested in determining whether the differential distribution of calcium regulatory proteins like the IP3 and ryanodine receptors reflected the presence of multiple, physically separate networks of SER within the dendrites of Purkinje neurons specialized for different aspects of calcium regulation. Using several 3-dimensional visualization techniques including serial section reconstruction, electron microscopic tomography and selective staining combined with intermediate high voltage electron microscopy (IVEM), we found that the majority of SER was contained within a highly branched network of cisterns and tubules extending throughout the dendritic shaft and into the dendritic spines (figures 1 and 2).[7]

The high degree of connectivity among the various components of the SER combined with immunocytochemical results suggests that it is a single organelle which possesses specialized subdomains for calcium uptake, storage and release. Unfortunately, the complex 3-dimensional structure of the SER poses a formidable obstacle for elucidating the precise spatial organization of calcium regulatory proteins within this organelle. To map the distribution of calcium regulatory proteins onto the three-dimensional SER network, we are employing methods for three-dimensional immunolabeling at both the light microscopic level using high resolution confocal microscopy and at the ultrastructural level by immunolabeling of semi-thick ultracryosections. We have achieved immunolabeling with 5 nm colloidal gold throughout the depth of a 0.3 um section by using extended incubation times and pretreatments with either ethanol or glycerol, although the degree of penetration is highly dependent upon the type of antigen to be localized. For example, labeling for membrane proteins such as the Ca^{++} ATPase is consistently seen throughout the thickness of the section while labeling for calsequestrin, a calcium binding protein within the lumen of the SER, is more difficult to achieve and tends to be strongest at the top and bottom of the section (figure 3). Preliminary results suggest that both the IP3 and Ca^{++}ATPase are widely distributed among the membranes of the SER while the ryanodine receptor and calsequestrin are more discretely localized. The localization of calsequestrin is of particular interest because analysis from thin sections has suggested that calsequestrin containing profiles are not physically continuous with the SER but represent a distinct vesicular organelle, the calciosome, specialized for the storage and release of intracellular calcium.[4] However, when viewed in three-dimensions, calsequestrin-containing profiles do not appear to be isolated but rather form a loose network (figure 3) similar in appearance and distribution to the cisternal SER seen in selectively stained material (figure 2). We are currently employing double labeling techniques to determine how the calsequestrin-containing regions of the SER relate to the IP3 and ryanodine receptors, both of which release calcium from intracellular stores upon stimulation. [8] Determining the 3-dimensional organization of these proteins and calcium regulatory sites within the SER will increase our understanding of the mechanisms by which neurons control intracellular calcium responses.

References
1. M. H. Ellisman et al., Neuron. (1990) 5, 135.
2. C. A. Ross et al., Nature (1989) 339, 468.
3. P. D. Walton et al., J. Cell Biol. (1991) 113, 1145.
4. A. Villa et al., J. Cell Biol (1991) 113, 779.
5. T. Satoh et al. J. Cell Biol. (1990) 111, 615.
6. R. D. Burgoyne et al. (1989) 342, 72.
7. M. E. Martone, J. Neurosci., in press.
8. V. Henzi and A. B. MacDermott Neuroscience (1992) 46, 251.
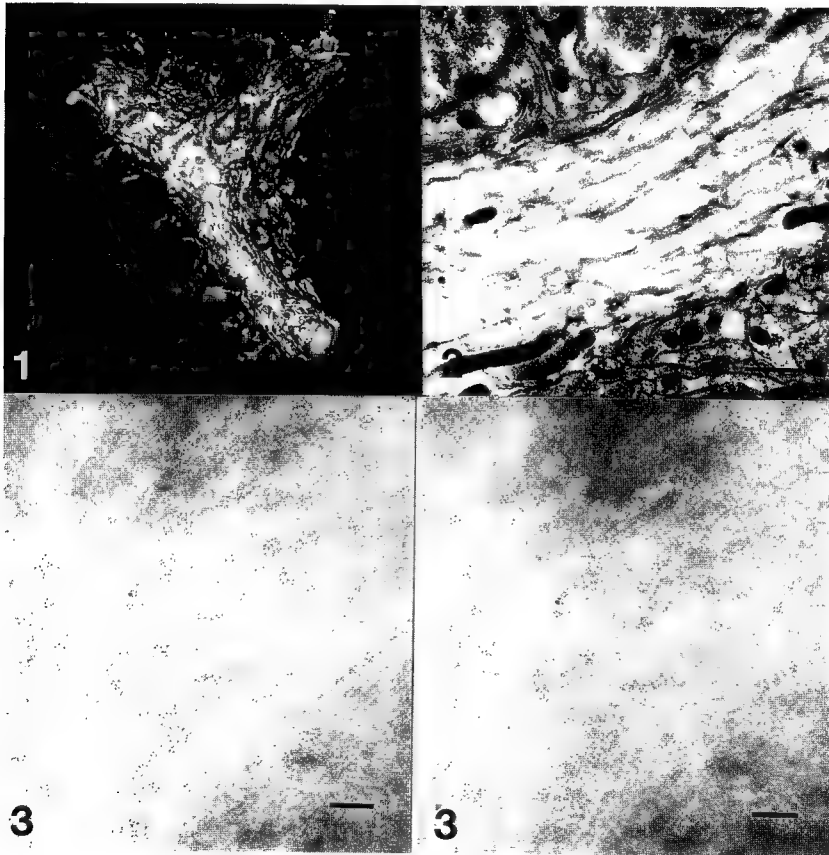
FIG. 1: Three-dimensional reconstruction from serial sections of the SER (light gray) in a branch point of a Purkinje cell dendrite.

FIG. 2: Semithick section (0.5 um) of a Purkinje cell dendrite stained by osmium-reduced potassium ferrocyanide. Scale bar=1 um.

FIG 3: Stereopair of 0.3 um thick cryosection immunolabeled with 5 nm colloidal gold for calsequestrin. Scale bar=200 um.

THE DYNAMICS OF SYNAPSE FORMATION: TIME-LAPSE OBSERVATIONS BY CONFOCAL FLUORESCENCE MICROSCOPY IN HIPPOCAMPAL SLICES AND ZEBRA-FISH EMBRYOS

Stephen J Smith, Michael E. Dailey, Susan Pike, JoAnn Buchanan and Dwight E. Bergles

Department of Molecular and Cellular Physiology, Beckman Center, Stanford University School of Medicine, Stanford, CA 94305

Our present information about the formation of synapses in the central nervous system is based almost exclusively on observations of fixed tissue specimens. Such observations can only provide very limited inference about the dynamics of the underlying developmental processes. In the hopes of obtaining direct information about the dynamics of synapse formation, we have explored new methods that allow repeated, high-resolution optical imaging of synapse formation events in live neural tissues.

Our efforts have focused on specific excitatory synapses in two vertebrate nervous systems: (1) the mossy-fiber-to-CA3-pyramidal-cell synapse in the hippocampus of postnatal day 4-8 rats and (2) the mauthner-fiber-to-motoneuron synapse in intact early embryos of the zebrafish *Brachydanio rerio*. We are using laser-scanning confocal fluorescence microscopy and fluorescent membrane stains such as di-I and di-O. Individual neurons or limited subsets of the neurons within a tissue are stained by applying these dyes in dimethylformamide solution through micropipettes.

In both the rat hippocampus and the zebrafish systems, we have succeeded in obtaining high quality images that clearly resolve the subcellular structures involved in synapse formation such as growth cones, fine dendritic branches and individual filopodia. Our imaging process can be repeated hundreds of times on individual specimens over periods of hours to days without appearing to disrupt the developmental processes of interest. We have also decisively established that many aspects of the glutamatergic mossy-fiber synapse formation process proceed toward a functionally normal end-point, unaffected by the hippocampal slice isolation procedure. In this symposium, we shall present video and still confocal microscopy results, electron micrographs and electrophysiological recordings that document our progress to date in the efforts outlined above.

Fig. 1 illustrates one substantive (although still preliminary) result from our time-lapse studies of hippocampal synapse formation. We have observed several instances where initial contact between the growing mossy fiber and a putative target pyramidal cell occurs between the mossy-fiber growth cone and a filopodial branch of a pyramidal cell dendrite. We are now exploring the hypothesis that this is a very common mode of initial contact between synapse formation partners. It is even interesting to speculate that active growth by post-synaptic target cells might be a general biological solution to the difficult navigational problems that are involved in final target cell selection in the complex three-dimensional environment of the developing nervous system.

Fig. 2 illustrates the quality of images it is possible to obtain of the growth cone of descending axons growing down the spinal cord in an intact Zebrafish embryo. The sequence of images in this figure were collected over the time period indicated and document the high rate of fiber growth (> 50 um/hr) we observe in this system.

t=0   t=4   t=90   t=444 min
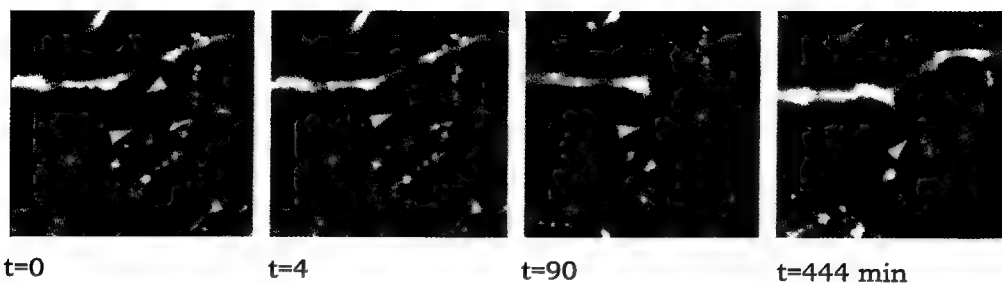
Fig. 1. Time-lapse sequence of possible early stage in formation of a rat hippocampal synapse. Cells in hippocampal slice were stained with di-I and visualized by confocal fluorescence microscopy. Upper arrowhead in first panel indicates tip of a filopodium sprouting from the large dendrite running across the top half of the panel. The lower arrowhead indicates a growth cone at the tip of an axon growing vertically toward the dendrite. In the second panel, the filopodium and the growth cone make contact, at the point indicated by the arrowhead. The contact persists for several hours. The third and fourth panels show a bending of the dendrite at the point of contact. In the full video sequence, it seems fairly clear that this bending is a result of tension developed from adhesion to the axon.
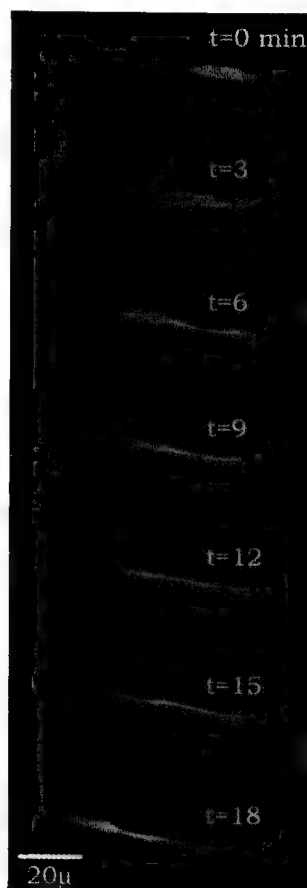
Fig. 2. Time-lapse sequence showing growth-cone motility and axon extension in an intact, developing zebrafish embryo. The mauthner cell axon was stained by a di-O injection and images were obtained by laser confocal microscopy.

101

IN SITU CRYOFIXATION OF RAT SPINAL CORD BY A NEW PROPANE JET FREEZING DEVICE

William B. Greene

Department of Pathology & Laboratory Medicine, Medical University of South Carolina, Charleston

Spinal cord trauma is a major health problem in terms of morbidity and mortality[1]. It is clear that traumatic spinal cord injury is related to the death of a cord segment which results in the structural and functional disruption of key pathways vital to the maintenance of normal neurological function. The injured area of the cord eventually becomes a zone of segmental necrosis which, in the more severe cases, involves all but a thin rim of sub-pial white matter[2]. The clinical consequences of segmental necrosis can be consistently reproduced in experimental animals by dropping weights onto the surgically exposed cord[3]. At the moment of impact and during the primary injury phase, there are changes in the spinal cord which indicate that neural membranes are altered[4]. The extent and reversibility of these alterations are being investigated for therapeutic treatment. Emphasis has been placed principally on secondary events leading to calcium toxicity[5]. An ultra-rapid freezing technique evolved from the necessity of preserving diffusible ions in situ before and after spinal cord injury.

The prototype cryo-jet apparatus (Fig. 1) was constructed by the modification of a model 4770 Parr critical point drying bomb and the addition of an indwelling, resistance thermometer. The pressure jet consists of a low temperature spring valve with a stainless steel, 5mm orifice tube that is the outlet for the pressurized liquid propane. Attached to the base of the pressure jet nozzle is a dip tube that serves to draw up the super cooled liquid propane from the bottom of the chamber. The internal pressure of the reaction chamber is constantly monitored by a low temperature pressure gauge that is mounted onto the top surface via a manifold. The external, pressurizing dry nitrogen gas flows into the manifold valve through a quvalve through a quick connect nipple. A 1500 pound blow out device is connected directly to the main valve. External pressure is supplied from a dry nitrogen cylinder. Dry nitrogen pressure is maintained throughout use.

This cryo-jet freezing technique provides a means for relatively deep, in situ preservation of sub pial axons in experimental rat spinal cord trauma studies (Fig. 2). The effects of trauma, in particular, the small, intra-cellular perturbations of calcium and other diffusible ions, can be analyzed and recorded by qualitative and quantitative Electron Probe Microanalysis (Fig. 3). Fixation regimens, other than cryofixation, have the potential to artifactually shift chemical elements from one cellular compartment to another or dilute them, either partially or completely, from the cell. The goal of this cryo-jet method is to confine axonal components and chemical elements to a biologically natural position.

References

1. J.F. Krause, in Central Nervous System Trauma Status Report, NIH (1985)319
2. J.D. Balentine, Lab. Invest.(1978)39,236
3. J.D. Balentine, Lab. Invest.(1978)39,254
4. J.D. Balentine, Surv. Synth. Path. Res.(1983)2,184
5. J.D. Balentine and W.B. Greene, J. Neuropath. Exp. Neurol.(1984)43,500
6. This work was supported by NIH Grant #2PO1 NS11066
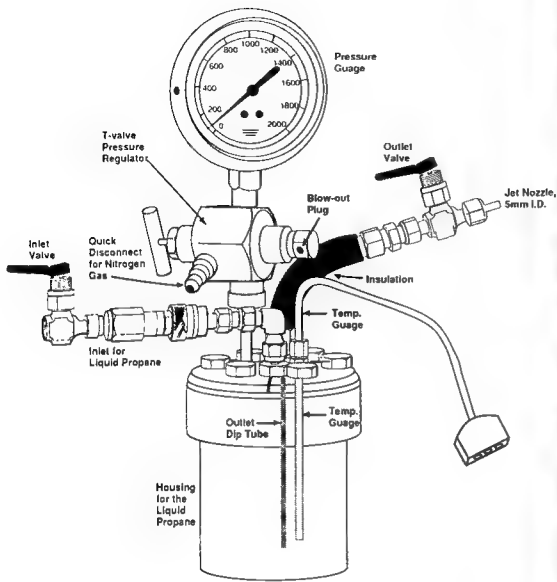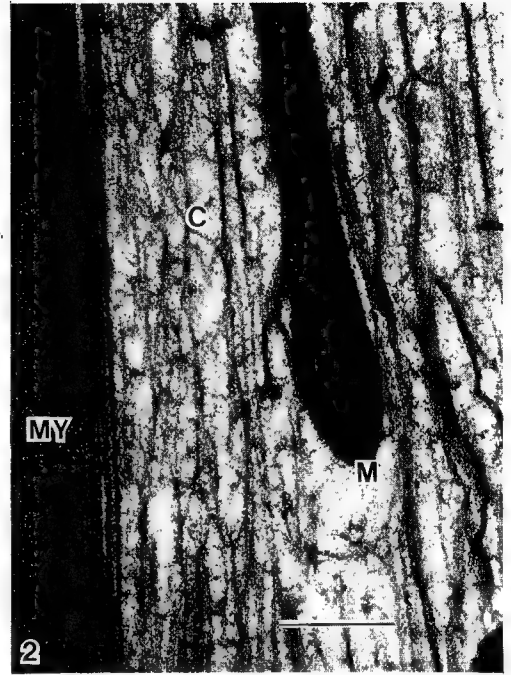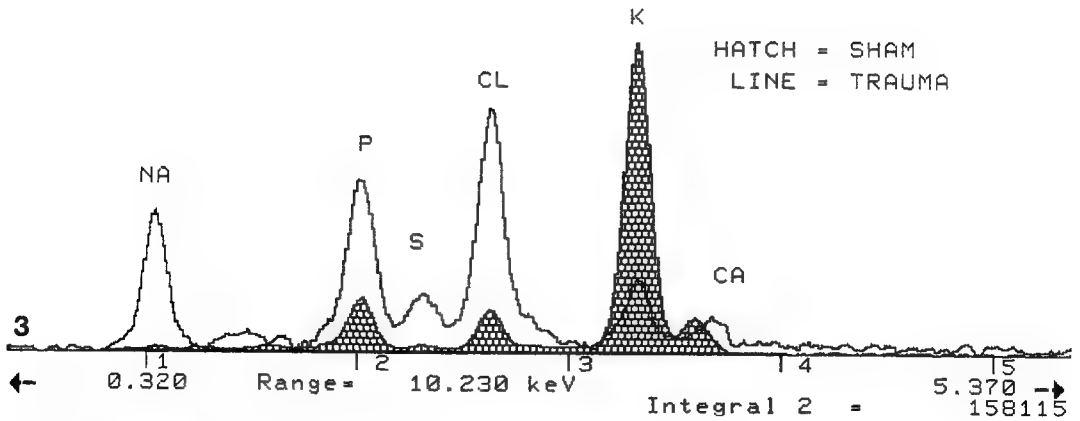
Fig. 1. Diagram of the cryo-jet freezer.

Fig. 2. Cryo section of rat spinal cord showing deep preservation of axoplasmic structures. Mitochondria (M), Cytoskeleton (C), Myelin sheath (MY). Bar = 5um.

Fig. 3. Typical x-ray spectrum of axoplasmic ER filaments. Sham operated control superimposed over a comparable traumatized area.

A NEWLY DEVELOPED CRYOFIXATION APPARTUS FOR PHYSIOLOGICAL
EXPERIMENTS AND ITS APPLICATION TO SQUID PHOTORECEPTOR CELLS

Michinori Ichikawa, Yoshiro Hanyu and Gen Matsumoto

Electrotechnical Laboratory, Tsukuba, Ibaraki 305 JAPAN

By cryofixation method for electron microscopy, structural change in squid
photoreceptor microvilli accompanied by long period of light illumination has
been studied by Tsukita *et al.*[1], resulting that there are two states of the
microvillar cytoskeletal structure under dark- and light-adapted conditions.
In this paper we report the structural changes as a function of time after the
light pulse application and their physiological significance.

For this experiment, we have developed a new cryofixation device which can
combine rapid freezing with physiological experiment2 (Fig. 1). The device
cryofixes biological specimen at precisely specified time after the light
illumination by driving a small silver block cooled down to 10°K with a
computer-controlled actuator; that is, for cryofixation, the cooled silver
block is pushed onto the specimen put on an experimental bench. Structural
change in the microvilli is observed to take place for the specimens cryofi-
xed at the time period over 50 msec after the light pulse is irradiated, but
is not observed for the 20-30 msec light-illuminated photoreceptors
(Fig. 2). The structural change takes place that the microvilli diameter of
70 nm for the dark-adapted cells increases to 120 nm after the 50 msec
light-illumination for 5-7% microvilli (Fig. 2), and that the change
accompanies the breakdown of the microvillar actin filament complex.
Further we have measured mechanical responses of squid retina to light
stimulation. Light stimulation induces an elongation of the retinal
photoreceptors. The time course of this mechanical response is similar to
that of the electrical response.

These clearly show that phototransduction is accompanied by some
morphological change: Light absorbance induces a swelling of the microvilli,
a break up of the microvillar actin filaments and a forward rolling of the
mitochondria. These phenomena indicate that phototransduction involves not
only enzymatic reactions, but also a dynamic mobilization of sub-cellular
components.

References
1. S. Tsukita, S. Tsukita and G. Matsumoto, J. Cell Biol. (1988)106, 1151.
2. M. Ichikawa, Y. Hanyu and G. Matsumoto, Biophys. J. (1993)64, A218.

FIG 1.

All of the moving parts are drived by stepping motors which are controlled by computer. The specimen is mounted on shock absorbing material outside of the cooling apparatus and its electrical responses are monitored.

For rapid cryofixation, the following commands are given.
1. Open door
2. Slide the stage into the cooling apparatus
3. Open valve
4. Bring the plunger down
5. Open shutter

Liquid Helium transfer tube
Wire
Plunger drive motor
Plunger
Silver block
Valve drive motor
Chamber
Wire
Door drive monitor
Shutter drive motor
Shutter
Specimen
Shock absorber
Stage drive motor
Valve
Door
Heater
Stage
Wire
Linear slider

FIG 2.

FIG 1.--A schematic drawing of a new cryofixation device.
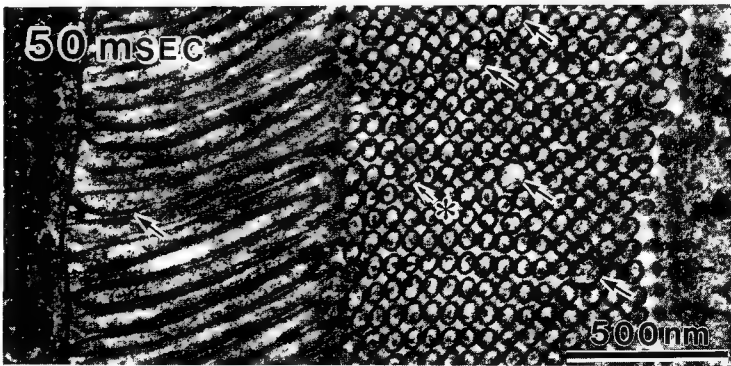
FIG 2.--Dark-adapted photoreceptors (DARK) and photoreceptors cryofixed at 50 msec after light stimulation (50 msec).

JET FREEZING OF CELLS AND TISSUES WITH AND WITHOUT CRYOPROTECTANTS

M.V. Parthasarathy, Carole Daugherty and T. Müller[*]

Section of Plant Biology, Cornell University, Ithaca, NY 14850
[*]BAL-TEC AG, FL-9496 Balzers, Principality of Liechtenstein

For the past several years cryofixation/freeze-substitution techniques have become valuable alternatives to chemical fixation of biological specimens. The superiority of cryofixation in preserving labile cell structures has been documented in several studies[1-2]. Commercially available jet freezers and the BAL-TEC HPM010 high pressure freezer have extended high quality cryofixation from monolayer cells to cells relatively deep inside tissues[3-5]. High pressure freezing can theoretically freeze biological materials of 0.5 mm thickness without the use of cryoprotectants[6] and propane jet freezing is reported to freeze biological samples up to 40 μm in thickness without cryoprotection[7]. Although high pressure freezing is the obvious method of choice for freezing large biological samples, its high cost combined with its apparent inability to consistently preserve microfilaments in some plant cells[8-10] has prompted us to explore the capability of jet freezing to yield well frozen samples with and without cryoprotectants.

We used the commercially available jet freezer JFD 030 (BAL-TEC) to obtain our results. Tightly pelleted cells sandwiched between 0.1 mm thick copper specimen carriers normally froze well without any cryoprotectants, after propane jet freezing (Figs. 1-2). However, good freezing of cells within tissues was obtained with propane jet freezing only when some cryoprotectant such as 0.1-0.2 M buffered sucrose[8] was used (Figs. 3-4). Cells of the phloem tissue, that naturally contain a high amount of sucrose, occasionally froze well without pretreatment with cryoprotectants. Variations in jet-pressures and thinner specimen carriers were tried in an effort to improve the freezing depth of cells in plant tissues that were not treated with cryoprotectants.

References

1.   B. Ding, R. Turgeon and M.V. Parthasarathy, Protoplasma (1991)165, 96
2.   S.A. Lancelle and P.K. Hepler, Protoplasma (1992)167, 215
3.   B. Ding, R. Turgeon and M.V. Parthasarathy, J.Electr. Microsc. Tech. (1991)19,107
4.   S.T. Craig and L.A. Staehelin, Europ. J. Cell Biol. (1988)46, 80
5.   D. Studer, M. Michel and M. Müller, Scanning Microsc. (1989)3, 253
6.   H. Moor, in Cryotechniques in Biological Microscopy, eds. R.A. Steinbrecht and K. Zierold, (1987), Springer-Verlag, 175
7.   J.C. Gilkey and L.A. Staehelin, J. Electr. Microsc. Tech. (1986)3,177
8.   B. Ding, R. Turgeon and M.V. Parthasarathy, J. Microscopy (1991)165, 367
9.   J. Z. Kiss, T.H. Giddings, L.A. Staehelin and F.D. Sack, Protoplasma (1990)157, 64
10.   U. Meindl, S. Lancelle and P.K. Hepler, Protoplasma (1992)170, 104
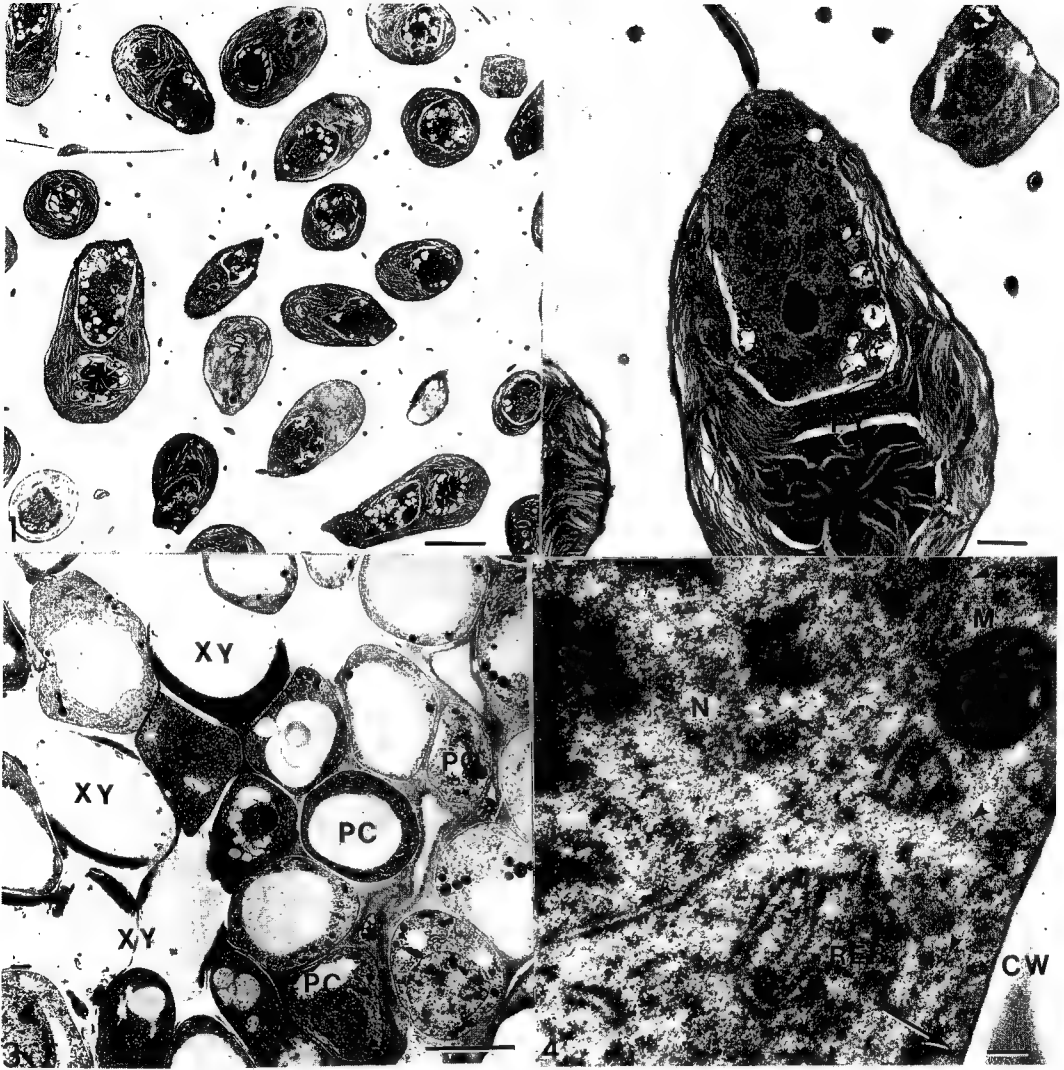
Figure 1. A portion of the pellet of the flagellated alga <u>Dunaliella salina</u> frozen without cryoprotectant. Bar= 5 μm

Figure 2. Higher magnification of the alga. Bar= 1 μm

Figure 3. Vascular bundle in oat coleoptile that was treated with buffered sucrose[8] before freezing. Note the good freezing of cells although the bundle was relatively deep within the coleoptile tissue. Bar= 5 μm

Figure 4. High magnification of a vascular cell showing good preservation of cytoskeletal elements. Bar= 0.1 μm

Key: C-chloroplast; CW-cell wall; M-mitochondrion; N-nucleus; PY-pyrenoid; PC-parenchymatous cell; RER-rough endoplasmic reticulum; XY-xylem element; arrow-microtubule; dart-microfilament bundle.

IMPROVED STRUCTURAL PRESERVATION OF HIGH-PRESSURE FROZEN CARTILAGE

Daniel Studer, Jeannine Wagner and Ernst B. Hunziker

M.E. Mueller Institute for Biomechanics, University of Berne, 3010 Berne, Switzerland

Adult cartilage is a unique tissue in that it is avascular and lacks innervation. The chondrocytes are embedded in an extracellular matrix which in most cases occupies 60 to 90% of the tissue volume. The ultrastructure and composition of rat growth plate cartilage has been investigated (1). It was found that during conventional chemical fixation of the tissue (2), about 60% of the extracellular matrix proteoglycans were lost (3). This artefact can be prevented if proteoglycans are precipitated by cationic dyes (eg. ruthenium hexaamine trichloride) during fixation (4) which forms relatively large precipitates by rendering high resolution imaging impossible. High pressure frozen extracellular matrix revealed a fine meshwork which was attributed to proteoglycan distribution (5). A meshwork due to segregation during freezing was not seen in recent experiments where adaequately frozen cartilage was investigated.

200μm thick sections of rat growth plate cartilage were excised in a bath of hexadecene (6). The sections were again processed under hexadecene, firstly punched (diameter 1.7mm) and then transferred to an aluminum sandwhich (corresponding in size to the sample). These samples were high pressure frozen in a PI-165 high pressure freezing machine (Fa. Wohlwend, 9466 Sennwald, Switzerland), freeze-substituted in acetone containing 2% OsO4 (16h at -90°C; 16h at -60°C; 12h at -30°C), embedded in epon and ultrathin sections were investigated in a Hitachi H 7100 electron microscope.

Parts of a cross-section of a growth-plate are shown (Fig. 1-4). The cells in the centre are not perfectly frozen (Fig.1). At high magnifications the meshwork in the matrix due to segregation patterns is illustrated (Fig. 2). Adaequately frozen cartilage cells close to the section surface (Fig. 3) lack this meshwork in the adjacent matrix (Fig.4), displaying instead an apparently uniform staining pattern that presumably corresponds to the proteoglycan distribution. After having assured a reproducible functioning mode for the high pressure freezer, the samples were consistently adaequately frozen to a depth of about 50μm. In one case (out of 30) the whole sample was adaequately frozen (i.e. to a depth of 100μm from both sides).

We found contrary to our previous description (5), that the matrix "meshwork" is absent in adaequately cryofixed cartilage matrix. Based on this result and the results of Michel et al. (7) we conclude, adaequate freezing is only achieved if the samples are vitrified. Vitrification is critically dependent on the composition of the ingredients in a tissue or cell, even within single cells the freezing quality of adjacent compartments can vary considerably and the same cell compartments in adjacent cells can show different freezing results. These remaining problems of cryofixation protocols can be overcome only by improving cryofixation techniques. Our aim is to be able to vitrify 200μm thick cartilage tissue slices. To achieve this goal, we are currently investigating the influence of different pressure levels with respect to time.

References

1. Hunziker E.B (1992) Biological regulation of the chondrocytes, ed. M. Adolphe, CRC Press :1-27.
2. Luft J.H. (1961) J. Biophys. Biochem. Cytol. 9: 409-414.
3. Engfeldt B. and Hjertquist S.O. (1968) Virchows Arch. 1: 222-229.
4. Hunziker E.B. et al. (1982) J. Ultrastruct. Res. 81: 1-12.
5. Hunziker E.B. and Schenk R.K. (1984) J. Cell Biol. 98: 277-282.
6. Studer D. et al. (1989) Scanning Microscopy, Supplement 3: 253-269.
7. Michel et al. (1991). J.Microsc.163: 3-18.
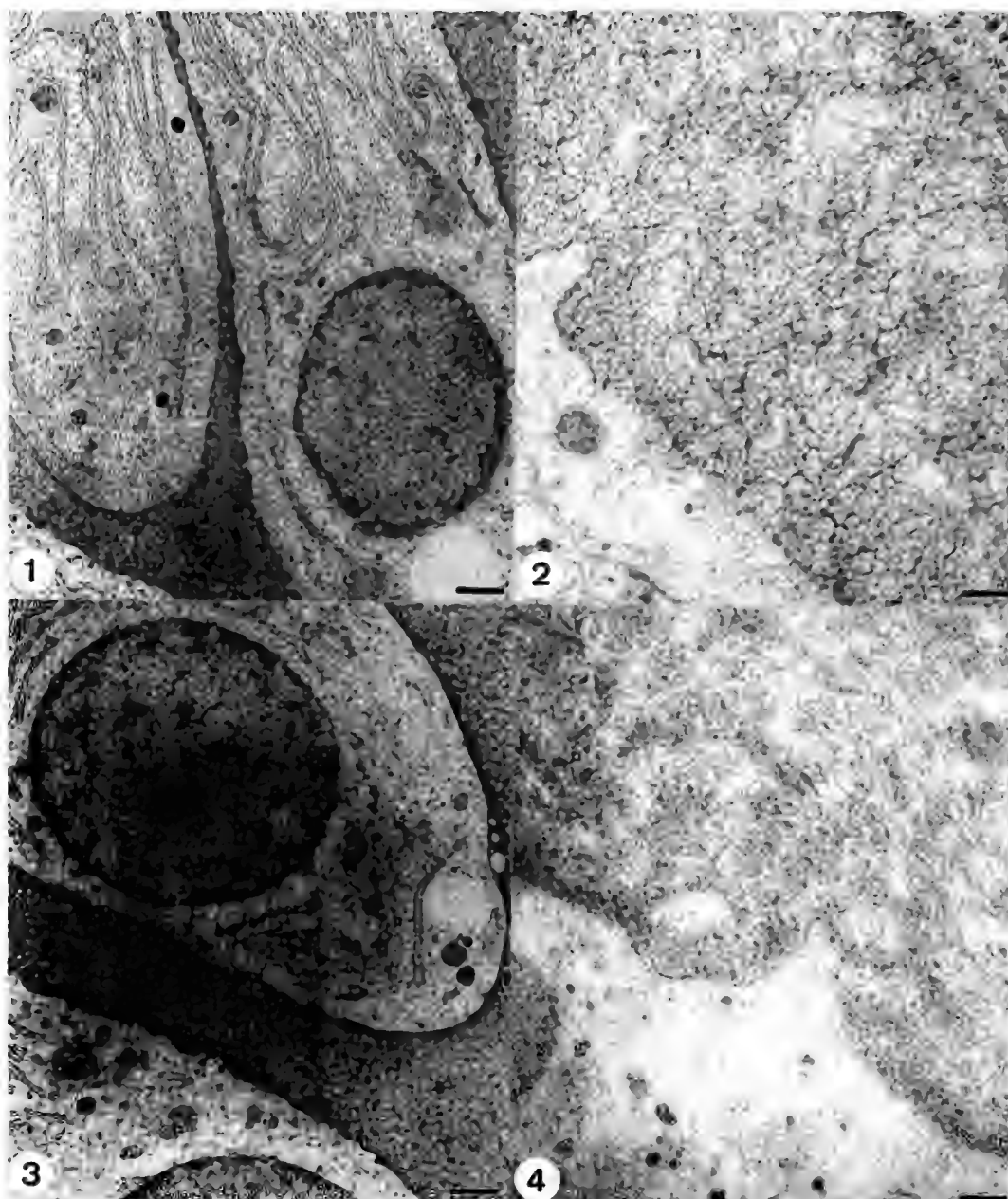
Fig. 1. Cartilage cells in the center of a 200μm thick section (bar 1μm).
Fig. 2. Matrix adjacent to the cells of Fig. 1; segregation patterns are apparent (bar 100nm).
Fig. 3. Cartilage cells close to the surface of a 200μm thick section (bar 1μm).
Fig. 4. Matrix adjacent to the cells of Fig. 2; no segregation patterns are present in the interfibrillar space (bar 100nm).

HIGH-PRESSURE FREEZING IMPROVES QUANTITATIVE AND QUALITATIVE STRUCTURAL DATA IN THE ACTINOMYCETE MICROSYMBIONT FRANKIA

R. Howard Berg

Department of Biology, Memphis State University, Memphis, TN, 38152

Symbiotic plant root nodules containing the nitrogen-fixing bacterium Frankia occur on a variety of woody shrubs and trees.[1] Ever since the first micrographs of freeze substituted cells of Frankia in culture were published[2] there has been impetus to see if freeze substitued nodule tissue will improve imaging of Frankia in vivo. High pressure freezing/freeze substitution (HPFS) accomplishes this.

Frankia is an actinomycete that fixes N_2 in a specialized multicellular, spherical structure termed the "symbiotic vesicle" that is surrounded by a multilamellate envelope (MLE) comprised of lipids. Early work based on MLE birefringence suggested the MLE was a O_2 diffusion barrier, thereby protecting nitrogenase from O_2-inactivation. Recently this has been challenged by freeze fracture data.[3] Traditionally it has been assumed that the MLE is electron-translucent because the lamina of the MLE are extracted by dehydration solvents, producing the "void space"--an extraction artifact hindering TEM analysis of MLE structure.

En bloc staining with chromic acid stains the MLE, showing that the MLE is present after exposure to dehydration solvents and that the void space results from tissue shrinkage in the symbiotic vesicle (Figure 1). In chemical fixation (CF), e.g. with glutaraldehyde and osmium, the MLE can not be imaged because the lamina are not stained and are indistinguishable from the void space artifact abutting the MLE (Figure 2). With HPFS (substitution in osmium/acetone, embedded in epon) the MLE is still unstained but it is readily imaged as an electron-translucent halo surrounding the symbiotic vesicle (Figure 3) because freeze substitution eliminates the void space. HPFS makes possible the quantitative analysis of MLE thickness in thin sections, allowing high resolution morphological studies of this important structure, both around a specific symbiotic vesicle and in comparison with those in other plant species. Furthermore, with HPFS there is better preservation of cytoplasmic structures such as the paracrystalline "striated body"(SB), which aligns in the center of young symbiotic vesicles, "directing" the formation of the first (longitudinal) septum (Figure 4). HPFS reveals a more detailed ultrastructure of mature SBs (Figure 5).[4]

References

1. C.R. Schwintzer and J.D. Tjepkema, Ed., Biology of Frankia, San Diego: Academic Press (1990):408.
2. S.A. Lancelle et al., Protoplasma (1985)127, 64.
3. R.M. Abeysekera et al., Can. J. Microbiol. (1990)36, 97.
4. This research was supported by NSF Instrumentation Grants DIR 9020299 and DIR 9102472.

Thin sections of symbiotic vesicles in root nodules of <u>Alnus</u> <u>serrulata</u> (Figs. 1,3-5) or <u>Elaeagnus</u> <u>pungens</u> (Fig. 2).
Fig. 1.--Fixation in chromic acid (0.5% aqueous, 1.5 h), embedded in epon. Void space (VS) forms between bacterial cytoplasm (BC) and the MLE. Bar = 1 μm. Inset: lamina of the MLE are stained by chromic acid. Bar = 0.1 μm.
Fig. 2.--CF symbiotic vesicle. Void space is indistinguishable from MLE. Bar = 1 μm.
Fig. 3.--Symbiotic vesicle after HPFS. MLE is unstained. Bar = 1 μm.
Fig. 4.--Striated body (arrow) in young symbiotic vesicle positions in the center; first septum (arrowhead) in stalk hypha. Bar = 1 μm.
Fig. 5.--Paracrystalline striated body in mature symbiotic vesicle. Bar = 50 nm.

EM IMMUNOCYTOCHEMISTRY FOLLOWING CRYOFIXATION BY HIGH-PRESSURE FREEZING AND LOW-TEMPERATURE EMBEDDING

Kent McDonald, Mary K. Morphew and J.R. McIntosh

Lab for 3-D Fine Structure, MCD Biology, U. Colorado, Boulder, CO 80309-0347, USA

A look at recent journals publishing cell and developmental biology papers shows that localization of antigens by immunoEM techniques is becoming increasingly popular. One can also see that a wide variety of immunoEM methods are being applied: pre-embed and post-embed labelling, cryofixation and room temperature fixation, cryosections and resin sections, LR White and Lowicryl resins, 5 - 10 nm gold and silver-enhanced 1 nm gold, and so on. This array of choices can be confusing to investigators unfamiliar with EM techniques but wanting to do EM immunolocalization of their antibodies. A very helpful overview of the problems can be found in the article by Kellenberger and Hayat[1] and in the series of books on colloidal gold methods edited by Hayat.[2] In this presentation, we will consider the different ways to fix cells for immunoEM and our experience with LR White and Lowicryl K4M resins.

Fixations for light microscope immunofluorescence usually involve some kind of extraction with either organic solvents and/or detergents. Unfortunately, these same methods cannot be used for EM studies because cell fine structure is poorly preserved (Fig. 1). We find that the best fixation for conventional EM (Fig. 2) and immunoEM (Figs. 3 & 4) is achieved by ultrarapid freezing followed by freeze substitution. For cells larger than about 10 um, high pressure freezing is the method of choice, though double propane jet freezing can be used on some larger cells. Our standard freeze substitution protocol for immunoEM uses 0.1% glutaraldehyde in acetone at -90 C for 2-3 days. Cells are warmed to about -40 C and infiltrated with either LR White or Lowicryl K4 M and polymerized by UV at the same temperature. Both methods work well with a variety of antibodies, however, we tend to prefer Lowicryl because there is less extraction of the ground cytoplasm (Figs. 3 & 4).[3]

1. E. Kellenberger and M.A. Hayat, in M.A. Hayat, Ed., Colloidal Gold, Vol. 3, San Diego, Academic Press (1991):1.
2. M.A. Hayat, Ed., Colloidal Gold, Vols 1 & 2, San Diego, Academic Press (1989).
3. This research was supported by grant RR00592 from the National Institutes of Health. We also wish to thank Dr. R.E. Boswell, MCD Biology, U. Colorado, Boulder for providing the *Drosophila* embryos.

FIG. 1. Posterior pole plasm of a *Drosophila* embryo fixed by immersion in cold methanol, then prepared for EM by glutaraldehyde - osmium fixation. Mitochondria (m) are discernible in the highly extracted cytoplasm. Bar = 0.5 um.
FIG. 2. Posterior pole plasm of a *Drosophila* embryo fixed by high pressure freezing, freeze substituted in 1% OsO_4 in acetone and embedded in Epon-Araldite. Mitochondria (m) and polar granules (p) are evident. Bar = 0.5 um.
FIG. 3. As in Fig. 2, except freeze substituted in 0.1% glutaraldehyde in acetone and embedded in Lowicryl K4M. 10 nm gold particles on polar granules (p) and mitochondria (m) recognize an antibody against tudor, a protein required for normal germ cell development in *Drosophila*. Bar = 0.5 um.
FIG. 4. As in Fig. 3, except embedment was in LR White. Note the white areas (arrows) which suggest extraction of the ground cytoplasm. Bar = 0.5 um.
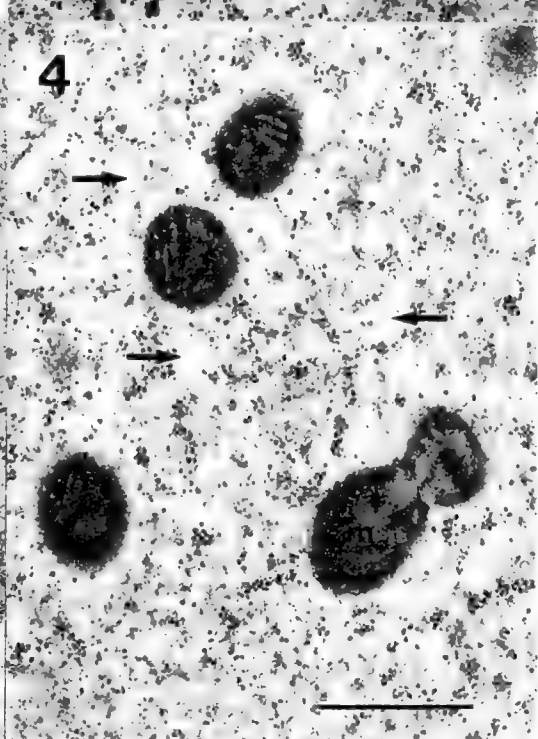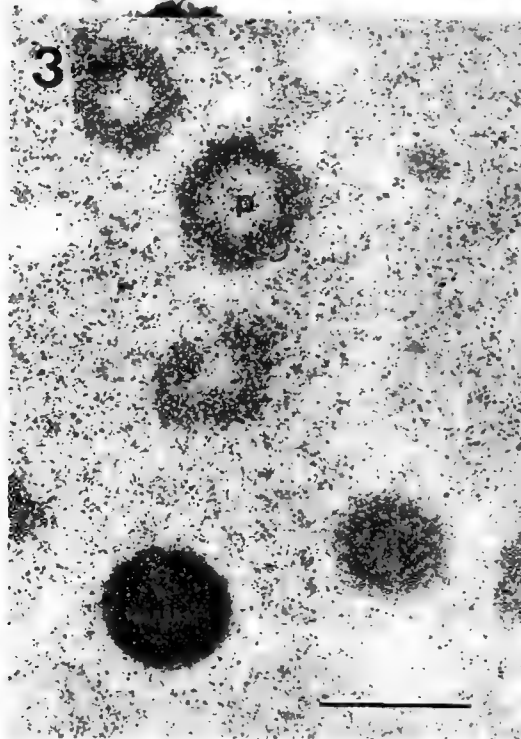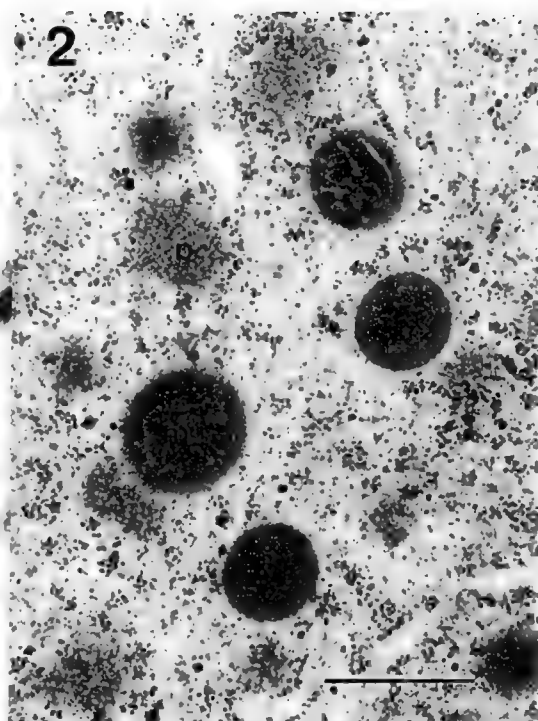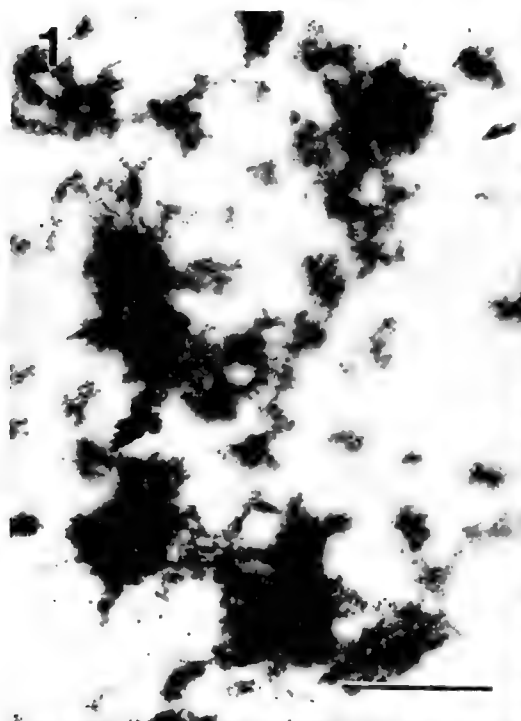
CRYO-ENHANCEMENT OF ULTRASTRUCTURAL, IMMUNOLOGICAL, CYTOCHEMICAL, AND LOW-VOLTAGE SEM CHARACTERIZATION OF FUNGAL GROWTH AND MORPHOGENESIS

Richard J. Howard and Timothy M. Bourett

DuPont Comapnay, Science and Engineering Laboratories, Wilmington, DE 19880-0402

Cells of filamentous fungi exhibit a characteristic somatic form, organized as a linear file of individual cells, known as the hypha. Growth of the fungus occurs primarily through expansion at the apex of the hyphal tip cell, where highly organized and localized exocytosis is thought to be responsible for the deposition of new cell wall. In pathogenic fungi, changes in the pattern of tip growth are the means by which specialized infection structures develop, enabling the fungus to adhere to and penetrate the host surface, establish infection and cause disease.[1,2] The use of cryo techniques has provided a vastly expanded knowledge of the cellular bases underlying these important morphogenetic events.

Hyphae are easily grown as a monolayer in culture, on pieces of cellophane overlying nutrient agar. These cell monolayers are easily manipulated for plunge freezing with minimal perturbation and no treatment necessary prior to quenching. In this sense, plunge freezing is superior to other cryo-fixation techniques that require pre-treatment or mounting of live specimens onto holders, hats or pistons. The subcellular organization of hyphal tips is exquisitely sensitive to environmental changes, and must be frozen within a few seconds from the time that the cellophane substratum is lifted from the agar surface. We obtain excellent results using a 9:1 mixture of propane and ethane.[3]

Freeze substitution of hyphal tip cells[4,5] has allowed for the observation of structures not recognized in chemically fixed specimens.[6] Elements of the cytoskeleton are obvious examples, including ubiquitous cytoplasmic microtubules (often associated with vesicular bodies),[7] intermediate tubular elements (16nm diam.), and various arrays of microfilaments.[8] Additional new cell constituents include an extensive system of endomembrane consisting of fenestrated single cisternae[4,6] (possibly representing a function equivalent to Golgi bodies which are not found in these organisms), a new organelle called the filasome,[6] and a vesicle-free core within the cloud of apical vesicles (the Spitzenkörper) lying adjacent to the site of mass exocytosis.[9] Modification of preparative protocol has allowed us to couple immunocytochemistry with freeze substitution for the post-embedment localization of actin within filasomes and the Spitzenkörper core.[9] Other modifications have enhanced our ability to detect intracellular lectin binding sites on thin sections and provide the first cytochemical marker for components of the secretory apparatus in a filamentous fungus.[10]

Low temperature low voltage field emission scanning electron microscopy has been an especially valuable tool in the study of extracellular, highly hydrated fungal mucilages. These substances are involved apparently in adhesion of fungal cells to the host surface,[11] and are found among a broad taxonomic spectrum of pathogens.

114

1. R.J. Howard et al., Proc. Natl. Acad. Sci. USA 88(1991)11281.
2. T.M. Bourett and R. J. Howard, Can. J. Bot. 68(1990)329.
3. H.C. Hoch, in H.C. Aldrich and W.J. Todd, Ed., Ultrastructure Techniques for Microorganisms, New York: Plenum Press (1986)183.
4. R.J. Howard and J.R. Aist, J. Ultrastruct. Res. 66(1979)224.
5. R.J. Howard and K.L. O'Donnell, Exp. Mycol. 11(1987)250.
6. R.J. Howard, J. Cell Sci. 48(1981)89
7. R.J. Howard and J.R. Aist, J. Cell Biol. 87(1980)55.
8. T.M. Bourett and R. J. Howard, Protoplasma 168(1992)20.
9. T.M. Bourett and R. J. Howard, Protoplasma 163(1991)199.
10. T.M. Bourett et al, Exp. Mycol (1993), in press.
11. J.E. Hamer et al., Science 239(1988)288.
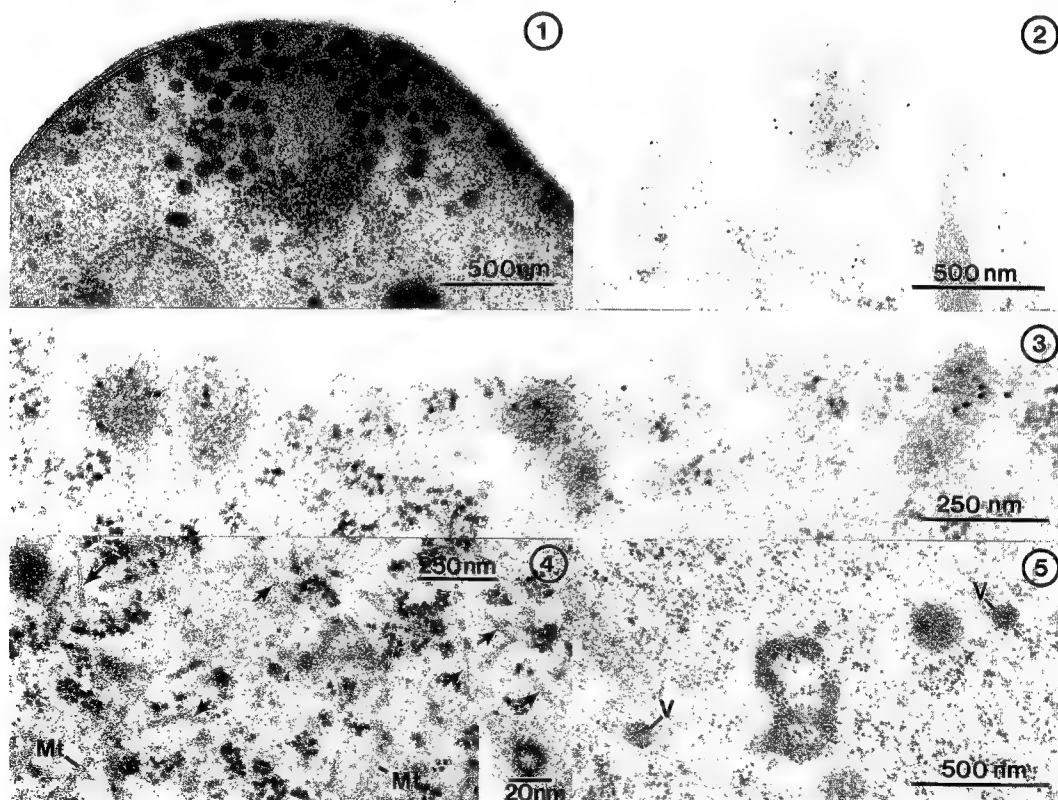
FIG. 1. HVEM micrograph of 250 nm thick section through hyphal tip of *Fusarium accuminatum* showing numerous vesicles and central core region of Spitzenkörper.
FIG. 2. Apical region of LR White-embedded hyphal tip of *Magnaporthe grisea*, prepared as in ref. 9, illustrating post-embedment actin localization within Spitzenkörper core.
FIG. 3. Post-embedment immunolocalization of actin within filasomes.
FIG. 4. Possible 16nm diam. cytoskeletal inclusions in germ tube of *M. grisea* (arrows), exhibit apparent protofilament-like substructure (inset). Mt, microtubule; F, filasome.
FIG. 5. Concanavalin A binding sites in smooth membrane cisterna and apical vesicles (V) of *Trichoderma viride*, localized using indirect method and HRP-gold probe.

115

CRYO-ELECTRON MICROSCOPY OF HUMAN ERYTHROCYTE MEMBRANE SKELETONS

Li Li and Robert Josephs

Laboratory for Electron Microscopy and Image Analysis, Department of Molecular Genetics and Cell Biology, The University of Chicago, Chicago, IL 60637

The membrane skeleton is a two-dimensional network of structural proteins attached to the cytoplasmic surface of the erythrocyte membrane. Spectrin, actin and band 4.1 are the major components in the skeleton network. It is generally believed that the membrane skeleton plays an important role in the deformability and stability of red cells. In this work we have used cryo-electron microscopy to examine the effect of ionic strength on skeleton size. Since the skeletons were unstained, unfixed and hydrated drying effects and the attendant changes in salt concentrations and pH associated with negative staining did not affect our results. The skeletons were embedded in a thin layer of vitreous ice supported by a fenestrated carbon film, which provided higher contrast than fenestrated carbon grids.

Ghosts derived from normal human red cells were incubated with 4 volumes of 2.5% Triton X-100 in 5 mM sodium phosphate (pH 7.4) for 1 hour at 4°C. The mixture was layered on top of a discontinuous density gradient of 10% and 60% sucrose. After centrifugation, the membrane skeletons were collected and dialyzed against 0.2 mM or 5 mM sodium phosphate buffer (pH 7.4) for 4-6 hours. Dialyzed skeletons were applied to carbon-coated fenestrated films that had been treated with 1% Alcian blue and rinsed thoroughly with distilled H_2O. The grids were then blotted to produce a thin layer of solution and immediately plunged into a liquid ethane slush. The grids were examined without any further processing under low dose conditions in a Philips CM10 microscope equipped with a Gatan cold stage and an anticontaminator. Contour lengths and end-to-end distances of spectrin tetramers in intact membrane skeletons were measured from enlarged prints using the computer program Macmeasure. The molecules' correlation length was calculated by iterative approximation using the following formula:

$$<R^2> = 2b^2[L/b-1+exp(-L/b)]$$

where R is the end-to-end distance of a particle, L is the contour length, and b is the correlation length.[1]

Figure 1 is an image of frozen-hydrated membrane skeletons showing a polygonal lattice of actin junctional complexes crosslinked by spectrin tetramers. There were generally 5 to 8 spectrin tetramers radiating from each junctional complex (Figure 1). Usually there was one spectrin molecule bridging adjacent actins but about 20% of the connections contained two spectrin tetramers (arrows). We noted that for skeletons in 5 mM NaPi buffer, because of the screening of electrostatic repulsion at higher ionic strength, it was more difficult to obtain large areas of expanded lattice than in 0.2 mM buffer.

For skeletons embedded in 0.2 mM sodium phosphate buffer (pH 7.4), the average distance between actin protofilaments was 151.2 nm (data not shown). The average contour length of spectrins was 174.9 nm and the correlation length was 255.8 nm (Figure 2). When skeletons were embedded in 5 mM sodium phosphate buffer (pH 7.4), which was obtained by rinsing with 5 mM NaPi buffer (pH 7.4) after the skeletons dialyzed in 0.2 mM NaPi buffer were applied onto the grids, the average contour length and correlation length were 153.9 nm and 536.0 nm, respectively (Figure 3). The average end-to-end distance decreased to 143.3 nm. The results were similar for skeletons dialyzed in 5 mM NaPi buffer. Since the average correlation length increased at higher ionic strength the shorter particles are straighter. This observation supports the model[2] of spectrin as a two stranded helix which contracts in a spring-like manner with increasing ionic strength.[3]

References

1. T. R. Coleman et al., Cell Motil. Cytoskel. 12(1989)248
2. A. M. McGough and R. Josephs, Proc. Natl. Acad. Sci. USA 87(1990)5208
3. This work was supported by NIH Grant HL22654
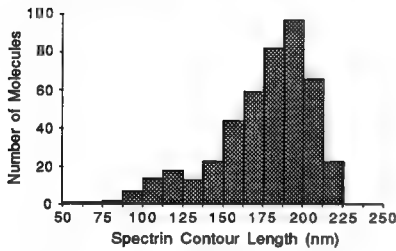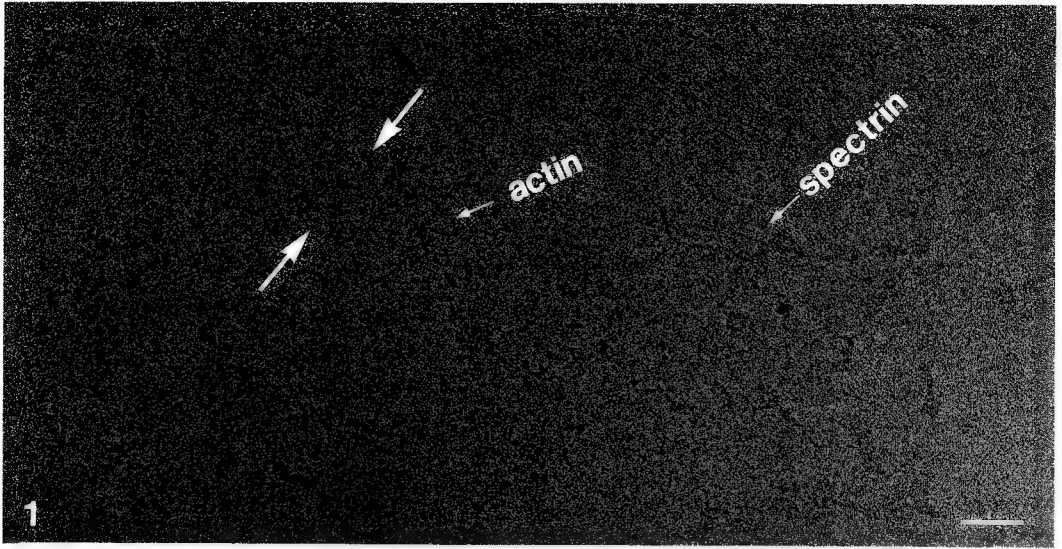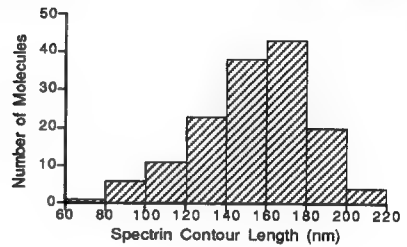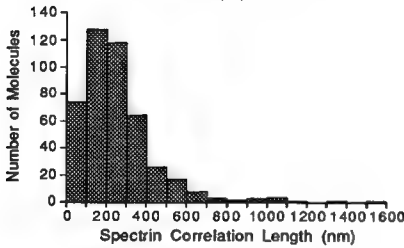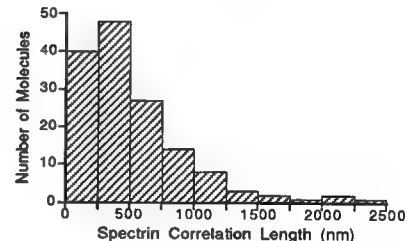
Figure 1.---Cryo-electron micrograph of expanded membrane skeleton embedded in a thin layer of vitreous ice crossing a hole in the supporting carbon film. Bar=50 nm.

Figure 2.---Contour length and correlation length of spectrin tetramers in 0.2 mM NaPi (pH 7.4). (a). Histogram showing the spectrin contour length distribution (mean=174.9±30.5 nm). (b). Histogram showing the spectrin correlation length distribution (mean=255.8±194.9 nm).

Figure 3.---Contour length and correlation length of spectrin tetramers in 5 mM NaPi (pH 7.4). (a). Histogram showing the spectrin contour length distribution (mean=153.9±27.7 nm). (b). Histogram showing the spectrin correlation length distribution (mean=536.0±437.5 nm).

ENERGY FILTERING AND CORRECTION FOR THE CONTRAST TRANSFER FUNCTION (CTF) OF FROZEN HYDRATED OBJECTS AS ILLUSTRATED BY A RECONSTRUCTION OF *DICTYOSTELIUM* S1 DECORATED ACTIN

Rasmus R. Schröder[*], Dietmar Manstein[§], Werner Jahn[*] and James A. Spudich[$]

[*]Department of Biophysics, Max-Planck-Institute for Medical Research, P.O. Box 103820, W-6900 Heidelberg, Germany, [§]National Institute for Medical Research, London NW7 1AA, U.K., [$]Department of Biochemistry, Beckman Center, Stanford University, School of Medicine, Stanford, CA 94305, USA

Ice embedded samples can not be simply described as weak phase objects, but as strong interacting specimens with inelastically dominated multiple scattering[1]. Removal of the inelastically scattered electrons allows closer to focus imaging and improves the structural signal to noise ratio, both leading to a higher structural information content[2]. Recent work demonstrated, that for radial density distributions the CTF correction of energy filtered images was necessary and sufficient to obtain good agreement with X-ray data[3]. Here we present the fully CTF-corrected three dimensional structure of F-actin decorated with Dictyostelium myosin head fragment (MHF). The results show aggreement to the known protein structure after CTF correction. In addition to the radial density profile also amplitudes of Bessel terms in the Fourier Transform are changing.

Actin from rabbit muscle was decorated with Dictyostelium myosin head fragment under the usual buffer conditions. Images were taken with a Zeiss EFTEM EM902. Magnification was 50000x, electron energy 80kV, electron energy loss $\delta E=0eV$ (zero-loss mode), energy width $\Delta E=20eV$, defocus values were in the range of 500-900nm. Vitrified samples were observed at a temperature of 90K. All images were taken at an specimen electron dose of 500 e^-/nm^2, negative material was Kodak SO163 developed for 12 min in undiluted Kodak D19. For image processing and the helical reconstruction a new set of computer programs was written.

Figure 1 gives a typical example of the protein complex. Single straight filaments show structural signal up to the 8th layerline (ca 4nm resolution) in the diffractometer pattern, as seen in Figure 2. Before averaging filaments from different negatives the CTF was corrected: Figure 3 shows an CTF uncorrected map of filaments from one micrograph. The ratio of amplitude to phase contrast in the CTF was then fitted ca 15% by adjusting the radial density distribution to the assumed mass distribution of actin and myosin. Figure 4 shows an unrealistic distribution for 10% amplitude contrast, values bigger than 20% again give meaningless results. The defocus of the individual negatives can be determined by the Thon rings visible in the optical diffraction of large negative areas. After averaging strong signal at higher resolution becomes apparent. An averaged map is shown in figures 5 and 6. Alterations in the weighting of individual Bessel terms of the helical Fourier synthesis show as changes in the overall structure. An apparent left handed helix in Figure 3 is reduced, whereas the right-handed long pitch helix of F-actin is increased. This is in good agreement with an atomic F-actin model.[4]

References

1. R.R. Schröder, J. Microsc. (1992)166, 389.
2. R.R. Schröder, et al., J. Struct. Biol. (1990)105, 34.
3. M.F. Smith, and J.P. Langmore, Mol. Biol. (1992)226,763.
4. K.C. Holmes et al., Nature (1990)347, 44.
5. We thank K.C. Holmes for his support and help with the helical reconstruction programs. This work was supported by grants to JAS from the NIH and the Alexander von Humboldt Stiftung.
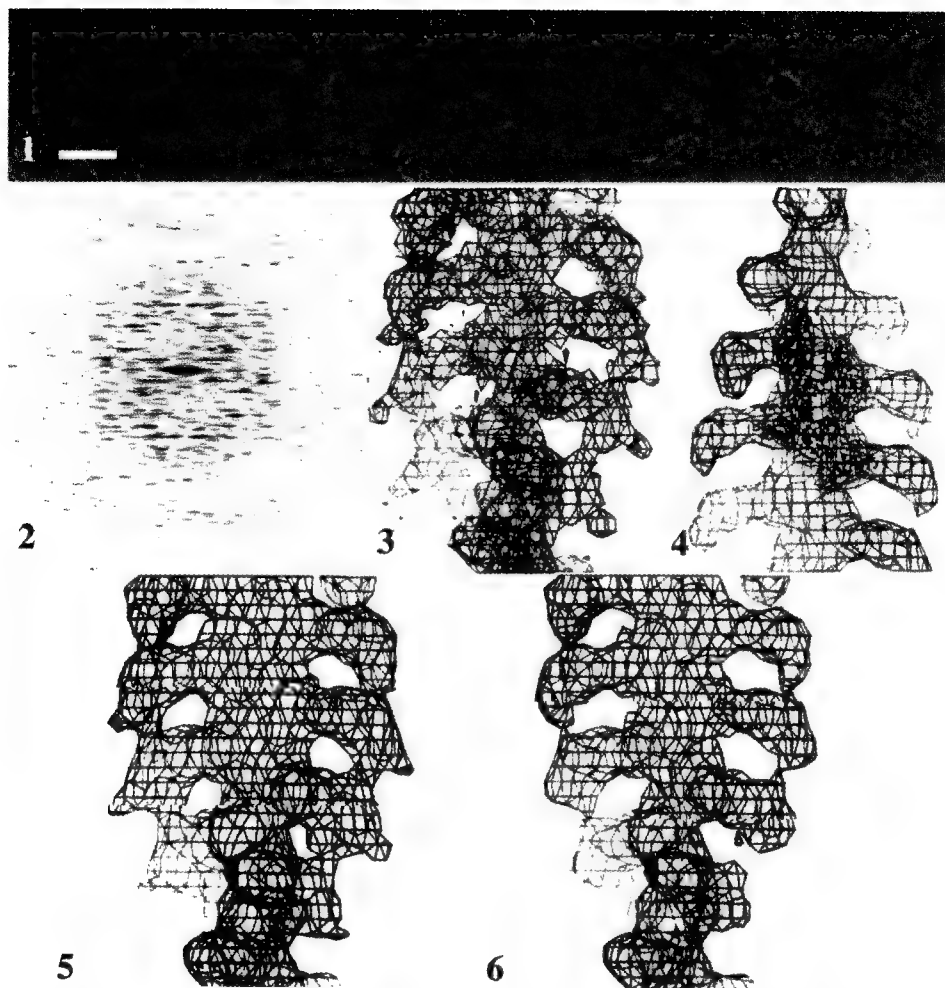
FIG. 1.--F-actin decorated with *Dictyostelium* myosin head fragment embedded in vitrious ice. Defocus ca 900nm, scale bar =35.4nm. Note the high contrast and the good visibility of the individual myosin moieties in single arrowheads along the filament.

FIG. 2.--Computed diffraction pattern of one single filament consisting of six arrowheads. Already from one filament a clear helical diffraction pattern is observable.

FIG. 3.--3D map uncorrected for the effects of the contrast transfer function. A strong left-handed helix in the F-actin part of the map is found. The densities of adjacent actin monomers show less contact than predicted by an atomic F-actin model.

FIG. 4.--CTF-corrected reconstruction with an assumed ratio of amplitude to phase contrast of 10%. The actin density changes, adjacent monomers in the left-handed helices are now connected. In the centre of the filament 4 individual actin monomers are shown. The myosin head fragment mass is too low, indicating a false radial density profile.

FIG. 5.--CTF-corrected reconstruction (42 arrowheads, i.e. 546 single myosins) with a density distribution as assumed from the actin and myosin masses. The ratio of amplitude to phase contrast is fitted to 14%., Resolution is restricted to 2nm, strong data exist up to 2.7nm resolution.

FIG. 6.--Another representation of the protein density of Figure 5 at a higher cutoff level, i.e. showing a closer protein envelope. All density maps are displayed on a 1nm grid.

119

3-D IMAGING OF FREEZE-DRIED ACTIN FILAMENTS IN FIBROBLAST USING HIGH-RESOLUTION CRYO-SEM

Ya Chen, Alexander B. Verkhovsky and Gary G. Borisy

Integrated Microscopy Resource (IMR) for Biomedical Research--An NIH Biotechnological Center, University of Wisconsin, 1675 Observatory Drive, Madison, WI 53706, U.S.A.

A new approach to image the macromolecular structure of actin filaments from detergent-extracted cultured cells using high resolution low-temperature scanning electron microscopy (cryo-SEM) is described. An advantage of studying the cytoskeleton by SEM is its large depth of focus which makes it easy to reveal the three-dimensional relationship between the cytoskeleton filaments. Recently, procedures have been investigated for high resolution visualization of biological samples by SEM.[1,3,5,8,9] These studies have demonstrated the importance of cryo preparation techniques for preserving the morphology of the specimen and advanced metal coating techniques for revealing its topography.

Coating for HRSEM requires a metal layer that will not obscure fine details while still yielding adequate SE signal. Magnetron-sputter coating of the samples with an ultrathin layer of metal at low temperature provides finer grain size than coating at ambient temperature. Chromium has many properties that make it suitable as coating metal for cytoskeleton: it has fine grain size, low BSE yield due to its low Z number, and it provides adequate SE signal.[6] This work was aimed to image the macromolecular structure of cytoskeletons *in situ* using freeze-drying, cryo-coating, and cryo-SEM.

Swiss 3T3 fibroblasts were grown on carbon-coated formvar grids in HAM's F-10 medium supplemented with 10% fetal bovine serum and antibiotics. Cells were extracted with 1% Triton X-100 solution as described[7], fixed in 2% glutaraldehyde for 30 min, and washed several times in distilled water. The grid was plunge-frozen in liquid ethane cooled by liquid nitrogen, transferred into a Gatan cold-stage, and freeze-dried at -85°C for 2 hours in the MED 010 (Bal-Tac) cryo-sputtering unit. Under these controlled conditions, all the bulk water is sublimated, but the protein-bound water, which is necessary for retention of the structural integrity and mechanical stability of the protein, is retained.[2] Cryo-sputtering with chromium was performed at -85°C and a 1.5 nm mass thickness was measured during coating with a quartz-crystal monitor (STM-100, Sycon) mounted at the same level as specimen. Specimens were examined at -110°C in a field emission "in-lens" type high resolution low-voltage SEM (Hitachi S-900).[1] Stereo pair images were taken at tilt angles of ±4°.

Stereo pair micrographs (Figure 1) illustrate a region of the fibroblast cytoskeleton showing a bundle of filaments with diameter of 8-9 nm, which were identified as actin filaments by their general morphology. A short repeat of 5.5 nm produced by the actin subunits was also clearly identified. The chromium coating layer provides sufficient topographic contrast, and the grain size is small enough not to hide small features such as the actin subunits.

In conclusion, success in the visualization of the macromolecular structure of actin filaments *in situ* in the fibroblast cytoskeleton was attributed to fast freezing, controlled

freeze drying and chromium thin coating. The resolution achieved was comparable to previously attained by TEM using the freeze-fracture, replica technique.[4] Application of these techniques offers a powerful approach for studying cytoskeleton organization.

Reference:
[1] Chen Y & Walther P (1992) *50th EMSA*, pp. 1280-81
[2] Gross H (1987) *Cryotechniques in Biological Electron Microscopy* (ed. by R.A. Steinbrecht & K. Zierold), Springer-Verlag, Berlin Heidelberg, PP. 205-215
[3] Hermann R & Müller M (1991) *Scanning Microscopy*, 5(3):653-664
[4] Heuser JE & Kirschner MW (1980) *J Cell Biol.*, 86, 212-234
[5] Lindroth M, Bell PB & Fredriksson BA (1988) *J Microsc.*, 151:996-
[6] Peters KR (1985) *Scanning Electron Microsc.*, IV:1519-1544.
[7] Verkhovsky AB, Surgucheva IG, Svitkina TM, Tint IS & Gelfand VI (1987) *Exp. Cell Res.*, 173:244-255.
[8] Walther P, Chen Y, Pech LL & Pawley JB (1992) *J. Microsc.*, 168:169-180
[9] Wepf R, Bremer A, Amrein M, Aebi U & Gross H (1992) *10th EUREM 92*, 3:751-753
[10] We thank Mr. Charles Thomas for editorial assistance. This work was supported by NIH Grant RR-0570 to the Integrated Microscopy Resource (IMR), Madison, Wisconsin.
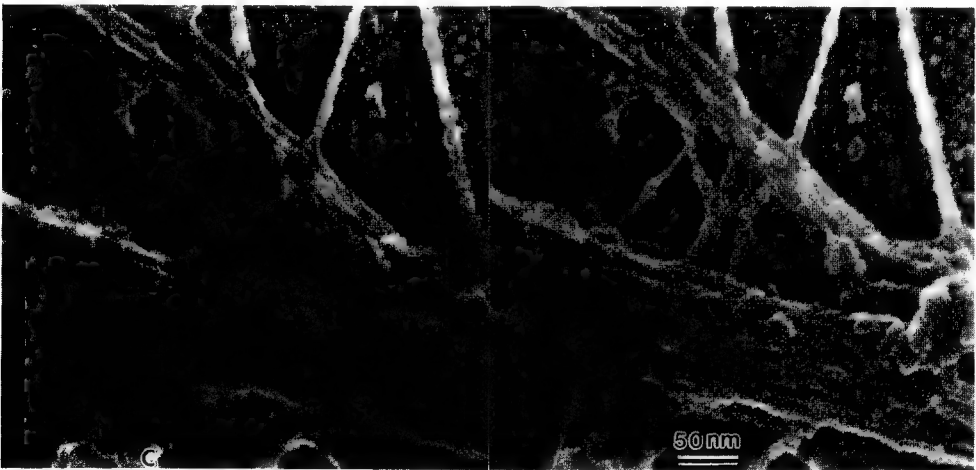
Figure 1--Stereo pair of micrographs illustrate cytoskeletons of extracted fibroblast. The specimen was plunge frozen, freeze-dried, cryo-coated with 1.5 nm chromium, and viewed in the Hitachi S-900 high-resolution SEM equipped with a Gatan cold-stage. A region of the fibroblast cytoskeleton shows a bundle of filaments with diameter of 8-9 nm, which were identified as actin filaments by their general morphology. A short repeat of 5.5 nm produced by the actin subunits was clearly seen.

USE OF PLATINUM SHADOWING AND MAGNETRON SPUTTER COATING IN AN OXFORD CRYOTRANS SYSTEM TO INCREASE LOW TEMPERATURE RESOLUTION OF BIOLOGICAL SAMPLES IN A HITACHI FIELD-EMISSION SCANNING ELECTRON MICROSCOPE

William P. Wergin, Eric F. Erbe and Alan Robins[*]

Electron Microscopy Laboratory; ARS-BARC; Beltsville, MD 20705-2350 and
[*]Oxford Instruments Limited; Scientific Research Division; Eynsham, England

Previous studies in this laboratory have shown that the resolution of biological specimens could be increased at least two fold in a conventional[1,2] as well as a field emission SEM[3] by substituting high vacuum evaporation of Pt for standard sputter coating. Because the EMscope SP2000A Sputter Cryo System and the Oxford CT 1500 Cryotrans System, which were used in these experiments, employed standard sputter coating, Pt shadowing and C evaporation were carried out in a modified Denton DFE-3 freeze-etch module on a DV-503 high vacuum evaporator and the coated specimens were transferred to the cryostage (EMscope) or the prechamber (Oxford) of the cryosystem. Not only did this procedure require a high vacuum evaporator but as a result of a through air transfer into LN_2, considerable contamination condensed on the surface of the specimen.[2,3,4] Most of this contamination consisted of water ice that could be easily sublimed; however, other unidentifiable contaminants remained. To increase the versatility of the cryosystem, reduce surface contamination of the specimen and evaluate alternative coating procedures, Oxford Cryotrans Systems were equipped and tested with a Pt evaporator and a high resolution magnetron sputter head. Low temperature observation and evaluation of the coated specimens were performed in a Hitachi S4100 field emission scanning electron microscope.

For Pt shadowing in an Oxford CT 1500, a suspension of yeast cells was mounted in hinged specimen holders, frozen in LN_2, and transferred through the uncooled prechamber to the precooled cold stage on the microscope. The stage in the prechamber was then cooled and the specimen was moved from the microscope to the prechamber where the specimen was fractured and shadowed. For magnetron sputter coating in the Oxford CT 1500-HR, a yeast suspension was mounted on a standard specimen holder, frozen in LN_2 and inserted into the prechamber where it was cleaved with a rotary knife and coated with Au/Pd.

Procedural changes in specimen handling combined with either high vacuum evaporation or magnetron sputter coating resulted in resolution sufficient to image nuclear pores much more clearly than was apparent after standard sputter coating (**Figs. 1 & 2**). Membrane particles could be observed on the fractured plasma membranes after shadowing as well as magnetron sputter coating (**Figs. 3 & 4**); these details could not be resolved after standard sputter coating. In conclusion, these simple modifications in the coating and handling procedures, which have been incorporated into the Oxford CT 1500 Cryotrans System, can be used to increase resolution of biological specimens to less than 10 nm.

1. W. P. Wergin et al., Proc. Ann. EMSA Meeting **46**(1988)256.
2. W. P. Wergin and E. F. Erbe, Scanning Microscopy **5**(1991)927.
3. W. P. Wergin and E. F. Erbe, Proc. Ann. EMSA Meeting **49**(1991)514.
4. W. P. Wergin and E. F. Erbe, Scanning **14**(1992)II40.

Figures 1 & 2. Freeze-fractured yeast cells illustrating nuclear pores (arrows) after standard sputter coating (**Fig. 1**) and Pt shadowing (**Fig. 2**). Bars = 0.2 μm.
Figures 3 & 4. P-faces of plasma membranes from yeast cells showing membrane particles (arrows) following Pt shadowing (**Fig. 3**) and magnetron sputter coating (**Fig. 4**). Bars = 0.4 μm.
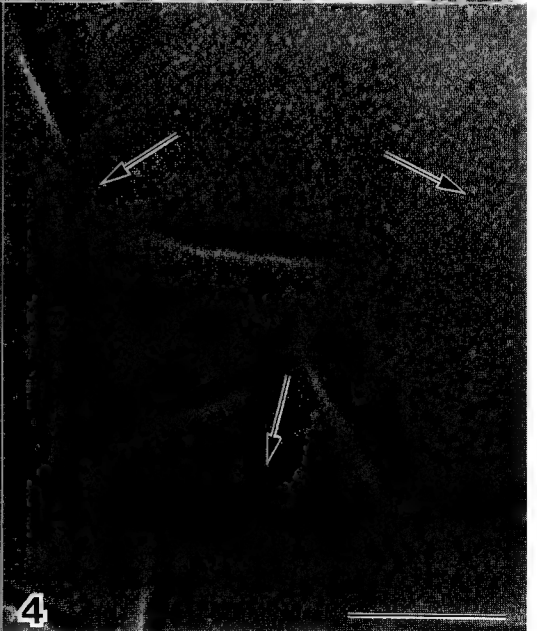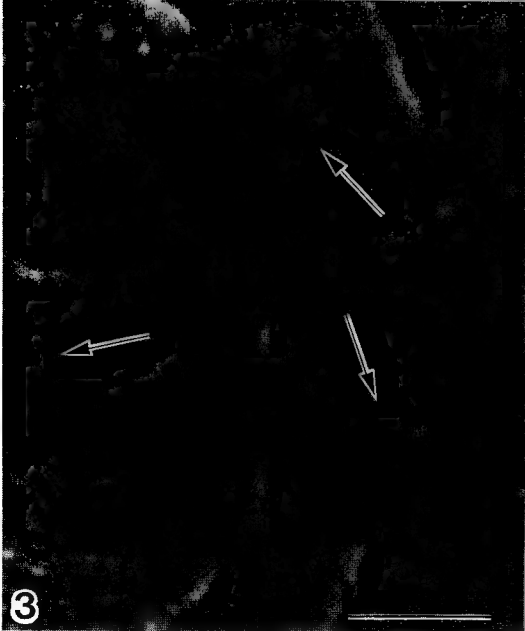
LOW-TEMPERATURE EVALUATION OF HIGH-PRESSURE FROZEN BIOLOGICAL SAMPLES BY TEM CRYOSECTIONS AND HIGH-RESOLUTION SEM

Martin Müller

Labor f. Elektronenmikroskopie I, ETH, Schmelzbergstrasse 7, CH-8092 Zürich

The unique ability of electron microscopy in biology is its power to describe and integrate structural details down to molecular dimensions within the context of a complex living system.

Structural information closely related to the living state may be achieved by cryoimmobilisation techniques that vitrify the cellular water and, at the same time rapidly arrest all physiological processes.

High-pressure freezing (Müller and Moor 198, Moor 1987) is at present the only practical way of cryofixing larger non-pretreated samples up to a thickness of 500 µm. A very high yield of adequately frozen specimens was demonstrated in TEM using suspensions of microorganisms as well as plant and animal tissue (i. e. no detectable effects of ice crystal damage are visible after freeze substitution) (Studer et al. 1989). High-pressure freezing can vitrify biological samples sometimes up to a thickness of 200 µm, as extrapolated from electron diffraction of cryosections (Michel et al 1991) The actual thickness that can be vitrified depends on the specimen, particularly on the presence of substances that exhibit cryoprotectant activity and also depends on the optimum transfer of pressure and cold to the sample and on the sample geometry (thickness and shape of the aquous layer, and the mass of the specimen planchettes necessery to protect the biological sample from direct pressure effects).

New sample preparation procedures were established in order to optimize the various parameters. Suspensions of cells are cryo-immobilized in porous cellulose tubing (inner diameter 200 µm) and cylinders of 300 µm in diameter of plant or animal tissue are produced by a special fine needle biopsy system. The samples are then sandwiched between two aluminum platelets with a cylindrical cavity that exatly matches the dimensions of the specimen. 1-Hexadecene (Studer et al. 1989) was employed to optimize the transfer of temperature and pressure.

It is preferable to process samples that have been successfully cryo-immobilised by physical protocols for microscopic observation, e. g. cryosectioning, or freeze fracturing. Once the structures and the vitrified state of the sample are established by cryosectioning and electron diffraction, they can provide reference information, against which the effects of additional preparation procedures e. g. freeze-substitution

and freeze-drying can be judged.

Cryosectioning:

Adequate cryosections were obtained by optimizing the cutting-parameters i. e. sectioning temperature, fixation of the sample, sectioning-velocity. Cutting artefacts were minimized by reducing the electrostatic interactions between the knife surface and the cryosection. The reduction of electrostatic forces on glass knives was accomplished by covering the knife surface with a very thin layer of frozen water (Michel et. al., 1991). The same method did not work with diamond-knives. A high yield of thin cryosections was however obtained with diamond knives by sectioning the sample in the presence of an ionisation electrode (Haug, Diatome AG, Biel, Switzerland). The electrode, with a field strength of 8 kV, produces positively and negatively charged nitrogen ions which neutralize the surface-charges of the knife and the section. This minimizes the friction on the knife surface and permits one to cut very thin sections without crevasses or knife marks. Compression could be further reduced by reducing the knife angle to 30 degrees. Samples vitrified under high pressure are relativeidy easily sectioned as compared to crystalline samples (Michel et al 1992).

High resolution cryo -SEM:

Cryoimmobilized bulk samples, frozen-hydrated or partially freeze-dried (etched), are frequently examined by TEM freeze-fracture replica techniques, or by low-temperature scanning electron microscopy (LTSEM). The latter technique eliminates the tedious task of digesting the biological material away, which often results in fractionation of the heavy metal replica. LTSEM can provide structural information that parallels that of TEM freeze-fracture techniques, provided that adequate specimen preparation procedures and an in-lens field-emission SEM are available. A high-vacuum cryotransfer system, that interconnects our freeze-fracture/metal coating unit and the Hitachi S-900 „In-lens" field emission SEM greatly facilitates low temperature analysis of high pressure frozen samples and provides ultrastructural data within 45 Minutes after tissue excision.

References

Michel M., Hillmann T. & Müller M. (1991) J . Microsc., 163, 3 - 18

Michel M. Gnägi H., Müller M. (1992) J. Microsc., 166, 43-56

Müller M. Moor H. (1983) The science of biological specimen preparation. SEM, 131-138

Moor H (1987) Cryotechniques in biological electron microscopy. Berlin, Springer. 175-191

Studer D. Michel M. and Müller M. (1989) Scanning microscopy suppl. 3, 253-269

PLANT ANATOMY, HISTOCHEMISTRY, AND GENE EXPRESSION AS VISUALIZED BY TISSUE PRINTING

Philip D. Reid* and David Bickar**

*Department of Biological Sciences and **Department of Chemistry, Smith College, Northampton, MA 01063

Tissue printing on nitrocellulose membranes followed by localization with appropriate probes has been used to study the distribution of protein and mRNA as well as the timing of gene expression in a variety of plant tissues.[2] Included in these studies are cell wall proteins in soybean and cellulase activity in relation to abscission in kidney bean.[3,4] Our recent studies have focused on the distribution of enzymes involved in crassulacean acid metabolism in the leaves of various species of *Peperomia*, the localization of ubiquitinated protein in various plant tissues, and the development of a stain for total protein transferred to nitrocellulose by tissue printing.[1]

Tissue prints made on dry nitrocellulose membranes (0.45μm pore size) and viewed with side illumination at low (10X) magnification show the characteristic morphology and anatomical organization of the printed tissue (Figs. 1 and 2). Treatment of the membranes with 12 mM HCl followed by a two minute incubation in an acidic 0.05% solution of copper phthalocyanine 3,4′,4″,4‴-tetrasulfonic acid tetrasodium salt (CPTS) (Figs. 3 and 4) shows the distribution of total protein transferred to the membrane. Tissue prints incubated with rabbit antibodies to ribulose bis-phosphate carboxylase/oxygenase (Fig. 5) or to ubiquitin-protein conjugate (Fig. 6) followed by exposure to an alkaline phosphatase-conjugated goat anti-rabbit antibody show the distribution of these two proteins within the tissue. Color was developed using standard alkaline phosphatase substrates.

The technique of tissue printing followed by indirect immuno-labelling with appropriate antibodies provides a tool for visualizing the tissue specific localization of proteins which may be of particular importance in the regulation of plant development.[5]

References

1. D. Bickar and P.D. Reid (1992) Anal. Biochem. 203, 109-115.
2. P.D. Reid and R. Pont-Lezica, eds. Tissue Printing, Academic Press (1992).
3. P.D, Reid, E. delCampillo and L.N. Lewis (1990) Plant Physiol. 93:160-165.
4. Z.H. Ye and J.E. Varner (1991) The Plant Cell 3:23-37.
5. The authors acknowledge the collaboration of I.P. Ting and B. Rubinstein.
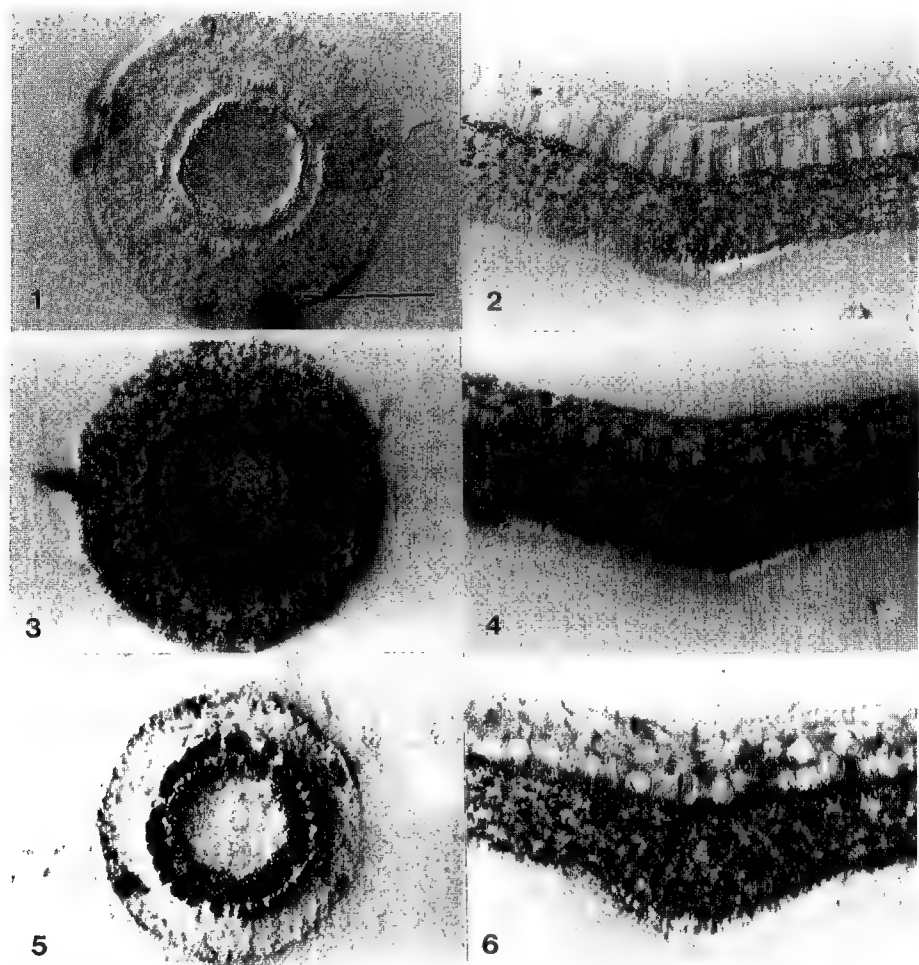
FIGS. 1.-6.--All tissue prints photographed at 10X magnification with side illumination. Bar = 1 mm.

FIG. 1.--Unstained tissue print of *Gossypium hirsutum* hypocotyl.

FIG. 2.--Unstained tissue print of *Peperomia orba* leaf.

FIG. 3.--CPTS stained tissue print of *Gossypium hirsutum* hypocotyl.

FIG. 4.--CPTS stained tissue print of *Peperomia orba* leaf.

FIG. 5.--Indirect immuno-labelled tissue print of *Gossypium hirsutum* hypocotyl showing localization of ubiquitin-protein conjugate.

FIG. 6.-- Indirect immuno-labelled tissue print of *Peperomia orba* leaf showing distribution of ribulose bis-phosphate carboxylase/oxygenase.

EXPLORATION OF CELL WALL ARCHITECTURE WITH THE RAPID-FREEZE DEEP-ETCH TECHNIQUE

Béatrice Satiat-Jeunemaitre(*) and Chris Hawes (**)

(*) C.N.R.S., Biomembranes et Surfaces Cellulaires Végétales, Ecole Normale Supérieure, Paris, FRANCE. (**) B.M.S., Oxford Brookes University, Oxford, ENGLAND

The comprehension of the molecular architecture of plant cell walls is one of the best examples in cell biology which illustrates how developments in microscopy have extended the frontiers of a topic. Indeed from the first electron microscope observation of cell walls it has become apparent that our understanding of wall structure has advanced hand in hand with improvements in the technology of specimen preparation for electron microscopy. Cell walls are sub-cellular compartments outside the peripheral plasma membrane, the construction of which depends on a complex cellular biosynthetic and secretory activity (1). They are composed of interwoven polymers, synthesised independently, which together perform a number of varied functions. Biochemical studies have provided us with much data on the varied molecular composition of plant cell walls. However, the detailed intermolecular relationships and the three dimensional arrangement of the polymers *in situ* remains a mystery. The difficulty in establishing a general molecular model for plant cell walls is also complicated by the vast diversity in wall composition among plant species.

The development of cytochemical, immunogold and affinity staining techniques, which can be used to detect various cell wall components, have provided invaluable data on the potential intermolecular relationships within the wall (2). However, with these techniques it is still impossible to visualise directly the macromolecular chains *in muro*. It is only by the recent application of the rapid-freeze deep-etch technique to plant cell studies that major progress has been made in our understanding of wall architecture as the method permits direct visualisation of three dimensional organisation of the wall macromolecules (3,4,5).

In this paper we report on a comparison of the three dimensional organisation of the cell walls in plants exhibiting varying degrees of wall organisation from random, through to complex helicoidal structures (4). The degree of complexity in wall architecture appears to correspond to a specific organisation of matrix sub-units around the backbone framework of cellulose microfibrils. Hemicelluloses appear as short cross-bridges (16-30 nm long) which are perpendicular to, and regularly space along the microfibrils. Observations of similar structures in cell walls exhibiting various hemicellulosic compositions, supports the hypothesis that the most important feature of the structural property of a wall molecule is not so much its chemical nature, but rather the shape of its backbone. These data will be compared with the existing models of cell wall architecture.

1. B. Satiat-Jeunemaitre, Tissue and Cell (1992)24, 315.
2. B. Vian, M. Temsah, D. Reis and J.C. Roland, J. Microsc. (1992)166, 111.
3. M. McCann, B. Wells, and K. Roberts, J. Microsc.(1992)166, 123.
4. B. Satiat-Jeunemaitre, B. Martin and C. Hawes, Protoplasma (1992)167, 3342.
5. S. Tamura and T. Senda, J. Elect. Microsc. (1992)41, 91.
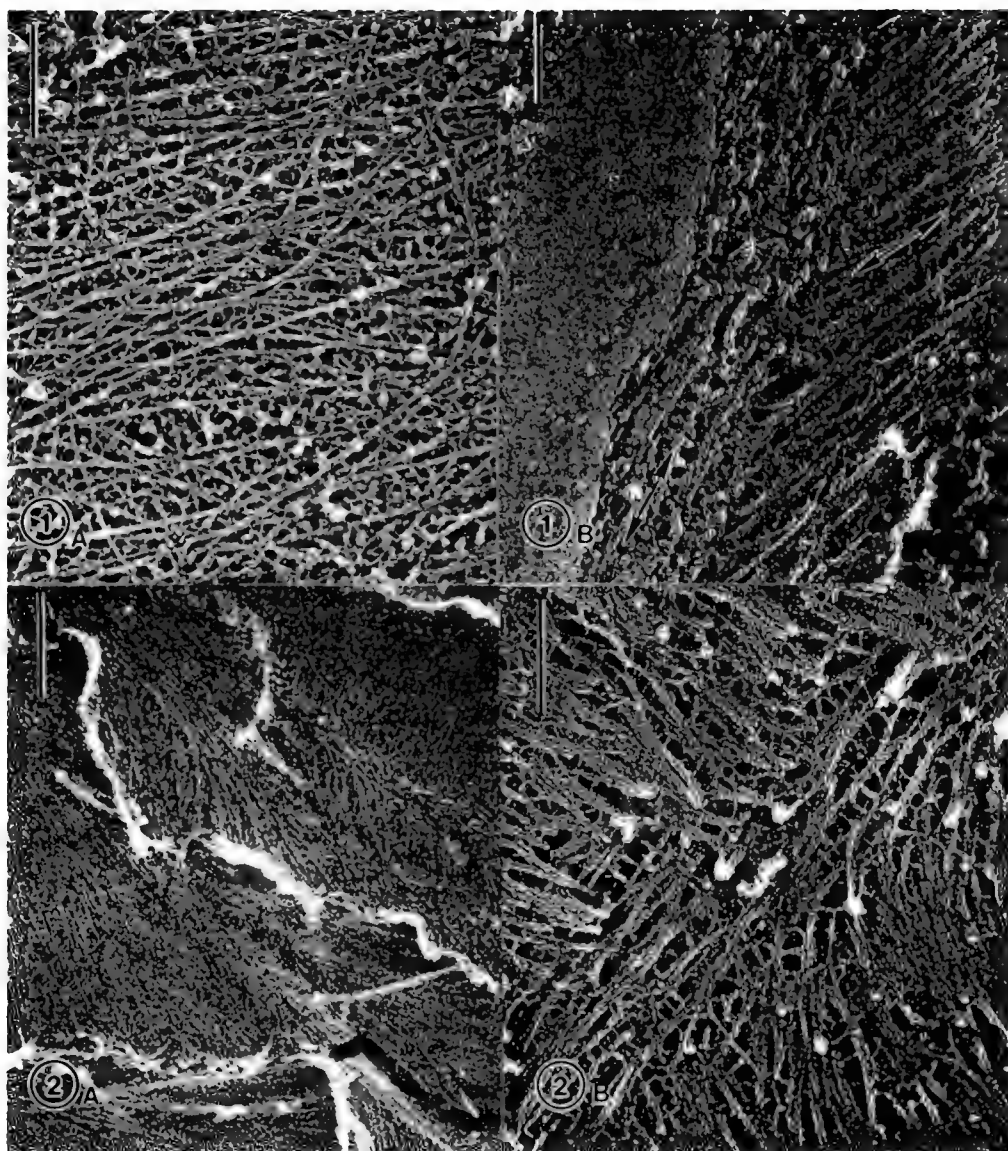
FIG. 1.--Carrot cell walls. (A) A randomly organised fibrillar network coexists with a lattice of shorter ramified units. Bar = 0.2μm. (B) Adjacent walls in aggregated cells. A higher degree of organisation can be detected, each cell wall exhibiting parallel microfibrils (arrows). Note the occurrence of perpendicular interconnecting bridges between some of the long microfibrils. Bar = 0.1μm.

FIG. 2.--Mung bean hypocotyl cell walls. (A) Polylamellate aspect of cell walls. Long microfibrils exhibit progressive rotation from one plane to the other. Bar = 0.2μm. (B) Regular cross-bridges between the microfibrils give a "ladder pattern" to the wall architecture. Bar = 0.2μm.

129

CONFOCAL MICROSCOPY OF THE CYTOSKELETON IN LIVING PLANT CELLS
FOLLOWING MICROINJECTION OF FLUORESCENT PROBES

Ann Cleary

Plant Cell Biology Group, Research School of Biological Sciences, The Australian National University, Canberra, ACT 2601, AUSTRALIA

Microinjection of fluorescent probes into living plant cells reveals new aspects of cell structure and function.[1] Microtubules and actin filaments are dynamic components of the cytoskeleton and are involved in cell growth, division and intracellular transport. To date, cytoskeletal probes used in microinjection studies have included rhodamine-phalloidin for labelling actin filaments and fluorescently labelled animal tubulin for incorporation into microtubules. From a recent study of *Tradescantia* stamen hair cells it appears that actin may have a role in defining the plane of cell division.[2] Unlike microtubules, actin is present in the cell cortex and delimits the division site throughout mitosis. Herein, I shall describe actin, its arrangement and putative role in cell plate placement, in another material, living cells of *Tradescantia* leaf epidermis.

The epidermis is peeled from the abaxial surface of young leaves usually without disruption to cytoplasmic streaming or cell division. The peel is stuck to the base of a well slide using 0.1% polyethylenimine and bathed in a solution of 1% mannitol +/- 1 mM probenecid. Rhodamine-phalloidin is loaded into the tip of a micropipette needle. The needle is back filled with water and attached via a water filled line to a micrometer syringe.[1] Delivery of the probe is regulated by applying hydraulic pressure. Injections are preformed directly on the stage of a Biorad MRC-600 confocal laser scanning microscope.

The leaf epidermis is composed of non-specialised epidermal cells and cells at all stages of stomatogenesis. The mature stoma consists of a pair of guard cells flanked by two lateral and two terminal subsidiary cells (SC). Epidermal and guard mother cells (GMC) divide in their equatorial plane producing cells of equal size. In SMCs the nuclei are polarised towards the inducing GMC. The subsequent terminal divisions cut off small rectangular SCs while the lateral divisions produce lens shaped SCs.

A network of actin can be visualised in the cortex of all cells. The arrangement of actin varies with cell type and stage of division. Non-dividing epidermal cells and SMCs have cortical actin filaments oriented randomly, as well as a subset of finer transverse filaments (Fig. 1). Actin is randomly distributed in GMCs (Fig. 2) but organised into radial arrays in mature guard cells (Fig. 3). At preprophase, cortical bands of actin circumscribe cells of all types and mark the future plane of division (Fig. 4). Preprophase bands of actin are less well defined in lateral SMCs (Fig. 5) and GMCs than in other cell types. Once the nucleus is polarised in a SMC, actin concentrates adjacent to the anticlinal wall in the region where it abuts the GMC (Fig. 6). In face view the bright region appears as a disc of predominantly anticlinally oriented actin filaments (Fig. 7). Following the breakdown of the nuclear envelope actin disassembles at the division site but remains elsewhere in the cell cortex (Fig. 8). The division site, marked by the absence of actin, is conspicuous throughout mitosis in epidermal cells, GMCs and lateral SMCs. In terminal SMCs the division site is detectable but less clearly delineated than in the other cells. The phragmoplast, containing microtubules and actin filaments, expands to fuse with the parental cell wall in the region that is devoid of cortical actin.

In all types of living cells examined by microinjection, and in fixed root tip cells,[3] there is some degree of cytoskeletal delineation of the division site maintained throughout division. It is proposed that cortical actin may have a role in guiding the cell plate to its final position. There is no evidence of phragmosomal actin leading the edge of the phragmoplast to the division site.

1. P. K. Hepler et al., Cell Biology Int. Reps (1993)In Press.
2. A. L. Cleary et al., J. Cell Sci. 103(1992)977.
3. B. Lui and B. A. Palevitz, Cell Motil. Cytoskel. 23(1992)252.
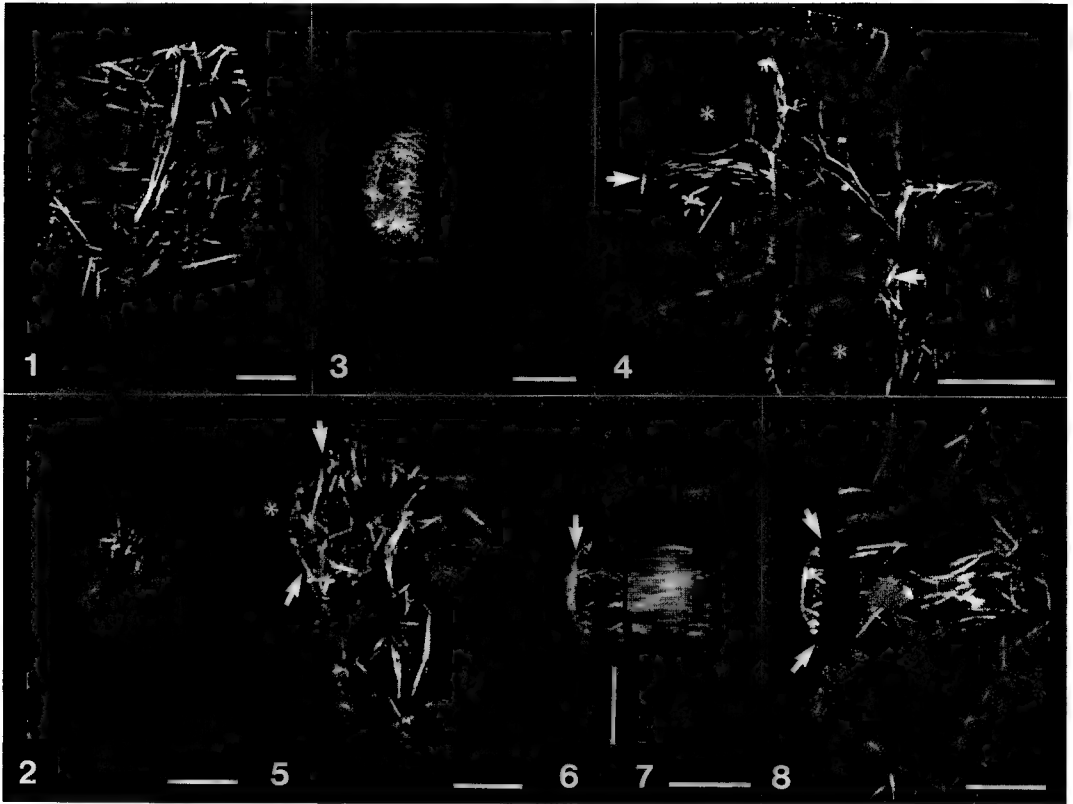
FIG. 1.--Random and transverse cortical actin in SMC. Projection of 12 images taken at 1 μm intervals. Bar = 10 μm.

FIG. 2.--Random cortical actin in GMC. Bar = 10 μm.

FIG. 3.--Radial cortical actin in mature guard cell. Bar = 10 μm.

FIG. 4.--Preprophase bands of actin (arrows) in cortex of two adjacent terminal SMCs. GMCs (*). Projection of 21 images taken at 1 μm intervals. Bar = 25 μm.

FIG. 5.--Preprophase band of actin (arrows) in lateral SMC. GMC (*). Projection of 10 images taken at 1 μm intervals. Bar = 10 μm.

FIG. 6.--Projection of 17 images taken at 1 μm intervals. Part of lateral SMC with bright band of actin (arrow) on the anticlinal wall adjacent to GMC. Bar = 10 μm.

FIG. 7.--Cell in Fig. 6 rotated 90° showing anticlinal wall in face view. Parallel actin filaments in bright zone. Bar = 10 μm.

FIG. 8.--Projection of 9 images taken at 1 μm intervals showing entire surface of cell in Fig. 6. Actin is absent from the division site (arrows). Bar = 10 μm.

CALCIUM ION IMAGING IN PLANT CELLS

Peter K. Hepler and Dale A. Callaham
Department of Biology, University of Massachusetts, Amherst, MA 01003

Calcium ions (Ca) participate in many signal transduction processes, and for that reason it is important to determine where these ions are located within the living cell, and when and to what extent they change their local concentration. Of the different Ca-specific indicators, the fluorescent dyes, developed by Grynkiewicz et al. (1), have proved most efficacious, however, their use on plants has met with several problems (2). First, the dyes as acetoxy-methyl esters are often cleaved by extracellular esterases in the plant cell wall, and thus they do not enter the cell. Second, if the dye crosses the plasma membrane it may continue into non-cytoplasmic membrane compartments. Third, even if cleaved by esterases in the cytoplasm, or introduced as the free acid into the cytoplasmic compartment, the dyes often become quickly sequestered into vacuoles and organelles, or extruded from the cell. Finally, the free acid form of the dye readily complexes with proteins reducing its ability to detect free calcium. All these problems lead to an erroneous measurement of calcium (2). Recently, these issues have been solved through the production of dextran-coupled forms of the dye. We have had extensive experience with fura-2-dextran and find that it remains in the cytoplasmic compartment for hours and acts as a reliable indicator for calcium (3).

Imaging is achieved through the use of thermoelectrically cooled (-45° C) charge couple device (CCD) detector array with 500 kHz data conversion rate (12 bit resolution). The characteristics of this system (high sensitivity, photometric stability, photometric linearity, defined pixel geometry) make it superior to any video camera for this work. We have written our own drivers for the camera system in assembly language giving complete control of all image acquisition and readout parameters and enabling tight coordination with the dual fluorescence excitation hardware and other features. The ability to operate the camera in a pseudo-frame-transfer mode (Miller et al., 1992) means that the images used to compute the ratio can be acquired with a limiting dead-time between images of only 2 ms., practically limited at present by filter changer hardware to 25 ms. The imaging system is operated on a 33 Mhz 80486DX computer with a 16 image RAM buffer capacity. The system provides the capacity and speed for time-sequence experiments and a practical environment for effective image analysis.

Images of lily pollen tubes that have been loaded by microinjection with fura-2-dextran are shown in Fig. 1a-g. Particularly pertinent is the demonstration of a steep gradient in free Ca that is focused at the extreme apex of the growing pollen tube. Treatment of the tube with the Ca ionophore, bromo-A-23187, causes the intracellular Ca to markedly elevate. Cytoplasmic streaming, a Ca sensitive process, stops and after a few minutes so does tube elongation. Of interest is the observation, shown in Fig. 1f, that in the continued presence of bromo-A-23187, the intracellular Ca drops apparently due to action of Ca pumps, which extrude the ion from the cytoplasm. Finally, removal of the bromo-A-23187, allows the intracellular Ca to return to basal levels (Fig. 1g).

References

1. Grynkiewicz, G., Poenie, M. and Tsien, R.Y. (1985) J. Biol. Chem. 260: 3440.
2. Callaham, D.A. and Hepler, P.K. In: "Cellular Calcium: A Practical Approach", McCormack, J.G. and Cobbold, P.H., eds. Oxford University Press. (1991) pp. 383-412.
3. Miller, D.D., Callaham, D.A., Gross, D.J. and Hepler, P.K. (1992) J. Cell Sci. 101, 7.

Figure 1a-h
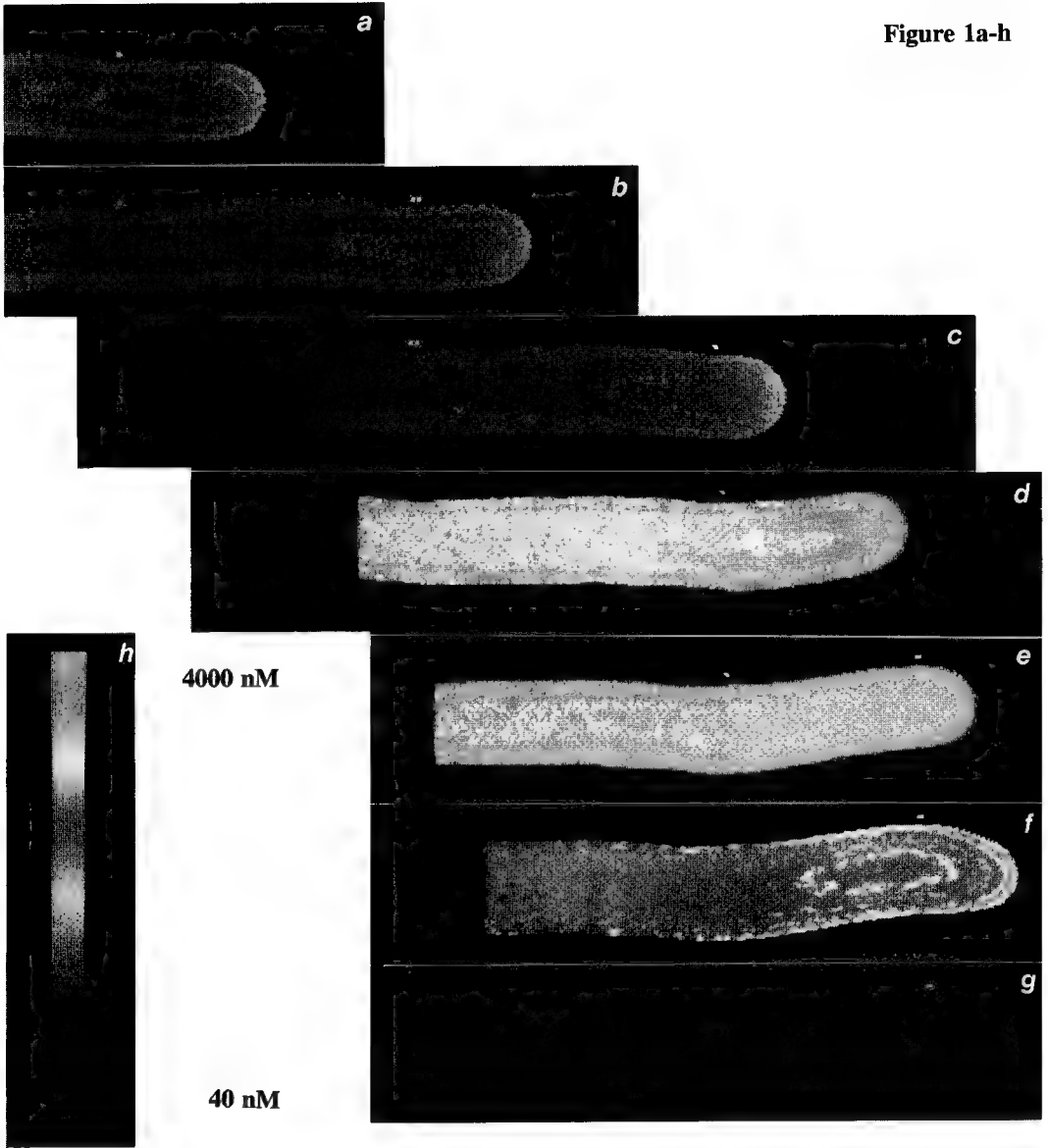
Fig. 1a-h. Images of a lily pollen tube loaded with fura-2-dextran and imaged in our CCD system.
Fig. 1a-c. Control conditions. Times post injection; a-0:00; b-0:06, c-0:13. Under control conditions the pollen tube grows rapidly (see reference marks) and exhibits a zone or elevated free Ca only at the extreme apex of the tube.
Fig. 1d-f. Treatment with bromo-A-23187 induces Ca entry. d-0:16; e-0:19; f-0:23. Cytoplasmic streaming stops within 3 min, whereas elongation ceases after 7 min. Note that in the continued presence of bromo-A-23187 the Ca level drops from peak levels (f).
Fig, 1g. Removal of bromo-A-23187 allows Ca to return to basal levels.
Fig. 1h. Color bar; the range extends from 40 nM (blue) to 400 nM (red).

133

SPRAY-FREEZING APPARATUS FOR CRYOFIXATION OF UNICELLULAR ALGAE

Stephen D. Fields, Gregory W. Strout and Scott D. Russell

Department of Botany and Microbiology, University of Oklahoma, Norman, OK 73019

Spray freezing unicellular organisms directly from the culture medium is an attractive alternative to other methods of rapid freezing because the possibility of pre-freezing artifacts is minimized.[1] However, the utility of spray-freezing has been limited due to difficulties in obtaining satisfactory freezing in large specimens and in collecting and processing specimens after freezing.[2] Consequently, the design of many spray-freezing devices is somewhat complicated, of limited application and often difficult to use.[3-5] A simple, inexpensive spray-freezing apparatus of our own design was developed with the purpose of rapid freezing unicellular algal suspensions for freeze substitution. A naked, freshwater dinoflagellate was used to determine the effectiveness of the freezing device and the associated freeze substitution protocol.

Approximately 70 ml of liquid propane is condensed in LN_2-cooled copper coils and collected in an aluminum chamber (Fig. 1). Using nitrogen gas as the propellant, a Paasche airbrush is used to spray concentrated cell suspensions at 138 - 207 kPa into the liquid propane from a height of 10 cm (droplet sizes range from 30 - 70 μm). The cold gas layer above the liquid propane is approximately 10 mm. Cells are collected in a nylon mesh basket inserted in the chamber containing liquid propane. Mesh sizes of 10 to 40 μm retain cells while allowing free flow of liquid propane. Warm pockets of propane are prevented from forming by mixing the cryogen with a magnetic stir bar. After freezing, the entire mesh basket is lifted out of the chamber and transferred through several rinses of acetone at -85° C to remove all residual liquid propane. Cells are then substituted in 1% tannic acid in acetone at -85° C, cryofixed in a 1% OsO_4/acetone solution at -20°C to 4°C, embedded in Spurr's resin, and sectioned with a diamond knife.

Cells sprayed at 138 - 175 kPa are usually undistorted and well frozen (Fig. 2), but cells sprayed at higher pressures apparently shear in the airbrush, resulting in empty or highly distorted cells. A drawback of spray-freezing cell suspensions is the relatively large volume of water associated with the cells. In order to remove all water and prevent damage from recrystallization, long freeze substitution times are required. However, the quality of ultrastructural preservation is directly affected by the length of the freeze substitution protocol.[6] Processing times longer than 8 days result in extensive extraction of membranes and other cytosolic components (Fig. 3) whereas cells processed for shorter time periods display distinct membranes and dense cytoplasm (Figs. 4, 5). Freeze substitution times can be reduced by constant mixing of the substitution medium.

This spray-freezing device is attractive because it yields excellent freezing in a high percentage of cells, its design is simple and the materials required for its construction are inexpensive. The rapid removal of the cryogen integrated with the freeze substitution protocol enhances the utility of the device and makes its use more convenient than other methods of rapid freezing we have employed for cryofixation of single cells.

References

1. L. Bachmann and W. W. Schmitt, Proc. Nat. Acad. Sci. USA 68(1971)2149.
2. J. C. Gilkey and L. A. Staehelin, J. Electr. Microsc. Tech. 3(1986)177.
3. R. D. A. Lang et al., J. Microsc. 108(1976)101.
4. M. Geanacopoulos and A. R. L. Gear, Thromb. R. 52(1988)599.
5. G. Knoll et al., J. Cell Biol. 113(1991)1295.
6. F. S. Sjöstrand, J. Struct. Biol. 103(1990)135.
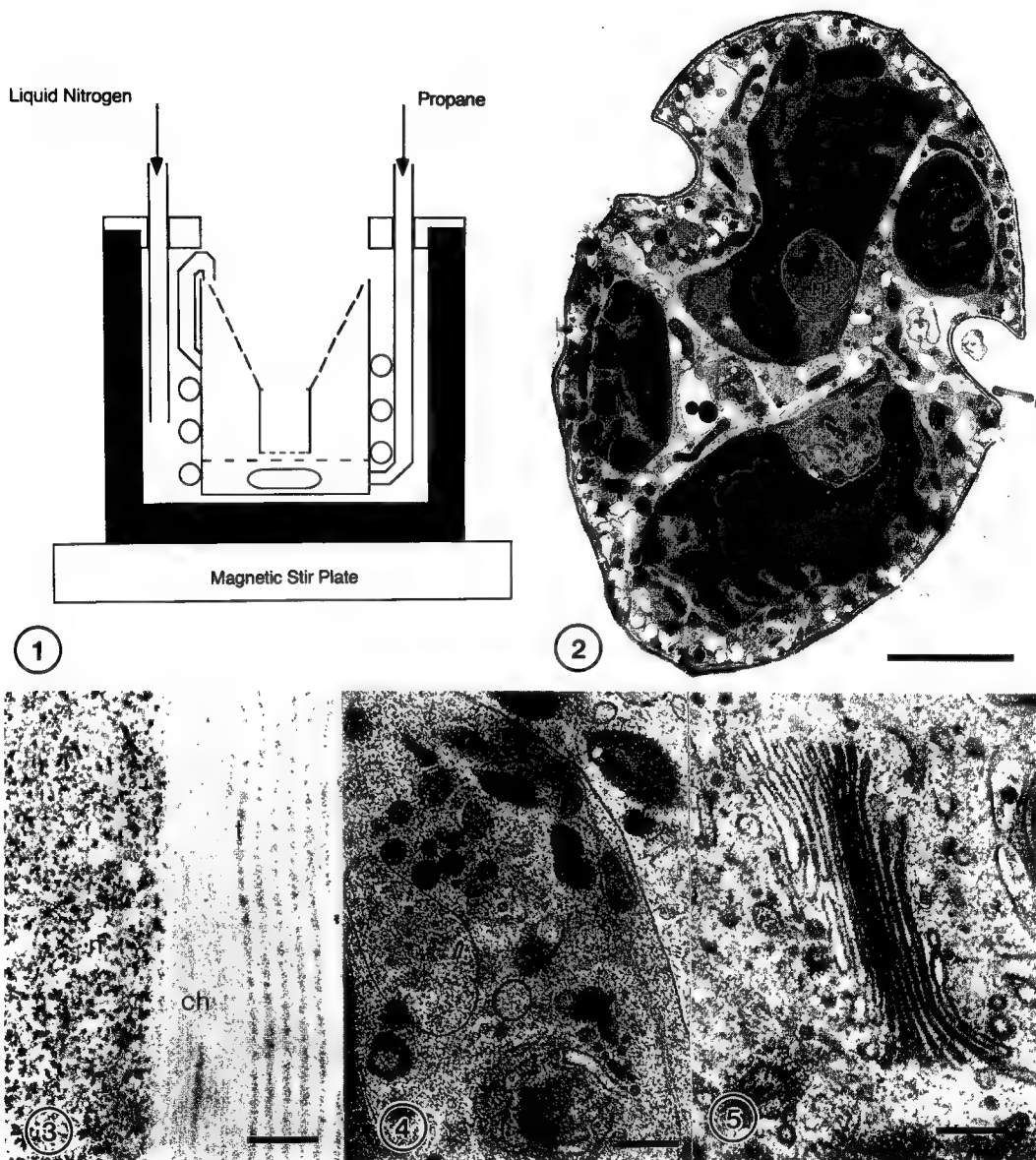
Abbr.: *Ch* chloroplast; *G* golgi body; *N* nucleus; *T* thylakoid

Fig. 1.--Cross sectional schematic of cryogenic chamber with inserted nylon mesh collecting basket.

Fig. 2.--Whole cell of *Gymnodinium acidotum* spray-frozen at 175 kPa and freeze substituted for 6 days. Cell is well frozen and displays native cell shape. Bar = 5 μm.

Fig. 3.--Extracted nuclear and chloroplast membranes of cell freeze-substituted for 14 days. Bar = 0.5 μm.

Fig. 4.--Endosymbiotic compartment of cell freeze-substituted for 6 days. Bar = 0.3 μm.

Fig. 5.--Golgi body of cell freeze-substituted for 6 days. Bar = 0.2 μm.

135

MICROTUBULE ORGANIZATION IN THE SIPHONOUS GREEN ALGA BRYOPSIS: AN ULTRASTRUC-
TURAL OBSERVATION WITH ELECTRONSPECTROSCOPIC IMAGING (ESI)

Sheng Jun Wei, Kyle Bishop

RJ Lee Group, Inc., 2424 Sixth St., Berkeley, CA 94710, USA

Transmission electron microscopy (TEM) has been routinely used to study the ultrastructure of microtubules (MT). However, we found that some MTs in the filamentous green alga we examined could not be easily recognized using conventional brightfield imaging, because of low contrast. Electronspectroscopic imaging (ESI) microscopy using the imaging electron energy filter solves many problems involving low contrast and feature resolution. By ESI, the contrast can be tuned and optimized so that images with higher resolution can be produced. In the present study we used ESI to improve the image quality in order to clearly resolve the MTs.

A specimen of the giant marine green alga Bryopsis sp. was prepared following a new modified double fixation procedure of our own to preserve cell structures (Fig. 1). In brief, the branched alga was cut into small segments of about 1 cm in length in 2% glutaraldehyde in 0.1 M phosphate at pH 7.2. It was neccessary to dissect the specimen in 2% glutaraldehyde, rather than in culture medium, in order to minimize cytoplasm damage. The sample was fixed in 4% glutaraldehyde in 0.1M phosphate pH 7.2, at room temperature (RT) for two hours. Postfixation was in 1% osmium in the same buffer at RT for one hour. One mL of 2% glutaraldehyde was then added to five mL of secondary fixative, with final concentrations of about 0.3% for glutaraldehyde and about 0.8% for OsO_4, at RT for 0.5 hour to reduce the osmium and to increase organelle osmication. Following a buffer rinse, the sample was dehydrated with ethanol, flat-embedded in Araldite 6005, cross and longitudinally sectioned, doubly stained with 2% aqueous uranyl acetate (UA) and 0.5% lead citrate, and observed in the JEOL-1200EX TEM at 80kV. MTs were photographed in the Zeiss-902A TEM at 80kV, either using conventional brightfield imaging or using ESI at $\triangle E=OeV$, to enhance contrast.

The thin cortical cytoplasm of Bryopsis contains numerous microtubules which are thought to be involved in the intracellular movements of organelles.[1] As shown in   Figs. 2-7, MTs in this alga are distributed in specific regions of cytoplasm, either in organized bundles or individually. The cross section shows that many circular microtubular profiles are located just underneath the plasma membrane or close to particular organelles, such as chloroplasts.[1,2] These circular structures have diameters of about 22-24nm and electron-translucent cores. The longitudinally sectioned microtubules display straight or slightly wavy and cylindrical morphologies with less dense central regions; they are parallel to the long axis of the cell as well as to each other. They also exist in similar areas in which cross sectioned MTs are located, possibly to maintain a spatial association with the adjacent organelles.[1,2] These observations confirm that MTs are present in the cortical cytoplasm of Bryopsis and provide ultrastructural evidence of the relationship between MTs and the particular organelles.

References

1. D. Menzel, M. Schliwa, European J. Cell Biol. (1986)40, 275-285
2. M. Schliwa, Cell and Muscle Motility (1984)5, 1-82

136
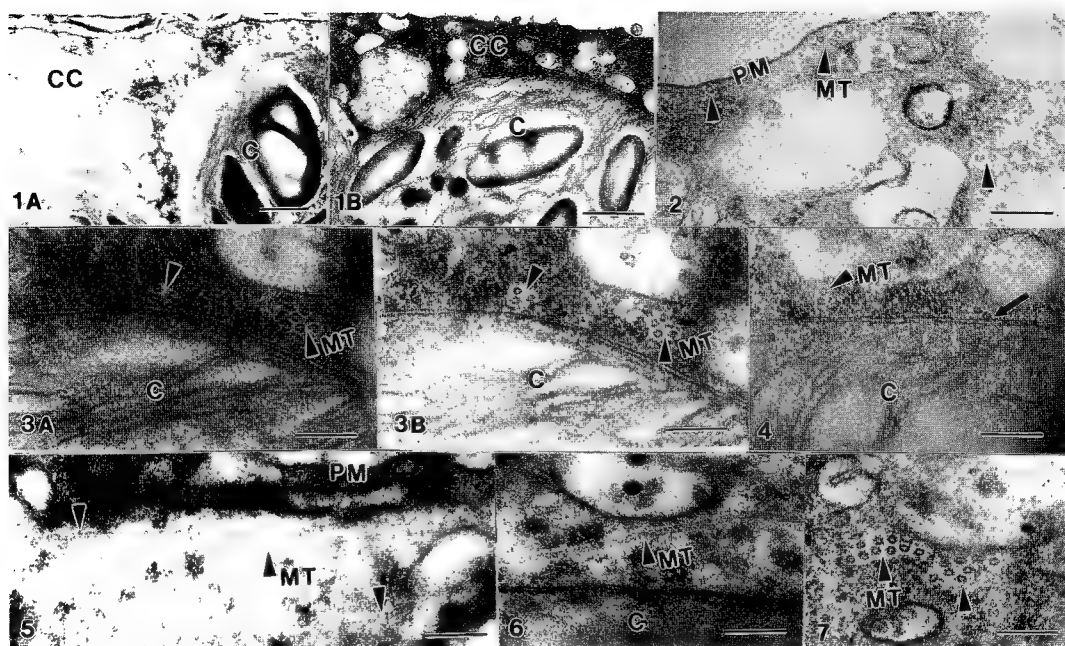
Fig. 1A-1B: Micrographs showing the results of different preparations. A) Conventional fixation procedure. Most of cortical cytoplasm (CC) was lost because of poor preservation. B) New modified procedure. Cortical cytoplasm (CC) appears dense and intact, with chloroplast (C) attached to its inner surface. Conventional brightfield imaging. Bars=1μ

Fig. 2: Cross sectioned microtubules (MTs) (arrowheads) close to plasma membrane (PM) in bundle and individually. ESI at △E=OeV. Bar=0.2μ

Fig. 3A-3B: Bundles of cross sectioned MTs (arrowheads) close to chloroplast (C). Micrographs demostrate the difference between two imaging modes. A) Conventional brightfield imaging, showing lower contrast and relatively fuzzy morphologies of MTs. B) ESI at △E=OeV, showing higher contrast and sharper appearance of MTs. Bars=0.2μ

Fig. 4: MTs (arrowheads) close to chloroplast (C). One of them is closely associated with the outer membrane of the chloroplast (arrow). ESI at △E=OeV. Bar=0.2μ

Fig. 5: Longitudinally sectioned MTs (arrowheads) parallel to plasma membrane (PM) as well as to each other. ESI at △E=OeV. Bar=0.2μ

Fig. 6: Longitudinally sectioned MTs (arrowheads) close to chloroplast (C). ESI at △E=OeV. Bar=0.2μ

Fig. 7: Bundles of cross sectioned MTs (arrowheads) close to an empty organelle. ESI at △E=OeV. Bar=0.2μ

UV ABSORPTION MICROSPECTROSCOPY AND ALKALI EXTRACTION TO CHARACTERIZE AROMATIC CONSTITUENTS IN PLANT CELL WALLS

D. E. Akin, W. H. Morrison III, and L. L. Rigsby

U.S. Department of Agriculture, Agricultural Research Service, Richard B. Russell Agricultural Research Center, Athens, Georgia 30613

Aromatic compounds bound to structural carbohydrates in plant cell walls limit the microbial utilization of otherwise biodegradable polysaccharides. Such limitations have important consequences in conversion of plant biomass to useful products and in carbon recycling. These aromatic constituents are chemically diverse, with further variations occurring in chemical linkages. Microspectroscopy and chemical analysis of alkali-treated plant walls was used to investigate aromatics.

Pearl millet (*Pennisetum glaucum*) stems (Fig. 1) were separated into pith parenchyma, pith vascular bundles, and rind (vascular and sclerenchyma cells combined). A normal (N) line and a counterpart brown midrib (bmr) mutant line, which has modified lignins, were both sampled. Ground (~ 1 mm) walls of these cell types were sequentially treated with 1M NaOH at 25°C for 20 h to remove ester-linked phenolic acids, and the residues were then treated with 4M NaOH in Teflon polyfluoro-alkoxy copolymer vials which were placed in stainless steel vessels at 170°C for 2 h to remove more resistant ether-linked and polymerized aromatics. Aromatics in supernatants from each treatment were evaluated by gas chromatography. Residues from each treatment and untreated cell walls were evaluated by UV absorption microspectrophotometry using a Zeiss UMSP-80 system equipped with a 75 W xenon lamp.[1, 2]

UV absorption spectra (Figs. 2,3) showed that the combined 1M,4M treatments removed all aromatics from wall residues, thus supernatants contained all aromatic constituents for analysis. Spectral patterns of untreated parenchyma walls (Fig. 2) indicated that both N and bmr cells contained substantial amounts of ester-linked phenolic acids. The λ_{max} in N walls of 312 nm indicated a predominance of *p*-coumaric acid.[1] UV absorption was reduced after treatment with 1M NaOH, and a small absorbance near 274 nm remained only in N walls. The more highly lignified vascular cells (Fig. 3) had higher absorption than parenchyma in both N and bmr stems. Spectral patterns indicated that aromatics were more condensed in N walls. Treatment with 1M NaOH resulted in loss of most all UV absorption in bmr walls. In contrast, N walls had a λ_{max} near 284 nm with a shoulder near 308 nm, the absorption ratio was increased indicating that ester-linked phenolic acids were removed, and condensed aromatics indicative of polymerized lignin remained. Microspectrophotometry and chemical analysis both indicated that N walls had higher concentrations of ester-linked *p*-coumaric acids, possessed a more condensed type of lignin, and retained more aromatics after 1M NaOH treatment. Microspectrophotometry identified sites for particular aromatics and linkages.

References

1. D. E. Akin and R. D. Hartley, J. Sci. Food Agric. (1992)59, 437.
2. Reference to specific products is made for identification purposes only and does not imply endorsement by the United States government.
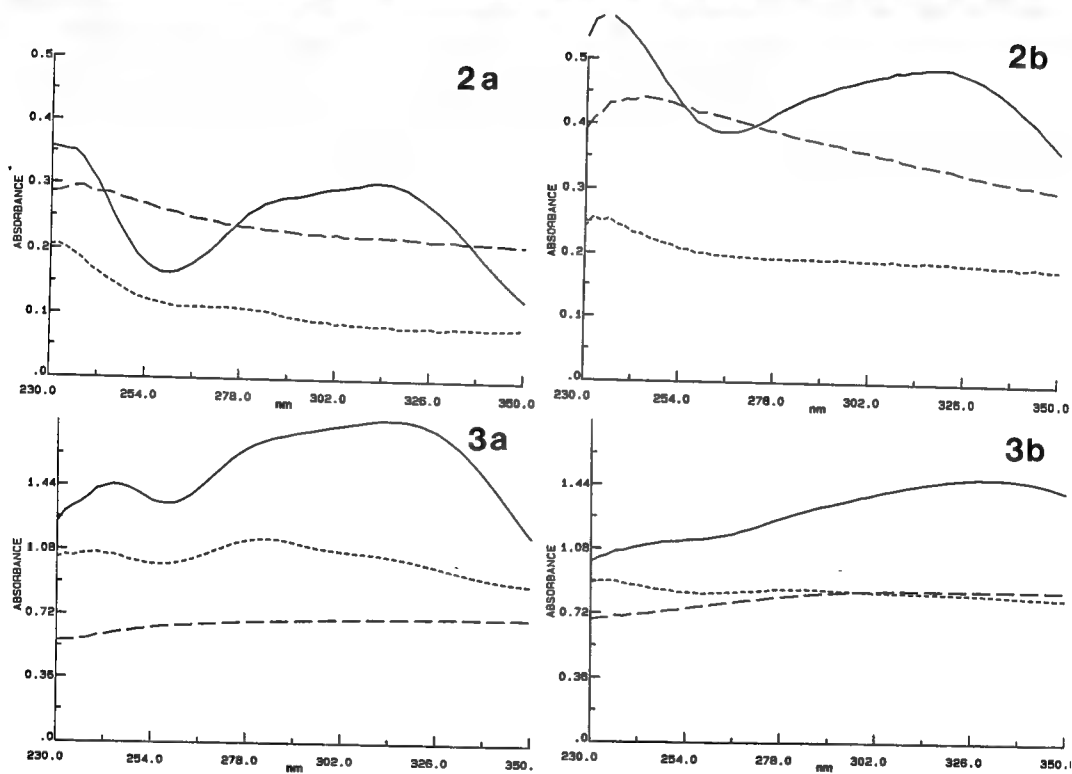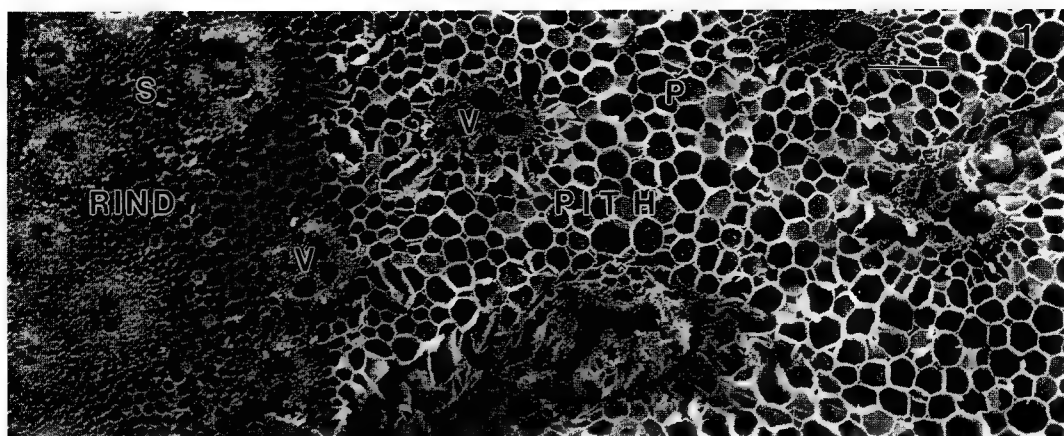
FIG. 1.—SEM of pearl millet stem. Pith is comprised of parenchyma (P) and vascular bundles (V). Rind is comprised of sclerenchyma (S) and embedded vascular bundles (V). Bar = 200 μm.

FIG. 2.—UV absorption spectra of parenchyma cells. **a.** Normal. **b.** Bmr mutant. Untreated (————), 1M NaOH-treated (- - -), 4M NaOH-treated (— —).

Fig. 3.—UV absorption spectra of rind vascular cells. **a.** Normal. **b.** Bmr mutant. Untreated (————), 1M NaOH-treated (- - -), 4M NaOH-treated (— —).

139

TISSUE PRINTING FOR SCANNING ELECTRON MICROSCOPY AND MICROANALYSIS

Barbara A. Reine

Botany Dept. KB-15, University of Washington, Seattle, WA 98195

The study of plant morphology and plant cells in the scanning electron microscope is often compromised by the limitations of specimen preparation techniques. Simple natural dehydration usually results in unacceptable shrinkage and distortion of the normal surface morphology of plant cells. Chemical fixation followed by critical point drying or some substitute for critical point drying such as Peldri II or HMDS (hexamethyldisilazane) improves morphological results but still imparts artifacts, adds chemical constituents to the specimen, and requires the use of toxic chemicals, a hood, and much time.

One technique that eliminates many of these disadvantages and is even suitable for specimen preparation in the field is tissue printing. For low magnification imaging and chemical analysis its "elegant simplicity" (2) is compelling. Historically, the application of tissue printing has been in connection with optical microscopy (1, 2). However, this technique works very well for low magnification SEM and associated elemental characterization of residues by x-ray microanalysis. The tissue print technique applied to SEM is much the same as for optical microscopy.

This work reports the use of tissue printing to reveal both anatomical stem structure and chemical analysis of cell exudates in a SEM equipped with an energy dispersive spectrometer. Various species of *Equisetum* were collected from the environs of Seattle, WA and one tropical species, *Equisetum giganteum*, was collected from the Caracas Botanical Garden in Venezuela. Stems of these various species were cut transversely and longitudinally and imprinted on 0.45 µm pore size nitrocellulose membranes as shown in Figure 1. A variation on this technique omits the top protective paper and the hand-cut section, substituting an entire stem freshly cut at the desired position. This variation is especially desirable for field work and for increasing the amount of cell sap collected. Either method creates both an anatomical and chemical imprint. The clarity of the anatomical print in the whole stem variation of this technique is dependent on the rigidity of the cell walls of the stem being imprinted. These imprinted nitrocellulose membranes are then dried, cut to size, attached to specimen mounts and coated with either carbon or gold-palladium. Imaging and x-ray microanalysis are performed directly on the imprinted membrane. Because there is little 3-dimensional relief on a tissue print, imaging the imprint in the SEM is improved by tilting the stage to an angle of ~30°, using care in making measurements and spatial interpretations.

These anatomical and chemical imprints allow morphological and analytical determination of differences between species and/or growth conditions. Figure 2 shows the anatomical detail present in an imprint of a stem cross-section of *Equisetum arvense*. This imprint exhibits stem anatomy reflecting the epidermal layer (EL), the vallecular canal (VC), the carinal canal (cc) and the central cavity (C), as well as individual cell outlines from the outer epidermis to the central cavity. Cell sap or exudate from *Equisetum telmateia* collected on a membrane is shown in Fig. 3 and that collected from *E. giganteum* is seen in Fig. 4. The appearance of these two residues is strikingly different and x-ray microanalysis corroborates this difference. The exudate from *E. telmateia* is virtually pure silica while the exudate from *E. giganteum* is composed of calcium, potassium, chlorine, magnesium and very little silica. These differences might be a function of age, growing conditions or actual species differences as suggested by previous work on ashed material (3).

REFERENCES

1. P. D. Reid, E. del Campillo and L. N. Lewis. Plant Physiol. (1990)93, 160.
2. P. D. Reid & R. F. Pont-Lezica, ED., TISSUE PRINTING: Tools for the Study of Anatomy, Histochemistry, and Gene Expression. New York: Academic Press, Inc. (1992) 188.
3. B. A. Reine. Proc. EMSA 1992, San Francisco Press, (1992) 856.

Fig. 1. Diagram of tissue print technique.
Fig. 2. SEM image of tissue print of *Equisetum arvense* stem cross-section. Bar = 145 µm.
Fig. 3. SEM image of cell exudate on tissue print of *Equisetum telmateia* stem. Bar = 65 µm.
Fig. 4. SEM image of cell exudate on tissue print of *Equisetum giganteum* stem cut longitudinally. Bar = 10 µm.

TISSUE PRINT TECHNIQUE
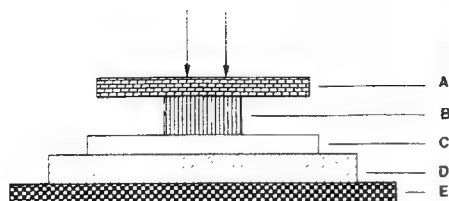
A - protective paper

B - razor blade hand section, 200 to 500 um thick

C - dry nitrocellulose membrane, 0.45 um pore size

D - 2 to 4 layers of paper towels

E - smooth solid surface such as a piece of plate glass

Firm pressure is applied from above.
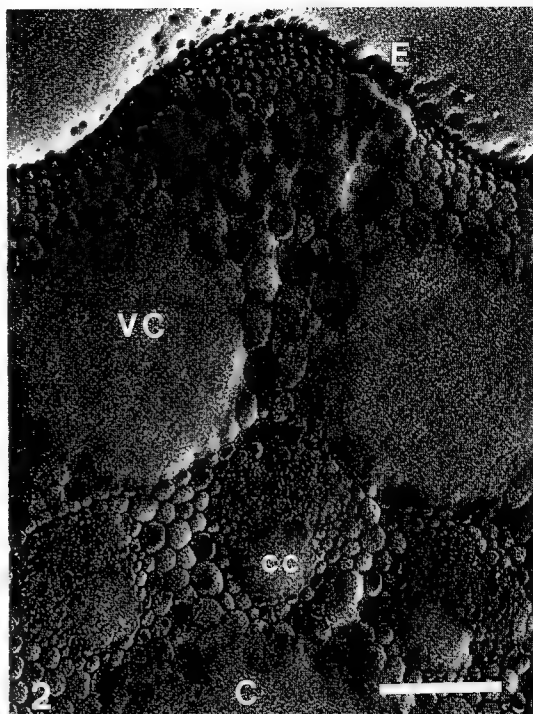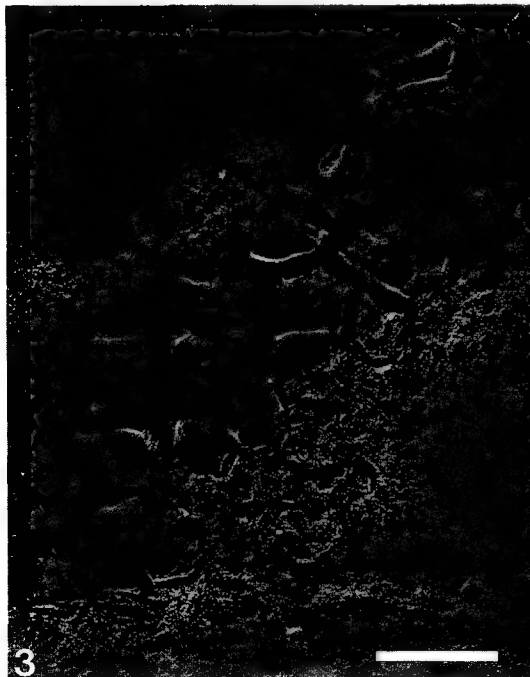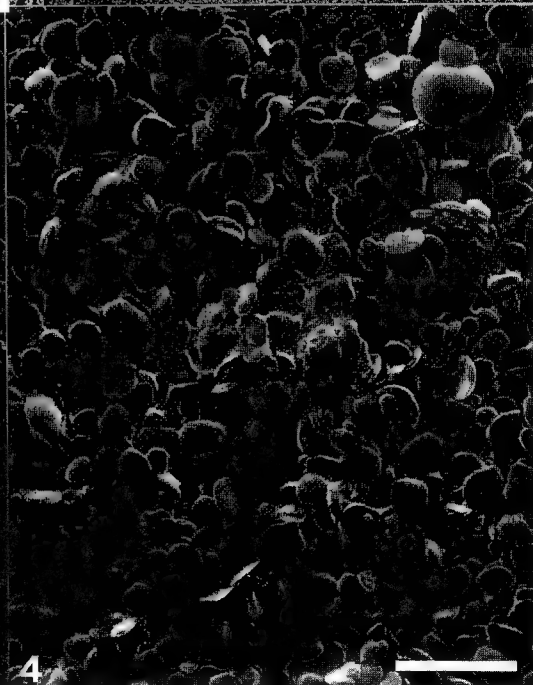
IMMUNOCYTOCHEMICAL LOCALIZATION OF NICOTINE IN DEVELOPING LEAVES OF TWO CULTIVARS OF NICOTIANA TABACUM

Patrick Echlin

Department of Plant Sciences, University of Cambridge, Cambridge CB4 1XA UK

Improved techniques have been developed for the *in situ* localization of nicotine in developing leaves of *Nicotiana tabacum.* Earlier studies[1] had shown that aldehyde fixed and partially dehydrated material embedded in different hydrophillic resins at low temperatures, retained up to 50% of the nicotine but invariably at the expense of good structural preservation. Significant improvements have now been made to the methods and it is now possible to obtain excellent structural preservation with high retention of nicotine.

Tobacco plants were grown in a glasshouse maintained at 23-26⁰C with 16H light and were well watered and fed with a high nitrogen fertilizer. The flower heads were removed from the plants as they appeared. Samples were taken from between the main veins at a distance 10mm from the edge of the mid part of the leaf at 10, 13, 16, 20, and 22 weeks from the time of seed germination which corresponded to the Juvenile, Mature, Ripe, Senescent and Old stages of leaf development. Thin strips of tissue no bigger than 500μm by 250μm were fixed for two hours at 277K in a mixture of 2% formaldehyde and 0.05% glutaraldehye in 50mM PIPES buffer pH 7.0. The tissue was dehydrated for 30mins in 30% ethanol at 277K, 30mins in 50% ethanol and 2 x 15mins in 80% ethanol at 248K. The partially dehydrated leaf fragments were placed in LR White acrylic resin for 1H at 248K, 16H at 248K and finally 1H at 248K. The infiltrated fragments were placed in capsules with fresh resin and polymerized for 24-36H at 248K Thick (2μm) sections were cut dry for immunocytochemical staining and subsequent light microscopy. These procedures resulted in excellent structural preservation in which 80-90% of the nicotine remained in the tissue as measured by HPLC and UV spectroscopy on extracts from larger samples of the same material treated in parallel.

The sections were immersed in a blocking buffer containing bovine serum albumin, foetal calf serum and fish gelatine for 30min at 298K. The buffer was replaced by mouse anti-nicotine serum for 16H at 298K. Both monoclonal and polyclonal mouse anti-nicotine antibodies were used. Sections were washed in phosphate buffered saline containing fish gelatine and bovine serum albumin (PBS-GB) and immersed for 90min at 298K in Ig biotinylated species specific whole antibody from sheep. The sections were washed in PBS-GB and immersed in either Streptavidin-fluorescein or Streptavidin-Texas Red for 90min at 298K. The stained sections were washed in PBS-GB, mounted in anti-fade mounting media and stored in the dark until examined using epi-fluorescence at 495nm for FITC or 596nm for Texas Red and photographed on either Ektar 1000 colour print film or Kodak 5020 EES colour slide film.

At all stages of leaf development and in both cultivars, the nicotine appears associated with the sieve elements of the phloem tissue. (Fig 1 and 2) The xylem tracheids of the small vascular bundles can be distinguished by their pale auto-fluorescence, and irregular thickening of the cell walls. Most photographs show cross sections of vascular bundles, but the occasional longitudinal sections show that it is the long sieve elements which are stained and that the xylem tracheids are unstained. Samples treated with pre-immune serum (Fig 3) show no staining associated with the phloem.There is a suggestion that the nicotine may be associated with the chloroplasts. This is a much less satisfactory result because it is difficult to distinguish the bright green fluorescence of fluorescein from the auto-fluorescence of chlorophyll. However, it is encouraging that a bright green fluorescent signal can be seen in the pale yellow Senescent leaves which have lost most of their chlorophyll and in the pale brown Old leaves which have lost all their chlorophyll. The use of Texas Red obviates most of these problems There appears to be less staining for nicotine in the Juvenile and Old leaves compared to the

Mature, Ripe and Senescent leaves. This is in agreement with the results of the chemical analysis for nicotine. In the occasional sections which pass through the glandular trichomes (Fig.4), staining can be seen associated with both the shaft and the terminal bulb of the trichome.
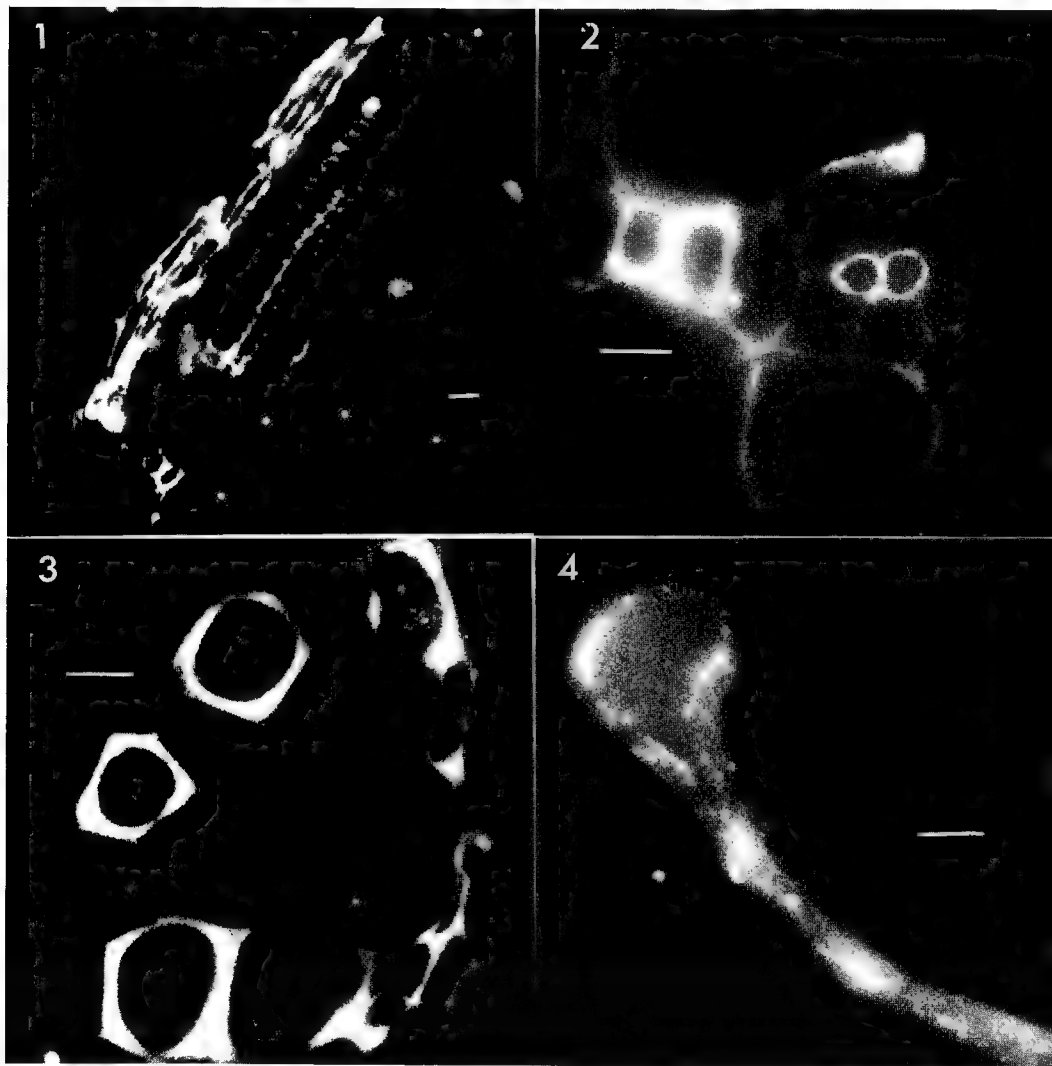
Fig 1. LS of Senescent Burley leaf with brightly stained sieve tubes and unstained xylem vessels.
Fig 2. TS of an Old Burley leaf showing brightly stained phloem tissue and unstained xylem tissue.
Fig 3. TS of a Juvenile Bright leaf showing no specific staining when pre-immune serum is use
Fig 4. TS of a trichome from Ripe Bright leaf showing positve staining for nicotine.
The marker bar on all four micrographs is equal to 10μm.

The nicotine antisera were supplied by Philp Morris Inc USA

[1] Echlin, P., Monaghan, P.M., & Robertson, D. *Proc. 50th Meeting EMSA* 1992, 854.

THE INFLUENCE OF CONFOCAL MICROSCOPE DESIGN ON IMAGING PERFORMANCE

C J R Sheppard

Physical Optics Department, School of Physics, University of Sydney, NSW 2006 Australia

The confocal microscope is now widely used in both biomedical and industrial applications for imaging, in three dimensions, objects with appreciable depth. There are now a range of different microscopes on the market, which have adopted a variety of different designs. The aim of this paper is to explore the effects on imaging performance of design parameters including the method of scanning, the type of detector, and the size and shape of the confocal aperture.

It is becoming apparent that there is no such thing as an ideal confocal microscope: all systems have limitations and the best compromise depends on what the microscope is used for and how it is used. The most important compromise at present is between image quality and speed of scanning, which is particularly apparent when imaging with very weak signals. If great speed is not of importance, then the fundamental limitation for fluorescence imaging is the detection of sufficient numbers of photons before the fluorochrome bleaches. This is a very different situation from the case where it is required to form an image in a very short time, when the number of photons is limited by saturation effects.

For the former case the weak fluorescent signal must be detected in a background of autofluorescence from either the specimen itself or the cements and coatings of the microscope objective. Autofluorescence from the objective can be considered as a constant source of stray light which reduces the signal to noise ratio of the imaging process.[1] To describe the effects of autofluorescence from the specimen it is useful to introduce the property of detectability, which must be defined according to the form of object and imaging geometry.[2,3] It is found that there is an optimum size of pinhole which maximizes the signal to noise ratio, the optimum size differing for different forms of object. For these two cases of noise originating from the optics or from the specimen itself, the behavior is quite different as the background increases as the square of the pinhole diameter if it comes from the objective but as the first power of the pinhole diameter if it comes from the specimen itself. This means that the confocal microscope is particularly advantageous compared with a conventional microscope when the limitation in performance stems from the autofluorescence from the objective.

For the case when it is necessary to image in a short time there is a limit, set by saturation, to the number of fluorescent photons which can be detected. The only way around this problem, which arises from the serial nature of scanned imagery, is to observe multiple points in parallel. This can be done using arrays of points, as in the tandem scanning microscope, or by using line illumination from a slit.[4] There are a variety of different optical arrangement using slits in use, which exhibit differences in their behavior.[5] Use of arrays of points, slits, or arrays of slits always result in a degraded imaging performance. The stray light from autofluorescence from the objective, for example, is proportional to the area of the detector aperture, so that, if line illumination is used and the slit is assumed just long enough to image a single line of the object, the noise performance is intermediate between that for a confocal microscope with a pinhole and that for a conventional microscope. The poorer performance comes from the fact that the length of the slit increases the stray light without increasing the signal appreciably. Similarly, a slit results in decreased optical sectioning, the signal from out of focus regions only decaying as the first power of the distance from focus rather than as the square of the distance as is the case for a pinhole aperture, so that detectability is also reduced. Hence the price one pays for an increase in speed is a reduction of image quality.

Whether one is aiming to record the best image possible, or to acquire an acceptable image in a short time, the performance of the detector is of great importance. Most commercial confocal microscopes use a photomultier tube as a detector which, although having high gain, has a quantum efficiency of only perhaps 13%. On the other hand CCD detectors can exhibit a quantum efficiency of 70% or more. The combined effect of quantum efficiency and noise can be considered by examining the signal to noise ratio S/N in the detection of a certain number of photons per pixel.[6] The ratio S/N determines the number of distinguishable grey levels in the image. It is found that for greater than about 20 photons per pixel a cooled frame transfer CCD exhibits superior performance compared with a photomultiplier tube with an S20 photocathode, so that to produce very high quality images a CCD is the better choice. On the other hand, if very few photons per pixel are available the photomultiplier tube will give the better image, but with only perhaps two or three grey levels.

If the number of the photons per pixel is not sufficient to produce an adequate image it is not a good idea to increase the pinhole size to increase the signal level, as the noise also increases so that the signal to noise ratio is reduced. In this case the number of photons per pixel can be increased if we are prepared to sacrifice spatial (or temporal) resolution.

References

1.   C.J.R. Sheppard et al., Scanning (1991) **13**, 233.
2.   C.J.R. Sheppard and X.S. Gan, submitted to J. Microscopy.
3.   C.J.R. Sheppard, Micron and Microscopia Acta (1991) **22**, 239.
4.   C.J.R. Sheppard and X.Q. Mao, J. Modern Optics (1988) **35**, 1169.
5.   D. Awamura and T. Ode, New Trends on Scanning Optical Microscopy, Okinawa, Japan (1992), Proceedings, p.43.
6.   C.J.R. Sheppard et al., J. Microscopy (1992) **168**, 209.

CONFOCAL MICROSCOPY, IMAGE RESTORATION, AND NUCLEAR STRUCTURE

Peter Shaw, Alison Beven, David Rawlins and Martin Highett

Department of Cell Biology, John Innes Institute, Colney Lane, Norwich NR4 7UH, UK

Fluorescent *in situ* hybridization and 3-D confocal microscopy have been used to study the arrangement of genes and transcripts in interphase plant nuclei. Wide-field fluorescence microscopy coupled with computer deconvolution has also been used on the same specimens and gives comparable results to confocal imaging. When image deconvolution is applied to confocal images, these show a significant improvement[1]. A comparison of confocal and wide-field (CCD) images of the same specimen (a plant nucleolus labelled with probe to the rRNA genes) is shown in Figure 1. The deconvoluted wide-field data (Fig 1b) and the raw confocal data (Fig 1c) are remarkably similar; the former is somewhat clearer. The deconvoluted confocal data (Fig 1d) is clearest of all.

Double-stranded DNA and single-stranded RNA probes to the 45S and 5S RNA genes have been used to investigate the functional organization of the nucleolus in pea root tissue[2]. *In situ* hybridization was carried out on vibratome slices approximately $50 \mu m$ thick (about 3 cells). With the DNA or sense RNA 45S probes all cells show 4 bright perinucleolar knobs, corresponding to the condensed, transcriptionally inactive rDNA from the two pairs of nucleolar organizer chromosomes in this species. Analysis of the various cell types observable in root tip tissue shows several characteristic patterns of internal nucleolar labelling, including bright foci, large central chromatin masses, and fine interconnecting fibres. An example is shown in Figure 2. The larger and more active the nucleolus, the smaller the proportion of condensed perinucleolar rDNA, and the smaller the proportion of labelling seen as foci.

The 5S genes are not linked to the 45S genes, and are located outside the nucleolus. Labelling with sense probe to th 5S genes shows six clusters in pea, occurring on 3 pairs of chromosomes. At least one 5S cluster, and often several, are located at the nucleolar periphery, and suggest that this may have functional significance[3]. (See Figure 3).

Labelling with 5S anti-sense probe shows a concentration of labelling in a cage-like network (see Fig 3), and this is closely paralleled by the labelling with 45S anti-sense probe. Double labelling experiments show that the larger foci and chromatin masses are located in the 'cavities' in the cage-work. However labelling with anti-sense probe to the external transcribed spacer portion of the 45S transcript, which is only present on initial transcripts before the first processing event, shows a distribution corresponding to the cavities in the cage-work. We interpret these observations in terms of a model of transcription and trancript processing which is highly organized in a sequential manner on an underlying structural matrix.[4]

References

1. P.J.Shaw and D.J.Rawlins, J. Microsc. (1991) 163, 151-165.
2. M.I.Highett, D.J.Rawlins and P.J.Shaw, J.Cell Science (1993) 104 (in press).
3. M.I.Highett, A.F.Beven and P.J.Shaw, J.Cell Science (1993) (in press).
4. This research was supported by the Agricultural and Food Research Council of the UK.
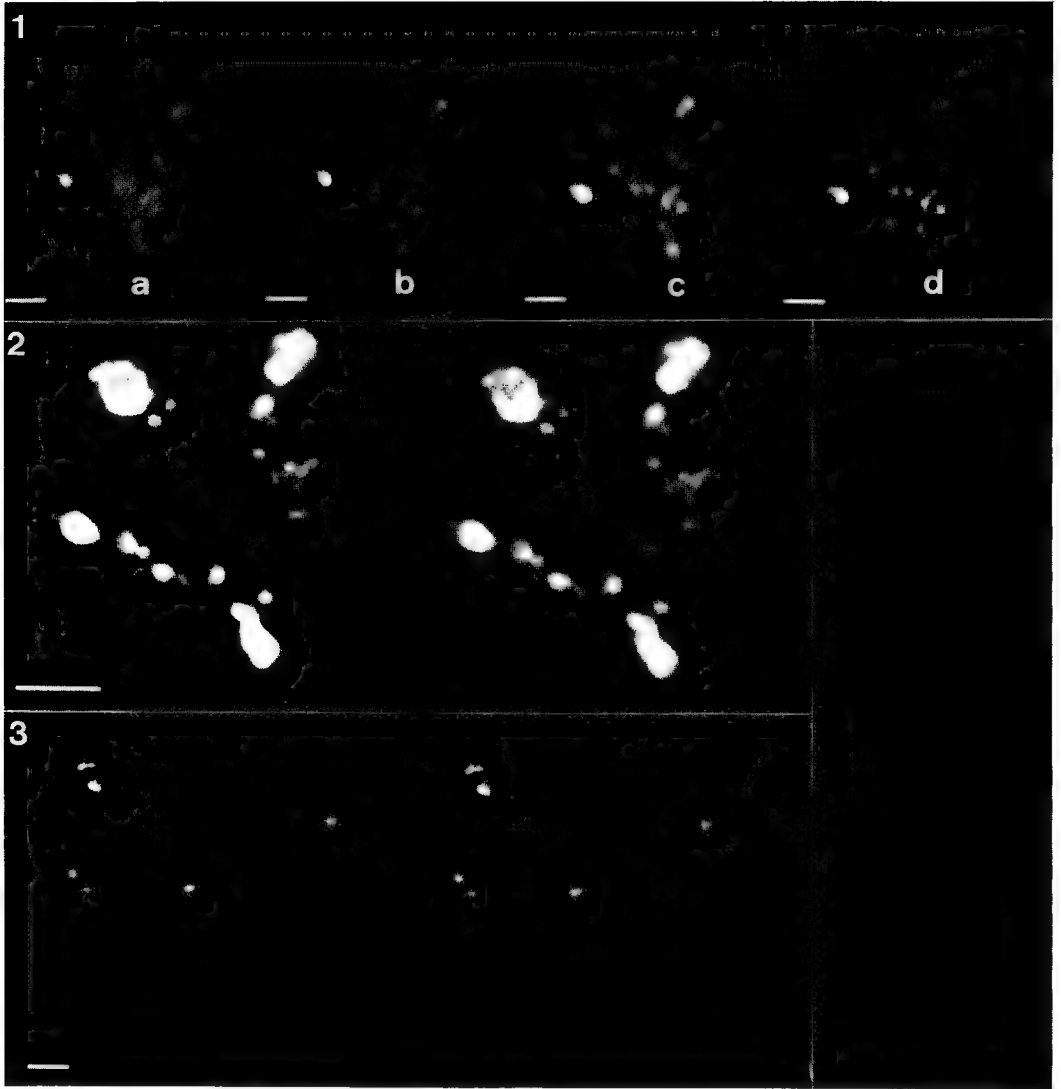
FIG. 1. Comparison of wide-field, confocal and deconvoluted data from the same nucleolus, *in situ* labelled with 45S sense RNA probe. An equivalent single section from the 3-D data set is shown in each case. A) Wide-field (CCD) data. B) Wide-field data after deconvolution. C) Confocal data. D) Confocal data after deconvolution. Bar=2μm.

FIG 2. Stereo pair of a projection of a single nucleolus labelled with 45S sense probe to show the position of the rDNA. Deconvoluted confocal data. Bar=2μm.

FIG 3. Stereo pair of a projection of a single nucleus labelled with 5S anti-sense probe to show the location of the genes in the nucleus and the transcripts in the nucleolus. Bar=2μm.

3-D IMAGE RESTORATION OF FLUORESCENCE MICROSCOPE IMAGES BY REGULARIZATION

Walter A. Carrington

Molecular Medicine, University of Massachusetts Medical School, Worcester, MA 01605

By combining optical sections of a fluorescently labelled cell with quantitative calibration of the microscope's blurring, we are able to computationally reverse the blurring of the microscope. We apply this approach to images taken on a conventional wide field microscope using a cooled CCD camera. Our algorithm is flexible in its use of data, which enables us to obtain good results with a small number of optical sections.[1,2] We use this flexibility to minimize photodamage and photobleaching, so that we are able to obtain 3-D movies of living cells with high spatial and temporal resolution. We obtain rejection of out of focus light, resolution and accuracy of quantitative fluorescent measurement superior to confocal microscopes with substantially less photobleaching and photodamage to the sample.[3] Recent algorithmic advances have enabled us to achieve transverse resolution as good as 100nm and axial resolution as good as 400nm.

The wide variety of cells and labels examined in 3-D in our lab illustrate the robustness and effectiveness of our image restoration approach. These applications range from samples as sparsely labelled as single copy genes in lymphocytes and fibroblasts labelled by in situ hybridization to densely labelled cells with fluorescently labelled dextran or Fura-2 that completely fill the cell volume. The sizes of cells examined range from newt eosinophils which are over 100 micrometers across and up to 20 micrometers deep to yeast cells which 2-3 micrometers in diameter. Recent collaborative work has examined the 3-D distribution of pre-messenger RNA and splicing enzymes in the nucleus.[4] Applicationof of our method to living cells has produced 3-D time series of lightly labelled cells at high resolution and with accurate quantitative fluorescence measurements; we routinely use 5-7 optical sections with non-uniform spacing on these experiments on living cells. Experiments on living cells have studied phenomenon in 3-D on time scales ranging from milliseconds ($[Ca^{+2}]$ in smooth muscle) to days (growth of axons in neuroblastoma cells).[5]

References

1. W.A. Carrington, et al, in K.Foskett, Grinstein,S., eds., Noninvasive Techniques in Cell Biology, Wiley-Liss, N.Y.(1990)53.
2. W.A. Carrington, in L.C. Smith, ed., Bioimaging and Two-Dimensional Spectroscopy, SPIE Proc., Vol. 1205 (1990)72.
3. W.A Carrington, et al, in J. Pawley, ed., Handbook of Biological Confocal Microscopy, Plenum Press, N.Y.(1990)151.
4. K.C. Carter, et al, Science, Vol.259,26 Feb. (1993)1330.
5. This work was supported by NSF grant DIR-9200027.
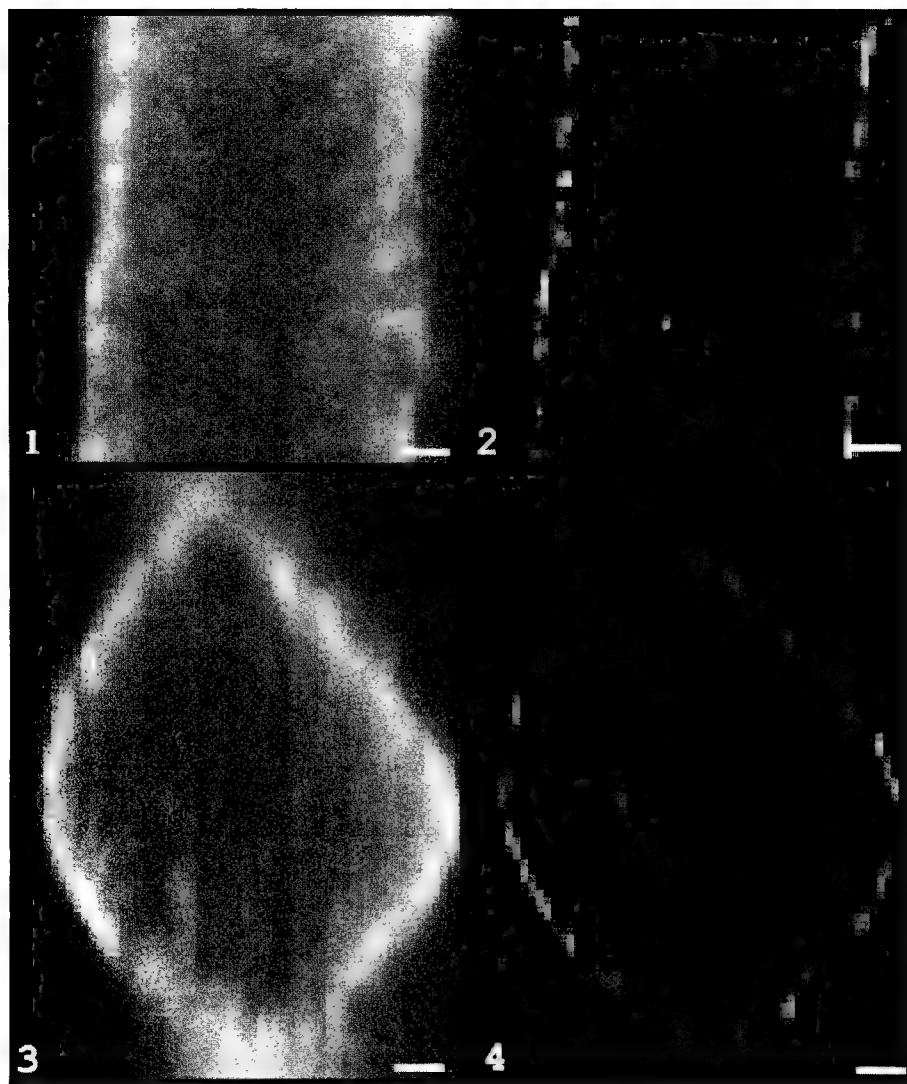
Fig. 1. One optical section before image restoration of smooth muscle cell with beta unit of the sodium–potassium pump labelled by indirect immunofluorescence. (XY section).
Fig. 2. Same cell after image restoration. (XY section).
Fig. 3. Same cell before image restoration (XZ section). Axis of the microscope (Z axis) is vertical.
Fig. 4. Same cell after image restoration (XZ section). Axis of the microscope (Z axis) is vertical.
All bars are 1 μm.

149

HIGH-RESOLUTION 3-D AND 4-D IMAGING USING WIDE-FIELD CCD-BASED MICROSCOPY

Jason R. Swedlow, Bethe A. Scalettar, John W. Sedat, David A. Agard

Graduate Group in Biophysics, Howard Hughes Medical Institute, Dept. of Biochemistry and Biophysics, University of California, San Francisco, San Francisco, CA 94143-0448

Because of the limited numerical aperture of a light microscope objective lens, every image recorded from a microscope is blurred and therefore degraded. This problem is particularly acute when a full three-dimensional image stack is viewed in projection. The blurred image is a convolution between every light source in an object and the point-spread function (PSF) of the objective lens and can be mathematically calculated or empirically measured.[1, 2] To eliminate blurring, we record three- and four-dimensional images with a charge-coupled device (CCD) -based computerized optical sectioning microscope and mathematically deconvolve out-of-focus photons using the appropriate three-dimensional, empirically measured PSF.[3] The use of the empirical PSF is important because of the presence of a partial confocal effect in a wide field microscope caused by the presence of the field diaphragm.[1] The advantage in this method is that collection and restoration of out-of-focus photons results in high sensitivity and resolution.

In order to follow nuclear and chromosome dynamics, we have injected *Drosophila melanogaster* embryos with various fluorescent proteins and then monitored the distribution of these proteins during mitosis by recording a series of three-dimensional data sets at regular time intervals-- a four dimensional data set. Two aspects of fluorescent imaging of living specimens are different from imaging of fixed specimens. First, embryos injected with fluorescent protein are quite photosensitive, so excitation light intensity from a Hg arc lamp is generally attenuated with a 10% transmittance neutral density filter and exposure times are limited to 10-200 ms. Disproportionately greater light intensity can be used with shorter exposure times. Second, the speed of the mitotic cycles in the *Drosophila* embryo means that only short three-dimensional data stacks can be recorded. Typically, 12 optical sections, each with a 50 ms exposure, separated by 0.5 μm, and consisting of 256 x 256 12-bit pixel elements, are recorded every 17 seconds. Instead of processing four-dimensional data sets by two-dimensional deconvolution of projections of individual three-dimensional images[4], we now use the full three-dimensional deconvolution on each three-dimensional image, thereby giving a much improved restoration (Fig. 1). Twenty cycles of iterative deconvolution on a three dimensional data set similar to that described above only takes 2.5 minutes on a DEC Alpha RISC Workstation. Deconvolution of four-dimensional data sets proceeds by sequentially processing individual (generally 200-300) three-dimensional images. The combination of wide-field microscopy and deconvolution has allowed exceptional spatial and temporal resolution for *in vivo* fluorescence studies which, to date, has not been equaled in reported studies using laser scanning confocal microscopes.

A useful feature of fluorescent imaging is the ability to study multiple probes simultaneously in space and time. Bandpass excitation and emission filters mounted on motorized wheels can be switched without changing a multi-wavelength dichroic mirror. Since the optical path length through the sample, coverslip, immersion oil and lens are a function of the wavelength, the PSF will vary with the choice of emission wavelength in a fluorescence microscope. As has been previously discussed, this greatly affects the symmetry of the PSF along the optical axis and degrades the resolution of the image.[1, 2]. When images are recorded using a fixed wavelength of light, axial asymmetry can be eliminated by adjusting the refractive index of the immersion oil.[1] In this case, the deconvolution algorithm can use a PSF which is axially symmetric. However, in multi-wavelength imaging with high numerical aperture lenses, this relationship between optical path length and wavelength makes it necessary to include axial asymmetry in the PSF and deconvolution. We have therefore explored the

improvement in image restoration when the axial asymmetry is included in deconvolution. PSFs of an Olympus 60x/NA1.4 lens were measured at 635 nm using 0.12 μm beads (Molecular Probes, Inc.) and immersion oil ranging in refractive index from 1.5000 to 1.5300. The PSFs were then deconvolved using algorithms that either ignored or included axial asymmetry. Inclusion of axial asymmetry produced up to a two-fold improvement in the full-width at half maximum intensity falloff along the optical axis in highly asymmetric images. As previously noted, highly asymmetric images are easily obtained: images of beads which appear symmetric using an oil of $n_D = 1.5180$ become very asymmetric under an oil of $n_D = 1.5150$.[1, 2] The use of axially asymmetric PSFs promises to be an important addition to deconvolution algorithms. Since empirical PSFs represent all the imaging properties of the microscope, including the partial confocal effect, it will probably be necessary to measure a number of asymmetric functions for asymmetric deconvolution.

With the increasing power of computer workstations, the capability to run three-dimensional deconvolutions on large images is now available for a modest investment. Nonetheless, we have explored the potential of accelerating the iterative deconvolution by a multi-resolution approach. The method works by running the deconvolution for one-quarter to one-half the normal number of iteration cycles on an image sub-sampled two-fold in the image plane. The intermediate result is then interpolated back to the original sampling size and used as a starting point for the rest of the iteration cycles. The result is 1.5 - 2 fold acceleration in running time and a final reconstruction which differs from the result from the full deconvolution in only the highest spatial frequencies and is therefore suitable for most analyses. In fact, this concept can be used for any image processing scheme to quickly test the validity of the choice of parameters. It is possible to store images of different resolutions within one file, since the sub-sampled images are small compared to the size of the fully sampled image. Information in the file header directs processing programs to the correct location of sub-sampled data.

References

1. Y. Hiraoka et al., Biophysical J. (1990)57, 325.
2. S. F. Gibson and F. Lanni, J. Opt. Soc. Am. (1991)8, 1601.
3. Y. Hiraoka et al., Semin. Cell Biol. (1991)2, 153.
4. Y. Hiraoka et al., Nature (1989)342, 293.
5. This work was supported by the Howard Hughes Medical Institute (J. W. S. and D. A. A.) and by grants from the National Institutes of Health to J. W. S. (GM-25101) and D. A. A. (GM-31627).
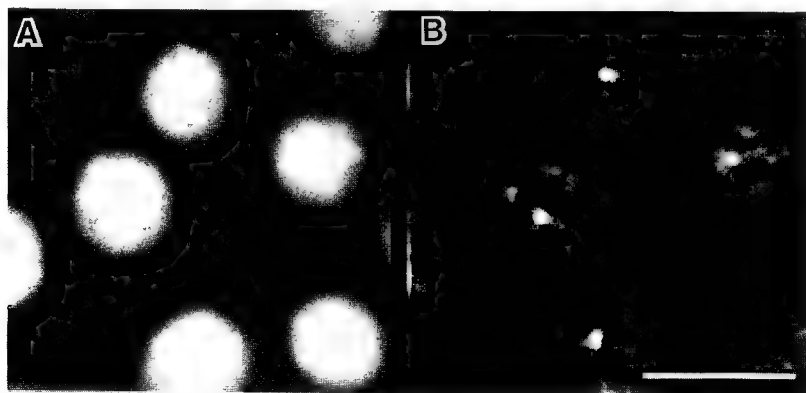
Figure 1. (A) Optical section recorded with a 60x/NA1.4 lens of living Drosophila embryonic nuclei injected with rhodamine-topoisomerase II. (B) Same optical section after deconvolution with empirically measured PSF. Scale bar = 10 μm.

THREE-DIMENSIONAL IMAGE RECONSTRUCTION OF FLUORESCENCE MICROGRAPHS WITHOUT KNOWING THE POINT SPREAD FUNCTION

Timothy J. Holmes, Vijaykumar Krishnamurthi and Yi-Hwa Liu

Biomedical Engineering Department, Rensselaer Polytechnic Institute, Troy, NY 12180-3590

The term *blind deconvolution* refers to the deconvolution, or deblurring, of a signal (optical, sound, or other) without explicit knowledge of the point spread function (PSF). The PSF is, instead, reconstructed concurrently with the deblurred signal from the collected, noisy data. Blind deconvolution methodologies have been under study for general signal processing applications, such as in restoring phonographs, as early as 1968 [1]. Ayers and Dainty have performed pioneering blind deconvolution research for deblurring 2D images [2], which has been applied to astronomy [3]. Inspired by this earlier blind deconvolution research, we have taken a new approach which is based on maximum likelihood estimation (MLE). Our approach is extended from previous research in applying MLE to positron-emission tomography (PET) [4]. A novelty of our research is in the application of MLE and blind deconvolution to 2D and 3D fluorescence microscopy [5-7].

The fundamental advantage of the MLE approach over some of the other blind deconvolution approaches is that it is a mathematical optimization approach, wherein the likelihood functional of the collected image data, the fluorescence probe concentration and the PSF is maximized. This type of optimization approach has an engineering advantage in that it removes guesswork in designing the algorithm and thereby tends to avoid *ad-hoc* remedies in refining and robustizing it. Rather than robustizing the algorithm in a trial and error fashion, we are able to, instead, formulate constrained solutions to the likelihood functional. Such constraints are what makes a blind deconvolution feasible, because we are able to constrain the properties of the PSF, thereby precluding ambiguous solutions. For example, it is well known that the PSF is bandlimited and that it has a well defined bandlimit.

The fundamental advantage of using a blind deconvolution over other 3D image reconstruction algorithms, used in fluorescence microscopy, is that it avoids the need to measure the PSF. Measuring the PSF typically involves imaging of small (<0.2 μm) fluorescent microspheres. Meticulous care must be taken in preparing the microsphere sample and in collecting and processing its calibration data. This procedure can be difficult, especially in the case of confocal fluorescence microscopy where low-light levels and photomultiplier tube noise are severe compared to widefield microscopy. Wide routine usage would be facilitated by a cut-and-dry procedure, not involving a PSF calibration. Another potential advantage is that we speculate that the blind deconvolution may conform to changes in the PSF. Since the PSF itself depends upon the specimen, it may change between the calibration of the PSF and the insertion of the specimen. The blind deconvolution potentially may avoid this problem, since it produces a PSF estimate from the specimen data itself. We expect that, at the very least, a blind deconvolution will ultimately be a useful addition to a comprehensive 3D image reconstruction toolbox, which may be called upon in cases where it is difficult, or impossible, to measure the PSF.

The derivation of the algorithm, its flowchart, its testing with computer simulations and its testing with 2D and 3D fluorescence micrographs are published elsewhere [5-7]. Fig. 1 demonstrates the axial deblurring and inherent noise reduction that is achieved with confocal data. To summarize: The algorithm is an iterative solution to the MLE criterion. The reconstruction of the probe concentration and the PSF are inherently constrained to be nonnegative. It produces images which compare well with former nonblind versions of the algorithm, where the PSF has been measured. For widefield microscopy, in all of the simulation and experiments run thus far, it has robustly and consistently done so, so long as the PSF is reasonably constrained, for instance, to be bandlimited with respect to all three dimensions (x, y and z) and to have the well known missing cone region.

Presently, reconstructions require on the order of 300 to 3,000 iterations, with corresponding processing times of 3 to 30 hours, for a 128x128x64 image, with a 15 Mflop computer (IBM 3090 with a vector processor), which is not a particularly fast computer by present standards. Estimated times with modern, faster, less expensive computers, such as the CSPI (Bellerica, MA) 3-Slot Multiprocessor having 3 parallel SC-3XL's (each with 2 Intel i860 XP processors), are 15 minutes to 2.5 hours. An algorithmic acceleration scheme, which we have applied previously to the nonblind version of the algorithm [7], is expected to reduce the number of iterations by a factor of 10 (30 to 300 iterations are expected). Estimated times with this accelerated algorithm and this CSPI computer are 2 to 20 minutes. These faster speeds will also allow larger dimensioned images, such as 256x256x256 or 512x512x128 dimensioned images, to be processed with a reasonable trade-off in processing time and memory size.

1. T.G. Stockham, T.M. Cannon and R.B. Ingebretsen, Proc. IEEE (1968)63, 678.
2. G.R. Ayers and J.C. Dainty, Opt. Lett. (1988)13, 547.
3. M. Karovska and S.R. Habbal, Astrophysical J. (1991)371, 402.
4. L.A. Shepp and Y. Vardi, IEEE Trans. Med. Imag. (1982)1, 113.
5. T.J. Holmes, J.O.S.A.-A (1992)9, 1052.
6. V. Krishnamurthi, Y. Liu, T.J. Holmes, B. Roysam and J.N. Turner, SPIE (1992)1660, 95.
6. V. Krishnamurthi, T.J. Holmes and Y. Liu, Applied Optics, in review.
7. T.J. Holmes and Y. Liu, J.O.S.A.-A, (1991)8, 893.

Fig. 1. Lateral ray-summed views of confocal data (64x64x64 sampling; 50x50x25 μm) of rat hippocampal dendrites stained with lucifer yellow. Left: Original orthogonal views; Right: Deblurred, noise reduced views after 1,000 iterations.

TWO-PHOTON EXCITATION FLUORESCENCE MICROSCOPY IN LIVING SYSTEMS

David W. Piston

Department of Molecular Physiology and Biophysics, Vanderbilt University, Nashville, TN 37232

Two-photon excitation fluorescence microscopy[1] provides attractive advantages over confocal microscopy for three-dimensionally resolved fluorescence imaging.[2-5] Two-photon excitation arises from the simultaneous absorption of two photons in a single quantitized event whose probability is proportional to the square of the instantaneous intensity.[6] For example, two red photons can cause the transition to an excited electronic state normally reached by absorption in the ultraviolet. In our fluorescence experiments, the final excited state is the same singlet state that is populated during a conventional fluorescence experiment. Thus, the fluorophore exhibits the same emission properties (e.g. wavelength shifts, environmental sensitivity) used in typical biological microscopy studies. In practice, two-photon excitation is made possible by the very high local instantaneous intensity provided by a combination of diffraction-limited focusing of a single laser beam in the microscope and the temporal concentration of 100 femtosecond pulses generated by a mode-locked laser. Resultant peak excitation intensities are 10^6 times greater than the CW intensities used in confocal microscopy, but the pulse duty cycle of 10^{-5} maintains the average input power on the order of 10 mW, only slightly greater than the power normally used in confocal microscopy.

Three properties of two-photon excitation give this method a tremendous advantage over conventional optical sectioning microscopies for the study of UV excitable fluorophores in thick samples: **1)** The excitation is limited to the focal volume because of the intensity-squared dependence of the two-photon absorption. This inherent localization provides three-dimensional resolution and eliminates background *equivalent to an ideal confocal microscope* without requiring a confocal spatial filter, whose absence enhances fluorescence collection efficiency. Confinement of excitation to the focal volume also *minimizes photobleaching and photodamage* - the ultimate limiting factors in fluorescence microscopy of living cells and tissues. This localization is demonstrated in Figure 1, which shows the XZ bleaching pattern that arises from repeated scanning of a single XY plane in a stained polymer film. Figure 1(a) shows the conventional single photon bleach, while 1(b) is for two-photon excitation. **2)** The two-photon technique allows imaging of UV fluorophores with conventional visible light optics in both the scanning and imaging systems, because both the red excitation light (~700 nm) and the blue fluorescence (>400 nm) are within the visible spectrum. **3)** Red light is far less damaging to most living cells and tissues than UV light because fewer biological molecules absorb at the higher wavelengths. Longer wavelength excitation also reduces scattering of the incident light by the specimen, thus allowing more of the input power to reach the focal plane. This relative transparency of biological specimens to 700 nm light *permits deeper sectioning*, since both absorbance and scattering are reduced.

Many cell biological applications of two-photon excitation microscopy have been successfully realized. Two-photon excitation of Indo-1 has allowed three-dimensionally resolved, dynamic quantification of intracellular calcium activity ($[Ca^{2+}]_i$) in motile cells[2], cardiac myocytes and excitable cells.[3] These measurements permit visualization of both standing calcium gradients and transient heterogeneities in $[Ca^{2+}]_i$. Cell autofluorescence arising from NADH has been imaged in corneal cells and myocytes. Figure 2 shows (a) an NADH auto fluorescence image and (b) a transmitted light image of a rat cardiac myocyte, acquired in 10 sec total exposure. The myocytes survive under continuous two-photon excitation imaging for over two minutes, which is considerably better than under conventional UV excitation. We have also used Hoechst 33342 to image nuclear division in living sea urchin embryos. Figure 3 shows a single optical section through the metaphase plate of a single nucleus of a living 8-cell embryo. The embryos remain healthy through two division cycles (90 min) with a complete 3-D data set acquisition every ten minutes. Finally, we have utilized the pulsed nature of mode-locked excitation to efficiently realize fluorescence decay time imaging.[7,8] Fluorescence decay times (~1-10 nsec) are sensitive to the local environment of the fluorophore, and therefore a useful quantity for determination of intracellular chemistry. The excellent background elimination of the two-photon excitation allows accurate, spatially resolved decay time images to be acquired in as little as 10 sec exposure time. These

examples, which demonstrate the wide ranging power of two-photon excitation microscopy, represent only a small subset of the possible future applications of this technique.[9]

[1] Denk W., J.H. Strickler and W.W. Webb *Science* **248**:73-76 (1990).
[2] Williams, R.M., I. Brust-Macher, D.W. Piston and W.W. Webb. *Biophys. J.* **63**:A367 (1993).
[3] Piston, D.W. and W.W. Webb. *Biophys J.* **59**:156a (1991).
[4] Summers, R.G., J.B. Morrill, A. Lieth, M. Marko, D.W. Piston and A.T. Stonbreaker. *Dev. Growth Diff.* (1993) In Press.
[5] Piston, D.W., R.G. Summers and W.W. Webb. *Biophys. J.* **63**:A110 (1993).
[6] Goppert-Mayer, M. *Ann. Phys.* **9** :273-294 (1931).
[7] Piston, D.W., D.R. Sandison, W.W. Webb. *Proc. SPIE* **1 640**:379-389 (1992).
[8] Guild, J.B., D.W. Piston, D.R. Sandison and W.W. Webb. *Biophys. J.* **63**:A110 (1993).
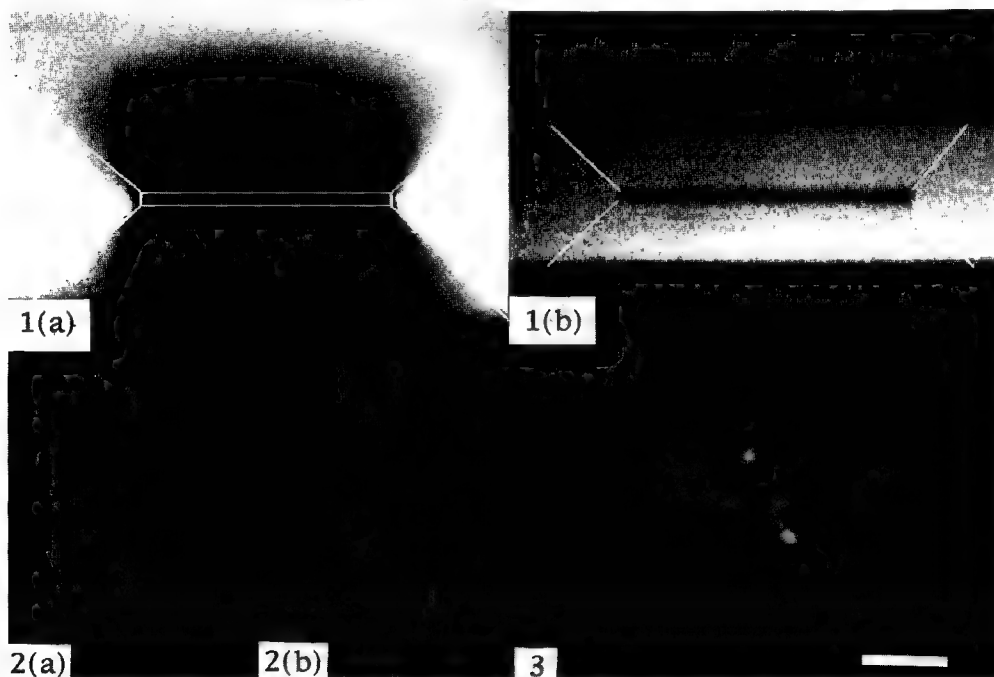
FIG 1. (a) XZ profile of the excitation pattern in a confocal microscope formed by repeatedly scanning a single XY optical section in a thick film of rhodamine-formvar until fluorescence was completely bleached. The box represents the region from where data was be collected by the confocal microscope for this optical section. Nearly uniform bleaching occurred both above and below the focal plane. (b) Same excitation pattern, but for two-photon excitation. Slanted lines denote excitation light path as in (a), yet bleaching only occurred in the focal plane. Scale bar (located in Figure 3) represents 35 μm.
FIG 2. (a) Two-photon excited NADH autofluorescence (normal excitation ~350 nm) image of a rat cardiac myocyte. Nuclei are clearly visible as dark spots. (b) Transmitted light image acquired simultaneously shows no Z plane detail, i.e. nuclei are not visible. Scale bar is 25 μm.
FIG 3. Single optical section of Hoechst 33342 stained chromosomes within a sea urchin embryo nucleus. Nucleus was located 30 μm from the top of the embryo. Scale bar is 5 μm.

SIMULTANEOUS, NON-INTERFERING COLLECTION OF OPTIMAL FLUORESCENT AND BACKSCATTERED LIGHT SIGNALS ON THE MRC 500/600

JB Pawley, WB Amos*, A Dixon** and TC Brelje§

IMR, 1675 Observatory Dr. Madison WI, 53706 USA, *MRC Molecular Biology, Hills Rd, Cambridge UK, **Bio-Rad Ltd., Maylands Ave. Hemel Hempstead, Herts,HP2-7TD,UK, §University of Minnesota Medical School, Dept. of Cell Biology and Neuroanatomy, 321 Church St.SE,Minneapolis, MN 66455

One of the most important attributes of the confocal LM is that it can be used for imaging living cells. Unfortunately, cells that contain fluorescent dyes are far less tolerant of the intense illumination characteristic of microscopical examination than unstained cells. As a result, it early became evident that every effort should be made to extract as much information as possible from every photon striking the specimen. This implies not only utilizing detectors with high quantum efficiency but also detecting the light which is back-scattered by (BSL), or passing through, the specimen in addition to any fluorescent signal. Both transmitted light and BSL carry information about the optical properties of the specimen and it is possible to detect this information without compromising fluorescent signal collection [1].

The fraction of incident light, I_0, passing through a surface separating regions having differing indices of refraction, n_1 and n_2, that is scattered is, $I_s = I_0\{(n_1 - n_2)/(n_1 + n_2)\}$. If the surface is optically smooth over the diameter of the probe, the scattering is coherent and becomes reflection. Reflected light obeys the Reflection Law, $\angle_{inc.} = \angle_{refl.}$, and therefore, the amount of light re-entering the objective lens, and being subsequently recorded by the detector, will vary strongly with the local inclination of the surface. The fraction reflected also varies with $\angle_{inc.}$ or α, as $1/(\alpha - 90^0)$, where $\alpha = 0$ at normal incidence[2].

The optical inhomogeneities commonly present in most biological tissue scatter a only a small fraction of the incident light back towards the objective lens: about 10^{-4} to 10^{-6} or about the same as is usually produced by fluorescence[2]. Collection of this weak BSL signal in the laser-scanning confocal microscope (LSCM) has always been complicated by the fact that a much larger fraction (0.5-3%) of the highly-coherent incident laser illumination is specularly reflected at each optical surface in the excitation path. This reflected light is not usually troublesome when the instrument is used for fluorescence because, unless the reflecting surface is conjugate with an image plane, most of the reflected light is removed by the confocal pinhole and the remainder is stopped by the long-pass, barrier filter in front of the detector. However, the barrier filter cannot be used when one wishes to treat the light scattered back by optical inhomogeneities in the specimen as the signal and, unless precautions are taken, the specular reflections appear in the BSL image as a number of more-or-less concentric bright rings near the axis which obscure the BSL signal from the specimen. While the effect of this artifact can be reduced by panning the scanning system so that one uses a peripheral part of the lens field, this reduces optical performance and so it is preferable to use "Anti-flex" polarizing techniques [3,4,5]

We have developed a system of two filter blocks for use with the Bio-Rad MRC-500/600 which permit optimal removal of these reflection artifacts and the simultaneous collection of BSL and fluorescence signals (Fig 1). The Block I contains a laser -line filter followed by a beam-splitter consisting of a 6 mm thick Pyrex optical flat, anti-reflection coated on its rear (upper) side. A 1/2-wave plate after the laser is used to rotate the laser polarization so that 0.8 -5% of the laser light is reflected down the optic axis and through a 1/4-wave plate between the ocular and the objective. Almost all of the returning BSL and fluorescent light passes through this beam-splitter to Block II where the BSL and fluorescent signals are separated with a dichroic mirror. The long wave signal passes to PMT 1 via an emission filter. Signal at the excitation wavelength passes through a 1/4-wave plate and analyzer (both rotatable) and a laser line filter to PMT 2. The orientation of the 1/2-wave plate is adjusted to give maximum light from the objective then the rotatable elements in Block II are adjusted to eliminate spurious reflections (Fig 2). Finally, the 1/4-wave p;late in the microscope body is rotated to produce the maximum BSL signal from a living cell. (Fig 3). As expected, the BSL image demonstrates optical sectioning when compared to phase contrast (Fig 4). Fig. 5 is a BSL/Fluor stereo pair of part of a cheek cell. It shows punctate cytoplasmic features.

References: 1)EHK Stelzer, Chapter 9 & JB Pawley, Chapter 2, in Handbook of Biological. Confocal Microscopy., Plenum NY, 15-26 & 86. (1989); 2) PC Cheng and R. Summers, Chapter 17, 181-83, IBID; 3) HE Keller, , Chapter 7, 85, IBID; 4) Swarzowski DH *et. al.* Scanning 14:104-111, (1991). 5)WA Shurcliffe & SS Ballard *Polarized Light,* Van Nostrand, Princeton, 104-106.
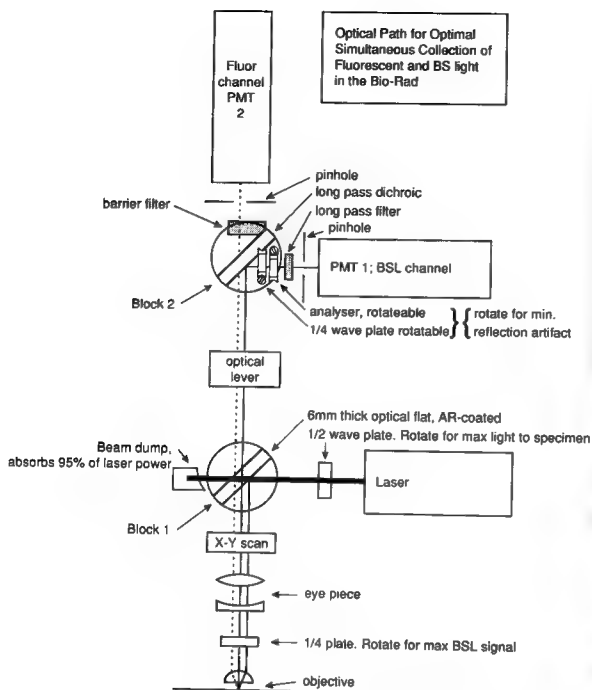
Fig.1.Diagram of BSL/Fluor.system for MRC-500/600.

Fig. 4. Focus series images of a cheek cell, acquired simultaneously using BSL and non-confocal phase contrast ($\Delta z = 0.5 \mu$m, second pair focussed at glass surface). The BSL series shows greatly reduced depth-of-field.

Fig. 5. (below) Stereo pair made using a 0, 2 pixel shift on a stack of 15 images acquired simultaneously using the BSL/Fluor system shown in Fig.1. The specimen was part of a cheek cell stained with Acridine Orange.

Fig.2 Reflection artifacts before (a) and after (b) adjustment. All other settings constant.
Fig. 3. Increase of signal produced by adjustment of 1/4 wave plate in microscope body.
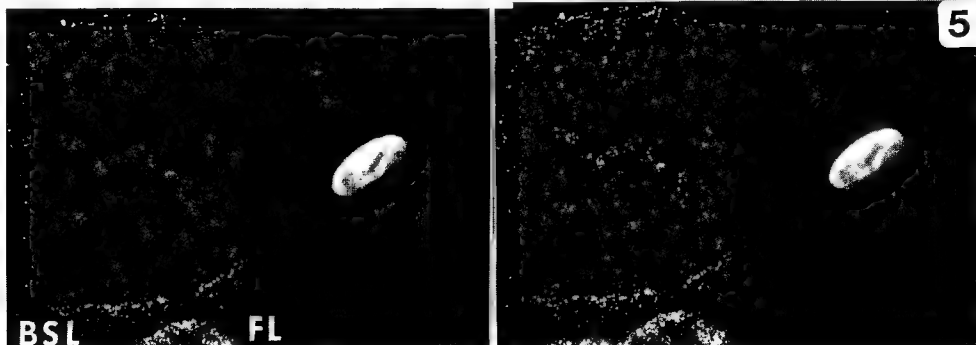
THREE-DIMENSIONAL IMAGE ANALYSIS AND VISUALIZATION IN CONFOCAL LIGHT MICROSCOPY

J. K. Samarabandu, R. Acharya, D. R. Pareddy and P. C. Cheng

Advanced Microscopy and Imaging Laboratory (AMIL), Department of Electrical and Computer Engineering, University of New York at Buffalo, Buffalo, NY 14260 USA

In the study of cell organization in a maize meristem, direct viewing of confocal optical sections in 3D (by means of 3D projection of the volumetric data set, Figure 1) becomes very difficult and confusing because of the large number of nucleus involved. Numerical description of the cellular organization (*e.g.* position, size and orientation of each structure) and computer graphic presentation are some of the solutions to effectively study the structure of such a complex system. An attempt at data-reduction by means of manually contouring cell nucleus in 3D was reported (Summers *et al.*, 1990). Apart from being labour intensive, this 3D digitization technique suffers from the inaccuracies of manual 3D tracing related to the depth perception of the operator. However, it does demonstrate that reducing stack of confocal images to a 3D graphic representation helps to visualize and analyze complex tissues (Figure 2). This procedure also significantly reduce computational burden in an interactive operation. These image analysis tools can also be employed for numerical and volumetric study of cellular organization such as the position of the individual cells, the surface area and volume of nucleus and the orientation of cell division axis. To overcome the disadvantage of manual tracing, an automatic data reduction procedure based on multi-dimensional image analysis algorithms was developed in our laboratory. We also developed a system to visualize and extract morphometrical parameters from the data generated by this method (Acharya et.al 1990). Our confocal image processing system is implemented as a set of tools whose activities are coordinated by a blackboard control structure and is modeled after the image understanding model introduced by Kanade (1980). In contrast, the analysis of the 3D arrangement of string-like structures, such as chromosomes, requires a different approach. For example, the possibility of studying chromosomes in 3-D has been of significant interest in cytogenetics. In the past decade, some progress has been made in studying *Drosophila* chromosomes (Agard and Sedat, 1983) and maize pachytene chromosomes (Dawe *et al.*, 1992) by digital deconvolution of bright field images. Using computer programs, three dimensional path of each chromosome was traced and recorded to produce a straightened map of the chromosome. Major obstacle in the analysis of such structure is the requirement of a large computational resource, and also the manual tracing of chromosomes is very tedious and time consuming. On the other hand, confocal microscopy can achieve similar optical sectioning results with significantly less computational resource (Figure 3). To assist such an operation, our laboratory has developed a semi-automatic tracing program which can significantly reduce the tedious tracing work (Figure 4). In the context of analyzing chromosomal arrangement, the "structural knowledge" consists of identifying chromosomal strands in a given subvolume using features such as center of mass and orientation.

References

1. R. G. Summers *et al.*, J. Electron Microscopy Tech. (1990)
2. R. S. Acharya, P. C. Cheng, J. K. Samarabandu, R. G. Summers, L. H. Chen, and C. E. Musial, Trans. Royal Microscopical Society (1990)1,289
3. T. Kanade, Computer Graphics and Image Processing (1980)13,279
4. Agard, D. A. and Sedat, J. W. Nature (1982)302: 676-681.
5. R. K. Dawe *et al.*, Maize Genetics Cooperation Newsletter, (1992)66,23
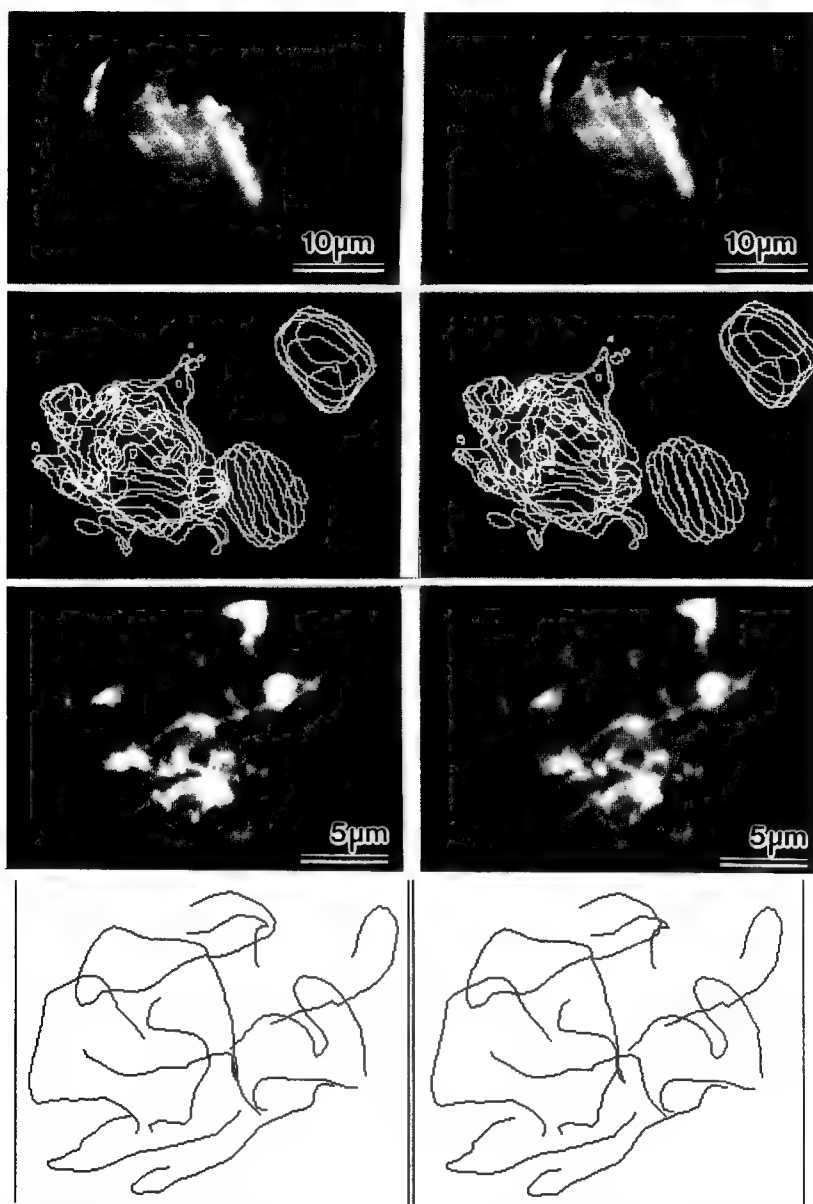
Figure 1. Stereogram shows DAPI stained nucleus (two sperm and one vegetative nucleus) in the pollen grain of maize (*Zea mays L.*). The image was reconstructed from a stack of confocal images obtained by using an Olympus UV laser scanning confocal microscope (LSM-GB200UV) with UVAPO40XLSM water immersion objective. excitation: 351 and 364nm.

Figure 2. Surface contours of the three nucleus similar to those shown in Figure 1. The image was obtained from 60 confocal optical sections by our multi-dimensional image analysis system.

Figure 3. Stereogram of maize pachytene chromosomes stained by Feulgen. The stereogram was reconstructed from 40 optical sections obtained by using an Olympus laser scanning confocal microscope (LSM-GB200) in epi-fluorescent mode. excitation: 514nm.

Figure 4. Partially traced chromosomes shown in Figure 3.

159

INTELLIGENT COMPUTATIONAL 3-D MICROSCOPY: NEW RESULTS IN SEGMENTATION, NOISE REMOVAL, CELL COUNTING, AND AUTOMATED NEURON TRACING

Badrinath Roysam, Anoop K. Bhattacharjya, Hakan Ancin, Andrew R. Cohen, Robert W. Mackin, Douglas E. Becker, and Carlos Rodriguez

ECSE Department, Rensselaer Polytechnic Institute, Troy, New York 12180, USA

This paper presents a review of recent advances made by us in the broad area of intelligent computational 3-D microscopy. This research involves the development and application of automated pattern recognition, computer vision and image interpretation algorithms to problems in 3-D biological microscopy. The broad goal of this work is to develop computational tools for rapid, unsupervised, flexible, quantitative and unbiased analysis of large sets of complex 3-D images of thick biological specimens. The imaging modalities used in this work have thus far involved laser-scanning confocal microscopy (LSCM) and 3-D brightfield microscopy.[1] The specimens of interest have been thick slices of brain tissue, large selectively-stained neurons, indocyanin green and fluorescein retinal angiograms, and thick overlapping cell clusters in cytological preparations such as Papanicolaou smears.

Image segmentation is an essential first step for most forms of analysis. This task is straightforward when the image data is isotropic, has uniform high contrast, and is free of noise. Under these conditions, a simple thresholding operation, followed by morphological processing is adequate. Unfortunately, these conditions are rarely met. The LSCM images of interest to us exhibit non-isotropic axial blurs, spatially-varying quantum noise, and sometimes, low and/or spatially-varying contrast.[2,3] The brightfield images of thick cytological preparations are characterized by non-isotropic blurs and missing frequencies, extremely high variability in image intensity and contrast due to the unpredictable nature of cell overlaps and staining variations. In either case, there exists an inherently high variability in the shapes, sizes, orientations, and overlap patterns among biological structures. Finally, the large volume of 3-D data presents serious computational challenges.

The above challenges are being addressed as follows. The non-isotropic nature of the data is handled by using image reconstruction algorithms, usually based on the EM algorithm.[3,4] The problem of imaging noise is handled by the use of statistical models of noise in the reconstruction algorithm, and the incorporation of region-dependent smoothing priors. Usually, background regions are smoothed significantly, whereas foreground regions are smoothed minimally, or not at all.[2,5] The forbidding computational requirements of this task are met in two ways: (i) data reduction; and (ii) the use of parallel and vector computers. The technique of data reduction is useful when the object(s) of interest occupy a small fraction of the 3-D image space. In this method, the set of voxels corresponding to the foreground, and a limited neighborhood of the same are extracted into an active voxel data structure. Subsequent computations occur over this reduced data set.

The challenge of image variability is addressed in several ways. For the LSCM images, fixed intensity thresholds are replaced by Poisson intensity models based on intensity intervals. The upper and lower bounds on these intervals are computed over local voxel neighborhoods using an unsupervised clustering procedure.[6,7] The bounds are allowed to vary slowly over the 3-D image. The brightfield cytological images exhibit a more extreme form of image variability, requiring a different approach. For these images, a combination of two methods has been developed. First, the segmentation is made to proceed in a nested fashion. In this method, the image is segmented into a set of unconnected blobs. These blobs are then re-segmented repeatedly, in a nested fashion, using locally-derived intensity intervals. Second, spatial localization constraints are introduced into the segmentation algorithm. This method is useful when the objects of interest (eg. cells, nuclei, dendrites) are spatially localized. In this approach, densitometric and geometric feature distance metrics are defined for each voxel-region pair. These metrics are incorporated into an ISODATA cluster analysis procedure.[7] This method has a significant side benefit in that it provides a well-founded mechanism for disambiguating overlapping clusters of localized objects.

160

Our current efforts are focussed on embedding known priors related to region shapes, in combination with spatial localization constraints. The region shape models are expressed in terms of partially-flexible polygonal templates that are constructed from user-supplied examples of cell shapes.

Significant progress is achieved by posing the segmentation problem in combination with other operations, rather than in isolation. For example, the generalized EM algorithm provides a sound basis for combining segmentation with deblurring.[8] Gibbs' energy representations of generalized Bayesian hypothesis tests and syntactic pattern constraints can be used to effect a joint solution of intensity estimation (noise removal), boundary estimation and segmentation problems. Such synergistic solutions not only result in improved segmentations, but also in improved intensity estimation.[2,5]

The problem of cell counting is an important application of segmentation. The problem of counting is a specific instance of the more general problem of cell population analysis. This includes the measurement of various cell properties such as volumes, 3-D locations, staining levels and shape descriptors, and subsequent analysis of the entire cell population with respect to these measurements. The population may be analyzed to detect unusual cells and imaging artifacts automatically , and to organize the cells into a hierarchy of groups reflecting similar properties. Hierarchical representations based on dendrograms have proven to be invaluable in this regard.[7]

A fundamental difficulty in cell population analysis is the specification by a user as to what constitutes a cell. Indeed, in any given ensemble of cells, one finds significant variations in intensity, size, shape, orientation and spatial clustering patterns. These variations are compounded when the population contains a mixture of two or more different types of cells. The most extreme images of interest contain densely-overlapping clusters of different types of cells. While sophisticated mathematical tools exist for modelling quantifiable cell parameters, they are difficult to construct, especially in 3-D. Our current efforts are focussed on developing bootstrap-based methods that automatically construct such models from user-supplied examples and counterexamples.

The detailed tracing of neuronal topologies and accurate measurement of sizes and volumes of various structures is vital for a large number of studies in biology and medicine. Currently, most of the tracing is carried out by laborious and time-consuming manual and semi-automated processes.[9] We have been successful in automating this process completely. The approach is based on imaging selectively-stained neurons in 3-D using LSCM, and subsequent image analysis. The image analysis is based on deblurring and segmenting the data, followed by a high-quality 3-D skeletonization operation. Fine dendritic fragments that are disconnected from the main skeleton are selectively rejoined using a combinatorial algorithm. The completed neuronal skeleton is converted to a graph-theoretic structure. The somas are localized using mathematical morphology operators over the 3-D segmentation. Selective and accurate model-free volumetric measurements of various neuronal structures are made by locating specific structures on the graph-theoretic representation, and using cutting planes to isolate and count the voxels corresponding to the structure of interest.

References:
1. B. Willis et al. Journal of Microscopy, (in press).
2. Roysam, B. et al., Micron and Microscopica Acta, 23(1992):447-461.
3. T. J. Holmes, J. Opt. Soc. Am. A, 6(1989):1006-1014.
4. M. I. Miller and B. Roysam, Proc. Natl. Acad. Sci., 88(1991):3223-3227.
5. B. Roysam and M. I. Miller, Digital Signal Processing, 2(1992):48-64.
6. T. N. Pappas, IEEE-PAMI,40(1992)901-914.
7. A. K. Jain and R. C. Dubes, Algorithms for Clustering Data, Prentice-Hall (1988).
8. A. D. Dempster et al., J. Royal Statistical Society, B39(1977):1-37.
9. J. J. Capowski (ed.) Computer Techniques in Neuroanatomy, Plenum Press, (1989).
10. Acknowledgements: Digital Equipment Corp., AT&T Foundation, NSF, MSA, Colleagues.

THREE-DIMENSIONAL IMAGING AND PHYSIOLOGY OF LIVE NEURONS AND GLIA: CONFOCAL LIGHT AND CORRELATIVE HIGH-VOLTAGE ELECTRON MICROSCOPY

J.N. Turner, D.H. Szarowski, W. Shain, M. Davis-Cox, D.O. Carpenter and M. Fejtl

Wadsworth Center for Laboratories and Research, New York State Dept. of Health, and School of Public Health, The University at Albany, Albany, NY 12201-0509

Correlating physiologic measures with three-dimensional (3D) imaging at the light and electron microscopic levels is a powerful combination of methods for studying the structure and function of biological systems. Neurobiology is an ideal field for the application of these methods because neurons and glia have complex and extensive 3D structure, and their physiology is under intense study. Neurons, such as those studied here from *Aplysia*, can be more than 100 μm in diameter, and glia undergo large scale 3D shape change as a function of a number of physiologic parameters.[1] The ability to accurately quantitate the 3D structure, volume and surface area of live neurons and glia is important to our understanding of the complex function of these cells.

Neurons were isolated from the major ganglia of juvenile *Aplysia Californica* and glia were obtained from long term cultures of LRM 55 cells[1] or as primary isolates from rats. Cultures were exposed to DiI dissolved in DMSO with or without 20% Pluronic F-127 and added to the culture media. The imaging instrument was an Olympus IMT-2 and a Bio-Rad MRC-600. A plexiglass perfusion stage with a ceramic insert ensured electrical isolation for the high resistance probes (10 to 25 MΩ) used to monitor intracellular potential, inject current, and measure the plasma membrane capacitance and resistance. It also provided rapid fluid transfer and a humidified environment. Images were recorded as a function of the z-dimension or as a function of time at a constant z-position, and reconstructed on an IBM RISC-6000 graphics workstation using ANALYZE[2] or VoxelView (Vital Images).

Fig. 1 shows an optical section through the center of an *Aplysia* neuron in control media (A) and after exposure to 30% hypertonic media (B). The change in size and surface structure is obvious and is shown from the side as a function of time (increasing vertically) in (C). The lines a and b indicate the times for (A) and (B), and the arrow indicates the media change. The membrane time constant, τ, serves as a measure of membrane surface area. (D) depicts intracellular recordings that determine τ by injecting hyperpolarizing current pulses. τ increases in 30% hypotonic media indicating an increase in surface area due to cell swelling. The opposite result is expected for hypertonic media, and we are correlating surface area measures by 3D reconstruction.

Glial cells are shown to change shape in response to exposure to isoproterenol in Fig. 2. (A) is representative of control cells and are about 4 μm in height while those that have changed shape (B) are about 18 μm. The withdrawal of the cytoplasm toward the nucleus and into a few highly polarized processes is dramatic.

References

1. W. Shain et al., Glia (1992)5, 223.
2. R. Robb and C. Barillot, in IEEE Transactions on Medical Imaging (1989)8, 217.
3. Work partially supported by grants NIH RR 06904, RR01219, NS 21229 and NSF DIR 9108492.
MF is sponsored by a Schrödinger Fellowship from the Austrian Science Foundation.

Fig. 1

A   B

C   D

τ=47.5 ms (30% hypotonic)

τ=27.6 ms (back in ASW)

b

a

τ=25.2 ms (control ASW)

Fig. 2

A   B
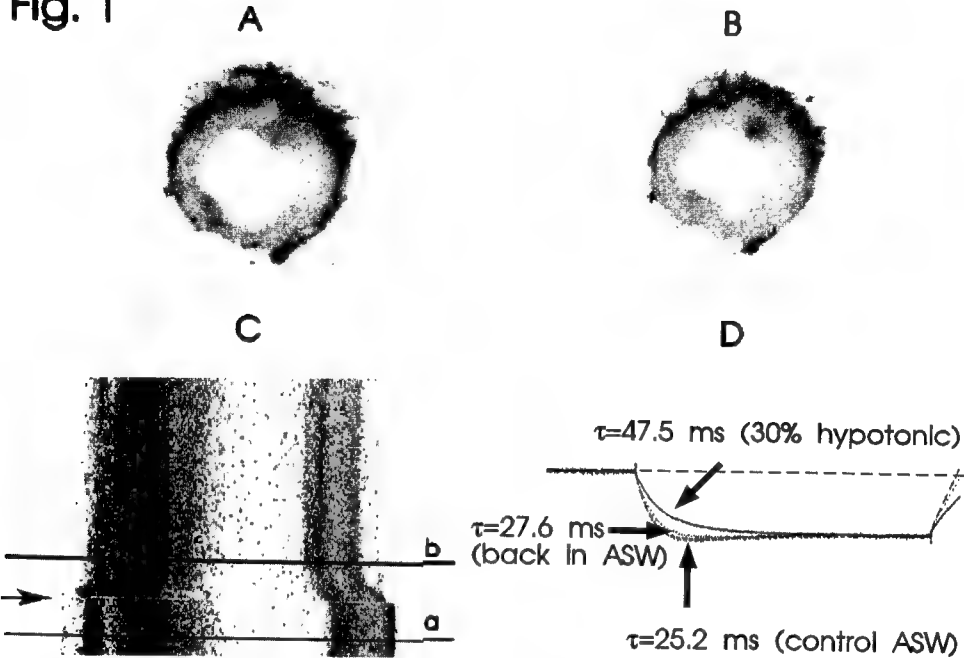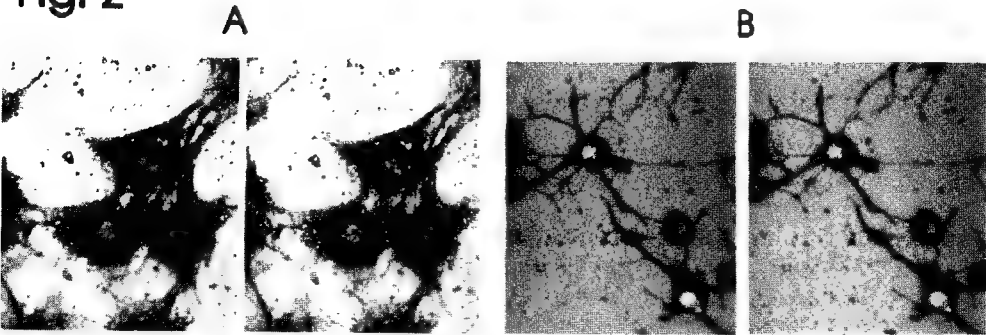
IMAGING IN 5 DIMENSIONS: QUANTITATIVE MEASUREMENT OF MEMBRANE POTENTIAL FROM SINGLE MITOCHONDRIA IN LIVING CELLS

Leslie M. Loew,[*] Richard A. Tuft,[**] Walter Carrington,[**] and Fredric S. Fay[**]

[*]Department of Physiology, University of Connecticut Health Center, Farmington, CT 06030
[**]Biomedical Imaging Group, University of Massachusetts Medical School, Worcester, MA

The energy released during the oxidation reactions in the mitochondrial respiratory chain is stored as an electrochemical potential consisting of a transmembrane electrical potential (V_{mit}) of about -180 mV and a proton gradient of about 1 pH unit; this drives the synthesis of the ATP required to fuel the cell's energy-dependent processes.[1] This key cellular system has been the subject of thousands of studies. However, data on how it is regulated by the physiological state of the cell has only been gathered via indirect studies on isolated mitochondrial suspensions; quantitative studies on individual mitochondria *in situ* have been precluded by their small size, their high motility, and the absence of appropriate methodologies.

An approach toward a more quantitative assessment of V_{mit} within intact cells was based on the development of the potentiometric fluorescent dyes TMRE and TMRM,[2] which rapidly equilibrate across membranes in accord with the Nernst equation. It was possible to follow changes V_{mit} with widefield video microscopy,[3] but the mitochondria are too small to permit accurate measurements. This is because both the relative fluorescence from the mitochondrion and an adjacent equivalent cytosolic volume must be accurately determined, but the thickness of the optically sampled volume dilutes the true emission emanating from a mitochondrion. Confocal microscopy has been used to provide better estimates.[3,4] But V_{mit} obtained in this way can only be considered a lower limit because even a confocal optical section may be significantly thicker than a given mitochondrion and is not necessarily accurately centered on it. A stratagem complementary to confocal microscopy involves computer algorithms which use the experimental point spread function of the microscope optics to deconvolve 3D widefield datasets.[5,6] This method, effectively, takes the out-of-focus fluorescence measured in the experimental data and restores it to its appropriate point of origin. Image restoration has been confined to studies where precise high resolution 3D structural information is required. In this paper, we show that it can also be used to obtain accurate fluorescent intensities from objects at or even below the resolution limit of the light microscope. By employing a fast 3D microscope to freeze mitochondrial motion (Figure 1), and mathematical modelling to calibrate intensities in restored 3D images, V_{mit} may be determined from individual motile mitochondria inside living cells (Figure 2).

1. Mitchell, P. *Nature* **1961**, *191*, 144-8.
2. Ehrenberg,B.; Montana, V.; Wei,M.; Wuskell,J.P.; Loew,L.M. *Biophys. J.* **1988**, *53*, 785-94.
3. Farkas,D.L.; Wei,M.; Febbroriello,P.; Carson,J.H.; Loew,L.M. *Biophys. J.* **1989**, *56*, 1053-69.
4. Loew,L.M. In "Methods in Cell Biology" v. 38; Matsumoto,B., Ed.; Academic Press, 1992.
5. Carrington,W.; Fogarty,K.E. In "Proceedings of the 13th annual Northeast Bioengineering Conference"; Foster,K., Ed.; IEEE:, 1987.
6. Agard,D.A. *Ann. Rev. Biophys. Bioeng.* **1984**, *13*, 191-219.

1
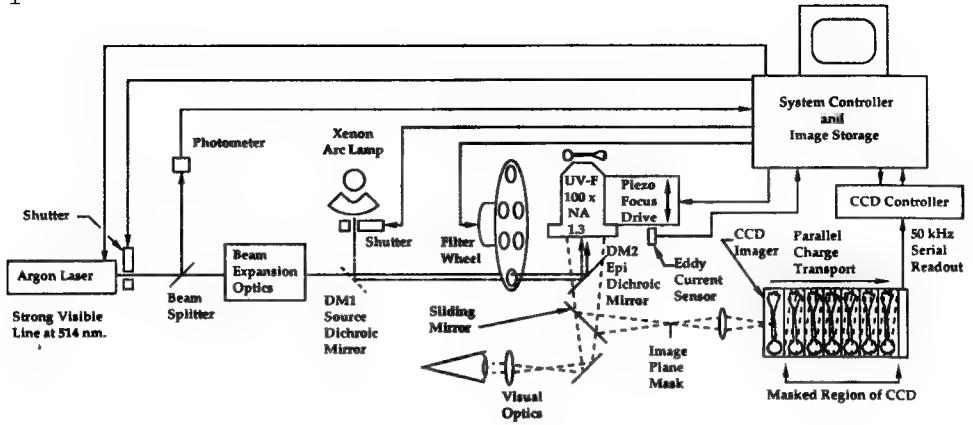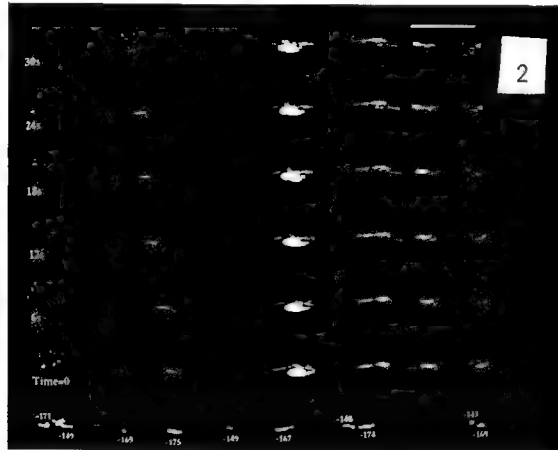
Fig. 1.-- Fast 3D imaging is based on a custom-built microscope incorporating a frame transfer cooled ccd imager, fast piezoelectric focus driver, and an argon ion laser for fluorescence excitation of TMRE. Intracellular calcium measurements may be made via a second excitation path set for the fluorescent calcium indicator fura-2.

Fig. 2.-- After image restoration and calibration, V_{mit} is determined within long neuronal processes via a modified form of the Nernst equation. The bottom strip shows V_{mit} assigned to individual mitochondria in the 3D image by this process. The 6 images above are projections onto a single plane of 3D images taken at 6 second intervals. Scale bar = 10 μm.

165

REAL-TIME CONFOCAL MICROSCOPY OF THE HUMAN *IN VIVO* CORNEA

Barry R. Masters,*   Andreas A. Thaer **

* Department of Anatomy and Cell Biology, Uniformed Services University of the Health Sciences, 4301 Jones Bridge Road, Bethesda, MD 20814
**In cooperation with Institute for Medical Vision Aid, and Helmut Hund GmBH, Bahnhofstrasse 12, 6330 Wetzlar, F.R.G.

A new confocal microscope has several unique features which differentiates it from other *in vivo* confocal imaging systems.is described.[1-5] • The light source is a halogen lamp. This source has many advantages over the mercury or xenon arc lamps used in other confocal designs. The mercury or xenon arc lamps have the problem of arc jitter which results in changing illumination intensity. Filters are inserted in the lamp housing to remove both short ultraviolet and infrared light. • The microscope uses standard microscope objectives which are readily interchangeable. Other *in vivo* confocal systems are limited to a built in objective which is not removable. In these studies we used a Leitz 50X, NA 1.0 water immersion objective.• The detection system consists of an intensitified video camera with video output to a Sony U-matic tape recorder. In parallel with the video recording there is a video monitor in order that the operator can observe in real-time the confocal images of the subject's eye. •Hard copy of individual video frames is obtained with either a video printer or by displaying single video frames on the monitor and photographing the screen with a 35 mm film camera.

The real-time *in vivo* confocal microscope is based on two sets of adjustable conjugate slits[6-8]. The slits are located in conjugate planes in front of the halogen source and in front of the detector. The advantages of slits over confocal microscope systems based on Nipkow disks containing pinholes are the following. Slits have the possibility of continually adjusting the depth of focus in the z-axis. In addition, a slit confocal system passes many-fold more light from the eye to the detector as compared to pinhole type confocal systems[1,4,5]. Another advantage of adjustable slits is that the scanned field of view and the light intensity incident on the field of view can be easily varied. Scanning of the image of the slit over the plane of the cornea is accomplished with the use of a rotating mirror two sided mirror.

The confocal microscope is mounted on a standard ophthalmic head rest. Immediately before the corneal examination, a drop of methylcellulose gel was applied to the tip of the microscope objective and the microscope was slowly positioned to make contact between the gel and the cornea. The tip of the microscope objective never touches or flattens the corneal surface; a layer of gel was always between the objective and the eye.The z-axis position of the confocal microscope was controlled by manual movement of the microscope stage with a joystick. Alternatively, computer controlled stepping motor scanned the focal plane of the confocal microscope across the full thickness of the cornea.

The following *in vivo* human corneal confocal microscopic images were made by photographing the still video frames on the monitor with a film camera. **These photographs are made from single video frames without image processing or frame averaging; they represent typical raw data.** Fig.1.shows the superficial cells of the epithelium.   Fig. 2. shows the wing cells just posterior to the ocular surface. Fig. 3 shows nerve fibers and keratocyte nuclei in the anterior stroma.Fig. 4. shows the basal epithelial cells and their distinct cell borders.

1. Lemp. M.A., Dilly, P.N., Boyde, A., (1986). Cornea 4, 205-209.
2. Koester, C.J., Roberts, C.W. (1990). in: **Noninvasive Diagnostic Techniques in Ophthalmology**, Barry R. Masters, Editor, Springer-Verlag, New York, 99-121.
3. Koester, C.J, Auran, J.D., Rosskothen, H.D., Trokel, S.L., Tackaberry, R.B. (1992) Invest. Ophthalmol Vis. Sci, 33, no. 4, suppl. p. 1233.
4 Jester, J. et al., (1992), Invest. Ophthalmol. Vis. Sci vol 33, no. 12, pp. 3255-3270.
5. Wegener, A.R., Gaida, G., Massig, J.H., Breipohl, (1992) . Invest. Ophthalmol Vis. Sci, 33, no. 4, suppl. p. 1234.
6. Masters, B.R., Thaer, A. (1993), Biophys. J. 64, no. 2, part 2, p. A108.
7. Masters, B.R., Thaer, A., (1993), International Conference on Confocal Microscopy & 3D Image Processing, Sydney, Australia.
8. Masters, B.R., Thaer, A., (1993) Ophthalmic and Visual Opttics, Technical Digest of the Optical Society of America, pp. 133-136.
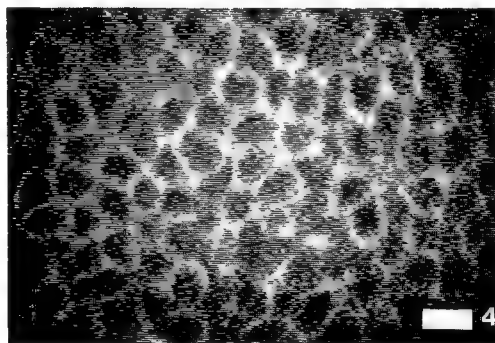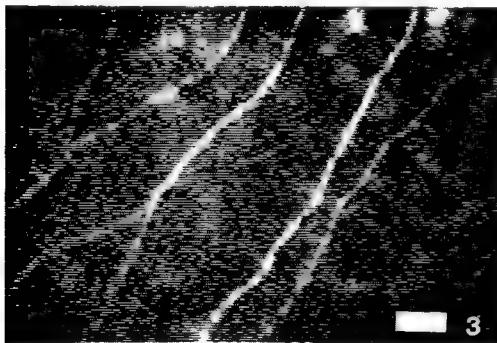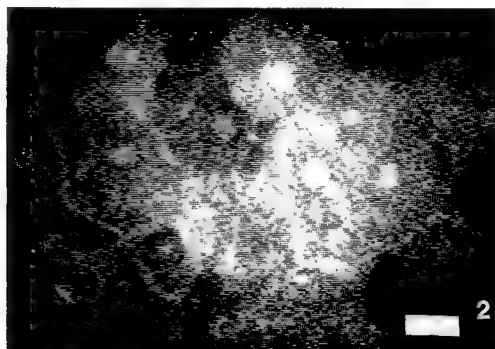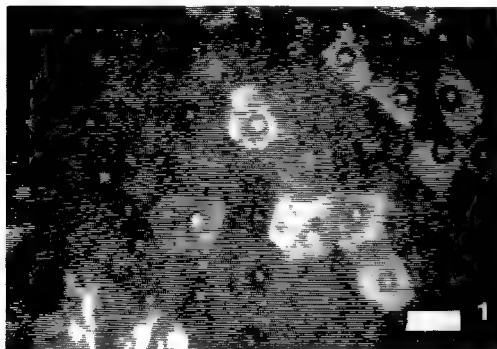
All figures are single video frames of live human cornea. No image processing or frame averaging was used. Scale bar 20 microns on alll figures.

Fig.1.shows the superficial cells of the epithelium.

Fig. 2. shows the wing cells just posterior to the ocular surface.

Fig. 3 shows nerve fibers and keratocyte nuclei in the anterior stroma.

Fig. 4. shows the basal epithelial cells and their distinct cell borders.

CONFOCAL STUDY OF MICROAGGREGATES IN 2.5 BILLION YEAR-OLD SEDIMENTS

G.Y. Fan, S. Mojzsis[†] and G. Arrhenius[†]

San Diego Microscopy and Imaging Resource and
[†]NASA Exobiology Center, Scripps Institution of Oceanography
University of California at San Diego, La Jolla, California 92093

Light microscopy conducted on samples of Archean sediments reveals microaggregates (Fig. 1) which are suggestive of a biotic origin. These aggregates, typically 15 μm wide and 50 μm long, are thought to be the mineral remains of colonies of microorganisms that lived 2.5 billion years ago.[1] Confocal microscopy is used to study the structures of these microaggregates in 3-D.

Samples under study are from the lowest section drill core taken from the Dales Gorge Member of the Brockman Iron-Formation (Hamersley Basin) in Western Australia.[2] These sediments are well preserved and escaped metamorphic conditions typically experienced by older rocks of this type. Two types of samples were prepared for study under the microscope: thin sections (~40 μm) for transmitted light microscopy to study the general rock texture and to locate the features of interest, and thick sections (3 mm) for confocal microscopy to determine the 3-D structure of the aggregates in their undisturbed state. The samples have been carefully polished so that they may be directly placed on the oil-immersion lens without the use of a cover slip. No chemical treatments of the surfaces have been performed. Fig. 1 shows the general nature of the sample as seen in transmitted light. Visible are the rod-shaped, brownish calcium-phosphate (apatite) aggregates, some of which are enlarged in the insert. Similar aggregates can be found in ocean sediments which are forming today. The apatites often form clusters, although isolated aggregates have also been found. The clusters tend to distribute along the microbands of the rocks. Electron microprobe analyses show that the interiors of the aggregates, besides calcium and phosphorus, contain no major elements heavier than sodium.

Confocal microscopy is carried out on a Zeiss Axiovert 35M microscope with a Bio-Rad MRC600 laser scanning attachment.[3] Optical sections are acquired in the reflected mode from the thick section in the corresponding locations determined by transmitted light microscopy on the thin section so that the searching time is minimized. The 3-D reconstruction of an area containing the calcium-phosphate aggregates is carried out on a Silicon Graphics computer using the Synu rendering software,[4] an example of which is shown in Fig. 2. An optical section series containing 15 sections, acquired with a x63 objective lens and an electronic zoom factor of 4.5, is used in the reconstruction. The z increment is 0.5 μm. Fig. 3 shows a stereopair reconstructed from the same section series, using the maximum intensity projection algorithm, with a shift of ±4 pixels/section. The bright background seen is an artifact of the rock polished surface, and the minute features within the aggregate are thought to be the remains of individual microorganisms. Further TEM studies are under way to investigate the composition of these micron- and submicron-sized inclusions.

References

1. S. Mojzsis, G.Y. Fan and G. Arrhenius, to be submitted to Nature (1993).
2. A.F. Trendall, in Iron-Formations: Facts and Problems, Eds. A.F. Trendall and R.C. Morris, Elsevier (1983) 69-129.
3. J.G. White and W.B. Amos, Nature328 (1987) 183.
4. D. Hessler et al, NEORIMAGE 1 (1992) 55.
5. Supported by NSF grant EAR 8916467, NASA grant NAGW 1031 and NIH grant RR04050.
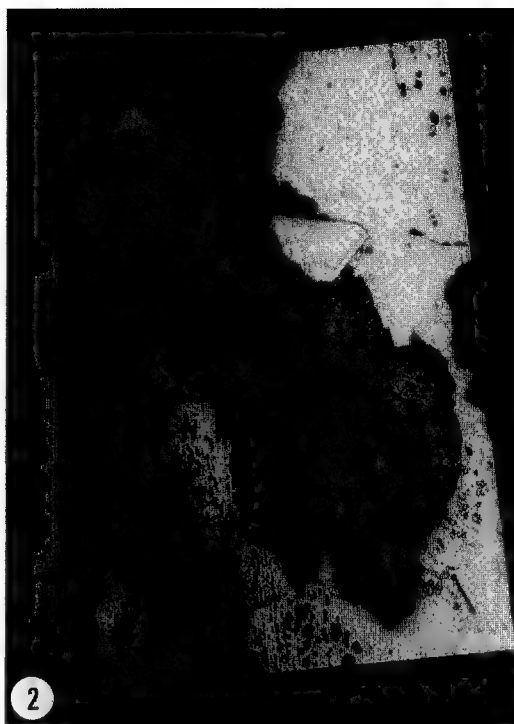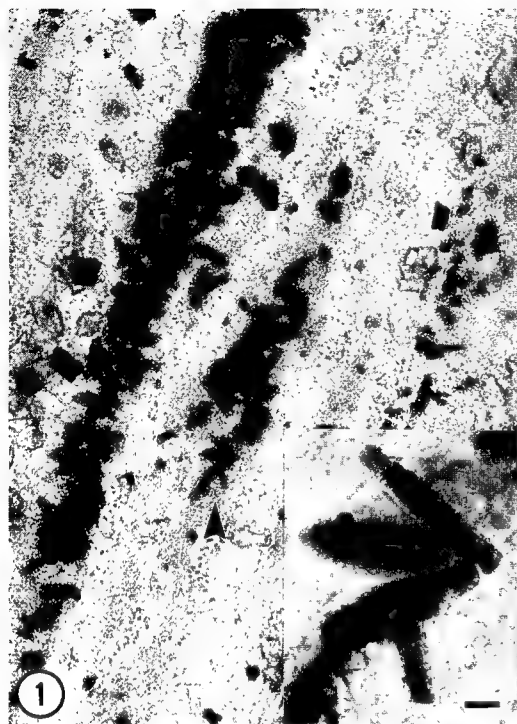
FIG. 1.--2.5 billion-year old Hamersley sediment, showing mciroaggregates of a possible biotic origin. Insert shows enlargement of the region pointed to by arrow. Bar = 10 µm.

FIG. 2.--3-D reconstruction of an isolated micrograin of calcium-phosphate aggregate. Inclusions are thought to consist of graphite or a less mature species of carbon compound, derived from the organic component left behind by the organisms.

FIG. 3.--Stereopair of the same aggregate shown in Fig. 2, created from an optical section series using the maximum intensity projection method.

MICROSTRUCTURE OF THE AVIAN EGGSHELL

S.Q. Xiao, M. Agarwal and A.H. Heuer
Department of Materials Science and Engineering, Case Western Reserve University
Cleveland, OH 44106

Fresh white and dry brown eggshells were studied by TEM and SEM. For TEM, thin sections of the eggshell were prepared by both ultramicrotomy and ion-beam thinning.

The various regions from the inner to the outer part of the eggshell can be summarized as follows : the shell membrane, the mammillary layer, the palisade layer and the cuticle. The shell membrane is about 80 μm thick and is composed of collagen fibers with a mantle and core structure. The mammillary layer is a mixture of calcite crystallites, organic matrix and collagen fibers; it starts at the outer shell membrane and merges gradually into the palisade layer. The collagen fibers present near the palisade are surrounded by tiny calcite crystals (Fig. 1). In this region, the periphery of fibers are calcified. The SEM study of the etched cross section [1] revealed clusters of fine organic sheets at the junction of the membrane and the palisade layer (Fig. 2). Further etching results in the collapse of these sheets, to form knob-like features on the surface of the membrane.

The palisade layer is about 250 μm thick and is mainly calcitic. Specimens prepared by ultramicrotomy revealed pseudo single crystals (PSC) of ~ 100-200 μm in size [2], within the palisade layer. Thin foils prepared by ion-beam thinning shows the presence of more perfect single crystals, about 100 μm in size. More detailed experiments are being performed to explore the relative advantages and disadvantages of the two techniques.

The cuticle can be divided into the inner and outer regions, ~4 μm and ~1 μm thick, respectively. The inner cuticle has a higher content of Ca and P, and is composed of small needle-like features of approximately 10nm X 100nm in size (Fig. 3). Selected area diffraction pattern (insert) of these needles revealed them to be crystalline hydroxyapatite.

References

1. M. Agarwal, S.Q. Xiao and A.H. Heuer, Proceedings volume for Symposium S of the Fall 1992 MRS meeting (In press).
2. S.Q. Xiao, S. Baden and A.H. Heuer, Proceedings of EMSA, 1102-1103 (1992).
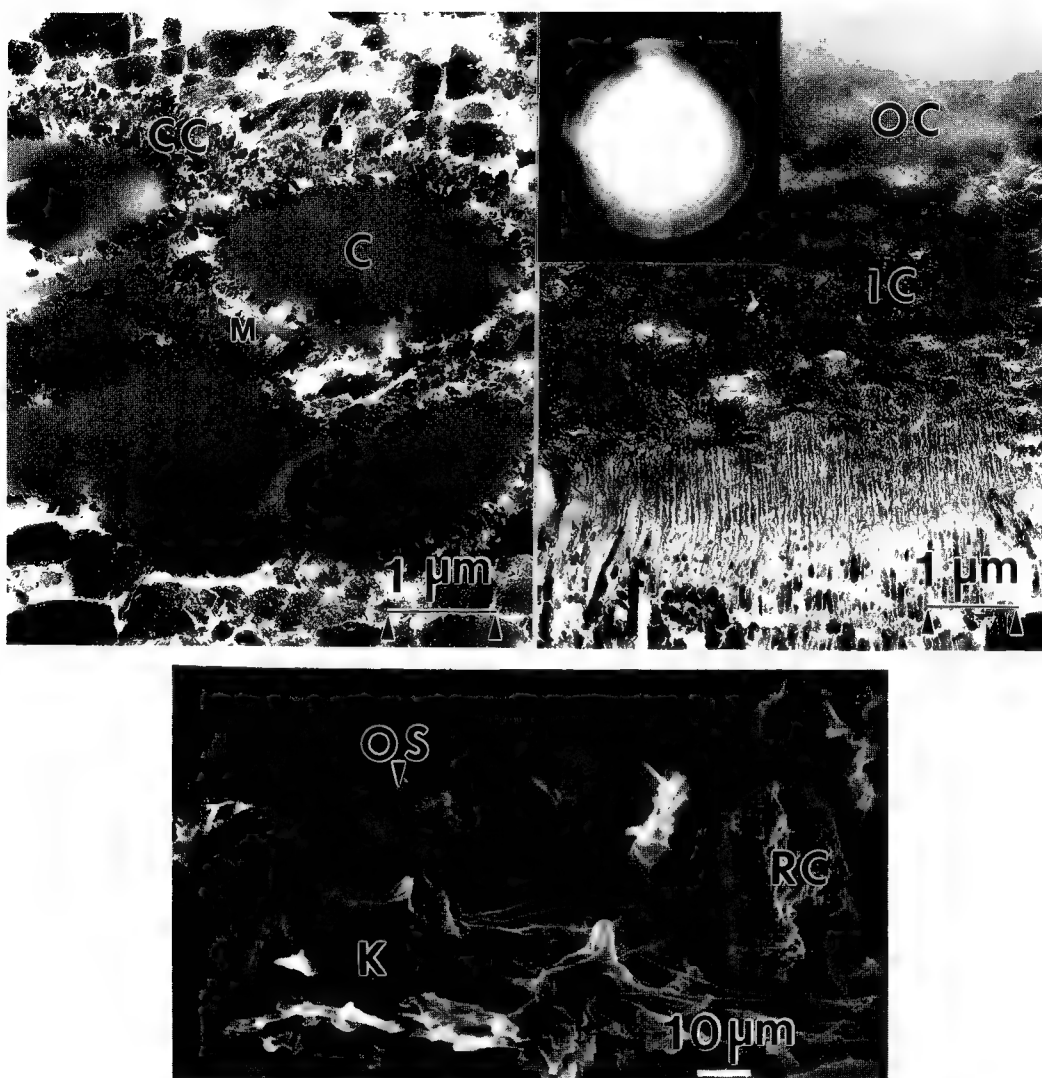
Figure 1: Bright field TEM micrograph of the mammillary region from a fresh white eggshell showing the collagen fibres . The core (C) and mantle (M) structure of the fibres, as well as tiny calcite crystals (CC) surrounding the fibres are indicated.

Figure 2: SEM micrograph of the mammillary region from an etched cross section of the eggshell. After etching, fine organic sheets (OS) and the knob-like (K) feature can be seen on the outer membrane. Residual calcite (RC) is also present.

Figure 3: Bright field TEM micrograph of the cuticle region of the eggshell. The outer cuticle (OC) and the inner cuticle (IC) containing needles of hydroxyapatite are indicated.

171

MORPHOGENETIC MACHINES REVEALED: MICROSCOPY OF LIVING CELLS IN THE EMBRYO OF THE FROG, XENOPUS LAEVIS

Ray Keller

Department of Molecular and Cell Biology, University of California, Berkeley, CA 94720

The amphibian embryo offers advantages of size, availability, and ease of use with both microsurgical and molecular methods in the analysis of fundamental developmental and cell biological problems.[1] However, conventional wisdom holds that the opacity of this embryo limits the use of methods in optical microscopy to resolve the cell motility underlying the major shape-generating processes in early development.

These difficulties have been circumvented by refining and adapting several methods. First, methods of explanting and culturing tissues were developed that expose the deep, nonepithelial cells, as well as the superficial epithelial cells, to the view of the microscope. Second, low angle epi-illumination with video image processing and recording was used to follow patterns of cell movement in large populations of cells. Lastly, cells were labeled with vital, fluorescent dyes, and their behavior recorded, using low-light, fluorescence microscopy and image processing. Using these methods, the details of the cellular protrusive activity that drives the powerful convergence (narrowing) and extension (lengthening) movements that shape the dorsal mesoderm and neural tissue of the vertebrate embryo were
resolved. [2,3,4]

The results have significance for understanding the behavioral and biomechanical aspects of how cell motility actually produces change in tissue shape. Moreover, the spatial and temporal patterns of cell motility suggest novel patterns in the underlying processes of cell-cell communication that organize cell behavior and tissue differentiation. By combining high resolution microscopy of cell behavior in explants with molecular methods of altering cell-cell signalling [5], and microsurgical methods of generating chimeric cell populations, we hope to resolve some of the molecular signals underlying the development of specific cell behaviors.

Although these methods are being applied to all major regional morphogenetic processes shaping the gastrula and neurula in amphibians, principally *Xenopus*, as well as in other vertebrates, the focus in this paper will be on the methods developed to resolve the cell motility underlying convergence and extension of the mesoderm and neural tissue of *Xenopus*.

Previous evidence suggested that the deep, non-epithelial cells were the cells generating the forces that produce convergence and extension, so the "open-faced" explant of the relevant dorsal axial tissues of the gastrula was developed, which exposes the deep cells to microscopy.[2] However, the exposed deep cells do not behave normally in most media, and a special saline, "Danilchik's solution", was developed, based on an analysis of blastocoel fluid.[6] The original solution and several modifications have been described elsewhere. [7] This solution allows deep cells to carry out movements judged by indirect methods to occur in vivo.[2] It is characterized by relatively low levels of chloride and high pH (8.3), both of which seem essential for the health and motility of deep cells.

The open-faced explant is pressed lightly against a #1.5 coverslip, glued across a hole in a culture dish, with another small coverslip fragment, supported on both ends by high vacuum grease or clay, thus restricting the cells to a planar configuration. For following gross movements of individual cells in large fields, containing hundreds of cells, the explant is illuminated at low angles (nearly perpendicular to the optical axis) with fiber optic lights, thus shadowing the boundaries of individual cells.[2] Tracing the movements of large numbers of cells shows that convergence and extension occurs in two phases.

To resolve the details of the protrusive activity underlying mediolateral cell intercalation, individual cells were labeled with fluorescein dextran amine (FDA) or with DiI, a lipid soluble fluorescent compound (Molecular Probes, Inc.)[7]. In the first case, whole embryos were injected with FDA at the one cell stage and the labeled progeny cells transfered in small groups or as individual cells to corresponding regions of unlabeled explants at gastrula stages. In the second case, a solution of 1 mg/ml DiI in ethanol was dried on to small fragments of coverslips or glass filaments, and the coverslips or filaments placed across the explant, allowing a number of cells to contact and pick up the dye. In 3-10 minutes the coverslip was removed. Low light fluorescence microscopy was done, using a Nikon Diaphot and a halogen lamp at low levels of illumination. Cells were exposed to illumination by an electronic shutter (Uniblitz, Inc.) only while recording images, which occurred at intervals of 30 sec to 2 min (time-lapse). Both the electronic shutter and the interval was controlled by an Image I, image processor (Universal Imaging, Inc). Image processing consisted of frame averaging (8-16 frames), sharpening, and background subtraction. Processed images were stored on an optical disc recorder. FDA labeling was appropriate for use with 10x (0.5) and 20x (0.75) fluorescence objectives for periods of 6-8 hours, at intervals of 1 min, without killing the cells. Although DiI labeling was less predictable in terms of exactly which cells were labeled, this method was less toxic to cells under high numerical aperture objectives, and allowed high resolution analysis of fine filiform and lamelliform protrusive activity using a 60x (1.4) fluorescence objective at shorter intervals for several hours.

Using these methods, it was shown that the mediolateral cell intercalation described above is brought about as the mesodermal cells confine nearly all their protrusive activity to their medial and lateral ends, thus becoming bipolar and elongated in the mediolateral direction (transversely). This bipolar protrusive activity is applied directly to the surfaces of adjacent cells and appears to pull the cells together along the mediolateral axis, thus producing mediolateral cell intercalation, which in turn, produces convergence and extension.

These methods are adaptable for use in studying the cell motility underlying other morphogenetic processes in early development of amphibians and other embryos as well.[8]

1. B. Kay and B. Peng, Methods in Cell Biology, San Diego: Academic Press (1991) 36.
2. J. Shih and R. Keller, Development (1992) 116, 901-914.
3. J. Shih and R. Keller, Development (1992) 116, 915-930.
4. R.Keller et al., Development (1992) Supplement, 81-91.
5. E. Amaya et al., Cell (1991) 66, 257-270.
6. J. I. Gillespie, J. Physiol. (1983) 344, 359-377.
7. R. Keller, Methods in Cell Biology, San Diego: Academic Press (1991) 36, 61-113.
8. This was supported by NIH grant HD25594 and NSF grant DCB89052

LASER SCANNING CONFOCAL MICROSCOPIC ANALYSIS OF
CYTOSKELETAL AND NUCLEAR REORGANIZATION IN LIVE DROSOPHILA
EMBRYOS

William Theurkauf

Department of Biochemistry and Cell Biology, SUNY at Stony Brook,
Sony Brook, NY   11794-5215

Cell division in eucaryotes depends on coordinated changes in
nuclear and cytoskeletal components.   In Drosophila melanogaster
embryos, the first 13 nuclear divisions occur without cytokinesis.
During the final four divisions, nuclei divide in a uniform monolayer
at the surface of the embryo. These surface divisions are
accompanied by dramatic changes in cortical actin and microtubule
structure (Karr and Alberts, 1986), and inhibitor studies indicate
that these changes are essential to orderly mitosis (Zalokar and Erk,
1976).   Because the early embryo is syncytial, fluorescent probes
introduced by microinjection are incorporated in structures
associated with all of the nuclei in the blastoderm.   In addition, the
nuclei divide synchronously every 10 to 20 min.   These
characteristics make the syncytial blastoderm embryo an excellent
system for the analysis of mitotic reorganization of both nuclear
and cytoskeletal elements.   However, the Drosophila embryo is a
large cell, and   resolution of cytoskeletal filaments and nuclear
structure is hampered by out-of focus signal.   This problem can be
overcome by computationally eliminating unwanted signal (Minden
and Sedat references).   We have found that live Drosophila embryos,
microinjected with fluorescently labeled protein, can also be
examined directly using a laser scanning confocal microscope.   We
have used this technique to examine reorganization of actin
filaments, microtubules, and nuclei in living embryos microinjected
with fluorescently-conjugated actin, tubulin, and histones. This
technique allows resolution of single microtubules and time-lapse
analysis of cell cycle changes in cytoskeletal dynamics.

The syncytial blastoderm stage of Drosophila embryogenesis is
genetically tractable, and mutations that specifically disrupt the
syncytial mitoses have been identified (Sullivan, Fogarty, and
Theurkauf, submitted).   Cytological analysis of these mutations
indicate that they include lesions in genes required for the assembly
of specific cytoskeletal elements.   One of these mutations, which

we have named *scrambled* , has been analyzed in detail. The scrambled mutation causes fusion of neighboring spindles during the surface divisions. These fusions lead to division errors and loss of nuclei from the surface monolayer. Microinjecting embryos with the actin-depolymerizing drug cytochalasin D phenocopies the spindle assembly defect observed in *scrambled* embryos. Cytochalasin treatment also leads to gross disorganization of the surface nuclear monolayer, while interphase nuclear distribution is relatively normal in scrambled mutant embryos. These observations indicate that the actin caps function in spacing interphase nuclei, and that the pseudocleavage furrows prevent spindle fusions at mitosis.

The product of the scrambled gene appears to play a central role in actin reorganization at mitosis. Molecular characterization of this gene should therefore provided important insights into cell cycle regulation of the cytoskeleton. The scrambled mutation was induced by the insertion of a single transposable P element. Genomic sequences flanking the P element have been isolated and used to clone candidate cDNAs. We are currently characterizing these cDNAs.

References:

Sullivan, W., Fogarty, P. and Theurkauf, W. Mutations affecting the cytoskeletal organization of syncytial Drosophila embryos. Submitted.

Karr, T., and Alberts, B. (1986). Organization of the cytoskeleton in early Drosophila embryos. J. Cell Biol. 102, 1494-1509.

Kellogg, D., Mitchison, T., and Alberts, B. (1988). Behavior of microtubules and actin filaments in living Drosophila embryos. Development 103, 675-686.

Minden, J., Agard, D., Sedat, J. and Alberts, B. (1989). Direct lineage analysis in Drosophila melanogaster by time lapse three dimensional microscopy of living embryos. J. Cell Biol. 109, 505-516.

Zalokar, M., and Erk, I. (1976). Division and migration of nuclei during early embryogenesis of Drosophila melanogaster. J. Microbio. Cell. 25, 97-106.

CONFOCAL MICROSCOPY OF CYTOSKELETAL ORGANIZATION IN AMPHIBIAN OOCYTES AND EGGS

David L. Gard, Amy D. Roeder, and Marianne M. Schroeder

Department of Biology, University of Utah, Salt Lake City, Utah 84112

Amphibian oocytes, eggs, and early embryos have been increasingly used as models for studying the regulation of microtubule assembly, the regulation and mechanics of spindle assembly, and the generation of cellular and embryonic axes. However, little information has been available regarding the organization of cytoskeletal elements in vivo during oogenesis. In large part, this results from the unique challenges posed by immunofluorescence microscopy of these large cells (up to 2 mm in diameter). Preservation and staining of labile cytoskeletal elements is often difficult in large cells, due to the limited penetration of fixative and antibodies or other dyes. In addition, the accumulation of yolk during oogenesis renders larger oocytes, eggs, and early embryos opaque. Finally, cell size also often limits the magnification and resolution possible, since the details of cytoskeletal organization in large oocytes and eggs often are obscured by fluorescence from outside of the focal plane when objectives with high numerical aperture are used. Our interest in the role of microtubules and actin filaments in establishment of the animal-vegetal axis of amphibian (*Xenopus laevis* and *Rana pipiens*) oocytes led us to evaluate different methods of sample preparation, resulting in fixation and staining protocols which adequately preserve microtubule and actin organization in amphibian oocytes. We have successfully used these techniques, in conjunction with laser-scanning confocal microscopy, to examine the distribution of microtubules and actin filaments throughout oogenesis and early embryogenesis in *Xenopus laevis*.[1-4]

Confocal immunofluorescence microscopy revealed that stage I *Xenopus* oocytes contain elaborate cytoskeletal networks composed of microtubules and actin filaments. Microtubules were observed in the perinuclear and cortical cytoplasm (Fig. 1), and were associated with the mitochondrial mass of diplotene oocytes (Fig. 2). No evidence for localized microtubule organizing centers was observed, indicating that the maternally-derived centrosome is inactivated early in oogenesis, prior to establishment of the A-V axis. Staining with rhodamine-conjugated phalloidin revealed that diplotene oocytes (> 35 μm in diameter) contained dense networks of actin cables linking the germinal vesical (GV: the oocyte nucleus), mitochondrial mass (Fig. 3), and cortical actin band. In addition, the GV of oocytes greater than 35 μm diameter was brightly stained with rhodamine-phalloidin (Fig. 4). The GV of Rana oocytes also stained with rhodamine-phalloidin, suggesting that f-actin may play an important role in nuclear organization during amphibian oogenesis.

The A-V axis of *Xenopus* oocytes first becomes apparent during stage IV of oogenesis. Polarization of the cytoplasmic microtubule network coincides with axis formation. By stage VI, the animal hemisphere of *Xenopus* oocytes contains a dense array of microtubules and microtubule bundles radiating from the GV and extending to the animal cortex. Microtubules in the vegetal hemisphere appear less ordered. Cytoplasmic cables of actin filaments surrounded the GV of stage VI *Xenopus* oocytes, extending into the animal and vegetal cytoplasm.

Finally, confocal immunofluorescence microscopy and time-lapse microscopy of living oocytes microinjected with fluorescein-conjugated tubulin revealed a complex pathway of meiotic spindle assembly during maturation of *Xenopus* oocytes.[6]

References

1. *D.L. Gard, Dev. Biol 143(1991)346.*
2. *D.L. Gard, Dev. Biol 151(1992)516.*
3. *M.M. Schroeder and D.L. Gard, Development 114(1992)699.*
4. *A.D. Roeder and D.L. Gard, (manuscript in preparation).*
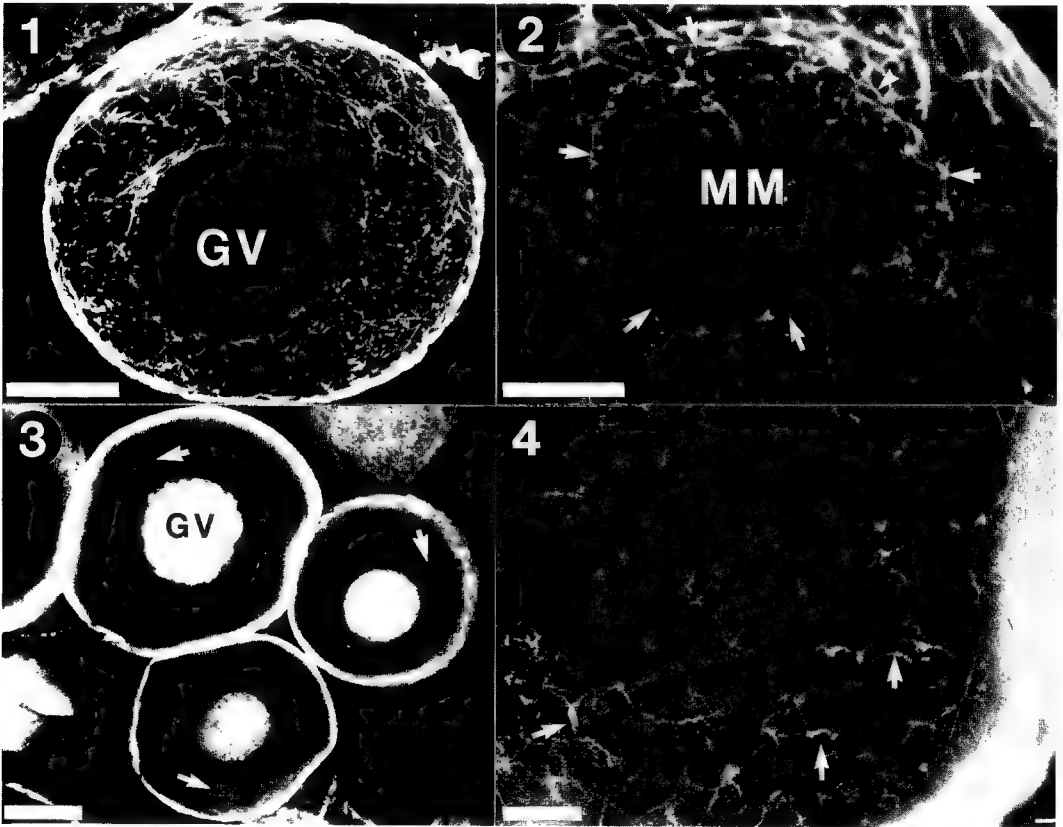
FIG. 1- Optical section of stage I Xenopus oocyte stained with anti-tubulin. Note germinal vesicle (GV). Bar = 25 μm.
FIG. 2- Mitochondrial mass (MM) in stage I oocyte stained with anti-tubulin. Note microtubules (arrows) surrounding and penetrating mass. Bar = 10 μm.
FIG. 3- Optical section of stage I oocytes stained with rhodamine-conjugated phalloidin. Note prominent staining of GV (GV) and mitochondrial mass (arrows). Bar = 100 μm.
FIG. 4- Mitochondrial mass in stage I oocyte stained with rhodamine-phalloidin. Note network of f-actin cables (arrows). Bar = 10 μm.

CORRELATIVE LIGHT AND ELECTRON MICROSCOPY: COUNTING CENTRIOLES IN INDIVIDUAL SEA URCHIN ZYGOTES PREVIOUSLY FOLLOWED *IN VIVO*

Greenfield Sluder and Frederick J. Miller

Worcester Foundation for Experimental Biology, Shrewsbury, MA 01545

Centrosomes are the ensembles of structures that define the poles of the mitotic apparatus. In animal cells, a centrosome typically consists of a pair of orthogonally arranged centrioles associated with osmiophilic pericentriolar material which nucleates the microtubules of the aster and central spindle. The precise doubling, or reproduction, of the centrosome during interphase is an important event in the cell's preparations for mitosis.

To characterize the mechanisms that control centrosome reproduction we need to follow the behavior of centrosomes within individual cells over several cell cycles. We use sea urchin zygotes as an experimental system because they have a rapid cell cycle, are large enough (100 um diameter) to easily manipulate, and are optically clear. However, the experiments pose two challenges. The first is to follow the behavior of centrosomes within individual zygotes for several hours with the light microscope and then recover just those individuals from a large population for ultrastructural analysis. The second is to precisely determine the number of centrioles in all centrosomes of each recovered zygote. Conventional thin section methodology would require at least 1000 serial sections, of which only a small percentage would contain centrioles. Compounding this difficulty is the extremely small size of a centriole relative to the zygote (the centriole to zygote volume ratio is approximately $1:1 \times 10^6$). Despite these technical difficulties, the power of our approach is that the history of each centrosome examined at the ultrastructural level is known and our prior characterization of the experimental system allows us to predict how each centrosome would have behaved had the zygote not been fixed.

Centrioles and the Reproductive Capacity of Centrosomes: For a normal mitosis the cell can have only two centrosomes at the onset of mitosis. Functional analysis of centrosome reproduction indicates that there is a counting mechanism within each centrosome that limits the number of daughter centrosomes that can arise from the parent. To determine the basis for this we examined the relationship between the reproductive capacity of centrosomes *in vivo* and the number of centrioles they contain.[1,2] Experimentally manipulated zygotes are loosely adhered to coverslips with protamine sulfate and mounted over fluorocarbon oil for *in vivo* observations. At the time of fixation, individual zygotes are circled on the coverslip with a diamond scribe just before the coverslip is removed from the preparation and immersed in fixative. After dehydration and embedding on the coverslip, the zygote(s) previously followed *in vivo* are relocated and excised for serial semi-thick (0.25 um) sectioning as described by Rieder et al..[3] An important feature of their method is that the ribbons of serial sections are mounted on formvar coated slot grids and screened with the phase contrast microscope to identify those sections that have clear areas formed by astral arrays of microtubules around each centrosome. By examining only those sections with asters one need not examine all 250-300 serial sections of each zygote to find all centrosomes. Finding the relatively small centrioles is facilitated by examining at higher magnification only the astral regions within each section.

This work shows that the ability of a centrosome to reproduce is correlated with the number of centrioles it contains. Centrosomes with two centrioles reproduce in a normal fashion while those with only one centriole do not reproduce until the centriole has doubled.

Centrosomes that have no centrioles do not double between mitoses. We conclude that the molecules that control centrosome reproduction are spatially and mechanically associated with centrioles for cells that have these organelles.

Role of Nuclear Activities in the Control of Centrosome Reproduction: Cells precisely coordinate centrosomal and nuclear events during the cell cycle. To investigate the role of nuclear activities in controlling the reproduction of centrosomes, individual zygotes were enucleated with a micropipette leaving one centrosome in the cell. We then characterized the behavior and ultrastructure of this centrosome in individual zygotes.[4] Zygotes are held in a microinjection chamber filled with sea water for *in vivo* observations. At the time of fixation, the individual zygote followed *in vivo* is pulled out of the holding portion of the chamber with the micropipette and allowed to sink to the bottom of the preparation. The zygote of interest is recognized from the population of the zygotes at the bottom of the preparation by a refractile oil droplet injected at the time of enucleation. This zygote is then transferred with a mouth controlled pipette to a 1.5 ml Eppendorf style test tube with 3 mm of the tip cut off and a piece of 53 um mesh nylon screen fused over the opening that is suspended in a 5 ml test tube filled with fixative. Dehydration and embedding is readily accomplished by lifting the Eppendorf tube from one 5 ml tube and placing it gently into another containing the next solution. Later, the plastic tube is cut away and the zygote is located with a dissecting microscope for excision, remounting, and serial semi-thick sectioning.

The results of this study show that asters repeatedly double in enucleated zygotes. Ultrastructural analysis shows that centrioles also reproduce in a normal fashion in proper coordination with the doubling of the centrosome as a whole. Thus, nuclear activities, such as DNA synthesis, transcription, or putative nuclear signals, do not control the reproduction of centrosomes in cells that do not need to grow before division.[5]

1. G. Sluder, and C.L. Rieder. J. Cell Biol. 100(1985):887.
2. G. Sluder et al. Cell Motil. Cytoskel. 13(1989):264.
3. C.L. Rieder et al. J. Elect. Microsc. Tech. 2(1985):11.
4. G. Sluder et al. J. Cell Biol. 103(1986):1873.

MEIOTIC SPINDLE ASSEMBLY IN CYTOPLASMIC EXTRACTS OF *SPISULA SOLIDISSIMA* OOCYTES

Robert E. Palazzo*#, Eugeni Vaisberg#, Richard W. Cole^, and Conly L. Rieder^#

*Department of Physiology and Cell Biology, University of Kansas, Lawrence, KS. 66045; ^The Wadsworth Center for Laboratories and Research, Albany, NY 12201-0509; #Department of Molecular Cell and Developmental Biology, University of Colorado, Boulder, CO 80309-0347; and #The Marine Biological Laboratory, Woods Hole, MA 02543

Critical for karyokinesis in animal cells, is the assembly of a spindle-chromosome-aster complex which serves as the force-generation system for chromosome segregation. *Spisula solidissima* oocytes offer a unique system for the study of spindle assembly since they can be obtained in large quantities, are naturally synchronized in the cell cycle and can be induced to assemble meiotic spindles within 15 min after parthenogenetic activation[1]. Oocytes contain a large nucleus [germinal vesicle (GV)] and are arrested at the G2/M border of meiosis I. No centrosomes or asters have been observed in oocytes at this stage by either electron microscopy or fluorescence microscopy using anti-tubulin antibodies. Observation of live oocytes with polarized light microscopy revealed that within 4-6 min after parthenogenetic activation, asters appeared and invaded the GV as it breaks down (GVBD). 15 min after activation a complete bipolar meiotic spindle was observed.

As a first step towards the development of an *in vitro* biochemical reconstitution system for the study of spindle assembly, concentrated lysates were prepared at various times following parthenogenetic activation and analyzed by phase-contrast microscopy. Lysates prepared from unactivated oocytes (U-lysates) contained GV's which remained intact. In contrast, lysates prepared 4 min after activation (A-lysates) contained GV's which underwent GVBD within 2-4 min after warming to room temperature. Lysates warmed to room temperature for 15 min were analyzed by immunofluorescence microscopy using anti-tubulin antibodies. U-lysates displayed a complex meshwork of polymerized microtubules. In contrast, A-lysates contained no such meshwork but displayed prominent asters. In attempts to induce GVBD and aster formation, fresh A-lysates were repeatedly centrifuged to remove particulate materials. Analysis by polarized light and immunofluorescence microscopy revealed that these high-speed A-lysates (HSA-lysates) were depleted of asters, microtubules, GV's and chromosomes. HSA-lysates were added to U-lysates, incubated for 15 min and prepared for double fluorescence analysis using a DNA specific dye (Hoechst 33342) and anti-tubulin antibodies. Analysis revealed that the characteristic microtubule meshwork of U-lysates had not formed, GV's disappeared, and asters assembled and captured chromosomes to form monopolar, bipolar and multipolar spindle-like complexes. Spindles isolated from living cells 15 min after activation were compared to bipolar spindles assembled *in vitro* by polarized light and video microscopy. Although less birefringent, spindles assembled *in vitro* exhibited a striking similarity to those assembled in living cells.

As a final analysis, the centriole content of asters assembled *in vitro* was compared to asters assembled in living cells by High Voltage Electron Microscopy (HVEM) of serial thick sections.

Analysis of asters isolated from living cells following parthenogenetic activation revealed that 4 min asters contained a single centriole[2]. Asters isolated from oocytes 15 min after activation contained two centrioles per aster. HSA-lysate was added to U-Lysates *in vitro* and incubated at room temperature to induce aster formation. Asters were isolated at 4 and 15 min during incubation. HVEM analysis revealed that 4 min asters contained a single centriole, while 15 min asters contained two centrioles per aster[3]. We conclude that centrioles assembled in this cell-free system reflecting high fidelity to the events occuring in living oocytes. Further, *in vitro*, centrioles assembled in a sequential manner, first one and then a second, reflecting one phase of the centriole replication process which we call the centriole duplication phase.

In summary, we have taken advantage of the unique properties of the *Spisula solidissima* oocyte model system, coupled with the swift assays offered by light, fluorescent and video-microscopy, to develop an inducible *in vitro* system which carries out the all the major strucutural events leading to spindle assembly. Importantly, high resolution structural analysis by HVEM demonstrated that this system is capable of assembling and duplicating centrioles outside the confines of the living cell.

References

1. R.D. Allen, Biol. Bull. (1953)105, 213.
2. R.E. Palazzo, J.B. Brawley, and L.I. Rebhun, Zool. Sci. (Japan) (1988)5, 603.
3. R.E. Palazzo, E. Vaisberg, R.W. Cole, C.L. Rieder, Science (1992)256, 219.

THREE-DIMENSIONAL RECONSTRUCTION OF THE SYNAPTONEMAL COMPLEX FROM PACHYTENE MAIZE MEIOCYTES USING EM TOMOGRAPHY

Jennifer C. Fung*, Bethe A. Scalettar**, David A. Agard**, and John W. Sedat**

* Graduate Program in Biophysics, University of California, San Francisco, CA 94143
**Howard Hughes Medical Institute, Department of Biochemistry and Biophysics, University of California, San Francisco, CA 94143-0448

The synaptonemal complex (SC) is a structure involved in the synapsis of homologous chromosomes during the prophase I stage of meiosis. Although the exact function of the complex is unknown, it has been suggested that one possible role might be to promote recombination by ensuring close synapsis of the homologous chromosomes. In addition, it is thought that the SC may also be required to convert the resulting recombination events into functional chiasmata to provide for proper chromosome segregation at the end of the first stage of meiosis.

The SC structure itself is highly conserved across a variety of species[1]. The organization of the SC is tripartite consisting of lateral, central and transverse elements. Two-dimensional cytological observations have been made to characterize the general features of these SC components[2]. The lateral elements are 300 - 500 Å wide proteinaceous structures which flank the synapsed regions of the chromosome bivalent. Between the two lateral elements is a central region containing the central element commonly characterized as a less dense amorphous structure. Running perpendicular to both the lateral and central elements in the central region are the transverse elements. Each transverse element is generally considered to be a single structure directly spanning the distance between the two lateral elements. Recently, genetic analysis of meiosis in yeast has identified a putative structural component of the transverse element[3]. As more studies continue to uncover more of the proteins involved in the SC formation, a higher resolution analysis of the SC structure will be required in order to accomodate this type of information into the overall architecture of the SC.

Intermediate voltage electron tomographic microscopy is one such method which will allow a more detailed determination of the three-dimensional structure of the SC. For our studies, we are using meiocytes isolated from anthers from the W23 stock of maize *Zea mays L*. The meiocytes are prepared under conditions which preserve not only the synaptonemal complex but also the surrounding chromatin. The fixed meiocyte preparations are embedded in Epon from which 0.3 um semi-thick sections containing the 0.1 um wide SC are cut. Sections are later stained with uranyl acetate and lead citrate to provide greater contrast. A tomographic data set is collected by obtaining a stack of images from a series of tilts over an angular range of +/-75 degrees incrementing every 1.25º at 300 kV using a Phillips 430. All images were recorded directly using a cooled slow scan CCD with 2x2 binning resulting in a 27.7 Å/pixel resolution for each 480 pixel-squared image. All data sets were collected using an automated data collection scheme to minimize overall electron dose and specimen shrinkage[4]. Alignment of the images used 15 nm gold beads as fiducial markers. After mass-normalization (conversion of intensity to mass density), images were reconstructed using a resolution weighted back projection scheme.

The results from our initial reconstructions show that the synaptonemal complex is a more complicated structure than has been previously observed. Fig 1. is a two-dimensional slice from the center of the three-dimensional reconstruction of a maize meiocyte synaptonemal complex. All components of the tripartite structure are displayed in this slice: lateral elements (filled arrows), central element (open arrow) and transverse elements (arrow head). The most striking feature of this reconstruction is the additional substructure seen in both the central and transverse elements. It can now be clearly seen that the central element consists of at least two distinct fibrous subdomains 80 and 220 Å in width. Both fibrous elements run longitudinally down the central element with the 220 Å subdomain making up the

bulk of the architecture. Furthermore, the components of the transverse elements can now also be examined in more structural detail. One observation that can be obtained from this higher resolution study is that the transverse elements connect solely from the lateral to the central element rather than the previously assumed direct connection between the two lateral elements. In addition, each transverse element seems to consist of more than one fibrous structure exhibiting a twisted rather than straight path to the central element.

References

1. von Wettstein D. et al., Annu. Rev. Genet. 18 (1984) 331
2. Westergaard M. et al., Ann. Rev. Genet. 6 (1972) 71
3. Sym M. et al., Cell 72 (1993) 365
4. Koster A.J. et al., EMSA Bulletin 23 (1993) in press

Fig. 1. A single slice from a three-dimensional reconstruction of a synaptonemal complex from isolated maize meiocytes. The synaptonemal complex is flanked by the synapsed homologous chromosomes.

THREE-DIMENSIONAL RECONSTRUCTION OF THE GOLGI COMPLEX AND TRANS-GOLGI NETWORK: A HVEM TOMOGRAPHIC STUDY

Mark S. Ladinsky,[*] James R. Kremer, Paul S. Furcinitti, J. Richard McIntosh, and Kathryn E. Howell[*]

[*] Department of Cellular and Structural Biology, University of Colorado Health Sciences Center, Denver, Colorado 80262
Department of Molecular, Cellular and Developmental Biology, Boulder Laboratory for Three-Dimensional Fine Structure, University of Colorado, Boulder, CO 80309

The Golgi complex is the central organelle in the secretory pathway of eukaryotic cells. It is composed of multiple cisternae that contain various enzymes involved in posttranslational modification of newly synthesized proteins. The cisternae are connected to a reticular lattice, the trans-Golgi Network (TGN), which is responsible for sorting and targeting proteins and lipids to other cellular locations. Transport between the Golgi cisternae is thought to occur largely via carrier vesicles, but recent studies suggest that some transport may be via tubules which link the cisternae and TGN. Although the Golgi complex has been well characterized biochemically, only a few studies have addressed its 3-D fine structure.[1]

Specific staining, high voltage electron microscopy (HVEM), and computer axial tomography were used to visualize the structure of the Golgi cisternae and the TGN in 3-D. A technique developed by R. E. Pagano was used to facilitate the visualization of the TGN and trans-most cisternae: Normal rat kidney (NRK) cells are treated with a fluorescent analog of ceramide (BODIPY-cer) which is internalized and metabolized in the Golgi complex (Fig. 1a).[2] Cells are fixed at times when the probe is localized in the TGN. The cells are then placed in a solution of diaminobenzidine (DAB) and irradiated with an argon-ion laser (λ=488 nm, 5 mW/mm^2) to excite the BODIPY fluorophore, resulting in the formation of an electron dense DAB reaction product in the TGN and trans-most Golgi cisternae (Fig. 1b). The "photoconverted" cells are then postfixed and processed for electron microscopy (Fig. 1c). Semi-thick sections (250 nm) were cut and transferred to formvar coated 1 mm slot grids and poststained with 2% uranyl acetate and Reynold's lead citrate. Colloidal gold particles (15 nm) were added to one or both surfaces of the grid to serve as fiducial points for image alignment. Grids were carbon-coated prior to viewing.

For each data set, a single 250 nm section was imaged near focus at a magnification of 18,300X by a JEOL-1000 operating at 1 MV with a 30 μm objective aperture. The nominal dose was 35 e/A^2 for each tilt in a ±60° tilt series with 2.0° tilt increments. The dose was minimized by focusing each tilted view away from the specimen along the tilt axis and recording images on Kodak SO-163 (high-speed) film. Negatives were digitized with 3.8 nm square pixels (Fig. 2). Transmitted light intensity was converted to optical density as previously described.[3] A computer program was used to align the tilt series based on a model of the positions of the fiducial markers in each tilt view and the known tilt angles. A tomographic reconstruction was calculated using the aligned tilt series and the R-weighted back-projection algorithm.[4] Slices of the reconstructed volume can be cut and visualized either parallel or perpendicular to the tilt axis (Fig 3). The resolution of the reconstruction was 13 nm.

Our initial results indicate that the Golgi complex is highly convoluted, with the

whole complex sometimes reversing polarity within a short distance. In addition, the TGN appears as extended tubules connected to the trans cisternae. Future studies will include analysis of high-resolution data obtained by improved specimen prepartion via cryo-fixation or progressive lowering of temperature after fixation.[5]

References

1. A. Rambourg and Y. Clermont, *Eur. J. Cell Biol.* 51 (1990) 189.
2. R. E. Pagano et al., *J. Cell Biol.* 113 (1991) 1267.
3. G. Devaud et al., *Biophys. J.* 63 (1992) 630.
4. C. J. Wilson et al., *Neuroimage* 1 (1992) 11.
5. This research was supported by NIH Biotechnology Resources grant RR00592 to the Boulder Laboratory for 3-D Fine Structure and NIH grant GM42629 to K. E. Howell.
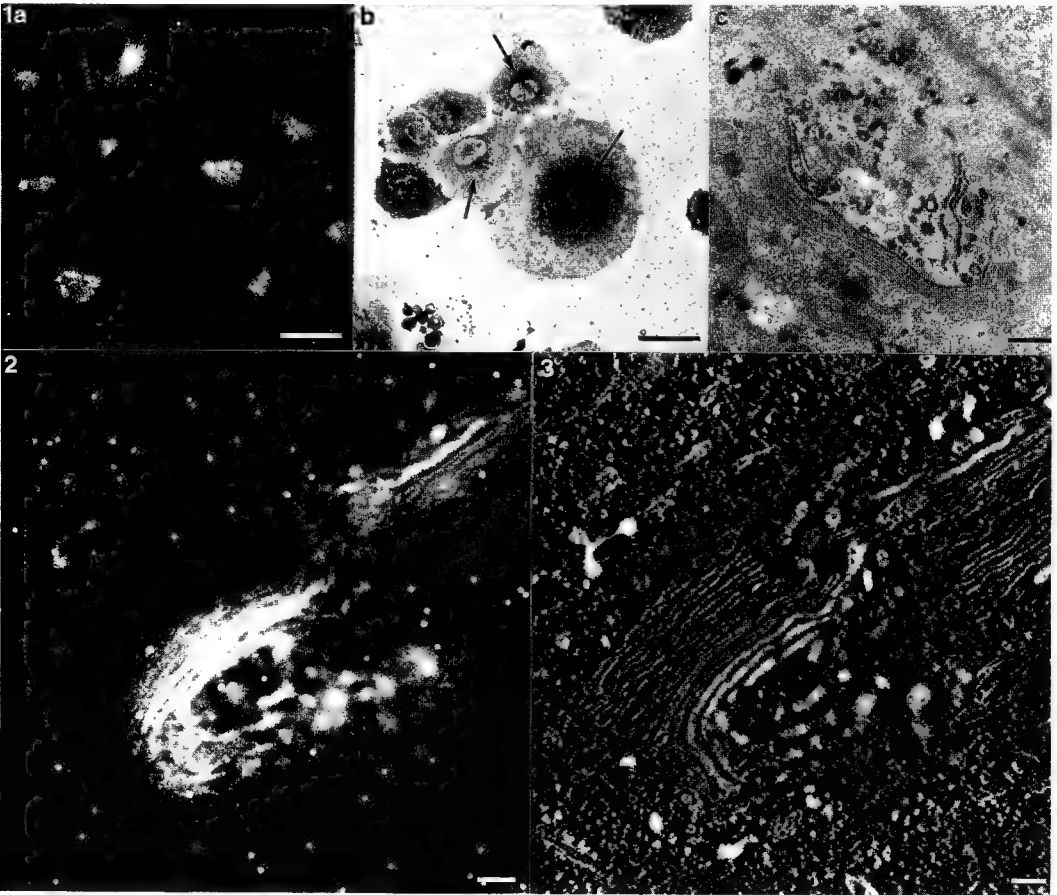
FIG. 1.-- Photoconversion of internalized BODIPY-cer: a) Fluorescence Light Microscopy in live NRK cells. Bar = 100 μm. b) Phase contrast image of cells after photoconversion. Bar = 100 μm. c) TEM of thin section (40 nm) showing specificity of labelling in a photoconverted Golgi complex. Bar = 200 nm.
FIG. 2.-- HVEM of 0° tilt view of Golgi complex. Bar = 100 nm.
FIG. 3.-- Slice (4 nm) of reconstruction perpendicular to axis of the electron beam. TGN and unstained cisternae are clearly visible. Bar = 100 nm.

DEEP NEGATIVE STAINING OF CELL WHOLE MOUNTS
FOR HIGH VOLTAGE ELECTRON MICROSCOPY

Marek Malecki and Hans Ris

Integrated Microscopy Resource, National Institutes of Health Biotechnology Resource, Molecular Biology Laboratories and Department of Zoology, University of Wisconsin, Madison, Wisconsin, U.S.A.

High voltage electron microscopy (HVEM) offers greatly enhanced beam penetration, reduced radiation damage, and increased resolution over conventional transmission electron microscopy (CTEM). Thus, HVEM is specially suitable for spatial organization studies on cell whole mounts [7,1,2] rather than CTEM of cell freeze fracture replicas[3] (Fig.2) or extracted cell thin negative stainings[8,4] (Fig.3). These studies are particularly interesting, if the observations of a living cell can be correlated with the HVEM images of the same cell after either chemical fixation [9,5] or rapid freezing [6]. We present here a novel and simple procedure to study threedimensional organization of cell whole mounts with the aid of HVEM.

Human neuroblastoma cells were grown on polystyrene films [5]. These cells were gently extracted and fixed. Then, after brief washing, they were infiltrated with the staining and embedding mixture: 3% polyvinylpyrrolidone - as an embedment and 3% ammonium molybdate - as a negative stain (Fig.4). Finally, samples were air dried. Whole mounts were observed in our AEI Mark II 7 HVEM equipped with a rotating-tilting stage and operating at 1MeV.

In the HVEM-stereopair (Fig.5), we can appreciate threedimensional organization of actin cytoarchitecture. Two types of filamentous actin organization are recognized: networks and bundles. The individual filaments can be traced over long distances. Intersecting filaments do not create any fusions, but their interrelationships can be spatially analysed. These filaments are uniform in thickness (6nm) and actin monomers can be recognized over the entire filament length.

The procedure presented here offers important advantages for studies on the cell whole mounts. This procedure is fast and simple, allowing us to evaluate samples within minutes; thus results can be quickly applied to ongoing experiments. The samples are maintained in aqeous media during all procedures, while deleterious effects of organic solvents are avoided. Threedimensional organization is preserved due to embedding simultaneous with air drying. This procedure, when compared to freeze drying, does not require expensive cryo-equipment; also, it does not expose samples to possible freezing artifacts. Finally, embedment and staining make samples easy to prepare and resistant to storage and shipment; therefore the procedure is suitable to pursue collaborations between: biochemical and cell biology laboratories nation-wide and our facility as a National Resource.

LEGENDS. Fig. 1- diagram of a living cell. Fig.2-4 - diagrams of specimen preparations. Fig. 5 - the HVEM stereo-micrograph of actin filamentous architecture prepared by deep negative staining, bar 100nm.
REFERENCES. 1.Bridgman PC & Reese TS 1984, J.Cell Biol.99:1655. 2. Buckley IK & Porter KR 1973, J.Cell Biol. 59:273a. 3. Heuser JE & Kirschner MW 1980, J.Cell Biol. 86:212. 4. Lewis AK & Bridgman PC 1992, J.Cell Biol.119,5:1219. 5. Malecki M 1990, SMI Sup.5:53. 6. Malecki M 1992, Proc. 50th Ann. Mtg. EMSA: 566. 7. Ris H 1985, J.Cell Biol. 100:1474. 8. Small JV & Celis JE 1978, Cytobiologie 16,308. 9. Wetzel B & Albrecht RM 1989, SMI Sup.3:1.

① LIVING CELL

② FREEZE FRACTURE REPLICA

③ NEGATIVE STAINING

④ DEEP NEGATIVE STAINING

186

⑤
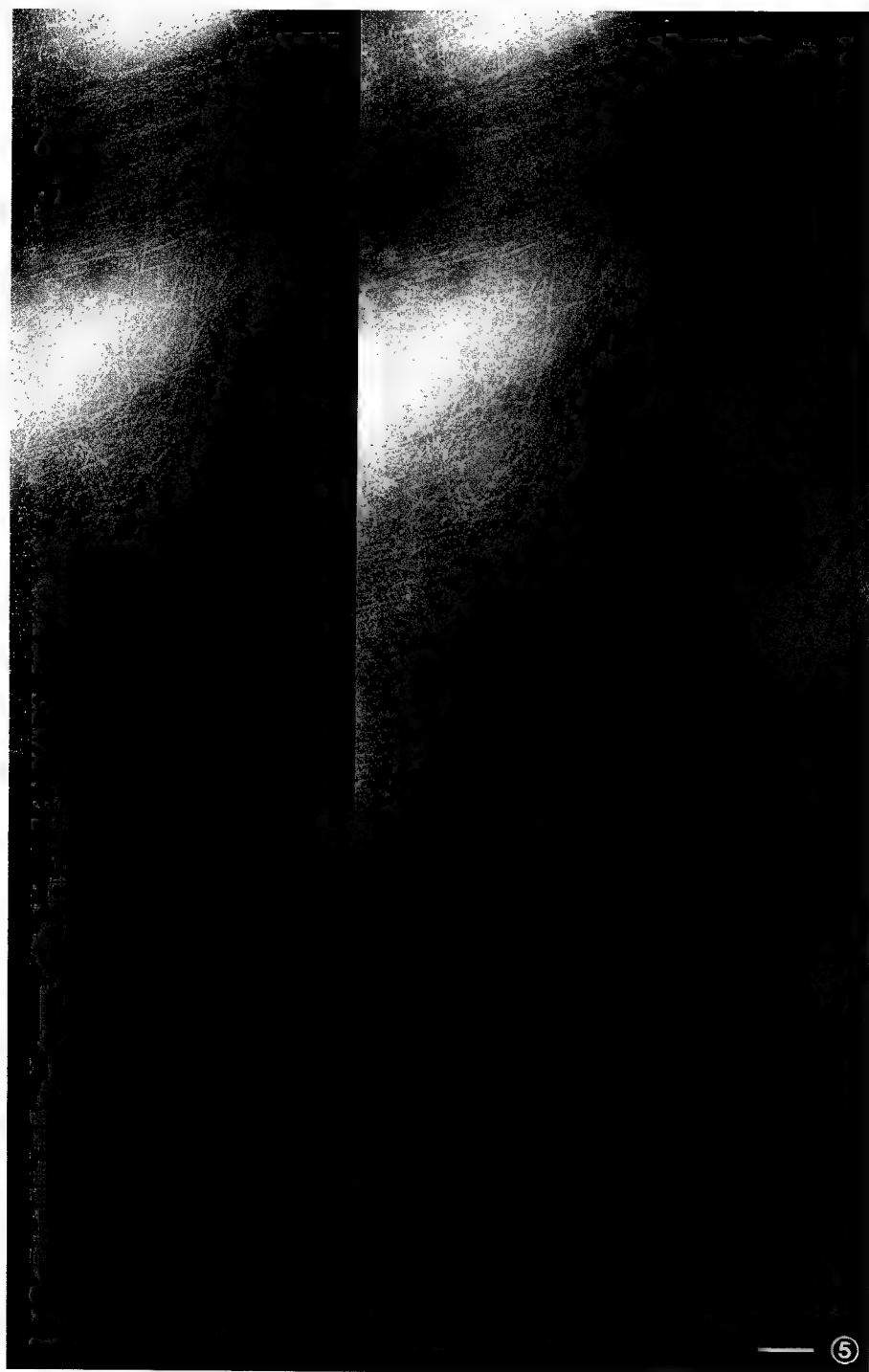
VIDEO-MICROSCOPIC MEASUREMENT OF CELL-SUBSTRATUM TRACTION FORCES GENERATED BY LOCOMOTING KERATOCYTES

Tim Oliver, Michelle Leonard, Juliet Lee, Akira Ishihara and Ken Jacobson

Department of Cell Biology and Anatomy, University of North Carolina at Chapel Hill, NC 27599

We are using video-enhanced light microscopy to investigate the pattern and magnitude of forces that fish keratocytes exert on flexible silicone rubber substrata.Our goal is a clearer understanding of the way molecular motors acting through the cytoskeleton co-ordinate their efforts into locomotion at cell velocities up to 1μm/sec. Cell traction forces were previously observed as wrinkles(Fig.1) in strong silicone rubber films by Harris.(1) These forces are now measureable by two independant means.

In the first of these assays, weakly crosslinked films are made, into which latex beads have been embedded.(Fig.2) These films report local cell-mediated traction forces as bead displacements in the plane of the film(Fig.3), which recover when the applied force is released. Calibrated flexible glass microneedles are then used to reproduce the translation of individual beads. We estimate the force required to distort these films to be 0.5 mdyne/μm of bead movement. Video-frame analysis of bead trajectories is providing data on the relative localisation, dissipation and kinetics of traction forces. There are strong traction forces acting transiently and centripetally on beads near the rear-lateral edges of the cell's lamella. These beads move up to 5μm and are close to regions of the cell where lamellar retraction occurs symmetrically about the cell's mid-line(Fig.3). Beads directly in the path of the cell and up to 5 cell widths away are slowly pushed forward as the cell approaches(data not shown).

We have also measured the deflection of calibrated microneedles, used to directly block locomoting keratocytes(Fig.4). By this means we have estimated a cell's maximum rearward-directed traction force on silicone rubber to be 6 mdyne, before it is brought to a halt or changes its direction.

References

1. A.K. Harris et al., Science (1980) *208*, pp 177-9.

FIG.1--Phase contrast image of fish epithelial explant on strongly crosslinked silicone rubber showing long, tension wrinkles(arrows) beneath and beyond the cell sheet. Individual keratocytes can be seen at the edge of the cell sheet(arrowhead). Bar=50μm.

FIG.2--DIC image of a keratocyte moving left to right on weakly crosslinked silicone rubber that incoporates 1um beads(arrow). Box illustrates area chosen for kymographic display of traction-force assay. Loose bead at centre of box subsequently disappears from view. Box width =15μm.

FIG.3a through b--Kymograph of boxed region in fig.2. over a total time of 3.25 minutes. First panel is coincident with fig.2. Cell traction causes deflection of beads, particularly those close to and beneath the rear and lateral lamella(arrows). Boxwidth=15μm.

FIG.4--Phase contrast images of locomotion on silicon rubber. a) Cell approaches suspended needle until nuclear region is obstructed. b) Cell maintains direction of locomotion while retraction of cell rear is blocked c) Cell assumes complex morphology and turns aside, displacing needle tip to the left as it does so. Bar=20μm.
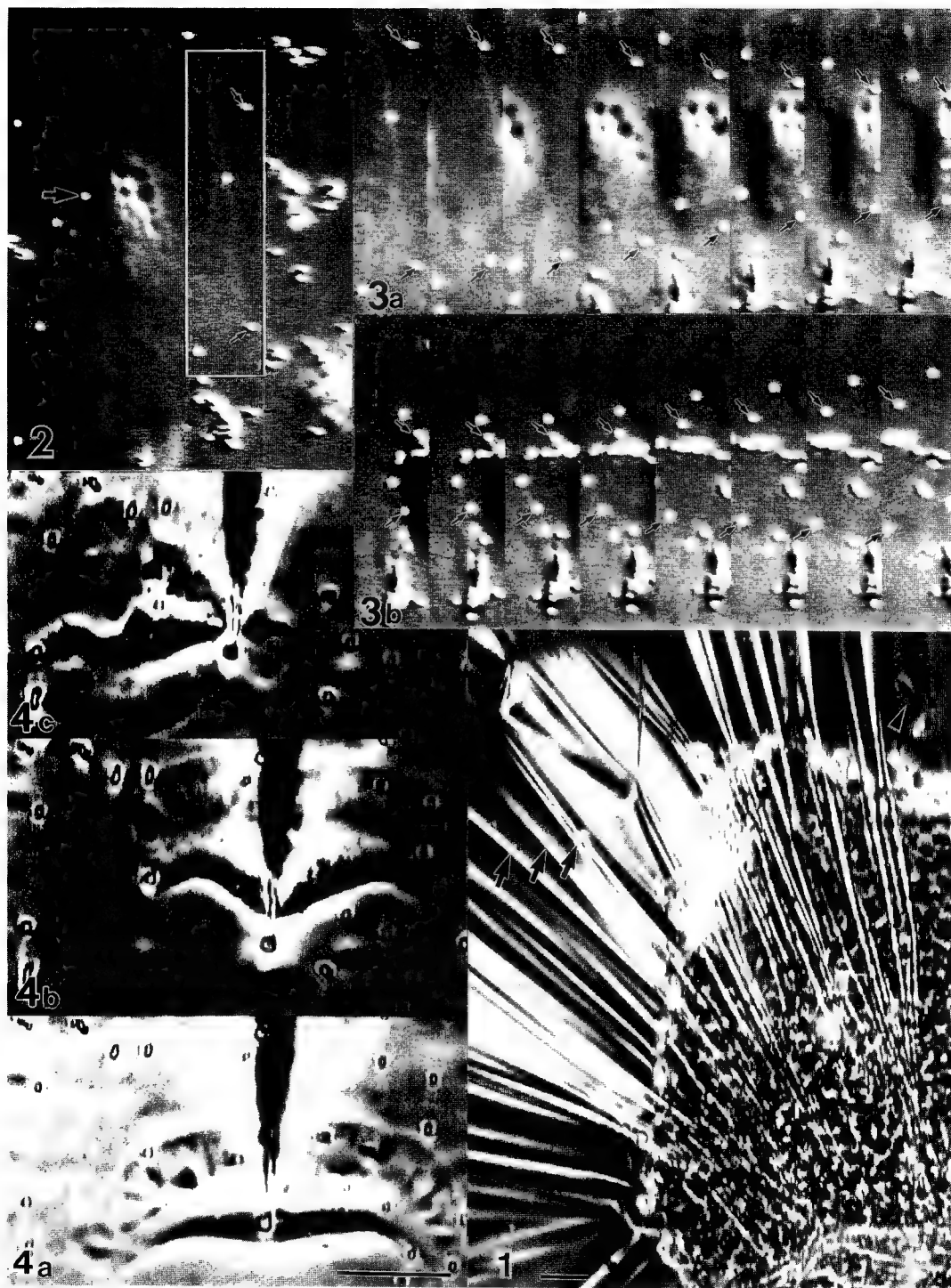
THE ORGANIZATION OF THE MICROTUBULE ASSOCIATED PROTEIN TAU IN ALZHEIMER PAIRED HELICAL FILAMENTS

George C. Ruben*, Khalid Iqbal°, Inge Grundke-Iqbal°, and John E. Johnson, Jr.[+]

*Depart. of Biol. Sciences, Dartmouth College, Hanover, NH 03755; ° Institute for Basic Research in Developmental Disabilities, Staten Island, NY 10314; [+] Depart. of Neuroscience, SRI, Menlo Park , CA

Neurofibrillary tangles (NFT) of paired helical filaments (PHF) are the most characteristic brain lesions of Alzheimer disease[1,2] and their abundance determines the diagnosis. This histopathological hallmark occurs with greater frequency in patients with clinical dementia of the Alzheimer type than in normal individuals of the same age.[8] Therefore, it is important that we establish and understand the arrangement of subunits in PHF. This knowledge, we believe, could be key to understanding the pathogenesis of neurofibrillary degeneration.

Intracellular Alzheimer NFT fixed in OsO_4 or $KMnO_4$ in the absence of glutaraldehyde treatment were first observed by transmission electron microscopy (TEM) of thin sections and reported by Kidd.[1] The tangles he observed contained helical pairs of ~10 nm filaments separated center to center by 15 nm with a double helical period of ~160 nm that he named paired helical filaments. Subsequent thin sectioning work with a similar fixation treatment confirmed that the PHF were helical with crossover width, T=12.8±2 nm, and a wide region , W=24±3.1 nm, which occured every L=65-80 nm .[3] Negatively stained isolated PHF were observed with crossover widths of T=6-11 nm, and wide regions of W=15-22 nm which occured every L=60-90 nm.[4,5] In contrast to the thin sectioned PHF images, the wide regions in a normal negatively stained PHF image rarely split into two filaments. Periodic PHF structural models have been advanced within the constraints of the negative stain dimensions but none has garnered consensus status.[9]

Tau has been found in PHF as the integral protein subunit of PHF.[9] Tau has also been shown to form ~2.1 nm triple-stranded left-hand helical polymers of ~1.0 nm strands which we think may be its native form.[7] In addition, ~2.1 nm triple-stranded left-hand helical filaments structurally identical to tau polymer filaments have been found condensed in tangles with PHF.[8] Although direct visualization of tau in PHF has been an important research objective for years, conventional sample preparation methods using thin sectioning and negative staining techniques for TEM have not achieved this goal.[8,9]

A new freeze-drying vertical replication method for TEM allows observation of single PHF and their upper surface within NFT isolated without detergent at a 0.6-0.7 nm resolution and a 260 nm depth of field on a JEOL 100cx TEM.[6] Resolution in replicas is directly related to the Pt-C deposition angle to a surface and to the final Pt-C film thickness.[6] The PHF we observed made one helical turn (L) in 74±8.5 nm with a wide region (W) of 14.8±0.6 nm similar to PHF previously modeled with a periodic morphology. The PHF thin region (T) measured ~2.4 nm, ~4.9 nm, ~7.4 nm, and ~9.7 nm and the most often observed width was ~2.4 nm. No surface features regularly divide the PHF into two filaments. Morphologically the PHF are thin helical ribbons with an often observed thickness of ~2.4 nm. At high magnification, ~1.0 nm and some ~0.4 nm strands identical to normal and denatured tau monomer covered PHF surfaces and were aggregated in nonperiodic fashion.[9]

References

1. M. Kidd, Nature (1963) 197, 192; Brain 87 (1964) 307.
2. R.D.Terry et al., Am J. Pathol. (1964) 44, 269.
3. H.M.Wisniewski et al., J. Neurol. Sci. (1976) 27, 173.
4. J.Brion et al., Acta Neuropathol. (Berl).(1984) 64, 148; C.M.Wischik et al., J. Cell Biol. (1985) 100, 1905.
5. H.M. Wisniewski et al., J. Neuropathol. Exper. Neurol. (1984) 43 643.
6. G.C.Ruben , JEMT (1989) 13, 335.
7. G.C.Ruben et al., J. Biol. Chem. (1991) 266, 22019.
8. G.C.Ruben et al., Brain Research (1993) 602, [2] E2.
9. G.C.Ruben et al., Brain Research, (1993) 602, 1.
10. GCR thanks GeoM Co & Dartmouth Rippel EM Lab, KI thanks NIH grants. AG05892, AG04220, AG08076, NS18105, & Alz. grant from Amer. Health Assist. Foundation, Rockville, MD
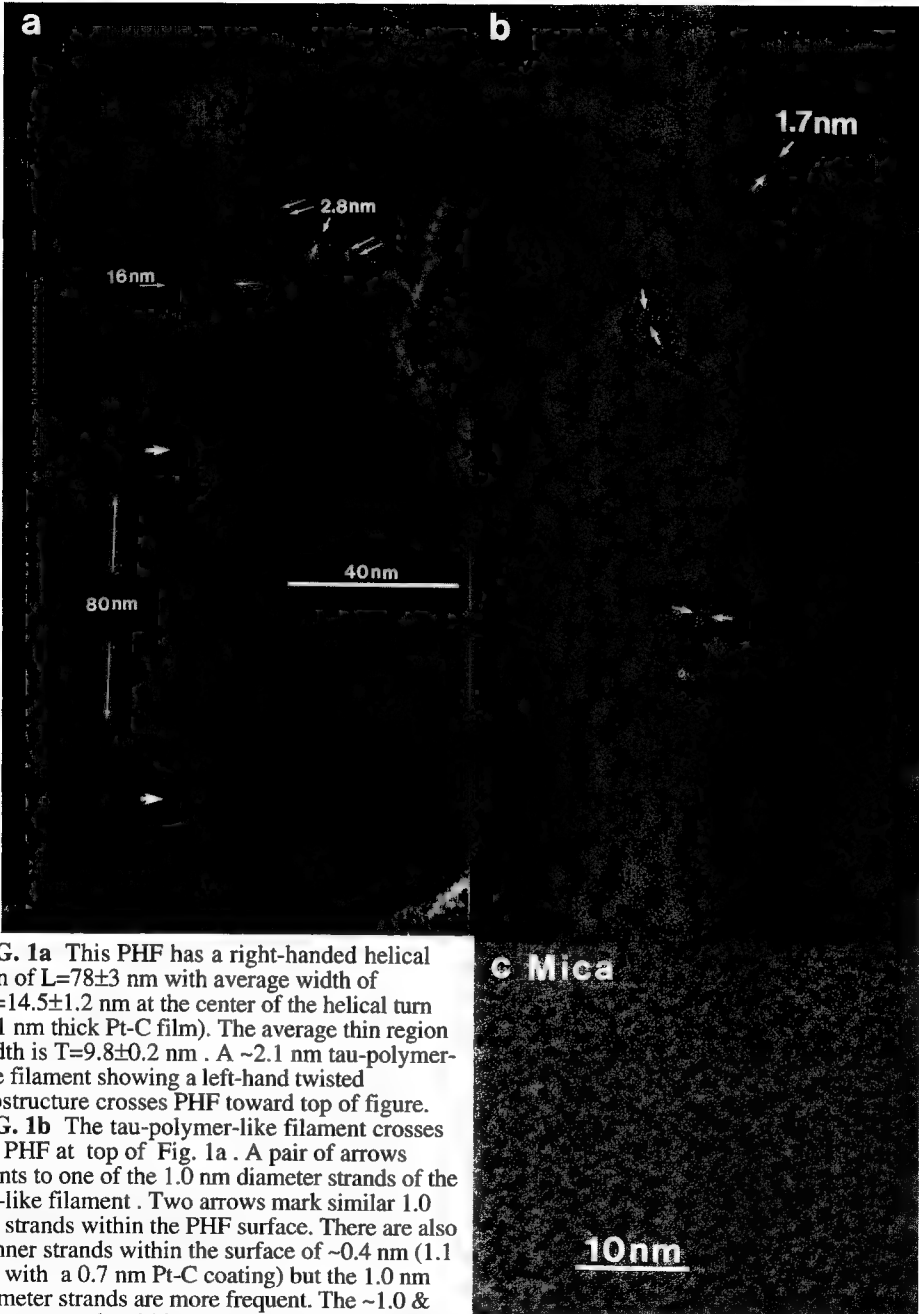
FIG. 1a This PHF has a right-handed helical turn of L=78±3 nm with average width of W=14.5±1.2 nm at the center of the helical turn (1.1 nm thick Pt-C film). The average thin region width is T=9.8±0.2 nm . A ~2.1 nm tau-polymer-like filament showing a left-hand twisted substructure crosses PHF toward top of figure.
FIG. 1b The tau-polymer-like filament crosses the PHF at top of Fig. 1a . A pair of arrows points to one of the 1.0 nm diameter strands of the tau-like filament . Two arrows mark similar 1.0 nm strands within the PHF surface. There are also thinner strands within the surface of ~0.4 nm (1.1 nm with a 0.7 nm Pt-C coating) but the 1.0 nm diameter strands are more frequent. The ~1.0 & 0.4 nm strands within PHF are disordered. bar =10nm as in Fig.1c. **FIG. 1c** 1.0 nm Pt-C film on mica shows structures at the 0.5-0.6 nm level.[6] Strands in Fig. 1b are 2-3 times larger than the 0.5-0.6 nm chain-like structures in Fig. 1c.

191

BREFELDIN A AFFECTS THE ENDOMEMBRANE SYSTEM AND VESICLE TRAFFICKING IN HIGHER PLANTS

Béatrice Satiat-Jeunemaitre [1], Jancy Henderson [2], David Evans[2], Kim Crooks[2], Mark Fricker[3], Richard Napier[4] and Chris Hawes [2].

[1]C.N.R.S. Biomembranes et Surfaces Cellulaires Végétales, Ecole Normale Supérieure, Paris, FRANCE. [2]B.M.S., Oxford Brookes University, Oxford, UK. [3]Department of Plant Sciences, Oxford University, Oxford, UK. [4]H.R.I., East Malling, Kent. U.K.

In plant cells, as in animal cells, many macromolecules and membranes are transported by vesicle vectors through both the exocytotic and endocytotic pathways. In order to elucidate the mechanisms and molecular events of such trafficking we are using a set of drugs known to perturb membrane flow in plant cells in combination with immunocytochemical studies using a bank of monoclonal antibodies to various components of the endomembrane system and cell surface. In animal cells, one such drug, Brefeldin A, a fungal fatty acid derivative which causes disruption of the Golgi apparatus, has recently been used as a tool to dissect the mechanisms of vesicle flow from the endoplasmic reticulum to the Golgi apparatus and down the cisternae of the Golgi stack (1). It has been demonstrated that BFA also has a dramatic effect on the Golgi apparatus in higher plant cells (2,3,4).

In this paper we report on recent work on the disruption of the plant Golgi apparatus with BFA and the redistribution of endomembrane marker epitopes after drug treatment of roots and suspension culture cells. BFA induces a reversible rearrangement of the Golgi stacks into circular formations which are generally perinuclear. In roots this movement is followed by a dramatic reduction in the number of stacks which is parallelled with the formation of large clusters of Golgi derived vesicles. In these accumulations of vesicles, the Golgi membrane glycoprotein recognised by monoclonal antibody JIM84 can be detected by fluorescence and gold labelling. A build up of Golgi derived secretory products (cell surface glycoproteins recognised by JIM1 and wall pectins recognised by JIM7) also occurs after a BFA treatment. At the light level, such accumulations are clearly depicted as the occurrence of numerous fluorescent spots, often in a perinuclear location. At the electron microscope level, accumulation of secretory products is seen at the *trans*-Golgi and in the large vesiculated areas of BFA treated cells. Also, enhanced labelling of the tonoplast with JIM1 is observed after BFA treatment, indicating some redirection of product to the vacuole. The endoplasmic reticulum, when localised by staining with a monoclonal antibody to the carboxy-terminal tetrapeptide HDEL (4), appears swollen on incubation with BFA. However, in contrast to reports from the animal literature (1), we have observed no redistribution of Golgi products or Golgi marker epitopes into the endoplasmic reticulum as a result of BFA action.

1. R.D. Klausner, J.G. Donaldson and J. Lippincott-Schwartz, J. Cell Biol. (1992)116,1071.
2. B. Satiat-Jeunemaitre and C. Hawes, J. Cell Sci. (1992)103, 1153.
3. B. Satiat-Jeunemaitre and C. Hawes, Cell Biol. Int. (1993)17, in press.
4. A. Driouich, G.F. Zhang and L.A. Staehelin, Plant Physiol. (1993), in press.
5. R. Napier, L.C. Fowke, C. Hawes, M. Lewis and H.R.B. Pelham J. Cell Sci.(1992)102, 261.
6. Dr Paul Knox (University of Leeds, U.K.) kindly supplied JIM7 and JIM1.
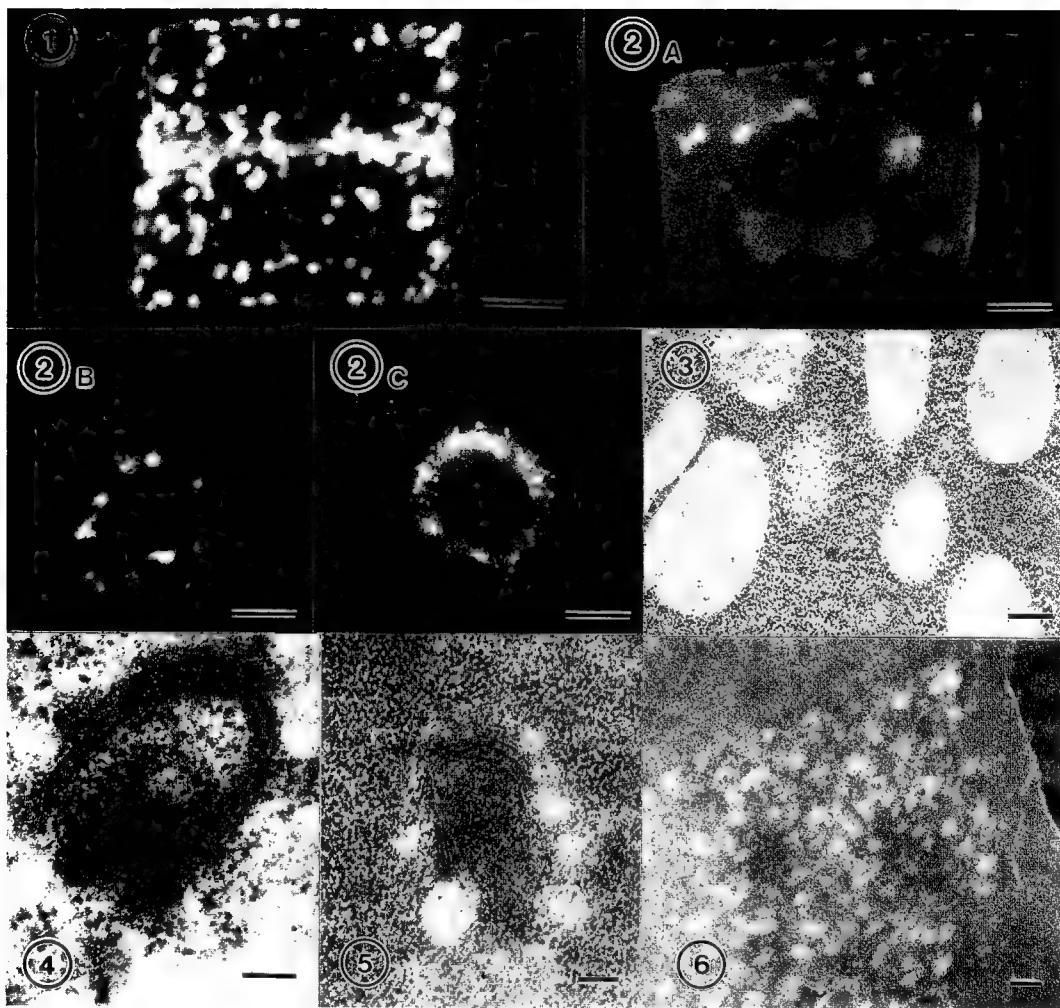
FIG. 1--Confocal laser scanning micrograph of root cells stained with JIM84. Note the Golgi staining throughout the cytoplasm. Bar = 10µm.

FIG. 2--Immunofluorescence staining of BFA treated root cells. Bar = 10µm. (A) JIM84, fluorescence concentrates in discrete cellular compartments. (B) JIM1, fluorescent aggregates accumulate mainly around the nucleus.(C) JIM7, occurrence of numerous vesicles (not seen in control cells).

FIG. 3--In some BFA-treated onion root cells, there is an increased localisation of JIM1 epitopes on vacuolar membranes. Bar = 0.25µm

FIG. 4--Accumulation of JIM7 epitopes at the *trans*-face of BFA-distorted Golgi stacks. Bar = 0.1µm.

FIG. 5--JIM84 epitopes remain associated with Golgi membranes after BFA treatment. Bar = 0.1µm.

FIG. 6--BFA-induced vesicular compartment, trapping both JIM84, JIM1 and JIM7. (JIM1) on the micrograph). Bar = 0.2µm.

193

CONFORMATIONAL CHARACTERIZATION OF NUCLEOSOME STRUCTURE BY ELECTRON MICROSCOPY

Gregory J. Czarnota

Department of Medical Biophysics, University of Toronto and Ontario Cancer Institute
500 Sherbourne Street, Toronto, Ontario, Canada M4X 1K9

Chromatin structure at the fundamental level of the nucleosome is important in vital cellular processes. Recent biochemical and genetic analyses show that nucleosome structure and structural changes are very active participants in gene expression, facilitating or inhibiting transcription and reflecting the physiological state of the cell.[1] Structural states and transitions for this macromolecular complex, composed of DNA wound about a heterotypic octamer of variously modified histone proteins, have been measured by physico-chemical techniques and by enzyme-accessibility and are recognized to occur with various post-translational modifications, gene activation, transformation and with ionic-environment.[2] In spite of studies which indicate various forms of nucleosome structure, all current x-ray and neutron diffraction studies have consistently resulted in only one structure, suggestive of a static conformation.[3] In contrast, two-dimensional electron microscopy studies and three-dimensional reconstruction techniques have yielded different structures.[4, 5] These fundamental differences between EM and other ultrastructural studies have created a long standing quandary, which I have addressed and resolved using spectroscopic electron microscopy and statistical analyses of nucleosome images in a study of nucleosome structure with ionic environment.

In carrying out a systematic analysis of nucleosome structure and ionic environment I have observed changes in nucleosome structure occurring over a spectrum of ionic-strengths. Purified calf-thymus nucleosomes were prepared in monovalent-salt at selected ionic-strengths corresponding to ionic strengths midway between putative structural transitions, and fixed using optimized fixation conditions. Nucleosomes were then either critical-point-dried or air-dried and imaged unstained using spectroscopic electron microscopy to provide a darkfield image with additional contrast from electrons scattered by DNA phosphorus. Images of unstained nucleosomes prepared at a variety of selected salt concentrations indicate a pleomorphic structure for the nucleosome dependent on ionic strength (Fig.1). For example, nucleosomes prepared in the presence of 10 mM NaCl, 15 mM TEA-HCl, pH 7.4 (Fig.1b) appear in projection as well defined elliptical shapes, whereas at 150 mM, 15 mM TEA-Cl, pH 7.4 (Fig.1d) nucleosomes appear in projection predominantly with circular morphology.

To correlate two-dimensional images to a three dimensional structure statistical analyses of nucleosome images were carried out using principal component analysis, a technique which permits direct inferences of three-dimensional structure from two-dimensional distributions of measured particle dimensions.[6] Principal component analysis of particle dimensions for nucleosomes at 10 mM NaCl (Fig.2a) indicates that the structure is a prolate ellipsoid, consistent with a previous 3D reconstruction from electron micrographs of the unstained particle. This conformation produces images in projection with a mean length of 100 Å and a mean width of 68 Å. In contrast, principal component analysis of particle dimensions at 150 mM NaCl (Fig.2b) indicates an oblate ellipsoidal

194

structure consistent with x-ray crystallographic determinations. This conformation produces images in projection with a mean length of 114 Å and a mean width of 91 Å. Images and analyses of nucleosomes prepared at other ionic strengths indicate other forms, including a more extended form observed at low ionic strength (Fig.1a). Preliminary investigations using divalent cations indicate other forms and differential effects with respect to monovalent salts in eliciting observable transitions in nucleosome structure.

References

1. R.K. Mann, and M. Grunstein, *EMBO. J.*, 11(1992), 3297.
2. P.S. Kayne *et al.*, *Cell*, 55(1988), 27.
3. I., Oohara, and A. Wada, *J. Mol. Biol.* 196,(1987), 399.
4. T.J. Richmond *et al.*, *Nature* 311(1984), 532.
5. G. Harauz, and F.P. Ottensmeyer, *Science* 226(1984), 936.
6. M. Zahn-Zabal *et al.* (submitted).
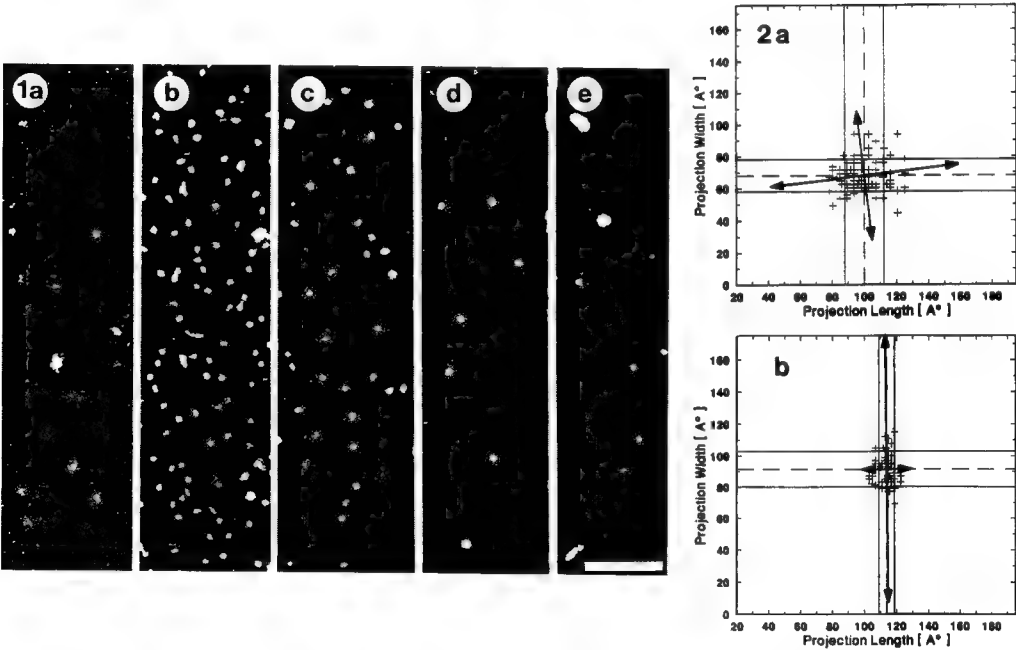
FIG. 1. 150 eV energy-loss images of critical-point-dried calf-thymus nucleosomes prepared for electron microscopy in 3mM (a), 10 mM (b), 33 mM (c), 150 mM (d), and 400 mM NaCl in 15mM TEA-HCl, pH 7.4 (e). Scale bar indicates 1000 Å.

FIG. 2. Results of principal component analysis for calf-thymus nucleosomes in 10 mM NaCl (a) and 150 mM NaCl (b). The longest arrow superimposed on each distribution corresponds to the first principal component (FPC) which represents the best-fit line through the scatter of paired measurements. A horizontal FPC is indicative of a prolate ellipsoidal structure (a), whereas a vertical FPC indicates a oblate ellipsoidal structure (b). Dashed lines indicate mean values and solid lines correspond to one standard deviation from the mean of each dimension.

SUBCELLULAR DISTRIBUTION OF AN ETHIDIUM BROMIDE/POLY r(A-U) COMPLEX

J.M. Jamison*, J.L. Summers[+], and J. Gilloteaux**

Departments of Microbiology and Immunology*, Urology[+] and Anatomy**, Northeastern Ohio Universities College of Medicine, Rootstown, OH 44272, U.S.A.

Previous results have shown that drug uptake by cells is enhanced when the drug is bound to DNA.[1,2] Chick embryo fibroblasts (CEF) treated with ethidium bromide (EB) exhibit inhibited cell multiplication, mitochondrial swelling and nucleolar segregation. However, EB-DNA treated CEF cells exhibit a much lower cytotoxicity than the EB-treated CEF cells and the mitochondrial and nucleolar alterations are reversible. Conversely, in Ehrlich ascites tumor cells exposed to EB or EB-DNA complexes, the toxicity of the DNA bound EB (as measured by inhibition of cell multiplication, nucleolar segregation, mitochondrial swelling and intramitochondrial inclusions) is more pronounced and appears earlier after treatment than the EB induced cytotoxicity. More recent results have shown that when EB was combined with double stranded RNA (poly r(A-U)) and then added to human foreskin fibroblasts (HSF), the 50% effective dose of the poly r(A-U) was 154-fold lower.[3,4] The results of additional studies demonstrated that the enhanced antiviral activity was not due to superinduction of interferon, direct viral inactivation, or host cell cytotoxicity. Phase contrast, fluorescence and confocal micrographs of HSF cells following a 3 h exposure to 50 μM EB alone or a 50 μM EB/200 μM poly r(A-U) combination, showed that EB alone stained the chromatin, but not the nucleolus, while the EB/poly r(A-U) combination stained the nucleolus, but not the chromatin. These results suggested that the enhanced antiviral activity of the EB/poly r(A-U) combination may be related to its altered distribution and to its ability to interfere with the synthesis and processing of rRNA.

The results of the current study examine effects of an EB/poly r(A-U) combination on human bladder carcinoma cells (RT4). RT4 cells were incubated with a 50 μM EB/200 μM poly r(A-U) combination for 3 h at 37 ° C and 5% CO_2. Subsequently, the RT4 cells were fixed in buffered 3.2% glutaraldehyde (0.1 M Na cacodylate, pH 7.4), fast fixed by 1% aqueous osmium tetroxide and embedded in epoxy resin. Sections were all contrasted with uranyl acetate except figure 8. The bar in figure 1 is 10 μm and the bars in figures 2-8 equal 100 nm. Figure 1 depicts an entire EB/poly r(A-U) treated RT4 cell. The arrow denotes the presence of a nuclear vacuole while the arrowheads indicate cytoplasmic vacuoles. Figure 2 is an enlargement of the nuclear vacuole of figure 1 which is adjacent to the nucleolus (n). Notice the presence of the electron dense material (EDM) in the nuclear vacuole. The arrows in figure 3 show the accumulation of electron dense EB or EB/poly r(A-U) in blebs at the cell surface. Accumulation of EDM occurs in a clathrin coated pits (c) adjacent to the smooth ER (r); w indicates the presence of a membranous whorl. Figures 4 and 5 show EDM in a clathrin coated pit (c), a mitochondrion (m) and a membranous whorl (w). Double arrows denote an electron dense filamentous structure (d = 1.5 nm) which may be the poly r(A-U). Figure 6 is an enlargement of the membranous whorl where the double arrows denote filamentous/membranous structures with a thickness of 1.5 nm and a periodicity of 3.5 - 5 nm. Figure 7 shows EDM in an endocytotic vesicles (e) and mitochondria (m). The arrows denote EB stained mitochondrial DNA (mtDNA). Figure 8 is a damaged mitochondrion with the arrows indicating EB stained mtDNA. Taken together these figures suggest a model in which EB/poly r(A-U) is endocytosed and follows a pathway to the nucleus which includes the ER which is continuous with the outer nuclear envelope.

References

1. A. Trouet, *et al.*, Nature New Biol. (1972) 239, 110.
2. E. Heinen, *et al.*, Biochem. Pharmacol. (1974) 23, 1549.
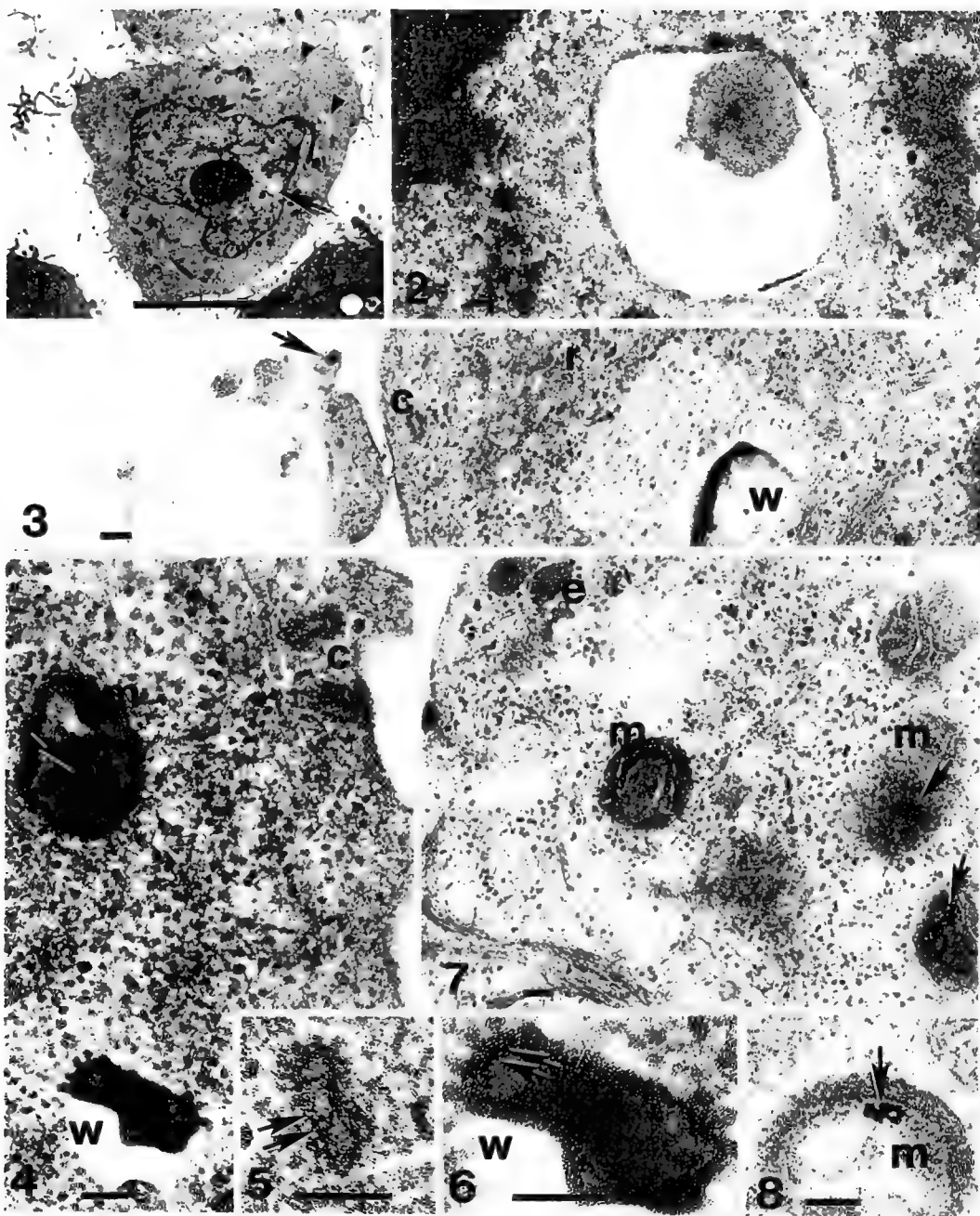
3. K. Krabill, *et al.*, Cell Biol. Int'l. Rep.(1992) 16, 975.
4. J.M. Jamison, J. Gilloteaux and J.L. Summers, in Progress in Molecular and Subcellular Biology. Double-Stranded RNA as Immunomodulator. (1993) (in press).

DEFEROXAMINE–INDUCED ULTRASTRUCTURAL LESIONS OF NUCLEOLI IN MCF-7 CARCINOMA CELL LINE

Fen Wang, Jonathan F. Head, and Robert L. Elliott

The Elliott Mastology Center and Research Institute, Baton Rouge, LA 70816

Deferoxamine(DFO), an iron chelator, has been demonstrated to inhibit the growth of a variety of human malignant cell lines[1]. Evidence suggests that DFO exerts its primary effect by chelating ferric iron and inhibiting DNA and RNA synthesis[2].

The effects of DFO on MCF-7 cells have been investigated. The IC_{50} and IC_{90} inhibitory concentrations of DFO on MCF-7 cells were 4.8 uM and 9.5 uM, respectively. This inhibition can be reversed by equimolar concentrations of iron and iron-loaded transferrin[3]. Alterations in the ultrastructure of nucleoli of MCF-7 cells exposed to the DFO in the concentrations of 4.8uM and 9.5uM for 24 hours, 48 hours and 72 hours were studied by transmission electron microscopy. The cells were grown in 24 well plates in alpha-MEM supplemented with 10% FCS and incubated at 37°C. They were harvested with trypsin-EDTA, pelleted into Beem capsules and centrifuged. A standard specimen preparation procedure was employed for transmission electron microscopy.

Nucleolar alterations progressed as the treatment time and DFO concentration increased, and there were dissociation and segregation of fibrillar and granular components. Control nucleoli were irregularly shaped and contained interdispersed granular and fibrillar components (Fig.1). 24 hours after exposure to 4.8 uM DFO, nucleoli appeared dense and contained fibrillar centers and vacuoles (Fig. 2). Fibrillar centers were more apparent after 48 hours exposure. The fibrillar components accumulated around the fibrillar center and localized at the periphery (Fig. 3). After 72 hours fibrillar centers were enlarged, collapsed and there was vacuolization of the fibrillar center matrix (Fig. 4). After 24 hours exposure to 9.5 uM DFO, marked nucleolar segregation of granular and fibrillar components were noted (Fig. 5). There was further dissociation of granular and fibrillar components after 48 hours (Fig. 6). After 72 hours the granular and fibrillar components were completely segregated (Fig. 7).

This study shows a series of nucleolar changes that progress to complete segregation. These alterations are dose and time dependent. Similar results induced by anthracyclines have been reported[4]. Nucleolar lesions induced by DFO indicate that this organelle is the principal intracellular target.

References:

1. D.L. Becten and B. Roberts, Cancer Res., (1989) 49:4809-4812.
2. H.M. Lederman, A. Cohen, J.W.W. Lee, M.H. Freedman and E.W. Gelfand, Blood, (1984) 64(3):748-753.
3. J.F. Head, T.L. Bruce and R.L. Elliott, Proc. AACR, (1992) 33:505.
4. Y. Daskal, C. Woodard, S.T. Crooke and H. Busch, Cancer Res., (1978) 38:467-473
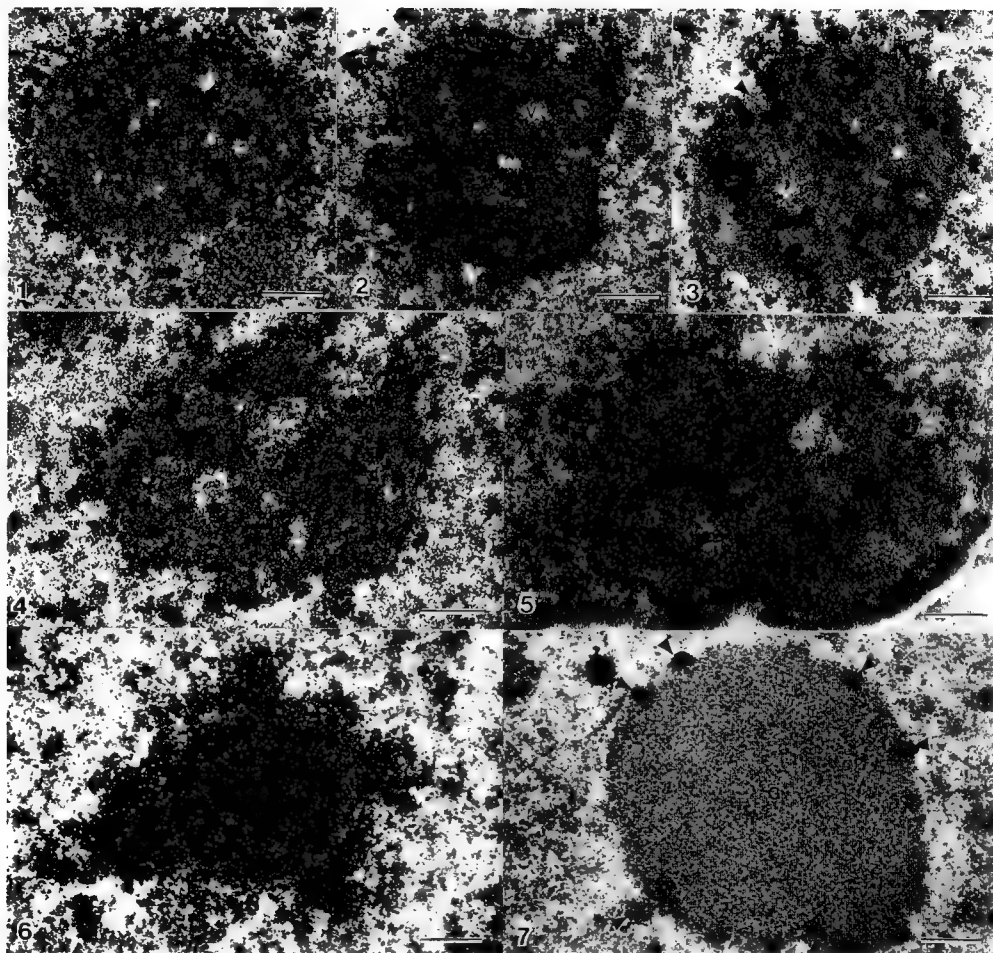
Fig.1.--Control MCF-7 cell nucleolus. The granular components(G) are distributed randomly throughout the nucleolus. The fibrillar centers(FC) are circled by denser fibrillar component(F). Bar=0.45um

Fig.2.--After 24-hr. treatment with 4.8 uM DFO, nucleolus appears compact and contains well-defined fibrillar centers(FC) and vacuoles(V). Bar=0.56um

Fig.3.--Nucleolus after 48-hr.exposure to 4.8 uM DFO, more fibrillar centers(FC) are formed. A fibrillar center matrix appears extruding from the nucleolus body(arrow). Bar=0.47um

Fig.4.--Following 72-hr. exposure to 4.8 uM DFO, fibrillar centers(FC) are enlarged and collapsed with vacuolization of fibrillar center matrix(arrow). Bar=0.47um

Fig.5.--Exposure to 9.5uM DFO for 24-hr. causes collapse and fusion of both fibrillar center-associated fibrillar component and fibrillar center matrix(arrows). Bar=0.28um

Fig.6.--After treatment with 9.5 uM for 48-hr., marked polarized dissociation of granular(G) and fibrillar components(F) occurs. Bar=0.31um

Fig.7.--A complete segregation of granular(G) and fibrillar(F) components is shown. The denser fibrillar component forming the cap is indicated by (C). The extruded microspherules form a ring around the nucleolus(arrows). Bar=0.30um

199

POLYMORPHISM OF FIBER CELL JUNCTIONS IN MAMMALIAN LENS

M. Joseph Costello, Kristin J. Al -Ghoul, Timothy N. Oliver, C. Wesley Lane, Magdalena Wodnicka and Pawel Wodnicki

Department of Cell Biology and Anatomy, University of North Carolina at Chapel Hill, Chapel Hill, NC 27599

Previous studies of junctional specializations between bovine lens fiber cells have indicated that pentalamellar profiles in isolated membranes correspond to gap junctions (GJs), undulating square array junctions (SAJs) and thin symmetric junctions (TSJs).[1-3] We show here that this same junctional diversity occurs in the intact tissue and that the differences in thickness and staining patterns can be documented by density profiles from thin-section TEM images of *in vivo* and isolated membranes.

Fresh bovine lenses were mounted on edge and vibratome sectioned parallel the optic axis. Sections near the center were fixed (paraformaldehyde, glutaraldehyde, and tannic acid) for thin-section analysis or were dissected on a glass slide to select a group of fiber cells within a narrow region, such as the deep cortex about 2 mm from the lens surface. Membranes were isolated from this small fraction of cells using a new procedure, essentially, suspending in buffer, washing 30 min in 4M urea and pelleting at low speed in an AirFuge (Beckman). This procedure takes about 2 h and gives excellent preservation with minimal vesiculation compared to the full urea washing procedure used previously.[1] The pelleted membranes were resuspended in 100 μl buffer and aliquots placed in microtitre wells, treated polylysine to promote membrane adhesion. The membranes were spun gently to form a loose pellet. The fixation and processing steps for thin-section TEM were performed in the wells.[4]

Cells near the vibratome cut surface show good contrast of membranes and cytoplasm (Figs. 1 & 2). Undulating membranes (Fig. 2, solid line) and gap junctions (Fig. 2, dotted line) have been interpreted diagrammatically (Fig. 3) based on the presence of MIP26 in curved square arrays of the SAJs[2,5,6] and connexin proteins in the GJs.[6,7] We also hypothesize that the TSJ contains arrays of MIP26 in both membranes[6] and serves as an adherens junction. These three distinct junctions are visible in thin sections of intact fiber cells (Fig. 4) and isolated membranes (Fig. 5 & 6). The tilt series demonstrates that the asymmetry in the SAJ is not due to tilt or curvature within the section because both membranes come into optimum view together at 0° (Fig. 7, lower arrowhead, indicates thin membrane on concave side). Further tilt shows the extent of the crystalline segment and the overlap with an adjacent segment (Fig. 6, upper arrowhead). The dimensions and staining patterns of the junctions can be distinguished in optical density scans (Fig. 8). Each plot is an average of 100 scans performed automatically on 4096x4096 digitized images. The dimensions confirm the close association of the junctional membranes of the lens and suggest that the concave thin membrane in the SAJ is 5 nm or less.

These images support the molecular interpretation that the curved membranes of the SAJs contain crystalline arrays of MIP26 paired with lipid bilayers,[2,5,6] and confirm that urea washed isolated membranes are representative of membranes in the intact lens.

References

1. G. Zampighi et al., J. Cell Biol. (1982)93, 175.
2. M. J. Costello et al., Curr. Eye Res. (1985)4, 1183.
3. M. J. Costello et al., Invest. Ophthalmol. Vis. Sci. (1989)30, 975.
4. B. E. Wray and R. Sealock, J. Histochem. Cytochem. (1984)32, 1117.
5. W.-K. Lo and C. V. Harding, J. Ultrastr. Res. (1984)86, 228.
6. G. Zampighi et al., J. Cell Biol. (1989)108, 2255.
7. D. L. Paul and D. A. Goodenough, J. Cell Biol. (1983)87, 708.
8. This research was supported by grant EY08148 from the National Institutes of Health.
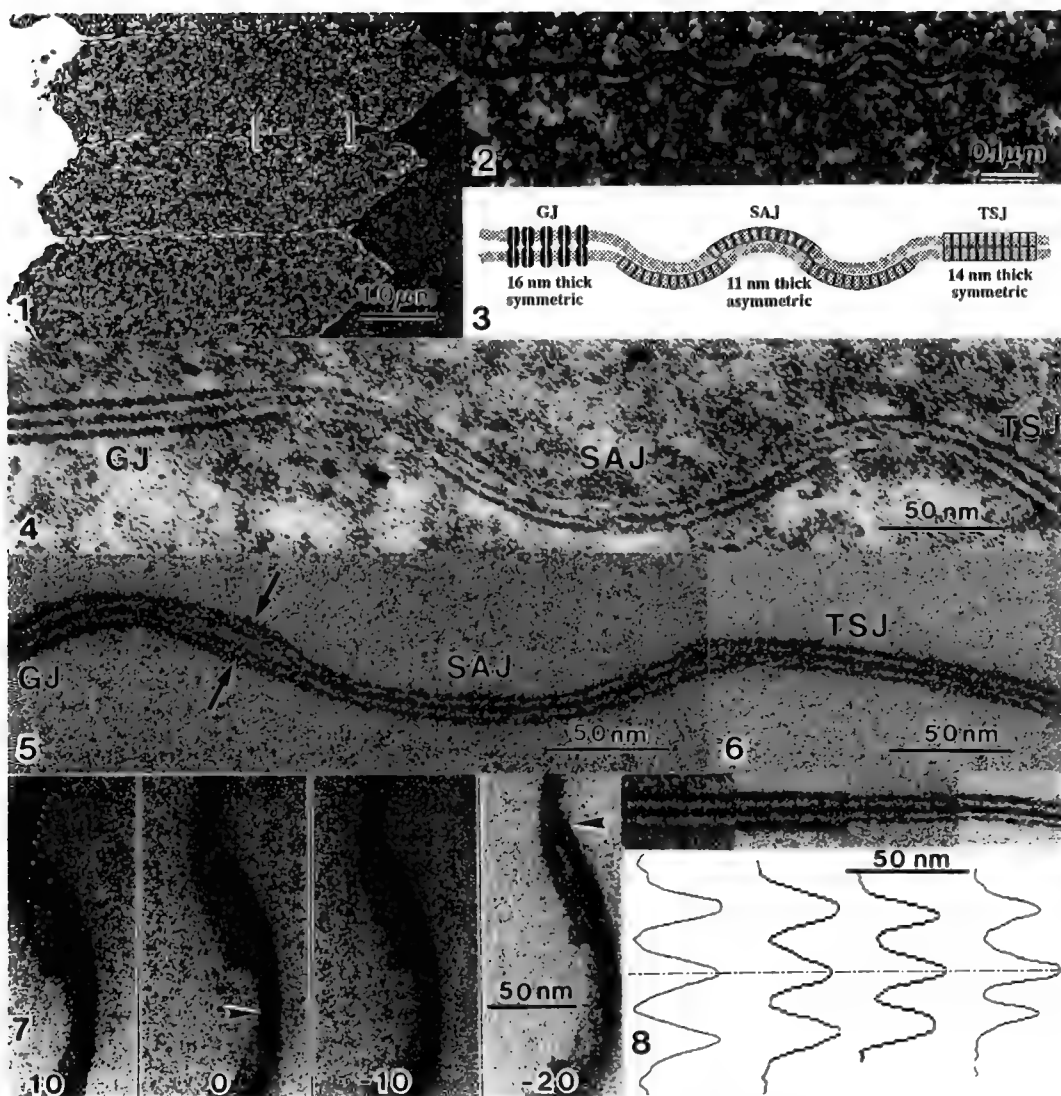
FIG. 1.--TEM of bovine fiber cell cut in cross-section. Vibratome cut at left edge.
FIG. 2.--Intermediate magnification of region of intercellular junctions in FIG. 1 (brackets).
FIG. 3.--Interpretation of junctions. GJ = gap junction; SAJ = square array junction; TSJ = thin symmetric junction.
FIG. 4.--TEM of junctions from deep cortex in intact lens at high magnification.
FIG. 5.--TEM of isolated bovine junctions from deep cortex. GJ, SAJ and single membranes (arrows) are present.
FIG. 6.--TEM similar to FIG. 4 showing TSJ.
FIG. 7.--Tilt series of SAJ showing that thick and thin membranes (lower arrowhead) come into optimum orientation together at 0°. End of a crystalline segment is visible at -20° (upper arrowhead).
FIG. 8.--Gallery of junctions (l. to r.) GJ from intact cell, and GJ, TSJ and SAJ, from isolated membranes. Corresponding optical density plots are shown below aligned at the intercellular space.

On-line alignment and astigmatism correction using a TV and personal computer

F. Hosokawa, Y. Kondo, T. Honda, Y. Ishida and M. Kersker

JEOL Ltd. 1-2 Musashino 3-chome Akishima Tokyo Japan

High-resolution transmission electron microscopy must attain utmost accuracy in the alignment of incident beam direction and in astigmatism correction, and that, in the shortest possible time. As a method to eliminate this troublesome work, an automatic alignment system using the Slow-Scan CCD camera has been introduced recently.[1] In this method, diffractograms of amorphous images are calculated and analyzed to detect misalignment and astigmatism automatically. In the present study , we also examined diffractogram analysis using a personal computer and digitized TV images, and found that TV images provided enough quality for the on-line alignment procedure of high-resolution work in TEM. Fig.1 shows a block diagram of our system. The averaged image is digitized by a TV board and is transported to a computer memory, then a diffractogram is calculated using an FFT board, and the feedback parameters which are determined by diffractogram analysis are sent to the microscope(JEM-2010) through the RS232C interface. The on-line correction system has the following three modes.

1) Diffractogram monitor
An amorphous TV image and its diffractogram calculated by the FFT board are displayed side by side on the computer CRT. The pair is refreshed every second, so that the microscope operator can check the response of astigmatism to his manual correction procedure. Fig.2a and b respectively show an amorphous image and its diffractogram in the monitor mode. In this mode, one may roughly correct astigmatism and set the defocus value to about 2 Sch in preparation for the beam alignment described next.

2) Coma-free alignment
The incident beam must be aligned in parallel with the true (coma-free) optical axis before precise correction of astigmatism, since the misalignment which causes the frequency-dependent defocus cannot be distinguished from astigmatism when one diffractogram is used. The method of coma-free alignment was first introduced by Zemlin et al.[2] and this basic method gives one of the fundamentals for the recent computer aided alignment procedure,[1,3,4] and is also referred to our algorithm. Fig.3a, b and c show an example of alignment steps in our system. In each set of diffractograms, a diffractogram by the primary beam is placed at the center, and diffractograms by ±6.0 mrad tilted beam along the x and y axes are placed laterally and lengthways, respectively. Fig.3a is the start point which is roughly aligned; Fig3.b shows that the primary beam is corrected -0.7 mrad in the x direction and +1.0 mrad in the y direction; and Fig.3c is the final state in which there are beam corrections of -0.15 mrad tilt x and -0.2 mrad tilt y from b. Now, the practical calculation of the true axis position is on trial (not yet automated), so the operator must type in the correction value by his own decision, observing the symmetry in the opposite tilt pair. As an aid to decide the first correction value, previously simulated diffractograms and images are usable. They were calculated under a defocus of 2 Sch, at which we start the alignment after checking in the monitor mode. Fig.4a, b and c are observed diffractograms; and d,e and f are pairs of simulated diffractograms and images. In this case, the first correction of beam tilt is 0.7 mrad along the y axis.

3) Astigmatism correction
The computer calculates the value and direction of the astigmatism from the defocus values of the 8 azimuth directions of the diffractograms using the least squares method, and corrects the astigmatism coil current of the microscope. Fig.5 shows an example of correction. Fig.5a is the start point of correction with 33 nm astigmatism. After one path, the astigmatism is corrected 7 nm in b, and c is the final state of correction in which astigmatism is less than 3 nm. Each path took 10 seconds.

References

1) O.L.Krivanek and G.Y.Fan, Proc.50-th EMSA Meeting(1992),91
2) F.Zemlin et al., Ultramicroscopy 3, 49(1978)
3) L.D.Marks, Proc.12-th ICEM(Seattle)1, 152(1990)
4) W.J. de Ruijter et al., Proc.12-th ICEM(Seattle)1, 154(1990)

Fig. 1. A block diagram of system.

Fig. 2. A diffractogram monitor mode display. In a and b are shown an amorphous Ge image and its diffractogram, respectively. Image was recorded with standard TV and JEM-2010 at 200kV.

Fig. 3. The coma-free alignment process using ±tilt method. The tilt angle is 6 mrad. Fig.3a is the start point, b is an intermediate and c is the final state in which opposite tilt pairs show a good symmetry. In each step, the correction value must be decided by the operator.

Fig. 4. Comparison of observed data(a ～c) with simulated data(d ～f) for the purpose of estimating the first correction of beam alignment. Fig.4d, e and f correspond to +5.3 mrad, 0.0mrad and -6.7 mrad beam tilt, respectively. The true axis was supposed to be at +0.7 mrad from the primary position.

Fig. 5. The astigmatism correction process. Fig.5a is the start point at which the detected astigmatism was 33 nm, b is the first corrected with the astigmatism reduced to 7 nm, and c is the final state with an astigmatism of less than 3 nm. Each path took 10 seconds.

ANALYSIS OF ELECTRON-SPECIMEN INTERACTIONS OF THICK BIOLOGICAL SPECIMENS IN TRANSMISSION ELECTRON MICROSCOPY AT 200 KEV

Karen F. Han, Alexander J. Gubbens*, Abraham J. Koster, Michael B. Braunfeld, John W. Sedat, and David A. Agard

Graduate Group in Biophysics, Howard Hughes Medical Institute, Dept. of Biochemistry and Biophysics, Univ. of California San Francisco, CA 94143
*Gatan Research and Development, Pleasanton, CA 94588

The primary project of our laboratory is the investigation of chromatin structure by three dimensional electron microscope tomography. The goal is to understand how 30nm fibers fold into higher order chromatin structures. Three dimensional tomography involves the reconstruction of an object by combining multiple projection views of the object at different tilt angles. Due to the electron-specimen interaction and the characteristics of lens aberration in the electron microscope, however, the image is not always an accurate representation of the projected object mass density. In this abstract, we analyze the various types of electron-specimen interaction for thick biological specimens up to 0.7 microns thickness.

Electron-specimen interactions include single elastic and inelastic, and multiple elastic and inelastic scattering. Of the imaging electrons, the single elastic and the plasmon electrons give rise to image intensities that can be linearly related to the projected object mass density. Multiply scattered elastic electrons contribute to an increase in background intensity. In addition, due to the chromatic aberration of the TEM's objective lens, multiply scattered inelastic electrons cause a blurring of the image because of an effective broadening of the focus spread.

Many authors have analyzed the relative magnitude of the various types of scattering events for energies below 100 keV [1-7]. In our lab, a typical electron tomographic reconstruction is done at 300 keV. It was thus appropriate to repeat such analysis at this higher beam energy. We were able to do the analysis at 200 keV using a Gatan Imaging Filter mounted on a JEOL 2010 TEM.

Our typical specimens are cell nuclei embedded in epon, stained with uranyl-acetate and lead-citrate, and cut to 0.3 microns thick. In a tomography data set, the effective thickness for a 0.3 micron specimen at high tilts can be up to 0.7 microns (65⁰ tilt). In this analysis, we used Drosophila Fat-body cell nuclei embedded in epon and cut to 0.3, 0.5 and 0.7 microns thick.

We found that at 200 keV, there is still a fair amount of elastic scattering, around 39%, 18%, and 8% for 0.3, 0.5, and 0.7 micron thick specimens respectively (fig.1). This is to be compared with less than 1% elastic scattering for a 0.5 micron thick specimen at 80 keV[1,7]. It is worth noting that the spectral maximum is at the zero energy loss, even for the 0.7 micron thick specimen. We further investigated the energy loss spectra as a function of aperture sizes (fig.2). We showed that the application of the objective aperture increases the relative number of elastically scattered electrons contributing to the image, as relatively more inelastically scattered electrons are blocked out by the aperture. This is in agreement with the angular resolved EELS analysis done by Reimer et al[8]. Depending on the specimen, the relative increase in the amount of elastically scattered electrons is different. For some specimens, the proportional increase of elastically scattered electrons can be up to 45% when applying a small objective aperture.

We showed that with electron spectroscopic imaging of thick biological specimens, much of the chromatic aberration effects due to multiple inelastic scattering are excluded from the image formation (fig.3a). We showed that high resolution signal is present when imaging using the plasmon energy loss electrons (25eV loss) (fig. 3b). Images taken with an energy window covering the zero to 25eV energy losses are not significantly degraded from chromatic aberration when compared with the zero-loss filtered image (fig. 3c).

We calculated the approximate elastic mean free path for our 0.3 micron thick specimen to be 250 nm at 200 keV. Extrapolated to 300 keV, the approximate mean free path is 540 nm. This implies that the electron-specimen interactions for a 0.7 micron thick epon-embedded specimen at 300 keV will

microscope lens aberration correction using multiple focus images. See our abstract, "Image Reconstruction Using a Focus Series on Thick Biological Specimens-- TEM CTF Correction," elsewhere in these proceedings for a discussion of this method.

References
1. Olins, A. et al. J Microscopy **154** (1989) 257.
2. Colliex, A. et al. J Microscopy **153** (1989) 1.
3. Gubbens, A. and Krivanek, O. Proc. 50th Ann. EMSA (1992) 1570.
4. Bazett-Jones, D. Electron Microsc. Rev. **5** (1992) 37..
5. Reimer, L. and Ross-Messemer, M. J. Microscopy **155** (1989) 169.
6. Reimer, L. and Ross-Messemer, M. J. Microscopy **159** (1990) 143.
7. Reimer, L. et al. J. Microscopy **155** (1991) 3.
8. Reimer, L. and Rennekamp, R. Ultramicroscopy **28** (1989) 258.

Figure Captions
1. EELS of 0.3, 0.5, 0.7 micron specimen at 200 keV, normalized to total counts.
2. EELS of 0.7 micron specimen using 40, 30, 10-micron apertures, and no aperture.
3a. Zero-loss image of a 0.7 micron specimen.
3b. Plasmon energy loss (25 eV) image of a 0.7 micron specimen.
3c. Zero to 25 eV loss windowed image of a 0.7 microns specimen.
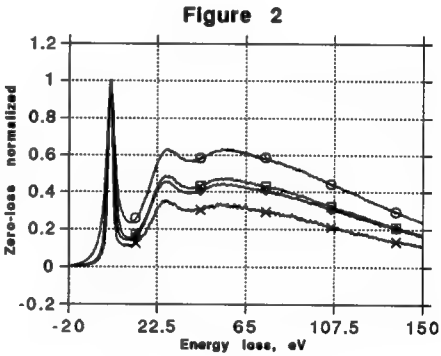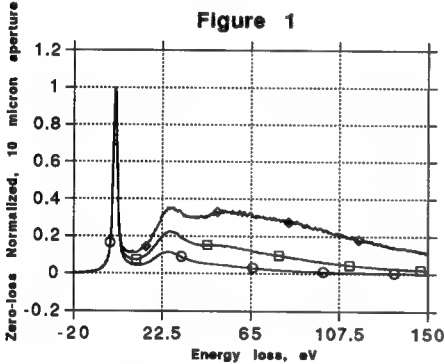
IMAGE COMPRESSION AND DATA INTEGRITY IN CONFOCAL MICROSCOPY

Gopal B. Avinash

NORAN Instruments, Inc., 2551 W. Beltline Hwy, Middleton WI 53562

In confocal microscopy, one method of managing large data is to store the data in a compressed form using image compression algorithms. These algorithms can be either lossless or lossy. Lossless algorithms compress images without losing any information with modest compression ratios (memory for the original / memory for the compressed) which are usually between 1 and 2 for typical confocal 2-D images. However, lossy algorithms can provide higher compression ratios (3 to 8) at the expense of information content in the images. The main purpose of this study is to empirically demonstrate the use of lossy compression techniques to images obtained from a confocal microscope while retaining the qualitative and quantitative image integrity under certain criteria.

A fluorescent pollen specimen was imaged using ODYSSEY, a real-time laser scanning confocal microscope from NORAN Instruments, Inc. The images (128 by 128) consisted of a single frame (scanned in 33ms), a 4-frame average, a 64-frame average and an edge-preserving smoothed image of the single frame. Images were compressed with (1) the lossless Lempel-Ziv-Welch (LZW) algorithm and (2) a lossy algorithm called Joint Photo Experts Group (JPEG) standard. Using the JPEG algorithm, one can trade-off between the image quality and the compression ratio by changing a quality control factor called the Q-value. The following criteria were used for determining the acceptability of the information content of images: (1) In the qualitative visual criterion, a decompressed image that could not be visually distinguished from the original was acceptable. (2) In the global quantitative criterion, a decompressed image was acceptable if the variance of the difference image defined as (original image - decompressed image) was less than 10% of the variance of the image noise computed from a "uniform" background in the image. (3) In the local quantitative criterion, a decompressed image was acceptable if the local quantitative measurements such as profiles made on the original matched well with those made on the compressed image.

Figure 1 shows the compression ratios obtained at various Q-values. The JPEG compression yielded better compression ratios at lower Q -values but the difference variance was higher than 10% of the noise variance (Figure 2 and Table 1). Figures 3 and 4 show the original and the decompressed images (64 frame average) at a Q-value of 75 using JPEG. Note that these images are visually indistinguishable from one another. As shown in Figures 5-8, at this Q-value, the intensity profiles are within the variations due to the noise in these images indicating the quantitative integrity of the compression. As can be expected, better quantitative agreement was obtained for images containing less randomness (image noise). For these images, lossless compression did not provide any compression at all. This empirical study, therefore, suggests that the lossy JPEG compression can qualitatively and quantitatively maintain image integrity when used with an appropriate Q-value. Further, the results imply that when the same qualitative and quantitative information is available, one can take advantage of the better compression of a lossy method.
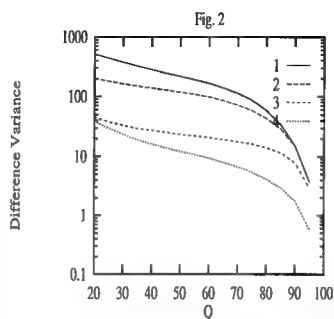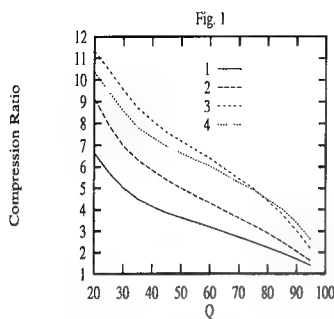
Fig. 1

Fig. 2

Fig. 3

Fig. 4

Fig. 5

Fig. 6

Fig. 7

Fig. 8
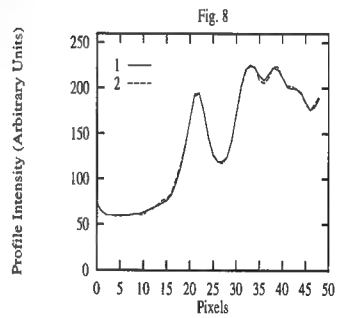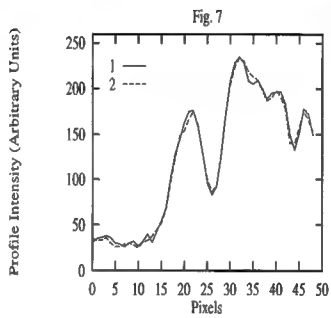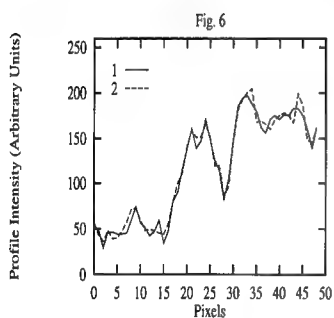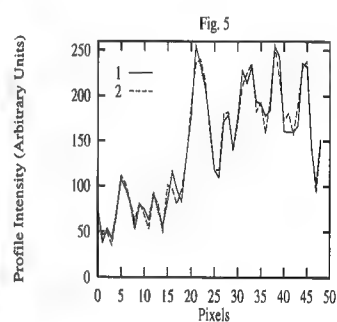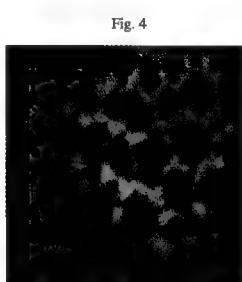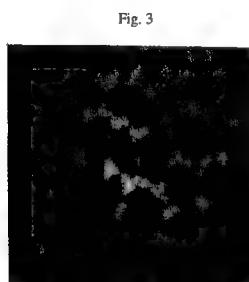
Fig. 1 Compression ratio decreases with increasing Q-values. 1) 1-frame; 2) 4-frame average; 3) 64-frame average; 4) 1-frame smoothed with an edge preserving algorithm.

Fig. 2 Difference variance and hence the image integrity increases with increasing Q-value. 1) 1-frame; 2) 4-frame average; 3) 64-frame average; 4) 1-frame smoothed.

Fig. 3 Original pollen image (128 by 128) 64-frame average.

Fig. 4 Compressed/decompressed version of Fig. 3 at Q-value of 75.

Fig. 5 - Fig. 8 Intensity profiles along the same location in 1) original and 2) compressed/ decompressed images from 1-frame, 4-frame average, 64-frame average, and 1-frame smoothed respectively at Q-values of 75.

207

IMAGE PROCESSING TO EXTRACT LINE INFORMATION FROM MICROGRAPHS

John H. Turner, Michael A. O'Keefe and Sidnei Paciornik◇

National Center for Electron Microscopy, University of California, LBL B72, Berkeley, CA 94720
◇Permanent address: D.C.M.M. - PUC/Rio, P.O. Box 38008, Rio de Janeiro, 22452 RJ, Brasil

In processing microscope images, it is sometimes important to be able to extract the lengths and directions of linear features. For example, in characterizing transmission electron microscope images of faceted grain boundaries, the desired information is the length of grain boundary lying along each direction[1]. In this case we require the sum of the lengths of the facets as a function of direction, but not their positions.

The problem of having the computer recognize and extract lines from images is not trivial. In order to measure grain boundary lengths automatically, micrographs must be digitized and the linear features (e.g. the grain boundaries) binarized and reduced to a single pixel width. Then the problem requires finding two simple parameters for each line in the image, its direction and number of pixels. A new approach to this problem is to project the intensities of the source image in all possible directions, and to collect the projection results into a new two-dimensional "image" with one dimension representing the projection direction. This new image is the sinogram of the source image[2]. Each peak in the sinogram represents a line, with one coordinate of the peak equal to the line's angle, and the other to its position (actually, the perpendicular distance of the line from the center of rotation of the source image). Intensities of peaks in the sinogram should then be equal to the numbers of pixels in the equivalent lines. Images were also processed using the very similar Hough transform[3], but this produced less-discernible peaks and significantly less-accurate line lengths. Figure 1 shows a typical test picture of 512x512 pixels.

Because lines in a digital image are "pixelated" (fig. 2a), the ratio of the number of pixels (p) to the line length (r) varies with angle. Once the number of pixels in each peak is determined, the peak values are transformed into line lengths by dividing by the cosine of the angle (from $0°$ to $45°$ and $135°$ to $180°$), or the sine ($45°$ through $135°$). Because of "pixelation", the number of different angles at which lines can be drawn in a digital image is limited; for an image of nxn pixels, a useful number of sampling angles is 2n, giving an angular resolution of $90°/n$; for a 512x512 image this value is $0.18°$. In using the sinogram peak to determine the number of pixels in a given line, two adjacent pixels are used because most pixelated lines project as two pixels (except for the special cases of $0°$, $90°$ and $45°$). Figure 2b illustrates how the peak pixel (A) and the highest pixel next to it (A') are summed and the next-highest pixel (B) subtracted as a measure of the background caused by the presence of other lines in the source image.

The algorithm for the sinogram of an nxn (square) binary image over 2n angles was written as a library function in the image processing program Semper[4]. Figure 3 shows the sinogram of the 512x512 test picture in figure 1. The accuracy of the method is illustrated in figure 4 by plotting sinogram results for length (a) and angle (b) against original values in the test image, and percentage errors (c,d). Length error is less than 8% for all the lines, except the shortest, and two (1 and 2 in fig. 1) that meet at a low angle of $5°$; the sinogram peaks from these two lines interfere because they lie in each other's "wake" and thus include high background levels. Angular error is less than $0.3°$ for all lines longer than 50 pixels.[5]

References
1. U. Dahmen and K.H. Westmacott, *Mat. Res. Soc. Symp. Proc* **229** (1991) 167-178.
2. J. Radon, *Berlin Sächsische Akad. Wissen.* **29** (1917) 262-279.
3. P.V.C. Hough, U.S. Patent 3,069,654 (1962).
4. W.O. Saxton, T.J. Pitt and M. Horner, *Ultramicroscopy* **4** (1979) 343.
5. This work was supported by the Director, Office of Energy Research, Office of Basic Energy Sciences, Material Sciences Division of the U.S. Department of Energy, under contract No. DE-AC03-76SF00098. SP acknowledges support from Conselho Nacional de Desenvolvimento Científico e Tecnológico -CNPq, Brasil.
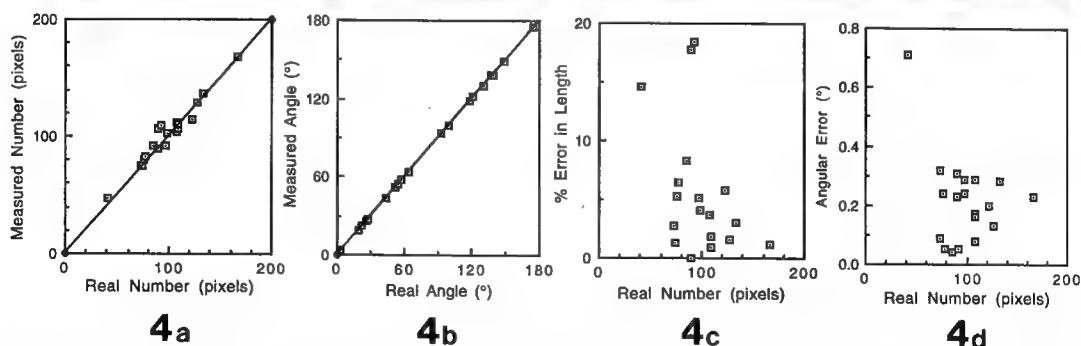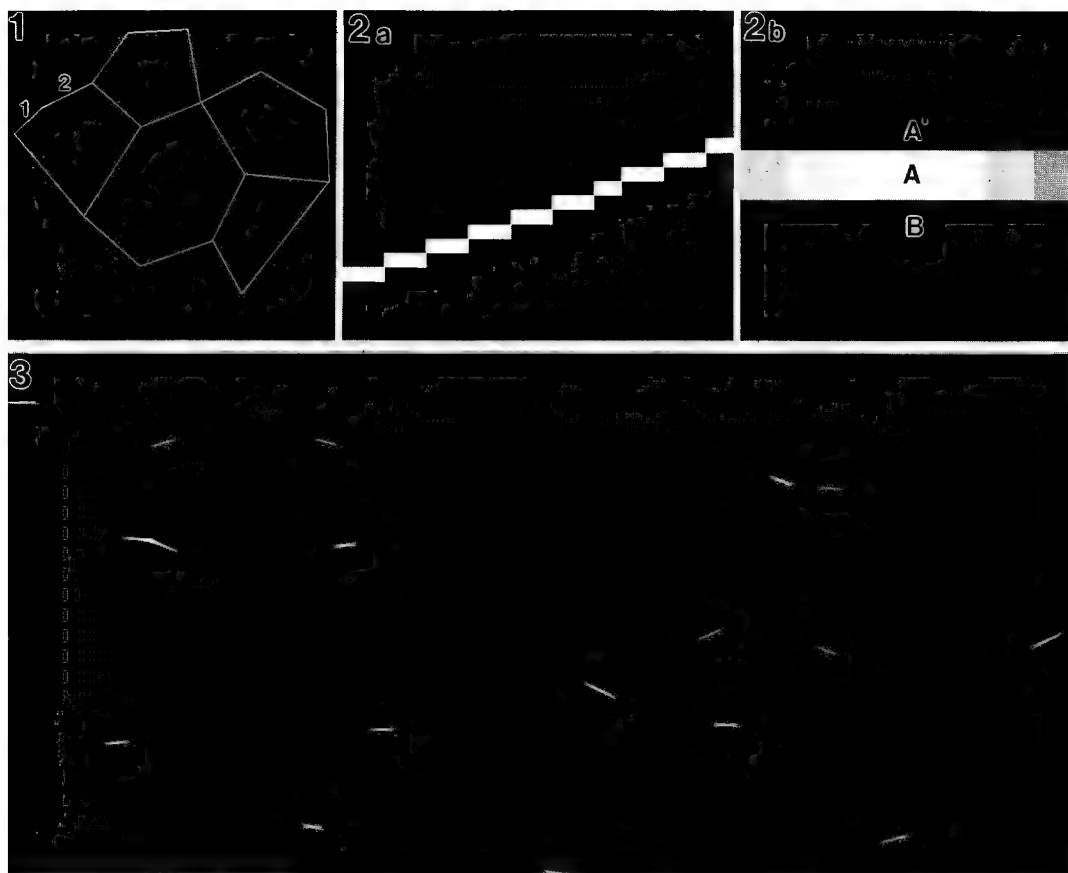
Figure 1. Test picture containing 19 lines, including two (marked 1 and 2) that are only 5.2° apart. All lines lie within an interior circle in order to simplify the implementation of the sinogram transform

Figure 2. (a) Blow up of a typical line showing pixelation. (b) its sinogram peak showing the two line pixels (A and A'), and the background pixel (B).

Figure 3. Sinogram of the test image in figure 1 from 0° (left) to 180° (right). Each line now appears as a surface that "folds" to a point as the projection direction becomes parallel to it.

Figure 4. Line lengths (a) and angles (b) extracted by sinogram from the test image plotted against the lengths and angles of the lines in the test image. Percentage error in line length (c) and angular error (d).

PROCESSING OF HIGH-RESOLUTION IMAGES OF IRRADIATED CERAMICS

M.E. Lewis, L.C. Qin, A.N. Sreeram, L.W. Hobbs

Department of Materials Science and Engineering
Massachusetts Institute of Technology
Cambridge, MA 02139

Mathematical morphology as an image processing and analysis tools is both a science and an art. The theory of mathematical morphology is rooted in topology, where a set-theoretic framework is the basis of binary morphology. Gray-scale morphology is an extension into the space of functions. This rigorous formulation has provided powerful transformations, operating directly on the information content of an image.[1] However, it is up to the investigator's creativity to devise the appropriate criteria for each problem at hand.

The main focus of the present study is the analysis of image contrast and the relationship with the underlying structure of the material. Image processing and analysis methods based on mathematical morphology were applied to high resolution micrographs of irradiated ceramics: electron-irradiated tridymite[2] and ion-irradiated lead pyrophosphate single crystal[3].

The interesting feature of these images is the presence of periodic, aperiodic and partially ordered structures, Fig.s 1a and 2a. Specific criteria for detecting these different contrast patterns are presently being developed and tested. Since contrast enhancement plays an important role in texture characterization, several morphological filters were applied as an alternative to the Fourier space methods[4]: alternating sequential filters (ASF) and grey-level top hat. This approach explores the information present in the spatial domain of the image. These filters resulted in a certain degree of homogenization of the image background and an enhancement of the contrast level.

The ASF filters comprise a series of openings and closings, which are less drastic operators than erosion or dilation. By increasing the size of the ASF filter, details of increasing size are removed. The grey-level top hat is another filter that detects structures based on contrast and is shown in Figs. 1b and 2b. There are inumerable variations of these filters, each adapted to the specific features of the image.

In order to detect the variations in contrast periodicity, the distance transform was applied to binary images, obtained by filtering and thresholding the original images. The distance function associates with each point of the image the distance to the background. Some initial results are shown in Figs. 1c and 2c. Though not conclusive, there are indications of increased distance in the aperiodic regions of the image.

There is yet so much more to explore, develop and test, that these preliminary results provide only an indication of what future research may bring forth for the application of mathematical morphology techniques to high-resolution electron microscopy images.[5]

References

1. J. Serra, Image Analysis and Mathematical Morphology, London: Academic Press (1982).
2. L.C. Qin, these proceedings.
3. A.N. Sreeram, L.W. Hobbs, Mat. Res. Soc. Symp. Proc. A8.6 (1993), in press
4. J.C. Russ, Computer-Assisted Microscopy, New York: Plenum Press (1990).
5. The authors acknowledge H. Talbot, CMM, for helpful discussions.
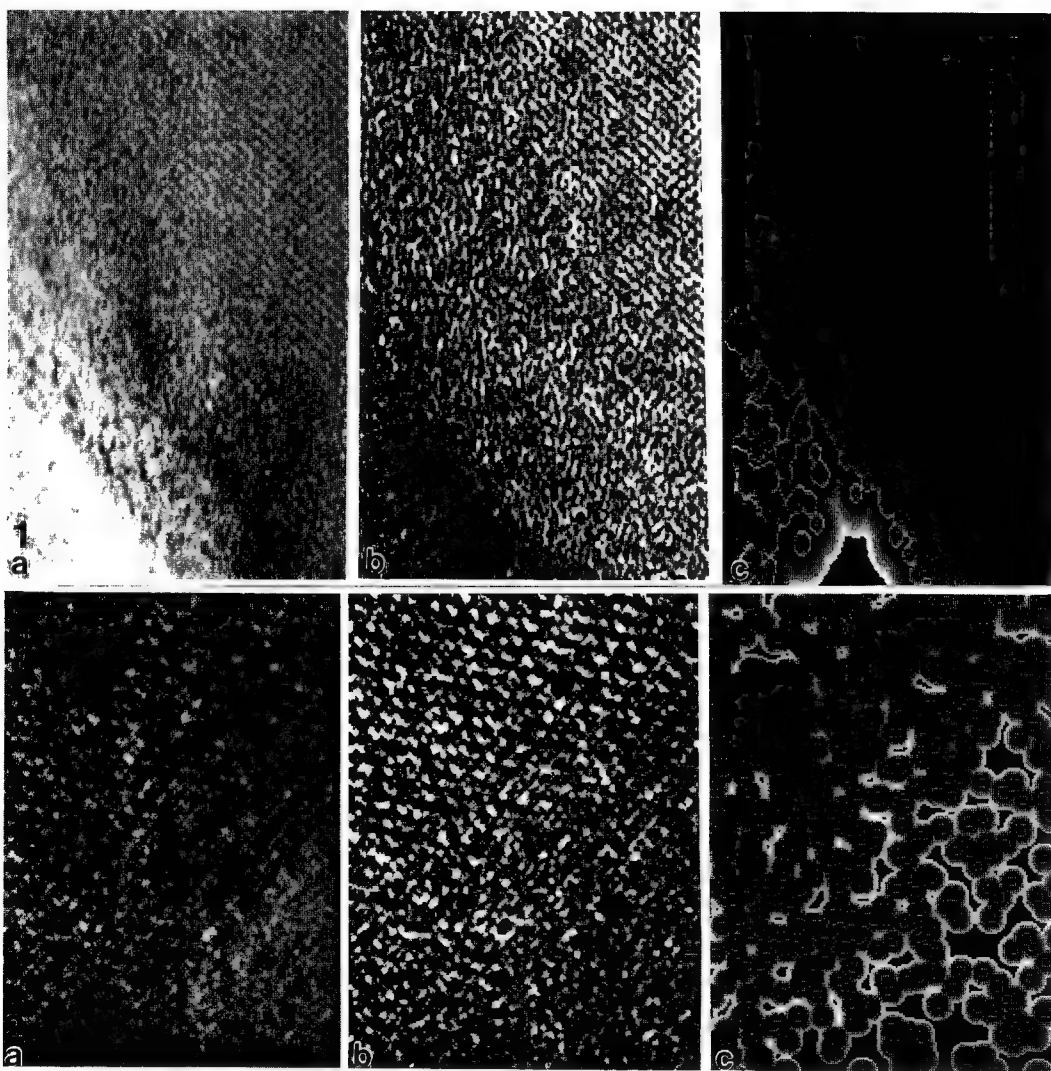
Figure 1. Image processing of HREM micrograph of irradiated-tridymite:
(a) original image with three well defined texture regions; (b) application of the white top hat transform of size 6; (c) distance transform.

Figure 2. Image processing of HREM micrograph of irradiated lead pyrophospate (single crystal):
(a) 256X256 section of original image with two distint textures; (b) application of white top hat transform of size 4; (c) distance transform.

NEW DIGITAL IMAGE PROCESSING TECHNOLOGY FOR FSEM MICROSCOPY

Klaus-Ruediger Peters* and Eisaku Oho**

*Molecular Imaging Laboratory, Biomolecular Structure Analysis Center, University of Connecticut
Health Center, Farmington, CT 06030-2017
** Department of Electrical Engineering, Kogakuin University, Tokyo 163-91 JAPAN

Digital image acquisition and processing can provide many advantages over conventional analog image information handling, i.e., undisturbed access to the "raw data set",[1] quantitative analysis of the image information, and reduced costs and increased flexibility of image data handling. However, it may principally change microscopy by providing a new facility for instant exhaustive data presentation in acquired images. Detail imaging is one of the basic microscopic tasks but visual access to detail information is cumbersome and often left to post-session data analysis. A dedicated software/hardware technique is now available for automatic "near-real-time" enhancement of image detail information visually not accessible in the "raw data" image. Pertinent image details include spatial dimensions of only a few pixels in size (spatial details) and intensity variations of only a few intensity steps in height (intensity details). While conventional image enhancement techniques often produce serious image artifacts which exclude a closer inspection of enhanced detail information, the new pixel-accurate processing (PAP) technology allows instant image evaluation at an accuracy-level of the raw data through detail enhancement in full-frame images,[2] digital zoom and noise smoothing. Adequate high speed processing is provided by a 486/50 MHz PC using a high level AP_x parallel processing technology (PAP IMAGE WORKSTATION, Molecular Visions, Science Park, New Haven, CT 06511).

Most important in detail evaluation is the management of noise inherent to most microscopic images. In single images, smallest intensity fluctuations can not be classified as noise or data and may be reduced only at cost of spatial detail loss. However, processing artifacts of such data reduction should be kept at a minimum. The noise smoothing capability of the PAP imaging system was evaluated using a test pattern derived from Gaussian noise of +/- 4 standard deviations (SD) width (1024x1024x8bit, mean pixel value of 127, minimum and maximum pixel values of 43 and 211, standard deviation of 21, and 0.000% clipping). A superimposed special test pattern consisted of only one pixel wide features, i.e., two perpendicular double lines of 0 and 255 intensities, and two sets of small crosses of either +/- 2 SD (top half) or +/- 3 SD (bottom half) intensities (Fig. left: circles). PAP smoothing at a +/- 2 SD intensity level maintained all features and noise pixels of higher/lower intensity values without distorting their spatial integrity (Fig. right: arrow heads) and improved dramatically their S/N ratio. Commonly, noise reduction algorithm utilize spatial masks (in the space or Fourier domain) and may produce spatial distortions of image details at a maximum level set by the mask size. The PAP technology maintains the spatial integrity of image details at the raw data pixel level and thus is ideally suited for image processing in microscopy in which the primary objective is detail acquisition and evaluation.

We expanded our analog FSEM (JEOL JSM-890) with a SEMICAPS image acquisition and provided it with a large "raw data" display (see schematic). After acquisition, the raw data image was automatically PAP processed and displayed on a same-sized monitor side-by-side with the raw data. PAP image evaluation produced a large number of image documents which were cost-efficiently protocolled with a video printer. All images acquired during a session were documented through a session editor with a laserjet printer on plain paper. The PAP image evaluation became an essential tool for FSEM work since it reduces excessive image acquisitions and refined in-depth data analysis and presentation. In addition, PAP evaluation was effective on all other images irrespective of origin, content , size or depth.[3]

References
1. E. Oho and K. Kanaya , Scanning 12(1990), 141.
2. E. Oho, Scanning 14(1992),335.
3. Supported by Connecticut Department of Economic Development Grant 92H018 and Seikosha Co., LTD., Japan providing a prototype 4500 video printer.
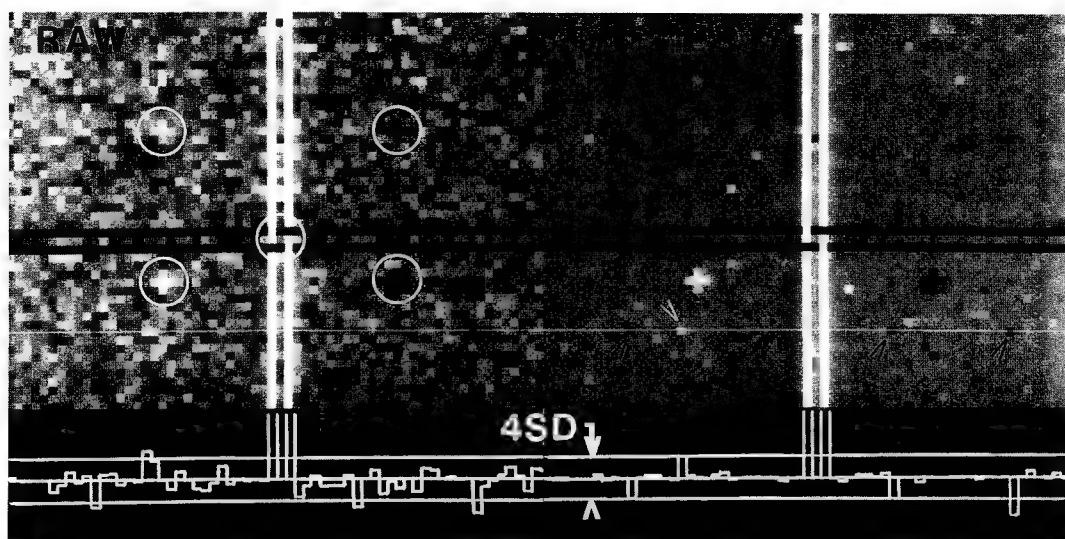
Digital FSEM: Pixel-Accurate Processing (PAP)
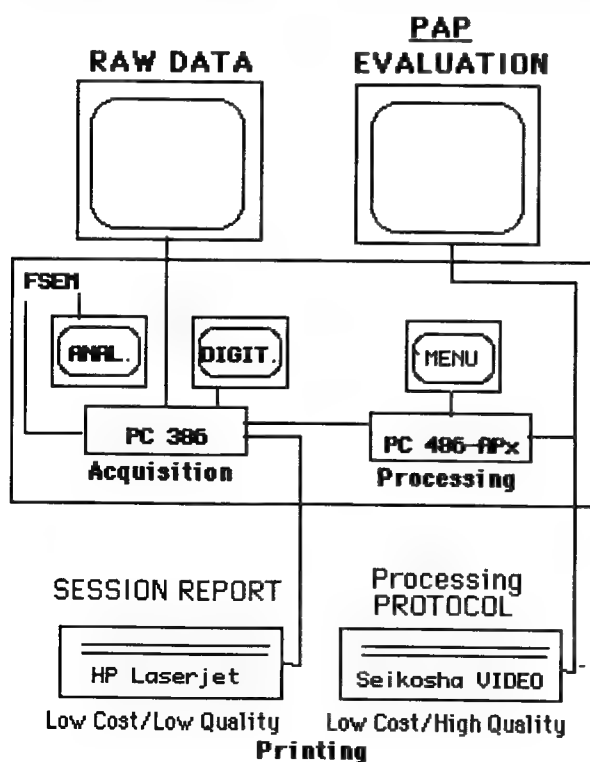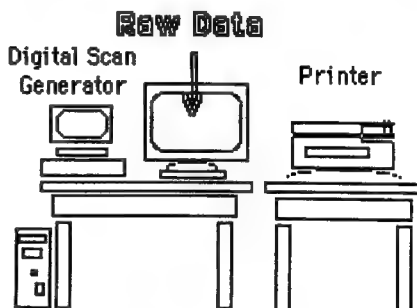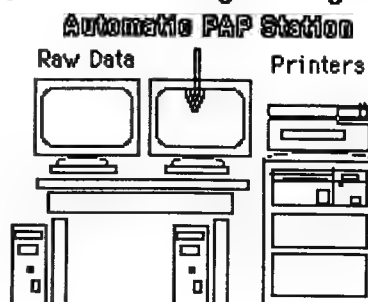
CHARACTERIZATION OF HF-TREATED Si(111) SURFACES USING REM, SEM, AND XPS

Y. Ma, S. Lordi and J. A. Eades

Materials Research Laboratory, University of Illinois at Urbana-Champaign

The imperfections on silicon wafers have become more and more crucial as the dimensions of integrated circuits are progressively reduced in the submicron range. The problems relating to the HF acid etching of Si surfaces have recently been studied using different techniques.[1,2] It has been found that Si-H bonding is responsible for the passivation of HF-treated surfaces[3], and the roughness of the surfaces is related to the pH value of HF acid used for etching.[4] The roughness of those surfaces was in most cases characterized indirectly by the width of the Si-H absorption peaks in IR spectra. Only in limited cases, were they studied by STM, a direct imaging technique.[5]

Here, we try to characterize the HF-treated Si(111) surfaces using direct imaging techniques, REM and SEM and a spectroscopy technique, XPS. The morphology of Si(111) surfaces HF-treated under different conditions was directly imaged in TEM, and SEM for comparison. The chemical status of these processed Si(111) wafers was examined by XPS to confirm the cleanliness and passivation of the treated surfaces. The Si(111) surfaces were first thermally and chemically oxidized for the removal of the damage caused by polishing, before HF treatment. Fig.1 shows three REM images of the Si(111) surfaces dipped for 10 minutes in three HF solutions whose pH value were chemically adjusted by NH_4F, NH_4OH and HCl: pH=1.0(a), 4.0(b) and 9.5(c). The RHEED pattern on the corner of each picture shows the spot used for imaging and indicates that the identical imaging condition was used for each image. The images demonstrate that the surface roughness of HF-treated Si(111) is related to the adjusted pH-value of HF: rough with pH<4.0, smoother with pH>4.0 and the best around pH=9.5. This is consistent with the finding of IR absorption spectroscopy.[4] The reason why the atomic steps of the passivated surface were not seen in the REM images is likely to be the low vacuum in a conventional TEM and the ionization of H atoms by the high energy electron beam of the TEM. Since SEM is more a convenient surface imaging technique and it is necessary to confirm what was observed using REM by comparing it with different techniques, SEM analysis was also carried out. Fig.2 shows three images of the surfaces corresponding to Fig.1. The surface was tilted such that the angle between the electron beam and the surfaces was about 10° in order to enhance the contrast. Thus the geometry was similar to that of REM analysis. It is clear that what was observed in SEM was consistent what was seen in the REM mode. Fig.3 shows the XPS survey spectra of the thermally and chemically oxidized Si(111) surface (a) and the HF-treated Si(111) surface shown in Fig.1(b) and 2(b) (b). Both O and C signals drop dramatically after the treatment, which means that the surface was cleaned and passivated.

1. B. F. Phillips et al., J. Vac. Sci. Technol., A1(2)(1982)646.
2. D. Graf et al., J. Vac. Sci. Technol., A7(3)(1988)808.
3. H. Ubara et al., Solid State Comm., 50(1984)673.

4. G. S. Higashi et al., Appl. Phys. Lett. 56(7)(1990)656.
5. G. S. Higashi et al., Appl. Phys. Lett. 58(15)(1991)1656.
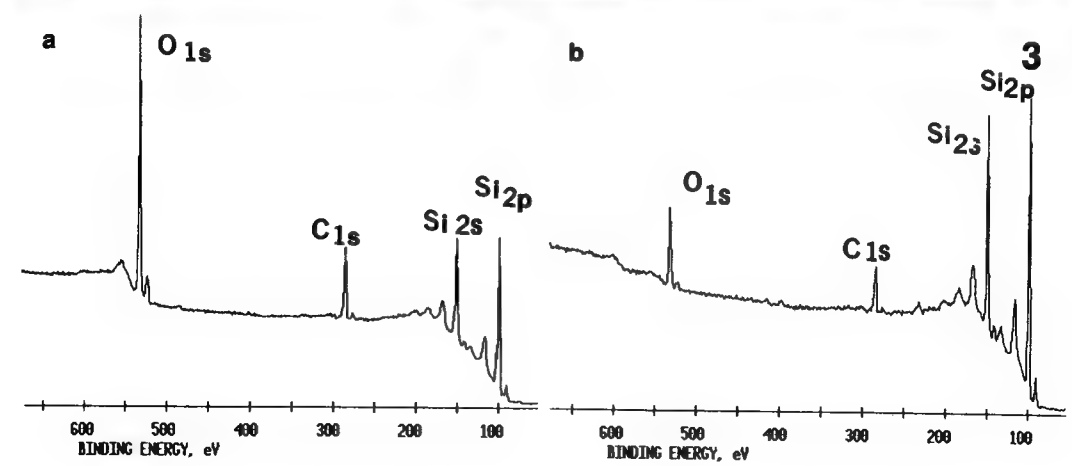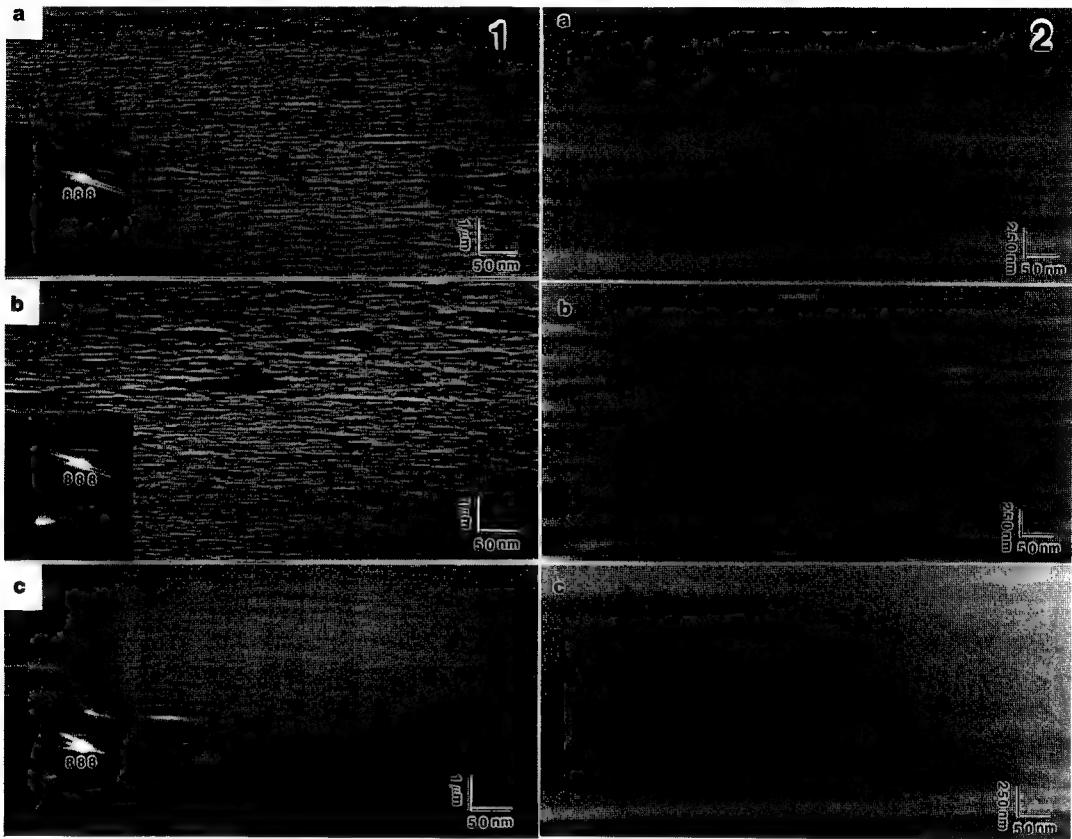
GENDER DETERMINATION OF CAUCASOID HAIR USING IMAGE ANALYSIS

T.B. Ball* and W.M. Hess**

*Department of Ancient Scripture and **Department of Botany and Range Science, Brigham Young University, Provo, UT 84602

It has been demonstrated that cross sections of bundles of hair can be effectively studied using image analysis.[1,2] These studies can help to elucidate morphological differences of hair from one region of the body to another.[2] The purpose of the present investigation was to use image analysis to determine whether morphological differences could be demonstrated between male and female human caucasian terminal scalp hair.

Hair samples were taken from the back of the head from 18 caucasoid males and 13 caucasoid females (Figs. 1-2). Bundles of 50 hairs were processed for cross-sectional examination[1] and then analyzed using Prism Image Analysis software on a Macintosh IIci computer.[3] Twenty morphological parameters of size and shape were evaluated for each hair cross-section. The size parameters evaluated were area, convex area, perimeter, convex perimeter, length, breadth, fiber length, width, equivalent diameter, and inscribed radius. The shape parameters considered were formfactor, roundness, convexity, solidity, compactness, aspect ratio, elongation, curl, and fractal dimension.

ANOVA and Tukey HSD Multiple Comparison tests of the data obtained indicated that the means of all of the parameters of size differed significantly ($p \leq 0.05$) between male and female hair, but of the parameters of shape, only extent and aspect ratio differed. Discriminant analysis based on the parameters that differed was able to correctly classify 58% of male and 68% of female samples. Tests for adequate sample size indicated that 25 hairs from 10 individuals was sufficient to estimate within 10% of the population mean at a 95% confidence level for any of the parameters considered.

References

1. W. M. Hess and R. E. Seegmiller, Trans. Am. Microsc. Soc. (1988)107, 421.
2. W. M. Hess, R. E. Seegmiller, J. S. Gardner, J. V. Allen, and Susan Barendregt Scanning Microsc. (1990)4, 375.
3. T. Ball, J. S. Gardner, D. A. Johnson and W. M. Hess, Phytopathology (1992)82, 1168.
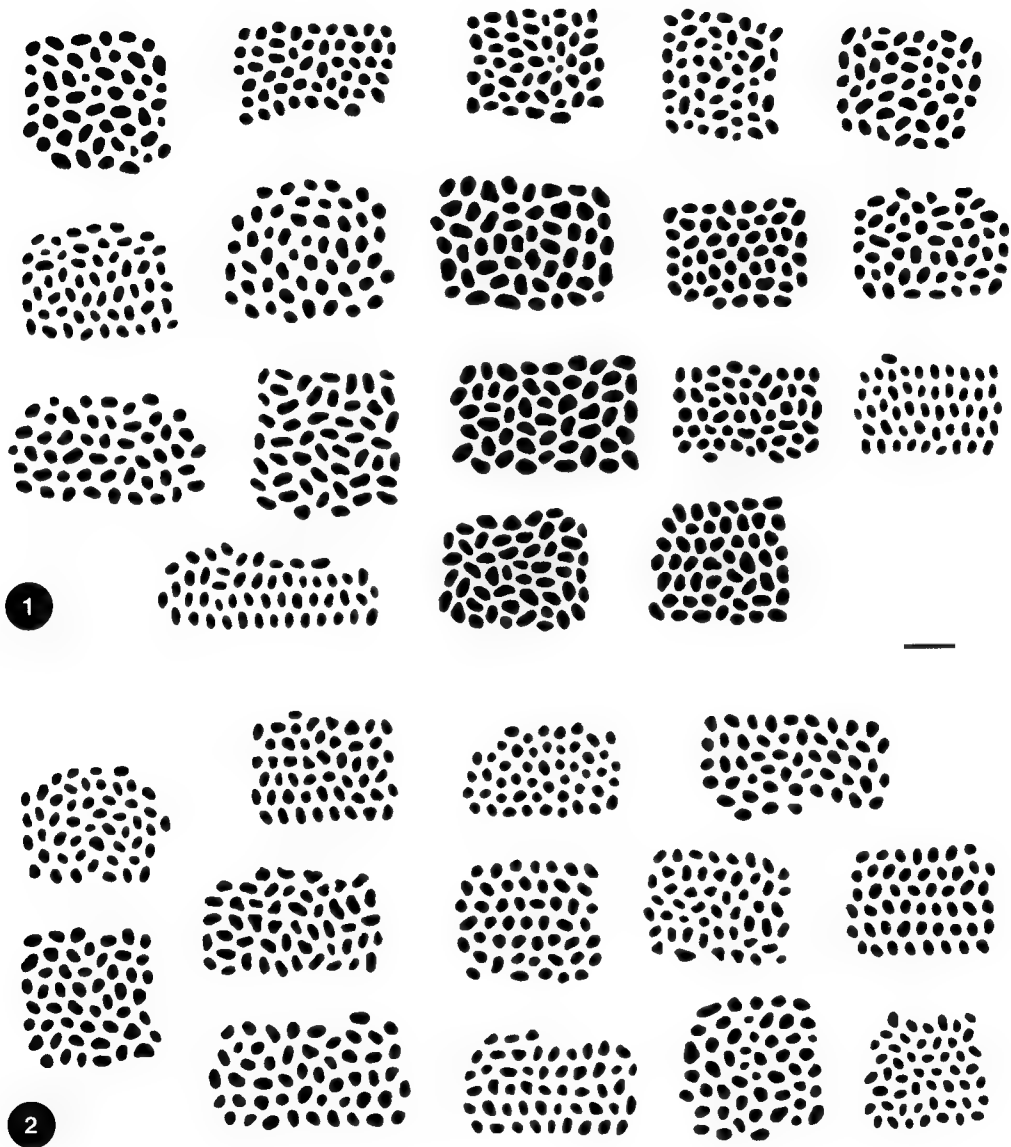
FIG. 1.   Cross section images of male caucasoid terminal scalp hair samples.
FIG. 2.   Cross section images of female caucasoid terminal scalp hair samples.
Bar = 100 μm.

THE VERSATILITY OF THE LIGHT MICROSCOPE IMAGE ANALYZER

E.L. Cardell and R.R. Cardell

Department of Anatomy and Cell Biology, University of Cincinnati
College of Medicine, Cincinnati, OH 45267

The centralization of resources means equipment and technical staff
must be versatile since their services will be used by various
investigators evaluating different applications and tissues. The
Nikon Microphot light microscope (LM) equipped with MTI video
camera, Gateway 2000 computer, Image-1 imaging system, and Sony
Color Video Printer is helpful for the evaluation of sections of
tissue from different projects, most of which are also electron
microscope studies that benefit from LM analysis. The high
resolution prints are immediately available to the researcher. The
various computer manipulations facilitate the visualization of
routinely stained sections and sections after autoradiography, β-
galactosidase localization, and immunogold-silver cytochemistry,
etc. Monochrome or color prints are possible with the display
modes provided, or display modes may be edited as beneficial for a
particular application. We have designed display modes that allow
monochrome and color images in the same print. NIH Grant DK27097.

Fig. 1.   Mitotic figures in Absolute Mode; Microtubules and
            condensed chromosomes are outstanding in these routinely
            stained sections. Bar, 20μm.
Fig. 2A.   Brightfield immunogold localization of PEPCK in
            hepatocytes after silver enhancement. The enzyme is
            located in glycogen regions only. Bar, 10μm.
      2B.   Negative image of 2A in which the gold particles resemble
            a darkfield image. Bar, 10μm.
Fig. 3.   Semithin epon section of pancreatic acinar (A) cells
            stained with toluidine blue. The secretory granules (G),
            acinar cells and ducts (D) differ in contrast to allow
            easy distinction. Bar, 20μm.
Fig. 4.   Semithin epon section of kidney, toluidine blue stained.
            Proximal (P) and distal (D) convoluted tubules are
            readily distinguished as are ducts (*) and glomerulae
            (G). This image contrast was enhanced by "Adjust
            Digital" manipulation of a low contrast stored image.
            Bar, 50μm.
Fig. 5A.   Brightfield image of transfected cells expressing *lacZ*.
            The bacterial β-galactosidase reaction product is easily
            viewed in semithin epon sections not counterstained.
      5B.   Darkfield image of 5A. Bars, 20μm.
Fig. 6.   PAS stained liver without counterstain. Both clumped and
            dispersed glycogen can be seen. Bar, 20μm.
Fig. 7.   Brightfield (A) and negative (B) images of developing
            mouse cortex 24 hours after 1 hr ^{3}H-thymidine pulse
            reveals the large number of neuroepithelial cells that
            had entered S-phase. Bars, 20μm.

218
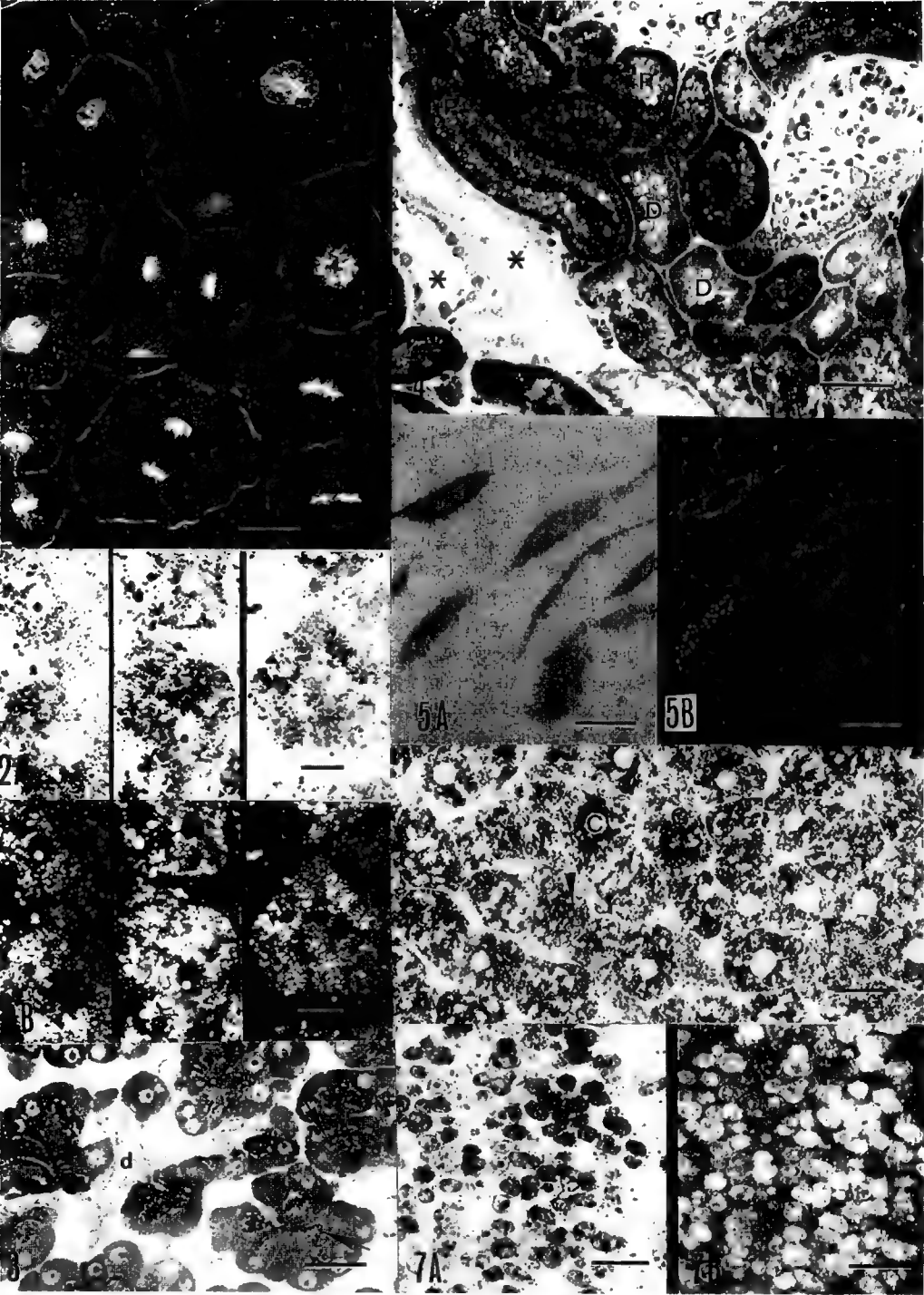
STANDARD FORMATS FOR THE EXCHANGE AND STORAGE OF IMAGE DATA

R.F. Egerton[α], D.S. Bright[β], S.D. Davilla[γ], P. Ingram[δ], E.J. Kirkland[ε], M. Kundmann[φ], C.E. Lyman[η], P.Rez[φ], E. Steele[β] and N.J. Zaluzec[κ]

[α]Physics Department, University of Alberta, Edmonton, Canada T6G 2J1;
[β]National Institutes for Science and Technology, Gaithersburg, MD 20899, USA;
[γ] 4pi Systems, 117 West Lynch St., Durham, NC 27701-1929, USA;
[δ]Departments of Cell Biology and Physiology, Duke University, NC 27710, USA;
[ε]Department of Applied Physics, Cornell University, NY 14853, USA;
[φ]Gatan Inc., 6040 Washington Street, Downers Grove, IL 60516, USA;
[η]Department of Metallurgy, Lehigh University, Bethlehem, PA 18015, USA;
[φ]Physics Department, Arizona State University, Tempe, AZ 85281, USA;
[κ]Electron Microscopy Center, Argonne National Laboratory, Illinois 60439; USA

In microscopy, there is an increasing need for images to be recorded electronically and stored digitally on disk or tape. This image data can be shared by mailing these magnetic media or by electronic transmission along telephone lines (e.g. modem transfer) or special networks, such as Bitnet and Internet. In each case, the format in which the image is stored or transmitted must be known to the recipient in order to correctly recover all the information. Because there are many image formats to choose from, it would undoubtedly save misunderstanding and frustration if a group of individuals with similar interests and needs could agree upon a common format. The MSA Standards Committee has surveyed several formats which could be of particular interest to microscopists, with a view to making a recommendation to our community.[1]

Our chief concern has been compatibility with existing software, combined with an adequate representation of the data, compactness of data storage (on disk) and reasonable rate of data transfer. In some forms of microscopy, the image intensity covers a wide dynamic range, demanding a large number of bits per pixel or representation by floating-point numbers. Although data transfer rates can be increased through various forms of data compression, compactness of storage demands that the image be represented in binary code rather than in more immediately readable ASCII numbers. The formats which we have considered include raw binary files, PICT, GIF, FITS, TIFF and HDF. A raw binary file is highly compact but not self-describing: the dimensions of the data array have to be specified external to the dataset. Such a format is too rigid for general use.

PICT is the main graphics format used by Macintosh computers and is recognised by many software programs. In its most recent manifestation (PICT2), grey-scale and color images are supported. Data can be represented by 8-, 16- or 32-bit integers and the file contains other information describing the image. But because this format is not commonly supported by computers which use the DOS and Unix operating systems, we do not recommend PICT as a general standard.

GIF (Graphics Interchange Format) was originally developed for the interchange of files over

the Compuserve network. A compression scheme can be used to compact the data and thereby shorten the transmission time. Support for color tables is included, but not floating-point numbers, so we feel that this format is not flexible enough for general microscopy.

FITS (Flexible Image Transport System) is a standard format used by optical and radio astronomers. It is capable of handling large, multidimensional arrays and can support several data types, including ASCII characters, 8-, 16- and 24-bit integers and floating-point numbers. Each file contains a header (written in ASCII text) to describe the data, which is usually in binary form.

TIFF (Tagged Image File Format) was developed jointly by the Microsoft and Aldus companies in order to store images from scanners and other desktop-publishing equipment in a machine-independent form. It has become the mostly widely used format for Macintosh and IBM-type personal computers. The data itself can be stored as 8-,16-, or 32-bit unsigned integers, and (in version 6.0) as signed integers and floating-point numbers. Besides the picture data, a TIFF file may contain supplementary information concerning the ownership, acquisition conditions etc., and even extensive documentation about the image. Each particular element of information is identified by a tag - a label which the computer needs to interpret the information.

HDF (Hierarchical Data Format) was developed by the National Centre for Supercomputing Applications (NCSA) at the University of Illinois (Urbana). It uses a machine-independent binary-file standard for recording matrix arrays and other types of scientific data, which can be quite extensive. This format permits flexibility; for example, subarrays corresponding to part of an image can be accessed for read/write purposes. Data are stored as 1- or 3-byte integers, or as floating-point numbers, in a binary-format continuous-byte file (not subdivided into blocks).

We see both TIFF and HDF as suitable formats for microscopy. In terms of immediate use, TIFF has the largest amount of support; it is used by all IBM-PC and Macintosh page-scanner programs, by page-layout applications such as Ventura Publisher, QuarkXPress and Aldus PageMaker, and by image-editing programs such as Image, Digital Darkroom, Photoshop, ImageStudio, ImageEdit and Snapshot. Because these applications typically read several formats, they can be used to translate TIFF files into other forms. TIFF is flexible and still evolving; it currently allows multiple images per file, several types of data compression, and various types of color image. Because the image data is organized into 'strips', an application program can call into memory only those parts of an image which require processing. TIFF documentation is available over the Internet network from several FTP sources,including zippy.nimh.nih.gov (see the /pub directory).

Microscopists should remain aware of the HDF standard, which might grow in popularity within the scientific community. NCSA's program Import2HDF can read several 'foreign' formats including TIFF, FITS,PICT, GIF and ASCII Text Files. HDF documentation, source code and Macintosh applications are available free of charge (via anonymous FTP) over Internet (ftp.ncsa.uiuc.edu).

1. MSA Standards Committee report, MSA Bulletin, vol.23, No.2, 1993.

DETERMINING CHROMATIN STRUCTURE BY COMPUTER-AIDED IMAGE ANALYSIS

James B. Olesen and Carol A. Heckman

Center for Microscopy and Microanalysis, Bowling Green State University, Bowling Green, Ohio 43403

In the present research, we address the problem of how chromatin fibers are ordered in band and interband regions along the length of a *Drosophila* polytene chromosome. Our approach employs image processing as a preliminary step to amplify the image contrast. Then, computerized pattern recognition methods are used to study how the chromatin is arranged.

Polytene chromosomes were isolated from salivary glands and squashed on glass microscope slides.[1,2] The slides were immersed in liquid nitrogen and the coverslips were removed with a razor blade. Small droplets of a polymer developed in our laboratory called HACH (a mixture of 2-hydroxyhexanedial, carbohydrazide and hydrazine) were then placed over individual chromosome spreads and the slides were left at 26°C overnight to allow for HACH polymerization.[3] HACH-embedded samples were removed from the slides, mounted on resin blocks, trimmed and thin-sectioned at a thickness of approximately 100 nm. Sections were floated onto formvar-coated gold grids and viewed with a Zeiss 10C transmission electron microscope operated at 80kV.

Images of polytene chromosomes (Fig. 1) were acquired via a Photometrics charge-coupled device camera linked to a Sun 4/260 workstation. Subsequently, the digital images were transferred to a Sun SPARCstation running SunVision/SunIP image processing software. The images were treated with several filter and processing operations from the IP library. Edge enhancement was performed to emphasize feature boundaries and the enhanced images were thresholded to create an image with binary contrast (Fig. 2). Regions of interest were identified by a program that outlined a boundary of continuously filled pixels and reported their coordinates. The output was then subjected to a program designed to search for ellipsoidal contours. Then, the area, ellipse of concentration, lengths of major and minor axes of the ellipse, centroid position, and other relevant data about each figure were reported. Structures corresponding to the expected range of areas for a 30 nm fiber were selected out of the data set. The locations of their centroids were mapped and compared to the original image (Fig. 3).

In order to determine whether a periodic structure could be detected in these data, the distance between the centroids of all structures having an area similar to the 30 nm fiber were calculated. When the distribution of such distances was plotted in histogram form, there appeared to be an anomalous, high frequency of values around 80 nm (Fig. 4). Since this distance is obviously larger than the closest possible packing distance for two 30 nm fibers, it was thought to reflect some higher order of organization in the chromosome. We then examined the entire range of area values generated by the contour evaluation program. The area distribution showed several peaks in the range from 1000-3000 nm^2 (Fig. 5). Thus, it was possible that there were also intermediate levels of structure between the 30 nm fiber and the spacing that appeared to center around 80 nm.[4]

References

1. J.S. Yoon et al., Experientia (1973) 29, 639.
2 M. Ashburner *Drosophila*: A Laboratory Manual, Cold Spring Harbor: Cold Spring Harbor Laboratory Press (1989) 28.
3. J.B. Olesen et al., Proc. XIIth Intern. Congr. Elect. Micro. (1990) 3, 790.
4. Research supported by NSF DIR-9009697 and Ohio Board of Regents Academic Challenge.
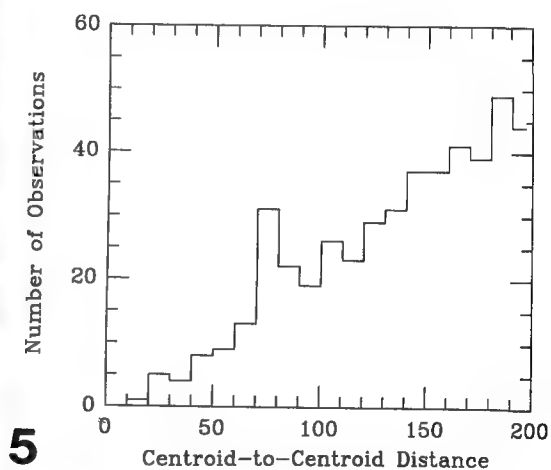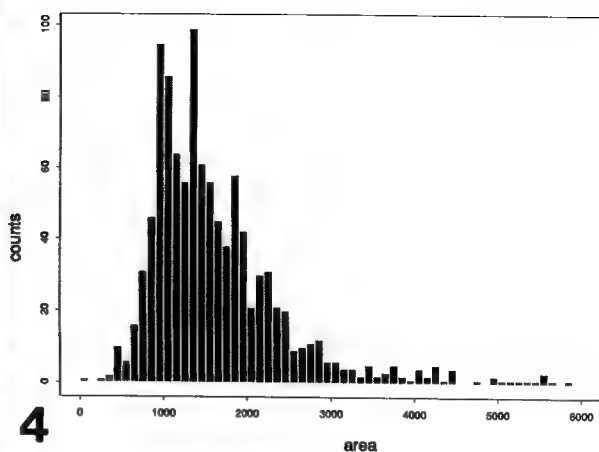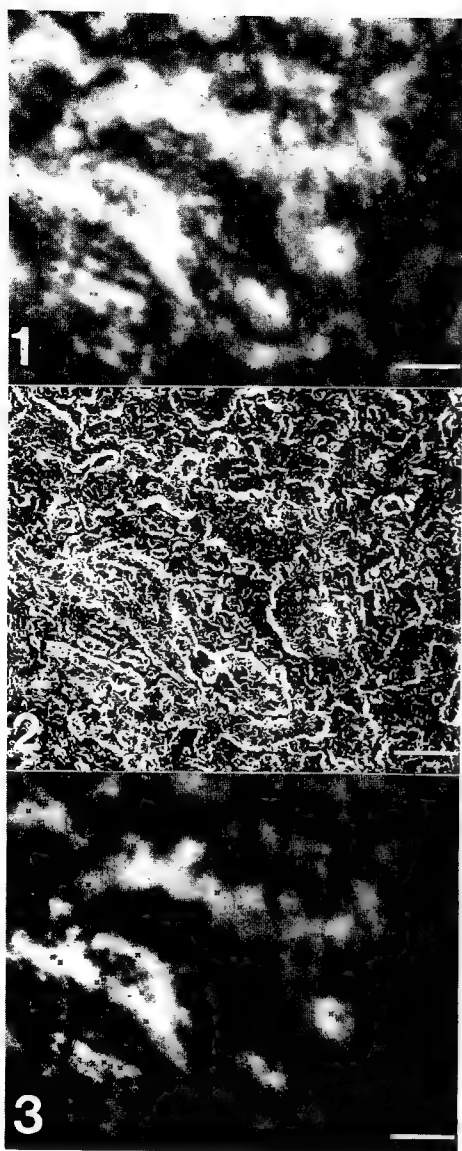
FIG. 1.   Thin-section of HACH-embedded polytene chromosome. Bar = 0.25μm.

FIG. 2.   Thresholded image of chromosome shown in FIG. 1. Bar = 0.25μm.

FIG. 3.   Original image of chromosome with locations of structures marked that had areas similar to that of 30nm chromatin fiber. Bar = 0.25μm.

FIG. 4.   Histogram of distances between structures identified in FIG. 3.

FIG. 5.   Histogram of area values of all structures identified by contour evaluation program.

LOG-LOG SCALE ROUGHNESS SPECTROSCOPY OF SURFACES

P. Fraundorf and B. Armbruster*

Center for Molecular Electronics and Department of Physics, University of Missouri-SL, St. Louis MO 63121. *Also Monsanto Corporate Research, 800 N. Lindbergh Blvd, St. Louis MO 63166

Optical interferometry, confocal light microscopy, stereopair scanning electron microscopy, scanning tunneling microscopy, and scanning force microscopy, can produce topographic images of surfaces on size scales reaching from centimeters to Angstroms. Second moment (height variance) statistics of surface topography can be very helpful in quantifying "visually suggested" differences from one surface to the next. The two most common methods for displaying this information are the Fourier power spectrum and its direct space transform, the autocorrelation function or interferogram. Unfortunately, for a surface exhibiting lateral structure over several orders of magnitude in size, both the power spectrum and the autocorrelation function will find most of the information they contain pressed into the plot's origin. This suggests that we plot power in units of LOG(frequency)≡-LOG(period), but rather than add this logarithmic constraint as another element of abstraction to the analysis of power spectra, we further recommend a shift in paradigm.

Any given topographic image will boast some average level of vertical fluctuations, measureable by the rms variation in heights across the image. The question we pose is simple: Over what lateral size scales is this rms variation distributed? More specifically, how many Angstroms of rms variation, per decade in the range of lateral sizes, does the image contain for spatial periods throughout the range represented in the image? A plot of this quantity on a LOG-LOG scale *by inspection* lets us estimate both the rms variation as a function of image size, and the impact of any given range of frequencies on the total rms variation observed.

Figure 1 shows calculated surfaces consisting of Poisson distributed 5nm-high hemispheres and Gaussian bumps whose volume is set equal to a hemisphere of equal height, along with their two-dimensional (2D) roughness spectra on size scales ranging between 1 nm (origin) and 100 nm (perimeter). Figure 2 shows analytical 1D (azimuthally averaged) spectra for Gaussian bumps of several sizes, and Figure 3 shows a similar 1D spectrum for a 2048x2048 image of 55nm-high hemispheres Poisson distributed on a surface. In this latter image, dotted curves showing the envelope of rms variations in this quantity as a function of azimuth are plotted as well. This envelope is very helpful in showing up deviations from isotropy in experimental images. The dashed "line of hemispheres" basically flags the transition between "smooth surfaces" populated by oblate (pancake-like) protrusions below the line, and "forested surfaces" populated by prolate (rod-like) protrusions above the line. The lower "dot-dash" line illustrates schematically where we expect very smooth surfaces (like polished VLSI wafer silicon) to plot.

As you can see, these plots provide a context in which to examine quantitative roughness variations measured over a wide range of sizes, with a wide range of techniques. Application of these plots to the scanning probe study of surface nucleation and growth, as well as to time-domain and feedback loop artifacts in such images, are discussed in two separate papers submitted to this conference. Semper 6 macros have been used for doing the 2D and 1D calculations described here.
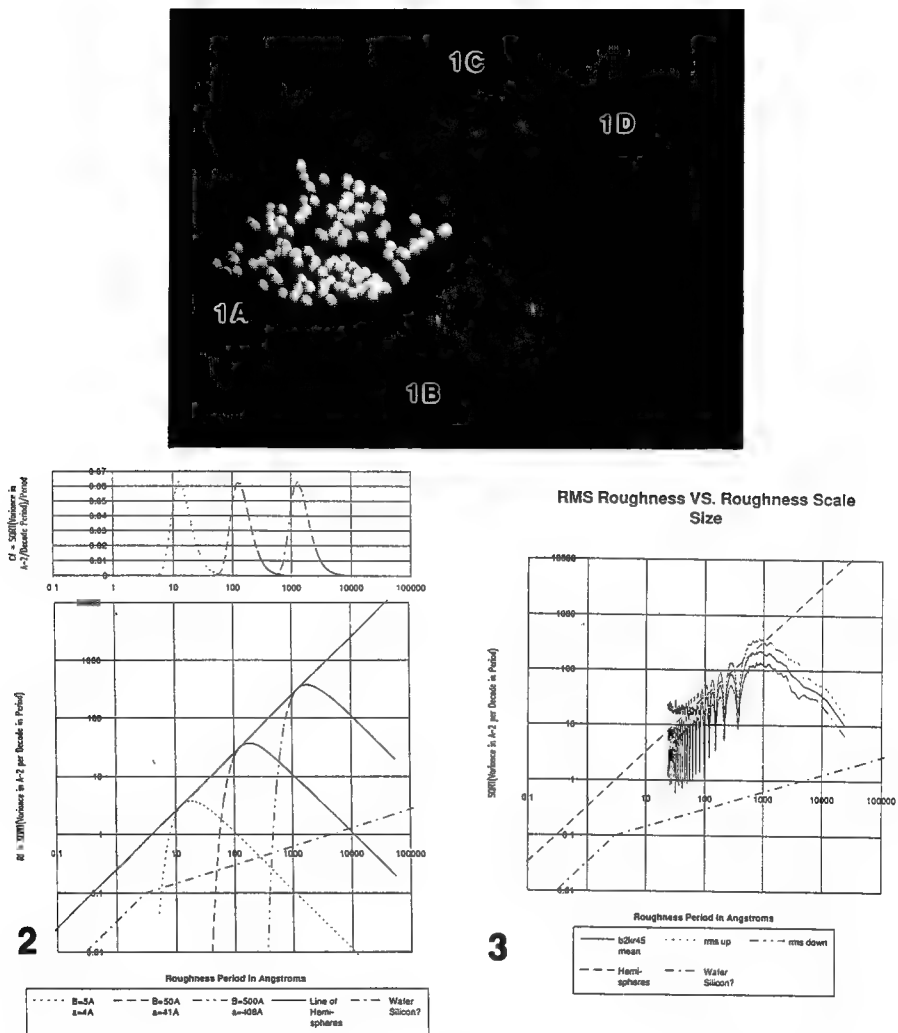
Fig. 1A: Poisson distributed hemispheres on a surface; **Fig. 1B:** Two-dimensional roughness spectrum of the hemispheres in 1A. The plot is radially logarithmic, with rms variation per decade displayed near the center of the plot for small size scales, and near the perimeter for large size scales; **Fig. 1C:** Poisson distributed Gaussian bumps, shown with the same vertical scale as 1A; **Fig. 1D:** Two-dimensional roughness spectrum of the bumps in 1C. Same vertical scale as 1B.

Fig. 2: One-dimensional (azimuthally averaged) roughness spectrum for Gaussian bumps whose volume is equal to that of a hemisphere of the same height, for heights of 5, 50 and 500 Angstroms. This analytical plot illustrates the kind of "line-widths" you might expect in such spectra for non-periodic surfaces.

Fig. 3: One-dimensional (azimuthally averaged) roughness spectrum computed from a 2048x2048 floating point image of 550 Angstrom radius hemispheres Poisson distributed on a surface. The beats (which are periodic in frequency) will be damped if experimental images as the spread in hemispheres becomes finite.

ATOMIC-FORCE IMAGING OF BIOLOGICAL MOLECULES USING AN ENVIROMENTAL
CELL WITH SAMPLE TRANSLATION CAPABILITY

Silvio P. Marchese-Ragona, Briggs Christie and Renee Jobe

TopoMetrix Applications Laboratory, 1505 Wyatt Drive, Santa Clara, CA   95054
(408) 982-9700

Atomic force microscope images of well-characterized biological
macromolecules always appear wider and flatter than expected. These
dimensional artifacts can be explained in part by tip convolution and tip
compression as well as the relative strengths of the tip-sample and tip-
substrate interactions.   The effects of tip convolution and tip compression can
be manipulated by knowing the tip geometry and applied force, however the
tip-sample interaction strength is highly dependent on the environment in
which the specimen is scanned.   In order to manipulate the environmental
conditions under which images are obtained we have constructed an
enviromental cell (Fig. 1.) that allows us to simultaneously image molecules in
the topographic and lateral force modes in almost any gas or liquid at ambient
temperatures and pressures.   The design of the enviromental cell allows the
sample to be translated in the x and y directions, and also allows the sample to
be viewed optically at magnifications up to 400 times.   As a model test object we
have used plasmid DNA physically adsorbed to a   magnesium acetate treated
mica substrate (Fig. 2.).   DNA is the "yardstick" molecule used by most AFM
research groups to study biological specimen preparation procedures.   DNA's
popularity is largely due to its ability to tenaciously stick to mica and its
extremely robust nature.   However, the imaging conditions for DNA are rather
strict.   DNA is extremely stable   when imaged in an enviromental cell under a
continuos flow of dry nitrogen.   When DNA is imaged in air, however, a
number of interesting artifacts can be seen that are largly dependent on the
relative humidity.   A very common observation when imaging under ambient
conditions is that a small fragment of the sample becomes detached from the
surface   and sticks to the tip (Fig. 3.).   This uncontrolled tip-sample interaction
severely reduces the image quality and resolution.   Changing the scan
direction by 90 degrees can often dislodge the contaminant (Fig. 4.) but this at
best is only a temporary solution at best, since another fragment will soon
adhere to the tip.   While this can be currently viewed as an artifact it may also
represent a very crude form of protein manipulation.   In humid environments
DNA molecules can often appear to be "sunk" when imaged in the topographic
mode (Fig. 5.).   This particular artifact is derived from a strong tip-sample
interaction relative to the tip-substrate interaction.   The corresonding lateral
force image is shown in Fig. 6.
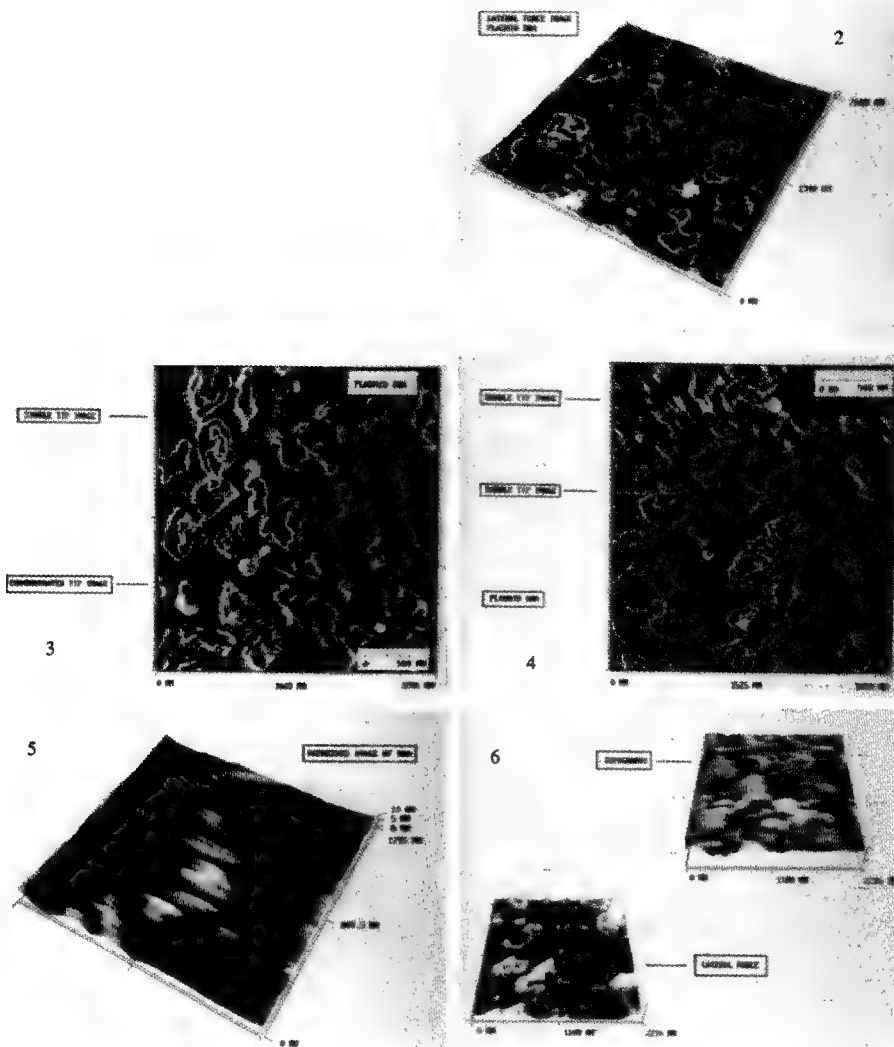
FIGURE. 1. Schematic diagram of AFM enviromental cell.
FIGURE. 2. Lateral force image of Plasmid DNA bound to magnesium acetate
treated mica. The specimen was scanned under a constant flow of
dry nitrogen.
FIGURES 3. and 4. Figure 3. shows the effect of tip contamination occurring
in the last one-third of the scan. The contaminant can be
removed by rotating the scan direction by 90 deg.
FIGURE. 5. DNA scanned in high relative humidity. The DNA appears to have
a negative height because of a strong tip-sample interaction.
FIGURE. 6. Simultaneous acquisition of Topographic and Lateral force
images.

227

EFFECT OF RAISED TEMPERATURE ON A STAINLESS-STEEL SURFACE BY AMBIENT ATOMIC-FORCE MICROSCOPY

Pan S. Jung

AT Corporation, 1815 1st Ave., Suite 102, Mesa, AZ 85202

We report images from atomic force microscopy (AFM) of a heated metallic surface performed under an ambient environment. The stainless steel surface was heated up to 121C, which is limited only by the capacitive heating element used (100W). We observed that the topography of the surface changes dramatically. It is found that at high temperatures, the surface appears flat compared with the presence of many round bumps observed on the same sample at room temperature when the ambient humidity is high. To the best of our knowledge, this is the first report on ambient AFM performed on a metallic surface above 100C.

Most AFM systems adopt moving sample stages [1]. In this case, it is difficult to implement heavy heating heating elements and a heat reservoir block. For this experiment, the TAK3 from AT Corporation [2] is used. The sample stage is kept stationary and the heating element (the tip of a soldering iron) is fixed firmly on one side of a surface of the block using a screw. The AFM head uses the optical lever method, and it includes a piezo scanner which scans the cantilever-probe in both the X- and Y-directions on the sample surface. The details are published elsewhere [3]. The temperature is monitored by a thermocouple fixed at a distance approximately equal to the AFM probe distance from the heating point to minimize the temperature measurement error.

Figure 1 is one image of the sample (the stage was of commercial stainless steel 1 inch in diameter and 3/4 inch thick) at 18C. The topography is composed of many round structures, the size of which are of the order of 100 nm. The force on the sample was kept close to zero as it appears in the force-distance curve before the scanning is performed. The surface was then heated up to the maximum temperature supplied by the heater. The maximum temperature observed was 121C. Due to the large heat capacity of the sample, the temperature reaches its steady state in one hour. A few images were taken at intermediate temperatures. A typical image at 93C is shown in Figure 2. It can be seen that the topography is not very similar to Figure 1. The surface is relatively smooth with no hint of the 100 nm bumps. This effect seems to be consistent at several positions on the sample although it was difficult to scan the exact same area due to the large drift at the high temperatures.

The images indicate that the bumps seen on the surface were missing at the higher temperatures. They could be adsorbents from the air, possibly due to water condensation since the images were taken during a humid (90%) day. Repeated experiments performed in air during a dry spell (20% humidity) do not show such bumps. Similar bumps are occasionally observed on the images of gold-coated gratings, while the surfaces are free of such structures in most cases. Similar bumps are also occasionally seen on silicon samples in ambient. The exact identity of the adsorbents is yet to be determined. In between the highest and lowest temperatures, isolated islands are formed similar to those structures at the top of Figure 1. When the temperature is then lowered after reaching the maximum, the bumps appear ultimately covering almost all the surface at 37C. This shows that the process of adsorption is reversible, thus indicating a physical process rather than a

chemical one. At a temperature higher than 70C, it is noticed that the cantilever experiences a series of small jumps at a low non-periodic rate. The image improves considerably at higher scanning rates (up to 70 lines per second was tried). The exact cause of this disturbance is under investigation.

References
[1] G. Meyer and N. M. Amer, Appl. Phys. Lett., 53 1045 (1988)
[2] AT Corporation, 1815 W. 1st Ave., Suite 102, Mesa, Arizona 85202
[3] P.S. Jung and D. R. Yaniv, Electron. Lett., 29 264 (1993)
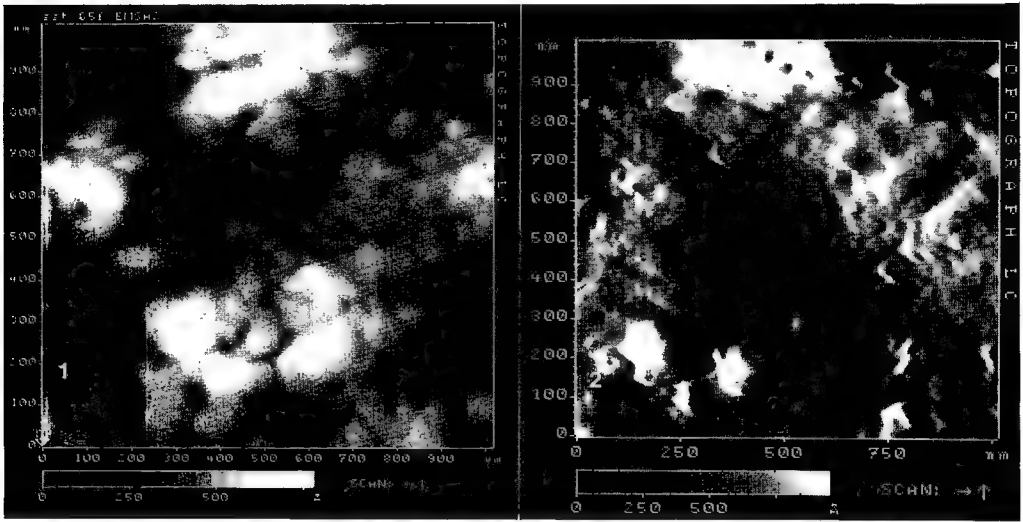
Figure 1. Surface of a machined stainless steel sample stage observed by AFM at room temperature (18C). Many round bumps are covering the surface.

Figure 2. A higher temperature image taken at 93C. This image was taken one hour after the heater was turned on. The surface is closer in appearance to that of machined stainless steel with a few machined grooves at the center. On the top and near the bottom, islands of residue are formed.

Correlative atomic-force microscopy and high-resolution scanning electron microscopy of proteins attached to platelet surfaces

S.R. Simmons[1], S.J. Eppell[2], R.E. Marchant[2], R.M. Albrecht[1]

1. Animal Health and Biomedical Sciences, University of Wisconsin, Madison, WI 53508

2. Biomedical Engineering, Case Western Reserve University, Cleveland, OH 44106

The atomic force microscope (AFM) has provided images at submolecular or atomic scale resolution of biological macromolecules attached to surfaces such as mica, graphite, or synthetic phospholipid membranes.[1-3] Because the AFM can be operated with the sample in air, vacuum, or immersed in a liquid such as a biological buffer, it has the potential for high resolution imaging of the structure and organization of macromolecules on surfaces of cells in the hydrated or even living state.[4] Realization of this potential would allow observation of molecular processes at the cell surface without the necessity for preparation of the sample for electron microscopy. To date, however, the AFM has yielded images of cell surfaces only at relatively low magnifications, and has not provided the atomic resolution achieved on hard, crystalline surfaces.

Previously we have utilized correlative video-enhanced light microscopy, high voltage transmission electron microscopy, and low voltage, high resolution scanning electron microscopy (HRSEM) in conjunction with colloidal gold labeling to investigate the binding of fibrinogen molecules to receptors on platelet surfaces and the subsequent movement of the ligand/receptor complexes on the membrane surfaces.[5] To extend these studies to include the AFM and assess the utility of colloidal gold labeling for AFM we have compared images of proteins bound to a platelet surface obtained by AFM with images of the exact spot on the same platelet by HRSEM. Platelets adherent to formvar-filmed finder grids were labeled with fibrinogen or IgG antibody to the fibrinogen receptor, either soluble or gold conjugated. Labeled platelets were prepared for electron microscopy by glutaraldehyde and osmium fixation, ethanol dehydration, and drying by the critical point method. The dried specimens were imaged in air with a Digital Instruments Nanoscope II AFM using either a Si_3N_4 integrated pyramidal tip or the same tip with a carbon spike grown on the end of the pyramid with the HRSEM. The specimen was then sputter coated with 1-2 nm of platinum and imaged in a Hitachi S-900 HRSEM (Integrated Microscopy Resource, University of Wisconsin, Madison) at 1-2 kV accelerating voltage in the SE mode, providing a topographical image of the surface, or at 5-10 kV in the BSE mode for identification of gold labels.

At lower magnifications, up to 10000x, platelet outlines and distances between features on the platelet surface as seen by AFM or HRSEM were comparable, facilitating identification of the same platelet in each microscope (Fig. 1). At higher magnifications the information gained from the AFM begins to diverge from that of the HRSEM. Fibrinogen molecules bound to the platelet surface can be visualized by either technique, as can particles in the platelet surface membrane which are the appropriate size for glycoprotein receptors (Fig. 3). However, the AFM produces an image of a small feature such as a protein molecule or gold particle that is laterally inflated. At the same time the AFM provides accurate height information that is not readily available from the HRSEM and shows edges of small structures which in the HRSEM are less clearly defined. Thus, at the highest magnifications used (100000x final magnification) surface features which were not obvious by HRSEM could be visualized by AFM, and the topography of the surface could be seen by AFM in much more detail (Fig. 3). Gold labels could be identified by AFM by their regular, spherical shapes. Correlative

electron microscopy confirmed the identity and position of gold labels on the cell surface (Fig.2).

AFM imaging of platelet surfaces provides images of such resolution as to permit visualization of individual protein molecules on the platelet surface membrane. By using small colloidal gold labels to identify surface receptors or bound ligands it will be possible to follow processes such as receptor expression, movement, and organization on living cells. Subsequent examination of fixed and dried cells by scanning or transmission electron microscopy can provide confirmation of the identity of gold labeled proteins and permit correlation of the final positions of the labels with surface and internal ultrastructure.

1. H.G. Hansma et al., Clin. Chem. 37(1991)1497.
2. J. Yang et al., FEBS Letters 279(1991)295.
3. R. Wigren et al., FEBS Letters 280(1991)225.
4. H.J. Butt et al., J. Struct. Biol. 105(1990)54.
5. R.M. Albrecht et al., Am. J. Anat. 185(1989)1.
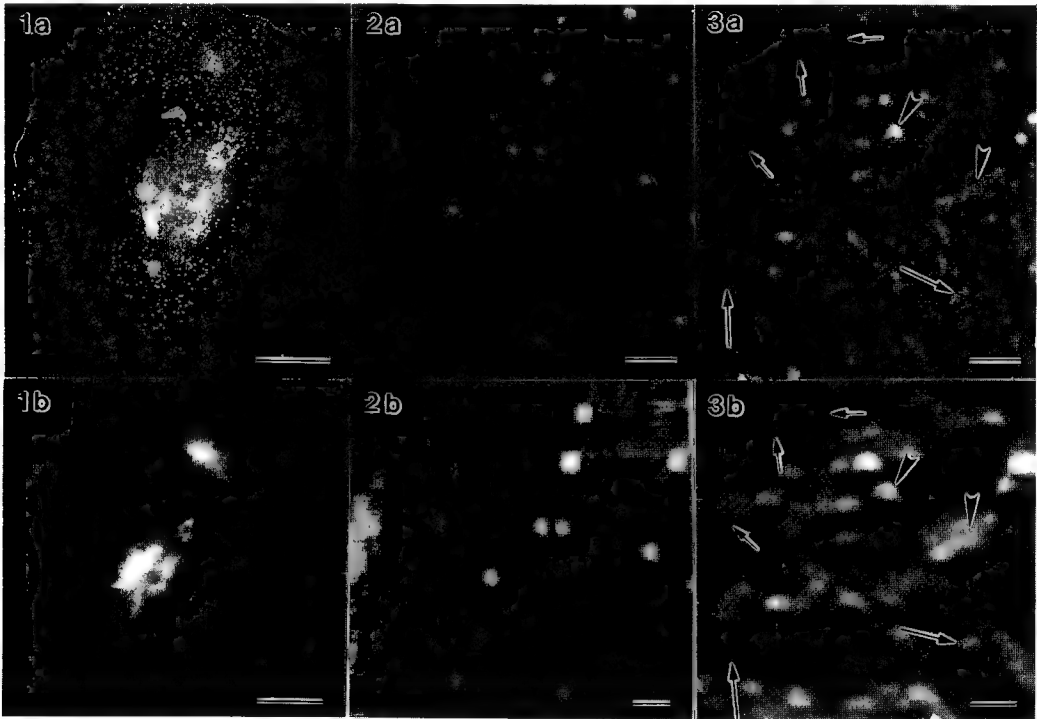
Fig. 1. Surface adherent platelet labeled with gold particles (small white spheres) conjugated to antibody to fibrinogen receptor. Bar = 1μm. a. HRSEM 10 kV BSE. b. AFM of same platelet as in 1a. Height mode.

Fig. 2. Detail of platelet shown in Fig. 1. Bar = 0.1 μm. a. HRSEM 1 kV SE. Beam penetration at this low voltage is slight, showing membrane surface and surface of protein coating on gold particles. Overall dimensions of protein/gold probes are 25 nm. b. AFM of same area as in 2a. Height mode. Inter-particle distances are comparable to those measured by HRSEM. Overall probe diameters are more than twice those measured by HRSEM.

Fig 3. Fibrinogen on platelet surface. Bar = 0.1 μm. a. HRSEM at 3.0 kV SE. Rod-shaped fibrinogen molecules are bound individually (large arrows) and in small aggregates (arrowheads) to platelet surface. Structures of appropriate size for integral membrane receptors (small arrows) can also be seen. b. AFM deflection mode of same area as in Fig 3a. Arrows indicate same structures as in Fig 3a. Lateral dimensions of proteins are inflated. However, AFM provides increased topographic detail and clearly defined edges.

APPLICATIONS OF ULTRAMICROTOMY FOR MATERIALS CHARACTERIZATION

R.T. Blackham, J.J. Haugh, C.W. Hughes and M.G. Burke

Westinghouse Science and Technology Center, Pittsburgh, PA   15235

Essential to the characterization of materials using analytical electron microscopy (AEM) techniques is the specimen itself. Without suitable samples, detailed microstructural analysis is not possible. Ultramicrotomy, or diamond knife sectioning, is a well-known mechanical specimen preparation technique which has been gaining attention in the materials science area. Malis and co-workers[1,2] and Glanvill[3] have demonstrated the usefulness and applicability of this technique to the study of a wide variety of materials including Al alloys, composites, and semiconductors. Ultramicrotomed specimens have uniform thickness with relatively large electron-transparent areas which are suitable for AEM anaysis.

Interface Analysis in Type 316 Austenitic Stainless Steel: STEM-EDS microanalysis of grain boundaries in austenitic stainless steels provides important information concerning the development of Cr-depleted zones which accompany $M_{23}C_6$ precipitation[4], and documentation of radiation induced segregation (RIS).[5,6] Conventional methods of TEM sample preparation are suitable for the evaluation of thermally induced segregation, but neutron irradiated samples present a variety of problems in both the preparation and in the AEM analysis, in addition to the handling hazard. The intrinsic activity of a conventional sample can swamp the energy dispersive x-ray spectrometer so that no analysis is possible. By minimizing the sample volume, it is possible to significantly reduce or eliminate the problem. Ultramicrotomy represents one way in which this can be accomplished. As an example of the feasibility of this technique for the preparation of thin (<50 nm) sections of stainless steel, a specimen of Type 316 stainless steel was embedded in Epox 812 and sectioned using a 45° diamond knife. The cutting speed was 1 mm/sec. Figure 1 shows the presence of a grain boundary in ultramicrotomed Type 316 stainless steel. The sectioning operation results in extensive deformation of the material, but it is still possible to identify grain boundaries in the deformed structure.

Phase Identification in metal matrix composites (MMC): 6061 Al-graphite composites contain several phases that form during processing and critically affect the mechanical performance of the composite. Ultramicrotomy provides a method for providing samples that are suitable for AEM analysis of both the graphite reinforcement and the intermetallic phases. A small slice (~0.3 mm in thickness) of the MMC was mounted in the ultramicrotome, and sliced with a cutting speed of 2 mm/sec. Due to the deleterious effect of H_2O on the structure of selected phases in the MMC, the ultramicrotomy operation was performed "dry" (sections were not floated off the knife in H_2O). An example of the ultramicrotomed MMC microstructure is shown in Figure 2. Like the austenitic stainless steel, the aluminum matrix was heavily deformed during the slicing operation. However, it was possible to retain portions of the graphite reinforcement in the structure. The identification of the graphite was performed using both electron diffraction and EDS microanalysis techniques.

Although these examples represent initial efforts in the application of ultramicrotomy to materials of current industrial significance, the results obtained to date are encouraging. With further development, it should be possible to extend this technique to several other

232

industrially significant systems including oxide films on metal substrates, and the preparation
of irradiated alloys for the evaluation of intergranular segregation.[7]

References

1. T.F. Malis and D. Steele, Proc. MRS **Vol. 199**(1990)3.
2. D. Steele and T.F. Malis, Proc. Annual EMSA, **49**(1991)1110.
3. S.R. Glanvill, Proc. XIIth ICEM (1990)428.
4. E.P. Butler and M.G. Burke, Acta Met. **34**(1986)557.
5. E.A. Kenik et al., J. Nucl. Mater. **183**(1991)145.
6. E.A. Kenik, Met. Trans. **22A**(1991)253.
7. The authors are grateful to Dr. T.F. Malis and Mr. G. Williams for their assistance,
valuable discussions, and encouragement in furthering the applications of ultramicrotomy.
The authors also thank Dr. M.N. Gungor for providing the MMC material for
ultramicrotomy experiments.
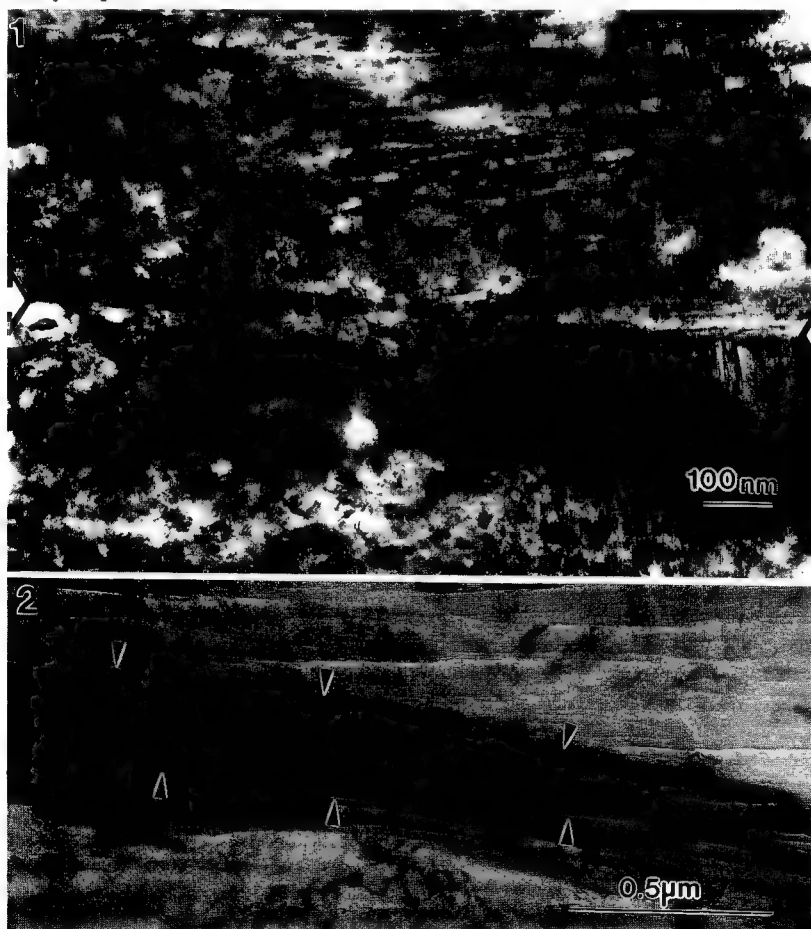
FIG. 1.--TEM of ultramicrotomed Type 316 SS containing a grain boundary (arrowed).
FIG. 2.--TEM of ultramicrotomed MMC sample showing extensive deformation and a
graphite flake (arrowed).

FEATURE ENHANCEMENT BY NON-UNIFORM ION-MILLING FOR SEM OF INTEGRATED CIRCUITS

F. Shaapur

National Center for High Resolution Electron Microscopy, Center for Solid State Science, Arizona State University, Tempe, AZ 85287

A variety of techniques has been developed to enhance the image contrast of EM specimens in both physical and biological sciences. In SEM of materials, feature enhancement is mainly based on augmentation of surface topography by non-uniform material removal from different structural elements and preferential erosion at adjoining interfaces. The enhanced surface topography, in turn, translates into better response to the probing beam resulting in higher image contrast.

In cross-sectional imaging by SEM (XSEM) of ICs, feature enhancement has been carried out by chemical[1] or mechanical,[2] i.e., ion-milling, surface treatments. Ion-milling has been used to clean surfaces and to enhance their topography. The non-uniform material removal from the surface, in this case, merely relies on an inherent characteristic of the structural elements, i.e., their relative erosion rates during the ion-thinning. An additional factor, i..e., minimization of the "shadowing" effect by adjusting the orientation of ion incidence[3] may also be used to elevate the non-uniform ion-milling even further. In this work, the effectiveness of the above factor has been evaluated using a previously developed[4], and now commercially available[5], ion-milling auxiliary specimen rotation system.

As a representative IC sample, a SRAM device was used to provide a number of XSEM specimens. The ion-milling was carried out for a duration of 15 minutes using a Gatan DuoMill model 600 generating a 6kV Ar ion beam of 1mA current aimed at the specimen surface at a 20° angle of incidence. The specimens were rotated in a "rocking" mode within a 40° sector, centered around the device/viewing-glass glue-line, at a constant speed of 2 rpm. In order to establish a reference for the evaluation of results a number of specimens were ion-milled with regular unidirectional constant rotation speed of 2 rpm. The samples were later examined in a Hitachi S-5000 FEG-SEM operated at 1.5 kV.

Figure 1 shows a poly-Si feature in contact with the Si substrate and embedded in a CVD Si-oxide layer in a specimen ion-milled in the "rocking" mode. The overall surface augmentation and the resulting feature enhancement are readily visible in this micrograph. Figure 2 presents a portion of the above feature at higher magnification. The erosion pattern on the surface indicates the preferential ion-milling orientation. The specimens treated by standard ion-milling produced only a slightly better image contrast than those untreated for surface enhancement and noticeably inferior to those ion-milled in a "rocking" mode. Figure 3 displays a different region of the Figure 1 specimen showing two distinct IC structural features enhanced by the above procedure.

In conclusion, ion-milling with a "rocking" mode of specimen rotation greatly enhances the structural features in a XSEM IC specimen leading to improved image contrast. This technique may also be employed in surface augmentation of IC cross-sectional specimens for other surface microscopy applications, e.g., scanning probe microscopy (SPM).[6]

References

1. R.B. Marcus and T.T. Sheng Electron Microscopy of Silicon VLSI Circuits and Structures (John Wiley & Sons, New York, NY, 1983), p. 28.

2. S.J. Klepeise et al. in Proc. 47th EMSA Ann. Meeting ed. by G.W. Bailey (San Francisco, CA, 1989), p. 712.

3. U. Helmersson and J.E. Sundgren, J. Elec. Micr. Tech. 4, 361 (1986).

4. F. Shaapur and K.A. Watson, in Specimen Preparation for Transmission Electron Microscopy of Materials ed. by R.M. Anderson (Mat. Res. Soc. Proc. 254, Pittsburgh, PA, 1990), p. 153.

5. VCR , S. San Francisco, CA and RTCC, Tempe, AZ.

6. This work was supported by a grant from the National Science Foundation (Grant No. DMR-91-15680). The author is grateful to Mark Appleget and Hitachi Scientific Instruments for providing access to the Hitachi S-5000 FEG-SEM. The critical review of the manuscript by professor David J. Smith is also greatly appreciated.
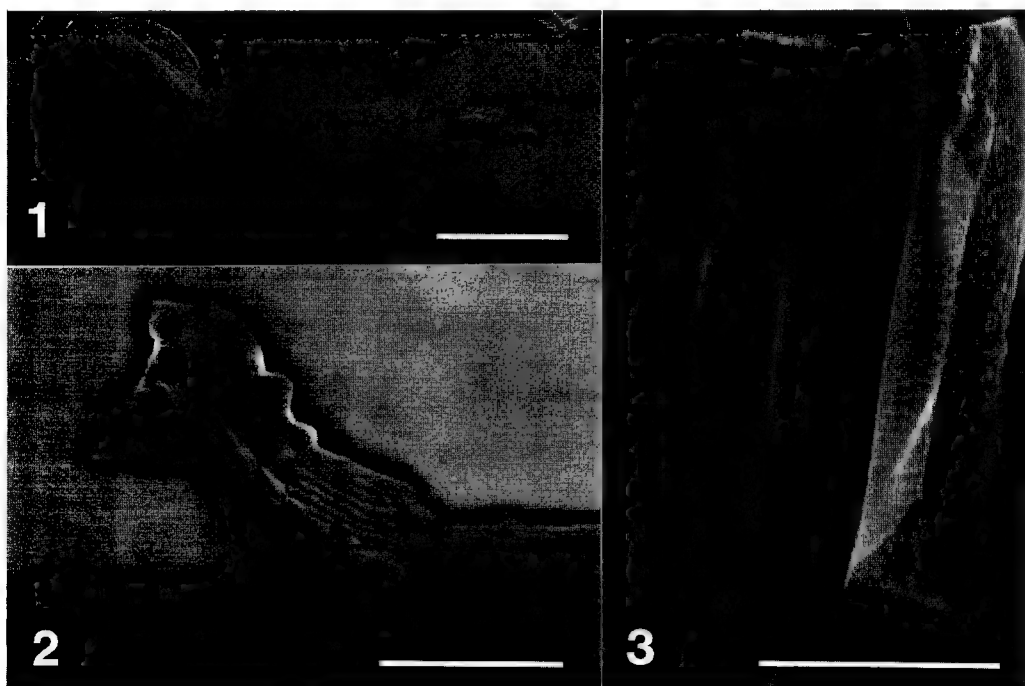
FIG. 1. Poly-Si feature enhanced by ion-milling in "rocking" mode. Bar= 2 μm.

FIG. 2. Portion of Figure 1 feature at higher magnification showing typical erosion pattern associated with this ion-milling procedure. Bar= 1 μm.

FIG. 3. Various enhanced features buried in insulating oxide layer. Bar=1 μm.

CROSS-SECTIONAL TEM SPECIMEN PREPARATION FROM MAGNETO-OPTICAL DISK BY ULTRAMICROTOMY

F. Shaapur,* M.J. Kim,* Seh Kwang Lee** and Soon Gwang Kim**

*Center for Solid State Science, Arizona State University, Tempe, AZ 85287-1704
**Materials Design Laboratory, Korea Institute of Science and Technology, Cheongryang, Seoul, Korea

TEM characterization and microanalysis of the recording media is crucial and complementary to new material system development as well as quality control applications. Due to the type of material generally used for supporting the medium, i.e., a polymer, conventional macro- and microthinning procedures for thin foil preparation are not applicable. Ultramicrotomy (UM) is a viable option and has been employed in previous similar studies.[1,2] In this work UM has been used for preparation of XTEM samples from a magneto-optical (MO) recording medium in its original production format.

The as-received material system consisted of a 4-layer, 2100 Å thick medium including a 300 Å TbFeCo layer enveloped by silicon nitride protective layers supported on a 1.2 mm thick x 135 mm (5.25 in.) diameter polycarbonate disk. Recording tracks had an approximate pitch of 1.6 μm separated by 800 Å deep peripheral grooves. Using a Buehler Isomet low-speed diamond saw, 1 mm wide and 20 mm long strips were cut out of the disk along the recording tracks. The thin film surface was degreased and cleaned by gently scrubbing with a cotton swab soaked in isopropyl alcohol. As shown schematically in Figure 1, the strip was placed in a size 00 (20 mm long x 7 mm diameter) gelatine capsule axially, using a holding clip, and subsequently embedded with medium grade LR White (London Resin Co., UK) acrylic resin. Following the curing step and the dissolving of the gelatine molding shell in hot water the resin block was trimmed to a tapered end. The square-shaped (250 μm x 250 μm) block-face configuration showing the relative position of the thin film is presented in Figure 2. The cutting stroke direction is also indicated on this diagram. UM was carried out using an MRC MT-6000 system equipped with a 45° diamond knife and operated at a cutting stroke speed of 0.6 mm/sec. Various feed values were taken to produce slices ranging in thickness from 500 to 3000 Å. The prepared slices were collected on holey-carbon-coated copper grids and later examined in a JEOL 2000FX and a Topcon 002B TEM both operated at 200 kV. A liquid-nitrogen-cooled specimen holder was used to minimize the beam heating effects.

Figure 3 shows a typical bright field image of the medium's multi-layered structure. In order to minimize image doubling, specimens were tilted as required to ensure a close alignment of the film/substrate interface with the transmitted beam during microscopy. Figure 4 presents the film structure at a higher magnification showing its four distinct sublayers and their morphologies. A comparison of the as-deposited layers thicknesses with those measured from the TEM images indicated minimal structural deformation due to the UM procedure.

In summary, XTEM specimens were prepared from a magneto-optical disk in its original production format by UM for the first time. Damage and plastic deformation associated with the UM technique were negligible in the as-prepared specimens.[3]

References

1. P.B. Narayan, in Proc. 43rd EMSA Ann. Meeting, Ed. by G.W. Bailey (San Francisco, CA, 1985), p. 212.
2. H.M. Ho et al., in Specimen Preparation for Transmission Electron Microscopy of Materials, Ed. by J.C. Bravman (Mater. Res. Soc. Symp. 115, Pittsburgh, PA 1988), p. 149.
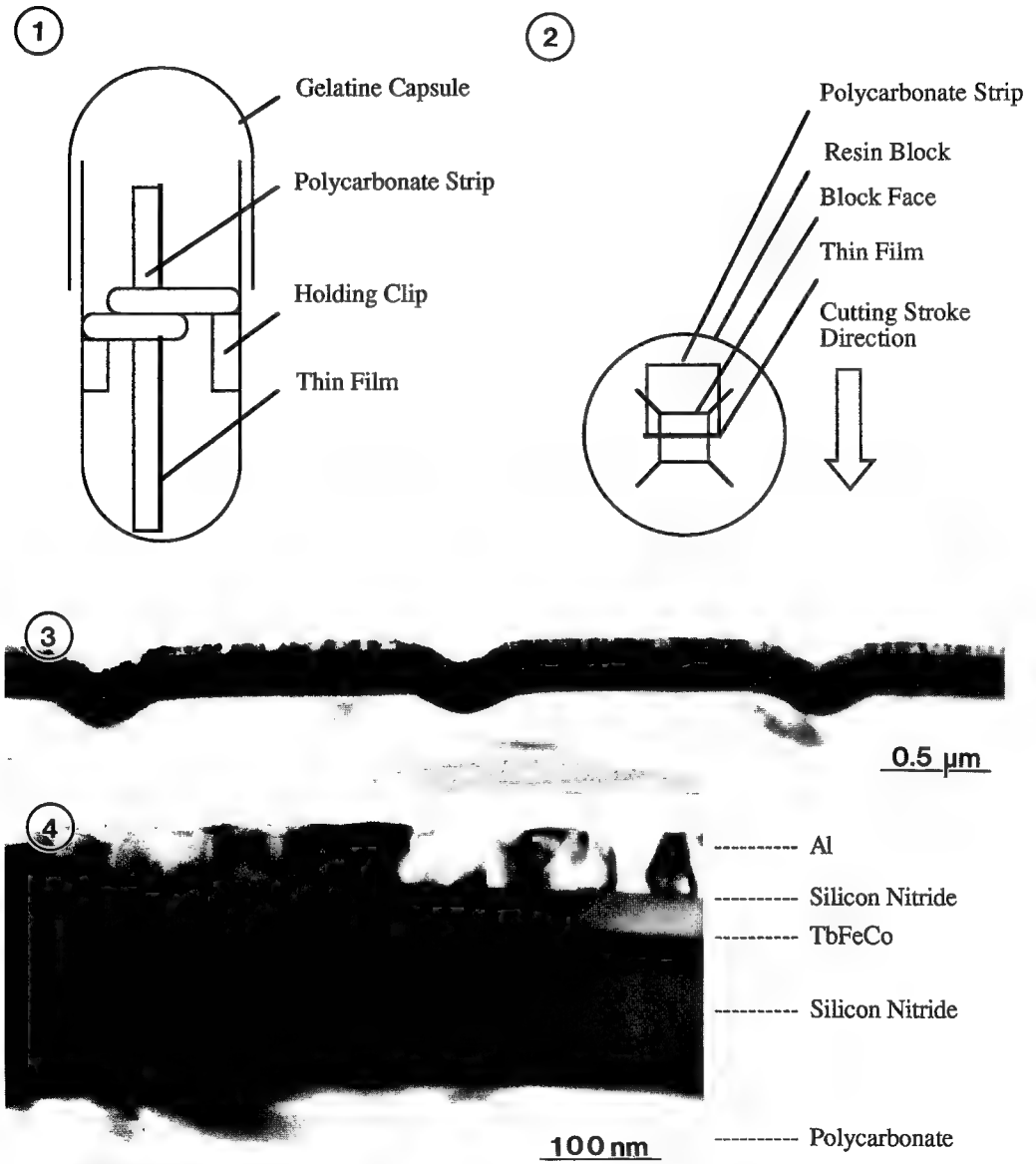
FIG. 1.--Relative position of various components inside gelatine capsule.
FIG. 2.--Schematic front-view of resin block after trimming.
FIG. 3.--Bright field XTEM image of recording tracks in magneto-optical (MO) disk.
FIG. 4.--Substructural layers of medium showing at higher magnification.

A STUDY OF THE MICROVASCULATURE OF THE NORMAL RABBIT BLADDER WITH VASCULAR CORROSION CASTING, SEM AND TEM

Fred E. Hossler*, and Frederick C. Monson**

*Department of Anatomy, J. H. Quillen College of Medicine, East Tennessee State University, Johnson City, TN 37614
**Division of Urology, Hospital of the University of Pennsylvania, Philadelphia, PA 19104

The mammalian urinary bladder performs two functions, urine storage and expulsion. Bladder function is dependent upon the delivery of oxygen and nutrients via a rich blood supply, yet studies of the bladder vasculature during distension have concluded that blood flow is restricted during filling.[1] Following surgically induced ischemia, regeneration of the wall and its vasculature have been reported but not described in detail.[2] Beyond the gross level, the functional vascular anatomy of the bladder wall is poorly understood.[3] Preliminary to studies of angiogenesis and mucosal regeneration following ischemia, and vascular accommodation during distension, the present study utilizes routine transmission (TEM) and scanning (SEM) electron microscopy, and vascular corrosion casting (VCC) to describe the normal microvasculature of the rabbit bladder.

Bladders were perfuse fixed with 2% glutaraldehyde in 0.1 M cacodylate buffer, pH 7.3, for routine TEM and SEM. Thin sections were cut from Araldyte and stained with lead and uranium for TEM, and samples were critical point dried from ethanol and CO_2 for SEM. For VCC, resin (Mercox diluted with methylmethacrylate, 4:1) was infused at physiological pressure using a mercury manometer.[4] Cast tissues were macerated with 10% KOH, washed in H_2O, and critical point dried for routine SEM.

The bladder is supplied by inferior and superior vesicular branches of the abdominal aorta. The vesicular arteries extend from the base to the apex of the bladder in the serosa on the superior and inferior surfaces, branch freely, anastomose at the level of small arterioles along the lateral walls, and supply a rich mucosal capillary plexus (Fig. 1). Accompanying the arteries are straight, unbranched vessels with dense capillary terminals of unknown function. Many of the mucosal capillaries lie in very close association with the urothelium, commonly lying within grooves interdigitated with the basal layers of the transitional epithelium[3] (Fig. 2). The capillaries are often fenestrated and invested with pericytes (Figs. 3, 4). The diameter of the smallest capillaries is about 5-8 um, and the intercapillary distances range from 10-100 um in the partially distended state (Figs 1, 5). The venous drainage exhibits numerous valves, and parallels the arterial supply.

These methods provide a clear 3-D view of the microvasculature of the normal rabbit bladder, which should be valuable in elucidating
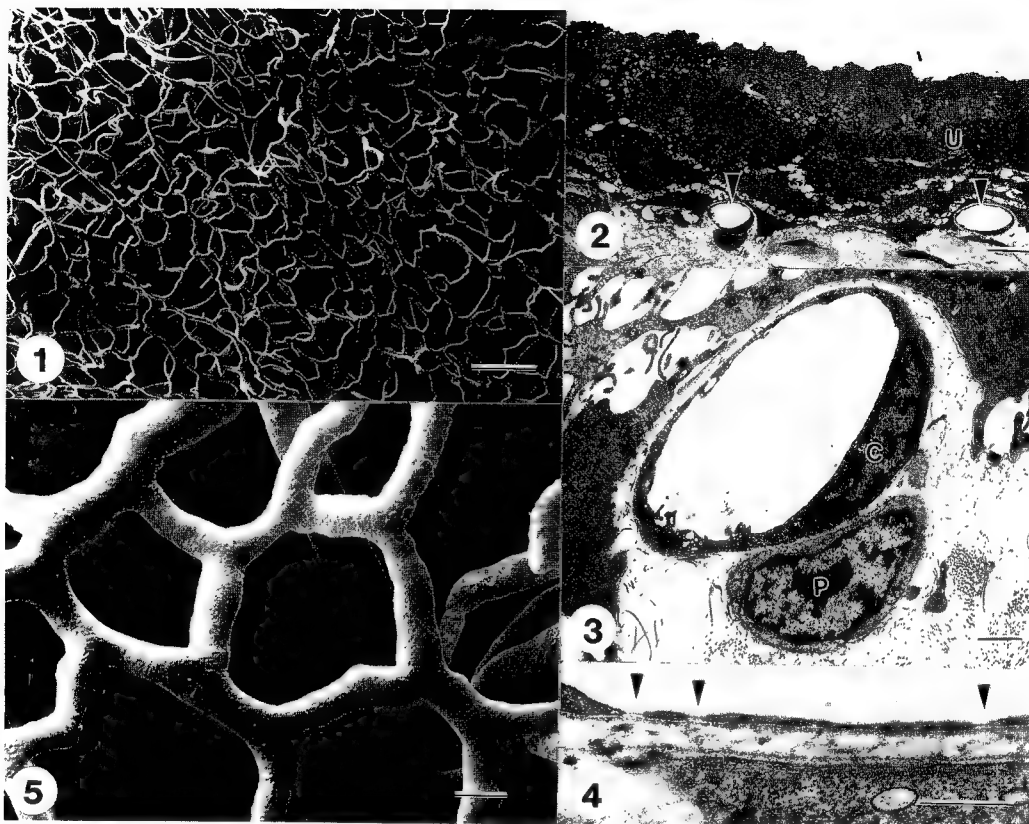
Fig. 1--Vascular corrosion cast of bladder mucosa. Bar = 100 μm.
Fig. 2--Capillaries (arrows) associated with the urothelium (U).
Bar = 10 μm.
Fig. 3--Pericyte (P) associated with capillary (C). Bar = 1 μm.
Fig. 4--Fenestrations (arrows) of the mucosal capillaries. Bar =
0.5 μm.
Fig. 5--Capillaries of mucosa - corrosion cast. Bar = 10 μm.

relationships between the submucosal and mucosal vasculature, and
in identifying possible sites for collateral circulation and
angiogenesis in the regenerating bladder wall[5].

References

1. M. Dunn, Brit. J. Urol. (1974)46, 67.
2. H. S. Gill, F. C. Monson, A. J. Wein, M. R. Ruggieri and R. M.
Levin, J. Urol. (1988)139, 1350.
3. T. Inoue and G. Gabella, Cell Tiss. Res. (1991)263, 137.
4. F. E. Hossler, J. E. Douglas, A. Verghese and L. Neal, J.
Electron Micros. Tech. (1991)19, 406.
5. This research is supported in part by a grant from the Research
Development Committee of East Tennessee State University.

GUM ARABIC HELPS PREPARE BETTER LACEY POLYMER FILMS FOR SPECIMEN SUPPORT IN
ELECTRON MICROSCOPY

Shailesh R. Sheth and Jayesh R. Bellare

MicroLab, Department of Chemical Engineering, I.I.T., Bombay 400 076, India

Specimen support and astigmatism correction in Electron Microscopy are at least two
areas in which lacey polymer films find extensive applications. Although their
preparation has been studied for a very long time[1], present techniques[1,2] still
suffer from incomplete release of the film from its substrate and presence of a
large number of pseudo holes in the film. Our method ensures complete removal of
the entire lacey film from the substrate and fewer pseudo holes by pre-treating the
substrate with Gum Arabic, which acts as a film release agent.

The method is based on the classical condensation technique[1] for preparing lacey
films which is essentially deposition of minute water or ice droplets on the
substrate and laying the polymer film over it, so that micro holes are formed
corresponding to the droplets. A microscope glass slide (the substrate) is immersed
in 2.0% (w/v) aq. CTAB (cetyl trimethyl ammonium bromide)-0.22% (w/v) aq. Gum
Arabic solution for about 6-10 hours. The CTAB in the solution renders the slide
surface hydrophobic. After this the slide is washed with distilled water and
allowed to dry at room temperature. Next, the slide is held by its longer edge and
is completely immersed in liquid nitrogen for about one to two seconds to ensure
uniform chilling of the slide surface. Next, the slide is exposed to the atmosphere
(temperature = 22°C; relative humidity = 85%) for about three seconds, during which
dew drops condense on the slide surface. Thereafter, the slide is dip-coated in a
0.5% (w/v) polymer solution of cellulose acetate butyrate in ethyl acetate. The
dip-coating is done slowly at an angle of 40-45° with the horizontal. The slide is
then rested on its other longer edge on a tissue paper till all the excess polymer
solution drains off. Ethyl acetate quickly evaporates away, leaving behind a lacey
polymer film on the slide. In order to release the film, the slide is first
subjected to re-hydrophilic treatment by immersing it in 1.0% (w/v) aq. solution of
Aerosol OT (AOT) for about two hours. The slide is then immersed through a
dome-shaped water meniscus at an angle of less than 10° with the horizontal which
finally releases the film onto the water surface. The film is then collected on a
brass stub for examination under the SEM or on grids for TEM use.

Unlike the classical techniques, this method ensures complete removal of the entire
film from the slide surface in one piece. The films are uniform, have fewer pseudo
holes and possess high porosity (refer Figure 1). While previous techniques used
slides treated with only the hydrophobic agent (CTAB solution), this method uses
slides treated with both the hydrophobic agent and Gum Arabic simultaneously. Gum
Arabic acts as a release agent and enhances the structure and the quality of the
film and thereby provides us with this simple and reproducible technique for
preparing lacey polymer films.

REFERENCES
1. A. Fukami and K.Adachi, J. Electron Microscopy (1965) 14(2), 112.
2. P.K. Vinson, Ph.D. Thesis, The University of Minnesota, Minneapolis, USA(1990)
and Proc. 45 th Annual Meeting of the Electron Microscopy Society of America, G.W.
Bailey, Ed., San Francisco Press, San Francisco, (1987), 644.
3. This work was supported by a Thrust-Area Grant from MHRD, Govt. of India.
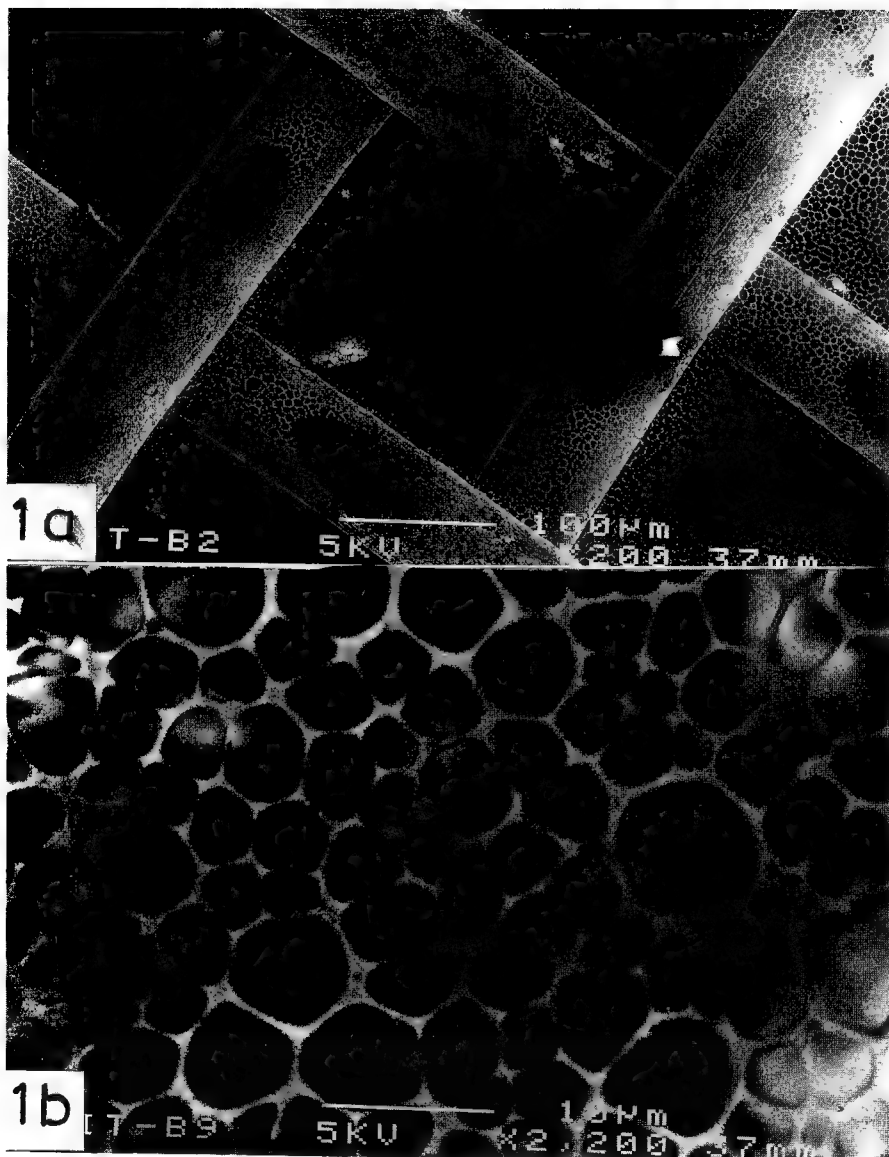
Fig.1.-- Lacey polymer film over copper wire mesh mounted on a brass stub as seen under JEOL JSM 6400 scanning microscope. Due to the Gum Arabic release agent incorporated, the film released easily from the substrate. Note absence of pseudo holes and high porosity. a) Bar = 100 μm; b) Bar = 10 μm.

241

A rapid silver-impregnation technique on ultra-thin sections for EM

K. Chien, R.C. Heusser, M.L. Jones and R.L. Van de Velde

Pathology & Laboratory Medicine, Cedars-Sinai Medical Center
Los Angeles, California 90048

Silver impregnation techniques have been used for the demonstration of the complex carbohydrates in electron microscopy.[1,2] However, the silver stains were believed to be technically sensitive and time consumming to perform. Currently, due to the need to more specifically evaluate immune complex for localization in certain renal diseases, a simplified procedure in conjunction with the use of the microwave has been developed and applied to renal and other biopsies. The procedure is as follows:

Preparation of silver methenamine solution:
1. 15ml graduated, clear polystyrene centrifuge tube (Falcon, No. 2099) was rinsed once with distilled water.
2. 3% hexamethylene tetramine (methenamine) was added into the centrifuge tube to the 6ml mark.
3. 3% silver nitrate was added slowly to the methenamine to the 7ml mark while agitating. (Solution will instantly turn milky in color and then clear rapidly by mixing. No precipitate should be formed).
4. 2% sodium borate was added to the solution to the 8ml mark, mixed and centrifuged before use.

Staining procedures:
1. Glutaraldehyde/osmium fixed kidney specimens were embedded in epoxy resin. Ultra-thin sections (pale gold) were collected on Gilder 300 mesh nickel grids and inserted vertically into the slots of a silicone rubber staining pad.
2. 2% periodic acid was dropped onto the grids and the staining pad was placed in a moisture chamber (pre-heated Petri dish with wetted filter paper) in a microwave oven (Sharp, R-2A82B) for 50 seconds at full power.
3. Grids incubated in solution for 1 minute, thoroughly rinsed with a jet of distilled water, dried with filter paper and inserted into new slots (or another staining pad)to avoid contamination.
4. Silver staining solution was dropped onto the grids in the moisture chamber and then stained in the microwave oven at full power for approximately 100 seconds (sections will turn brown).
5. Grids incubated in solution for 2 minutes, rinsed with distilled water, dried and examined by TEM without U/Pb staining.
* For routine electron microscopy, ultra-thin sections were collected on copper grids and stained with U/Pb in the microwave oven at full power for 20 and 18 seconds respectively.

In renal specimens, glomerular basement membranes (fig.1) were strongly stained and clearly distinguishable from the immune complexes. Also, in the cytomegalovirus infected duodenal biopsies, nucleocapsids and virions were stained by this method (fig.2). The silver particles were fine and background staining is minimal.

This silver impregnation technique demonstrates the simplicity of chemical preparations and staining procedure. Disposable plastic centrifuge tubes are used instead of acid-washed glassware. Ratios between chemicals are important but not critical. Uncoated nickel grids are inserted vertically in a staining pad which allows silver staining on both sides of the ultra-thin sections for high contrast and minimal handling. The use of microwave shortens the staining time and makes this silver stain valuable for practical application.

References

1. H. Z. Movat, Amer. J. Clin. Path. 35(1961)528.
2. A. Rambourg, J. Histochem. Cytochem. 15(1967)409.
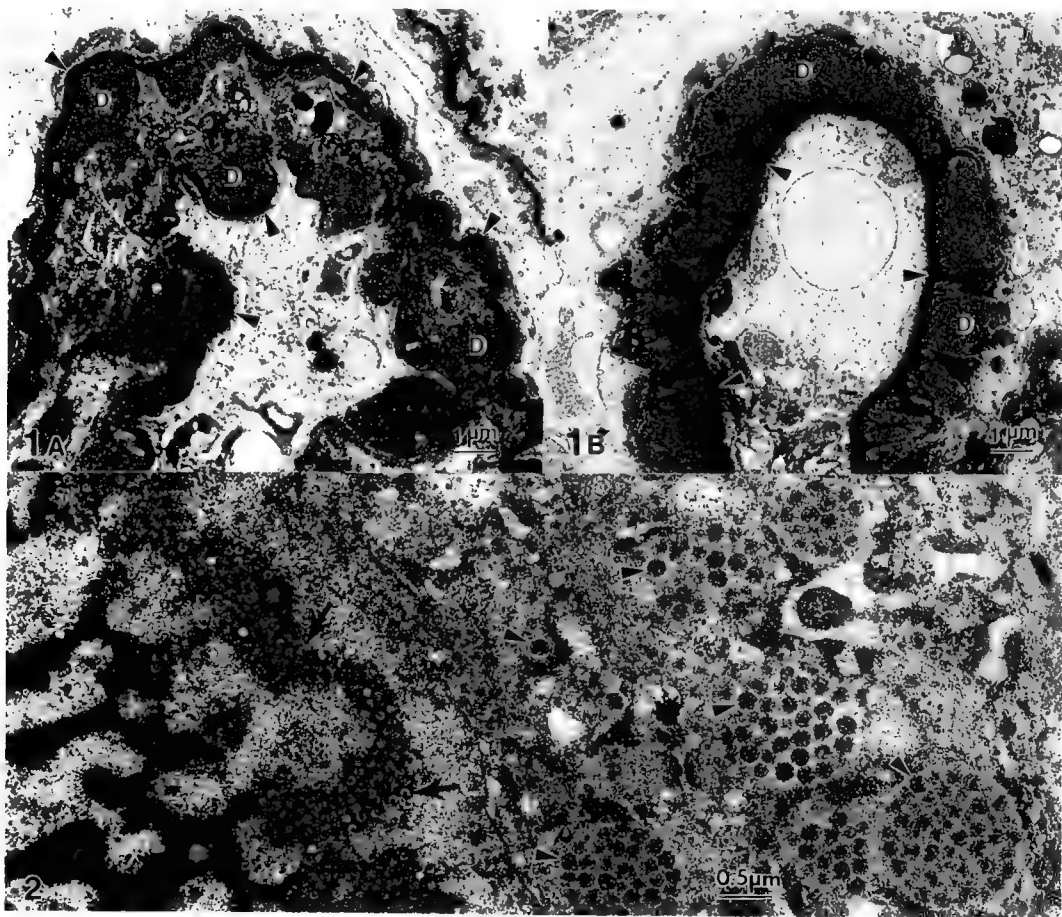
FIG. 1--Glomerular capillary basement membranes (arrowheads) are strongly stained by silver and clearly distinguished from immune complex deposits (D) in membranoproliferative (A) and membranous glomerulonephritis (B).
FIG. 2--Nucleocapsids (arrows) and virions (arrowheads) of human cytomegalovirus in infected cells are identified by silver.

A MODIFICATION OF THE HUMPHREY'S STAIN FOR EPOXY SECTIONS: A SUITABLE
ALTERNATIVE TO TOLUIDINE BLUE FOR ROUTINE SECTION STAINING

E.P. Calomeni and W.T. Gunning

Department of Pathology, Medical College of Ohio, Toledo, Ohio, 43699

We have abandoned the use of toluidine blue as a routine stain for light microscopy of epoxy
embedded tissues. As an alternative, we utilize a three-component stain described by Humphrey
and Pittman (1974) with minimal modifications to render the procedure substantially more timely
(1). Numerous publications in the early 60's through mid 70's proposed a variety of polychromatic
stains for light microscopic evaluation of epoxy sections. Most of these reports cited the difficulties
involved in using a reliable method of staining epoxy sections in a timely and non-cumbersome
fashion (2). One of the most successful stains to address these concerns is toluidine blue, first
described by Trump *et al.* in 1961 (3), which is undoubtedly the stain of choice in most
laboratories. We have found that the differentiation of stained tissues when using the Humphrey's
stain is superior to that rendered by toluidine blue. This stain differentiates cellular detail from
connective tissue in brilliant fashion as most cells will appear in various shades of blue (quite similar
to shades produced by toluidine blue) and collagen appears a vivid deep pink to bright red. It has
proven to be a valuable stain when evaluating fibrosis in fine needle liver biopsies (Figure 1).
Another example of its superior staining differentiation is seen in sections of peripheral nerve
(Figures 2-4). Myelinated axons stain dark blue for the myelin sheath, axon bodies stain pale blue,
and unmyelinated fibers are easily seen due to the red color of connective tissue surrounding them.

Some disadvantages when using this stain include color variability when comparing sections
embedded in a variety of epoxy resins, variability in time required to stain sections (also dependent
upon epoxy resin type), and fading of the stain over time if sections are heat dried before the
staining procedure (1, 4).

We use a rapid cure, "firm" mixture of Spurr's epoxy resin as the sole embedding media in our
laboratory. The only modification we have made to the procedure as described by Humphrey and
Pittman (1, 4) is to increase the staining temperature and decrease the time. Two dye solutions are
used:

Solution A.	Methylene blue-azure II	0.13 g	Methanol	10 ml
	Azure II	0.02 g	Phosphate buffer, pH 6.9	30 ml
	Glycerol	10 ml	Distilled H_2O	50 ml

Solution B.   Basic fuchsin , 1% in 50% ethanol

The protocol we follow is to place glass sides with dried epoxy sections in a coplin jar containing
solution A (methylene blue-azure II) in a water bath at 80° C for 5 minutes. Slides are then washed
with warm running tap water and subsequently placed upon a 60° C hot plate for staining with the
counter stain, basic fuchsin applied by dropper, for 25 seconds. This procedure has proven to be
easy, reliable, and most definitely beneficial in our opinion. The purpose of this report is to draw

attention to a method of staining epoxy sections for light microscopy, established many years ago, which enhances detail available in sections that are thinner than paraffin sections used for routine histology.

1. Humphrey, CD and Pittman, FE (1974) Stain Technol 49(1):9-14
2. Spurlock, BO *et al.*, (1966) Am J Clin Pathol 46(2): 252-258.
3. Trump, BF, Smuckler, EA, and Benditt, EP (1961) J Ultrastruct Research 5:343-348.
4. Andersson, M (1977) Application note 303, LKB, Bromma, Sweden.
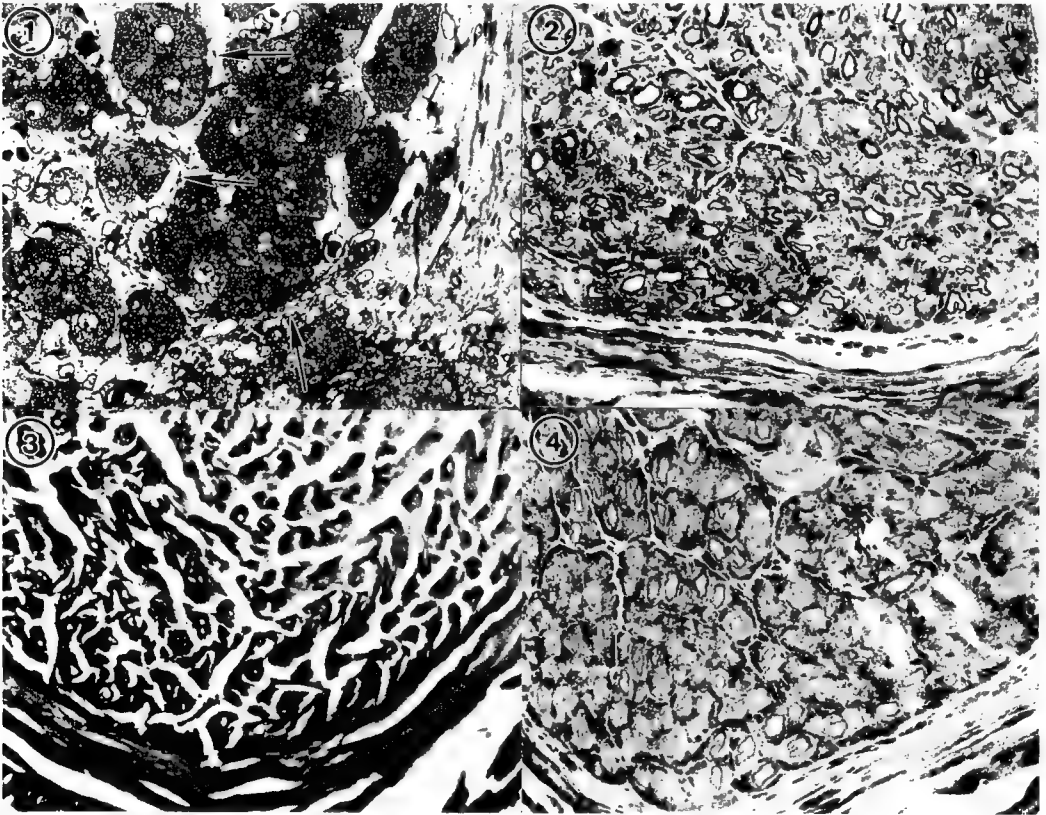
Figure 1. Epoxy section of liver stained with Humphrey's stain shows early fibrosis between hepatocytes (arrows). 300 X

Figure 2. Epoxy section of peripheral nerve stained with Humphrey's stain shows fine detail including unmyelinated fibers. 300 X

Figure 3. Paraffin section of peripheral nerve (Hematoxylin and eosin stain) demonstrates that epoxy sections offer more detail due to section thickness and attention paid to fixation of tissues which may be ultimately viewed by electron microscopy. 300 X

Figure 4. Epoxy section of peripheral nerve stained with toluidine blue for comparison with Figure 2; black and white photographs are limited for such comparisons. 300 X

NANOSURGERY OF BIOLOGICAL SPECIMENS USING A FOCUSED ION BEAM

John M. Mackenzie, Tracy H. Woodward[1] Dieter P. Griffis and Phillip E. Russell

Analytical Instrumentation Facility, Box 7916, North Carolina State University, Raleigh, NC 27695
[1]Materials Analytical Services, 2418 Blue Ridge Road, Suite 105, Raleigh, NC 27607

While ion beams have been utilized for sample preparation in Materials Science for many years, this technology has rarely been applied to biological sample preparation. With the advent of computer controlled, finely focused ion beam technology (also widely used for modification and preparation of materials samples[1]), many opportunities exist for nanosurgery of biological specimens at particular locations of interest e.g. many biological interactions, such as parasites/host interactions, occur as rare events at specific binding sites. In order to visualize the binding sites of viruses to their host cells with thin sectioning, cells are commonly infected with a thousand fold more viruses than would be present in the case of a normal infection. Although this technique allows visualization of the interaction site, this is clearly not a natural state and may bias the results. Utilizing a technique such as freeze etching that exposes large surfaces , one can locate rare events such as an isolated viral infection site. However, this techniques relies on free running fracture planes and thus provides no control of the surfaces exposed for examination. Most current methods, therefore, do not allow location of rare events over large surfaces which can then be cross sectioned at the specific point of interest. A high resolution (50nm minimum spot size), computer controlled focused ion beam provides the capability of both imaging the sample to find the location of interest and the provide controlled erosion of the sample while simultaneously allowing visualization of the surfaces as they are eroded.

Samples were prepared by fixation in 3% glutaraldehyde followed by dehydration in ethanol, critical point drying and sputter coating with a light coating of gold/palladium (20nm). The sample was mounted on a standard metal stub that could be transferred between the scanning and focused ion beam instruments. All focused ion beam micromachining was performed using an FEI Model 610 Workstation. For imaging of samples to locate areas of interest, the Ga^+ ion gun was operated at 25keV, 64pa providing a beam spot size of approximately 64 nanmeters. The area of sample to be micro machined was then selected from the acquired image and Ga^+ current was increased to approximately 250na to reduce cutting time. The ion gun was then retuned to the imaging conditions described above to polish the face of the cross section and to acquire an ion image. Samples were then transferred to a Phillips 505T SEM for further examination. See representative examples in figures 1 and 2.

1. J. G. Pellerin, D.P. Griffis, P.E. Russell, J. Vac. Sci. Technol. (1990) B8(6), 1945.
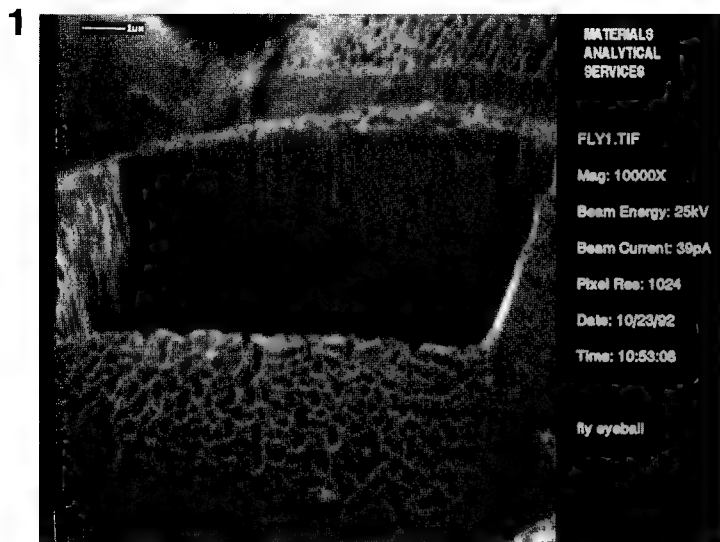
Fig 1. Secondary electron micrograph of housefly eye cross section generated using the focused ion beam.

Fig 2. Scanning electron micrograph of same field shown in Figure 1.

DUAL STAIN KIT FOR THE MICROSCOPIC GRAM CLASSIFICATION OF OCULAR INFECTION BACTERIA

Jacob S. Hanker*, Dale N. Holdren**, Kenneth L. Cohen** and Beverly L. Giammara+

*Biomedical Engineering Dept., University of North Carolina, Chapel Hill, NC 27599-7455

**Ophthalmology Dept., University of North Carolina, Chapel Hill, NC 27599-7545

+Analytical Electron Microscopy Laboratory, Graduate Programs and Research, University of Louisville, Louisville, KY 40292

Keratitis and conjunctivitis (infections of the cornea or conjunctiva) are ocular infections caused by various bacteria, fungi, viruses or parasites; bacteria, however, are usually prominent. Systemic conditions such as alcoholism, diabetes, debilitating disease, AIDS and immunosuppressive therapy can lead to increased susceptibility but trauma and contact lens use are very important factors. Gram-negative bacteria are most frequently cultured in these situations and Pseudomonas aeruginosa is most usually isolated from culture-positive ulcers of patients using contact lenses.[1] Smears for staining can be obtained with a special swab or spatula and Gram staining frequently guides choice of a therapeutic rinse prior to the report of the culture results upon which specific antibiotic therapy is based. In some cases staining of the direct smear may be diagnostic in situations where the culture will not grow.[2,3] In these cases different types of stains occasionally assist in guiding therapy.

Our laboratories have recently developed a rapid microwave-accelerated silver methenamine PATS-TS stain for lipopolysaccharide(LPS) or endotoxin which stains gram-negative (but not gram-positive) bacteria for both light and electron microscopy.[4-10] This Giammara-Hanker PATS-TS reaction also stains mannans and glucans in the walls of fungi such as Candida. By elimination of a step in this reaction involving condensation of the dialdehyde (produced by periodate oxidation of the vicinal diglycol of the LPS KDO) with thiocarbohydrazide(TCH), fungi but not gram-negative bacteria are stained.[9,10] Over the past two years the staining of duplicate smears of a large number of bacterial cultures or of aspirates from many infected patient sites, one with the Sigma Diagnostics HT90 Gram Stain (which is primarily for gram-positive bacteria) and one with the PATS-TS stain (positive for gram-negative bacteria) has indicated the possible importance of a dual stain kit (PATS-TS stain and Sigma HT90 Gram Stain) for the rapid classification of bacterial infections.[6-10] This could be especially important where gram-negative bacteria or microorganisms such as Pneumocystis carinii or Candida might be suspected as in AIDS.[10]

Preliminary studies in 15 ocular infections have shown the benefits of comparing the results with these two stains on duplicate smears taken directly from patients (and from cultures when available) for classifying ocular infections.

Thus, Gram classification of a number of ocular infections that could not be classified by culture was accomplished with our dual stain kit on duplicate smears (Table 1). In other situations it could be important to compare the dual stain kit results with the Sigma Diagnostics HT100 Silver Stain version of our PATS stain (without the TCH step) which shows fungi positively but not gram-negative

bacteria. Thus, a treble kit, containing the stains in our dual kit and the Sigma Diagnostics HT100 Silver Stain could be important for many other types of infections as well as ocular. Positively-stained gram-negative rods (arrows, Fig. 1) and diplococci (arrows, Fig. 2) were clearly seen in PATS-TS stained smears from ocular infections whose duplicate Gram-stained smears showed no safranin-stained rods or many safranin-stained diplococci respectively.

Silver-methenamine stained slides of gram-negative bacteria or of fungi can be mapped with a Microlator Slide™ and directly studied by the BEI or SEI modes of SEM by a Xeroxographic technique reported last year.[11]

References

1. J. Perrigin, J. Am. Optom. Assoc. (1992)63, 243.
2. T. Merrick, Lab. Med. (1982)13, 498.
3. E. Bottone, Lab. Med. (1988)19, 288.
4. B. Giammara et al., Proc. 47th Ann. Meet. Electr. Microsc. Soc. Amer. (1989)1082.
5. J. Hanker et al., Microsc. Res. Tech., in press.
6. J. Hanker et al., Proc. 49th Ann. Meet. Electr. Microsc. Soc. Amer. (1991)120.
7. J. Hanker, et al., Proc. 50th Ann. Meet. Electr. Microsc. Soc. Amer. (1992)686.
8. J. Hanker et al., Mater. Res. Soc. Symp. Proc. (1991)189, 355.
9. J. Hanker et al., Mater. Res. Soc. Symp. Proc. (1991)189, 371.
10. J. Hanker and B. Giammara, Scanning, in press.
11. B. Giammara and J. Hanker, Proc. 50th Ann. Meet. Electr. Microsc. Soc. Amer. (1992)770.

TABLE I

DUAL STAINING POSITIVITY* OF GRAM-NEGATIVE
OCULAR INFECTIONS

	Cultures With No Growth	Cultures With Gram-Negative Microbes
Gram Safranin Stain	10%	50%
PATS-TS Stain	50%	100%

*ca percentage

1   x 1000   2   x 1000
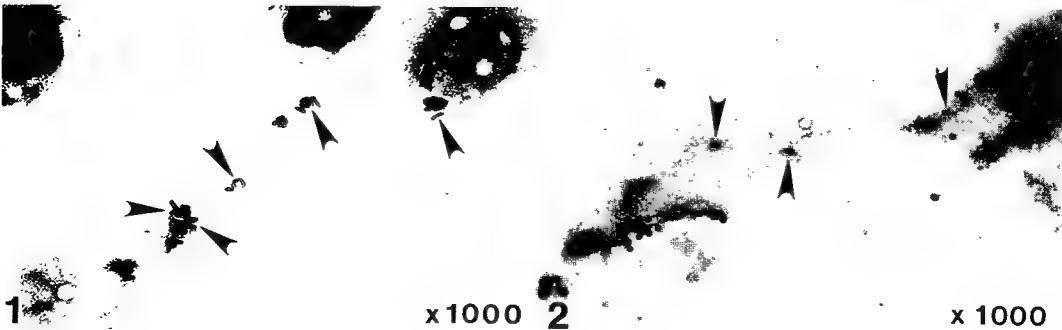
X-RAY DETECTION PERFORMANCE OF A 300KV FIELD-EMISSION ANALYTICAL
ELECTRON MICROSCOPE

C. E. Lyman, J. I. Goldstein, D.B. Williams, D.W. Ackland, S. von Harrach*, A. W. Nicholls*,
and P.J. Statham**

Dept. of Materials Science and Engineering, Lehigh University, 5 East Packer Ave., Bethlehem,
PA 18015; * Fisons Instruments/VG Microscopes, Birches Industrial Estate, Imberhorne Lane,
East Grinstead, West Sussex, RH19 1UB, U.K.; **Oxford Instruments, Microanalysis Group,
Halifax Road, High Wycombe, Buckinghamshire, HP12 3SE, U.K.

A major goal of analytical electron micrsocopy (AEM) is to detect small amounts of an element in a
given matrix at high spatial resolution. While there is a tradeoff between low detection limit and
high spatial resolution,[1] a field emission electron gun allows detection of small amounts of an
element at sub-10nm spatial resolution. The minimum mass fraction of one element measured in
another is proportional to $[(P/B) \cdot P]^{-1/2}$ where the peak-to-background ratio P/B and the peak intensity
P both must be high to detect the smallest amount of an element. Thus, the x-ray detection
performance of an analytical electron microscope may be characterized in terms of standardized
measurements of peak-to-background[2], x-ray intensity[3], the level of spurious x-rays (hole count)[4],
and x-ray detector performance in terms of energy resolution and peak shape.

This paper provides measurements of these parameters from Lehigh's VG Microscopes HB-603
field emission AEM. This AEM was designed[5] to provide the best x-ray detection possible. The
instrument has two Oxford Instruments (Link Analytical) energy-dispersive x-ray spectrometers
which can each collect x-rays at a 20° take-off angle while the specimen is at 0° tilt. One detector is
a windowless Si(Li) detector with a nominal 30 mm[2] active area the other is an ultra-thin-window
intrinsic germanium (IG) detector of the same physical size. In each case the detector cryostat has
been designed to provide the detector crystal a 0.3 steradian collection solid angle from the center
of the specimen. Both detectors retract along the line-of-sight to the specimen on motorized tracks.
To reduce background x-rays generated in the specimen stage area of the microscope, the specimen
cup and retaining ring were of Be, and inserts of Al (to be replaced by Be) were fitted on the top
and bottom polepieces. While not used for the present measurements, electrostatic beam blanking
has been used to gate the x-ray detector, providing the highest count rate capability available.

The specimen used in the P/B and x-ray intensity measurements was the NIST chromium thin film
of 104 nm thickness described by Williams and Steel.[2] This specimen was kept at 0° tilt and data
was taken on the Cr film at the center of the grid squares. For the P/B measurement, the CrK-
alpha peak was divided by a 10 eV-wide background B as defined by Fiori.[2] Figure 1 shows that
P/B increases smoothly from 100 to 300 kV. Similar measurements[3] from a Philips EM430 are
shown for comparison. The IG detector exhibited the highest values at each kV with P/B = 6300
at 300 kV. This appears to be the highest value of P/B yet recorded, equalling that reported by
Zaluzec with a Si(Li) detector on a similar instrument.[6]

Figure 2 shows x-ray intensity (in units of cps/nA) collected by the two detectors as a function of
accelerating voltage. The x-ray intensity decreases with kV which is expected since the cross-
section for x-ray excitation decreases over the same range.[3] Figure 3 shows the hole count for the
HB-603 compared to measurements on the same specimen from a Philips EM430 with a standard
"hard x-ray" second condenser aperture.[4] The data from the HB-603 show an order of magnitude
improvement in spurious x-ray generation at 300 kV. Figure 4 shows the performance of the IG x-
ray detector in measuring light elements. The specimen was a 100 nm NiO particle supported on a
carbon film. This spectrum is superior in P/B and energy resolution compared to a similar
spectrum from the same particle taken with the Si(Li) detector.

250

References

1. J. I. Goldstein, C. E. Lyman, and J. Zhang, *Microbeam Analysis - 1990*, J. R. Michael and P. Ingram (eds.), San Francisco Press, San Francisco, CA, (1990) 265.
2. D. B. Williams and E. B. Steel, *Analytical Electron Microscopy-1987*, D. C. Joy (ed.), San Francisco Press, (1987) 228.
3. M. Zemyan and D. B. Williams, submitted to *Journal of Microscopy*.
4. C. E. Lyman and D. W. Ackland, *Proceedings of the 49th Annual Meeting Electron Microscopy Society of America*, San Francisco Press, (1991) 720.
5. D. B. Williams et al., Proceedings of the Microbeam Analysis Society - 1993, in press.
6. N. J. Zaluzec, *Proceedings of the 50th Annual Meeting Electron Microscopy Society of America*, San Francisco Press, (1992) 1466.
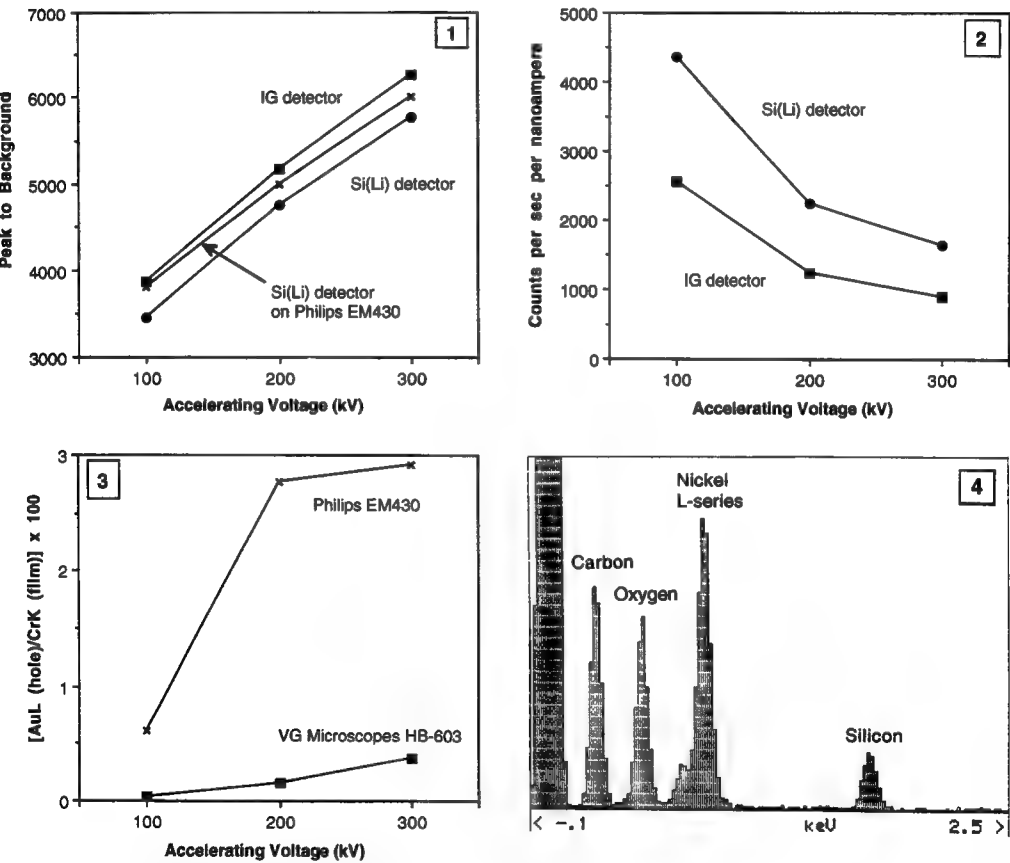
Figure 1. P/B versus accelerating voltage for the Si(Li) and IG detectors on the VG Microscopes HB-603 AEM. The IG detector exhibits the highest P/B yet obtained. Philips EM430 data[3] is shown for comparison.

Figure 2. X-ray intensity (counts/sec/nA) versus accelerating voltage for Si(Li) and IG detectors in the HB-603.

Figure 3. Hole count in the VG Microscopes HB-603 dedicated STEM compared with that of the Philips EM430 conventional TEM/STEM. Specimen was Cr film over two gold grids.[4]

Figure 4. Spectrum from 100nm NiO particle on a carbon film with IG detector at 300 kV.

COMPARISON OF HIGH-ANGLE TAKE-OFF AND LOW-ANGLE TAKE-OFF EDX DETECTOR GEOMETRY OF THE HF-2000 FE-TEM

Y. Sato, T. Hashimoto, M. Ichihashi, Y.Ueki*, K. Hirose*, and T. Kamino*

Instrument Division, Hitachi Ltd., Ibaraki, 312 Japan
* Hitachi Instruments Engineering Co.Ltd.,Ibaraki, 312 Japan

Analytical TEMs have two variations in x-ray detector geometry, high and low angle take off. The high take off angle is advantageous for accuracy of quantitative analysis, because the x rays are less absorbed when they go through the sample. The low take off angle geometry enables better sensitivity because of larger detector solid angle.

Hitachi HF-2000 cold field emission TEM[1, 2] has two versions; high angle take off and low angle take off. The former allows an energy dispersive x-ray detector above the objective lens. The latter allows the detector beside the objective lens. The x-ray take off angle is 68° for the high take off angle with the specimen held at right angles to the beam, and 22° for the low angle take off. The solid angle is 0.037 sr for the high angle take off, and 0.12 sr for the low angle take off, using a 30 mm^2 detector.

To compare analytical performance of two versions, direction dependency of the results from unisotropic sample was investigated. For this purpose, line profiles of Cr concentration in a stainless steel (SUS-304) across the same grain boundary were measured with 1 nm probe, 1nm step, 0.4 nA probe current, and acquisition time of 50 sec. for each point. Measurements were carried out with each microscope version under the condition that the boundary is placed both parallel and perpendicular to the detector axis. The sample was not tilted, but the area was selected at off-Bragg condition to avoid the channeling effect[3]. Configuration of the high angle detector with the perpendicular grain boundary (G.B.) and that of the low angle detector with the parallel grain boundary are shown in figures 1 and 2.

Experimental results are shown in figures 3~6. Figures 3 and 4 were measured with top take off detector from the same area of grain boundary parallel and perpendicular to the detector axis. As shown in these figures, both concentration curves are in good agreement, and spatial resolution measured with the high angle version is not affected by the direction of the grain boundary. Figures 5 and 6 were obtained with the low angle detector from the grain boundary parallel and perpendicular to the detector axis respectively. The x ray count with the is approximately 4 times of the high angle version. The spatial resolution of figure 5 is as good as the high angle version. However, figure 6 shows that the spatial resolution is reduced when the measurement is done with the grain boundary perpendicular to the detector direction. In this case, experimental results seems to be affected by electron beam broadening and x-ray absorption in the sample.

The high angle version is suitable for analyzing nanoscale orders sample with unisotropic distribution. From smaller influences of the beam broadening and the x-ray absorption, it is also derived that accurate quantitative analysis is done with the high angle version more easily. With the low angle version, x-ray sensitivity is higher than the high angle version, so that many x-ray photons are detectable in shorter time. However, careful alignment of the sample to the detector is required if one may expect spatial resolution as good as the high angle version.

References
1. T.Hashimoto and D.C.Joy, Proc. 50th EMSA (1992), 1208.
2. T.Hashimoto et al, Proc.49th EMSA (1991), 352.
3. K.M.Krishnan, Scanning Microscopy Supplement 4 (1990), 157-170

Fig. 1

68°

G.B

Fig. 2

22°

G.B
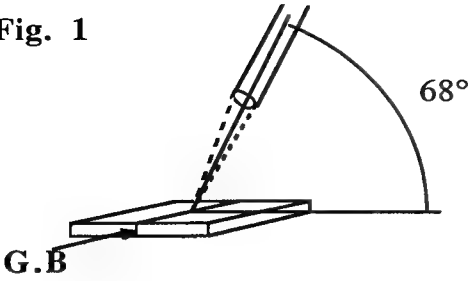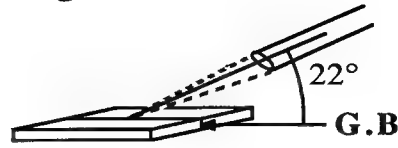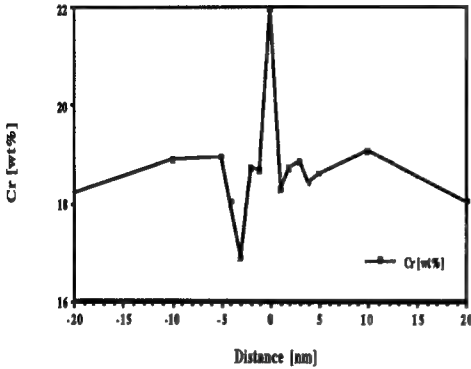
Fig. 3

Fig. 4
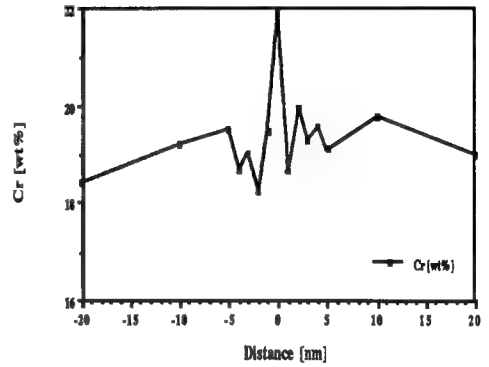
Fig. 5
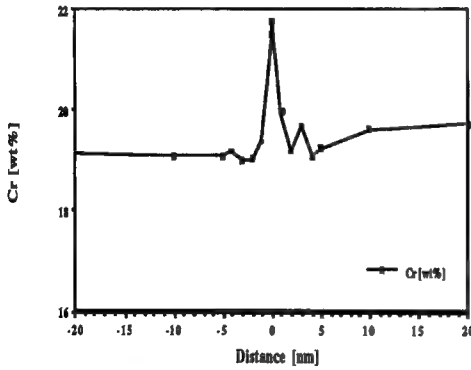
Fig. 6
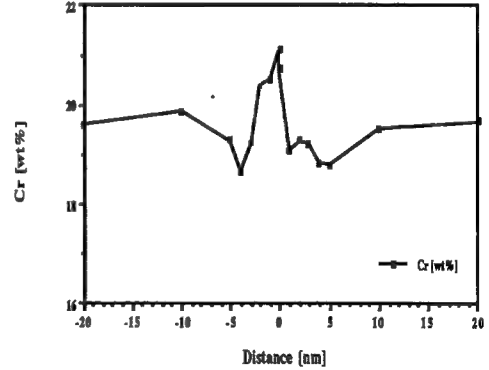
Fig. 1.___ Top take off geometry with grain boundary perpendicular to detector axis.
Fig. 2.___Side take off geometry with grain boundary parallel to detector axis.
Fig. 3.___Cr weight % across grain boundary (Distance=0)parallel to top take off detector.
Fig. 4.___Cr weight % across grain boundary perpendicular to top take off detector.
Fig. 5.___Cr weight % across grain boundary parallel to side take off detector.
Fig. 6.___Cr weight % across grain boundary perpendicular to side take off detector.

DEVELOPMENT OF HIGH-PERFORMANCE OBJECTIVE LENS POLEPIECE FOR ULTRAHIGH RESOLUTION ANALYTICAL ELECTRN MICROSCOPE

K. Fukushima, T .Kaneyama, F. Hosokawa, H. Tsuno, T. Honda and M. Kersker*

JEOL Ltd., 1-2, Musashino 3-chome, Akishima, Tokyo, 196 JAPAN
* JEOL (U.S.A.) Inc., 11 Dearborn Road, Peabody, MA 01960

Recently, in the materials science field, the ultrahigh resolution analytical electron microscope (UHRAEM) has become a very important instrument to study extremely fine areas of the specimen. The requirements related to the performance of the UHRAEM are becoming gradually severer. Some basic characteristic features required of an objective lens are as follows, and the practical performance of the UHRAEM should be judged by totally evaluating them.

1) Ultrahigh resolution to resolve ultrafine structure by atomic-level observation.
2) Nanometer probe analysis to analyse the constituent elements in nm-areas of the specimen.
3) Better performance of x-ray detection for EDS analysis, that is, higher take-off angle and larger detection solid angle.
4) Higher specimen tilting angle to adjust the specimen orientation.

To attain these requirements simultaneously, the objective lens polepiece must have smaller spherical and chromatic aberration coefficients and must keep enough open space around the specimen holder in it.

We have newly developed high-performance objective lens polepieces for a 200 kV and a 300 kV UHRAEM separately. In order to obtain an optimum shape of these polepieces, the optical constants for various shapes which were obtained by altering the lens shape parameters, such as the bore diameter, lens gap, and tapered angle were calculated by the finite element method (FEM). In designing the shape, we paid attention to sufficiently satisfy the requirements descrebed above. As the concrete aim for the development of the new polepieces, we decided the following items.

1) Spherical abberation coefficients ; less than 0.5 mm for 200 kV and 0.6 mm for 300 kV, respectively.
2) Specimen tilting angle ; higher than $\pm 20°$ as a combined angle of X-tilt and Y-tilt.
3) Take-off angle and solid angle ; higher than $20°$ and larger than 0.1 st.

From the results of FEM calculation, it was ascertained that the optimum shape for 300 kV was a little different from that for 200 kV. The theoretical characteristic features of the two best-shaped polepieces are shown in Table 1. The values for the detection solid angle in this table correspond to the detector which has a $30mm^2$ window.

Two new polepieces for 200 kV and 300 kV were made trially, based on the design decided by theoretical calculation and on the necessity of open space. And their features were ascertained experimentally. As a result, their spherical aberration coefficients obtained by the diffractogram analysis method[1] agreed with the theoretical values. A specimen tilting angle of $20°$ was achieved. X-ray detection sensitivity for Al K α using the new 300 kV polepiece (solid angle 0.1 sr) compared with that of the present 300 kV polepiece (0.068 sr) is shown in Fig.1. The sensitivity ratio between them was 1.35. Figure 2 shows a Scherzer focused image of amorphous germanium thin film deposited with evaporated gold particles and its optical diffractogram, using the new 300kV polepiece. This image demonstrates a point resolution of 0.167 nm which is led by theoretical calculation.

1) O.L. Krivanek, Optik 45(1976)97

Table 1 Characteristic features of newly designed objective lens polepieces.

	Accelerating voltage (kV)	
	200	300
Spherical abberation coefficient Cs (mm)	0.5	0.57
Chromatic abberation coefficient Cc (mm)	1.0	1.3
Focal length Fo (mm)	1.7	2.5
Theoretical resolution d (nm)	0.194	0.167
Specimen tilting angle θ (deg)	±20	±20
EDS take-off angle (deg)	25	20
EDS detection solid angle (sr)	0.13	0.1
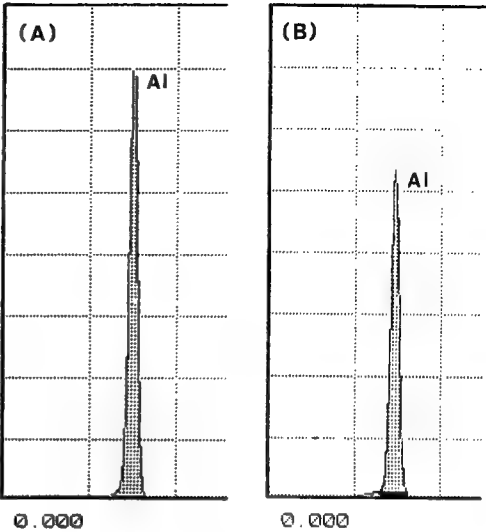
Fig.1 Comparison of x-ray detection sensitivity for Al K α. A: new polepiece (334373 counts) and B:present polepiece (247678 counts). VFS 32768 counts, thickness of Al foil 15 μm, probe current 50 pA, and live time 100 sec.
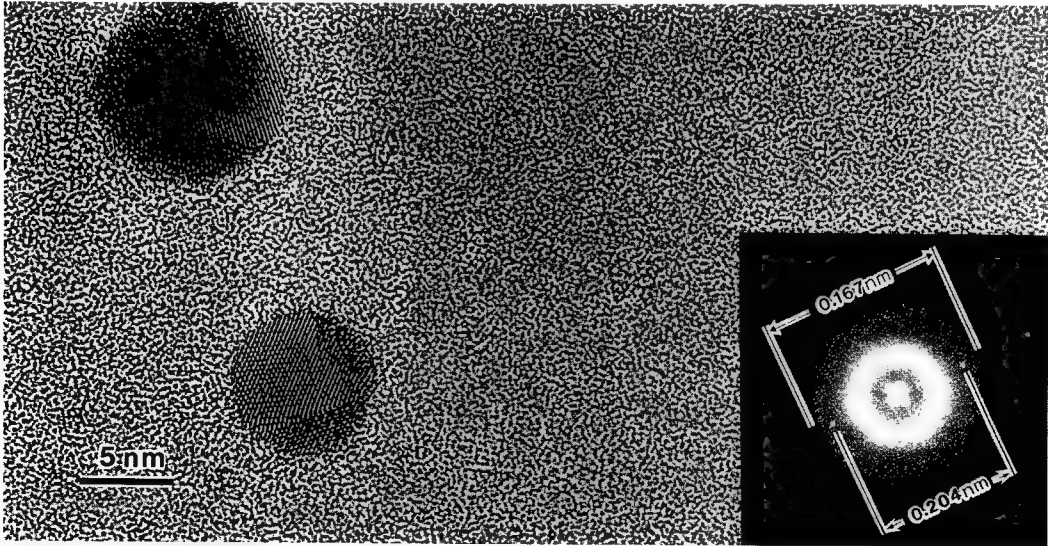
Fig. 2 Scherzer focused image and its optical diffractogram (inset) of amorphous Ge film deposited with evaporated Au particles, obtained using newly designed polepiece for 300 kV UHRAEM.

255

HIGH-PERFORMANCE EM-002B OPTICAL COLUMN CONSTRUCTION FOR FUTURE EXPANSION

K.Shirota, K.Moriyama, S.Mikami, A.Ando, O.Nakamura and T.Yanaka

Electron Beam Engineering Dept., TOPCON Corporation, Itabashi, Tokyo, 174 Japan

Since modern analytical transmission electron microscopes must have a wide range of illumination conditions (from "mm" to "nm" probe size), an additional lens (one of the condenser lenses, usually called the "mini-lens") is arranged immediately above the objective lens pole pieces. As a result, it has become very difficult to install an exchange mechanism for the objective pole pieces, which used to be done routinely.

To overcome this, TOPCON Electron Microscope EM-002B incorporated a new mechanism which can be exchanged quite easily and reliably by the user. This mechanism makes a space to exchange pole pieces, without column disassembly, by precisely driven external mechanisms (Fig. 1). The time required for a typical user to carry out such exchange is usually 15 to 20 minutes, and it will take not more than two hours for high resolution image or analysis after exchange. This time is also shortened by the fact that an anti-contamination cold trap is not generally required in the case of EM-00 2B. So, this is quite a practical way to exchange pole pieces. With this characteristic, EM-002B not only can maintain basic performance of 0.18nm ultra-high resolution image(UHR) and nano-area analysis , but also provides a universal and extremely high performance electron microscope currently available for many anticipated fields of research, with specially developed pole pieces such as high resolution higher tilt (P-20,P-30), high tilt (HTs), high resolution & specimen heating (PH), a very wide field of view & high contrast image (PBio) and magnetic material observation (PMG) (table 1). With UHR system, the specimen can be tilted to ±10° double tilt with 0.18 nm resolution and cooling down to -170°C with the same specimen tilt. HTs gives us the performance of a wide range of holders such as ±60° specimen tilt or a cooling holder cooled down by liquid Helium. As for PH, it is possible to heat up to 1,000°C using double tilt (x,y ±15° respectively) or up to 1,300°C using single tilt, with a theoretical resolution of 0.22 nm. PMG enables magnetic material application through magnetic domain observation with a very weak field specimen area (Fig. 2) . Applying the magnetic field to the specimen is also possible. For plural pole pieces, an EDX detector can be set in the optimal position for each pair of pole pieces by way of a special flange called "SUPER FLANGE" (Fig. 3).

The P-20, in particular, effectively provides ultra high resolution images with a point resolution of 0.19 nm, and a specimen tilt up to x: ±22°, y: ±15° and extremely large solid angle such as 0.2str or more for x-ray detection. With this lens system, the analysis of a ultra fine area at the 1 nm level strictly corresponding to the ultra high resolution image using a LaB6 cathode can be practically realized. This results from three important points: (a) a very small spherical aberration constant of the pre- and after-field of the objective lens, (b) extremely large solid angle for x-ray detection, and (c) higher precision of the electron optical axis. These have been simultaneously established for the first time in the world. Consequently, this system has enabled elemental analysis from a 1 nm probe with a LaB6 cathode, successfully producing about 1/2 - 1/3 of the x-ray detection count per second (CPS) of a Field Emission Electron Microscope (FETEM), and with a 1.5 nm probe has provided higher CPS than an FETEM. This system also greatly reduces beam irradiation which would damage the specimen. With this construction, elemental analysis from a 1 nm area is actually more practical when one considers specimen damage and also specimen contamination problems. Fig. 4 shows an example of elemental analysis made with the P-20 and an EDX (detector: NORAN NORVA), which gives information on element analysis with a 1 nm probe. Table 2 shows the relationship between the probe diameter and its current with the UHR, P-20 and P-30 lens systems, while Fig. 5 shows the relationship

between the probe size, the spherical aberration constant of the pre-field lens and the probe current with a LaB6 cathode.

Although it requires an extremely high level of technique for lens design to realize 1 nm area analysis with a LaB6 cathode, especially in a pole pieces exchange system, EM-002B provides the highest performance applicable to a wide range of research. It also assures the possibility to maintain the highest performance of an electron microscope for a long period of time since the pole pieces are readily cleaned. This is important if we take into consideration the fact that contaminated pole pieces affect the performance of an electron microscope adversely.

[references]
1) W.D.Riecke & E.Ruska, Proc. 6th Int.Cong. on Electron Microscopy, 1(1966)19
2) K.Shirota et al. J.Electron Microsc.,25(4),303(1976)
3) M.N.Thompson, Proc. EUREM 80, (1980)526
4) T.Yanaka, A.Yonezawa et al., Proc. 41th EMSA, (1983)312
5) T.Yanaka, Proc.XIth Int. Cong. on Electron Microscopy, Kyoto, (1986)243
6) T.Yanaka, K.Moriyama, R.Buchanan MRS Proc. 139(1989)271
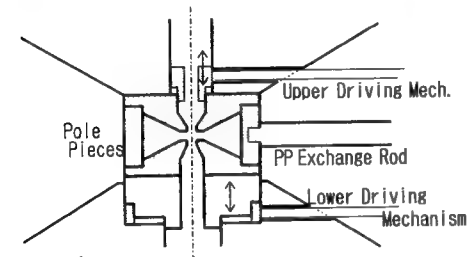
Fig. 1
Pole pieces exchange mechanism of EM-002B

Fig. 2
Magnetic domain observation lens.
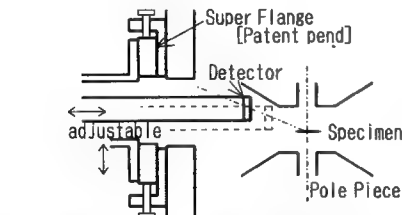
Fig. 3
Special flange for positioning EDX detector to the best point for each lens

P P	UHR	HTs	P-20	P-30	PH	PBio	PMG
Cs(mm)	0.4	2.7	0.5	1.2	0.9	2.7	—
Cc(mm)	0.8	2.4	1.0	1.2	1.0	2.4	—
δ (nm)	0.18	0.3	0.19	0.24	0.22	0.3	(0.8)
αx(str)	0.075	0.075	>0.2	>0.2	>0.2	—	
holders	±10° cold ±10°	±45~60° Liq.He etc.	22° etc.	±30° etc.	heat ±15°	quick 7mmgrid rotation	±10° heat ±15°

Table 1 Specification of exchangeable pole pieces of EM-002B (Cs: spherical aberration, Cc: chromatic aberration constants, δ: resolution, αx: solid angle for x-ray detection)

Fig. 4 Example of 1 nm probe analytical application from semiconductor(thickness: approx. 25nm), with P-20 lens system.

	1 nm	2 nm
UHR	0.06 nA	0.4 nA
P-20	0.05	0.3
P-30	0.03	0.2

Table 2 Probe current for 1nm and 2nm probe size of each lens
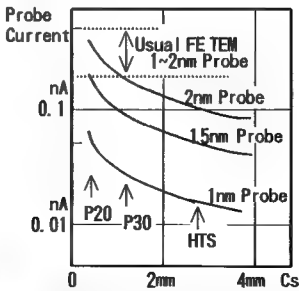
Fig. 5 Probe current as functions of spherical aberration constant(Cs) of pre-field lens and probe size.

257

THE NEW CM-SERIES TEMs: INTEGRATION OF A FIVE-AXIS MOTORIZED, FULLY COMPUTER-CONTROLLED GONIOMETER

Marc J.C. de Jong, P. Emile S.J. Asselbergs and Max T. Otten

Philips Electron Optics, Building AAE, 5600 MD Eindhoven, The Netherlands

A new step forward in Transmission Electron Microscopy has been made with the introduction of the CompuStage on the CM-series TEMs: CM120, CM200, CM200 FEG and CM300. This new goniometer has motorization on five axes (X, Y, Z, α, β), all under full computer control by a dedicated microprocessor that is in communication with the main CM processor. Positions on all five axes are read out directly — not via a system counting motor revolutions — thereby providing a high degree of accuracy. The CompuStage enters the octagonal block around the specimen through a single port, allowing the specimen stage to float freely in the vacuum between the objective-lens pole pieces, thereby improving vibration stability and freeing up one access port. Improvements in the mechanical design ensure higher stability with regard to vibration and drift. During stage movement the holder O-ring no longer slides, providing higher drift stability and positioning accuracy as well as better vacuum. The CompuStage has a number of unique features that make full use of the possibilities provided by computer control such as:

- A combination of high maximum tilts and absolute safety against damage of specimen holder, objective aperture and pole pieces.
- Speed of movement and direction are linked to the magnification on the microscope, with a speed reduction when the image is seen on a TV camera (with its higher magnification).
- Storage and recall of up to 25 five-dimensional positions as well external control of all five axes.

A unique feature of the new CompuStage is the MaxiTilt boundary check system that provides a flexible method for obtaining the highest tilts that are physically possible (Fig. 1). On instruments with ultra-high resolution objective lenses, the maximum tilt varies strongly as a function of X, Y, Z, α, β position. Normally two limiting choices exist: 1. absolute safety against damage of specimen holder, objective aperture and pole pieces, thereby strongly limiting the accessible tilt; 2. maximum tilt and hence no safety. Most microscopes fall somewhere between these extremes — a little tilt but no absolute safety. On the CM microscopes, the MaxiTilt system determines — 800 times per second when the stage is moving — what the accessible tilts are for the current combination of X, Y, Z, α and β and will not exceed these. At any combination of the five axes the maximum tilt that is physically possible is thus available to the operator, while absolute safety against damage is ensured.

The accurate read-out of all five axes makes it possible to store and recall specimen positions *and* orientations. Within seconds, orientations stored previously can be recalled (Figs. 2 and 3), thereby greatly speeding up many types of diffraction experiments. The five-axis recall facility is also accessible through remote control, allowing interfacing with external programs, e.g., for photomontage, systematic scanning of grids and computer-controlled tomography. The ease of external access to specimen position and orientation will allow us to test the feasibility of compucentricity (pseudo-eucentricity of the β tilt axis through computer-controlled feedback on X, Y and Z) and further automation.

With the introduction of the new CompuStage and its single-port entry a change has been made on the octagonal block surrounding the specimen area (Fig. 4). The access port freed has the dimensions standardized for EDX detectors, making it possible to mount more than one EDX detector or interfacing other detectors with the same, standard dimensions.
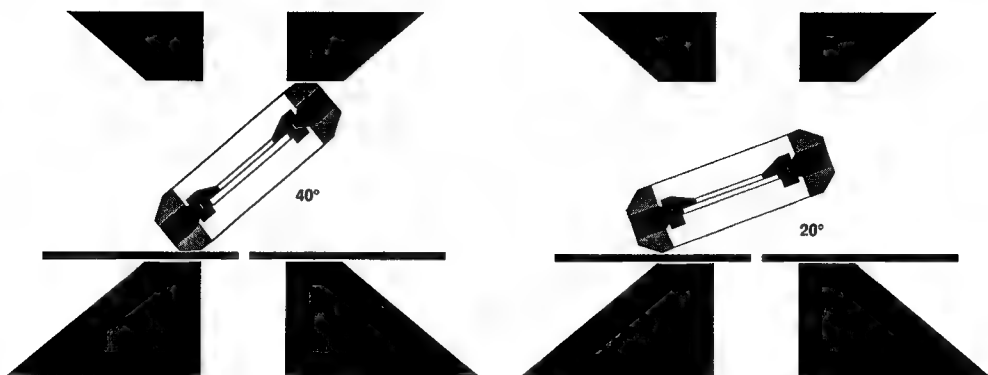
FIG. 1. For each combination of X, Y, Z, α and β, the MaxiTilt system determines the maximum tilts that are physically possible, combining high accessible tilts with absolute safety.
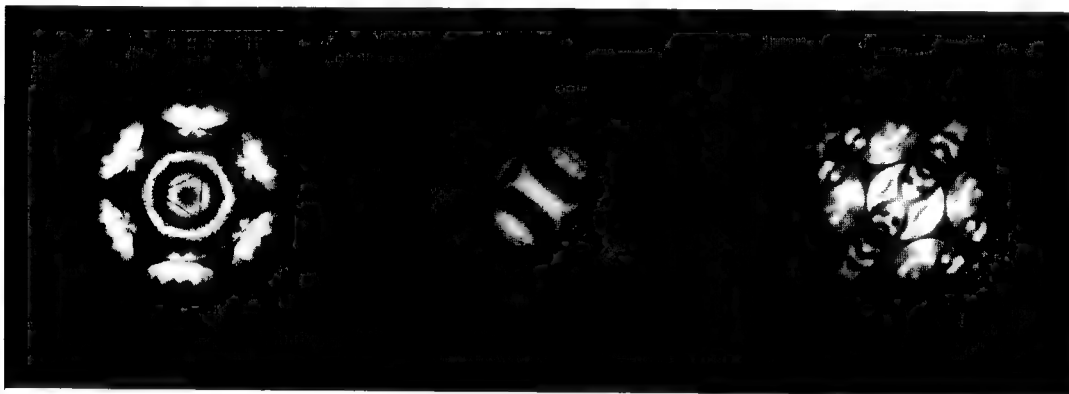
FIG. 2. Si diffraction patterns from three zone axes, stored and recalled using the 5-D recall facility.

FIG. 3. MICROCONTROLLER page showing the storage of the three axes of Fig. 2 in the registers on the right-hand side.
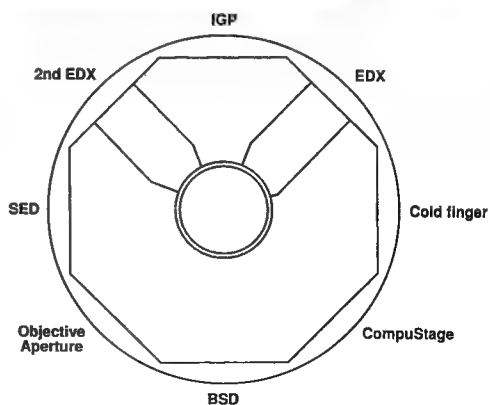
FIG. 4. Octagonal block around the specimen area — seen from above — showing the allocation of entry ports.

259

SCANNING ELECTRON MICROSCOPY OF PLANT CELLS USING A VARIABLE-PRESSURE SEM AND CRYOGENIC
TECHNIQUES

M. Yamada, K. Ueda, K. Kuboki*, H. Matsushima** and S. Joens***

Hitachi Instruments Engineering Co.,Ltd., Katsuta 312 JAPAN
*Hitachi Science Systems Co.,Ltd., Katsuta 312 JAPAN
**Faculty of Science,Saitama University, Urawa 338 JAPAN
***Nissei Sangyo America, Ltd.,Mountain View,CA 94043 USA

Use of variable pressure SEMs is spreading among electron microscopists. The variable
pressure SEM does not necessarily require specimen preparation such as fixation, dehydration,
coating,etc. which have been required for conventional scanning electron microscopy. The
variable pressure SEM allows operating pressure of 1~270 Pa in specimen chamber. It does not
allow microscopy of water-containing specimens under a saturated vapor pressure of water.
Therefore, it may cause shrink or deformation of water-containing soft specimens such as
plant cells due to evaporation of water. A solution to this problem is to lower the specimen
temperature and maintain saturated vapor pressures of water at low as shown in Fig.1. On
this technique, there is a published report of experiment to have sufficient signal to noise
ratio for scondary electron imaging at a relatively long working distance using an environ-
mental SEM.[1],[2] We report here a new low temperature microscopy of soft plant cells using a
variable pressure SEM (Hitachi S-2250N).

Fig.2 shows the instrument consisting of the S-2250N and a builtin cryostage. A specimen
mounted on a holder is cooled by liquid nitrogen. The ultimate specimen temperature depends
on the operating pressure in the specimen chamber. It reached down to about -70°C at 270 Pa.
There is a heater built-in the specimen holder. The specimen temperature can be set and
maintained at any point between the lowest and ambient conditions by controlling the heater
current. Leaves of <u>Pharbitis nil</u> (cb. Violet) seedling and the first leaves of mung bean
seedling were examined. Specimens were directly introduced in the specimen chamber after
cooling at 0°C for more than 10 minutes. Images were recorded at operating pressures of
1~270 Pa in backscttered electron image mode. The specimen temperature was varied 0~-40°C
during the microscopy. Most of the image recording was performed at about 0°C in order to
prevent cell damage by ice crystals.

In the microscopy of leaves of <u>Pharbitis nil</u> seedling at an ambient temperature and a
pressure of 130 Pa,cells started to shrink immediately and in 10 minutes they were deformed
thoroughly to such an extent that no one would recognize the original structure (Fig.3). At
about 0°C, the leaf primordia were clearly recorded (Fig.4). The first leaves of the mung
bean seedling were examined at about 0°C and at various specimen chamber pressures. Serious
deformation of the cells was observed at 1.3 Pa(Fig.5). At 130Pa,cells and pores were
preserved(Fig.6). We have confirmed that the low temperature microscopy using the variable
pressure SEM allows observation of water-containing soft plant cells without seriously
deforming the original structures.

References
1) G.D. Danilatos, EMAG-MICRO(1989)13
2) K.R. Peters,Electron Microscopy(1990)1,374
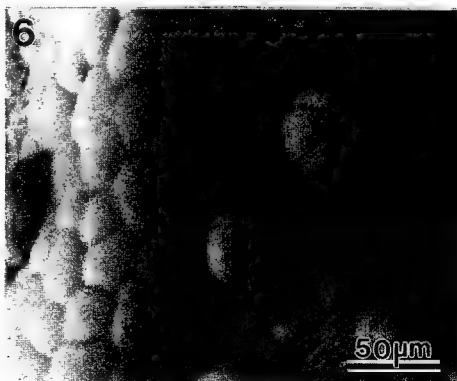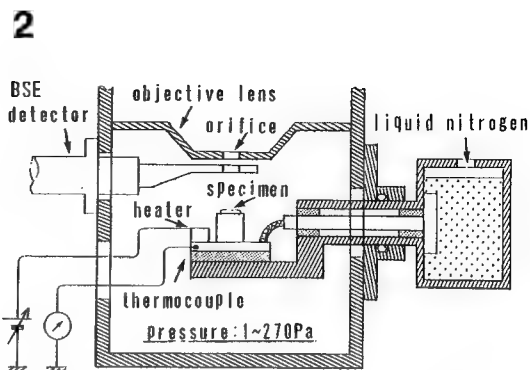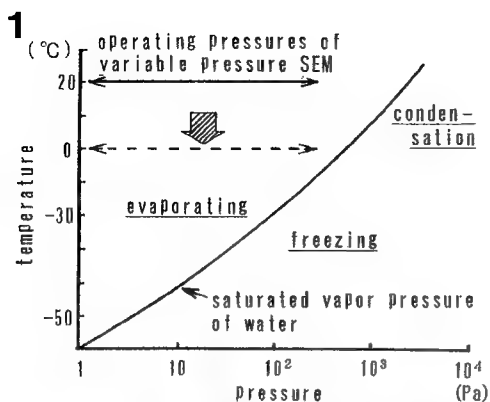
Fig. 1 —Saturated vapor pressure of water for each temperature and operating pressure of variable pressure SEM.

Fig. 2 —Specimen cooling apparatus built in the specimen chamber of S-2250N.

Fig. 3 —Leaf of _Pharbitis_ _nil_ seedling observed for 10 minutes at an ambient temp., 130 Pa.

Fig. 4 —Leaf of _Pharbitis_ _nil_ seedling observed for 10 minutes at about 0°C, 130 Pa.

Fig. 5 —The fist leaf of mung bean examined for 10 minutes at about 0°C, 1.3 Pa.

Fig. 6 —The fist leaf of mung bean examined for 10 minutes at about 0°C, 130 Pa.

MTF RESTORATION WITH SLOW-SCAN CCD CAMERAS

P.E. Mooney, W.J. de Ruijter and O.L. Krivanek

Gatan Research and Development, 6678 Owens Drive, Pleasanton, CA 94588, USA

Slow-scan CCD cameras (SSCs) attached to transmission electron microscopes (TEMs) are proving invaluable in the acquisition of TEM images and in providing high quality data for on-line analysis and autotuning procedures[1-3]. When equipped with a sensitive phosphor and an efficient fiber-optical coupling, they are able to record the arrival of single fast electrons[3]. At more typical exposure levels of 10 - 1000 fast electrons per pixel, they are able to capture images while adding less noise than the Poisson noise inherent in any electron image[4].

The raw images captured by the SSC suffer from various defects, but these can be corrected on-line in the computer used to record the images. The most familiar defect is the pixel-to-pixel gain variation, which is readily corrected by capturing a gain-reference image and then performing on-line gain-normalization[3,4]. Another significant defect in raw images is that the signal due to each arriving electron is spread over several pixels. This effect is particularly significant in an SSC using a single crystal scintillator, in which some 80% of the light generated by each incident electron is channeled sideways by the scintillator, but can become dechanneled and arrive at the CCD sensor some distance from its correct origin (Fig. 1). It leads to a point-spread function (PSF) with long "tails", which can contain as much as 50% of the total signal produced by the electron. The effect can be minimized by using powder phosphors and fiber optics with small angles of acceptance, but is still significant even with fully optimized hardware.

Just like with the pixel-to-pixel gain variation, the spreading can be characterized, and removed by image processing. The characterization can be performed most simply by recording the image of an electron-opaque edge such as that produced by a beam stop imaged by the SSC. The profile through the edge should ideally be 100% abrupt, but in reality will be broadened by the finite width of the PSF. A Fourier transform of the profile can be used to work out the modulation transfer function (MTF) of the SSC. Once the MTF is known, it is a simple procedure to restore it close to the ideal value by taking a Fourier transform of each new image, multiplying the transform by MTF_{min}/MTF, and Fourier transforming back. Since the image is digitized with little noise added, restoration can leave the signal to noise ratio unaffected[5]. The complete procedure takes about 1 minute for a 1k x 1k image using a Macintosh Quadra computer, and less than 10 seconds if an 80 MFlop array processor is installed.

Figs 2-5 illustrate the procedure graphically. An image of a beam stop captured by an SSC equipped with a YAG single crystal scintillator and fiber optics with a numerical aperture of 1 shows significant broadening (Figs 2a and b). Averaging the beam stop image in the direction parallel to the edge, performing the Fourier transform, and taking account of the fact that the beam stop actually consist of two edges that give a Fourier transform resembling the diffraction pattern of a single slit, yields the MTF shown in Fig. 3. The most significant feature of the MTF is the spike at the origin, which is due to the long-range tail of the PSF. Fig. 4 shows the restoration filter, MTF_{min}/MTF, which attenuates low frequencies and leaves high frequencies unaffected. Figure 5 shows the profile through the MTF-restored image of the beam stop. MTF restoration produced slight ringing due to the fact that high spatial frequency detail is strongly dependent on the position of the discrete pixels relative to the sharp features in the beam stop image, and that this dependence is not characterized by the measured MTF. The ringing can be prevented by adhering to the criterion that detail in the projected microscope image not exceed a spatial frequency of half the pixel frequency. Finally, Figs 6a and b illustrate the effect of MTF restoration on the image of a biological sample. The unrestored image (Fig. 6a) has a slightly unsharp appearance, as though it was photographed through a "soft" lens. The restored image (Fig. 6b) shows the small-scale detail much more clearly (this is especially evident in the original prints).

In summary, all TEM cameras (including ones using photographic film) have an MTF that falls of at higher spatial frequencies, which causes sharp detail to be attenuated in recorded images. The MTF of the SSC can, however, be characterized and restored, giving the SSC nearly ideal image detection properties in all significant respects.

References

1. P.E. Mooney et al., Proc. 12th Int. EM Congr. (Seattle) 1, 164 (1990).
2. O.L. Krivanek and G.Y. Fan, Proc. 50th EMSA meet., part 1, 95 (1992).
3. O.L. Krivanek and P.E. Mooney, Ultramicroscopy, to be published (1993).
4. K. Ishizuka, Ultramicroscopy, to be published (1993).
5. W.J. de Ruijter, P.E. Mooney and O.L. Krivanek, these proceedings.
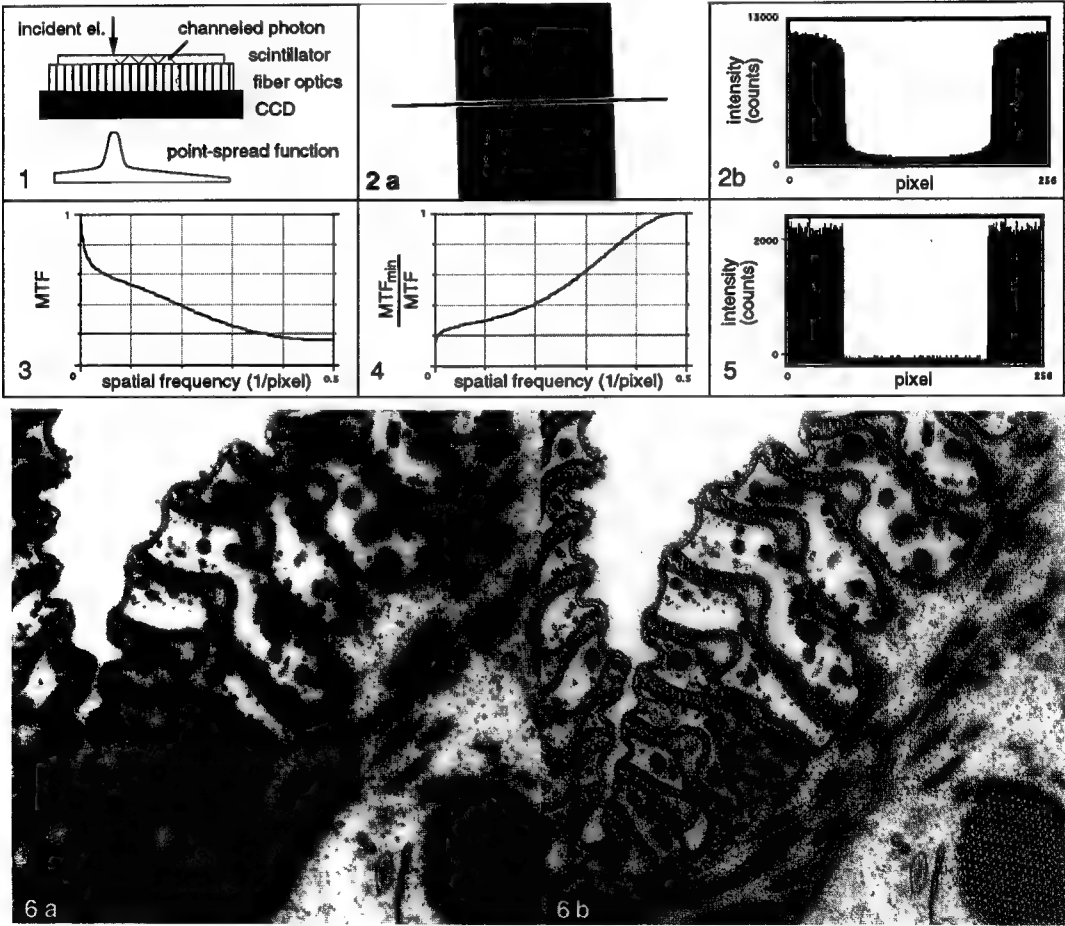
Fig. 1. Origin of a long point spread function (PSF) tail in single-crystal scintillator SSCs.
Fig. 2. Image (a) and profile (b) of TEM beam stop captured by a YAG-equipped SSC at 120 kV.
Fig. 3. The modulation transfer function (MTF) derived from Fig. 2.
Fig. 4. The MTF restoration filter, MTF_{min}/MTF .
Fig. 5. Profile through the restored image of the beam stop.
Fig. 6. Unrestored SSC image of a biological sample (prorodon ciliate) (a), restored image (b).

DEVELOPMENT OF AN AUTOMATED ANALYZER FOR TEM DIFFRACTION PATTERNS

A. G. Jackson*, J. Park*, D. Wood*, and S. LeClair†
*ThinkAlong Software, Inc., Brownsville, CA 95116; WL/MLIM, Wright Patterson AF Base, Ohio 45433

An application of self-adaptive algorithms to TEM is presented. Analysis of diffraction patterns is an integral part of an experiment because of the need to control contrast conditions. Obtaining two-beam conditions or locating a zone axis can be time consuming or not possible, because of restrictions in the tilt ranges of the holder being used. The present approach is to manually search reciprocal space in the instrument to find zones of interest and that are accessible, visually identify the zone axis, or, analyze the patterns and plot on a stereogram the locations of major zones. Once the experimenter has plotted the orientation, then locating desired zone axes is accomplished by manually tilting. This process can be relatively easy, as in the case of a cubic crystal, or very difficult as in the the cases of hexagonal, trigonal, triclinic, monoclinic or orthorhombic crystals, particularly when the crystalline region is a few microns or less in size.

Algorithms for calculating any zone axis location given two known zone axes are described by Jackson et al[1]. Although this is of considerable help, one must still be able to identify the zone axes either by inspection or by analysis. We have developed a program that accomplishes not only the location of the zone axes, but also identifies them and the planes they contain. The TEM Companion program utilizes quantitative information on the crystal system that is available to calculate the location of the zone axes, simulate the diffraction pattern at that zone axis, and, via self-adaptive algorithms, recognize the symmetry present in the pattern and identify the plane indices in the zone.

The TEM Companion consists of two parts: a Simulator and an Analyzer. The Simulator generates diffraction patterns based on the information entered by a user. In initializing the program, the user is asked for the crystal system, lattice parameters, atom symbols on each Wyckoff site, and the Wyckoff site symbol (and x, y, or z if needed). Atomic scattering factors and structure factors are included in the simulation using kinematic assumptions. Unlike the present approach used by an experimenter, no Kikuchi simulation has been included, because the Analyzer portion does not need the information to accomplish the orientation task. The Analyzer portion receives from the Simulator information about the tilts of specimen and the locations of spots in the diffraction pattern, and, when available, any information on the specimen. The Analyzer processes the data and generates a list containing the zone axis indices, planes in the zone, and tilt angles (holder and cup angles). It then generates a stereographic projection of the accessible region and marks the location of the two reference zone axes. The user can then enter the indices of any desired zone axis, have its location marked, and the tilts and indices displayed (Figures 1 and 2). The user can have the Analyzer pick two reference zones, or tilts of two reference zones can be entered along with indices. In addition to this mode, the user can also pick any position on the displayed stereogram by double clicking at the point of interest. The point is marked and the diffraction pattern corresponding to that tilt is plotted regardless of whether or not a zone is located there. Hence, the user can explore the reciprocal space by using the mouse to find two-beam conditions of interest. The Analyzer can also be used for such a search if desired.

References

1. A. G. Jackson, J. Woodhouse, and H. Fraser, submitted to J. Microsc. Tech.
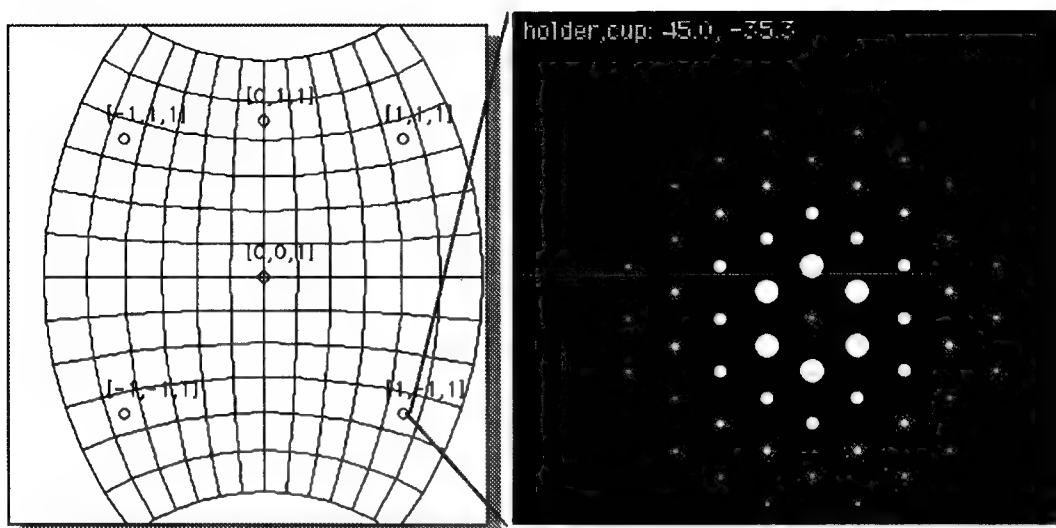
Figure 1. Example of the display in the Simulator; left: stereographic projection of accessible region of tilts; holder axis is vertical, cup axis horizontal; right: simulated diffraction pattern corresponding to [1-11] zone in lower right quadrant.
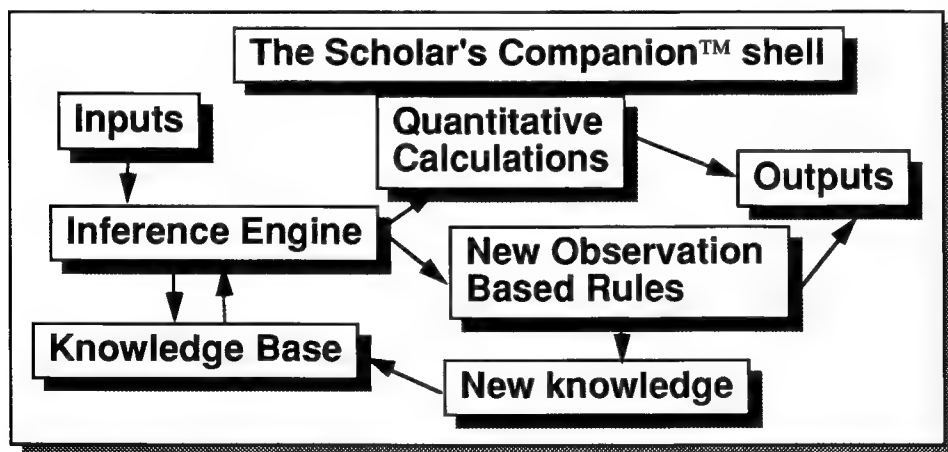
Figure 2. Schematic diagram of The Scholar's Companion shell used with TEM Companion. Inputs can be from user or from simulator; the inference engine processes inputs to generate quantitative outputs and to create new rules based on the data that are added to the existing knowledge base for future use.

CONFOCAL SCANNING LASER MICROSCOPY APPLIED TO QUANTIFY GAP JUNCTION EXPRESSION AND DISCRIMINATE DIFFERENT CONNEXIN ISOFORMS

Robert G Gourdie,* Colin R Green,* Robert P Thompson** Stephen Rothery,*** Nicholas S Peters*** and Nicholas J Severs***

*Dept Anatomy & Developmental Biology, University College London, Gower Street, London WC1E 6BT, ENGLAND; **Dept Anatomy & Cell Biology, Medical University of South Carolina, Charleston, South Carolina 29425, USA; ***Dept Cardiac Medicine, National Heart & Lung Institute, Dovehouse Street, London SW3 6LY, ENGLAND

The principles of confocal scanning laser microscopy, and the ability of the technique to provide serial optical sections free from out-of-focus blur for three-dimensional image reconstruction, are now well known to most microscopists. Current studies have entered a new phase — how best to exploit the high definition digital images for maximizing information in specific research applications. Here we report methods for the quantitative analysis of gap junction content per unit volume of tissue and per cell, and for qualitative analysis of the expression of different gap junctional proteins (connexins) in the heart.

The first requirements for developing these methods are properly characterized antibodies that, under standardized conditions, give reproducible results in immunofluorescence staining protocols.[1,2] The strategy as applied to cardiac gap junctions takes account of the unique organization of the junctions into intercalated disks at the end-on abutments between myocytes. Serial optical sectioning techniques are used to prepare projections revealing the entire gap junction population of *en face*-viewed disks.[2,3] Automatic measurement of the number and long axis length of individually labeled junctions is carried out using PC_IMAGE, an analysis package supplied by Foster Findlay Associates Ltd (Newcastle-upon-Tyne, England). The content (area) of immunostained junction can readily be determined per unit volume of tissue. In studies of cardiac development and disease, myocyte size may alter markedly; thus, measures of gap junction content per myocyte are particularly informative.[4-6] These measures can be derived using nuclear counts in preparations that have been double-stained with propidium iodide; alternatively, they can be derived via an index of myocyte volume, obtained from the ratio of the number of cross-sectioned cells to the number of disks present in the sample volume.[5-7]

To establish whether more than one connexin is expressed at precisely the same cellular site, a photobleach/double labeling procedure has been developed to permit relabeling a section that has previously been labeled. Figures 1-4 illustrate this method in action. The first immunolabeling step is done with a primary rabbit polyclonal antibody against connexin40, followed by a biotinylated second antibody and streptavidin conjugated to Texas red for visualization (Figs. 1 & 2). After photobleaching using the confocal scanning laser (25 milliwatt Argon ion laser, high power, 0 neutral density, 40 minutes), optical sectioning of the photobleached region reveals no detectable fluorescence from the previously labeled structures (Fig. 3). The section is then refixed for 5 minutes in 2% paraformaldehyde, washed and relabeled using a mouse monoclonal antibody against connexin43 (Zymed, California) followed by an anti-mouse secondary antibody conjugated to fluoroscein. The second connexin isoform can then be visualized within the photobleached zone (and elsewhere) (Fig. 4). In this way, it can be demonstrated that Purkinje fibers (the ventricular branches of the conduction system) express both connexin40 and connexin43. This co-expression of connexins by Purkinje fibers provides the physical basis by which connexin40-expressing conduction tissues electrically couple to working ventricular muscle which expresses only connexin43.

References

1. E. Harfst et al., J. Cell Sci. (1990)96, 591.
2. R. G. Gourdie et al., J. Cell Sci. (1991)99, 41.
3. R. G. Gourdie et al., Anat. Embryol. (1992)185, 363.
4. J. H. Smith et al., Am. J. Pathol. (1991)139, 801.
5. N. S. Peters et al., Circulation (1992)86Supl.1, 425.
6. N. J. Severs et al., J. Microsc. (1993)169, 299.
7. R. G. Gourdie et al., Circ. Res. (1993)72, 278.
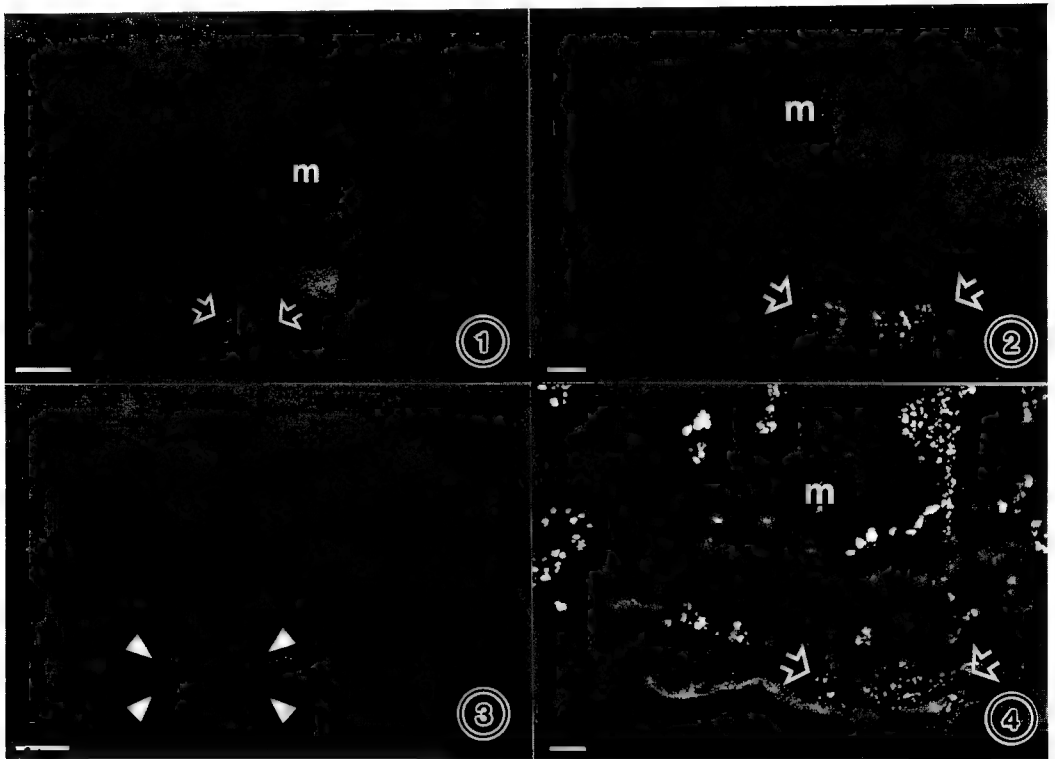
FIG. 1.—Survey view of section though left ventricle after immunolabeling for connexin40. Working myocytes of ventricle wall (m) are immunonegative; arrows indicate small group of immunopositive Purkinje cells. Bar = 10 μm.

FIG. 2.—Projection showing detail of immunopositive Purkinje cells indicated in Fig. 1. Bar = 5 μm.

FIG. 3.—After photobleaching (arrowheads indicate corners of photobleached region corresponding to total field of Fig. 2). Optical sectioning demonstrates no fluorescence from previously labeled structures. Bar = 10 μm.

FIG. 4.—Projection of photobleached region after relabeling for connexin43. Note group of Purkinje cells that were immunopositive for connexin40 are also immunopositive for connexin43 (compare arrowed regions in Figs 4 & 2. Working ventricular myocytes (m) that were immunonegative for connexin40 are immunopositive for connexin43. Bar = 5 μm.

267

THREE-DIMENSIONAL LIGHT MICROSCOPY, OPTIMIZED STAINING, AND AUTOMATED IMAGE ANALYSIS OF CELL NUCLEI IN THICK TISSUE SLICES

W. Lin, T. Holmes, H. Ancin, B. Roysam, D.H. Szarowski and J.N. Turner

Departments of Biomedical Engineering and Electrical, Computer and Systems Engineering, Rensselaer Polytechnic Institute, Troy, NY, 12180, and Wadsworth Center for Laboratories and Research, Albany, NY 12201-0509

The number, size, shape and three-dimensional (3D) distribution of cell nuclei in thick tissue samples is often critical to our understanding of tissue level organization and function. Examples include the analysis of neurons in brain tissue as a function of development, electrical activity, and exposure to toxins as well as the development of whole embryos. The sample is stained with a fluorescent dye selective for nucleic acid, and observed with a confocal light microscope. The classic Feulgen stain, although primarily an absorption stain, is often used for this purpose[1]. However, it is unreliable for fluorescence due to the mixture of compounds usually present in Fuchsin[2]. We have optimized a procedure using acriflavine as the Schiff reagent for staining thick (100 - 500 μm) brain slices[3]. In addition, Ancin and Roysam have developed software for automatically analyzing 3D objects, which are classified by volume, shape, intensity and relative 3D spatial locations.

Slices of rat hippocampus were fixed in paraformaldehyde, hydrolyzed in 6N HCl and stained in acriflavine. Samples were imaged using an Olympus IMT-2 inverted light microscope and a Bio-Rad MRC 600 confocal attachment. The acquired 3D image data was subjected to axial deblurring, constrained 3D segmentation, and disambiguation of overlapping objects. The resulting population was subjected to a hierarchical cluster analysis using volume and shape parameters, 3D location and intensity. Microspectrophotometric data were obtained using a Zeiss Zonax and spectrophotometer.

Fig. 1 is a stereo pair of nuclei in the pyramidal cell layer. Fig. 2 is composed of optical sections at various depths (11, 21, and 31 μm) in the specimen, and shows that the stain adequately penetrates the thick slice. Fig. 3 shows the absorption and emission spectra for the pyramidal cell layer. The maximum absorption is at 480 nm and the emission peak is at 510 nm. Thus, we used the 488 line of the Argon ion laser and a 540 high pass barrier filter. It is clear that the standard rhodamine filter set often used for this type of observation is not optimal. Automated cell counting and quantitative analysis of nuclei in thick brain slices is underway.

References

1. R.G. Summers, et al., J. Elect. Microsc. Tech. (1991)18, 24.
2. G.S. Nettleton and A.V. Martin, Stain Technology (1979)54, 213.
3. E. Schulte, personal communication.
4. Work partially supported by NIH grant R55 06904; NSF grants MIP-9013247 and DIR 9108492, AT&T and Digital Equipment Corp.

Fig. 3

Extinction(-+) and emission(-o) spectra of acriflavine stained nuclei

<----- Extinction spectrum

480 nm

510 nm

<----- Emission spectrum
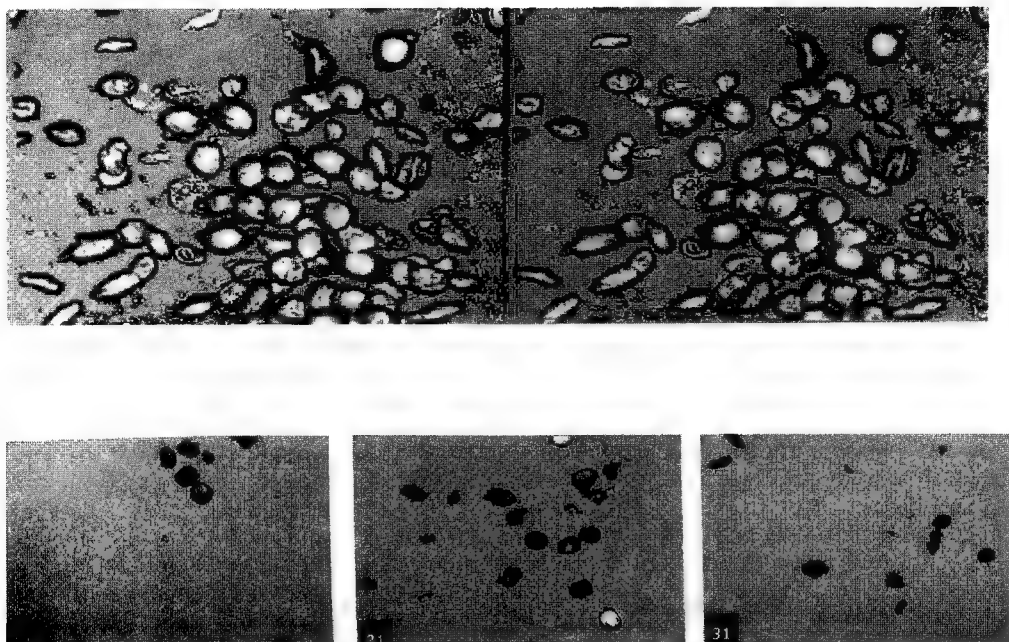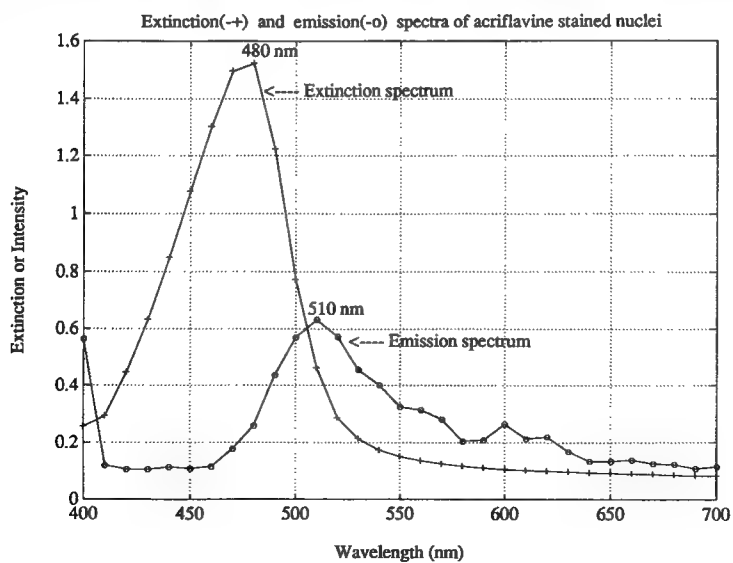
DISCRIMINATION OF THE ASSEMBLY STATES OF CYTOSKELETAL PROTEINS IN CULTURED CELLS USING CONFOCAL MICROSCOPY

David A. Carpenter, Sohaib A. Khan and Wallace Ip

Department of Anatomy and Cell Biology, University of Cincinnati College of Medicine, Cincinnati, Ohio 45267-0521

The cytoskeleton is a three-dimensional network of cytoplasmic filaments that mediates many processes involving motility, and the specification and maintenance of cell form. In recent years, it has become evident that all three major components of the cytoskeleton—microfilaments, microtubules, and intermediate filaments (IF)—are dynamic structures that undergo reversible assembly-disassembly as required by the physiologic needs of the cell. While the *assembled* form of the cytoskeleton—the filamentous network—is readily visible by conventional immunofluorescence microscopy, it is often difficult to visualize the non-filamentous form of a cytoskeletal protein because the subunits or oligomeric assemblies are small and because the images tend to be diffused due to interference from fluorescently labelled subunits above and below the plane of focus. Confocal microscopy offers a convenient solution to this problem at the light microscope level, because optical sections of fluorescently immunolabelled cytoskeletal networks do not suffer from such out-of-focus interference. We have combined this approach with molecular genetic manipulations to study the assembly dynamics of vimentin IF networks in several cell types during mitosis.

A vimentin cDNA is modified by site-directed mutagenesis (Carpenter et al., 1991) to generate several mutants, such that the encoded proteins contain ser→ala mutations at position 55 (Chou et al., 1991), a target site for p34[cdc2], the kinase responsible for the phosphorylation of many molecules in a cell cycle dependent manner. The mutant proteins are then expressed in cultured cells by calcium phosphate mediated transfection and stably transfected cell lines are established. Since phosphorylation of vimentin at the onset of mitosis disassembles the IF network (Rosevear et al., 1990), cells expressing the phosphorylation-defective vimentins are expected to be incapable of doing so. This is indeed observed to be the case by conventional immunofluorescence microscopy, but the distinction between filamentous and non-filamentous proteins is not always unambiguous, for reasons discussed above. In contrast, confocal microscopy of the same cells permits clear discrimination between assembled and disassembled IF proteins. In addition, by double labelling the cells with anti-vimentin and anti-tubulin antibodies (to visualize the mitotic apparatus), the stages of mitosis are accurately identified and correlated with the assembly state of the vimentin. Using this approach, we have determined that (1) all ser-55 phosphorylation-defective vimentins assemble into normal-looking IF networks in transfected cells, (2) they remain assembled during mitosis, and (3) IF disassembly appears not a requisite event for the progression through mitosis for many cell types.

References:
Carpenter, D.A., W. Ip, and S.A. Khan (1991) *J. Cell Biol.* 115:335a.
Chou, Y.H., K. Ngai, and R. Goldman (1991) *J. Biol. Chem.* 266:7325-7328.
Rosevear, E.R., M. McReynolds and R.D. Goldman (1990) *Cell Motil. Cytoskel.* 17:150-166.
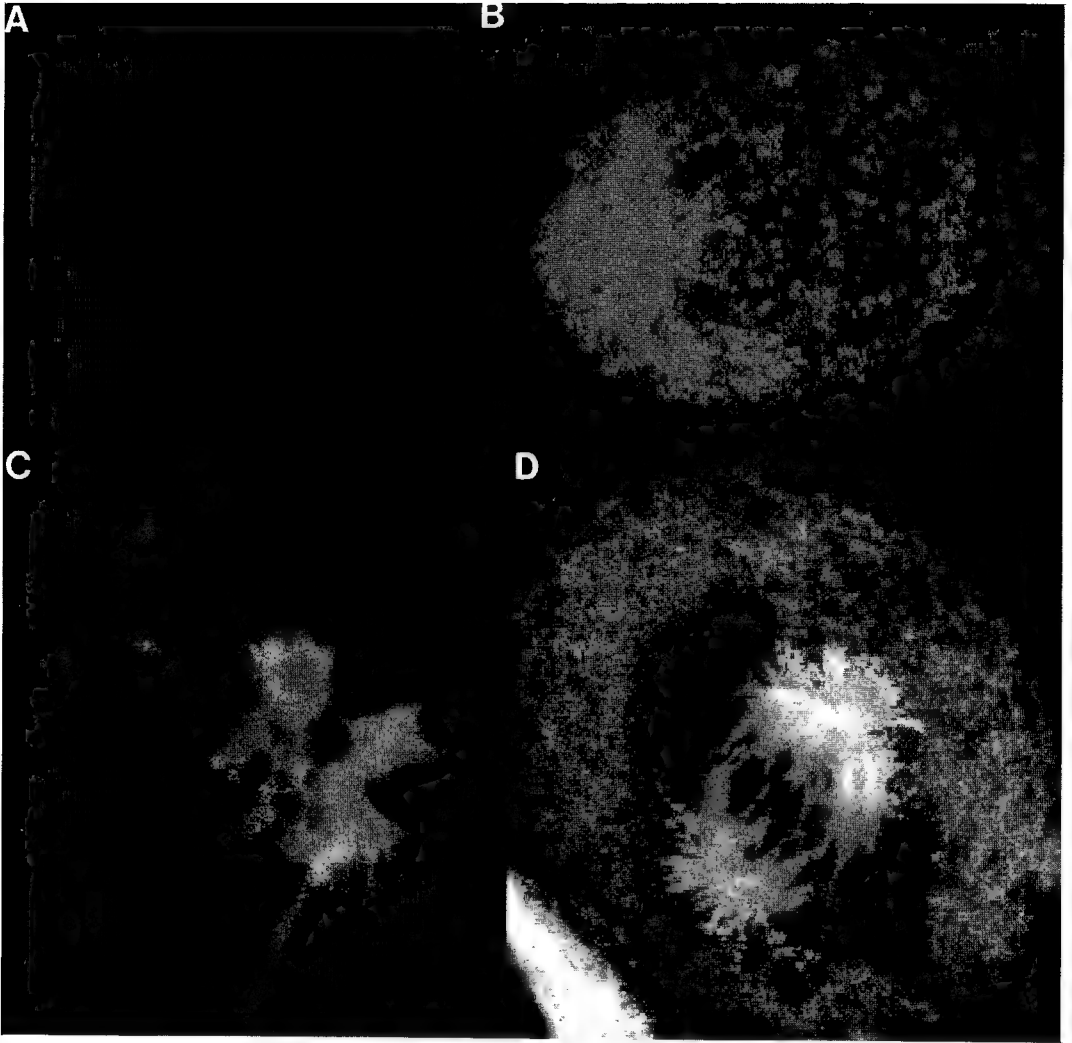
A. An untransfected BHK21 cell in interphase, immunolabelled with anti-vimentin antibodies by the indirect method and imaged by confocal microscopy. Note the extensive, pan-cellular filamentous network. This is a 0.5 μm optical section.
B. An untransfected BHK21 cell in prophase or prometaphase, immunolabelled for vimentin. The IF network is disassembled into small aggregates that appear in a punctate staining pattern. In conventional immunofluorescence, this pattern would suffer from out-of-focus inteference so that the entire cell would be diffusedly stained.
C. A BHK21 cell expressing the phosphorylation site mutant vimentin at ser55, fixed and labelled for vimentin during prophase. Vimentin protein appears green. In contrast to the wild-type cell shown in panel B, the vimentin filament network is intact, because phosphorylation-induced disassembly is blocked by the mutation. The mitotic apparatus is labelled with anti-tubulin and appears in red. Both green and red are pseudocolors.
D. A BHK21 cell expressing the ser55 mutant vimentin, fixed and processed during early metaphase. The IF network remains intact and persists throughout the entire cell cycle.

DETERMINING DNA STRAND BREAKS USING THE LASER SCANNING MICROSCOPE

M.K. Winters*, D.W. Fairbairn*, M.D. Standing† and K.L. O'Neill*

*Department of Microbiology †Department of Botany and Range Science
Brigham Young University, Provo, Utah, 84602

The single cell gel assay has been proven to be an effective, fast and accurate method of determining the amount of DNA single or double stranded breaks[1]. The possible uses of this assay have already reached into some aspects of DNA damage caused by chemicals or other destructive agents. It has yet to reach even deeper into mutagenesis and carcinogenesis, both of which may show single or double stranded breaks to the DNA. Here we explore the effects that different concentrations of H_2O_2 have on the DNA of cells. The assay is performed by suspending cells in a low melt point agarose, spreading the agarose out on a frosted slide and letting it gel over ice. The cells are then treated with H_2O_2 to induce single strand DNA breakage. The cells are lysed in an alkaline environment, which separates the DNA into single strands and then electrophoresed. The gel is then stained with ethidium bromide. The resulting DNA migration pattern produces a comet-like image. Imaging and measuring the comets is performed using the fluorescent image generated by the laser scanning microscope[2]. The relative amount of DNA strand damage generated by the H_2O_2 is derived by comparing the size of the comets of the damaged cells with undamaged controls.

Cells were treated with varying concentrations of H_2O_2 on ice to prevent DNA repair[3] and electrophoresed for 10 minutes at 1.5V/cm. A Carl Zeiss laser scanning microscope (LSM 10) was used to view the comets and measured using the microscope's system software (2.08). Red/blue color thresholding was used in the photographs to facilitate visualization of the comet head and tail.

The relative amount of damage induced in the DNA is determined by measuring the distance from the tip of the head of the comet to the tip of the tail. Figures 1-4 show the difference in the size of the comets according to the damage caused by the different concentrations of H_2O_2.

As shown by the photographs, the single cell gel assay does accurately and effectively determine DNA damage. Applying the technology of the laser scanning microscope to the single cell assay is becoming invaluable in the detection of DNA damage and analysis of repair.

References
1. P.L. Olive *et al.,* Experimental Cell Research (1992b), 198, 259-267.
2. D.W. Fairbairn *et al.,* Scanning (1993), in press.
3. J.F. Ward *et al.,* Radiation Research (1985), 103, 383-392.
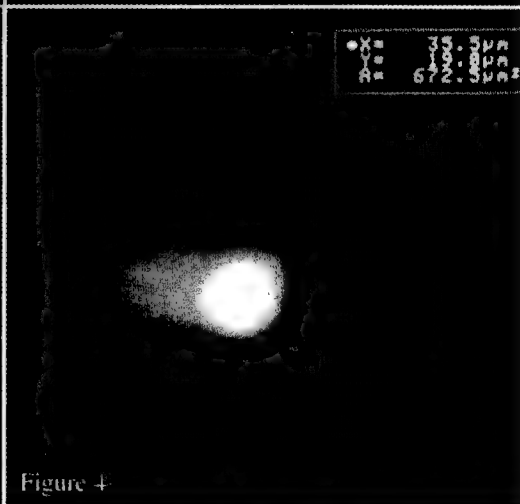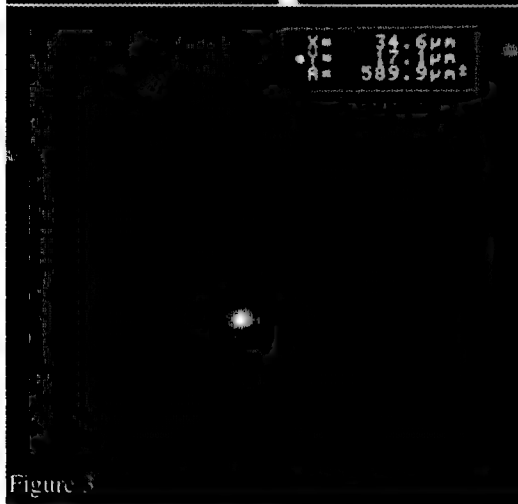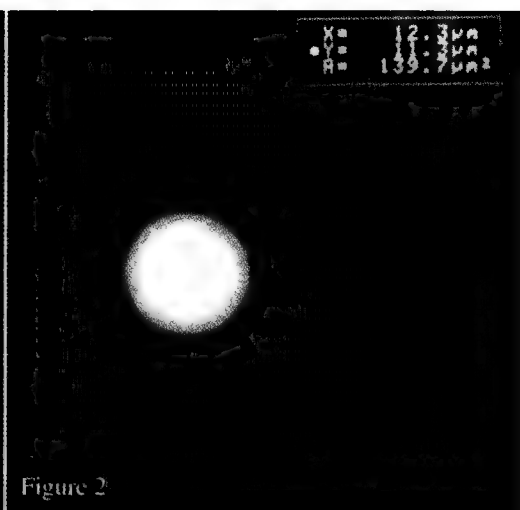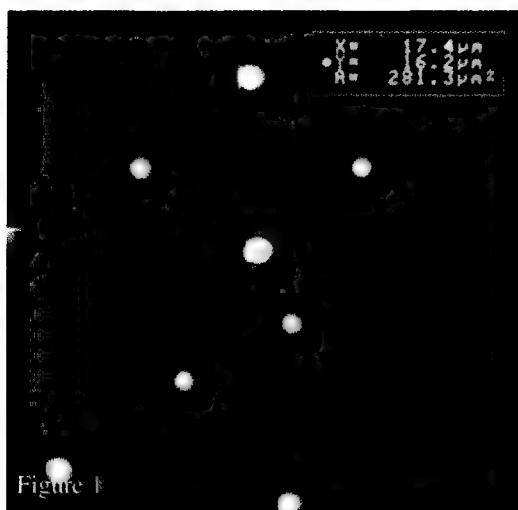
Figure 1: Undamaged controls. A field of comets to show typical control cell comet morphology.
Figure 2: Undamaged control. Single comet at greater magnification.
Figure 3: H2O2 damage induced cells. A fieldof comets to show typical damaged cell comet morphology.
Figure 4: H2O2 damage induced cell. Single comet at greater magnification. Note in the figures above the similarities in the Y values of all the cells (vertical measurements) and the differences in the X values between the control cells and the damaged cells (horizontal measurements).

273

VISUALIZING THE INTRACELLULAR MEMBRANE SYSTEM OF YEAST CELLS USING A LASER SCANNING CONFOCAL MICROSCOPE

Karen L. McCoy, Andrew G. Dillin[*], and Ardythe A. McCracken[*]

Electron Microscopy Facility, University of Nevada School of Medicine, and the Department of Biology[*], University of Nevada, Reno NV 89557

Progress has been made in developing new preparative techniques for electron microscopic visualization of the intracellular structures of yeast[1]. In addition, development of the laser scanning confocal microscope (LSCM) has provided improved resolution for fluorescent microscopy. We asked whether the LSCM in combination with new preparative techniques could be used for comparable investigative research of the intracellular organizaton of the yeast cell.

To investigate this possibility, a BioRad MRC600 LSCM equipped with a krypton/argon laser and integrated computer imaging capabilities, was used to study various dipliod strains of the yeast *Saccharomyces cerevisiae*. Cells were treated with the lipophilic, cationic fluorescent dye $DiOC_6$ (3,3'-dihexyloxacarbocyanine iodide), which has been used to visualize intracellular membrane structures, and in particular the endoplasmic reticulum of mammalian cells[2] and living yeast cells[3]. Since one of our interests is the intracellular localization of proteins in the yeast cell, we utilized transformed yeast cells expressing a human gene encoding a protein that inappropriately accumulates in the endoplasmic reticulum (ER)[4].

Our studies showed that the intracellular pattern of membranes visualized by $DiOC_6$ staining of living cells can be reproduced in fixed cells (figure 1, b and a respectively). Discrete intracellular membrane structures were seen by LSCM imaging of living cells. This membrane network was not efficiently resolved using the conventional fluorescent microscope. Fixed cells revealed the same discrete intracellular structures when staining with $DiOC_6$ followed the fixation procedure (3.7% formaldehyde[5], with conditions established to maintain the integrity of intracellular structures[1]). Such patterns are reminiscent of the morphological structure of the *S. cerevisiae* ER, which has recently been described at the EM level as membranes that envelope the nucleus, extend into the cytoplasm, and frequently juxtapose the plasma membrane[5]. To investigate the possibility that the $DiOC_6$ staining pattern seen in our studies represented the ER of these cells, we counter stained the cell nucleus with various DNA binding dyes. A discrete circular compartment, the nucleus, was found within a ring of the $DiOC_6$ stained membranes (arrows, figure 1). Together, these observations suggest that the $DiOC_6$ pattern represents the yeast cell ER. A second line of evidence which implicates the $DiOC_6$ stained membrane network as ER, was obtained by indirect immunofluorescence. Antibodies which specifically bind to alpha-1-proteinase inhibitor (A1Pi, the human protein expressed by these transformed cells), were

used in combination with fluorescein-conjugated secondary antibodies to localize A1Pi in these cells. It has previously been shown that this protein accumulates in the ER of the yeast cell.[4] The immunofluorescent pattern seen in the A1Pi expressing cells (figure 1d) was quite similar to that seen using $DiOC_6$ staining. Cells which do not express A1Pi did not show this immunofluorescent pattern (figure 1c).

These results suggest that the LSCM can be used in combination with fluorescent dyes and antibodies to accurately identify intracellular compartments within the yeast cell. Our intent is to substantiate these observations and thus establish these techniques for use in intracellular localization studies of yeast.[6]

1. D. Preuss et al., 1993. Molecular Biology Cell 3:1-15
2. M. Terasake et al., 1984. Cell 38:101:108
3. R. Wright et al., 1992. ASCB meeting, Denver, CO.
4. A.A. McCracken et al., 1993. Molecular Biology Cell in press
5. J.R. Pringle et al. 1991. Methods in Enzymology 194:565-601
6. This research was supported by American Cancer Society grant MV551; LSCM supported by NIH grant S10 RR06507-01
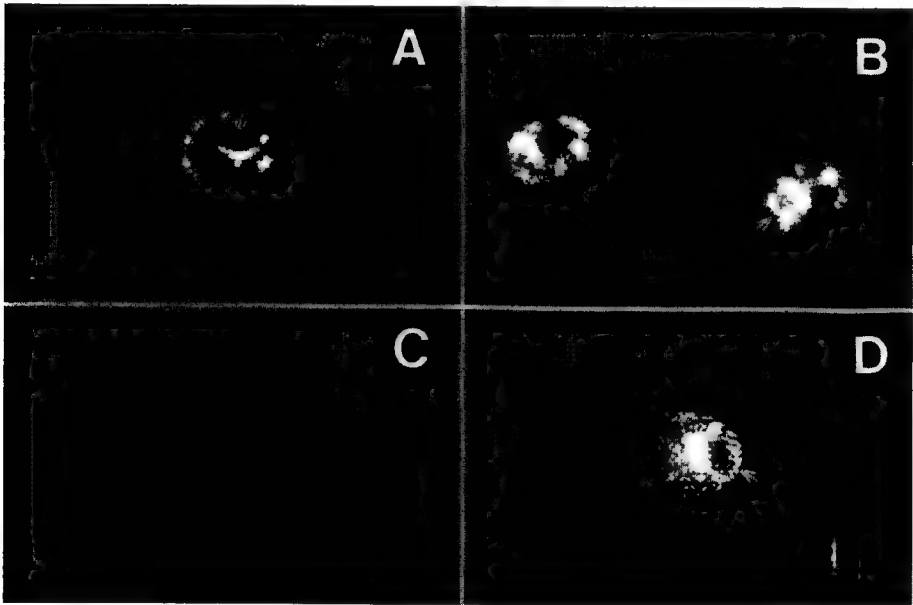
Figure 1. **LSCM single 0.5um step images from a Z-series section through the cell.** Panel a, $DiOC_6$ treated fixed cell; panel b, $DiOC_6$ treated living cell; panel c, FITC-antibody treated control cell with no A1Pi expression; d, FITC-antibody treated cell expressing A1Pi.

THREE-DIMENSIONAL TRANSMITTED BRIGHTFIELD IMAGING: PRAGMATIC DATA COLLECTION AND PREPROCESSING CONSIDERATIONS

J.A. Cooper[1], S. Bhattacharyya[1], J.N. Turner[2,1] and T.J. Holmes[1,2]

[1]Biomedical Engineering Department, Rensselaer Polytechnic Institute, Troy NY 12180-3590

[2]Wadsworth Center for Laboratories and Research, New York State Department of Health, Albany NY

We have been developing algorithms for 3D image reconstruction of biological specimens with absorbing stains. This is important because there are many absorbing stains which are widely used in conjunction with transmitted light brightfield (TLB) microscopy, yet most of the 3D microscopic imaging research has been directed toward fluorescence microscopy. For instance, horseradish peroxidase (HRP) is used widely in the neurosciences for its many advantages as a tracer and intracellular marker. It is readily injected into individual neurons, transported long distances, and fills both the dendritic and axonal fields, while it may double as an electron microscopy stain for correlative analysis. With such advantages, it is clear that absorbing stains will continue to be widely used. Their utility will furthermore broaden with 3D visualization and quantitation.

The main principles behind our methodology are the following. Standard optical serial sectioning data collection is used [1]. The iterative, constrained image reconstruction algorithm is designed to reconstruct the 3D optical density distribution [2,3].

There are a number of pragmatic considerations in implementing a 3D TLB system, particularly in the data collection and preprocessing. Our system uses a Spectra-Source Instruments (Westlake Village, CA) MCD 220 (192x165) thermoelectrically cooled, slow scan CCD camera, which was chosen for its outstanding price/performance ratio. It is interfaced to a 386 computer for data collection, which in turn is attached to a network of more powerful Unix-based computers for executing the image reconstruction.

The important advantages of using a slow-scan cooled CCD camera is that, compared to video-rate cameras, it has superior linearity, a 12-bit dynamic range and low-noise. Also, the ability to integrate charge on the CCD camera, with selectable integration times, inherently allows for a much more precise data precorrection procedure, as explained below.

Our own methodology, summarized below, is a novel extension to previous methods of others [4]. The data are precorrected by a procedure which may be summarized by the expression:

$$I_{corrected}(i,j,k) = \frac{I_{uncorrected}(i,j,k) - I_{preamp}(i,j) - D(i,j)\,T(k)}{T(k)\,q(i,j)} \tag{1}$$

where i, j and k are the voxel indices along x, y and z, respectively, $I_{uncorrected}$ is the uncorrected image, I_{preamp} is a bias image originating from the camera's preamplifier, $D(i,j)$ is the dark current component (electrons/sec.), $T(k)$ is the exposure time and $q(i,j)$ is the

276

quantum efficiency. The terms which need to be calibrated prior to this correction are $I_{preamp}(i,j)$, $D(i,j)$, $T(k)$ and $q(i,j)$. $T(k)$ is nonuniform because the exposure time has random fluctuations on the order of milliseconds. This effect is pronounced for exposures on the order of 100 milliseconds or less.

$I_{preamp}(i,j)$ and $D(i,j)$ are calibrated simultaneously, by collecting two *dark* frames wherein the shutter is held closed, at two separate charge integration times T_{cal}. These two terms are then obtained by solving for them from the expression,

$$I_{cal}(i,j) = I_{preamp}(i,j) + D(i,j) \, T_{cal} \qquad (2)$$

while treating this expression as two simultaneous equations, each with a different T_{cal}. Relatively large T_{cal}'s are used (60 and 120 sec., typically) to produce a high signal to noise ratio in the Poisson electron counting statistics. Subsequently, $q(i,j)$ is measured by collecting a flat-field image I_{flat}, which may be obtained by taking the microscope extremely out of focus, and solving for I_{flat} from the expression,

$$I_{flat}(i,j) = q(i,j) \, T_{flat} + I_{preamp}(i,j) + D(i,j) \, T_{flat} \qquad (3)$$

with a known T_{flat}, selected for approximately a 3/4 CCD well capacity to ensure a high SNR, and with the other terms in this expression known from the above described calibration. $T(k)$ is calibrated directly from the optically sectioned data by understanding from geometrical optics that the summation of the intensity values over (i,j) should be approximately uniform with respect to k. In other words, with proper correction software,

$$S(k) = \sum_{i,j} I_{corrected}(i,j) \qquad (4)$$

should be equal to a constant S_{ave} with respect to k. $T(k)$ is estimated by, first, postulating that it is equal to T_{nom}, which is its nominal, chosen value and then substituting T_{nom} for $T(k)$ in Eq. 1. Then, $S(k)$ is calculated by substituting this expression into Eq. 4, and subsequently S_{ave} is found by averaging the resulting $S(k)$ over k. Finally, the estimated $T(k)$ is found by the expression $T(k) = [T_{nom}S(k)]/S_{ave}$. It is this last $T(k)$ estimate that is substituted, again, into Eq. 1 to finalize the correction of the data.

1. D.A. Agard, Am. Rev. Biophys. Bioeng. (1984) 13, 191.
2. S. Bhattacharrya, MSA Annual Meeting, 1993.
3. B.H. Willis et al., J. of Microscopy (1993), in press.
4. R.S. Aikens, D.A. Agard and J.W. Sedat, Methods in Cell Biology (1989) 29, 291.

INTRACELLULAR EDEMA DOES NOT ADVERSELY AFFECT THE ABILITY TO CRYOPRESERVE INTACT HEARTS

CL Hastings, RD Carlton, FG Lightfoot[1], AF Tryka

Department of Pathology, Arkansas Children's Hospital and University of Arkansas for Medical Sciences, Little Rock AR 72202 and [1]Department of Anatomy, George Washington University, Washington, DC 20037

The earliest ultrastructural manifestation of hypoxic cell injury is the presence of intracellular edema. Does this intracellular edema affect the ability to cryopreserve intact myocardium? To answer this question, a model for anoxia induced intracellular edema (IE) was designed based on clinical intraoperative myocardial preservation protocol. The aortas of 250 gm male Sprague-Dawley rats were cannulated and a retrograde flush of Plegisol at 8°C was infused over 90 sec. The hearts were excised and placed in a 28°C bath of Lactated Ringers for 1 h. The left ventricular free wall was then sliced and the myocardium was slam frozen. Control rats (C) were anesthetized, the hearts approached by median sternotomy, and the left ventricular free wall frozen in situ immediately after slicing. The slam frozen samples were obtained utilizing the DDK PS1000, which was precooled to -185°C in liquid nitrogen. The tissue was in contact with the metal mirror for a dwell time of 20 sec, and stored in liquid nitrogen until freeze dry processing (Lightfoot, 1990). Samples in a pre-cooled brass drying block were placed into a vacuum of 10^{-5} torr for 48-72 h of evaporation. The dried tissue was then vapor fixed by osmium tetroxide in a desiccator, and embedded in Spurr's resin. For comparison, myocardium from the same animals fixed in cold 2% osmium tetroxide were processed and embedded in Araldite. 70 nm sections stained with UA/Pb were examined on a Zeiss 902.

The osmium fixed IE group demonstrated intracytoplasmic lucencies separating mitochondria and sarcomeres. The mitochondria showed swelling and separation of the cristae (fig. 1), indicative of anoxic cell injury (Jennings, 1985). Adequate cryopreservation of structures along the leading edge in both cryopreserved C and IE groups was obtained (fig. 2). Mitochondrial morphology of the cryopreserved C myocardium demonstrated clearly visible tightly packed cristae, while the IE group demonstrated separation of cristae (Fig. 3), similar to that visualized in the convention-al ultrastructural preparations. We conclude that the hand held PS 1000 provides a convenient method for cryopreservation of an intact organ, and that the presence of intracellular edema does not adversely affect the quality.

References
Jennings RB et al. Circ Res 56:262-78, 1985.
Lightfoot F, et al. XIIth EMSA Proc 792, 1990.
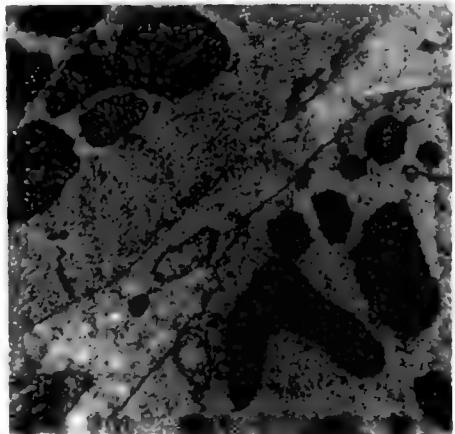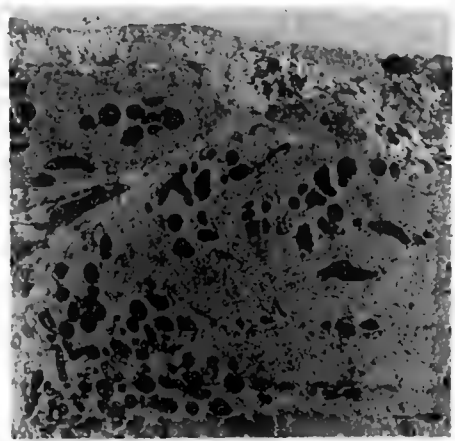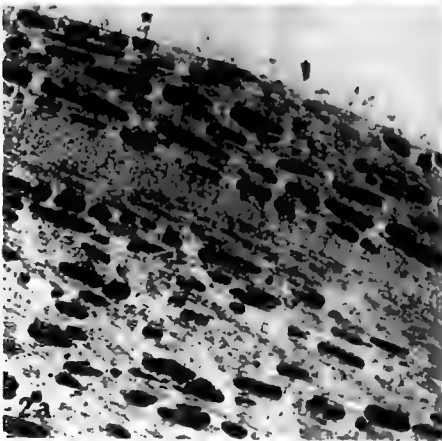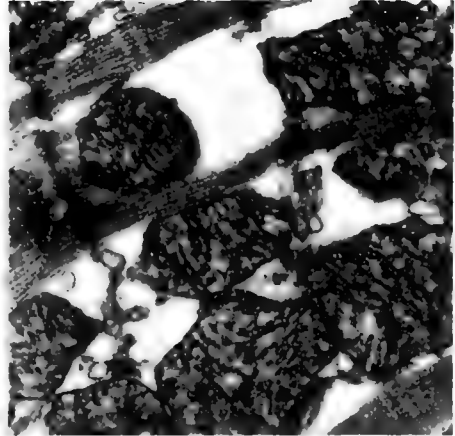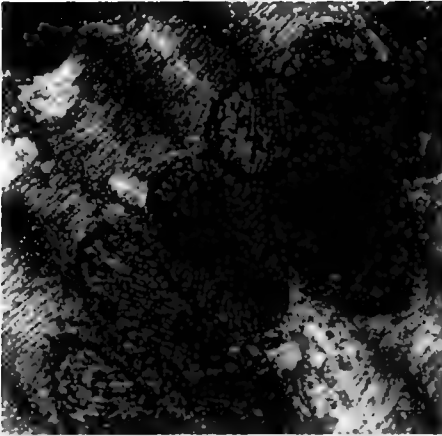
Figure 1a and b.--Osmium fixed C and IE myocardium. Bar =.05um.
Figure 2a and b.--Cryopreserved C and IE myocardium.   Arrows
indicate leading edge of slam frozen surface.   Bar =.20um.
Figure 3a and b.--Cryopreserved C and IE myocardium.   Bar =.05um.

LOSS OF MEMBRANE STRUCTURE AND CYTOPLASMIC VOLUME IN GLUTARALDEHYDE-FIXED NEUTROPHILS COMPARED TO CRYOFIXED-FREEZE-SUBSTITUTED NEUTROPHILS

Charles S. Gilbert, Richard T. Parmley

The University of Texas Health Science Center at San Antonio, Department of Pediatrics, San Antonio, Texas

Cryofixation instantly preserves cell processes without chemical alteration and freeze-substitution (FS) preserves cell constituents.[1] Investigation has shown that cell membranes and microfilaments appear better preserved in cryofixed-freeze-substituted (CFFS) specimens[1], including basophils.[2] However, the cells have not been looked at morphometrically nor have neutrophils been looked at specifically.

Peripheral blood was collected in heparin from four male donors by venipuncture. Blood was centrifuged at 500 x g for 45 min to separate the granulocytes using a one-step density gradient approach,[3] and then washed in RPMI 1640. Cells were split and half were resuspended in RPMI with 10% DMSO, cryofixed using the Eiko RF-2 and stored in liquid N_2 until FS processing in 4% OsO_4 in acetone with embedment in Spurr's resin.[4] The other half were resuspended and fixed in 3% glutaraldehyde in 0.1M Cacodylate, pH 7.35 for 1 hr at 4-6°C. Cells were dehydrated, embedded in Spurr's resin, counterstained with UALC and examined using a Zeiss EM109.[5] Consecutive neutrophils were photographed and 15 cells were analyzed per donor for each treatment using computerized planimetry.[5] Areas (A) and perimeters (P) of the cell and nuclei were measured. Magnification correction factors were used.[5] A cell form factor [$FF_C = (4\pi A)/P^2$] with a value of 1.0 being a perfect circle and surface volume density [$S_{VC} = (4/\pi)(P/A)$] were calculated.[6,7] Cell volume (V_C) and surface area (S_C) were calculated assuming the cell to be a sphere with radius based on profile area.[8] Statistical analysis was performed using NCSS.[5] Normality and variance checks and t-tests were run.

The data for different treatments is presented in the table. The FF_C showed that CFFS cells were significantly rounder than glutaraldehyde-fixed (GLUT) cells which had a more irregular surface with membrane projections. The V_C was about 27% smaller in GLUT cells while the S_C remained constant. The membranes of cells, granules, mitochondria and nuclei appeared more intact and distinct with CFFS. Endocytic caveolae were more prominent in CFFS samples and submembraneous material coating vesicles was more distinct. Morphometric data showed that the nuclear compartment did not shrink and shrinkage in neutrophils was largely limited to the cytoplasm and its associated compartments. This was consistent with the more dense cytoplasm in GLUT cells, suggesting loss of less dense cytoplasmic content, presumably due to fixation. Increased cytoplasmic volume in CFFS cells did not appear to be due to abnormal cell swelling since membranes, nuclear envelope and mitochondrial cristae were more intact than in GLUT cells. In summary, CFFS appears to be an excellent method for preserving neutrophil membranes and cytoplasm; and prevents a number of artifacts caused by glutaraldehyde fixation.

References:

1. M.A. Hayat, Principles and Techniques of Electron Microscopy: Biological Applications, 3d Ed., CRC Press (1989).
2. R. Hastie, Lab. Invest. (1990)62:119.
3. J. R. Kalmar et al., J. Immunol. Meth. (1988)110:275.
4. M. Takagi et al., J. Histochem. Cytochem. (1989)37:1025.
5. C. S. Gilbert et al., J. Histochem. Cytochem. (1993)In Press.
6. C. M. Payne and L. Glasser, Blood (1986)67:299.
7. E. R. Weibel, in M. A. Hayat, Ed., Principles and Techniques in Electron Microscopy, 3d Ed., Van Nostrand Reinhold (1973)237.
8. R. J. Sokol et al., Acta Anat. (1987)129:211.
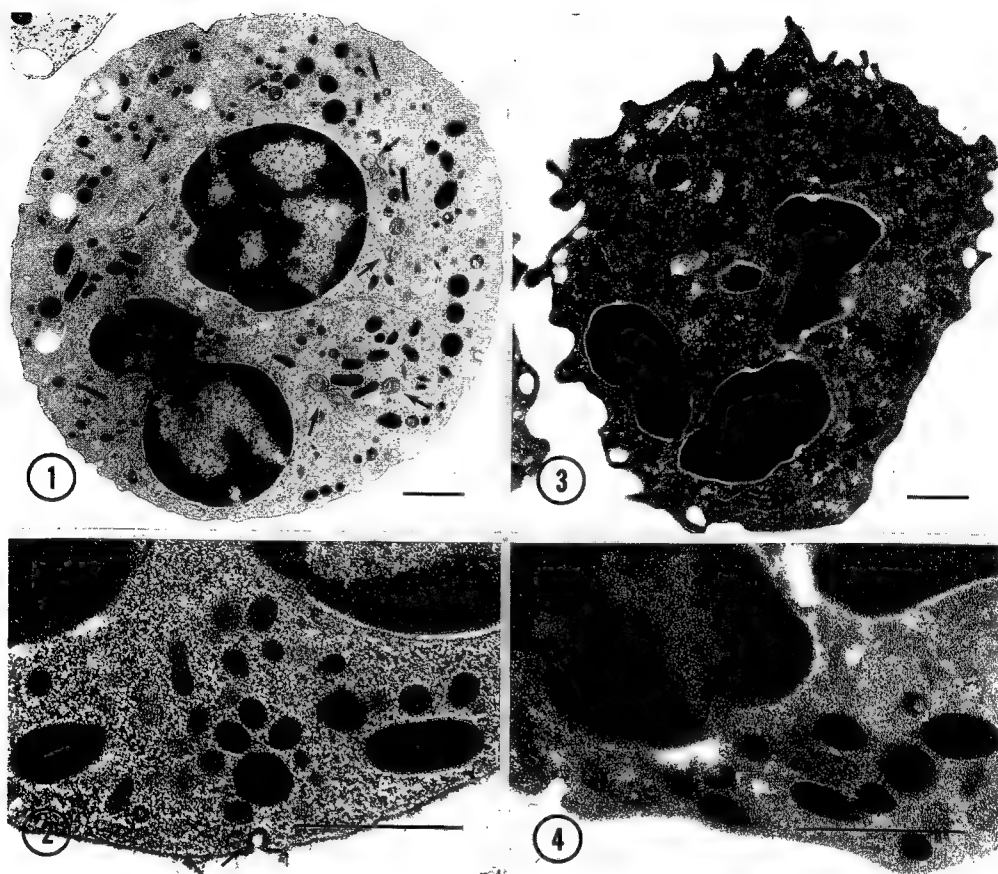
FIG. 1.--CFFS neutrophil shows round profile, multiple cytoplasmic granules, distinct mitochondria (arrows) and two nuclear lobes (n) with intact membranes. Cytoplasmic matrix is minimally dense. Bar = 1 μm.
FIG. 2.--Bilayer of plasmalemma and coating material beneath endocytic caveolus (arrow) are very distinct and well preserved. Similarly granule and nuclear membranes are well delineated. Bar = 1 μm.
FIG. 3.--This GLUT neutrophil has a more irregular surface and denser cytoplasmic matrix. Separation of nuclear membranes is more prominent; shrunken mitochondria cannot be seen. Bar = 1 μm.
FIG. 4.--Membranes of this GLUT neutrophil lack details seen with CFFS (cf Fig. 2). Bar = 1 μm.

TABLE ($\mu \pm$ sd)	Cell Area (μm^2)	Cell Peri (μm)	FF_C	S_{VC} (μm^2/fl)	Nuc area (μm^2)	Nuc Peri (μm)	V_C (fl)	S_C (μm^2)
CFFS (n=60)	37.9 ±5.6	25.0 ±3.1	0.77 ±0.13	0.85 ±0.10	9.4 ±2.9	18.2 ±4.4	325 ±70	272 ±49
GLUT (n=60)	30.6 ±5.2	28.4 ±3.7	0.49 ±0.10	1.20 ±0.16	8.5 ±2.4	19.5 ±5.0	236 ±60	277 ±54
t-test	<.001	<.001	<.001	<.001	.071	.137	<.001	.615

Use of a Post-Embedding, Indirect, Double-Sided Labeling Procedure to Identify ConA Binding Sites within Apical Vesicles of a Filamentous Fungus

Timothy M. Bourett and Richard J. Howard

Dupont Company Science and Engineering Laboratories, Wilmington DE 19880-0402

Vesicles are thought to play an important role in the polarized apical extension of fungal hyphae. These vesicles are likely to contain cell wall precursors and other molecules destined for exocytosis at the hyphal apex, including polysaccharides and/or other glycosylated molecules which should be recognized by certain lectins, including Concanavalin A (ConA). Here we describe the presence of ConA binding sites (CABS) within the apical vesicles of *Trichoderma viride*. In addition, we compare single- and double-sided ConA labeling patterns to assess the impact of these different techniques on the interpretation of results.

Somatic hyphae of *T. viride* were grown as a cell monolayer over pieces of cellophane on the surface of nutrient agar plates. The cellophane pieces and cells were plunge-frozen in a liquid propane/ethane mixture,[1] freeze-substituted in 2% OsO_4 in acetone,[2] and subsequently embedded in Quetol resin.[3] Thin sections were picked up with empty, formvar-dipped, single-slot, gold grids. The single-slot grids were used much like a loop to transfer sections from the surface of one drop to another, and facilitated the examination and quantitation of CABS in serial sections.[4] After equilibrating for 15 min in the lectin labeling buffer (50mM Tris-HCl pH 7.2, with 150mM NaCl, 0.05% PEG 20,000, and 1mM each of $CaCl_2$, $MnCl_2$ and $MgCl_2$), the sections were floated on a drop containing 30µg/ml ConA in the same buffer for 60 min. After a thorough series of rinses in buffer the sections were treated with a horseradish peroxidase-gold complex for 30 min in the same manner. Following another series of rinses in buffer and then double-distilled water the grids were transferred to a formvar film on a perforated, aluminum platform,[5] and allowed to dry at 60°C for 15 min.[6] To label the opposite face of the sections, the grids were punched out from the platform, inverted, floated on drops and treated as above. Before examination in the TEM, grids were stained with 4% uranyl acetate in 40% methanol and lead citrate for 5 min each.

Initial experiments, employing a single-sided labeling procedure in conjunction with methanolic UAc post-staining, showed two differentially stained populations of apical vesicles in hyphae of *T. viride*.. Electron translucent vesicles were labeled with ConA and electron opaque vesicles were unlabeled. However, when a double-sided labeling technique was employed both populations of vesicles were shown to contain CABS. In subsequent experiments employing single-sided labeling, it was determined that the electron-translucent vesicles had been destained by the methanol used to initially rinse the grids after uranyl acetate staining. All of the destained, electron translucent vesicles were positioned within the sections so that their contents were exposed to the methanol rinse, and to the ConA probe. Vesicles buried within the section, or exposed to the surface on the opposite side, were protected from destaining by the formvar support film and were not labeled with ConA.

References

1. H.C. Hoch, in H.C. Aldrich and W.J. Todd Eds., Ultrastructure Techniques for Microorganisms, New York: Plenum Press (1986)183.
2. R.J. Howard and K.L. O'Donnell, Exp. Mycol. 11(1987)250.
3. T.M. Bourett and R.J. Howard, Can. J. Bot. 68(1990)329.
4. T.M. Bourett et al., Exp. Mycol. (1993) in press.
5. J.C. Rowley and D.T. Moran, Ultramicroscopy 1(1975)151.
6. A. Abad, J. Electron Microsc. Tech. 8(1988)217.
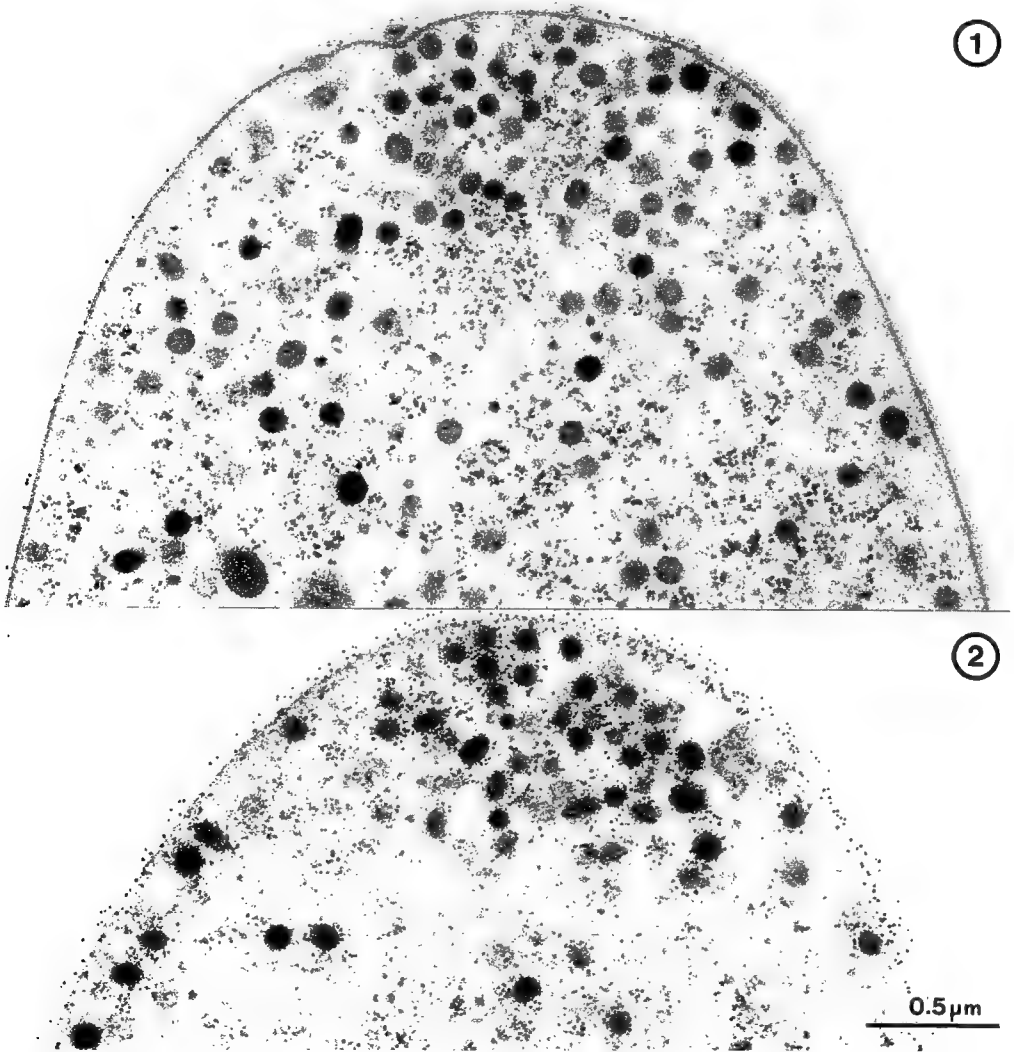
FIG. 1. Median section through apical region of *Trichoderma viride* hyphal tip labeled with ConA-HRP-gold on upper surface only. None of darker vesicles were labeled.
FIG. 2. Similar section but labeled on both sides. All vesicles show ConA binding sites.

A CRYO-SEM TECHNIQUE DEVELOPED AND APPLIED TO SURFACTANT LIPOSOMES

Kiran Bhadriraju and Jayesh Bellare

Microlab, Department of Chemical Engineering, I.I.T., Bombay-400 076, India

Freeze-fracture replication TEM and Cryo-TEM are developed techniques for studying surfactant dispersions. Application of freeze-fracture cryo-SEM[1] with direct imaging to such systems has the advantages of observing a greater range of particle sizes, large depth of field implying larger tilts together with rotation, and freeze-etching/freeze drying the sample while imaging it. A procedure for cryo-SEM of liquid colloids,which uses a simple sample preparation setup, and its results for liposomal dispersions, are described here.

Samples are plunge-frozen by a freezing device (Fig.1) made from a standard desoldering tool (Fig.2) used as a plunging unit. Fracture plates (Fig.3) are made from 0.1 mm thin copper sheet made adhesive to the liquid by 400 mesh TEM grids that are bent over the two edges of the plates and stuck on the non-sample side with a rubber adhesive. The sample is sandwiched between a pair of fracture plates (Fig.3) and plunged into liquid Freon-22 kept at its freezing point ($-160°$C) in an electrically heated cup (Fig.1) cooled by a liquid liquid nitrogen bath. The sandwich, while still fixed to plunging unit, is quickly transferred into liquid nitrogen, where it is clamped onto a custom designed specimen holder (Fig.4). The sandwich is transferred to the preparative cold-stage of a JEOL SEM, JSM-6400, via an air-lock and left there for 30 min to stabilize. It is then fractured by removing the top plate using a cryo-fracture knife, optionally coated with a thin layer of gold, placed on the observation stage, left for 20 min to stabilize again, and then imaged while at liquid nitrogen temperatures.

Sample results of liposomal dispersions are shown in Figs.5,6 and 7. Liposomes were made by adding weighed amounts of surfactant to 20 ml distilled water, gently shaken and hydrated for 48 h. Surfactants used were AOT (Sodium di-2-ethylhexylsulfosucci- nate) and soya lecithin. Fig.5 shows a large liposome with a horned Dupin cyclide- like[2] structure. This image was taken without gold or any other coating at 5KV. Fig.6 shows a fractured soya pc liposome which is apparently spherical, similar to freeze- fracture TEM results[2]. Fig.7 shows a multilamellar vesicle structure similar to those imaged by cryo-TEM[3]. These results show that cryo-SEM could conveniently be used for studying membrane transitions, biological fluids, polymer latex, etc., along with elemental analysis which is possible with uncoated samples. Thus these cryo-SEM results are a valuable adjunct to optical microscopy, environmental SEM, FFTEM and cryo-TEM of colloidal dispersions[4].

REFERENCES

1. J.G. Sheehan and W.Walen Shaw, Tappi (1990), 73, 171-178.
2. J.A.N. Zasadzinsky et al., Phil.Mag.A (1985), 51, 287-302.
3. J.R Bellare et al., J.Electron Microsc.Tech. (1988), 10, 87-111.
4. This work was supported by a Thrust-Area Grant from MHRD, Govt. of India.

FIG.1.- Freezing set-up A-liquid nitrogen B-liquid freon C-Specimen D-tweezers E-plunging shaft F-heater coil Gtweezers clamp

FIG.2.-Plunging unit. A-fixed end of spring Bmoving end of spring C-trigger D-locking mechanism E-plunging shaft F-step

FIG.3.-Specimen fracture plate pair. A-0.1 mm thick copper sheet B-TEM grid C-clamping area (on one plate of pair) D-sample sandwiched in between (plate spacing exaggerated for clarity)

FIG.4.-Specimen holder with specimen plates affixed. A-2 mm thick Cu sheet B-0.5 mm thick phosphor-bronze strip C-washer D-screw E-specimen plates F-stub (fits cryo stub holder of JSM 6400)

FIG.5.-A 2% AOT liposome (uncoated). The structure appears to be a horn shaped Dupin cyclide. Bar = 10,000 nm

FIG.6.-A 2% Soya pc liposome (coated with gold). The micrograph is similar to FFTEM micrograph of liposomes. Bar = 10,000 nm

FIG.7.-A 2% Soya pc multilamellar vesicle (coated with gold). Bar = 1000 nm

285

RETENTION OF VANADIUM COMPOUNDS IN CELLS AND TISSUES DURING PROCESSING FOR ANALYTICAL MICROSCOPY

Victoria Hatch, Rebecca C. Stearns, Marshall Katler, and John J. Godleski

Respiratory Biology Program, Harvard School of Public Health, 665 Huntington Avenue, Boston, MA 02115

Previous studies from our laboratory have shown that soluble vanadium compounds accumulate in phagolysosomes of alveolar macrophages. In routinely fixed and processed material, the vanadium appears primarily as a precipitate in the phagolysosomes when examined using the Zeiss CEM902.[1] Although macrophages respond to vanadium exposure with a massive respiratory burst within minutes of exposure, vanadium is not detected by Electron Energy Loss Spectroscopy (EELS) or Electron Spectroscopic Imaging (ESI) in these cells prepared by glutaraldehyde and OsO_4 liquid fixation.[2] However, if the cells are prepared by rapid cryofixation and freeze drying, vanadium can be detected at these very early stages of exposure. Work is now in progress to define the pathways used by vanadium ions in moving from the cell membrane to the phagolysosome. The purpose of the study reported here is to directly compare the retention of radioactive vanadium, ^{48}V, in lung macrophages prepared by conventional liquid fixation protocols and by cryomethodology. We also compare uptake and retention of ^{48}V in cryofixed peripheral lung tissue.

Alveolar macrophages were collected by lavage with phosphate buffered saline from hamsters euthanized with sodium pentobarbital. The cells were pelleted, washed with Medium 199 supplemented with 5% fetal bovine serum and antibiotics, resuspended to a concentration of 2-4 x 10^6 cells/ml, and incubated for 3 hours at 37°C with Med 199 plus 0.1 mM VCl_3 + $^{48}VCl_3$ (approximately 0.25 µCi). Uptake of ^{48}V was measured at 15, 30, 60, and 180 minutes. Cell viability was measured by Trypan blue exclusion. The cells to be liquid fixed were washed twice remove free ^{48}V and then the ^{48}V activity in the cell pellet was counted as fixation was started with 2.5% glutaraldehyde in 0.1 m potassium phosphate buffer with 0.01% $CaCl_2$ for 1 hour. The pellet was then washed with buffer, post-fixed in 1% OsO_4 in 0.085 m Na Cacodylate buffer, washed, and dehydrated through a graded series of ethanol. All fixation and dehydration fluids were retained and ^{48}V activity was determined in each with a gamma scintillation counter. The cells to be cryofixed were washed twice to remove free ^{48}V and collected into clean brass 22 caliber shell casings. The opening was capped with Nucleopore® Filter membrane secured by a rubber O-ring. The ^{48}V activity was determined for the contents of the brass casings, after which they were plunge frozen in liquid nitrogen. The shell casings and their frozen cells were then placed into the sample wells of the MDD-C and freeze dried using a Lifecell® MDD-C molecular distillation dryer. Pieces of peripheral lung 2 mm on a side were incubated for 2.75 hours in Med 199 with VCl_3 and $^{48}VCl_3$ or with $^{48}VCl_3$ alone, washed with Med 199, loaded 3 pieces each into brass casings, counted, frozen, and dried as above. The ^{48}V activity of the dried casings was counted and corrected for expected radioactive decay (half life = 16 days).

The cells took up between 1.5 and 2 percent of the available ^{48}V (Fig. 1), the lung tissue took up about 25%. Cell viabilities were not affected by uptake of the radioactive vanadium. After

processing in the MDD-C, cryofixed cells retained 84% of the expected ^{48}V activity and lung tissue retained a mean of 80% activity. Cells which had been liquid fixed and dehydrated retained 57% activity (Fig. 2). The greatest losses of vanadium occurred in the glutaraldehyde and OsO_4 fixation steps of the liquid processing (Fig. 3). Cryofixation and freeze drying in the Lifecell® MDD-C results in excellent morphology (Fig. 4) as well as substantially greater retention of ionic constituents for EELS and ESI studies.

References

1. Godleski, J.J., *et al.* Proc. EMSA. 1992, p. 638-9.
2. Lalani, T. Master's Thesis, Respiratory Biology, Harvard School of Public Health, 1992.
3. This research was supported by NIH grants ES00002 and ES05947. Technical contribution of Cindy Hastings is acknowledged.

1 ^{48}V UPTAKE BY CELLS

2 ^{48}V LOST FROM PELLET DURING PROCESSING

3 ^{48}V RETENTION

4
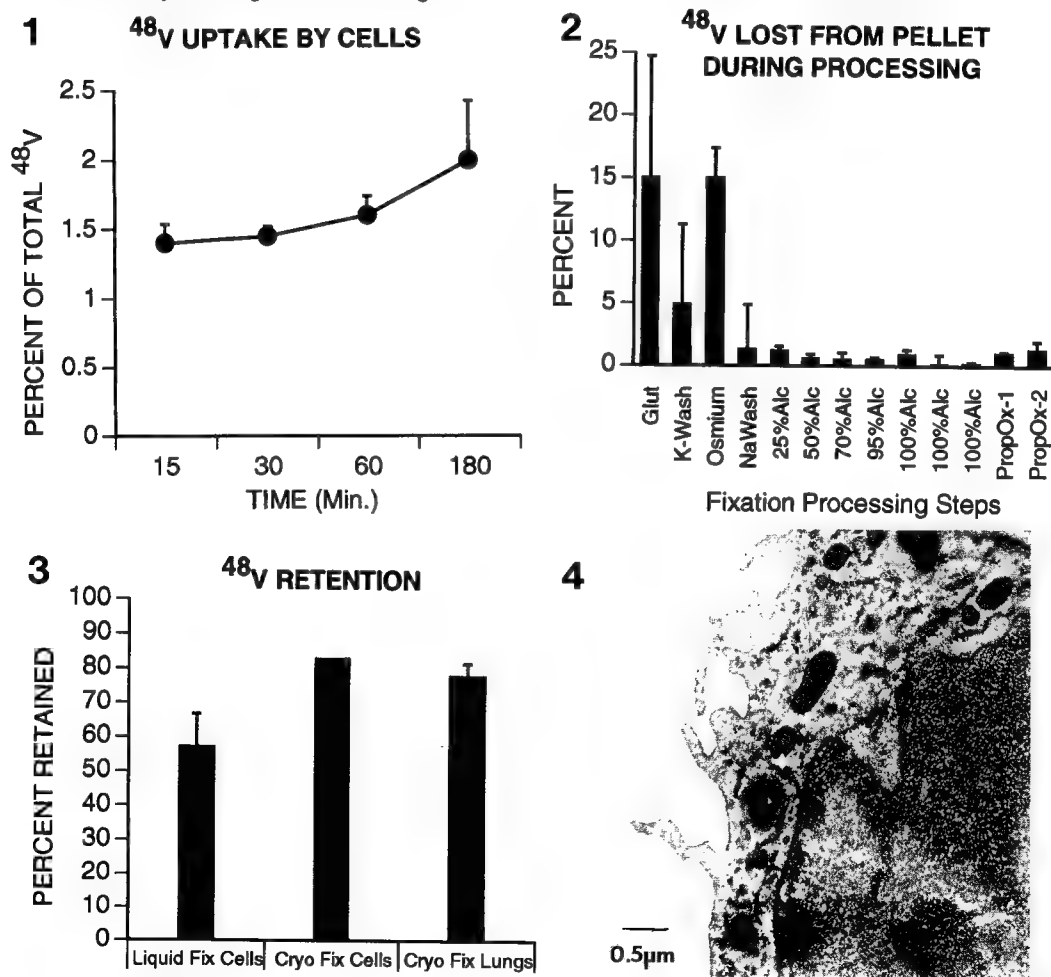
Fig. 4--Cryofixed freeze-dried hamster macrophage exposed to VCl_3. Bar = 0.5μ.

DEMONSTRATION OF GAD IN PURKINJE-CELL TERMINALS WITH SILVER ENHANCED GOLD IMMUNOCYTOCHEMISTRY

Helen G. Gilerovitch, Georgia A. Bishop, James S. King and Richard W. Burry

Dept. of Cell Biology, Neurobiology and Anatomy, The Ohio State Univ., Columbus, OH 43210

The neurotransmitter gamma-amino butyric acid (GABA) is synthesized in presynaptic terminals by glutamic acid decarboxylase (GAD). Antibodies to GAD have been used to localize presynaptic terminals in the cerebellar cortex that use GABA as a neurotransmitter.[1] In the cerebellum, the Purkinje cell makes synaptic contacts on dendrites and somata of neurons in the cerebellar nuclei. We were interested in developing a technique that combined light microscopic analysis of GAD distribution in Purkinje cell terminals with high quality electron microscopic localization of GAD.

The approach taken in this study was to combine high glutaraldehyde/metabisulfite fixation technique[2] with the preembedding N-propyl gallate (NPG) silver enhanced gold procedure.[3] Mice were perfused with buffered 3% glutaraldehyde and 0.4% sodium metabisulfite. Vibratome sections (60 μm) were permeabilized with 0.3% Triton, and incubated with a monoclonal anti-GAD antibody.[4] The sections were incubated in goat-anti-mouse 1 nm Nanogold, and the gold was enhanced with the NPG silver enhancement solution for 10 minutes. After embedding in Spurrs resin between two sheets of teflon, the sections were photographed with a light microscope and then remounted for thin sectioning.

Light microscopic examination of vibratome sections revealed punctate labeling (Fig. 1, arrows) around neurons (Fig. 1, stars) in the cerebellar nuclei. Individual neurons were seen to be associated with GAD reactive terminals as has been reported previously.[5] Electron microscopic examination of thin sections showed a good level of cytological preservation in the cerebellar nuclei (Fig. 2). GAD positive terminals were seen to encircle the neurons (Fig. 2, block arrows). With NPG silver enhancement of 10 minutes, particles were small enough to allow detailed analysis of cytological features. These results indicate that the combined techniques of fixation with glutaraldehyde in the presence of metabisulfite and the preembedding NPG silver enhanced gold procedure can be used together for localization of GAD in synaptic terminals in the CNS.

References
1. Bishop et al., Neurosci. Abst. 18(1992)854
2. Oleskevich et al., Neurosci. 42(1991) 777-791
3. Burry et al., J. Histochem. Cytochem. 40(1992)1849-1856
4. Chang & Gottleib, J. Neurosci. 8(1988)2123-2130
5. Wassef et al., Brain Res. 399(1986)125-135
6. This work was supported by an Interdisciplinary Seed Grant from the Office of Research, The Ohio State University.

Fig. 1. Light micrograph of cerebellar nuclear neurons encircled (asterisk) by GAD positive terminals (small arrows). Blood vessels are also seen (star). Bar = 50 μm

Fig. 2. Electron micrograph of cerebellar nuclear neuron (CN) with nucleus in lower left. GAD positive terminals (block arrows) are seen making contact with the membrane of the neuron. Bar = 1 μm
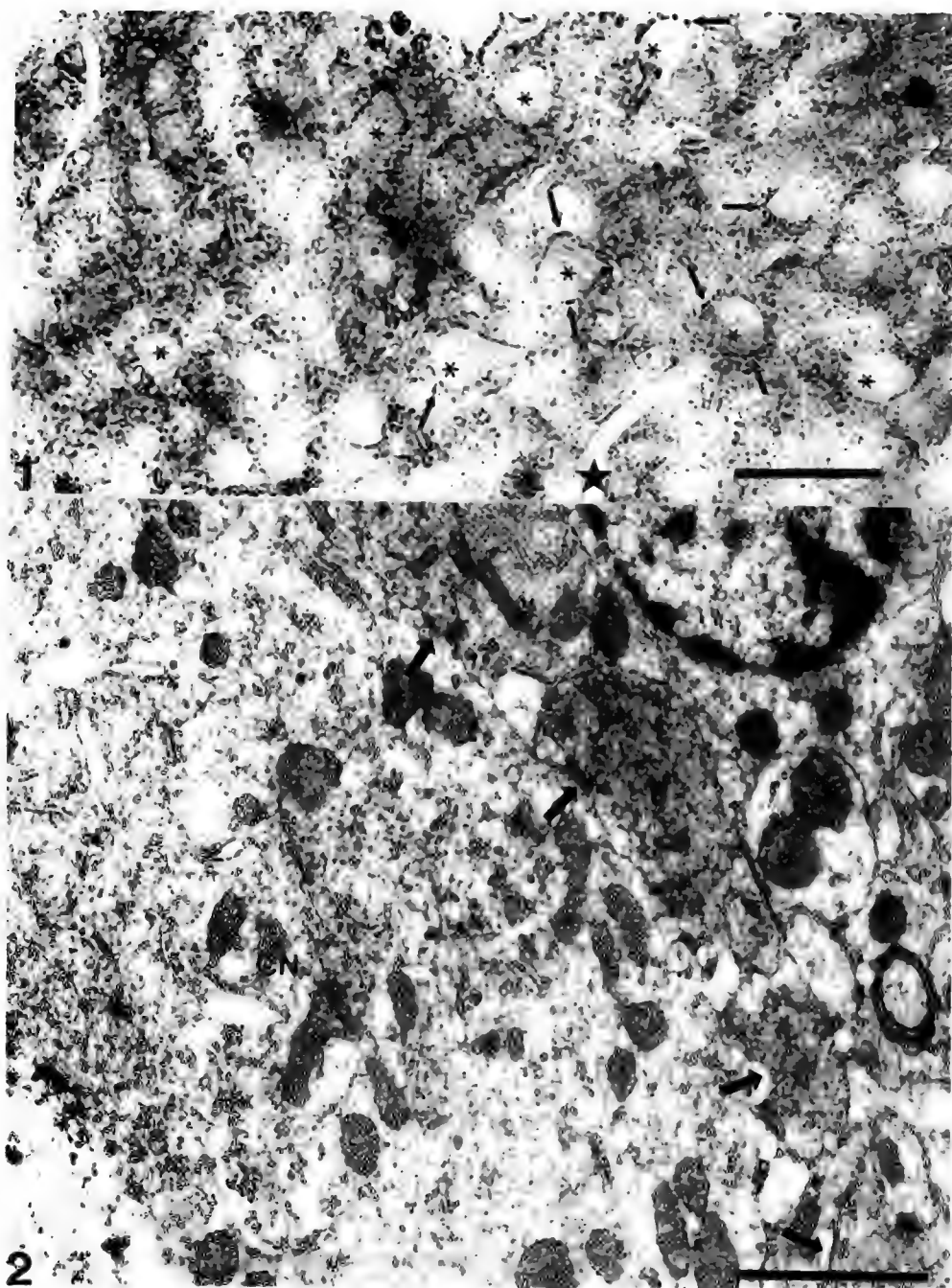
FROM LIGHT TO ELECTRON MICROSCOPIC ANALYSIS OF NEURONS INTRACELLULARLY INJECTED IN FIXED SLICES WITH "MINIRUBY", A FLUORESCENT BIOCYTIN COMPOUND

Wei-lin Liu and Michael T. Shipley

Department of Anatomy and Cell Biology, University of Cincinnati College of Medicine, 231 Bethesda Ave. Cincinnati OH 45267-0521

Intracellular labeling of neurons in fixed slices is a very useful method for studying morphological structures of neurons both at light and electron microscopic levels. Recently, biocytin has been widely used for intracellular labeling in living slices because this molecule is highly soluble, has high electrophoretic mobility and has high affinity for avidin.[1] However, biocytin cannot be used in fixed slices because in fixed slices membrane potential cannot be used to signify that a cell is impaled. Thus, in fixed slices it is necessary to inject cells with a fluorescent compound so that impalement and filling can be visualized under fluorescent microscope. We have developed a fluorescent biocytin compound, "Miniruby" (MR), dextran-tetramethylrhodamine-biocytin. previously, we showed that this molecule provides excellent intracellular labels in fixed slices at the light microscopic level.[2] Here, we demonstrate MR can also be visualized at the electron microscopic level.

Fixed slices (200-400 µm) of adult rat olfactory bulb, piriform cortex and periaqeductal gray were used. Slices were stained by 0.001% ethidium bromide so that cell bodies could be visualized under fluorescent illumination. A cell was impaled with a pipette (tip diameter 0.5-1.2 µm) containing 3-5% MR; positive constant current (1-5 nA; 300-400 msec. on, 600-700 msec. off -10 min.) was applied until the fine dendrites were brightly fluorescent. In most cases, the cell body, dendrites and spines were well filled in about 10 min. For LM, slices were post-fixed for 2-12 hours, then reacted by ABC-DAB. For EM, the reacted slices were osmicated with 0.5% osmium for 20 min, dehydrated and flat embedded in Epon. Ultrathin sections were cut on a ultramicrotome, stained with uranyl acetate and lead citrate and analyzed in a electron microscope (JEOL JEM-100 CX II).

Many neurons were filled within a single slice. After ABC-DAB reaction, all filled neurons could be visualized by bright field microscopy (Figs 1-4). Neurons of widely varying size and morphology were filled in piriform cortex, periaqeductal gray and olfactory bulb. Dendritic trees and spines were clearly and densely labeled (Figs 4, 5). In addition, the fine terminal ramifications of the apical dendrite of olfactory tufted cell were also labeled (Fig 3). At the EM level, the MR filled neurons and their processes were shown as dark dense structures. This enables us to analyze the ultrastructures of pre- and postsynaptic elements of MR filled neurons. Figures 6 & 7 show the secondary dendrite of a filled mitral cell. Several dendro-dendritic synapses are clearly seen.

Intracellular filling with MR in fixed slices overcomes several limitations of other intracellular markers: (1) it is easy to visualize the electrode in relation to the cell bodies; (2) the histochemical staining is very sensitive and light stable; (3) injected neurons, dendrites are well visualized by bright field microscopy; and (4) electron microscopic analysis of MR filled cells can be done. This method provides detailed analysis not only of the morphology of the filled neurons at the LM level, but also identification of the pre- and postsymaptic elements at the EM level. MR, combined with immunocytochemical detection of other antigens or tract-tracing techniques, can be used to identify and characterize the organization and molecular profiles of synapses on MR filled neurons.

References

1. K. Horikawa and W. E. Armstrong, J. Neurosci. Methods. (1988)25, 1.
2. W-L. Liu et al., Brain Res. (in press).
3. This research was supported by NIH DC00347, NS20643, NS24698, NS29635, NS29218 and US Army DAMD 17-91-C-1071.
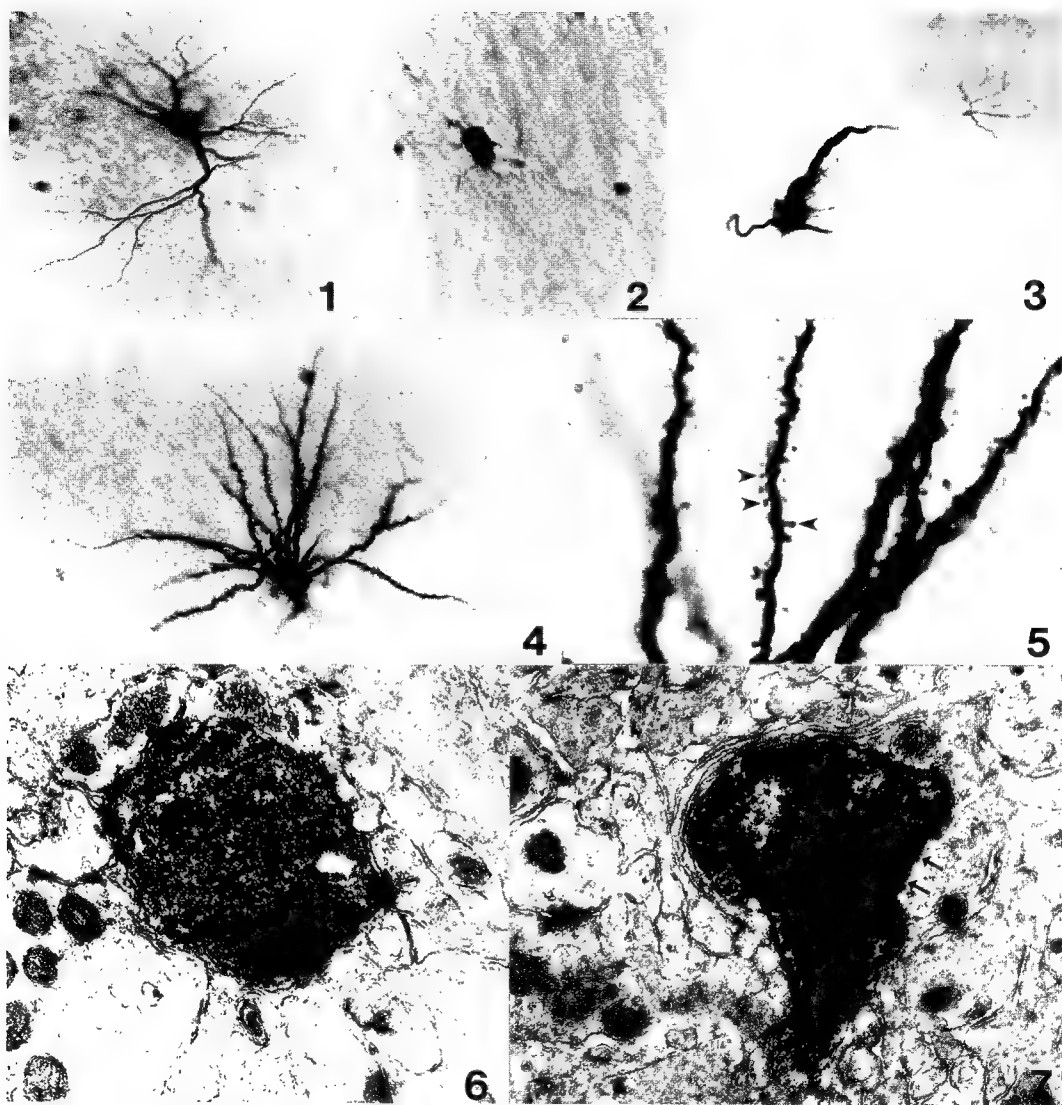
Fig 1: One MR filled neuron in piriform cortex.

Fig 2: A MR filled cell in the periaqeductal gray. This cell might be a glia cell.

Fig 3: A tufted cell filled with MR in the olfactory bulb. Note that the fine terminal ramifications of the apical dendrite of the tufted cell were well filled.

Figs 4&5: One MR filled neuron in piriform cortex has dendritic spines shown at higher magnification (arrowheads) in panel 5.

Figs 6&7: A secondary dendrite of a MR filled mitral cell in external plexiform layer of the olfactory bulb at the EM level. Several dendro-dendritic synapses (arrows) are clearly seen.

PROJECTIONS FROM THE PERIAQUEDUCTAL GRAY (PAG) TO THE PERIAMBIGUAL AREA: RELATION TO CHOLINERGIC VAGO-CARDIAC NEURONS

Shuang-jin Xu, Tilat A. Rizvi, Maorong Jiang, Matthew Ennis and Michael T. Shipley

Department of Anatomy and Cell Biology, University of Cincinnati College of Medicine, 231 Bethesda Ave., Cincinnati, OH 45267-0521

Activation of the midbrain periaqueductal gray (PAG) elicits species specific defense reactions and marked autonomic adjustments. In agreement with recent studies by Bandler and colleagues in the cat, we found that activation of rostrocaudally-oriented, longitudinally organized columns in PAG elicit differential cardiovascular and behavioral responses. Activation of dorsolateral/lateral PAG produces aggressive/flight behaviors accompanied by pressor responses while stimulation of ventrolateral PAG produces immobility and depressor responses. The pathways mediating these selective behavioral and autonomic responses are poorly understood.

The projection from PAG to the sympathoexcitatory zone in the rostral ventrolateral medulla is a likely substrate for PAG-evoked pressor responses. However, circuits mediating PAG-evoked depressor responses are not known. The present studies have identified a robust, focal projection from PAG to the nucleus ambiguus (NA), a potent depressor area in the ventral medulla. In addition, we have used tract tracing techniques and immunocytochemistry to examine the organization of PAG projections in relation to cholinergic preganglionic parasympathetic NA neurons that innervate the heart.

Physiologically-guided injections of wheat germ agglutinin-horseradish peroxidase (WGA-HRP) into NA and the region immediately surrounding NA, here defined as the periambigual area (pNA), retrogradely labeled neurons in the ventromedial supraoculomotor, lateral and ventrolateral parts of PAG. Labeled neurons in ventromedial PAG formed a discrete cluster centered immediately dorsal to the contralateral oculomotor nucleus. Labeled neurons in the lateral and ventrolateral parts of PAG formed longitudinal columns that extended substantially along the rostrocaudal axis of PAG; the lateral column occupied the rostral two-thirds of PAG, while the ventrolateral column extended along the caudal one-third of PAG. Thus, the spatial organization of these two columns of medullary output neurons is similar to that of the pressor and depressor columns in PAG.

WGA-HRP or phaseolus vulgaris leucoagglutinin (PHA-L) injections into lateral and ventrolateral PAG labeled a longitudinally-organized fiber plexus that densely innervates the entire rostrocaudal axis of NA and pNA. Labeling begins at the level of the facial nucleus, corresponding to the compact formation of NA; labeled fibers at this level are primarily located in the region immediately surrounding, and to a lesser extent, within NA. The density of labeled fibers progressively increases along the rostral to caudal axis of pNA, terminating most heavily in the loose and caudal, external formation of pNA. In contrast to these results, tracer injections into dorsomedial, dorsolateral, or ventromedial parts of PAG produced only sparse fiber labeling in the ventrolateral medulla, including NA and pNA.

These anterograde tracing results indicate that PAG densely innervates medullary regions containing preganglionic vagal neurons. Bieger and Hopkins (1987) demonstrated the caudal external formation of pNA, shown here to be heavily targeted by PAG inputs, contains the majority of neurons that innervate the heart. Previous studies hace shown that preganglionic parasympathetic vagal neurons contain the neurotransmitter acetylcholine. To directly assess the relationship between PAG projections and

292

cholinergic vagal neurons, anterograde tracing was combined with immunohistochemical staining for choline acetyltransferase (ChAT), the synthetic enzyme for acetylcholine. At the light microscopic level, anterogradely labeled fibers densely innervated regions containing ChAT-positive neurons. Labeled fibers and terminals were most dense among groups of ChAT-positive neurons in the loose and caudal, external divisions of pNA.

To assess PAG projections in relation to cardiac-projecting neurons, the retrograde tracers WGA-HRP or Fluorogold were injected directly into 1-2 cardiac ganglia. In agreement with Bieger and Hopkins (1987), these injections retrogradely labeled neurons that were primarily located in caudal pNA, although some labeled neurons were located immediately ventral to the compact formation of NA. The distribution and density of pNA cells labeled after tracer injections into the heart overlaps substantially with fibers anterogradely labeled from PAG.

These results indicate that PAG has direct, robust connections with NA and pNA. This projection terminates most heavily in the caudal pNA region containing preganglionic parasympathetic vagal neurons that project to the heart. Projections from PAG terminate in close proximity to cholinergic vago-cardiac pNA neurons. The PAG-NA projection may comprise a direct anatomical substrate that mediates the potent depressor responses produced by PAG stimulation. In addition, the projection from PAG to the rostral, compact division of NA may mediate the respiratory and vocalization responses produced by activation of PAG. Experiments in progress will determine if PAG innervates identified vagocardiac neurons and if this pathway mediates PAG-evoked depressor responses.

References:
1. Bandler, R., Carrive, P. and Zhang, S.P. Integration of somatic and autonomic reactions within the midbrain periaqueductal grey: Viscerotopic, somatotopic and functional organization. Prog. Brain. Res. 67 (1991) 269-305.

2. Bieger, D and Hopkins, D.A. Viscerotopic representation of the upper alimentary tract in the medulla oblongata in the rat: the nucleus ambiguus. J. Comp. Neurol. 262 (1987) 546-562.

IMMUNOELECTRON MICROSCOPIC LOCALIZATION OF ACTIN IN DEVELOPING RAT LEG MUSCLE

Theresa A. Fassel and Marion L. Greaser

Muscle Biology Laboratory, University of Wisconsin-Madison, Madison, Wisconsin 53706

Studies were conducted on the arrangement of α-actin in muscle cells in Sprague-Dawley rats at 1, 3, 5, 7, 30 and over 100 days of age. The α-actin isoform was distinguished from the nonmuscle ß- and τ- isoforms by using the α-specific monoclonal antibody HUC1-1.[1] The antibody was used in a two stage post-embedding procedure with colloidal gold conjugated to goat anti-mouse IgG.

Muscle samples were placed in a relaxing solution (100 mM KCl, 10mM Imidazole, 10mM $MgCl_2$, 2mM EGTA, 4mM ATP, 1mM $NiCl_2$, 1mM PMSF, 100 μM leupeptin, 50% glycerol) for 1 hr on ice or overnight at -20°C. Samples were transferred to a skinning solution (100mM KCl, 10mM KH_2PO_4, 5mM $MgCl_2$, 1mM EGTA, 1% glucose, 0.2% Triton X-100, 0.02% NaN_3) for 1 hr on ice and then into 3.7% formaldehyde in rigor buffer (RB - 75mM KCl, 5mM K_2HPO_4, 2mM $MgCl_2$, 2mM EGTA, 2mM NaN_3) for 1 hr for fixation. Samples were washed in RB, dehydrated in a graded ethanol series, and embedded in LR White resin. Thin sections on nickel grids were exposed to a blocking buffer (10% goat serum-1% BSA- 0.4% fish gelatin in RB) for 1 hr at room temperature. Samples were incubated with primary anti- α-actin antibody for 4 hours at room temperature in a hydration chamber. They were then washed three times in RB and incubated in 15nm gold labelled goat anti-mouse IgG (Fc) (Amersham, UK) in a hydration chamber overnight at room temperature. Samples were washed 3x in RB, 1x in 1% glutaraldehyde in RB, 3x in RB, and 3x in distilled water for 5 minutes each. Samples were post-stained in 2% uranyl acetate and Reynold's lead citrate and observed in a Hitachi H-600 at 50 KV. Controls in which the primary antibody was replaced with blocking buffer were included with each group of grids processed.

Day 1 muscle cells had few myofibrils and those which were present appeared poorly organized (Figs. 1 & 2). Most of the actin was contained in individual filaments and bundles of filaments not associated with distinct sarcomeres. Z-line structures were identifiable but A-bands were often not clearly defined. Ribosomes were abundant and typically associated with filaments. A considerable increase in myofibril density was found in muscle cells at Day 3 (Fig. 3). Myofibrils resembled mature structures with A-bands more frequently identifiable. Labelling was frequently observed throughout the sarcomere, although restriction of labelling to I bands and regions of overlap of the thick filaments were observed. Primitive myofibrils with barely discernable Z-lines between masses of filaments were still observed in Day 5 cells. Again, in more mature areas some restriction of label to the I band and overlap with the thick filament occurred. For Day 7 cells (Figs. 4 & 5), some mature-like sarcomeres with distinct A bands and straighter Z-lines were observed. Bundles of less well organized filaments were also labelled. Day 30 cells (Figs. 6) had abundant mature myofibrils.

References

1. N.M. Sawtell et al., Cell Motil. Cytoskeleton (1988)11, 318.
2. The authors thank Dr. J. Lessard for providing the HUC 1-1 antibody.

FIGS. 1. and 2.--Longitudinal and cross sections of Day 1 rat muscle cells labelled for α-actin. The actin is present in loosely organized filaments and bundles.

FIG. 3.--Longitudinal section of Day 3 myofibrils. A bands and Z lines are visible; actin labelling is sometimes excluded from the H-zone.

FIGS. 4 and 5.--Longitudinal and cross sections of Day 7 myofibrils show more mature appearing sarcomeres. Actin labelling is abundant.

FIG. 6.--Cross section of Day 30 myofibrils show considerable increase in density of actin labelling.

Magnification bars equal 1 μm.

ULTRASTRUCTURAL LOCALIZATION OF ANTIGENIC SITES IN PANCREATIC TISSUE USING IN SITU (METAL-MIRROR) CRYOFIXATION

Fred G. Lightfoot

Department of Anatomy, The George Washington University Medical Center, 2300 I St. N.W., Washington, D.C. 20037

There have been previously reported methods using in situ cryofixation via metal mirror freezing to study the ultrastructural characteristics of lung tissue while in its native state (inflated), as well as the elemental composition in subcellular compartments of the proximal tubule in whole (unexcised) tissue.[1,2] Many studies have been done to determine the most appropriate way to conserve both antigenicity and structural integrity of various tissues.[3,4] In most of these protocols there are steps which are likely to reduce or destroy the tissue antigenicity. In this report, an application using in situ cryofixation of pancreatic tissue for optimal ultrastructure and antigenicity will be described.

Male rats were anesthetized with sodium pentobarbital (50mg/kg). The abdomen was opened and the pancreas was carefully elevated, using forceps, being careful to maintain integrity of the mesentery of the duodenum and pancreas along with their blood supply. The tissue was rapidly frozen using the PS1000 cryofixation unit (Delaware Diamond Knives, Wilmington, DE), a pneumatically operated metal mirror instrument precooled to nitrogen temperature. The tissue was immediately returned to a liquid nitrogen bath and never exposed to atmosphere thereafter prior to embedding. The specimens were freeze-dried, embedded in spurr resin, sectioned at 90 nm and placed on nickel grids. Sections, etched with sodium metaperiodate or unetched, were immunocytochemically labeled using anti-human α-amylase followed by incubating sections with 10 nm protein A gold. Figure 1 shows an overview of well preserved exocrine tissue with characteristic masses of granular reticulum and dense secretory droplets. In Figure 2 the fine structure is more clearly discerned and shows no ice artifact in the granular reticulum, nucleus and mitochondria. When immunolabeling tissue sections for amylase (Figs. 3 and 4) the intensity of the gold label was similar in both etched or unetched sections and was concentrated within zymogen granules, condensing vacuoles and endoplasmic reticulum.

It is suggested that the intensity of cellular antigenic sites may be greatly enhanced by the use of cryofixation followed by freeze drying and embedding in spurr resin. This enhancement is achieved since contributing factors to degradation of antigenicity are removed, i.e. chemical fixation and dehydrating agents.

References

1. J.J. Godleski, et al. Proc. of EMSA. (1992) 740
2. C.C. Freudenrich, et al. Proc. of EMSA. (1992) 742
3. M. Bendayan, et al. The Am. J. of Anat. (1986) 175, 379
4. P. Klosen, et al. The J. of Histo. & Cyto. Chem. (1993) 41, 455
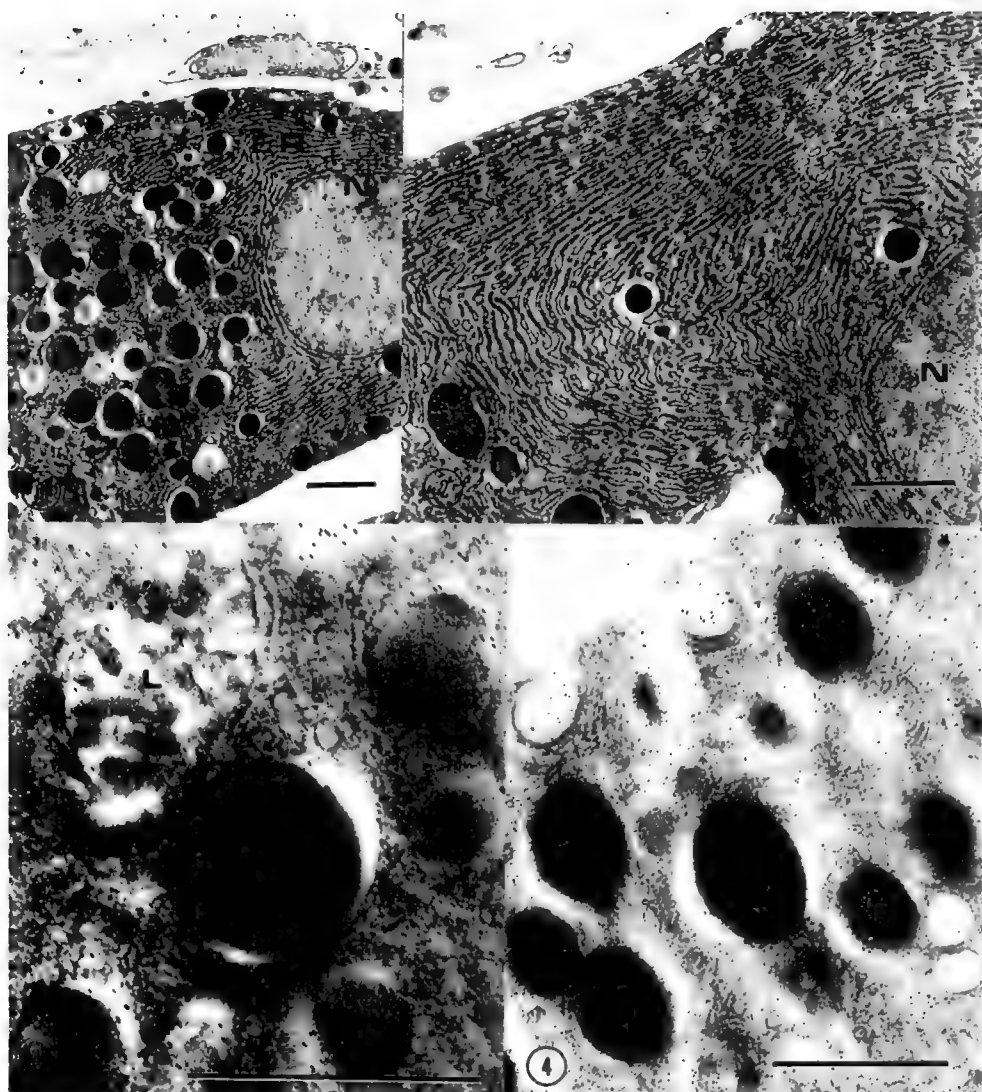
Fig. 1 Unstained control in situ cryofixed rat exocrine pancreas. Uppermost area is leading edge of fixation revealing characteristic fine structure with no visible ice reticulation. ER (endoplasmic reticulum) N (nucleus) Bar=1μm

Fig. 2 Higher magnifaction of control tissue clearly demonstrates the excellent structure of in situ cryofixed exocrine pancreas. N (nucleus) M (mitochondria) Bar=1μm

Fig. 3 The lumen of an acinus is seen with microvilli projections. Gold particles are seen over zymogen granules and lumen: section treated with sodium metaperiodate. L (lumen) Z (zymogen granules) Bar=1μm

Fig. 4 The gold labeling for amylase is over secretory granules of varying density: section treated with sodium metaperiodate. Z=secretory granule Bar=1μm

297

CYTOCHEMICAL LOCALIZATION OF GLYCOGEN PHOSPHORYLASE ACTIVITY IN RAT LIVER

John E. Michaels and Robert R. Cardell

Dept.of Anatomy and Cell Biology, Univ.of Cincinnati College of Medicine, Cincinnati, OH 45267

Glycogen phosphorylase (GP) is a key enzyme in liver glycogen breakdown. GP activity is altered with its state of phosphorylation. In the current study, the intralobular distribution of GP activity was observed histochemically in frozen sections of rat liver during fasting and after stimulation of glycogen synthesis.

Normal and adrenalectomized (ADX) rats were fasted overnight to reduce liver glycogen to minimal levels. Fasted ADX rats received 2 mg dexamethasone (DEX) 0-8 h prior to sacrifice to stimulate glycogen synthesis. Liver was removed, rapidly frozen in isopentane cooled in liquid nitrogen, then cryostat sectioned. In order to determine sites of GP activity, sections were incubated in medium that contained glucose 1-phosphate as substrate. Under the incubation conditions used, GP synthesized glycogen as the reaction product.[1,2] Glycogen was identified by two staining methods: 1) iodine staining has been shown to be rather specific for newly synthesized glycogen produced during the histochemical procedure (Figs. 1-6), whereas 2) periodic acid-Schiff (PAS) stained both native and nascent glycogen.

In the normal fasted rats liver GP activity was variable. Many hepatocytes showed substantial enzyme activity whereas adjacent cells showed little or none. Overall, in many instances activity was somewhat more concentrated in the centrilobular region of the lobules (Fig. 1). In contrast to the fasted normal rats in which activity was distributed throughout the positive cells, in the fasted ADX rats (Fig. 2), GP reaction product was highly concentrated in small discrete aggregates in random hepatocytes throughout the lobule.

After 2 h DEX treatment (Fig. 3), overall GP activity increased. In some hepatocytes enzyme activity remained aggregated, in other cells GP activity was dispersed or absent. After 4 h DEX treatment (Figs. 4 and 5), the majority of hepatocytes contained GP reaction product. GP activity was more concentrated in centrilobular cells. After 8 h DEX treatment (Fig. 6), substantial GP activity was evident throughout the lobules that was more uniformly distributed than at the 4 h interval. In general, GP reaction product appeared more aggregated in periportal cells and more dispersed in centrilobular hepatocytes.

The results show that GP activity increased as glycogen synthesis was stimulated. Although progressively more hepatocytes acquired enzyme activity throughout the lobules, the observations suggest that in this ADX-DEX model of glycogen synthesis, a transient centrilobular pattern of concentration of GP activity was generated after 4 h DEX treatment. The change in patterns was consistent with glycogen patterns during early glycogen synthesis described previously.[3] Also, localization by immunocytochemistry of GP enzyme protein in fed and fasted rats revealed centrilobular patterns.[4] At both the 2 h and 4 h intervals GP activity was variable in adjacent cells suggesting diversity in the metabolic state of neighboring hepatocytes in different lobular regions. By the 8 h interval, GP activity was more intense and occurred in virtually all hepatocytes. The centrilobular pattern was not apparent.[5]

References
1.   O. Eränkö and A. Palkama, J. Histochem. Cytochem. 9(1961) 585.
2.   L. A. Lindberg and A. Palkama, J. Histochem. Cytochem. 20(1972) 331.
3.   M. Babcock and R. R. Cardell, Amer. J. Anat. 140(1974) 299.
4.   B. Giffin et al., J. Histochem. Cytochem. (In review)
5.   Supported by NIH Grant #DK27097.
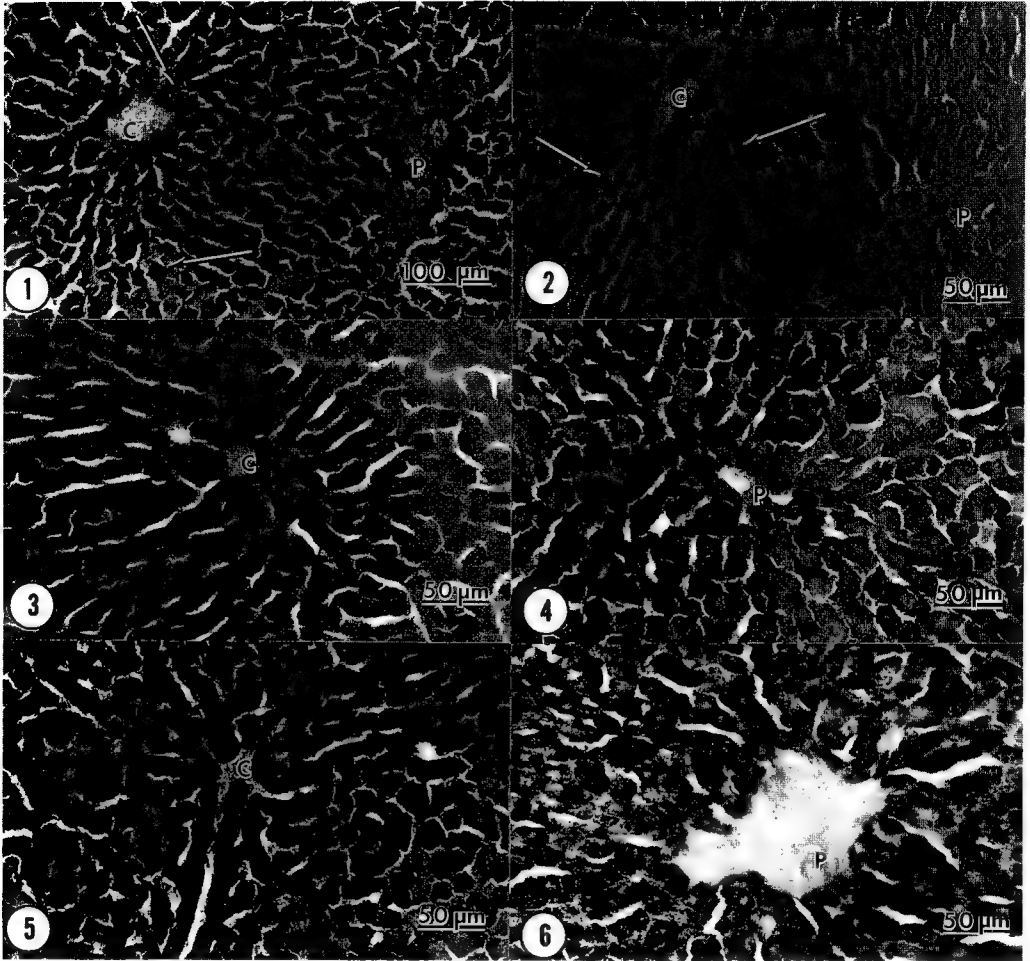
All figures from cryostat sections, incubated 1 h, iodine stained to demonstrate GP activity (new glycogen) and counterstained with light green.

Fig. 1. Periportal (P) and centrilobular (C) regions from fasted normal rat shows random cells with GP activity (arrows).

Fig. 2. Periportal (P) and centrilobular (C) regions from fasted ADX rat. GP activity appears as aggregates of glycogen (arrows).

Fig. 3. Centrilobular (C) region from fasted ADX rat after 2 h DEX. GP activity is dispersed in some hepatocytes and occurs as small aggregates in other cells.

Fig. 4 and 5. Periportal (P, Fig. 4) and centrilobular (C, Fig. 5) regions from fasted rat after 4 h DEX. GP activity is more concentrated in centrilobular cells. Some hepatocytes show little activity.

Fig. 6. Periportal (P) region from fasted ADX rat after 8 h DEX. Virtually all cells show GP activity.

299

IMMUNOGOLD ELECTRON MICROSCOPIC LOCALIZATION OF PHOSPHOENOLPYRUVATE CARBOXYKINASE IN RAT LIVER

Kuixiong Gao, Randal E. Morris, Bruce F. Giffin, Emma Lou Cardell and Robert R. Cardell

Department of Anatomy and Cell Biology, University of Cincinnati College of Medicine, Cincinnati, Ohio 45267-0521

Phosphoenolpyruvate carboxykinase (PEPCK) is a rate-limiting gluconeogenic enzyme which catalyzes the conversion of oxaloacetate to phosphoenolpyruvate. A gradient of PEPCK from periportal hepatocytes to pericentral hepatocytes has been demonstrated in normal rat liver;[1-4] however, the subcellular distribution of PEPCK molecules within hepatocytes could not be determined from these light microscope studies.

We have used two immunogold histochemical approaches to study the subcellar distribution of PEPCK in normal rat hepatocytes. In the first procedure 10μm cyrosections of 4% paraformaldehyde perfusion-fixed rat liver were collected on silanated slides and immunostained with goat anti-rat PEPCK (normal goat serum served as a control), and incubated in a secondary antibody (5nm gold-labeled rabbit anti-goat IgG) and a tertiary antibody (5nm gold-labeled goat anti-rabbit IgG). The immunogold stained samples, with or without silver enhancement (IGSS), were counterstained with pyronine Y, re-embedded in Visio-Bond and removed from the slides and semithin sectioned for epipolarized illumination combined with transmitted light microscopy (Figs. 1 and 2), or re-embedded in epoxy resin and sectioned for electron microscopy (EM, Fig. 4) In the second procedure 25, 50 and 100 μm free-floating vibratome sections of well fixed rat liver (4% paraformaldehyde plus 0.5% glutaraldehyde perfusion-fixed, immersion fixed overnight at 4°C) were immunogold stained using a 5nm gold labeled secondary antibody, with and without IGSS, osmicated, embedded in epoxy resin and sectioned for EM (Figure 3).

The gold-labeled antibodies penetrated the entire thickness of the cryosection. PEPCK antigenic sites were highly labeled (Figs. 1 and 4), but membranes, especially smooth endoplasmic reticulum (SER) were not preserved. Penetration of the gold-labeled antibody was limited to cells at the surface of the vibratome sections; however, the longer fixation preserved the membranes, including SER. In both procedures the PEPCK antigenic sites (indicated by gold particles or silver enhanced gold) are predominantly in the glycogen areas of cytosome and not in the mitochondria, lipid droplets, nuclei, Gogli apparatus, or other organelles. Periportal hepatocytes have a compact subcellular distribution of PEPCK, glycogen and more gold particles; while those in pericentral hepatocytes have a diffuse subcellular distribution of PEPCK, glycogen and few gold particles. In control experiments (normal goat serum replaced the goat anti-rat PEPCK antibody in the immunogold staining procedures), the background was very low with no specific staining patterns. The results support the SERGE concept proposed by Cardell et al.[5] describing restricted regions within hepatocytes specialized for glycogen metabolism that including glycogen (and/or precursors), SER, enzymes and other essentials for glycogen deposition and breakdown.

Literature
1. Anderson, B., et al., Eur. J. Cell Biol. 30 (1983) 126.
2. Guder, W. and Schmidt, U., Hoppe Seyler's Z. Physiol. Chem. 357 (1976) 1793.
3. Wimmer, M. et al., Histochem. 93 (1990) 409.
4. Giffin, B. F., et al., In Bailey, G. W. et al. (eds.) Electron Microscopy; Proc. EMSA 50th, MAS 27th, MSC 19th Annual Meeting, San Francisco, CA. San Francisco Press, Inc. 1992, p.828.
5. Cardell, et al., J. Cell Biol. 101 (1985) 201.
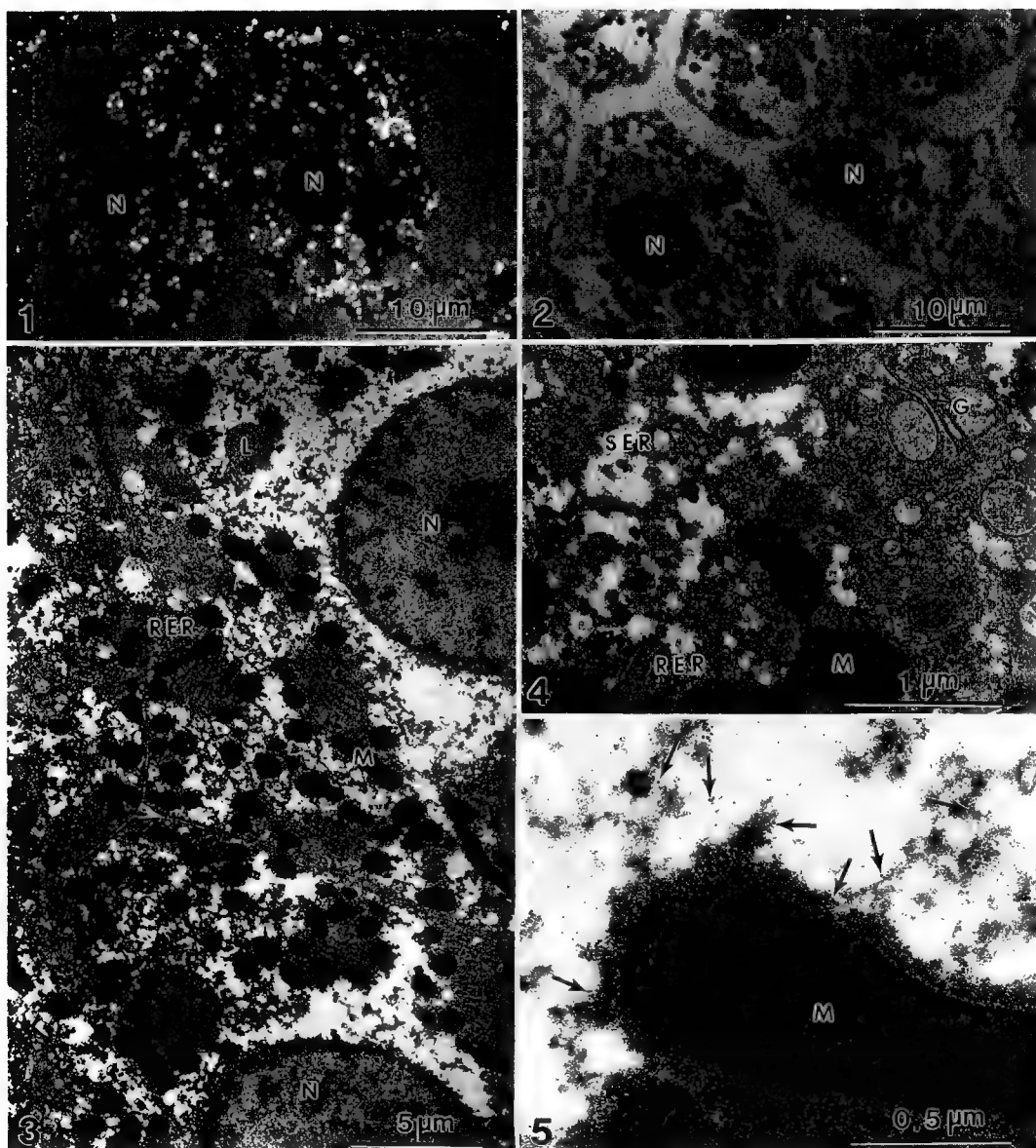
Figures: 1. Hepatic PEPCK antigen sites (white dots) in pyromin stained $0.5\mu m$ section of $10\mu m$ IGSS cyrosection. Nuclei (N) are not immunostained. 2. Control: normal goat serum replaced anti-PEPCK antibody. 3. EM localization of PEPCK antigenic sites (black particles) in hepatocyte. Thin section of IGSS vibratome section. Nuclei (N), mitochondria (M), rough endoplasmic reticulum (RER) and lipid (L) are not immunostained. 4. Higher magnification of region in 3, showing RER, SER, mitochondria and Golgi apparatus (G) and their relationship to PEPCK (dark particles) in glycogen areas (white) 5. Immunogold localization of PEPCK antigenic sites. Thin section of $10\mu m$ cryosection stained with 5nm immunogold labeled secondary and tertiary antibodies. Some less obvious gold particles are identified by arrows.

301

THE CATALYTIC ACTIVITY OF ADENOSINE MONOPHOSPHATE DEAMINASE IN MURINE DUODENUM AS REVEALED BY TRANSMISSION ELECTRON MICROSCOPY

K. Bielat* and G. Tritsch**

*Department of Pathology, Roswell Park Cancer Institute, Buffalo, NY 14263
**Department of Experimental Biology, Roswell Park Cancer Institute, Buffalo, NY 14263

AMP deaminase was visualized in a manner analogous to our previous approach with adenosine deaminase (1). The chloro-analog of AMP, i.e., 6 Chloropurine riboside 5′ monophosphate (CPRMP) (from Sigma) was shown to be a substrate of this enzyme which liberates Cl⁻ which is precipitated with added Ag^+, and, after exposure to light electron dense Ag° grains are deposited at loci of enzyme activity. The substrate at a concentration of 1.1 mM in 50 mM HEPES buffer, pH 7.2, in the presence of 150 mM K^+ (as the acetate), 3mM ATP and 10μM pentostatin (deoxycoformycin) was incubated with freshly excised tissue from a female C-57 BL/6 mouse. The substrate concentration is 1.4 times Km for rabbit muscle enzyme (Sigma), and K^+ and ATP are allosteric activators of this enzyme. Because many cells have ecto 5′-nucleotidase activity, pentostatin was added to prevent manifestation of adenosine deaminase activity of dechlorination of any nucleoside that might be formed.

The mice were sacrificed by cervical dislocation and the gastrocnemius muscle was dissected from the animal. Tissue blocks of $0.5mm^3$ or less were incubated in the assay mixture for 10 minutes at 37°C with agitation. The control medium lacked the substrate. The incubation medium was replaced with 2.5% glutaraldehyde in 0.1 HEPES containing silver nitrate at a final concentration of 2mM and the blocks were allowed to fix for 1 hour at room temperature. The fixative was removed and the blocks were washed 3X with 0.2M HEPES buffer, pH 7.4, for 5 minutes each. Osmication was achieved with 2% osmium tetroxide in 0.15M cacodylate buffer, pH 7.4 for 3 hours at room temperature. The fixative was removed and the blocks were washed 3X for 5 minutes each in 0.2M cacodylate buffer. Dehydration was performed with a graded series of ethanol 30%, 50%, 70%, 90% for 5 minutes each and 2X in 100%. Infiltration was conducted with 100% ethanol-Spurr epoxy resin 1:1 for 2 hours at room temperature followed with pure Spurr resin for an additional 3 hours also at room temperature. Embedding was done in #00 gelatin capsules filled with pure Spurr resin and polymerized at 70°C for 24 hours. The tissue blocks were trimmed with razor blades to a trapezoid shaped face and thin sections were cut with glass knives on a Porter-Blum MT-2 ultramicrotome and collected on uncoated 200 mesh copper grids and examined unstained in a Siemens 1A transmission electron microscope operating at a potential of 80kv.

Figure 1 is a transmission electron micrograph of an unstained section of murine duodenum allowed to react with CPRMP in the presence of deoxycoformycin and Ag^+. Electron dense silver grains of relatively uniform size are visible throughout the tissue section with the greatest amount localized at the level of the microvilli projecting into the duodenal lumen. The localization of silver grains represents discrete microloci of catalytically active AMP deaminase.

This communication visualizes loci of enzyme activity and is therefore different from the use of antibodies against enzyme protein, which need not necessarily represent catalytically active entities. The relative uniformity in size of the silver grains indicates that the enzyme activity at the various locations is uniform and that we are not seeing regions with markedly different levels of activity. It is also evident from the micrograph, that our reagents were able to diffuse to all parts of the tissue under our experimental conditions. This technique is an improvement of the original developed by Nakatsu (2) for light microscopy, the advantage being increased resolution of the localization of the catalytic activity.

1.   K.L. Bielat and G. Tritsch, Molecular and Cellular Biochemistry (1989) 86:135-142.
2.   K. Nakatsu, Journal of Histochemistry and Cytochemistry (1975) 23:194-199.

Figure 1: An unstained section of duodenal epithelium with numerous electron dense silver grains of relatively uniform size visible throughout the section. The greatest amount of silver grains are localized at the level of the microvilli. Original magnification - 10,000X.

303

EOSINOPHILS IN THE LAMINA PROPRIA OF THE RAT STOMACH BIND A BIOTINYLATED GASTRIN ANALOG

Caroline A. Miller, David H. Nichols, Richard F. Murphy and D. David Smith

Department of Biomedical Science, Creighton University School of Medicine, Omaha, NE 68178

Gastrin is a small peptide known to function as both a stimulator of gastric acid secretion and as a growth factor. Eosinophils are white blood cells which form a part of the body's defenses against invading microorganisms. Douglas et al. have reported staining, using a biotinylated gastrin analog (biotinyl-L-Trp-L-Leu-ß-Ala), of unidentified cells in the lamina propria of the rat fundic stomach.[1] This gastrin analog has been shown to suppress gastric acid secretion in dogs.[2] We here identify the cells binding this analog as eosinophils. We have perfused and fixed small pieces of fundic stomach with 2% paraformaldehyde/ 0.5% glutaraldehyde in 0.1 M phosphate buffer, pH 7.4 for 1 hour. The tissue was then embedded in 5% agar and 50 μm sections were cut on a vibratome. Sections were incubated for 30 min. with 1.63×10^{-6} M biotinylated gastrin analog, rinsed, and exposed to an avidin-biotin-glucose oxidase complex (ABC-GO; Vector). Tetranitroblue tetrazolium (TNBT) was used as a substrate for visualizing the glucose oxidase. Sections were then embedded in Embed 812 and alternate 2μm thick and 70 nm thin sections cut. Cells found to be stained using light microscopy of thick sections matched with cells which could be identified as eosinophils (Figs. 1-3) on the transmission electron microscope. All matchable stained cells were eosinophils, and cells identifiable as plasma cells and mast cells in the transmission electron microscope did not stain. Indirect matching was used because while the glucose oxidase reaction eliminated the possibility of endogenous artifact, we were unsuccessful in attempts to form an electron dense reaction product. Gastrin binding was insensitive to the presence of high concentrations of bovine serum albumin (1%) or Polypep (1%; Sigma) in the incubation solution and no staining was observed when the biotinylated gastrin analog was eliminated from the reaction solution. In addition, staining was reduced when a 10 fold excess of unlabeled whole gastrin was added to the reaction solution and eliminated when a 100 fold excess was used. While the significance of these observations is unclear, one additional observation may be relevant. Eosinophils commonly form close associations, some involving contact, others across minimal intervening extracellular matrix, with overlying epithelial cells. When they do (Fig. 1), staining is frequently observed on the faces of parietal cells (acid secretors) but not chief cells (protease secretors) closest to the eosinophils. This staining is tentatively presumed to result from a product of eosinophil degranulation, capable of binding the biotinylated gastrin analog, adhering to the parietal cells. Thus eosinophils might play an intermediary role in normal and/or pathological gastric acid secretion.

References

1. A. J. Douglas et al., Int. J. Peptide Protein Res. 35 (1990), 306.
2. A. Yasui et al., Int. J. Peptide Protein Res. 35 (1990), 301.
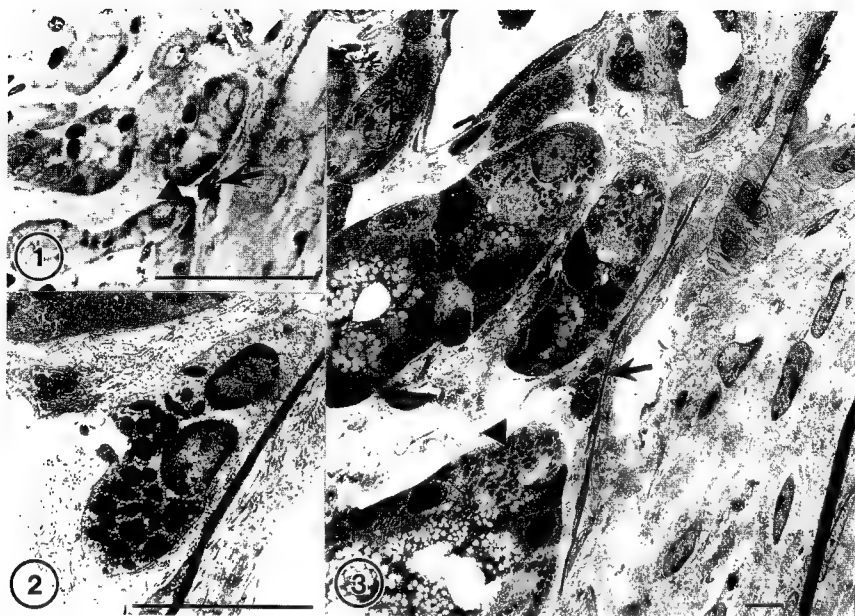
FIGURE 1. Light micrograph of rat fundic stomach. Arrow indicates the stained cell identified as a eosinophil in Figures 2. and 3. Arrowhead marks stain on a cell which can be identified as a parietal cell in Figure 3. Bar = 10 μm.
FIGURE 2. Eosinophil stained in Figure 1. Bar = 5 μm.
FIGURE 3. Transmission electron micrograph of the same field shown in Figure 1. Arrow indicates the eosinophil stained in Figure 1. Arrowhead indicates the parietal cell stained in Figure 1. Bar = 5 μm.

DISTRIBUTION OF VLA-5 AND VLA-4 FIBRONECTIN RECEPTORS IN HUMAN MONOCYTES DEMONSTRATED BY IMMUNOFLUORESCENCE, IMMUNOCYTOCHEMISTRY, AND AUTORADIOGRAPHY

Robert Williams, Che-Hung Lee, Sara E. Quella, David M. Harlan, and Yuan-Hsu Kang

Naval Medical Research Institute, Bethesda, Maryland 20889-5055

Monocyte adherence to endothelial or extracellular matrices plays an important role in triggering monocyte activation in extravascular sites of infection, chronic inflammatory disorders, and tissue damage.[1] Migration of monocytes in the tissues involves the response to a chemoattractant and movement by a series of attachments and detachments to the extracellular matrices which are regulated by expression and distribution of specific receptors for the matrix proteins such as fibronectin (FN).[2] The VLAs (very late antigens or beta integrins), a subfamily of the transmembrane heterodimeric integrin receptors, have been thought to play a major role in monocyte adherence to the extracellular matrices and cells.[3] In this subfamily, VLA-5 and VLA-4 are believed to be the most essential integrins mediating monocyte adherence to FN.[4] In the present report, we have established and compared different procedures for morphological evaluation of the expression and distribution of the FN receptors on human monocytes in order to investigate their response to endotoxin or cytokine stimulation.

Human peripheral blood monocytes from normal donors were allowed to adhere to 6-well plates, glass coverslips or 8-well chamber slides in Iscove's medium overnight and processed for demonstration of the expression and distribution of the receptors by immunofluorescence, immunogold and immunoperoxidase electron microscopy, and autoradiography. Incubation of live cells with blocking agent and antibodies was carried out on ice to prevent internalization of the reagents. Cells were incubated with 1% BSA for 30 min and then reacted with anti-VLA-5 antiserum or murine anti-VLA-4 antibody for 60 min. For immunofluorescence, cells grown on coverslips were fixed in 3.5% paraformaldehyde for 30 min following incubation with the primary antibodies and then reacted with anti-rabbit IgG or anti-mouse IgG linked to FITC after 3 washings in PBS. Cells cultured in 6-well plates were harvested by vigorous flushing with PBS, collected in 1.5 ml microcentrifuge tubes, incubated with the primary antibodies and then reacted with anti-rabbit IgG or anti-mouse IgG linked to HRP, carboxylate beads or colloidal gold. Cells were then incubated in diaminobenzidine and H_2O_2 solution to visualize HRP and endogenous peroxidase in monocytes and processed for transmission and scanning electron microscopy. Cells cultured in chamber slides were incubated with the primary antibodies, reacted with ^{125}I-anti-rabbit IgG or ^{125}I-anti-mouse IgG, and fixed in 2% glutaraldehyde/1% paraformaldehyde for 30 min. The slides were coated with Ilford K5D emulsion and developed in D-19 Kodak developer.

Immunofluorescence, autoradiography, and immunoelectron microscopy showed that both VLA-5 and VLA-4 integrins were constitutively expressed on the cell surface by the monocytes (Figs. 1,2,3,4,5). However, VLA-5 was more densely expressed than VLA-4 as indicated by autoradiography and immunogold electron microscopy (Figs. 2,4). Only a few carboxylate beads were observed attached to the basal portion of the cell by immunobead SEM (Fig. 3). Immunoperoxidase TEM illustrated uniform staining of VLA-5 on the cell surface (Fig. 4). Immunoelectron microscopy, particularly immunogold labeling revealed that both integrins were concentrated at the microvillar and pseudopod regions (Fig. 5), suggesting that both integrins are possibly involved in monocyte anchorage and movement in tissues. The results also indicate that the methods established in this study can be used for quantitative assessment of the receptors using photometry, confocal microscopy, and morphometry.[5]

References
1. J. S. Pober and R. S. Cotran, Transplant. 50(1990)537.
2. T. A. Springer, Nature 346(1990)425.
3. R. O. Hynes, Cell 48(1987)549.
4. M. E. Hemler, Ann. Rev. Immunol. 8(1990)365.
5. This work was supported by a Navy R & D research fund (61152N.MR00001.001.1398) to Dr. Y. H. Kang.
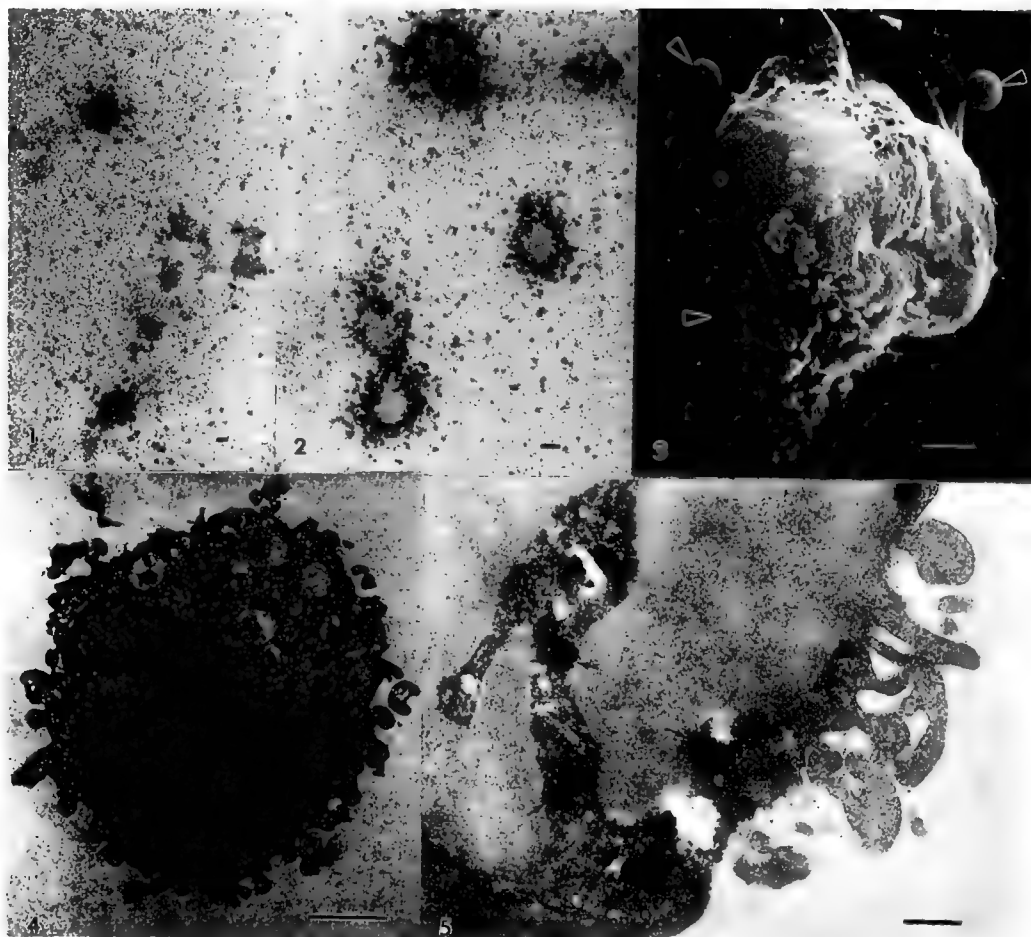
FIG. 1.--LM autoradiograph of VLA-5 shows dense silver grains on the cell surface.
Bar = 1 um
FIG. 2.--LM autoradiograph of VLA-4 depicting that the cell surface is less densely
labeled by silver grains than VLA-5. Bar = 1 um
FIG. 3.--SEM of immunobead labeling of VLA-5. Only a few beads are seen attached
to the basal sides of the cell (arrowheads). Bar = 1 um
FIG. 4.--TEM of immunoperoxidase localization of VLA-5 on the cell surface. Note
the myeloperoxidase granules (arrows). Bar = 2 um
FIG. 5.--TEM of VLA-5 localization by immunogold method. The Receptors are
concentrated at the microvillar and pseudopodial areas. Arrows indicate
myeloperoxidase granules. Bar = 0.5 um

307

ULTRASTRUCTURAL APPLICATION OF THE PATSC-GMS STAINING IN VARIOUS KIDNEY DISEASES

Shigeki Namimatsu, Shin-ichi Nakamura, Yoshizo Nakagami,
Tatsuo Oguro*, Goro Asano**

Central Research Institute, 1st. Hospital Nippon Medical School,
Central Institute for Electron Microscopic Research*, Department
of Pathology**, Nippon Medical School, 3-5-5, Iidabashi,
Chiyoda-ku, Tokyo 102, Japan

We have previously reported a new staining method, PATSC-GMS, [1,2,3] for transmission electron microscopy. In the present study, we evaluated the stainability and usefulness of the PATSC-GMS method in tissues from renal diseases.

Fifty human kidney biopsies comprising normal (n=2), membranous glomerulonephritis (n=10), Alport's syndrome (n=1), IgA nephropathy (n=4), and other cases (n=33) were studied. Samples were pre-fixed in 2.5% glutaraldehyde, post-fixed in 1% osmium tetroxide, and embedded in Epok-812 after dehydration. Ultrathin sections were made and placed on nickel grid mesh. The sections of the tissues were Pre-incubated in ammonia water(25%) for 10minutes, oxidized in 1% periodic acid for 20 minutes, reacted in 0.1% thiosemicarbazid (TSC) for 1minute, post-incubated in ammonia water(25%) for 5minutes and stained with gelatin methenamine silver(GMS) solution: (50ml of 3% methenamine, 5ml of 2% gelatin, 5ml of 5% silver nitrate, 40ml of distilled water, and 5-6ml of 5% sodium tetraborate) was performed for 50C 50minutes in the oven. Observation was done under a Hitachi H-7100 transmission electron microscope.

PATSC-GMS method stained basement membranes of the glomeruli in normal and diseased kidney biopsies with no background silver grains. Improved staining of collagen fibers was also observed. Heterochromatin in the nucleus was not stained. In renal diseases, basement membrane showed thickening, duplication and the presence of immuno-deposits, and specific fibers of mesangial matrix proliferated. Compared with ordinary PAM staining, PATSC-GMS method showed markedly improved results. The ordinary PAM staining is done in a floating fashion and often produces background silver grains. PATSC-GMS staining is performed on ultrathin sections on the grid mesh, and can be applied to every tissue and embedding material of epoxy resin.

References

1. S. Namimatsu, et al. : J. Clin. Electron Microscopy (1989) 22 (5-6), 928-929.
2. S. Namimatsu, J. Submicros. Cytol. Pathol. (1992) 24 (1), 19-28.
3. S. Namimatsu, et al. : J. Clin. Electron Microscopy (1992) 25 (5-6).
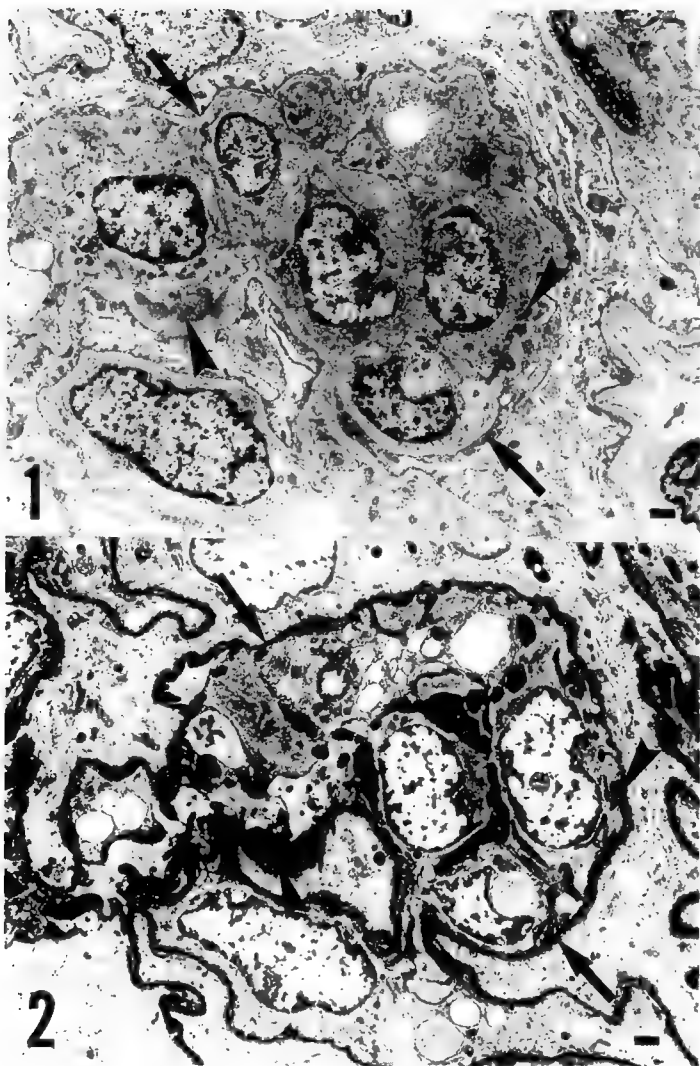
FIG. 1.   __TEM of IgA nephropathy GN
A portion of glomerulus stained uranyl acetate and lead
citrate is demonstrated.
Not poor staining of basement membranes(arrows) and
absence of staining of immuno-deposit(arrowheads).
X3,000

FIG. 2.   __TEM of IgA nephropathy GN
Comparable area from the same glomerulus as in Fig. 1.
stained with the method of PATSC-GMS.
Note significant enhancement of staining in the basement
membranes(arrows)and immuno-deposit(arrowheads).
X3,000

VIRAL PROTEINS ARE EXPRESSED ON MEMBRANOUS VESICLES IN THE ENDOPLASMIC RETICULUM OF FLAVIVIRUS-INFECTED CELLS

Mary Beth Downs,* and Peter Summers **

*Pathology Division and ** Virology Division, United States Army Medical Research Institute for Infectious Diseases, Ft. Detrick, Maryland, USA 21702

Japanese encephalitis virus is a member of the family Flaviviridae, a group that includes yellow fever virus and dengue virus. Flaviviruses contain a central nucleocapsid made of a capsid protein (C) and a single-stranded RNA genome surrounded by a membranous envelope with two associated proteins: the surface envelope glycoprotein (E), which forms projecting spikes, and the non-glycosylated membrane protein (M). Infected cells also synthesize seven non-structural viral proteins, including the NS1 protein which is found on the cell surface and is secreted in particulate form. Replication of flaviviruses appears to involve the endoplasmic reticulum (ER) as (1) proliferation of ER membranes and formation of intracisternal vesicles are characteristic of flavivirus infection, (2) essentially all viral proteins are membrane associated, and (3) mature virions are first seen in the lumen of the ER[1].

The method by which flaviviruses acquire their envelopes is unknown as no cytoplasmic nucleocapsids or budding virions have been seen. Leary and Blair[2] suggest that the intracisternal vesicles condense to form virions while others[3] believe virions bud through the ER membrane. To investigate these theories we permeabilized and labeled living cells with immunogold. MPF (ferret brain derived) cells were infected with Japanese encephalitis virus at a MOI of 10. After incubation for 3 days, the cells were permeabilized for 40 minutes at 37°C with 100 U streptolysin O per ml of Eagle's minimal essential medium (EMEM). The monolayers were washed, then incubated overnight with hyperimmune mouse ascites fluid (HMAF), which reacts with the E and NS1 proteins, as determined by Western blot analysis. The cells were rinsed in EMEM, then incubated with goat anti-mouse IgG conjugated to 5nm colloidal gold (Amersham) diluted 1:40 in EMEM at 37°C for 2 hours. The cells were then fixed for 24 hours with 4% formaldehyde and 2% glutaraldehyde in cacodylate buffer (pH 7.4), post-fixed with OsO_4, and routinely processed for TEM.

As shown in Figure 1, the soluble cytoplasmic elements leached out of the

cells during incubation, leaving only cellular membranes and attached proteins. Gold label was localized only on the surface of intracisternal vesicles. We acquired monoclonal antibodies directed against E and against NS1. Immunogold labeling of L.R. White-embedded material suggests that the anti-NS1, but not the anti-E antibody labels the vesicles, which supports the theory that they are by-products of viral replication and precursors of the particulate NS1 secreted by infected cells.

References:

1. M. A. Brinton, in The Togaviridae and Flaviviridae, Plenum Press (1986), 327.
2. K. R. Leary and C. D. Blair, J. Ultrastruct. Res. (1980)72, 123.
3. T. Hase, P. L. Summers, K. H. Eckels, and W. B. Baze, Arch. Virol. (1987)92, 273.
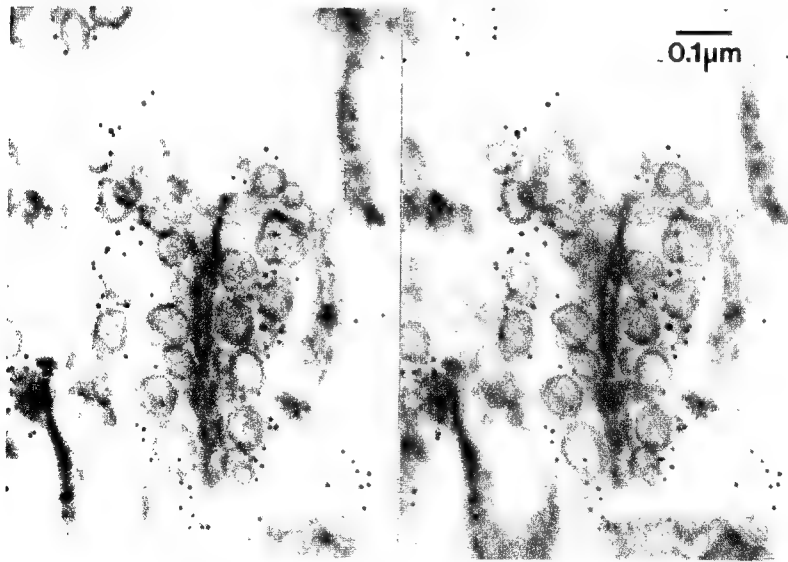
Figure 1 -- Stereo electron micrographs of intracisternal vesicles from JEV-infected cells permeabilized with streptolysin O. 5nm immunogold labels viral proteins E and NS1.

DIFFERENTIATION OF MALIGNANT MESOTHELIOMA (MM) FROM ADENOCARCINOMA

John Garancis, John Cafaro, Anthony Cafaro Jr., and Raymond Venezia

Department of Pathology, St. Joseph's Hospital, Milwaukee, Wisconsin 53210

Malignant mesothelioma (MM) is a rare tumor arising predominantly from either the visceral or parietal pleura or peritoneal surfaces. It primarily effects individuals between 45 and 75 years of age and asbestos is felt to be the single most important etiologic agent[1,2]. Studies suggest that the incidence of MM is increasing perhaps at a rate of as high as 13% per year. The diagnosis of MM can be difficult and is often complicated by the tumors similarity to metastatic adenocarcinoma, both in it's microscopic appearance and to some extent clinical course.

In this particular study the immunohistochemical properties of 22 malignant mesotheliomas (20 pleural and two peritoneal) are compared with 20 pulmonary adenocarcinomas. Each tissue was examined using monoclonal antibodies to wide-spectrum cytokeratin, CEA, Leu-M1 and B72.3. Extensive asbestos exposure was identified in all but 1 of the mesothelioma cases. The cases of peritoneal MM were found to have a history of chrysotile exposure only (Fig. 1). Distant metastases were present in four cases of MM. Ten cases of MM were examined by electron microscopy.

All cases of mesothelioma exhibited positive staining for wide-spectrum cytokeratin and negative staining for the presence of CEA, Leu-M1 and B72.3. In examining the adenocarcinomas, again 100% were positive for cytokeratin; however, 90% exhibited CEA and Leu-M1 positivity, and 80% showed positivity for B72.3. Electron microscopic examination of the mesothelioma cells revealed characteristic narrow long microvilli and pools of cytoplasmic glycogen and abundant intracytoplasmic filaments (Fig. 2). The mean ratio of length to diameter (LDR) of microvilli was 12.5. For adenocarcinoma, the mean LDR was 5.3.

In conclusion, malignant mesothelioma appears to be reliably differentiated from pulmonary adenocarcinoma using the above mentioned immunohistochemical panel and additional confirmation can be provided using the electron microscopic findings. Characteristic features of malignant mesothelioma include: Negative immunoreactivity to CEA, Leu-M1 and B72.3. Electron microscopy demonstrates long narrow microvilli of the mesothelial cells associated with pools of cytoplasmic glycogen and abundant intracytoplasmic filaments[3].

REFERENCES:
1. I.J. Selikoff, D.K.H. Lee: asbestos and disease. New York Academic Press (1978). p 1977.
2. MJ.R. Becklake: Asbestos-related disease of the lung and other organs: Their epidemiology and implications for clinical practice. AM Rev. Respir. Dis. (1976) p 114,187.
3. C.S. Bodrossian, S. Bonsib, and C. Moran. Differential diagnosis between mesothelioma and adenocarcinoma: A multimodal approach based on ultra-structure and immunocytochemistry. Sem. Diagn. Patholo. (1992), p 9, 24.
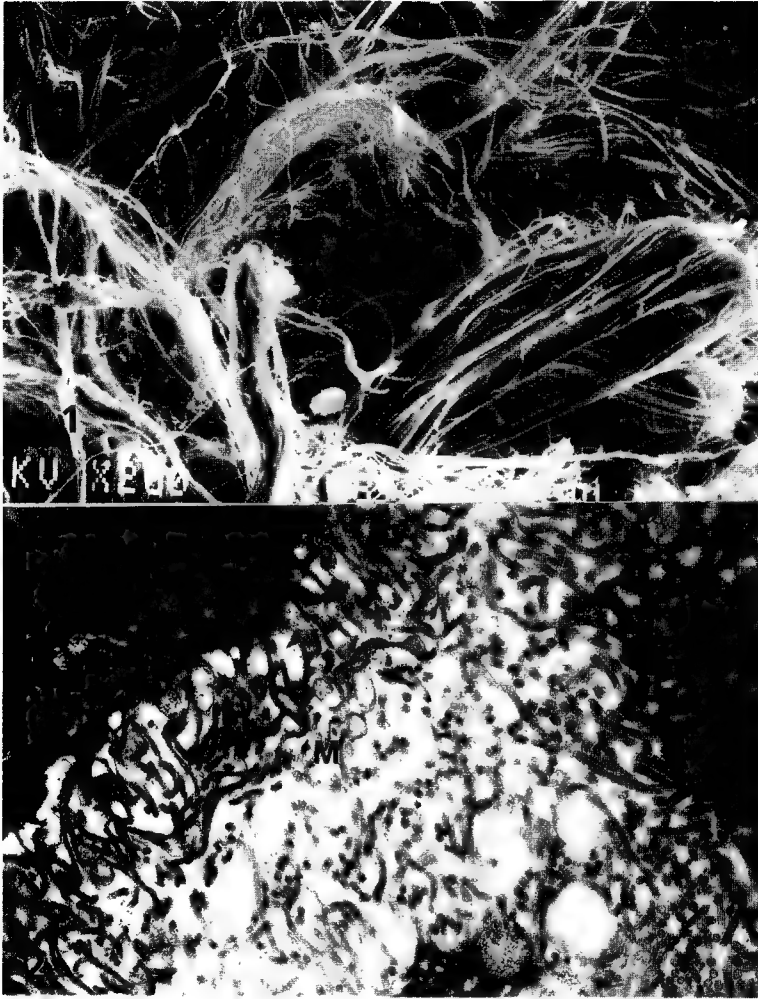
FIGURE 1:   Scanning electron micrograph of chrysotile fibers exhibiting
            longitudinal curvatures.   The asbestos rope which was used for
            insulation purposes consisted of chrysotile. X 200

FIGURE 2:   Electron (TEM) micrograph of malignant mesothelioma cells with
            narrow, elongated surface microvilli (M) frequently reaching
            considerable length. X 6000

TRANSPORT PATHWAYS OF LOW-DENSITY LIPOPROTEINS BY ARTERIAL ENDOTHELIUM OF HYPERCHOLESTEROLEMIC RATS

C.H. Kao[a], V. C. Yang[a], J.K. Chen[*], and J.S. Kuo[+]

[a]Department of Biology, Tunghai University, Taichung, Taiwan, Republic of China
[*]Department of Physiology, Chang Gung Memorial Hospital, Lin-Kou, Taiwan, Republic of China
[+]Department of Medical Research, Veteran General Hospital, Taichung, Taiwan, Republic of China

Atherosclerosis is more likely to occur at the branched regions of the large or medium-sized arteries.[1] Physiological evidences show that changes in endothelial permeability at the branched regions can cause low density lipoproteins (LDL) to filtrate and accumulate in the intima.[2] However, the LDL transport pathways across the arterial endothelium at the ultrastructural level still remain uncertain. The purpose of this experiment is utilizing fluorescein 1,1'-dioctadecyl-3,3,3',3'-tetramethylindocarbocyanine perchlorate (DiI) and colloidal gold as the tracer substances to investigate the transport pathways of LDL in the branched and the unbranched regions of arteries in the diet-induced hypercholesterolemic rats.

Rat or human LDL was coupled to DiI or to 10-15nm colloidal gold particles according to the standard procedures. Male Srague-Dawley rats, weighing approximately 250 gm were fed high-cholesterol diets over a period of 12 months. At 6 and 12 months after feeding, animals were anesthetized by intraperitoneal injections of sodium pentobarbitol. The vascular bed was cleared of blood by perfusion with oxygenated PBS supplemented with 0.25% glucose and 1 mM CaCl$_2$ at 37°C through the left ventricle. After the blood washed out, the right and the left femoral arteries and the left ventricle, the thoracic and the abdominal aorta were cannulated with polyethylene tubings. The tubings between the left ventricle and the thoracic aorta and the tubings between the abdominal aorta and the femoral arteries were connected with peristaltic pump to form two closed circuits. Then, LDL-DiI or LDL-colloidal gold conjugate was infused to recirculate in the two closed circuit systems for 5 minutes. The vasculatures were then perfused with modified Karnofsky's fixative, or with 3% formaldehyde. The carotid artery, aortic arch, thoracic aorta, abdominal aorta and their branched regions were then collected and prepared for light and electron microscopy.

The intimal injuries occurred in the arteries after high-cholesterol feeding (Fig. 1). LDL-DiI was detected in the intimal layers at both branched and unbranched regions of the arteries. However, there was more LDL-DiI in the branched regions than that in the unbranched regions. LDL-DiI was also observed in the medial layers at the branched regions of the arteries. The intima of outer wall of the carotid artery and the intima of inner wall of the aortic arch with low shear stresses contained more LDL-DiI than other areas of the vessel wall. LDL-colloidal gold was observed in the intracytoplasmic vesicles either free within the cytoplasm or attached to the luminal surface or abluminal surface (Fig. 2). Some of the tracer molecules were found in the open junctions between the endothelial cells of the aortic arch (Fig. 3). It is concluded that the major visible route for transport of LDL across the endothelium in the branched and the unbranched regions of the arteries is intracytoplasmic vesicles. The open junctions may also play an important role in the LDL transport at certain loci of the vessels.[3]

References

1. R. Ross, New Engl. J. Med. (1986)314, 488.
2. L. B. Nielsen et al., Arterioscler. Thromb. (1992)12, 1402.
3. This research was supported by a grant from the National Science Council, Taiwan, Republic of China, No. NSC-80-0211-B029-501.
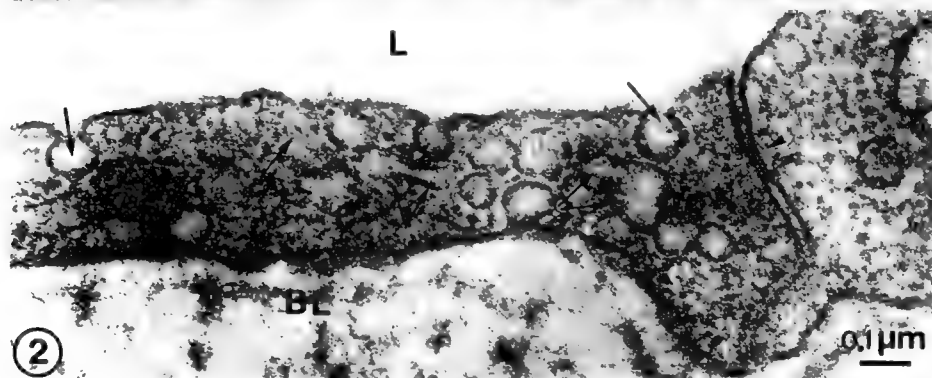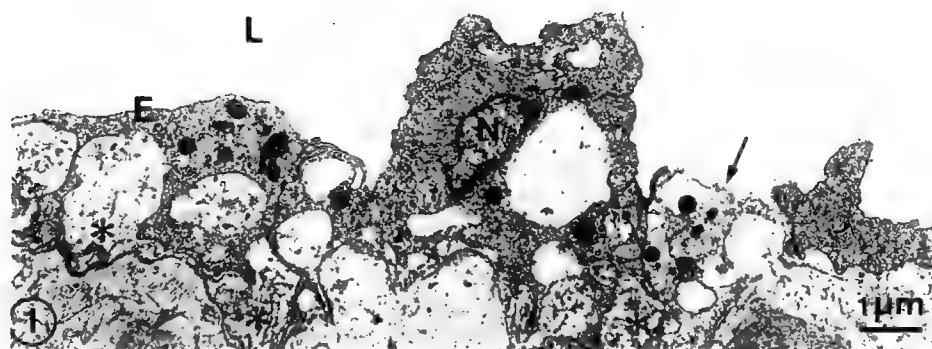
Fig. 1.-- Endothelia and internal elastica of aortic arch from a hypercholesterolemic rat. Denuded endothelial cell (arrow); severe degenerative changes of internal elastica (asterisks). Lumen (L). Endothelial cell (E). Nucleus (N).

Fig. 2.-- Endothelial cells of aortic arch from a hypercholesterolemic rat. LDL-colloidal gold particles are found in the intracytoplasmic vesicles (arrows). Lumen (L). Tight junction (double arrow heads). Basal lamina (BL).

Fig. 3.-- Endothelial cells of aortic arch from a hypercholesterolemic rat after infusion of LDL-colloidal gold. Tracer molecules are observed in the open junction (double arrow heads) and in the internal elastica (arrow). Lumen (L). Myelin figure (MF).

LOCALIZATION OF ATRIAL NATRIURETIC PEPTIDE IN NORMAL HUMAN ATRIAL TISSUE BY IMMUNOELECTRON MICROSCOPY

Chi-Ming Wei, Margaret Hukee, Christopher G.A. McGregor, John C. Burnett, Jr.

Cardiovascular Diseases and Cardiovascular Surgery and Electron Microscopy Core Facility, Mayo Clinic and Foundation, Rochester, MN 55905

Atrial natriuretic peptide (ANP) is a 28-amino acid peptide which is secreted from atrial myocytes and possesses natriuretic, vasoactive and renin inhibiting actions. In chronic congestive heart failure (CHF), plasma concentrations of ANP are significantly increased in the circulation secondary to enhanced atrial and ventricular synthesis. In a variety of non-human species, ANP has been detected by light and electron microscopy. However, the localization of ANP in normal human cardiac tissue remains unclear. Therefore, the current studies were designed to determine the localization of ANP in normal human atrial tissue.

Cardiac tissue of three normal human right atria were obtained from the donor heart undergoing primary cardiac transplantation. Atrial tissue was fixed for 24 hours at 4°C in 4% formaldehyde and 1% glutaraldehyde in 0.1M phosphate buffer. These specimens were rinsed in phosphate buffer, dehydrated in a series of ethyl alcohols, embedded in Quetol 651, and polymerized at 42°C for 48 hours. Thin sections were pretreated with sodium metaperiodate and rinsed with distilled water. Non-specific sites were blocked with 1% bovine serum albumin (BSA) in Triz buffered saline with 0.1% Tween-20 added (TBS-T). Rabbit antisera to alpha atrial natriuretic peptide containing sequences 1-28 (ANP) was obtained from Pennisula Laboratories. Antibody was diluted 1:1000, and sections were incubated for 16 hours at 4°C and 2 hours at room temperature. Controls without primary antigen were included. After rinsing in TBS-T, the sections were incubated in Protein A + Au conjugate (15 nm) for 1 hour at room temperature and rinsed again in TBS-T. Sections were stained with uranyl acetate and lead citrate prior to examination in the transmission electron microscope.

Characteristic membrane-bound secretory granules were identified in all atrial specimens examined. In the atrial myocytes of the normal human heart, abundant electron-dense secretory granules were observed. Most labeling of ANP was found associated with the atrial granules. Gold particles were found both within granules and on the granule periphery (Figure 1). Controls without primary antibody had no gold label present (Figure 2).

In normal human atrial tissue, this study clearly demonstrates that ANP is localized to secretory granules. This study extends to the normal human our understanding of the biology of atrial regulation of this important peptide of cardiac origin.

References

1. J.C.Burnett Jr et al., Science (1986)231, 1145.
2. C.M.Wei et al., Am. J. Physiol. (1993)264, H71.
3. A.J.Stingo et al., Am. J. Physiol. (1992)263, H1318.
4. C.M. Wei et al., J. Am. Soc. Nephrology (1991)2, 422.
5. K. Hasegawa et al., Circulation (1991)84:1203.
6. This research was supported by grants from the Minnesota Affiliate of the American Heart Association MHA-103 and National Heart, Lung, and Blood Institute (NHLBI) Grants HL-36634, HL-07111. J.C. Burnett, Jr. is an Established Investigator of the American Heart Association.
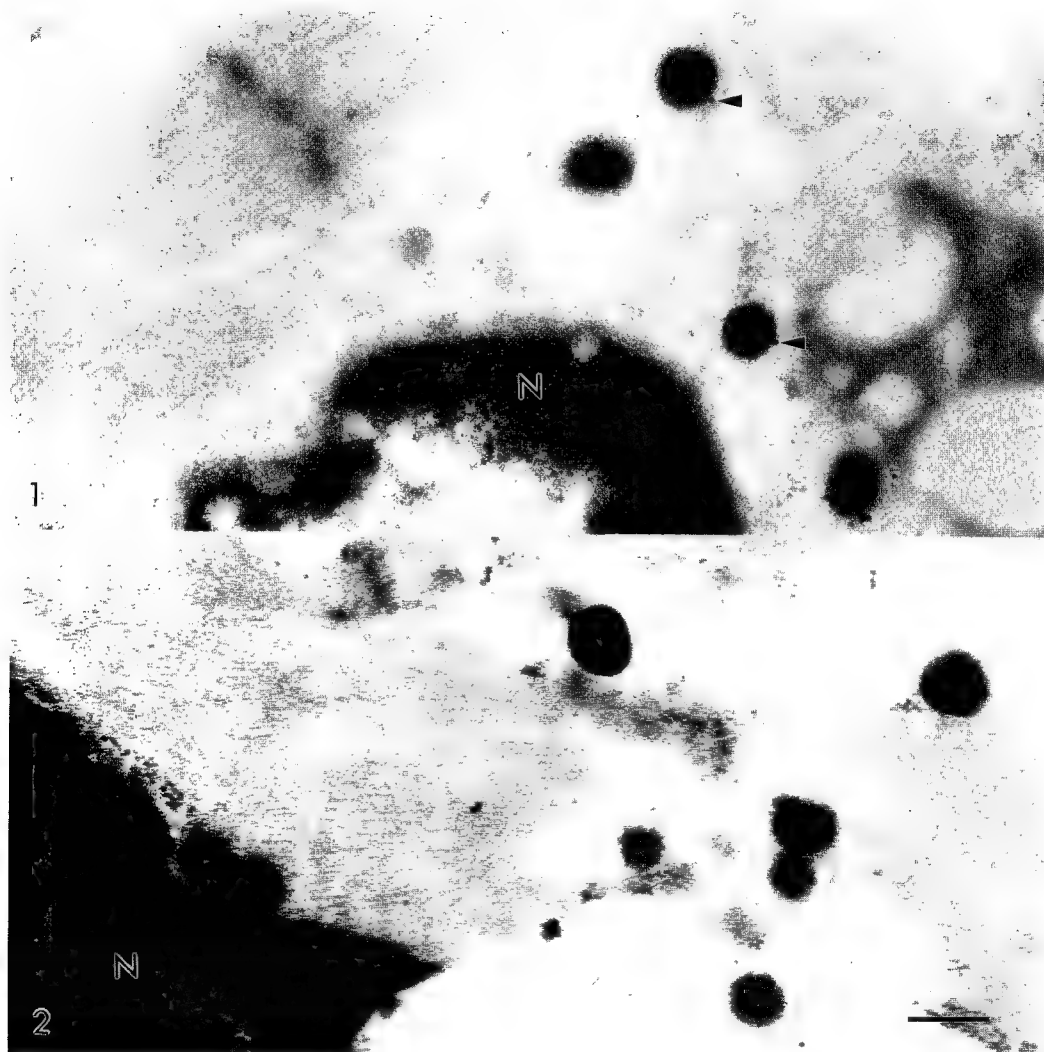
LEGEND:

Figure 1: Atrial granules showing the localization of ANP (arrows) within and on the periphery of granules. nucleus (N).
Figure 2: Atrial granules from control incubated without primary antibody and showing the absence of colloidal gold. (Bar = 200 nm.).

CYTOCHEMICAL LOCALIZATION OF FREE-RADICAL-DERIVED OXIDANTS IN HUMAN CORONARY ATHERECTOMY PLAQUES

E. Ann Ellis, Maria B. Grant and Thomas J. Wargovich

Department of Medicine, College of Medicine, University of Florida, Gainesville, FL 32610

Atherosclerosis is a multifactorial disease which leads to occlusion of vessels and potentially fatal intravascular thrombosis. Biochemical and immunocytochemical studies of oxidized low density lipoprotein (LDL) and treatment with antioxidants have demonstrated a role for oxidation in antherogenesis in animal models.[1] The enzyme NADH-oxidase produces superoxide radicals ($O_2^{\cdot-}$) and the free radical derived oxidant, hydrogen peroxide (H_2O_2). We used the cerium NADH-oxidase cytochemical localization[2] technique to identify sites of free radical derived oxidation in coronary artery atherosclerotic lesions removed from patients undergoing coronary atherectomy.

Atherectomy plaques were fixed in cold, sodium cacodylate buffered (pH 7.4) 5% acrolein within 5 min after removal from patients. Specimens were washed in buffer and processed as previously described for cytochemical localization of NADH-oxidase.[3] Cross sections of the plaques were examined and photographed, without post staining, at 75 kV in the transmission electron microscope.

NADH-oxidase activity, shown by cerium perhydroxide precipitate, was confined to the extracellular matrix and foam cells of the fatty streak. There was increased activity around cholesterol crystal clefts (Fig. 1) and in the cytoplasm and phagocytic vacuoles of remnants of macrophage foam cells (Fig. 2). NADH-oxidase localized in the cytoplasm and on the plasma membrane of foam cells as well as in the surrounding extracellular matrix (Figs. 3, 4). There was no localization of NADH-oxidase activity in the fibrous cap or the core region adjacent to the vessel intima.

Previous immunohistochemical studies demonstrated the accumulation of lipid peroxidation products in the fatty streak of atherosclerotic lesions. This work shows that the monocyte derived NADH-oxidase which generates the free radical derived oxidants involved in lipid peroxidation is produced by foam cells with both intracellular and extracellular activity which is confined to the fatty streak. These findings provide additional _in vivo_ evidence for an active role of free radical derived oxidants in the fatty streak in atherogenesis.

References

1. M. E. Rosenfeld et al., Atheroscler. Rev. (1991)23, 229.
2. R. T. Briggs et al., J. Cell Biol. (1975)67, 566.
3. J. Guy et al., Arch. Ophthalmol. (1990)108, 1614.
4. Supported by American Heart Grant #92GIA/862.
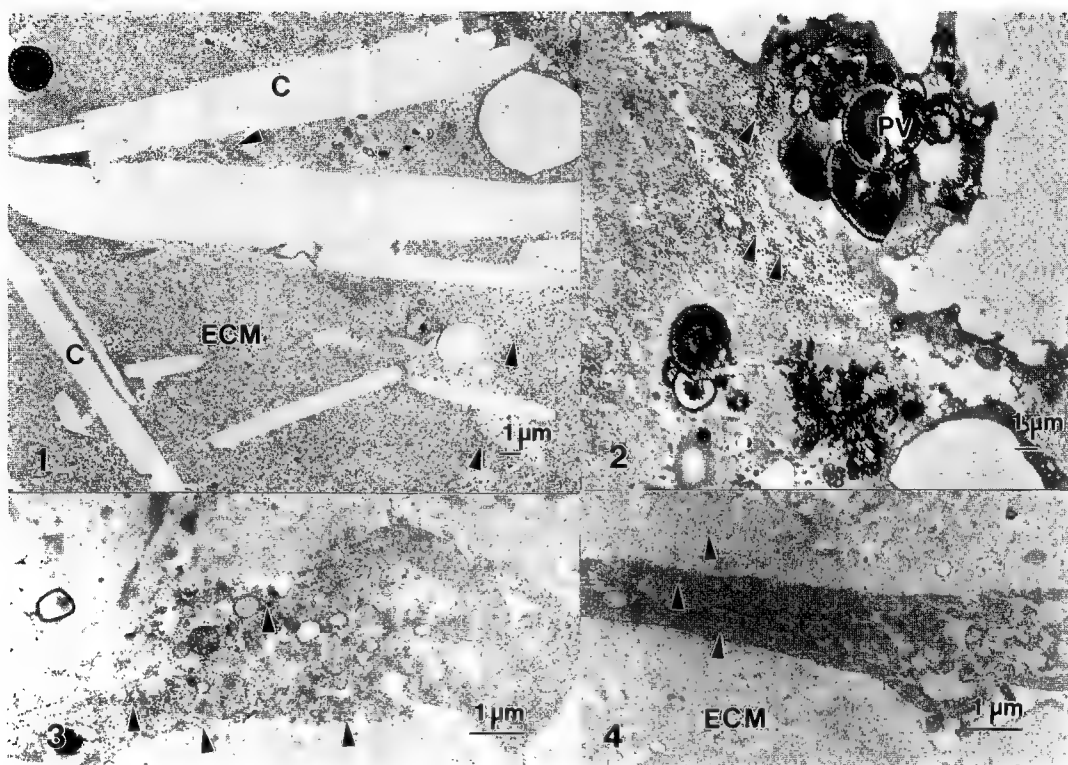
FIG. 1.--H$_2$O$_2$, cerium perhydroxide precipitate (arrowheads), localization in extracellular matrix (ECM) around cholesterol crystal clefts (C). 3,500 X

FIG. 2.--H$_2$O$_2$ in cytoplasm (arrowheads) and phagacytic vacuole (PV) of a remnant of a macrophage. 3,500 X

FIG. 3.--H$_2$O$_2$ precipitate in cytoplasm and on plasma membrane (arrowheads) of a foam cell. 9,000 X

FIG. 4.--H$_2$O$_2$ precipitate (arrowheads) in cytoplasm and extracellular matrix around foam cell. 9,000 X

VISUALIZATION OF THE ANIONIC SITES IN THE CELL WALL OF APPLE FRUIT USING A CATIONIC COLLOIDAL GOLD PROBE

Stéphane Roy*, William S. Conway*, Alley E. Watada*, Christopher D. Pooley** and William P. Wergin**

*Horticultural Crops Quality Laboratory and **Electron Microscopy Laboratory; USDA-ARS; Beltsville, MD 20705-2350

The ripening of fleshy fruits involves a softening process that consists of biochemical changes in the cell wall and leads to cell separation. Calcium is an important constituent of the cell wall and plays roles in maintaining the firmness of fruit[1] and in reducing postharvest decay[2]. The modification of cell wall strength is believed to be influenced by calcium that interacts with acidic pectic polymers to form cross-bridges[3]. This study examined how the frequency and distribution of anionic binding sites in the cell walls of apple fruit were influenced by calcium infiltration.

Mature "Golden Delicious" apple fruits were pressure infiltrated with either H_2O or a 4% solution of $CaCl_2$ and the pericarp was sampled and processed according to standard procedures[4]. Cationic poly-L-lysine colloidal gold complex was used in a one-step procedure to visualize anionic sites *in muro*[5]. Observations were performed with light microscopy, following silver intensification, and with transmission electron microscopy.

Results indicated that gold labelling was intense and uniformly distributed throughout the cell wall of the pericarp of H_2O-treated fruits. The labelling of the cell wall of the pericarp of calcium-treated fruits, remained intense in the middle lamella, was greatly reduced in the primary wall and was nearly absent in the angles of the intercellular space. Light microscopic observations after silver intensification gave similar results. No differences in distribution were noted from the epidermis to the inner part of the mesocarp.

In conclusion, the decrease and distribution of the anionic binding sites that were observed in cell walls of apple tissue suggests that $CaCl_2$ infiltration resulted in new calcium cross-bridges that were localized at the angles of the intercellular space and along the primary cell wall on both sides of the middle lamella.

1. B.W. Poovaiah et al., Hort. Rev. **10**(1988)107.
2. W.S. Conway et al., Plant Disease, **76**(1992)329.
3. M.C. Jarvis, Plant Cell Environ. **7**(1984)153.
4. J.C. Roland and B. Vian, Electron microscopy of plant cells, New York: Academic Press (1991)1.
5. E. Skutelsky and J. Roth, J. Histochem. Cytochem. **34**(1986)693.

Figures 1 & 2: Light micrographs showing the cationic gold labelling of anionic sites after silver intensification. Heavy labelling on the cell walls of H_2O-treated fruits (Fig 1). The labelling on the cell walls of calcium-treated fruits was reduced (Fig. 2). Bars = 30 μm.
Figures 3 to 6: Electron micrographs of *in muro* visualization of anionic sites after cationic gold labelling of ultrathin sections. Homogeneous distribution of labelling throughout the cell wall of H_2O-treated fruits (Fig 3). A control after preincubation with poly-L-Lysine did not show any labelling (Fig. 4). Cell walls of calcium-treated fruits: absence of labelling (arrows) in the angle of the intercellular space and decrease in the labelling in the primary cell wall (Fig. 5); conversely the middle lamella remained heavily labelled (Fig. 6). Bars = 1 μm. Abbreviations: e = epidermis; i = intercellular space; m = middle lamella; mi = mitochondria; p = plastid; v = vacuole; w = primary cell wall.
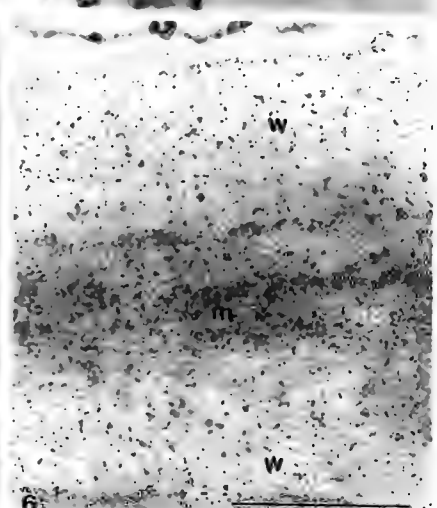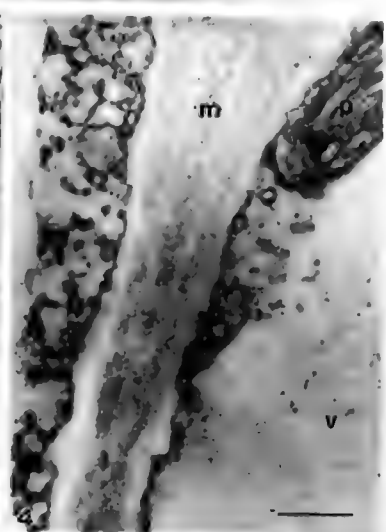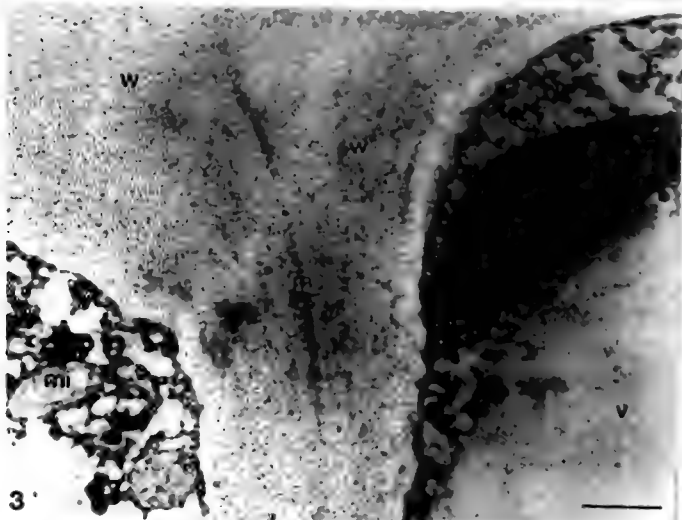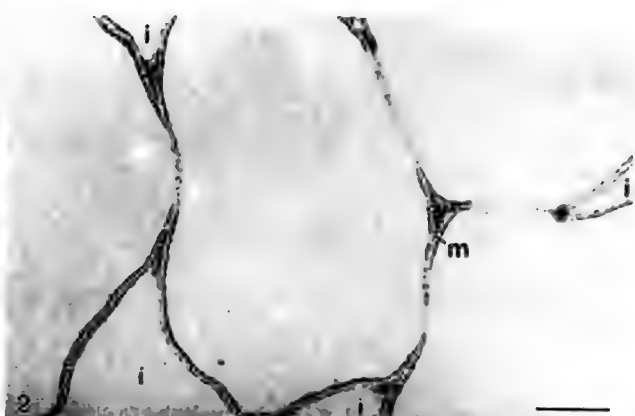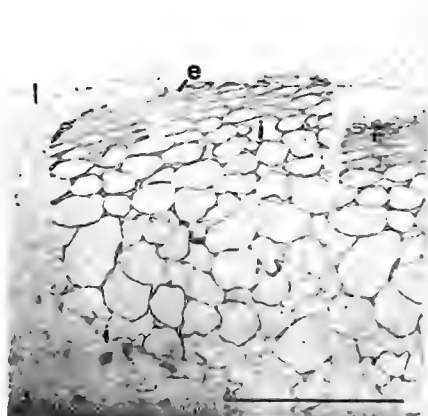
CELL INJURY AND CALCIUM ACCUMULATION FOLLOWING SULFUR MUSTARD EXPOSURE

J.P. Petrali, T.A. Hamilton, K.R. Mills and R. Ray

Comparative Pathology, USAMRICD, Aberdeen Proving Ground, Maryland 21010-5425

Cellular injury, irrespective of causative agents, is associated with a change in the transmembrane potential for calcium with subsequent accumulations of calcium to intracellular domains. At this time however, the association of sulfur mustard (HD)-induced cytotoxicity and calcium metabolism remains at controversy. This study correlates the ultrastructural cytopathology, cytochemical localization and x-ray microanalysis of calcium in cultured cells exposed to HD in vitro.

NG108-15 and HeLa cells, exposed to 300 and 500 μM HD respectively and harvested at 1 to 24h post exposure, were fixed in 1.6% formaldehyde and 2.5% glutaraldehyde for 3 h at 4°C and processed for routine ultrastructural evaluation. Replicate populations were cytochemically processed for precipitation of calcium by incubating in a medium of 2% potassium pyroantimonate and 1% osmium tetroxide for 90 min in the dark at 20°C. Cells were then placed in a secondary medium of 0.5% tannic acid for 15 min, rinsed in 1% sodium sulfate, dehydrated in graded ethanols and embedded in epoxy resin.[1] Ultrathin sections were analyzed without counterstaining to maximize visualization of calcium-pyroantimonate precipitates. X-ray microanalysis of ultrathin sections was performed with a KEVEX 8000 system interfaced to a JEOL 1200EX. X-ray spectra were acquired at an accelerating voltage of 60kv, 30,000X magnification and at fixed lens currents. Calcium and antimony x-ray energies, collected at 3.69 and 3.605 keV respectively and expressed as counts per second (cps), were used to measure calcium accumulations. Newman-Keul's multiple comparison strategies were used to obtain statistical comparisons of cps of HD-exposed and non-exposed cells.

Results indicate that cell injury and intracellular accumulations of calcium appear to coincide. Evidence of cytopathology appeared after a latency of 6 h with margination of chromatin, loss of microvilli, focal swelling of endoplasmic reticulum and subplasmalemmal rarefaction of cytoplasm. At 12 to 24 h the process deepened with condensation of mitochondria, coalescing of cytoplasmic vacuoles, progressive swelling of endoplasmic reticulum, evagination of the nuclear envelope, nuclear pyknosis, blebbing of the plasmalemma and frank necrosis (*Fig.1*). Cytochemical localizations of calcium-antimonate precipitates at 0 to 3 h were largely confined to extracellular domains. At 6 through 24 h precipitates were specific to euchromatin regions of the nucleus, dilated endoplasmic reticulum, the cytosol and condensed mitochondria (*Fig.2*). X-ray micro-analytical quantification of calcium and calcium-antimonate precipitates revealed that significant accumulations began at 6 h and were maintained at 12 to 24 h. The time-course accumulation of calcium correlated strongly with the time-course of the observed cytopathology induced by HD (*Fig.3*).[2]

References

1. C.K. Meshul and W.F. Hopkins, Brain Research, (1990) 514, 310-319.
2. The authors gratefully acknowledge Dr. William Smith, Biochemical Pharmacology, USAMRICD, for management of HD exposures of Hela cells.
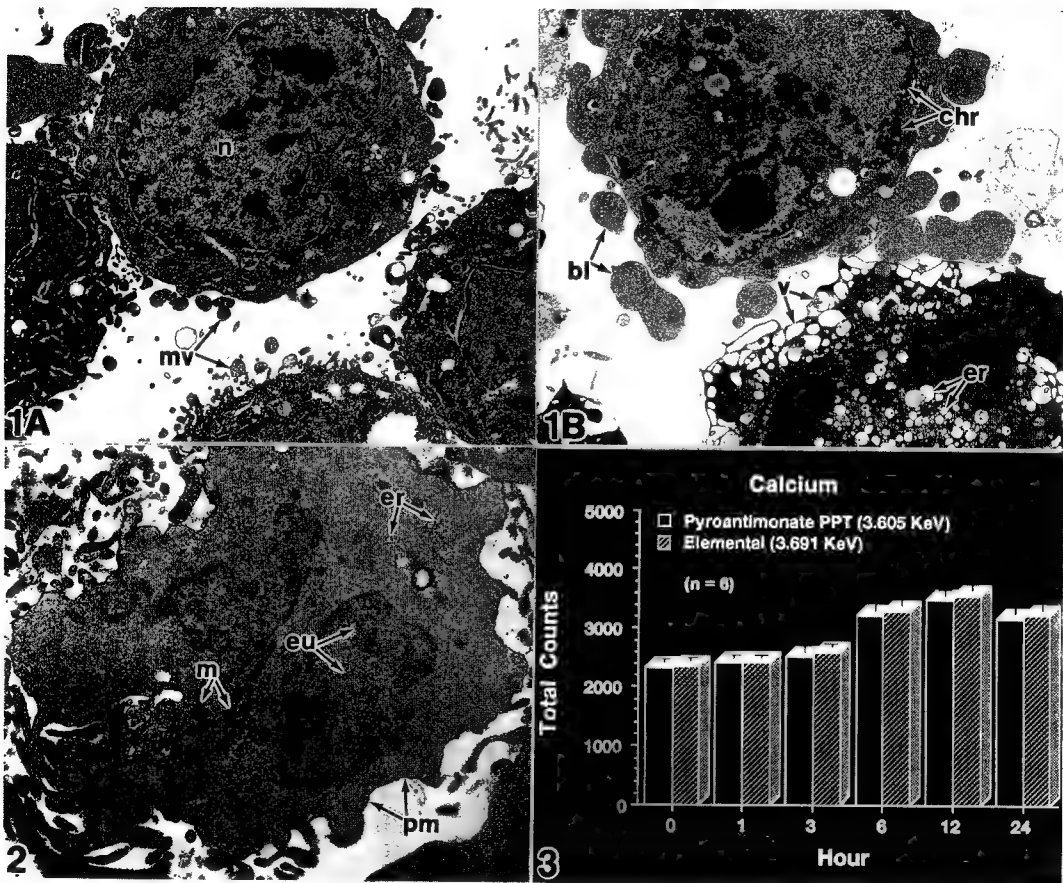
FIG 1. *A.* HeLa cells not exposed to HD; nuclei (n), microvilli (mv). *B.* Twelve hours after HD exposure with margination of chromatin (chr), cytoplasmic blebs (bl), dilated endoplasmic reticulum (er), cytoplasmic vacuoles (v). Magnifications 5000X.

FIG 2. Twenty four hours after HD exposure calcium precipitates are localized to nuclear euchromatin (eu), endoplasmic reticulum (er), mitochondria (m), and plasmamembrane (pm). Magnification 8000X.

FIG 3. X-ray microanalytical quantification of calcium precipitates represented as cps. Significant accumulation begins at 6 hours post exposure.

PEANUT AGGLUTININ RECEPTORS IN THE EPIDIDYMAL SPERMATOZOA OF THE PALM SQUIRREL (FUNAMBULUS PENANTI)

S. R. Bawa, R. Bawa*, and H. K. Bains

Department of Biophysics, Panjab University, Chandigarh 14, India
***U. S. Department of Commerce, Patent and Trademark Office, Washington, D. C. 20231, U. S. A.**

Physiological ripening of the mammalian spermatozoa during their sojourn in the epididymal duct is also mirrored on the morphological plane by lectin-labeling studies (1). In this report peanut agglutinin (PNA), which specifically labels methyl α-D-galactopyranoside, has been employed to monitor the maturation process of the epididymal spermatozoa of the Indian palm squirrel (Funambulus penanti) employing fluorescence microscopy and transmission electron microscopy (TEM in toto).

Spermatozoa were released from the epididymis by gently mincing the tissues in phosphate-buffered saline (pH 7.4). For fluorescence microscopy, sperm suspensions were smeared onto poly-L-lysine coated coverslips and labeled with 10 µl of fluorescein isothiocyanate-linked PNA (100 µl/L). For TEM in toto, sperm suspensions were adsorbed onto poly-L-lysine and Formvar coated grids and subsequently labeled with colloidal gold-linked PNA. After washing in buffer the grids were examined with a JEOL 1200 EX transmission electron microscope. Controls were prepared by incubating sperm samples in 0.2 M α-D-galactopyranoside.

Changes in the labeling pattern of PNA on the acrosome are observed during epididymal transit of the spermatozoa. In the caput epididymal spermatozoa the acrosome is faint with only the margin of the acrosomal cap sharply stained (Figure 1). Upon reaching the cauda epididymis the plasma membrane of the spermatozoa overlying the acrosomal cap appears faint (Figure 3). In the corpus epididymis the sperm head looses substantial staining along the margin of the acrosomal cap (Figure 2). However, the cytoplasmic droplet is intensely stained throughout the passage of the spermatozoa in the epididymal duct. Colloidal gold-linked PNA labeling also reveals restricted localization along the acrosome margin in the caput epididymal spermatozoa (Figures 4 and 5).

We and others believe that epididymal secretions are producing alterations in the PNA receptor sites as the spermatozoa travel through the caput, corpus and cauda regions of the epididymis (2, 3). The diffusion of the label on the corpus and the cauda epididymal spermatozoa is difficult to correlate with the distribution of the intramembranous particles (IMPs) on the plasma membrane overlying the acrosome. The disposition of IMPs on the plasma membrane remains unchanged during the passage of the spermatozoa in the epididymis in the squirrel (4).

References:
1. Koehler, J. K. (1981). *Archives of Andrology* **6:**197-217.
2. Bains, H. K., S. R. Bawa, M. A. Pabst, and S. Sehgal. (1993). *Cell and Tissue Research* **271:**159-168.
3. Voglmayr, J. K., G. Fairbanks, and R. G. Lewis. (1983). *Biology of Reproduction* **29:**767-775.
4. Bawa, S. R. (1993). Unpublished results.
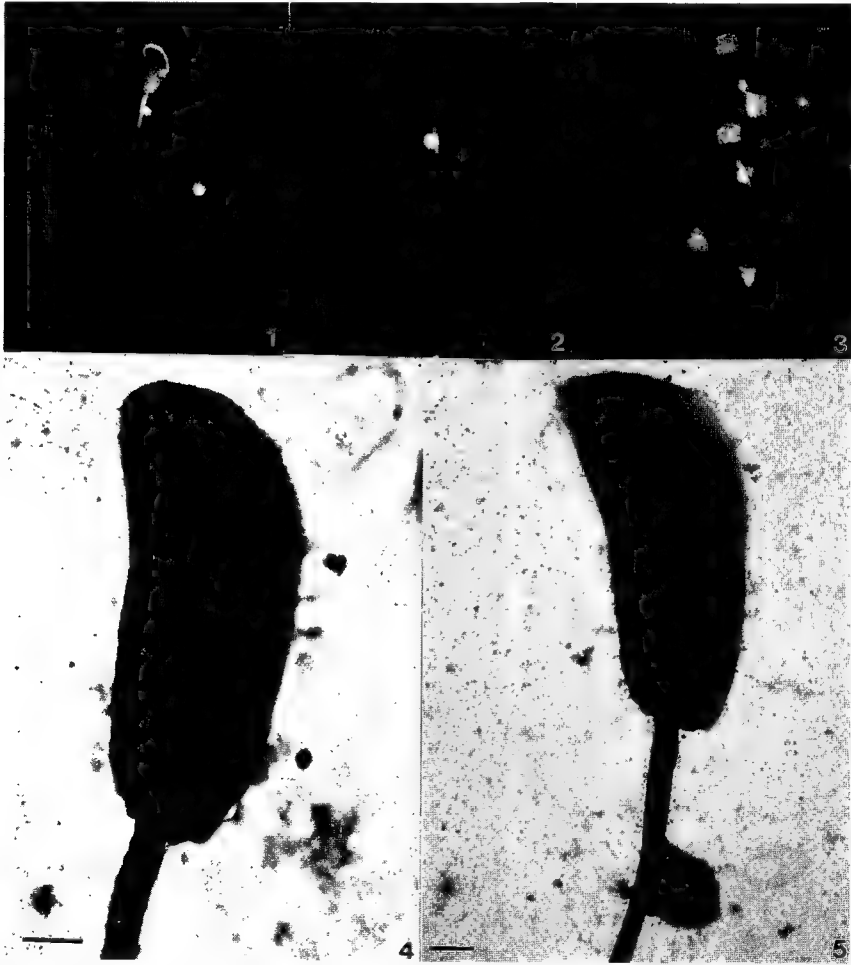
Figures 1-3: Fluorescence micrographs of squirrel caput, corpus and cauda epididymal spermatozoa respectively, labeled with fluorescein isothiocyanate-linked PNA.
Figure 4: TEM *in toto* of colloidal gold-linked PNA labeled caput epididymal spermatozoa. Note the restricted labeling along the margin of the acrosomal cap. Bar = 2 μm.
Figure 5: TEM *in toto* of the caput epididymal sperm (Control Sample) showing specificity of the PNA label. Bar = 2 μm.

325

A NEW CYTOCHEMICAL METHOD: COMBINED ENZYME CYTOCHEMISTRY AND IMMUNOCYTOCHEMISTRY ON ULTRATHIN CRYOSECTIONS

Toshihiro TAKIZAWA and John M. ROBINSON

Department of Cell Biology, Neurobiology & Anatomy, Ohio State University, Columbus, OH 43210

Cryo-ultramicrotomy has been a useful method for immunocytochemistry because it can preserve the ultrastructure of cells and also display antigenic sites in cells. Recently, cryo-ultramicrotomy has been successfully applied to enzyme cytochemistry for the demonstration of some phosphatases with lead as the capture metal.[1] However, this application has some problems. The lead reaction product is unstable with uranyl acetate staining, thus leading to poor ultrastructural detail. The purpose of this study is to develop the new method of enzyme cytochemistry using cerium as the capture metal on ultrathin cryosections labeled with immunogold probes. This method should be of importance for demonstrating the ultrastructure localization of certain enzymes and the simultaneous localization of antigens in a variety of cell types.

Freshly isolated human neutrophils were fixed with paraformaldehyde and/or glutaraldehyde in 0.1 M cacodylate buffer (pH 7.2) with 5 % sucrose, then pelleted into 10 % gelatin and subsequently infiltrated with 2.3 M sucrose. The pellets were frozen in nitrogen slush; ultrathin cryosections (90 nm in thickness) were cut with a Reichert Ultracut E equipped with a FC 4D cryounit and collected on formvar-coated copper grids. The sections were blocked with 2 % BSA in PBS prior to incubation with the primary antibody [rabbit anti-human lactoferrin (LF)] and the subsequent incubation with goat anti-rabbit IgG- 15 nm gold. The cryosections were then incubated in reaction medium for the cytochemical detection of alkaline phosphatase (ALPase).[2] After cytochemistry was carried out, the ultrathin cryosections were negatively stained with 2 % phosphotungstic acid (PTA) at pH 7.0 and simultaneously covered with formvar-films.[3]

ALPase activity was present in small cytoplasmic structures on Epon-sections following conventional cerium cytochemistry (Fig. 1). In ultrathin cryosections of human neutrophils, the numerous granules dispersed throughout the cytoplasm as well as the Golgi complex were well-preserved (Figs. 2a and 2b). Immunogold labeling of LF was present in an abundant population of granules the so-called specific granules (Fig. 2a). A population of large granules lack immunogold particles; these are the azurophilic granules (Fig. 2a). ALPase activity in cryosections was detected in small compartments similar to the ALPase-positive compartments on Epon-sections (Figs. 3a and 3b). There was no evidence for LF being localized within the ALPase-positive compartments (Figs. 3a and 3b). These results indicate that the ALPase-positive compartment is not part of the population of specific granules.

The cerium method is suitable for enzyme cytochemistry on cryosections because cerium is an efficient capture metal and is stable following negative-staining. We developed this new method in order to combine immunocytochemistry and enzyme cytochemistry on ultrathin cryosections. It should be noted that the immunocytochemistry was carried out on ultrathin cryosections prior to enzyme cytochemistry on the same cryosections so that the cerium reaction product for the detection of enzyme activity would not inhibit the function of antibodies on cryosections. It should also be noted that PTA was very useful as a negative-staining reagent since PTA was used at neutral pH and produced a good contrast with the cerium reaction product and the colloidal gold particles.

References
1. O. Fukushima et al., Acta Histochem. Cytochem., 22(1989)131.
2. T. Kobayashi and J.M. Robinson, J. Cell Biol., 113(1991)1743.
3. T. Sakai et al., J. Electron Microsc., 35(1986)Suppl:2221
4. This work was supported by the Council for Tobacco Research. T. Takizawa was supported by a study abroad grant from The Naito Foundation, Japan.
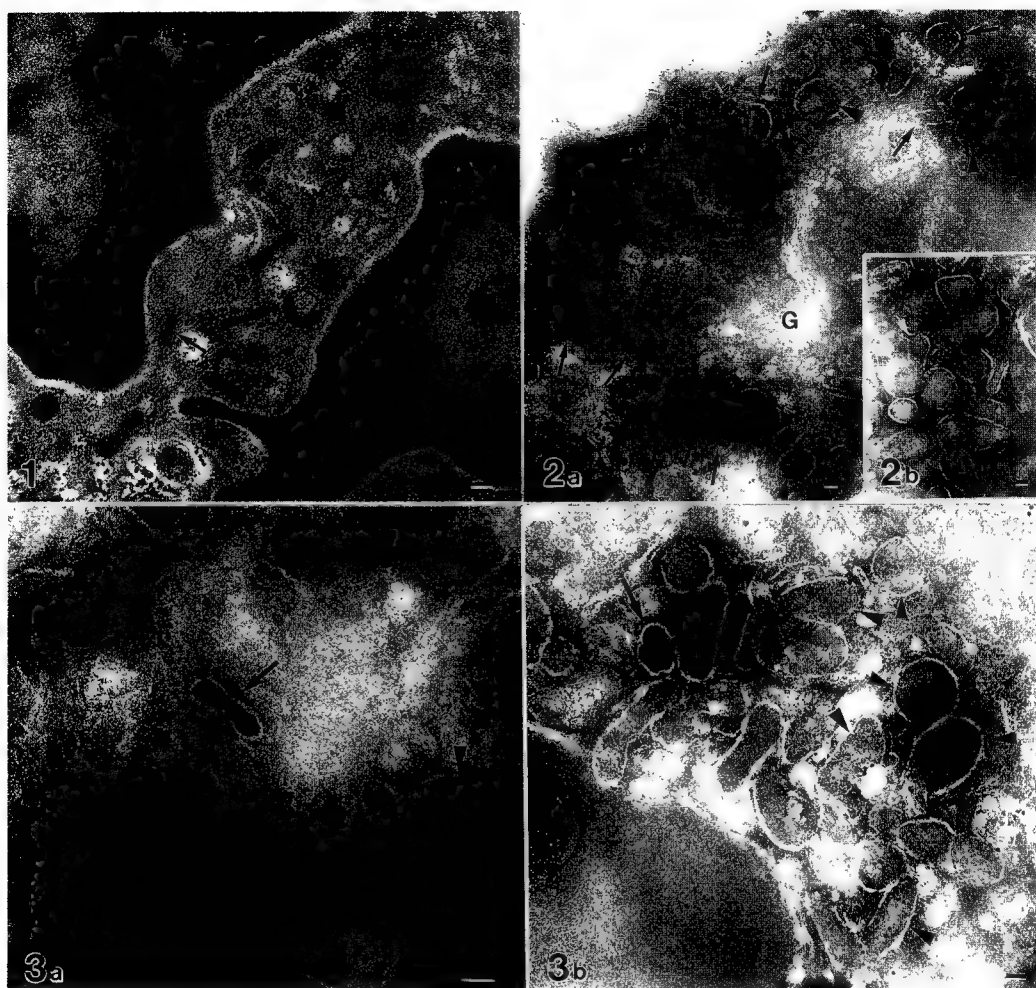
FIG. 1. Electron micrograph of ALPase activity in human neutrophils using conventional cerium cytochemistry. ALPase activity was present in small cytoplasmic structures (arrows). Bar = 0.1 μm.

FIGS. 2a. and 2b. Immunocytochemistry of lactoferrin. 2a: Immunogold particles indicating the distribution of LF were present in an abundant population of granules (arrows). Some large granules lack immunogold particles (arrowheads). The various membrane systems including the Golgi complex (G) were well-preserved. 2b: Control experiment in which primary antibody was omitted; note the absence of gold labeling. Bar = 0.1 μm.

FIGS. 3a. and 3b. Electron micrographs of the combination of LF-immunocytochemistry and ALPase enzyme cytochemistry. Immunogold labeling of LF (arrowheads) was present in specific granules and was not localized within the ALPase-positive compartments (arrows). Bar = 0.1 μm.

SERIAL THIN SECTIONING FOR PRE- AND POST-EMBEDDING IMMUNOHISTOCHEMISTRY: ACHIEVING CONSISTENT AND RELIABLE RESULTS FOR A 3-D RECONSTRUCTION

Antonia M. Milroy

Department of Anatomy and W.M.Keck Foundation Center for Integrative Neurosciences, University of California, San Francisco CA 94143-0452, USA

In recent years many new techniques and instruments for 3-Dimensional visualization of electron microscopic images have become available. Higher accelerating voltage through thicker sections, photographed at a tilt for stereo viewing, or the use of confocal microscopy, help to analyze biological material without the necessity of serial sectioning. However, when determining the presence of neurotransmitter receptors or biochemical substances present within the nervous system, the need for good serial sectioning (Fig.1+2) remains. The advent of computer assisted reconstruction and the possibility of feeding information from the specimen viewing chamber directly into a computer via a camera mounted on the electron microscope column, facilitates serial analysis. Detailed information observed at the subcellular level is more precise and extensive and the complexities of interactions within the nervous system can be further elucidated.

We emphasize that serial ultra thin sectioning can be performed routinely and consistently in multiple user electron microscopy laboratories. Initial tissue fixation and embedding must be of high quality. The use of a harder epoxy facilitates the separating of sections. We trim the specimen block to a thin, one-sided rhomboid which assists cutting, orientation of the tissue and numbering of sections on the grid (Fig.3) during collection in the diamond knife boat. In addition, the rhomboid shape allows proper numerical sequence when viewing sections at a low magnification in the electron microscope. The skill of vertical alignment of the specimen face to the knife (i.e. same distance between the edge of the diamond knife and top and bottom of specimen face, Fig.4) allows one to cut serial sections, remove the block and, at a later time, re-enter the same block in the microtome holder for further serial sectioning. For collecting serial sections from the water bath we use Butvar coated single slot copper or nickel grids. The Butvar coating provides a very tough and elastic support film and is essential for extensive immunohistochemical manipulation of the sections on the grid and for multiple entries into a high vacuum. For example, in our laboratory the block size is such that 5 sections can fit on one open slot grid. We cut 25 sections, separating each set of 5 sections with two eyelash manipulators during sectioning. At this point the microtome is stopped and the sections are collected. After repeating this step 4 times, one has a collection of 100 serial electron microscopic sections for photography followed by a computer assisted 3-D reconstruction (Fig.5). The loss of a section or grid should be recorded for proper continuity of the reconstruction. In addition, when doing electron microscopy of serial sections, each grid should be kept at low magnification with the beam spread for about 1 minute to stabilize support film and sections before extensive repeated viewing and photography.
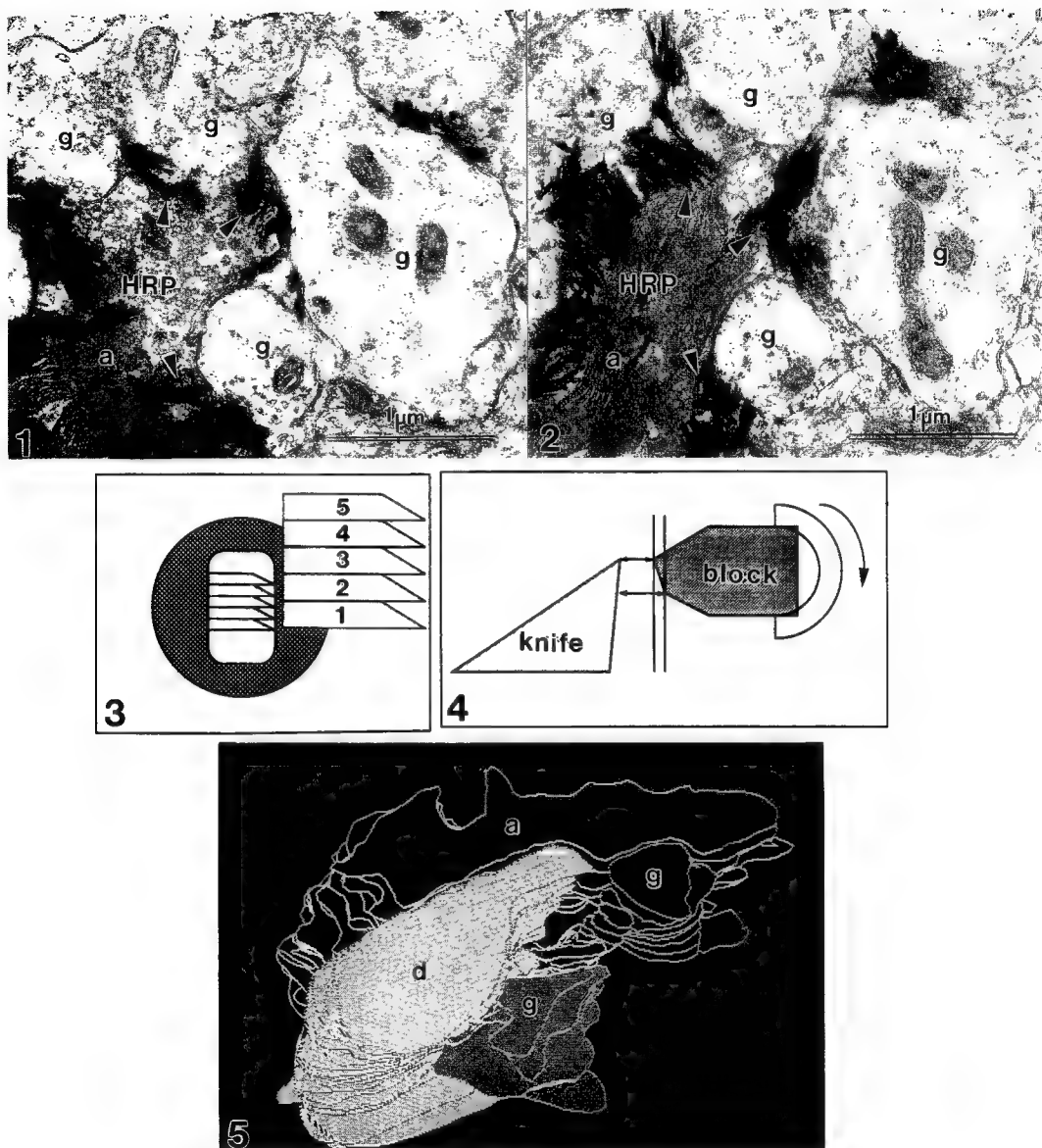
Fig. 1+2:   – Serial micrographs of thalamic profiles in consecutive sections.
a = lemniscal afferent. HRP/ arrow heads = crystals showing horseradish
peroxidase transport. g = profiles with 10 nm gold particles indicating the
presence of GABA neurotransmitter, presumably inhibitory.

Fig. 3:   – Schematic grid with 5 rhomboid sections.

Fig. 4:   – Schematic alignment of block face to knife.

Fig. 5:   – 3-D computer reconstruction of serial thalamic sections. a = lemniscal
afferents, d = dendrite, g = GABA containing profiles.

      (Reconstruction courtesy of Henry J. Ralston, III.)

329

HIGH-RESOLUTION GOLD LABELING

James F. Hainfeld*, Frederic R. Furuya*, Kyra Carbone*, Martha Simon*, Beth Lin*, Kerstin Braig**, Arthur L. Horwich**, Daniel Safer***, Bernd Blechschmidt****, Mathias Sprinzl****, James Ofengand*****, and Milas Boublik*****

* Biology Department, Brookhaven National Laboratory, Upton, N.Y., 11973
** Howard Hughes Medical Institute and Department of Genetics, Yale School of Medicine, New Haven, CT 06510
*** Department of Cell and Developmental Biology, The School of Medicine, University of Pennsylvania, Philadelphia, PA 19104-6058
**** Laboratorium fur Biochemie, Universitat Bayreuth, Bayreuth, Germany
***** Roche Institute of Molecular Biology, Hoffmann-La Roche Inc., Nutley, NJ 07110-1199

A recently developed 1.4 nm gold cluster (1-3) has been found to be useful in labeling macromolecular sites to 1-3 nm resolution. The gold compound is organically derivatized to contain a monofunctional arm for covalent linking to biomolecules. This may be used to mark a specific site on a structure, or to first label a component and then reassemble a multi-component macromolecular complex. Two examples are given here: the chaperonin groEL and ribosomes.

Chaperonins are essential oligomeric complexes that mediate nascent polypeptide chain folding to produce active proteins. The E. coli chaperonin, groEL, has two stacked rings with a central hole ~6 nm in diameter. The protein dihydrofolate reductase (DHFR) is a small protein that has been used in chain folding experiments, and serves as a model substrate for groEL. By labeling the DHFR with gold, its position with respect to the groEL complex can be followed. In particular, it was sought to determine if DHFR refolds on the external surface of the groEL complex, or whether it interacts in the central cavity. DHFR was labeled as shown in Fig. 1, then denatured and bound to groEL. Gold was observed in the cavities in top views (Fig. 2), and in side views (not shown), gold was localized to each ring, sometimes two golds being observed, one associated with the top and one with the bottom ring (4).

Subunit structure is often lost in freeze dried unstained samples (Fig. 2). Use of usual stains such as uranyl acetate obscures the 1.4 nm gold. However, a lower density vanadate stain (5), which is more dense than the protein but less dense than the gold, yields good visibility of both components. The DHFR-Au$_{1.4nm}$ complexed with groEL is shown in Fig. 3 and the subunit detail of the groEL and the gold are clearly seen.

The second example is the use of Au$_{1.4nm}$-labeled tRNA to probe its position on ribosomes. First, a specific base on the tRNA was used to covalently link the 1.4nm gold in ~100% yield (6,7). This was then bound to 30s subunits (Fig. 4) or 70s ribosomes (Fig. 5), and column chromatography used to remove unbound tRNA. Labeling yield at this step was low, but the sites labeled were very reproducible.

References

1. J. F. Hainfeld, F. R. Furuya, and R. D. Powell, EMSA Proceedings (1991) 284.
3. J. F. Hainfeld and F. R. Furuya, J. Histochem. Cytochem. (1992) 40, 177.
3. 1.4 nm gold cluster is "Nanogold", available from Nanoprobes, Inc. or E.F. Fullam.

4. K. Braig, et al. Proc. Nat. Acad. Sci. (1993) in press.
5. Available from Nanoprobes, Inc. or E.F. Fullam as "NanoVan".
6. J. F. Hainfeld et al. J. Struct. Biol. (1991)107, 1.
7. J. F. Hainfeld, F. R. Furuya, and K. Carbone, EMSA Proceedings (1992) 526.
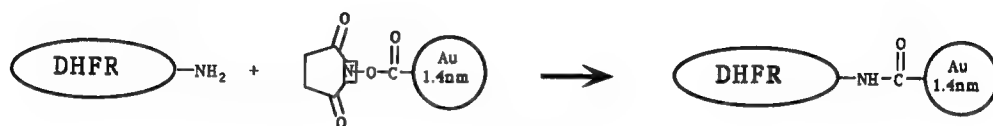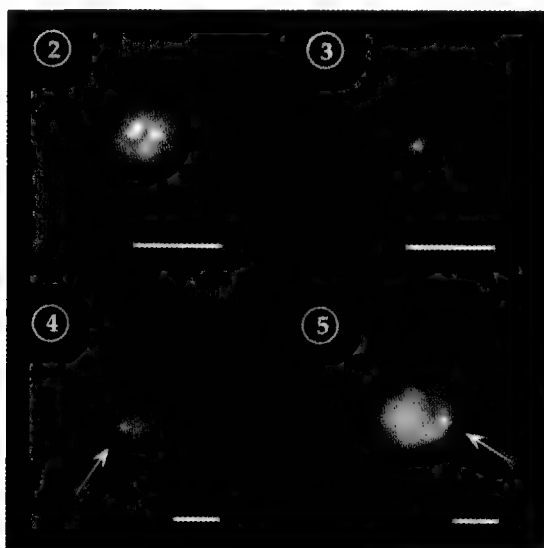
Fig. 1

Fig. 1.--Coupling reaction of $Au_{1.4nm}$ to DHFR.

Fig. 2.--STEM darkfield micrograph of freeze dried unstained groEL with two gold labeled DHFR molecules (bright spots) in the central cavity. Bar=10 nm.

Fig. 3.--STEM darkfield micrograph of vanadate stained groEL with one gold labeled DHFR molecules (bright spot) in the central cavity. Bar=10 nm.

Fig. 4.--STEM darkfield micrograph of gold labeled tRNA (arrow, bright spot) bound to 30S ribosomal subunit. Bar=10 nm.

Fig. 5.--STEM darkfield micrograph of gold labeled tRNA (arrow, bright spot) bound to 70S ribosome. Bar=10 nm.

PYOSPERMIA AND SPERMOPHAGY IN SEMEN OF THE RED WOLF

James K. Koehler, Carrol C. Platz, Jr.*, Will Waddell**, Michael H. Jones**

Department of Biological Structure, University of Washington, Seattle, WA 98195,*ICSB, Sandy, OR 97055, **Point Defiance Zoo and Aquarium, Tacoma, WA 98407

The red wolf (*Canis rufus*) inhabited the Southeastern United States until the early 1900's when aggressive hunting and a shrinking primitive habitat virtually eradicated the species. *C. rufus* was certified as an endangered species in 1967 and was essentially extinct in the wild by 1980. About 200 animals are preserved in zoos and captive breeding facilities where efforts are underway to increase the stock.[1] Since a shrinking gene pool and captive stress may reduce reproductive vigor, we undertook an electron microscopic examination of red wolf semen used for artificial insemination at the Graham, WA breeding facility of the Point Defiance Zoo.

Animals were anesthetized with 175 mg. Telazol, IM before electroejaculation using a rectal probe[2] Semen was washed in PBS prior to fixation in 1.25% glutaraldehyde in 0.1M cacodylate, post fixed in OsO4, dehydrated in alcohol and propylene oxide and embedded in Epon 812. Some samples were incubated in capacitation or maintenance media for several hours before fixation as above. Thin sections, cut with a diamond knife were double stained and viewed in a Phillips EM 420 TEM. Although many morphologically normal sperm (Fig. 1) were seen in the semen of the five wolves used in this study, most specimens showed mild to extensive white cell infiltration (pyospermia) and accompanying spermophagy. Figure 2 shows a typical L.M. field dominated by neutrophils, many of which have phagocytosed sperm(arrows). Similar fields were seen immediately after collection as well as after culture in capacitation media indicating that phagocytosis was not induced by culture, but was initially present. A sequence can be suggested regarding the uptake and endosomal processing of sperm including attachment, incorporation (Figure 3) and degradation (Figure 4). Occasionally, a membrane complex consisting of endosomal membrane, sperm plasma membrane and a dense intermembrane material envelops the engulfed sperm (Figure 5, arrows). Sperm so enshrouded seem to be in excellent condition and may be protected from enzymatic degradation by this dense lamina.

Pyospermia and spermophagy have been documented in (human) cases of idiopathic and infective prostatitis[3] as well as post-vasectomy[4] but have not received much attention in animal models. As these conditions constitute a negative indicator of fertility[5], it is of some concern that this subpopulation of wolves show a high incidence of white cell infiltration and sperm phagocytosis. Captive stress and the effects of a shrinking gene pool may be contributing factors to this phenomenon, but further studies are necessary before generalizing these observations.

References

1. U.S. Fish and Wildlife Service (1989) Red Wolf Recovery Plan, Atlanta, GA.
2. C.C. Platz and S.W.J. Seager, J. Amer. Vet. Med. Assoc.(1978) 173, 1353.
3. R.E. Berger, et al., J. Urol. (1979) 121, 750.
4. Alexander, N.J., Fed.Proc. (1975) 34, 1962.
5. R.E. Berger et al.,Fertil. Steril. (1982) 37, 557.
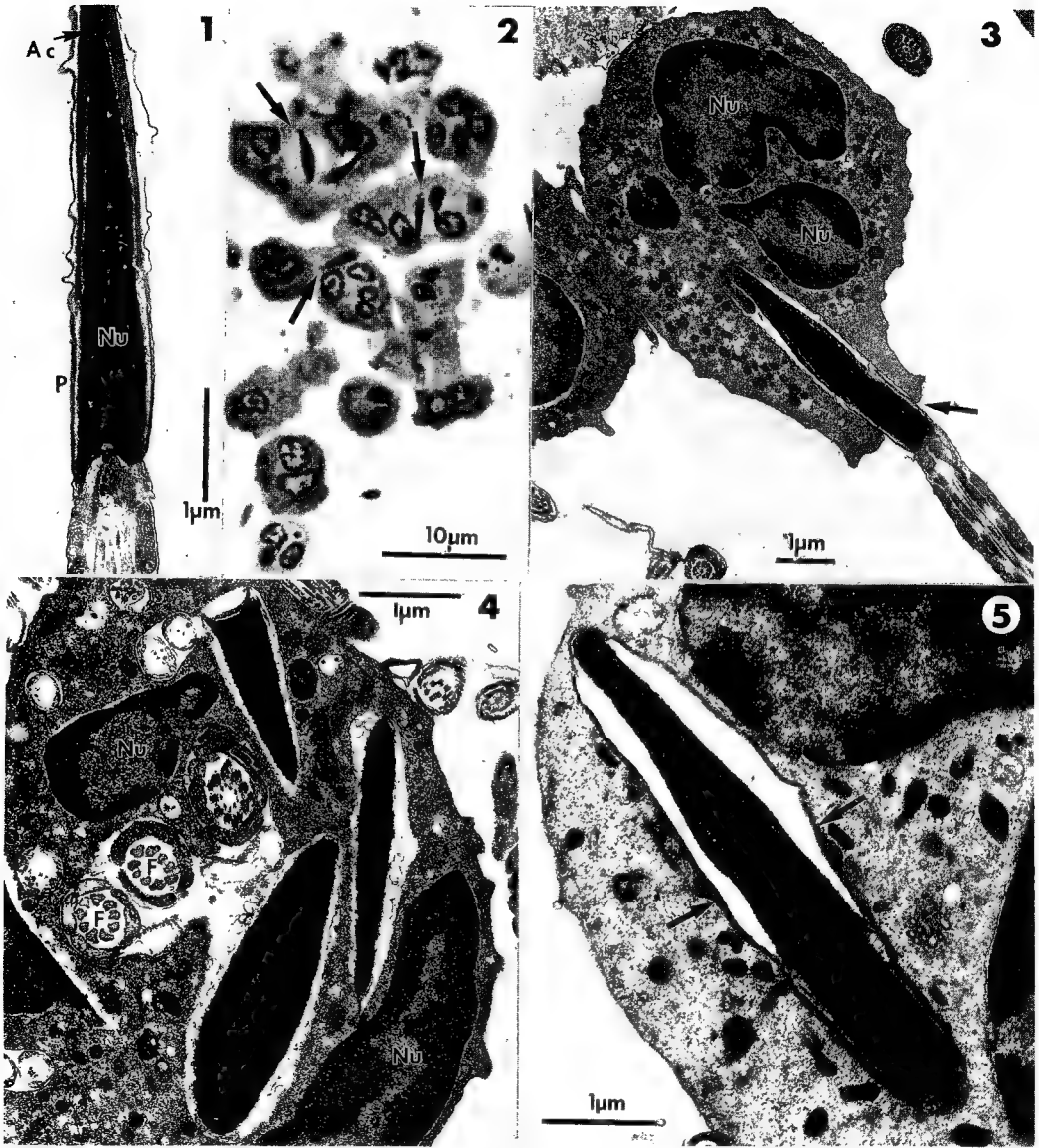
Fig. 1   TEM of red wolf sperm fixed immediately after semen collection showing typical features including fully condensed nucleus (Nu), acrosome (Ac) and post acrosomal region (P). X 18,400

Fig. 2   LM showing extensive neutrophil infiltation of semen with many sperm (arrows) incorporated into phagocytic vesicles. X 2,200

Fig. 3 Initial stage of incorportation of a red wolf sperm (arrow) into a neutrophil (Nu, nuclei). X 9,800

Fig. 4   Later stage of phagocytic activity in a neutrophil (Nu, nuclei) showing several dense sperm nuclei and flagellae(F) in endosomes undergoing partial digestion. X 16,700.

Fig. 5 Red wolf sperm incorporated into a phagosome showing a dense, membrane complex (arrows) enveloping the endosome. Note the "normal" appearance of the entrapped sperm. X 19,500.

ELECTRON MICROSCOPY OF THE CHANGES IN THE SPERM HEAD CURVATURE OF THE PALM SQUIRREL (FUNAMBULUS PENANTI)

S. R. BAWA, R. BAWA*, AND H. K. BAINS

Department of Biophysics, Panjab University, Chandigarh 14, India
*U. S. Department of Commerce, Patent and Trademark Office, Washington, D. C. 20231, U. S. A.

Examination of ultrathin sections of the spermatozoa recovered from the epididymis of the Indian palm squirrel (Funambulus penanti) indicates that the sperm head undergoes changes in its curvature during epididymal transit.

Testis and epididymis of an adult male squirrel were dissected and small pieces of tissue fixed in 2.0% glutaraldehyde in 0.1 M phosphate buffer and post-fixed in osmium tetroxide. After dehydration in graded acetone the material was embedded in Araldite. Ultrathin sections were cut on a Reichert Jung Ultracut, picked-up on copper grids, stained with Reynold's lead citrate-uranyl acetate and examined with a JEOL 1200 EX transmission electron microscope.

Ultrathin sections of the caput epididymal spermatozoa reveal that their plasma membrane is adherent to the underlying acrosome (Figure 1). When these spermatozoa reach the corpus epididymis the plasma membrane surrounding the head becomes ruffled (Figure 2). The lifting-up of the plasma membrane around the head is restricted to the posterior bend of the acrosome. The membrane covering the post-acrosome region is in intimate contact with the underlying portion of the head. In the caput and corpus epididymal spermatozoa the acrosome is in line with the nuclear axis with a sharp bend at the rostral part of the acrosome. When the spermatozoa pass down to the cauda epididymis there is reduction in the curvature of their acrosome (Figure 3). In these spermatozoa there is incorporation of granular material between the plasma and outer acrosomal membranes. This material appears similar to that found in the lumen of the epididymis. The plasma membrane overlying the acrosome of the cauda epididymal spermatozoa is taut as compared to the ruffled appearance of the plasma membrane in the corpus epididymal spermatozoa.

Epididymal maturation of the squirrel spermatozoa is accompanied by a progressive loss of acrosomal curvature in asmuchas the rostral segment of the caudal spermatozoa is less sharply bent vis-a-vis the acute bending of the caput epididymal spermatozoa. Such a change in the sperm head curvature has also been reported in the maturing spermatozoa of the rat (Fornes and de Rosas, 1989). These authors opine that decrease of the head surface area in the epididymal maturation of rat spermatozoa may be due to compaction of the nucleus. In most of the mammalian species it has been reported that the sperm head undergoes alterations due to the influence of the Sertoli cell cytoskeleton and/or microtubules of the spermatid (Bawa and Werner, 1983; Vogl, 1983). However, in the squirrel post-testicular changes enumerated above manifest during sojourn of the spermatozoa in the epididymis. We believe that in the

squirrel the sperm head streches out with concomitant accumulation of granular material between the plasma membrane and the acrosomal surface, thereby causing this altered curvature of the head.

References:
1. Bawa, S. R., and G. Werner. (1983). *In:* J. Andre (editor). *The Sperm Cell.* Martinus Nijhoff Publishers, The Hague, Boston and London, pages 245-248.
2. Fornes, M. W., and J. C. de Rosas. (1989). *Gamete Research* **24:**453-459.
3. Vogl, A. W. , V. C. Lin, M. Dym, and D. W. Fawcett. (1983). *American Journal of Anatomy* **168:**83-98.
4. Supported by research grants to SRB from the Alexander von Humboldt Foundation, Germany and the Panjab University, India.
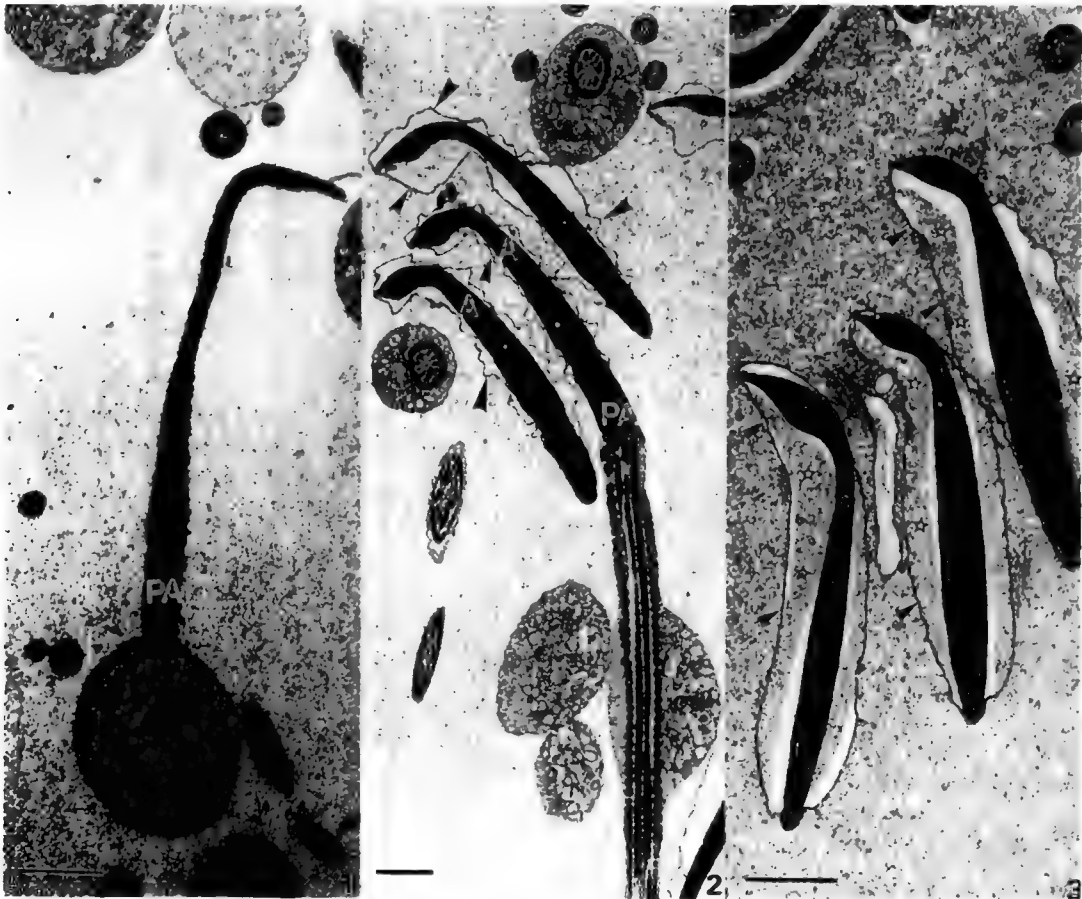
Figures 1-3: Transmission electron micrographs of the caput, corpus and cauda epididymal spermatozoa respectively of squirrel. Note the ballooned plasma membrane over the acrosome and the fine granular material (star) between the plasma and outer acrosomal membranes. acrosome (A), post-acrosome (PA), cytoplasmic droplet (cd), plasma membrane (arrowheads). Bar = 2 μm.

PATHOLOGY OF THE SPERMATIC MIDDLE PIECE AND INFERTILITY

G. Gallegos de L., E. Ramírez B.,L. Gómez G. and M. Díaz G.

Departamento de Patologia, Fac. de Medicina, Universidad Autónoma de Nuevo León
International Center of Cell and Molecular Biology, Monterrey, N.L. México

On the pathology of spermatozoa associated to infertility, it has been described a variety of alterations that include subtle axonemal defects such as lack of dineyn arms [1], and altered microtubular pattern (9+0)[2]. Also it has been reported acrosomal agenesy in round head sperms[3], and altered acrosomal modelation[4]. All these alterations become responsible of sperm motility disarrangement that impair procreation. In these cases it is convenient the ultrasructural study with the purpose of a more correct and precise diagnosis and prognosis.

Thus, we studied the subcellular spermatic pathology in semen of infertile men obteined by masturbation. The specimens were proccesed for electron microscopy by the usual method, after washing in phosphate buffer. Thin sections were observed in Carl Zeiss EM 109 electron microscope.

In this series of 21 patients studied, 43% have showed alterations of the flagellar middle piece.At the optical microscope, the sperms showed short tail and were immotile or presented a big cytoplasmic drop and movement grade I or II (according to WHO classification). At the ultrastructural level , we observed a middle piece totally disorganized with mitochondria disarrangement in their helical periaxonemal pattern (fig.1). In the cytoplasm appeared dense fibers dispersed , or in small aggregates as well as microtubular doublets (Fig.2). Concomitantly, we observed alterations in the nuclear an acrosomal shape and frequently with excesive perinuclear cytoplasm. The observed alterations seems to have a common base that implies an altered pattern of microtubular distribution, whose role in spermatogenesis process is well recognized .The ultraultrastructural alterations present in short tailed sperm , not only involve the axoneme but include the rest of cell components of this segment , and are similars to those reported by Gallegos et al. (1991)[5] in mice treated with the mutagen ethyl methane sulphonate.

References

1.- B.A. Afzelius et al. (1975) J. Cell Biology 66:225

2.- B. Bacceti et al. (1979) Andrologia 11: 437

3.- R.S. Jeyendram et al. (1985) Andrologia 17:31

4.- A.F. Holstein et al. (1975) Virchow Arch. A. Pathol., Anat.,Histol. 367:93

5.- G. Gallegos et al. (1991) EMSA Proc. p.p. 140.
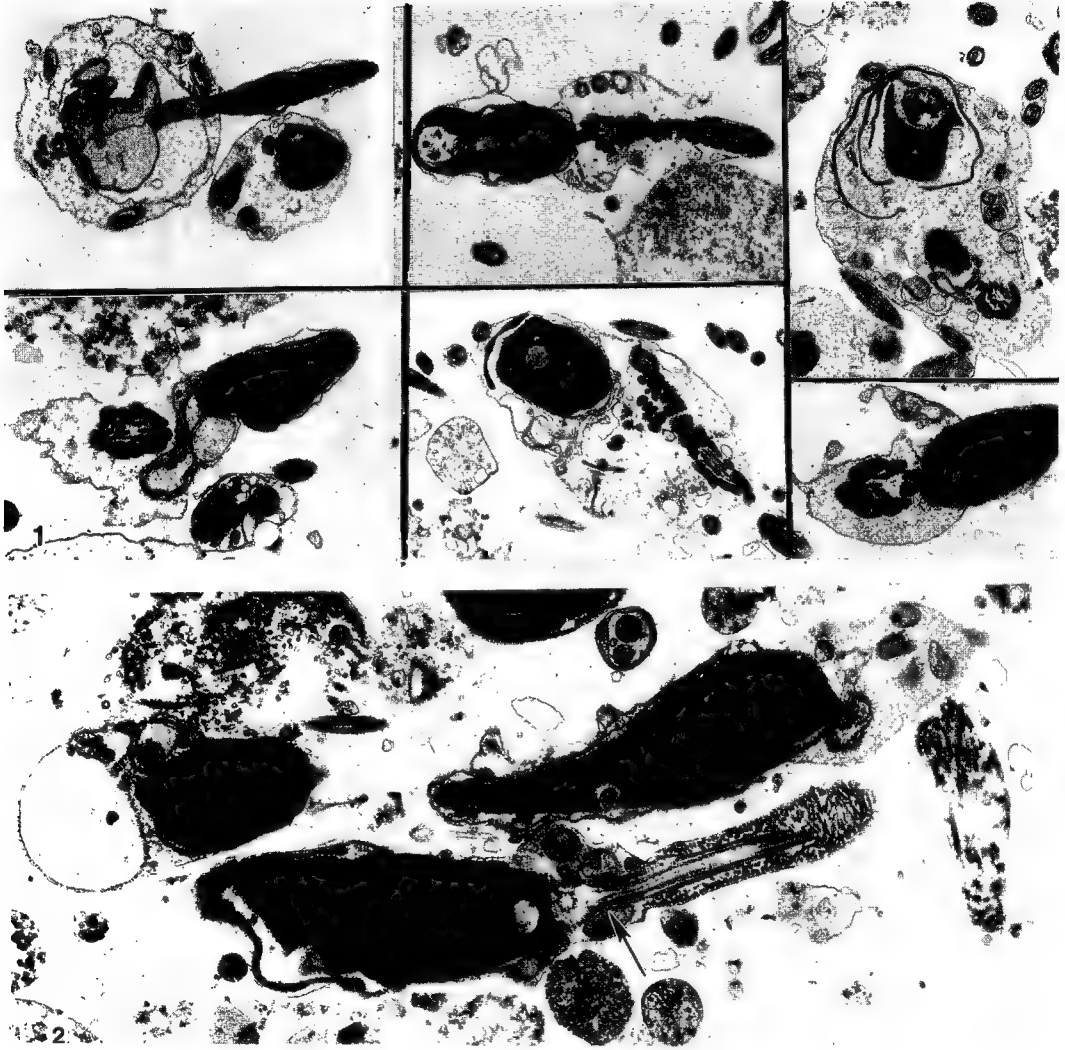
Fig.1. Abnormal sperms of a subfertile asthenozoospermic patient. The middle
piece of the flagellum in completely altered, the helicoidal arrangement
of the mitochondria was absent. None cell present a charasteristic axonema
at middle piece. ———————— 5μm

Fig.2. Shorted tails spermatozoa in a normozoospermic patient with a total sperm
motility: the middle piece is very short (arrow), and the dense fibers at
the principal piece are in altered pattern. ————1μm

ATYPICAL BASAL BODIES FOUND IN CILIATED CELLS OF AN ASTHMATIC PATIENT: AN ACQUIRED ULTRASTRUCTURAL ALTERATION OR EVIDENCE OF A DISORDER OF CILIOGENESIS?

W.T. Gunning, R.F. Judkins, and B.E. Akpunonu

Numerous reports of abnormal cilia in human respiratory epithelium have been published within the last ten years; most of these studies have described alterations of the axoneme and attributed these changes to a dysfunction of the ciliary apparatus, otherwise labeled immotile cilia syndrome or primary ciliary dyskinesia (1). In general, dysfunctional or ineffective mucociliary clearing of the respiratory tract is a prime factor contributing to chronic respiratory tract infections, and while patients with chronic respiratory tract infections do not necessarily have an immotile cilia syndrome, this history is the norm for patients suffering from the congenital disorder (2). More than 20 alterations of the cilia axoneme have been observed. The most common is the loss of dynein arms and other frequently seen abnormalities include loss of radial spokes and transposition of ciliary microtubules (2). Approximately one half of the patients found to have ciliary abnormalities also have *situs inversus*, bronchiectasis, and chronic sinusitis, a triad of manifestations known as Kartagener's syndrome. Males with Kartagener's syndrome are usually found to have immotile spermatozoa as well. In addition, many patients having congenital ciliary defects have a long history of rhinitis and nasal polyps.

In contrast to congenital alterations of cilia usually involving multiple tissues and organs, acquired ciliary defects have been reported as focal in nature, an alteration of the normal arrangement of 9 plus 2 microtubular pattern (not a defect of the dynein arm or radial spoke), and in errors of the ciliary necklace, the basal body, or rootlets at the apex of ciliated cells (3). Other abnormal cilia thought to be of an acquired etiology include megacilia (numerous axonemes within a single membrane), naked cilia, and intracytoplasmic cilia. Causes for such acquired defects include long-lasting viral colds, bacterial infections (e.g. *Mycoplasma pneumoniae*) of the upper respiratory tract, and exposures to environmental toxins, especially cigarette smoke.

We have recently evaluated the nasal mucosa of a 30 year old male with a history of asthma, first diagnosed when he was 3 months old. He had a familial history of asthma and he had developed a progressive asthma which was increasingly difficult to control with steroids. Surgery was performed to correct a chronic obstructive polypoid rhinosinusitis. The ultrastructural morphology of cilia appeared to be within normal limits as no congenital or acquired alterations of the axonemes were seen (Fig. 1). However, the basal bodies of numerous cilia contained an unusual round dense "granule" (Fig. 2-3). The significance of these bodies is unknown and only a few original reports have described their occurrence (4, 5). The presence of such granular densities within the basal body apparatus may interfere with ciliary function, or be the result of a disorder of ciliogenesis, and may be another of the many ultrastructural alterations included as criteria for a diagnosis of immotile cilia syndrome.

1. Afzelius, BA (1979) Interntnl Rev Exp Pathol 19:1-43.
2. Rubin, BK (1988) Clin Chest Med 9(4):657-668.
3. Ballinger, JJ (1988) Ann Otol Rhinol Laryngol 97:253-258.
4. Lungarella, G, *et al.* (1985) Eur J Respir Dis 66:165-172.
5. Stockinger, L, *et al.* (1989) Exp Lung Res 15:925-941.
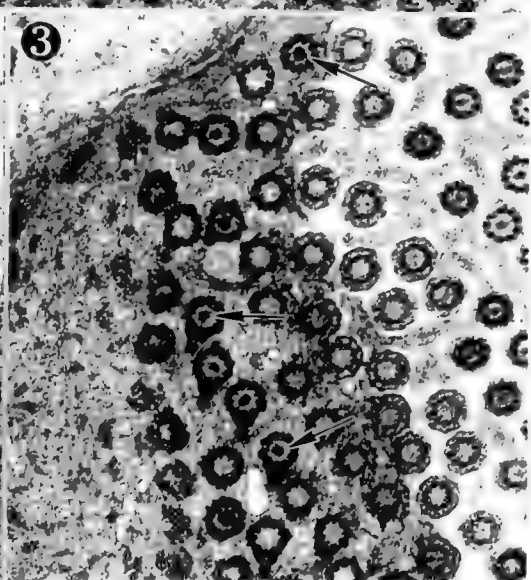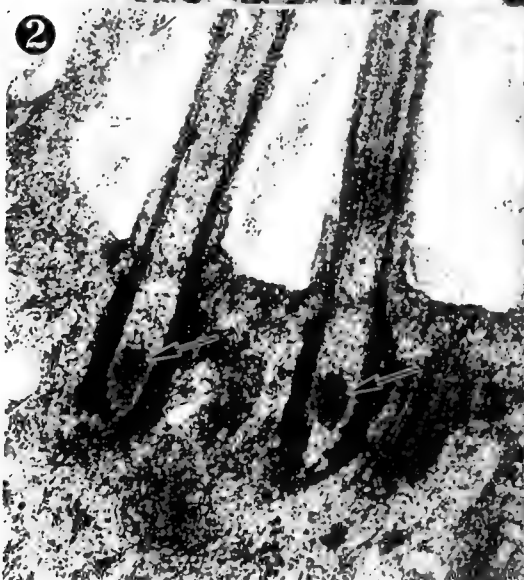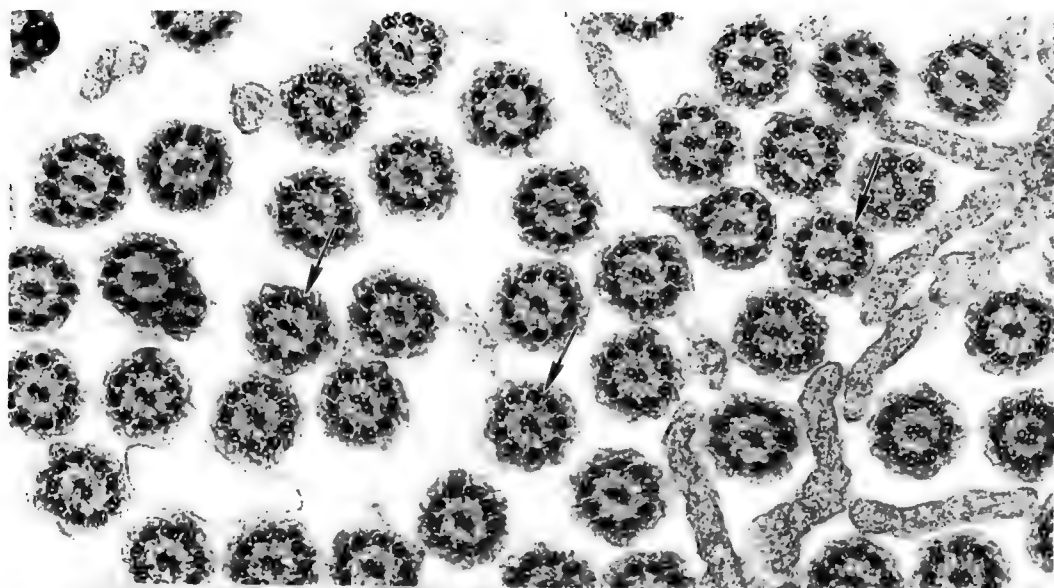
Figure 1. Cross-section of cilia shows the normal axoneme structure of 9 doublet plus 2 singlelet microtubules with intact dynein arms (arrows). 66,000 X

Figure 2. Apex of a ciliated cell with unusual dense granules (arrows) located within basal bodies. 65,000 X

Figure 3. *En face* section through the apex of a ciliated cell shows many basal bodies containing granules (arrows). 27,500 X

PROLIFERATION OF MICROTUBULES FROM DISCRETE ELECTRON-DENSE BODIES IN THE CILIARY DENDRITIC PORTION OF MECHANOSENSORY SETAE OF COPEPOD ANTENNAE

Tina M. Weatherby* and Petra H. Lenz**

*Biological Electron Microscope Facility and **Békésy Laboratory of Neurobiology, Pacific Biomedical Research Center, University of Hawaii, Honolulu, HI 96822

Sensory setae on the appendages of most arthropods contain microtubules in their innervating dendrites. Both mechano- and chemoreceptors are of ciliary origin. Mechanoreceptive dendrites typically contain more microtubules than do chemoreceptive dendrites, perhaps reflecting a role for microtubules in stiffening the setae. The presence of microtubules may also increase the sensitivity of mechanotransduction.

The overall arrangement of calanoid copepod mechanoreceptors has been described elsewhere.[1,2] In calanoid copepods the arrangement of microtubules in the distal ciliary segment of the dendrites is dramatic: as many as 3000 microtubules per dendrite are found in parallel rows (fig. 1,3a). These bundles of microtubules extend some distance into the setae themselves. The basal bodies within these dendrites are especially electron-dense and give rise to a circlet of 9 + 0 microtubules (fig. 2,3f). Just distal to the circlet electron-dense material begins to form adjacent to the microtubules (fig. 3e), eventually forming elongate electron-dense bodies radiating outward (fig. 3d). These dense outer bodies appear to be solid, discrete structures, containing a homogenous, very electron-dense material, unlike the more usual amorphous outer dense fibers found peripheral to the 9 + 2 basal body structure in some mammalian sperm, or the pericentriolar material found in most microtubule organizing centers. Microtubules sprout from the internal tip of these bodies (fig. 3b-d), indicating that they are nucleating centers for microtubule polymerization. The dense bodies persist for most of the length of the distal dendrite that lies within the antennal shaft, a distance ranging from <20 to >100 μm. Microtubules form in bridged rows from the internal tip of these nucleating bodies throughout the length of these structures. The microtubules stay in register and bridges occur both within rows and between rows. As the strands of microtubules elongate, they fill the center of the dendrites and the dendrites enlarge from a circular shape to a rectangular shape. As the dense rods proceed distally, they shorten until they appear only as electron-dense microtubule doublet-sized dots. At their point of origin all the microtubules have electron-dense centers, in contrast to the more usual hollow tubes. Microtubules with lucent centers appear more distally in the dendrites with the highest numbers appearing where the dense-bodied nucleating sites are no longer visible (fig. 3a).

We hypothesize that the dense outer bodies are composed of microtubule associated proteins involved in the initiation of polymerization of microtubules, and that the dense material within the microtubules also contributes towards this function.[3]

References
1. T.M. Weatherby *et al.*, submitted.
2. T.M. Weatherby and P.H. Lenz, in prep.
3. Supported by NSF grant OCE 89-18019 to D. Hartline and NIH grant RR03061 (RCMI).
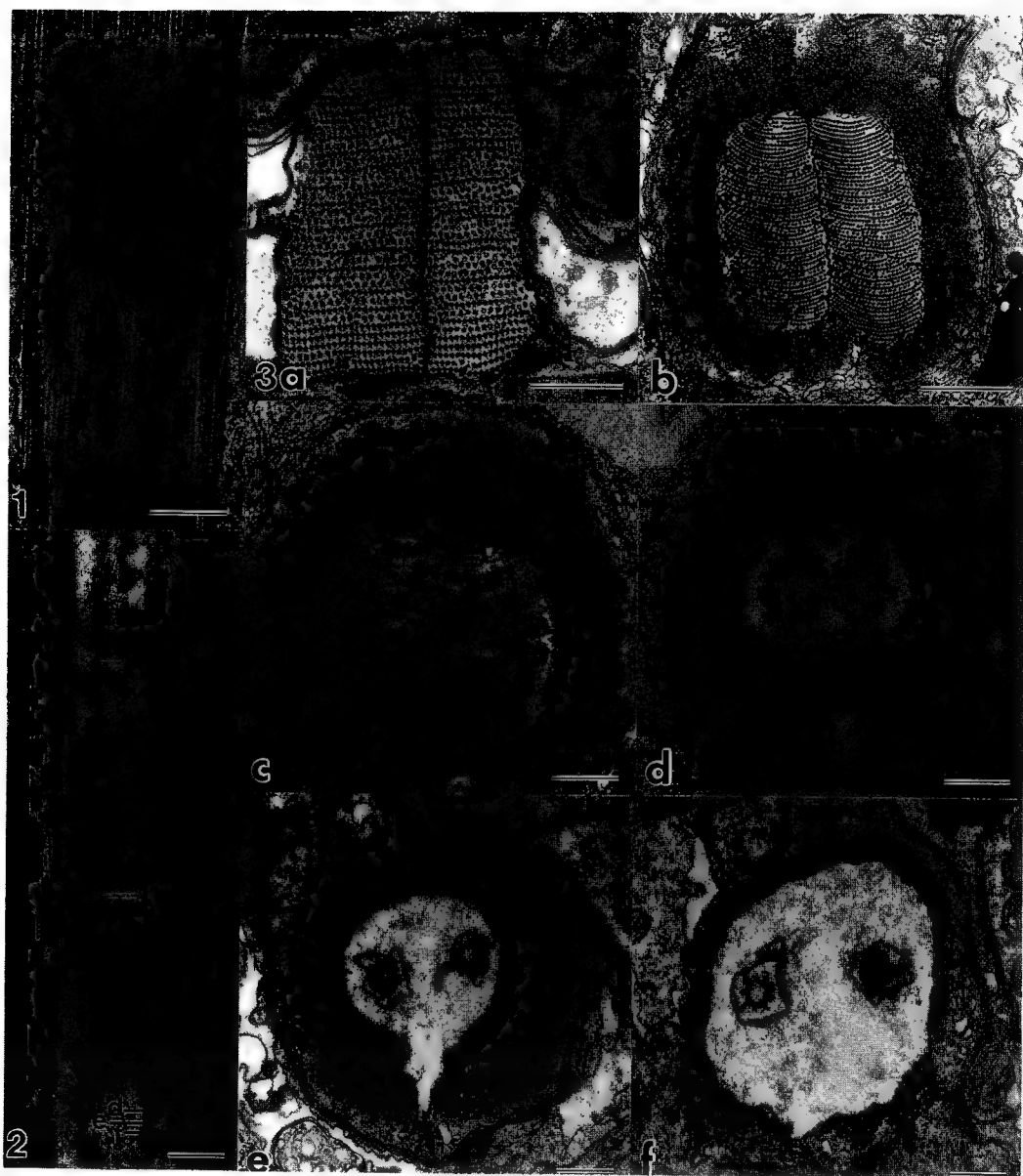
FIG. 1 Longitudinal section through two dendrites containing parallel arrays of microtubules in antennal mechanosensory seta, *Pleuromamma xiphias*.

FIG. 2 Longitudinal section through ciliary segment of dendrite within antennal shaft. **a-f** approx. levels of cross-sections in Fig. 3a-f.

FIG. 3 Cross-sections through pairs of ciliary dendrites. **a** rows of electron-dense and -lucent microtubules as they appear before entering the seta. **b-c** elaboration of rows of microtubules with dense centers. **d** initiation of proliferation of microtubules from outer dense bodies. **e** 9 + 0 circlet and forming outer dense bodies. **f** basal body and 9 + 0 circlet. Bars = 0.5 μm

SULFHYDRYL BOND FORMATION IS A PREREQUISITE FOR PROPER CYCLING OF CENTROSOMES AND CHROMOSOMES IN MAMMALIAN TISSUE CULTURE CELLS

Heide Schatten,* Neidhard Paweletz,** and Ron Balczon***

*Department of Zoology, University of Wisconsin, Madison, WI 53706, **German Cancer Research Center, Division: Growth and Division of the Cell, D-69 Heidelberg, Germany, ***Department of Structural and Cellular Biology, University of South Alabama, Mobile, Alabama, 36688.

To study the role of sulfhydryl group formation during cell cycle progression, mammalian tissue culture cells (PTK2) were exposed to 100μM 2-mercaptoethanol for 2 to 6 h during their exponential phase of growth. The effects of 2-mercaptoethanol on centrosomes, chromosomes, microtubules, membranes and intermediate filaments were analyzed by transmission electron microscopy (TEM) and by immunofluorescence microscopy (IFM) methods using a human autoimmune antibody directed against centrosomes (SPJ),[1] and a mouse monoclonal antibody directed against tubulin (E7). Chromosomes were affected most by this treatment: premature chromosome condensation was detected in interphase nuclei, and the structure in mitotic chromosomes was altered compared to control cells. This would support previous findings in dividing sea urchin cells in which chromosomes are arrested at metaphase while the centrosome splitting cycle continues.[2] It might also support findings that certain sulfhydryl-blocking agents block cyclin destruction.[3] The organization of the microtubule network was scattered probably due to a looser organization of centrosomal material at the interphase centers and at the mitotic poles. Centrioles appeared to be normal exhibiting their regular microtubule pattern in a perpendicular orientation. Striking was the abundance of intermediate filaments in these treated cells.

These results demonstrate the requirement for reduction of disulfide groups to sulfhydryl group formation for proper progression of chromosome and other cyclical events during the cell cycle.

REFERENCES

1. R. Balczon and K. West, Cell Motil. Cytoskel. (1991) **20**, 121.
2. H. Schatten, M. Walter, D. Mazia, H. Biessmann, N. Paweletz, G. Coffe, and G. Schatten, Proc. Natl. Acad. Sci. (1987) **84**, 8488.
3. F.C. Luca and J.V. Ruderman, J. Cell Biol.(1989) **109**, 1895.
4. This research was supported by a grant from the German Cancer Research Center, Germany.
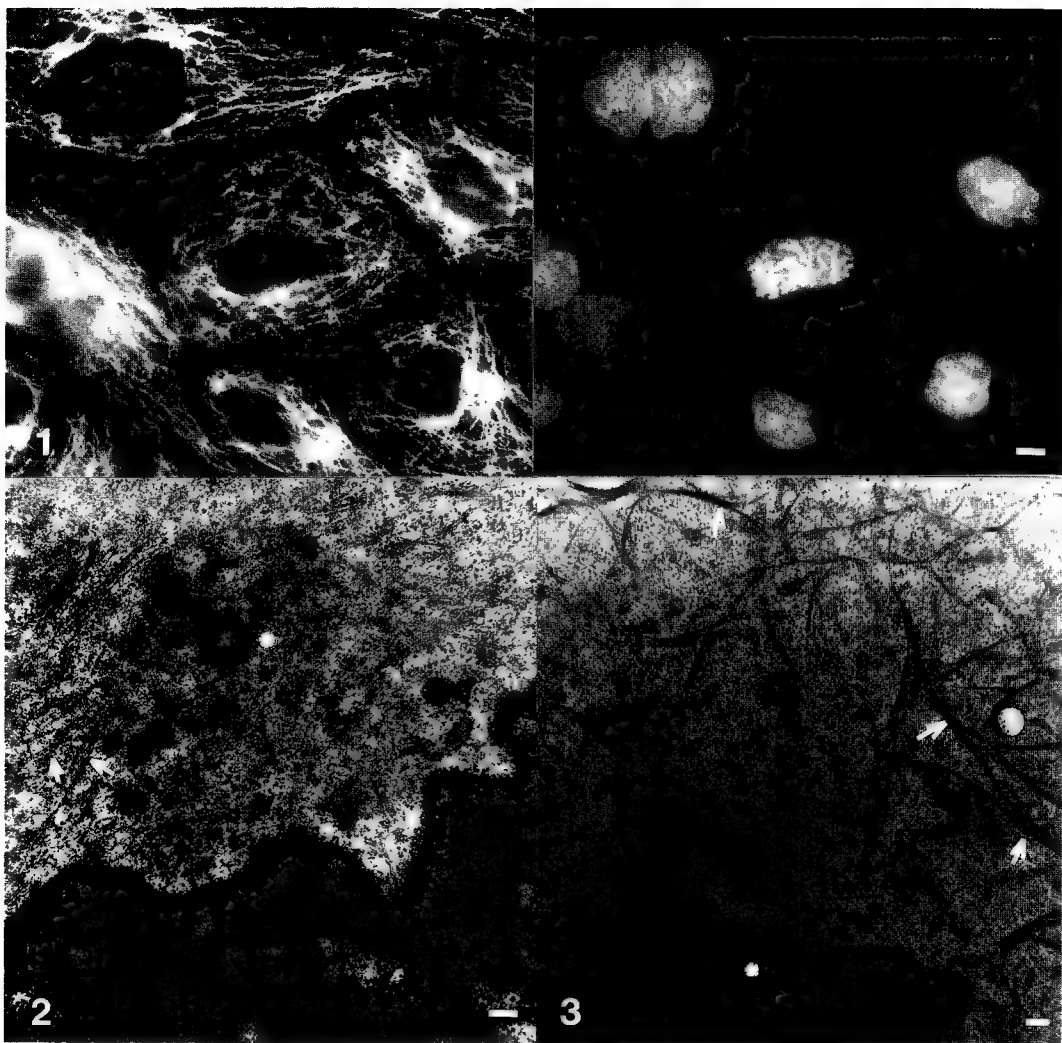
FIG. 1.-- LM of PTK$_2$ cells in interphase treated with 100 uM
2-mercaptoethanol for 4 h, stained for microtubules (left) and
DNA (right). Note that microtubule organization is without
distinct center normally associated with the nucleus (left),
and that chromosomes are prematurely condensed (right). Bar
= 1 μm.
FIG. 2.-- TEM of PTK$_2$ cell in mitosis treated with 100 uM 2-
mercaptoethanol for 4 h. Note the presence of microtubules
(arrows) and centrioles (asterisk). Bar = 0.5 μm.
FIG. 3.-- TEM of PTK$_2$ cell in mitosis treated with 100 uM 2-
mercaptoethanol for 4 h. Note the abundance of intermediate
filament bundles (arrows) and irregularities in chromatin
organization (asterisk). Bar = 0.5 μm.

LIGHT-MICROSCOPIC IDENTIFICATION OF GOLGI STAINING PATTERNS IN EMBEDDED BLOCKS OF
MUSCLE TISSUE PRIOR TO SECTIONING FOR ELECTRON MICROSCOPY

Noboru Fujimaki,* Lee D. Peachey,** and Harunori Ishikawa*

*Department of Anatomy, Gunma University, Maebashi, 371 JAPAN and **Department of
Biology, University of Pennsylvania, Philadelphia, PA 19104-6018, USA

The Golgi stain (1-2) is very useful for selective staining of membrane systems in
muscle cells, especially for HVEM and IVEM where thick sections can be examined and
three-dimensional information obtained. However, the staining intensity and
pattern are highly variable from preparation to preparation, among fibers in the
same preparation, and within individual fibers. Staining can be absent altogether,
or can involve the T-system (T) or the sarcoplasmic reticulum (SR) alone, or both T
and SR. Considerable time can be spent sectioning blocks and scanning the sections
in the electron microscope, searching for the desired staining pattern, sometimes
without success. We have found that examination of the trimmed face of an embedded
block under a dissecting microscope with oblique reflected light reveals a pattern
of colors in muscle fibers and parts of muscle fibers. The origin of the colors
and the reason that the different staining patterns show different colors are not
clear. Nevertheless, the colors can be related to the staining pattern that will
be seen in the electron microscope in sections cut from the same blocks, thus
facilitating trimming of the block to areas of interest, both saving time and
reducing the likelihood of missing rare staining patterns or paticularly
interesting parts of the embedding.

The specimens shown are frog (Rana temporaria) sartorius muscles prepared using the
three-cycle Golgi method (2). Figure 1 shows a black/white view of an entire block
face (color images are more informative). The smooth, light regions in Figure 1,
as in the fiber marked * and part of the fiber marked with the open star, are red,
and show staining of the SR in the electron microscope (Figures 2 & 3) and in high-
power light micrographs of sections (Figure 4). Less bright, mottled regions in
Figure 1, for example parts of the fibers marked with stars, are yellow in color
and correlate with staining of the T-system, without SR staining in micrographs of
sections (Figures 4 & 5). Many fibers and parts of other fibers appear black, and
these show no staining of either T-system or SR.

FIG. 1. Black/white light micrograph of a block face taken on Kodak TMAX film
using conical oblique illumination and a dissecting microscope at 45x. The
specimen is frog skeletal muscle, oriented for transverse sectioning. The size of
the block face is 1.5 x 0.8 mm.
FIGS. 2 & 3. Low magnification electron micrographs taken using a JEOL 4000-EX TEM
at 350 kV, showing a 1 micrometer thick section of the block face shown in Fig. 1.

References
1. E. Veratti, J. Biophysic. Biochem. Cytol. 10, sup. 3-59 (1961).
2. C. Franzini-Armstrong and L. Peachey, J. Histochem. Cytochem. 30, 99-105 (1982).
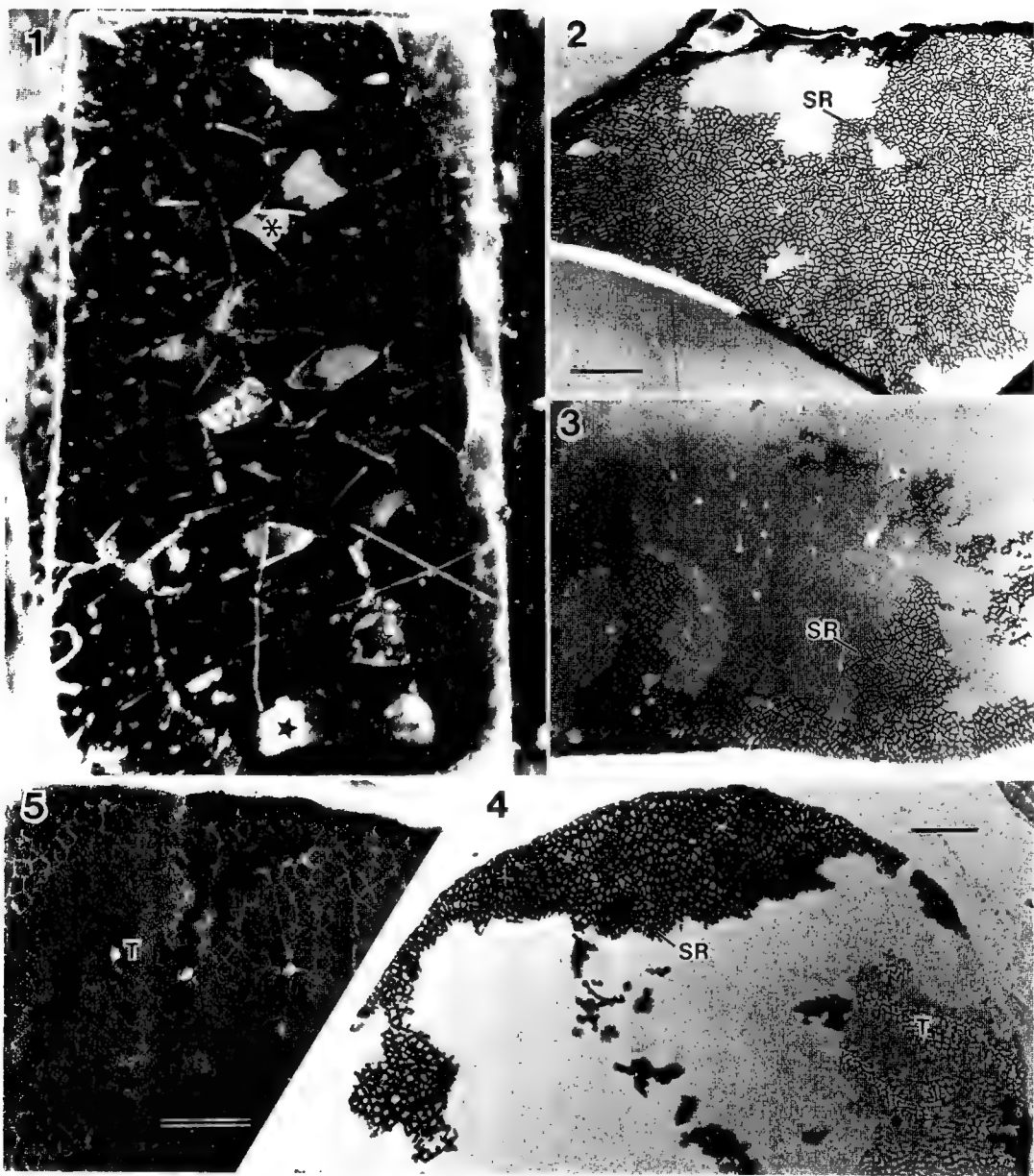
The fiber in Fig. 2 is marked with * in Fig. 1, and the fiber in Fig. 3 is marked with an open star in Fig. 1. Both fibers show staining of the SR in regions that appear red in the block face. Bar 10 micrometers.

FIG. 4. Light micrograph, 1 micrometer section, same fiber as Fig. 3, which shows both red and yellow colored regions in the block face. The yellow region corresponds to T-system staining in the EM. Bar = 10 micrometers.

FIG. 5. Higher magnification electron micrograph of part of the fiber marked with a closed star in Fig. 1, showing T-system staining. Bar = 5 micrometers.

A FREEZE-FRACTURE-ETCHED STUDY OF THE PHYSARUM POLYCEPHALUM PLASMA MEMBRANE DURING EARLY FORMATION OF THE MACROPLASMODIAL STAGE

Randolph W. Taylor and Henrie Treadwell, Ph.D.

Department of Biology, Electron Microscopy Section, Morris Brown College, Atlanta, Georgia. 30314 and The Kellogg Foundation, Battle Creek, MI. 48075

The plasma membrane of the Slime Mold, Physarum polycephalum, process unique morphological distinctions at different stages of the life cycle. Investigations of the plasma membrane of P. polycephalum, particularly, the arrangements of the intramembranous particles has provided useful information concerning possible changes occurring in higher organisms.[1,2,4] In this report Freeze-fracture-etched techniques were used to investigate 3 hours post-fusion of the macroplasmodia stage of the P. polycephalum plasma membrane.

Microplasmodia of Physarum polycephalum (M3C), axenically maintained, were collected in mid-expotential growth phase by centrifugation.[3] Aliquots of microplasmodia were spread in 3 cm circles with a wide mouth pipette onto sterile filter paper which was supported on a wire screen contained in a petri dish. The cells were starved for 2 hrs at 24°C. After starvation, the cells were feed semidefined medium supplemented with hemin and incubated at 24°C. Three hours after incubation, samples were collected randomly from the petri plates, placed in plancettes and frozen with a propane-nitrogen jet freezer. Frozen specimens were placed immediately in liquid nitrogen, fractured, etched and shadow-coated with platinum and carbon using the Blazars BAF 360. Following the cleaning of the replicas with sulfuric acid, and acetone, the replicas were washed several times in distilled water. The replicas were mounted on uncoated grids and examined with a Hitachi 300 transmission electron microscope.

A freeze-fracture-etched profile of a microplasmodia plasma membrane delineating the protoplasmic half (PF) and the extracellular half (EF) is shown in figure 1. Three hours post-fusion the macro-plasmodia reveal the formation of a tight junction (arrows) on the E-face between two microplasmodia cells (figure 2). Whether these cells are actually joined together during the macroplasmodia stages by tight junction require further investigations. The IMPs have similar morphological arrangements with few clusters (3 or more IMPs per cluster) on both cell plasma membrane extracellular half (figure 2). The IMPs at eight hours post-fusion were more numerous and the aggregations of particles were more evident.[3] Depressions are apparent throughout the macroplasmodia. These depressions seem to become more pronunced as fusion of the plasma membrane progresses. This supports the premises that IMPs can serve as indicators of increased plasma membrane component activity in communication with the environment and that it is possible to correlate IMP arrangement distribution and density with morphogenesis. In addition, probing the IMP structure and arrangement at different time points during the macroplasmodia formation may provide valuable clues to events

occurring at early – S, late – S and G$_2$ of the Physarum cell cycle.

1. Affolter, H. U., Behreno, K. Seebeck, T. and Brown, R. FEBS letters. (1970), Vol. 107, No. 2.
2. Shraideh, Z.et al. Cell Biology International Reports, (1982), Vol. 6. 851.
3. Taylor, R.W. and H.M. Turner, Proceedings. EMSA, 50th Ann. Meeting. p 866.
4. Turner, H., Hogan, T.C., J. Protozool. (1982), 29 (3), p 341-347.
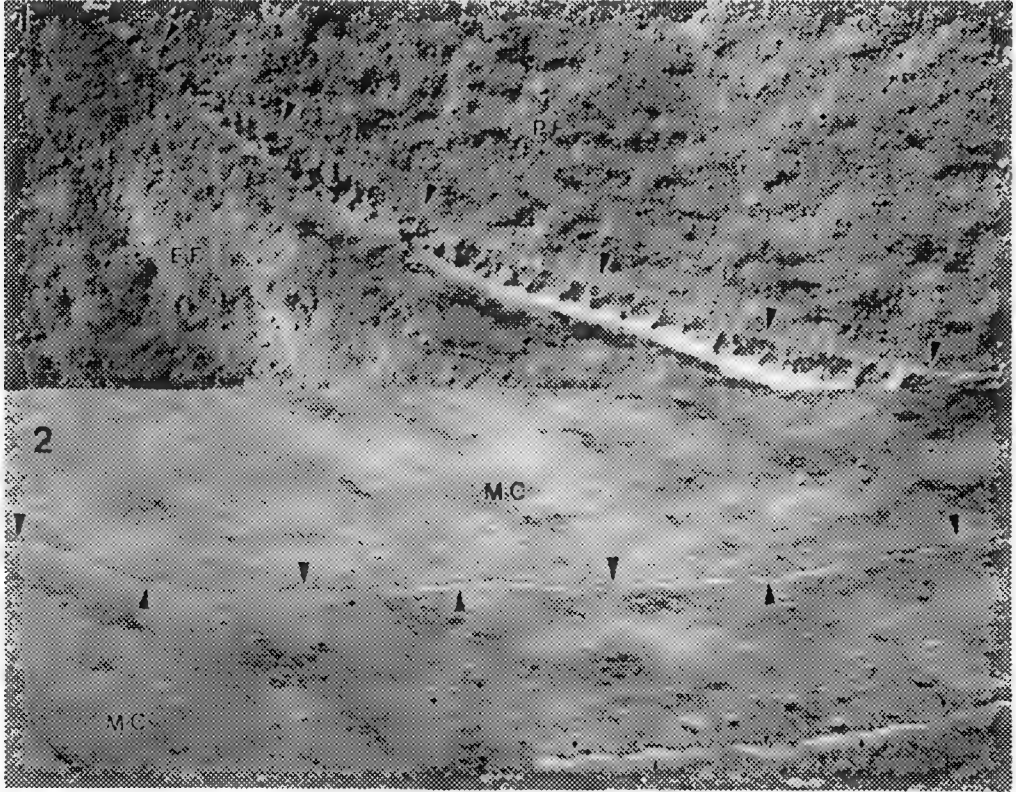
FIG. 1. Electron micrograph of a microplasmodial cell revealing both the protoplasmodic half (P-face) and the extracellular half (E-face). Intramembrane particles are more numerous on the protoplasmic half as compared to the extracellular half. X100,000.
FIG. 2. Electron micrograph depicting the formation of a tight junction between two microplasmodia cells extracellular half of the plasma membranes shown by arrows. X100,000. The inset reveals a high magnification of the tight junction. X208,000.

SOYBEAN CHLOROPLAST RESPONSES TO ENHANCED ULTRAVIOLET IRRADIATION

Richard F.E. Crang[1], Andrey E. Vassilyev[2], and Yevgeney A. Miroslavov[2]

[1]Department of Plant Biology, University of Illinois, Urbana, IL 61801, USA; and [2]Komarov Botanical Institute, 197376 St. Petersburg, RUSSIA

Environmental concerns over the degradation of the earth's stratospheric ozone layer have been expressed for the past decade in recognition that with ozone depletion, enhanced ultraviolet irradiation will be received at the earth's surface[1,2]. Such increase in ultraviolet irradiation can be hypothetically determined by making appropriate computer calculations based on proposed cloud cover, season, latitude, elevation, and percent of stratospheric ozone depletion. We have proposed a 40% reduction in the ozone layer corresponding to a daily increase of 19.1 kJ in the limits of ultraviolet-B (UV-B) spectral irradiation (280-320 nm). This is within the range of realistic possibilities based on current estimated ozone depletion rates for the next 40–50 years. We wish to determine the extent to which chloroplasts are ultrastructurally altered compared with those from plants raised under ambient conditions lacking an UV-B irradiation component.

Uninoculated seeds of soybean (*Glycine max*), cv. "Forrest" were sown in standardized greenhouse soil in 4" clay pots, watered daily, and fertilized once per week. The plants were divided into two groups of matching environmental conditions except that one group received supplemental UV-B irradiation as indicated above. The length of exposure was 8 hr per day, each day, from the time that seedling emergence was first noted until 22 days post-germination when the third trifoliate leaves had fully expanded. Interveinal leaf samples, 1×3 mm, were then taken from each of 12 plants from each group, and conventionally prepared for observation with light microscopy (LM) and transmission electron microscopy (TEM). All attempts possible were made in order to quantify the data as statistically significant and for comparison between the two groups, as well as in comparison with previous studies[3]. Magnifications with the TEM were standardized, as well as photographic enlargements. For additional purposes of standardization, only chloroplasts from upper palisade mesophyll cells were analyzed.

As illustrated in Figures 1 and 2, the morphology of the chloroplasts from the two groups shows that with enhanced ultraviolet irradiation, the size and shape of the chloroplasts changes. Additional observations were made in which the data was tabulated as shown in Table 1. Most of these structural changes were not evident from direct observations of the micrographs obtained. Starch grain numbers were reduced in the no-lamp control set of plants examined, and there were fewer numbers of plastoglobuli per plastid. In addition, the dimensions of chloroplasts from the UV-B treated group consistently showed greater size than that of control, and with noticeable invaginations taking the form of extensions and/or the inclusion of organelles such as mitochondria. Certainly, the results clearly indicate that a variety of sometimes subtle, although significant, changes are obtained including starch composition, the size and number of plastoglobuli, average maximum thylakoid number, and plastid shape and dimensions.

References

1. A.H. Teramura and M.M. Caldwell, Amer. J. Bot. (1981) **68**: 934-941.
2. S.D. Flint, P.W. Jordan and M.M. Caldwell, Photochem. and Photobiol. (1985) **41**: 95-99.
3. C.V. Allen and J.H. Garrard, Environ. and Expt. Bot. (1982) **22**: 465-473.

Table 1. Mean parameters (with standard errors as appropriate) of chloroplast measurements from TEM sections of upper palisade layer cells.

Character	No-Lamp Control	UV-Treated
Diameter of Plastoglobuli, µm	0.13±0.04	0.15±0.04
No. plastoglobuli/plastid	3.6±0.6	7.0±3.1
Surface fraction of starch, %	23.4	11.6
Max. thylakoid number	11±2.1	15±3.2
Long. axis chloroplast, µm	5.6	6.7
Trans. axis chloroplast, µm	1.8	2.1
Invaginations/plastid, %	6.0	35.0
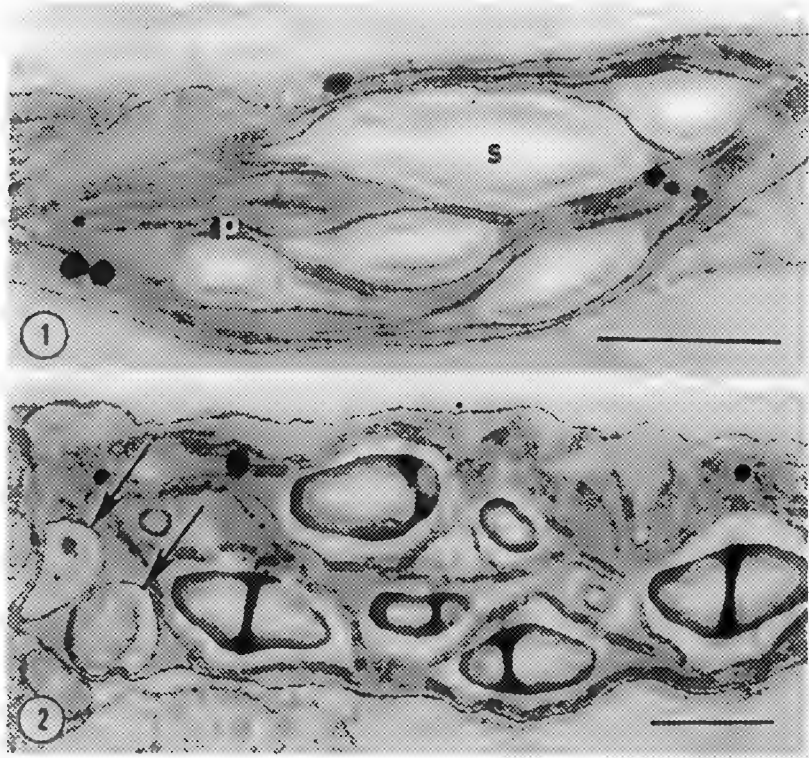
FIG. 1. Palisade chloroplast from no-lamp control set of *G. max* cv. "Forrest" plants, taken from 3rd trifoliate leaf. Simple, starch grains (S) are evident, along with plastoglobuli (p). The plastids typically have a regular shape with large amounts of stroma present containing a rudimentary system of thylakoid membranes and grana. Bar = 1.0 µm.

FIG. 2. Palisade chloroplast from *G. max* cv. "Forrest" plant (3rd trifoliate leaf) which has received enhanced UV-B irradiation from the time of germination. Overall size is greater than that of control (Fig. 1), and starch grains are more abundant, along with a more highly developed thylakoid system. Also note evidence of stroma invaginations (arrows). Bar = 1.0 µm.

STRUCTURE OF SEEDS AND DEVELOPING SEEDLINGS OF HYDRILLA VERTICILLATA

D. L. Holmberg and F. J. Ryan

USDA ARS Aquatic Weed Control Lab., Botany Department, University of California, Davis, CA 95616-8537

Until recently, it was believed that Hydrilla verticillata, a widespread aquatic weed, did not generally produce seeds. There were reports that the monoecious biotype from the U. S. was sometimes capable of producing viable seeds [1,2], although these were not described in any detail. Recent work at the USDA ARS Aquatic Weed Research Laboratory, Ft. Lauderdale, FL, identified a monoecious biotype of H. verticillata from Penang Island (Malaysia) that is self-fertile and reliably produces viable seed. This biotype may also be crossed with other biotypes including the female dioecious plant from Florida. This work was undertaken to describe the anatomical characteristics of seeds and developing seedlings, using light and electron microscopy.

Seeds and seedlings of the Penang Island biotype and Florida X Penang Island cross were processed for light and scanning electron microscopy (SEM). Fixed and fresh material was used. Seeds and seedlings were fixed in 2% paraformaldehyde and 0.1% gluteraldehyde in 0.1M phosphate buffer, pH 7.0. and dehydrated to 100% ethanol. Material for light microscopy was embedded in paraplast. Material for SEM was infiltrated in Peldri II© at 28°C. Sublimation to dryness was carried out at room temperature. Tissue was sputter-coated with gold for observation on a Hitachi SEM 4000. Other specimens were observed in the living state on a Hitachi S2250 N "Nature" SEM or on a Zeiss MC 63 stereomicroscope.

Seeds of Hydrilla verticillata were oval, brown-black and 0.5 mm by 2.0 mm. The seed coat had a dense network of coiled hairs (Fig. 1a) attached in a hexagonal pattern, coincident to the outline of the cells (Fig. 1b). The hairs extended from the seed coats (Fig. 1c) and promoted aggregation. This might provide more effective water dispersal. These hairs also might allow anchorage to a substrate. When seed tissue was stained with Amido Black 10B (Fig. 2), meristematic tissue in the embryo displayed high concentrations of protein, while cotyledonary tissue had lower concentrations. As the seedling elongated, the radicle emerged from the cotyledon and was surrounded by fine roots (Fig. 3). The cotyledonary pocket (Fig. 4) enlarged as the cotyledon extended. The first true leaf emerged from this pocket. Subsequently, more leaves grew out of this pocket to form the seedling. Leaves developed in whorls at nodal regions (Fig. 5a & b) to form the characteristic plant. The lack of structural tissue in seed hairs and seedlings from the aquatic habitat cause problems for conventional SEM, since the tissue collapsed and was distorted upon fixation and dehydration. Observations in the living state eliminated these problems. Some of this work has been previously reported. [3]

References
1. RD Conant, TK Van and KK Steward (1984) Monoecious hydrilla produces viable seeds in the United States. Aquatics 6: 10.
2. K Langeland and CB Smith (1984) Hydrilla produces viable seeds in North Carolina lakes-mechanism for long distance dispersal. Aquatics 6: 20-21.
3. DL Holmberg and FJ Ryan (1992) Structure and protein composition of seeds of Hydrilla verticillata Plant Physiol. 99S: 114.
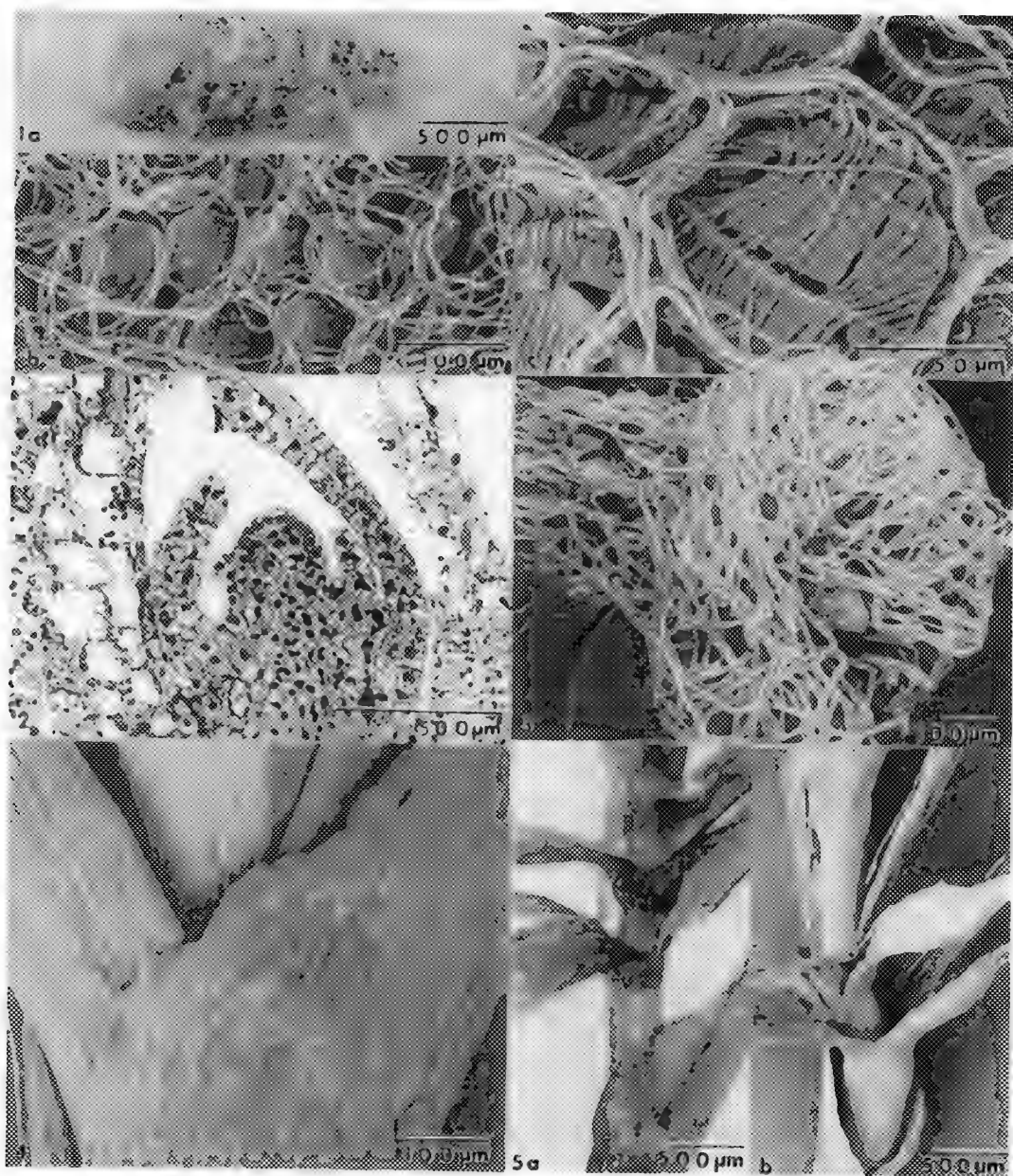
Fig. 1a Entire seed processed with Peldri II©. Image from a dissecting microscope.
    b SEM of a portion of a dry seed.
    c SEM of a portion of a living seed.
Fig. 2 Light micrograph showing apical meristem of germinating seed stained with Amido Black
Fig. 3 SEM of living seedling showing radicle surrounded by roots
Fig. 4 SEM of living seedling showing leaves extending from the cotyledonary pocket.
Fig. 5a Light micrograph of developing seedling.
    b SEM of live, developing seedling arising from the cotyledonary pocket.

UNDEVELOPED FIBERS: A SOURCE OF DYEING PROBLEMS IN COTTON TEXTILES

W. R. Goynes, B. F. Ingber, and D. P. Thibodeaux

USDA, ARS, Southern Regional Research Center, P.O. Box 19687, New Orleans, LA 70179

In the growth and development process of cotton fibers, during approximately the first 17 days only elongation of the primary wall structure occurs. As the elongation process is being completed, secondary layers of cellulose fibrils begin to be deposited within the primary wall to form the main body of the fiber. This developing wall provides the fibers with a dimensional rigidity. When the boll opens and the fibers dry, they are able to maintain a dimensional structure, as illustrated in figure 1. Samples of harvested cotton fibers normally contain fibers whose walls have completely developed, as well as some whose walls are thin because of a short development time. Fully developed fibers are referred to as "mature" and incompletely developed fibers are referred to as "immature." There may also be fibers that are essentially undeveloped beyond the primary wall stage. Undeveloped cotton fibers are produced by seed whose development was interrupted before maturity (motes). These undeveloped fibers may be considered immature, but are different from fibers commonly called immature in that they are composed only of a cuticle and primary wall. Little or no secondary layers are present. Because of their extremely thin walls, undeveloped fibers have no structural rigidity, and form flat ribbons when they dry from the boll (figure 2). These flat, thin-walled fibers often collapse upon each other, forming masses that are difficult to separate. Many of these adhering masses are sticky and also adhere to other materials during processing. These fibers are a problem because they do not blend or parallelize with other fibers during processing, and form bundles or knots that usually adhere to other fibers throughout processing. The primary wall of the fiber contains noncellulosic materials bound in a matrix of cellulose fibrils. However, the secondary wall makes up the main body of the fiber, and is considered to be pure cellulose. Undeveloped fibers have little secondary wall, and their very low cellulose content causes them to be unreceptive to cellulose dyes. Cotton textiles are dyed with cellulose dyes, and since bundles of undeveloped fibers do not accept cellulose dyes, these bundles were a logical suspect as a source of white specks that appear on darkly dyed textiles.

To confirm this premise, fabrics containing surface white specks were examined by scanning electron microscopy. Figure 3 shows an example of this surface imperfection. At this low magnification it simply appears as an unidentified mass. However, on examination at higher magnification, very thin undeveloped fibers similar to undeveloped fibers from motes were evident. It is possible to distinguish in the micrograph shown at figure 4 layers of fiber "shells" that are stuck together. In figure 5, a very immature fiber is seem lying diagonally across the mass, with an undeveloped fiber draped across it. The immature fiber is likely a fiber from a mote that has had some secondary wall layers deposited. The undeveloped fiber is so thin that even the small wrinkles on the surface of the immature fiber can be seen through it. This thin-walled fiber apparently adheres tenaciously to the surface of the other fiber, and this type of adhesion binds the bundle of undeveloped fibers into a larger mat with other fibers. It appears likely that these masses of undeveloped fibers are a source of the white specks that are present on the surfaces of some dyed cotton fabrics.
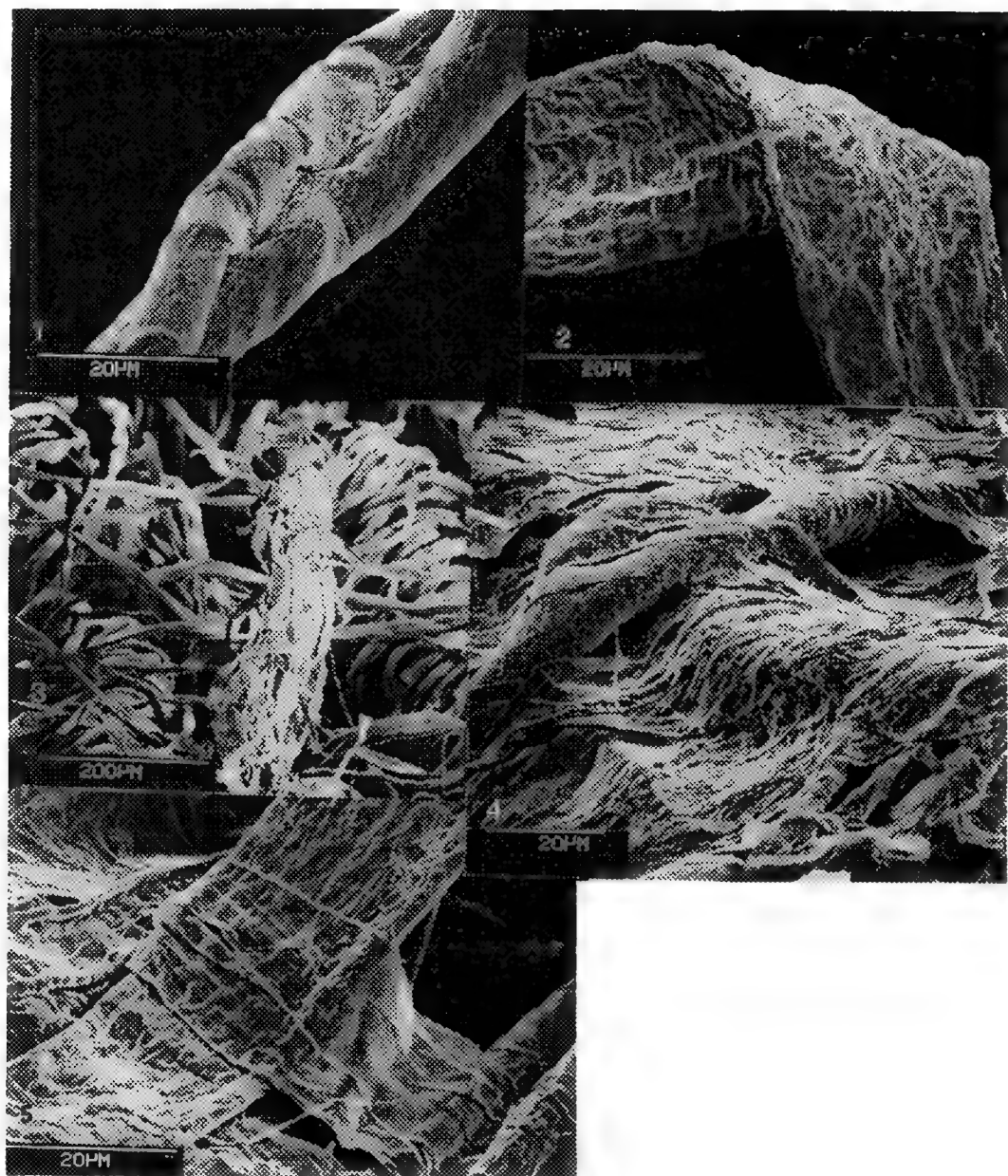
FIG. 1. Segment of a typical mature cotton fiber
FIG. 2. Ribbon-like undeveloped fiber
FIG. 3. Fabric with surface imperfection
FIG. 4. Mat of fiber shells composing imperfection
FIG. 5. Undeveloped fiber on surface of imperfection

FEMALE SEX STEROID INDUCED GALLBLADDER EPITHELIUM CHANGES AND GALLSTONE DEPOSITS IN FEMALE HAMSTERS: TEM AND SEM ASPECTS

S. Karkare *, J. Gilloteaux *, and T. R. Kelly **

* Dept of Anatomy and ** Dept of Surgery, Akron City Hospital, N E O U College of Medicine, Rootstown OH 44272

Approximately 1 million people in the United States alone develop gallstones each year. The incidence is higher in women than in men and the ratio being $4 \geq 1$. A correlation has also been suggested between oral contraceptives and cholelithiasis[1]. In addition, postmenopausal or cancer estrogen therapy has been reported to be a factor responsible for gallstone formation [2]. Female sex hormone receptors have been detected not only in the gallbladder musculature, but also in its epithelium [3]. As a follow up to experiments effectuated in the male [4] and the ovariectomized Syrian hamster [8], this report shows that, a combination of a low cholesterol diet with female sex steroid treatment contributes to the formation of gallstone-like deposits, while modifying the surface epithelium morphology. Syrian hamsters (F_1B strain, BioBreeders, Watertown MA) were housed under 12h light:12 h dark cycle, at 20 °C, fed Purina chow and water ad libitum. Several duration/treatment groups were studied, but this report will focus on data obtained with the group injected weekly with estradiol valerate (E weekly, s.c. 8-10 μg/100 g.b.w., in corn oil) and with i.m. medroxyprogesterone acetate (DepoProvera Upjohn Co., Kalamazoo, MI; 8-10 mg/100 g.b.w.) for a 3-month period. Other parameters (blood and bile) were also studied but not reported here.

In response to this treatment, apical and subapical accumulations of electron dense mucus granules are detected by TEM in the surface epithelial cells (Fig. 1 and insert). SEM of the fundic, body, and neck portions of the gallbladder epithelium provides a view of uniform microvilli which populate pleomorphic cell apices. Isolated areas show clusters of cell apices projecting blebs (0.5-1.0 to 4.0-5.0 μm) and instances of cellular excrescences and dead cell extrusions (Figs. 2-4)). Except for these changes and remnants of cell decapitation events, the epithelium appears unaltered, almost resembling the control group epithelium. The most striking feature however is the abundance of gallstone-like deposits of diverse morphology (triangular plate-like [Fig. 5] to amorphic with an uneven surface [Fig. 6]) and size (15 by 20 μm to 20 by 25 μm).

These observations, confirmed those obtained from other treatments, and from human cholelithiasis. A combined change in mucus and in bile quality, decreased contractility and cell sloughings to induce formation of cholelithiasis.

References

1. T. Jorgensen, Gut (1988) 29, 433.
2. M. Yamamoto, et al., Acta Pathol. Jap. (1990) 40, 14.
3. J. Gilloteaux et al., J. Submicrosc. Cytol. Pathol. (1993) in press.
4. J. Gilloteaux et al., Tissue and Cell (1992) 24, 869.
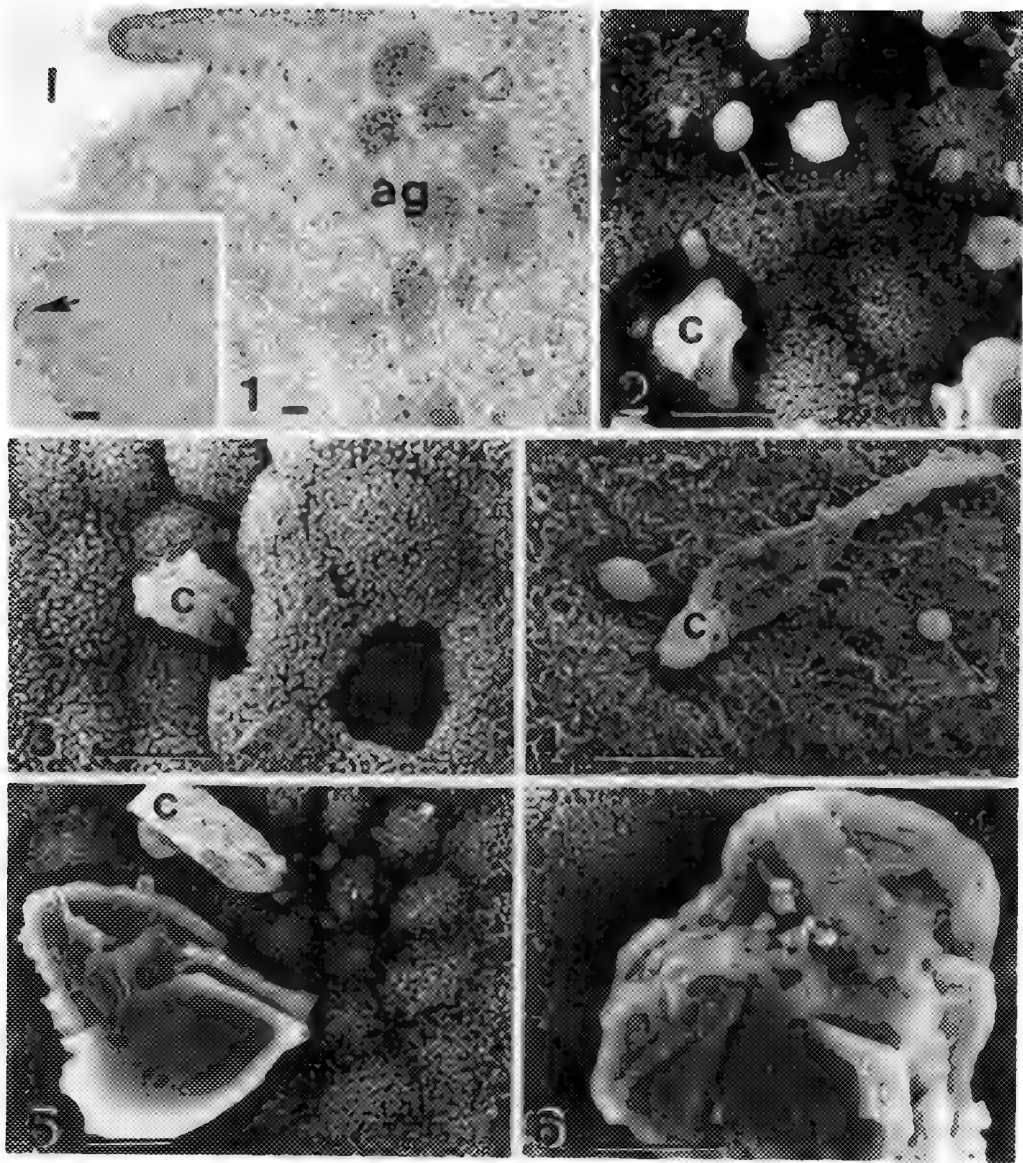
FIG. 1.--TEM depicting anionic apical granules (ag) and bulging (arrow in insert);
l: gallbladder lumen. Bar = 100nm; Bar in insert equals 1µm.

FIG. 2.--SEM of bulgings (arrowed), cell extrusions (c) and calculi. Bar equals 5µm.

FIG. 3,4, and 5--SEM of cell extrusions (c) and apical blebs (arrowed). Bars equals 5µm

FIG. 5 and 6:--Example of small showing plate-like (in 5) and heterogenous gallstones. Bars
= 5 µm.

ULTRASTRUCTURAL CHANGE OF THE CELL MEMBRANES ON MYOCARDIUM FOLLOWING TREATMENT WITH H_2O_2

Tatsuo Oguro[1], Kaoru Aihara[1], Kuniharu Aida[2], Goro Asano[2], Muhammad Ashraf[3]

Central Institute for Electron Microscopic Researches[1], The Second Department of Pathology[2],
Nippon Medical School, Tokyo 113 Japan
Department of Pathology and Laboratory Medicine, University of Cincinnati, Ohio 45267 USA[3]

It has been suggested that hydrogen peroxide (H_2O_2) is indirectly associated with postischemic-reperfusion injury of the heart. Previously, we reported that the heart was not damaged when perfused with exogenously generated superoxide anions. However, H_2O_2 which is a dismutation product of superoxide anion severely affected the heart structure and function[1], and the combined effects of H_2O_2 on membrane lipid and proteins result in the formation of membranous bleb.[2]

In this study, we evaluated the ultrastructural changes of the cell membranes in isolated rat hearts and cultured myocytes following treatment with exogenous H_2O_2. In the isolated hearts, $300\mu M$ H_2O_2 was perfused for 15 min and in the isolated cultured myocytes an equal amount of H_2O_2 was added to the culture medium for 30 min. This dosage of H_2O_2 was found to be injurious to the heart in our previous study. In the isolated cultured myocytes, $300\mu M$ H_2O_2 was added to the medium for 30 min. Both the hearts and the cultured myocytes were fixed in 2.5% buffered glutaraldehyde, post-fixed in 1% osmium tetroxide and processed for transmission and scanning electron microscopy.

In the isolated hearts, bleb formation and rupture of the cell membrane of the myocytes were seen. The cell membrane was lifted from the cytoplasm of cells. (Type I & II blebs)
Many blebs were seen in the interstitium between the myocyte and capillary(Type III blebs)[3]. On the other hand, the cultured myocytes showed many blebs which stemmed from the plasma membrane and were released into the medium in the form of soap bubbles.

These findings suggest that blebs originated from sarcolemmal membranes undergoing lipid peroxidation and these blebs appear to play an important role in "No-reflow" phenomenon commonly observed after ischemia/reperfusion.

References
1. S.Miki et al.; J Mol Cell Cardiol (1988) 20, 1009.
2. T.Oguro et al.; Am J Cardiovasc Path (1992) 4(3), 265.
3. M.D.Sage et al.; Am J Pathol (1988) 133, 327.
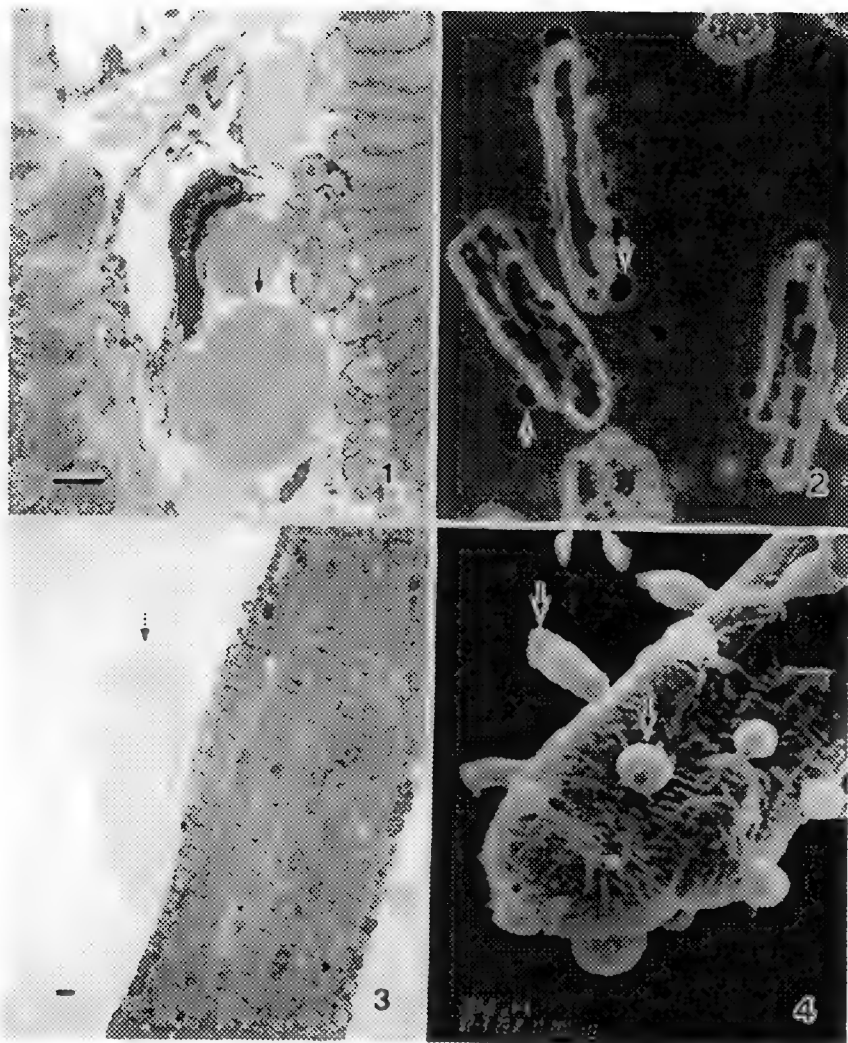
Fig 1. TEM of the isolated heart perfused with 300μM H_2O_2. Type III blebs were seen in the interstitium between the myocytes and capillary.

Fig 2. LM of the isolated cultured myocytes treated with 300μM H_2O_2.

Fig 3. TEM of the isolated cultured myocytes treated with 300μM H_2O_2.

Fig 4. SEM of the isolated cultured myocytes treated with 300μM H_2O_2.

EFFECT OF MATRIGEL ON DEVELOPMENT OF A549 LUNG EPITHELIAL CELLS

Yvonne Kress[1], Barry R. Bloom[2,3] and Kathleen A. McDonough[2,3]

Departments of [1]Pathology and [2]Microbiology and Immunology, and [3]Howard Hughes Medical
Institute, Albert Einstein College of Medicine, 1300 Morris Park Avenue,
Bronx, NY 10461

Extracellular matrix components are known to influence the growth and differentiation of cultured cells, often causing them to behave more like their *in vivo* counterparts than cells grown on plastic. To develop an *in vitro* model in which to study the interaction of pathogenic microorganisms with the lung epithelium, we have undertaken a morphological study of the effects of extracellular matrix components on the human lung alveolar epithelial cell line A549. A549 cells were grown for varying amounts of time on plastic; Costar polycarbonate membrane filter inserts; or on Matrigel coated polycarbonate filter inserts. Cells were fixed for 1 h in 2% glutaraldehyde in 0.1 M cacodylate buffer, post-fixed in 1% OsO4 for 45 min, dehydrated in ascending ethanol, and embedded in Spurr's resin.

A549 cells grown on a plastic slide formed an even monolayer with cells connected by well-formed junctional complexes or separated by interdigitating microvilli. The cytoplasm showed many polyribosomes, rough endoplasmic reticulum, small golgi complexes, mitochondria, occasional lysosomes and bundles of microfilaments. Cells grown on a polycarbonate filter for 4 to 5 weeks appeared mostly cuboidal with well defined basolateral and apical domains. Pseudopodia on the basolateral side inserted into the filter pores, and the apical side of the cells was lined with short microvilli (Figure a). In contrast to the cells grown on plastic, most of the cells contained large lysosomes, some secretory granules, and pools of particulate glycogen, but the junctional complexes were poorly developed (Figure e). Cells grown for 3 days on a Matrigel-coated filter formed several layers of interconnected flattened to cuboidal cells (Figure b). Microvilli covered the apical side of the cells, and some were connected with well-developed junctions (Figure f). Morphologically, these cells bore more resemblance to cells grown on plastic than to those grown on polycarbonate filters. After 5 days, the cells had undergone a dramatic structural reorganization, as they surrounded themselves with the extracellular matrix and appeared to form lumen with microvilli projecting into the luminal space (Figure c). Secretory granuoles were often seen near the apical surfaces of these cells, and a secreted substance was apparent in the luminal spaces (Figure g). Morphologically the cells resembled Clara cells with pools of glycogen, large lysosomes, microvilli and lipid droplets. After 21 days in culture, most cells maintained their cuboidal form, although some were elongated with long thin processes (Figures d and h).

These studies demonstrate that extracellular matrix components have a striking effect on the organization of A549 lung cells in culture, causing them to form alveolar-like structures *in vitro*. Additional studies will include biochemical and histochemical analyses of these cells, as well as examination of the effects on cell development of varying media components.

Figure Legends:
    a, e: A549 cells grown on Costar polycarbonate filter inserts for 35 days. F denotes filter side of cells. Bar = (a) 10 and (e) 1 micron.
    b, f: A549 cells grown on matrigel (M) coated filters for 3 days. Note microvilli and junctional complex at apical side. Bar = (b) 10 and (f) 0.5 micron.
    c, g: 5 day culture of A549 cells on Matrigel coated filter. F = filter; M = Matrigel; L = luminal space; G = glycogen pools; and S = secretory granules. Bar = (c) 10 and (g) 1 micron.
    d,h: 21 day culture of A549 cells on Matrigel coated filter. Bar = (d) 10 and (h) 0.5 micron.
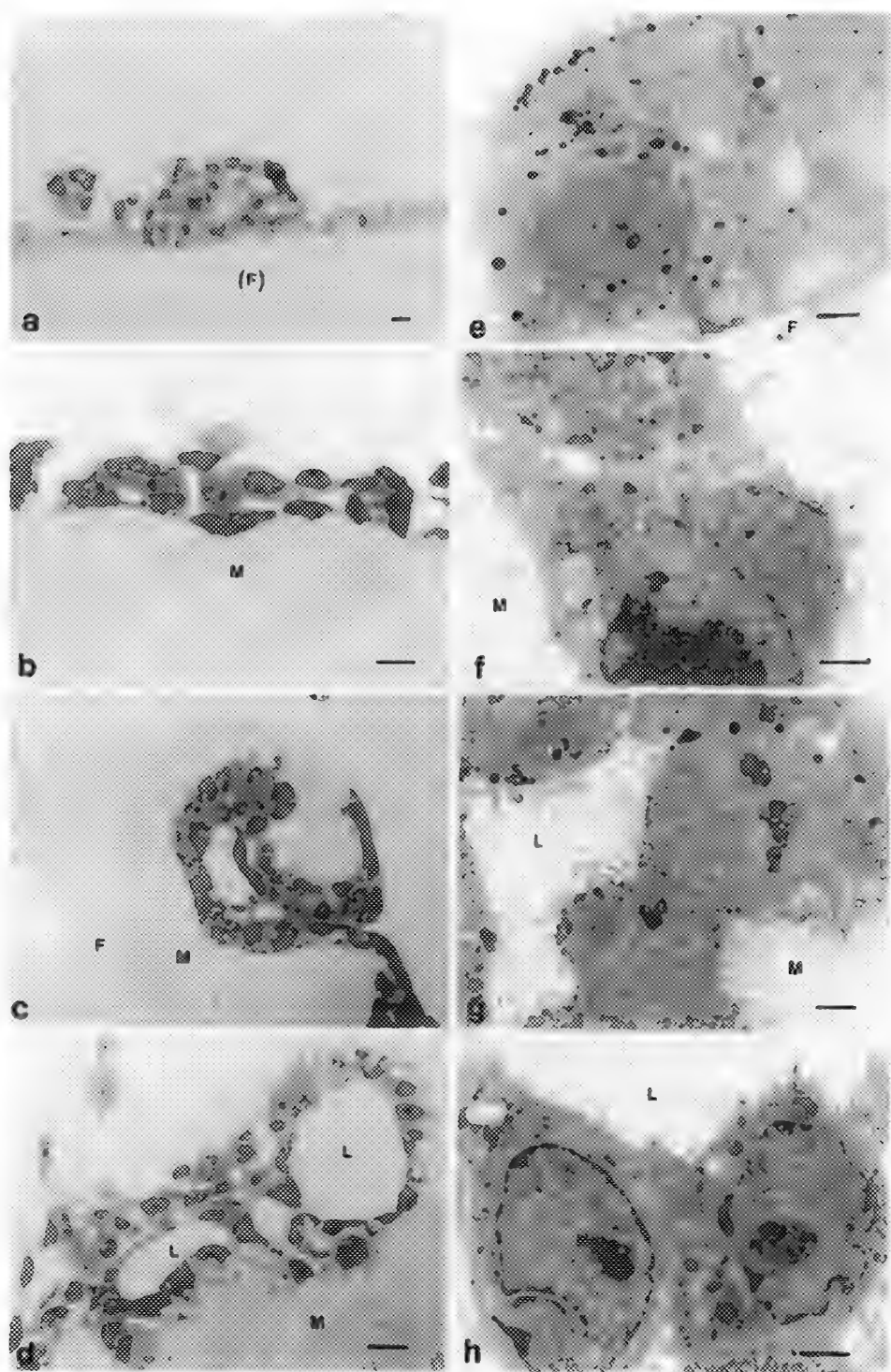
ULTRASTRUCTURAL STUDY OF BASEMENT MEMBRANE RE-FORMATION AFTER INTIMAL
DENUDATION

Munehiro Yokoyama, Toshiyuki Ishiwata and Goro Asano

Department of Pathology, Nippon Medical School, Tokyo, Japan

The basement membrane (BM) underneath the endothelial cell(EC) layer plays
important roles in the maintenance of cell polarity and the regulation of
cell migration, adhesion, proliferation and differentiation(1, 2). The model
of denudation of the aortic intima with a balloon catheter is useful in
research into interactions among cell components and extra-cellular matrix in
the regenerative process of ECs in atherogenesis. In this study, re-formation
of BM was examined during re-endothelialization after intimal denudation,
using transmission electron microscopy.

Male Wistar rats, weighing about 400 g were used and endothelial denudation
of the thoracic aorta was performed with a vascular balloon catheter (1.5 Fr.,
DOW CORNING, CORP). The catheter was inserted into the thoracic aorta via the
left common carotid artery. After inflation of the balloon with saline
solution, the catheter was passed through the length of the aorta about 2.5
cm three times. The animals were sacrificed at 15 min, 3, 7, 14, 21 and 28
days after endothelial denudation and the thoracic aortas were removed. For
transmission electron microscopy, aortic tissues were fixed in 2.5%
glutaraldehyde in 0.1 M cacodylate buffer (pH 7.3), post-fixed in 1% osmium
tetroxide and embedded in Epon 812 after dehydration in a graded ethanol
series. Ultrathin sections were placed on the nickel grids and stained with
uranyl acetate and lead citrate. To make the BM structure conspicuous,
periodic acid-thiosemicarbazide gelatin-methenamine silver (PATSC-GMS)
staining was performed according to the method originally described by
Namimatsu(3). Observation was performed using a Hitachi H-7100 transmission
electron microscope.

Although the luminal surface of the aortic wall was covered by round-shaped
regenerating ECs by 7 days after intimal injury, no continuous BM structure
was detectable until 21 days. PATSC-GMS staining demonstrated the
accumulation of BM components underneath the regenerating ECs at 14 days
(Fig1). A continuous BM structure firstly appeared at 21 days after intimal
removal and was almost complete by 28 days(Fig2,3). Simultaneously, the
regenerating ECs became flattened in shape and attached more closely to the
BM compared with earlier phases. These findings suggest production of the BM
components by the regenerating ECs and a role of re-formed BM in the growth
and differentiation of regenerating ECs.

References
1.D.S.Grant, P.I.Lelkes, In Vitro Cell Dev. Biol. (1991) 27A,327.
2.K.Kubota, H.K.Kleinman, J. Cell Biol. (1988) 107, 1589.
3.S.Namimatsu, J. Submicrosc. Cytol. Pathol. (1988) 24, 19.
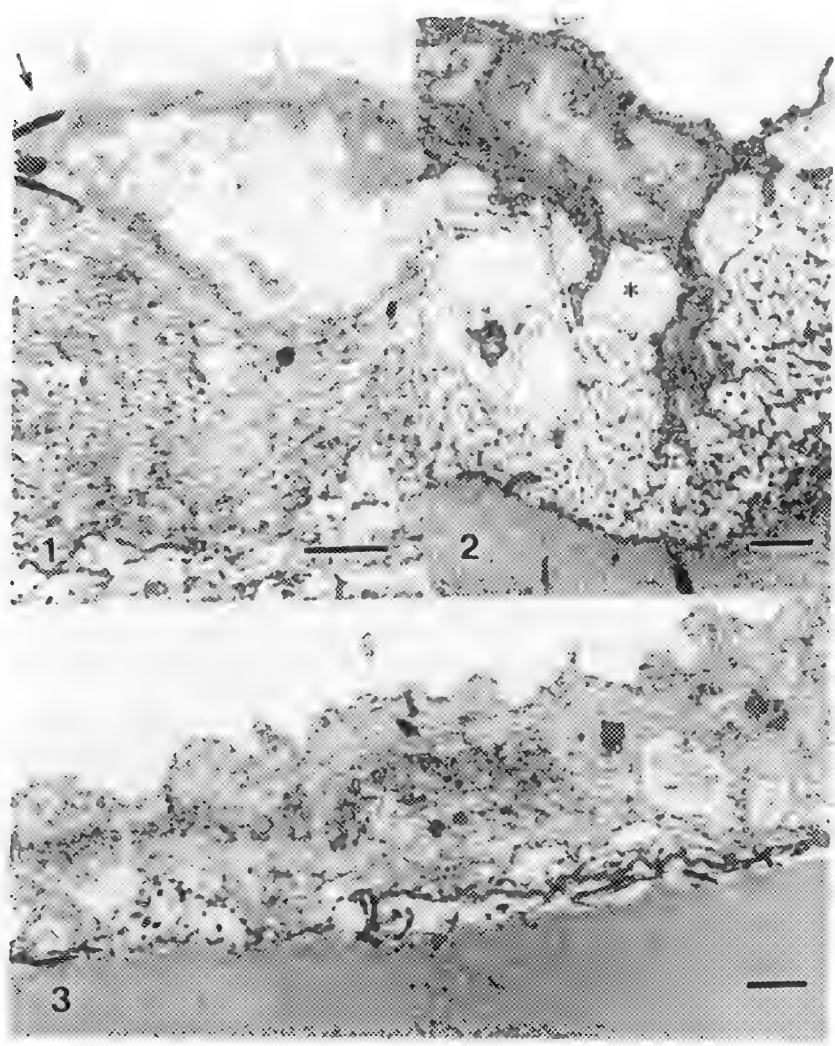
Fig 1 Electron microscopic findings at 14 days after intimal denudation. PATSC-GMS staining. The cytoplasm of regenerating cells bulges toward the lumen and frequently containes Weibel-Palade bodies (arrow). Increased subendothelial matrix consists of irregularly accumulated PATSC-GMS-positive materials. Bar: 1 μm.

Fig 2 Electron micrographs obtained at 21 days after intimal injury. PATSC-GMS staining. The regenerating ECs extend cytoplasmic processes toward the elastic lamina. Bar: 1 μm.

Fig 3 The density of PATSC-GMS-positive materials has become more rarefied than on day 14 in the upper layer of the subendothelial space (*).
A partially continuous BM structure is evident just above the elastic lamina. Bar: 1 μm.

COLLAGEN RATIOS IN EXERCISE-TRAINED AND PRESSURE-OVERLOADED RAT HEARTS

ML Burgess, RL Price, *FL Abel, GP Jones, *J Buggy, L Terracio and TK Borg

Depts. of Developmental Biology & Anatomy and *Physiology, School of Medicine, University of South Carolina, Columbia, SC 29208

The cardiac extracellular matrix (ECM) is composed of components known to affect cardiac function. Specifically, collagens (types III and I) provide a network integral to cardiac myocyte metabolism and function. Collagens promote the recoil action following contraction and maintain vascular patency during contraction. Chronic pressure-overload adversely affects cardiac compliance and function, and ultimately leads to heart failure. Fibrosis is common in pressure-overloaded hearts, partially accounting for the ventricular "stiffness" and reduced function. Chronic exercise training, however, is identified by enhanced cardiac function. Currently, little is known about ECM cellular biology and of exercised hearts and its relationship to cardiac function (1). This study examined the morphology, biochemistry and function of chronically exercised versus pressure-overloaded rat hearts to further delineate the role of the ECM in cardiac function.

Male Sprague-Dawley rats were adapted to treadmill running and randomly divided into four groups: coarctation of abdominal aorta (Coarc) to induce pressure-overload, sham operated and sedentary controls (Cont) and exercise-trained (XT). After 12 wk, all animals were anesthetized and subjected to cardiac functional measurements. A carotid pressure transducer was advanced into the left ventricle (LV) for pressure measurements. Another catheter was placed in the left brachial artery for measurement of arterial pressure. Chronotropic stimulation was achieved by a 3 ug/mg dose of isoproteronol infused via brachial vein catheter. LV and arterial pressures were recorded before, and at various timepoints after drug infusion. A Codas software program converted LV pressure to the derivatives $\pm$dP/dT (maximal change in pressure/time). The heart was then excised, rinsed in buffer, trimmed and sectioned. LVs were either prepared for TEM by routine methods, or frozen for hydroxyproline (OH-P) and collagen types III and I analysis. OH-P was analyzed by colormetric analysis. Collagen types III and I were separated by non-interrupted SDS-PAGE with negatively charged reduced, thioglycolic acid. Stained gels were subjected to scanning densitometry. Pearson's correlations were used to analyze the relationship between collagen type ratio and -dP/dT. Statistical significance was achieved if $p < 0.05$.

TEM showed a marked increase in collagen in Coarc vs XT and Cont hearts (Figs 1-2). OH-P analysis of total collagen content confirmed the increase in Coarc (3.9 vs 2.4 ug/ml in Cont). The collagen type III:I ratio was decreased in Coarc (0.54) and maintained in XT (0.82) vs. Cont (Fig 3), which may indicate an increase in type I collagen in Coarc. Diastolic compliance (-dP/dT) was greater in XT than in Coarc and Cont (Fig 4), which indicates a greater relaxation capacity in XT hearts. Correlational analysis of collagen type III:I ratio and -dP/dT exhibited a statistically significant negative correlation ($r = -0.90$, $p < 0.05$).

Chronic pressure-overload and exercise training result in selective adaptations by the heart. Specifically: 1) chronic run training maintains the ratio of collagen types III and I in the heart with no change in overall collagen; 2) chronic run training enhances diastolic function as evidenced by greater relaxation capacity; 3) chronic pressure-overload results in a lower cardiac collagen III:I ratio; 4) chronically pressure-overloaded hearts exhibit impaired diastolic relaxing function, as evidenced by decreased -dP/dT; and 5) an association exists between cellular collagen adjustments and myocardial functional parameters in both chronic exercise and pressure-overload. These data suggest an important role for ECM components in cardiac adaptation to exercise and pressure-overload.

References

1   Thomas, DP et al. *Am J Physiol* 263 (*Heart Circ Physiol* 32):H778-H783, 1992.
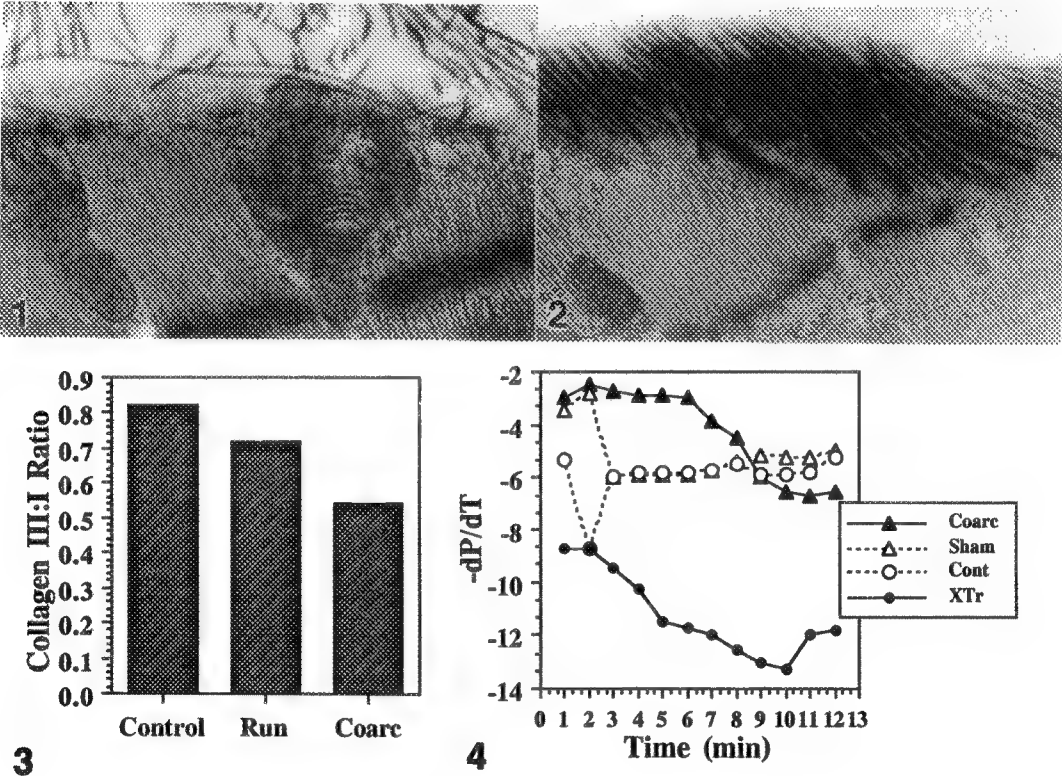
Figure Legends

Fig 1-2   TEMs of LVs from XT (1) and Coarc (2) animals. Collagen content was greater in Coarc than in XT or Cont.

Fig 3   Collagen type III:I ratio was lower in the Coarc hearts vs XT and Cont.

Fig 4   Ventricular relaxation capacity (-dP/dT) was markedly increased in XT and attenuated in Coarc vs Cont.

CONFOCAL AND ELECTRON MICROSCOPY OF CULTURED CARDIAC MYOCYTES

D.G. Simpson, R.L. Price, M. Terracio, L. Terracio, T.K. Borg

Department of Developmental Biology and Anatomy, School of
Medicine University of South Carolina, Columbia, SC 29208

Early in heart development cardiac myocytes are spherical in shape,
intercellular junctions are distributed at irregular intervals
around the periphery of the cell, and myofibrillar organization is
essentially random. As myocytes mature, they undergo extensive
morphogenesis during which the phenotype changes to a tubular rod-
like shape, cell junctions congregate at the distal ends of cells
to form intercalated disks, and myofibrils become organized in
parallel arrays typical of striated muscle. Although not fully
understood, it is known that these changes are a result of
interactive processes between intracellular components of the
cytoskeleton, integrin membrane receptors, and the extracellular
matrix (ECM).

In vivo studies on the process of cardiac myocyte maturation and
myofibrillogenesis are difficult because of the complex biochemical
environment of the intact animal and the many extra- and
intracellular interactions which are required for proper
development and myofibrillogenesis. Unfortunately, in previously
available in vitro modelling systems, isolated myocytes spread out
over the culture substratum, assume a stellate nonpolar shape, and
myofibril organization remains essentially random. Although
considerable information on the process of myofibrillogenesis has
been obtained from these culture systems (1), comparison of data
with in vivo development of cardiac myocytes is difficult due to
organizational differences in the developing cells.

We have recently developed an aligned thin collagen gel culture
system in which isolated cardiac myocytes develop a phenotype
similar to the in vivo situation (2). For confocal microscopy,
cultured myocytes were fixed for 10 min in 2% paraformaldehyde in
Sorensen's phosphate buffer, extracted for 10 min in 0.5% triton,
and stained for localization of vinculin, actin, laminin, and β-1
integrin. Cells were washed in PBS and counterstained with goat
anti-rabbit antibodies conjugated with Texas red or FITC. For
electron microscopy, cells were fixed in 2.5% glutaraldehyde in
Sorensen's phosphate buffer, rinsed in buffer, post fixed in 2%
OsO_4, dehydrated in ethanol, and embedded in Poly/Bed 812.

After 24 hours in culture, myofibrils were primarily in the central
areas of the cells and filaments extended into developing cell
processes. Confocal microscopy indicated vinculin was in the
developing Z-disks in the central areas of the cells, and β-1
integrin and laminin were localized in distinct patches on the
sarcolemma. These staining patterns are similar to those seen in
developing myocytes in vivo (3). By 96 hours, myocytes were

elongate, arranged in parallel arrays and cultures had established a coordinated rhythmic beating pattern. Myofibrils were organized in the long axis of myocytes and had well developed Z-bands and intercalated discs (Figs 1,2). Laminin and β-1 integrin distribution was more extensive than in earlier stages and was in a relatively uniform pattern along the sarcolemma which is similar to the staining pattern of adult myocytes in vivo (Figs 3,4).

These results indicate the phenotype of myocytes cultured on thin collagen gels closely resembles that of in vivo myocytes. This system will provide an improved in vitro model for controlled investigation of the intrinsic and extrinsic factors which affect cardiac myocyte morphogenesis.

REFERENCES

1. Hilenski, LL. et al. 1991. Cell Tiss Res 264:577-587.
2. Simpson, DG. et al. Submitted. Circ Res.
3. Price, RL. et al. 1992. J Histochem Cytochem 40:1373-1381.
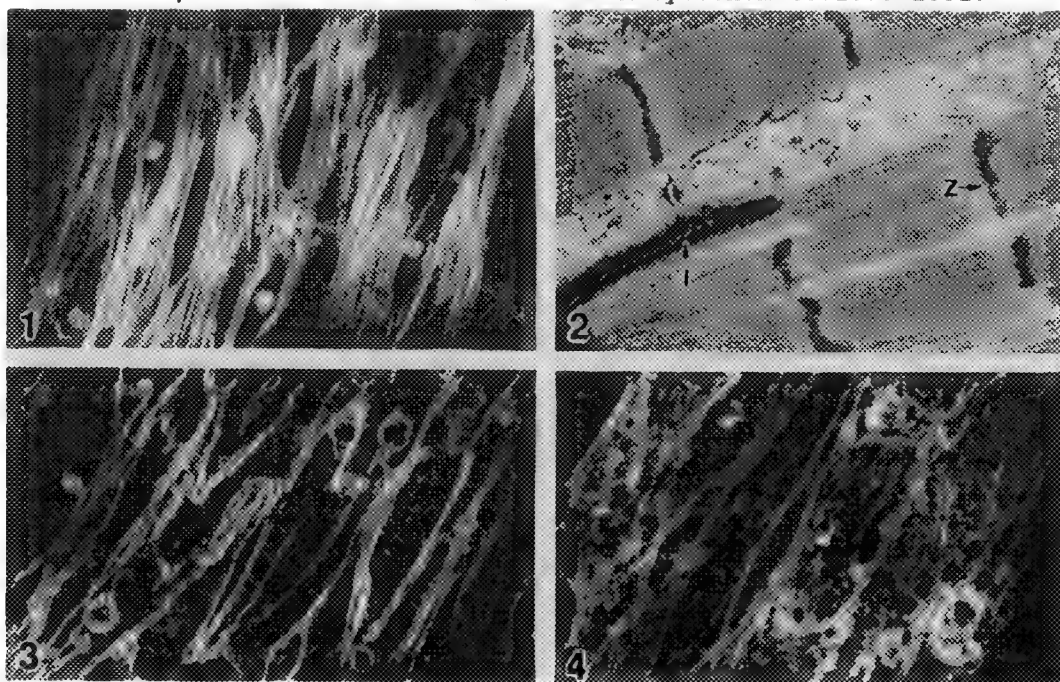
Figure 1. Confocal micrograph of cardiac myocyte from 96 hour collagen gel culture stained for actin. Myocytes are aligned in parallel and Z-bands are well developed.
Figure 2. Electron micrograph of cardiac myocytes from 96 hour collagen gel culture showing well developed Z-bands (Z), intercalated disks (I), and organization of myofibrils.
Figures 3-4. Confocal micrographs of cardiac myocytes from 96 hour collagen gel culture showing distribution of β-1 integrin (3) and laminin (4) along sarcolemma.

COMPARATIVE STUDIES OF ALARIA AND DIPLOSTOMUM METACERCARIAE USING SCANNING ELECTRON MICROSCOPY

M. Ujiie *, R. A. Heckmann *, and J. S. Gardner **

* Department of Zoology, WIDB 109, Brigham Young University, Provo, Utah 84602; ** Electron Optics Lab, 128 WIDB, Brigham Young University, Provo, Utah 84602

Two species of metacercariae belonging to the genera Alaria and Diplostomum were obtained from lizards in Mexico and fish in Peru. Alaria was found in the lungs of Scleroporus grammicus (Mesquito lizard) and Diplostomum was in the intestines of Orestias agasii (Carachi). To study the taxonomy and morphology of these two parasites, their integuments were compared using SEM.

The parasites were fixed in 10% formalin, transferred into 2.5% glutaraldehyde and kept in 70% ethanol to be sent to Brigham Young University. Specimens were dehydrated to 100% ETOH and critical point dried [1]. Samples were mounted on stubs using double-stick tape and were coated with approximately 30 nm of gold. The two species were compared using SEM.

The integuments of the two species of metacercariae exhibited major differences. In order to achieve maximum absorption, modification of the surface area of primitive parasites is more extensive than in subsequent species. Alaria was uniformly covered with microvilli -- characteristic seen in many of the trematodes -- including its anterior sucker region [2] (Fig. 1, 3). The folded integument of Diplostomum, however, was covered with rough projections and numerous pores (Fig. 2, 4, 5). Specific to the integument of Diplostomum were surface structures arranged in spirals which may be sensory regions [3] (Fig. 5). These were evenly spaced over the complete surface of the metacercariae. These "sensory regions" will be further analyzed with TEM.

References

1. M. T. Posteck et al., Scanning electron microscopy, Ladd Research Industries (1980)115.
2. M. Katz et al., Parasitic Diseases, Springer-Verlag (1989) 95.
3. M. S. Alyousif, Ann. Zool. (Agra). (1986)24, 1.
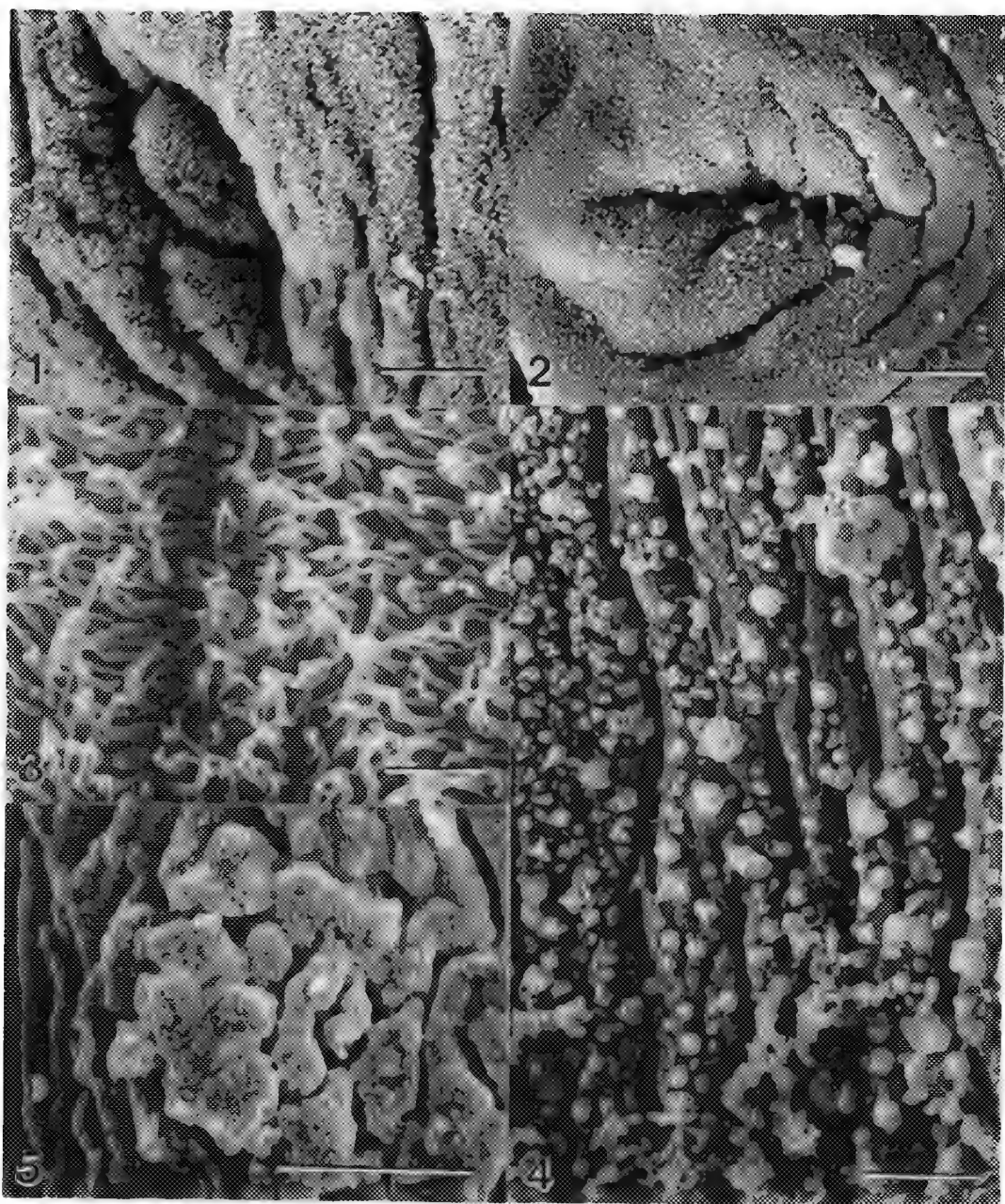
Fig. 1 Anterior sucker of *Alaria* covered with microvilli. Bar = 10 μm.
Fig. 2 Anterior sucker of *Diplostomum*. Bar = 10 μm.
Fig. 3 Numerous microvilli on the integument of *Alaria*. Bar = 1 μm.
Fig. 4 Integument of *Diplostomum*. Many folds are present. Bar = 10 μm.
Fig. 5 Spiral structures observed on *Diplostomum*. Bar = 1 μm.

ADHERENCE OF ENTEROTOXIGENIC *KLEBSIELLA PNEUMONIAE* TO HELA CELLS AND EXPRESSION OF TYPE 3 FIMBRIAE

M.D. Miliotis, B.D. Tall, R.T. Gray, and R.H. Hall. Food and Drug Administration, Washington, DC 20204

In 1986, an outbreak of diarrheal disease in Texas was attributed to contaminated iced tea in which *Klebsiella pneumoniae* was the predominant flora. Although the ten strains tested were of different serotypes, they all produced a heat labile enterotoxin[1]. Some of these enterotoxigenic strains (ETKP) also exhibited mannose-resistant hemagglutinins, which were later found to be type 3 MR/K fimbriae[2]. In this study we extended our observations and investigated fimbrial expression, as well as HeLa cell adherence behavior, using negative staining, immunogold labeling, and scanning electron microscopy (SEM).

ETKP strains were grown on colonization factor antigen agar overnight at 37° C for expression of fimbriae. The presence of fimbriae and immunogold labeling of the cells was determined as described by Wolfe *et al*[3]. Antiserum was prepared against purified fimbriae in rabbits and dilutions of primary and secondary antibodies (goat anti-rabbit IgG conjugated with 10 nm gold particles) in phosphate buffered saline, pH 7.2, containing 1% bovine serum albumin and 0.5% Tween 20 were used to label cells. Samples were prepared for negative staining by contrasting with 1% sodium phosphotungstatic acid (PTA), pH 7.2, prior to examination with a Philips 400 HM transmission electron microscope operating at an accelerating voltage of 80 kV. Adherence studies were performed with monolayer cultures of HeLa cells grown on 13-mm glass coverslips. The monolayers were infected with ETKP ($\sim 10^8$ cells/ml) either alone or in the presence of mannose. The infected cells were incubated for 3 hours at 37° C, washed, fixed in 4% paraformaldehyde/1% glutaraldehyde in 0.2 M sodium cacodylate, pH 7.2, and processed for scanning electron microscopy by standard methods[4]. The coverslips were evaluated in an ISI super IIIA SEM, operating at an accelerating voltage of 15 kV.

Negative stain results (Figs. 1 and 2) showed an abundance of rigid, 4-6 nm fimbriae radiating from the cell surfaces. Differences in fimbrial expression among similarly cultured ETKP strains and the known MR/K expressing type strain, IA565 were noted (compare Fig. 1 with Fig. 2). Immunogold labeling results showed immune complexes, recognizing fimbriae in "railroad rail fashion" in the homologous labeling reaction (Fig. 3). However, the heterologous immune reaction shown in Fig.4, displayed a more random labeling pattern, suggesting minor fimbrial antigenic differences expressed by these strains. SEM results showed that the strains adhered to the surface of the HeLa cell in a localized mannose-resistant manner (Fig. 5). These data indicate that structurally similar fimbriae expressed by some ETKP strains may possess minor antigenic differences and that fimbriae may play a role in adherence.

1. M. D. Miliotis *et al*, Abstr. Annu. ASM Meeting (1990), 44.
2. M. D. Miliotis *et al*, Abstr. Annu. ASM Meeting (1993), Submitted.
3. M. K. Wolfe *et al*, Infect. Immun. (1989) 57, 164.
4. B. D. Tall *et al*, Proc. Annu. EMSA Meeting (1992), 882.
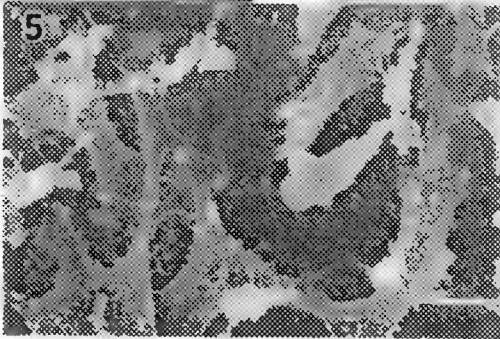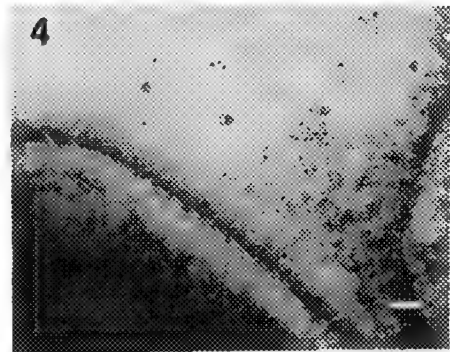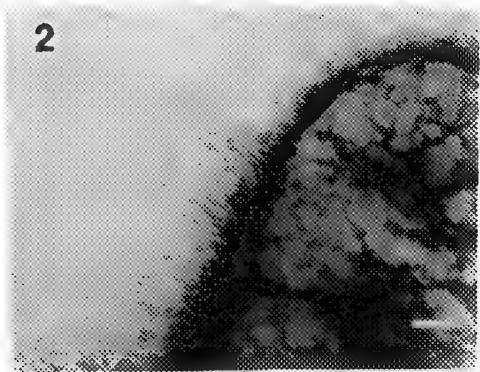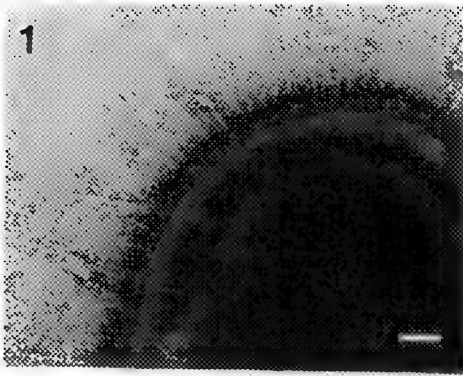
Fig. 1.--Enterotoxigenic *Klebsiella pneumoniae* strain K7 negatively stained with 1% sodium phosphotungstate, pH 7.2. Bar maker = 0.1 μm.

Fig. 2.--MR/K expressing *Klebsiella pneumoniae* type strain IA565 negatively stained with 1% sodium phosphotungstate, pH 7.2. Bar maker = 0.1 μm.

Fig. 3.--Enterotoxigenic *Klebsiella pneumoniae* strain K7 labeled by immunogold technique. Primary antibody was anti-K7 fimbriae diluted to 1:500. Secondary antibody dilution was 1:10. Cells stained with 1% sodium phosphotungstate, pH 7.2. Bar marker = 0.1 μm.

Fig. 4.--Enterotoxigenic *Klebsiella pneumoniae* strain K5 labeled by immunogold technique. Primary antibody was anti-K7 fimbriae diluted to 1:500. Secondary antibody dilution was 1:10. Cells stained with 1% sodium phosphotungstate, pH 7.2. Bar marker = 0.1 μm.

Fig. 5.--SEM of enterotoxigenic *Klebsiella pneumoniae* strain K7 adhering to the surface of HeLa cell in localized fashion. Bar marker = 10 μm.

HIGH-RESOLUTION SEM STUDIES OF THE ATTACHMENT OF GIARDIA TROPHOZOITES TO THE MICROVILLOUS BORDER OF CULTURED INTESTINAL EPITHELIAL CELLS

Muriel Gavin[1], Carol L. Wells[1], and Stanley L. Erlandsen[2]

Departments of Laboratory Medicine and Pathology[1] and Cell Biology and Neuroanatomy[2], University of Minnesota School of Medicine, Minneapolis, MN 55455

Trophozoites or the free-swimming form of the intestinal protozoan, *Giardia*, resides within the host small intestine where they attach to the microvillous border by means of a grasping organelle, the ventral adhesive disc. Several mechanisms have been proposed to explain trophozoite attachment including contractile activity[1], microtubular coiling-uncoiling[2], hydryodynamic activity of the ventral flagella[3], and activated lectin binding[4].

We have developed a model for investigating the mechanism of attachment of *Giardia* trophozoites to the microvillous border of cultured intestinal epithelial cells. Caco-2 cells, a human colonic intestinal cell line was grown for 14 days on glass cover slips in Delbeccos' modified Eagle's medium. *Giardia* trophozoites (Be-1;IP-0482:1) were cultured in TYI medium for 3 days, then harvested and resuspended in modified Eagle's medium prior to incubation for 30 minutes on Caco-2 cells. Coverslips were rinsed with warm Hanks balanced salt solution, fixed overnight in 3% glutaraldehye - 0.1 M cacodylate buffer, pH 7.2, dehydrated in ethanol, and critical point dried in CO_2. Portions of the coverslips were mounted perpendicular or parallel to the axis of the beam, and coated with ≤1 nm of platinum by ion beam sputtering before examination at low voltage (<4 keV) in the Hitach S-900 field emission SEM.

Numerous trophozoites of *Giardia* were observed attached by their ventral surface to the microvillous border of the Caco-2 cells (Fig. 1). At higher magnification (Figs. 2 & 3), the microvilli near the circumerference of the ventrolateral flange (VLF) appeared to be oriented centripitally toward the center of the adhesive disk, suggesting that a grasping activity of the disk or ventrolateral flange might have produced this radial microvillar pattern. Mounting coverslips parallel with the beam axis (Fig. 4) permitted better visualization of the interaction of Caco-2 cell microvilli with the VLF. Individual microvilli directly attached to the serrated edges of the VLF, suggesting a strong cell-cell interaction related to contractile activity and possibly lectin-like binding. A space estimated at ~30-60 nm was observed between the trophozoite VLF and the cell surface, and would argue against the hydrodynamic mechanism for attachment which requires active beating of flagella. These results suggest that the VLF, in part, may help mediate attachment by forming strong focal adhesions with microvilli on the Caco-2 cell surface, and that the strength of these adhesions is sufficient to deform the edge of the VLF.

References

1. S.L. Erlandsen and D.G. Feely, Giardia and Giardiasis, Plenum Press (1984) 33.
2. J.C. Muller et al, Scann. Elect. Micros. (1973) 557.
3. D.V. Holberton, J. Exp. Biol. (1974) 60: 207.
4. H.D. Ward et al, Biochem. (1987) 26: 8669.
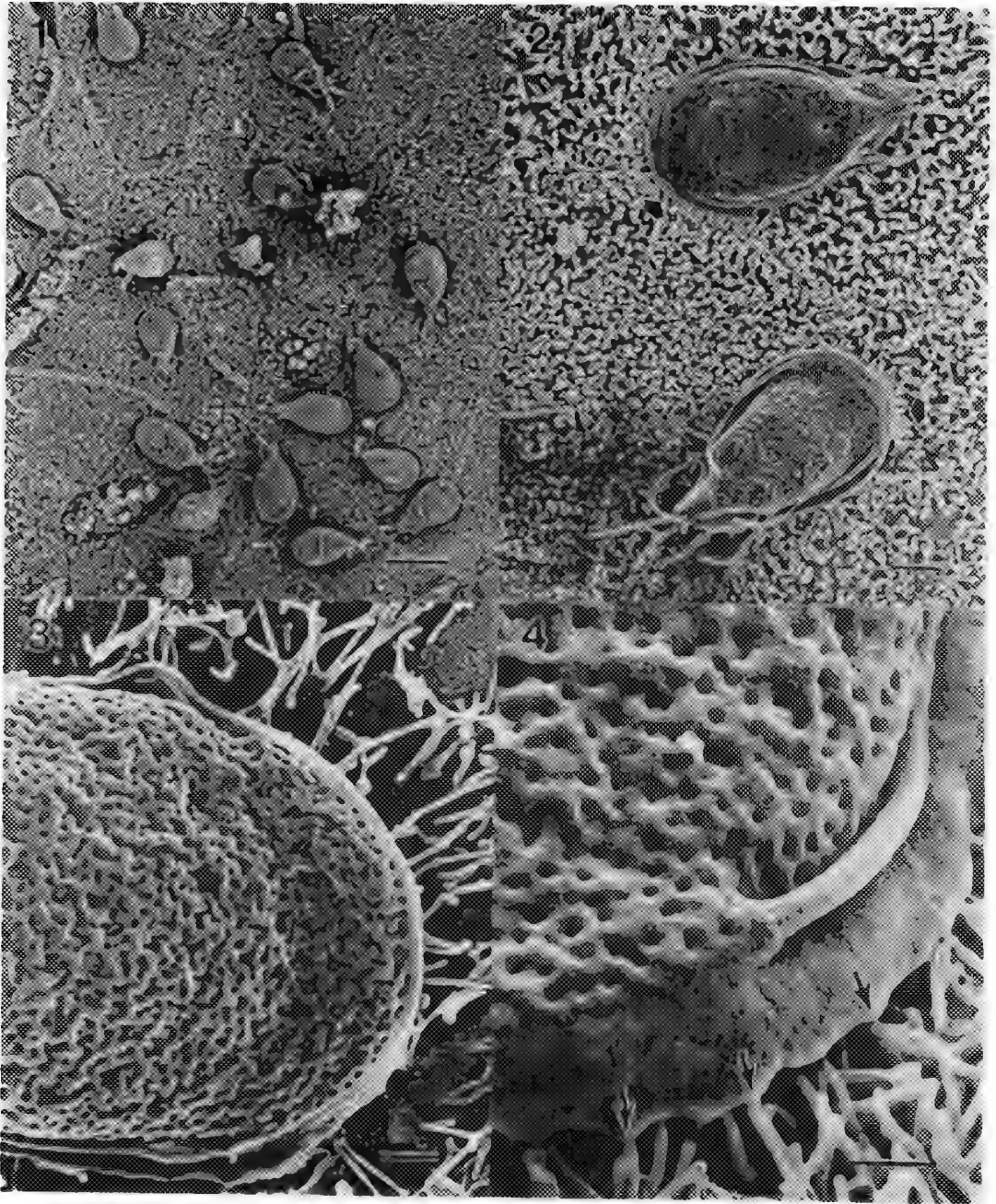
Figure 1. Apical surface of Caco-2 cells showing attached *Giardia* trophozoites. Bar, 10 microns
Figure 2. Note centripetal orientation of microvilli (arrowheads) near the edge of VLF. Bar, 2 microns
Figure 3. Vertical view shows radial orientation of microvilli beneath VLF of trophozoite. Bar, 1 micron
Figure 4. High tilt reveals microvilli attached (arrowheads) to serrated edge of VLF. Bar, 0 5 microns

USE OF LOW-VOLTAGE SEM (LVSEM) TO EVALUATE CELLULAR MORPHOLOGY AND EXTRACELLULAR POLYSACCHARIDE PRODUCTION BY *Pseudomonas fragi (ATCC 4973)*, *Listeria monocytogenes (Scott A)*, AND *Salmonella typhimurium*

Tina Schwach and E. A. Zottola

Department of Food Science and Nutrition, University of Minnesota, St. Paul, Minnesota 55108

LVSEM offers the microbiologist a unique view of the microbial cell surface. Colony morphology is used by microbiologists to distinguish between organisms. Some bacteria exhibit different colony morphologies when grown on solid media. *P. fragi* ATCC 4973 exhibits both rough (R) and smooth (S) colonies. It is not known why different morphologies form, but there is some speculation that their expression may be affected by nutrient conditions[1] ,other physical parameters, such as growth in a non-static environment[2], and may involve extracellular polysaccharide (EPS) formation[3]. EPS has also been implicated in bacterial attachment to surfaces[4].

In this study, three organisms of importance to the food industry were grown in Trypticase Soy Broth (TSB) at 21C. Growth rates, EPS production, and cell surface morphologies were evaluated in both 3% TSB and 0.3% TSB. The lower concentration was used to simulate decreased availability of nutrients. Two glass chips (3mm x 6mm) were added to small petri dishes containing the culture medium and the organism. Care was taken to have the top surface of the chips equal with the liquid level, since this air-liquid interface is the site of pellicle formation and is associated with EPS. In the case of *L. monocytogenes*, where no distinct pellicle is formed, the chips were immersed in the media and the bottoms of the chips were viewed. One chip was removed after 4h and the other after 24h. These times represented early logarithmic growth and late log or early stationary phase. Samples for LVSEM were fixed and dehydrated in a graded acetone series according to conventional procedures. They were coated with platinum by ion sputtering in argon and viewed on a Hitachi S-900 SEM at 3.7 keV.

As shown in Figures 1 and 2, after 4h, the surface morphology of *P. fragi* differed between the two media. This was true for both colony types. After 24h (Figure 3), morphological differences were still evident. Also evident, were extracellular fibrils (Figure 4), possibly EPS, running between and over the cells. This was seen in both the 3% and 0.3% TSB samples. Surface detail was easily distinguished as the polymer appeared not to enrobe the cells. One possible explanation for this is that the EPS from *P. fragi* is released into the media and does not remain completely adherent to the cells. After 4h, *S. typhimurium* also exhibited a distinct surface morphology in both dilutions of TSB. However, after 24h this surface detail became blurred by a layer of EPS which coated the cells (Figures 5 and 6). This was also seen with *L. monocytogenes* (Figure 7). It was also noted that the thickness of the pellicle (when present) and the amount of EPS formed by all three organisms was always less in 0.3% TSB than in 3% TSB.[5]

References
1. J. R. W. Govan, J. Med. Microbiol. (1975)8, 513.
2. J. H. Pringle et al. J. Gen. Microbiol. (1983)129, 2557.
3. P. J. Herald. M. S. Thesis. University of Minnesota, St. Paul, Minnesota (1989)
4. E. A. Zottola. Biofouling. (1991)5,37.
5. This research is supported in part by a USDA fellowship and the Mn. Ag. Exp. Stat.
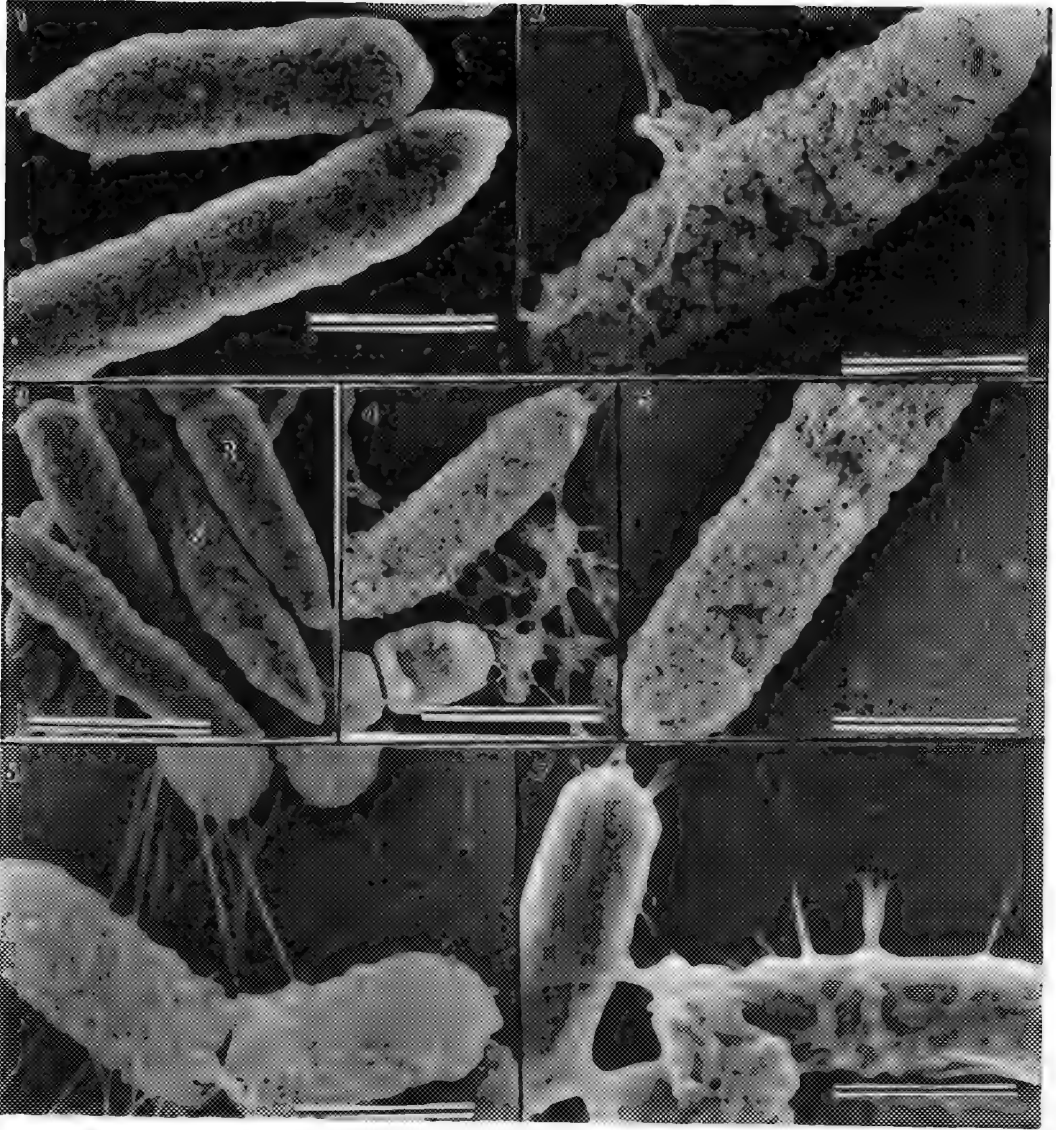
FIG. 1. -- SEM of *P. fragi* ATCC 4973 (S) after 4 hr in 3% TSB at 21C. Bar = 860 nm.
FIG. 2. -- SEM of *P. fragi* ATCC 4973 (S) after 4 hr in 0.3% TSB at 21C. Bar = 600 nm.
FIG. 3. -- SEM of *P. fragi* ATCC 4973 (R and S) after 24 hr in 0.3% TSB at 21C. Bar = 1.2μm.
FIG. 4. -- SEM of *P. fragi* ATCC 4973 (R) after 24 hr. in 0.3% TSB at 21C. Bar = 1.5 μm.
FIG. 5. -- SEM of *S. typhimurium* after 4 hr in 3% TSB at 21C. Bar = 670 nm.
FIG. 6. -- SEM of *S. typhimurium* after 24 hr in 3% TSB at 21C. Bar = 750 nm.
FIG. 7. -- SEM of *L. monocytogenes (Scott A)* after 24 hr in 3% TSB at 21C. Bar = 600 nm.

LYSINE EFFECT ON RUTHENIUM RED AND ALCIAN BLUE PRESERVATION OF THE STAPHYLOCOCCI GLYCOCALYX

Theresa A. Fassel[*], James R. Sanger[**] and Charles E. Edmiston[**]

[*]University of Wisconsin-Madison, Madison, WI 53706; [**]Medical College of Wisconsin, Milwaukee, Wisconsin 53226

The gram-positive coagulase-negative staphylococci are opportunistic organisms important in latent infection associated with prosthetic biomaterials. Their highly charged polysaccharide glycocalyx, or slime, aids in proliferation of bacteria on surfaces after an initial adhesion event, possibly at the time of surgical insertion.[1] The cationic reagents, ruthenium red (RR) and alcian blue (AB), in en bloc procedures have aided visualization of the polysaccharide glycocalyx material in TEM or SEM applications.[2,3] Further, enhancement of RR preservation or staining of slime by inclusion of lysine in a prefixation stage has been observed.[3,4] The effect of lysine with and without RR and AB on preservation/staining of the staphylococci glycocalyx is investigated further in this study.

Staphylococcus aureus ATCC 25923, Staphylococcus epidermidis RP62 (RP62) and *Staphylococcus hominis SP2* (SP2) were cultured in trypticase soy broth for 18 hrs at 35°C, following recovery from frozen storage and plating on blood agar plates for 24 hrs. Cells with 75mM lysine in the prefixation were incubated for 20 minutes with 2.5% glutaraldehyde (GA), 2.5% GA and 0.075% RR, or 2.5% GA and 0.075% AB, respectively. Parallel samples without lysine were simultaneously processed. Fixation was in 2.5% GA, 2.5% GA and 0.075% RR, or 2.5% GA and 0.075% AB, for 2 hrs. Samples were washed 3X 10 minutes in buffer. Postfixation was in 1% OsO_4 for 2 hrs followed by washes. The buffer for these washes and all solutions was 0.1 M cacodylate buffer pH 7.2. Samples were dehydrated in a graded ethanol series and infiltrated and embedded in LR White. Thin sections were cut using a Reichert Jung Ultracut and post-stained in 2% uranyl acetate and Reynolds lead citrate. Observations were made in a Hitachi H-600 at 75 KV.

When no lysine and no cationic reagent are present in the prefixation, glycocalyx material is minimal for all species studied (Fig. 1). With 75 mM lysine, some fibrous material is observed (Fig. 2). With 75 mM lysine and RR, considerable fibrous material surrounds cells (Figs. 3 and 4). With 75mM lysine and AB, the glycocalyx material appears comparable to the lysine and RR preparation for SP2 (Fig. 5). For RP62, the material does not appear as condensed with lysine and AB (Fig. 6) vs. the more discrete condensations seen with only AB (Fig. 7). Thus, lysine seems to enhance the effect of RR and AB.

References
1. Edmiston, CE et al., 1989 Infect. Control.Hosp. Epidemiol. 10:11-117.
2. Fassel, TA et al 1991 Cell and Materials 1:199-208.
3. Fassel, TA et al., 1992 Cell and Materials 2:37-48.
4. Jacques, M and Graham, L 1989 J.Electron Microsc. Tech. 11:167-169.
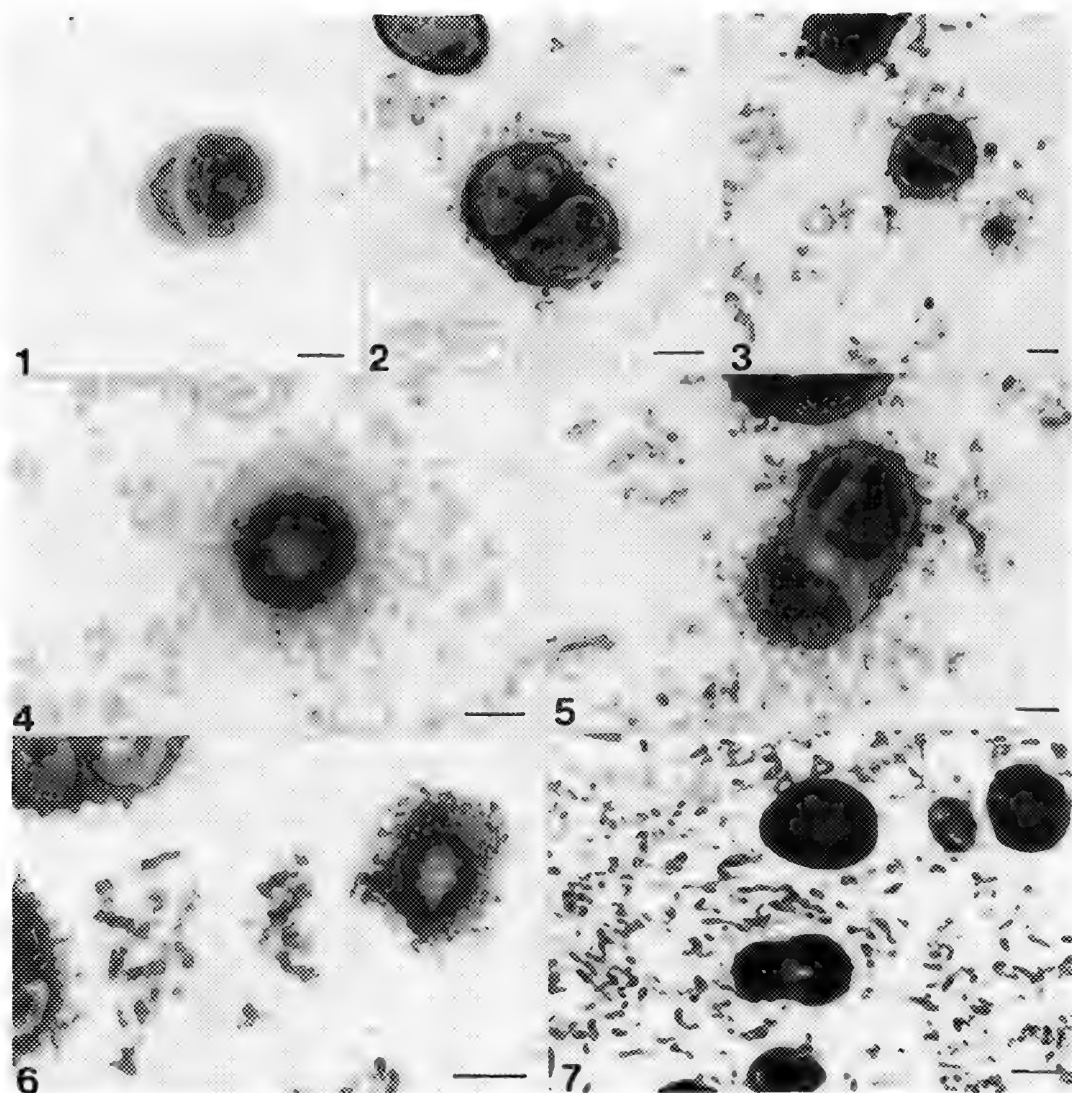
FIGS. 1 AND 2.--For *S. aureus*, minimal glycocalyx material is seen by glutaraldehyde prefixation (FIG. 1). Addition of lysine, improves observation of fibrous material (FIG. 2).
FIGS. 3 AND 4.--Enhanced glycocalyx is also observed with lysine and RR for *S. aureus* (FIG. 3) and SP2 (FIG. 4).
FIGS. 5, 6 AND 7.--Lysine enhances the effect of AB, in a manner apparently similar to RR for SP2 (FIG. 5). Discrete curved condensations without lysine added to AB (FIG. 7) contrasts the fibrous material seen when lysine is included with AB, for RP62 (FIG. 7). All magnification bars = 0.25 μm.

BACTERIAL ADHERENCE AND BIOFILM BEHAVIOR OF *VIBRIO VULNIFICUS*

B. D. Tall, R. T. Gray, and D. B. Shah. FDA, Washington, DC 20204

Vibrio vulnificus, an opportunistic human pathogen, is found as member of the normal microflora of shellfish and other seafoods, many of which are eaten raw. Though usually not harmful, *V. vulnificus* is responsible for causing fulminating septicemia in immunocompromised individuals. In previous light microscopic studies, we showed data suggesting that isogenic unencapsulated phase variants were more adherent to HeLa cells than were counterpart encapsulated phase variants[1]. In this study, we extended our observations by comparing phase variant capsular morphology stained with Alcian blue (AB) and Ruthenium red (RR), and investigated the dynamics of biofilm formation by these organisms to glass coverslips (CS) using quantitative plate counts and scanning electron microscopy (SEM).

To characterize the morphology of capsules expressed by these organisms, we stained cells grown on trypticase soy agar containing 1% NaCl (TSA/NaCl) with AB and then prepared them for electron microscopy (EM) according to the method described by Hendley *et al*[2]. Cells stained with RR were prepared for EM by modifications of the method described by Hendley *et al*[2]. Briefly these modifications consisted of using a fixative buffer pH of 7.2 instead of 6.5 and incorporating wash buffers and dehydrating solvents containing 0.05% RR. After EPON embedding, thin sections of AB and RR stained cells were contrasted with lead citrate and uranyl acetate and viewed in a Philips 400 transmission electron microscope, operating at an accelerating voltage of 80 kV. Biofilm formation of *V. vulnificus* to glass CS was investigated by separately inoculating 10^5 CFU/ml of each isogenic variant into wells of a sterile 24-well tissue culture plate containing artificial sea water (salinity 10 ppt) and an acid-cleaned, sterile glass CS. Duplicate samples of the sessile population and the planktonic population (population of cells adherent to the CS vs. population of cells in liquid culture phase) were obtained at 0, 3, and 18 h and were inoculated onto TSA/NaCl plates for quantitative viable cultures. A third corresponding CS was fixed and processed for SEM as described previously[3].

AB stained encapsulated cells were seen covered by a thick layer of fibers radiating from the cell surface (Fig. 1). Whereas, the unencapsulated AB stained cells did not have this surface layer (Fig. 1). Additionally, there was no surface layer observed in cells stained with RR or unstained control cells suggesting that AB had imparted stability to the capsule enabling preservation throughout processing (compare Fig. 1 with 2). Viable plate count results showed (Table 1) that immediately after inoculation, 0.7% of the unencapsulated cell population colonized the glass coverslip. In contrast, only 0.02% of the encapsulated cell population colonized the coverslip. After 3 h of incubation at 37° C, 1.3% of unencapsulated cell population had colonized the coverslip, whereas only 0.1% of the encapsulated cell population had colonized the coverslip. There was no difference in the percentage of cells of either phase variant colonized overnight. SEM results corroborated the viable plate count data and the results from our previous study. As seen in Fig. 3, many cells were observed adhering to the coverslip. These results suggest that the unencapsulated phase variant may be more ecologically adept at the initial colonization stage of biofilm formation than its isogenic encapsulated counterpart and that AB may be useful as a capsule stain to study these organism's capsule ultrastructural detail.

1. B. D. Tall *et al*, Abstr. Annu. ASM Meeting (1992), 138.
2. J. O. Hendley *et al*, J. Infect. Dis. (1981) 143, 796.
3. B. D. Tall *et al*, Proc. Annu. EMSA Meeting (1992), 882.

Table 1. Population Dynamics of Biofilm Formation of *V. vulnificus.*

Phase Variant	Incubation Time (h)	Viable Count, CS	Viable Count, Sup.	% Population Colonizing CS
Capsule⁻	0	7.0×10^3	9.0×10^5	0.7
Capsule⁺	0	2.0×10^2	8.5×10^5	0.02
Capsule⁻	3	9.3×10^4	6.9×10^6	1.3
Capsule⁺	3	2.2×10^3	2.2×10^6	0.1
Capsule⁻	18	1.1×10^7	1.2×10^{10}	0.1
Capsule⁺	18	1.3×10^7	1.4×10^{10}	0.1
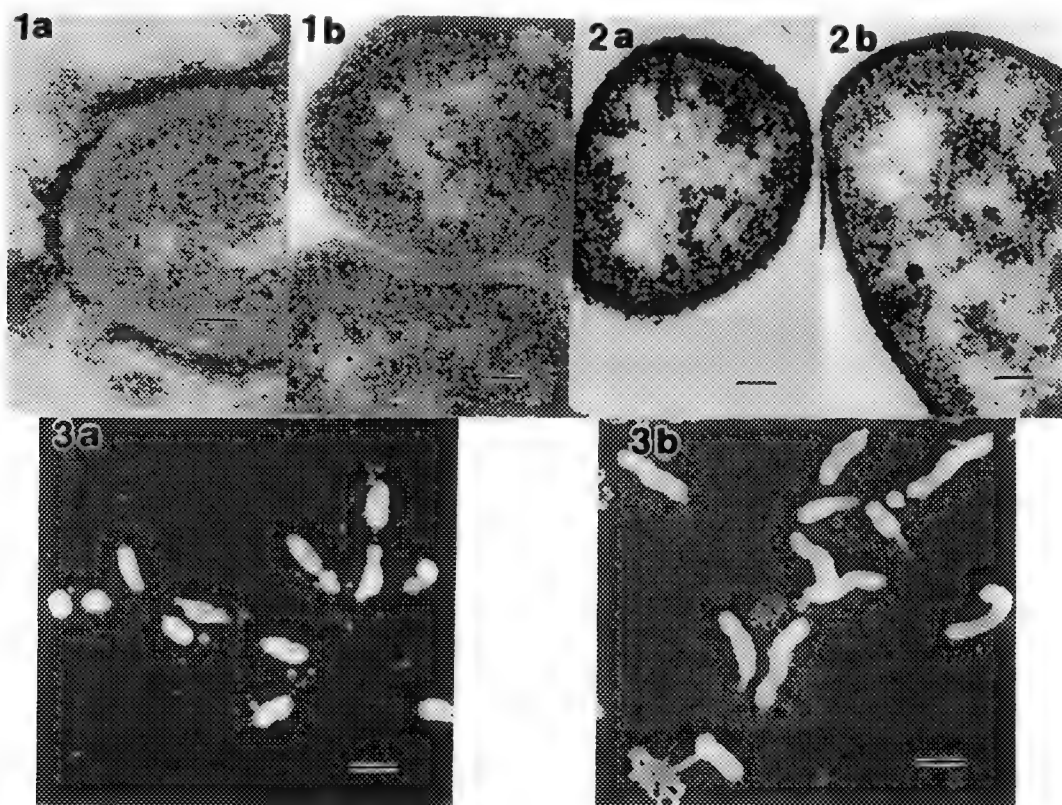
Fig. 1. --Transmission electron photomicrograph showing encapsulated (A) and unencapsulated (B) phase variant *V. vulnificus* cells stained with Alcian blue. Bar markers = 0.1 μm.

Fig. 2. --Transmission electron photomicrograph showing encapsulated (A) and unencapsulated (B) phase variant *V. vulnificus* cells stained with Ruthenium red. Bar markers = 0.1 μm.

Fig.3. --Scanning electron photomicrograph of biofilm formation on glass coverslips colonized by unencapsulated *V. vulnificus* cells obtained at 0 (A), and at 18 h (B). Bar markers = 1 μm.

MICROSCOPY OF *TAXOMYCES ANDREANAE* A NEW TAXON ISOLATED FROM *TAXUS*

Gary A. Strobel*, M. D. Standing** and W. M. Hess**

*Department of Plant Pathology, Montana State University, Bozeman, MT 59717 and **Department of Botany and Range Science, Brigham Young University, Provo, UT 84602

A newly described fungus,*Taxomyces andreanae* Strobel, Stierle, & Hess. has also been isolated from (*Taxus brevifolia* Nutt.),[1] The growth pattern of the fungus was determined by growing it on various plant species, plant parts and agar cultures. The morphological characteristics appeared to be more diverse when the fungus was grown on twigs of yew wood. Therefore, the purpose of these investigations was to use electron microscopy to more carefully observe the nature of fungal growth and bulbil formation of *T. andreanae* on twigs of yew wood.

Small pieces of sterile plant tissues were used to grow the fungus. For microscopy studies, procedures outlined by Upadhyay et al.[2] were used, which consisted of fixation and dehydration followed by critical point drying and sputter coating for SEM, and embedment in Spurr resin for TEM. All SEM photos were taken at 10 kV. Fungal colonies had sparse to very dense concentrations of hyphal cells (Fig. 1) which, in some areas of cultures, produced hyphal cells which averaged from 1.25 μm to larger cells which averaged 3.75 μm in diameter.[1] Characteristically hyphal cells did not have crystals on their surfaces (Figs. 1-2). However, in some areas of colonies crystals on surfaces of hyphal cells were sparse (Figs. 2-3) to heavily concentrated (Figs. 5-6). The crystals were not water soluble and energy dispersive X-ray microanalysis revealed the presence of only light elements. Calcium oxylate crystals of various morphologies have been reported for other fungi.[3-5]

1. G. Strobel, A. Stierle, D. Stierle, and W. M. Hess, Mycotaxon (1993)47,71.
2. R. Upadhyay, D. Kenfield, G. A. Strobel, and W. M. Hess, Can. J. Bot. (1991)69, 797.
3. K. D. Whitney and H. J. Arnott, Mycologia (1986)78,42.
4. K. D. Whitney and H. J. Arnott, Mycologia (1986)78,649.
5. K. D. Whitney and H. J. Arnott, Mycologia (1987)79,180
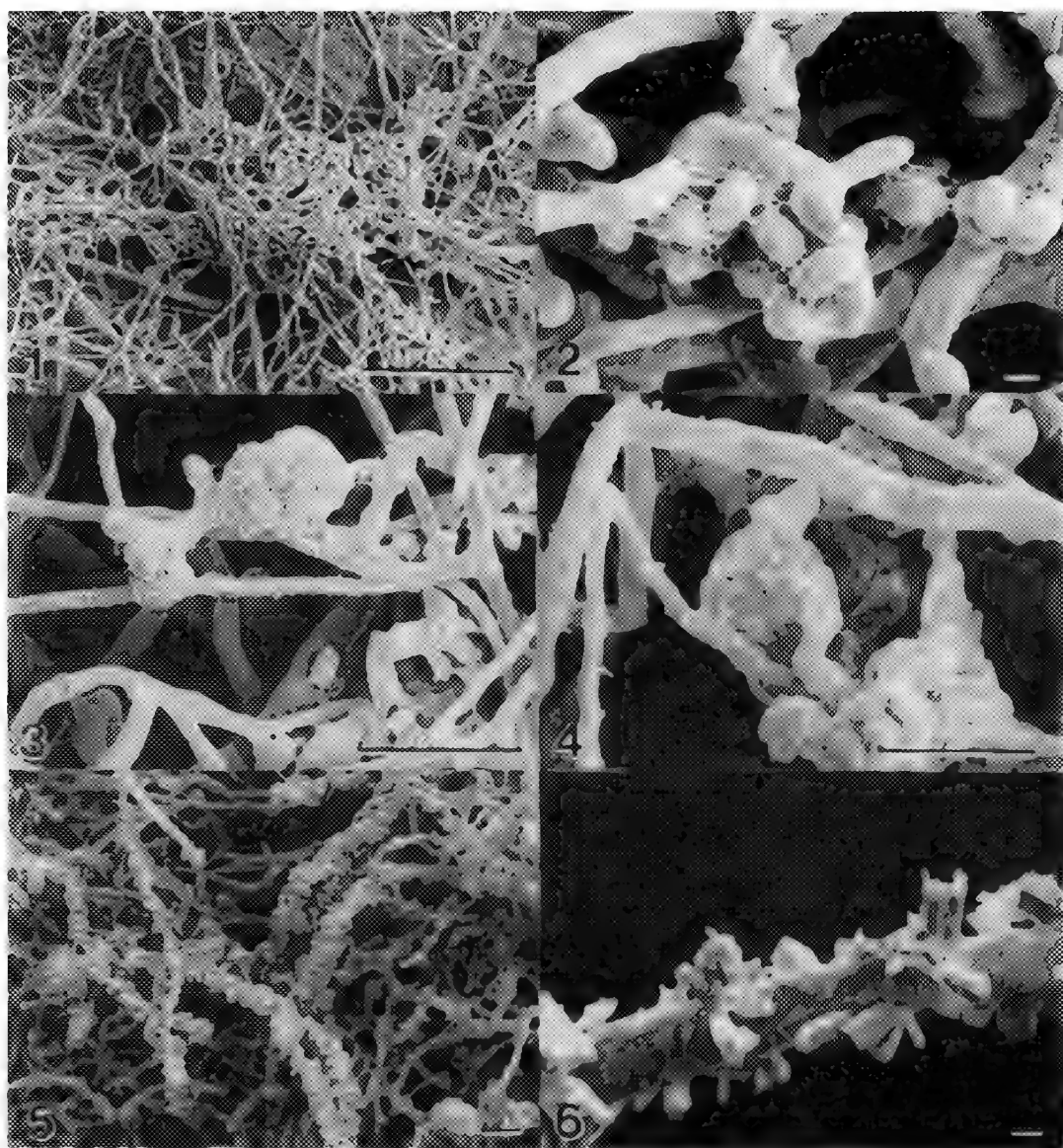
Figs. 1-6. SEM images of *Taxomyces andraea* grown on yew wood twigs. Fig. 1. Colony characteristics. Bar =100 μm. Fig. 2. Bulbil cells and hyphal cells without crystals. Bar =1μm. Figs. 3-4. Hyphal cells with sparse crystals and bulbils without crystals. Fig. 3, Bar =10 μm . Fig. 4, Bar =10 μm. Figs. 5-6. Hyphal cells densely covered with crystals. Fig. 5, Bar = 10 μm. Fig. 6, Bar =1μm.

MICROSCOPIC STUDY OF MALE MORPHO RHETENOR WING SCALES

L. Bingham*, I. Bingham*, J. Tanner*1, C. Driscoll*1, S. Geary*, J. Hollingshead*, B. Hansen**, and J. S. Gardner**

* Timpview High School, Provo, Utah 84604
** Electron Optics Lab, 128 WIDB, Brigham Young University, Provo, Utah 84602

The morphology of pigmented ventral scales and non-pigmented iridescent dorsal scales of Morpho rhetenor wings were compared using scanning electron microscopy and light microscopy. Sections of wing and individual scales were mounted at various angles on stubs for SEM evaluation. Some scales were embedded in Spurr's resin [1] and sectioned for LM and SEM.

Pigmented scales are ornamented by ridges parallel to the axis of the scale (Fig. 1). They are approximately 1.5 µm apart with holes through the membrane between ridges. The non-pigmented iridescent scales similarly contain a series of parallel ridges, but with several layers of lamellae (Fig. 2). The distance between these ridges is only approximately 0.7 µm (Fig. 3). Much smaller and more frequent holes can be observed between these ridges (compare Figs. 1 and 3). The overlapping layers of lamellae form stacks of thin films, which resemble a "Christmas tree" structure. [2] The space between the overlapping lamellae is 0.05 µm and there appear to be holes through the midrib between lamellar stacks (Fig. 4). In resin embedded sections, dorsal and ventral scales are separated by a central membrane of the wing (Fig. 5). The base of each scale is attached to this central membrane. In the SEM these sections reveal the electron dense nature of the lamellae (Fig. 6).

Morpho rhetenor scales with iridescent properties are morphologically much more complex than pigmented scales. The structural color arising from dorsal iridescent scales is a result of an overlapping of lamellae to form stacks of thin films which act as interference mirrors. [2] Ventral scales do not possess the necessary structures to be iridescent and exhibit only pigmented coloration.

References

1. A.R. Spurr, J. Utrastruct. Res. (1969)26, 31.
2. H. Ghiradella, Ann. Entomol. Soc. Am. (1985)78, 252.
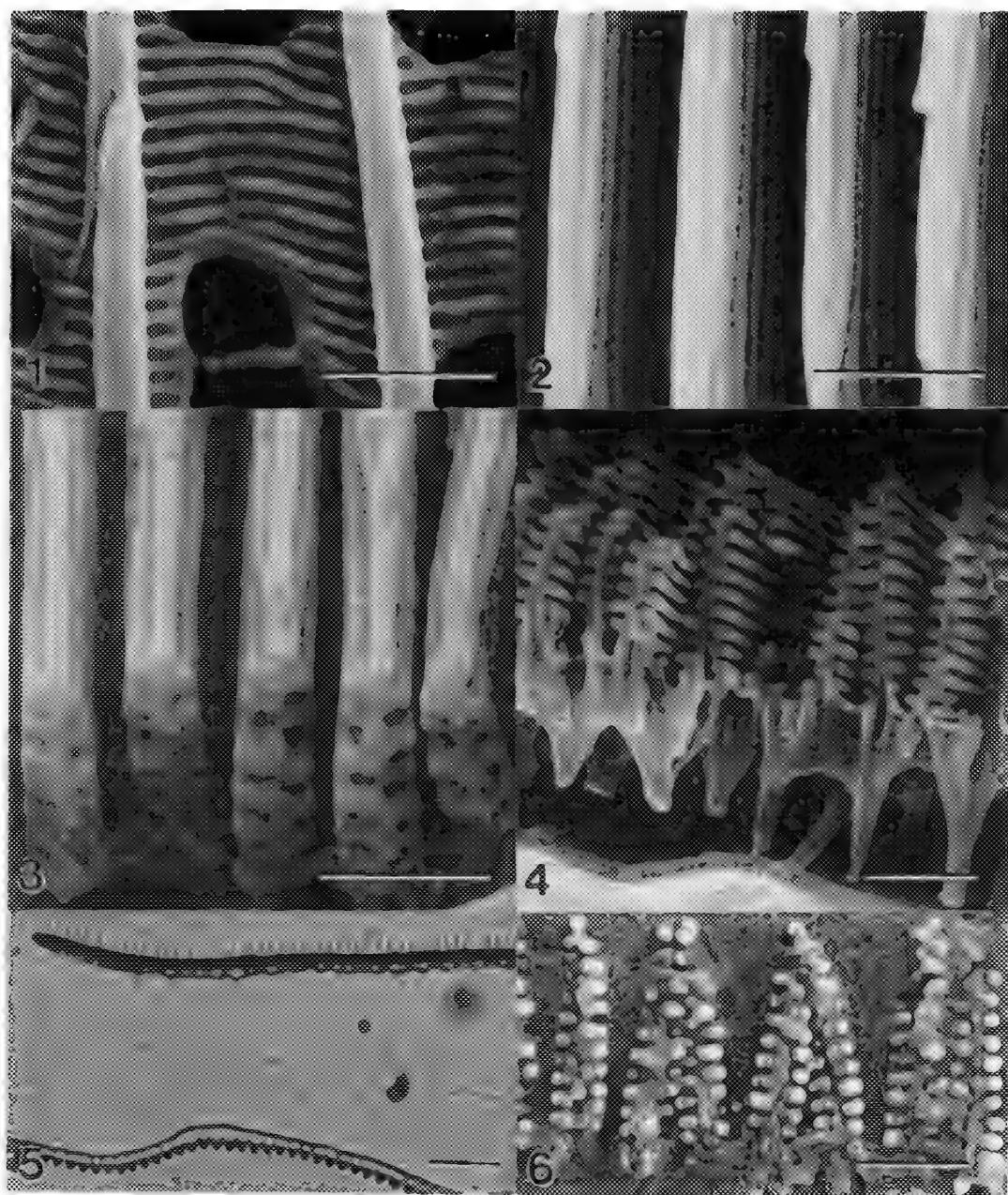
Fig. 1-4 & 6. SEM images. Bar = 1µm. Fig. 1. Ventral pigmented scale. Note ridge spacing and holes. Fig. 2-4. Dorsal iridescent scales. Fig. 2. Note narrow spacing of ridges. Fig. 3. Note numerous holes in connecting membrane. Fig. 4. Note spacing of lamellae. Fig. 5. LM image of cross section through wing. Bar = 10 µm. Fig. 6. Note electron dense lamellae.

THE EFFECT OF TORBAFYLLINE ON CAPILLARY MORPHOLOGY IN PRIMATE SKELETAL MUSCLE AFTER ISCHEMIC REPERFUSION INJURY

Michael A Gregory and Maurice Mars*

Electron Microscope Unit, University of Durban-Westville, P.Bag X54001, Durban 4000, Natal, South Africa and *Department of Physiology, University of Natal, Durban, South Africa

Morphometric studies have shown that experimental drug Torbafylline (T) alters the response of skeletal myofibres to ischemic reperfusion injury (IRI)[1,2]. An ultrastructural study has been instituted to determine if and/or how T may "protect" the muscle from IRI. This report outlines the effect that 3 hours of tourniquet mediated ischemia and up to 24 hours of reperfusion has on the capillaries of primate skeletal muscle, with and without prior administration of T.

Sixteen adult vervet monkeys (8 control - 8 experimental) were studied under general anesthesia. In each case, a hindlimb was exsanguinated using an Esmarch bandage. To induce lower limb ischemia, a pneumatic tourniquet was applied to the thigh at 100mm Hg above systolic pressure for 3 hours. In 4 control animals, open muscle biopsies were taken from the tibilais anterior before tourniquet application (BTA), just prior to tourniquet deflation, and after 3 and 6 hours of reperfusion. In the remaining 4 animals, biopsies were taken BTA and after 12, 18 and 24 hours of reperfusion. The other 8 animals received drug T (20 mg/kg) intravenously over 30 minutes BTA. Open muscle biopsies were taken as for the control groups. The tissue was immediately immersed in Karnovskys' fixative for 1 hour prior to osmication and preparation for TEM using conventional techniques.

Morphological observations were confined to cross or oblique sections of the small capillaries in spaces between the individual myofibres of muscle bundles. The ultrastructure of capillaries in all control specimens BTA was normal (Fig.1). The interlocking endothelial cells (EC) were from ±130nm - ±370nm in width over most of their length, thickening to ±2.5um at the position of the EC nucleus. Numerous ±5nm pinocytic vesicles were arrayed along both the outer and luminal (inner) membranes. After 3 hours ischemia, at least one and often both endothelial cells were swollen (Fig.2), in some cases to 4 times their normal width. Pathomorphology was at its worst 12 hours after reperfusion. However, some capillaries with severly edematous EC were present in specimens 24 hours after reperfusion. Pathomorphology included reduced numbers of pinocytic vesicles, myelin figures dilatation of rough endoplasmic reticulum and the absence of glycogen and ribosomes (Fig.3). The lumen of "edematous capillaries" was often completely occluded. In T treated tissue, similar edematous changes were noted in one or both EC in some capillaries after the ischemic episode and at every time post-reperfusion. However, the number of affected capillaries was substantially reduced as was the overall severity of EC oedema (Fig.4).

The results suggest that Torbafylline may ameliorate skeletal myofibre IRI by reducing the degree of EC edema in the post-ischemic period thereby improving vascular perfusion to the muscle.

References

1. M.A. Gregory and M. Mars, Comm. Electron Microsc. Soc. South Afr. (1991) 21, 217.
2. M.A. Gregory and M. Mars, Comm. Electron Microsc. Soc. South Afr. (1992) 22, 115.
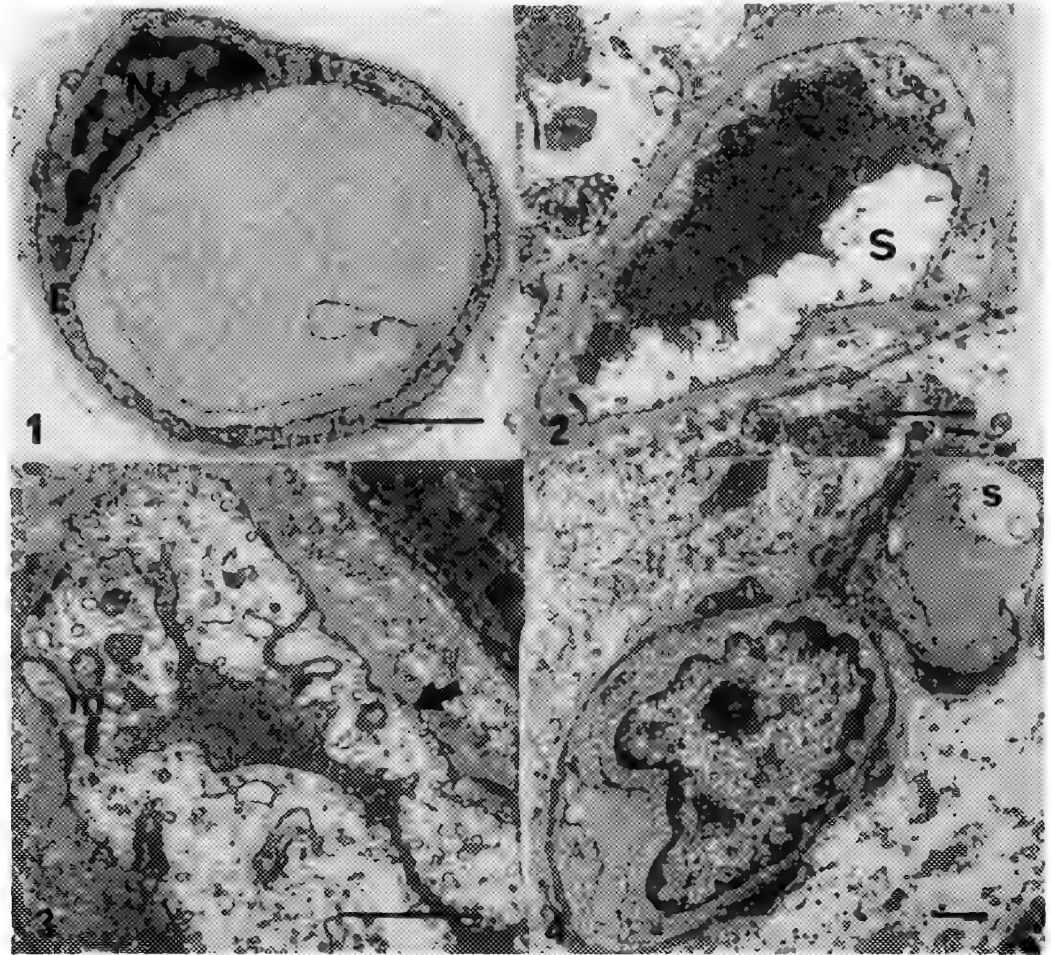
Fig.1. BTA: Normal capillary with erythrocyte in lumen. E = endothelial cell; N = nucleus. Bar = 1um.
Fig.2. 3 hours ischemia: No T: Swollen endothelial cell (S) in abnormal capillary. Bar = 1um.
Fig.3. 24 hours reperfusion: No T: Swollen EC's in almost occluded capillary. Pinocytic vesicle (arrowed); myelin figure (m). Bar = 1um
Fig.4. 24 hours reperfusion: T treated: Normal capillary and capillary with swollen EC. Bar = 1um.

APPEARANCE OF MYOFIBROBLAST DURING THE HEALING OF EXPERIMENTAL CORNEAL WOUND

Masamichi Ishizaki[1,3], Kyoko Wakamatsu[1], Takakuni Matsunami[1], Nobuaki Yamanaka[1]
Toshikazu Saiga[2] and Winston W.-Y. Kao[3]

Department of Pathology[1] and Ophthalmology[2], Nippon Medical School, Tokyo, Japan, 113.
Department of Ophthalmology[3], University of Cincinnati, Cincinnati, OH 45267-0527

It is well known that corneal stroma cells (keratocytes) can transform to fibroblasts during the corneal wound healing.[1]   We have studied the expression of α-smooth muscle actin, vimentin and desmin in fibroblastic cells of the alkali-burned and lacerated corneas in the rabbits by means of immunohistochemistry and electron microscopy.

Methods.   Rabbits were anesthetized, and central corneal alkali-burn and laceration were produced. The injured corneas healed for 1 day to 45 days, and 18 days embryonic rabbit corneas were immunostained with monoclonal antibodies against α-smooth muscle actin, vimentin and desmin.   For transmission electron microscopy, two techniques were used for the staining of ultra-thin sections: 1) uranyl acetate and Reynold's lead citrate and 2) the tannic acid method of Kajikawa.[2]

Results.   Antibody against α-smooth muscle actin reacted with fibroblastic cells in injured corneas (Fig 1) but not with stromal cells in normal and embryonic corneas. Anti-vimentin antibody strongly reacted with the fibroblastic cells in injured corneas (Fig 2) and stromal cells in normal and embryonic corneas.   Anti-desmin antibody did not react with any cell types in normal, embryonic and injured corneas, except ocular muscles. These results are summarized in Table 1. Transmission electron microscopy demonstrated the presence of basal lamina (microtendon) associated with fibroblastic cells in injured corneas (Fig 3).   Many "dense bodies" or "attachment site" were scattered within fibroblastic cells in injured corneas (Fig 4). These findings were not seen with stroma in normal and embryonic corneas.

Conclusion.   The fibroblastic cells in injured corneas show the characteristics of myofibroblast. The fibroblastic cells contain an extensive cytoplasmic fibrillar system and change their expression of α-smooth muscle actin and vimentin during the healing of injured corneas.   The stromal cells (keratocytes) can transform to myofibroblasts during the corneal wound healing.

References
1. S. Kitano and J.N. Goldman, Arch. Ophth., (1966) 76, 345.
2. K. Kajikawa, et al, J. Electron. Microsc. (Tokyo), (1975) 24, 287.
3. This study is in part supported by grants from NEI (#EYO05629), RPB, Inc., New York, NY, and OLERF, Columbus, OH.
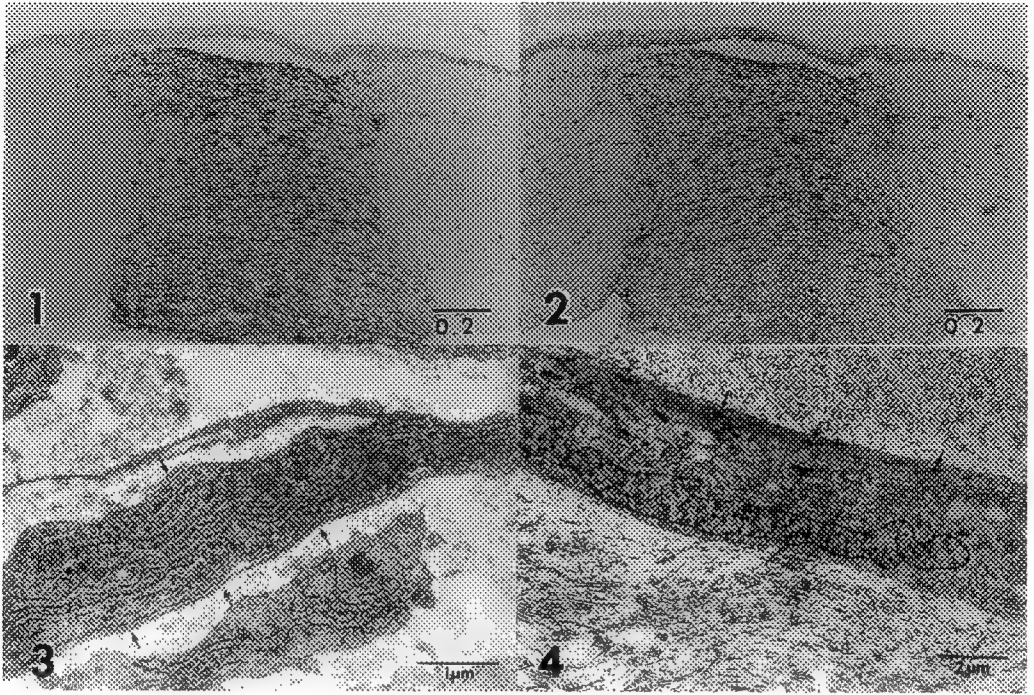
Fig. 1 Anti-smooth muscle α-actin reacts with fibroblastic cells in the granulation tissues of lacerated cornea which have healed for 14 days.

Fig. 2 Anti-vimentin reacts with fibroblastic cells in the granulation tissues of lacerated cornea which have healed for 14 days.

Fig. 3 Microtendons (arrows) are closely associated with a fibroblastic cell.

Fig. 4 The presence of electron dence bodies (arrows) stained by tannic acid in a fibroblastic cell.

Table 1   Summary of immunostaining of stromal cells in normal and injured corneas.

	Fibroblast*	Myofibroblast*	Fetal cornea cell	Normal cornea cell	Injured cornea cell
α-SMA	–	+	–	–	+
Vimentin	+	+	+	+	+
Desmin	–	–	–	–	–

α-SMA: α-Smooth Muscle Actin

* A. P. Sappino et. al. Lab. Invest. (1990) 63, 144.

IMMUNOELECTRON MICROSCOPIC DETECTION OF C-TYPE NATRIURETIC PEPTIDE IN NORMAL HUMAN ATRIAL TISSUE

Chi-Ming Wei, Margaret Hukee, Christopher G.A. McGregor, John C. Burnett, Jr.

Cardiovascular Diseases and Cardiovascular Surgery and Electron Microscopy Core Facility, Mayo Clinic and Foundation, Rochester, MN 55905

C-type natriuretic peptide (CNP) is a newly identified peptide that is structurally related to atrial (ANP) and brain natriuretic peptide (BNP). CNP exists as a 22-amino acid peptide and like ANP and BNP has a 17-amino acid ring formed by a disulfide bond. Unlike these two previously identified cardiac peptides, CNP lacks the COOH-terminal amino acid extension from the ring structure. ANP, BNP and CNP decrease cardiac preload, but unlike ANP and BNP, CNP is not natriuretic. While ANP and BNP have been localized to the heart, recent investigations have failed to detect CNP mRNA in the myocardium although small concentrations of CNP are detectable in the porcine myocardium. While originally localized to the brain, recent investigations have localized CNP to endothelial cells consistent with a paracrine role for CNP in the control of vascular tone. While CNP has been detected in cardiac tissue by radioimmunoassay, no studies have demonstrated CNP localization in normal human heart by immunoelectron microscopy. Therefore, the present studies were designed to detect the cardiac CNP localization in normal human atrial tissue by immunoelectron microscopy.

Cardiac tissue of three normal human right atria were obtained from the donor heart undergoing primary cardiac transplantation. Atrial tissue was fixed for 24 hours at 4°C in 4% formaldehyde and 1% glutaraldehyde in 0.1M phosphate buffer. These specimens were rinsed in phosphate buffer, dehydrated in a series of ethyl alcohols, embedded in Quetol 651, and polymerized at 42°C for 48 hours. Thin sections were pretreated with sodium metaperiodate and rinsed with distilled water. Non-specific sites were blocked with 1% bovine serum albumin (BSA) in Triz buffered saline with 0.1% Tween-20 added (TBS-T). Rabbit anti-C type natriuretic peptide was obtained from Pennisula Laboratories with no reported cross-reactivity with human BNP or with alpha or beta ANP. Antibody was diluted 1:1000, and sections were incubated for 16 hours at 4°C and 2 hours at room temperature. Controls without primary antigen were included. After rinsing in TBS-T, the sections were incubated in Protein A + Au conjugate (15 nm) for 1 hour at room temperature and rinsed again in TBS-T. Sections were stained with uranyl acetate and lead citrate prior to examination by transmission electron microscopy.

In normal human atria, modest but positive labeling of CNP was observed. Gold particles were found within and on the periphery of the atrial granules (Figure 1). Controls without primary antibody had no gold label present (Figure 2).

The present study is the first report demonstrating that CNP may be localized to normal atrial tissue. Recognizing that CNP may be of endothelial cell origin, the current findings may support of paracrine role for CNP in the control of myocardial function.

References

1. J.C.Burnett Jr et al., Science (1986)231, 1145.
2. C.M.Wei et al., Am. J. Physiol. (1993)264, H71.
3. A.J.Stingo et al., Am. J. Physiol. (1992)263, H1318.
4. C.M. Wei et al., J. Am. Soc. Nephrology (1991)2, 422.
5. This research was supported by grants from the Minnesota Affiliate of the American Heart Association MHA-103 and National Heart, Lung, and Blood Institute (NHLBI) Grants HL-36634, HL-07111. J.C. Burnett, Jr. is an Established Investigator of the American Heart Association.
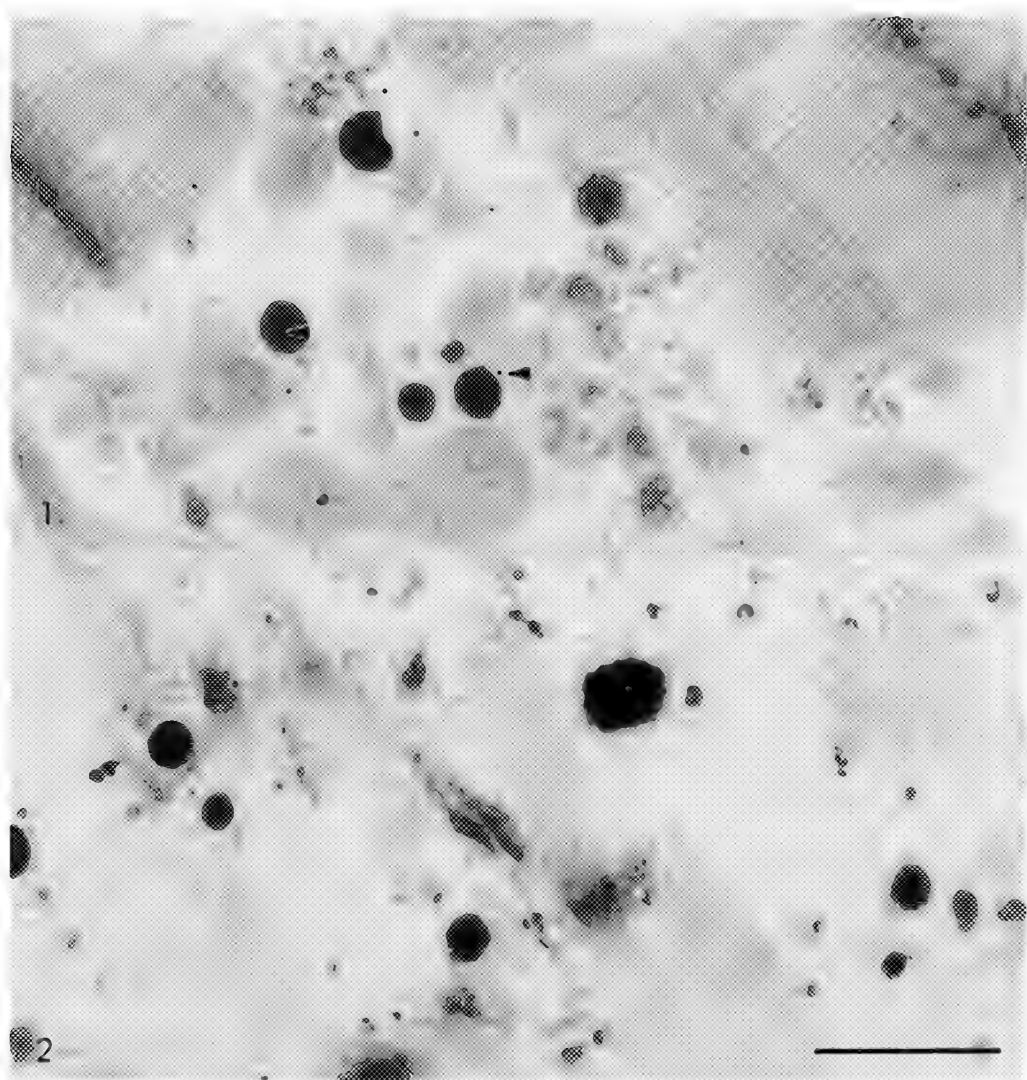
LEGEND:

Figure 1: Atrial granules showing the localization of CNP (arrows) within and on the periphery of the granule.
Figure 2: Atrial granules from controls incubated without primary antibody and showing the absence of colloidal gold label. (Bar = 500 nm.)

389

DRUG-INDUCED MORPHOLOGICAL ALTERATIONS IN LIVER

Moustafa Mohamad, Richard L. Drake, and Robert R. Cardell

Dept. of Anatomy and Cell Biology, Uni. of Cincinnati, Cincinnati, OH 45267

Chronic administration of phenobarbital, an anticonvulsant drug, or rifampicin, an antituberculous drug, alters hepatocyte ultrastructure by inducing the proliferation of smooth endoplasmic reticulum (SER) and changes in glycogen content. While these generalized effects are important, the lobular location of hepatocytes must be considered since pericentral and periportal hepatocytes differ morphologically and most hepatotoxic compounds affect specific zones of the liver. We treated adult male rats with phenobarbital or rifampicin for 5 days to evaluate the effect of each drug on hepatic glycogen levels, glycogen distribution across the liver lobule, and hepatocyte ultrastructure, especially the SER. Our results show a decrease in hepatic glycogen levels as determined biochemically in both treatment groups. Semithin sections of liver specifically stained for glycogen (Figs. 1-3) show that in treated animals glycogen in pericentral and periportal hepatocytes is reduced (Figs. 2,3). Ultrastructurally, periportal hepatocytes typically have clumped glycogen (Fig. 4); however, in treated animals periportal hepatocytes that show the greatest reduction of glycogen contain extensive SER (Fig. 5). Since pericentral hepatocytes normally contain more SER than periportal hepatocytes, and enzymes related to glycogen breakdown reside in SER, the tendency for pericentral cells to lose glycogen readily is expected. Furthermore, drug detoxifying enzymes are known to be synthesized in the SER. The induction of SER membranes by a 5 day drug treatment results in some periportal cells, which normally have relatively little SER, becoming more like pericentral hepatocytes ultrastructurally. The presence of more SER in some periportal hepatocytes results in the dispersal of compact glycogen masses as the SER appears to infiltrate the glycogen, and glycogen apparently is broken down. The coincidence of SER induced by drugs and glycogen breakdown is of interest since the clinical use of phenobarbital and rifampicin is widespread. (Supported by NIH Grant #DK27097)

Fig. 1. Light micrograph of liver lobule from a normal rat. Dark staining compact glycogen is observed near the portal vein (P). Diffuse and smaller glycogen patches are observed near the central vein (C). Bar=50 μm.

Fig. 2. Light micrograph of liver lobule from a rifampicin-treated rat. Cells near the portal vein (P) have both compact and more dispersed glycogen. Glycogen in hepatocytes near the central vein (C) is greatly reduced. Bar=50 μm.

Fig.3. Light micrograph of liver lobule from a phenobarbital-treated rat. Cells near the portal vein (P) have both compact and more dispersed glycogen. Glycogen in hepatocytes near the central vein (C) is greatly reduced. Bar=50 μm.

Fig. 4. Compact glycogen in a periportal hepatocyte from a normal rat. M:mitochondria. Arrows:α-particles of glycogen. Arrowheads: smooth endoplasmic reticulum. Bar=1.0 μm.

Fig. 5. Dispersed glycogen in a periportal hepatocyte from a phenobarbital-treated rat typifies the hepatocytes most affected by the drug. M:mitochondria. Pe:peroxisomes. Arrows:α-particles of glycogen. Arrowheads: smooth endoplasmic reticulum. Bar=1.0 μm.
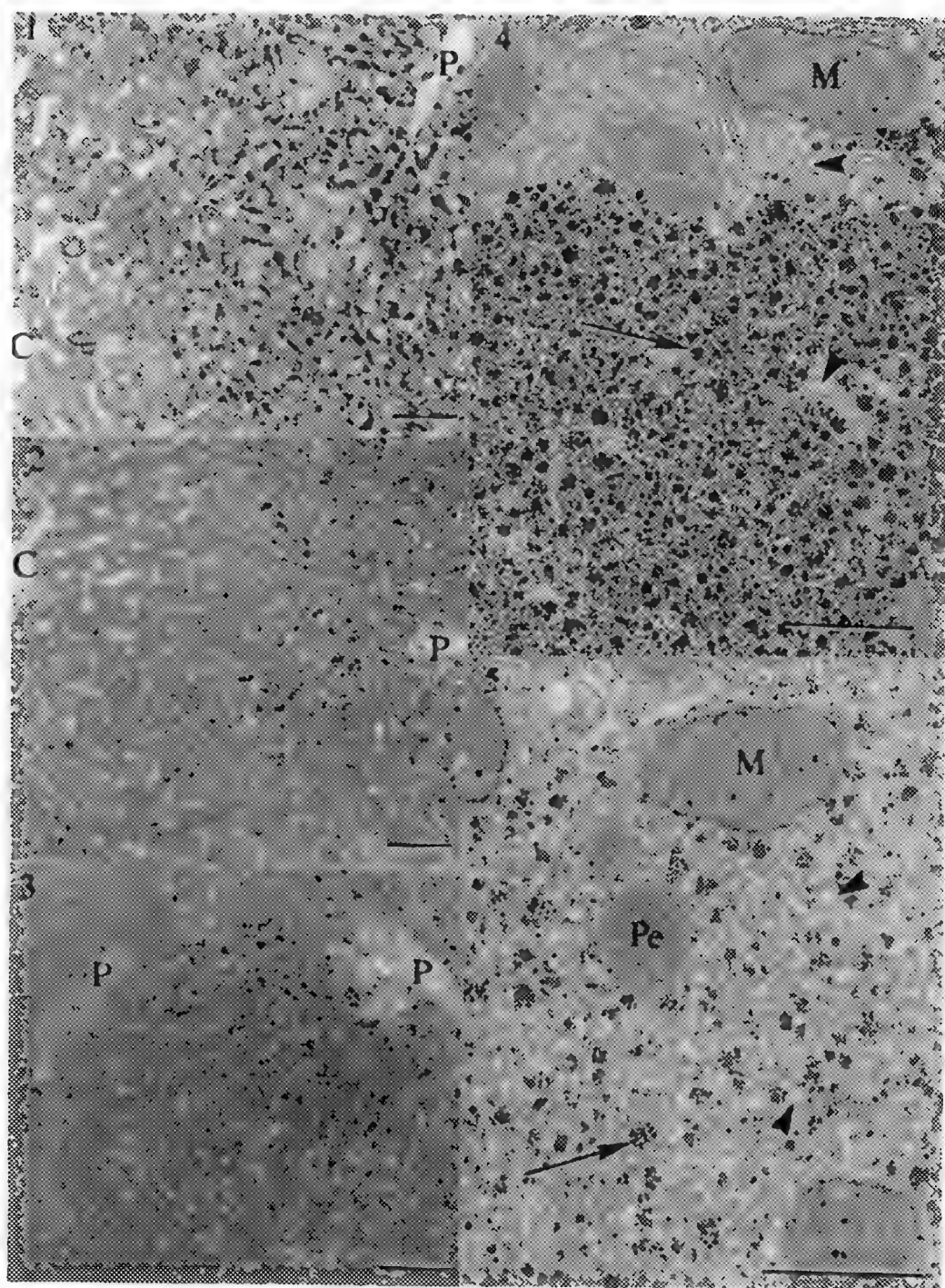
ROLE OF KUPFFER CELLS IN CCL4-INDUCED HEPATOCYTIC TOXICITY: A PRELIMINARY STUDY

S. Yamashiro, T. Bast, R.A. Towner, E.G. Janzen and L.A. Reinke[*]

Departments of Biomedical Sciences and MRI, Ontario Veterinary College, University of Guelph, Guelph, Ontario N1G 2W1, Canada, and [*]Department of Pharmacology, College of Medicine, Oklahoma State University, Oklahoma City, OK 73190, U.S.A.

Carbon tetrachloride (CCl_4) hepatotoxicity is one of the most frequently used experimental models to study the mechanism of cell damage by metabolites of xenobiotics (1,2). Cytochrome P-450 enzymes are considered to be involved in the metabolic activation of CCl_4 to generate the trichloromethyl ($.CCl_3$), which in turn may be converted to the peroxy radical ($.OO-CCl_3$) (3,4). In our previous studies, we have demonstrated CCl_4-induced edematous response by using proton magnetic resonance imaging and electron microscopy (2,5). However, these studies have not given any consideration to Kupffer cells, which could act as an interphase between the sinusoid and hepatocytes.

Three male Wistar rats (200-250 g) were given two doses of CCL_4 one hour apart (160 $\mu l/kg$ bodyweight, with 5% Emulphor in 0.85% saline) intraperitoneally (i.p.). The same number of rats received phenyl tert-butyl nitrone (PBN), 25 mg/200 g in a 0.07 M pH 7.4 phosphate buffer and corn oil i.p. 30 min prior to the administration of CCl_4 as above. Equal numbers of rats received either Emulphor in 0.85% saline or PBN only acted as controls.

The rats were euthanized with an overdose of sodium pentobarbital (i.p.). The livers were perfused with universal fixative via the hepatic portal vein (5). Small pieces of the liver tissues were collected and processed for transmission electron microscopy.

Hepatocytes from the rats treated with CCl_4 contained many vacuoles and swollen mitochondria as reported previously (2). Kupffer cells in these livers contained many secondary lysosomes and residual bodies (Fig. 1). Occasionally, these Kupffer cells were seen to be associated with electron dense particles. Some of these particles were surrounded by the Kupffer cell membrane (Fig. 2). Kupffer cells, endothelial cells and hepatocytes of the control, PBN and PBN plus CCl_4 were apparently normal.

This preliminary observation suggests that the Kupffer cells in the CCl_4 treated rats not only interfere with sinusoidal blood flow but also may be involved in the formation of metabolites to be released into the perisinusoidal space. Further studies on the role of Kupffer cells in CCl_4 hepatic toxicity are being carried out by manipulating the Kupffer cell activity.

REFERENCES

1. Traiger, G.F. and Plaa, G.L. Toxicol. Appl. Pharmacol. 20 (1971), 105.
2. Janzen, E.G., Towner, R.A. and Yamashiro, S. Free Rad. Comms. 9 (1990), 325.
3. Brattin, W.I., Glende, R.A. and Recknagel, R.O. J. Free Rad. Biol. Med. 1 (1985), 27.
4. Frank, H., Thiel, D. and MacLeod. Biochem. J. 260 (1989), 873.
5. Towner, R.A., Reinke, L.A., Janzen, E.G. and Yamashiro, S. Biochem. Biophys. Acta. 1096 (1991), 222.
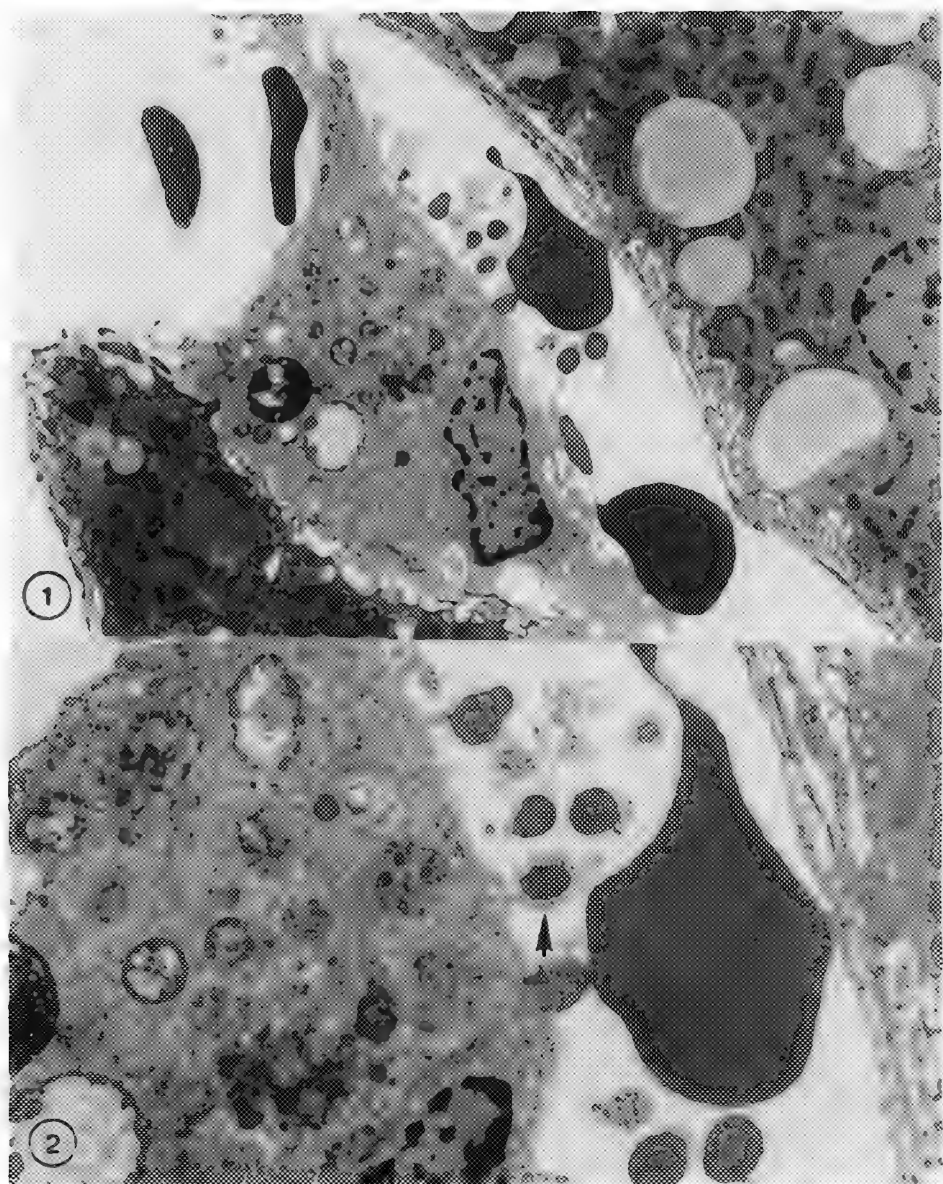
Fig. 1.   A Kupffer cells from CCl₄-treated rat depicting lysosomal bodies in the cytoplasm and electron dense bodies on the sinusoidal surface. X 5400.

Fig. 2.   Higher magnification of Fig 1 showing electron dense bodies near the cell membrane. One of them (arrow) is surrounded by the Kupffer cell membrane. X 14,400.

LOBULAR AND CELLULAR DISTRIBUTION AND CONTENT OF GLYCOGEN SYNTHASE IN PERIPORTAL AND PERICENTRAL HEPATOCYTES OF THE RAT LIVER

Bruce F. Giffin, Randal E. Morris, Richard L. Drake and Robert R. Cardell

Dept. of Anatomy and Cell Biology, Univ. of Cincinnati College of Medicine, Cincinnati, OH

Glycogen[1] and the enzymes involved in hepatic carbohydrate metabolism[2] have a heterogeneous distribution throughout the parenchyma of the liver. Although the precise lobular localization for many of these enzymes has been determined[3], information on the distribution and content of glycogen synthase (GS) has not been published. These studies were undertaken to determine: (1) the lobular and cellular distribution of GS in the fed rat; (2) any relationship between glycogen patterns and the distribution of GS.

Livers of fed male Spraque-Dawley rats were perfused with cold 30% sucrose and 10 um frozen sections collected on Vectabond treated slides. After fixation for 5 min in 4% paraformaldehyde at room temperature, tissue sections were incubated in polyethylene slide boxes with blocking buffer (PBS, 0.5% Triton X-100, 5% fetal calf serum, 2% bovine serum albumin, 0.95% fish gelatin, pH 7.5) overnight at 4°C. Tissue sections were incubated for 6 hours at room temperature with goat anti-rat liver GS diluted in blocking buffer (1:1000) followed by 5 nm gold conjugated rabbit anti-goat IgG overnight at 4°C and 3 hours with 5 nm gold conjugated goat anti-rabbit IgG at room temperature. An immunogold-silver physical development technique was used to visualize the lobular and cellular distribution of the gold conjugated antibodies by light microscopy. Serial sections were stained with hematoxylin to evaluate morphology and the PAS reaction for the determination of hepatic glycogen. Photometric image analysis was used to determined the intensity of GS immunoreactive material in pericentral (n=52) and periportal (n=52) hepatocytes.

Although GS was distributed throughout the liver parenchyma (Fig. 1), periportal and pericentral hepatocytes displayed different cellular patterns of enzyme distribution. GS in periportal cells (Fig. 2) occured in discrete clumps while pericentral cells (Fig. 3) had a more dispersed distribution of the enzyme. These cellular patterns were reminiscent of periportal (Fig. 4) and pericentral hepatocyte (Fig. 5) glycogen distributions. Quantitative photometric measurements showed 22% more GS in pericentral cells when compared to periportal cells. This finding is consistent with previous biochemical studies[2] which indicated higher rates of glycogen synthesis in the pericentral zone. The similarity between the cellular distribution of GS and glycogen suggest an association of the enzyme with glycogen synthesis occuring in the SERGE[4] compartments. Further studies are in progress to relate the cellular distribution of GS and a functional understanding of the periportal and pericentral hepatocytes.

References
1. R.R. Cardell and E.L. Cardell, J. Elec. Microscop. Tech. 14 (1990), 126.
2. K. Jungermann and N. Katz, Physiol. Rev. 69 (1989), 708.
3. H. Bartels et al., Histochemistry 95 (1990), 637.
4. R.R. Cardell et al., J. Cell Bio. 101 (1985), 201.
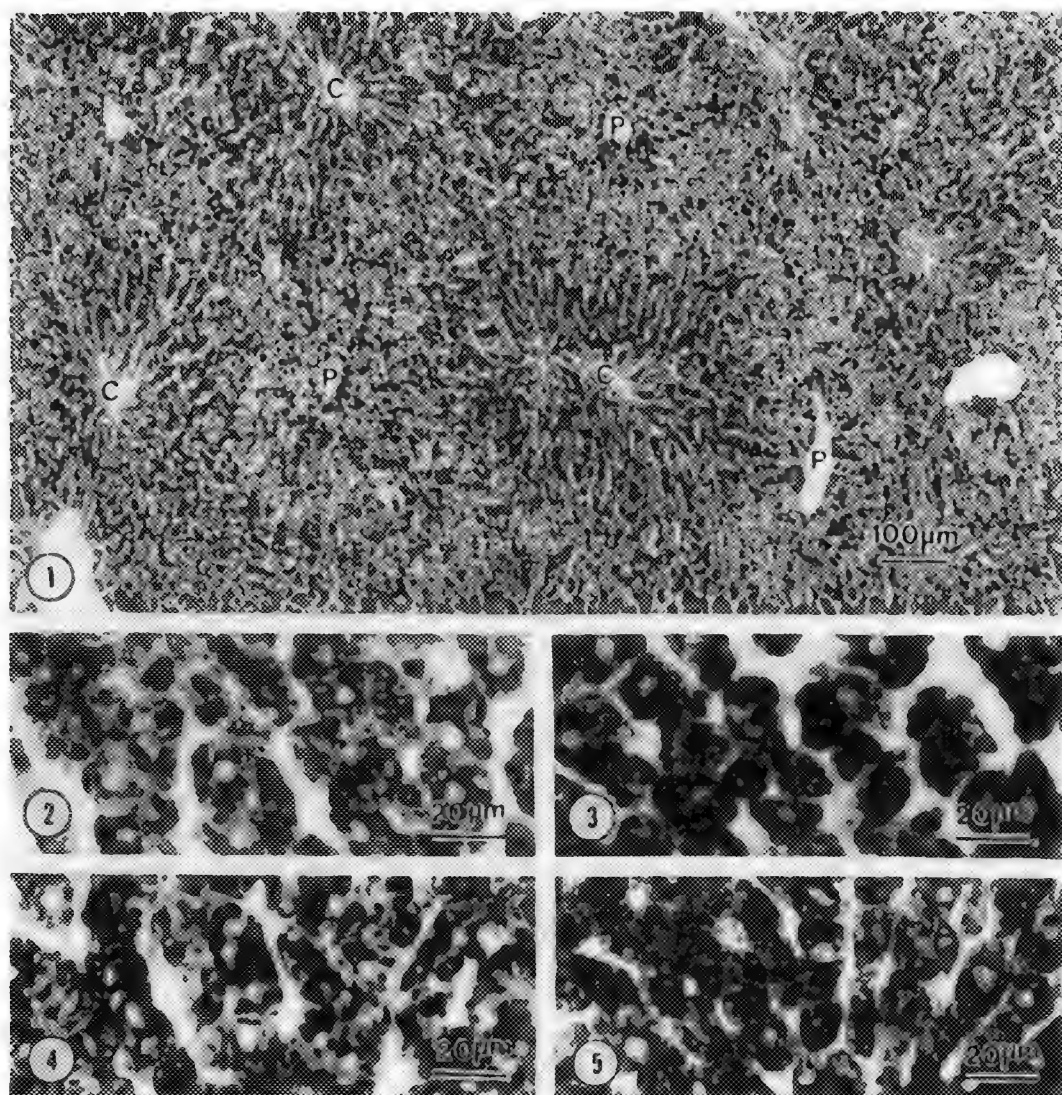
Figure 1. GS is distributed throughout the liver lobule with some heterogeneity in the cellular distribution of periportal (P) and pericentral (C) hepatocytes.

Figure 2. Dense compact masses characteristic of GS distribution in periportal hepatocytes.

Figure 3. GS is more homogeneously dispersed in pericentral hepatocytes.

Figure 4. PAS staining of hepatic glycogen shows discrete masses in periportal hepatocytes.

Figure 5. PAS staining of hepatic glycogen shows a dispersed distribution in pericentral hepatocytes.

PEROXISOME PROLIFERATION: ORGANELLES OR ACTIVITY AS AN ENDPOINT?

Catherine A. Taylor[1] and Bruce M. Jarnot[2]

[1]Department of Anatomy, Wright State University School of Medicine, Dayton OH 45435
[2]Toxicology Division, Armstrong Laboratory, Wright-Patterson AFB OH 45433

Peroxisome induction can be expressed as an increase in peroxisome area (proliferation) or as an increase in peroxisomal fatty acid oxidation (activity). This study compares proliferation and activity as endpoints for hepatic peroxisome induction by perfluorodecanoic acid (PFDA). Fluorocarboxylic acids such as PFDA represent a class of compounds possessing commercially important surfactant properties. A single 50 mg/Kg ip. dose of PFDA produces a characteristic "wasting syndrome" in male F-344 rats. Symptoms include hypophagia, weight loss, hepatomegaly, and delayed lethality. Hepatic studies reveal changes similar to those seen with the hypolipidemic agent clofibrate. These include mitochondrial disruption, endoplasmic reticulum and peroxisome proliferation, and increased peroxisomal acyl-CoA oxidase activity.

Male Fisher-344 rats received a single ip. dose of 2, 20, or 50mg/Kg PFDA dissolved in 1:1 propylene glycol/water and were sacrificed 8 days post-dose. All control rats received an equal volume of vehicle ip. Animals were provided food and water *ad libitum*, except pair-fed controls which received the same restrictive food intake consumed by their weight-paired dosed partners (50mg/Kg PFDA group) to simulate the hypophagia associated with PFDA. Peroxisome ultrastructural morphometry was performed on sections of liver selectively reacted with diaminobenzidine (DAB). 0.5mm^3 cubes were briefly fixed in buffered 4% formaldehyde, incubated with alkali DAB in the presence of KCN and H_2O_2 for catalase (peroxidase) cytochemistry, and processed for conventional transmission electron microscopy. Three photographs were generated from each liver section at 11,500x magnification. Total peroxisome area (Pa) and cytoplasmic area (Ca) were determined for each photograph and Pa/Ca ratios calculated. Peroxisome activity was assessed in fresh liver homogenates by the cyanide-insensitive oxidation of palmitoyl-CoA, expressed as nmol NADH produced/mg protein/minute.

Representative transmission electron micrographs of liver sections from control and 50mg/Kg PFDA induced rats reacted with DAB for peroxisome cytochemistry are shown in Figure 1. These micrographs present the area (15x16uM) and magnification (11,500x) used for morphometric analyses and typify the increased peroxisome area density seen following exposure. PFDA dose response and pair-fed (hypophagic) response are presented in Figure 2. Solid bars indicate average hepatic peroxisomal acyl-CoA oxidase activity in calculated as nmol NADH produced/mg protein/minute (n=5). Hatched bars present average peroxisomal content as percent cytoplasmic area, calculated by ultrastructural morphometry (n=5).

1. R.A. Gunther, Ind. Eng. Chem. Prod. Res. Dev. (1962) 1, 165.
2. C.T. Olson, Toxicol. App. Pharmacol. (1983) 70, 362.
3. F. Roels, J. Histochem. Cytochem. (1979) 27:11, 1471.
4. P.B. Lazarow, Methods Enzymol. (1981) 72, 315.
5. Research supported by a grant from the Air Force Office of Scientific Research.
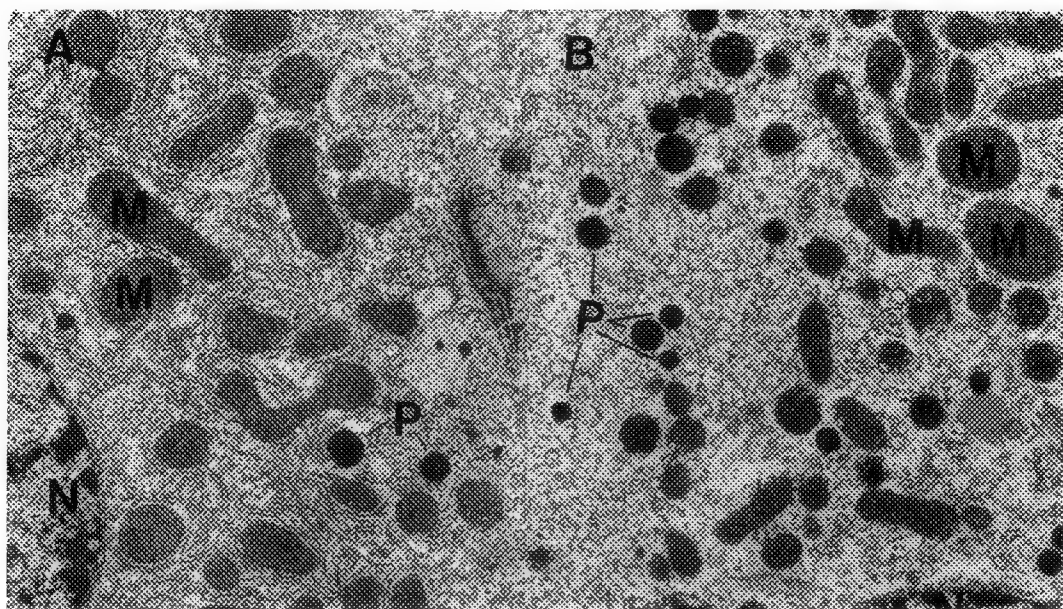
Figure 1 Representative transmission electron micrographs of liver sections from **A**) control and **B**) induced (50mg PFDA) rats reacted with DAB for peroxisome cytochemistry. Photos present magnification (11,500x) used in morphometric analyses; **N**ucleus, **M**itochondrion, **P**eroxisome.
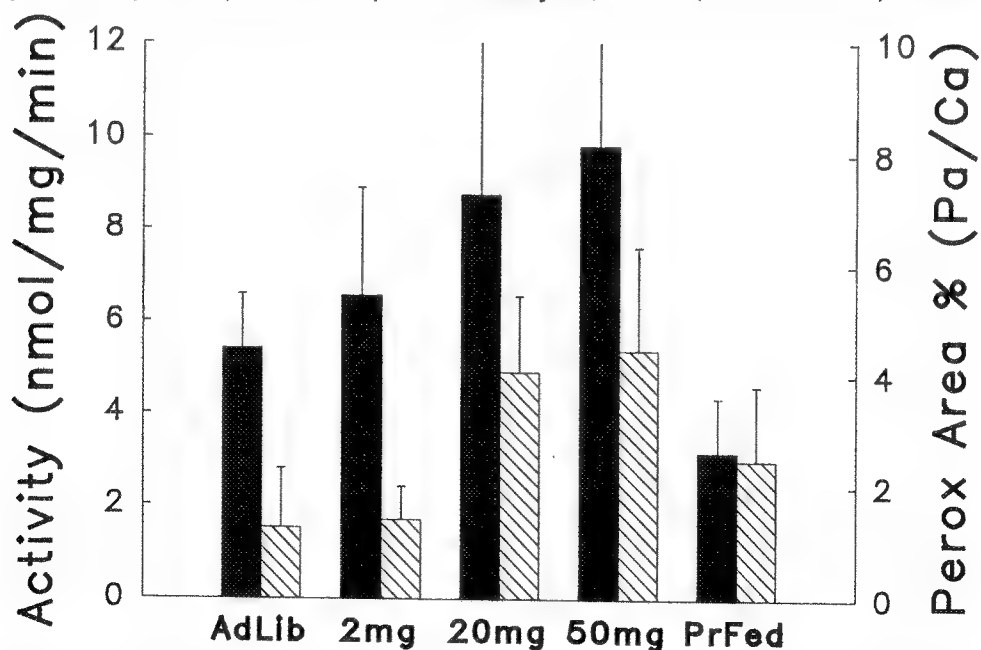
Figure 2 Comparison of hepatic peroxisomal acyl-CoA oxidase activity and area density following exposure to 2, 20, & 50mg/Kg PFDA, and in *ad lib* and pair-fed control rats.

CHEMICALLY INDUCED ACCUMULATION OF PHOSPHOLIPIDS IN CANINE ORGAN SYSTEMS

Beverly E. Maleeff[1], Charles H. Kircher[1], Alison M. Badger[2], Timothy K. Hart[1] and Peter J. Bugelski[1]

Departments of Toxicology-US[1] and Cell Sciences[2], SmithKline Beecham Pharmaceuticals,
King of Prussia, PA

Cationic amphiphilic drugs (CAD) are structurally characterized by their hydrophobic ring structure and hydrophilic side chain. Studies have shown that over 30 CADs with various pharmacological activities have the ability to induce phospholipid-like inclusions in peripheral blood cells[1] and in organs such as lung, liver and spleen.[2] SK&F 105685 is a novel cationic amphiphilic compound with immunomodulatory activity. It induces immune suppressor cell activity in many species.[3] The purpose of this study was to determine if this compound induces cytoplasmic phospholipid inclusions in dogs.

Heparinized blood samples were collected from male and female dogs after 14 and 85 days of treatment. Buffy coats were prepared and fixed with 2.5% glutaraldehyde - 2.0% paraformaldehyde with 50 µM $CaCl_2$ in 0.1M cacodylate buffer, pH 7.2. The pellets were processed to epoxy resin. Tissues from all organs were collected at necropsy in buffered formalin following 30 or 90 days of treatment, and processed for histopathologic evaluation. Portions of liver from the 30 day study were then transferred to glutaraldehyde and processed for TEM. Thin sections were mounted on 200 mesh grids and stained with uranyl acetate and lead citrate. Sections were examined with a JEOL 1200EX transmission electron microscope operating at 80 kV.

Differential evaluation of buffy coats revealed one or two electron-dense multilamellar phospholipid-like inclusions in lymphocytes and monocytes from dogs treated for 14 and 85 days (Figure 1). The presence of phospholipid-like inclusions in peripheral blood was found to be dose-related. However, there was no significant increase in phospholipid-like inclusions with time. No inclusions were seen in peripheral blood cells from the control dogs at either time point (Table 1).

Light microscopic evaluation revealed that the liver from animals treated for 30 and 90 days was affected. Diffuse microvesicular vacuolation of hepatocytes and Kupffer cells was observed. Ultrastructurally, multilamellar electron dense inclusions were observed in hepatocytes (Figure 2) and Kupffer cells. In addition, phospholipid-like inclusions were detected in bile duct epithelium.

We conclude that oral dosing of dogs with SK&F 105685, like other CADs, results in phospholipid-like inclusions in liver and peripheral blood mononuclear cells. Electron microscopy is more sensitive than light microscopy for identification of phospholipid-like inclusions in cells. Since electron microscopic examination of peripheral blood cells is a practical tool for determining if a CAD induces phospholipid accumulation in humans,[4] our data suggest that evaluation of human peripheral blood from clinical trials by electron microscopy may be a suitable diagnostic tool.[5]

References
1. Reasor, M.J., Tox. Appl. Pharmacol. 97: 47-56, 1989.
2. Kodavanti, U.P. and Mehendale, H.M., Pharmacol. Rev. 42: 327-354, 1990.
3. Kaplan, J.M., et al., J. Clin. Lab. Immunol. 36:49-58, 1991.
4. Hein, L., Xenobiotica 11: 1259-1267, 1990.
5. This work was supported by SmithKline Beecham Pharmaceuticals.
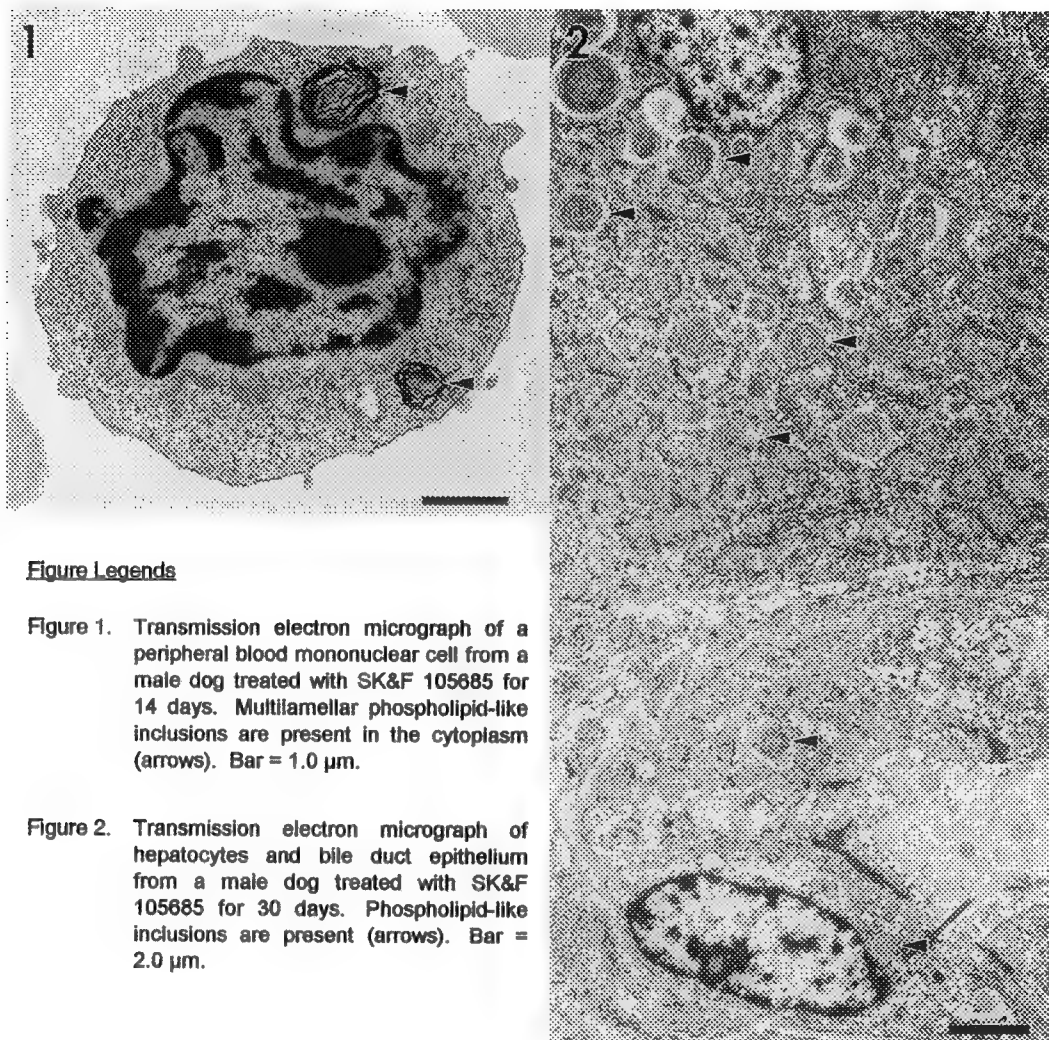
Figure Legends

Figure 1. Transmission electron micrograph of a peripheral blood mononuclear cell from a male dog treated with SK&F 105685 for 14 days. Multilamellar phospholipid-like inclusions are present in the cytoplasm (arrows). Bar = 1.0 μm.

Figure 2. Transmission electron micrograph of hepatocytes and bile duct epithelium from a male dog treated with SK&F 105685 for 30 days. Phospholipid-like inclusions are present (arrows). Bar = 2.0 μm.

Table 1.   PHOSPHOLIPID INCLUSIONS IN CANINE PERIPHERAL BLOOD
(% cells with phospholipid inclusions)*

		PMN	Eosinophils	Lymphocytes/ Monocytes
Day 14	Control	0	0	0
	Treated	0	0	15.2
Day 85	Control	0	0	0
	Treated	0	0	5.2

* Mean of 4 animals/group at day 14 and 6 animals/group at day 85

HUMAN MELANOCYTES TRANSFER PIGMENT TO EPIDERMAL KERATINOCYTES AFTER GRAFTING OF A CULTURED SKIN SUBSTITUTE TO ATHYMIC MICE

M. Dana Harriger and Steven T. Boyce

University of Cincinnati, Department of Surgery, Cincinnati, OH 45267; and Shriners Burns Institute, Cincinnati, OH 45229

Melanocytes are pigment-synthesizing cells intercalated among the basal keratinocytes along the dermal-epidermal junction of the skin. Through production of melanin, melanocytes generate skin pigmentation that provides the ultraviolet barrier in the epidermis. Melanosomes are very electron-dense, membrane-bound organelles that package and transfer pigment throughout the epidermis. Melanocytes transfer melanosomes to nearby keratinocytes in the basal layer of the epidermis. The mechanism of pigment transfer may involve either the fusion and breakdown of plasma membranes of both melanocyte and keratinocyte, establishing cytoplasmic communication, or phagocytosis of melanosome containing dendritic processes by the keratinocyte. Most melanosomes within keratinocytes are degraded by lysosomal enzymes as the cells differentiate and move upward. However, some keratinocytes retain melanosomes into the stratum corneum. Melanocytes are identified in light micrographs by their palely staining cytoplasm, ovoid nucleus, and cytoplasmic granules (Figs. 1,3) and in electron micrographs by the absence of keratin filaments and presence of melanosomes (Figs. 2,4,5,6).

Composite cultured skin substitutes (CSS) consisting of a collagen-glycosaminoglycan (C-GAG) substrate populated with human epidermal keratinocytes and fibroblasts develops into skin tissue with histologic and ultrastructural properties that closely resemble uninjured human skin within 2-4 weeks after grafting to full-thickness wounds on athymic mice.[1] Recently, human melanocytes were inoculated with the keratinocytes onto the C-GAG matrix resulting in areas of pigmentation in the graft.[2] (Figs. 1,2) Pigmented skin samples (Fig. 3) were excised from sacrificed animals, fixed with 2% glutaraldehyde/2% paraformaldehyde in 0.1M sodium cacodylate (pH 7.4), post-fixed with 1% osmium tetroxide in 0.1M sodium cacodylate buffer, and embedded in glycol methacrylate for light microscopy, or in epon-araldite for electron microscopy.[3]

Melanocytes are evident in the basal layer of the epidermis and in the dermis underlying the epidermal-dermal junction. Melanosomes are present in the cytoplasm of adjacent keratinocytes demonstrating pigment transfer has occurred (Figs. 4,5,6). However, the mechanism of transfer cannot be determined from this study. These results demonstrate that cultured melanocytes persist after grafting, and transfer melanosomes to keratinocytes to restore pigmentation in healed skin.

References
1. S.T. Boyce, et al., Surgery 110 (1991) 866.
2. S.T. Boyce, et al., J Invest Dermatol (1993) in press.
3. J.J. Wolosewick and K.R. Porter, in Maramorosh and Hirumi, Eds., Practical Tissue Culture Applications, New York: Academic Press (1979) 58.
4. Supported in part by Shriners Hospitals for Crippled Children grants #15837 and #15893.
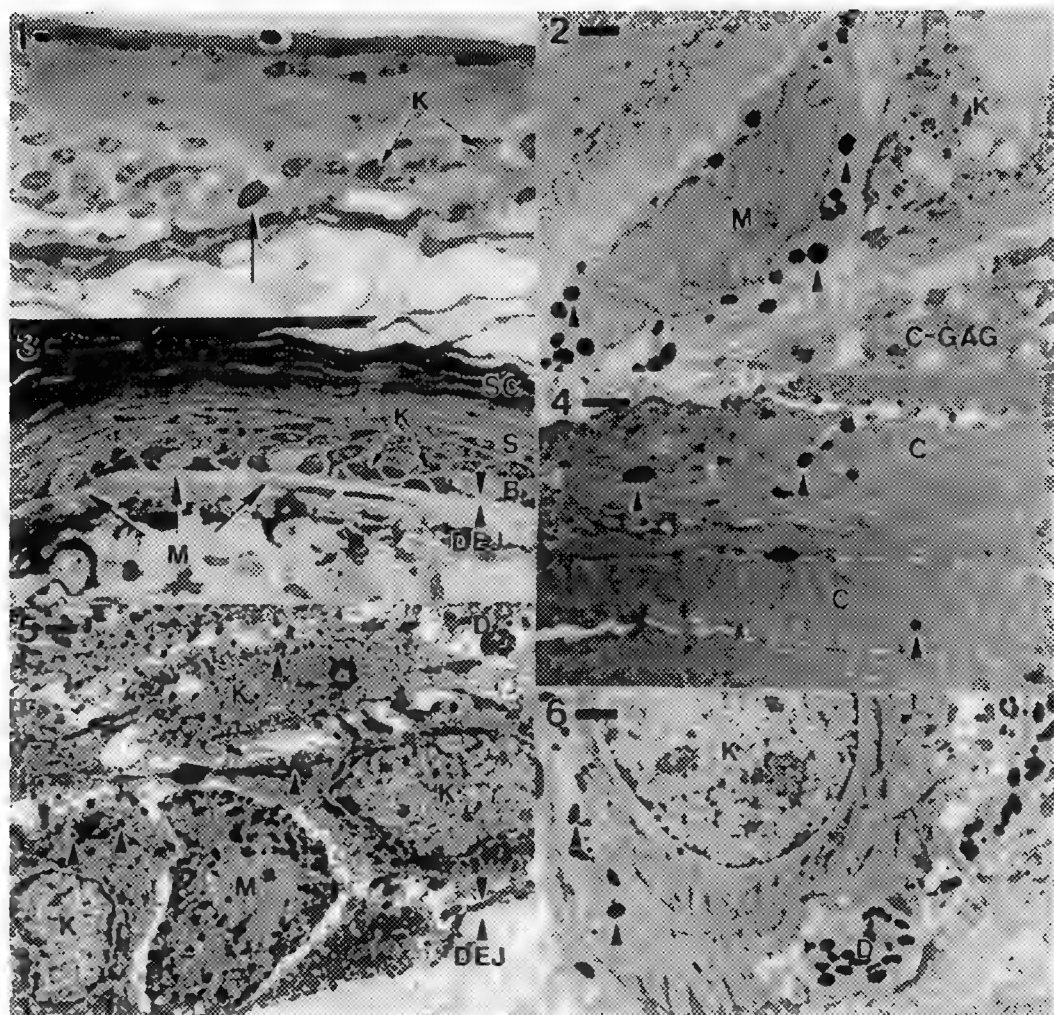
Fig. 1. CSS indicating melanocyte (arrow) among cultured keratinocytes (K). Bar =10μm.

Fig. 2. CSS demonstrating association of melanocyte (M) with melanosomes (arrowheads) and cultured keratinocyte (K) on C-GAG substrate. Bar = 1μm.

Fig. 3. Healed skin with melanocytes (arrows) among basal keratinocytes (K); dermal-epidermal junction (DEJ), basal layer (B), spinosal layer (S), stratum corneum (SC). Bar =10μm.

Fig. 4. Stratum corneum of healed skin demonstrating retention of melanosomes (arrowheads) within corneocytes (C). Bar = 1μm.

Fig. 5. Pigment transfer via melanosomes (arrowheads) from melanocyte (M) to adjacent keratinocytes (K); melanocyte dendrite (D). Note circular distribution of melanosomes in keratinocyte (asterisk) suggesting dendrite phagocytosis. Bar = 1μm.

Fig. 6. Basal keratinocyte (K) with melanosomes (arrowheads) completely surrounds melanocyte dendrite (D). Bar = 1μm.

HISTOCHEMICAL AND IMMUNOCYTOCHEMICAL ULTRASTRUCTURAL LOCALIZATION OF MELANOCYTE SPECIFIC PROTEINS

Ying L. Boissy, Seth J. Orlow[*] and Raymond E. Boissy

Departments of Dermatology & Cell Biology, University of Cincinnati College of Medicine, Cincinnati, OH, and [*]New York University School of Medicine, New York, NY

Melanin synthesis in melanocytes is localized to melanosomes, where enzymatic and structural gene products must be targeted. Some gene products are translocated through different pathways (*i.e.*, tyrosinase travels through the Golgi apparatus during processing[1], whereas a putative matrix glycoprotein does not[2]). To visualize trafficking routes, we used post-embedding immunocytochemistry to compliment DOPA-histochemistry. We report on the localization of tyrosinase, matrix glycoprotein, tyrosinase-related protein 1 (TRP-1)[3] and lysosome-associated membrane protein-1 (LAMP-1)[4].

DOPA histochemistry: Cultured melanoma cells were fixed in half-strength Karnovsky's, incubated in 0.1% l-DOPA 2X for 2.5 h and embedded in Eponate 12. For immunocytochemistry, cells were fixed with 4% paraformaldehyde, 1% glutaraldehyde, and 0.2% picric acid with 0.5 mM $CaCl_2$ (pH 7.4) for 20 m at RT, quenched in 50 mM NH_4Cl for 20 m at 0°C, washed in 0.1 M maleate buffer (pH 6.5), and treated with 2% uranyl acetate (pH 4.0) for 30 m at 0° C.[5] Cells were embedded in Lowicryl K4M at -20°C. Immunolabelling: Sections washed with 50 mM Tris containing 150 mM NaCl at pH 7.4 (TBS) were blocked with 1% BSA/0.02% Tween 20 (TBS-ICC) for 10 m. Specimens were treated with primary antisera (PEP-1 and PEP-2 [against the carboxy and amino termini of TRP-1 respectively][3], antivesicle/LAMP-1[4] and normal rabbit serum at 1:100-1:200, and antimatrix (MX)[2] at 1:10,000) diluted in TBS-ICC for 2 h at RT. Specimens were incubated with Protein A conjugated to 5 nm or 18 nm colloidal gold particles (from Randall Morris) diluted 1:10 in TBS for 1 h at RT, stabilized with 2% glutaraldehyde for 5 m and stained with 2% O_SO_4/Reynold's lead citrate.

Tyrosinase was histochemically localized to the trans-Golgi network (TGN), coated vesicles, and premelanosomes (Figs. 1 & 2). By immunocytochemistry, TRP-1 localizes to the TGN (Figs. 3 & 4) and vesicles by the TGN (Figs. 5 & 6). These vesicles, which also contain LAMP-1 (not shown), may be a pre-melanosomal/lysosomal organelle.[6] Gold staining for TRP-1 subjectively differs between the two PEPs in that PEP-1/gold appears predominantly on the cytoplasmic side or on the membrane (Figs. 3 & 5), whereas PEP-2/gold appears within the lumen (Figs. 4 & 6), of the TGN cisternae or vesicles. Antibodies against a melanocyte vesicle preparation (which contains LAMP-1) or purified melanosome matrix demonstrate specificity for the melanosome (Figs. 7 & 8). This report demonstrates post-embedding immunocytochemistry for preliminary cellular localization of melanocyte specific proteins.

References

1. A. B. Novikoff et al., J. Histochem. Cytochem. (1968)16, 299.
2. S. J. Orlow et al., J. Invest. Dermatol. (1993) submitted.
3. M. Jimenez et al., J. Biol. Chem. (1991)266, 1147.
4. B-K Zhou et al., J Invest. Dermatol. (1993)100, 110.
5. M. A. Berryman and R. D. Rodewald, J. Histochem. Cytochem. (1990)38, 159.
6. S. J. Orlow et al., J Invest. Dermatol. (1993)100, 55.
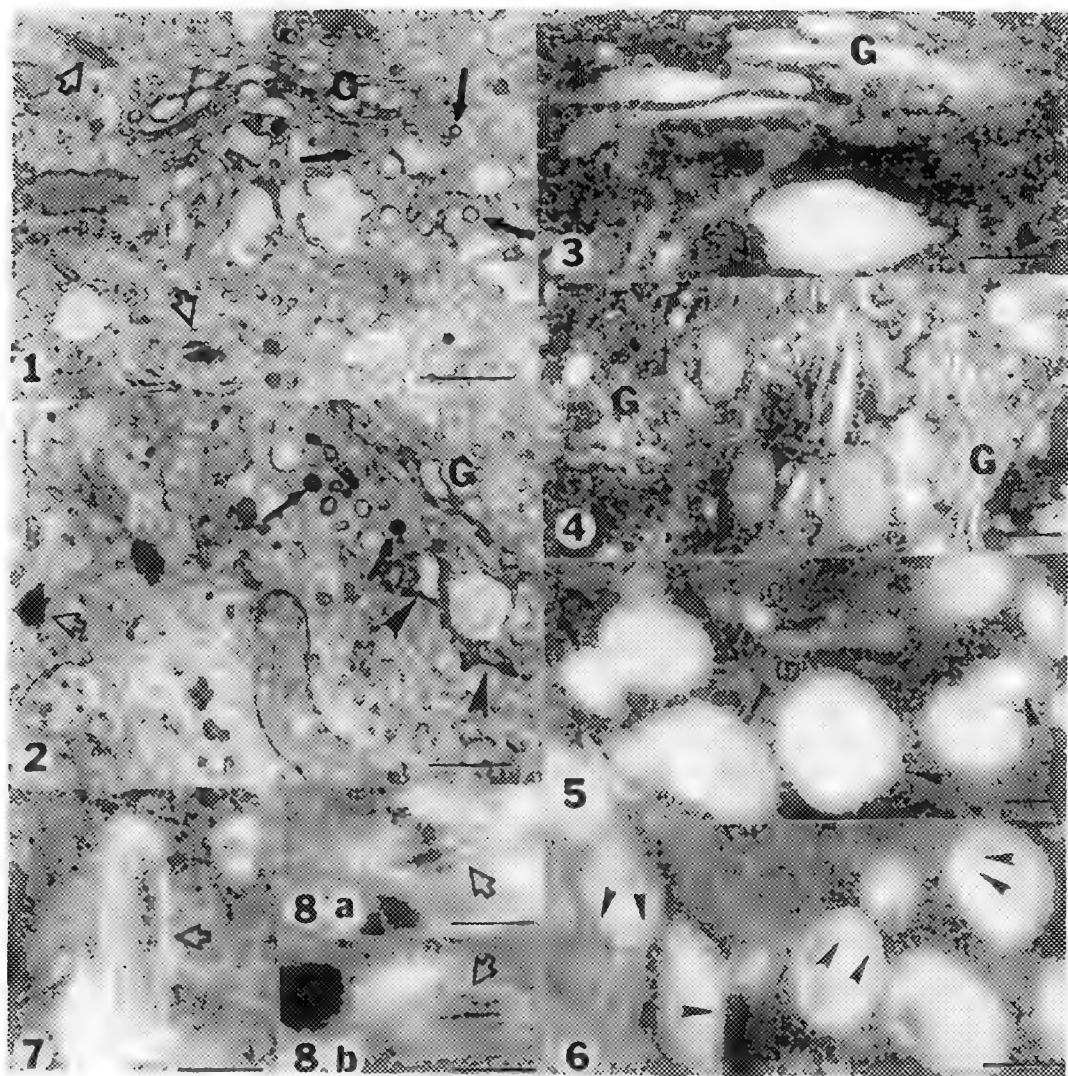
FIG. 1 - Perinuclear area of cultured melanoma cell demonstrating Golgi apparatus (G), associated coated vesicles (arrows), and unmelanized premelanosomes (open arrows). Bar = 0.4 μm.

FIG. 2 - Melanoma cell incubated in l-DOPA demonstrating reaction product within cisterna (arrowheads) and coated vesicles (arrows) of TGN and premelanosomes (open arrow). Bar = 0.4 μm.

FIG. 3 & 4 - TRP-1 immunolocalized with PEP-1 & PEP-2 respectively within Golgi apparatus (G) and TGN. Bars = 0.2 μm.

FIG. 5 & 6 - TRP-1 immunolocalized with PEP-1 & PEP-2 respectively (arrowheads) within early premelanosomes. Bars = 0.2 μm.

FIG. 7 & 8 - Immunolocalization using antisera produced against isolated melanocyte vesicles & melanosome matrix respectively within premelanosomes (open arrows). Bars = 0.2 μm.

INTRACYTOPLASMIC LUMINA IN EPENDYMOMAS: AN ULTRASTRUCTURAL STUDY

Khang L. Ho, Dario V. Caccamo and Julio H. Garcia

Department of Pathology, Henry Ford Hospital, Detroit, MI 48202

Intracytoplasmic lumina (ICL) are round to oval, single membrane bound spaces bearing microvilli that may or may not contain secretory material. The morphogenesis of ICL remains controversial and their biological significance and diagnostic implication of this structure have not been fully explored[1,2,3]. ICL have been reported in a variety of epithelial tumors outside the central nervous system, but this structure is rarely described in tumors of the central nervous system[4].

We analyzed ultrastructural features of ICL in six ependymomas (1 from lateral ventricle, 3 from fourth ventricle and 2 from the spinal cord) and three myxopapillary ependymomas of the filum terminale. Two types of ICL were identified: (1) ICL with both microvilli and cilia and (2) ICL with only microvilli (Fig.1). Ciliated ICL were common in ependymomas of the ventricles whereas non-ciliated ICL were frequently seen in myxopapillary variant. Various stages of formation and development were observed in ciliated ICL (Fig. 2,3). The first stage was characterized by the distension of an intracytoplasmic cilium. The second stage was featured by the formation of microvilli resulting from protrusion of the cytoplasm into the distended ciliary cistern. The third stage was characterized by enlargement of their size which resulted partly from the fusion of adjacent ICL or fusion of ICL with cytoplasmic vesicles. The fourth stage was characterized by fusion of ICL with cytoplasmic membrane. After fusion, ICL opened into the extracellular space or into the intercellular space between two closely apposed ependymal cells (Fig. 3). The origin of non-ciliated ICL was not clear. There was no evidence that non-ciliated ICL were closely related to Golgi apparatus, endoplasmic reticulum or mitochondria. Non-ciliated ICL may represent pseudo-lumina which resulted from invagination of extracellular space within the cytoplasm.

Large ciliated and non-ciliated ICL frequently contained loose or condensed granulo-fibrillary material in the lumen. The cytoplasm surrounding ICL did not show any unusual features. Aggregate of cytoplasmic filaments at the periphery of ICL, which is a common finding in ICL of meningioma [5] and ICL of neoplasms outside the central nervous system, is not seen in ependymomas.

Ciliated ICL have not been described in other neoplasms[6]. They may represent a characteristic ultrastructural feature of ependymomas. We suggest that fusion between ciliated ICL and the cytoplasmic membrane and subsequent opening of ciliated ICL into the narrow intercellular space may lead to the formation of intercellular microrosette which is a characteristic feature of ependymomas[7].

References

1. FN Ghadially: Ultrastructure pathology of the cell and matrix. 3rd Edition, Butterworths, London. (1988), p 1010.
2. M Sobrinho-Simoes, JV Johannessen and VE Gould: Ultrastruct Pathol. (1981) 2, 327.
3. K Donhijsen, U Schmidt, etc.: Hum Pathol. (1992), 23, 860.
4. KL Ho, DV Caccamo and JH Garcia: J Neuropathol Exp Neurol. (1992) 51, 300.
5. A Alguacil-Garcia, NM Pettigrew and AAF Sima, Am J Surg Pathol. (1986) 10, 102.
6. M Boysen, A Reith : Ultrastruct Pathol. (1980), 1; 477.
7. DS Russell and LJ Rubinstein: Pathology of tumors of the nervous system. 5th Edition, Williams and Wilkins, Baltimore. (1989) p 196.
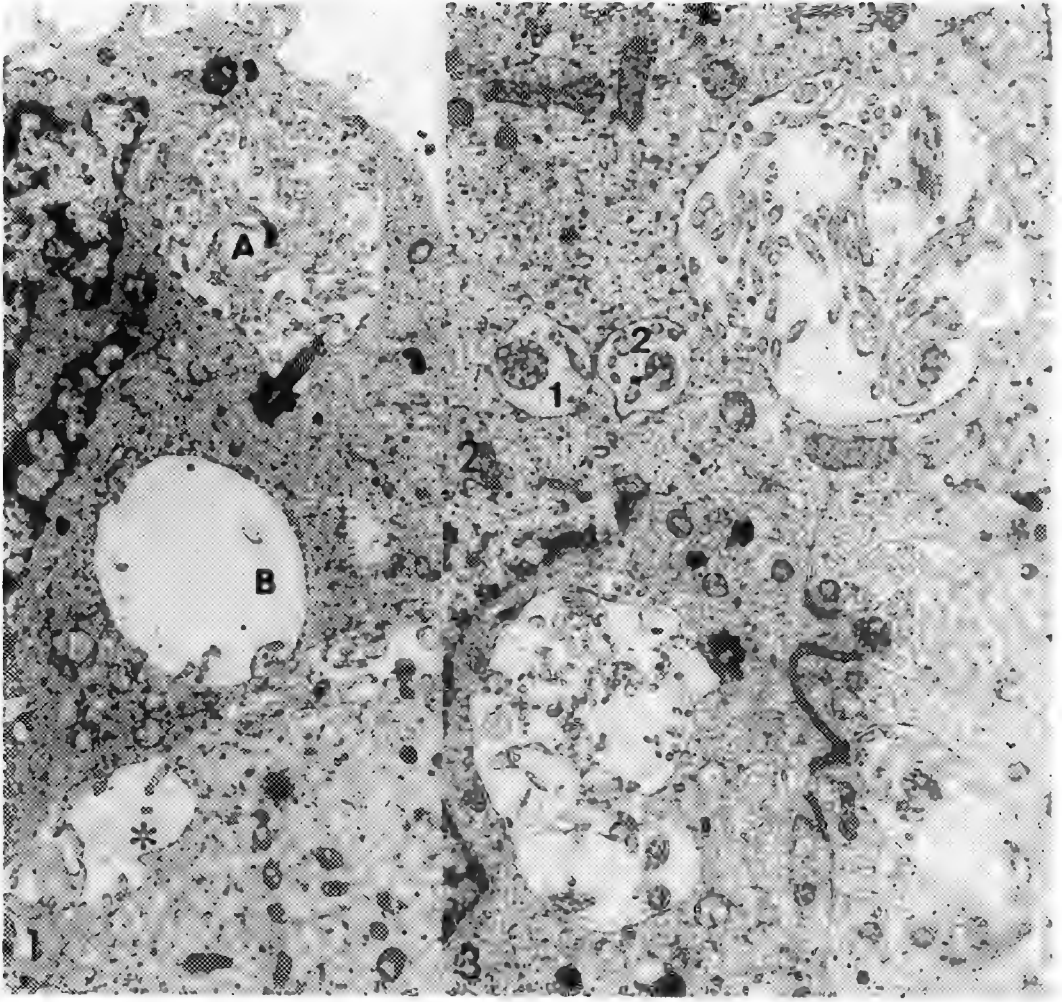
FIG. 1.--An ependymomal cell contains both ciliated (A) and non-ciliated (B) ICL. Asterisk indicates the intercellular space. X13,000

Fig. 2 --An ependymoma cell contains three ciliated ICL in different stages of development. ICL 1 represents early stage of development showing distension of the peniciliary cistern with one microvillus. ICL 2 shows fusion of a coated vesicle. The cilium in both ICL 1 and ICL 2 is abnormal in the microtubular pattern. x15,000

FIG 3.--Three ciliated ICL are fused with the cytoplasmic membrane and open into a narrow intercellular space. Note the presence of prominent and elongated zonulae adherentes at the sites of opening. x 15,000.

ADRENAL AND VAGUS MODULATION OF CISPLATIN-INDUCED GASTRIC EMPTYING
AND ULCERATION

Surinder K. Aggarwal

Department of Zoology, Michigan State University, East Lansing,
Michigan 48824-1115 U.S.A.

Cisplatin is a most valuable broad spectrum antineoplastic drug
available for the treatment of testicular and ovarian cancers.[1] It
has several severe toxic side effects of which gastrointestinal and
nephrotoxicity are the major dose limiting.[2,3] It also induces
hypocalcemia and hypomagnesemia that have been demonstrated to
effect the secretory activity of the neurohypophysis and the
parathyroid glands.[4] In rats cisplatin treatment causes stomach
bloating and ulceration that can be ablated by daily injections of
calcium just before the treatment and during the treatment or using
vagotomy.[5] Adrenalectomy has also been shown to prevent ulceration.
Present study is an effort to determine the effect of cisplatin on
morphological and cytochemical changes in the neuromuscular
interactions of the stomach smooth muscle and the adrenal glands
before and after vagotomy.

Male Wistar rats [Crl:(WI)BR] weighing 200-300 g were given
intraperitoneal injection of 9 mg/kg in 0.85% saline. Alternate
group of animals received in addition daily injections of calcium
(1 ml of 1.3% calcium chloride). Bilateral cervical vagotomy was
performed on anaesthetized rats. All animals were killed on day 6
of the treatment. Three days after cisplatin treatment 6 animals
were given choline chloride (Methyl-^{3}H) as intraperitoneal injection
(6 μC/kg) and were sacrificed at 5 min, 3 and 12 h intervals.
Cardiac, pyloric and sphincter tissues were digested in protosol
and radioactivity measured. Autoradiograms of the same tissues were
prepared to localize the incorporation of ^{3}H-choline.

Cisplatin treatment strongly inhibits gastric emptying after 3 days
and one can observe elevated levels of gastric acid secretions with
prominent ulcer lesions at day 5. Cisplatin causes significant
telangiectasia both in the cortex and the medulla of the adrenal
gland. There is observed a sharp decrease in the lipid content of
the zona fasciculata and zona reticularis of the adrenal cortex
(Figures 1, 2) with little change in the zona glomerulosa. The
inner mitochondrial membranes show a pronounced swelling and there
is a general cavitation in the mitochondria. The medullary portion
of the adrenal shows atrophy with swollen epinephrine and
norepinephrine granules.

Bilateral cervical vagotomy causes an increase in the lipid
droplets of both the aldosterone and the corticosterone cells of
the cortex within two days indicating a steroidal hormonal
precursor accumulation and a reflection of the suppression in the
functional activity of the regions. Simultaneously, there are
observed no lesions in the gastric walls after vagotomy and the

gastric acid levels are also depressed. Choline-^{3}H incorporation studies show an accumulation of choline in the synaptic vesicles after cisplatin treatment. Vagotomy or calcium supplements in the form of daily injections (iv) seem to protect the normal stomach functions from cisplatin induced gastric emptying and ulceration.

1.   Nicolini M. 1988. Platinum and other metal coordination compounds in cancer chemotherapy. Boston: Martinus Nijhoff.
2.   Hacker MP, et al. 1984. Platinum coordination complexes in cancer chemotherapy. Boston: Martinus Nijhoff.
3.   Schaeppi J, et al. 1973. Toxicol Appl Pharmacol.**25**, 230
4.   Aggarwal SK and Fadool JM. 1993. Anti-Cancer Drugs **4**, 2.
5.   Valen B, et al. 1991. Surgery, **110**, 824
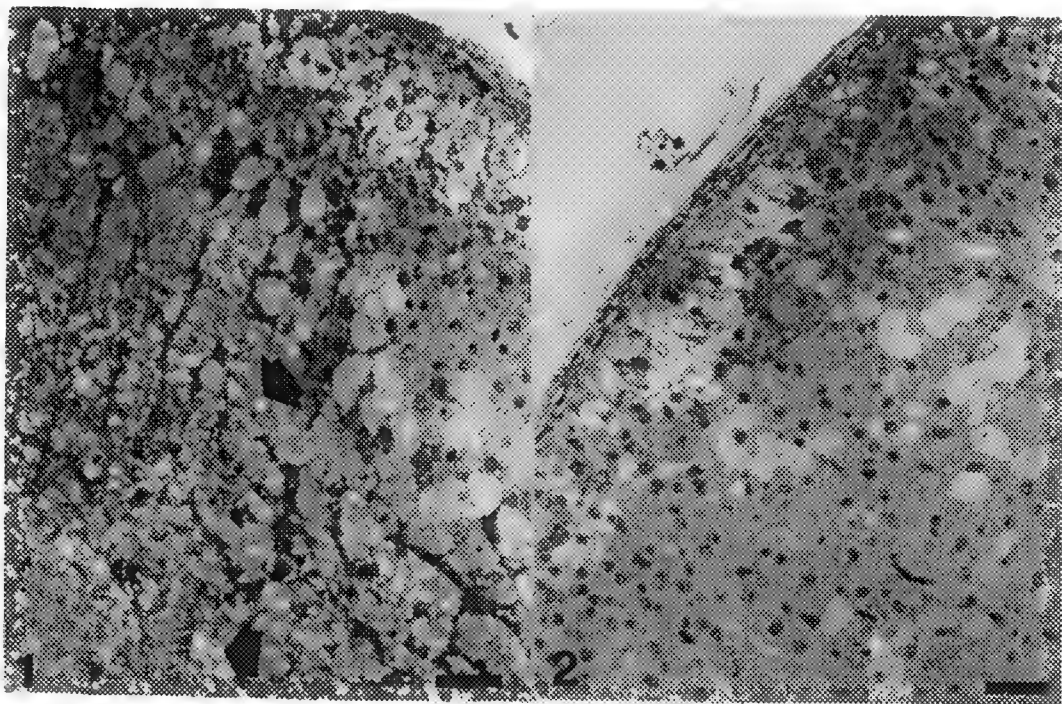
Figure 1. Cross section through the cortex of the rat adrenal stained with methylene blue showing the distribution of lipids (arrows).
Figure 2. Cross section through the cortex of the rat adrenal treated with cisplatin (9 mg/kg) for 5 days. Note the absence of lipids from the zona fasciculata and zona reticularis. Bar=0.05mm

407

CYTOARCHITECTURE OF CULTURED OLFACTORY NEUROEPITHELIAL SPHERES: THE ROLE OF OLFACTORY SUSTENTACULAR CELLS IN CAVITY FORMATION

Sarah K. Pixley and Marian Miller

Departments of Anatomy and Cell Biology, and Environmental Health, University of Cincinnati, Cincinnati, OH 45276

When newborn rat olfactory mucosal cells were dissaggregated and plated as single cells onto astrocyte bed layers, abundant generation and maturation of olfactory receptor neurons was observed[1]. Both immature and mature neurons were found in large multicellular spheres after 15 days in culture,[1]. In sections of the spheres, almost all had central cavities, and the neurons were located almost exclusively in the external 1-2 cell layers[2]. We show here that the spheres also contain olfactory sustentacular cells, neuronal supporting cells similar to retinal Muller cells. Sustentacular cell presence was shown by immunostaining cultured cells with a monoclonal antibody, SUS, which has previously been shown to recognize only sustentacular cells and a subset of the Bowman's gland cells[3]. Fig. 1 shows that cultured cellular spheres contained numerous SUS-positive, roughly bipolar cells. These cells appear to be located internally rather than on the external surface. Sustentacular cell presence was further confirmed by immunostaining with a monoclonal antibody, 1F4, developed in this laboratory[4]. 1F4 binds, at the EM level, to bind to only the microvilli of sustentacular cells in the olfactory epithelium[4]. 1F4 staining of the cultures is shown in Fig. 2. To determine the location relative to neurons, cultures were double immunostained with SUS and an antibody marker for mature neurons, anti-olfactory marker protein (OMP). Fluorescent secondary antibodies were used and imaging was done with confocal microscopy (Fig. 3). SUS-positive cells (a) were located around the central cavity and internal to OMP-positive neurons (b). The internal location of sustentacular cells was further confirmed by sectioning SUS-stained cultures after plastic embedding. Fig. 4 (a) shows toluidine blue staining of a sectioned sphere, and Fig. 4 (b) shows the same sphere viewed through a dark blue filter, allowing visualization of the SUS-positive cells bordering the cavity. To further identify the sustentacular cells and to determine their role in formation of the cavities, cultures were examined by TEM. Fig. 5 shows that cells with microvilli formed the lining of the cavities. Sustentacular cells are the only microvillar-bearing cells of the olfactory epithelia. The microvilli had an unusual glycocalyx coating and external strands of material, suggesting the presence in the cavity of proteinaceous material (perhaps similar to nasal mucus). The microvilli-bearing cells contained numerous tight junctions, Fig. 6, arrows. The tight junctional placement suggests that the olfactory sustentacular cells had created a a fluid barrier between the cavity and the cells within the wall of the cavity. This further suggests that the sustentacular cells play a role in the formation of the central cavity, and thus a role in formation of the multicellular spheres. These spheres are the only sites of neurogenesis and neuronal maturation in these cultures.

1. S.K. Pixley, Neuron. (1992)8, 1191.
2. S.K. Pixley, L. Hastings, D. Miller, and M.L. Miller, AchemS. Abs. (1993), April, 1993.
3. Hempstead, J.L. and J.I. Morgan, Brain Res. (1983) 288, 289.
4. Pixley, S.K. and B. Menco, Chem. Senses. (1991)16, 568.
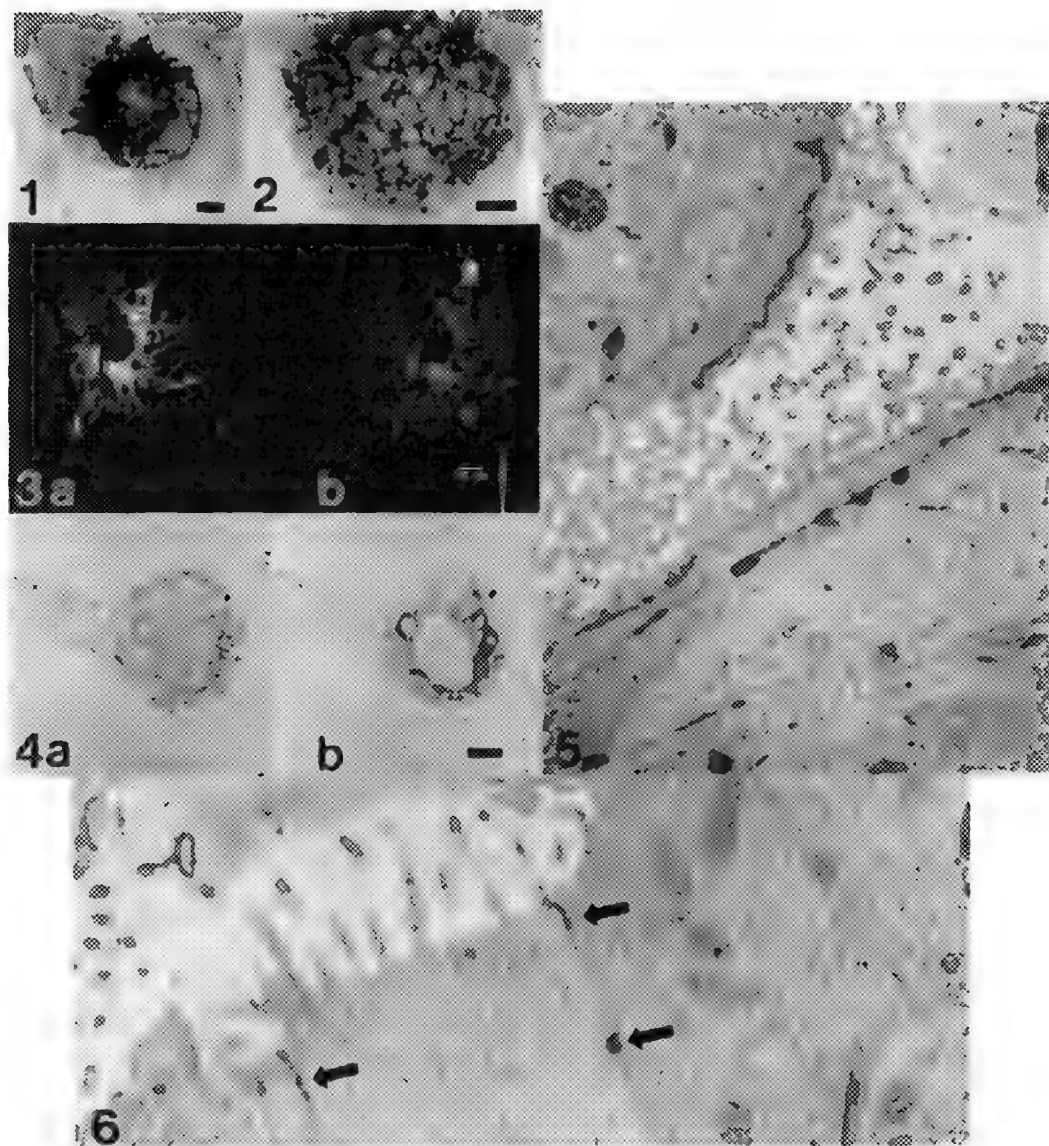
FIG 1 --LM of whole mount of 15 day olfactory epithelial sphere immunostained with SUS (ABC immunostaining techniques with horseradish peroxidase and diaminobenzidine, no counterstain Bar=20 µm
FIG 2 --LM of whole mount of 15 day olfactory epithelial sphere immunsotained as in Fig. 1, using the 1F4 monoclonal antibody. Bar=20 µm.
FIG 3 --Confocal Microscopy of SUS (a) and OMP (b) double immunolabelled olfactory epithelial sphere
FIG 4. --LM of sectioned olfactory epithelial sphere immunostained with SUS (a) shows toluidine blue counterstaining, while use of a dark filter allows visualization of the peroxidase staining in (b) Bar= 10 µm
FIG 5. --TEM of olfactory epithelial sphere Central cavity is shown It contains numerous microvilli
FIG. 6. --TEM of olfactory epithelial sphere Microvilli-bearing cells have tight junctions (arrows)

AN SEM EVALUATION OF NORMAL, HYPERMINERALIZED, AND DEMINERALIZED HUMAN DENTIN AND ITS INTERACTION WITH DENTIN BONDING SYSTEMS

Jorge Perdigao

Department of Operative Dentistry and Central Electron Microscopy Research Facility, The University of Iowa, Iowa City, IA 52242, USA

The mechanism of bonding to enamel has been described as tag-like resin extensions into the etched enamel structure.[1] However, the mechanism by which resins bond to dentin has not been fully elucidated. Bonding to dentin represents a greater challenge than bonding to enamel due to the organic composition of dentin, the presence of fluid-filled tubules, variations in intrinsic composition, and the presence of the odontoblastic process in dentinal tubules. Bonding to mineralized dentin surfaces is more difficult than bonding to normal dentin.[2] The purpose of this study was to evaluate the morphology of three different dentin substrates and their interaction with four different dentin bonding systems (DBS).

One-hundred twenty caries-free human molar teeth stored in an thymol solution were randomly assigned into three groups (n=40), according to the type of surface treatment. After removing the occlusal dentin, forty teeth were suspended in 600 ml of a mineralizing solution for two weeks. The mineralizing solution (pH=7) contained 1.5 mM $CaCl_2.2H_2O$ + 0.9 mM K_2PO_4 + 0.15 M KCl. Another group of 40 teeth was suspended in a demineralizing solution of 0.1 mol/L acetic acid at $4^{\circ}C$, for one week. The remaining 40 teeth were kept in distilled water at room temperature. The teeth were further assigned to one of the DBS's: All-Bond 2 (AB2), Amalgambond Plus (AM), Prisma Universal Bond 3 (PUB3), and Scotchbond Multi-Purpose (SB). After bonding and thermocycling, the specimens were tested in shear. Two specimens of each of the 12 bonding groups plus two for each of the dentin substrates were processed for SEM observation. Longitudinal 300 μm sections were taken using a Silverstone-Taylor microtome. Sections of the restored specimens were immersed in 6 ML HCl for 30 s and 1% NaOCl for 12 h to demineralize and deproteinize dentin. All specimens were mounted on aluminum stubs with colloidal silver, vacuum-desiccated for 24 h, sputter-coated with gold-palladium, and examined in a Hitachi S-4000 Field Emission SEM at 12 kV Vacc and 10 mm WD.

The intertubular dentin in mineralized specimens seemed to be covered with a mineral deposit. In cross-section, demineralized dentin showed exposed collagen fibers. The morphology of the dentin-resin interface of the restored specimens is shown in micrographs 5 to 8. Funnel-shaped rough resin tags were evident in AB2 and AM specimens, when applied to normal dentin. AB2 and AM also displayed a hybrid layer. PUB3 generally did not penetrate the dentinal tubules, which is in agreement with the presence of the smear layer. The hybrid layer was generally absent in demineralized and hypermineralized specimens. The bond strengths to normal dentin were higher than to mineralized dentin; the bond strengths to mineralized dentin were higher than to demineralized dentin. This may be related to the partial obliteration of intertubular dentin by mineral deposition in hypermineralized dentin, and to calcium removal in demineralized dentin. Our results on mineralized dentin confirm that the mineral content of intertubular dentin is an important factor in bonding. The results with demineralized dentin suggest that a micromechanical infiltration into etched hydroxyapatite may be a major component of the bonding process. Clinically, hypermineralized substrates occur with sclerotic dentin and under carious lesions.[2,3] Thus, the use of these adhesive systems in these clinical situations without appropriate mechanical retention may be contraindicated.[4]

References
1.   A.J.Gwinnett and A.Matsui, Arch.Oral Biol.(1967)12,1615.

2. E.S.Duke and J.Lindemuth, Am.J.Dent.(1991)4,241.
3. N.Kurosaki et al., Quintessence Int.(1990)21,87.
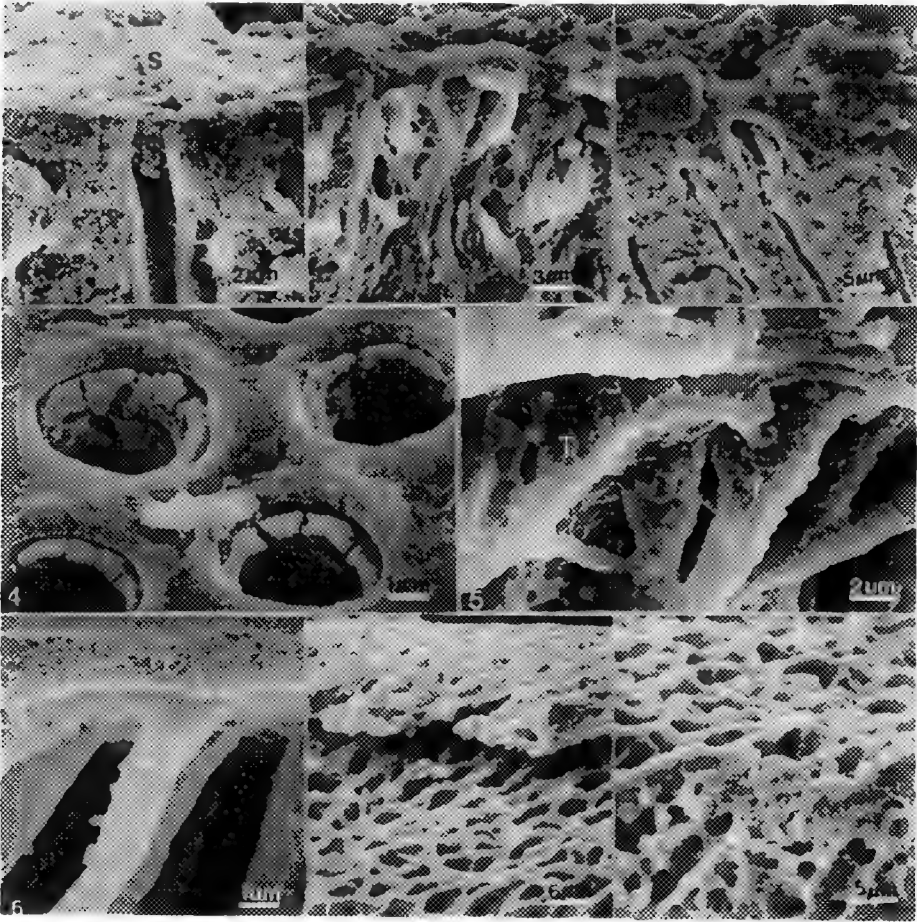
Fig.1. Cross-sectional view of untreated dentin. S - smear layer.
Fig.2. Cross-sectional view of demineralized dentin.
Fig.3. Cross-sectional view of hypermineralized dentin.
Fig.4. Hypermineralized dentin: deposition of mineral on the intertubular dentin.
Fig.5. Penetration of AB2 into normal dentin. T - resin tag.
Fig.6. Penetration of AM into normal dentin. H - Hybrid layer.
Fig.7. Penetration of PUB3 into mineralized dentin.
Fig 8. SB interaction with demineralized dentin.

SEM COMPARISON BETWEEN DENTIN SURFACES ETCHED WITH ACID AGENTS AND DENTIN SURFACES IRRADIATED WITH LASER

Jaime Silberman, D.D.S., Marcos Vargas, D.D.S., Gerald Denehy, D.D.S., M.S.

College of Dentistry, The University of Iowa, Iowa City, Iowa, 52242

Preliminary research has indicated that laser etching may create a roughened dentin surface similar to that produced by enamel acid etching. Localized melting and recrystallization produce fungiform projections on dentinal surfaces (1,2). Consequently, this surface may present potential for bonding composite resin restorations (3,4). The purpose of this investigation was to compare using SEM and dentin topography that results from both acid etching and laser treatment, and also make comparisons between the effectiveness of various laser exposure parameters. In addition, a shear bond strength pilot study was done to corroborate the SEM results.

Forty-two molars were collected and randomly divided into six groups. Dentin surfaces were prepared by horizontal section through the middle third of the teeth crown and finished with 600-grit paper. Five of the groups were laser treated with LX-20 CO_2 surgical laser. The dentin treatments of each group were as follows: Group #1: Dentin etched with 10% Maleic Acid, Group #2: Dentin irradiated with CO_2 laser at 2W mode 5, Group #3: Dentin etched with 10% Maleic acid and 3W mode 5 and then etched with 10% Maleic acid, Group #5: Dentin irradiated at 3W mode 7, Group #6: Dentin irradiated at 3W mode 9.

Twelve prepared teeth were used for SEM analysis. For the bond strength pilot study, the dentin surfaces of five teeth in each group were properly treated with a hydrophilic dentin bonding agent (Scotchbond Multi Purpose). A hybrid composite resin (Z-100) was attached to the tooth using 4.5 mm diameter capsules and polymerized. The samples were tested for shear strength of the bonded composite cylinders using an Instron testing machine.

SEM observations showed different topographic characteristics in the six groups relating to the intertubular dentin, peritubular dentin and the presence of smear layer (fig. 2,3,4,5,6). It appears that the laser treatment at 3W mode 9 melts the dentin surface resulting in a partially or totally obstructed micromechanical attachment with the bonding system. The presence of smear layer at 3W mode 5 and at 3W mode 7 apparently produce the same effect. Both observations would minimize the possible formation of the hybrid layer.

The bond strength pilot study showed that the samples only with 10% Maleic acid demonstrated higher bond strength that the samples irradiated with laser.

Maleic acid treatment appears to be a better option than the CO_2 laser irradiation for dentin surface preparation in effectively utilizing the new generation hydrophilic dentin bonding system.

REFERENCES

1. Zakariasen K. (1991) Spotlight of lasers: A look at potential benefits,. JADA, vol 122, July, pp. 58-62.
2. Cooper L.F. (1988) Shear strength of composite bonded to laser treated dentin. The Journal of Prosthetic Dentistry, vol 60 no. 1, pp. 45-49.
3. White J.M (1991 b) Shear bond strength of ND: YAG laser treated dentin. Journal of Dental Research 70, Abstract of papers, Abstract 1048, p. 397.
4. Dederich D. (1989) Effects of Carbon Dioxide laser on dentinal bonding. Journal of Dental Research 68, Abstract of papers, Abstract 10, p. 868.
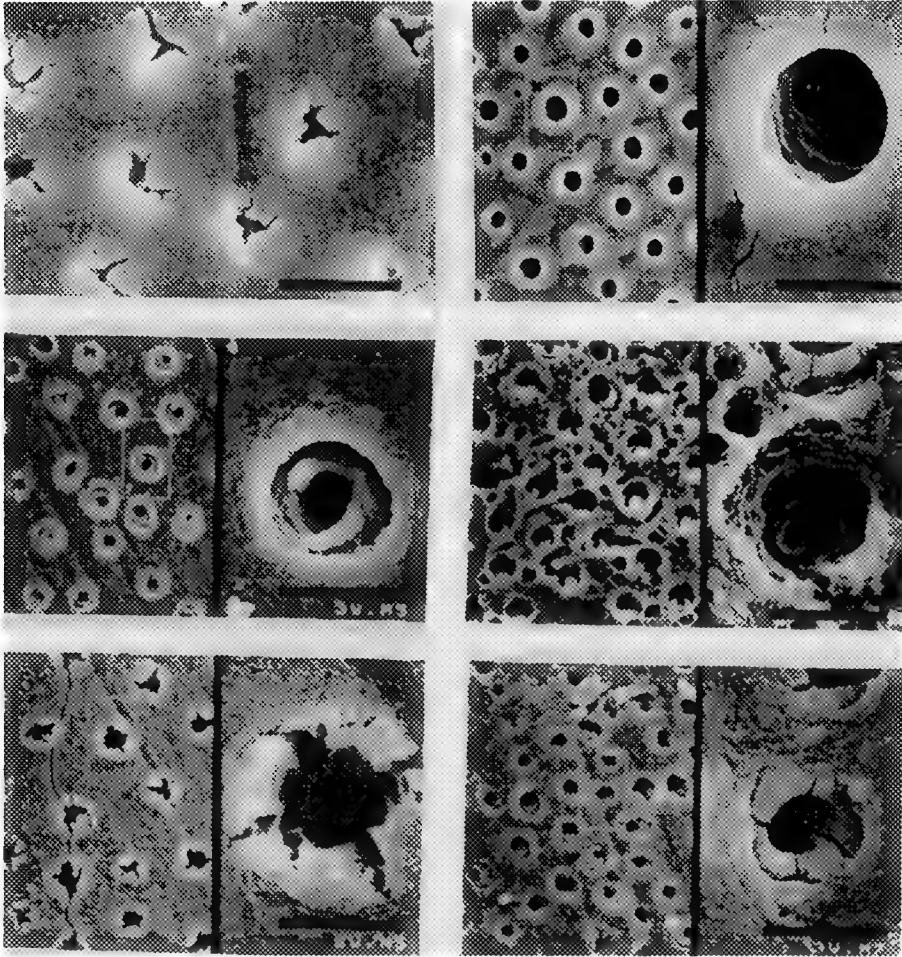
Figure 1: Normal dentin surface polished with 600-grit paper. Bar = 6μm.

Figure 2: Dentin etched with 10% Maleic acid. Bar = 15μm.

Figure 3: Dentin irradiated at 3W mode 5. Bar = 15μm.

Figure 4: Dentin etched with 10% Maleic acid and then irradiated at 3W mode 5. Bar = 15μm.

Figure 5: Dentin irradiated at 3W mode 5 and then etched with 10% Maleic acid. Bar = 15μm.

Figure 6: Dentin irradiated at 3W mode 7. Bar = 15μm.

HUMAN, BOVINE, AND PIG TEETH SURFACE CHARACTERIZATION OF ENAMEL AND DENTIN: AN SEM STUDY

Daniel Fortin

College of Dentistry, The University of Iowa, Iowa City IA 52242

Many researchers use extracted human teeth to evaluate the adhesive strength of restorative materials. Attachment to tooth hard tissues in the oral cavity is a complex and difficult problem that has challenged investigators. An important step in dealing with this problem is a thorough characterization of the substrate. Extracted human teeth are, however, becoming increasingly difficult to obtain due to recent progress in conservative dental treatment. Other mammalian teeth, such as bovine teeth have been tested. Although slightly different in composition and structure, bovine teeth have been used as substitute for human teeth and their use has been documented in different papers.[1,2,3,4] While using such teeth does not lead to results that are identical with those obtained when the enamel and dentin of human teeth is used, they do produce results that are comparable and certainly useful in evaluating the influence of various methods of enamel and dentin treatment.

In order to find a substitute for human teeth in laboratory studies, surface characterization of enamel and dentin from bovine and pig teeth were compared using the SEM to human teeth. The teeth were extracted and stored in thymol. The individual teeth were cut with a hard tissue microtom (Silverstone-Taylor hard tissue microtom). The sections were made from the occlusal to the gingival. The thin slices of teeth were then treated with different acids to remove the smear layer. The term smear layer is used often to describe the grinding debris left on dentin by cavity preparation.[5] The specimens were treated with 10% maleic acid for both 20 seconds and 45 seconds., or 37% phosphoric acid for both 20 seconds and 45 seconds. The acids selected are normally utilized in current dentin bonding systems. After acid treatment and rinsing with water for 15 seconds, the specimens were mounted on aluminium stubs with colloidal silver and vacuum dessicated. The surface characterization was done by scanning electron microscopy (Hitachie S-4000 Field Emision SEM at 12kV Vacc and 12 mm WD) after gold paladium coating (sputter-coated).

Result of this study showed that pig enamel is very different to human or bovine. Dentin surfaces, however, appear to be similar with tubules comparable in concentration, shape and distribution. Etching of the dentin with maleic acid and phosphoric acid gives similar results on human, bovine and pig. Based on this study pig enamel is not suitable because of the morphology, as a substrate to replace human enamel for in vitro study. Although bovine enamel appeared to be somewhat similar to human enamel, slight differences were still present. Research on materials to be used on human teeth should be conducted on an appropriate substrate, not only similar in appearence, but identical in physical properties. Based on the literature cited, further research is needed to determine a suitable and practical substrate for testing restorative materials to human teeth. If direct comparisons with living, human teeth are to be made, experiments must be designed to determine the differences in not only morphology, but biochemistry and relative bond strengths between human and non human substrates as well as between vital and preserved dentin.

References

1. M. Nakamichi and T. Fusayama, J. Dent. Res.(1983) 10,1076.
2. N.D. Ruse and D.C Smith, J. Dent.Res.(1991) 6,1002.
3. D.H. Retief et al., J.Dent.(1990) 6,253.
4. C.D. Torneck et al., J. Endo.(1990) 3,123.
5. D.H. Pashley, Oper.Dent.(1984) Suppl.3,13.
6. This study was supported by the University of Iowa Graduate College.
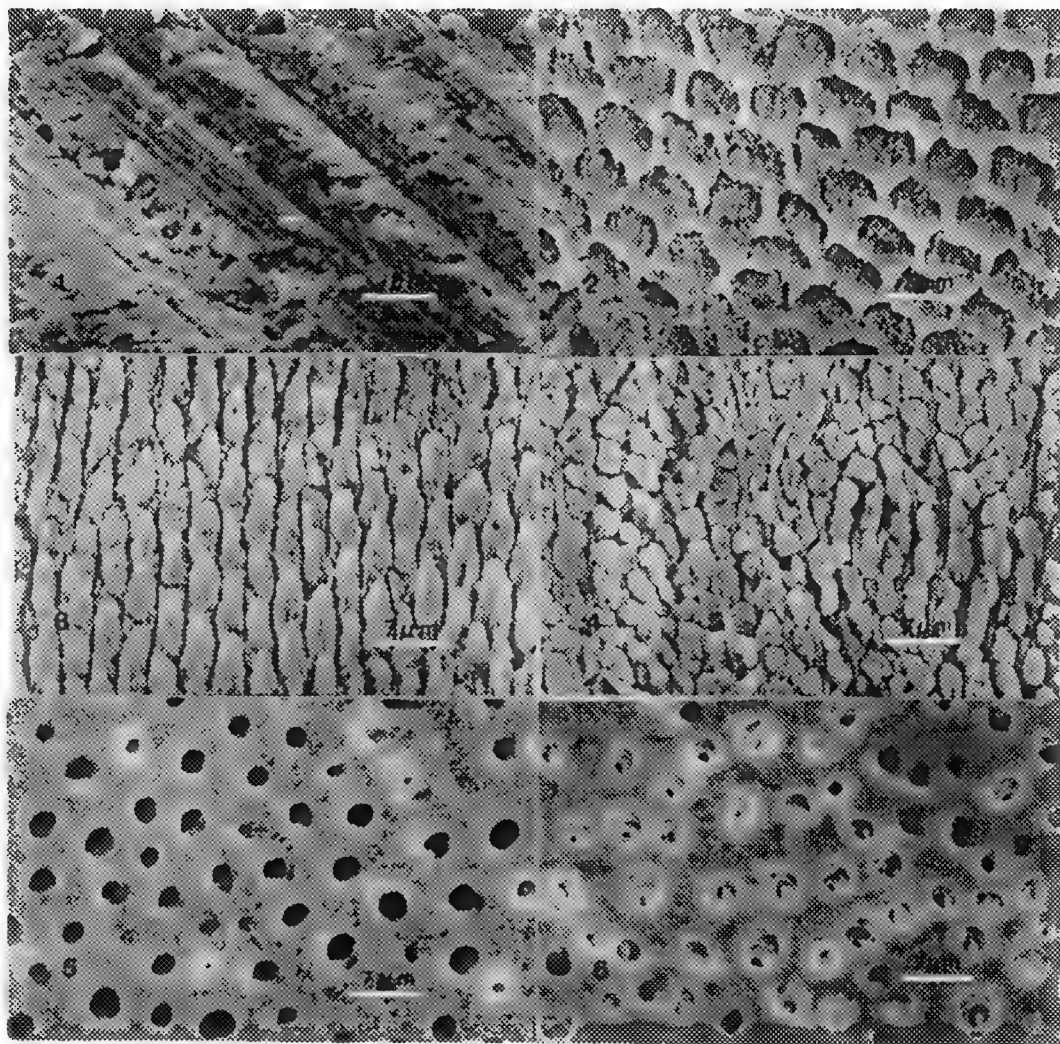
Fig.1. Human, dentin smear layer, before acid treatment. Bar 7μm.

Fig.2. Human enamel prism, 37% phosphoric acid 20 sec. Prism core material was preferentially removed leaving the prism peripheries relatively intact. Bar 7 μm.

Fig.3. Bovine enamel prism, 37% phosphoric acid 40 sec. Prism peripheries have been removed preferentially, leaving the prism cores projecting towards the original enamel surface. Bar 7 μm.

Fig.4. Pig enamel prism, 10% maleic acid 40 sec. Longitudinal rows of prism separated by inter-rows sheets. Bar 7 μm.

Fig.5. Human dentin, 37% phosphoric acid 20 sec. Etching removed the smear layer, open and widens the dentinal tubules. The grainy debris left on the surface is silica which is used to thicken the gel etchant. Bar 7 μm.

Fig.6. Pig dentin, maleic acid 20 sec. Maleic acid is thickened with polivinyl alcohol instead of silica, and left no debris on the surface. Dentinal tubules were opened and a very clean surface is seen. Bar 7 μm.

LOW-VOLTAGE SCANNING ELECTRON MICROSCOPY OF URINARY STONES

Peter Rez, Center for Solid State Science and Physics Dept, Arizona State University, Tempe, AZ 85287
Michail Reilly, Chem. Bio and Materials Engineering Dept, Arizona State University, Tempe, AZ 85287

Urinary stones are predominantly composed of calcium oxalate and calcium apatite while a minority of stones are formed from uric acid[1]. The oxalate stones occur with greatest frequency, mainly in the form of the monohydrate (whellewite) with some dihydrate (wedellite) present. Despite many years of extensive research, the mechanisms for kidney stone nucleation and growth are still unknown. In particular the urine from recurrent stone formers, and the urine from those who do not form stones, does not show large differences in concentration of either calcium or oxalate ions. Recent work has emphasised the role of possible "inhibitors" or "promoters" in the growth of urinary stones though the quest for these substances remains elusive. Much effort has been devoted to the study of crystallization[2] of calcium oxalates in an attempt to understand nucleation, aggregation and growth as a function of pH and the presence of possible promoters or inhibitors.

Many analytical techniques have been applied to urinary stone analysis with X-ray diffraction, wet chemistry and infrared spectroscopy being the most successful for routine characterisation. There has not been as much emphasis on the microstructural characterisation of stones. In the early work of Prien and Prien[3] the crystallographic forms of the microcrystallites making up a typical urinary stone were analysed. Polarized light optical microscopy was used to both determine the constituents and delineate the growth patterns. Scanning microscopy has been limited to low resolution studies, primarily because calcium oxalate is an insulator. It has also been applied in the characterisation of the products of crystallization experiments.

The development of the field emission low voltage scanning electron microscope has opened up the possibility of high resolution imaging of insulating materials. In particular it is possible to achieve less than 10nm spatial resolution with an accelerating voltage of a few kilovolts, which should be sufficiently low to avoid charging of uncoated specimens. It should therefore be possible to examine in more detail the morphology of the microcrytallites and the way they fit together. On the basis of relationships between the lattices of the various constituents of kidney stones Lonsdale[4] proposed that epitaxy was important in the growth process. The crystallographic orientations could be assessed by both morphology and electron channeling patterns.

An oxalate stone passed by the author was examined in a Hitachi S 5000 field emission SEM. Fig. 1 shows an overall view taken at 3.0kV . The morphology is similar to others that have been shown in the literature. At higher magnifications, as shown in Fig 3, the outside surface was shown to be composed of numerous crystallites, about 5μm in length and 0.5μm wide . Higher magnification images (up 1000,000 times) showed that these crystallites were not necessarily smooth, some have protrusions of about 100nm in size. Features that could be growth spirals as shown in Fig 3 were seen in many places on the surface. A non crystalline plaque, about 40 micron, across was shown to be organic material (Fig. 2). At first it was thought that the crater at the top was the nucleation site. The stone was embedded in epoxy and sectioned through the crater. A polarised light optical micrograph revealed growth rings as seen by Prien and Prien as well as possible secondary nucleation sites (Figs 5 and 6). It also appears that the primary nucleation site is displaced from the center of the crater. Another stone examined in a JEOL 840 SEM (Fig. 4) showed a different crystal morphology. Further studies will use low voltage high resolution SEM of the sectioned stone, and possibly high resolution transmission microscopy, to understand how the crystallites bind together and whether there are other phases present.

1. F.M. Driessens and R.M.H. Verbeek (eds), Biominerals, CRC Press, (1990).
2. E.L. Prien and E.L. Prien (1968) Amer. J. of Medicine, 45, 654.
3. J.P. Kavanagh, Scanning Microscopy (1992) 6, 685.
4. K. Lonsdale (1968) Science, 159, 1199.
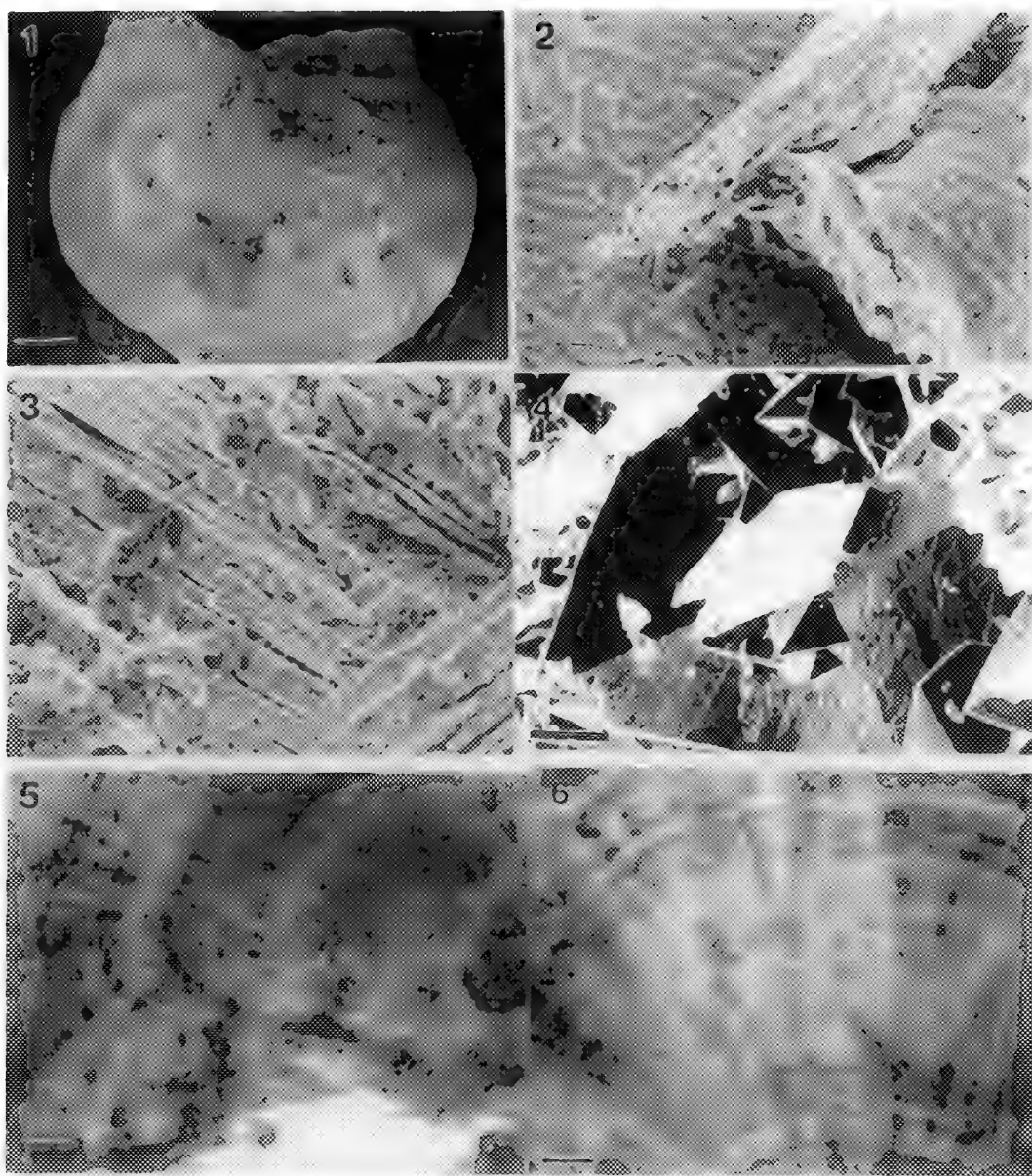
Fig. 1.-- Overall view of kidney stone imaged at 3.0kV Bar = 220 μ.
Fig. 2.-- Organic plaque on the surface of kidney stone imaged at 3.0kV. Bar = 3 μ.
Fig. 3.-- Crystallites on the surface of the stone imaged at 3.0kV. Bar = 0.5 μ.
Fig. 4.-- Different stone showing surface crystallites imaged at 20kV using JEOL 840. Bar = 1.5 μ.
Fig. 5.-- Polarised light reflection optical micrograph showing nucleation site.   Bar = 35 μ.
Fig. 6.-- Polarised light reflection optical micrograph showing possible secondary nucleation sites.
Bar = 70 μ.

ULTRASTRUCTURAL DIAGNOSIS OF CRYPTOSPORIDIUM IN A PATIENT WITH ACQUIRED IMMUNODEFICIENCY SYNDROME (AIDS)

E. Ramirez B.,L. A. Ceseñas , F. Segovia
DEPARTAMENTO DE PATOLOGIA,FACULTAD DE MEDICINA
UNIVERSIDAD AUTONOMA DE NUEVO LEON, MONETERREY N.L. MEXICO

Cryptosporidium sp is an intestinal protozoan that is well known as parasite of different animals,but recently it has been recognized as a cause of human disease, principally since apparition of the acquired immunodeficiency syndrome (AIDS). In this kind of patients it produces severe diarrhea (loss of a stool volume up to 17 liters per day), this condition may be a major factor leading to death.

Information about Cryptosporidiosis and AIDS incidence in developing countries is limited. In this paper we report the ultrastructural study of an intestinal biopsy from an hemophilic man,infected wit HIV through a blood transfussion that presented severe diarrhea.

Jejunal biopsy specimen was obtained and prepared for electron microscope study. The specimen was fixed in 2.5% glutaraldehyde in 0.2 M phosphate buffer pH 7.2;postfixed in 1% osmium tetroxide in 0.2M phosphate buffer pH 7.2;dehydrated in ethanol and embedded in epoxy resin (Medcast). Thin sections obtained in a LKB ultratome V with a diamond knife, stained with uranyl acetate and lead citrate, were observed in a Zeiss EM109 electron microscope.

Results.- Numerous Cryptosporidia were observed, attached to the brush border of surface epithelial cells. At the contact site,there is a dense platelike that substitute the microvilli. Out of this zone, they looked normal. We observed four membranes surrounding the parasite and the two outermost appear to be derived from the epithelial cell. Different phases of Cryptosporidium life cyclewere identified: Trophozoites, Mature merozoites, microgametes, and macrogametes.

Despite that Cryptosporidiosis can be diagnosed with optical methods, using modifications of Acid Fast Stain or even fluorescent antibodies, Electron microscopic method still is the only one that permit identification of Cryptosporidium without doubt.

References

1. M. Kenneth S. and G.M. Dickinson, PostGrad.Medicine (1989)85:309
2. W.O. Dobbins and W.M. Weinstein, Gastroenterology (1985)88:738
3. R. Modigliani et al. Gut (1985)26:179
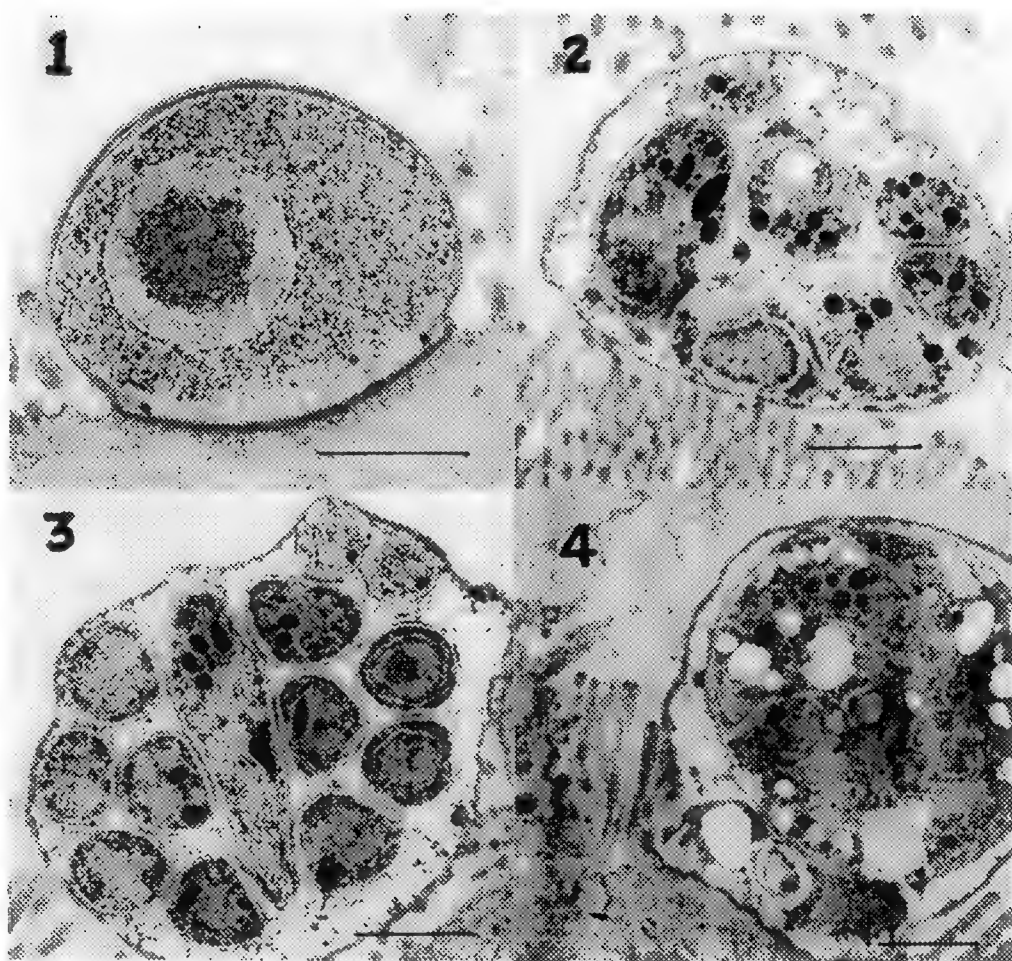
Different phases of Cryptosporidium life cycle.   Barr= 1um

Fig.1. Trophozoite
Fig.2. Mature merozoite
Fig.3. Microgametes
Fig.4. Macrogamete

PREDATION-INDUCED *E. COLI* FILAMENTS: ARE THEY MULTICELLULAR?

Marcelle A. Gillott, Dale Holen, Jonathan Ekman, Michelle Harry and Martin Boraas

Department of Biological Sciences and
Center for Great Lakes Studies
University of Wisconsin-Milwaukee
Milwaukee, WI 53201

Escherichia coli can have a filamentous growth form due to mutation or, in the current study, selection of predator-resistance when preyed on by a bactivorus protozoan.[1,2] When used as food for the mixotrophic flagellate, *Poterioochromonas malhamensis*, filamentous *E. coli* appeared in continuous and batch cultures. The filamentous morphology of *E. coli* is persistent in plate and liquid culture in the absence of the flagellate. Typically, filament length is long in exponential growth and short in stationary phase.

A major question in the morphology of these filamentous *E. coli* (Fig. 1) is whether they are chains of cells that have failed to separate or whether they are a continuous filament without septa. Fluorescence light microscopy using DAPI, a DNA-specific stain, indicates that the filaments show both continuous fluorescence (Fig. 2a), indicating a continuous filament, and discrete units of fluorescence (Fig. 2b), indicating separate cells. Division patterns of living filaments observed with video microscopy show that cell division does occur, but it has been observed only at 10-20 μm from the ends of filaments. Therefore, light microscopy alone did not reveal whether the filaments were cellular or non-septate in nature.

Transmission electron microscopy of bacterial filaments indicates they are free of septa (Fig. 3a), except in short filaments (Fig. 3b) and near the ends of long filaments (Fig. 3c,d). These data agree with the observations of living cells with the light microscope. The patchy DAPI staining could be explained by the presence of large vacuoles observed in thin sections of some of the long filaments.

Separate genes govern septum formation and the formation of the tubular cell wall.[3] Thus, the formation of filaments in this strain of *E. coli* may have been due to a change in the genetic control of septum formation. One hypothesis about the control of septum formation consistent with our results is that septa typically form only when physically near other septa or end caps. Thus, when the filaments are growing rapidly the mean length tends to be long, but when in stationary phase, cell formation occurs without biomass growth and the mean filament length declines to a minimum.

References

1. Alder, H.I. and A.A. Hardigree. 1965. J. Bact. 90:223-226.

2. Begg, K.J. and W.D. Donachie. 1985. J. Bact. 163:615-622.

3. Donachie, W.D. and A.C. Robinson. 1987. In: *Escherichia coli* and *Salmonella typhimurium*. Cellular and Molecular Biology. F.C. Neidhardt, ed. Am. Soc. for Microbiol., pp. 1578-1593.
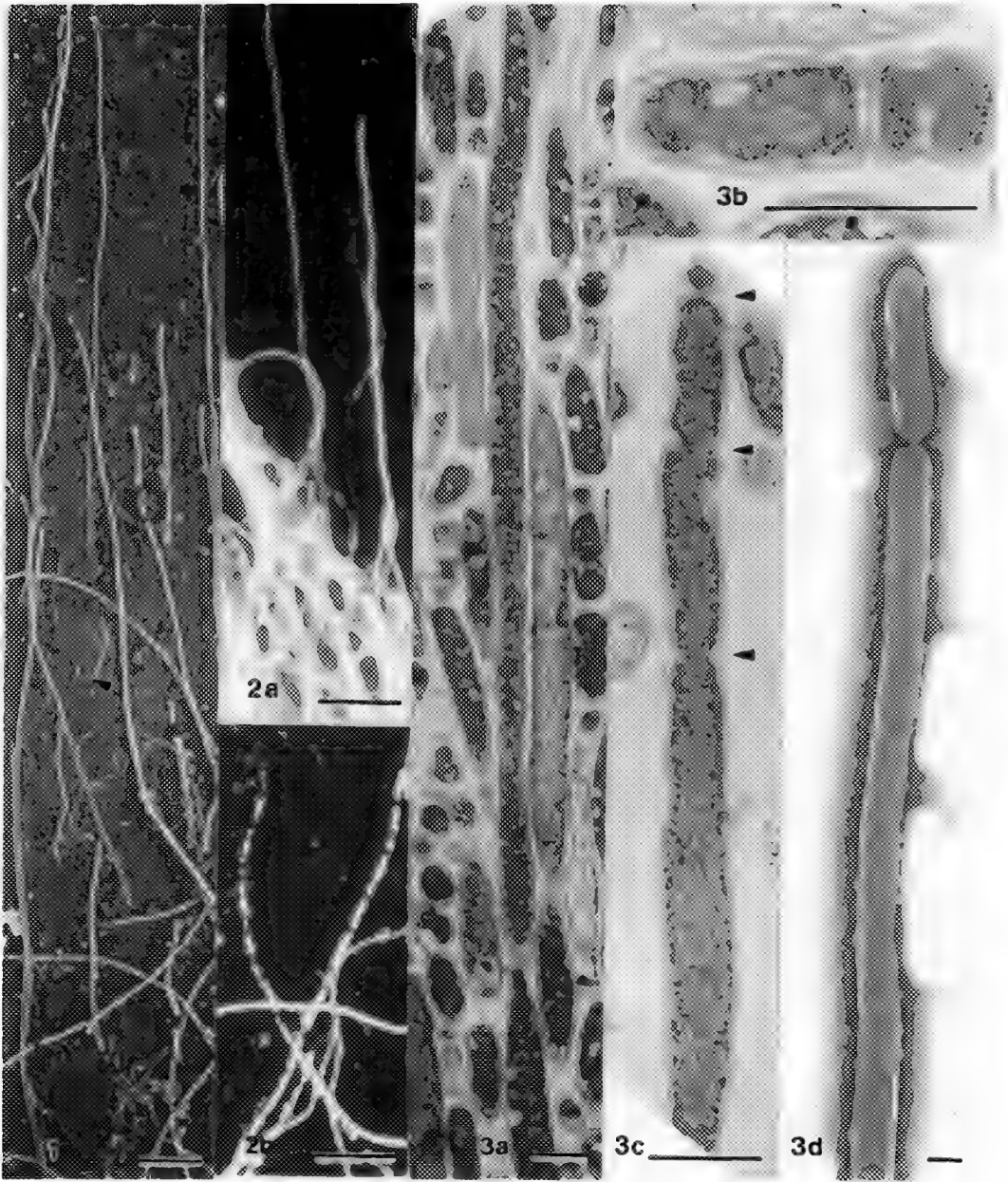
Figure 1. Low mag SEM of predation-induced filamentous *E. coli*. Note the presence of some small "wild-type" rods (arrow). Scale = 10 μm. Figure 2. (2a) DAPI fluorescence of DNA may be septa-free single cells or (2b) chains of septated filaments (scale = 10 μm). Figure 3. (3a) Absence of septa in long filaments in TEM thin sections (scale = 10 μm); (3b) short filaments indicating septation and subsequent cell division (scale = 1 μm); early (3c) stages of septa formation (arrows) at the end of a long filament (scale = 1 μm); and (3d) negative stain showing septation at end of filament (scale = 1 μm).

RAPIDLY DEVELOPING TISSUE UNDERGOING DRAMATIC DECREASE IN SIZE

V. Lindley and E. Pfeiler*

Electron Microscopy Consultants, 1304 N. Euclid Avenue, Tucson, Arizona 85719, U.S.A.
*Departamento de Ciencias Marinas, Instituto Tecnológico y de Estudios Superiores de Monterrey, Guaymas, Sonora, 85400, MEXICO

The purpose of this study was to look at rapidly developing tissues in a system that is undergoing a dramatic decrease in size. Metamorphosing bonefish (Albula sp.) larvae (leptocephali) undergo major changes in morphology[1] and biochemical composition in a period of less than two weeks. Total body length decreases by 60-65%, losing approximately 80% of the total body mass[2], an average loss of 3.5 um/min. Biochemical changes include about a 50% decrease in total lipid and about an 80% decrease in total carbohydrate[3]. Metamorphosing larvae do not begin feeding until late in the process; nutritional requirements are probably provided by breakdown and metabolism of endogenous lipid and carbohydrate. Light microscopy (LM) and transmission electron microscopy (TEM) were performed on the fore-, mid- and hindgut (and adjacent tissues) of early, intermediate and advanced metamorphosing larvae. Changes in ultrastructure correlate well with the biochemical and physiological data. The most dramatic changes are seen in the gut. Figures 1-3 show well-developed microvilli in the lumen of the gut in all larvae. Figure 1 shows epithelial cells of the midgut of early larvae separated by saturated (osmiophobic) lipid deposits. These deposits disappear during metamorphosis (fig 1-3). Mucous cells were not evident in early larvae but were abundant in hindgut of advanced larvae (fig 4). Development of other tissues: muscle, skin and internal organs were also investigated. Figure 5 shows well developed epithelium, basement membrane, collagen and muscle in the early larvae. The basement membrane decreases in thickness during metamorphosis (data not shown). The ultrastructural information provided by the electron micrographs clearly demonstrates developmental processes of an organism decreasing it's total mass 80 percent.

1. P. Rasquin. J. Morphol. (1955) 97, 77.
2. E. Pfeiler. Bull. Mar. Sci. (1884) 34, 177.
3. E. Pfeiler and A. Luna. Envir. Biol. Fish. (1984) 10, 243.
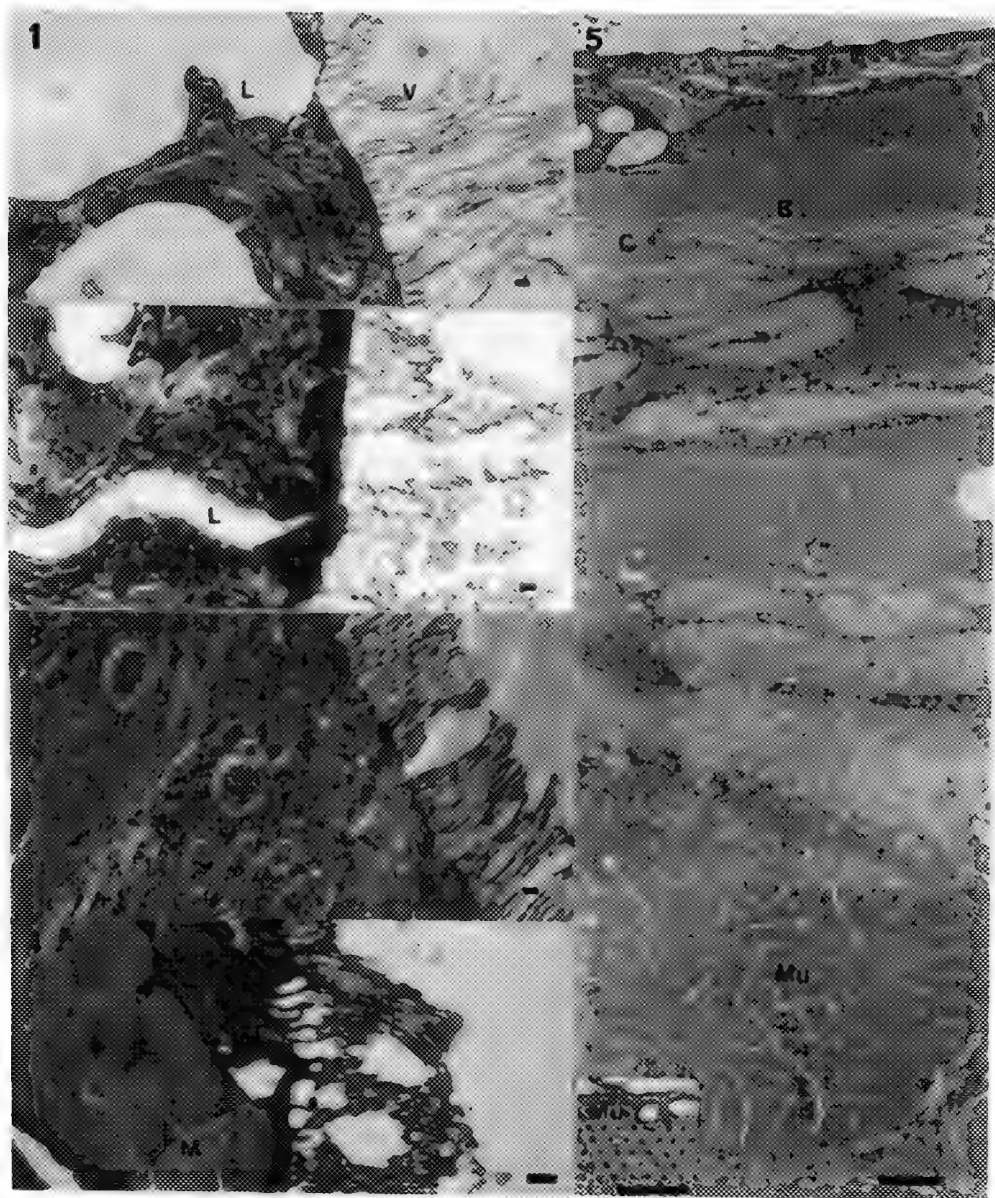
FIG. 1.-- TEM of the midgut of early larvae showing well developed microvilli (V) and areas of saturated (osmiophobic) lipid deposits (L). Bar = 400 nm.

FIG. 2.-- TEM of midgut of intermediate larvae showing the reduction of lipid deposits (L). Bar = 400 nm.

FIG. 3.-- TEM of midgut of advanced larvae showing no lipid deposits. Bar = 400 nm.

FIG. 4.-- TEM of hindgut of advanced larvae showing developed a mucous cell (M). Bar = 400 nm.

FIG. 5.-- TEM of tissue adjacent to the gut in the early larvae. Epithelium (E), basement membrane (B), collagen (C) and muscle (Mu) are all well developed. Bar = 2.5 um. Inset Bar = 200 nm.

EPENDYMAL MORPHOGENESIS IN A SIMPLE VERTEBRATE SPINAL CORD

Jill K. Frey, Aileen Chen and R. David Heathcote

Department of Biological Sciences, Box 413, University of Wisconsin, Milwaukee, WI 53201

All cells of the spinal cord originate from the single layer of neuroepithelium that lines the central canal. Since the turn of the century, it has been known that a subclass of these ependymal cells can differentiate into neurons and extend cytoplasmic projections and cilia into the central canal. We have recently used tyrosine hydroxylase immunocytochemistry to identify a catecholaminergic subpopulation of cerebrospinal fluid (CSF) contacting ependymal neurons in the developing spinal cord of the frog *Xenopus laevis* (Fig. 1).[1] The interneurons are located in the floor plate region of the spinal cord and have axons that extend rostrally toward the hindbrain. During the morphogenesis of the catecholaminergic population of cells, two longitudinal columns gradually appear and then rapidly "converge" at the ventral midline. Transverse sections of embryonic spinal cord (see Fig. 1) showed that the cell bodies decreased in size and underwent changes in shape, number and position within the spinal cord.[2] In order to understand the mechanisms underlying the changes in catecholaminergic neurons, we have begun a study on the morphogenesis of the ependymal layer of the spinal cord.

Extensive remodeling occurred during the first week of spinal cord development. Starting at neural tube closure (stage 19; 0.9 days) quantitative analysis of light micrographs showed an increase in cell number accompanied by a decrease in cell size at the seventh somite level of the spinal cord (Table 1). Although initially there was a dramatic increase in the size of the central canal, its volume stayed roughly constant up to hatching (stage 35/36; 2.1 days; Table 1). However, the shape of the central canal changed in concert with the increasing volume of white matter. Differentiation of the ependymal layer of cells was examined with electron microscopy. A montage of a transverse section of the spinal cord at stage 27 (1.3 days) is shown in figure 2. Enlargement of the ventral region (boxed area) shows that cytoplasmic processes and cilia are present (Fig. 3) just before the initial appearance of tyrosine hydroxylase immunoreactivity at stage 28.[2] The ventral spinal canal contained motile cilia with the 9+2 arrangement of microtubules (Fig.4). Ciliated processes lacking the two central microtubule singlets (characteristic of nonmotile neuronal processes[3]) were also present in the central canal (Fig. 5). These characteristics of differentiated ependymal neurons were not present at the time of neural tube closure (stage 19), but were observed at stage 23, very close to the stage that differentiating axons first appear in the spinal cord.[4,5] Thus CSF contacting cells differentiate along with the earliest neurons in the spinal cord. The remodeling of the spinal cord that occurs during the morphogenesis of the catecholaminergic interneurons apparently involves changes in size, shape and position of all spinal cord cells.

1. R.D. Heathcote and A. Chen (1993) J. Comp. Neurol. *328*, 437-448.
2. A. Chen and R.D. Heathcote (1992) Soc. Neurosci. *18*, 621.
3. A. Peters, S.L. Palay and H. deF. Webster (1991) *The fine structure of the nervous system.*
4. B.P. Hayes and A. Roberts (1973) Z. Zellforsch. *137*, 251-269.
5. M. Jacobson and S. Huang (1985) Devl. Biol. *110*, 102-113.

Table 1. Spinal cord morphogenesis

Age	Stage	Spinal Cord Area	Central Canal Area	Cell #	Cell Area
0.9 days	19	18,291.7 μm^2	129.7 μm^2	15(4)	613.6 μm^2
1.3	27	25,100.7	1944.7	85(31)	215.4
2.1	35/36	24,299.6	2148.1	122(56)	144.0

Cell # were total number of nuclei in section; those in cells bordering the central canal (ependymal nuclei) are in parentheses.

Areas were measured from transverse sections.
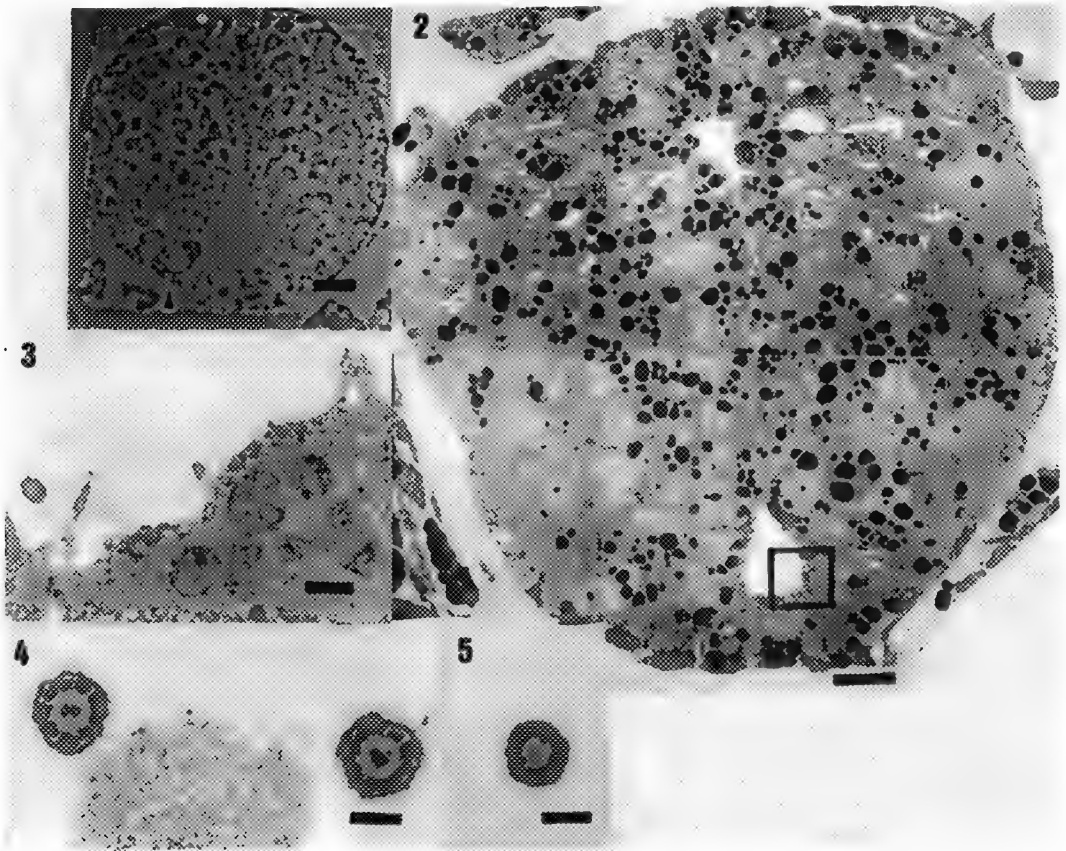
FIG. 1: 1 μm (LM) transverse section of immunostained cell (arrow) at stage 33/34. Bar: 10 μm.

FIG. 2: Montage (TEM) of transverse section of spinal cord at stage 27. Bar: 10 μm.

FIG. 3: Ependymal processes extend into central canal (boxed region of Fig.2). Bar: 1 μm.

FIG. 4: Motile cilia (9+2) in central canal at stage 27. Bar: 0.5μm.

FIG. 5: Nonmotile neuronal cilia (9+0) in central canal at stage 27. Bar: 0.5 μm.

EFFECT OF CYCLICAL STRETCHING ON CULTURED RAT CEREBRAL VASCULAR SMOOTH MUSCLE CELLS: A FLOW CYTOMETRIC, CONFOCAL LASER SCANNING, AND TRANSMISSION ELECTRON MICROSCOPY STUDY

Shams Ghoneim, Thomas Waldschmidt, Elizabeth Yoder, Steven Moore and Gary Baumbach

Department of Pathology, University of Iowa, Iowa City, IA 52242

Vascular hypertrophy during chronic hypertension has been linked to a variety of potential determinants including increased intravascular pressure, neurohumoral factors and genetic factors. Of the various determinants, one might assume that arterial pressure per se would play an especially important role. Nonetheless, the role of intravascular pressure has remained unclear. Based on findings in vivo, we recently proposed that increases in pulse pressure, as opposed to mean pressure, may be an important determinant of cerebral vascular hypertrophy (3).

The goal of the present study was to further explore the possible link between pulse pressure and hypertrophy using a combination of tissue culture, fluorescent-activated cell sorting (FACS), transmission electron microscopy, and confocal laser fluorescent microscopy techniques. Cultured smooth muscle cells derived from rat cerebral microvessels were used for these experiments. Flex culture plates with rigid (control) or flexible (elastomer), collagen-coated bottoms were seeded with smooth muscle cells. After 48 hours to allow for attachment, the culture plates were placed in a Flexercell Strain Unit (model FX-2000) (1, 2), and exposed to continuous cyclical stretching at 20 k Pascals unit pressure and 60 cycles per minute for 5 days. After stretching, the cells were harvested by trypsinization, and divided into two equal portions. One portion was fixed in 1% paraformaldehyde in phosphate buffer saline for 10 minutes. The other portion remained in fresh media. Both portions were then examined with FACS. Forward and orthogonal light scatter were calculated.

Both unstretched and stretched cells were immunostained for alpha actin, a marker for smooth muscle cells. The images obtained with confocal microscopy clearly demonstrated a high level of smooth muscle culture purity (Figures 1a and 1b). However, confocal microscopy did not show a visually recognizable difference between stretched and unstretched cells. We also processed stretched and unstretched cell samples for routine transmission electron microscopy (TEM). Here too, no significant ultrastructural differences could be demonstrated between stretched (Figure 2a) and unstretched cells (Figure 2b). In contrast to the inability to demonstrate differences with confocal and transmission electron microroscpy, examination of the cells with flow cytometric analysis demonstrated an increase in both size and complexity of fresh stretched cells (Figure 3a) as compared to fresh non-stretched, cells (Figure 3b). Fixation normalized the differences in cell size and complexity.

In conclusion, the present study demonstrates the value of using flow cytometric analysis in obtaining useful information in relation to adaptive mechanisms of cerebral vascular smooth muscle to pulsatile stretching that may shed some light on the capability of these cells to adjust to increased high blood pressure during hypertension. This information could not be obtained by either transmission electron microscopy or confocal laser microscopy alone.

References

1.   H. G. Predel et al, The Lancet. (1992) 340, 878.
2.   J. A. Carosi, S. G. Eskin and L.V. Mcintire, J. of Cellular Phys.(1992) 151, 29.
3.   G. L. Baumbach, J. E. Siems and D. D. Heistad, Circulation Research.(1991) 68, 338.
4.   This research was supported by NIH grants HL-22149 and NS-24621.
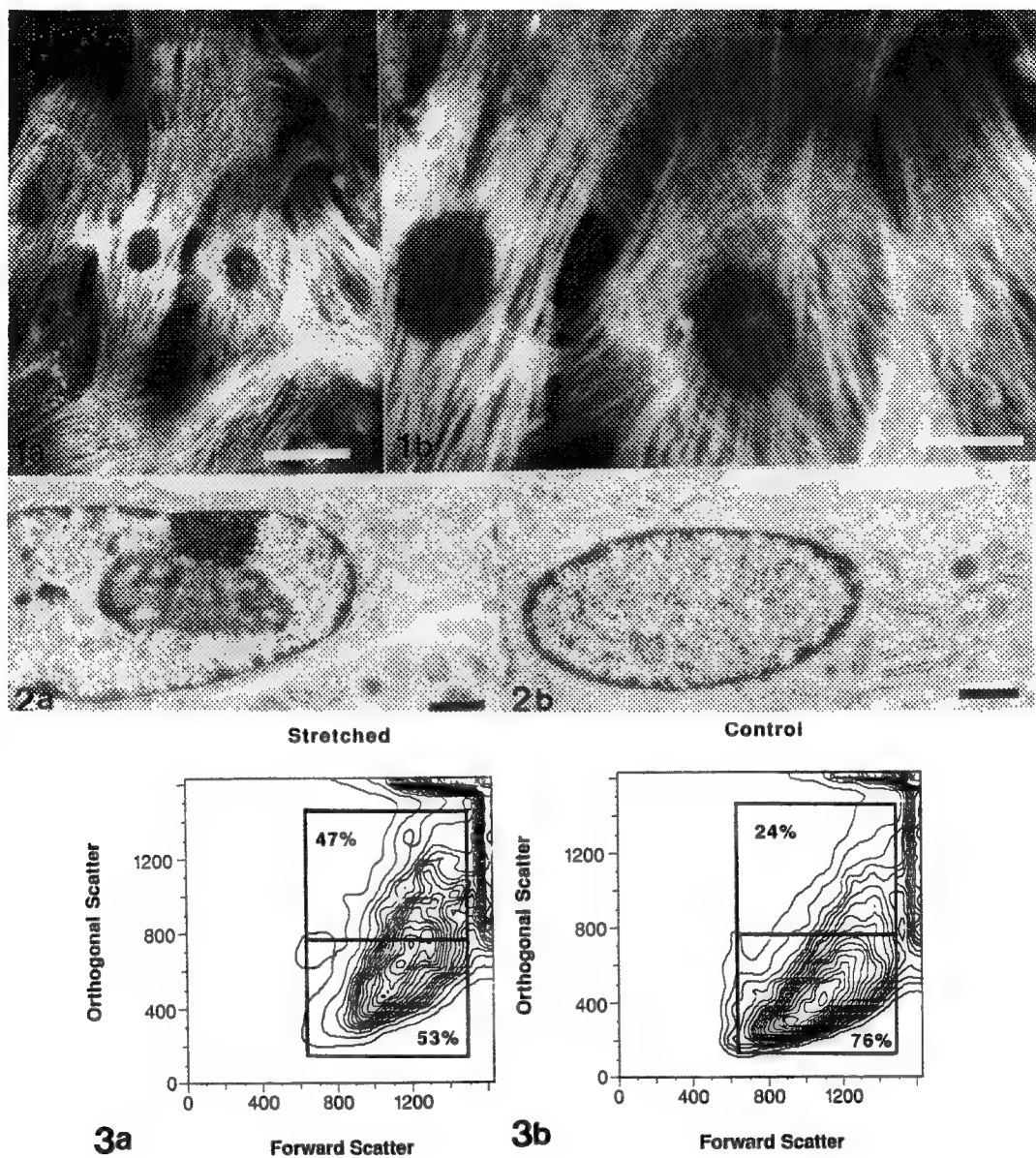
FIG. 1 a and b. -- Confocal image of stretched smooth muscle cells immunostained for alpha actin. Bars = 10 μm (Fig. 1a) and 25 μm (Fig. 1b).
FIG. 2 a and b. -- TEM of 5 day stretched and 5 day control smooth muscle cell. Bar = 12.5 μm.
FIG. 3 a and b. -- FACS contour plots showing differences between orthogonal and forward light scatter of stretched and unstretched smooth muscle cells.

THE NUMBER AND SIZE OF RAT TUBULAR CELLS IN DIABETIC GROWTH, REGRESSION, AND REGROWTH USING THE OPTICAL DISECTOR

Jens Randel Nyengaard†, Allan Flyvbjerg°, Ruth Rasch#

Stereological Research Laboratory†, Institute of Experimental Clinical Research and Department of Medicine°, Aarhus Kommunehospital, Department of Cell Biology#, Institute of Anatomy, University of Aarhus, Århus, Denmark

Diabetic renal growth, regression and regrowth was studied using stereological methods on perfusion-fixed rat kidneys. A razor blade tissue slicer was used for cutting the entire kidney into 2-mm-thick slices and every second slice was sampled systematically random. Every sampled slice from each kidney was embedded in a single capsule using glycolmethacrylate. From every plastic block one 35-μm-thick section and one 2-μm-thick section was cut and stained with PAS. The volume of kidney cortex was estimated on the thin sections using the Cavalieri principle[1]. Total volume of proximal and distal tubules (V(tub)) were estimated by point-counting on the thin sections at a magnification of 332x using a projection microscope. Using an optical disector[2] (Fig. 1a-d) on the thick sections, the numerical densities (N_V) of proximal and distal tubular cells were estimated. The total number of tubular cells: $N(total)=N_V*V(tub)$. The mean volume of a tubular cell ($\bar{v}(tub)$) including basement membrane and lumen was calculated as: $\bar{v}(tub)=V(tub)/N(total)$. Lumen of the tubular cell was excluded by point-counting using the thin sections and the microscope mentioned in Fig. 1.

An analysis of variances of the stereological estimators equal to the coefficient of error, $CE_{ste}=SEM/mean$, was performed on the level of tissue slices. The coefficient of error was estimated of the Cavalieri estimator[1] as well as for the point-counting and the optical disector[3]. The variation of the stereological estimators can be expressed in relation to the coefficient of variation of the above-mentioned estimates, $CV_{tot}=SD/mean$, where CV_{bio} expresses the true biological variation between animals: $CV^2_{tot}=CV^2_{bio}+CE^2_{ste}$ (see Table 1 for data).

The 13-week-study comprised one control group (C) and three diabetic groups (D-H, D-HN, D-HNH). D-H rats were hyperglycaemic for 13 weeks. D-HN rats were hyperglycaemic for 10 weeks and then normoglycaemic for 3 weeks. D-HNH rats were similar to D-HN rats except that during the last week the animals were again hyperglycaemic. The number of proximal and distal tubular cells increased by 37% and 36% in D-H rats and the mean volume of the proximal and distal tubular cells increased by 12% and 16%, respectively as compared to C rats. Normoglycaemia for 3 weeks normalized the mean volume of distal tubular cells but the proximal tubular cells were 7% smaller than those in C rats. The number of proximal cells remained increased by 21% compared with C rats and the number of distal tubular cells retained a 17% insignificant increase. After regrowth the volume of proximal tubular cells was 20% greater than in D-HN rats and the other parameters were unchanged.

428

References
1. H.J.G. Gundersen and E.B. Jensen; J. Microsc. (1987)147, 229.
2. D.C. Sterio; J. Microsc. (1984)134, 127.
3. J.P. Kroustrup and H.J.G. Gundersen; J. Microsc. (1983)132, 43.
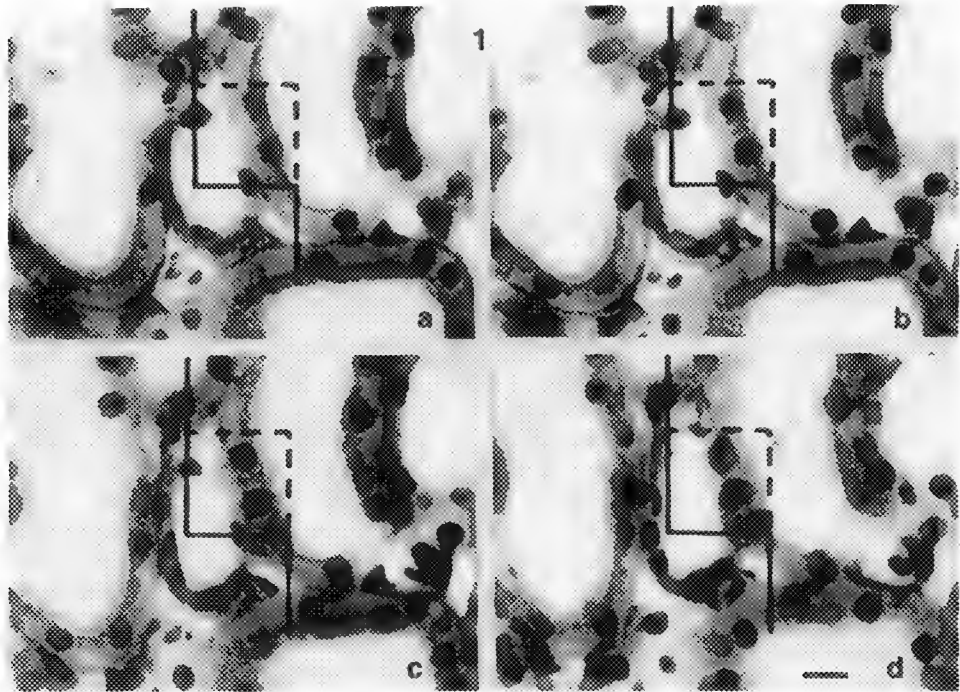
FIG. 1a-d. Four optical sections 2 μm apart in the middle of a modified periodic acid-Schiff-stained glycolmethacrylate section of 35 μm thickness, are shown. Originally, the thick sections were displayed on a SONY Trinitron television screen by the use of an Olympus BHS microscope equipped with a SONY CCD color video camera. The video camera was interfaced through an Amiga 2000 computer loaded with software superimposing the area of the two-dimensional, unbiased counting frame as indicated by the full drawn lines and dotted lines on this figure. All nuclear profiles with anything inside the counting frame, provided they do not touch or intersect the full drawn exclusion lines, are considered for counting. The observer focuses through a distance of 20 μm counting any proximal or distal tubular cell nuclei coming into focus, excluding those in the first optical section and including those in the last optical section. Nuclei are counted when they are clearly in focus in the disector counting frame as is the case for the two proximal tubular cell nuclei shown in c. The bar indicates 10 μm.

Table 1. CE_{ste} and CV_{tot} are shown for the stereological estimators of total number of proximal tubular cells (N(prox)) total number of distal tubular cells (N(dist)) mean volume of proximal tubular cells ($\bar{v}(prox)$) and mean volume of distal tubular cells ($\bar{v}(dist)$).

	N(prox)	N(dist)	$\bar{v}(prox)$	$\bar{v}(dist)$
CE_{ste}	0.08	0.09	0.04	0.04
CV_{tot}	0.13	0.18	0.08	0.12

ELECTRON MICROSCOPIC STUDY ON INNER EAR OF GUINEA PIG WITH SPECIAL REFERENCE TO MORPHOLOGICAL CHANGES OF VESTIBULAR MACULA IN HYPERCHOLESTEROLEMIA

Yan Qiao[1], Goro Asano[1], Izumi Kashiwado[2] and Yasuo Hattori[2]

[1] Department of Pathology, and [2] Department of Otorhinolaryngology,
Nippon Medical School, Tokyo 113 JAPAN

Vertigo may be induced by various factors such as vascular changes including arteriosclerosis and hypercholesterolemia in the inner ear. In orter to clarify the mechanism of vertigo, the inner ear of guinea pig in hypercholesterolemic condition was investigated by electron microscopic techniques.

The guinea pigs have served as experimental materials. They were divided into two groups: one received non-administration of cholesterol and the other received the administration of cholesterol. The vestibular macula in inner ear were observed at 1, 2 and 3 months after the administration of cholesterol and also vascular function was investigated by using horseradish peroxidase as tracer.

Ultrastructural changes such as the depletion of microvilli on the cell surface and increased microvesicles were detected in the cytoplasm of sensory cell after cholesterol administration. After two months, lipid droplets were demonstrated in the cytoplasm, associated with intercellular edema. The cytoplasmic projection with vacuolization was demonstrated in the surface of sensory cells in the vestibular macula after three months of cholesterol administration. In the dark cell or transitional cells, mitochodrial degeneration and lipid accumulation were noted, and associated with vacuolization of endothelial cells and perivascular edema. The electron dense tracers such as horseradish peroxidase were localized in the vesicular system through the intercellular space and pinocytotic vesicles in endothelial cells.

The administration of cholesterol hypercholesterolemia may induce membrane damage resulted in the hypercholesterol permeability and morphological changes of in the vestibular macula which may induce functional changes such as vertigo, in the inner ear.

References

1. Y. Qiao et al. J. Clin. Electr. Microsc. (1988)21, 781.
2. Y. Qiao et al. J.Clin. Electr. Microsc. (1989)22, 566.
3. Y. Qiao et al. J. Clin. Electr. Microsc. (1990)23, 95.
4. Y. Qiao et al. J. Jpn Atheroscler. Soc. (1990)18, 711.
5. Y. Qiao et al. J.Shen Yang Medical College. (1991)1,49.
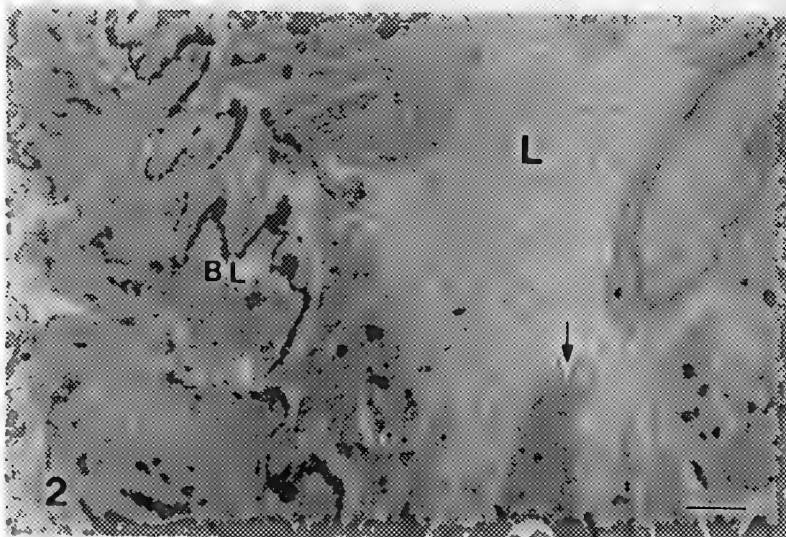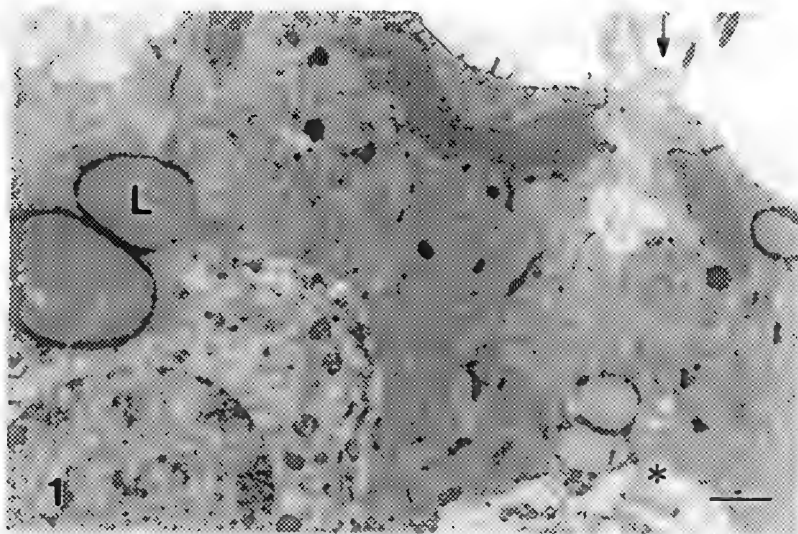
FIG. 1.--TEM of vestibular macula. Cytoplasmic projection of sensory cell (arrow),
mitochondrial degeneration(*) and lipid droplets(L) are noted in the
cytoplasm of transitional cells in macula after three months of choleterol
administration. Bar=0.8 μm.

FIG. 2.--TEM of labyrinthine artery. Cytoplasmic projection(arrow). The swollen
endothelial cell is associated with lamellar thickening of basal lamina(BL)
after three months of cholesterol adminitration. L=vascular lumen,
Bar=1.2 μm.

ULTRASTRUCTURAL CHANGES IN THE COCHLEA OF THE INNER EAR IN GUINEA PIGS WITH
HYPERCHOLESTEROLEMIA

Izumi Kashiwado, Kurata Yuge, Yasuo Hattori, Yan Qiao and Goro Asano

Department of Otolaryngology, Department of Pathology, Nippon Medical School, Tokyo
113, Japan

Although sensory neural hearing loss stemming from hypercholesterolemia has
received attention in recent year, nothing has been made known about inner ear
injuries resulting from this condition.
In this study, we prepared guinea pig models with hypercholesterolemia and observed
inner ear with a transmission electron microscope, and also investigated the effect
of vitamin E therapy on injuries.
Materials and Methods: Ninetyth white female Hartley guinea pigs weighing 250-300g
each were divided into three groups. Group A consisted of the control animals,
which were fed by a stock diet. Group B was fed by a hyperlipid diet (2.5%
cholesterol, 0.25% bile acid, and 7.5% cattle fat). Group C was given a vitamin E-
added hyperlipid diet. All animals were sacrificed at either one, two or three
months after treatment, and cochlear duct vasculature was observed with a
transmission electron microscope. Cholesterol, triglyceride, and TBARS values were
concurrently measured in serum.
Results: In group B and C, cholesterol and triglyceride levels remainedon control
levels. The TBARS level was elevated in group B but remained unchanged in groups A
and C.
Ultrastructural changes: In group B, lipid droplets markedly increased in the
endothelial cells, along with manifestation of vacuolar degeneration and an
increase in the pinocytotic vesicles of the modiolus capillaries. In group C, the
increase in lipid droplets was slight and number of pnocytotic vesciels were
basically the same as in group A, with minor vacuolar degeneration.
Observation of the stria vascularis revealed that in group B, vacuolar degeneration
had progressed in the capillary endothlial cells and density of the marginal cells
decreased. In group C, few structural changes in the capillaries and the marginal
cells were detected.
Examination of the outer hair cells revealed marked vacuolar degeneration in group
B along with cytoplasm leakage in the cell membranes. In group C, cell membranes
were well preserved and intracellular organelles were not markedly different from
those in group A.
Discussion and Conclusion: These results suggest that cholesterol load is
accompanied by hypercholesterolemia, which in turn injury the endothelium of the
vasculature dominating the inner ear. This is followed by an anomaly affecting
cochlear lipid metabolism that results in ultrastructural changes Corti's organ and
the spiral ganglia. However, vessel and cell injuries in the vitamin E-added
hyperlipid diet group seemed to have been inhibited by the antioxidation activity
of vitamin E.
References
1. I. Kashiwado, et al.: J. Clin. Electron Microscopy 25 (5-6), (1992)
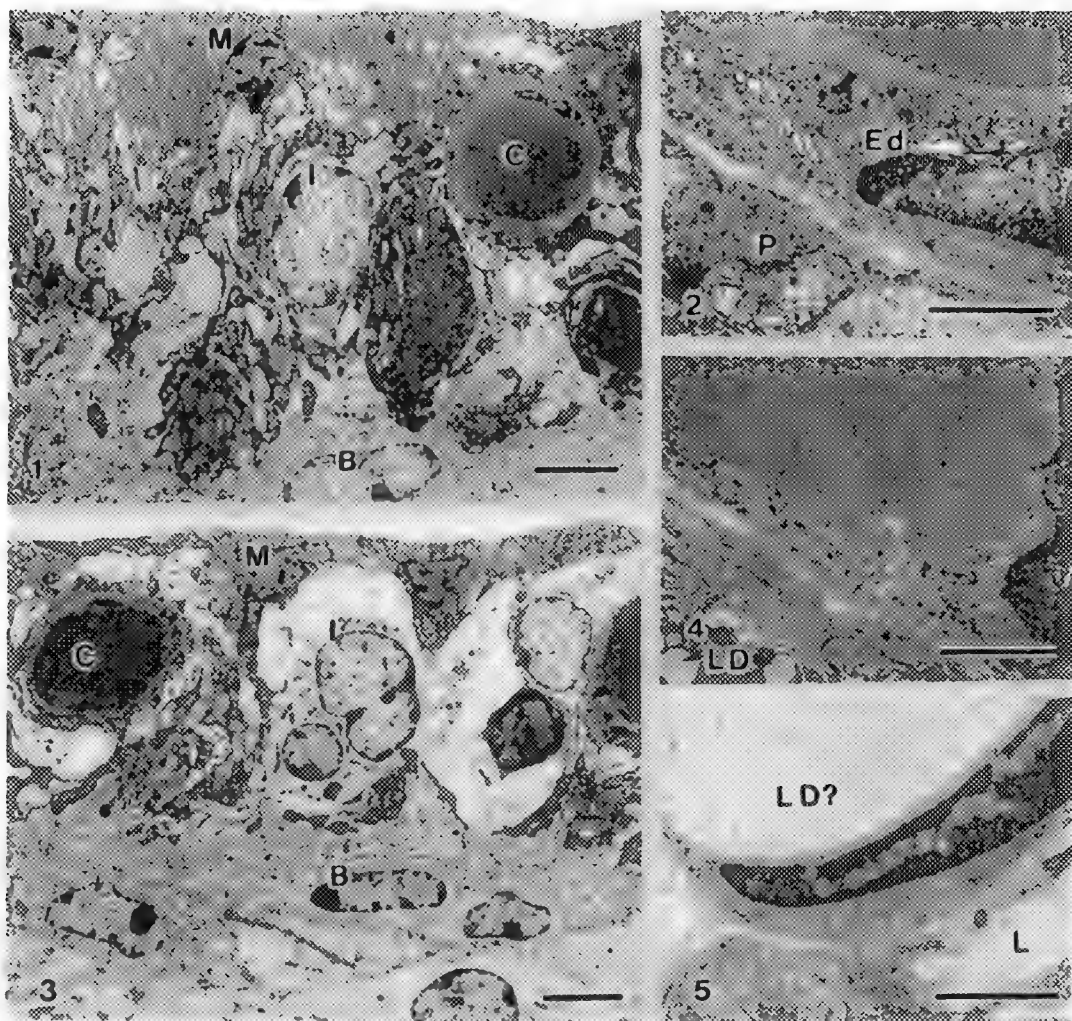
Fig. 1.--Stria vascularis of control guinea pig consist of marginal cell(M), intermediate cell(I), basal cell(B) and capillary(C). Bar=5 μm.
Fig. 2.--Capillary wall of the control stria vascularis consist of the well developed endothelium (Ed) and the pericyte (P). Bar=1 μm.
Fig. 3.--Stria vascularis of guniea pig fed by hyperlipid diet for three months. The degeneration of intermediate cells are suspected. Bar=5 μm.
Fig. 4.--Capillary wall of stria vascularis of guinea pig fed by hyperlipid diet for three months. There are two lipid droplets (LD) in the pericyte. Bar=1 μm.
Fig. 5.--Capillary wall of spiral ligament of guinea pig fed by hyperlipid diet for three months. The pericyte has a huge vacuole (lipid droplet?). L:lumen. Bar=1 μm.

THICKNESS MEASUREMENTS BY ELECTRON ENERGY LOSS SPECTROSCOPY (EELS)

Ruoya Ho, Lijie Zhao, Yun-Yu Wang, Zhifeng Shao and Andrew P. Somlyo

Department of Molecular Physiology and Biological Physics
Box 449, University of Virginia, Charlottesville, VA 22908

An estimate of specimen mass-thickness is an essential requirement for evaluate with EELS the absolute elemental concentration in biological specimens[1-9]. The conventional method[2,3,5,8] used for measuring specimen thickness by EELS is:

$$t/\lambda_i = ln(I_t/I_0)$$

where t is the specimen thickness, λ_i is the total inelastic mean free path, I_t is the total count in an EELS spectrum and I_0 is the count in the zero loss peak. This equation is rigorously correct, only if the electrons are collected over all scattering angles and the spectrum covers all energy losses. But in most experiments with a finite energy loss region, because of the limited collection semi-angle, we can only collect a fraction of scattered electrons. Omitting the high loss electrons will result in a cut-off error that is usually less than 5%, if we use an energy window from 0 eV to 150 eV or above. But the effect of the limited semi-angle is more serious[10]. Fig. 1 shows the $ln(I_t/I_0)$ measured on the same specimen in both TEM and STEM mode at 80 keV with a magnetic sector spectrometer equipped with a parallel detector on Philips 400 FEG[11]. The $ln(I_t/I_0)$ ratio between STEM and TEM for the same specimen is about 0.83. In our system the estimated collection semi-angle is about 100 mrad for TEM and 11.6 mrad for STEM[10]. Therefore, one must be extremely careful when comparing specimen thickness measured in different modes or under different optical conditions.

For a limited collection semi-angle α, the collection efficiencies for each order of elastic scattering (α_n) and for inelastic scatterings (γ_n) are intrinsically different. However, for most experimental conditions, it was shown that $\gamma_n = (\gamma)^n$ is a good approximation[12]. It is also easy to show that, if α is small, the effect of elastic scattering on the thickness measurement by the conventional method can be omitted under the first order approximation. In this case, we have $\gamma_1 t/\lambda_i = ln(I_t/I_0)$. Obviously, this thickness is spectrometer dependent, due to the explicit inclusion of γ_1 in the measured value.

When it is not convenient to measure the zero loss, it is sometimes easier to determine the specimen thickness ($\gamma_1 t/\lambda_i$) by using the ratios of the multiple least-squares fitting coefficients of a sharp core edge of an abundant element, such as the carbon K-edge. The excellent agreement of this method with the conventional method is shown in Fig. 2. The small "systematic" error might be accounted for, if we consider that the conventional method should always give an under estimate of $\gamma_1 t/\lambda_i$, due to the finite energy window used[10].

When the specimen is not uniform in the area covered by the probe, which is common for most biological sections, some error is introduced by both methods. For the conventional method, an under estimate often results, which could be up to 20%, while for the fitting method, an over estimate of up to 50% often results, due to the dominance of plural scattering of the thicker part of the specimen. This conclusion indicates that the thickness determined by spot analysis is not a very reliable indication for estimation of pixel time for mapping at a predetermined accuracy, because it dose affect the uncertainty in trace element quantitation[7]. Therefore, it is very desirable to use a probe that is smaller than the spatial variations in mass-thickness within a given specimen.

The STEM dark field signal can also be used to estimate local thickness[13]. In the presence of significant gun current fluctuations (up to 20% on our microscope), however, the normalization based on transmitted signal should be used, but sometimes this normalization is not available.

In conclusion, the mass-thickness determination by using the ratios of the fitting coefficients of a core edge of one of the abundant element is equivalent with the conventional method. The relative

spectrometer dependent mass-thickness can be determined quite reliably by EELS, but the absolute value of mass-thickness can not be determined by EELS. In the presence of significant mass-thickness variation, the average thickness determined by EELS is not reliable, which also affects the estimation of uncertainty in EELS quantitation. In the later case, a smaller probe should be preferred[14].

References

1. M. Isaacson, in: "Principle and Techniques of Electron Microscopy, Biological Applications",.(Ed. M.A. Hayat), Vol. 7, Van Nostrand Reinhold Company, New York, (1977) 1.
2. R.F. Egerton, "Electron Energy Loss Spectroscopy in the Electron Microscope", Plenum Press, New York, (1986).
3. R.D. Leapman, C.E. Fiori and C.R. Swyt, Journal of Microscopy 133 (1984) 239.
4. H. Shuman and A.P. Somlyo, Ultramicroscopy, 21 (1987) 23.
5. R.F. Egerton and S.C. Cheng, Ultramicroscopy, 21 (1987) 231.
6. R.D. Leapman and R.L. Ornberg, Ultramicroscopy, 24 (1988) 251
7. Y.Y. Wang, R. Ho, Z. Shao and A.P. Somlyo, Ultramicroscopy, 41 (1992) 11.
8. P.Rez, W. Chiu, J.K. Weiss and J. Brink, Microscopy Research and Technique, 21 (1992) 166.
9. Y.Y. Wang, R. Ho, Z. Shao and A.P. Somlyo, Ultramicroscopy, submitted.
10. L. Zhao, Y.Y. Wang, R. Ho, Z. Shao, A.V. Smolyo and A.P. Somlyo, Ultramicroscopy, in press
11. H. Shuman and P. Kruit, Rev. Sci. Instrum., 56 (1985) 231.
12. R.F.Egerton and Z.L.Wang, Ultramicroscopy, 32 (1990) 137.
13. J. Wall, in:"Introduction to Analytical Electron Microscopy", Edited by J.J Hren, J.I. Goldstein, D.C. Joy, (Plenum Press, New York and London 1979) p. 333.
14. This work was supported by NIH grant PO1 HL48807 and the Whitaker Foundation.
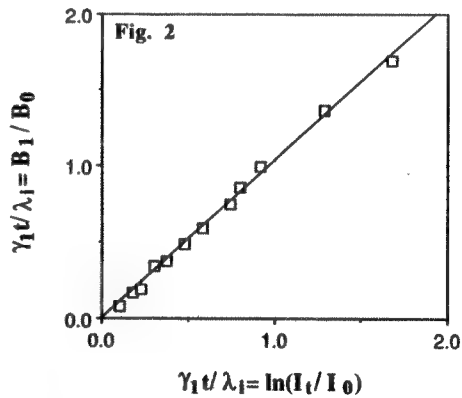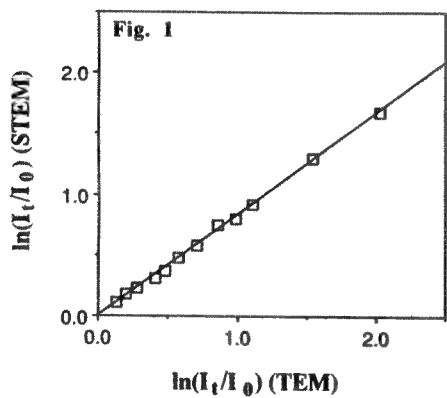
Fig.1.-- $\ln(I_t/I_0)$ values plotted on abscissa were measured by TEM imaging mode for which collection semi-angle is about 100 mrad; $\ln(I_t/I_0)$ values on ordinate were measured in STEM mode, for which collection semi-angle is 11.6 mrad at 80 keV[10].

Fig.2 -- Ratios of double scattering(core loss ⊗ single plasmon)/single scattering(core loss) fitting coefficients (B_1/B_0) are shown as squares, solid line is the best fitted regression line of data points; slope of line is 1.04; STEM mode, E_0=80 keV and collection semi-angle α is 11.6 mrad[10].

PROPERTIES AND DOSE DEPENDENCE OF EMBEDDING MEDIA FOR CRYO-AUTOMATED ELECTRON TOMOGRAPHY

M.B. Braunfeld, A.J. Koster, J.W. Sedat, D.A. Agard

The Howard Hughes Medical Institute and the Department of Biochemistry and Biophysics, University of California at San Francisco, CA 94143-0448

Electron tomography is well suited to the study of complicated, non symmetric biological structures[1]. In our laboratory, we use intermediate voltage electron microscopic tomography to follow complex paths of chromatin fibers within intact sections of Hela telophase chromosomes. In order to accurately reconstruct these features at resolutions beyond 50Å, precise imaging conditions and data collection schemes have been developed and employed[2].

To obtain useful high resolution information, the specimen needs to be well preserved. Data collection must also be accurate and self-consistent. However, a serious limitation has been radiation damage to the specimen during scanning, and data collection[3]. Because of the high doses required for tomography, the standard approach has been to accept the inevitability of serious radiation damage, and to heavily pre-irradiate the sample in an attempt to provide stability and consistency during data collection.

The use of fully-automated data collection methods allows a substantial decrease in beam dose, suggesting that the entire approach should be reevaluated. Our goal has been to develop new protocols for data collection defining optimal approaches for both self-consistency and useful resolution. We have examined the effects of irradiation on a variety of embedding media in order to quantitative beam damage and hopefully to identify a beam stable embedding medium. We have sought to minimize damage by substantially reducing the total dose during data collection. And finally, we have investigated the use of cryogenic data collection to minimize the effects of secondary radiation damage.

The results of our resin studies on epon, epox, and lowicryl show similar shrinkage profiles for all resins. As expected, shrinkage in the X-Y plane was much less (final values = 4-8%) than in the Z direction (final values=26-35%). Shrinkage data fit a first-order decay process: half the Z shrinkage occurs after 100 $e^-/Å^2$, 99% of the total shrinkage occurs after ~600 $e^-/Å^2$. The total amount of Z shrinkage was approximately the same for each resin and quite consistent from sample to sample. None of the resins is particularly remarkable in their ability to withstand high electron doses.

436

Contrary to some other reports, we find no improved beam stability is provided by microwaving the samples; epox behaves similarly to the other resins.

Unlike manual tomographic data collection where the sample is continuously irradiated during the entire collection process, automated tomography results in stroboscopic beam irradiation. Surprisingly, even with specimens that were exceptionally well stabilized (~125,000e$^-$/Å^2), automatic data collection resulted in a further 8% Z shrinkage for a dose of only 5,000 e$^-$/Å^2.

The stroboscopic effect can be completely eliminated by collecting data at cryogenic temperatures. Our cryogenic data shows that shrinkage is slowed by at least a factor of 5 compared to room temperature data; half the Z shrinkage occurred after a dose of ~800e$^-$/Å^2. Most desirable would be to avoid all radiation damage. Based on our cryo-shrinkage data, total electron doses up to 50e$^-$/Å^2 can be tolerated, at which shrinkage of 0.7% was observed. Assuming collecting data at ~1e$^-$/Å^2, this would allow 50 tilted views. Obviously, there is a trade-off between more views and lowered statistical accuracy in the data.

In some case higher doses are required. For example if the desired specimen is rare, prescanning can involve substantial doses. In such cases, minimizing variability during collection is paramount. We have found that with pre irradiation kept between 800-1000 e$^-$/Å^2, very high quality cryo automated data collection can be accomplished using 300 e$^-$/Å^2. Under these conditions, the total lateral shrinkage is 1%, and z shrinkage is 1%. Furthermore this is accomplished while maintaining proper CCD counting statistics, tilt ranges and resolution.

By utilizing automated data collection at low temperatures, the damaging effects of the beam are greatly reduced. Hence, both the total electron dose and shrinkage are minimized. This will result in much higher quality biological raw data and an improved overall tomographic data set.

1. B. F. McEwen et al., Proc. Nat. Acad. Sci. USA 83(1986)9040-9044.
2. A. J. Koster et al., Ultramicroscopy 46(1992)207-227.
3. P.K. Luther, in: Electron Tomography, J. Frank (ed.), Plenum Press, New York, 1992, 39-60.

MICROANALYSIS OF SILICATE GLASS FILMS GROWN ON α-Al$_2$O$_3$ BY PULSED-LASER DEPOSITION

Michael P. Mallamaci, James Bentley,* and C. Barry Carter

Department of Chemical Engineering and Materials Science, University of Minnesota,
421 Washington Avenue SE, Minneapolis, MN 55455-0132
*Metals and Ceramics Division, Oak Ridge National Laboratory, P. O. Box 2008,
Oak Ridge, TN 37831-6376

Glass-oxide interfaces play important roles in developing the properties of liquid-phase sintered ceramics and glass-ceramic materials. Deposition of glasses in thin-film form on oxide substrates is a potential way to determine the properties of such interfaces directly. Pulsed-laser deposition (PLD) has been successful in growing stoichiometric thin films of multicomponent oxides.[1] Since traditional glasses are multicomponent oxides, there is the potential for PLD to provide a unique method for growing amorphous coatings on ceramics with precise control of the glass composition. Deposition of an anorthite-based (CaAl$_2$Si$_2$O$_8$) glass on single-crystal α-Al$_2$O$_3$ was chosen as a model system to explore the feasibility of PLD for growing glass layers, since anorthite-based glass films are commonly found in the grain boundaries and triple junctions of liquid-phase sintered α-Al$_2$O$_3$ ceramics.

Single-crystal (0001) α-Al$_2$O$_3$ substrates in pre-thinned form were used for film depositions. Pre-thinned substrates were prepared by polishing the side intended for deposition, then dimpling and polishing the opposite side, and finally ion-milling to perforation. Prior to deposition, all substrates were acid-cleaned and annealed in air at 1400°C to recrystallize regions amorphized by the ion beam and form clean (0001) surface terraces.[2] Film deposition was achieved using a KrF excimer laser operating at 10-20 Hz with a 200mJ pulse energy. The laser was focused on a rotating target inside a vacuum chamber, where an oxygen partial pressure of 5-10 mTorr was maintained during deposition. Both polycrystalline and glass targets were used, and in each case the deposited film was amorphous. The substrates were mounted on a resistively-heated block, and a series of substrate temperatures ranging from ambient to 950°C was used to determine any effect of substrate temperature on the film composition or structure.

Deposition onto pre-thinned substrates allowed plan-view observation of the as-deposited film microstructure without the possibility of artifacts being introduced by post-deposition specimen preparation. In this case, direct x-ray microanalysis of the film is complicated by the presence of aluminum in both the substrate and the glass film. To overcome this complication, the composition of the glass film on the surface of the substrate was determined by removing the x-ray intensity contributed by the substrate itself. The analysis relied on three assumptions: (1) the glass film was uniform in thickness across the substrate surface; (2) all Si and Ca intensity was generated in the glass film, whereas the Al intensity was contributed from both the film and the substrate; and (3) the Al intensity generated from the substrate fell to zero when the substrate was of zero thickness (i.e. the foil edge), and scaled linearly with substrate thickness. Each film composition was determined using energy-dispersive x-ray spectrometry (EDS) in Philips CM12 and EM400T/FEG analytical electron microscopes (AEM). Quantitative analysis was performed with an updated version of the computer code (NEDQNT2) based on the standardless approach of Zaluzec assuming that the thin-foil criterion was valid for the specimens.[3,4] Since the glass films were susceptible to electron beam damage, a defocused probe was used to limit the current density during analysis. Thus, an area approximately 1 μm in diameter was sampled to obtain an average film composition in that region. X-ray spectra were collected from areas of different substrate thickness, which was determined by measuring the spacings of the Kossel-Möllenstedt fringes in convergent-beam electron-diffraction patterns obtained from the center of each analysis area.[5] Since these fringes are related to the thickness of the substrate alone, a linear regression to zero substrate thickness was used to determine the Al x-ray intensity generated by the glass film. Quantification was then performed using the x-ray intensities at zero substrate thickness. Figure 1 illustrates a typical linear regression to obtain substrate-subtracted intensity values.

The reliability of this method of microanalysis was tested using a pre-thinned substrate on which a relatively thick (50nm) glass film was grown. In addition to the presence of a uniform film on the substrate surface, a significant amount of glass was deposited on the edge of the substrate as shown in Figure 2. The small probe of a field-emission gun (FEG) AEM was used to analyze the edge film, eliminating any contribution from the substrate. The film composition determined from the edge of the substrate was found to agree with the composition determined by removal of the substrate contribution, as presented in Table 1. The substrate-subtraction method will be used to determine the composition of thinner glass films deposited on pre-thinned substrates and to systematically track variations in film composition with substrate temperature during growth. Preliminary data have shown a decrease in silicon content as substrate temperature increases; further quantitative measurements are in progress. Use of the method to analyze crystallized films is also underway.[6]

1. D.H. Lowndes, Proc. 8th International Summer School on Crystal Growth, in press.
2. D.W. Susnitzky and C.B. Carter, J. Am. Cer. Soc. **75**, 2463 (1992).
3. N.J. Zaluzec, ch. 4 in Introduction to Analytical Electron Microscopy, eds. J.J. Hren et al. (Plenum Press, New York, 1979).
4. D.B. Williams, Practical Analytical Electron Microscopy in Materials Science. (Philips Electronic Instruments, Inc., Electron Optics Publishing Group, Mahwah, New Jersey, 1984), pp. 67–89.
5. P.M. Kelly et al., Phys. Stat. Sol. (a) **31**, 771 (1975).
6. Research supported by the U. S. Department of Energy under Grant No. DE-FG02-92ER45465 and partially supported by the Division of Materials Sciences, U. S. Department of Energy, under contract DE-AC05-84OR21400 with Martin Marietta Energy Systems, Inc., and through the SHaRE Program under contract DE-AC05-76OR00033 with Oak Ridge Associated Universities. MPM is also with the Department of Materials Science and Engineering, Cornell University, Ithaca, NY.

TABLE 1. Comparison of two methods used to obtain the composition of a glass film deposited with an alumina-rich polycrystalline target at a substrate temperature of 750°C.

atomic % ratios	substrate-edge film	substrate-subtraction method
Si/Al	0.43	0.44
Ca/Al	0.37	0.38

1

2
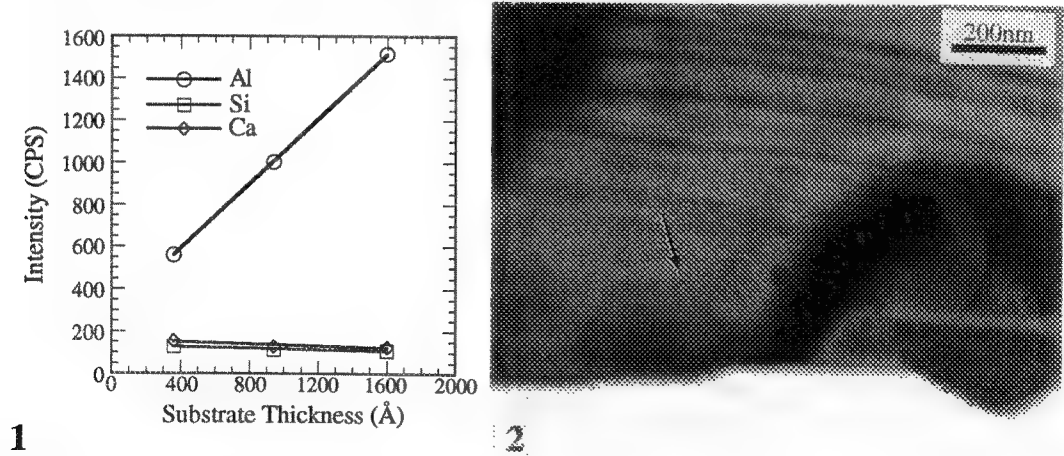
FIG. 1. X-ray intensity from each element as a function of substrate thickness from a glass film deposited at a substrate temperature of 750°C.
FIG. 2. Bright-field image showing the deposited glass film on the edge of the substrate. Surface steps on the substrate are visible at arrow.

TEM AND AEM STUDY OF POLYCRYSTALLINE CdS/CdTe HETEROSTRUCTURES FOR PHOTOVOLTAIC APPLICATIONS

K.M. Jones, M.M. Al-Jassim, R.W. Birkmire* and B.E. McCandless*

National Renewable Energy Laboratory, Golden, CO 80401

* Institute of Energy Conversion, University of Delaware, Newark, DE 19716

CdTe-based solar cells are attracting increasing attention due to their potential for low-cost, large-area high-efficiency photovoltaic applications. Recently, conversion efficiencies exceeding 15% have been reproducibly demonstrated for small area devices. However, the morphology, microstructure and interface properties have not been studied in a systematic manner. Additionally, these structures are normally subjected to at least one heat treatment step prior to device fabrication. The effects of such heat treatment on the microstructure and the CdS/CdTe interface are not well understood. In this work TEM, AEM and secondary ion mass spectrometry (SIMS) were used to study the morphology, microstructure and the CdS/CdTe interface as a function of deposition parameters and post deposition heat treatment. The solar cells used have the following structure:

Si (substrate)/SnO$_2$/CdS/CdTe/Cu-Au (contact)

The CdS and CdTe films were grown by physical vapor deposition. The thickness of these films is 0.5µm for CdS and 2-3µm for CdTe. In some cases, the CdS was heat treated at 400°C for 20-30 min prior to the deposition of CdTe. After the deposition of the latter, the samples were heat treated in the presence of CdCl$_2$ at 400°C for 20-30 min in air. TEM, STEM/EDS, and SIMS were used to characterize the CdTe, CdS films and the CdS/CdTe interface.

TEM cross-sectional examination of an as-deposited structure (figure 1) shows that the grain size and morphology in the CdTe films is similar to that in CdS. Detailed study of the CdS/CdTe interface revealed that the majority of grain boundaries and planar defects propagate across the interface. Furthermore, high resolution lattice imaging showed that a large percentage of the CdTe grains are epitaxially related to the underlying CdS grains (figure 2). Selected area electron diffraction examination of the films showed that the CdS is constituted of a mixture of cubic and hexagonal phases, while the CdTe is predominantly cubic. Such a difference in the crystal structure is thought to complicate the interface considerably. STEM/EDS measurements were performed in several areas across the interface. No evidence of Te or S interdiffusion was observed in the as-deposited structures. These results were corroborated by SIMS measurements.

Heat treated samples exhibited a markedly different microstructure and interface properties. Figure 3 is a TEM cross-section that demonstrates the considerable grain growth that was observed in both CdS and CdTe films. However, the grain growth was an order of magnitude higher in CdTe than in CdS. Additionally, high resolution lattice imaging of the CdTe/CdS interface (figure 4) shows that the CdTe grains appear less oriented with respect to the underlying CdS grains. This is believed to be due to the fact that the CdS grains are larger in number and exhibit no preferred orientation. Hence, a CdTe grain can only be oriented epitaxially with one CdS grain.

440

Unlike the as-deposited structure, STEM/EDS analyses across the interface of the heat treated sample detected sulphur diffusion into CdTe. However, the concentration of sulphur varied considerably along the interface. In the CdTe grains, increased levels of sulphur were detected particularly in regions with a high density of planar defects.

This work clearly demonstrated the effects and importance of heat treatment on CdS/CdTe solar cell structures. The optimization of such treatment and the preservation of the CdS/CdTe interface is the goal of this study.
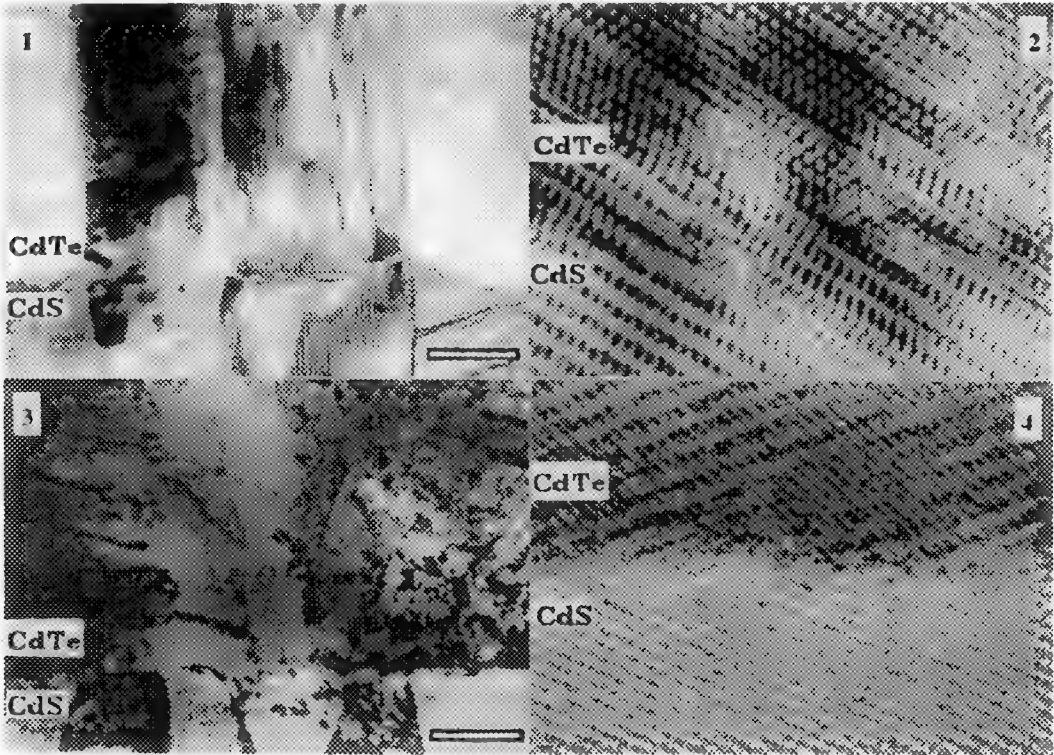
FIG. 1.--TEM cross-section of as-deposited polycrystalline CdS/CdTe structure. Bar = 50nm.

FIG. 2.--High resolution lattice image of the as-deposited CdS/CdTe interface.

FIG. 3.--TEM cross-section of heat treated polycrystalline CdS/CdTe structure. Bar = 0.5μm.

FIG. 4.--High resolution lattice image of heat treated polycrystalline CdS/CdTe interface.

ENERGY-DISPERSIVE X-RAY MAPPING OF GRAIN BOUNDARIES IN HIGH-T_C SUPERCONDUCTORS

J.C. Barry and G.J. Auchterlonie

Centre for Microscopy and Microanalysis, University of Queensland, Brisbane Queensland 4072, AUSTRALIA

Superconductors are materials which carry electrical current without resistive loss below a certain critical temperature (T_c). There are many potential uses for materials that are superconducting, but until recently the T_c's of known materials were too low to be useful in large-scale applications such as power transmission. However, with the discovery of high T_c oxide superconductors, the feasibility of such projects are now being considered. The problem with the oxide superconductors is *not* that their critical temperature is too low (the T_c's of the oxides are almost an order of magnitude better than the metal superconductors), *but rather* that in bulk form their current carrying capacity (J_c) is too low[1]. It is known that the bulk J_c is determined by intergranular conductivity. Low values for J_c may occur because of: (a) a change of stoichiometry at the grain boundaries, or (b) because of misorientation of adjacent grains. High J_c's can be achieved in thin films by texturing the material so that there are few grain boundaries across the direction of current flow but many grain boundaries perpendicular to the current flow. In this study, we use EDS X-ray mapping to analyse stoichiometry at grain boundaries in bulk $YBa_2Cu_3O_{7-x}$.

The $YBa_2Cu_3O_{7-x}$ material was embedded in epoxy, thinned by ultramicrotomy, and examined in a 4000FX electron microscope. It has been shown[2,3] that J_c and T_c are strongly dependent on the oxygen stoichiometry of $YBa_2Cu_3O_7$ -x. So, in order to distinguish between the effects of structural versus chemical change, we find grain boundaries which are clean as seen by lattice imaging, and apply EDS mapping to measure (at 60Å resolution) any stoichiometric changes (if any) at the grain boundaries. The EDS mapping is done on a 6400F FEG SEM. A carbon-cup holder on the SEM was modified to accept 3.0mm grids. The SEM has an ultra-thin window Ge detector. Maps of oxygen, yttrium, copper and barium are collected simultaneously.

In the X-ray maps of many grain boundaries we did find some evidence for a variation in oxygen stoichiometry at the grain boundaries, but this variation was not well localised. A typical X-ray map series from the region near to a grain boundary is shown in Fig. 1. The interface between grain 1 and 2 (in Fig. 1) is oxygen rich, but that grain boundary is also deficient in copper and barium. Grain 1 contains a sub grain boundary which is rich in barium and copper (arrowed). The sub grain boundary is not visible in the oxygen and yttrium maps. Fig. 2 shows a series of X-ray line profiles across a different boundary. The barium profile differs significantly from the yttrium and oxygen profiles[4].

References

1. S.E. Babcock, MRS Bulletin, (1992) 15, no. 8, 20.
2. N. McN. Alford, W.J. Clegg, M.A. Harmer, J.D. Burchall, K. Kendall and D.J. Jones, Nature, (1988) 332, 58.
3. A. Fujimori, E. Takayama-Muromachi and Y. Uchida, Solid State Communications, (1987) 63, 857.
4. The authors would like to acknowledge support from the Australian Research Council, and also the support of, and the use of the facilities at the Centre for Microscopy and Microanalysis at the University of Queensland.
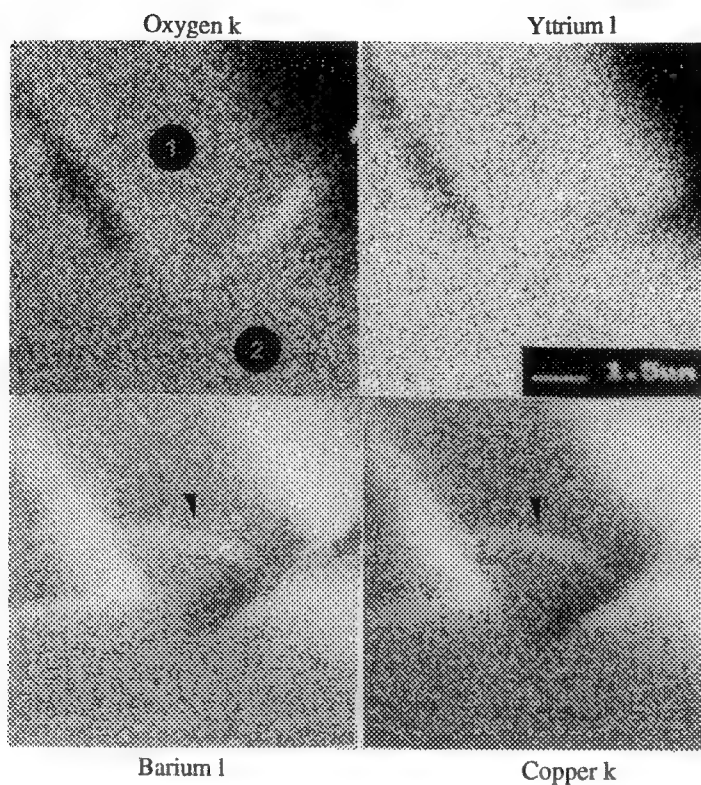
Figure 1. X-ray maps of a region encompassing a grain boundary.
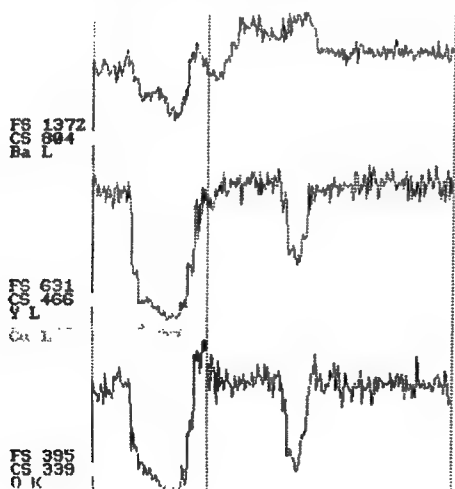
Fig. 2. X-ray Line profiles across a grain boundary.

443

BIOMINERALIZATION IN LORICATE GREEN ALGAE

John R. Dunlap and Patricia L. Walne

Program in Microscopy and Department of Botany, The University of Tennessee, Knoxville, TN 37996-0810

Members of the green algal family Phacotaceae are characterized by the presence of an extracellular wall-like structure termed a lorica. A complex assemblage of mucopolysaccharides and metals, primarily calcium and iron, the lorica is considered to be a highly conserved structure. Hence, lorica morphology has served as a basic criterion for classification at both the generic and species levels. Although lorica development is thought to be genetically controlled in the phacotacean algae[1] the extent of cellular control over development and mineralization is largely unknown. This study was initiated to gain a better understanding of lorica microarchitecture and mineralization patterns in this unusual group of organisms.

Three members of the Phacotaceae are reported on here: Pteromonas, Phacotus and Dysmorphococcus. Samples for the present study were fixed in glutaraldehyde; some were post-fixed in osmium tetroxide and all were dehydrated in alcohol and embedded in Spurr's low-viscosity resin. Thin and thick sections were examined and analyzed on an Hitachi H-800 TEM/STEM operating at 200kV. Energy dispersive x-ray spectra were collected with a Link Pentafet detector and QX 2000 processing system.

In all three genera lorica microarchitecture is characterized by interwoven granulo-fibrillar material. In the lorica of both Pteromonas and Phacotus this fibrillar material appears as a loosely woven mat encircling the cell (Figures 1 & 2). Calcium and phosphorus are the primary mineralizing elements in the loricae of both genera (Figure 3). In Pteromonas, calcified material has been localized in Golgi-derived vesicles near, at and outside the cell surface (Figures 4 & 5). In Dysmorphococcus the lorica may also have electron-opaque needle-like components (Figure 6) in addition to the granulo-fibrillar material (Figure 7). Such components have not been observed in either of the other two genera. In Dysmorphococcus loricae, phosphorus, iron, manganese and calcium are typical elements. In the areas where needle-like components are present Mn is the predominant element (Figure 8) and in areas with electron opaque granular components Fe is the predominant element (Figure 9).

In summary, the lorica of Dysmorphococcus is a single, porate unit, and Fe and Mn are the primary mineralizing elements. These features, combined with lorica microarchitecture, make Dysmorphococcus more reminiscent of the euglenoid system characterized by Trachelomonas, where Fe and Mn are also the primary elements in the lorica, and mineralization appears to be a passive extracellular process[2,3]. In contrast, in both Pteromonas[4] and Phacotus[5] the loricae are bivalved and Ca is the primary mineralizing element. Further, in Pteromonas lorica development and mineralization appear to be under active cellular control in that Ca-enriched presumptive lorica material is found in Golgi cisternae and in vesicles throughout the cytoplasm and at the cell surface adjacent to the plasmalemma.

References

1. B. Giering et al., Arch. Protistenkd. (1990)138, 75.
2. J. Dunlap et al., Protoplasma. (1983)117, 97.
3. J. Dunlap and P. Walne, J. Protozool. (1985)32, 437.
4. D. Gerard and P. Walne, J. Phycol. (1979)15, 15.
5. L. Pocratsky and P. Walne, J. Phycol. (1981)17, 76.
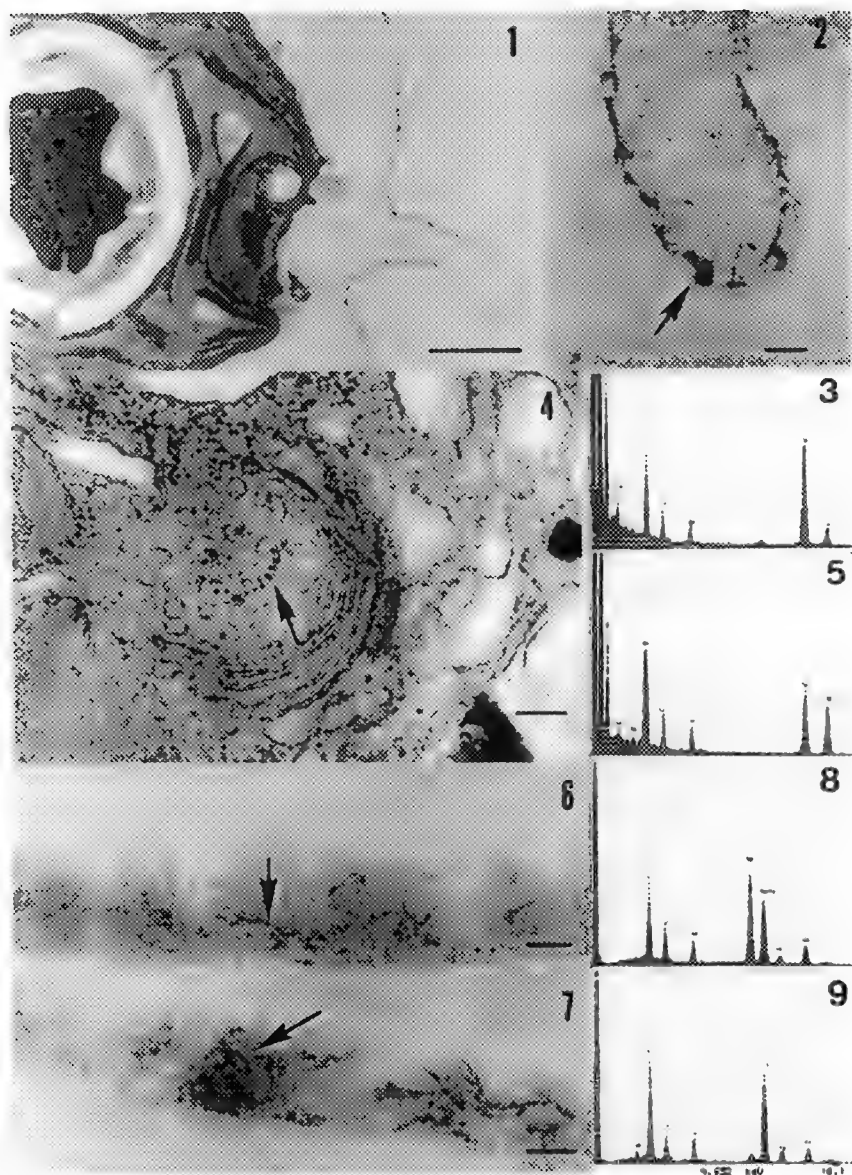
FIG. 1. Section through <u>Pteromonas</u> shows juxtaposition of cell and lorica. Bar = 1μm
FIG. 2. Higher magnification of portion of lorica shown in Fig. 1. Bar = 100nm
FIG. 3. X-ray spectrum taken from lorica shown in Fig. 2.
FIG. 4. Section through <u>Pteromonas</u> shows electron opaque inclusions in Golgi cisternae   and
     vesicle. Bar = 100nm
FIG. 5. X-ray spectrum taken from vesicle material shown in Fig. 4.
FIG. 6. Section through <u>Dysmorphococcus</u> lorica with needle-like components. Bar = 100nm
FIG. 7. Section through <u>Dysmorphococcus</u> lorica with granular components. Bar = 100nm
FIG. 8. X-ray spectrum taken from lorica shown in Fig. 6.
FIG. 9. X-ray spectrum taken from lorica shown in Fig. 7.

445

A VACUUM MODIFICATION FOR THE PHILIPS CM30 ELECTRON MICROSCOPE

N. D. Evans[*], J. Bentley and A. T. Fisher

[*] Oak Ridge Institute for Science and Education, P.O. Box 117, Oak Ridge, TN 37831-0117
Metals and Ceramics Division, Oak Ridge National Laboratory, P.O. Box 2008, Oak Ridge, TN 37831-6376

For the Philips CM30 (or earlier EM430), the large surface area in the gun, the relatively poor pumping speed at the base of the gun, and the use of the same 100 l/s ion getter pump (IGP) for the column and gun, all lead to a significant degradation of gun vacuum (and slow recovery) following the gas burst involved in specimen exchange, even with extended pumping in the airlock. Since the vacuum quality in the gun is important for LaB_6 filament life and high voltage stability, we adopted a conservative approach to the maximum pressure P_c allowed for the application of high voltage or filament emission; we chose an IGP reading of 22 (5×10^{-5} Pa). Delays of ~15 min typically occurred following specimen insertion. To avoid these problems the vacuum system has been modified. The goals were threefold: (1) To increase the pumping speed at the gun. The conductance of the original 600-mm-long vacuum line with three 90° elbows and a valve (V5) results in a pumping speed of <10 l/s at the base of the emission chamber and a routine pressure of 3×10^{-5} Pa (1.5×10^{-7} torr).[1] (2) To prevent the specimen exchange gas burst travelling through the IGP to the gun. It was determined that the gun isolation valve V7 has such a small conductance that it does not provide an effective path. (3) To add a residual gas analyzer (RGA) for vacuum diagnostics.

The original arrangement (thin lines) and modification (overlayed thick lines) to accomplish the above goals are shown schematically in Fig. 1. After considering sublimation and active getter pumps, a conventional 45 l/s StarCell● ion pump (Varian Vacuum Products, Lexington, MA) was chosen for the supplemental pump. The original 90° elbow and bellows between the base of the gun and valve V5 were replaced with a custom-built (MDC Vacuum Products Co., Hayward, CA) 5-way cross, which has a special flange to mate with the base of the gun, conflat flanges to accommodate the new ion pump and RGA, a spare 70 mm flange, and a manual butterfly valve (V_b, Fig. 1) with attached bellows for connection to the V5 assembly. To place minimal load on the cross, the pump is supported from tapped holes already available in the rear of the gun and is configured so as not to interfere with removal of the high voltage cable, if necessary. In fact, returning to the original configuration is easily achieved. No changes to the microscope software or vacuum logic have been necessary and, importantly, no X-ray leakage has been detected from the modification, even under severe and abnormal operating conditions. The total cost of hardware acquisition and fabrication was less than $10,000.

Figure 2 shows vacuum response curves following specimen insertion with the supplemental ion pump off and V_b open. The behavior is expected to represent that of the unmodified system. The column pressure was recorded from an analog readout of the IGP current (the microscope display is too slow) and the gun pressure was obtained from the RGA mounted on the cross. With the 45 l/s ion pump operating and V_b open, typical vacuum recovery following specimen insertion is as presented in Fig. 3. The pressure in both the gun and column recover much more quickly. When V_b is closed, the emission chamber is isolated from the IGP and the pressure in the gun is maintained by the supplemental ion pump. The pumping speed at the base of the emission chamber was calculated to be 27 l/s. Under these conditions (Fig. 4), the gun pressure measured by the RGA is 4×10^{-6} Pa (3×10^{-8} torr). High voltage and emission current can be applied immediately following specimen exchange, or may even remain on continually, since the pressure in the gun is not detectably impacted by the specimen exchange.

The high voltage interlock, which prevents the application of high voltage if the pressure exceeds a critical level, is governed by the IGP current. This interlock is effectively bypassed with V_b closed. We plan to correct this condition by using the setpoint facility of the supplemental ion pump controller to provide vacuum interlock protection for the microscope. An alternative procedure that we have used is to close V_b only during specimen exchange and for a short time afterwards when the pressure can be monitored without undue burden on the operator.[2]

1. A. Roth, *Vacuum Technology*, 3d ed, Elsevier Pub. (1990) 80-96.
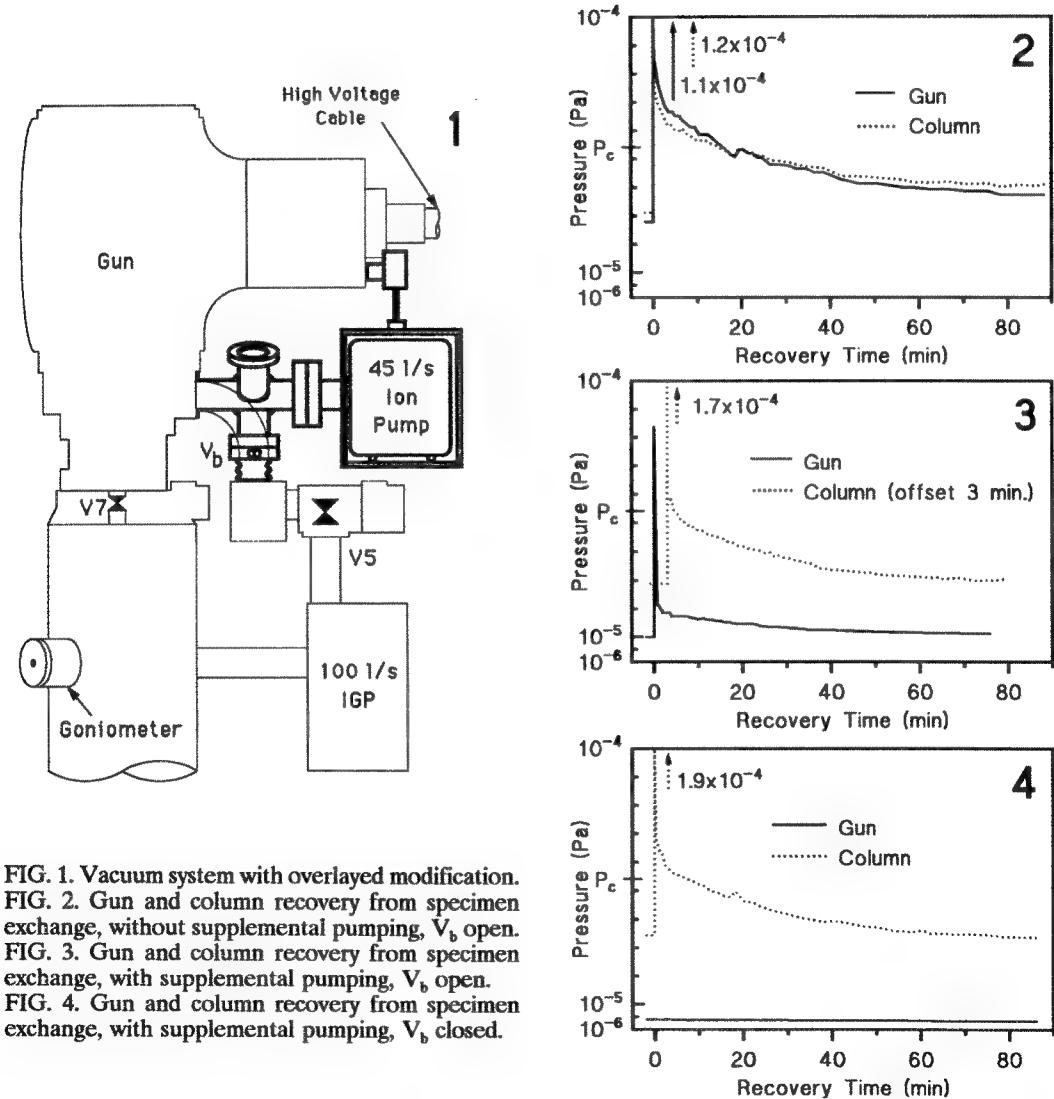
FIG. 1. Vacuum system with overlayed modification.
FIG. 2. Gun and column recovery from specimen exchange, without supplemental pumping, V_b open.
FIG. 3. Gun and column recovery from specimen exchange, with supplemental pumping, V_b open.
FIG. 4. Gun and column recovery from specimen exchange, with supplemental pumping, V_b closed.

447

DESIGN AND PERFORMANCE OF INSTRUMENTATION FOR AUTOMATED SINGLE-TILT-AXIS ELECTRON TOMOGRAPHY

A.J. Koster, H. Chen, W. Clyborne, J.W. Sedat, D.A. Agard

The Howard Hughes Medical Institute and the Department of Biochemistry and Biophysics, University of California at San Francisco, San Francisco, CA 94143-0448

One of the driving questions in our group is into understanding how chromosomes are constructed from fibers of DNA wrapped around histones in their native form. To permit high resolution analysis of these highly complex fibers, we use intermediate voltage electron tomography[1]. To obtain 50Å resolutions, we incorporate new approaches to overcome the resolution limiting factors determined by specimen fixation and staining techniques, data collection and 3D reconstruction algorithms[2].

With our present instrumentation we can automatically collect a series of projection data of large, radiation sensitive objects with only a minimum of manual operation[3,4], with high accuracy and consistency. The images are recorded directly in digital format to overcome the time consuming task of digitizing negatives. Furthermore, the system offers automated eucentricity setting, automatic tracking of image shifts, and automatic focusing during data collection. Highly reliable data collection is ensured by closely monitoring the variation in image shift, defocus, average image intensity, and exposure time throughout the tilt series.

Typically, we record data sets at a magnification of 13,600, containing 121 views of 512^2 superpixels of 2.1nm (due to limited transfer function of the scintillator at 300kV, we bin 2x2 pixels into 1 superpixel), over a tilt range of ±75° with 1.25° increments. Normally, we collect data sets using ~5,000e-/Å^2; 10-100 fold less compared to manual data collection. Collecting data using far less dose per view is possible (0.5-1e/Å^2), but will lower the statistical accuracy. To minimize shrinkage[5] of the resin during data collection, we pre-irradiate the specimen with a dose of 125,000e-/Å^2. Without human intervention, it takes less than 3h to collect a data set. The sample is exposed to the beam for ~3min. Most of the data collection time is required for readout of the CCD camera (200 kpixels/s) and the writing of data to the harddisk (45 %), and the computation of correlation functions (used to track image shift and defocus) (24 %).

Presently, we are expanding the capabilities of our data collection system by including functionality which increases the resolution and interpretability of our 3D reconstructions. This includes (a) image montage[6]; to increase the number of resolvable details from 512^2 to, for example, 1024^2, (b) image restoration[7,8] to combine several images taken at different defocus into one image with higher resolution and better contrast (at every tilt angle), and (c) low dose data collection by performing the tracking of shift and defocus on another area than for taking the data[9]. Preliminary results show that we are able to collect 23 views over a ±55° with a total dose of less than 25e-/Å^2.

Due to restrictions in speed and capacity of our present instrumental setup based on a microVAX III computer, we are in the process of upgrading our data collection system. The upgrade involves in particular the computer system and readout rate of the CCD camera. In the new setup both the TEM and CCD camera are controlled by a Silicon Graphics Personal Iris workstation, equipped with a Sky Shamrock 320 Mflops array processor. The readout rate will be increased by a factor 2.5. In total, we expect a five fold increase in data collection speed, mainly due to faster disk access and more efficient use of the array processor.

A new, menu driven data collection package has been developed. The package meets the demands on flexibility required for the recording of low-dose data sets, as well as of (real-time) image montage and object restoration. The setup of the software is built within the structure of the IVE (Interactive Visualization Environment) software developed in our group. IVE offers a great variety of tools to generate applications for the recording, display and processing of multi-dimensional data sets. The package consists of a set of fully independent modules, written in both C and Fortran. Each module is self-contained, and can perform a limited number of (related) tasks. The modules run simultaneously as background processes, and communicate with each other through shared memory areas. For example, some of the modules are dedicated solely to control instrumentation (TEM, CCD camera, display); others to interact with the user (data collection status, input data windows).

1. C.L. Woodcock, in: Electron Tomography, J. Frank (ed.), Plenum Press, New York, 1992, 313-357
2. A.S. Belmont et al., Chromosoma 98 (1989)129-143.
3. A.J. Koster et al., Ultramicroscopy 46(1992)207-228.
4. A.J. Koster et al., EMSA Bulletin, Vol. 23, No. 2, 1993, in press.
5. M.B. Braunfeld et al., these proceedings.
6. J.C. Fung, these proceedings.
7. D. Typke et a., Ultramicroscopy 46(1992)157-173.
8. K.H. Han, these proceedings.
9. K. Dierksen et al., Ultramicroscopy, in press.
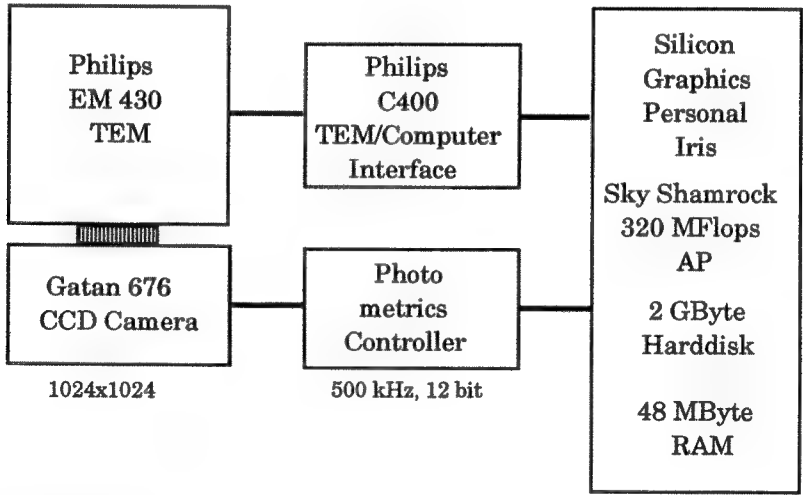
FIG.1.-- Instrumental setup for automated electron tomography at UCSF.

EFFECTS OF HIGHER-ORDER LAUE ZONE REFLECTIONS ON STRUCTURE IMAGES

*H. S. Kim and **S. S. Sheinin

*Department of Physics, Kyungsung University, Pusan 608-736, South Korea
**Department of Physics, University of Alberta, Edmonton, Alberta, Canada T6G 2J1

The importance of image simulation in interpreting experimental lattice images is well established. Normally, in carrying out the required theoretical calculations, only zero order Laue zone reflections are taken into account. In this paper we assess the conditions for which this procedure is valid and indicate circumstances in which higher order Laue zone reflections may be important. Our work is based on an analysis of the requirements for obtaining structure images i.e. images directly related to the projected potential. In the considerations to follow, the Bloch wave formulation of the dynamical theory has been used.

The intensity in a lattice image can be obtained from the total wave function at the image plane is given by:

$$\Psi(\mathbf{r}) = \sum_g \phi_g(z) \exp[2\pi i(\mathbf{K}+\mathbf{g}) \cdot \mathbf{r}] \tag{1a}$$

where $\phi_g(z)$ is the diffracted beam amplitide given by

$$\phi_g(z) = \sum_i \chi^{(i)} C_g^{(i)} \exp(2\pi i \gamma^{(i)} z) T(q) D(q) \tag{1b}$$

In these equations, the z direction is perpendicular to the entrance surface, $\mathbf{g}$ is a reciprocal lattice vector, the $C_g^{(i)}$ are Fourier coefficients in the expression for a Bloch wave, $b^{(i)}$, $\chi^{(i)}$ is the Bloch wave excitation coefficient, $\gamma^{(i)} = k^{(i)} - K$, $k^{(i)}$ is a Bloch wave vector, $\mathbf{K}$ is the electron wave vector after correction for the mean inner potential of the crystal, $T(q)$ and $D(q)$ are the transfer function and damping function respectively, q is a scattering vector and the summation is over i=1,N where N is the number of beams taken into account. In order to obtain structure images $T(q) \approx \pm i$, $D(q) \approx 1$ and the crystal thickness z should be small.

In order to gain some insight into the relative importance of zero and higher order Laue zone reflections, $\phi_g(z)$ in (1a) can be estimated by using a two beam approach and assuming that the diffracted beams to be weak (a reasonable assumption for the thin crystals required for structure images). Under these circumstances $|\gamma^{(1)}| \gg |\gamma^{(2)}|$ and the extinction distance for the diffracted beam, $\mathbf{g}$, is given by $\xi_g \approx (1/\gamma^{(1)})$. It can be shown that under these circumstances

$$\phi_g(z) \approx (\xi_g \sigma V_g / 2\pi)[1 - \exp(-2\pi i z / \xi_g)] \tag{2}$$

where σ is the equivalent to the interaction constant in the phase object approximation and V_g is a Fourier coefficient of the lattice potential. (2) can now be used to estimate the relative importance of

450

zero order and higher order Laue zone reflections if the extinction distances of these reflections are known. In gold, for example, extinction distances for zero order Laue zone reflections are one to two orders of magnitude greater than the lattice parameter, a_0. For higher order Laue zone reflections the extinction distances can be shown to be $\xi_g \approx a_0$. Substituting these characteristic values of extinction distance into (2) indicates that diffracted beam amplitudes for zero and higher order Laue zone reflections are comparable for crystal thicknesses less that about $0.5a_0$. As crystal thickness increases beyond this value, the effects of higher order Laue zone reflections become less important. In order to test these conclusions, calculations of image contrast have been carried for a crystal thickness of $0.25a_0$. Fig. 1a shows the results obtained for a [100] zone axis orientation and including 37 zero order Laue zone reflections only. Fig. 1b shows the results obtained when 32 beams from the first, 8 from the second and 4 from the third upper and lower Laue zones are also included. It should be noted that in order to correctly take the higher order Laue zone reflections into account, a form of the dynamical theory which permits the non-symmetrical Laue case to be taken into account must be used.[1] It is clear from these results, keeping in mind that gold has an FCC structure, that the correct structure image can only be obtained if the higher order Laue zone reflections are taken into account in the calculations.[2]

References

1. H. S. Kim and S. S. Sheinin, Ultramicroscopy, in the press
2. This research was funded by the Natural Sciences and Engineering Research Council of Canada and the Korea Science and Engineering Foundation

(a)   (b)
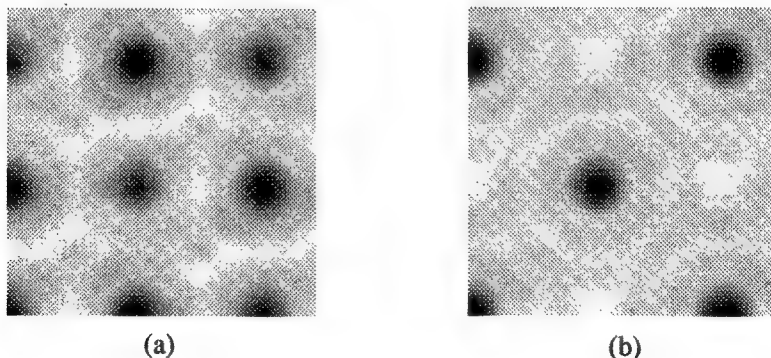
Fig. 1.-- Structure images for gold in a [100] zone axis orientation at 400 kV and a crystal thickness of $a_0/4$. a) includes zero order Laue zone reflections only and b) includes both zero and higher order Laue zone reflections in the calculations.

ANALYSIS OF PHOTOGRAPHIC EMULSIONS FOR HIGH-VOLTAGE ELECTRON MICROSCOPY

James R. Kremer, Paul S. Furcinitti, Eileen O'Toole, and J. Richard McIntosh

Department of Molecular, Cellular and Developmental Biology, Boulder Laboratory for Three-Dimensional Fine Structure, University of Colorado, Boulder, Colorado 80309-0347

Characteristics of electron microscope film emulsions, such as the speed, the modulation transfer function, and the exposure dependence of the noise power spectrum, have been studied for electron energies (80-100keV) used in conventional transmission microscopy.[1] However, limited information is available for electron energies in the intermediate to high voltage range, 300-1000keV.[2,3] Furthermore, emulsion characteristics, such as optical density versus exposure, for new or improved emulsions are usually only quoted by film manufacturers for 80keV electrons. The need for further film emulsion studies at higher voltages becomes apparent when searching for a film to record low dose images of radiation sensitive biological specimens in the frozen hydrated state. Here, we report the optical density, speed and relative resolution of a few of the more popular electron microscope films after exposure to 1MeV electrons.

Three electron microscope films, Kodak S0-163, Kodak 4489, and Agfa Scientia 23D56 were tested with a JEOL JEM-1000 electron microscope operating at an accelerating voltage of 1000keV. Test films were exposed to a total electron dose ranging from 0.1 to 60 e/μm^2. The electron dose was calculated using a faraday cup to calibrate the screen current meter. The Kodak S0-163 film and the Agfa film were both developed for 12 minutes in full strength Kodak D-19 developer and the Kodak 4489 film was developed for 5 minutes in Kodak HRP developer. All films were processed at a temperature of 20° C and were placed in Kodak rapid fix for 3 minutes, and washed for 20 minutes.

The optical density (OD) is defined as $\log_{10} 1/T$, where T is the ratio of transmitted light through the film to incident light. The OD for each film was calculated by measuring the incident light and the transmitted light with a Photometrics STAR 1 slow scan CCD camera operated at -45° C. Corrections for the dark current and variations in the incident light and CCD cell variations were made. The CCD camera was also calibrated against a Kodak Step Tablet #2. The speed of each type of film was determined by the reciprocal of the amount of electron exposure (e/μm^2) needed to give an optical density of 1 above the background fog. The results in order of increasing sensitivity are 0.03 for Kodak 4489, 0.17 for Agfa 23D56 and 0.31 for Kodak SO-163. The response of electron microscope film emulsions to 1Mev electrons is slower than that reported for 80keV electrons.[1] The graphs in Figure 1 show the relationship between optical density and electron dose. Images obtained with the two fastest films are compared in figures 2 and 3, which show a Triton extracted PTK cell that has been fixed with glutaraldehyde, post-fixed with OsO_4, dehydrated and critical point dried. The faster film SO-163 shows a higher contrast image but the Agfa film shows finer detail. The best film to use will therefore depend on the radiation sensitivity of the specimen and the resolution required to answer the question of interest.[4]

452

References

1. Kenneth H. Downing and David A. Grano. Ultramicroscopy 7 (1982) 381.
2. Murray Vernon King and Donald F. Parsons. Ultramicroscopy 2 (1977)371.
3. V. Matricardi, G. Wray. Micron, 1972,3:526.
4. This research was supported by NIH Biotechnology Resources grant RR00592.
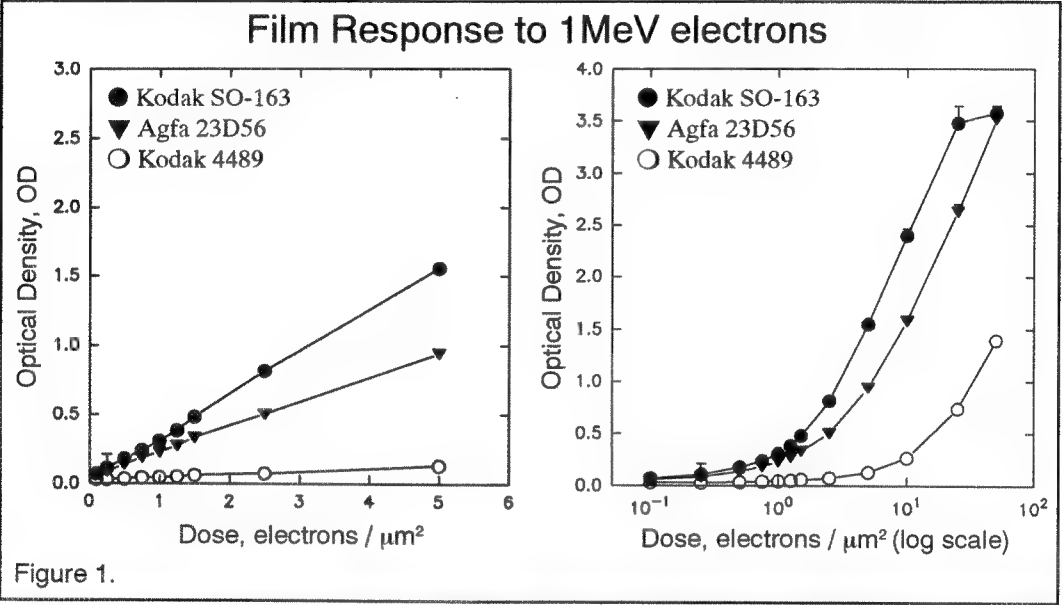
Figure 1.
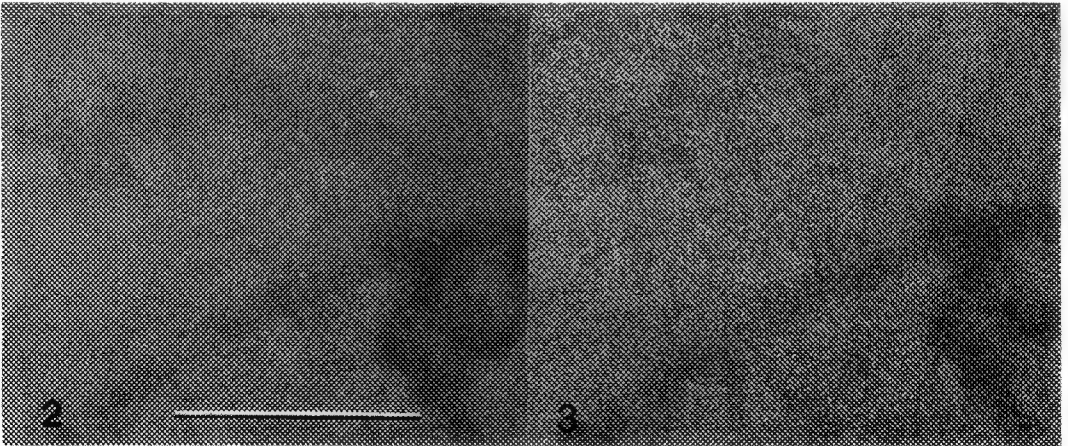
FIG. 1.-- Graphs showing the relationship between optical density and electron dose. Graph on the left shows a linear relationship at lower dose rates, and graph on the right is plotted on a log scale.
FIG. 2.-- Low dose image (1.0 e/μm^2) of the thin cell margin in a PTK cell taken with Agfa 23D56 film. Print magnification is 16x film magnification in order to show film grain. Bar = 500 nm.
FIG. 3.-- Image with same conditions as figure two, but taken with Kodak SO-163 film.

MODULATION ELECTRON ENERGY LOSS SPECTROSCOPY AND ITS APPLICATION OF QUANTITATIVE ANALYSIS

Suichu Luo, John R Dunlap and David C Joy[*]

EM Facility, University of Tennessee, Knoxville, TN 37996-0810,
[*]Oak Ridge National Laboratory, Oak Ridge, TN 37831

Electron energy loss spectroscopy (EELS) gives an inportant insight into the variety of excitations a sample may undergo when irradiated by an electron beam.[1,2,3] The focus of this work was to simulate electronic excitations within the energy range from a few to several hundred eV. Our recently developed modulation scheme, combines both convolution and deconvolution techniques, to provide quantitative information about elementary inelastic scattering processes without knowledge of sample parameters such as thickness or optical constants.

In the low energy loss region of the spectrum the primary excitation mechanisms include interband transitions, and surface and bulk plasmons. In general these individual excitation events overlap in the spectrum. A FFT convolution procedure was developed where the basic inelastic processes may be represented by the dielectric theory . The dielectric function ε is used to describe both single excitations and collective excitations[4], where

$$\varepsilon = 1 + \frac{4\pi Ne^2/m}{\omega^2 - \omega_0^2 - i\,\omega/\tau} \qquad (1)$$

Here $\omega_p^2 = 4\pi Ne^2/m$ is the bulk plasmon frequency, N is number of free electrons per unit volume, e and m are the charge and mass of the electron respectively and ω_0 is a constant which is finite for a bound state but zero for a free electron . τ is a constant which describes the damping suffered by the excitation.Thus, from equation 1, the energy loss function for bulk plusmon and interband transitions is:

$$\text{Im}\{-1/\varepsilon\} = \frac{\omega\,\tau\,\omega_p^2}{(\omega^2 - \omega_x^2)^2 + \omega^2\tau^2} \qquad (2)$$

The energy loss function $\text{Im}\{-1/(1+\varepsilon)\}$ used to describe the surface plasmon is also computed from equation (1).[5] Inner shell excitations are represented by ' saw tooth' curves, with a post-edge slope given by the analytical expression E^{-r}.[3] Single scattering distributions are productions of energy loss functions and Lorentzian angle distribution function.[3]

The first step is to use an FFT deconvolution procedure to obtain a single scattering distribution from the experimental EEL spectrum. Second, the parameters τ and ω_x are chosen for fitting to the observed profiles. Finally , an FFT convolution process is used to change the simulated single profile into a plural scattering profile for fitting to the experimental EEL spectra by adjusting these parameters iteratively. A sum rule is applied for the absolute scale of $\text{Im}\{-1/\varepsilon\}$, so that either the specimen thickness or its refractive index can be estimated. Figures 1, 2, and 4 show comparisons of our simulation results with the experimental EEL spectra. Figure 3 shows the stopping powers of C for total and K-shell seperately and the comparison with Bethe formula. According to our simulation results the scattering mechanisms for AL are composed of a main single bulk plasmon at 16eV, a double bulk plasmon at 32eV, a surface plasmon at 11eV and a double surface plasmon at 22eV.

To test our method the calculated total inelastic mean free path, the sample thickness, k-shell excitation cross section (for carbon only), the optical function ε, ε_r, ε_i for both C and AL are compared with other methods [3,6] and good results are obtained. Our method is of particular value for materials for which it is difficult to obtain information on the thickness, or refractive index.

References

1. G. Zanchi et al., Proceedings of theXIIth International Congress for Electron Microscopy. (1990),18.
2. Y. Kihn et al., Inst. Phys. Conf.Ser. (1991),**119**,143.
3. R. F. Egerton, 'Electron Energy-Loss Spectroscopy in the Electron Microscope', (1986), Plenum Press.
4. R. H. Ritchie and A. Howie, Phil. Mag. (1977), **36**, 463.
5. E. W. Plummer et al., in Proceeding of 14th Werner Brandt Workshop on charged particle penetration phenomena, Oak Ridge National Laboratory, (1991), 140
6. R. F. Egerton et al., 45th annual Meeting of the Electron Microscopy Society of America(1987), 122.
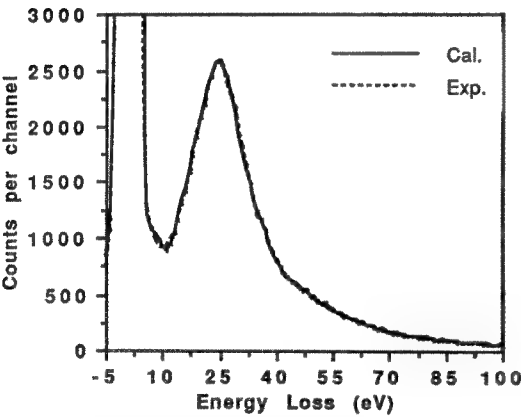
Fig.1 Comparison of simulated and experimental EELS data for carbon. Recorded at 100keV and with 5-mrad collection semiangle.
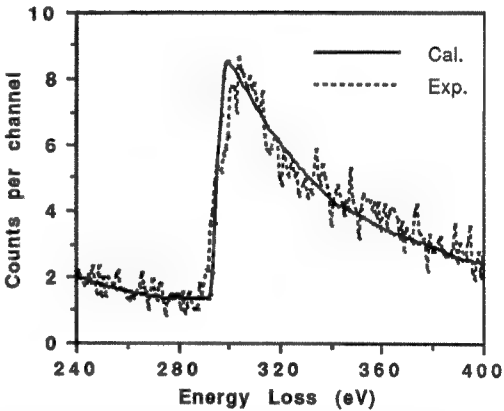
Fig.2 Comparison of simulated and experimental EELS data for carbon K shell . Recorded at 100keV and with 5.3-mrad collection semiangle.
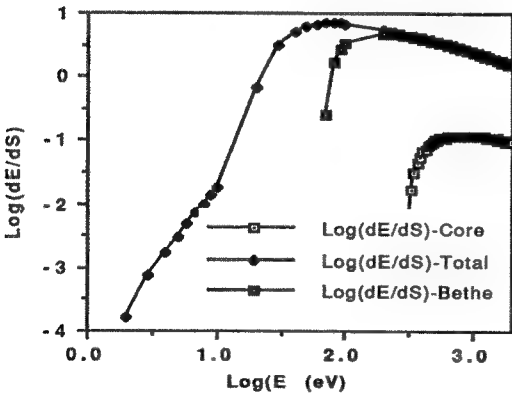
Fig.3 Comparison of calculated data from experimental EELS and Bethe formula for Carbon. At 100keV and with 5.3- mrad collection semiangle.
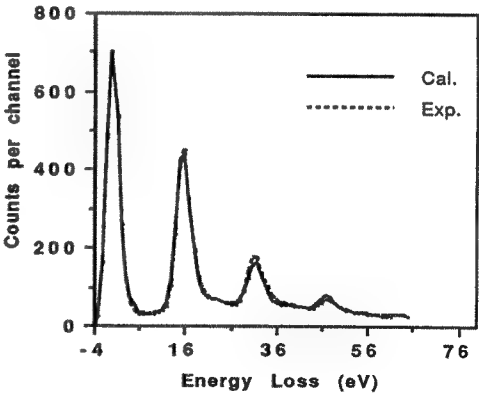
Fig.4 Comparison of simulated and experimental EELS data for aluminum[3]. At 100keV and with 5.3- mrad collection semiangle.

455

DETERMINATION OF REFRACTIVE INDEX OF SOLIDS BY DISPERSION STAINING METHOD: AN ANALYTICAL APPROACH

Shu-Chun Su

Hercules Incorporated, Research Center, 500 Hercules Road, Wilmington, DE 19808-1599, USA

When immersion liquids are used to determine the refractive index (RI) of non-opaque solids, the dispersion staining method is a simple, effective and precise way to determine the matching wavelength, λ_0, at which the RI of an immersion liquid equals that of the solid. A series of equations has been derived to calculate the RI at any given visible wavelength such as n_F, n_D and n_C, i.e. the RI's at Fraunhöfer spectral lines F (486 nm), D (589 nm), and C (656 nm), from λ_0 data obtained by the dispersion staining method. Two methods have been established: the *Single Liquid Method* and the *Double Liquid Method*.

The *Single Liquid Method* is applicable for solids with known dispersion coefficients, which is defined as $(n_F\text{-}n_C)$. This method uses only one immersion liquid whose RI is close to the RI of the solid to be measured so that a match between the liquid and the solid occurs in the visible range. If the matching wavelength is determined to be λ_0 (nm), the RI of the solid at wavelength i (nm) can be readily calculated using the following equation:

$$n_i^S = n_i^L + (\Delta^L - \Delta^S) \cdot k_i,$$

where n_i^S is the RI of the solid at wavelength i (nm); n_i^L the RI of the liquid at wavelength i , Δ^L the dispersion coefficient of the liquid, $(n_F^L\text{-}n_C^L)$; Δ^S the dispersion coefficient of the solid, $(n_F^S\text{-}n_C^S)$; and k_i equals $(X_0\text{-}X_i)/(X_F\text{-}X_C)$. X_0, X_i, X_F, and X_C are defined by replacing the λ in the expression $(\lambda-200)^{-1}$ with λ_0, i, 486 and 656, respectively. Therefore, $k_i = [(\lambda_0\text{-}200)^{-1}\text{-}(i\text{-}200)^{-1}]/[(486\text{-}200)^{-1}\text{-}(656\text{-}200)^{-1}]$, or $[(\lambda_0\text{-}200)^{-1}\text{-}(i\text{-}200)^{-1}]/0.001304$. In most cases, n_D^S, the RI of the solid at 589 nm, is to be determined. The above equation then becomes

$$n_D^S = n_D^L + (\Delta^L - \Delta^S) \cdot k_D,$$

where n_D^L is the RI of the liquid at 589 nm and k_D equals $[(\lambda_0\text{-}200)^{-1}\text{-}(589\text{-}200)^{-1}]/[(486\text{-}200)^{-1}\text{-}(656\text{-}200)^{-1}]$ or $[(\lambda_0\text{-}200)^{-1}\text{-}0.002571]/0.001304$. Because n_D^L, Δ^L, and Δ^S are known, the only parameter that needs to be measured is λ_0. A table for quick conversion of λ_0 to k_D is provided to minimize the calculations involved.

The *Single Liquid Method* is extremely useful for rapid identification of synthetic and natural fibers, such as polypropylene, polyethylene, nylon, cellulose, etc., as well as fibrous components in bulk insulation samples, such as the six fibrous asbestos minerals regulated by the Environmental Protection Agency: chrysotile, grunerite (or amosite), riebeckite (or crocidolite), tremolite, actinolite, anthophylite. A single RI liquid mount (1.550 for chrysotile, 1.680 or 1.700 for grunerite and riebeckite and 1.605 for tremolite, actinolite and anthophylite) is sufficient for

rapidly determining both $n_\perp$ and $n_\parallel$, the RI's perpendicular and parallel to the fiber elongation, respectively, with reasonable accuracy. A series of conversion tables for the six asbestos minerals are presented in this paper to aid the conversion of an observed λ_0 to its corresponding n_D^s value. Other applications of this method include the estimation of the composition of common rock-forming minerals such as plagioclase, olivine, orthopyroxene and augite.

The **Double Liquid Method** is applicable to any solid and requires **no** knowledge about its dispersion coefficient, $(n_F^s - n_C^s)$, or other optical properties. This method uses two immersion liquids whose RI's at 589 nm bracket the RI at 589 nm of the solid to be measured. If the matching wavelengths for Liquid #1 and Liquid #2 are measured to be λ_0^1 (nm) and λ_0^2 (nm), respectively, the RI of the solid at wavelength i (nm), n_i^s, can be readily calculated using the following equation:

$$n_i^s = n_i^1 + (n_i^2 - n_i^1) \cdot k_i,$$

where n_i^1 is the RI of Liquid #1 at i; n_i^2 the RI of Liquid #2 at i; and k_i equals $(X_0^1 - X_i)/(X_0^1 - X_0^2)$. X_i, X_0^1 and X_0^2 are defined by replacing the λ in the expression $(\lambda - 200)^{-1}$ with i, λ_0^1 and λ_0^2, respectively. Therefore, $k_i = [(\lambda_0^1 - 200)^{-1} - (i - 200)^{-1}]/[(\lambda_0^1 - 200)^{-1} - (\lambda_0^2 - 200)^{-1}]$. In most cases, n_D^s, the RI of the solid at 589 nm, is to be determined. The above equation then becomes

$$n_D^s = n_D^1 + (n_D^2 - n_D^1) \cdot k_D,$$

where n_D^1 is the RI of Liquid #1 at 589 nm; n_D^2 the RI of Liquid #2 at 589 nm; and k_D equals $[(\lambda_0^1 - 200)^{-1} - 0.00257]/[(\lambda_0^1 - 200)^{-1} - (\lambda_0^2 - 200)^{-1}]$. Because n_D^1 and n_D^2 are known, the parameters that need to be measured are λ_0^1 and λ_0^2. A table for quick conversion of λ_0^1 and λ_0^2 to k_D is provided to minimize the calculations involved. Apparently, the **Double Liquid Method** is more accurate than the **Single Liquid Method**.

If t, the temperature of the liquid at the time of determination, is not 25°C, temperature correction must be applied to all RI's of the liquids used in the above calculations. The equation used for this purpose is

$$n_i^t = n_i^{25°C} + (t - 25) \cdot dn/dt,$$

where n_i^t is the RI of a liquid at temperature t (°C) and wavelength i (nm); $n_i^{25°C}$ the RI of the liquid at 25°C and wavelength i (nm); and dn/dt the temperature coefficient of the liquid. It should be noted that dn/dt is a negative value. Therefore, if the t is higher than 25°C, n_i^t is lower than $n_i^{25°C}$.

Besides dispersion staining, there are other techniques for determining the matching wavelength λ_0 between the RI of a solid and that of its surrounding liquid medium, e.g., the traditional wavelength-variation method, double-variation method, oblique illumination method, etc. The above equations are equally applicable to the λ_0 data obtained by these and **any** other techniques.

A METHOD FOR DIRECT MEASUREMENT OF SPECIMEN NOISE IN HREM IMAGES

Sidnei Paciornik[#], Roar Kilaas, Ulrich Dahmen, Michael Adrian O'Keefe

National Center for Electron Microscopy, University of California, LBL B72, Berkeley CA 94720
#, Permanent Address: DCMM, PUC-Rio, P.O BOX 38008, Rio de Janeiro, RJ 22452, Brasil

High resolution electron microscopy (HREM) is a primary tool for studying the atomic structure of defects in crystals. However, the quantitative analysis of defect structures is often seriously limited by specimen noise due to contamination or oxide layers on the surfaces of a thin foil.

For simple monatomic structures such as fcc or bcc metals observed in directions where the crystal projects into well-separated atomic columns, HREM image interpretation is relatively simple: under weak phase object, Scherzer imaging conditions, each atomic column is imaged as a black dot. Variations in intensity and position of individual image dots can be due to variations in composition or location of atomic columns. Unfortunately, both types of variation may also arise from random noise superimposed on the periodic image due to an amorphous oxide or contamination film on the surfaces of the thin foil. For example, image simulations have shown that a layer of amorphous oxide (random noise) on the surfaces of a thin foil of perfect crystalline Si can lead to significant shifts in image intensities and centroid positions for individual atomic columns [1]. This effect on *compositional* analysis by HREM has been examined previously [2,3], assuming a fixed structure with no atomic displacements. Here, we consider the complementary problem, the effect of noise on the *structural* analysis by HREM, assuming a lattice of fixed composition.

The image simulation in figure 1 illustrates that in the absence of specimen noise (under optimum conditions and subject to limitations not discussed here), a small displacement of a single atomic column can be imaged faithfully and measured directly from the image. However, the accuracy of such a measurement is compromised by specimen noise. This is illustrated in figure 2 which shows the effect of specimen noise on apparent atom positions, using simulated images of crystalline material with varying amorphous surface layer thickness fraction.

The present method for noise assessment is based on the average displacement of image intensity peaks due to contamination or oxide layers. To determine this average displacement, it is necessary to extract the image peak positions and compare them with a set of reference peak positions. The list of peak positions is obtained by finding the center of mass of intensity peaks located near atomic positions in the experimental image. Then a reference list is created by performing a least-squares fit of a 2D lattice upon the positions of the first list. Assuming a perfect periodic lattice, this reference list approximates the positions of intensity peaks in the absence of noise. The root mean square (rms) deviation between the lists is used as a direct measure of the noise in the image. In Figure 3 the rms deviation obtained is plotted against the amorphous to crystalline thickness ratio. As can be seen from this figure, there is a direct relationship between the amorphous layer thickness and the rms deviation. This result validates the use of the rms value as a direct assessment of atomic positioning error.

The rms deviations obtained are average values for the regions considered. By reducing the size of the region, the variation in the ratio of amorphous to crystalline material can be sampled at smaller intervals. However, when the region becomes too small, the accuracy in the fitted lattice decreases, since the number of peaks enclosed is too small to give good statistical values for the lattice parameters. In order to determine an optimum size for the region, the rms deviation was obtained for different sized windows. A plot of resulting values against the number of atoms inside each window is shown in figure 4. The optimum number of atoms is ≈100. The decrease in rms for smaller numbers is a statistical artifact as commented above. The method described here allows a clear assessment of the specimen noise-imposed limitations to structural defect analysis in simple materials[4].

458

References
1. R. Kilaas and R. Gronsky, Ultramicroscopy 16, 193 (1985)
2. J.M. Gibson and M.L. McDonald, Mat. Res. Soc. Symp. Proc. Vol. 82, 109 (1987)
3. A. Ourmazd, F.H. Baumann, M. Bode and Y. Kim, Ultramicroscopy 34, 237, (1990)
4. This work is supported by the Director, Office of Energy Research, Office of Basic Energy Sciences, Materials Sciences Division of the U.S. Department of Energy under Contract No. DE-ACO3-76SFOOO98. One of the authors (S.P.) acknowledges the support from Conselho Nacional de Desenvolvimento Científico e Tecnológico - CNPq, Brasil.
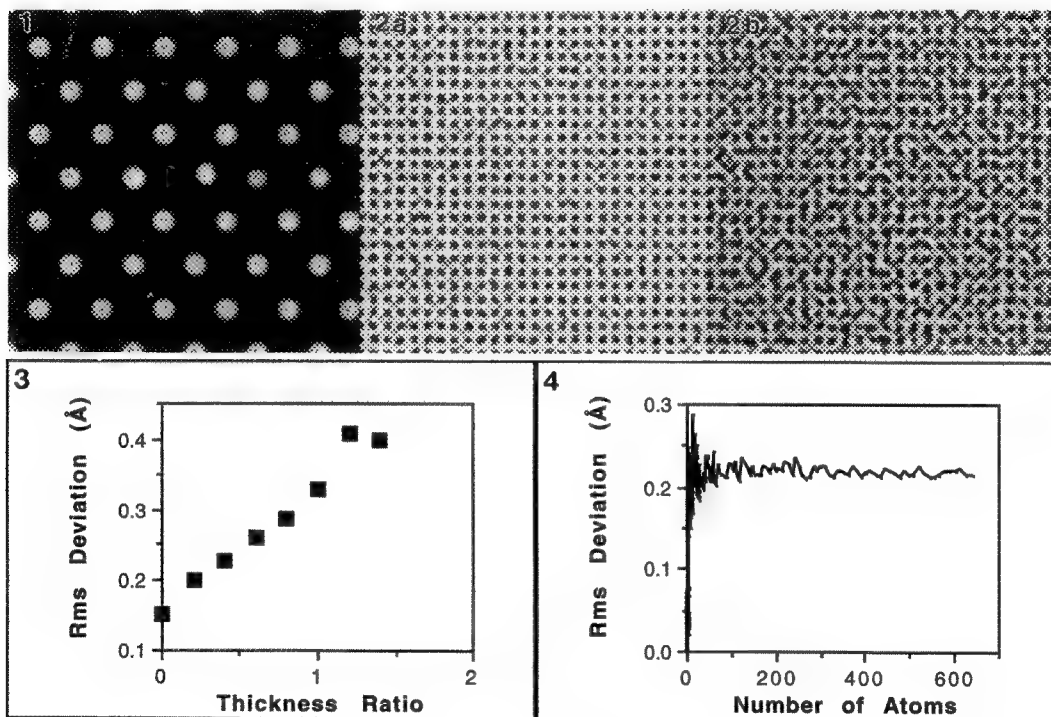
Figure 1 - Simulated image of 20Å thick Al specimen in [110] direction showing the effect of a single atom displacement of 0.5Å under Scherzer conditions. Image contrast is reversed for clarity.

Figure 2 - Simulated images showing the effect of amorphous contamination on apparent atomic positions for two amorphous to crystal thickness ratios of (a) 0.2 and (b) 1.4.

Figure 3.- Rms deviation versus amorphous to crystal thickness ratio.

Figure 4.- Rms deviation as a function of number of atoms inside the measurement window.

HIGH-RESOLUTION FIELD EMISSION SEM (FESEM) OF BULK BIOLOGICAL SAMPLES: RELATIONSHIP BETWEEN DIFFERENT METAL COATINGS, THEIR THICKNESSES, AND QUALITY OF BACKSCATTER ELECTRON (BSE) VERSUS SECONDARY-ELECTRON (SE) IMAGING

Chris Frethem[1], Carol Wells[2], Vince Carlino[3], and Stanley L. Erlandsen[1]

Department of Cell Biology and Neuroanatomy[1], Department of Laboratory Medicine and Pathology[2], University of Minnesota School of Medicine, Minneapolis, MN 55455; VCR Group, Inc.,[3] South San Francisco, CA 94080

High resolution visualization of cell surfaces in bulk biological samples can be obtained by low voltage FESEM using either SE or BSE imaging methods[1,2,3] and the preferred selection of low accelerating voltages (1-4 keV) has been based on theoretical considerations related to interaction volumes, electron charge, and potential radiation damage to the surface produced by direct exposure to the electron beam[4]. Fine metal coatings (≤ 1 nm) produced by ion sputtering for high resolution FESEM imaging are used to minimize charging and to increase SE contrast as well as BSE topographical contrast.

The purpose of this work was to investigate the relationship between the thickness of metal coatings produced by ion beam sputtering and the quality of imaging obtained by SE and BSE of biological samples. Cells of *Proteus mirabilus* were immunocytochemically labeled with 12 nm colloidal gold as previously described[5], fixed in glutaraldehyde followed by post-fixation in osmium, and critical point dried in CO_2. Biological specimens were examined by FESEM (V_0=1-4 keV) without any metal coating or after ion beam sputtering (IonTech, VCR Group, South San Francisco) the following film thicknesses: 0.5 nm, 1.0 nm, 1.5 nm, 2.0 nm of platinum (Pt), iridium (Ir), tungsten (W), or chromium (Cr). Metal film thickness was measured by a quartz crystal monitor during sputtering and the resistance (Ω) of metal films deposited on glass substrates was determined using a 2-point method. The substructure and granularity of the metal films were imaged at 300 kx in FESEM by BSE at 8 keV.

Electrical conductivity was detected at thicknesses of ≥ 1 nm for W and Cr and at ≥ 1.5 nm for Pt and Ir (Fig. 1). Pt, Ir, and W coatings of 0.5 nm were fine grained (~1 nm) while the 1 nm coating was more granular (1-4nm; see Pt in Figs. 2 & 3). SE image quality with Cr was poor, but a progressive improvement was obtained with increasing Pt coating (0.5 to 1.0 nm) despite their being nonconductive (compare Figs. 4-6). BSE atomic number contrast of colloidal gold could be achieved with no metal coating (Fig. 7). Imaging of surface topography by BSE was achieved at thinner metal coatings than by SE (compare Figs. 5 to 8, 6-9). Due to higher energy of BSE (90% of V_0) versus SE (~1-20 ev), the BSE imaging was relatively independent of local surface charging and likewise of contamination.

References

1. J. Pawley and D.C. Joy, Proc. 50th Ann. EMSA Mtg. (1992) 2: 1278.
2. D.C. Joy, J. Micros. (1991) 161: 343.
3. R. Wepf, et al., J. Micros. (1991) 163: 51.
4. J. Pawley, Advances in Electronics and Electron Physics, Academic Press (1992) 83:203.
5. C.L. Wells and S.L. Erlandsen, Infection & Immunity (1991) 59:4693
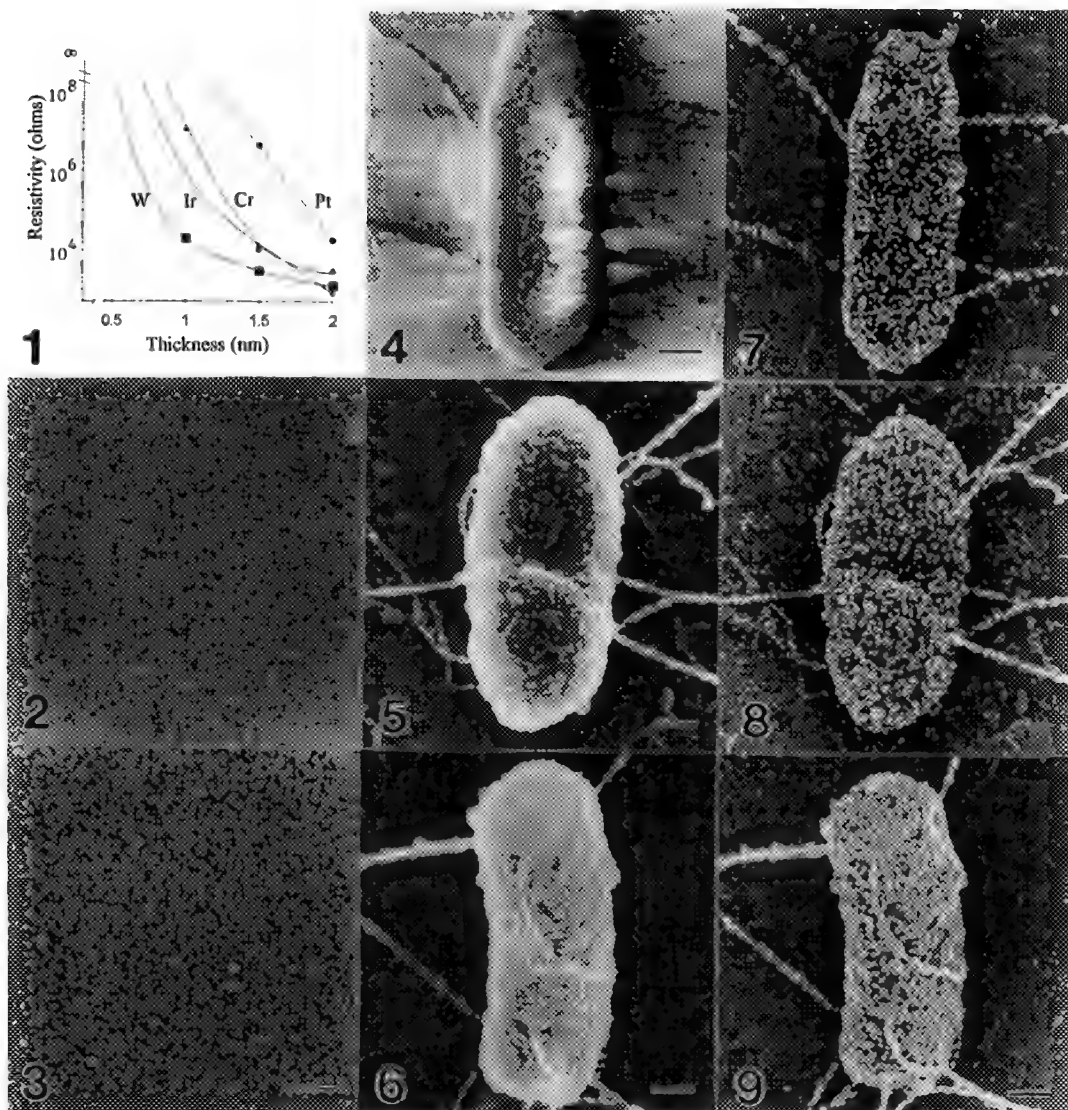
Figure 1. Relationship of resistivity (ohms) to sputtered metal coating thickness(Cr, Ir, Pt, W).

Figure 2 BSE image of 0 5 nm Pt coating on glass substrate Bar, 40 nm.

Figure 3. BSE image of 1 0 nm Pt coating on glass substrate Bar, 40 nm.

Figures 4-6 SE images of *Proteus mirabilus* with no coating (Fig. 4), coated with 0.5 nm Pt (Fig. 5), coated with 1.0 nm Pt (Fig. 6), Bar, 200 nm for all figures.

Figures 7-9. BSE images of *Proteus mirabilus* corresponding to Figures 4-6. No metal coating in Figure 7, Pt coating = 0.5 nm in Figure 8, and Pt coating = 1.0 nm in Figure 9. Bar, 200 nm for all figures.

SCANNING ELECTRON MICROSCOPY EVALUATION OF HEAT CURED COMPOSITE RESIN AFTER SURFACE PREPARATION TO ENHANCE BOND STRENGTH

Glen M. Imamura, John W. Reinhardt, Jorge Perdigao

Department of Operative Dentistry, The University of Iowa, Iowa City, IA 52242

Tooth shaded composite resin is frequently used as a direct restorative material in the oral cavity. However, during setting it undergoes a volumetric shrinkage which can result in leakage around margins of the restoration[1]. Indirect techniques avoid intraoral shrinkage by fabricating and curing the composite at elevated temperatures outside of the mouth. Higher curing temperatures also improve physical properties *in vitro*[2]. The completed restoration is then cemented into the prepared cavity with a low viscosity composite resin cement. This study evaluated the effect of varied surface preparation and chemical conditioning on the bond strength of two different indirect heat cured composite resins to a composite resin luting cement.

Well and disk specimens of a microfilled resin (Concept, Williams), groups 1-7, and a minifilled hybrid resin (Herculite-XRV-Lab, Kerr), groups 8-14, were fabricated and cured at 250° C and 85 psi pressure. Each resin set was randomly divided into 7 groups of 10 specimens. After preparation of opposing surfaces (Table. 1.), disks were bonded to wells with a dual-curing resin cement, stored for 7 days in water at 23° C, thermocycled 1000 times and fractured.

Both composite materials were evaluated independently (ANOVA/Duncan's) and significant differences for treatments were detected differences at $p < 0.05$. Rocatec treatment for the microfilled resin, group 7, provided the greatest shear bond strength of 41.5 MPa (Fig. 1.). This was followed by groups (shear strength in MPa); 2 (34.2), 3 (31.6), 4 (36.8), 5 (39.8), 6 (41.4) and 1 (control, 8.7). Microabrasion uses 50 μm aluminum oxide suspended in a high pressure air stream to create a roughened surface. The mechanical irregularities produced were critical to increased bond strengths (Fig. 2.). Further application of bonding agents to enhance resin penetration (Fig. 3) or silane solutions to form a polysiloxane layer[3] significantly improved bond strengths over microabrasion alone (Fig. 3.). Methods which used All-Bond 2 following microabrasion, as in group 10 (38.6), and Rocatec treatment, as in group 14, (34.5) were statistically equivalent. They provided the greatest bond strengths for the hybrid resin followed by group 9 (29.1). Any treatment involving surface conditioning with hydrofluoric acid (HF) acid resulted in weak bonds. Hybrid composites combine both large and small glass filler particles into a resin matrix. Their heavy loading with a large filler fraction leaves less surrounding matrix. Dissolution of the glass phase (especially large particles) by HF acid left a remnant resin shell which may have provided a poor bonding substrate (Fig. 5.). HF acid alone used with group 11 (13.5) was not significantly different from group 8 (control, 12.9). Microabrasion prior to HF acid application as with group 12 (19.5) significantly improved bond strength over group 11. Silanation following microabrasion and HF acid as in group 13 (26.5) improved bond strength significantly over group 12. Evaluation showed evidence of a polysiloxane layer on the hybrid surface also (Fig. 6.). However, the polymer layer was of a more porous and irregular nature when compared to the microfill.

In summary; 1.) microabrasion was a prerequisite to improve shear bond strength, 2.) Rocatec treatment provided the highest bond strengths for both materials. This procedure involves a preparatory surface abrasion step. It is unclear if the improved strength is due to the deposition of ceramic particles or a consequence of microabrasion, 3.) chemical primers (i.e. bonding agents, silanation etc.) significantly improved bond strengths when used in conjunction with microabrasion, and 4.) HF acid conditioning significantly decreased bond strengths on the hybrid resin. The microfilled resin was not affected to as great a degree by HF acid.

Table 1. Surface preparations.

PREPARATIONS	GROUPS													
	1	2	3	4	5	6	7	8	9	10	11	12	13	14
50 um microabrasion		X	X	X	X	X			X	X		X	X	
37% Phosphoric Acid	X	X			X			X	X					
Special Bond II[a]			X											
All-Bond 2[a]				X						X				
Silanation					X								X	
9.6% HF Acid						X					X	X	X	
Rocatec[b]							X							X

a. Bonding agents. b. Mechanically places ceramic particles on surfaces following microabrasion with a 30 μm abrasive.
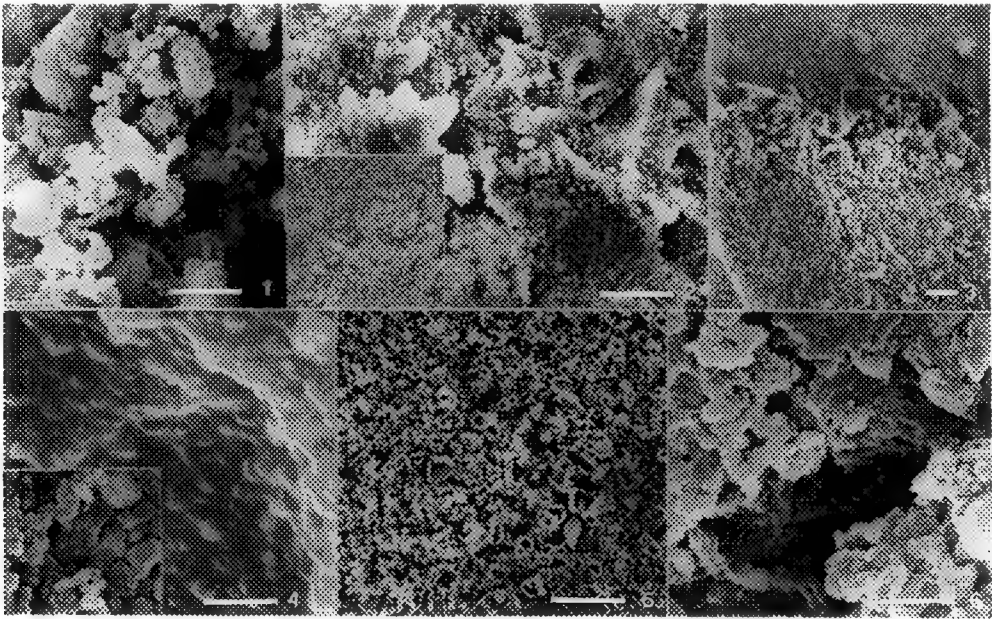
Fig. 1. Ceramic particles embedded in the surface following Rocatec treatment. Bar = 0.6 μm
Fig. 2. Microabrasion of the surface. No surface preparation, control (inset). Bar = 6.0 μm
Fig. 3. Cross section of resin penetration into the surface following microabrasion. Bar = 6.0 μm
Fig. 4. Polysiloxane layer on surface. Surface prior to silanation (inset). Bar = 6.0 μm
Fig. 5. Surface following HF acid conditioning. Bar = 6.0 μm
Fig. 6. Surface following microabrasion, HF acid conditioning and silanation. Bar = 0.6 μm

References

1. P. Lambrechts et al., Oper. Dent. 12(1987)53.
2. J.F. McCabe and S. Kagi, Br. Dent J. 171(1991)246.
3. B.I. Suh, J. Esthet. Dent. 3(1991)139.
4. Support from the Graduate College and CEMRF at the University of Iowa is greatfully acknowledged.

EFFECTS OF LOW-TEMPERATURE HEATING ON THE MORPHOLOGY OF BIRCH WOOD

Robert M. Fisher* and Barbara A. Reine**

*Department of Materials Science and Eng. FB-10, University of Washington, Seattle, WA 98195
**Botany Dept. KB-15, University of Washington, Seattle, WA 98195

The effects of heating wood have been studied for many years with much of the work focused on the curing, ignition, extraction of gaseous and liquid by-products, production of charcoal and, of course, high temperature oxidation, i.e. combustion. Research techniques include bulk weight-loss studies or differential gravimetric analysis (DTA), analyses of the evolution of a wide variety of C-O-H organic compounds by gas chromatography and mass spectroscopy, observing critical times and temperatures for piloted and smoldering ignition, analyses of heat energy absorption and release using Differential Thermal Analysis (DTA) and measurement of the caloric value of firewood and charcoal. Optical microscopy has been used in support of these studies but surprisingly little electron microscopy has been carried out (3).

The stimulus for this research was curiosity about structural changes during long term heating of wood that increase its' susceptibility to spontaneous, i.e., smoldering combustion. The literature on fire origin investigations contains numerous references to cases where fires were believed to have resulted from spontaneous ignition of structural wood members after years of exposure to steam heating pipes. The pyrophoric behavior of many materials is directly related to a surface area to volume parameter in relation to the kinetics of oxidation reactions. The shrinkage of wood during drying has its origin in a shrinkage of the cell walls and the dimensions of the cell walls are reduced remarkably (2). Therefore, it is reasonable to expect that wood would have similar pyrophoric behavior if the S/V ratio steadily increases as a result of inhomogeneous weight loss during long term heating creating thinner cell walls and increased porosity. The first step in a program to confirm this hypothesis is to establish a frame of reference for the gross structural changes that occur in the temperature range of importance in long term smoldering and spontaneous combustion. For this purpose, birch carpenter's screw plugs (1/2" in diameter by 1/4" thick) were used because they were readily available, clean, and very uniform in dimensions and mass. The weight loss during heating at 200°, 230°, and 260° C for extended periods was determined and corresponding samples sectioned and examined in a JEOL 840 SEM. Wood heated at temperature becomes relative easy to hand section but the unheated samples first were immersed in hot water for 24 hrs. and then were easily cut with a single edge razor blade essentially following Exley, et. al (1) except that the recommended treatment with sodium hypochlorite was not used.

Observations and discussion - The weight loss of birch samples heated at 260° C was essentially linear over a prolonged period corresponding to a 65% loss and then changed abruptly to a much lower rate. The rate was about 50% lower at 230° C and markedly lower at 200° C suggesting time different processes predominate in each regime. Various gases and liquids form when wood is heated including hydrocarbons, ethyl alcohol, and turpentine. The samples were noted to shrink uniformly in diameter with only a small change in length reflecting the weight loss seen in the earlier stages of heating. The remarkable uniform shrinkage in cell dimensions is seen in SEM images of cross-sections as shown in the figures and can be determined quantitatively by image analysis techniques (3).

REFERENCES
1. R. R. Exley, B. G. Butterfield and B. A. Meylan. J. of Microscopy (1974) 101, 21.
2. D. Fengel and G. Wegener. WOOD: Chemistry, Ultrastructure, Reactions. New York: W. de Gruyter. (1984). 613.
3. B. A. Reine, N. J. Fowler, and R. M. Fisher. Proc. ICEM 1990, San Francisco Press, (1990) 1, 854.

Fig. 1 SEM image showing representative cell size and shape in unheated birch. Bar = 14 μm
Fig. 2 SEM showing representative cell size and shape in birch heated 15 hrs. at 260° C. Bar = 14 μm
Fig. 3 SEM image showing cell wall structure and thickness in unheated birch. Bar = 4 μm.
Fig. 4 SEM of changes in cell wall structure and thickness in birch after 15 hrs. at 260° C. Bar = 4 μm.

465
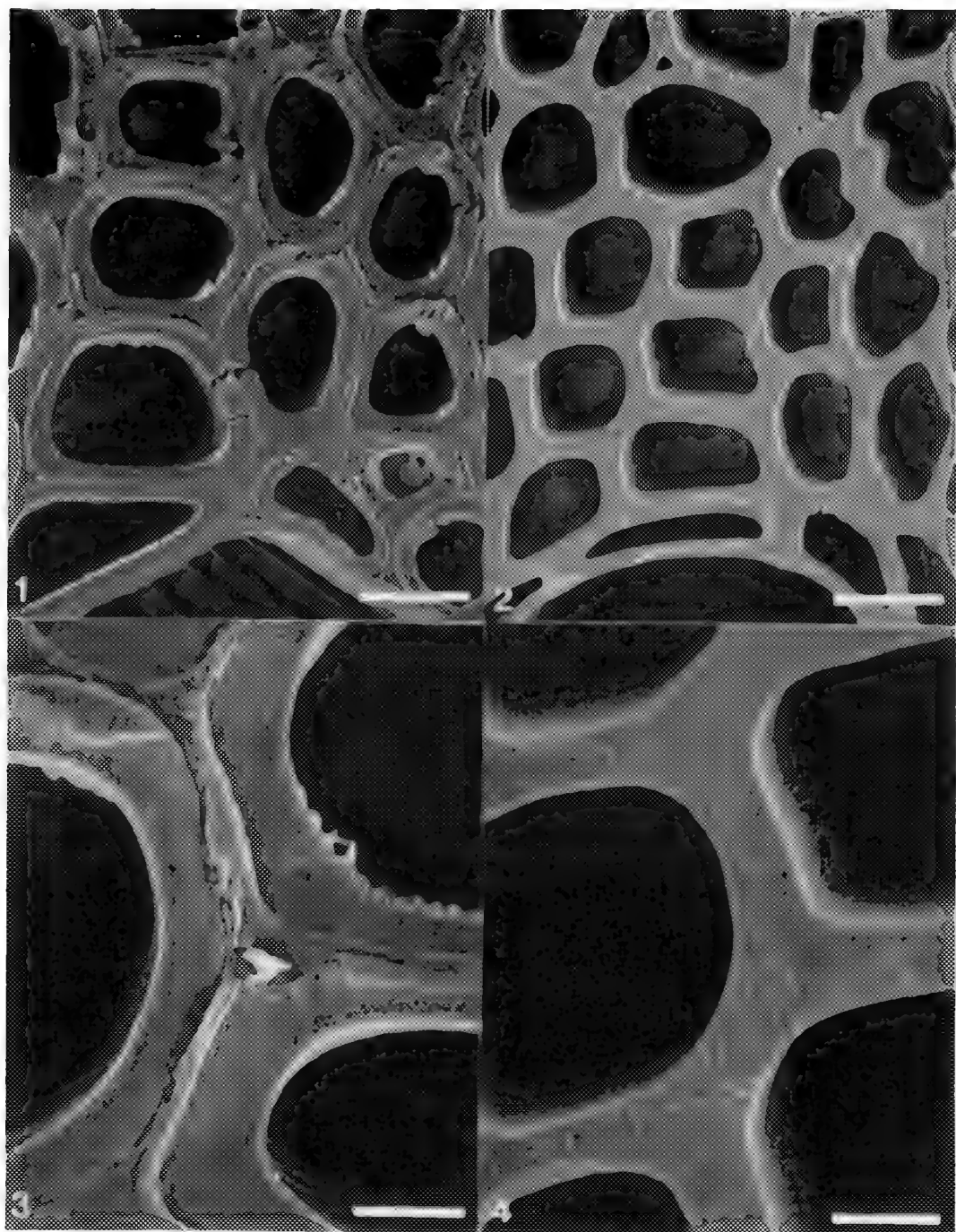
A COMPARATIVE SEM STUDY OF THE RELEASE OF THREE HERPES VIRUS PROGENY

Thomas Moninger, *Jose Rodriguez**

*Central Electron Microscopy Research Facility, University of Iowa, Iowa City Iowa
**Department of Microbiology, University of Iowa, Iowa City, Iowa

Human foreskin (HF) cells are permissive for three members of the herpesvirus family: herpes simplex virus (HSV), varicella-zoster virus (VZV) and human cytomegalovirus (HCMV). HSV and VZV belong to the alphaherpesvirinae subfamily, HCMV to the betaherpesvirinae. Cultures of the human melanoma line known as MEWO were also infected with VZV and HSV. The viruses cause different diseases in human beings.

In their interaction with cultured HF cells, HSV, VZV and HCMV differ in the effect they have on cell morphology (normally elongated), on the length of their replication cycle, and in the period of time during which progeny infectious virions are released, if they are released, since, unlike HSV and HCMV, infectious VZV virions are found only in small numbers in extracellular fluid from infected cultures. These observations led us to use scanning electron microscopy (SEM) to do a comparative study of progeny virion release with HF cells infected with one of the three herpesviruses under study.

Monolayer cultures of cells grown in 35mm plastic petri dishes were infected with one of the three viruses. At various times after infection (determined by the length of each virus' replication cycle) cultures were harvested and prepared for SEM using conventional techniques. Samples were fixed in glutaraldehyde and osmium tetroxide, dehydrated in ethanol, air-dried after hexamethyldisilizane treatment and sputter-coated with Au/Pd. Specimens were examined in an Hitachi S-4000 SEM. In HF cells HSV multiplies in hours and, depending on the multiplicity of infection (MOI), produces CPE between 2 and 3 days after infection and cell lysis within a day after the appearance of CPE. During the release stage, infected cells were found to show morphological abnormalities, the most obvious of which was rounding of the cells. At this time, infectious HSV was actually detaching from the cells in large numbers (infectious virus recoverable from the extracellular fluid) and, as seen with SEM, particles were being extruded from all portions of the cytoplasm. In contrast, HCMV was continuously released from cells for up to eight days after appearance of CPE (cell enlargement), as evidenced, again, by virus recoverable from the culture medium (100 infectious units per cell per day). SEM showed many more virus particles being extruded from all portions of the cytoplasmic membrane than infectious virions being released at any harvest time. In spite of the large number of particles being released, the cytoplasmic membrane showed no evidence of impending cell lysis or membrane disruption until a week after the appearance of CPE. HF cell infected with VZV exhibited CPE characterized by syncytium formation. Infectious virus could not be recovered from the culture fluid, but progeny virions were seen on the cells' surface. Similar observations wee made with VZV-infected human melanoma cells, which also support VZV replication, and where the virus replicates to higher titers and produces CPE in a much shorter time.

In HSV-infected HF cells, appearance of CPE and virus release occur together, and lysis of the infected cell follows within hours. Cells infected with HCMV and showing CPE extrude and release thousands of virion particles for days. Cells infected with VZV extrude progeny virions. At this time we do not know whether or not, and to what extent, these extruded particles are released into the extracellular medium

References
Grose, C., Brunell, P. A., Infect. Immun. (1978) 19:199-203
Johnson, D. C., Spear, P. B., J. Virol. (1982) 43:1102-1112
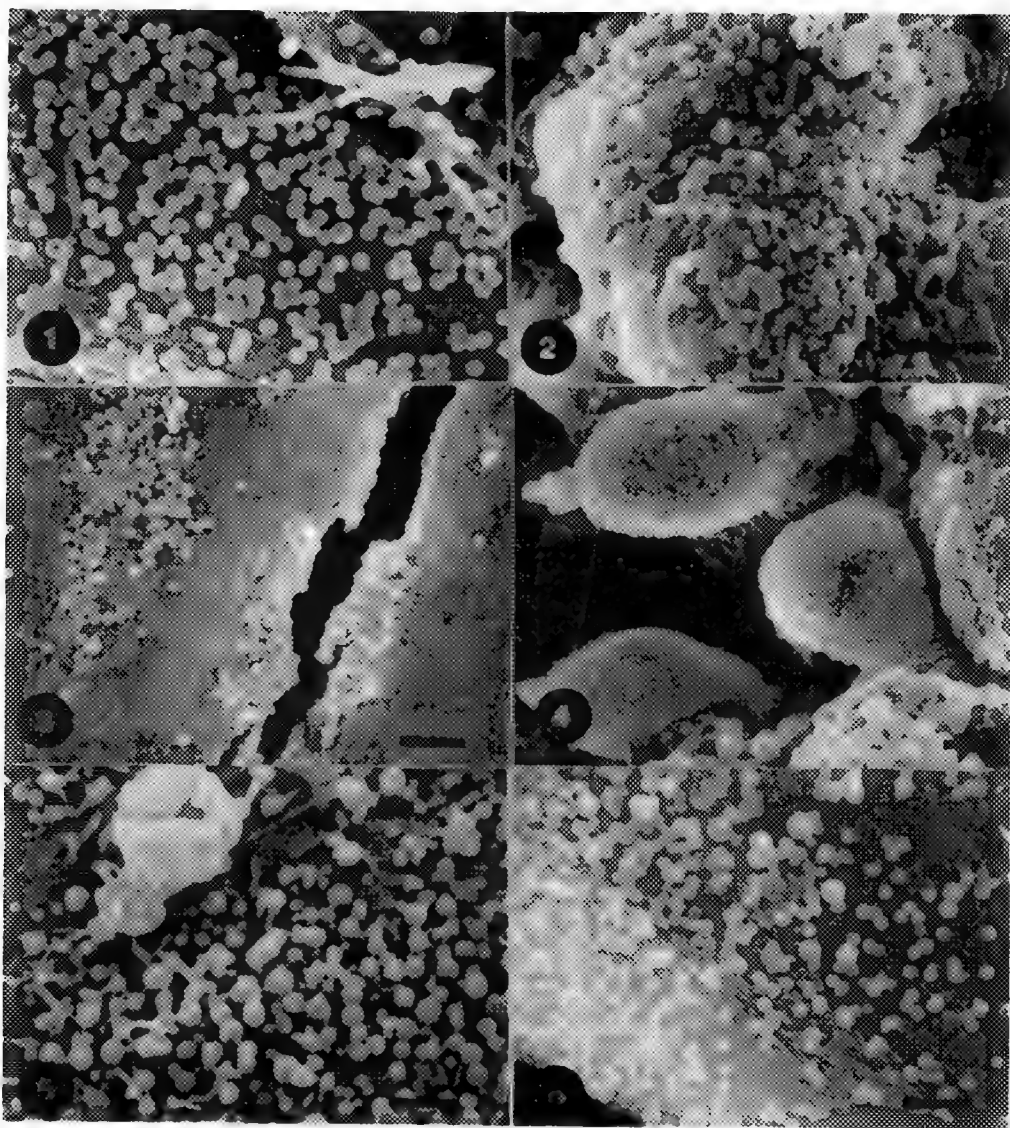
FIG. 1.--HSV infected HF cells. Bar = 1 um
FIG. 2.--HSV infected MEWO cells. Bar = 1 um
FIG 3.--VZV infected HF cells. Bar = 1 um
FIG. 4.--VZV infected MEWO cells. Bar = 1 um
FIG. 5.--HCMV infected HF cells. Bar = 1 um
FIG. 6.--HCMV infected HF cells. Bar = 1 um

SCANNING ELECTRON MICROSCOPY STUDIES ON THE MORPHOLOGY AND RELEASE OF VESICULAR STOMATITIS VIRUS

Thomas Moninger, *Jose Rodriguez**

*Central Electron Microscopy Research Facility, University of Iowa, Iowa City Iowa
**Department of Microbiology, University of Iowa, Iowa City, Iowa

In spite of convincing evidence to the contrary, the overwhelming majority of virologists still refer to vesicular stomatitis virus (VSV) as "bullet-shaped". The term bacilliform, which refers to a cylinder with 2 rounded ends, is used infrequently and conditionally to describe VSV.

We have used scanning electron microscopy (SEM) to study the morphology of the Indiana strain of VSV attached to, being, or having been released from 3 types of cultured cells, namely, a human melanoma line known as MEWO, human foreskin cells, and primary cultures of chick embryo cells. We have used crude virus suspensions and virus concentrated ten-fold by high-speed centrifugation and resuspension, as well as fresh virus preparations and virus suspensions that have been kept frozen at -70°C and thawed before use.

Virus suspended in medium containing 10% fetal bovine serum was used for transmission electron microscopy (TEM). The suspension were negative stained with 1% phosphotungstic acid containing 0.1% bacitracin and viewed in an Hitachi H-7000 TEM. For scanning electron microscopy, virus was adsorbed for 1.5 hours at 37°C unto confluent layers of cells grown in 35 mm plastic petri dishes. At the end of the adsorption period, the cultures were harvested and prepared for SEM examination using traditional techniques. Samples were fixed in glutaraldehyde and osmium tetroxide, dehydrated in ethanol, air-dried after hexamethyldisilizane treatment and sputter-coated with Au/Pd. Specimens were examined in an Hitachi S-4000 SEM. Cell cultures showing abut 50% CPE and producing progeny VSV were also used to examine released progeny VSVirions or virions on their way to being released.

Irrespective of the cell the virus was grown in or whether or not it was concentrated by centrifugation or frozen and thawed before use, VSVirions appeared bullet-shaped in TEM. In contrast, virus attached to any of the cells used in the study , as well as virus released from infected cells, had the shape of a cylinder with not one, but 2 rounded ends. Attached or released virions from virus suspensions that had been frozen or thawed once or had been concentrated before use had the same SEM morphology. An occasional bullet-shaped virion was seen in the SEM preparations, but there was little consistency to the shape of the blunt end, leading us to suspect that it was an artifact of the preparation procedure and one much more likely to occur with the phosphotungstic acid method used for TEM. VSVirions not fully released from the cytoplasm of infected cells always had rounded ends, supporting the belief that it is the round-end portion of the VSV nucleocapsid (itself definitely bullet-shaped) what gets extruded first from the infected cell.

References

Orenstein, J., L., Shelton, E., Lazzarini, R.A. Virology (1976) 71: 291-301.

Wagner, R., In Fields Virology, Second Edition, Chapter 31, pages 867-869. 1990. Raven Press, New York.
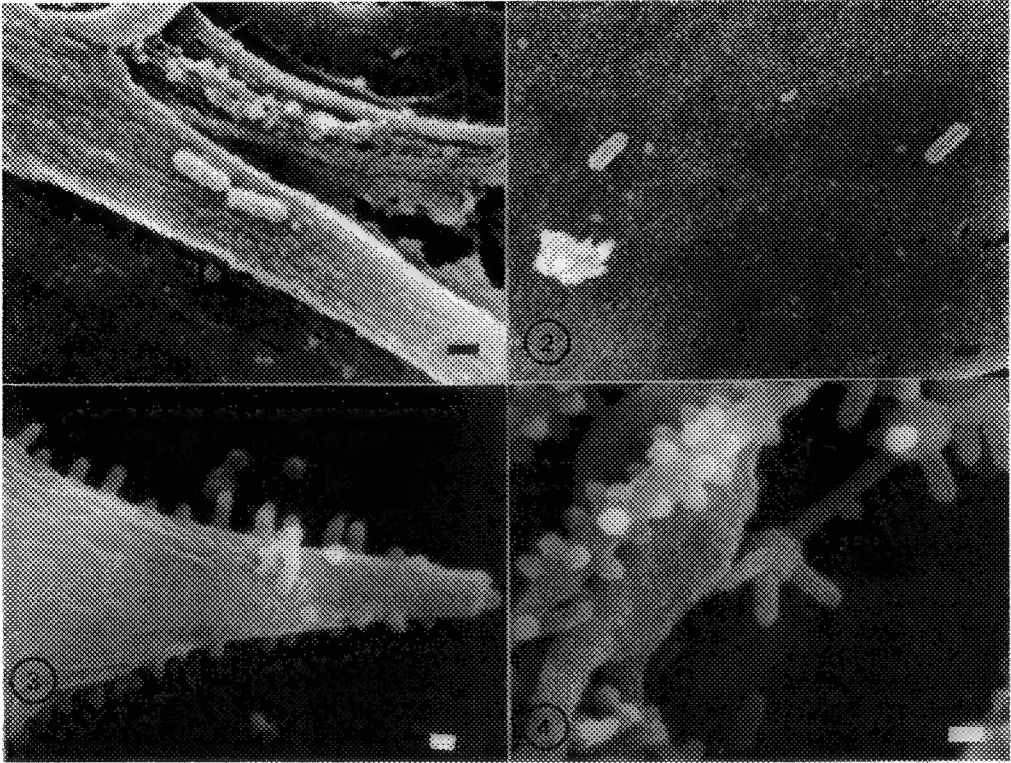
FIG. 1.--VZV infected MEWO cells. Bar = o.1 µm
FIG. 2.--VZV infected MEWO cells. Bar = 0.1 µm
FIG. 3.--VZV infected MEWO cells. Bar = 0.1 µm
FIG. 4.--VZV infected MEWO cells. Bar = 0.1 µm

ULTRASTRUCTURAL LOCALIZATION OF FIBRONECTIN IN PROCESS OF SERIAL INTIMAL REGENERATION

Toshiyuki Ishiwata , Munehiro Yokoyama and Goro Asano

Department of Pathology , Nippon Medical School , Tokyo , Japan

Intimal injury is considered as one of the initiation factors of atherosclerosis and intimal thickening. However the morphological elucidation after intimal injury is not so clear. On the other hand, fibronectin is a glycoprotein that play an important role in cell adhesion, migration, spreading, and differentiation[1]. This study was designed to examine the mechanism of serial intimal regeneration after intimal injury and the localization of fibronectin using scanning and transmission electron microscope.

Male Wistar rats, weighing 400g were used and endothelial denudation was produced by the modified methods of Baumgartner[2]. A deflated vascular balloon catheter(1.5F, DOW CORNING , Corp.) was introduced into the thoracic aorta, then inflated up to 2.5mm in diameter, and passed through the aorta three times to a length of 2.5cm. The animals were sacrificed at 15min, 3,7,14 and 28 days after denudation. For electron microscopic examination, the tissues were fixed in 2.5% glutaraldehyde in 0.1M phosphate buffer, treated with 1% osmium tetroxide in phosphate buffer, and dehydrated in a graded ethanol series. For scanning electron microscopic examination, the tissues were dried with critical point dryer, coated with gold paradium and observed with HITACHI S-430 scanning electron microscope. For transmission electron microscopic observation, the tissues were embedded in epoxy resin and ultrathin sections were cut and stained with uranyl acetate and lead citrate, and examined with a HITACHI H-7100 electron microscope. For immunoelectron microscopical examination, specimens were fixed in PLP solution and frozen in OCT compound. Frozen sections were cut and mounted on SILAN-coated slides. For enzyme immunohistochemistry of fibronectin, the indirect method was performred. Then the sections were post-fixed with 2% osmium tetroxide, dehydrated through a graded ethanol series, and embedded in epoxy resin. Ultrathin sections were cut and examined with a HITACHI H-7100 electron microscope.

At 15 minutes after intimal injury, fibrin nets with erythrocytes, leukocytes and platelets were focally adherent to the exposed internal elastic lamina(Fig 1a). At three days after intimal injury, neo-intima was thickened with collagen fibrils and smooth muscle cells. A great number of medial smooth muscle cells changed their phenotype from contractile to synthetic type in the intima. Most regenerated endothelial cells had cuboidal cytoplasm and were seen on the denuded vascular surface at fourteen days after intimal injury(Fig 1b).However most cells showed a flat appearance at 28days after injury. Fibronectin was localized at the thickened neo-intima and in the regenerated endothelial cells (Fig 2). Fibronectin is synthesized by regenerated endothelial cells and may play an important role in intimal regeneration.

References
1.R.O.Hynes and K.M.Yamada, J . Cell . Biol . (1985) 95, 369
2.H.R.Baumgartner , Z.Gesamte. Exp . Med . (1963) 137, 227
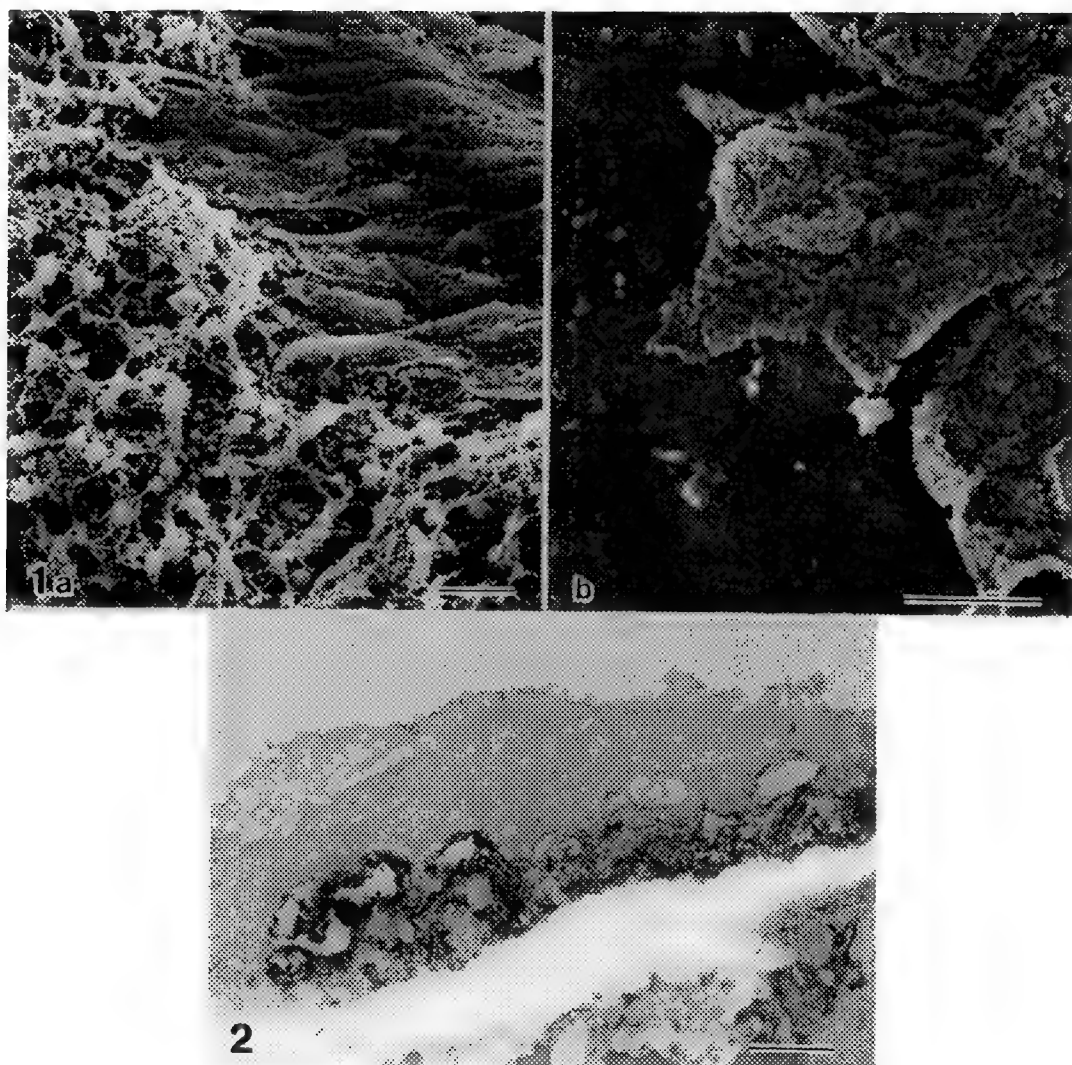
FIG. 1. SEM of injured rat aorta. a. At 15min after intimal injury, denuded area is covered with fibrin nets. Bar = 10μm.

b. At 14 days after intimal injury , regenerated endothelial cell is seen on the denuded vascular surface. Bar = 5μm.

FIG. 2. Immuno electron micrograph of injured rat aorta. Fibronectin is localized under the regenerated endothelial cell at 14 days after injury. Bar=1μm.

SCANNING ELECTRON MICROSCOPY OF ASBESTOS-CONTAINING MATERIAL WHERE THE ASBESTOS FIBERS ARE CONSIDERED LOCKED IN A BINDER

J. R. Millette and R. S. Brown

MVA, Inc., 5500 Oakbrook Parkway, Suite 200, Norcross, GA 30093

The United States Environmental Protection Agency (EPA) has labeled as "friable" those building materials that are likely to readily release fibers. Friable materials, when dry, can easily be crumbled, pulverized, or reduced to powder using hand pressure.[1] Other asbestos containing building materials (ACBM) where the asbestos fibers are in a matrix of cement or bituminous or resinous binders are considered non-friable. However, when subjected to sanding, grinding, cutting or other forms of abrasion, these non-friable materials are to be treated as friable asbestos material. There has been a hypothesis that all raw asbestos fibers are encapsulated in solvents and binders and are not released as individual fibers if the material is cut or abraded. Examination of a number of different types of non-friable materials under the SEM show that after cutting or abrasion, tuffs or bundles of fibers are evident on the surfaces of the materials. When these tuffs or bundles are examined, they are shown to contain asbestos fibers which are free from binder material. These free fibers may be released into the air upon further cutting or abrasion.

Gaskets[2], laminated asbestos board, floor tile and pipe elbow cement were sectioned and gold coated for analysis by scanning electron microscopy-energy dispersive x-ray spectrometry (SEM-EDS). In Figures 2, 3 and 4, chrysotile asbestos fiber bundles and chrysotile asbestos fibers can be seen protruding from the surfaces of these materials. The floor tile surface (Figures 1 and 2) was not abraded and, except for a sputtered gold coating, is in "as received" condition.

The presence of uncoated, unbound chrysotile asbestos fibers in these non-friable materials show that asbestos fibers are available for release into the environment.

References

1. National Emission Standards for Hazardous Air Pollutants; Asbestos NESHAP Revision USEPA, Federal Register Vol. 55 (224) Nov. 20, 1990.

2. J. Millette and R. Brown, The Microscope (1992) 40, 131.
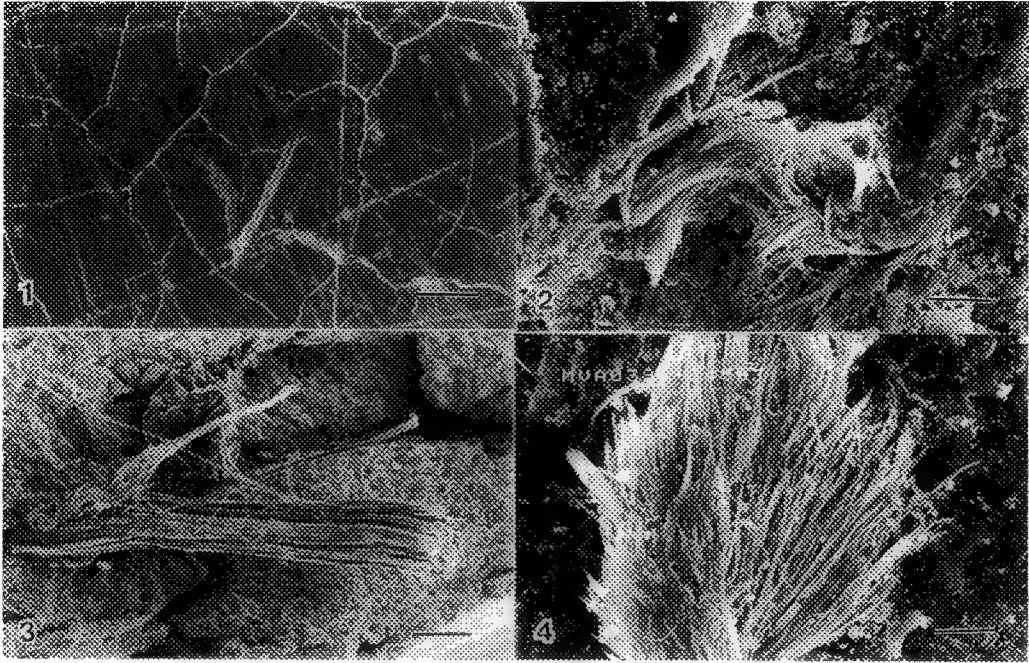
Figure 1. Secondary electron (SE) image of the surface of a chrysotile asbestos containing floor tile. Bar = 300 μm.

Figure 2. SE image of a chrysotile asbestos fiber bundle protruding from the surface of the floor tile in Figure 1 (arrow). Bar = 6 μm.

Figure 3. SE image of a chrysotile asbestos fiber bundle protruding from a fractured section of cured pipe elbow cement. Bar = 500 μm.

Figure 4. SE image of a chrysotile asbestos fiber bundle protruding from a cut edge of laminated asbestos board. Bar = 10 μm.

SEM STUDIES OF MEMBRANE ENDOCYTOSIS IN TOAD URINARY BLADDERS FOLLOWING WITHDRAWAL OF MEZEREIN

A.J.Mia, A.D. Davidson, L.X.Oakford* and T.Yorio*

Jarvis Christian College, Hawkins, TX 75765, * TCOM/UNT, Fort Worth, TX 76107-2690

Vasopressin (ADH), enhances fluid reabsorption through a complex process of water channel insertion into the apical membrane and retrieval during hormonal removal (1). These water channel membranes are thought to internalize by endocytosis resulting in down-regulation of the apical membrane permeability (2). ADH V_1-receptors, like ADH V_2-receptors, increased water flow, when mezerein (MZ), an activator of protein Kinase C, was added to the mucosal surface (3). This is accompanied by the activation of several protein Kinase C isozymes, as determined by protein A-immunogold labeling (4). However, little is known about the surface ultrastructural changes accompanying membrane retrieval in amphibian bladder tissues following removal of hormone (2,5). We reported an apparent membrane internalization process using scanning electron microscopy (SEM) following withdrawal of ADH (7). The current report is concerned with time-response surface studies of the apical membrane internalization process following withdrawal of MZ, and the role of protein Kinase C in this process.

Toad urinary hemibladders (Bufo marinus) were removed surgically from doubly-pithed animals, and were set up as sacs with an imposition of an osmotic gradient. Tissues were incubated in the absence (control) and presence of MZ, 10^{-6} for 10 min. At 10 min, MZ was withdrawn and the tissues incubated for an additional 5, 10 and 20 min. Tissues were fixed in 2% glutaraldehyde using PIPES buffer for 1 hr with a post-fixation in 1% osmium tetroxide for 1 hr. Tissues underwent dehydration using Peldri II and were mounted and prepared for viewing in the SEM.

Tissues were examined during onset of MZ action and following its removal. Control tissues retained in Ringer's solution under an osmotic gradient show a fairly smooth surface conformation. Figure 1 of a control tissue at 10 min retrieval shows no clear evidence of endocytosis, in the form of membrane surface invaginations. In contrast, tissues show surface membrane internalizations following withdrawal of MZ, (Fig. 2). MZ-treated tissues always show cellular swelling most apparent at cellular junctions. Although surface invaginations were induced in MZ-treated tissues during post buffer washes, their appearance was slower compared to ADH-exposed tissues. Therefore, at 10 min retrieval, fewer cells in MZ-treated tissues show surface invaginations in contrast to a greater number of ADH-treated cells. Figures 2 and 3 are comparative SEM images showing the relative number of cells with surface changes in MZ and ADH-stimulated tissues, respectively. Cell counts at 10 min retrieval, indicated that fewer than 8% of the cells showed surface invaginations and putative endocytosis in MZ-exposed tissues (n = 6), as compared to 45% of the cells in ADH-stimulated tissues (n = 6). The incidence of the proposed endocytosis in MZ and ADH-treated tissues reverses with time of retrieval. Therefore, at 20 min retrieval, 35% of the MZ cells showed endocytosis (Fig. 4) compared to 17% the ADH-treated cells. Some cells in the mezerein-treated tissues also lacked both microvilli and microridges during progressive restoration of the apical membrane permeability. This may represent a transition stage of the apical membrane prior to undergoing endocytosis during retrieval. These observations suggest that mezerein can mimic the actions of ADH in the induction of surface changes indicative of endocytosis. These observations further suggest that protein Kinase C may participate in the overall process of cycling of water channels in toad urinary   bladder.

References
1. A.J. Mia et al., Tissue and Cell 15: 737 (1983) .
3. R.A. Coleman et al., J. Histochem. Cytochem. 55: 1405 (1987).
4. T. Yorio and N. Satumtira, Biol. Cell 66:7 (1989).
5. A.J. Mia et al., EMSA 796 (1992).
6. D. Brown. Annu. Rev. Physiol. (1989).
7. A.J. Mia et al., SCANNING 93 (in press).
8. Supported by US Army grants DAMD17-19-C1096 and DAAL03-92-G- 0075.
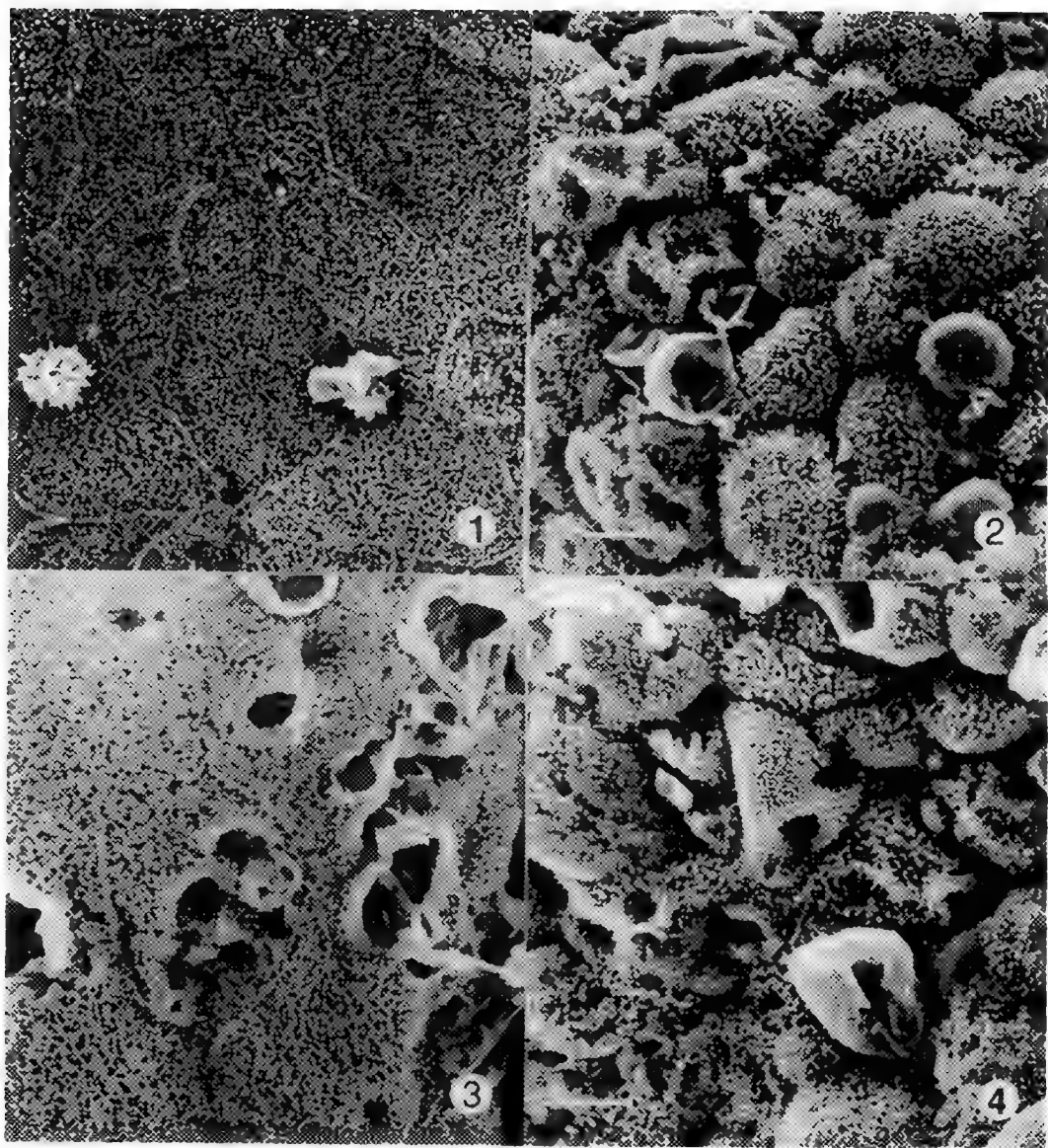
Fig. 1. SEM of control toad urinary bladder showing smooth mucosal membrane surface conformation following 10 min retrieval . Bar = 5 μm.

Fig. 2. SEM of mezerein exposed tissues at 10 min retrieval period showing surface invaginations involving only few cells. Bar = 5 μm.

Fig. 3. SEM of ADH-stimulated tissue at 10 min retrieval period showing endocytosis involving a large number of cells. Bar = 5 μm.

Fig. 4. SEM of mezerein exposed tissues at 20 min retrieval period showing endocytosis involving more cells than that at 10 min retrieval period of mezerein exposed tissues. Bar = 5 μm.

THE CONSOLIDATION OF MICROSCOPY TECHNOLOGY INTO A UNIVERSITY CENTRAL RESEARCH SUPPORT FACILITY: REFLECTIONS ON THE 1980'S AND PROJECTIONS FOR THE 1990'S AT THE UNIVERSITY OF IOWA

Kenneth C. Moore

Central Electron Microscopy Research Facility, 81 Eckstein Medical Research Building, University of Iowa, Iowa City, Iowa 52242

The University of Iowa Central Electron Microscopy Research Facility(CEMRF) was established in 1981 to support all faculty, staff and students needing this technology. Initially the CEMRF was operated with one TEM, one SEM, three staff members and supported about 30 projects a year. During the past twelve years, the facility has replaced all instrumentation pre-dating 1981, and now includes 2 TEM's, 2 SEM's, 2 EDS systems, cryo-transfer specimen holders for both TEM and SEM, 2 parafin microtomes, 4 ultamicrotomes including cryo-ultramicrotomy, a Laser Scanning Confocal microscope, a research grade light microscope, an Ion Mill, film and print processing equipment, a rapid cryo-freezer, freeze substitution apparatus, a freeze-fracture/etching system, vacuum evaporators, sputter coaters, a plasma asher, and is currently evaluating scanning probe microscopes for acquisition. The facility presently consists of 10 staff members and supports over 150 projects annually from 44 departments in 5 Colleges and 10 industrial laboratories. One of the unique strengths of the CEMRF is that both Biomedical and Physical scientists use the facility.

Projections for the 1990's will continue to involve diversification of equipment and techniques which may include scanning auger microscopy, a microprobe, an intermediate accelerating voltage TEM, in situ hybridization for both light and electron microscopy, high pressure freezing equipment, molecular distillation drying, environmental scanning electron microscopy, and integration of microscopes with computers for image recording and desk-top publication. The addition of any new equipment will be the direct result of faculty needs which are funded.

In addition, the CEMRF is involved with the organization of 4 teaching courses in electron microscopy, as well as assisting with sections of 8 other classes. With the addition of new techniques, the CEMRF will continue to offer at least 2 workshops a year. The facility will also continue to support the Iowa Microscopy Society, as well as other regional and national meetings. During the course of the year, the CEMRF provides tours to visiting scientists, faculty and student recruitment, high school students, business groups, and politicians. A totally new activity is currently being introduced in the facility. Along with faculty from different departments, high school students in eastern Iowa are being invited to participate in a "mentors" program. These students will spend several sessions in the CEMRF working on projects provided by the various faculty labs supporting this program. Our goal is to encourage more high school students to consider science as a career objective.

The development of the University of Iowa CEMRF has been made possible due in large part to the Central Administration's support of equipment acquisition over the past decade. Of the $2,000,000.00 invested in equipment, more than 70% was provided by the Graduate College and the Vice President for Research, with the other 30% obtained through equipment grants and user fees. 75% of the operating expenses for the facility are recovered by user fees from a large and well-funded group of investigators who are charged on an at-need, fee for service basis. Faculty recognize that they have a facility available to them that provides immediate access to state-of-the-art equipment and techniques, on a first-come, first-served basis, as well as one that provides training and supervision to all investigators.

A key element in the success of any centralized facility is the availability of a skilled and motivated staff. The CEMRF makes every effort to adequately compensate employees in terms of salary and the opportunity to improve themselves professionally. The recognition of an individuals contribution to the success of a project minimally includes technical acknowledgement, or co-authorship in the case of a strong intellectual commitment. Staff are also encouraged and supported to attend regional and national meetings, as well as to train in laboratories developing the latest techniques. As a result, new investigators to the facility have instant access on an at-need basis to research assistants who are familiar with the most recent procedures.

Consequently, concurrent with the development and success of the CEMRF, several departments have voluntarily divested themselves of their own E.M. equipment(28 E.Ms. on campus in 1981 as opposed to 11 E.Ms. in 1993). This represents a savings of more than $250,000.00 annually(1993 dollars), as well as releases 17 or more rooms for other use. In addition, the interaction between the remaining 6 E.M. laboratories is more positive as a result of this downsizing and centralization. The availability of user-friendly, quality equipment in the CEMRF operating on a first-come, first-served, at-need basis assures that E.M. is now accessible to all University faculty, staff, and students, and with many investigators sharing instruments, it is easier to justify acquisition of new equipment.

PARTICLE-NUMBER ESTIMATION WITH SPECIAL EMPHASIS ON THE DISECTOR AND FRACTIONATOR

Jens Randel Nyengaard

Stereological Research Laboratory, University Institute of Pathology and 2nd University Clinic of Internal Medicine, Institute of Experimental Clinical Research, University of Aarhus, Århus, Denmark

This abstract deals with how to stereologically estimate the number of particles in sections without making any assumptions about the size or shape of the particles. The usual term for this kind of particle estimation is design-based because by designing the study adequately any size or shape-assumptions are avoided in contrast to the obsolete model-based stereological methods. Design-based sampling of particles is performed when all particles have the same chance of being sampled, i.e., sampling particles with uniform probability. This points to the importance of proper particle *sampling* in stereology. Further, it is important to know what the dimension is of the sampled object, e.g., particle volume has a dimension of 3, particle length has a dimension of 1 whereas particle number has a dimension of 0. Thus, in order to make design-based particle number estimation 3-dimensional information is needed because the geometric characteristic of the 0-dimensional number is cardinality. A single, uniformly positioned thin section is not adequate for design-based particle number estimation because this sample is height-weighted; a cell twice as high as another cell has twice the chance of being hit by the section. The requirement is two parallel sections which do not need to be physically separate sections, since optical sections most frequently are easier to generate and use.

The disector[1] comprises two parallel section planes a known distance h apart and a 2-dimensional unbiased counting frame of area $[a(frame)]$ on the sampling plane. Particles are counted $[\Sigma Q^-]$ if they are sampled in one section plane but not the other section plane provided they do not violate the counting rule of the counting frame. The total number of particles $[N(total)]$ in a complete specimen with a certain volume $[V(ref)]$ is then calculated as:

$$N(total) = \frac{\Sigma Q^-}{h \cdot \Sigma a(frame)} * V(ref) = \frac{\Sigma Q^-}{\Sigma v(disector)} * V(ref)$$

The disectors must have a uniform position in the total space of the specimen. If the sections are not made for electron microscopy, the two parallel section planes can be optical, i.e., in one relatively thick section, 30 μm, say, thin optical sections are generated inside the thick section by moving the plane of focus up and down. Particles are then counted when they come into focus provided they do not violate the counting rule of the counting frame. In order to use the disector and optical sectioning with a normal light microscope (confocal microscopes are ideal for

478

optical sectioning!) a microcator needs to be attached to the microscope for measuring the distance h between the sampling planes. Secondly, only oil lenses can be used because the movement of the specimen stage as measured by the microcator then equals the movement of the plane of focus. The oil lenses should preferably have a high numerical aperture to give a small focal depth. The image of the section planes can optionally be projected onto a table with the counting frame in a darkened room or be displayed on a television screen where the video camera is interfaced through a computer that superimposes a counting frame on the video image. The disector provides a direct estimate of any particle number, however, one problem with the disector evolves around the estimation of $v(disector)$ and $V(ref)$. If there is differential tissue deformation behind these two estimates the final total particle number may be biased. This problem may even become crucial if differential tissue deformation is expected between two investigated groups, e.g., control and diseased tissue. In that case another stereological approach may be more suitable.

The fractionator[2] has the advantage of being completely independent of shape and size of the particles as well as any deformational changes of the tissue involved. Without deliberate cheating, it is not known how to provide a biased fractionator-estimate of particle number. The principle of the fractionator is very simple: a fraction of the specimen is sampled uniformly at random with a known and predetermined probability. The number of particles $[\Sigma Q^-]$ are counted in that fraction and the total number of particles is then calculated as:

$$N(total) = \Sigma Q^- \cdot (total\ sampling\ fraction)^{-1}$$

Thus, there is no need to know the section thickness even though the disector-principle is used for estimating the number of particles in the final tissue sample. The price paid is that the final tissue sample has to be serially sectioned entirely which makes the fractionator much more cumbersome than the pure disector-method. The observer therefore needs to address the type of problems involved with particle number estimation before choosing between the disector or fractionator.

Finally, it should be said that the disector counting-principle also provides the opportunity of estimating size of the particles. Moreover, it is also possible to estimate the methodological error of the stereological tools in order not to count too few or too many particles $[\Sigma Q^-]$. In general, ~100 particles counted are sufficient to obtain a methodological error of ~10%.

References
1. D.C. Sterio; J. Microsc. (1984)134, 127.
2. H.J.G. Gundersen; J. Microsc. (1986)143, 3.

THE FIRST DECADE OF THE DISECTOR

H.J.G. Gundersen

Stereological Research Laboratory, Bartholin Building, University of Aarhus, DK-8000 Århus Denmark

Nine years and eleven months ago the disector was described: a complete rule for uniform sampling of 3D structures strictly according to cardinality — and from sections, physical or just imaging planes.

Intuitively, the simplest situation is when particle number is wanted: with a uniform sample one just counts the number Q^- in the sample and estimate numerical density N_V or N directly (with the fractionator).

Along the way, it has been realized that under certain fortuitous circumstances one may also count other unique but not isolated features of structure, like 'trees' (ciliae, brush borders and other appendages on surfaces) and the complementary type, exemplified by glands and follicles. All these structures each have exactly one disk of connection to an easily recognizable surface, these disks may be counted in a disector.

The most basic mathematical definition of a 0-dimensional quantity or counting measure is that of the Euler number. The Euler number encompasses the number of isolated particles as a part of the definition, but is much more general. Also the Euler number may be estimated using disectors as already noted in the original publication. The special problems with artificial edges may be solved in various ways (the ConnEulor estimator) and as all other 0-dimensional counting measures, the Euler number may be estimated in disectors of arbitrary orientation distribution. The use of this estimater in histologically complex (but mathematically simple) networks have already revealed a lot of unknown facts about the development of trabecular bone and capillary networks.

Moreover, many complexly shaped particles fulfill the requirement that they are non-reentrant, i.e. their genus is 1. The number of such complicated particles may then be estimated unbiasedly with the ConnEulor-estimator, in just two sections irrespective of artificial edges and irrespective of how complicated the particle shape is. These requirements are much less than those of the disector for isolated particles.

With a uniform sample of particles in the first step, the disector also opened up for a wealth of particle size estimators: the selector, the nucleator, the rotator providing more and more information for less and less effort – when applicable.

In the nucleator and the rotator one makes <u>all</u> <u>observations</u> with respect to a fixed point. This has turned out to be a very direct way to simple and efficient estimators of a large range of <u>spatial</u> <u>distributions</u>.

References:

Sterio, D.C. (1984) The unbiased estimation of number and sizes of arbitrary particles using the disector. *J. Microsc.* <u>134</u>, 127-136.

Gundersen, H.J.G., Boyce, R.W., Nyengaard, J.R. & Odgaard, A. (1993) The ConnEulor: Unbiased estimation of connectivity using physical disectors under projection. *(in press)*.

THICKNESS MEASUREMENT IN QUANTITATIVE ELECTRON MICROSCOPY

Yew M. Heng

E.M. Facility, McMaster University Medical Centre, Hamilton, Ontario, Canada L8N 3Z5

Quantitative electron microscopy generally implies the measurement of elemental content and/or structures in a given specimen or the 3D reconstruction of a structure. When a feature in a specimen is being quantified in a transmission electron microscope (TEM), the specimen thickness has to be determined for at least two reasons. Firstly, thickness is a required parameter in the calculation, for example, of volume and secondly, it is required for the calibration of instrumental conditions or theoretical parameters such that correction for thickness effects due to conditions such as radiation damage, x-ray absorption or multiple scattering of electrons can be performed. However, it is a common knowledge that specimen thickness is difficult to be determined accurately. The difficulty is mainly due to the nature of TEM specimens. There is no universal method which can be used. Therefore, in order to select a few appropriate methods, it is necessary that a wide range of methods be reviewed and critically assessed.

Numerous methods are available for the measurement of the thickness of a specimen to be analysed in a TEM (Table 1). They can be performed either within an electron microscope following specific procedures or outside the TEM with accessory devices using light optics or mechanical methods. Electron microscopical methods have the advantage that certain procedures can be applied locally at the region where the quantitative analysis will be performed. For example, thickness information can be obtained using EELS or EDS while elemental composition is being analysed.[1,2] However, errors due to electron radiation damage are of serious concern using these kind of methods. Some of the methods such as convergent beam electron diffraction, cross sectioning, section of embedded spheres, shadowing, small fold and parallax methods allow direct measurement of thickness without having to use any thickness standard or to know any specific property of the specimen. These methods are usually useful for the calibration of indirect methods such as electron scattering and light interference.

The selection of a method depends on many conditions. An ideal technique should be accurate, reproducible, non-destructive, convenient and easy to perform. It should also allow local measurement as well as be capable of measuring a wide range of thicknesses. These criteria are rarely met by any one method. Therefore, a combination of at least two methods is usually necessary. The appropriate selection of methods and their application are sometimes difficult, however necessary to obtain absolute quantification.[3]

References

1. R.F. Egerton and S.C. Cheng, Ultramicroscopy (1987)21, 231.
2. T.A. Hall and B.L. Gupta, in T.A. Hall *et al.*, Eds., *Microprobe Analysis as Applied to Cells and Tissues*, New York: Academic Press (1974)147.
3. This work is supported by the Medical Research Council of Canada.

TABLE 1
Methods for the measurement of specimen thickness

Electron Microscopical Methods
Autoradiography
Backscattered electrons
Convergent Beam Electron Diffraction (CBED)
Cross sectioning
Electron scattering
- Beam current; Current density; Photographic densitometry
- Electron Energy Loss Spectroscopy (EELS) -- Relative to electron mean free path; Bethe-sum-rule; Kramers-Kronig-sum-rule
- Scanning Transmission Electron Microscopy (STEM) -- Multiple signals detection

Energy Dispersive X-ray Spectroscopy (EDS)
- Characteristic X-rays; X-ray continuum

Section of embedded spheres
Shadowing
Small fold
Tilting (parallax)
- Contamination cones; Particles on both surfaces (latex or gold particles); Features intersect both surfaces (membrane; fault lines)

Light Optical Methods
Confocal microscope
Ellipsometry and related methods
Film optical density
Interference phenomena
- Fizeau fringes (Tolansky technique);
- Fringes of equal chromatic order;
- Interference colour comparisons;
- Interference spectroscopy;
- Michelson interferometer;
- Polarization interferometer;
- Reflectivity intensity;
- Variable-Angle Monochromatic Fringe Observation (VAMFO)

Mechanical Methods
Microtome setting
Block face measurement
Stylus profilometry

Others
Microbalance weighing
Quartz crystal oscillation

References available upon request

QUANTITATIVE IMAGE ANALYSIS AND MORPHOMETRY (QIAM) OF ELECTRON MICROGRAPHS USING A COMPUTER-ASSISTED USER-DEFINED INTERFACE

Barbara A. Evans, Tamara A. Howard, Thomas M. Mahoney* and Michael J. Becich

Department of Pathology, Division of Cellular and Molecular Pathology, University of Pittsburgh School of Medicine, Pittsburgh, PA 15261; *B&B Microscopes, Warrendale, PA 15086

Quantitative Image Analysis and Morphometrics (QIAM) is a tedious and time-consuming process. The large number of micrographs examined leads to special data management problems. Analysis of multiple subcellular compartments in cells is complicated by the inability to resolve adjacent cellular compartments. In addition, capturing data via grey scale or thresholding techniques on electron micrographs is very difficult at the organelle level. Visual feedback from an image that is also captured by an integrated digitizing pad (to identify and edit the cellular compartments) is critical. Statistical evaluation of the large amounts of information generated further complicates data management and analysis. Computer assisted QIAM with a user defined interface in a Windows environment has helped make data collection and analysis a much simpler and efficient process. We used BioScan's Optimas software (Edmonds, WA) linked to a spreadsheet to analyze multiple intracellular compartments and other features of a variety of epithelial cells in vivo and in vitro.

We used a computer assisted QIAM system that ran on a user defined macro with Optimas software. Images were captured by a filtered DAGE video camera with a Cosmicar lens, via a Matrox IP8-AT image board run on a 486P/33 PC Professionals computer and displayed on a noninterlaced Mitsubishi direct display video monitor (#FA3425). A noninterlaced Goldstar terminal (#1465), fitted with a super VGA color adapter displayed command functions. Areas of interest were traced directly from micrographs on a SummaSketch Plus pad (#MM1201). Analysis of electron micrographs focused on cell area, nuclear area, cell height, microvillus height, endosomal and lysosomal compartments. Calibration of the system was via a carbon replica of a standard diffraction grating (2160 lines/mm). Data was transferred directly to an Excel spreadsheet. A custom designed user defined interface and macro program calculated the cytoplasmic area and % microvillus height.

Feedback from the monitor enables the user to assure the highest degree of accuracy by viewing the point to point tracing as an overlay on the digitized image. The sequential on line help simplifies operation by multiple users. These features, coupled with the custom designed user defined interface and macro programs, allow for efficient and reliable data capture. The user designed interface for quantitating intracellular compartments on transmission electron micrographs contains button palettes and on-line help (Panel A). This allows for efficient data capture and transfer to Excel 4.0 spreadsheets (Panel B), simplifying editing and statistical analysis (bottom of Panel B). The QIAM programs are easily modified by the user, interface to spreadsheet applications and statistical software, and operate in the Windows environment. This system easily and reliably aids us in quantitating various intracellular compartments and improves the efficiency and accuracy of the analysis of transmission electron micrographs.

Panel A

T. E. M. Measuring Program

	Objects	Sums		Count
Acquire	Cell Area	0.000000	ADD	0
Calibrate	Nuclei Area	0.000000	ADD	0
Save Data	Cyto Area	0.000000	ADD	0
Open file	Coated Ves.	0.000000	ADD	0
All Done	Coated Pits	0.000000	ADD	0

Micrograph # :

Endosomes 0.000000 ADD 0
Golgi Sac. 0.000000 ADD 0
Trans Golgi 0.000000 ADD 0

Comments :

Multi-Ves-Bod's 0.000000 ADD 0
Plasma Mem 0.000000 ADD 0

On Line Help

Choose ADD to make measurements !

Lysosomes 0.000000 ADD 0
2nd Granules 0.000000 ADD 0
Rough ER 0.000000 ADD 0
Mitochondria 0.000000 ADD 0
Cell Height1 0.000000 ADD 0

Shift Down | Loop | Cell Height2 0.000000 ADD 0

Panel B

Analysis of Intracellular Compartments and Microvillus Height in CaCo2 Cells

Micro #	Cell Area	Nuclei Area	Cyto Area	Endo- somes	Golgi Sac	Giant LysVac	Endo/ Cyt	Golgi/ Cyt	GLV/ Cyt	Cell Height (um)	MV Height (um)	% MV Height
D656-1	71.76	21.92	49.84	5.83	1.10	0.00	11.70%	2.21%	0.00%	11.12	0.75	6.74
D656-2	70.90	32.28	38.62	2.44	0.61	0.00	6.32%	1.58%	0.00%	11.97	0.68	5.66
D656-3	106.35	27.94	78.40	20.38	0.70	0.64	25.99%	0.89%	0.82%	14.87	1.10	7.42
D655-4	101.59	12.94	88.65	9.52	0.12	0.41	10.74%	0.14%	0.46%	18.36	1.27	6.93
D655-5	86.45	21.15	65.30	7.52	1.32	0.37	11.52%	2.02%	0.57%	19.76	1.95	9.87
D653-6	89.31	20.22	69.08	4.16	0.72	0.00	6.02%	1.04%	0.00%	15.86	1.70	10.71
D653-7	87.27	15.42	71.85	16.70	0.98	1.10	23.24%	1.36%	1.53%	18.38	1.24	6.77
D657-8	52.08	19.88	32.20	2.50	0.81	0.00	7.76%	2.52%	0.00%	11.49	0.75	6.51
D657-9	86.27	26.66	59.61	3.49	0.91	0.00	5.85%	1.53%	0.00%	18.51	1.04	5.60
D657-10	68.25	16.98	51.27	1.94	1.39	0.00	3.78%	2.71%	0.00%	16.03	1.01	6.30
Statistical Analysis												
Mean	82.02	21.54	60.48	7.45	0.87	0.25	0.113	0.016	0.003	15.64	1.15	7.25
Std. Error	5.17	1.88	5.60	2.02	0.12	0.12	0.024	0.003	0.002	1.01	0.13	0.54
Median	86.36	20.69	62.46	5.00	0.86	0.00	0.093	0.016	0.000	15.95	1.07	6.76
Mode	#N/A	#N/A	#N/A	#N/A	#N/A	0.00	#N/A	#N/A	0.000	#N/A	0.75	#N/A
Std. Dev.	16.36	5.96	17.69	6.38	0.37	0.38	0.075	0.008	0.005	3.20	0.41	1.70
Variance	267.59	35.50	313.06	40.68	0.14	0.14	0.006	0.000	0.000	10.23	0.17	2.91
Kurtosis	-0.17	-0.36	-0.68	0.65	0.81	1.66	0.594	-0.253	2.266	-1.50	0.16	0.96
Skewness	-0.30	0.44	-0.12	1.31	-0.52	1.48	1.296	-0.347	1.600	-0.33	0.88	1.38
Range	54.27	19.34	56.45	18.44	1.27	1.10	0.222	0.026	0.015	8.64	1.27	5.11
Minimum	52.08	12.94	32.20	1.94	0.12	0.00	0.038	0.001	0.000	11.12	0.68	5.60
Maximum	106.35	32.28	88.65	20.38	1.39	1.10	0.260	0.027	0.015	19.76	1.95	10.71
Sum	820.23	215.39	604.82	74.48	8.66	2.52	1.129	0.160	0.034	156.35	11.49	72.51
Count	10.00	10.00	10.00	10.00	10.00	10.00	10.000	10.000	10.000	10.00	10.00	10.00
95% Conf	10.14	3.69	10.97	3.95	0.23	0.23	0.047	0.005	0.003	1.98	0.26	1.06

MEASUREMENT OF THE GEOMETRIC PROPERTIES OF LINEAL FEATURES IN THREE-DIMENSIONAL MICROSTRUCTURES

R.T. DeHoff

Department of Materials Science and Engineering, University of Florida, Gainesville, FL 32611

In most applications of stereology the focus of the measurements is upon the volume fraction V_V, surface area density S_V and number density N_V of *three dimensional features* like particles, grains, cells, porosity, organelles, etc. Most microstructures contain features that are essentially *one dimensional*; their characterization is largely ignored.

This presentation reviews the geometric properties that may be defined for space curves and edges in microstructures and the stereological relationships that, in an appropriately designed sampling scheme, provide unbiased estimates of these geometric properties.

Space curves have a *length*, usually reported as a line length density, L_V in stereological analyses. The local geometry near a point on a space curve is characterized by two properties, the *curvature k*, which is the rate of rotation of the tangent vector along the arc length, and the *torsion τ*, which is the rate of rotation of the binormal vector.

Edges are space curves formed by the intersection of two surfaces. In addition to local curvature and torsion values an element of edge is characterized by a local *dihedral angle χ*, which is the angle between the normal vectors of the two surfaces that meet to form the edge.

A triple line may be thought of as the aggregate of three mutually meeting edges. The dihedral angles of three edges that meet to form a triple line must sum to π; the average dihedral angle along any triple line is $\pi/3$.

On a two dimensional section through a microstructure space curves appear as points of intersection with the test probe; triple lines intersect the probe to form triple points. A simple count of these points (P), normalized by dividing by the area of the probe scanned (A_o) provides an estimate of the length density of the corresponding lineal feature:[1,2]

$$\langle \frac{P}{A_o} \rangle = \langle P_A \rangle = \frac{1}{2} L_V \tag{1}$$

This estimate will be *unbiased* if and only if the set of probes is an *I*sotropic, *U*niform, *R*andom (*IUR*) sample of the population of planar probes that may be visualized. Sampling with a set of *parallel* test planes yields the total *projected* length of lineal features on the direction normal to the test plane set:[1,2]

$$\langle P_A \rangle_{oriented} = L_{V,projected} = L_V \langle \cos \phi \rangle \tag{2}$$

486

where ϕ is the angle between the local tangent direction an the normal to the test plane set.

For projected images *design based stereological procedures* have been devised that guarantee an IUR test probe set and thus provide *unbiased* estimates of L_v.[3]

The *average dihedral angle* $<\chi>$ at edges in a structure may be estimated by applying an area tangent count on representative plane sections. A test line is swept over a calibrated area A_0 and the number of tangents T formed with edge traces is counted. The ratio[4]

$$< \frac{T}{A_\square} > \ = \ <T_A> \ = \ \frac{1}{2} <\chi> L_V$$

yields the dihedral angle. Application of the tangent count to projected curves in a projected image yields the average line curvature:[4]

$$< \frac{T}{A_o} > \ = \ <T_A> \ = \ \frac{\delta}{\pi} <k> L_V \tag{4}$$

where δ is the thickness of the slice from which the projection is obtained. A simple count of *inflection points I* yields the average torsion $<\tau>$:[4]

$$< \frac{I}{A_o} > \ = \ <I_A> \ = \ \frac{\delta}{\pi} <\tau> L_V \tag{5}$$

References

1. F.N. Rhines and R.T. DeHoff, Quantitative Microscopy, New York: McGraw-Hill (1968).
2. E.E. Underwood, Quantitative Stereology, Reading, MA: Addison-Wesley (1970).
3. A.M. Gokhale, J. Microscopy, 167(1992)1.
4. R.T. DeHoff and S.M. Gehl, Proc., 4th Intl. Cong. for Stereology, NBS Special Publication 431(1976)29.

Fractal Geometry and its Uses for Characterizing Microstructure

John C. Russ

Materials Science and Engineering Dept., North Carolina State University, Raleigh, NC 27695

Observers of nature at scales from microscopic to global have long recognized that few structures are actually described by Euclidean geometry[5]. Mountains are not cones, clouds are not ellipsoids, and surfaces are not planes. Classical geometry allows dimensions of 0 (point), 1 (line), 2 (surface), and 3 (volume). The advent of a new geometry that allows for fractional dimensions between these integer topological values has stirred much interest because it seems to provide a tool for describing many natural objects. As is the case for many new tools, this fractal geometry is subject to some overuse and abuse.

A classic illustration of fractal dimension concerns the length of a boundary line, such as the coast of Britain. Measuring maps with different scales, or striding along the coastline with various measuring rods, produces a result that depends on the resolution. More than this is required for the coastline to be fractal, however: It must also be self-similar. That is, the reduction of measurement scale from 100km to 10km increases the measured perimeter by the same factor as reducing the measurement scale from 100m to 10m. Hence, plotting the total perimeter vs. measurement scale on log-log axes produces a straight line whose slope gives the fractal dimension of the coastline (Figure 1). A smooth coastline, such as the beaches of Florida, has a slope that is nearly zero (the measurement does not vary much with scale). Consequently the fractal dimension is nearly 1.0, the topological dimension of a Euclidean line. A very "rugged" coastline such as that of Maine has a steeper slope on the log-log plot, about 0.25, and the fractal dimension of this coastline is 1.25, a fractional number between that for a line and for a surface.

Fractals occur in microstructures in a number of situations. Some of the most common are the clustering of particles, the branching of networks, and the roughness of surfaces. Clustering is illustrated in Figure 2 using a model of "diffusion limited aggregation" in which particles random-walk until they touch the growing cluster, and then adhere to it. A new arrival will more likely encounter one of the long arms, rather than finding a way between them to an interior point. Changing parameters such as the probability of sticking, crystallographic effects, ballistic motion of the particles, etc., alter the structure and change the fractal dimension. The generated clusters mimic many real dendritic structures closely, and the dimensions correlate with history and properties[1,6,10]. Branching networks can be produced with iterative models such as the L-system[8] shown in Figure 3. Progressive refinement of the structure by repeating a simple substitution rule produces networks that mimic plants, rivers, blood vessels, bronchi[4], and so on. The fractal dimension of the network correlates with its appearance and behavior.

Surface roughness has been studied extensively using fractal geometry[2,3], including wear surfaces, fractures, deposited coatings, corrosion, and even the surface of human skin. In many cases, the dimension can be correlated with history or properties. Application of cosmetics "smooths" skin and reduces its fractal dimension. The "roughness" (i.e., fractal dimension) of brittle fractures[7] in metals, ceramics and glasses correlates with the fracture toughness (K_{IC}) as shown in Figure 4. Machined surfaces have a fractal dimension related to tool wear. The data used for such measurements come from profilometer traces, interference microscopes, and scanned probe instruments such as STM and AFM. The mathematical tools used to analyze the fractal dimension from such data each have some practical limitations, but include the measurement of elevation profiles, sectioning of the surface to create islands and coastlines, and measurement in Fourier space[9].

References
1. Avnir, D., D. Farin (1984) Nature 308(15): 261-263.
2. Church, E. L. (1988) Applied Optics 27(8): 1518-1526.
3. Feder, J. (1988). Fractals. New York, Plenum Press.
4. Goldberger, A. L., B. J. West (1987) Yale Journal of Biology and Medicine 60: 421-435.
5. Mandelbrot, B. B. (1982). The Fractal Geometry of Nature. New York, Freeman.
6. Meakin, P., S. Tolman (1990) Fractals in the Natural Sciences. Princeton University Press. 133-146.
7. Mecholsky, J. J., S. W. Freiman (1991) J. Am. Ceramic Soc. 84(12): 3136-3138.
8. Prusinkiewicz, P., A. Lindenmayer (1990). The Algorithmic Beauty of Plants. New York, Springer
9. Russ, J. C. (1991) Journal of Computer Assisted Microscopy 3(3): 127-144
10. Vicsek, T. (1992). Fractal Growth Phenomena (2nd. Edition). Singapore, World Scientific.
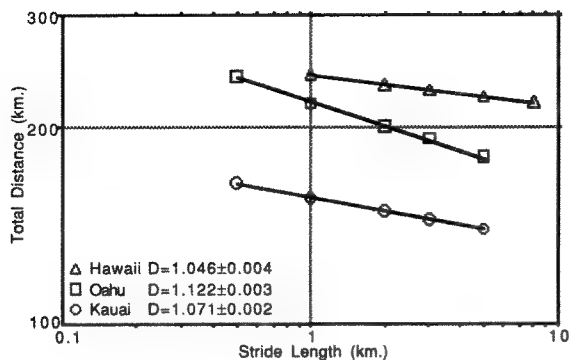
Figure 1. Richardson plots for three of the Hawaiian islands, showing the variation of the measured perimeter with the length of the measurement tool. The slope of each line is the fractal dimension.
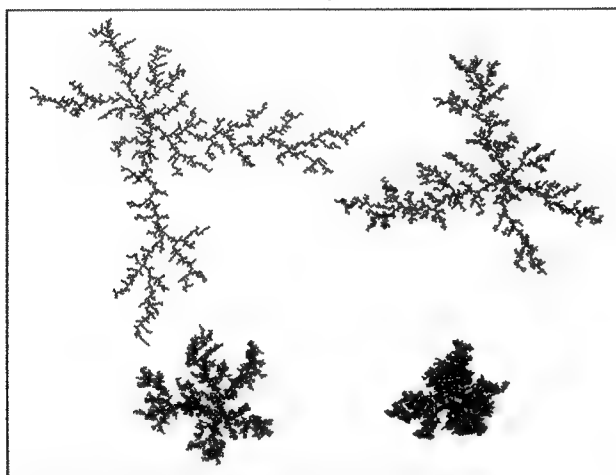
Figure 2. Clusters formed by Diffusion Limited Aggregation with varying sticking probabilities
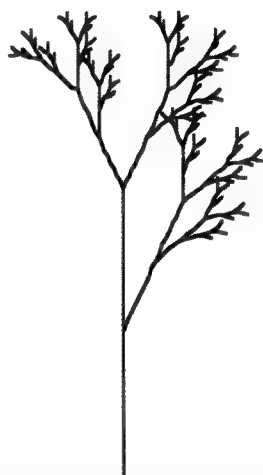
Figure 3. L-System network produced by iteratively applying one branching rule.
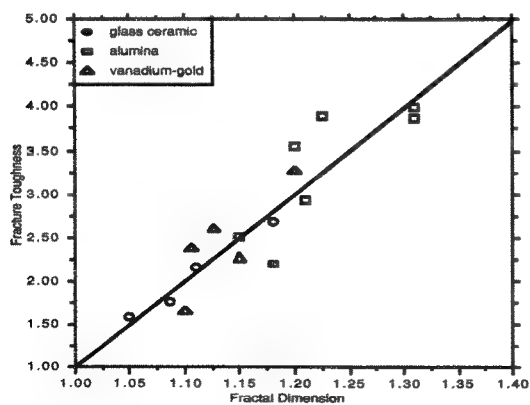
Figure 4. Observed correlation between fracture toughness and profile fractal dimension for different types of materials.

489

QUANTITATIVE MEASURE OF MIXTURE HOMOGENEITY OF AN ALUMINA SILICON CARBIDE COMPOSITE

James F. Kelly and Edwin R. Fuller, Jr.

National Institute of Standards and Technology, Gaithersburg, MD 20899

Homogeneity, defined in terms of spatial distribution uniformity of one phase or component within another, can be determined from the variation of the standard deviation of the measured volume fraction of one component with sampling area.[1] We have applied this concept to the evaluation of dispersions of SiC whiskers in an alumina matrix by using energy dispersive x-ray spectroscopy (EDS). The quantitative analysis measures the area to area variation in SiC fraction. The homogeneity distribution was obtained by calculating the variance in this fraction as a function of magnification (sampling area) in a scanning electron microscope. These data are compared to calculations of expected values based on a Poisson distribution model for the dispersion of SiC.

Compositions were prepared from two different SiC size distributions. The blending procedures and volume fractions (0.30) were the same for each composition. Six polished specimens were analyzed from each of two 100mm diameter hot-pressed alumina – SiC billets. The analytical procedure followed was to obtain a standard EDS X-ray spectrum representative of the bulk specimen composition by rastering the SEM electron beam over a large (3 mm by 4 mm) area of the specimen. The EDS spectra obtained when rastering over smaller areas (higher SEM magnification) were quantitatively compared with this standard spectrum to obtain the local area composition. The variability in local area composition wa obtained by measuring the composition of twenty-four areas at each of two magnifications (1kx and 10kx), corresponding to areas of 10,800 μm^2 and 108 μm^2, respectively. Multiple spectra were also collected from a single area to determine the expected variability in counting statistics and instrumentation.

The backscatter electron images in Figure 1 show the dispersion of SiC (dark areas) in the alumina matrix for each of the two magnifications. The two different types of SiC whiskers used in making these billets had mean sizes of 0.5 μm and 1.1 μm. Analysis of the expected variability, based on the simplifying assumption of a Poisson distribution of monosized features of area, a, making up an area fraction, F, predicts a variance, V, in measured area fractions within regions of area, A, given by:

$$V = (a/A) * F(1-F) \tag{1}$$

Results comparing the calculated and measured standard deviations for each composition and each magnification are given in Table 1. Comparison of measured and predicted values indicates that, although a relatively good dispersion of the whisker materials has been achieved, the deviation from purely random spatial distribution is clearly distinguished, with the lower magnification measurement being a more sensitive measure of the inhomogeneity. It is expected that at high magnifications the statistical assumption of many features within a field will not be met, while at very low magnifications only extreme inhomogeneity would be detected. The optimal magnification will depend on the particular composite under study. As indicated by Equation 1, the variability will be a function of material size, volume fraction, and measurement area. Expected applications of this type of analysis are in quality control after establishing the expected variability for a specific material.

1. F. F. Lange and K. T. Miller, J. Am. Ceram. Soc., 70(12) 896-900 (1987).

Table 1. -- Area to area Standard deviation of SiC area fraction

| | 1.1 μm Powder | | 0.5μm Powder | |
	Calculated	Measured	Calculated	Measured
10 kx	0.043	0.046	0.020	0.029
1 kx	0.004	0.010	0.002	0.007
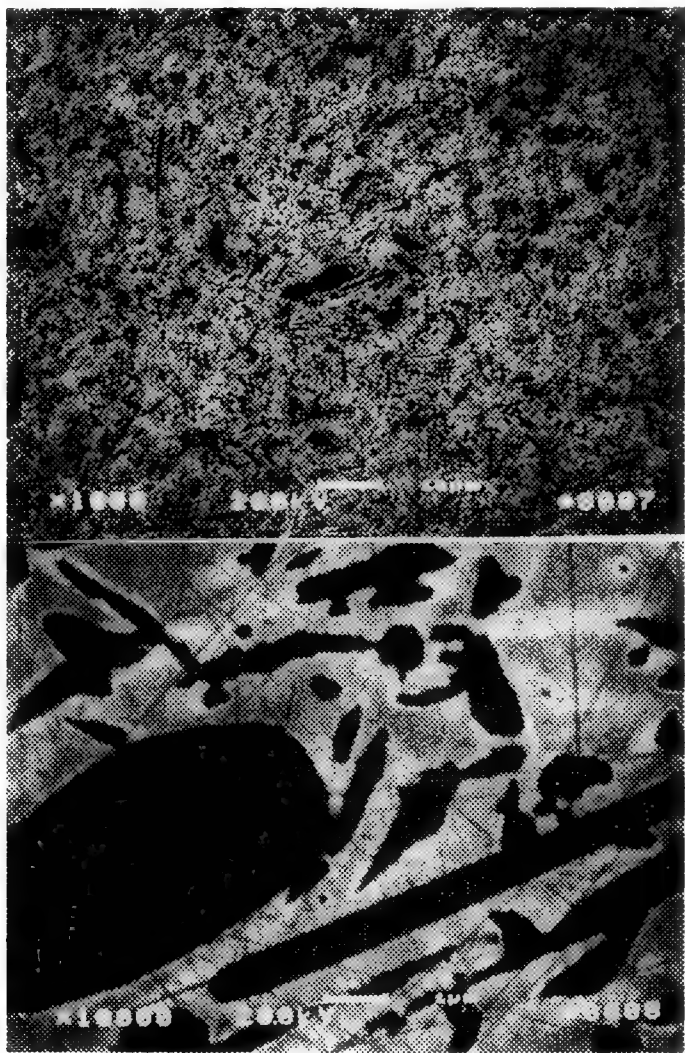
Figure 1. -- Backscattered electron SEM images of SiC in alumina

CRYOPRESERVATION OF BIOLOGICAL SPECIMENS

M. Joseph Costello

Department of Cell Biology & Anatomy, University of North Carolina at Chapel Hill, Chapel Hill, NC 27599

Rapid cooling is the first, critical step in the preservation of biological specimens for examination using a wide variety of electron microscopic techniques. The choice of which cooling method to use depends on many factors, such as the restrictions of specimen geometry, the type of structural information desired and the microscopic techniques to be employed. This summary will highlight some recent technical innovations and novel applications of cryopreservation of biological specimens to study ultrastructure, chemical composition, and dynamic processes.

For cryofixation to give realistic preservation of structural details, the specimen must be rapidly brought into intimate contact with the coolant and the contact must be maintained throughout the critical stages of the cooling process. During the last decade, four cooling methods have become prominent because they produce excellent preservation without cryoprotectants, are commercially available and are relatively simple to use: *plunge cooling, jet cooling, slam cooling*, and *high-pressure cooling*.[1-3]

Plunge cooling, the most commonly used method for cryofixation, is simply the immersion of a specimen into a liquid coolant usually held near its melting point.[3] We and others have had considerable success using thin specimens sandwiched between conductive metal sheets.[4] The streamlined profile of the sandwich ensures smooth entry into the coolant and a mechanical device controls the velocity of the plunge and brings the specimen gently to rest.[1-4] The optimum entry velocity is often debated. Our results indicate that velocities high enough to cause cavitation of the coolant, thus disturbing the coolant-specimen contact, degrade the cooling rate. The highest velocity without causing cavitation for copper sandwiches is about 2 m/s.[4] An important factor is the thickness of the specimen, ideally about 10 μm. Recently, however, we have demonstrated excellent preservation for freeze-fracture/etch by cooling thicker specimens without cryoprotectants, such as 20-40 μm thick vibratome sections of fresh ocular lens and fixed rat liver, and 30-50 μm thick clusters of insect endocrine gland cells.[5] In unpublished studies, the copper sandwich was used as a reaction vessel to study dynamic processes, such as vesicle fusion. A 0.05 μl specimen, insufficient to cover the available sample area in the sandwich, was exposed to a second fluid containing a modifying agent, such as Ca++. The solution was drawn in by capillary action and the gradient of the influence of the agent was observed in whole complementary replicas of the fractured surfaces.[6] In a published example, the copper strips of the sandwich served as electrodes to induce electroporation of erythrocyte membranes observed by freeze-fracture and freeze-substitution, which showed excellent preservation of the induced membrane pores.[7]

A great advance in plunge cooling technology was made with the demonstration that suspensions of biological material could be preserved in amorphous ice by plunging thin specimens into liquid coolants.[2,8] A specimen thickness of less than 100 nm is essential and is conveniently obtained by suspending the solution over holes in a thin film supported on an EM grid. The cooling rates needed to produce amorphous ice, estimated to be 10^5 to 10^6 °C/sec, require that the critical cooling occurs within the first 2-3 mm of the coolant surface for a plunge velocity of 2 m/s. Thus it is necessary to protect the exposed samples from precooling in the cold gas layer above the coolant and to maintain low coolant surface temperatures. Ethane and propane are at present the two preferred coolants, with propane having the advantage of remaining liquid for long periods surrounded by LN_2 and ethane giving slightly higher cooling rates.[3] This method has proven ideal for examination of cell fragments, organelles, viruses, lipid-protein vesicles and lipid phases.[2,8] Although obtaining usable images can be troublesome because the samples are extremely sensitive to beam damage, the images can yield high

resolution structural information. Importantly, the method has been used to study dynamic processes such as the assembly of microtubles[9] and fast phase transitions.[10]

Jet cooling is most often accomplished with a high velocity stream of propane (estimated to be > 10 m/s under 90 psi) directed at a sample sandwiched between copper supports.[11,12] Although several one-sided jet cooling devices have been reported, the best preservation is obtained with two-sided jets using similar holders to the copper sandwiches described for plunge freezing. The measured cooling rates for jet cooling are greater than for plunge cooling.[13] Thus, thicker samples can be rapidly cooled which are suitable for freeze substitution.[11,12]

Slam cooling is considered to be the ultimate cooling method when used with a liquid helium cooled copper block.[14] Specimens propelled onto a polished metal surface are held in contact with the surface by a mechanism that prevents bounce. This technique has been used to great advantage for revealing 3D structural details after deep etching and rotary replication of the cytoskeleton, membrane surfaces and macromolecules.[14] One novel approach has been to slam cool single muscle fibers at known intervals after stimulation for the study of excitation-contraction coupling.[15] The muscle fibers after cooling can be trisected to perform freeze-fracture/etch, freeze-substitution and elemental analysis on different segments.[15] This approach was also used to establish criteria for recognizing cooling induced cell damage (such as collapse of mitochondrial cristae) in the 15 μm thick layer where ice crystals are not readily visible.[16] A recent modification of slam cooling employs gold coated copper to aid in cleaning the surface, computer controlled cycling, and LN_2 to reduce cost.[17] The system gives good preservation while being simple and inexpensive to operate.

High pressure cooling has come of age[18] having been used effectively in the last few years to preserve thick specimens. The advantage is that hydrostatic pressure limits ice crystal nucleation and growth, producing ice-crystal-free specimens even though the freezing rates may be much slower than the slam cooling method. High pressure freezing is best suited for specimens that can be readily adapted to the holder so that the pressure is uniformly applied as the coolant reaches the specimen.[2,18]

References

1. R. A. Steinbrecht and K. Zierold, Eds., Cryotechniques in Biological Electron Microscopy, Berlin: Springer-Verlag (1987) 87.
2. A. W. Robards and U. B. Sleytr, in A. M. Glauert, Ed., Practical Methods in Electron Microscopy, Amsterdam: Elsevier Science Publishers B.V. (1985).
3. K. P. Ryan, Scanning Microsc. (1992)6, 715.
4. M. J. Costello et al., The Science of Biological Specimen Preparation (1984) 105.
5. J. Dai et al., Proc. Ann. EMSA Meeting (1992) 706.
6. R. D. Fetter and M. J. Costello, J. Micros. (1986)277.
7. D. C. Chang and T.S. Reese, Biophys. J. (1990)58, 1.
8. J. Dubochet et al., Q. Rev. Biophys. (1988)21, 129.
9. E. Mandelkow et al., J. Cell Biol. (1991)114, 977.
10. Y. Talmon et al., J. Electr. Microsc. Tech. (1990)14, 6.
11. M. Muller et al. Mikroskopie (1980)36, 129.
12. J. C. Gilkey and L. A. Staehelin, J. Elec. Micros. Tech. (1986)3, 177.
13. M. J. Costello et al., J. Micros. (1982)125, 125.
14. J. E. Heuser, Cells and Tissues: A Three-Dimensional Approach by Modern Techniques in Microscopy, New York: Alan Liss, Inc. (1989) 71.
15. R. Nassar et al., Scan. Elec. Micros. (1986)I, 309.
16. H. Dalen et al., J. Microsc. (1992)168, 259.
17. A. J. Jesaitis et al., J. Clin. Invest. (1990)85, 821.
18. D. Studer et al., Scan. Micros. Suppl. (1989)3, 253.

APPLICATION OF ELECTRON TOMOGRAPHY TO ELUCIDATE THE 3D ARCHITECTURE OF DIVERSE ASYMMETRIC BIOLOGICAL SPECIMENS

Bruce F. McEwen

Wadsworth Center Labs and Research, Box 509, Albany, NY 12201-0509

Electron tomography refers to the use of tomographic reconstruction methods to obtain three-dimensional (3D) information from transmission electron microscopy (TEM) (1). This is accomplished by tilting the sample over a wide angular range with 180° being ideal, but 120° to 140° more typical due to limitations imposed by the geometry of most TEM specimens (2). If symmetry is present in the sample then the full angular range is not required. Furthermore, if the specimen is present as identical units, either in crystalline arrays (3) or as single particles (4), the different tilts can be collected from different specimens and hence spare the total electron dose on any given particle. However, many important biological specimens are large, asymmetric objects which, due to their size, are not found as identical individual units (5). For such cases, the only recourse is to collect all the views from a single copy of the object, generally using a single axis tilt geometry.

Adequate sampling requires collecting the images with a small angular interval, usually between 1 and 5°. Thus the sample will be exposed to the electron beam between 24 and 140 times. At present, this requirement precludes using single-axis tomography with beam-labile frozen hydrated preparations unless a high degree of symmetry is present. In addition, embedded specimens will experience a shrinkage of about 25% in the depth dimension (reviewed in 6). Since most of this loss occurs after very little exposure to the electron beam, followed by a long, nearly flat plateau in the dose-mass loss curve, it is generally advisable to expose the sample to the electron beam for 5 to 10 minutes before collecting any data. Such a practice reduces the risk of the sample changing while the tilt series is being recorded. Once data collection is initiated, all efforts to minimize the electron dose, such as off-specimen focusing, should be employed. One of the consequences of the high beam exposure is that it limits the meaningful resolution available to about 4-5 nm. The mass loss also degrades resolution in the depth dimension which aggravates the loss of resolution in that direction due to the missing angular information. Nevertheless, resolution is still superior to what can be obtained from serial thin section reconstructions where the sampling size is at best 30-40 nm and hence the depth resolution limited to 60-80 nm.

Since most TEMs still record images onto film, the next step is usually digitization. Presently the preferred method is to use a CCD camera with a 1024 X 1024 chip and either 12 or 14 bit data readout although 16 bits may be desirable for thicker specimens. Alternatively a high-quality video camera can be use for most samples which is less expensive. Although the flatbed scanners still provide the highest quality of scanned image, they are not recommended for tomography because of the large amount of data that must be processed. Once scanned, the images are aligned to a common origin with the aid of fiduciary markers (7), and cross-correlation can be used for refinement. The fiduciary markers are usually colloidal gold particles added to the specimen surface before data collection. These gold particles are located either with a cursor or a feature recognition program that automatically finds particles the size and shape of the gold markers (8). The marker locations on each view are then entered into a least squares fitting program (7) that computes the position of each view relative to a common coordinate system.

After alignment, and subsequent density normalization, the data set can then be used to compute the 3D reconstruction using either the weighted backprojection or one of the iterative algebraic algorithms. Although they are the heart of the technique, and embody much of the theoretical knowledge, these algorithms tend to be transparent to the user. Once the reconstruction is computed, it must be probed for the desired information which is rarely obvious from a quick inspection of the 3D volumes. In fact this step usually consumes the majority of the time and effort in a project. Computer power and software in this area are improving at a rapid pace and several kinds of analyses are currently carried out that were not feasible a few years ago. Presently some of the more useful computer graphic tools include examining 2D slices, volume rendering, shaded surfaces and hand editing and volume segmentation in combination with the other approaches.

Single-axis electron tomography has been applied to a wide range of biological problems (9,10). Recent studies include investigations of the mammalian kinetochore (11), vertebrate mineralization (12) and Balbiani ring hnRNP substructure (12). The latter combines the 3D analysis with selective DNA staining and electroscopic imaging indicating the importance of specimen preparation and imaging technique to tomographic studies. One particularly exciting development is automated tomography (8,14,15). This technique is based on placing a CCD camera inside the TEM to enable direct digital recording. Aside from bypassing the need for film, and thereby the digitization step, this development allows for feedback between the image and the TEM controller. This in turn enables incrementation of the tilt angle, rough alignment, automatic focus adjustment, and image recording all without input from the operator. The major advantage of automated tomography is the possibility that the electron dose can be lowered to the point where mass loss is avoidable for embedded specimens and that studies with frozen hydrated specimens are feasible. Progress in automated tomography, improved specimen preparations, more powerful computer workstations, volume restoration methods and new volume visualization software, promise to make single-axis tomography an even more powerful and commonly used tool for ultrastructural investigations (16).

References

1. J. Frank in Electron Tomography, ed. J. Frank, Plenum 1992, p. 1.
2. D.P. Barnard et al., J. Microscopy (1992)167, 39.
3. L.A. Amos et al., Prog. Biophys. Mol. Biol. (1982)39, 183.
4. M. Radermacher, J. Electr. Microsc. Tech. (1988)9, 359.
5. B.F. McEwen and J. Frank, Proc. Ann. EMSA Meeting (1992)50, 580.
6. P.K. Luther in Electron Tomography, ed. J. Frank, Plenum 1992, p.39.
7. M.C. Lawrence in Electron Tomography, ed. J. Frank, Plenum 1992, p. 197.
8. A.J. Koster et al., Microsc. Soc. Amer. Bulletin (1993)23, in press.
9. B.F. McEwen in Electron Tomography, ed. J. Frank, Plenum 1992, p. 281.
10. C.L.F. Woodcock in Electron Tomography, ed. J. Frank, Plenum 1992, p. 313.
11. B.F. McEwen et al., J. Cell Biol. (1993)120, 301.
12. W.J. Landis et al., J. Structural Biol. (1993)110 in press.
13. A.L. Olins et al., Chromosoma (1993)102, 137.
14. K. Dierksen et al., Ultramicroscopy (1992)40, 71.
15. A.J. Koster et al., Ultramicroscopy (1992)46, 207.
16. Supported by NIH RR01219 to Wadsworth Center's Biological and Image Reconstruction Facility as a National Biotechnological Resource.

Computer-Aided Analytic and Visualization Tools for Structural Studies

Bridget Carragher

Beckman Institute, University of Illinois, Urbana, IL, 61801

Structural biologists typically acquire data in the form of a two-dimensional image (or set of images) from which the three-dimensional structure of the object of interest must be inferred. Examples can be found over a range of sizes spanning many orders of magnitude, and covering structures from the macroscopic to the atomic scale. A correspondingly wide range of different instruments is used in the collection of this data, from CT/MRI scanners, through light and electron microscopes, and recently, atomic force instruments. The images which are collected from these instruments may be in the form of a series of 2D slices through the 3D data set (and these may be either physical sections or optical sections) or a series of tomographic 2D projections of the 3D data set. In either case it is highly likely that computer software tools will be used on the data set either as an aid in the qualitative interpretation of the structure or as a means of extracting quantitative morphological measurements.

During this tutorial the following topics will be discussed:

1. Stereology: This refers to the set of procedures for determining the three-dimensional characteristics (such as volume, surface area, length and number) of inhomogeneous solids, such as tissue samples, from two dimensional planes through them.[1] Recent developments in the field of stereology have led to the development of a new class of stereological estimators that are not constrained by the geometrical approximations of previous methods.[2] Some practical examples of the use of these new techniques will be presented and the design of a stereology workstation attached to a light microscope will be discussed. See Figure 1a.

2. Three-dimensional representation in confocal microscopy: The unprocessed output of a confocal microscope is a set of optical sections through the 3D object. Before the data set may be visualized and interpreted it may need to be resampled onto a uniform sampling grid and renormalized to compensate for progressive attenuation of the signal at greater depths into the sample. These aspects will be discussed as well as techniques for surface and volume reconstruction.[3] See Figure 1b.

3. Reconstruction from serial sections in electron microscopy: The method used to reconstruct a 3D volume from a set of serial electron micrographs depends on how readily the structures of interest can be segmented. Procedures for both manual and automatic segmentation will be discussed as well as procedures for alignment of the data sets and subsequent rendering of the volumes.[4,5] See Figure 1c.

4. Tomographic techniques: The steps involved in tomographic reconstructions using both random conical tilt geometry and helical geometry will be discussed in some detail.[6] See Figure 1d.

In each of the topics discussed practical information will be provided about hardware requirements and software availability.

References

1. H.J.G. Gunderson et al., APMIS 96(1988)379.
2. H.J.G. Gunderson et al., APMIS 96(1988)857.
3. H.T.M. Van der Voort et al., J. Micros. 153(1989)123.
4. D. Hessler et al., Microscopy 22(1992)73.
5. S.J. Young et al., J. Electr. Micros. Tech. 6(1987)207.
6. M. Rademacher, in J. Frank Ed., Electron Tomography, Plenum Press (1991)91.
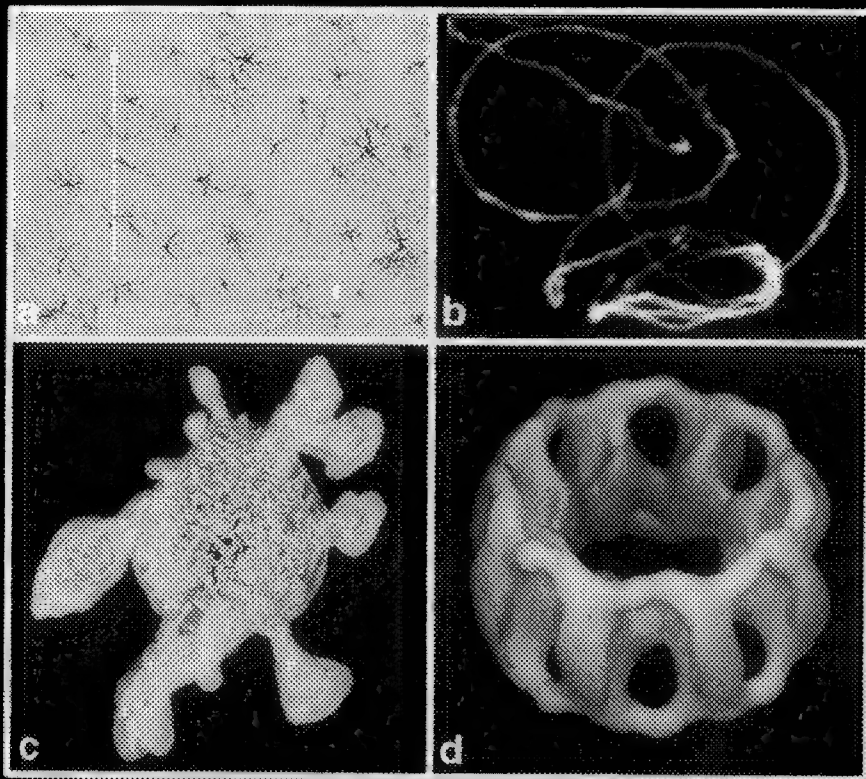
Fig. 1a--Stereology software allows measurement of 3D geometrical parameters (such as volume, surface area, length and number) from 2D sections. An unbiased sampling frame is shown superimposed onto a field of astrocytes.
(Image courtesy of Nick Hawrylak and Nick Kisseberth, Beckman Institute, University of Illinois.)
Fig. 1b--Three-dimensional reconstruction of a sperm tail inside a drosophilla egg obtained using optical sections from the confocal microscope.
(Image courtesy of Tim Karr, Beckman Institute, University of Illinois.)
Fig. 1c--Reconstruction of dendrite of Purkinje cell of chick cerebellum obtained from serial sections of electron micrographs.
(Image courtesy of Maryann Martone and Mark Ellisman, Microscopy and Imaging Resource, University of California, San Diego.)
Fig. 1d--Three-dimensional reconstruction of the nuclear pore complex obtained using random conical tilt tomographic techniques.
(Image courtesy of Jenny Hinshaw and Ron Milligan, Research Institute of Scripps Clinic, La Jolla.)

SECONDARY ION MASS SPECTROMETRY IN THE BIOLOGICAL AND MATERIALS SCIENCES

Richard W. Linton

Department of Chemistry - CB3290, The University of North Carolina, Chapel Hill, NC 27599-3290

Secondary ion mass spectrometry (SIMS) is based upon energetic ion bombardment of surfaces resulting in in the emission of sputtered particles, including both atomic and molecular ions.[1] The use of mass spectrometric detection provides a highly versatile and sensitive tool for surface and thin film chemical analysis. In recent years, the scope of the technique has broadened to include a variety of analysis modes including:

1. Elemental Depth Profiling (dynamic SIMS),
2. Laterally Resolved Imaging (ion microprobe or ion microscope analysis),
3. Image Depth Profiling (combination of modes 1 and 2 providing 3-D images),
4. Molecular Monolayer Analysis (static SIMS),
5. Sputtered Neutral Mass Spectrometry (post-ionization).

Much of the early work in dynamic SIMS centered on the development of depth profiling and imaging techniques, with an emphasis on applications to electronic materials.[2] SIMS has made extensive contributions to semiconductor materials science since the 1960's, including the development of new devices and processes, and in failure analysis. It is clear that as microelectronics technology continues to evolve into the realm of ultra-large scale integration (ULSI), techniques such as SIMS will become increasingly important in characterizing trace element dopants and contaminants within highly complex architectures. Previous research in dynamic SIMS has emphasized the optimization of useful secondary ion yields, and the understanding of sample matrix effects that influence absolute quantification of elemental concentration and depth scales. The recent advent of post-ionization techniques, such as the use of lasers to ionize sputtered neutral species, offers some promise for improving sensitivity or quantitative capabilities. For example, the use of high power density lasers for non-resonant post-ionization with high efficiency has the potential to significantly reduce matrix effects. Quantitative multielement depth profiling of multilayer film structures can be facilitated, although residual matrix effects such as sputter yield differences between various layers remains a concern. Other instrumental developments have included the incorporation of image array detectors, such as resistive anode encoders and charge-coupled devices, for digital image detection in a microscope mode. These are readily combined with dynamic SIMS, allowing three-dimensional imaging of near surface compositions.[3] Microprobe capabilities also have been greatly improved in recent years with the advent of liquid metal sources providing field emission ion guns with extremely high brightness.[4] Such sources are pushing dynamic SIMS lateral spatial resolution down to the 20nm range, thus approaching the fundamental limit of approximately 10nm imposed by the spatial distribution of sputtered ions from the cascade collisional volumes of single ion impacts. This tutorial will briefly review the physical basis, instrumentation, and materials science applications of dynamic and imaging SIMS, emphasizing the use of sector field instruments. New developments in image processing, such as volume rendering and pattern recognition, also will be introduced as means to enhance the interpretation of complex multi-dimensional SIMS data.

The biological and biomedical communities have benefited from the same developments in dynamic SIMS outlined above. A 1992 special issue of *Biology of the Cell*, highlighting the presentations made at a NATO-sponsored workshop on biological SIMS, provides an excellent overview of the state-of-the-art.[5] The ability of SIMS/ion microscopy to image trace element localizations within microvolumes of preserved cells and tissues is a major asset. Furthermore, the technique has a rather unique ability to experimentally vary the lateral and depth resolutions over a wide range to provide a suitable analytical volume for a given level of analytical precision. The technique is well suited to the detection of physiologically important elements, such as Na, K, Ca, Mg, as well as xenobiotic species, such as toxic heavy metals. Furthermore, since mass spectrometric detection is isotope specific, there are countless possibilities for using isotopically labelled elements or molecules for examining the chemistry of

biologically important species at the cellular level. Furthermore, the field emission ion source is allowing elegant elemental mapping studies at the sub-cellular level of resolution.[4] Paralleling the extensive work in electron microprobe applications, there has been considerable effort to characterize and minimize analytical artifacts involved in sample preparation, especially for easily diffusible elements that require cryo-preservation for accurate localization.[5] Analogous to the research on matrix effects in semiconductor applications, biological applications require major efforts to achieve quantification of elemental concentrations, including the development of appropriate standards and the evaluation of potential sources of image contrast unrelated to elemental concentration variations (e.g., topographic contrast, chromatic contrast, local matrix effects on sputter/ion yields).[5] This tutorial will illustrate the range of biological applications that benefit most effectively from the utilization of dynamic SIMS.

A major growth area for SIMS has been the static mode of analysis, in which a very low dose of primary ions is used to minimize beam damage to surface layers. Typically, only a very small fraction of the outermost monolayer is removed, resulting in a mass spectrum in which molecular or cluster ions can be correlated with molecular species on the solid surface. Since the sampling depth is severely constrained, the technique requires a mass spectrometer with extremely high ion transmission. Furthermore, since molecular spectra are usually very complex, the technique also demands high mass resolution and accurate mass measurement. The development of time-of-flight (TOF) instruments with suitable secondary ion energy compensation have provided one means to achieve high analytical performance over a broad mass range.[6] As a consequence, static SIMS measurements are increasingly constrained by the ability to sputter and ionize molecular surface species, rather than by the mass spectrometry of the secondary ions. In the most favorable instances of useful ion yields, the coupling of a pulsed liquid metal ion source with TOF detection allows molecular mapping in the outermost monolayer with lateral resolutions on the order of 1 μm. Improved ion yields have been achieved by deposition of samples as monolayers on metallic substrates, most commonly by the use of etched silver foil, resulting in the production of metal-cationized molecular ions. Within the past year, resonant photoionization by femtosecond UV laser pulses has been shown to improve the useful yield and molecular information of selected organic species.[7] The TOF-SIMS approach has been particularly promising for the characterization of polymer films, including the oligomer distribution and endgroup characterization of relatively low molecular weight materials.[8] It also shows promise for organic monolayers produced by Langmuir-Blodgett and self-assembly techniques. This tutorial will briefly summarize the development of static SIMS as a molecular spectroscopy, useful in both materials and biological science applications.

References

1. D. Briggs, M.P. Seah, Eds., Practical Surface Analysis- Volume 2: Ion and Neutral Spectroscopy, Chichester, England: Wiley (1992).
2. R.G. Wilson, F.A. Stevie, C.W. Magee, Secondary Ion Mass Spectrometry: A Practical Handbook for Depth Profiling and Impurity Analysis, New York: Wiley (1989).
3. K.H. Gray et al., J. Vac. Sci. Tech. A (1992)10, 2679.
4. R. Levi-Setti, J.M. Chabala, Y.-L. Wang, Ultramicroscopy (1988)24, 97.
5. P. Fragu, Ed., Biology of the Cell (1992)74, 1-160.
6. E. Niehuis, et al., Surf. Interface Anal. (1989)14, 135.
7. R. Möllers, et al., Resonant Photoionization of Sputtered Organic Molecules by Femtosecond UV Laser Pulses, Org. Mass Spec. (1992), in press.
8. I.V. Bletsos, et al., Anal. Chem. (1988)60, 938.

TAILORING MICROSTRUCTURES OF MATERIALS THROUGH BIOMIMETICS

Mehmet Sarikaya* and Ilhan A. Aksay**

*Materials Science and Engineering, University of Washington, Seattle, WA 98195
**Chemical Eng & Princeton Materials Inst, Princeton Univ, Princeton, NJ 08544

Biomimetics involves investigation of structure, function, and methods of synthesis of biological composite materials. The goal is to apply this information to the design and synthesis of materials for engineering applications.

Properties of engineering materials are structure sensitive through the whole spectrum of dimensions from nanometer to macro scale. The goal in designing and processing of technological materials, therefore, is to control microstructural evolution at each of these dimensions so as to achieve predictable physical and chemical properties. Control at each successive level of dimension, however, is a major challenge as is the retention of integrity between successive levels. Engineering materials are rarely fabricated to achieve more than a few of the desired properties and the synthesis techniques usually involve high temperature or low pressure conditions that are energy inefficient and environmentally damaging.

In contrast to human-made materials, organisms synthesize composites whose intricate structures are more controlled at each scale and hierarchical order. The properties of biological composites therefore, are optimized under a given set of environmental conditions. In addition, biomaterials are often multifunctional. The synthesis is performed at ambient temperatures efficiently in aqueous media using constituents collected from the environment. Some of the structural biomaterials include soft tissues, such as mucus, cartilage, cuticle, tendon, silk, and skin; and hard tissues such as skeletal units (bone), teeth, and mollusk shells. Although the constituent phases appear to be of simple character, they have a high degree of structural order. In hard tissues, for example, the inorganic component (calcite in sea-urchin spines- Fig.1- and aragonite in mother-of-pearl from mollusk shells- Fig. 2) is highly organized and uniquely associated with biological macromolecules (proteins, polysaccharides, and their fractions). The macromolecules appear to control nucleation and growth of the constituent phases, and the overall shape of the tissue. Furthermore, biogenic inorganic matrices exhibit substructural features that are not present in synthetic ones.

The realization by scientists that there must be a close relationship between the highly organized structures of biological composites, the unique biological synthesis mechanisms by which these structures are produced, and the resultant physical properties, has led to the creation of a new multidisciplinary field, incorporating biological and physical sciences, called biomimetics. Interrelationships among these three areas are critical for materials development and, therefore, biological composites offer inspirational sources and serve as guidelines in the development of new technological materials, either by biomimicry or bioduplication. This is schematically illustrated in Fig. 3. This presentation discusses some current issues in biomimetics, with emphasis on hard tissues, including: i) biomineralization; ii) structural hierarchy; iii) macromolecule-inorganic interface structure; iv) identification of macromolecules; and v) their self-assembly.
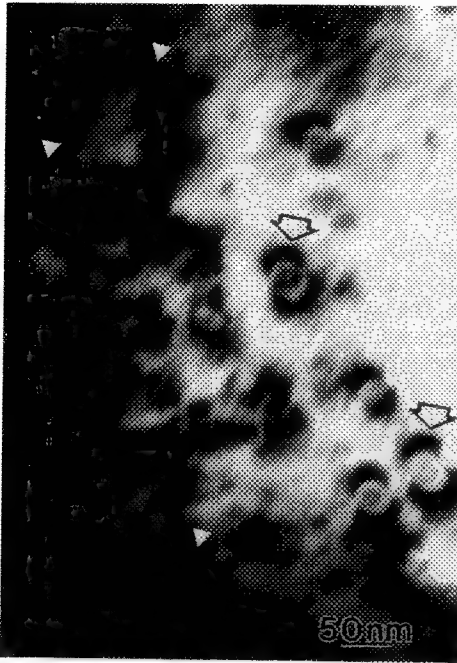
Fig. 1- A BF-TEM image of sea-urchin spine exhibiting ultrafine Mg containing precipitates within a calcitic matrix. Architecturally intricate spine is ~0.5 mm in diameter and ~3 mm in length and is single crystalline calcite.
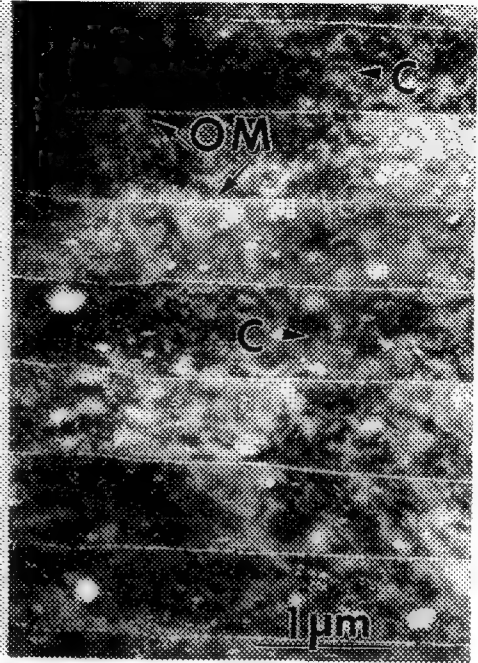
Fig. 2- A TEM cross-sectional image of nacre displaying brick and mortar nano-architecture of aragonite platelets (C) and organic matrix (OM) which in itself contains layers of proteins and polysaccharides. Note dislocations, voids, and other substructural features in aragonitic platelets.

Biomimetics

Biomimicking

Synthesis of technological materials based on artificial approaches to mimic biological microstructures

Bioduplication

Processing of technological materials based on biological approaches to mimic both biosynthesis and microstructures

Novel Materials
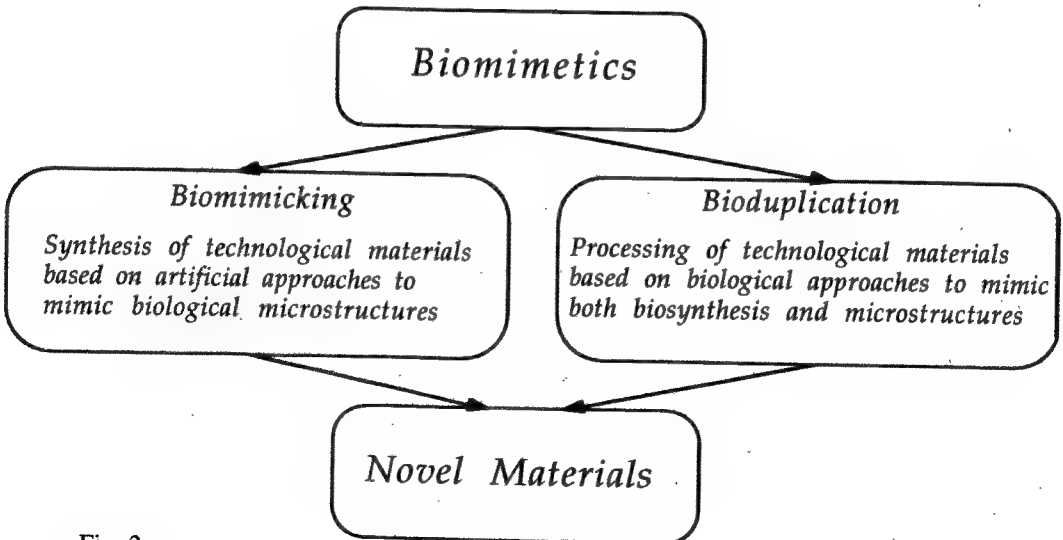
Fig. 3

BASIC LITERACY IN ELECTRON-EXCITED X-RAY MICROANALYSIS

Dale E. Newbury

National Institute of Standards and Technology, Gaithersburg, MD 20899

Electron beam x-ray microanalysis with energy dispersive x-ray spectrometry (EDS), as performed in electron probe microanalyzers (EPMA)/scanning electron microscopes (SEM) for thick specimens and analytical electron microscopes (AEM) for thin sections, is a powerful technique with wide applicability in the physical and biological sciences and technology communities.[1] The operation of an EDS x-ray microanalysis system has been automated to the point that many users now consider EDS to be a routine tool where the results reported by the automation system are always correct. Unfortunately, there are numerous pitfalls awaiting the unwary analyst. All EDS users require a basic level of literacy in x-ray microanalysis to properly interpret spectra and develop a sensible analysis strategy for their problems. This "basic literacy" includes knowledge of the factors controlling the efficiency of production of characteristic and continuum x-rays, the characteristic energies and structure of x-ray families that provide the basis for qualitative analysis, the operational characteristics of energy dispersive x-ray spectrometers, including artifacts, and the systematic procedures for qualitative and quantitative analysis. While it is useful to understand the physics of x-rays on a numerical basis, a pictorial approach is more accessible to the beginner in the field. One of the most valuable aids to achieving basic literacy is to develop a sense of what a "correct" x-ray spectrum actually looks like. Simulated spectra calculated from first principles as well as spectra measured under well-defined conditions can serve to graphically illustrate critical aspects of the generation, propagation, and EDS measurement of x-rays.[2] Some of the pertinent questions that can be considered by this pictorial approach include:

1. What is the basic form of the x-ray spectrum and how does the EDS measurement process affect it? An example of an ideal spectrum from a thick 75%Al-25% Zn target as generated within the specimen by incident 15 keV electrons is illustrated in Figure 1. The spectrum measured by EDS is superimposed. The measured spectrum deviates significantly from the generated spectrum. The peaks are broadened by a factor of 100 compared to the natural linewidth during the EDS measurement process, and the background shape is drastically altered as a result of absorption in the specimen and detector components. The efficiency of measurement varies markedly as a function of x-ray energy.

2. Can relative estimates of concentrations be made from comparisons of elemental peak height ratios? In addition to detection efficiency variations as a function of x-ray energy, the efficiency of characteristic x-ray generation depends strongly on the overvoltage (the ratio of beam energy to critical excitation energy), and x-ray self-absorption is strongly dependent on composition. Estimates of concentration ratios from raw interelement relative peak heights are therefore likely to be in considerable error, as illustrated in Figure 2 for a 75%Al-25% Zn specimen measured at 15 keV.

3. What is the role of artifacts in practical EDS measurements?
Artifacts always exist at some level in the spectrum measurement process and pose problems ranging from incorrect peak identification to increased errors in quantitative analysis. Artifacts can be divided conveniently into two classes: (1) physically inevitable and (2) experimentally preventable/reducible. Examples of physically inevitable artifacts include the peak broadening shown in Figure 1, as well as escape peaks, incomplete charge, and Si internal fluorescence. Experimentally preventable/reducible artifacts include pulse pileup, peak broadening due to ground loops, light leakage, and microphonics, and "system peaks" from scattered radiation. It is the responsibility of the analyst to recognize both types of artifacts and ensure that their presence does not compromise results, eliminating whenever possible the experimentally preventable artifacts. This can be a difficult task, since these artifacts may depend on the experimental details and may change unexpectedly with a change in operating parameters. Comparison of measured spectra to reference spectra which are artifact-free or which have known, well-characterized artifacts is an important part of good quality assurance procedures for EDS analysis.

References
1. Goldstein, J. I., Newbury, D. E., Echlin, P., Joy, D. C., Romig, A. D., Jr., Lyman, C. E., Fiori, C., and Lifshin, E., <u>Scanning Electron Microscopy and X-ray Microanalysis</u>, 2nd edition (Plenum Press, New York, 1992).
2. Fiori, C. E. and Swyt, C. R., Microbeam Analysis-1989, San Francisco Press, 236.
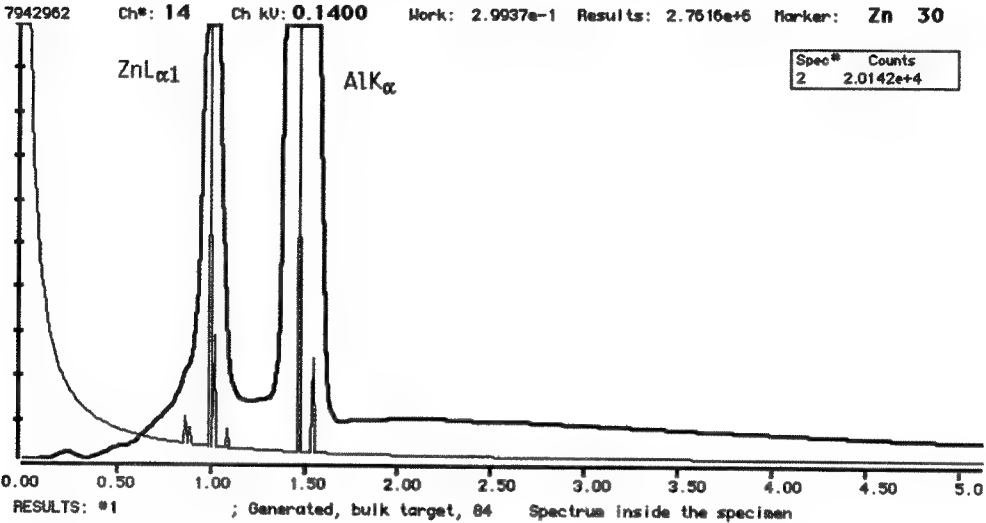
Figure 1 Simulated x-ray spectra for bulk 75%Al - 25%Zn, beam energy = 15 keV: thin trace = as generated within specimen; thick trace = as detected.
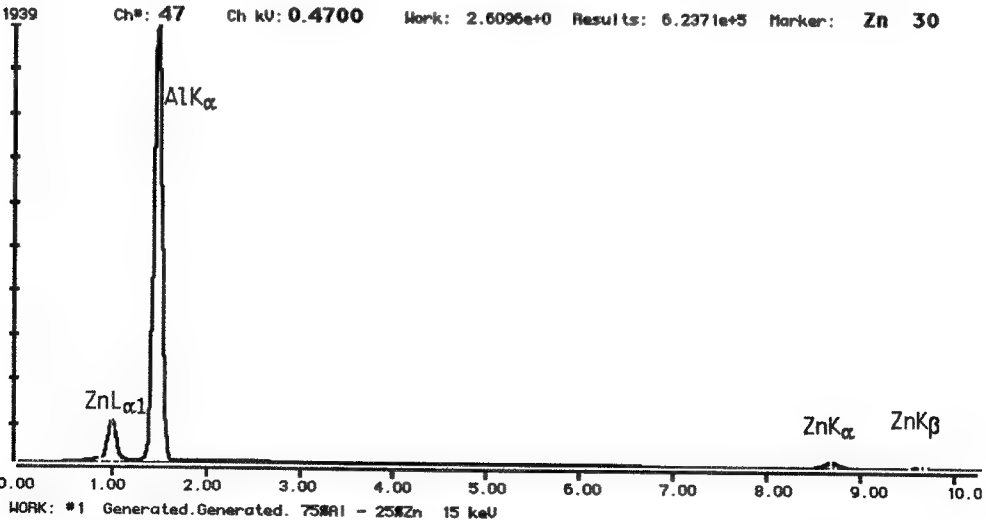
Figure 2 Calculated EDS spectrum as detected for bulk 75%Al - 25%Zn, beam energy = 15 keV, showing relative peak heights.

MICROSTRUCTURAL CHARACTERIZATION USING X-RAY DIFFRACTION IMAGING

David R. Black

Ceramics Division, National Institute of Standards and Technology, Gaithersburg, MD, 20899

X-ray diffraction imaging, also known as x-ray topography, is a powerful tool to study the defect microstructure of single crystals. As the name implies, this technique is based on recording an image of the diffracted x-ray beam from a crystal. Contrast in the image results from point-to-point variation in the diffracted intensity through the crystal. An example of a diffraction image is shown in figure 1. That this image is in some way a topographic representation of the sample can be seen in the impression of differing elevations and textures in different parts of the image. However, since this image is a result of diffraction from the sample the interpretation of the image is much more complex.

Diffraction contrast is usually separated into two types: mosaic contrast and extinction contrast. Mosaic contrast occurs for crystals considered to be formed from a collection of small perfect crystal blocks. These blocks have a well defined rocking curve width, the angular range over which they will diffract, and may be slightly misoriented with respect to each other and/or may have different lattice spacing. Diffraction from this type of crystal will produce regions of differing intensity and/or spatial separation or overlap of these different regions on the image. This type of contrast is seen in figure 1 where the images of different subgrains are shifted with respect to each other producing black and white boundaries as indicated on the image. Extinction contrast results from a change in the diffracted intensity from, for example, the deformed regions around localized lattice defects such as dislocations. This change in intensity is due to a reduction in primary extinction in these regions, hence the name extinction contrast. This type of contrast is shown in figure 2 where individual dislocations and stacking faults are visible. The different types of contrast, the experimental conditions required to produce them and the different types of defects that can be imaged will be discussed. Emphasis will be placed on experiments using synchrotron radiation.

The recent increase in the availability of high intensity x-ray beams from synchrotron radiation sources has opened the door to many experiments that would be either impractical or impossible using laboratory x-ray sources. A brief introduction to synchrotron radiation will be given and the advantages it brings to x-ray diffraction imaging will be discussed. Particular attention will be given to real time imaging experiments.

A bibliography of several review articles is given on page 2.

Bibliography

1) A. Authier, in Advances in X-ray Analysis Vol 10, New York: Plenum (1967) 9.
2) A. Authier, in Modern Diffraction and Imaging Techniques in Materials Science, Amsterdam: North-Holland (1969) 481.
3) B. Batterman and H. Cole, Reviews of Modern Physics, 36 #3, (1964) 681.
4) J. Chikawa and M. Kuriyama, in G. Brown and D. Moncton eds., Handbook on Synchrotron Radiation, 3 (1991) 3.
5) M. Kuriyama et al., Ann. Rev. Mater. Sci., 12, (1982) 23.
6) A. R. Lang, in Modern Diffraction and Imaging Techniques in Materials Science, Amsterdam: North-Holland (1969): 407.
7) B. K. Tanner, X-ray Diffraction Topography, Oxford: Pregamon (1976).
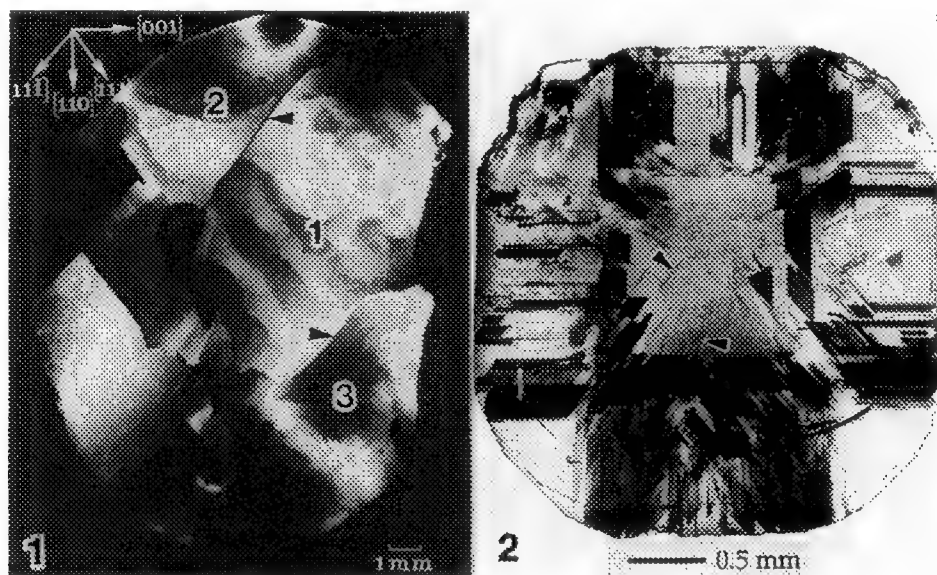
FIG 1. (220) surface reflection topograph from a nickel single crystal showing that this crystal is formed from several subgrains. The image from grain 1 overlaps grain 2, which produces the black boundary, and is shifted away from grain 3 which produces the white boundary.

FIG 2. (111) transmission topograph from an isotopically enriched man-made diamond crystal. Individual dislocations are visible in the central region, as indicated, while the black planar features towards the edges are stacking faults.

INTRODUCTION TO EMISSION ELECTRON MICROSCOPY FOR THE IN SITU STUDY OF SURFACES

Martin E. Kordesch

Condensed Matter and Surface Science Program, Department of Physics and Astronomy, Ohio University, Athens OH 45701 USA

The Photoelectron Emission Microscope (PEEM) and Low Energy Electron Microscope[1] (LEEM) are parallel-imaging electron microscopes with highly surface-sensitive image contrast mechanisms. In PEEM, the electron yield at the illumination wavelength determines image contrast, in LEEM, the intensity of low energy (< 100 eV) electrons back-diffracted from the surface, as well as interference effects, are responsible for image contrast. Mirror Electron Microscopy is also possible with the LEEM apparatus. In MEM, no electron penetration into the solid occurs, and an image of surface electronic potentials is obtained.

While the emission microscope techniques named above are not high resolution methods, the unique contrast mechanisms, the ability to use thick single crystal samples, their compatibility with uhv surface science methods and new material-growth methods, coupled with real-time imaging capability, make them very useful.

These microscopes do not depend on scanning probes, and some are compatible with pressures up to 10^{-3} Torr and specimen temperatures above 1300K. The use of such microscopes in situ, i.e. during a surface chemical reaction, during chemical vapor deposition, or during a surface process such as surface reconstruction, facetting or layer growth will be discussed.

References

1. W. Telieps and E. Bauer, Ultramicroscopy (1985) 17, 57.
2. This work was supported by the Office of Naval Research through SDIO/IST Grant No. N00014-J-1596, DARPA and NATO.

SELECTED BIBLIOGRAPHY:EMISSION MICROSCOPY IN PHYSICAL SCIENCES

I. General Introduction\References

1. Emission Microscopy and Related Techniques, Second International Symposium and Workshop, Seattle, WA. O.H. Griffith and W. Engel, editors. Ultramicroscopy (1991) 36, 1-275. Includes 20 articles, historical and technical reviews, newest hardware, and bibliography of PEEM, LEEM and related work: 1985-91. There is some duplication in the list below.

II. Photoelectron Emission Microscopy

2. A. Garcia. C. Wang and M.E. Kordesch, Appl. Phys. Lett. (1992) 61, 2984.

3. C. Wang, et al. Electronics Lett. (1991) 27, 1459.
** Carbon Monoxide/Platinum Systems:
4. H.H. Rotermund, Surf.Sci. (1993) 283, 87.
5. M. Ehsasi, et al., Ultramicroscopy (1993) in press.
6. H.H. Rotermund, et al. Surf. Sci. (1992) 275, L645.
7. G. Veser and R. Imbihl, Surf. Sci. (1992) 269/270, 465.
8. M. Bar, et al. Phys. Rev. Lett. (1992) 69, 945.
9. G. Ertl, Science (1991) 254, 1750.
10. M. Mundschau and B. Rausenberger, Platinum Metals Rev. (1991) 35, 188.
11. H.H. Rotermund, et al. Phys. Rev. Lett. (1991) 66, 3083.
12. H.H. Rotermund, et al. Nature (1990) 343, 355.
13. S. Jakubith, et al. Phys. Rev. Lett. (1990) 65, 3013.
14. M. Mundschau, et al. Surf. Sci. (1990) 227, 246.

III. Low Energy Electron Microscopy

15. B. Rausenberger, et al. Surf. Sci. in press.
** Silicon Surfaces
16. A.W. Denier van der Gon and R. M. Tromp, Phys. Rev. Lett. (1992) 69, 3519.
17. R.M. Tromp, A.W. Denier van der Gon and M.C. Reuter, Phys. Rev. Lett. (1992) 68, 2313.
18. R.M. Tromp and M.C. Reuter, Phys. Rev. Lett. (1992) 68, 954. and Phys. Rev. Lett. (1992)
19. R.J. Phaneuf, et al., Phys. Rev. Lett. (1991) 67, 2986.
** Spin Polarized LEEM
20. H. Pinkvos, et al. Ultramicroscopy (1992) 47, 339.
21. M.S. Altman, et al. Mater, Res. Soc. Symp. Proc. (1991) 232, 125.
** Bio LEEM
22. O.H. Griffith, et al., J. Microsc. (1992) 168, 249.

IV. Synchrotron PEEM

23. J. Stohr, et al. Science (1993) 259, 659.
24. G. Margaritondo and F. Cerrina, Nuc. Inst. Method.A (1990) 291, 26. Review

V. Electron Optics/prospects for improvement

25. G.F. Rempfer, O.H. Griffiths, Ultramicroscopy (1992) 47, 35.

VI. Miscellaneous Favorites

26. W. Telieps, Appl. Phys. A,(1987)44, 55.
27. E. Bauer and W. Telieps, in Surface and Interface Characaterization by Electron Optical Methods, A. Howie and U. Valdre, eds. New York: Plenum Publishing Corp. 1988.
28. R.A. Schwarzer, Microscopica Acta (1981) 84, 51.
29. J. Pohl, Physik. Zeitschr. (1934) 35, 1003.

SCANNED PROBE MICROSCOPY IN BIOLOGY

Knute A. Fisher

Departments of Anatomy and Biochemistry & Biophysics, and Francis I. Proctor Foundation, University of California, San Francisco, CA 94143-0944

HISTORY: Numerous scanned probe microscopes (SPM) have been developed over the past decade.[1] Most are based on the precise positioning of sample and probe using piezoelectric transducers, and some have the capability of imaging flat surfaces with atomic resolution. The first atomic resolution SPM applied to biological samples was the scanning tunneling microscope (STM).[2] The atomic force microscope (AFM) was subsequently developed[3] and over the past few years has become the instrument of choice for biological applications.

SCANNING TUNNELING MICROSCOPY: Early investigators applied the STM to examinations of organic and biological systems ranging from small molecules to nucleic acids, globular and fibrillar proteins, and larger structures such as viruses, membranes, and even whole cells.[4] Much of this work was done during the mid-80s using electrically-conductive highly-oriented pyrolytic graphite (HOPG) as a substrate. Images were often difficult to obtain and control experiments were lacking. Unfortunately, when careful experiments were undertaken, they revealed that HOPG itself was capable of generating images previously thought to be biological. The HOPG artifact problem was exacerbated by the absence of convincing explanations of image formation by non-conducting samples, and by the lack of information that wasn't of the "me-too" variety. The unfulfilled expectations of easily achieved atomic resolution images of biological samples, plus the concerns just outlined established a somewhat shaky beginning for SPM in biology. At the same time it should be remembered that some exquisite and reproducible high-resolution STM imaging was accomplished with planar two-dimensional arrays such as liquid crystals and Langmuir-Blodgett films. In addition, several studies of metal-coated samples mounted on glass or mica, or freeze-fractured, demonstrated that the STM could be used to study features of biological interest. For example, the height of a phospholipid ridge in a freeze-fractured replica, and the thickness of a biological membrane and change in thickness after enzymatic cleavage, were examined.

ATOMIC FORCE MICROSCOPY: The conductivity problem in STM was overcome by the development of AFM and subsequent development of an optical detector for reproducibly measuring the deflection of the AFM cantilever. Given suitable and commercially available instruments by the late-80s, the study of insulating as well as conductive samples could be initiated in earnest. For biological applications, several problems remain.[5] AFM resolution is limited by physical and chemical properties of the tip and by tip-sample interactions. Recently a variety of tips have been developed that are intended to improve resolution. With soft biological samples, however, simply reducing the size of the tip and/or producing more needle-like shapes has not significantly improved resolution, since the force is distributed over a larger area of the sample with a dull tip than with a sharp tip. Even with dull tips, the forces may still move or perturb soft samples. Nevertheless, exciting biological images are now being achieved at 2-10 nanometer resolution.

SAMPLE PREPARATION: In the past few years attention has been given to preparing samples especially suited to AFM. Most of these approaches have employed methods to tether the sample to the substrate. For STM, coating with metal stabilizes the sample for subsequent scanning. For AFM, attachment of samples to mica ionically or covalently has led to reproducible imaging.[6] Because sample preparation and reproducible imaging has been a significant problem for SPM, obtaining images with relative ease has been a significant recent advancement for the field.

APPLICATIONS: Although there continue to be STM studies of biological samples, SPM investigators have increasing turned to the AFM. For example, AFM is being used to examine single linear molecules such as nucleic acids and collagen monomers; model lipid monolayers, bilayers, and multilayers; native and reconstituted biomembranes; and intact hydrated cells.

FUTURE: Other SPM instruments such as the near-field scanning optical microscope will undoubtedly be developed for biological applications. For AFM, as high-resolution tips continue to be developed, it will be necessary to focus increasingly on sample stabilization methods and/or to explore alternative imaging modes such as the non-contact modes of scanning. One approach we have taken to improve sample stability has been to develop a low-temperature AFM that can scan frozen samples.[7] We have imaged nucleic acids, ferritin molecules, collagen monomers, and purple membrane at 143 K and have found improved reproducibility, and instrument stability and sensitivity, but with resolution still apparently tip limited. Clearly the future of AFM lies in its unique capability of imaging hydrated samples in real time. Perhaps the most important advance for AFM in biology will be in asking appropriate questions! For example, rather than asking for the atomic structure of an active site of an enzyme, one might more reasonably ask for details of hydrated enzyme-substrate interactions (protein-protein or protein-nucleic acid). The future also will increasingly demand labels and approaches to identify structures unequivocally. In summary, for AFM to continue as a viable and creditable microscopic method will require increasingly thoughtful approaches, from experiment design to image interpretation.

References

1. H.K. Wickramasinghe, *Sci. Amer.* (1989) **Oct**, 79.
2. G. Binnig and H. Rohrer, *IBM J. Res. Dev.* (1986) **30**, 355.
3. G. Binnig et al., *Phys. Rev. Lett.* (1986) **12**, 930.
4. K.A. Fisher, *J. Elect. Microsc. Tech.* (1989) **13**, 355.
5. P.K. Hansma et al., *Science* (1988) **242**, 209.
6. H.G. Hansma et al., *Science* (1992) **256**, 1180.
7. K.A. Fisher et al., *Proc. Ann. EMSA Meet.* (1991) **49**, 54.
8. Supported by grants from NIDA, number DA05043, and NEI, number EY02162.

QUANTITATIVE AFM OF LANGMUIR-BLODGETT FILMS

R. Viswanathan, J. Garnaes, D. K. Schwartz and J. A. N. Zasadzinski

Department of Chemical and Nuclear Engineering, University of California, Santa Barbara, CA 93106

Because of their applications in the areas of non-linear optics, molecular electronics, and biosensors, Langmuir-Blodgett (LB) films have been extensively studied by a wide variety of scattering and spectroscopic techniques. The atomic force microscope[1] has emerged as an important tool for studying LB films because of its unprecedented ability to quantitatively measure films with high resolution.

The unique abilities of quantitative AFM imaging motivated us to investigate the effect of incorporating different divalent metal cations and fatty acids of different chain length into films deposited on both amorphous and ordered substrates. Once substrate effects have been accounted for, multilayer Langmuir-Blodgett films of palmitic, stearic and arachidic acid salts show that the area per molecule is primarily controlled by the detailed interactions of the counterion with the carboxylic acid group. However, the lattice dimensions and symmetry are dictated by the close packing of the alkane chains, given the constraint of area per molecule set by the counterion. Hence, AFM studies of molecular organization of fatty acid LB films may be ideal systems to check molecular dynamics calculations of alkane packing. This limiting area per molecule decreases with the degree of ionic versus covalent bonding of the metal ion with the carboxylic acid moiety, with barium arachidate (BaA) > manganese arachidate (MnA) > cadmium arachidate > lead stearate (PbSt) (Figure 1). For BaA and MnA the increased molecular area is sufficient to induce tilt in the molecular packing. The lattice parameters, symmetry, and area per molecule are independent of the length of the alkane chain of the fatty acid for all cations and substrates examined (See Table 1).

However, the choice of substrate does have a dramatic effect on the structure of monolayer and multilayer films for both PbSt and MnA. Monolayers of PbSt deposited on crystalline mica have long range order while monolayers of MnA on mica show a distinct but short-ranged order. Otherwise identical PbSt and MnA monolayers are completely disordered on amorphous oxidized silicon. Both PbSt and MnA monolayers on mica have a significantly larger lattice spacing and molecular area than do the corresponding multilayers on mica, indicating a strong coupling to the mica lattice (Table 1). For PbSt trilayers on mica, the molecular area and lattice parameters were significantly larger than those of PbSt trilayers on oxidized silicon. The monolayers of both BaA and CdA were disordered, and for CdA no structural differences were observed between multilayer films deposited on oxidized silicon or mica. In addition, the periodic height modulation changed in wavelength from a value of ~ 1.9 nm in the case of Cd to ~ 1.2 nm for Mn.[2] The wavelength of the height modulation is independent of the length of the alkane chain for a given cation, in contradiction to theory. No height modulation was observed for Pb. BaA films had three distinct lattice arrangements that included stacking faults and offsets by individual methylene units; however, all BaA lattice structures had the same molecular area.

Atomic force microscopy can provide the most detailed real and Fourier space information available on the structure of Langmuir-Blodgett films of fatty acid salts. Although the multilayer films of all but BaA have similar packing symmetry, the variation in the unit cell dimensions is related to the degree of covalent bonding between the metal ion and the carboxylic acid group, and to specific interactions with the substrate. The structure and extent of positional correlations of the monolayer films are dramatically affected by a change in cation and are related to substrate interactions. The period of buckling modulation is also altered by a change in cation, but not by a change in the alkane chain length.[3]

1. G. Binnig, C. F. Quate, and Ch. Gerber, *Phys. Rev. Lett.,* (1986)56, 930.
2. J. Garnaes, et al. *Nature,* (1992) 357, 54.
3. This work was supported by the Office of Naval Research under grant #N00014-90-J-1551.

Material	layers	substrate	a_1 (nm)	a_2 (nm)	mol. area (Å^2)	tilt angle	corr. len. (nm)	mod. period (nm)
PbSt	1	mica	0.447 ± 0.006	0.922 ± 0.008	20.6	0°	>40	none
PbSt	3	mica	0.514 ± 0.006	0.752 ± 0.008	19.3	0°	>40	none
PbSt	5	mica	0.497 ± 0.006	0.739 ± 0.008	18.4	0°	>40	none
PbSt	7	mica	0.493 ± 0.006	0.728 ± 0.008	17.9	0°	>40	none
PbSt	3	silicon	0.492 ± 0.006	0.728 ± 0.008	17.9	0°	>40	none
PbSt	1	silicon	none	none	?	?	?	none
CdA	1	mica	none	none	19.4	?	0	none
CdA	3	mica	0.482 ± 0.006	0.748 ± 0.008	18.0	0°	>40	1.9 ± 0.3
CdA	3	silicon	0.482 ± 0.006	0.748 ± 0.008	18.0	0°	>40	1.9 ± 0.3
MnA	1	mica	0.46 ± 0.01	0.87 ± 0.02	20.0	?	~3	none
MnA	3	mica	0.495 ± 0.006	0.791 ± 0.008	19.6	19°	>40	1.18 ± 0.08
MnA	5	mica	0.481 ± 0.01	0.812 ± 0.01	19.5	19°	>40	1.18 ± 0.08
MnA	3	silicon	0.477 ± 0.006	0.834 ± 0.008	19.9	19°	>40	1.18 ± 0.08
MnA	1	silicon	none	none	none	?	0	none
BaA	1	mica	none	none	none	?	0	none
BaA (1)	3	mica	0.44 ± 0.01	1.52 ± 0.01	20.4	26°	>40	none
BaA (2)	3	mica	0.94 ± 0.01	0.94 ± 0.01	20.2	19°	>40	none
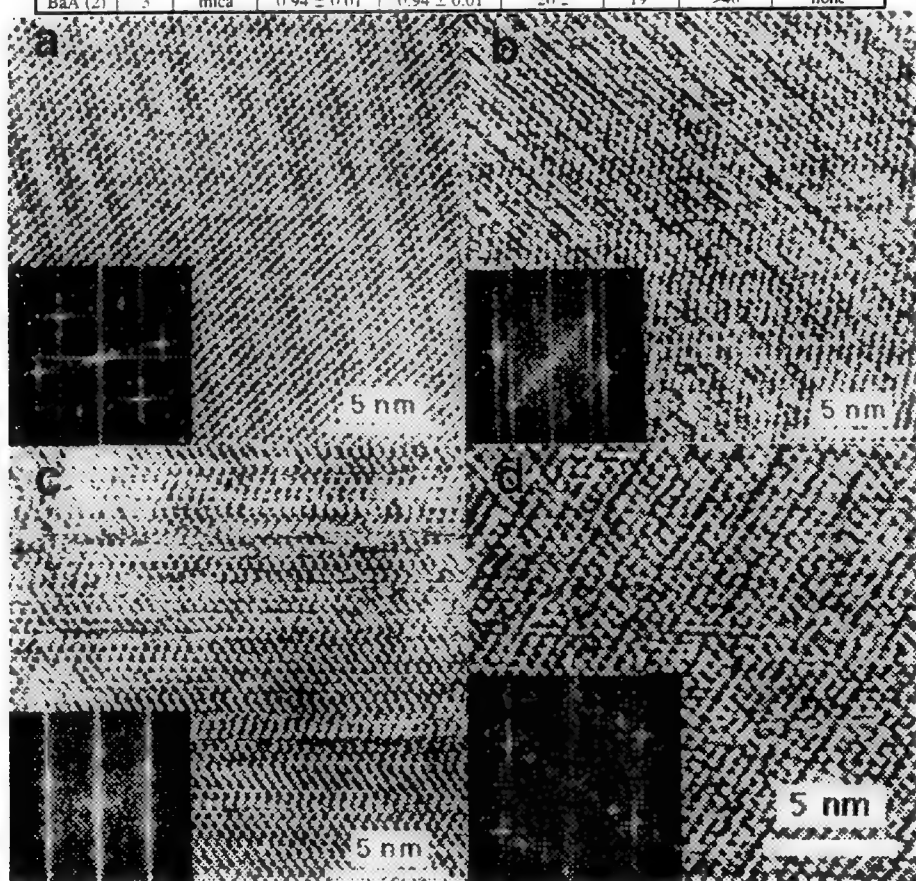
FIG. 1. AFM images of trilayer films of a) CdA; b) MnA; c) PbSt; and d)BaA with the Fourier transforms of the images inset. From the FT's we can quantitatively determine the lattice parameters and symmetry of the films, and by correlating with the images, we can determine the real space packing.

IMAGING BIOLOGICAL SAMPLES WITH THE ATOMIC-FORCE MICROSCOPE

Eric Henderson, Daniel Jondle, Thomas Marsh, Wen-Ling Shaiu, Luming Niu, James Vesenka, *Elis Stanley and Philip Haydon

2112 Molecular Biology, Department of Zoology and Genetics, Iowa State University, Ames, IA 50011. *National Institutes of Health, Bethesda, MD

The application of atomic force microscopy (AFM) to biological investigation is attractive for a number of reasons. Foremost among these is the ability of the AFM to image samples, even living cells, under near native conditions and at resolution equal to, or exceeding, that possible by the best light microscopes. Moreover, the ability of the AFM to manipulate samples it images provides a novel and far reaching application of this technology.

We have been studying a number of biological samples by AFM. These include conventional and non-conventional nucleic acid structures, ribosomes, neural cells and synapses, cellular organelles (chloroplasts and nuclei), among others. Each of these projects has its own set of associated difficulties and each reveals information about the uses and limits of the AFM in biology. Fig. 1 shows AFM images of various biological samples. In the case of nucleic acids, which have been extensively studied in a number of labs by AFM the problems of signal/noise sample deposition have been overcome in air and organic solvents. Recently imaging of DNA in aqueous environments has been accomplished. Small biomolecules like ribosomes present the problem of deconvolving the tip architecture from the image. Mathematical algorithms to do this have been developed and methods for tip shape characterization and new tip construction are ongoing. Successful imaging of living cells is very dependent upon the type of cell, the type of tip, the growth substrate and imaging parameters such as applied vertical force and scan rate. Cellular organelles, lacking the extensive supportive skeletal structures found in some cells, have been extremely difficult to image in their native state, although images of fixed samples are routinely obtained.

One of the obvious future developments in AFM is the integration of this method with other imaging methods, for example, fluorescence and light microscopy. We have constructed a prototype coaxial optical/atomic force microscope. Similar instruments have been constructed by other laboratories . With these instruments one can visualize a biological (or other) sample with bright field, dark field or fluorescence microscopy and position the scanning tip over a region of interest . Subsequent scans of this area reveal surface topography and other information about the sample. In our laboratory this approach has been applied to the study of cellular cytoskeleton and chromatin structure. Fig. 1 shows fluorescence and AFM micrographs of *Xenopus* retinal glial cells (panels g and h) and a *Drosophila* polytene chromosome (panel i). Further development in this area is ongoing.
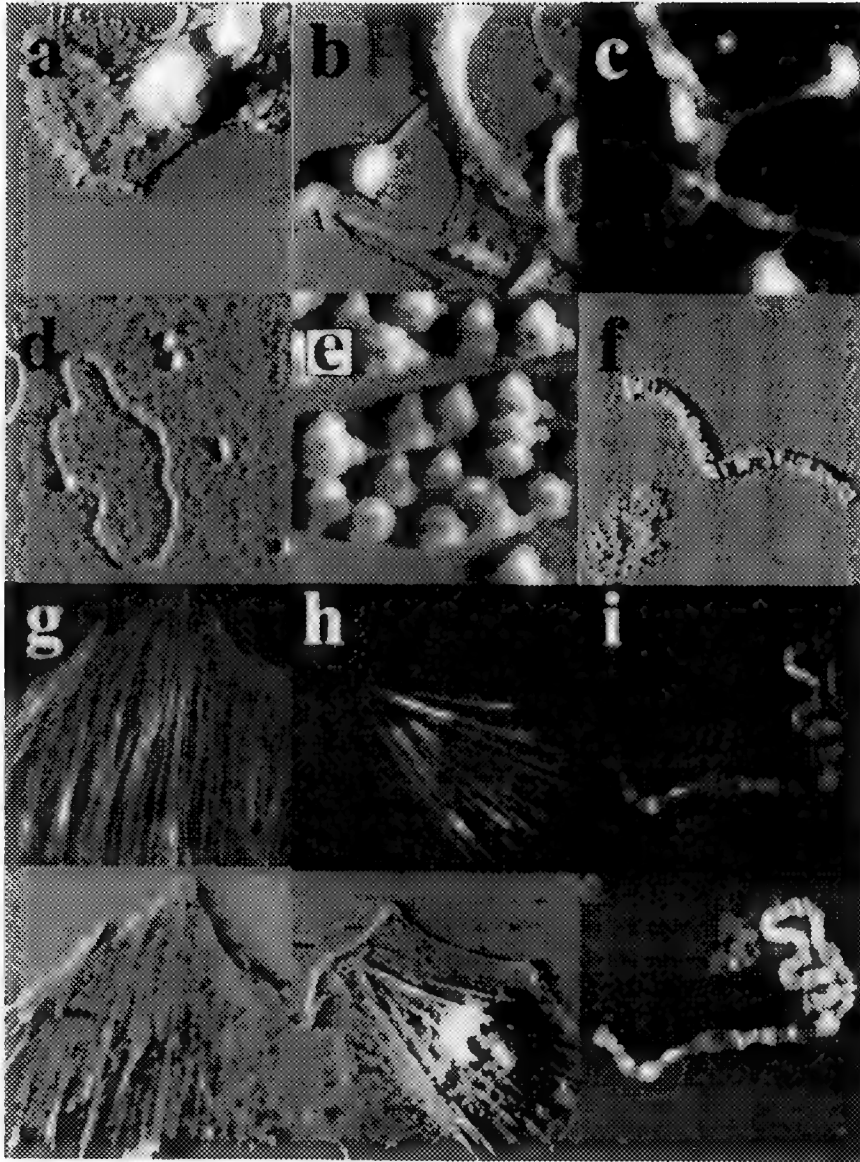
Fig. 1. AFM of biological samples. a, living *Xenopus* retinal glial cell, b, living rat hippocampal neuron and glial cells, c, specialized nerve terminal (calyx) from chicken, d, plasmid DNA bound by the restriction endonuclease EcoRI, d, bacterial large ribosomal subunits, f, fragment of a *Drosophila* polytene chromosome, g and h, fluorescence (top) and AFM micrographs of fixed *Xenopus* retinal glial cells, i, fluorescence (top) and AFM micrographs of *Drosophila* polytene chromosome. Approximate field sizes are, a, b, g and h, 80 μ^2; c, f and i, 20 μ^2; d, 1 μ^2; and e, 0.5 μ^2.

STRAINED-LAYER VAN DER WAALS EPITAXY IN A LANGMUIR-BLODGETT FILM

Ravi Viswanathan

Department of Chemical & Nuclear Engineering, University of California at Santa Barbara, Santa Barbara, CA 93106

Langmuir-Blodgett (LB) films are layered structures of amphiphilic molecules which are assembled by successive deposition on a solid substrate from a monolayer at the air water interface. Most of the potential applications of LB films (molecular electronics, cell membrane models, biosensors) are based on the premise of perfect molecular layering and orientation. The technique of atomic force microscopy (AFM), which probes only the outermost layer of the film, has opened up the study of the surfaces of these films which occupy a unique position at the intersection of surface science and complex fluids. We show here that the growth of lead stearate (PbSt) LB films on mica substrates proceeds by a new type of epitaxy which we call "strained layer van der Waals epitaxy" because it represents a compromise between the mechanisms of strained-layer epitaxy and van der Waals epitaxy.[1]

The PbSt films were prepared with the standard Langmuir-Blodgett vertical dipping method and imaged with the AFM in air at ambient temperature.[2] After the fatty acid films were imaged, the films were cleaved, and the underlying mica substrate was imaged. The concept of strained-layer epitaxy is familiar from semiconductor systems wherein the first monolayer of an adsorbed film, which has a bulk lattice constant no more that a few percent different from that of the substrate, replicates the in-plane structure of the substrate exactly and subsequent layers gradually relax to the bulk structure of the adsorbate. For PbSt films on mica, however, the bulk crystal structure has a significant mismatch with the substrate in both lattice constants and symmetry. Hence the ordering field of the mica, in addition to the strong intralayer interactions (surface viscosity, elasticity) within the PbSt film, helps to induce long-range positional order in a monolayer. The monolayer is aligned with respect to the mica substrate and has a similar repeat distance with the substrate in only one direction. The surface lattice constants gradually relax to their bulk values as successive bilayers are deposited. Our results suggest that better ordering in LB films might be achieved 1) by designing molecules to maximize intralayer interactions while minimizing interlayer interactions;[3] and 2) by coupling the LB films to a substrate with similar lattice symmetry. Table 1 shows the lattice parameters (a_1 & a_2) for all of the films. Note the dramatic decrease in molecular areas as number of layers increases. The figures show molecular resolution images of a monolayer and the underlying mica substrate, as well as the respective Fourier transforms.

The centered-rectangular PbSt monolayer is deposited on the hexagonal mica substrate in a well-defined orientation such that there is a close match between one set of lattice rows of monolayer and substrate. However, the other lattice constants of the monolayer are far from commensurate with the substrate. The adsorbed layer (as well as subsequent layers) is oriented with respect to the substrate and has long range positional and orientational order. This type of growth has been termed van der Waals epitaxy and is common to adsorbates and substrates that form bulk layered structures with strong intra-layer interactions but weak and non-specific inter-layer interactions. Subsequent bilayers revert to the thick film type of packing, non-centered rectangular, but the values of the lattice constants relax gradually from bilayer to bilayer towards the bulk values. PbSt films on mica reach their bulk structures after 7 layers. This is different from PbSt films on silicon, which reach their bulk structures at 3 layers. This is due to the amorphous silicon surface, which does not have an ordering field like mica to induce order in a monolayer.[1,4]

References

1. K. Ueno, et al., *J. Vac. Sci. Tech. A* (1990) **8**, 68; A. Koma, et al., *Appl. Surf. Sci.* (1989) **41/42**, 451; F.S. Ohuchi, et al., *J. Appl. Phys.* (1990) **68**, 2168.
2. D.K. Schwartz et al., *Science* (1992) **257**, 508.
3. C.J. Eckhardt, et al., *Langmuir* (1992) **8**, 2591.
4. This work was funded by the Office of Naval Research Grant #N00014-90-J1551.

Table 1

Material	layers	substrate	a$_1$ (nm)	a$_2$ (nm)	mol. area (Å^2)
PbSt	1	mica	0.447 ± 0.006	0.922 ± 0.008	20.6
PbSt	3	mica	0.514 ± 0.006	0.752 ± 0.008	19.3
PbSt	5	mica	0.497 ± 0.006	0.739 ± 0.008	18.4
PbSt	7	mica	0.493 ± 0.006	0.728 ± 0.008	17.9
PbSt	3	silicon	0.492 ± 0.006	0.728 ± 0.008	17.9
PbSt	1	silicon	none	none	?
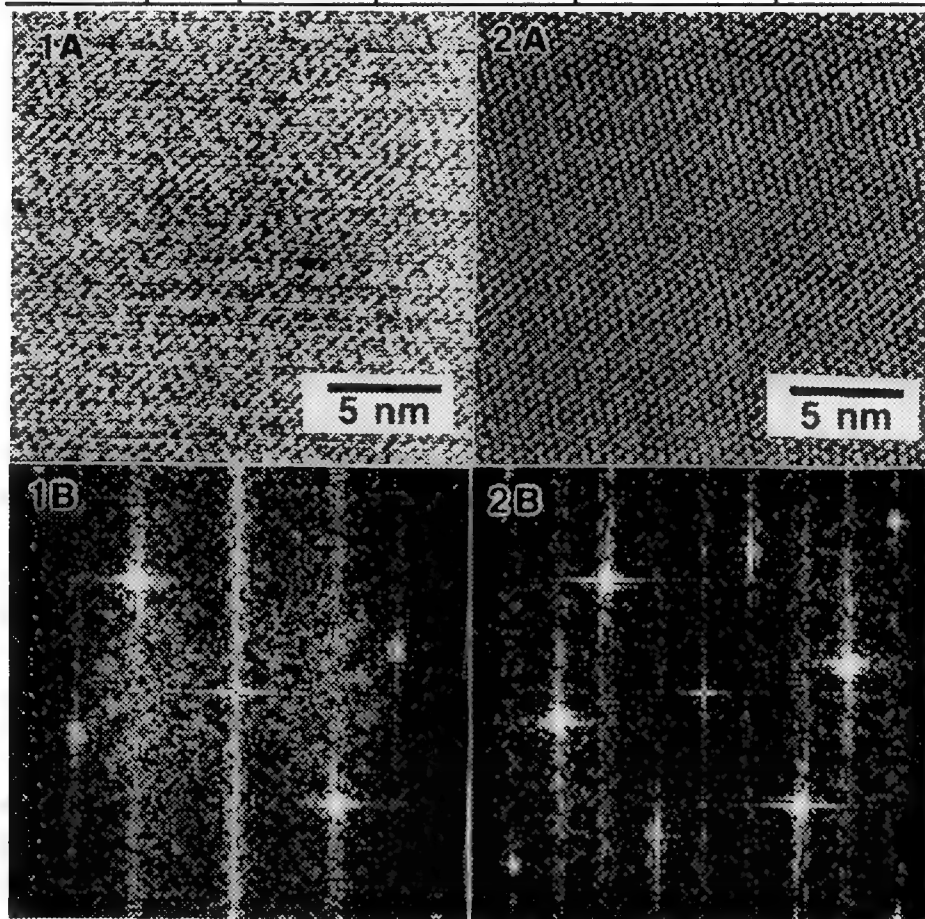
FIG. 1A -- Molecular resolution 20 nm x 20 nm image of monolayer of PbSt on mica.
FIG. 1B -- Fourier transform of FIG. 1A showing 3 pairs of spots, each corresponding to different lattice row direction.
FIG. 2A -- Molecular resolution 20 nm x 20 nm image of underlying mica lattice after cleavage.
FIG. 2B -- Fourier transform of FIG. 2A showing 3 pairs of spots. Note similarity in orientations of the spots as compared to monolayer (FIG. 1A & 1B).

NON-CONTACT ATOMIC-FORCE MICROSCOPY OF SOFT SURFACES

R. S. Howland*, D. F. Oot*, R. Nowroozi-Esfahani**, G. J. Maclay***, P. J. Hesketh***

*Park Scientific Instruments, 1171 Borregas Avenue, Sunnyvale, CA 94089
**SensAct, Inc., Chicago, IL 60680;
***EECS Department, University of Illinois at Chicago, Chicago, IL 60680

The atomic force microscope (AFM) was invented in the mid-1980s, in response to strong interest in the high resolution, real-space surface imaging capabilities of the scanning tunneling microscope (STM). The AFM provides one real benefit that the STM cannot: it is able to image insulating surfaces. As a result, the AFM can operate on a wider variety of samples; it also can image samples in air, where many conductors oxidize rapidly, and in solution. Essentially no surface preparation is necessary. Historically, however, even the AFM has had limitations. Until recently, the contact forces exerted by the AFM tip on the sample surface meant that AFM was limited to surfaces of substantial rigidity. Non-contact AFM removes that barrier, opening up the possibility of AFM imaging of very soft surfaces, or of surfaces that cannot be contaminated by contact with the tip.

An AFM uses a piezoelectric transducer to scan the sample beneath a sharp probe. The probe is mounted on a cantilever of very low force constant, which deflects as the atoms of the tip interact with the atoms of the sample surface. The deflection is typically read by bouncing a laser beam off the back of the cantilever, and into a position-sensitive photo detector. When the cantilever deflects, it changes the position of the beam on the photo detector, activating a feedback loop that causes the scanner to extend or contract to bring the cantilever deflection back to its operating position. A map of the extension of the scanner in Z as a function of its position in X and Y generates an image of the surface topography.

In traditional contact AFM, electrostatic repulsion from interpenetration of the electron clouds of the tip and sample causes the deflection of the cantilever and ultimately produces a topographic image. The size of the total force between tip and sample for contact AFM is on the nano-Newton scale, large enough to cause local deformations or even destruction in soft samples. Non-contact AFM employs the attractive van der Waals force that arises from induced dipole interactions between atoms separated by 50 to 100Å, to image the surface topography. The attractive van der Waals force is in the pico-Newton range, small enough that even a drop of liquid on the surface of a sample may be imaged without deformation.

Other solutions to AFM imaging of soft samples have also been employed. A technique popularly termed "tapping mode" removes the lateral component of the force in contact AFM by tapping the tip against the surface of the sample, and monitoring the damping of the tapping motion. The smearing effect often seen in contact AFM images of soft samples is removed; however, vertical forces remain in the nano-Newton range, and the contamination issue is not addressed. The most serious limitation, however, is that the resulting image can represent a convolution of topographic and elastic properties. True non-contact AFM is the preferable technique for imaging soft surfaces at present.

Because the deflections of the cantilever for non-contact AFM are too small to be detected using the optical-lever technique described for contact AFM, another detection method is used. Cantilevers are vibrated near their resonance frequency, and the amplitude shift that occurs when the tip and sample begin to interact is monitored. This method requires the fabrication of stiffer cantilevers than those typically used for contact AFM.

516
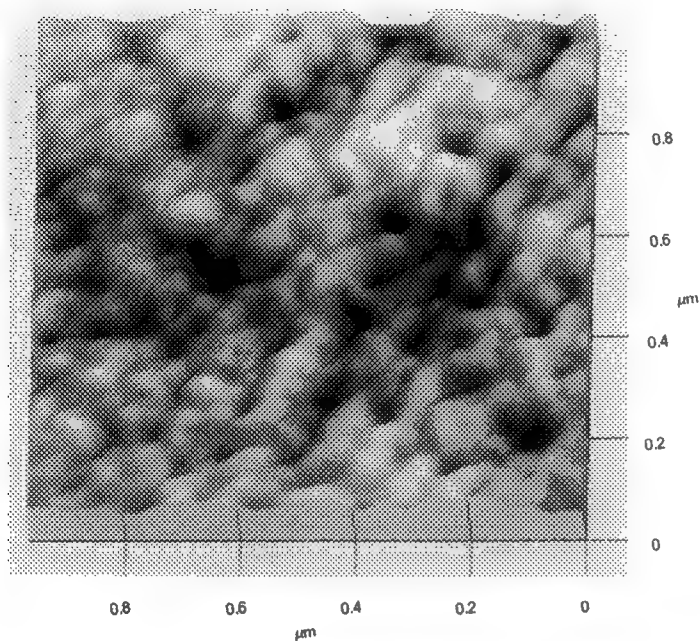
Traditional contact AFM image of surface of thin film of 25Å of platinum on 1000Å of SiO_2 on silicon substrate. The sample was prepared by electron-beam evaporation at 10^{-8} torr. Rounded depressions and asperities are evident, but finest details are obscured by deformation of surface by contact with AFM tip.
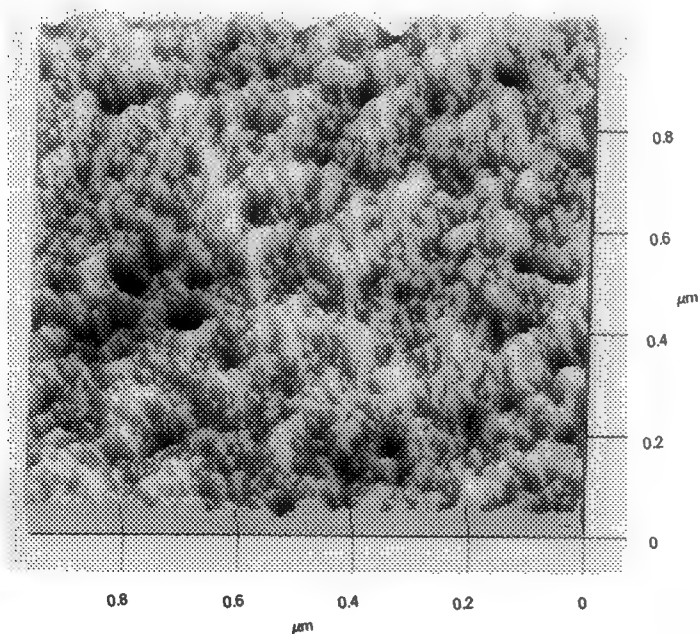
True non-contact AFM image of platinum film, showing not only larger-scale depressions and asperities, but also fine surface roughness. RMS roughness of the surface is measured by AFM as 3.2Å.

CONTACT AND NON-CONTACT ATOMIC-FORCE MICROSCOPY OF TYPE I COLLAGEN

Ellen A.G. Chernoff [a], Donald A. Chernoff [b], and Kevin Kjoller [c]

[a]Department of Biology, Indiana University-Purdue University at Indianapolis (IUPUI), 723 W. Michigan Street, Indianapolis, IN 46202; [b]Advanced Surface Microscopy, Inc., 6009 Knyghton Road, Indianapolis, IN 46220; [c]Digital Instruments, Inc., 520 E. Montecito, Santa Barbara, CA, 93103

Introduction. Type I collagen was examined using two types of atomic force microscopes (AFM) in a continuing effort to refine the process of obtaining molecular information from biological materials using scanning probe microscopy. Operating in air, a contact mode (Nanoscope II) and a non-contact mode AFM (Nanoscope III) were used to image collagen fibrils polymerized from pepsin-extracted type I bovine skin collagen adsorbed onto mica substrates. AFM is a practical method for high resolution examination of extracellular matrix material without the time consuming preparative techniques required for electron microscopy.

Methods. For fibrillar collagen samples, Vitrogen 100 (Collagen Corporation, Palo Alto, CA) was prepared according to a modification of the procedure provided by Collagen Corp. for neutralized isotonic collagen gels[1]. Monomeric collagen samples were prepared by diluting the vitrogen in 0.012M HCl[1].

Images captured with the Nanoscope II AFM (Digital Instruments, Santa Barbara, CA) used a "J" scanner (horizontal range of 120 um). "Medium" force constant probes were used (200 um silicon nitride cantilevers with 36 um wide legs). Contact AFM images are displayed in topview, height mode. Image files are presented essentially unfiltered; in some cases the "Flatten" filter was used to remove noise-induced steps parallel to the Y-axis. D-band measurements were made directly from screen displays using the Nanoscope II software. Images captured with the Nanoscope III (Non-contact AFM) used "tapping mode". Images are displayed in topview or perspective view using a combined height and slope mode.

Results. Monomeric collagen samples, examined by contact mode AFM, form a meshwork (Figure 1). Occasionally oligomeric structures are found in monomer samples (Figure 2). Contact mode fibrillar collagen images show well-defined D-banded fibrils with a banding period of 70nm (Figure 3). Using the non-contact AFM operating in "Tapping Mode" we obtained further, higher resolution information from the fibrillar samples (Figure 4). This mode provides higher resolution because the probe touches the soft sample more gently. Sub-bands at intervals as small as 30 nm are found in both the regions of subunit overlap and in the gap region in a repeating pattern ("wide valley-bump-bump"). The asymmetry of this pattern agrees with the banding pattern seen in TEM with negative staining and this allows us to identify the C-terminal direction of the fibril.

1. E.A.G. Chernoff and D.A. Chernoff, J. Vac. Sci. and Tech. A (1992)10, 596.
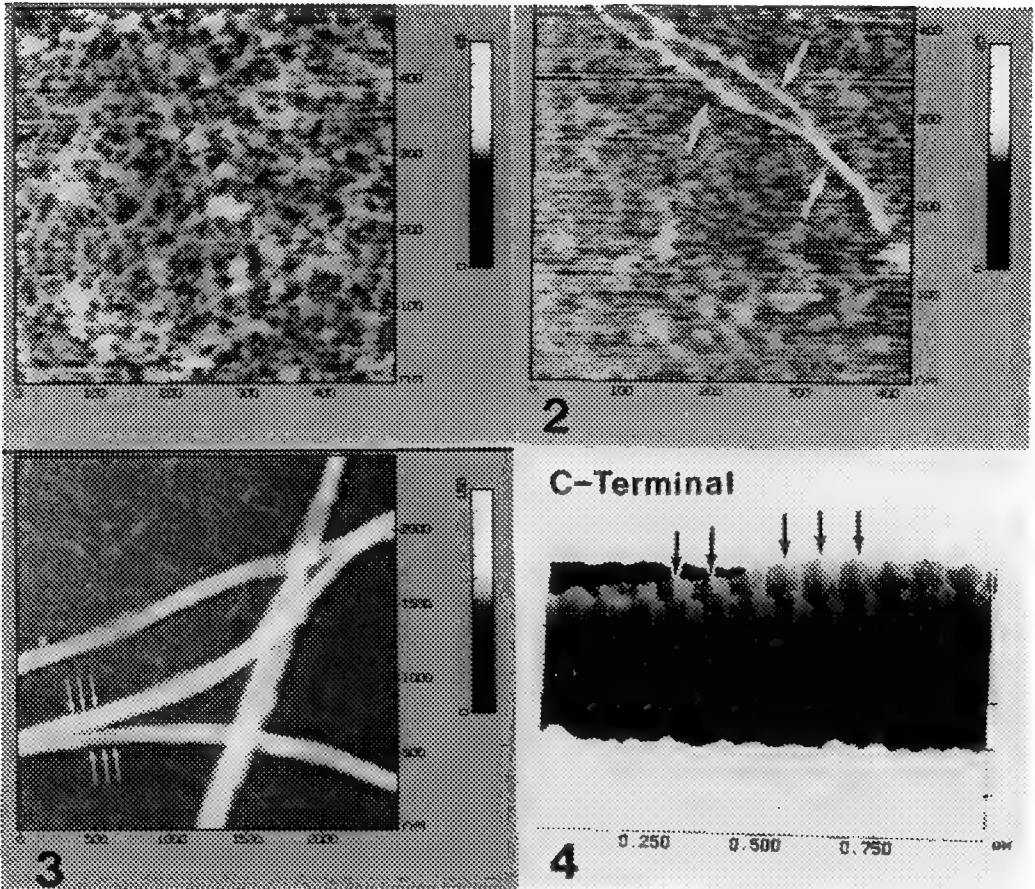
FIG. 1.--Contact mode AFM image showing collagen monomer preparation. The monomers form a fine meshwork. Horizontal range = 500 nm (0.5 μm)

FIG. 2.--Collagen monomer preparation in which a larger structure was seen (arrows), with dimensions suggesting that it was an oligomeric fibril. Horizontal range = 450 nm (0.45 μm).

FIG. 3.--Contact-mode AFM image of fibrillar collagen showing characteristic D-banded fibrils. Arrows indicate the location of the gap regions. Horizontal range = 2500 nm (2.5 μm)

FIG. 4.--Non-contact "tapping mode" AFM image of fibrillar collagen. The D-period and sub-bands are visible. Banding asymmetry indicated that the C-terminal is toward the left end of the fibril. Topview image, combined height and slope mode. Horizontal range = 2,000 nm (2.0 μm). Vertical range = 25 nm

THE EFFECT OF PROBE–TIP GEOMETRY ON FORCE MICROSCOPY IMAGES

J. T. Thornton[*], E. M. T. Velu[**], C. B. Mooney[*], and P. E. Russell[*]

[*] Department of Materials Science and Engineering, and Precision Engineering Center, North Carolina State University, Raleigh, NC

[**] Department of Electrical and Computer Engineering, and Data Storage Systems Center, Carnegie Mellon University, Pittsburgh, PA

The atomic force microscope (AFM) has been used to characterize a variety of surfaces to study the influence of the instrumental parameters and sample topography on the interpretation of the images and the data obtained. The effect of the tip shape on the resulting image resolution and artifacts has been studied. Test samples of varied topography have been used to establish imaging parameter optimization for specific sample topographies.

Chromium thin films of different thickness, deposited uniformly by rf diode sputtering, have been selected as test samples and imaged with a variety of tip shapes. These films were developed as underlayer films for magnetic recording media used in computer hard disks. The range of tips include commercial silicon nitride pyramidal tips, focused ion beam (FIB) sharpened silicon nitride pyramidal tips, and electron beam contamination induced tips (microtips) varying in growth time (i.e. length) from 10 to 40 seconds (approximately 0.40 to 0.65 μm). The silicon nitride pyramidal tips have a uniform geometry of a 3 μm square base and 55 degree sidewalls [1]. The FIB was used to sharpen these tips by scanning the ion beam in a circular pattern to produce a higher aspect ratio (length/width) tip [2]. The microtips have sidewalls which approach a vertical orientation and are approximately 0.1 μm wide at the base with a tip end of approximately 20 nm [3]. Figures 1-4 show the images of a 350 nm chromium film (approximately 35 nm peak-to-valley) imaged with a pyramidal tip, a FIB sharpened pyramidal tip, a 0.40 μm microtip, and a 0.65 μm microtip, respectively. The silicon nitride pyramidal tip produces a 'doublet' feature on each grain in the image as seen in Figure 1. The FIB sharpened pyramidal tip displays good definition of grains, however, significant smoothing is suspected in the image (Figure 2). The 0.40 μm tip produces an image with clear features and sharp definition between the grains (Figure 3). Increasing the tip length increases the degree of distortion in the image, which can be seen in Figure 4 with a 0.65 μm microtip. The increase in clarity of the features in the image of the 0.40 μm microtip is believed to be due to the ability of the microtip to image high aspect ratio protrusions and depressions which were smoothed over by the pyramidal tips. The decrease in feature clarity with an increase in tip length is believed to be caused by the bending of the long slender microtip under the influence of the repulsive and friction forces acting on the tip while imaging in contact mode [4].

The ability of the microtips to improve the clarity of surface features is not observed for all surface topography. A 105 nm thick chromium film of lower peak-to-valley roughness (approximately 15 nm) was imaged with the same range of tips. The pyramidal tips produced the clearest images of this film (Figure 5) and for thinner films with lower peak-to-valley values. Image distortion is present with each microtip and the degree of distortion increases with the length of the microtip (Figure 6), which was imaged with a 0.65 μm microtip. An increase in tip bending with length is believed to cause this behavior.

By imaging two chromium thin films of different scale topography with a range of tip shapes, two conclusions can be drawn: (1) For samples with a high aspect ratio topography (peak-to-valley > 35 nm), the microtips increase the image clarity significantly with respect to the pyramidal tips. (2) For samples with lower aspect ratio surface features (peak-to-valley < 15 nm), the pyramidal tips produce the clearest image with respect to the microtips. These experiments indicate a transition point at which the surface topography can best be characterized by either the pyramidal tips or the microtips depending of the aspect ratio and size of the features.

References:

1. T. R. Albrecht et al., *J. Vac. Sci. Technol.*, (1990) A8, 3386.
2. M. J. Vasile et al., *Rev. Sci. Instrum.*, (1991) 62, 2167.
3. H.Ximen and P. E. Russell, *Ultramicroscopy*, (1992) 42-44, 1526.
4. A. J. den Boef, *Rev. Sci. Instrum.*, (1991) 62, 88.
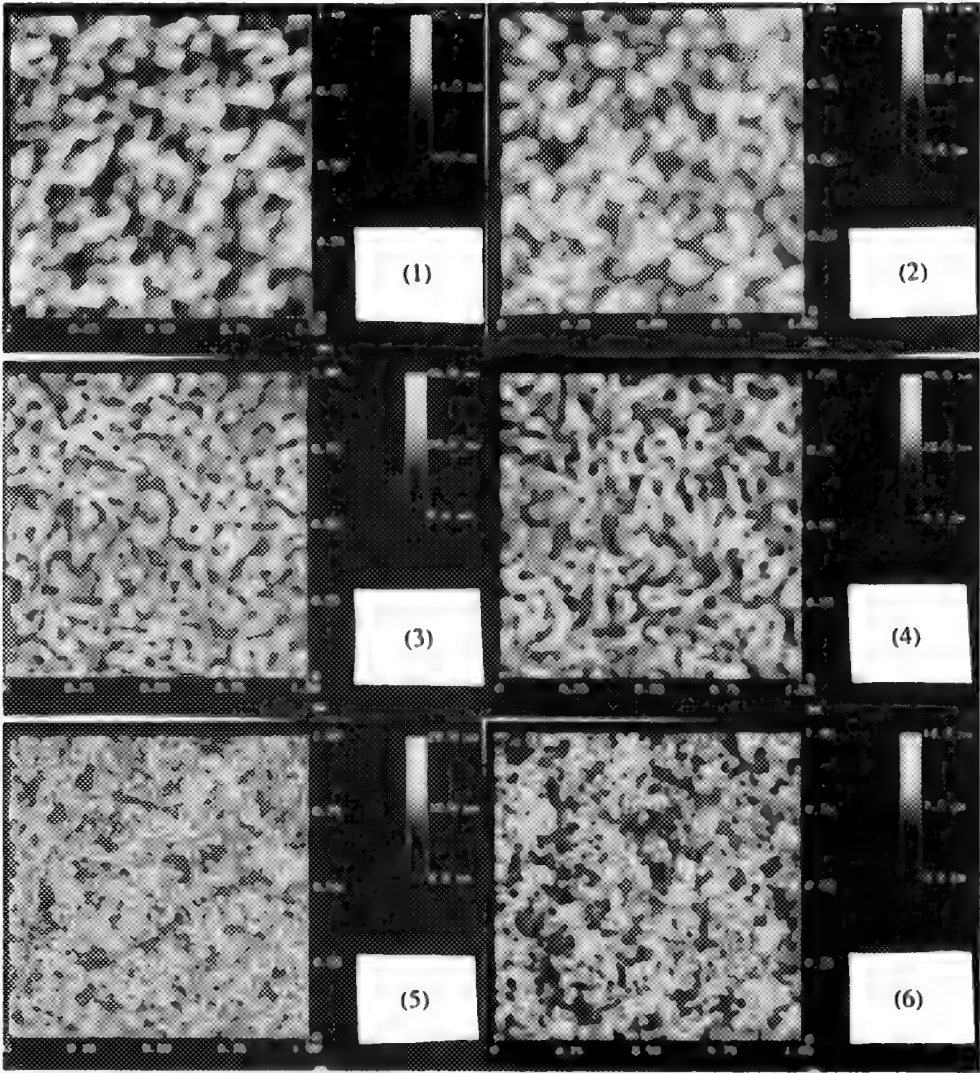
Figure 1: 350 nm Cr film image with pyramidal tip.
Figure 2: 350 nm Cr film imaged with focus ion beam sharpened pyramidal tip.
Figure 3: 350 nm Cr film imaged with 0.40 μm microtip.
Figure 4: 350 nm Cr film imaged with 0.65 μm microtip.
Figure 5: 105 nm Cr film imaged with pyramidal tip.
Figure 6: 105 nm Cr film imaged with 0.65 μm microtip.

DISTORTION IN LATTICE-RESOLUTION SCANNED-PROBE MICROSCOPE IMAGES

L. Fei

Department of Physics and Astronomy, University of Missouri-St. Louis, St. Louis, MO 63121

Scanned probe microscopes (SPM) have been widely used for studying the structure of a variety material surfaces and thin films. Interpretation of SPM images, however, remains a debatable subject at best. Unlike electron microscopes (EMs) where diffraction patterns and images regularly provide data on lattice spacings and angles within 1-2% and ~1° accuracy, our experience indicates that lattice distances and angles in raw SPM images can be off by as much as 10% and ~6°, respectively. Because SPM images can be affected by processes like the coupling between fast and slow scan direction, hysteresis of piezoelectric scanner, thermal drift, anisotropic tip and sample interaction, etc., the causes for such a large discrepancy maybe complex even though manufacturers suggest that the correction can be done through only instrument calibration.

We show here that scanning repulsive force microscope (SFM or AFM) images of freshly cleaved mica, a substrate material used for thin film studies as well as for SFM instrument calibration,[1] are distorted compared with the lattice structure expected for mica. Fig.1 (a) is a SFM (Digital Instruments, NanoScope III) image of Muscovite mica and (b) is central portion of the Fourier power spectrum of (a). Muscovite mica has C2/c(15) space group symmetry with $a=0.5203$ nm, $b=0.8995$ nm, $c=2.0030$ nm and $\beta=94.47°$.[2] The major diffraction spots positions calculated from these parameters are indicated in the fig. 1 (b) with "+" marks. The discrepancy of distances as well as angles between theoretical and experimental data is obvious and much larger than the instrument digitizing error. Our calculation show that the distances of diffraction spots are off from theoretical positions by as much as 10%, with angles are off by as much as 6°. Moreover, images taken with different scan angles (varies from 0°-115°) have been analyzed, and diffraction spot shifts in different directions are found in their power spectra. Our analysis of these distortions shows further that the distortion can not simply be corrected by resetting the fast and slow scan direction magnifications. For a first order correction, we have proposed that a two parameter mathematical model be used to restore images, according to known theoretical diffraction spot positions. The model assumes that the distortion is either a contraction or expansion (with coefficient c) along some azimuthal direction (of angle α). An rms minimizing best fitting algorithm has been used to determine the c and α from a given set of experimental and theoretical periodicities. A corrected image of fig.1 obtained with algorithm implemented in the Mathematica and Semper 6 program language is shown in fig.2 (a). The central portion of it's power spectrum is shown in fig.2 (b).

In conclusion, we have shown that raw SFM images often are distorted, with the distortion amount larger than digitizing error. We have separately seen such distortion in scanning tunneling microscope image of graphite. The distortion can not simply be restored by changing the fast and slow scan calibrations. A two parameter mathematical model is proposed to remove the distortion from images of known structure. Further work is needed to understand the behavior and mechanisms of this distortion, so that it can be removed from images of unknown structures when absolute angles and spacings in these images are of interests.

References

1. D. K. Schwartz et al., *Physical Review E*, **4 7** (1993)452.
2. D. R. Lide et al., *Handbook of Chemistry and Physics*, **73rd** ed. CRC press, (1992-1993)4-172.
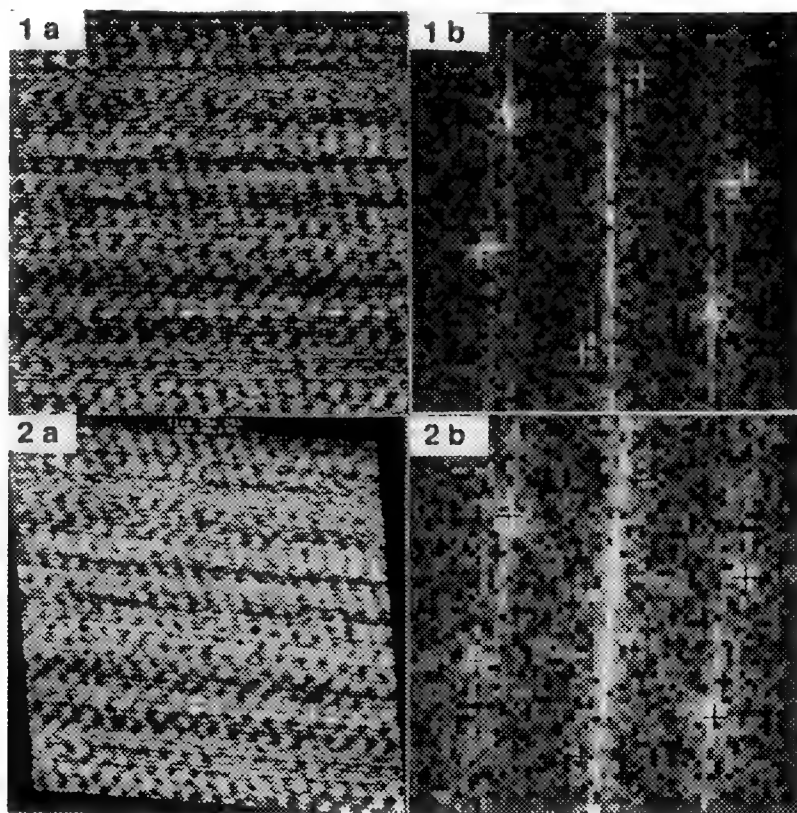
Fig.1--(a) Raw SFM (Digital Instruments, NanoScope III) image of Muscovite mica, field width is 10 nm, and (b)central portion of the power spectrum of (a), "+" marks are theoretical calculation of diffraction spot positions.
Fig.2--(a) Corrected image of fig.1 (a), and (b) central portion of the power spectrum of (a).

FINDING NOISE-RELATED ARTIFACTS IN SCANNED-PROBE MICROSCOPE IMAGES

H. Siriwardane, P.Fraundorf*, L Fei*, W.J. James, J.Newkirk, and O.A. Pringle

*Center for Molecular Electronics and Department of Physics, University of Missouri-SL, St. Louis MO 63121 USA

Departments of Physics, Chemistry & Metallurgical Engineering and Materials Research Center, University of Missouri-Rolla, Rolla MO 65401 USA

Scanned probe microscope images often contain structure which does not belong to the actual specimen. Some of this structure arises in time-domain instabilities of the microscope and its environment, some of it arises with imperfect attempts of the feedback loop to hold force or current constant, and some of it reflects tip (as opposed to specimen) structure.[1] We illustrate here: (i) artifacts of the first kind, i.e. those which are independent of tip shape and which exist in the slow-scan limit, (ii) the way in which low-pass filtering can give such artifacts three-dimensional character, and (iii) tests involving Fourier phases and amplitudes in scanned probe images which can signal the presence of such artifacts.

The first and best test for artifacts related to time-domain instability is simply to locate precisely the same feature in two micrographs, if possible taken with different scan speeds (e.g. at different magnfications). If the feature remains unchanged in structure and size, then it is unlikely to be a purely time domain artifact. Sometimes, however, such evidence is not available, and you are instead provided with only a single image like the scanning force image of plasma deposited carbide shown in Figure 1, in low-pass filtered and unfiltered form. Figure 2 illustrates how structures in the filtered image have a more 3D character than do structures in the unfiltered image, giving them a dangerously plausible appearance.

Because time-domain instabilities often will not show spatial correlations, a simple after the fact test is to randomize Fourier phases in the image to see if the image changes in character. Figure 3 shows how an edge dislocation in a periodic lattice disappears when this is done, as would your face if the image was a photograph of you, whereas both the unfiltered force images with or without phase randomization image, as well as the images resulting from filtering these, look quite similar in character. In other words, the absence of unlikely Fourier phase assignments in an image (like sharp edges) leaves open the possibility of a noise origin.

One can obtain quantitative information on time-domain instabilities in a scanned probe microscope by simply cutting scan amplitudes to zero and recording a "stationary-tip image". Such an image, along with a real scanning force image of iron carbide taken with the same instrument, is shown in Fig. 4. The rms "roughness" in the stationary tip image is around 0.67 nm, while that in the real image is only around 0.42 nm. Figure 5 shows these rms roughness values decomposed as a spectral function of log(spatial frequency), for which purpose we of course consider the stationary tip image "mapped" onto an image of the same width as the real image. The result shows that at high (non-physical) spatial frequencies the real image has more structure (feedback loop related?), while at low frequencies the stationary tip noise is higher (less damping from specimen contact?). Conclusion: The bumps may well be pure artifact.

---

[1] P. Fraundorf and J. Tentschert, Ultramicroscopy 37 (1991) 125-129.
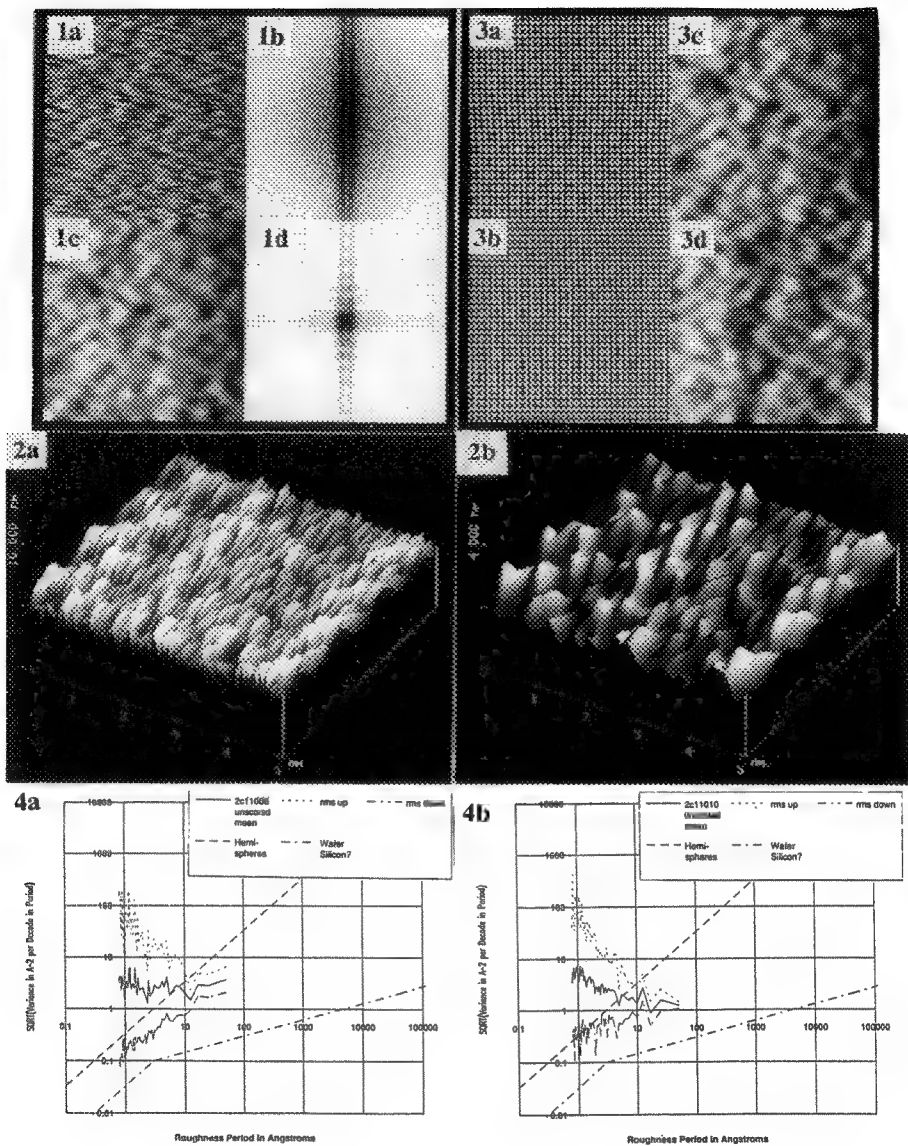
Fig 1. (a) Scanning force microscope image of a plasma deposited film. (b) Fourier spectrum of 1a.
   (c) Low pass filtered image of Figure 1a. (d) Fourier spectrum of 1c.
Fig 2. (a) Structure of an unfiltered carbide film in 3D. (b) Low pass filtered 3D image of 2a.
Fig 3. (a) Edge dislocation in a periodic lattice. (b) Phase randomized image of 3a.
   (c) Low pass filtered image of a plasma deposited film. (d) Phase randomized image of 3c.
Fig 4. (a) Roughness spectra of (a) stationary tip image. (b) Plasma deposited film carbide film.

ATOMIC-FORCE MICROSCOPY: EXOTIC INVENTION OR PRACTICAL TOOL?

Donald A. Chernoff

Advanced Surface Microscopy, Inc., 6009 Knyghton Road, Indianapolis, IN 46220-4955

The Scanning Tunneling and Atomic Force Microscopes are well-known due to their extraordinary capability of imaging atoms using a simple mechanism. However, atomic resolution is usually not needed to solve most problems in development and manufacturing. So, many scientists and engineers (mistakenly) regard these new microscopes as more "exotic" than practical.

Both the AFM and the STM make 3-dimensional images of solid surfaces, but the AFM has much broader applications. The reason for this is that the AFM uses a universal sensing mechanism (repulsive and attractive mechanical forces), whereas the STM uses an electrical signal, which requires that the surface be at least somewhat conductive.

Using the extraordinary height sensitivity and wide scan capability of the AFM, we easily answer simple (but important) questions about surfaces and surface features, including:
- Is a contaminant present?
- Is a feature a pit or a peak?
- How tall is it?
- What is the grain size of a coating?
- How rough is the surface?
This paper presents several applications which have practical value for a diverse group of industries.

AFM images of aluminum foil show many shallow bumps (5-25 nm high), which cover features associated with the rolling process (such as large tears and fine scratches). It is evident that the bumps are deposited after the foil emerges from the rollers. We believe this contaminant is a non-volatile residue derived from the rolling lubricant. The ability to detect the amount of residue on the foil surface helps metallurgists improve product cleanliness.

AFM images show the grains in polycrystalline silicon films clearly. We can judge the grain size and measure surface roughness quantitatively. For the process engineer, this structural information is a key link in understanding how process conditions determine device performance parameters such as resistance and capacitance.

High density magnetic data storage depends on precise fabrication of the recording head. Thin film heads are fabricated by deposition of alumina and ferrite layers on an alsimag substrate, followed by cross-sectional polishing to expose the ferrite pole tips. The layers and interfaces are crisply defined in the AFM images and we can determine the critical height information.

AFM images of optical disc stampers show the general shape of the data bumps, including the height, width, and wall slopes, as well as flaws and the fine grain structure of the Ni surface.
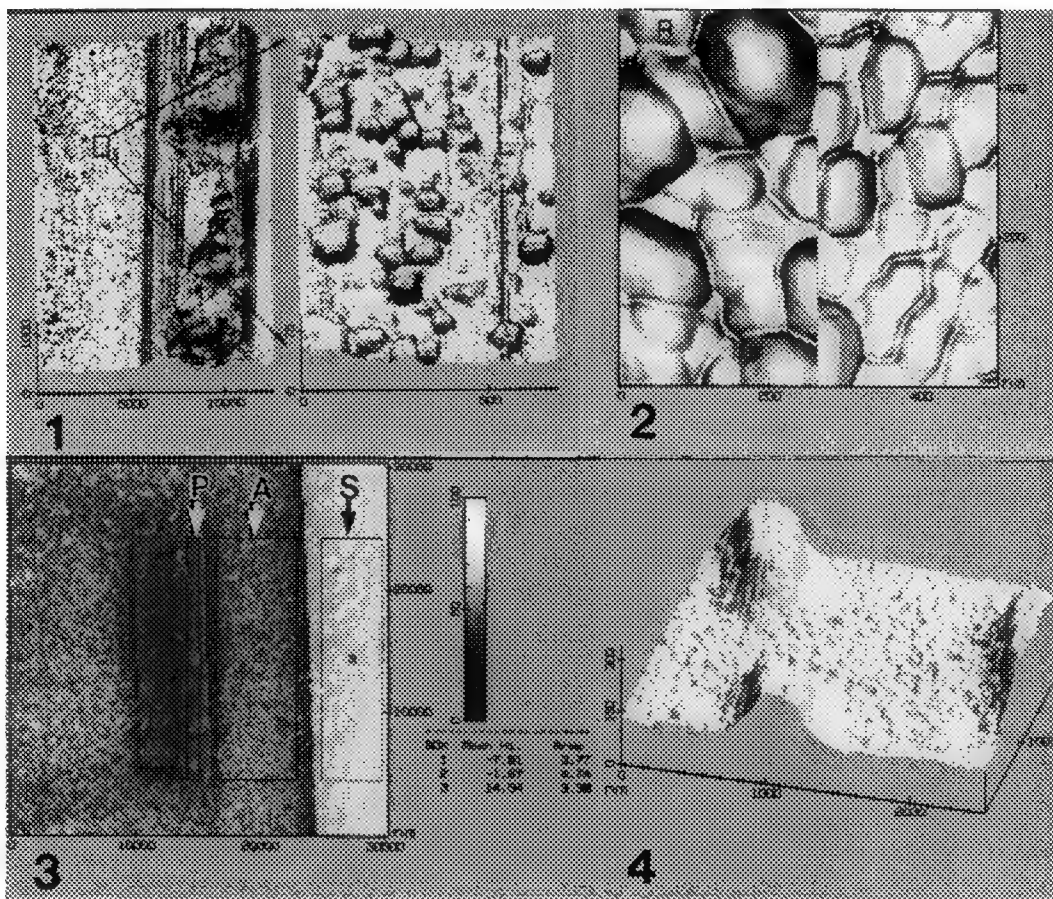
FIG. 1.--AFM images of aluminum foil, showing rolling marks such as ridges with tears and smooth valleys with fine scratches. Bumps 5 to 25 nm high are found everywhere overlying the rolling marks.

FIG. 2.--Composite AFM image showing polycrystalline Si thin films. Specimen A had larger grains and a rougher surface than specimen B.

FIG. 3.--AFM image of a thin film magnetic recording head, presented in height mode (white is high, black is low). The right pole tip (PT) and alumina (A) regions were lower than the substrate (S) by 22 and 16 nm, respectively.

FIG. 4.--AFM image of an optical disc stamper. Large features are data bumps. Small features are Ni grains.

In-situ measurements of scanned probe tip shape with etched nuclear tracks

J. Tentschert, P. Fraundorf, B. Armbruster*

Center for Molecular Electronics and Dept. of Physics, U. Missouri-SL, St. Louis, Missouri 63121, *
also Monsanto Corporate Research, Monsanto Co., St. Louis, Missouri 63166

In air based Scanning Tunneling Microscopy (STM), tip geometry is often unknown so effects in images due to tip shape are difficult to quantify. While the importance of tip structure is often discussed, the methods for getting this information tend to be unsatisfactory in that they often involve ad hoc assumptions (seeing carbon atoms means a good tip) or they lack the ability to make measurements necessary to make quantitative assertions about unknowns. By exploiting the reproducibility of etched nuclear track pits, we have measured the tip interaction profile for an STM tip in air to a resolution of better than 4 nm in three dimensions.

As a source of nuclear track pits we coated Nuclepore filters to make them conductive for STM. We used holes in both the 50nm and 200nm range. As a height calibration we took an image of 30nm colloidal Au on HOPG. Our method was as follows: We took an image of an area containing several pits. Next, the image was flattened, several holes were cut and averaged, and a standard deviation image was calculated using the programming language Semper 6, see Figure 1. Using these individual pits, their mean, and their standard deviation image, we were able to make quantitative comparisons both on individual tips and between multiple tips. From these mean images a tip interaction profile can be found from which will allow for measuring and removing tip shape effects in an image[1]. This technique can be used on other scanned probe instruments, and with pits on the size scale of 2 to 15nm available, even higher resolution is possible. Figure 1 is a look at an individual tip. In 1A the three holes not near an edge were cut and averaged. The depth of the mean image, 1B, was 77.4nm the while mean of the standard deviation image,1C, was 3.4nm. These holes are 200nm in diameter. The apparent asymmetry in the vertical and horizontal directions comes from a difference in the scan rates used while acquiring this image. Two tips at different times are compared in Figure 2. This graph shows the RMS difference between the pit images from one image and their mean on one axis and the RMS difference between those same pit images and the mean image of the pits taken at a later time on the other axis. The second group of points is the same comparison made with the individual pit images from the later time. By comparing pit images to a mean image in this way we can not only distinguish differences between tips, but can also measure the evolution of a single tip with time.

In conclusion, using nuclear track pits we measured the tip interaction profile to a resolution of better than 4nm. We also compared the pit images formed by two different tips and found the difference between them to be greater than the difference between the individual pits from each tip. This technique allows one to create a tip interaction profile and thus will allow for measuring and removing tip shape effects when looking at unknowns. By allowing a view of the tip as well as sample changes, *in-situ* techniques of this sort can open a world of 'nano-invention' by giving the operator a way to iteratively modify and apply the scanning probe.

---

1. P. Fraundorf and J. Tentschert, Ultramicroscopy 37 (1991) 125-129
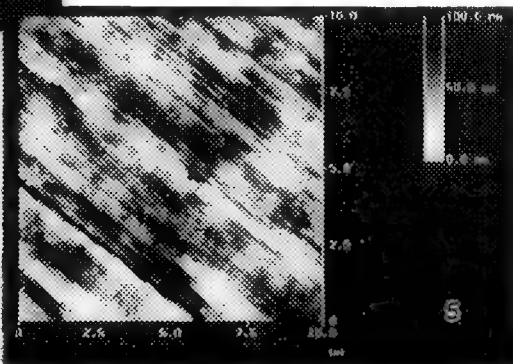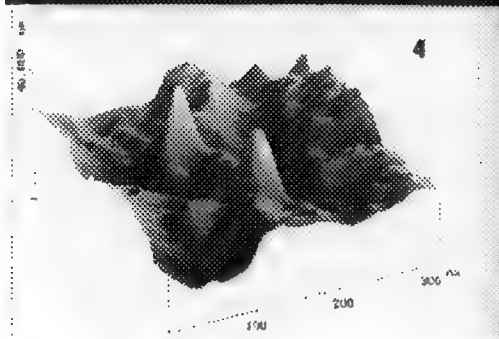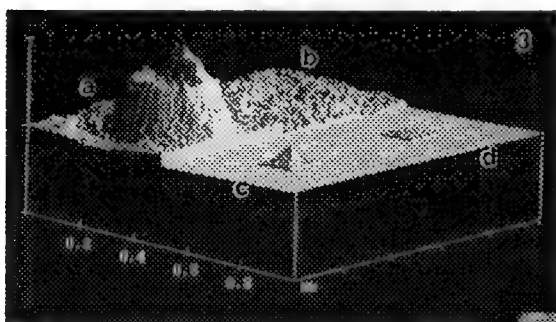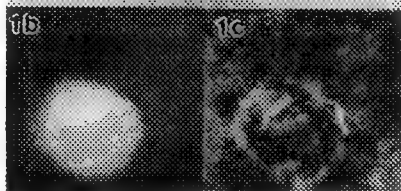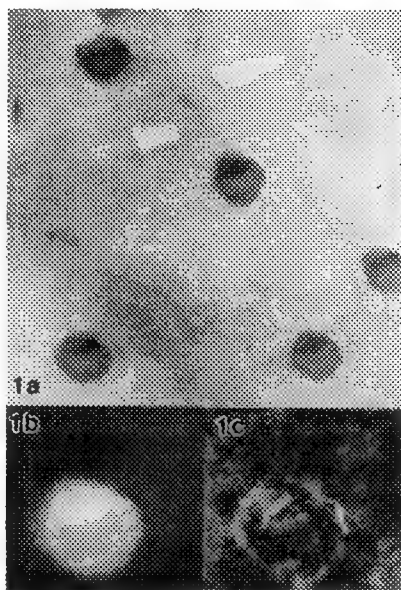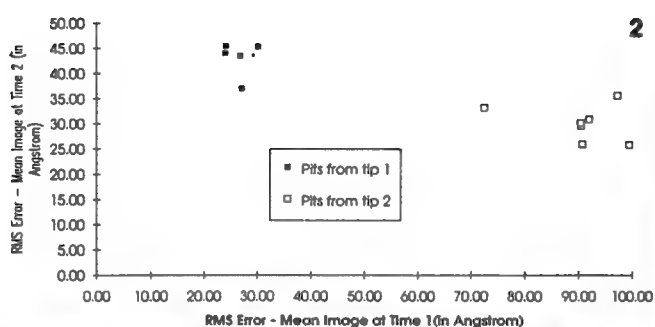
Figure 1A: Image of a coated Nuclepore filter showing multiple holes. Ledge structures are clearly visible and consistent in this image; 1B: Mean pit image made by averaging the three pits not near an edge in 1A; 1C: Standard deviation image calculated during the averaging process for image 1B. The holes are 200nm in diameter.

Figure 2: Graph comparing the same tip at two different times. The time evolution of the tip can be seen and measured in this way.

Figure 3: Composite of four images. 3A: The inverted average of several 200nm etched nuclear particle track images whose structure tells about the shape of the scanning tip being used to image them. Two semicircular ledges, in particular, reveal the location and height of two secondary tips on the scanning probe. The height of the image is around 70nm from the base to the top; 3B: The standard deviation image from the averaging process for 3A, which shows that from track to track the image has been quite repeatable; 3C: The inverted image of several 50nm etched nuclear particle track images, indicating how such images tell us about structure on the scanning tip closer to its very end; 3D: The standard deviation image from the averaging process for 3C, showing around 2nm vertical reproducibility in the profile shape from track to track.

Figure 4: Inverted image of two 15nm etched nuclear track pits in a commercial Nuclepore filter. Images of such tiny holes tell us about the size and shape of the scanning tip that the microscope is using. These pits were imaged by repulsive force (SFM) on *uncoated* Nuclepore filters.

Figure 5: "Large field width" repulsive force (SFM) image of 50 nm pits in *uncoated* filters.

529

SCANNED-PROBE MICROSCOPE ROUGHNESS SPECTROSCOPY

P. Fraundorf and B. Armbruster*

Center for Molecular Electronics and Department of Physics, University of Missouri-SL, St. Louis MO 63121. *Also Monsanto Corporate Research, 800 N. Lindbergh Blvd, St. Louis MO 63166

Air based scanning tunneling and scanning force microscopes are capable of producing images very easily, but oft-times that is all that they produce. Since microscopic regions of specimens of course differ in detail from one to another, often judgements about how two regions differ fundamentally are left to qualitative intuition. Given a quarter of a million numbers, in the case of a typical large SPM image, we should be able to quantitatively compare the statistical properties evidenced therein from one specimen to another. Such quantitative insight may also yield information on artifacts (like time-domain noise and feedback-loop effects) in an image. To accomplish this most intuitively, we recommend simply decomposing the rms height variations in the specimen into two and one dimensional (azimuthally averaged) logarithmic (per decade frequency) roughness spectra. The basic properties of such a decomposition of topographic images are discussed in a paper submitted separately to this conference. We here discuss scanned probe microscope results.

Figs. 1a and 1b show log-log roughness spectra obtained for 512x512 scanning tunneling microscope (STM) images of the same region on a metal-coated diamond-like carbon specimen, taken at two different scan speeds. The upper and lower curves define the azimuthal standard deviation (i.e. the directional anisotropy) of the image roughness as a function of LOG(period) = -LOG(frequency). As you can see, the fast scan image contains a bit more high frequency (low period) structure, and this high frequency structure is drastically more anisotropic. We find this effect in the roughness spectra to be characteristic of feedback loop artifacts (i.e. of deviations away from the slow scan limit[1]). In fact, if the tip is moving slow enough to allow images at two different speeds without such an enhancement in anisotropy at high frequencies, such spectra would provide evidence that feedback loop artifacts are not a problem (i.e. that slow-scan limit assumptions are plausible). Roughness spectra are similarly useful in investigating likely effects of time-domain (stationary-tip) noise on images (cf. another submission by this group to the conference).

Fig. 2b shows the two-dimensional roughness spectrum of an STM image (Fig. 2a) from a Cu surface exposed for 5 seconds to an Ag plating bath, while Fig.2d shows the analogous spectrum for an STM image (Fig. 2c) from a specimen with 60 seconds of Ag plating. Note that the second spectrum shows extra large size-scale anisotropy orthogonal to a deep crack running just to the left of center in Fig. 2c. Such large scale anisotropy should raise a flag of caution in considering Fig. 2d representative, since single sharp features like cracks can introduce significant roughness at all spatial frequencies. This anisotropy also shows up in the one-dimensional (azimuthally averaged) roughness spectra of these same specimens (Fig. 3a and 3b). Finally, note the peak near 50nm in the spectrum of Fig. 2b, associated with the mounds in the image. Bump nucleation/growth simulations predict well defined behavior for peaks in the roughness spectra, as a function of time. Thus roughness spectroscopy might aid in the quantitative detection and monitoring of such processes.

---

[1]   P. Fraundorf and J. Tentschert, Ultramicroscopy 37 (1991) 125-129.
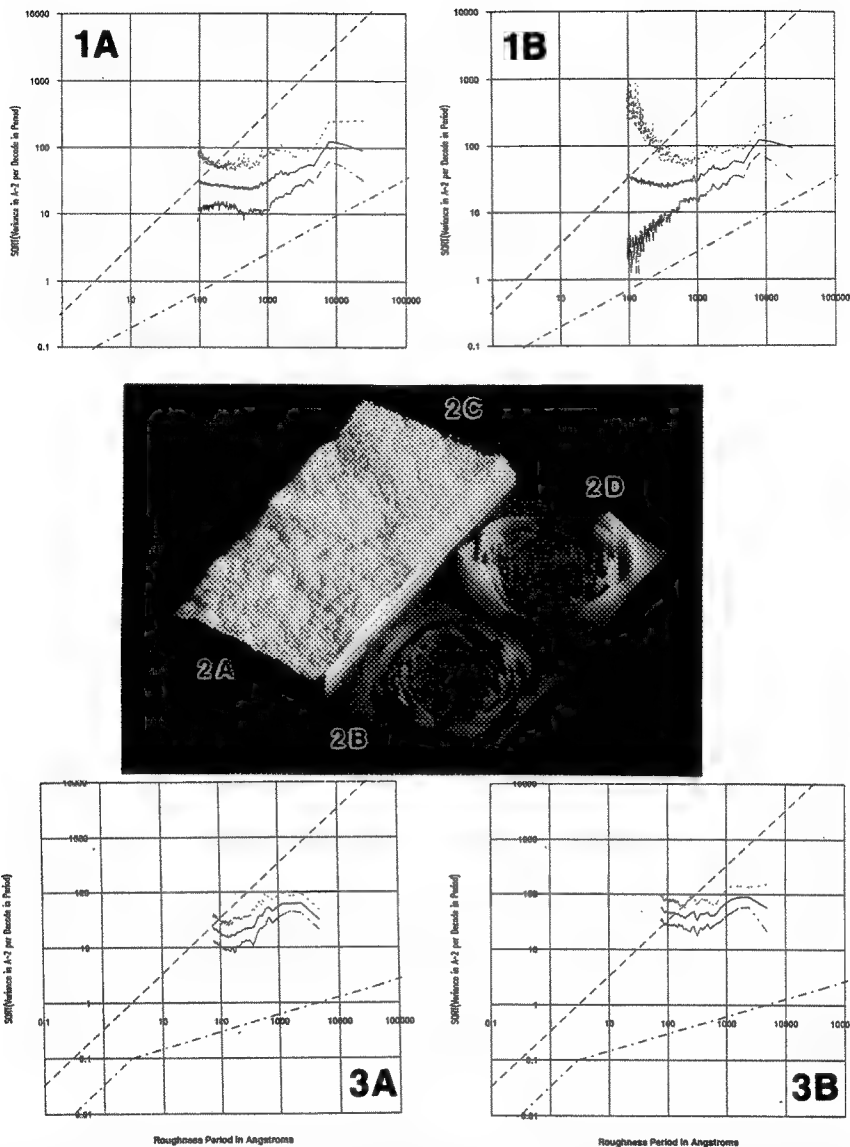
Fig. 1A: Azimuthally-averaged log-log roughness spectrum of a 512x512 STM slow-scan (e.g. 30 second) image of a metal-coated diamond-like carbon specimen.; **Fig. 1B:** Spectrum similar to 1A except of a fast-scan (e.g. 10 second) image.

Fig. 2A: STM image of a Cu surface exposed to a 5 second Ag plating bath; **Fig. 2B:** Two-dimensional roughness spectrum of the surface in 2A. The plot is radially logarithmic, with rms variation per decade displayed near the center of the plot for small size scales, and near the perimeter for large size scales; **Fig. 2C:** As in 2A, except exposure to bath is 60 seconds.; **Fig. 2D:** Two-dimensional roughness spectrum of the bumps in 2C. Same vertical scale as 2B.

Fig. 3A: One-dimensional (azimuthally averaged) roughness spectrum computed from the STM image shown in 2A. **Fig. 3B:** Same for image in 2C.

SCANNED TIP MEASUREMENT OF DEEP VERTICAL FACETS ON A FLAT SURFACE: MEASURING ROUGHNESS ON GaAs LASER WAVEGUIDE MIRRORS

Chang SHEN*, Phil FRAUNDORF* and Robert W. HARRICK**

*Center for Molecular Electronic and Dept. of Physics, U. of Missouri-SL, St. Louis,MO 63121
**McDonnell Douglas Electronic System Company, MO 63134
**Present address: Dept. of E. E., University of California-Santa Barbara, CA 93111

Monolithic integration of optoelectronic integrated circuits (OEIC) requires high quantity etched laser facets which prevent the developing of more-highly-integrated OEIC's. The causes of facet roughness are not well understood, and improvement of facet quality is hampered by the difficulty in measuring the surface roughness. There are several approaches to examining facet roughness qualitatively, such as scanning force microscopy (SFM), scanning tunneling microscopy (STM) and scanning electron microscopy (SEM).[1,2,3,4,6] The challenge here is to allow more straightforward monitoring of deep vertical etched facets, without the need to cleave out test samples. In this presentation, we show air based STM and SFM images of vertical dry-etched laser facets, and discuss the image acquisition and roughness measurement processes. Our technique does not require precision cleaving. We use a traditional tip instead of the T shape tip used elsewhere to preventing "shower curtain" profiling[5] of the sidewall. We tilt the sample about 30 to 50 degrees to avoid the curtain effect. The size of etched mirror facets are 11 microns wide by 2 microns deep, located at the end of a waveguide channel which is 4 microns wide and 2.2 microns deep. Tip landing, and the "curtain effect", are major difficulties for data acquisition. The sharper edge between mirror and its adjacent surface shown in the STM image of Fig 4, indicates that the non-mirror area (part A) was scanned by the sidewall of the tip. Protrusions on the sample surface sharper than the tip show the inverted images of the tip profile, instead of the defect itself. Due to the tilt surface, the scan region in the x-y plane of our case is about 10 microns. The curtain effect is becomes worse when we increase the scanning speed.

In summary, we use air-based STM and SFM for monitoring vertical mirrors by tilting the samples. The cantilever used (Digital Instrument's nanoprobe) has a long overhang which limits access to the tilted sample.

[1] D.K.Probst, L.G.Perrymore, B.C.Johnson, R.J.Blackwell,J.A.Priest and C.J.Balestra. "Demonstration of an Integrated,Active 4x4 Photonic Crossbar" IEEE photonics Technol. Lett.,Vol.PTL-4,#10 pp1139-1141
[2] F.Ren, S.J.Pearton,J.R.Lothian,C.R.Abernathy and W.S.Hobson. "Reduction of sidewall roughness during dry etching of SiO$_2$" J. Vac.Sci. & Technol. B, Vol 10,#6 pp2407-2411(Nov/Dec 1992)
[3] H.Saito and Y. Noguchi, Jpn. J. Appl. Phys.,Vol. 28, pp 1836-1841(1989)
[4] Robert W. Harrick, L.G. Sabo, and J.L.Levy, "Novel method for measuring and analyzing surface roughness semiconductor laser etched facet" J. Vac. Sci. Technol. B9 (6) Nov/Dec pp2278-2782 (1991)
[5] J.E. Griffth,D.A.Grigg,M.J.Vasile,P.E.Russell and E.A.Fitzgerald, "Characterization of scanning microscope tips for linewidth measurement" J. Vac. Sci. Technol. B9(6) Nov/Dec pp3586-3589 (1991)
[6] C.F.Lin Photonic Tech. Lett. Vol. 4, pp 127-130 (1992)
[7] B.C.Johnson,Unpublished,July 1992
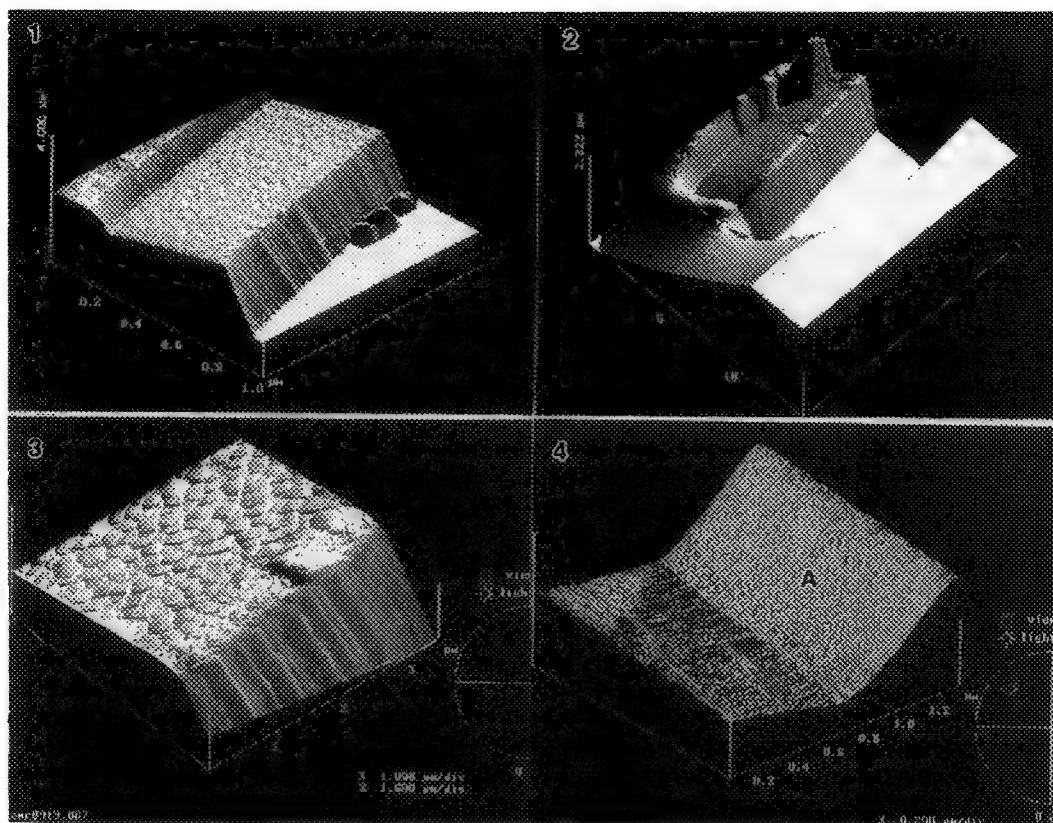
Fig.1: SFM image. Sharp protrusions give out the inverted tip images (3 pyramidal objects). The mirror facet partly hides behind a "shower curtain".

Fig 2: SFM image. We cannot take data in white region because the cantilever head is touching the surface of the tilted sample. Note the pyramid which maybe the tip's image. This pyramidal object is dulled after the next cantilever scan.

Fig.3: Zoomed-in image of Fig.2. It shows more details about the mirror facet and its adjacent area.

Fig.4: STM image. The clear edge of mirror (flat region) and non-mirror area (sloping region A) indicates that they were taken by different regions of the tip. The non-mirror area was likely scanned by the sidewall of the tip, so it looks smoother than the mirror area surveyed by the tip's head.

LATERAL DISPLACEMENT MICROSCOPY OF HOLOGRAMS USING SCANNED TIP IMAGE PAIRS

C. SHEN and P. Fraundorf

Center of Molecular Electronic and Dept. of Physics,University of Missouri-SL, St. Louis, MO 63121
*Supported by Monsanto Company External R&D

Tip displacements associated with lateral forces between specimen and tip can be quite large (e.g. microns in size) during repulsive force microscopy (SFM or AFM) and air-based scanning tunneling microscopy (STM) of soft samples. Both x and y components of the lateral tip displacement *due specifically to drag between the specimen and tip*, as separated from those components of the tip's displacement due solely to the geometry of mechanical equilibrium between the tip and a tilted surface, may be inferred from STM or SFM image pairs of the same region taken with the tip traveling in different directions (e.g. with the tip fast scan going left versus up). We refer to this process of inferring displacement from image pairs as displacement mapping. By comparison, *absolute* measurements of lateral force like those obtained by imaging cantilever twists in Digital Instrument's commercial lateral force microscope: (a) don't remove equilibrium (purely geometric) components of the lateral displacement from the often more interesting friction components, (b) measure the lateral force in only one of the two transverse directions, and (c) require special hardware, not available on conventional STM's for example, to measure transverse deflection.

Displacement mapping, which can also be useful for calculating topographic maps from stereopair images or in remote sensing and pattern recognition, is reported here on STM and SFM images of metallized holograms. The results are shown in Fig.3a-4b. The basic algorithm for displacement mapping makes heavy use of the cross-correlation analysis of small image regions in each image with the help of Semper 6 programming language. Clockwise/CounterClockwise helical scan STM images of a hologram show lateral tip displacements on the order of 0.5 micron. Displacement maps of a Left/Right Raster Scan Pair shows an x-displacement in which the spatial frequency of the corrugated structure is doubled.(Fig.1b,2b). The maximum displacements locate on the peak and trough region of the hologram. This is a clue that the double frequency feature may be explained by a friction force responsible for the tip's bending mechanism, and a normal force between tip and sample surface that is roughly constant.

In summary, x vs. y scanned tip *image pairs* can yield tip displacement images optimized for exploring the effects of friction in ANY scanned tip microscope. The major task is to take a pair of scanned tip image and find a better algorithm to retrieve the displacement components. We are presently collecting challenging image pairs for such calculation, and will also describe methods to create images with known displacement maps.

Reference:
[1] C. Shen, P. Fraundorf, APS march meeting, 1992. Vol 37. No.1 Pg167
[2] M.Radmacher,etc. Science, Sept. 1992 Vol 257, Pg1901
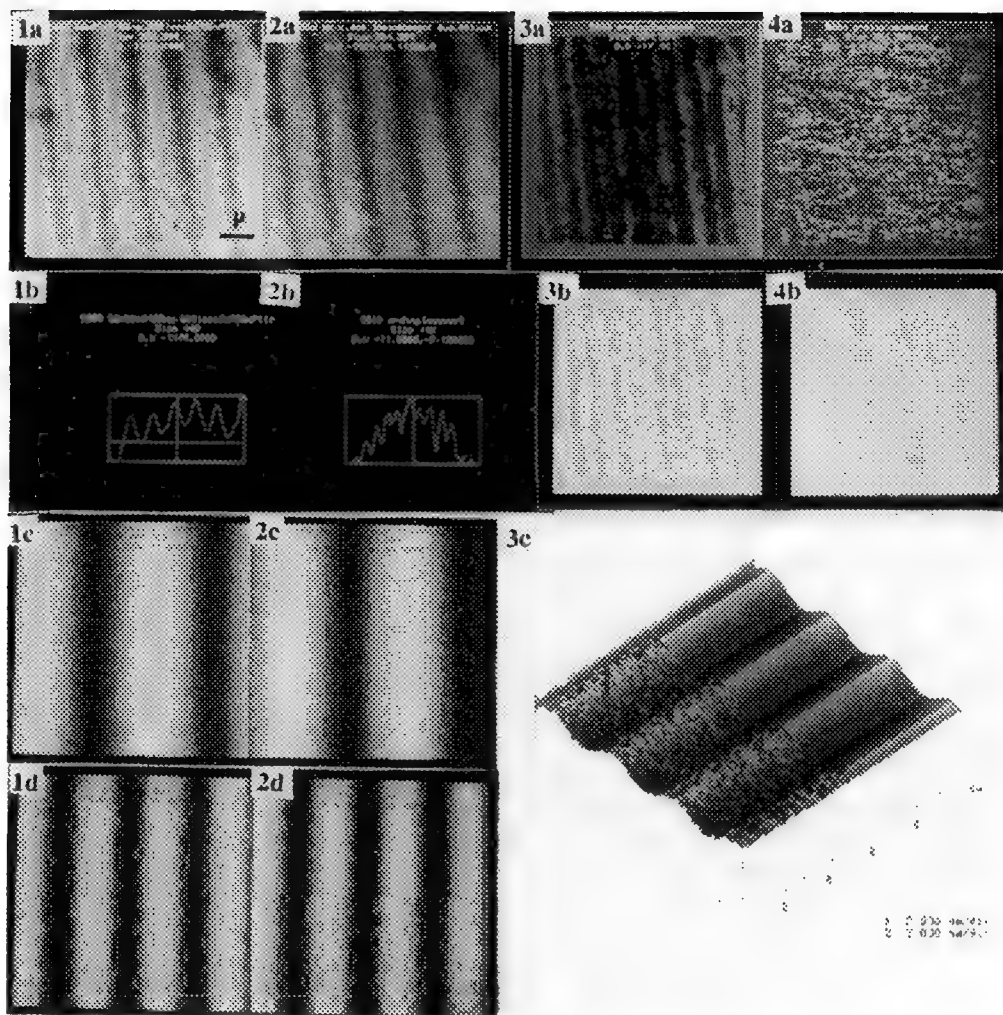
Fig.1a,2a are Left & Right STM image pair of hologram. Field with 5x5 microns. The displacement in horizontal direction (x-axis) is about .5 micron order.

Fig.3a is X-displacement image. The maximum displacement regions (dark area) locate in the peak and trough region of the corrugated structure of hologram. Fig.4a is Y-displacement image with no significant structure.

Fig. 1b is a projected image of Fig.1a. with the angle of 99 degrees to the horizontal direction. It has sine wave form.

Fig. 2b is projected from Fig.3a. with same angle of Fig. 1b. The spatial frequency of the sine wave structure is doubled and the maximum displacements is at the peak and trough of Fig.1b.

Fig. 3b. Optimal correlation range image. Gray value is the minimum size of the region correspondent to each pixel during the mapping calculation.

Fig. 4b is correlation coeff. image. The average correlation coeff. (average gray value) is 0.878.

Fig. 1c,2c are computer generated image pair for testing the algorithm. They are displaced by the displacement image shown as the up-half part of Fig. 2d.(smooth region). The displacement image is generated that its gray value is proportional to the gradient of the surface of Fig. 1c & 2c. It doubles the spatial frequency of Fig.1c & 2c.

Fig. 1d. is calculated from Fig. 1c & 2c by displacement-map algorithm. It recovers double spatial frequency feature.

Fig.2d shows original displacement image compared with the computer calculated one (Up half smooth region v.s. Low-half part, noisy region). Fig 3c. is the 3-dimension view of Fig. 2d.

IMAGE ANALYSIS: FROM PIXELS TO DATA

John C. Russ

Materials Science and Engineering Dept., North Carolina State Univ., Raleigh, NC 27695-7907

This meeting is about microscopy, which deals with images, and this special session is specifically concerned with the methods for interpretation of those images. It should not be necessary to preach to such an audience about the need for appropriate tools for performing quantitative measurements to extract numeric information from images. Most of these tools are based on the ready availability of computers and peripherals which allow the acquisition, storage, processing, measurement and interpretation of the data. Provided we can also teach the scientist to ask the right questions and correctly use the results, image analysis can offer a powerful tool for the understanding of structure. Since most of this structure is three-dimensional, whereas images are essentially two-dimensional, there is need for stereological interpretation, and for the construction of 3D visualization from multiple images. These are dealt with in subsequent papers in this session. This talk is primarily an introduction to the basics of computer-based image analysis - the tools for obtaining information from images, or "data from pixels."

An image is stored in the computer as an array of pixels ("picture elements"). The most common acquisition method uses a video camera and a frame grabber, which can digitize the array of about 300,000 pixels in 1/30 of a second, with each pixel's brightness represented by a number from 0 to 255 (8 bits). Standard video cameras are inexpensive, but both the tube and chip type cameras have shortcomings (e.g., geometric distortions and electronic noise). The choice of "real time" video imaging vs. integration of more signal over a period of seconds is driven more by the availability of standard consumer electronics than a consideration of the actual imaging needs in most instances. Recording an image with more pixels (up to several million), and more bits per pixel (from 12 to 16) for an extended grey scale dynamic range, is possible but comparatively slow and costly. Recording color is straightforward when appropriate, either by using multiple chip cameras or sequentially recording images through different filters, and then combining them in the computer. Alternate methods of acquiring images include the use of conventional film with flat bed scanners, which provides high resolution but may be inconvenient; videotape, which is convenient but of marginal quality; and the direct digitization of the signal from scanning microscopes such as the SEM or AFM, which requires an inexpensive analog-to-digital converter and appropriate cabling.

Once the images have been acquired, they are often stored or printed using the computer and its associated peripherals. Storage on removable magnetic, optical, or magneto-optical drives is straightforward if slow. File formats are beginning to become standardized, which will improve data exchange. Accessing the stored images requires designing a database structure and assigning meaningful descriptive keys, and is an area still little addressed by current software except in the medical imaging field. The advent of Kodak's Photo-CD format may force the pace of such developments. Printing of grey scale and color images is an active area of development, driven by a substantial consumer market. Hardcopy of acceptable quality, speed and cost is not yet quite available from printers that might be considered attachments for individual systems, but dye-sublimation printers and 600+ dpi laser printers are getting close.

A common defect in as-acquired images is non-uniform illumination, which may be caused by the microscope optics and alignment, camera vignetting, or variations in the sample thickness or surface orientation. Images may also require color correction or noise removal. Image warping may be used to correct for foreshortening, or to align multiple images of the same field (e.g., obtained using different signals, detectors or color filters) or of serial sections. All of these procedures are routinely handled in software. Appropriate standards are needed for calibration of the microscope and detector system, both to relate brightness values to density, dosage, atomic number, etc., and to establish dimensional values for the image magnification.

Image processing may be performed for simple visual enhancement, for example to increase contrast, sharpen the appearance of edges or increase color saturation. Processing may also be required as a

precursor to image segmentation, by delineating edges and boundaries, or extracting textural or directional information from pixel brightness patterns. Combination of multiple images is also used, for instance as the ratios of different signals, or temporal differences to detect motion. These steps may modify the pixels in the original image in ways that depend on the local neighborhood around each pixel. Some of the procedures are most efficiently performed in frequency space, similar to working with diffraction patterns in the TEM. The purpose is to assign new pixel values that can distinguish features of interest from their surroundings, so that thresholding can be used to isolate those features for measurement, producing a "binary" image. Segmentation remains one of the most difficult processes to automate, particularly in complex biological images where the same density may correspond to several structures.

Binary, or black and white, images that result from segmentation may also require processing. Classical morphological operations such as erosion and dilation selectively add or remove pixels according to local patterns, to fill holes, remove noise, smooth boundaries, join broken lines, or separate touching objects. Similar classes of operations based on the Euclidean distance map give improved isotropy and sometimes greater speed. In addition to their role in "cleaning up" images, these binary image operations may also be used to extract topological information about features, such as the ends, nodes and branches of the feature skeleton, or the distance of features from irregular boundaries.

Measurement of images falls into two broad categories. Global measurements of the entire field of view (or averages over many fields of view) provide robust descriptors of the entire microstructure. For instance, the area fraction of the structures of interest gives the volume fraction, and the length of boundary lines per unit area of image can be used to calculate the surface area per unit volume, and from that the "grain size" (actually a misnomer) parameter for materials. The number of features per unit area is only indirectly related to the number per unit volume, which may be calculated either by assuming that the size or shape of the features is known, or by comparing multiple serial section images through the structure. Recent developments in the field of Stereology address many of these microstructural characterization tools as well as associated methods for systematic or random sampling of structures.

Measurement of individual features can provide data for subsequent statistical analysis. Four classes of measurements may be considered: the brightness (or density, or color) of the features; their location (including orientation, neighbor distances, etc.); their size (area, length, breadth, etc.); and their shape. Shape is a particularly difficult concept to quantify. The standard methods include formally dimensionless ratios of size measurements, such as length/breadth, which are easily calculated but not unique. At the other extreme, harmonic analysis of the unrolled feature boundary can completely characterize the shape, but in a way that seems difficult for humans to interpret. Topological properties (e.g., number of end points or number of sides) and fractal dimension of the boundary both provide values that correlate well with human visual observation.

Statistical interpretation of imaging data generally requires nonparametric tools, since the measures are rarely normally distributed as required for common t-test or Anova procedures. The goals of such analysis may include characterizing sample parameters for correlation with history and properties, or comparing different populations of specimens to determine whether they are the same or different, or recognizing individual features as belonging to one of several populations based on multiple criteria. In addition to traditional statistical analysis approaches, methods based on fuzzy logic and neural nets have shown great promise for dealing with the complexity of the multi-dimensional data produced by image analysis.

Software and hardware tools to perform all of these operations are widely available. They offer powerful aids to the microscopist who is willing to invest time in learning their use and the interpretation of the results. The speed of operation is reasonable for typical laboratory operations, and as computer power continues to increase, two developments may be expected: the speed of the operations will increase to permit routine on-line use, and the complexity and "intelligence" of the algorithms will increase. This will enable the systems to function as an assistant to the microscopist, applying operations chosen from among the available tools based on image content and prior human decisions in similar cases.

Architectures/Environments for Image Processing: Hardware and Software for the microscopist

David S. Bright

Microanalysis Research Group, Surface and Microanalysis Science Division, National Institute of Standards and Technology, Gaithersburg MD 20899

Digital images are large arrays of data with array elements all treated in a similar way. "Architecures for image processing" immediately suggests parallel processors because of the enormous increase in speed. These processors enhance images in real time -- TV rates -- but this is less of a consideration where image collection takes more than a few seconds.   Further, these machines are expensive and programming is difficult. For example, when the image is divided among processors as in Fig. 1 and 2, problems arise at the edges of the pieces. Issues such as cost, flexibility, ease of use and data integrity are often of more interest to the microscopist.

Desktop computers present an ideal environment for off line processing of images with a few thousand pixels on an edge. These computers are adequately fast, they have sufficient storage and communication capability, and the software is less expensive than equivalent software for workstations or larger computers. Attachments for desktop computers that are especially useful for image processing and storage include scanners, the magneto-optical disk and the CD-ROM. The Kodak Photo CD™* system for data storage offers an inexpensive service for laboratories customarily using film to digitize their images onto CD-ROMs.

The Macintosh (Mac) is particularly useful for image processing because the user interface and image formats are standardized and highly developed and good commercial and public domain software is available for image processing. Image processing tools on the Mac treat images either as pictures or as arrays of data. The picture orientation is the more visual -- images are pieces of magical film that can be cut, pasted, enhanced, annotated, and drawn on. Adobe Photoshop™ has this orientation, where even very large color (24 bit) images are conveniently scanned (even from an electron microscope with a plug in board[1]), combined, enhanced and archived. Photoshop supports an especially large number of formats for storage on disk. Because Photoshop is designed primarily for graphic artists, data is usually not extracted from the images: no line scans or intensity averages for example. The maximum precision for gray levels or color components is 8 bits (0-255).

NIH Image, a public domain image analysis tool originally developed primarily for inspection of micrographs and images of chromatograms, combines the picture and the data array orientation. Images are stored internally as 256 levels (8 bits) of gray or false color. Images can be enhanced, annotated, and modified, and the pixel values accessed as scan lines, histograms, segmenting (blobbing) and averages of segmented regions such as particles. This data can be read by word processors, spread sheet, or plotting packages. This program has been adapted for spatial filtering with FFT's, as well as specific microscopic applications. Macros are easily written to combine the built-in operations to make special commands that access whole images, but individual pixel values are not accessed easily for special purposes.

Data often has more than 8 bits of precision. This precision is lost when the image is scaled to 8 bits. Among the tools that retain more than 8 bits are NCSA[2] Datascope®, and IPLab Spectrum™ that retain real or 16 bit precision respectively. The precision affects the results of even simple image processing (see Fig. 3).

For special analyses, one must manipulate pixel values directly, preferably with a standard programming language. I use an ANSII standard, object oriented language, Macintosh Common LISP, to implement image processing routines for use by the Microanalysis Group at NIST. A special purpose operation can be written with a minimum of lines of code (see Fig. 4) and then run without reloading data, recompiling, or restarting the system.

References

1. Scott Davilla, 4pi Analysis, Inc. , 117 W. Lynch St., Durham, NC 27701-1929
2. National Center for Supercomputing Applications, U. Ill, Urbana.
* Certain commercial equipment, and instruments, are identified in this paper to describe the subject more fully. Such identification does not imply recommendation or endorsement by the NIST, nor does it imply that the equipment identified is necessarily the best available for the purpose.


```
(defun histogram_equalize_to_byte (in_ara)       Define function name.
  (let* ((out_ara (make-array (array-dimensions in_ara)    Temporarily allocate output image array.
            :element-type '(unsigned-byte 8)))
      (hist (fixnum_+_histogram in_ara))          Calculate histogram.
      (h_sum 0))
    (declare (fixnum dx dy y1))                    **
    (dotimes (i (array-total-size hist))           Calculate cumulative histogram.
      (incf h_sum (aref hist i))
      (setf (aref hist i) h_sum))
    (multiple-value-bind (iav offset) (ccl::array-data-and-offset in_ara)   **
      (declare (ignore offset))                    **
      (multiple-value-bind (oav offset) (ccl::array-data-and-offset out_ara)  **
        (declare (ignore offset))                  **
        (dotimes (i (array-total-size iav))        Calculate equalized image.
          (setf (aref oav i)  (ccl::muldiv (aref hist (aref iav i)) 255 h_sum)))))
    out_ara))                                      ** Not absolutely necessary.
                                                      Added for speed.
```

Fig. 1.-- Diagram of image subdivided for four processors. Operation involves convolution kernel. Areas a, b, c have no result because too near edge. Areas d, f not needed by processor I, but areas e, g, h from processors II, III, IV respectively must be shared with processor I.

Fig. 2.-- Diagram of image subdivided for four processors. Pieces a, b, c, d of central particle can be segmented independently but later must be associated as one particle.

Fig. 3.-- Effect of numerical precision on enhancement of x-ray map of superconductor b in Ag-Pd capsule (a). Detail not seen in original. Some detail in region (b) seen with linear enhancement of only region (b). Histogram equalization with full (16 bit) precision shows diffusion of Pd into superconductor. Same equalization but with only 8 bits looses detail.

Fig. 4.-- Example of addition of code for "special" processing. Equalization shown in Fig. 3 possible after adding ONLY this code.

STEREOLOGICAL GROUND RULES

R.T. DeHoff

Department of Materials Science and Engineering, University of Florida, Gainesville, FL 32611

Microstructures have three primary attributes: chemistry; physics; and geometry. The chemical and physical attributes are routinely quantified. The geometry of microstructures is almost never quantified in spite of the existence of a sophisticated but easy to use measuring apparatus for the purpose called *stereology*.

Stereology is a mathematical apparatus that permits statistical inference of the geometric properties of three dimensional microstructures from information obtained from images of the structure that are essentially two dimensional. This tool is not widely used mostly because the ground rules have been presented vaguely, or with limited application, or perhaps because the basic relationships are too simple to be believable.

This presentation briefly reviews the geometric properties that may be accessed through the stereological apparatus, the kinds of measurements required, and the expected value theorems that connect the measurements to the three dimensional geometry.
Table 1 summarizes these three aspects of the content of stereology.[1,2]

The emphasis of the presentation is on the *ground rules*:

1. The theorems at the heart of stereology *make no simplifying geometric assumptions*.

2. The fundamental equations are *expected value theorems*; the left side of each equation in Table 1 is the value approached by the mean value of that measurement obtained from a sample as the size of the sample approaches the population.

3. *Unbiased estimates* of these expected values require that the set of test probes used for each measurement be chosen from an *I*sotropic, *U*niform distribution of probes *R*andomly.

So-called *IUR* sampling of test probes to obtain unbiased estimates of the stereological measures is the key ground rule that must be built into the conscious design of a sample of test probes for stereological analysis. Strategies for designing efficient sampling schemes that satisfy the *IUR* criteria have been devised[3,4] and are discussed.

Table 1. Stereological measurements and the geometric properties they access in any microstructure.

Stereological Measurement	Relation Symbol		Symbol	Microstructure Property
Point fraction	$<P_P>$	=	V_V	Volume Fraction
Line Intercept Count	$<P_L>$	=	$\frac{1}{2}S_V$	Surface Area Density
Area Point Count	$<P_A>$	=	$\frac{1}{2}L_V$	Line Length Density
Area Feature Count	$<N_A>$	=	$N_V<D>$	Number X Diameter
Disector Count	$<N_V>$	=	N_V	Number Density
Area Tangent Count	$<T_A>$	=	M_V/π	Total Curvature

References

1. F.N. Rhines and R.T. DeHoff, Quantitative Microscopy, New York: McGraw-Hill (1968).
2. E.E. Underwood, Quantitative Stereology, Reading, MA: Addison-Wesley (1970).
3. A.J. Baddeley, H.J.G. Gundersen and L.M. Cruz-Orive, J. Microscopy, 142(1986)259.
4. A.M. Gokhale, J. of Microscopy, 167(1992)1.

IMAGE SIMULATION IN ELECTRON MICROSCOPY

Roar Kilaas

National Center for Electron Microscopy, Lawrence Berkeley Laboratory, Berkeley CA 94720, USA

The theoretical calculation of High Resolution Transmission Electron Microscope (HRTEM) images has become a routine operation due largely to the existence of several commercially available computer programs. Associated with these "black box" calculations, exists a danger coming from the ease with which the programs can be used to produce images without any understanding of the underlying physical principles and approximations used in the calculations. While hopefully the majority of users of image simulation take the care to understand the limitations of the technique, there are several basic principles that must be understood in order to use the technique within the limits of its applicability. An example of this is shown in figure 1.

Although image simulation is fairly straightforward, and the technique has been applied successfully to many problems in HRTEM, figure 2, it is not an optimum tool for solving unknown structures. Each image depends on many adjustable parameters, the structure itself being the most important, and the task of computing hundreds of images and comparing them visually is a tedious task to say the least. It is not until recently that the computer is being used to compare calculated images with experimental data in an efficient way.[1,2] The emergence of the slow scan CCD cameras and the ability to readily record images and diffraction patterns quantitatively has accelerated the need for quantitative comparison between theory and experiment. An experimental image and a calculated image can easily be compared by calculating the cross correlation coefficient between the two. While this can be done in both image space and reciprocal space, it is often advantageous to use reciprocal space since there are usually less frequency components forming the image than pixel values in the image itself. Figure 3 shows four images in a through focal series compared quantitatively to a large number of calculated images. The four regions of good match lie on a straight line, indicating that the images were taken at constant thickness with varying defocus. This technique can be expanded to iteratively refine the structure model.[2]

In most cases, the inelastic scattering is neglected in image simulation, partly because there is no good theory that allows for all mechanisms of inelastic scattering to be included in the calculation in an efficient manner. While this is not a serious limitation in most cases, the use of energy filters makes it possible not only to form images from the elastically scattered electrons, but also from inelastically scattered electrons within a given energy window. One could form an image by selecting the energy of a core-electron excitation for a particular element and hope to create an image that would map out the chemical elements in the sample with atomic resolution. The simulation of this type of image would require the inelastic scattering to be treated much more accurately than what is current practice, but given the anticipated increased use of energy filtered imaging, it is an area that needs attention.

Because of the nature of image simulation; model, image, comparison, refinement of model, etc., it is clear that it is ultimately better to develop methods that deduces structural information directly from the experimental data. While there has been progress in this area, it will take some time before these methods can be readily employed by the EM community.[3] Since these techniques involve major changes to the microscope together with a tight coupling to a computer, it is likely that image simulation will continue to play an important role in the near future.

References

1. A. Thrust and K. Urban, Ultramicroscopy 45 (1992), 23-42.

2. W. King and B.S. Lawver, submitted for publication.

3. D. Van Dyck, and W. Coene, Optik 77, 3, 125 (1987)

4. This work is supported by the Director, Office of Energy Research, Office of Basic Energy Sciences, Materials Sciences Division of the U.S.Department of Energy under Contract No. DE-AC03-76SF00098.
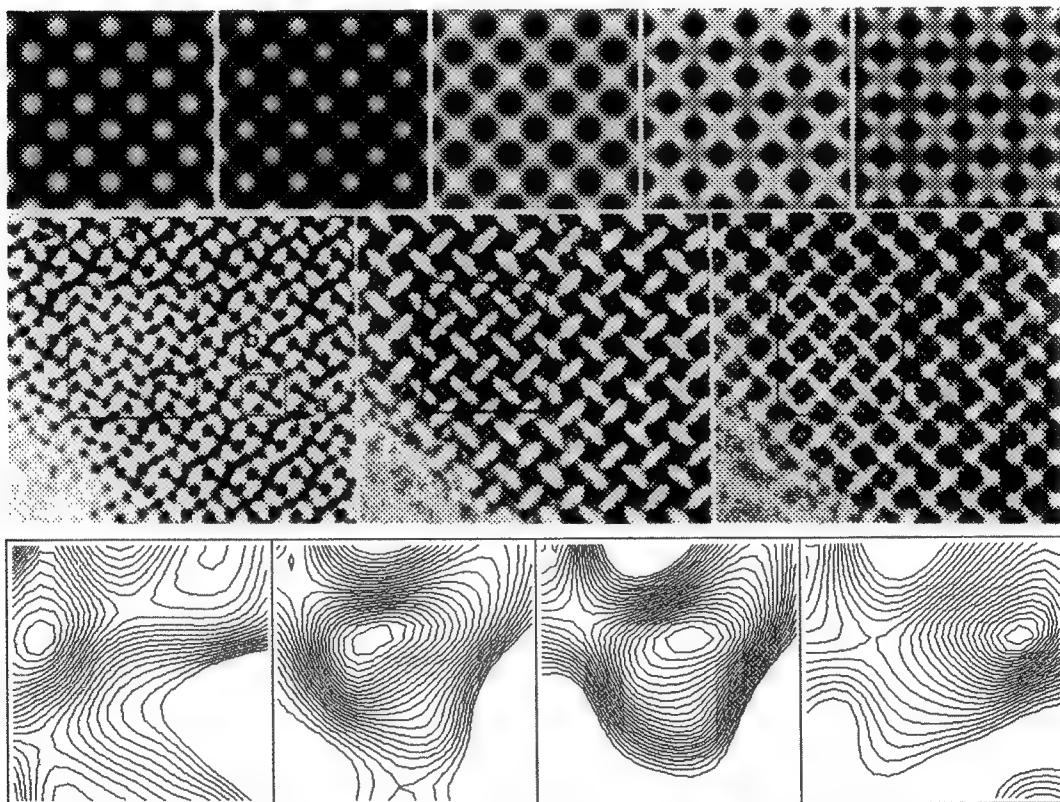
Figure 1.--Five calculated images of the same structure, $SrTiO_3$, using 5 different values for the maximum value of the scattering angle. Reflections whose scattering angle exceeds the imposed limit are not included in the dynamical calculation. In all but the first image, the maximum scattering angle is larger than what corresponds to the objective lens aperture.

Figure 2.--Examples of simulated images matching an experimental through focus series.

Figure 3.--Four calculated contour maps of the cross-correlation function between experimental and calculated images. Each map depicts the cross-correlation coefficient between a single experimental image in a through focus series and a set of calculated images. Within each map, the defocus changes from left to right and thickness of the specimen changes from top to bottom. The areas of good fit, high cross-correlation coefficient, lie on a straight line, showing that good fits are obtained for the same specimen thickness and four different values for defocus.

IMAGE SIMULATION IN SCANNING ELECTRON MICROSCOPY

Z. J. Radzimski[1]

Research Center for Integrated Systems, Hiroshima University, Higashi-Hiroshima 724, JAPAN

The development of image acquisition and processing software has made microscopy, including scanning electron microscopy (SEM), a very precise tool. Various processing techniques for image quality enhancement and image quantification have been introduced[2]. However, the theoretical bases for SEM analysis are not always fully understood. Using Monte-Carlo (MC) methods several important issues have been successfully addressed, for example, X-ray production and backscattered electron (BSE) simulation. MC methods provide insight into the physical basis of electron beam/solid interactions and offer a wide degree of freedom in setting the simulation conditions regarding sample geometry, the electron beam, and signal collection[3]. The results can be extracted at any stage of electron-target interactions to determine energy, angular and/or spatial distributions. MC programs with a single scattering approach, Mott scattering cross section and corrected Bethe's formula for energy loss can be used for both low and high energy electrons[4]. The simulation can be performed for complicated structures with multi-element phases of various shapes[5]. Traditionally, because of a long computation time, MC methods were used mainly to simulate a spot mode or line scan of SEM operation. With newer, faster computers more complicated structures and problems, including image simulation, can be addressed. At present, BSE images can be simulated with a good accuracy for relatively complicated structures. The prognosis for SEM imaging is an increased use of low energy BSE[6]. This offers advantages over secondary electrons (SE), such as less sensitivity to instability, distortion or charging. BSE imaging at low energies offers both high resolution and an image that is more topography specific than the SE signal, which is strongly affected by surface contamination and local electrical fields. Also, at low energy the BSE information depth is comparable with SE. It is important to add that the simulation of SE is quite complicated and only a few good examples for elemental targets can be found in the literature[7].

In this work, the simulation of BSE images was performed for a 3-dimensional structure, shown in Fig. 1a, with various elements (Si substrate and a pattern with combination of C, Cu and Au). The MC program is the further development of a single-scattering program widely distributed by David Joy[8] and modified later by Russ et. al.[5]. The present version, written in C language, runs on Sun workstations. The images shown in Fig. 1b - g were generated for 1 keV primary electrons using a 100x100 array of incident points with 2000 electrons at each point. The program separates backscattered electrons into four directions, similar to a solid state detector mounted below the polepiece. Various factors related to the image formation and efficiency of signal collection can be addressed by analyzing the simulated images. This includes: contrast formation, contrast versus spacing between features, edge brightening, and dimension evaluation. The quantification of these items is possible by a line scan analysis in any direction. In practice, the simulation can be performed on a selected area of a particular structure. In this way the computing time is reduced. Often, simulation of a line scan would be enough to distinguish between artifacts or reality. These issues will be discussed in detail during the presentation. Various examples of MC simulated images and their processing will be also included.

References
1. on leave from Analytical Instrum. Facility, North Carolina State Univ., Raleigh, NC 27695-7916.
2. J. C. Russ, Computer Assisted Microscopy, Plenum Press, NY, (1990)
3. D. E. Newbury, Microbeam Analysis (1992) **1**, 9.
4. A Macintosh version of such a program will be distributed at this meeting by the author.
5. J.C. Russ, Z.J.Radzimski, A. Buczkowski , L. Maynard, J. Comput. Assist. Microsc. (1990) **2**,53.
6. D.C. Joy, Microbeam Analysis (1992)**1**,19.
7. M. Kotera, T. Koshida, H. Suga, (1990), Scanning Microscopy Suppl. **4**, 111.
8. D. C. Joy, J. Microscopy, (1987), 147, 51.
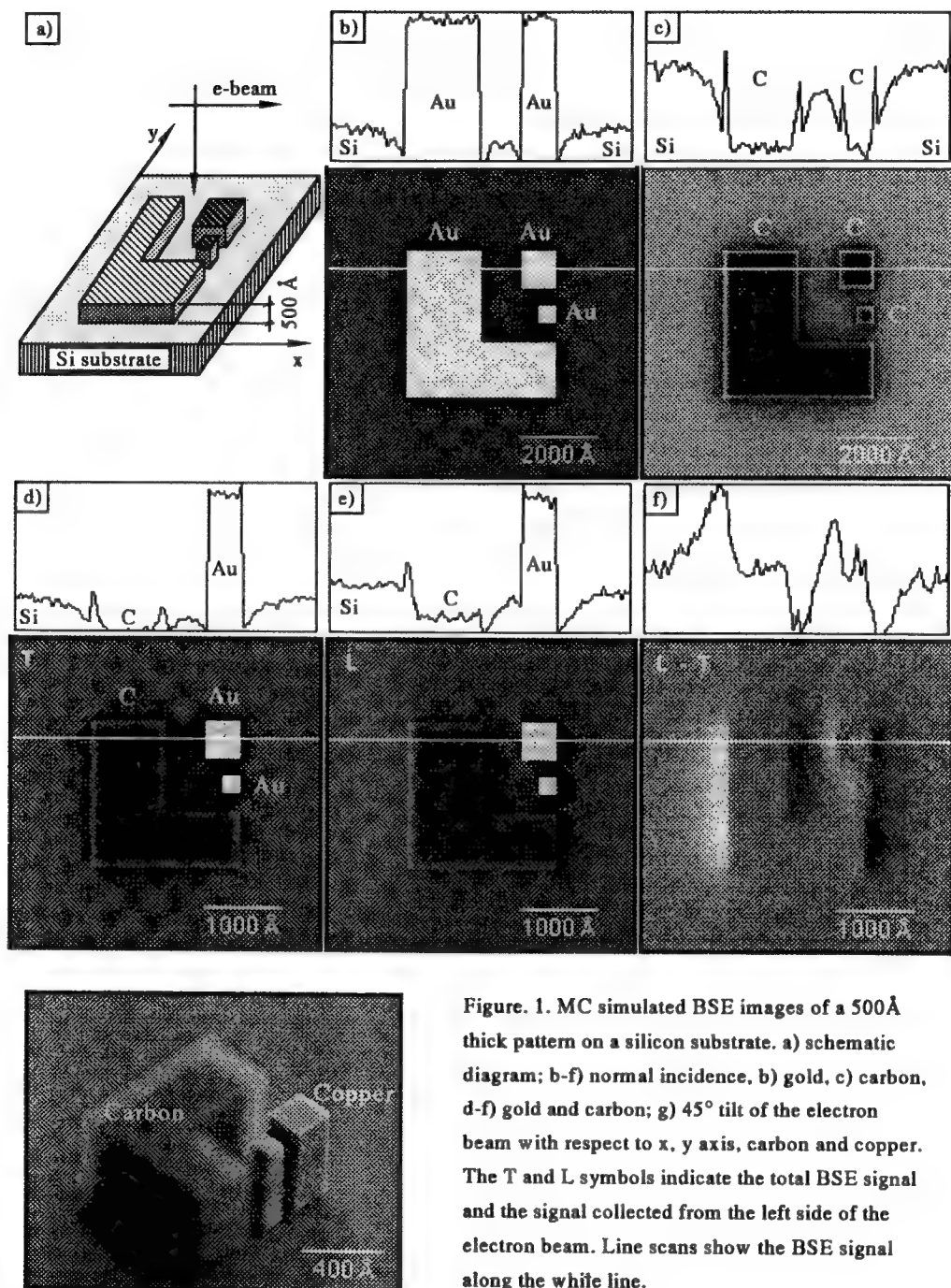
Figure. 1. MC simulated BSE images of a 500Å thick pattern on a silicon substrate. a) schematic diagram; b-f) normal incidence, b) gold, c) carbon, d-f) gold and carbon; g) 45° tilt of the electron beam with respect to x, y axis, carbon and copper. The T and L symbols indicate the total BSE signal and the signal collected from the left side of the electron beam. Line scans show the BSE signal along the white line.

545

DATA ACQUISITION AND PROCESSING FOR AUTOMATED ELECTRON MICROSCOPY

O.L. Krivanek, W.J. de Ruijter, C.E. Meyer, M.L. Leber, and J. Wilbrink

Gatan Research and Development, 6678 Owens Drive, Pleasanton, CA 94588, USA

Automated electron microscopy promises to perform many tasks better and faster than a human operator. It should also allow the operator to concentrate on the larger picture without having to worry about countless details that can be best handled by a computer. It requires three essential components: 1) data acquisition system that provides the computer with high-quality data on line, 2) computer and software able to analyze the incoming data in real time, and 3) control links that enable the computer to adjust the important microscope parameters.

An optimized system architecture is shown schematically in Fig. 1. The microscope is equipped with various microprocessors that control its hardware, and provide data processing abilities devoted to different types of signals (e.g., X-ray spectra). These microprocessors use a standardized communication protocol to communicate over a standard network (such as AppleTalk or Ethernet) with a "master computer", which provides the user interface, as well as the computing power necessary to handle the most demanding tasks. A large part of the software running on the master computer is devoted to collecting and analyzing image (or spectroscopy) data, which is furnished to the computer over a dedicated high-speed link, typically using block-mode direct-memory access (DMA) protocol.

In the case of TEM, the data is best provided by a slow-scan CCD (SSC) camera whose performance exceeds the performance of photographic film in most important aspects[1]. If enough processing power, the right software, and controlling links to the rest of the microscope are available, the system is able to perform various complicated tasks completely unassisted. Examples include high resolution autotuning that can align, focus, and stigmate a TEM faster and with better precision than any human operator[2], low dose image acquisition, and automated recording of tilt series data sets for 3-D reconstruction[3]. The accuracy of the autotuning is such that it has uncovered hitherto ignored imaging defects such as 3-fold astigmatism, and quantified them[4]. Fig. 2 illustrates the autotuning with diffractograms produced by a Macintosh Quadra 700 computer interfaced to a Philips CM12 ST, and running Gatan's DigitalMicrograph software. The computer aligned and stigmated the TEM, recorded SSC images optimized for first, second, third and fourth broad contrast transfer interval imaging, and computed and displayed their Fourier transforms.

In the case of STEM, there are typically several detectors that produce data at each image pixel. The resultant data set may consist of as many as 1024 image planes (in the case of a STEM equipped with a PEELS). The capture, analysis, and presentation of such data sets is called "spectrum imaging". Its ability to integrate imaging with ultra-sensitive analysis of any selected sample region, and the fact that it captures all the data in just a single pass of the electron beam over the sample, has made it into one of the most powerful techniques of electron microscopy available today[5].

The SEM case is similar to STEM, with the secondary and back-scattered electrons, and energy-dispersed X-ray spectroscopy (EDXS) providing the principal signals. Full control of the microscope from the master computer has lead to SEM autofocusing and precise beam control for minimum-dose imaging, as well as sophisticated "search and analyze" microanalysis procedures.

An important facet of automated microscopy is that the controlling software should include a high-level scripting language which gives users an ability to "program" experiments. The language should be simple enough to protect the users from the full complexity of the total system, yet powerful enough to enable them to do even the most complicated tasks. As an example, Gatan's DigitalMicrograph software includes a scripting language in which creating a new image C that is the product of existing images A and B is accomplished simply by writing C = A*B in a script window, and pressing Enter to execute. The command EMChangeFocus(10) changes the microscope focus by +10 DAC units, with DigitalMicrograph taking care

546

of the details of communicating with the microscope. Using this language, the 4 diffractograms of Fig. 2 were recorded automatically using a script 19 lines long, and many previously difficult tasks can be programmed in a few hours.

In summary, most of the important components for fully automated microscopy are in place, and several systems performing various automated procedures have been developed. Probably the single most important component still missing is a standardized communication language, which would enable separate pieces of hardware to work together. It would perform a function similar to that of the PostScript "page description language", which helped launch the desktop publishing revolution by enabling different personal computers and printers to work together. A standardized EM "experiment description language" would similarly accelerate automated microscopy developments into a full revolution, and it is to be hoped that MSA/MAS will have the foresight to encourage its development.

References

1. O.L. Krivanek and P.E. Mooney, Ultramicroscopy, in print.
2. O.L. Krivanek and G.Y. Fan, Proc. 50th EMSA meet., part 1, 95 (1992).
3. A.J. Koster, H. Chen, J.W. Sedat and D.A. Agard, Ultramicroscopy 46, 207 (1992).
4. O.L. Krivanek and M.L. Leber - these proceedings.
5. R.D. Leapman and J.A. Hunt - *in:* Microscopy, the Key Research Tool (EMSA, MA) p.39 (1992).
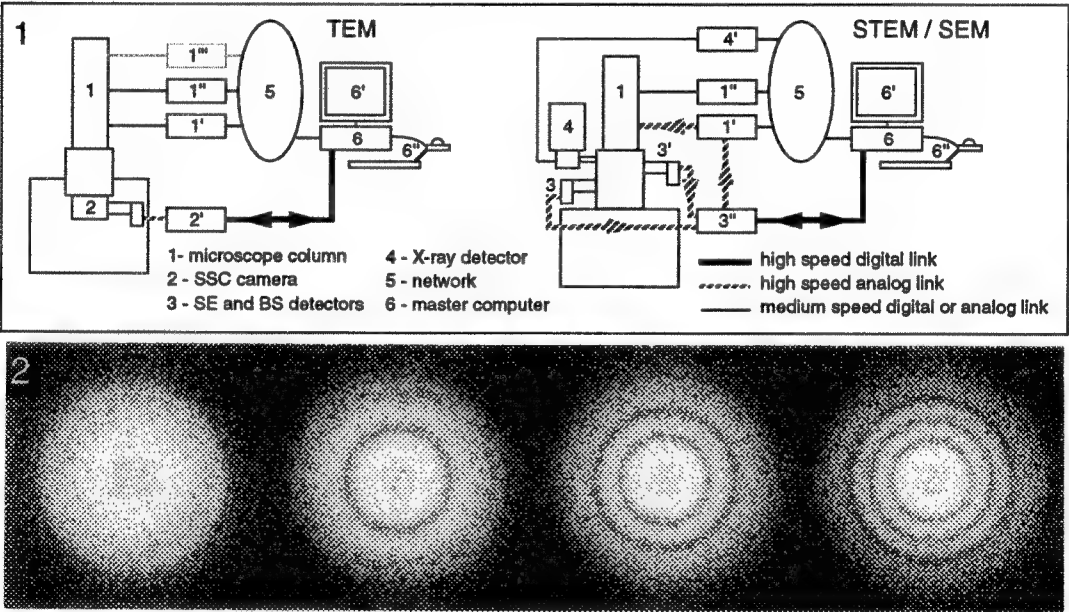
Fig. 1. Schematic diagrams of automated TEM and STEM/SEM systems. 1: microscope column, 1'-1''': column-controlling electronics with dedicated microprocessors, 2-2': SSC camera and its electronics, 3-3": SEM/STEM detectors and digitizing and scan-producing electronics, 4-4': X-ray detector and electronics, 5: medium speed (100-1000kB/s) network, 6-6": master computer, monitor and input devices.

Fig. 2. Experimental digital diffractograms of successive micrographs recorded by a Gatan 694 SSC using a 19-line DigitalMicrograph script controlling an autotuned microscope. They correspond to Scherzer defocus, and $\sqrt{3.5}$, $\sqrt{5.5}$, and $\sqrt{7.5}$ generalized defocus, respectively. No other diffractograms were taken in the series, illustrating the precision of the microscope control.

HVEM TOMOGRAPHY: A NEW TOOL FOR THE CELL BIOLOGIST

Joachim Frank

Wadsworth Center, New York State Department of Health, Albany, NY 12201-0509 and
Department of Biomedical Sciences, SUNY Albany

The technique of three-dimensional imaging with the transmission electron microscope [1] is a new tool ready to be used by the cell biologist. By itself, the transmission microscope is not capable of producing 3D images, but it allows collection of a tilt series of projections in a wide angular range. From such a series, a 3D image can be reconstructed using established mathematical principles. The first reconstructions of this kind were obtained by Walter Hoppe's group in 1974 [2], but the full potential of this approach was not realized until the mid-80's when computers with sufficient speed and memory became available [3-7].

Especially within the past three years, there has been a rapid development in the areas of instrumentation, computation, and visualization. New tilt stages meet the demands of high accuracy and wide angular coverage [8,9]. Direct image readout systems and on-line control of the microscope make it possible to design automated data collection systems [10]. Software for 3D reconstruction and restoration exists as part of major EM-oriented image processing packages [11]. Workstations with high-speed graphics enable the viewing of complex structures in motion, a capability necessary for the investigator to "grasp" and interpret the internal organization of an unknown biological object. Current development work in our group focuses on methods for eliminating the "missing wedge" in Fourier space so that structures are imaged without distortion, and on the development of tools for interacting with three-dimensional data. As yet there exists no general tool that would allow the cell biologist to isolate a structure from its complex surroundings in three dimensions. We plan to develop a 3D interactive environment that allows groups of voxels of a 3D structure to be transported from one viewing box to another. A three-dimensional cursor (TINKERBELL) will be used to select the regions to be isolated.

The combination of tomograpy with the high voltage electron microscope is particularly powerful, since it allows specimens up to several microns thick to be imaged [5,12]. Thus long-standing questions such as the organization of the mitotic apparatus, the higher-order structure of the chromosome and the architecture of mitochondria (Fig. 1) can be addressed. For example, the results of our recent tomographic electron study of the kinetochore [13] indicate that previous models, derived on the basis of interpreting projection images, are quite oversimplified.

At this stage there is a need to popularize the tomographic method and place it in the hands of adventurous graduate students in the field of cell biology who need to explore three-dimensional spatial organization of cell components in a "non-destructive" way, i.e., without having to resort to thin sectioning. The Albany Biological Microscopy and Image Reconstruction Resource, which is funded by the National Center for Research Resources of NIH, is available for HVEM tomographic studies at no cost.

References

[1]   Electron Tomography, ed. J. Frank, Plenum 1992.
[2]   W. Hoppe et al., Hoppe-Seyler's Z. Phys. Chem. (1974)355, 1483.
[3]   J.A. Subirana et al., J. Biomol. Struct. Dyn. (1983)1, 705.
[4]   B.F. McEwen et al., Proc. Natl. Acad. Sci. USA (1986)83, 9040.
[5]   J. Frank et al., J. Electron Microsc. Tech. (1987)6, 193.
[6]   D.E. Olins et al., Science (1983)220, 498.
[7]   U. Skoglund et al., Nature (London) (1986)319, 560.
[8]   J.N. Turner et al., Ultramicroscopy (1988)26, 337.
[9]   D.P. Barnard et al., J. Microscopy (1992)167, 39.
[10]   K. Dierksen et al., Ultrmamicroscopy (1992)40, 71.
[11]   R. Hegerl, Ultramicroscopy (1992)46, 415.
[12]   B.F. McEwen, in Electron Tomography, ed. J. Frank, Plenum, 1992.
[13]   B.F. McEwen et al., J. Cell Biol. (1993)120, 301.
[14]   M. Marko et al., J. Electron Microsc. Tech. (1988)9, 395.

FIG. 1--A tomographic reconstruction of a pair of rat-liver mitochondria, showing the organization of the predominantly tube-like cristae associated with the "orthodox" conformation (provided by C.A. Mannella and M. Marko). Membranes were contoured stereoscopically [14] in serial subsets of the tomographic volume, since segmentation by density or density gradient was unsuccessful.

SOFTWARE FOR THE RECONSTRUCTION OF OFF-AXIS ELECTRON HOLOGRAMS

David C Joy[+] and Rodney D Bunn

EM Facility, University of Tennessee, Knoxville, TN 37996-0810, and
[+] and Oak Ridge National Laboratory, Oak Ridge, TN 37831

Holography is a two step imaging process. After a hologram has been recorded it must then be reconstructed in order to obtain the stored image information. Gabor originally envisaged the use of optical reconstruction methods, but these are difficult to set up and limited in their flexibility.[1] The alternative is to use digital techniques to reconstruct and manipulate the hologram and its reconstructions. This paper describes a program designed for the reconstruction of off-axis electron holograms.

An off-axis electron hologram is an interferogram between a reference electron wave and the signal wave which has passed through the specimen. The hologram consists of a pattern of fringes modulated in position and amplitude as a result of phase shifts in, and scattering of, the signal wave. To recover phase and amplitude images from the hologram it is necessary to perform three operational steps. Firstly, the digitized hologram is Fourier transformed producing an array of complex numbers, one for each pixel in the original hologram. The intensity representation of this transform in reciprocal space contains an autocorrelation peak flanked by two sidebands. The two sidebands are complex conjugate to each other, and each contains the phase and amplitude information about the signal wave. A region of reciprocal space containing one of the sidebands is then selected and moved to the origin of coordinates. Finally, this region is again Fourier transformed producing an array with about 1/3 to 1/4 of the number of pixels of the original hologram. The modulus of the complex number at each pixel point represents the amplitude of the signal wave at that pixel and hence a gray scale display of the modulus gives an 'amplitude' image. The argument of the complex number at a pixel point represents the phase shift of the signal wave at that pixel and a gray scale display of the argument (zero shift =black, 2π radians =white) thus produces the 'phase' image of the specimen.

Although the processing steps employed are standard operations, and can thus be carried out by any one of several of the standard image processing packages which are commercially available , it is convenient to have a special purpose program available. We have therefore developed a program, Holographic Image Processing (HIP) for the Apple Macintosh™ II computer which implements the required steps, and also provides additional facilities for quantitative enhancement of the reconstructed images. The code is in MPW C and makes full use of the Macintosh graphical user interface. HIP can handle holograms up to 1024x1024 pixels in size, although manipulating and viewing images of this size requires large amounts of memory (> 24 Mbytes) and large display screens. However, HIP can also display images in a reduced format of 256x256 pixels while maintaining all of the 1024x1024 data and facilities are provided to allow for the viewing of limited areas of the full image while employing the 256x256 mode. The operations which determine the speed of the reconstruction are data formatting and the Fourier transform routines. When HIP is executed on a MacIIci not equipped with a 68881

floating point coprocessor (FPU) the reconstruction of a 256x256 pixel hologram requires in excess of 15 minutes processing time. Using a MacIIci equipped with a 68882 FPU, performance is increased by a factor of 15 times, a reconstruction now only requiring 1 minute and 9 seconds. Larger images require proportionally longer processing times.

To further enhance performance we have incorporated a National Instruments DSP2300 Digital Signal Processor (DSP) board. This NuBus board is constructed around the Texas Instruments TMS-320C30 DSP which is a specialized Reduced Instruction Set Computer (RISC) which can process data at a rate of 33 MFLOPS. In addition the DSP2300 has high speed dual ported, dual access 32-bit memory which maximizes throughput when performing floating point array maths and data transfers. The performance of HIP is enhanced by a further factor of 3 times as compared with the FPU benchmarks, and still further refinement and improvements in processing time are anticipated.

It should be noted that some diligent checking is necessary before applying either software, or DSP hardware-based, Fourier transform routines since many of the codes in common use employ techniques to speed up computation which may result in incorrect signs for the phase (i.e complex number is in the wrong quadrant) or even, in a few cases, incorrect amplitudes. The final amplitude and phase images, together with the original hologram and the intermediate transform, are all available on the screen for user interaction, and may be stored as standard TIFF files.

The phase shifts suffered by an electron wave travelling through a specimen, or through electric or magnetic fields, are usually small ($<\pi$) so provision is made to enhance the information content of the phase image. The technique of phase amplification multiplies the phase shift by N times (where N is an integer) and displays the phase variation modulo 2π so producing contours in the image at steps of $2\pi/N$ which help delineate surfaces features, edges etc. The phase image can also processed so as to simulate the effect of interfering the reconstructed image with the original reference beam. This produces an interferogram which reveals the three-dimensional shape of the specimen. Finally, the phase shift associated with each pixel can be plotted as a vertical offset to form a 'mesh' image which again displays the three-dimensionality of the sample and which can be rotated about all three axes on the display screen for detailed viewing.[2]

REFERENCES

(1) D. Gabor, (1948), Proc.Roy.Soc., **A197**, 45
(2) This work was sponsored in part by the Laboratory Directed Research and Development Program of Oak Ridge National Laboratory, managed by Martin Marietta Energy Systems Inc., for the United States Department of Energy under contract DE-AC05-84OR21400

HARD-COPY IMAGING OPTIONS

Dr. Leonard Polizzotto

Assistant Director of Research, Polaroid Corporation, 730 Main Street-1,
Cambridge, MA 02139

Photographic film has played a central role in the recording of microscope images since the invention of photography in the 1830s. Photography rapidly creates an accurate record of the microscopic specimen and avoids the subjectivity that was inherent in written and artistic descriptions of visual observations. Both instant and conventional films offer high resolution, the ability to record a large tonal gradation, and a stable media for long-term data storage.

Newer techniques, such as thermal, ink jet, and laser prints, have grown in popularity because they offer ease-of-use or lower per-image cost. Despite recent improvements, none of these techniques offer the resolution or stability of a photograph. In general, people have been forced to sacrifice quality and permanence in order to achieve the lower per-image cost and ease-of-use promised by alternative recording systems.

Photographic hard copy has traditionally served as both the communication and storage medium. The introduction of digital storage methods has made these functions more distinct. Therefore, it is important to understand the trade offs between hard copy images and electronically stored images. Magnetic, optical, and solid state electronic storage technologies differ significantly in their cost per image, time and ease to record and retrieve, and display flexibility. Photographic hard copy continues to offer some archival storage advantages, and hard copy remains a requirement for reports, presentations, and discussions.

Each of the current hard copy recording options offers a mix of advantages and disadvantages. The ideal hard copy medium for microscopy would combine the quality and permanence of photography with the price and ease-of-use of the alternative systems. This ideal hard copy system would also offer the correct contrast and dynamic range, so that all the important details in the micrograph will be visible within the print. A black-and-white system would be able to record a full range of gray values with rich whites and blacks, and a color system would be able to record a full range of colors.

In recent years, Polaroid Corporation has developed a variety of black-and-white and color imaging media that are activated by diode lasers. Unlike existing laser printers that produce an image by fusing toner to a paper or transparent base, these new imaging systems use laser power to print directly on the new media by creating phase transitions within it. The new laser imaging systems show promise for eliminating the current trade offs between cost, ease-of-use, quality, and permanence. The instant processes require no running water or wet chemistry, the imaging time is short, and the prints offer long term archival permanence.

A black-and-white laser imaging system was demonstrated at the "Future Directions in Microscopy and Imaging" workshop held before last year's EMSA meeting. This system has now been beta tested at a variety of large scientific imaging locations with outstanding results.

The new black-and-white process uses carbon particles instead of photographic silver and relies upon high power laser diodes to write the image. The film consists of a 7 mil polyester base, a laser sensitive layer, an imaging layer composed of carbon particles in a polymeric matrix, and a cover sheet.

The film is exposed with high-power gallium-arsenide solid state laser diodes that write a high-resolution image. When the laser strikes the film, its energy is absorbed by the laser sensitive layer. The absorbed energy causes a phase transformation that creates a permanent adhesion of the imaging layer to the laser sensitive layer. Following exposure, the cover sheet is peeled off, which removes the unactivated portions of the imaging layer. This leaves the positive image permanently affixed to the substrate.

There are some important variables that must be carefully controlled to produce a high-quality image with this new technique. The carbon particles must be small and have a narrow size distribution in order to create a uniform spot size. And the laser energy must be applied for very brief intervals--typically a few hundred nanoseconds--to prevent the energy from affecting areas that should remain unexposed. In addition, the separation of the film sandwich has to be carefully controlled, to ensure that all unexposed areas are removed and all exposed areas are kept in place.

The new laser imaging system produces a full range of grays by using a digital gray-scale rendering technique that subdivides each of the individual pixels into 4320 separate pels. Each pel is individually exposed by focusing the laser beam onto a small area of the film that is only a few microns square. The large number of individual pels per pixel creates a film with 4320 or 12 bits of gray value. The 4320 potential gray values in this laser printing system make it possible to precisely define any film response curve, by simply adjusting the subset of actual values that are used for a particular picture.

The new laser medium matches photographic permanence, because there are no fadeable dyes, such as those used in the thermal transfer and dye diffusion processes. Instead, the image is composed of stable carbon particles that are permanently affixed to the polyester base by an irreversible phase transformation.

Color images are becoming increasingly important in scientific imaging and a new color laser imaging method is also under development at Polaroid. This system uses laser energy to activate color dyes within the medium. The laser exposure transforms the medium into a full-color slide, reflective print, or overhead transparency.

While the black-and-white laser imaging system requires only a single laser wavelength, the new color system uses lasers with three different infrared wavelengths to create phase transitions for yellow, cyan, and magenta dyes in the single sheet, completely dry media. This new imaging system combines the resolution and permanence of photography with the ease-of-use and lower per-image cost of other current imaging methods. It is expected that the new color system will find many applications in microscopy and scientific imaging, including producing the slides that will be used in the presentation of this paper.

ALIGNMENT WITHOUT USING MARKERS IN ELECTRON TOMOGRAPHIC RECONSTRUCTION

Weiping Liu, David A. Agard and John Sedat

Department of Biochemistry and Biophysics and the Howard Hughes Medical Institute, University of California at San Francisco, San Francisco, CA 94143-0448

In the electron tomographic reconstruction process the mutual alignment between projections of different view angles is a crucial step. Thus far the only alignment method routinely used is based on fiducial markers[1]: gold particles are distributed on the specimen, and the relationship between the specimen and the digital projection coordinate systems is determined from least-square fitting the measured positions of colloidal gold beads on the projections. The inherent drawbacks with this method are that i) it is a tedious trial-and-error process to obtain the right amount of evenly distributed beads in the area of interest on the specimen and ii) the beads might obstruct the structural analysis since they are essentially opaque objects under the electron microscope (EM). The problems can become more acute if ice-embedded specimens are to be studied. The other two approaches to the alignment are the common line / moments method[2] which requires that the object has clear boundaries in its projections and the cross-correlation[3] method which assumes that the object has a flat structure. But for the studies of sub-cellular structures, these approaches are not valid since there are normally no well-defined structural boundaries in the projections due to the limited size of the detector (which introduces the so-called limited detector problem) and the structure is generally not flat. The sino-alignment approach, which aligns via comparing the re-projections of the reconstruction with the projections, has been proposed but has never been applied to experimental data[4].

In essence, the ultimate information for alignment lies in the redundancy of the data set. From the corresponding consistency requirement between projections in this set we can in principle achieve alignment without resorting to isolated prominent features in the projections (e.g., the gold beads). Thus the alignment problem can be generally defined: an optimal alignment of a projection set is achieved when the projections in this set are oriented in such a way that their mutual consistency is maximized. The consistency is measured and achieved through sino-alignment in an iterative fashion: in cycle k, i) the alignment parameters of cycle (k-1) are applied the projections, ii) the corresponding reconstructions are computed, and iii) the projections are aligned with the corresponding re-projections of the reconstruction to obtain the new alignment parameters (we use least-square fitting for the alignment).

There are five alignment parameters with each projection for a single-tilt data collection geometry: one tilt angle which can be obtained from the goniometer readings, one rotational angle of the projection relative to the 3-D tilt axis, one magnification which varies with the objective current that is adjusted to follow the changing specimen height during the data collection process, and two translational displacements. We have found that the sino-alignment is ill-behaved towards the rotational parameters: it is unable to correct if all projections in a set have a rotational offset, but it is effective with translational parameters. Thus the following alignment procedure has been devised:
1) Obtain rotational alignment parameters and magnifications via EM calibration. (this is applicable for our automated EM data collection system with CCD camera[5].)
2) Do initial translational alignments via cross-correlation between neighboring tilt projections, with the projections stretched according to their tilt angles.

3) Do sino-alignment with translational parameters using the result of 2) as the initial input.

In practice, to increase the computational efficiency, the raw projection data set is sampled down 5 times and the sino-alignment of step 3 is applied first to this reduced set. The resultant alignment parameters are then refined by applying the sino-alignment to the raw data set. To minimize the more severe limited detector problem in projections of high tilt angles, the projections of low tilt angles (normally within 55°) are sino-aligned first, then the high tilts are sino-aligned with the alignment parameters of the low tilts fixed. The choice of reconstruction algorithm is also important for the sino-alignment, and the Tomographic Alternating Projection Iterative Reconstruction (TAPIR) algorithm[5] is used. This algorithm is essentially a constrained iterative technique which incorporates constraints such as positivity, degree of smoothness of the reconstruction, and compact support (by choosing the dimensions of the reconstruction volume). It gives superior reconstructions than the weighted back-projection algorithms especially for distributed sub cellular structures. Also, to achieve good accuracy, fast convergence and high computational efficiency in the sino-alignment process, appropriate sizes of the projections should be used, the smoothness constraint in TAPIR for a given alignment cycle should be chosen according to the degree of misalignment in that cycle, and the amount of interpolations should be (and have been) minimized.

By adopting the above strategy, we have obtained alignment to within sub-pixel agreement with the bead alignment result. Finally, our approach is general in spirit, which can be applicable to many other alignment problems.

References:

1. M.C. Lawrence, In Electron Tomography, New York: Planum Press (1992), 197.
2. A.B. Goncharov and M.S. Gelfand, Ultramicroscopy 25 (1988), 317.
3. J. Frank and B.F. McEwen, In Electron Tomography, New York: Planum Press (1992), 205.
4. J. Dengler, Ultramicroscopy 30 (1989), 337.
5. A.J. Koster et al., Microscopy Society of America Bulletin 23(2) (1993), (in press).

ANALYSIS OF CRYO-ELECTRON MICROGRAPHS OF HbS FIBERS

Michael R. Lewis, Leon J. Gross, and Robert Josephs

Laboratory for Image Analysis and Electron Microscopy, Department of Molecular Genetics and Cell Biology, The University of Chicago, 920 East 58th Street, Chicago, Illinois 60637

We are studying the structure of deoxy-sickle hemoglobin (HbS) fibers by cryo-electron microscopy (cryo-EM). Cryo-EM affords potentially higher resolution than negative staining in part because the electron scattering by unstained protein includes internal structure which may be poorly depicted by an envelope of negative stain. This advantage, however, is partially compromised by a low signal to noise ratio (snr) and low image contrast. Our cryo-EM images were recorded with specimen doses of 7 e$^-$/Å^2 at 100 keV, *ca.* 100 nm defocus, and 39,000 magnification on Kodak SO-163 film.[1,2]

Helical particles usually have a constant pitch. Thus the rotation about the axis is coupled to translation along the length of the particle. HbS fibers, however, have a variable pitch which ranges from 6° to 12° rotation per unit cell length (63 Å). Consequently, the rotation of HbS fibers is partially decoupled from translation and the twist of each unit cell and its relative angular rotation about fiber the axis cannot be determined by particle symmetry. To determine these parameters for 3-dimensional reconstructions, we independently compare each unit cell to models based on a previous reconstruction of negatively stained fibers.[3] A 3-dimensional co-ordinate model of this reconstruction, calculated by Watowich et al.[4], was used to calculate provisional 4 Å per voxel electron density models of fibers. These models have different, but uniform, pitches ranging from 2° to 17° rotation per unit cell (figure 1).[2]

From each density model, fiber projections were calculated in order to display each angle of view from 1° to 360°. We determine the pitch and angle of view for a unit cell by its **similarity** to views in the model gallery. In our procedure a unit cell is first **aligned** within the gallery by cross-correlation, which locates the unit cell axis and identifies its phase along the fiber axis to ± 2 Å. The unit cell's similarity is then evaluated by calculating correlation coefficients at each pitch and angle of view in the gallery. For each unit cell this procedure produces a surface plot of image similarity (figure 1c), showing the correlation coefficients (z-axis) versus pitch (y-axis) and angular rotation (x-axis). We have found that in HbS fibers the image differences due to pitch are small, but significant enough to produce a distinct peak coefficient at the correct angle of view and pitch of the test unit cell. The mirror image, whose angle of view differs by 180°, also produces a peak because of the approximate 2-fold screw symmetry of HbS fibers. However this peak is lower than for the correct angle of view.

We are examining the properties this procedure using model images having limited resolution, low snr (figure 1b), rotational alignment errors, scaling errors, shifted phases, and reversed polarity. These tests are designed simulate actual cryo-electron micrographs. At snr 1, correlation coefficients identify both the pitch and angle of view of test unit cells to ± 2°, even though the peak coefficient is only *ca.* 0.33. At 32 Å resolution pitch discrimination is nearly abolished, and at 64 Å resolution the ability to discriminate mirror images is lost despite coefficients of *ca.* 0.96. Small (1.5°) axis tilt errors have no appreciable effect, whereas scaling errors introduce systematic shifts from the proper angle of view, apparently because the fiber width varies with angle of view. These results suggest that our procedure will successfully identify the pitch and angle of view in micrographs of frozen hydrated HbS fibers.

References

1. Lewis, M. R. & Josephs, R., Proc. Ann. EMSA meeting (1992) 50, 1036-7.
2. Lewis, M. R., et al., J. Micr. Res. Tech. (1993) in press
3. Carragher, B., et al., J. Mol. Biol. (1988) 199, 315-331.
4. Watowich, S. J., et al., J. Mol. Biol. (1989) 209, 821-828.
5. Supported by NIH grant HL30121 (R.J.) and Training Grant GM08282 (M.R.L.)
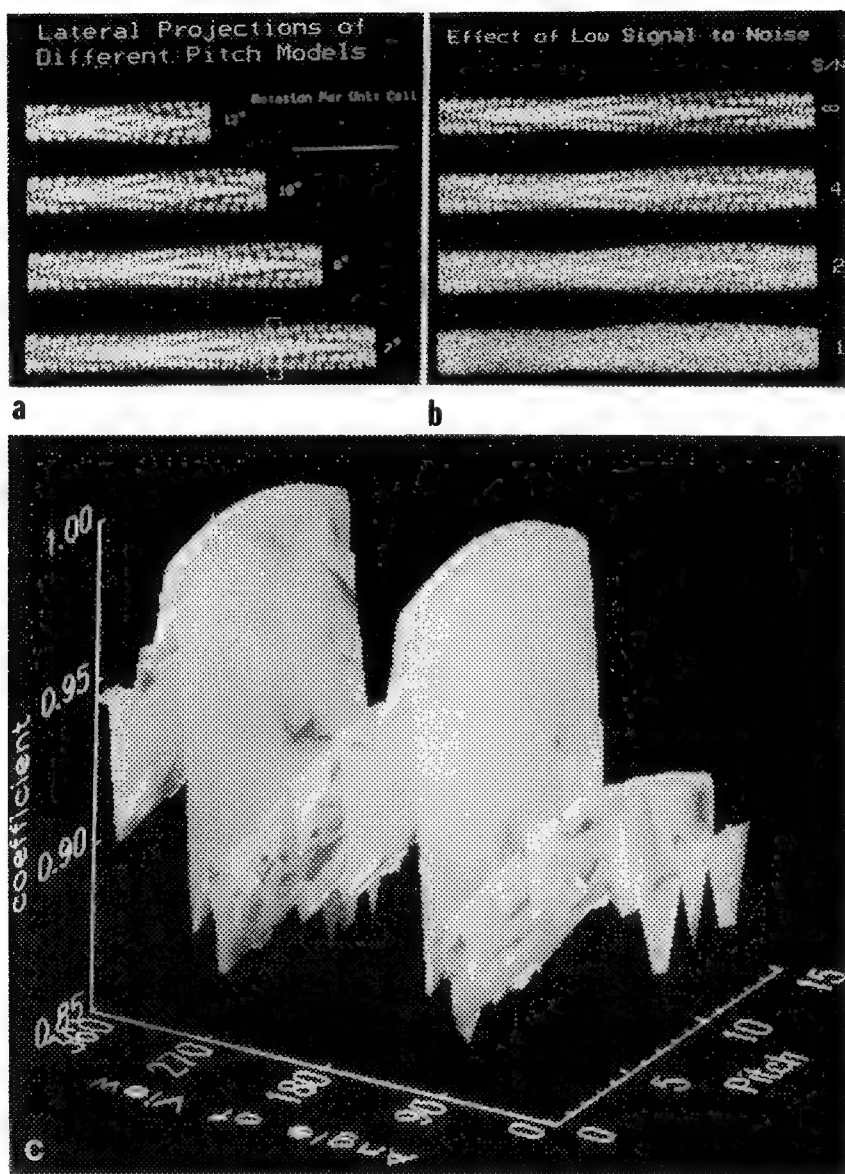
FIG. 1. a) Model deoxy-sickle hemoglobin fiber projections for four different pitches. Bar = 500 Å. The unit cell used to calculate the coefficients in panel c is outlined by the box in the bottom projection. b) The bottom projection of panel a (with 4 additional unit cells length) is shown with increasing amounts of noise. Our procedure identifies the correct pitch and angle of view of model unit cells even at snr 1. c) Surface plot of image similarity. Correlation coefficients are plotted for the unit cell image outlined in panel a.

IMAGE RECONSTRUCTION USING A FOCUS SERIES ON THICK BIOLOGICAL SPECIMENS: TEM CTF CORRECTION

Karen F. Han, John W. Sedat and David A. Agard

Graduate Group in Biophysics, Howard Hughes Medical Institute, Dept. of Biochemistry and Biophysics. University of California, San Francisco, CA 94143

The primary project of our laboratory is the investigation of chromatin structure by three dimensional electron microscope tomography. Three dimensional tomography involves the reconstruction of an object by combining multiple projection views of the object at different tilt angles. There are two complications that give rise to an inaccurate representation in the image of the projected object mass density: 1) electron-specimen interactions, and 2) electron microscope lens aberrations. In our abstract, "Analysis of Electron-specimen Interactions of Thick Biological Specimens in Transmission Electron Microscopy at 200 keV" elsewhere in these proceedings, we investigated image formation at the level of electron-specimen interactions at 200 keV. We extrapolated that at 300 keV, there is still a significant amount of elastic scattering for thick (up to 0.7 microns) biological specimens . Here, we demonstrate that this allows the correction of the microscope aberration function through multiple focus observations can enhance contrast.

For high resolution electron microscopy of crystalline materials, some authors have demonstrated that the focus variation method to reconstruct the specimen exit-surface electron wave can lead to an improvement in resolution [1-3]. Other authors have done CTF corrections at intermediate resolutions on thin biological specimens such as macromolecules and viruses[4,5]. We attempt to reconstruct images of 0.3 micron thick epon embedded, heavy-metal stained biological specimens at 300 keV, with a resolution down to 30 Å^{-1}. (Data collection system at UCSF[6] allows convenient on-line image processing of multiple focus data sets.)

Focus levels of the images were determined through beam tilt induced image displacement[6], with an accuracy of 0.1 micron. For the resolution of interest, we select large defocuses (10, 5 and 3 microns) for image restoration. Using the positions of the maxima and minima in the diffractogram, the relative amounts of phase and amplitude components of the CTF can be estimated. Many authors have done image restoration using many (usually more than 8) focus levels[1-5]. In a single axis tomographic reconstruction data set, it is impractical to take more than 3 focus level images for every projection. It is therefore necessary to develop a technique for image restoration that requires fewer focus levels and less computational time.

We experimentally showed that multiple scattering outside of the objective aperture (20 microns) contributes only to additional background noise and not object information (fig.1). From spectroscopic imaging analysis, we found that there were only very low resolution object features at energy losses beyond 50 eV. Therefore, we make the assumption that much of the multiple scattering component will contribute to a constant background that will not coherently follow the expected CTF fluctuations through focus at resolutions beyond 150 Å^{-1}. The technique of image restoration then involves the extraction of the imaging component that follows the expected fluctuations in the CTF.

Very simply, we do a least squares fit on the following function:

$$\text{Data}(k, \Delta f) = \text{Object}(k)\ \text{CTF}(k, \Delta f) + \text{Other}(k).$$

It is worth noting that this does not take into account all the partially coherent components that still follow the fluctuation of the CTF through focus. By using single value decomposition of the CTF matrix, one can allow a threshold for the fit such that it does not become too stringent. We show here that using this type of CTF correction, the fitted object does enhance image resolution as compared to the in focus image (fig.2). We note that the 'other' component still contained a fair amount of low resolution information that is not included in the object. This is not surprising since the CTF fluctuation through focus is most sensitive at high resolutions. We are in the process of comparing the reconstructed object with and without such CTF correction.

References:
1. D. van Dyck and M. Op de Beeck. Proc. 12th ICEM Meeting, Seattle (1990) 26.
2. D. van Dyck. Proc. 49th Annual EMSA Meeting, San Jose (1991) 654.
3. W. de Ruijter et al. Proc. 50th Annual EMSA Meeting, Boston (1992) 988.
4. D. Typke, R. Hegerl, and J. Kleinz. Ultramicroscopy **46** (1992) 157.
5. R. Vogel and S. Provencher. Ultramicroscopy **25** (1988) 223.
6. A. Koster et al. EMSA Bulletin **23** (1993) in press.

Figure Captions:
1. 0.3 micron thick specimen embedded in epon stained with uranyl acetate and lead citrate. Images were taken on the Philips EM430 at 10300X. A) Without an objective aperture, B) With a 20 micron objective aperture, C) Image difference between A and B.
2A. Object restored from 10, 5 and 3 microns underfocused images.
2B. Other component
2C. Same image taken in focus.
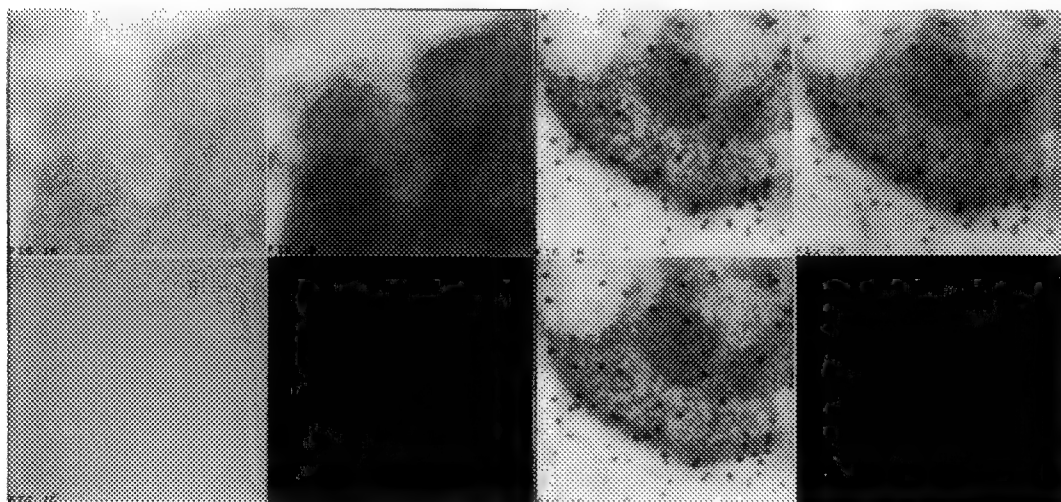
DETERMINATION OF THE DEFOCUS VALUE OF MICROGRAPHS OF ICE-EMBEDDED SPECIMEN WITHOUT CARBON SUPPORT FILM

Z. Hong Zhou

Verna and Marrs McLean Department of Biochemistry, and W. M. Keck Center for Computational Biology, Baylor College of Medicine, 1 Baylor Plaza, Houston, TX 77030

It is well recognized that the contrast transfer function (CTF) of an electron microscope modulates the image contrast. The effects of this CTF are to reverse the sign of the phases and to alter the amplitudes at different spatial frequencies. These changes are dependent on the defocus of the objective lens in a given microscope setting. Therefore, it is necessary to determine the defocus experimentally in order to correct the phase reversal and the amplitudes due to the CTF for attaining a high resolution reconstruction. The most straightforward way of determining the defocus value is to determine the positions of the Thon rings in the CTF by optical or computed transforms. In a crystalline specimen, the defocus value of an image can be refined against the electron diffraction amplitude[1]. For specimen of which the x-ray structure is known, one can also use the x-ray structure factor to determine the CTF parameters[2]. Since many of the ice-embedded specimens were prepared without carbon support film in order to enhance the image contrast, this has presented a difficulty in visualizing the CTF rings readily. This lack of visibility may be caused by the low scattering contrast of the ice-embedded specimen. We have evaluated in this paper how one may obtain the CTF rings and determine the defocus value of a micrograph by summing the computed Fourier transform amplitudes of individual images of the capsids of herpes simplex virus type 2 (HSV-2) taken with a 400 kV electron cryo-microscope.

Ice-embedded B capsids of HSV-2 were prepared by quick freezing and suspended on a holey-carbon grid without any support film. 400 kV images were recorded from the specimen kept at $-168°C$ in a JEOL 4000 electron microscope at $20,000 \times$ magnification with an electron dose of about 6 e/$Å^2$ on Kodak SO163 electron image films (figure 1). Each specimen area was imaged twice with a focal pair of 1μm defocus difference. The micrographs were then digitized with a step-size equivalent to 5.5 Å on the specimen. Capsid particles were boxed out into individual particle images of 256×256 pixels interactively on a Silicon Graphics Power Series computer and then Fourier transformed. After summing the amplitudes of the transforms of 606 particle images from the same micrograph, we were able to see the Thon rings of the CTF up to the fourth order (figure 2). The spatial frequencies of the minima of the CTF were used to calculate the defocus value of the micrograph. The agreement among the defocus values calculated from the frequencies of the different minima suggested that these minima were not due to the molecular transforms of the capsid particles. This conclusion was further confirmed when we compared the azimuthally averaged amplitudes of the transforms of the focal-pair images (figure 3). The number of Fourier transforms of the capsid particles needed to visualize the CTF rings is dependent on the defocus value of the micrograph as well as the molecular transform of the particles. At 7.3μm underfocus, 20 HSV-2 capsid particles are adequate to show the first two minima. At 2μm underfocus, 400 particles are required to show the first 2 CTF minima. This method has been tested to work for images of several specimens of single particle. This computational procedure can be essential for our attempt to extend the structural resolution of 3-dimensional reconstruction of single particles[3].

References:
1. R. Henderson, *et al.*, (1986), *Ultramicroscopy*, 19, 147.
2. R. H. Cheng, (1992) *EMSA Proceedings*, 996.
3. The author would like to thank Dr. W. Chiu for advise and guidance throughout this work. Many thanks to J. Jokana for recording the micrographs, to Drs. W. Batterson and M. Sarmiento for providing the virus capsid specimen. Research supported by W. M. Keck Foundation.
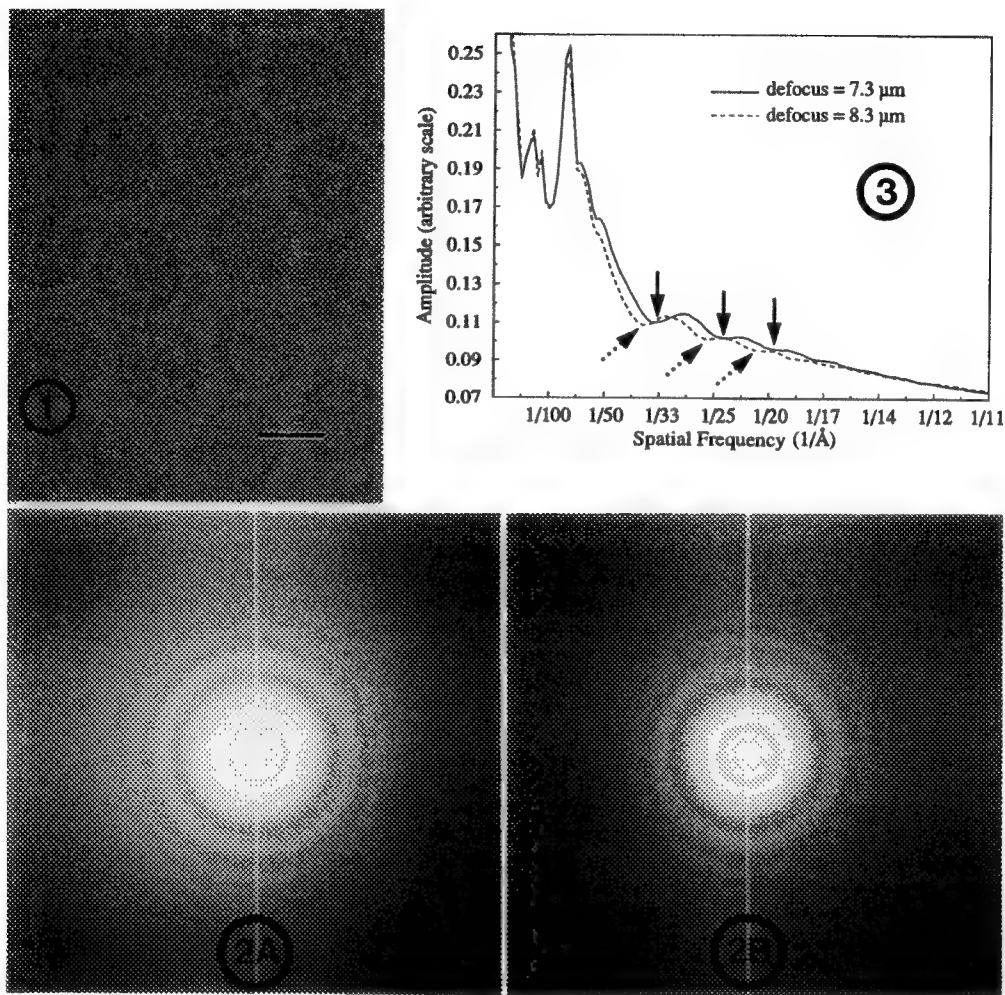
Figure 1. 400 kV electron image of ice-embedded B capsid particles of HSV-2 taken at 20,000 × magnification, with an electron dose of about 6 electrons/$Å^2$. The calculated defocus value is 7.3 μm. Scalebar = 1000 Å.

Figure 2. Sum of the amplitudes of the Fourier transforms from 606 individual capsid images boxed out from the focal-pair micrographs of 1μm defocus deference. The positions of the rings suggest the defocus values to be 7.3 (A) and 8.3 (B) μm respectively.

Figure 3. Azimuthally averaged Fourier transform amplitudes along a 10° arc as a function of spatial frequency. The amplitude profile of focal-pair micrographs can be compared with each other to distinguish the minima and maxima of CTF from those of the molecular transform. The low resolution peaks can be attributed to the molecular transforms of the viral capsid particles which occur at the same spatial frequencies in different defocused images. The minima at higher resolution (arrows), which occur at different frequencies in different focussed images, are due to CTF and we used the frequencies of these minima to determine the defocus values of the micrographs.

561

AUTOMATED 3-D CELL POPULATION ANALYSIS IN THICK TISSUE SECTIONS FROM LASER-SCANNING CONFOCAL-MICROSCOPY DATA

Hakan Ancin

ECSE Department, Rensselaer Polytechnic Institute, Troy, New York 12180-3590

This paper presents methods for performing detailed quantitative automated three dimensional (3-D) analysis of cell populations in thick tissue sections while preserving the relative 3-D locations of cells. Specifically, the method disambiguates overlapping clusters of cells, and accurately measures the volume, 3-D location, and shape parameters for each cell. Finally, the entire population of cells is analyzed to detect patterns and groupings with respect to various combinations of cell properties. All of the above is accomplished with zero subjective bias.

In this method, a laser-scanning confocal light microscope (LSCM) is used to collect optical sections through the entire thickness (100 - 500μm) of fluorescently-labelled tissue slices. The acquired stack of optical slices is first subjected to axial deblurring using the expectation maximization (EM) algorithm.[1,2]. The resulting isotropic 3-D image is segmented using a spatially-adaptive Poisson based image segmentation algorithm with region-dependent smoothing parameters.[3] Extracting the voxels that were labelled as "foreground" into an active voxel data structure results in a large data reduction. The reduced data set is subjected to two forms of cluster analysis. First, an ISODATA type partitional clustering algorithm is used to disambiguate overlapping cells.[4] This algorithm uses a combination of geometric and densitometric distance measures for implementing localization constraints essential for separating closely-spaced and overlapping cells. The splitting and merging of voxel clusters is guided by user-defined parameters. An agglomerative hierarchical clustering algorithm is then used to analyze the properties of the detected cell population.[4]

Figure 1 shows a 2-D projection of a 3-D image of a hippocampal slice from a rat's brain that has been counted manually.[5] Figure 2 shows a projection of the 3-D segmentation. Note the absence of artifacts and the high accuracy of this result. Figure 3 shows the result of the automatic counting and this result can be compared with the manual count result that is presented in Figure 1. Figures 4-6 show the resulting dendrogram representations of the cell population with respect to cell volumes, intensities, and locations respectively; the numbers in these dendrograms represent the cells that are shown in Figure 3. In addition to providing general insights about the population, these dendrograms also help detect unusual cells. In Figures 4 and 5, cell numbered 155 is more dissimilar than the rest of the cells and is in fact an artifact. From Figure 6 we can correlate the spatial cell clusters from original data. For instance cells numbered 157,154,156,158 are further from the rest of the cells and this can also be seen in Figure 6. Figure 7 shows the orthographic representation of the locations of the 3-D cell centroids.

References
1. T. J. Holmes, J. Opt. Soc. Am. A, 6(1989):1006-1014.
2. M. I. Miller and B. Roysam, Proc. Natl. Acad. Sci., 88(1991):3223-3227.
3. B. Roysam et al., Micron and Microscopica Acta, 23(1992):447-461.
4. A. K. Jain and R. C. Dubes, Algorithms for Clustering Data, Prentice-Hall (1988).
5. Acknowledgements: Prof B. Roysam, J. N. Turner, T. J. Holmes, M. A. Chisti

Fig. 1 Manual Count

Fig. 3 Automatic Count

155
87,126,83,0,148
59,127,62,98,135,23,99,112,69,129,52,122,6,44,55,30,63,138
24,80,22,136,78,104,3,110,142

84,11,76,10,9,25,97,92,114,140,40,54,68,90,111,144

100,137,42,88,119,124,149,2,20,21,95,26,38,75,56,150,4,81,105,45,46,67
134,29,85,94,13,115,109,145,117,17,74,128,34,32,141,93,33,118,66,71,65
53,1,151

36,35,60,102,70,103,57,116,89,101,123,125,19,61,131,15,64,91,132,152
153,47,120,8,143,31,41,28,96,107,18,43,146,48,58,154,27,79,49,106,130,158
86,139,7,12,50,121,14,77,108,133,82,147,37,157,51,73,156,5,16,39,72,113

Fig. 4: Volume-Based Dendrogram

155
3,2,4,81,58,60,31,101,109,123,134,157
1,80,56,119,33,121,128,54,135,10,22,111,99,126,44,78,100,140,17,94,92,104
77,28,57,117,5,142,24,90,97,110,83,69,53,84,108,136,144

122,150,39,148,151,138,105,156

45,68,32,20,112,55,106,98,116,40,8,63,62,120,74,127,43,25,72,76,23,64,75,130
6,9,26,52,96,35,70,145,95,125,146,37,30,87,93,66,141,34,86,149,7,154

73,18,46,102,21,71,103,29,51,48,49,13,47,79,16,50,81,139,12,88,107,42,129,59
113,67,114,131,89,137,65,115,85,147,38,36,27,124,118,132,133,41,19,153,0,91
11,82,15,143,152,14,158

Fig. 5: Intensity-Based Dendrogram

2,1,7,12,20,18,,22,26,17,24,32,36,35,39,55,64,69
50,59,67,92,79,81,96,38,44,45,54,48,51,57,66,68,75,78,83,84,98
91,102,111,93,94,100,103,114,107,108,120,122,128,129,125,131,132,140,141
117,123,124,126,139,148,136,142,143,152
63,0,3,4,13,31,5,8,10,23,27,30,21,28,29,37,46,41,47,52,58,70,74
6,16,15,19,25,34,11,9,14,42,43,33,40,49,104,109,118,105,119,121,138,145,146
53,56,61,60,62,82,76,65,72,77,85,89,71,73,88,80,86,90,87,95,99,110,112,113,116,97
101,106,115,134,137,127,130,144,150,133,135,149,147,151
153,155
157,154,156,158

Fig. 6: 3-D Location-Based Dendrogram

Fig. 7: Orthographic
Representation of 3-D
Cell Locations.

563

THREE DIMENSIONAL DEBLURRING OF TRANSMITTED-LIGHT BRIGHTFIELD MICROGRAPHS

Santosh Bhattacharyya

Biomedical Engineering Department, Rensselaer Polytechnic Institute, Troy NY 12180-3590

Three dimensional microscopic structures play an important role in the understanding of various biological and physiological phenomena. Structural details of neurons, such as the density, caliber and volumes of dendrites, are important in understanding physiological and pathological functioning of nervous systems. Even so, many of the widely used stains in biology and neurophysiology are absorbing stains, such as horseradish peroxidase (HRP), and yet most of the iterative, constrained 3D optical image reconstruction research has concentrated on fluorescence microscopy. It is clear that iterative, constrained 3D image reconstruction methodologies are needed for transmitted light brightfield (TLB) imaging as well. One of the difficulties in doing so, in the past, has been in determining the point spread function of the system.

We have been developing several variations of iterative, constrained image reconstruction algorithms for TLB imaging. Some of our early testing with one of them was reported previously [1]. These algorithms are based on a linearized model of TLB imaging [2,3]. What has made this development practical is that we have avoided the difficulties of measuring the PSF by incorporating a blind deconvolution variation [4,5], wherein the PSF is reconstructed along with the deblurred image, rather than having the PSF measured prior to executing the algorithm.

To summarize: The algorithm is iterative. It is formulated as an estimation of the 3D optical density of the stain, concurrent with an estimation of the PSF. It properly constrains these estimates to both be nonnegative. What makes the reconstruction of the PSF possible is that it is also constrained to have well known, reasonable properties. Such properties include its bandlimitedness [3] and its missing cone of frequencies.

Fig's. 1-a and -b, respectively, show axial and lateral views of a ray summed 3D data set, obtained from a section of a pyramidal neuron which was stained with HRP. A 1.25 N.A. lens was used. The sampling dimensions are 128x128x64 for a 12.8x15.4x13.4 µm field. Out of focus haze and blur are apparent in these photographs. Fig's. 1-c and -d show the reconstructed result following 500 iterations of the algorithm in [4]. The out of focus haze and blur removal is apparent. Fig's. 1-e and -f show the axial and lateral ray summed views of the reconstructed PSF. The general shape of this PSF agrees well with the general shape expected from theory [3].

Processing time was 137 minutes on a 15 Mflop IBM 3090 computer. We expect, conservatively, these times to be reduced by at least a factor of 20, by applying algorithmic acceleration schemes, as we have done previously for a former algorithm version [6] and by utilizing modern, faster, less expensive parallel computer architectures based on the i860 processor, such as those available from CSPI (CSPI, Inc., Bellerica MA).

1. B.H. Willis, B. Roysam, J.N. Turner and T.J. Holmes, J. of Microscopy (1993), in press.
2. F. Macias-Garza, K.R. Diller, A.C. Bovik and S.J. Aggarwal, J. Microscopy (1989)153, 205.
3. N. Striebl, J. Opt. Soc. Am. A 2 (1985)2, 121.
4. V. Krishnamurthi, Y.H. Liu, T.J. Holmes, B. Roysam and J.N. Turner, SPIE (1992)1660, 95.
5. T.J. Holmes, J.O.S.A.-A (1992)9, 1052.
6. T. J. Holmes and Y. H. Liu, J.O.S.A.-A (1991)8, 893.
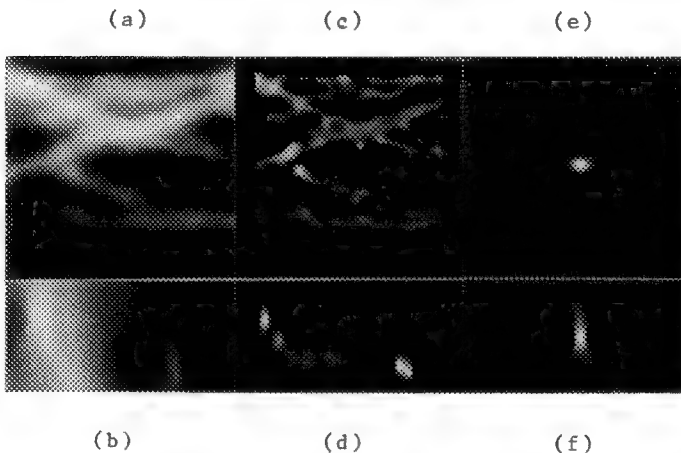
Fig. 1.   (a) Axial ray summed view of the 128x128x64 (12.8x15.4x13.4 μm) 3D dendritic data set prior to reconstruction.   This is of an HRP labelled neuron.   The gray levels have been inverted, so that the intensity in the image represents optical density units.   (b) Lateral view of the same sample as in (a).   (c) Deblurred axial view following 500 iterations.   (d) Deblurred lateral view. (e) Axial ray summed view of the reconstructed PSF.   (f) Lateral ray summed view of the reconstructed PSF.   The general shape of this PSF agrees well with the general shape expected from theory [3].

SOME PROBLEMS AND SOLUTIONS IN ELECTRON ENERGY LOSS SPECTROSCOPY OF CRYOSECTIONS

Zhifeng Shao, Ruoya Ho and Andrew P. Somlyo

Department of Molecular Physiology and Biological Physics
Box 449, University of Virginia, Charlottesville, VA 22908

Electron energy loss spectroscopy (EELS) has been a powerful tool for high resolution studies of elemental distribution, as well as electronic structure, in thin samples[1]. Its foundation for biological research has been laid out nearly two decades ago[2], and in the subsequent years it has been subjected to rigorous, but by no means extensive research. In particular, some problems unique to EELS of biological samples[3-7], have not been fully resolved. In this article we present a brief summary of recent methodological developments, related to biological applications of EELS, in our laboratory. The main purpose of this work was to maximize the signal to noise ratio (S/N) for trace elemental analysis at a minimum dose, in order to reduce the electron dose and/or time required for the acquisition of high resolution elemental maps of radiation sensitive biological materials.

Based on the simple assumption of Poisson distribution of independently scattered electrons, it had been generally assumed that the optimum specimen thickness, at which the S/N is a maximum, must be the total inelastic mean free path of the beam electron in the sample. This assumption, which is correct only for the case where the signal is dominant over the background, no longer holds for trace elemental analysis, where a very small signal is superimposed on a background consisting of plasmon plural scattering and other core edge losses. This problem was recently examined in detail[8,9]. In general, the EEL spectrum, excluding zero loss peak, can be simply written as[9]:

$$F(E) = I\,\tau \int_0^\alpha 2\pi\theta\,d\theta \left\{ \sum_{n=1}^\infty \frac{1}{n!}\left(\frac{t}{\lambda_i}\right)^n S_i^{(n)}(E,\theta) + \sum_{n=1}^\infty \frac{1}{n!}\left(\frac{t}{\lambda_i}\right)^n S_i^{(n)}(E,\theta) \otimes \sum_{m=1}^\infty \frac{1}{m!}\left(\frac{t}{\lambda_e}\right)^m \delta(E)\,S_e^{(m)}(\theta) \right\} \exp\left(-\frac{t}{\lambda_t}\right) \quad (1)$$

where $S_e^{(1)}(\theta)$ is the single elastic scattering distribution function, and $S_i^{(1)}(E,\theta)$ is the single inelastic scattering distribution function and both of them are normalized to 1. $1/\lambda_t = 1/\lambda_e + 1/\lambda_i$, where λ_t, λ_e, and λ_i are, respectively, the total mean free path, the elastic mean free path and the inelastic mean free path. I is the beam current, τ is the accumulation time, t is the thickness of the specimen, α is the collection semi-angle and (n) denotes the n-th convolution.

For the ideal case ($\alpha = \pi$), we have shown that the elastic scattering effect is cancelled out in the expression after the angular integration[9], because $\exp(t/\lambda_e) = \int_0^\pi 2\pi\theta\,d\theta \sum_{m=0}^\infty (1/m!)\,(t/\lambda_e)^m S_e^{(m)}(\theta)$. Even for the case of a limited collection angle at the spectrometer entrance, say $\alpha = 12$ mrad, the elastic scattering has only a small effect for thicker specimens. Based on both computer simulation and experimental measurements at 80 keV on the Philips 400 FEG, we found that the optimum specimen thickness is only $0.3\lambda_i$ for phosphorus and $0.44\lambda_i$ for calcium quantitation, primarily due to the plural scattering component in the background. Here, the total inelastic mean free path λ_i should be understood as defined by the actual entrance aperture of the spectrometer. Therefore, the actual optimum specimen thickness is spectrometer dependent. Although the optimum specimen thickness varies with the energy loss position of the element of interest, based on computer studies, we found that they remain roughly the same for different beam energies, if the thickness measurements are normalized to λ_i. Therefore, at 200 keV, the actual optimum specimen thickness will be 160% of that at 80 keV. Since thin cryosections are quite difficult to obtain, this 60% increase in thickness should be a particularly welcome improvement. The improvement in optimum thickness continues, albeit less steeply, for even higher beam energies, but the knock-on damage is expected to escalate [7]. Further experiments are required to determine the most suitable beam energy for analysis of biological cryosections, but at present, 200 keV appears to be a reasonable choice.

To minimize radiation damage, the use of a parallel detection EEL spectrometer[10-13] is almost mandatory. However, the channel to channel gain variations of such a multichannel device introduce an additional source of uncertainty. Depending on the detector used, this variation can be up to several percent, such as in a SIT camera[11]. To minimize this problem, the so-called difference method[3] was introduced. It is based on the fact that, for a slowly varying background, the subtraction of two spectra of a given energy shift ΔE can substantially reduce the contribution due to this gain variation η, provided that the signal is not completely cancelled out, because the uncertainty δS now becomes[5]:

$$\delta S = \eta(F(E) - F(E+\Delta E)) << \eta F(E) \approx \eta F((E+\Delta E) \qquad (2)$$

We see immediately that for $\Delta E \to 0$, $\delta S \to 0$. Thus a small shift should be preferred. But at the same time, the signal itself is also reduced or, for $\Delta E=0$, cancelled. The total statistical noise δP, which only depends on the total count at each channel of the final spectrum, remains roughly unchanged, difference or not:

$$\delta P \approx \sqrt{F(E) + F(E+\Delta E)} \qquad (3)$$

These factors determine that, for the given spectral profile of a trace element, there must be an optimum energy shift that should give the maximum S/N^8. Similar arguments were also presented recently under a slightly different condition[14]. Both experiments and computer simulation have confirmed this conclusion. We found that for phosphorus quantitation, the optimum energy shift is in the neighborhood of 15 eV. To preserve the maximum signal, obviously the best approach is to fit the original spectrum directly. To do this, a gain variation of $< 0.1\%$ was found necessary, where the statistical noise becomes dominant. We are currently designing a cooled CCD detector on order to utilize this advantage[15] In this case, the uncertainty of phosphorus detection in a biological specimen drops to 2.2 mmol/Kg for a specimen of $0.25\lambda_i$ at a beam current of 0.5 nA and a collection time of 100 s at the phosphorus L-edge. For a 0.8% gain variation and under the same conditions, this value becomes 16 mmol/Kg.

In conclusion, the optimum specimen thickness for elemental analysis of biological thin sections is much less than previously thought and, for most elements of interest, it is between 0.3-$0.5\lambda_i$. It appears that 200 keV is a reasonable compromise between analytical mapping of routinely obtainable cryosections and knock-on damage. When a parallel detector is used, the gain variation could be a limiting factor in quantitation. In this case, an optimum energy shift exists that provides the maximum S/N in the difference spectra. However, if gain variation can be substantially reduced, direct fitting should be the best approach. Attaining these optimum conditions can be particularly important for EELS mapping, because a factor of 2 improvement in S/N means a factor of 4 saving in actual mapping time for a given S/N. For a map requiring a collection time of 36 hrs, which is quite common, a reduction of 27 hrs is indeed substantial[16].

References

1. R.F. Egerton, "Electron Energy Loss Spectroscopy in the Electron Microscope", Plenum Press, New York, (1986).
2. M. Isaacson and D.E. Johnson, Ultramicroscopy, 1 (1975) 33.
3. A.P. Somlyo and H. Shuman, Ultramicroscopy, 8 (1982) 219.
4. H. Shuman and A.P. Somlyo, Ultramicroscopy, 21 (1987) 23.
5. R.D. Leapman, in: "Electron Probe Microanalysis, Applications in Biology and Medicine", Springer Series in Biophysics, Vol. 4 (Eds. K. Zierold and H.K. Hagler), Springer-Verlag, Berlin, Heidelberg, (1989) 113.
6. C. Mory and C. Colliex, Ultramicroscopy, 28 (1989) 339.
7. M. Isaacson, in: "Principle and Techniques of Electron Microscopy, Biological Applications", (Ed. M.A. Hayat), Vol. 7, Van Nostrand Reinhold Company, New York, (1977) 1.
8. Y.Y. Wang, R. Ho, Z. Shao and A.P. Somlyo, Ultramicroscopy, 41 (1992) 11.
9. Y.Y. Wang, R. Ho, Z. Shao and A.P. Somlyo, Ultramicroscopy, submitted.
10. H. Shuman, Ultramicroscopy, 6 (1981) 163.
11. H. Shuman and P. Kruit, Rev. Sci. Instrum., 56 (1985) 231.
12. D.E. Johnson and M. Connick, Rev. Sci. Instrum., 58 (1987)1822.
13. O.K. Krivanek et al., Ultramicroscopy, 22 (1987)103.
14. J. Michel et al., Ultramicroscopy, 48 (1993) 121
15. Z. Tang et al., manuscript in preparation.
16. This work was supported by NIH grant PO1 HL48807 and the Whitaker Foundation.

STEM MEASUREMENT OF SUBCELLULAR WATER DISTRIBUTIONS

R.D. Leapman, S.Q. Sun, S-L. Shi, R.A. Buchanan[*] and S.B. Andrews[*]

Biomedical Engineering and Instrumentation Program, NCRR; [*]Laboratory of Neurobiology, NINDS, National Institutes of Health, Bethesda, MD 20892.

Recent advances in rapid-freezing and cryosectioning techniques[1] coupled with use of the quantitative signals available in the scanning transmission electron microscope (STEM)[2] can provide us with new methods for determining the water distributions of subcellular compartments.[3-5] The water content is an important physiological quantity that reflects how fluid and electrolytes are regulated in the cell; it is also required to convert dry weight concentrations of ions obtained from x-ray microanalysis into the more relevant molar ionic concentrations. Here we compare the information about water concentrations from both elastic (annular dark-field) and inelastic (electron energy loss) scattering measurements.

In order to utilize the elastic signal it is first necessary to increase contrast by removing the water from the cryosection. After dehydration the tissue can be digitally imaged under low-dose conditions, in the same way that STEM mass mapping of macromolecules is performed.[6] The resulting pixel intensities are then converted into dry mass fractions by using an internal standard, e.g., the mean intensity of the whole image may be taken as representative of the bulk water content of the tissue. However, a correction must be applied to take account of the non-linearity of the dark-field signal as a function of thickness which cannot be assumed small compared with the elastic mean free path. In order to test this approach cryosections (prepared in a Reichert FC-4E cryoultramicrotome at a temperature of ~-160 C) were cut to a nominal thickness of 100 nm on a 35° Diatome diamond knife with the aid of an antistatic device. Hydrated sections mounted on carbon/Formvar-coated grids were transferred into a VG Microscopes HB501 field-emission STEM equipped with a cryotransfer stage.[7] The specimens were freeze-dried at -110°C and were recooled to -160°C before acquiring digital dark-field images at a dose of <100 e/nm^2. Fig. 1 shows part of a liver cell with contrast reversed for clarity. By analyzing the integrated intensities within this dark-field micrograph and assuming that hepatocytes have an overall dry mass fraction of 22%, the following dry mass percentages (± s.e.m.) were obtained for the different compartments: mitochondria, 35.2±0.5 %; endoplasmic reticulum, 24.0±0.6 %; nucleus, 20.6±0.5 %; and cytoplasm, 15.6±0.4 %. These values are plausible and indicate that it is possible to use quantitative dark-field STEM imaging to give information about water content. On the other hand, freeze-dried tissue is often found to suffer considerable lateral shrinkage that is not necessarily constant from organelle to organelle. Such differential shrinkage is likely to produce systematic errors in the dark-field water measurements. This has prompted us to develop an alternative direct approach that can be applied to hydrated cryosections.

Although the total inelastic signal from a hydrated cryosection also displays very weak contrast we can make use of subtle variations in the electron energy loss spectrum (EELS) between water and the organic components of the cell.[4] The single scattering EELS spectrum from ice has a plasmon maximum at 20.4 eV compared with 23.4 eV for protein. At lower energy losses there are differences too; the spectrum from ice contains a band-edge at 9.1 eV, whereas the protein spectrum contains a peak at 6.7 eV due to excitation of π-states. The single scattering distribution from a hydrated cryosection can be modeled as a linear combination of spectra from its separate constituents; these can be treated as standard reference spectra that can be fit by a multiple least squares (MLS) procedure. We have recorded energy loss spectra using a Gatan model 666 parallel-detection spectrometer interfaced to the ultra-high vacuum of the HB501 STEM.[8] This system provides an energy resolution of ~0.5 eV, as defined by the full-width at half maximum of the zero-loss peak. A typical spectrum recorded from a 0.5 μm diameter region of a frozen-hydrated erythrocyte is shown in Fig. 2 together with the fitted reference spectra. The MLS analysis of 13 such spectra yielded a water content of 70±2% (s.e.m.) for the erythrocyte which is consistent with the expected value.[9] The EELS approach has the advantage of not requiring

dehydration prior to analysis and the specimen is therefore not affected by differential shrinkage. The spatial resolution is limited by radiation damage and depends on the required accuracy in the measurement.[10] In order to attain an uncertainty of ±5% in the water determination the resolution is limited to ~100nm which is commensurate with the specimen thickness. The feasibility of utilizing the EELS spectrum-imaging technique to map the water distributions of hydrated tissue is also being explored.[11]

References:
1. M. Michel et al., J. Microsc. 166 (1992) 43.
2. C. Colliex et al., J. Ultrastruct. Res. 88 (1984) 177.
3. S.B. Andrews et al., Proc. 50th Ann. Mtg. EMSA (1992) 1574.
4. S. Sun and R.D. Leapman, Proc. 50th Ann. Mtg. EMSA (1992) 1572.
5. R.R. Warner et al., Proc. 50th Ann. Mtg. EMSA (1992) 1576.
6. J.S. Wall and J.F. Hainfeld, Ann. Rev. Biophys. Biophys. Chem. 15 (1986) 355.
7. R. D. Leapman & S. B. Andrews, J. Microsc. 161 (1990) 3.
8. O.L. Krivanek et al., Proc. 47th Ann. Mtg. EMSA (1989) 410.
9. S. Sun, S. Shi & R. D. Leapman, (to be published).
10. J. Dubochet et al., Q. Rev. Biophys. 21 (1988) 129.
11. J.A. Hunt and D.B. Williams, Ultramicroscopy 38 (1991) 47.
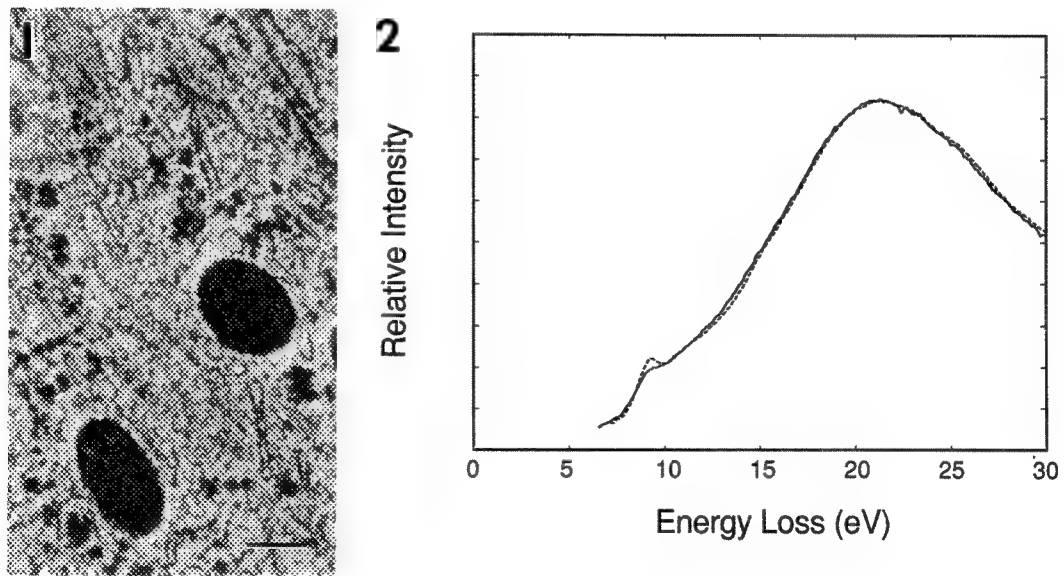
Fig.1 -- Low-dose dark-field STEM of freeze-dried cryosection of mouse hepatocyte. Bar = 200 nm.
Fig.2 -- Single-scattering EELS from frozen hydrated erythrocyte (solid line) and fit to reference spectra (dashed line).

DETERMINATION OF NUCLEIC ACID CONTENT OF VIRUSES BY ELECTRON SPECTROSCOPIC IMAGING AND CORRELATION AVERAGING

M. Misra[1], J. F. Conway[1], B. L. Trus[1,2] and A. C. Steven[1]

[1] Lab. of Structural Biology, NIAMS, and [2] Computer Systems Lab., DCRT, NIH, Bethesda, MD 20892

Energy filtering offers the potential to form element-specific images, and thus to quantitate and map various elements in biological specimens [1, 2]. To assess the sensitivity and reproducibility with which we can detect phosphorus using current technology, we have performed ESI experiments in a model system comprising three well-characterized viruses - tobacco mosaic virus (TMV), LA virus of yeast, and bacteriophage T4 - that differ widely in their contents and spatial distributions of nucleic acid. Here we make a preliminary report of experiments in which the data were recorded in a Zeiss EM902 electron microscope equipped with a Henry-Castaing energy filter.

An aliquot of the viral mixture was adsorbed to a thin, grid-mounted, carbon film, blotted to a thin film, rapidly frozen in liquid ethane, and transferred into the microscope in the frozen-hydrated state, where it was freeze-dried at 100^{0}K. A SIT camera was used to record images at energy losses of 105, 120 and 150 eV respectively, with an energy window of 10eV. The total dose was about 10^3 el/A^{2}. The images were acquired using a real-time Data Translation frame grabber (DT 2867) installed in an IBM PC, and transferred to a VAX 4000-200 for image processing. These operations included shading correction, alignment, formation of the "background" image at the phosphorus peak of 150 eV by extrapolating (pixel by pixel), from the 105 and 120eV reference images, and subtraction using the PIC program [3].

The field in Fig. 1 contains all three virions which are clearly recognizable, although their state of morphological preservation is poor, presumably on account of the high electron dose. The tail of the T4 virion (upper right), which should contain little or no DNA, is fainter in the 150eV image (Fig. 1b) than in the 105eV image (Fig. 1a), as expected. A similar observation applies to the TMV which contains only 5% (w/w) RNA. The difference map - shown in reverse contrast in Fig. 1d - represents our estimate of the net phosphorus distribution. This image is noisy, partly from the low number of counts per pixel. Only the T4 heads, each of which contains a densely packed viral chromosome of ~170 kbp, stand out. At the sites of some of the LA virions, there appear to be patches of density, but the signal is weak. To analyze them on a statistical basis, a set of virions from the 105eV image were aligned by correlation methods (Fig. 2a). The corresponding portions of the difference image (Fig. 1d) were also averaged (Fig. 2b), and reveal a positive concentration of phosphorus, centered on the virion. For comparison, a control image obtained by averaging 10 randomly chosen areas of background is shown in Fig. 2c. The amount of RNA per LA virion was calculated by integrating over the area of Fig 2b that is occupied by the particle, subtracting the (non-zero) background value, and calibrating on the corresponding integral for the T4 head. This procedure yielded a value of about 5 kbp of dsRNA which is in good agreement with the sequencing-derived value of 4.6 kbp [4]. Our "phosphorus map" difference images have low counts and high noise, reflecting the small fraction of electrons scattered into the 150 eV energy loss resonance. Nevertheless, our provisional conclusion is that sufficiently large concentrations of elements may be detected, and this sensitivity may be extended considerably by correlation averaging of the difference images with reference to the statistically better-defined reference images. This procedure also holds prospects for elemental mapping to within the resolution constraints imposed by radiation damage and specimen preservation.

References
1. Bazett-Jones, D., Electron Mic. Rev. 5(1991)37.
2. Buhle, E.L., et al, Proc. 43rd Ann. Mtg. EMSA (1985) 314.
3. Trus, B. L., and Steven, A. C., Ultramicroscopy, 6(1981)383.
4. Wickner, R. B., FASEB J. 3(1991)2257.
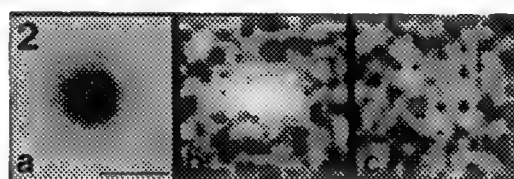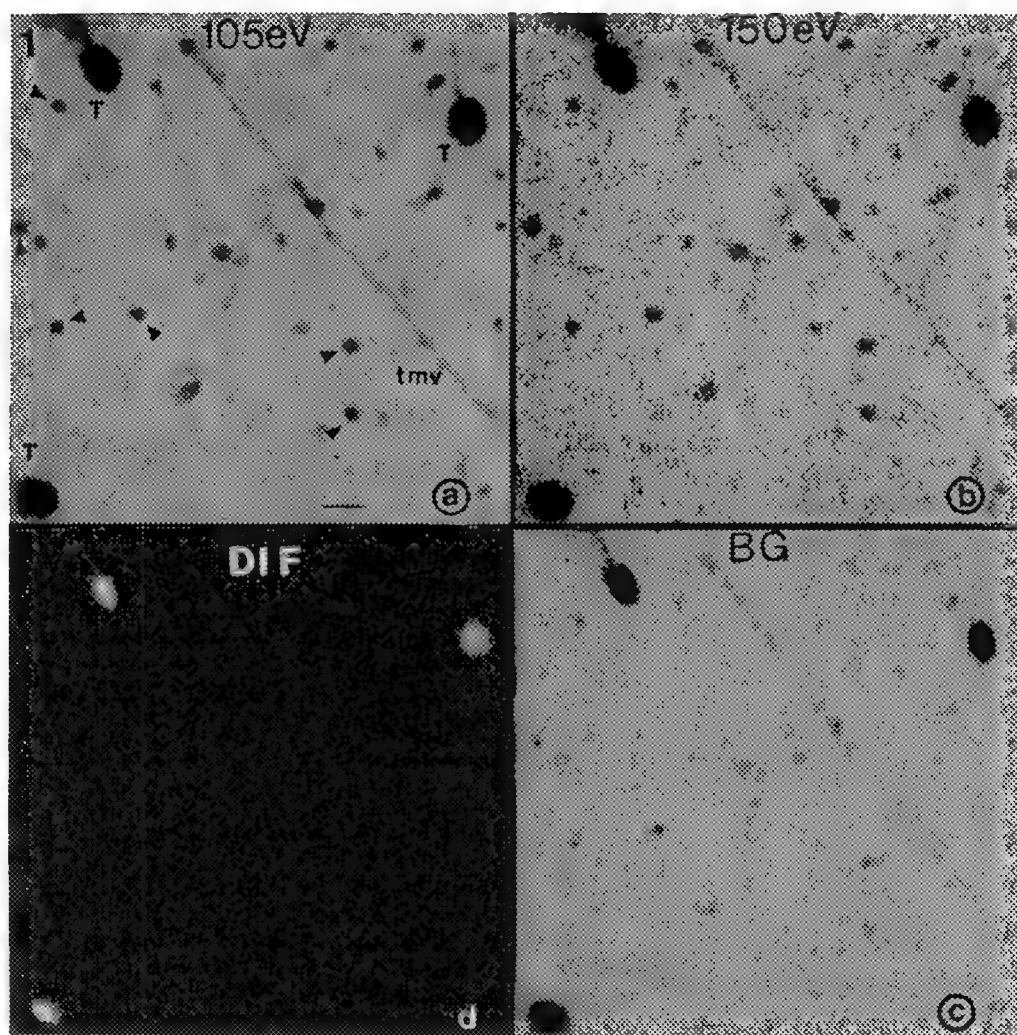
Fig. 1 : Energy-filtered images of unstained, frozen-dried, virus particles. This field contains three T4 virions, one TMV, and numerous LA virions, several of which are marked with arrows in (a). In addition to the 105eV (a) and 150eV (b) energy-loss images, the background obtained by extrapolation from the 105eV and 120 eV images to 150eV (c), and the resulting difference map (d) with contrast reversal so that phosphorus concentrations are shown as white. Bar = 100nm.

Fig. 2 : (a) Correlation-average of 10 LA virions: (a) - 105eV energy-loss image; (b) "phosphorus map"; (c) control image (background). Bar = 50nm.

EELS STUDY OF BULK Co AND CoSi$_2$

Kaikee Wong*

* Department of Applied Physics, Cornell University, Ithaca, NY 14853

CoSi$_2$ can grow epitaxially on Si and the Si/CoSi$_2$/Si heterostructure has potential uses in metal-based transistors. To fully utilize the device potential of CoSi$_2$, it is important to develop a thorough understanding of its electronic properties. By comparing the Co L$_{2,3}$ spectra of pure Co and CoSi$_2$, the bonding between Co and Si atoms can be studied.

A Si(111) wafer was treated by Shiraki cleaning before 500 Å of Co was deposited in an E-beam evaporator with a base pressure of 10^{-7} Torr. The wafer was then annealed in an UHV oven with a base pressure of 10^{-10} Torr at 950°C for 2 hrs.[1] A standard TEM plan view sample was then prepared from the wafer by dimpling and ion-milling, both from the Si side to preserve the silicide. The stochiometry of CoSi$_2$ was confirmed by SAD and EDS. EELS measurements were carried out in a VG-HB501A UHV STEM operating at 100 keV equipped with a serial EELS detector. The spot size was about 5 Å and the probe current was estimated to be 0.1 nAmp. Spectra were collected at areas where the Si had been milled away. The convergence and collecton half-angles were 20 and 2 mrad respectively.

Five Co L$_{2,3}$ spectra were recorded from the CoSi$_2$ sample with an energy resolution of 1.5 eV, a step size of 0.2 eV and a dwell time of 0.2 s per step. The spectra were taken at different thicknesses ranging from 0.28 to 0.68 λ, where λ is the plasmon mean free path. Since the measured plasmon peak of CoSi$_2$ at 20.3±0.3 eV is close to the spin orbit splitting of the L$_{2,3}$ edges (16 eV), multiple scattering can modify the shape of the core loss spectrum significantly. To recover the single scattering distribution (SSD), the Fourier ratio method was applied to the five spectra and a Wiener filter was used to reduce noise.[2] The resulting spectra were then added up to improve the signal. By taking five spectra instead of a single spectrum with a long dwell time, high voltage and specimen drifts can be reduced. Moreover, the five deconvoluted spectra can be compared to ensure the accuracy of the recovery scheme. Fig.1 shows a Co L$_{2,3}$ core loss spectrum taken at an area of thickness 0.68λ, the SSD and the low loss peak. The background of the core loss spectrum has been fitted to a E^{-r} power law and subtracted. The peak at 820 eV in the core loss spectrum is due to multiple scattering and is successfully removed by the deconvolution. Co L$_{2,3}$ edges were also recorded from a pure Co specimen with a resolution of 1.5 eV, a step size of 0.25 eV and a dwell time of 0.5 s per step. The SSD of Co and CoSi$_2$ L$_{2,3}$ edges are shown in fig.2. To match the two thresholds the SSD of CoSi$_2$ has to be shifted down 2.5±1.0 eV in energy . A theoretical calculation by Lambrecht et al. suggests that there is a transfer of 0.2 electrons from the two Si atoms to the Co atom and is consistent with the direction of the observed energy shift.[3]

The L$_3$ edges of Co and CoSi$_2$, as shown in fig.3, can be isolated from the L$_2$ edges by deconvoluting the SSD with two delta functions which are separated by the spin orbit coupling of 17 eV and are weighted by the white line intensity ratio.[4] The change in the L$_3$ edge reflects how the unoccupied d-density of states (DOS) is affected by the bonding of Ni and Si atoms in the silicide.[5] The FWHM of the L$_3$ white line increases from 2.1 eV in Co to 5.2 eV in CoSi$_2$ while that of L$_2$ increases from 2.8 eV to 5.6 eV. The intensity at E$_F$ is reduced. The change suggests there is a transfer of states with nonbonding character near E$_F$ to states with higher energy, consistent with the bonding theory of transition metal silicides.[6] The white line intensity ratio, which reflects the number of empty 3d$_{5/2}$ states relative to empty 3d$_{3/2}$ states, reduces from 3.3±0.2 in Co to 2.1±0.2 in CoSi$_2$. Such a large reduction suggests that the dependence of the ratio on d-band occupancy is complicated.

The low loss spectra of transition metals are known to be dominated by interband transitions. The relatively small width (6.7 eV) of the CoSi$_2$ plasmon compared to Co suggests that the system is free-electron like. To recover the dielectric functions ε$_1$ and ε$_2$, a Kramers-Kronig transformation is applied

to the low loss spectrum of CoSi$_2$.[7] The two functions are well described by the Drude model if a bound excitation at 6.5 eV is included. The origin of the excitation is still under investigation.[8]

References
1. J. N. Poate et al., Thin Film - Interdiffusion and Reactions, New York: Wiley (1978):359.
2. R. F. Egerton et al., Proc. R. Soc. Lond. A 398(1985)395.
3. W. R. L. Lambrecht et al., Phy. Rev. B 36(1987)2493.
4. R. D. Leapman et al., Phys. Rev. B 26(1982)614.
5. J. E. Muller et al., Phys. Rev. B 25(1982)365.
6. P. J. W. Weijs et al., Z. Phys. B - Condensed Matter 78(1990)423.
7. R. F. Egerton, in Electron Energy Loss Spectroscopy in the Electron Microscope, New York:Plenum Press (1986):362.
8. This work was supported by the MRL Program of the NSF under Award No. DMR-9121654.
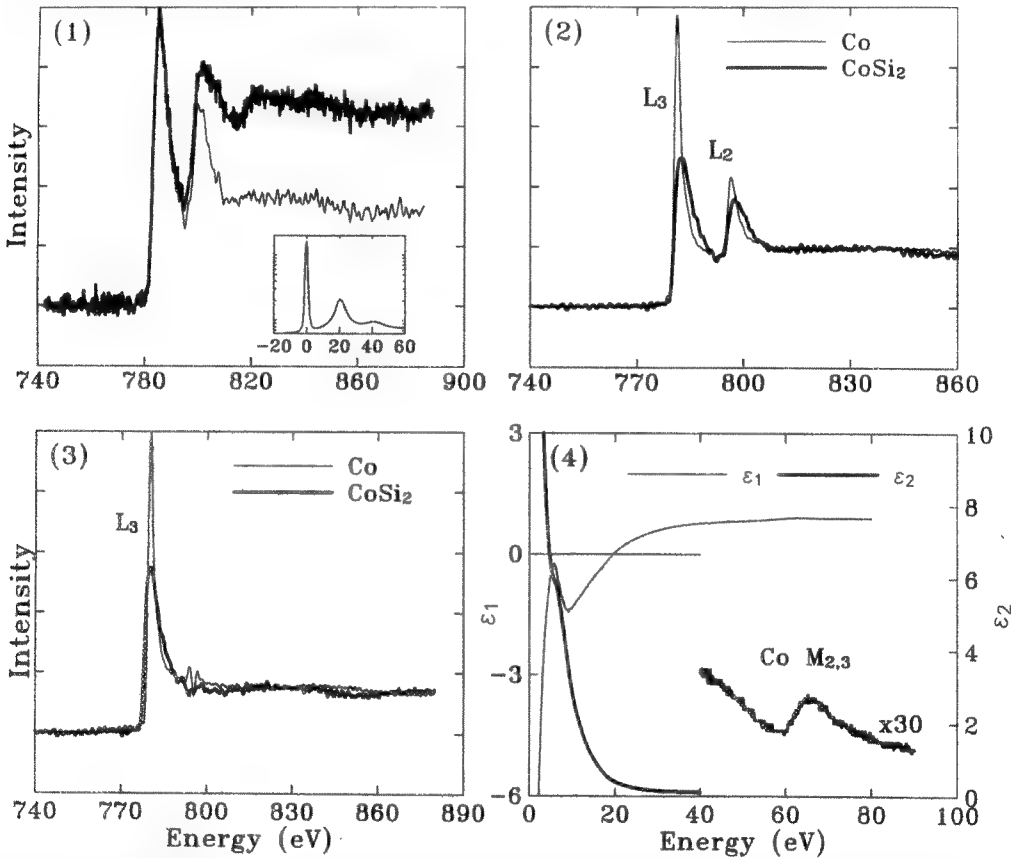
Fig.1: Core loss spectrum of CoSi$_2$ after background subtraction (light line) and single scattering distribution (dark line). Low loss spectrum is shown in insert with intensity in logarithmic scale.
Fig.2: Single scattering distribution of Co L$_{2,3}$ edges. in pure Co and CoSi$_2$. CoSi$_2$ spectra has been shifted down in energy by 2.5 eV. Spectra are scaled to same intensity after L$_2$ edge.
Fig.3: L$_3$ edge of Co and CoSi$_2$. CoSi$_2$ L$_3$ edge has been shifted down in energy by 2.5 eV.
Fig.4: Dielectric functions ε_1 and ε_2 of CoSi$_2$ with M$_{2,3}$ edge enlarged.

SYMMETRY-SELECTED ELECTRON ENERGY LOSS SCATTERING

P.E. Batson

IBM Thomas J. Watson Research Center, Yorktown Heights, New York 10598

The differential scattering cross section for EELS has long been described within the Born approximation: [1]

$$\frac{\partial \sigma^2}{\partial E \partial q} = \frac{4\pi e^4}{\hbar^2 v^2} \frac{1}{q^4} \mid \sum_j < \phi_n(r_j) \mid e^{iq \cdot r_j} \mid \phi_0(r_j) > \mid^2 = \frac{4\pi e^4}{\hbar^2 v^2} \mid M_{n,0} \mid^2 \tag{1}$$

where v is the incident electron velocity, $\mid \phi_0 >$ and $\mid \phi_n >$ are the initial and final one electron specimen states, and the sum is over the specimen electrons. This expression is suited to plane wave scattering where we have one well-defined momentum transfer given by q. We obtain equation (1) by expanding the swift electron coulomb interaction in a Fourier series and picking one momentum transfer. This is not very useful for scattering in the STEM, because we must sum coherently over many plane wave states to make a small probe. This produces many cross terms in equation (1) above, some of which may exactly cancel. Thus, the plane wave formulation can obscure a simple result by separating the scattering in a non-physical way. Following the notation of Pines and Nozieres,[2] we may instead express the matrix element as a sum over plane wave expansions of the specimen states,[3]

$$M_{n,0} = \sum_{q > 0} \frac{1}{q^2} < \psi_f(\mathbf{r}) \mid \rho_{-q} e^{-iq \cdot r} + \rho_q e^{iq \cdot r} \mid \psi_0(\mathbf{r}) >, \tag{2}$$

where $\rho_q \equiv (\rho \dagger_q)^{n0}$ is the matrix element for a charge density fluctuation taken between the ground state and the nth excited state of the specimen, and the ψ's are swift electron wavefunctions. This expression compactly displays wavefunctions for the swift electron rather than for the specimen. It brings no new information, since it is just a reordering of the terms present in equation (1). But it does put single particle and collective excitations within a single description through the use of ρ_q. Thus, ρ_q is an even function of q for plasmon scattering, but odd for interband losses.[2]

If we use well defined diffraction conditions, we can produce initial and final states of the swift electron that have chosen symmetries with respect to atom columns in a sample. I consider here a standard two-beam theory[3] for $g \equiv g_{220}$, the first allowed Bragg reflection for the [001] oriented diamond crystal. The general solution for ψ at a depth, z, and deviation, $\Delta\theta$, from the exact two beam conditions is given by[3,4]

$$\psi = e^{i2\pi \mathbf{K} \cdot \mathbf{r}} e^{i\pi s z} \{ \cos(\pi \Delta k z) - i \sin(\pi \Delta k z) [\cos\beta - \sin\beta e^{i2\pi g x}] \} \tag{3a}$$

$$s \approx g \tan\Delta\theta \; ; \quad \cot\beta = s\xi \; ; \quad \Delta k = \sqrt{s^2 + 1/\xi^2} \; ; \tag{3b}$$

where ξ is the extinction thickness. β is defined in the upper half plane, so that $s > 0$ implies $\beta < \pi/2$, and $s < 0$ implies $\beta > \pi/2$. Thus, $\cos\beta$ changes sign with s, causing a change in symmetry in the x-direction with deviation from the exact Bragg condition. This effect is maximized at the depth, $z = 1/2\Delta k$ where the first term in the curly brackets of equation (3a) is zero. At this depth, we may write in simplified form for $s = \pm 1/\xi$:

$$\psi^0_{\pm s} = e^{i2\pi \mathbf{K} \cdot \mathbf{r}} e^{\pm i\pi/2\sqrt{2}} \sqrt{2} \; e^{i\pi g x} \begin{Bmatrix} -\sin \pi g x \\ i \cos \pi g x \end{Bmatrix}. \tag{4}$$

There is another similar set of results, $\psi_{\pm s}{}^g$ for the beam positioned near the opposite Bragg condition. These are identical except for a change in sign of the $+s$ wavefunction.

If a scattering event occurs within the sample, and sufficient thickness of material exists below the scattering event, then the wave will be channeled into different directions depending on whether it is symmetric or anti-symmetric relative to the atom columns. The crystal defines a grating which, from certain directions, blocks waves except those of a certain symmetry. Thus, if channeling waves, of the type shown in equation (4), are established within a certain thickness, then both the initial and final states may be selected to some extent by working in a sample that is about twice that thickness.

Insertion of solutions (4) into expression (2), including information about ρ_q, tells us right away whether the inelastic scattering matrix integrand is odd or even in x, and so whether the matrix element is finite. I have performed the experiment in diamond, using $\psi_{-s}{}^{g}$ (case a) and $\psi_{+s}{}^{0}$ (case b) for ψ_i and $\psi_{-s}{}^{0}$ for ψ_f. In case (a), we force an even parity to even parity transition. The integrand in equation (2) will thus be finite only if ρ_q is an even function of q -- plasmon scattering. In case (b), we force odd to even parity in the swift electron, so that matrix element is finite only if ρ_q is an odd function of q -- interband or core loss scattering.

Figure 1. shows the swift electron dispersion surfaces near the Brillouin Zone boundary for the initial and final state energies, with cases (a) and (b) summarized. I fix the final state by positioning a collection aperture in the diffraction pattern. I fix the initial state with a small objective aperture, positioned using the STEM diffraction screen. I used a 2nm probe near the edge of a thin wedge of diamond to precisely fix the thickness. Figure 2 shows results for the low loss region after correction for multiple scattering compared with the standard small angle axial scattering result. Case (a) gives a strong plasmon with little interband scattering. Case (b) shows almost no plasmon scattering, with a strong interband component. In fact the interband component is so strong as to require a new "odd-parity" dielectric response function for understanding.

References:

1. M. Inokuti, Rev. Mod. Phys. 43, 297 (1971).
2. D. Pines, and P. Nozieres, Theory of Quantum Liquids (Benjamin, New York, 1966), pp. 85-87, 221.
3. P.B. Hirsch, A. Howie, R.B. Nicholson, D.W. Pashley, and M.J. Whelan, Electron Microscopy of Thin Crystals (Butterworths, London, 1965), Chapters 8,9.
4. This is a straightforward result using reference 3, but was not extensively discussed there.
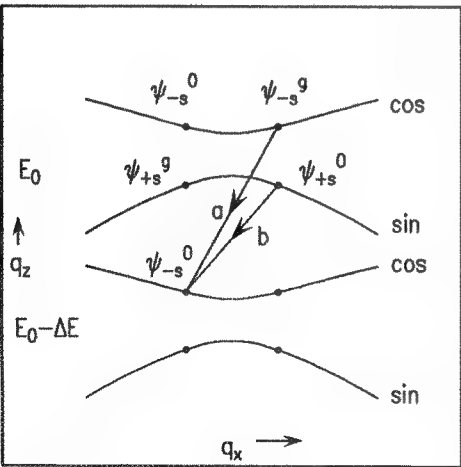
Figure 1. Summary of transitions for even parity (a) and odd parity (b) scattering. The dispersion surfaces follow the construction of reference 3.
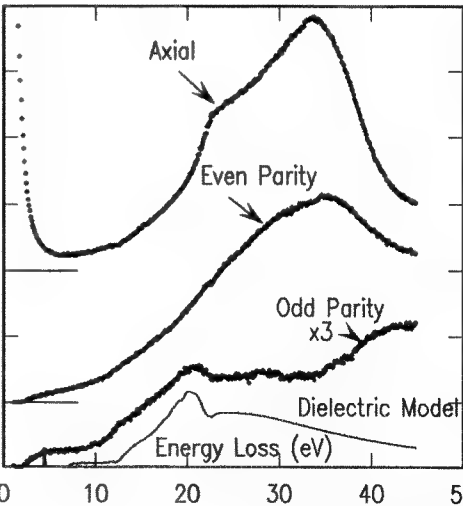
Figure 2. Results for non-channeling, axial scattering, and the two channeling cases after correction for multiple scattering. The plasmon and interband scattering are cleanly separated.

ATOMIC RESOLUTION CHARACTERISATION OF INTERFACE STRUCTURES BY ELECTRON ENERGY LOSS SPECTROSCOPY

N. D. Browning, M. M. McGibbon, M. F. Chisholm and S. J. Pennycook

Solid State Division, Oak Ridge National Laboratory, P. O. Box 2008, Oak Ridge, TN 37831, USA

The recent development of the Z-contrast imaging technique[1] for the VG HB501 UX dedicated STEM, has added a high-resolution imaging facility to a microscope used mainly for microanalysis. This imaging technique not only provides a high-resolution reference image, but as it can be performed simultaneously with electron energy loss spectroscopy (EELS), can be used to position the electron probe at the atomic scale. The spatial resolution of both the image and the energy loss spectrum can be identical, and in principle limited only by the 2.2 Å probe size of the microscope. There now exists, therefore, the possibility to perform chemical analysis of materials on the scale of single atomic columns or planes.[2]

In order to achieve atomic resolution energy loss spectroscopy, the range over which a fast electron can cause a particular excitation event, must be less than the interatomic spacing. This range is described classically by the impact parameter, b, which ranges from ~10 Å for the low loss region of the spectrum to <1Å for the core losses. In the STEM, the experimental spatial resolution limit is therefore given by adding the probe size and the impact parameter in quadrature. Figure 1 shows the expected spatial resolution of the energy loss signal as a function of collection angle for various energy losses. For energy losses above ~300eV and a collection angle of 30 mrad, the spatial resolution of the energy loss signal approaches the probe size.

The calculations of spatial resolution for the energy loss signal assume a very thin sample and ignore any beam broadening effects. For a zone-axis orientation, the Z-contrast result [1] shows however, that if the scattering event takes place in close proximity to the atom cores, the effect of beam channeling preserves the spatial resolution of the signal (figure 2). The effective spatial resolution is then limited only by the contribution of the probe tails (figure 3) on the surrounding columns to the spectral intensity. The extent of this contribution will be material dependent as the energy filtering of the spectrometer means that only those surrounding columns containing elements with core-edges in the same region of the spectrum will affect the result. From the probe profile calculations for silicon at the optimum focus condition, the intensity contribution of surrounding columns of the same element can be calculated to be ~15%. However, by reference to the image and using the calculated scattering cross-sections and probe profile, the effects of the tails can be deconvoluted from the spectrum, permitting quantitative analysis of single columns.

The anticipated high spatial resolution of the energy loss signal was confirmed by the study of cobalt silicide-silicon interfaces[3] using a CCD based parallel EELS system[2]. By using an oscilloscope linescan to center the beam accurately over successive planes across the interface, a series of 5 second exposure energy loss spectra were obtained of the cobalt $L_{2,3}$ edge (figure 4(a)) from atomically abrupt facets in the {111} planes (figure 4(b)). The intensity of the cobalt L_3 edge at each atomic plane relative to the intensity of the bulk gives a measurement of the variation in cobalt composition in the region of the interface. The intensity profile across the interface shows the energy loss spectra to have the same atomic resolution as the image (figure 4(c)). For a 3.1Å planar spacing, the effects of the probe tails should result in a ~7% change in intensity at the two planes either side of the interface. Although some effects are visible in figure 2(c), the signal-to-noise ratio ~10 makes it difficult to quantify. However, these results clearly demonstrate the possibility of obtaining atomic resolution chemical analysis by EELS.[4]

References

1. S. J. Pennycook and D. E. Jesson, Phys.Rev.Lett 64 (1990), 938

2. N. D. Browning and S. J. Pennycook, in press Microbeam Analysis
3. Sample from S. Mantl of Institut für Schicht-und Ionentechnik, Forschungzentrum Jülich, Germany
4. This research was sponsored by the Division of Materials Sciences, U. S. Department of Energy, under contract DE-AC05-84OR21400 with Martin Marietta Energy systems Inc, and in part by an appointment to the Oak Ridge National Laboratory Postdoctoral Research Program administered by the Oak Ridge Institute for Science and Education.
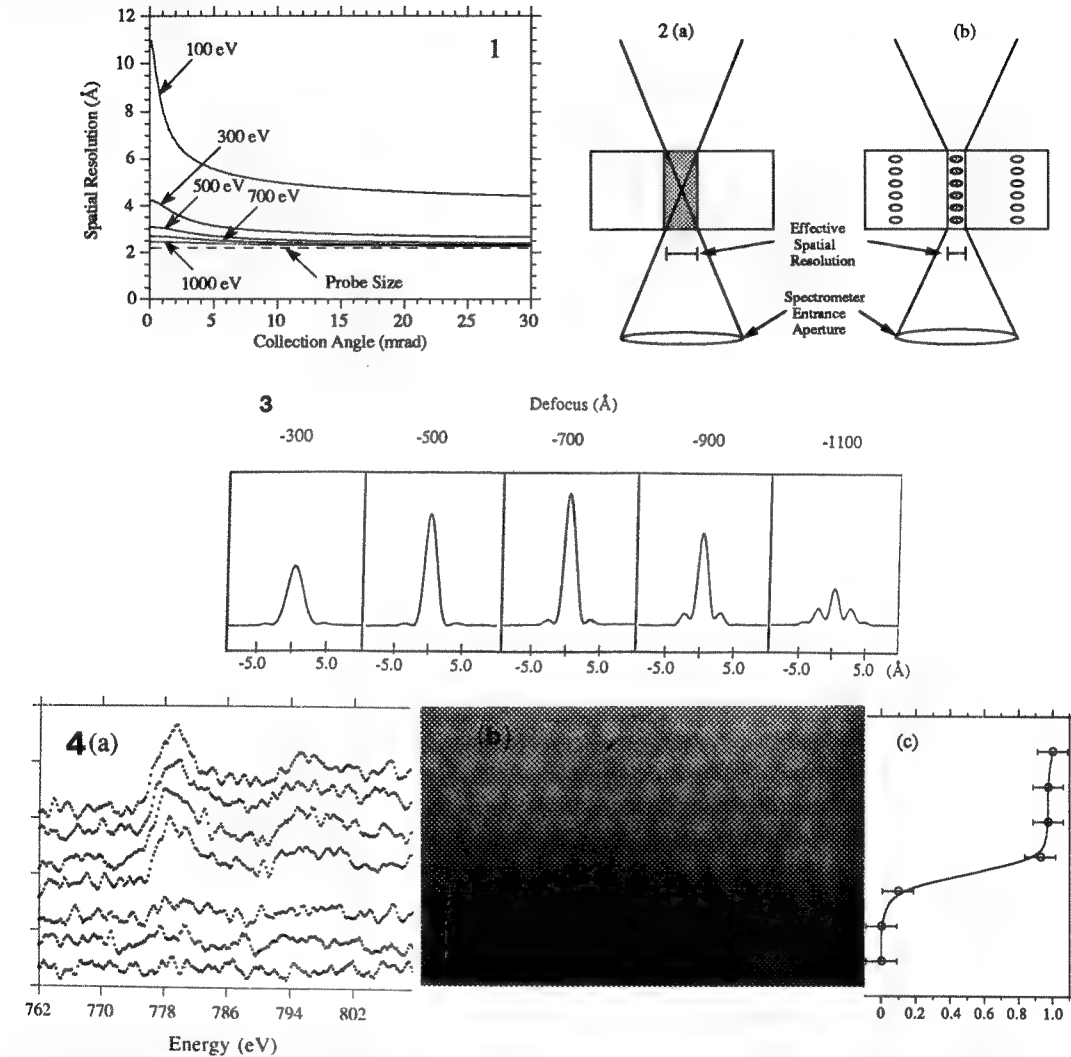
Figure 1. Theoretical spatial resolution of the energy loss signal as a function of collection angle.

Figure 2. The beam broadening seen in energy loss studies of amorphous materials or crystalline materials away from zone-axis orientation (a), is reduced in the case of a crystalline material in zone-axis orientation by the channeling of the electron beam down the atomic columns (b).

Figure 3. Effective probe intensity profiles as a function of defocus for an objective aperture of 10.3 mrad. The middle profile corresponds to the optimum Scherzer condition

Figure 4. (a) A 5 second exposure Cobalt $L_{2,3}$ spectrum scan in single plane steps across the cobalt silicide-silicon {111} facet interface (b). The cobalt L_3 edge intensity as a fraction of bulk intensity at each atomic plane shows the {111} facet interface to be atomically abrupt (c).

577

ACQUISITION OF EELS SPECTRA FOR HIGH-RESOLUTION SPECTROSCOPY

Maoxu Qian,* Mehmet Sarikaya,* and Edward A. Stern+
*Materials Science and Engineering and +Physics, University of Washington, Seattle, WA 98195

It is difficult, in general, to perform quantitative EELS to determine, for example, relative or absolute compositions of elements with relatively high atomic numbers (using, e.g., K edge energies from 500 eV to 2000 eV),[1] to study ELNES (energy loss near edge structure)[1] signal using the white lines to determine oxidation states, and to analyze EXELFS (extended energy loss fine structure)[1] to study short range ordering. In all these cases, it is essential to have high signal-to-noise (S/N) ratio (low systematical error) with high overall counts, and sufficient energy resolution (~1 eV), requirements which are, in general, difficult to attain. The reason is mainly due to three important inherent limitations in spectrum acquisition with EELS in the TEM. These are (i) large intrinsic background in EELS spectra, (ii) channel-to-channel gain variation (CCGV) in the parallel detection system, and (iii) difficulties in obtaining statistically high total counts (~10^6) per channel (CH). Except the high background in the EELS spectrum, the last two limitations may be circumvented, and the S/N ratio may be attained by the improvement in the on-line acquisition procedures. This short report addresses such procedures.

EELS spectra were acquired using the EL/P acquisition program[3] with a GATAN-666 parallel detection system attached to a Philips EM 430T operating at either 200 or 300 kV. Two major limitations were encountered in the acquisition program. Firstly, the present parallel EELS system has a CCGV of about 3%. This value, however, is already comparable to the fine structure features in, for example, EXELFS, and therefore, without correction of CCGV, fine structure analysis is meaningless. Secondly, statistical error in the spectrum should be at least 10 times smaller than the EXELFS signal which itself can be as small as few percentage of the background. This means that the statistical fluctuations should be only a few thousandths requiring measured counts of 10^6 level. Since the maximum count that can be acquired is limited to 16×10^3/CH, this necessitates about a few 100 scans with longer acquisition times (sometimes a few hours!). Due to the instability of the instrument, however, the edge will drift, smearing the spectrum.

Although in the current EELS acquisition program[3] a CCGV correction is provided, it does not reflect real acquisition conditions since it uses a 5 mm entrance aperture and a 0.0 eV/CH dispersion. A more accurtae correction is to locate a fairly smooth 50 eV energy band (without any spectral peaks or edges), usually in the low loss region of a spectrum, taken from a real sample with a 0.05 eV/CH dispersion. Any fluctuation would be due to the CCGV. As long as multiple plasmon peaks do not appear in this band, thickness is not a problem; in fact t = (1- 2) λ (mean-free-path) appears to be a good thickness for obtaining high total counts. Here, energy drift is not important since a smooth background is measured. However, care should be taken that no previous spectrum with prominent features was taken, such as zero loss peak or sharp inner shell edges, anywhere within the active channel region. The ratio of the measured data (Fig. 1a) to a cubic-spline fit (Fig. 1a) gives the normalized gain for each channel (Fig. 1b). By dividing each measured spectrum by the normalized gain for each channel will give the corrected CCGV distribution. The normalized CCGV distribution obtained using the EL/P software (Fig. 2) is significantly different than the one shown in Fig. 1(b).

A long acquisition time (e.g., > 10 s) may be used to attain high total counts, but this can cause spectrum drift detoriating energy resolution and limiting S/N ratio. An alternate way to obtain high counts/CH is to acquire many spectra by using a short dwell time and then summing them up, taking into account the drift between subsequent spectra. This can be done *on-line* by choosing a prominent feature, such as sharp white lines (with ΔE~10 eV) of the sample spectrum, and use it as a reference point for the alignment of the whole spectrum. Fig. 3 shows the quality of the spectrum obatained at the Mg-K edge. In practice, off-line alignment, that is often used, is not a good procedure since it requires large disk space and a longer total acquisition time, resulting in unnecessarily long exposure of the sample to the beam causing damage. In conclusion, with the above two functions, one can acquire spectra for long period of times (hours!), which is only limited by the sample damage, microscope conditions, and the patience of the operator.

1. *Electron Energy Loss Spectroscopy in the EM*, R. Egerton (Plenum, New York, 1986).
2. D. E. Sayers, E. A. Stern, and F. W. Lytle, Phys. Rev. Lett., **27**, 1204-1207 (1971).
3. M. Kundman, EL/P Software Instruction Manual, GATAN Inc. (1992).
4. Supported by NEDO Project, JAPAN, and Royalty Research Fund, University of Washington.
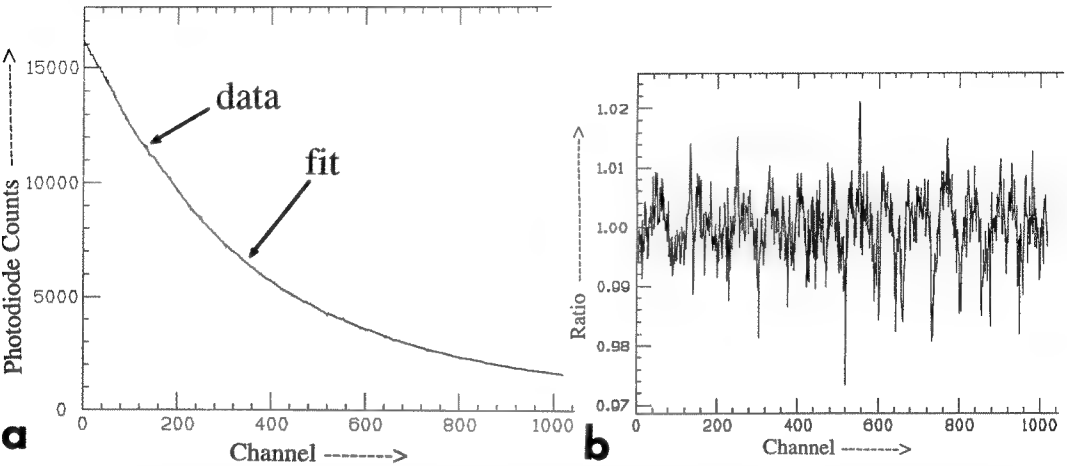
Fig. 1(a) A smooth 50 eV band from the low loss region of a thin C film (t ~ 1.5 mfp) (image mode, 10 kX mag., E_0=200 kV, 2 mm entrance aperture) with a superimposed cubic spline fit. (b) The ratio of the measured background to the smooth fit curve giving the normalized CCGV distribution.
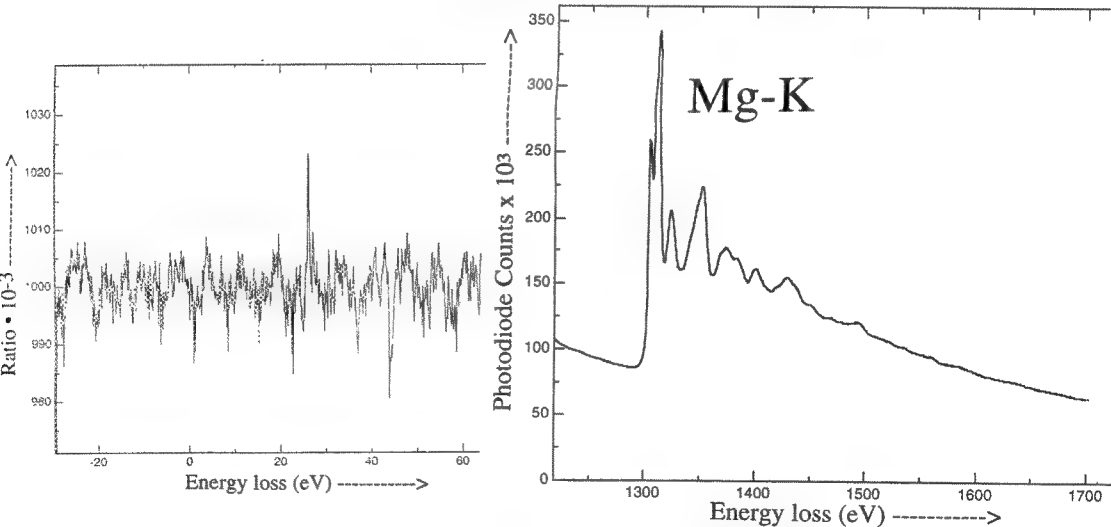
Fig. 2 - The CCGV obtained from EL/P, using a 5 mm aperture and 0.0 eV/CH dispersion. This CCGV distribution differs from that in Fig. 1(b) considerbly because of the differences in calibration conditions.

Fig. 3 - Mg-K edge taken from a single crystal MgO that was CCGV corrected and on-line acquired (sum over 1000 spectra) (E_0=200kV, 0.5 eV/CH, image mode, 10kX mag., EA=2 mm)

579

ENERGY-FILTERED REFLECTION ELECTRON MICROSCOPY AND REFLECTION HIGH-ENERGY ELECTRON DIFFRACTION ON ZEISS 912 TEM

JINGYUE LIU

Center for Solid State Science, Arizona State University, Tempe, AZ 85287

In reflection electron microscopy (REM) and reflection high energy electron diffraction (RHEED) the average path length of the elastically scattered electrons in the crystal ranges from 10 -100 nm and a significant portion of the electrons in the RHEED pattern spots used for imaging is inelastically scattered. The excitations of surface plasmons, bulk plasmons and valence electrons involves energy losses of 10 ~30 eV. Thus the image contrast and resolution in REM are degraded due to chromatic aberration of the objective lens. The use of energy filters in a TEM should offer significant improvement in resolution and contrast of REM images.[1] We present here some new results on the investigation of resolution limit and contrast mechanisms in energy filtered REM images.

The experiments were performed on a Zeiss 912 TEM fitted with an Omega magnetic imaging energy filter.[2] Digital RHEED patterns and REM images were acquired into 1024 pixels by 1024 pixels via a Gatan 679 CCD camera fitted to the microscope. The energy window used for imaging and diffraction was < 8 eV. A double-tilt cold stage was used to reduce phonon scattering and sample contamination. The sample temperature was at approximately -140°C during the experiment. Cleaved MgO (001) surface was used as a test sample.

Fig. 1a shows an unfiltered large-angle convergent beam RHEED pattern from a MgO (001) surface obtained with the incident beam azimuthal near the [100] zone axis. Figs. 1b, 1c and 1d show, respectively, RHEED patterns obtained with 0 eV (exposure time 0.02 sec), 22 eV (exposure time 0.02 sec) and 100 eV (exposure time 0.2 sec) energy loss electrons. The background intensity in the 0 eV loss RHEED pattern is significantly reduced. The surface loss signal (Fig. 1c), however, shows a RHEED pattern similar to the 0 eV loss RHEED pattern. Quantitative intensity line scans obtained by off line processing the digitally stored RHEED patterns reveal that the rocking curves of surface loss electrons have the same shapes and relative intensity ratios as the elastic rocking curves, in agreement with previous results.[3] RHEED patterns obtained with electrons having energy losses above 100 eV have a general form similar to that shown in Fig. 1d. These high energy loss events are mainly produced by core level excitations and multiple inelastic scattering of the incident electrons. A significant portion of these high energy loss signals may originate from the bulk of the sample and may have experienced multiple inelastic scattering inside the sample.

Fig. 2 shows the corresponding energy filtered REM images obtained with (008) specular beam satisfying surface resonance condition. By comparing images obtained with different energy loss electrons, it is not difficult to conclude that the elastic (0 eV loss) image gives the best contrast and resolution. Most of the inelastic scattering effects is removed in the elastic image (Fig. 2b) as compared with the unfiltered image (Fig. 2a). The effects of thermal diffuse scattering on REM images cannot be removed by using the energy filter but they are reduced due to the use of the cold stage. The surface loss image (Fig.2c) still reveals all the main surface features but with poorer image resolution and lower image contrast.[4] Quantitative information has been extracted from these digitally acquired REM images. An image resolution of approximately 0.9 nm has been achieved in Fig. 2b and in other higher magnification elastic REM images. The image contrast is also significantly improved in the elastic image as compared with that in the unfiltered image. For example, a step having a contrast of approximately 20% in the unfiltered REM image gives a contrast about 36% in the elastic image. Quantitative information about the contrast variations of surface steps with beam defocus has also been extracted from these energy filtered REM images. At high energy losses REM images (see Fig. 2d) show increasingly low surface sensitivity and poorer resolution since these signals are mainly generated by multiple inelastic scattering or are generated deep inside the crystal. Another adverse effect of using high energy loss electrons is that the field of view with resolvable features rapidly decreases with the increase of energy loss, presumably caused by incoherent effects which affect the effective convergence angle in the RHEED spot used to form REM images. Compositional imaging of bulk surfaces using core level excitations and other new features of energy filtered REM imaging will be discussed.[5]

References
1. J. C. H. Spence and J. Mayer, Proc. 49th Annu. Meeting of EMSA (1991) 616.
2. J. Mayer et al., Proc. 49th Annu. Meeting of EMSA (1991) 786.

3. M. Gajdardziska-Josifovska et al., Proc. 49th Annu. Meeting of EMSA (1991) 626.
4. J. Liu and J. M. Cowley, Ultramicroscopy, in press.
5. The author thanks professor J. M. Cowley for helpful discussions. This research was supported by Shell Development Company and made use of the ASU CHREM supported by NSF grant DMR-9115680.
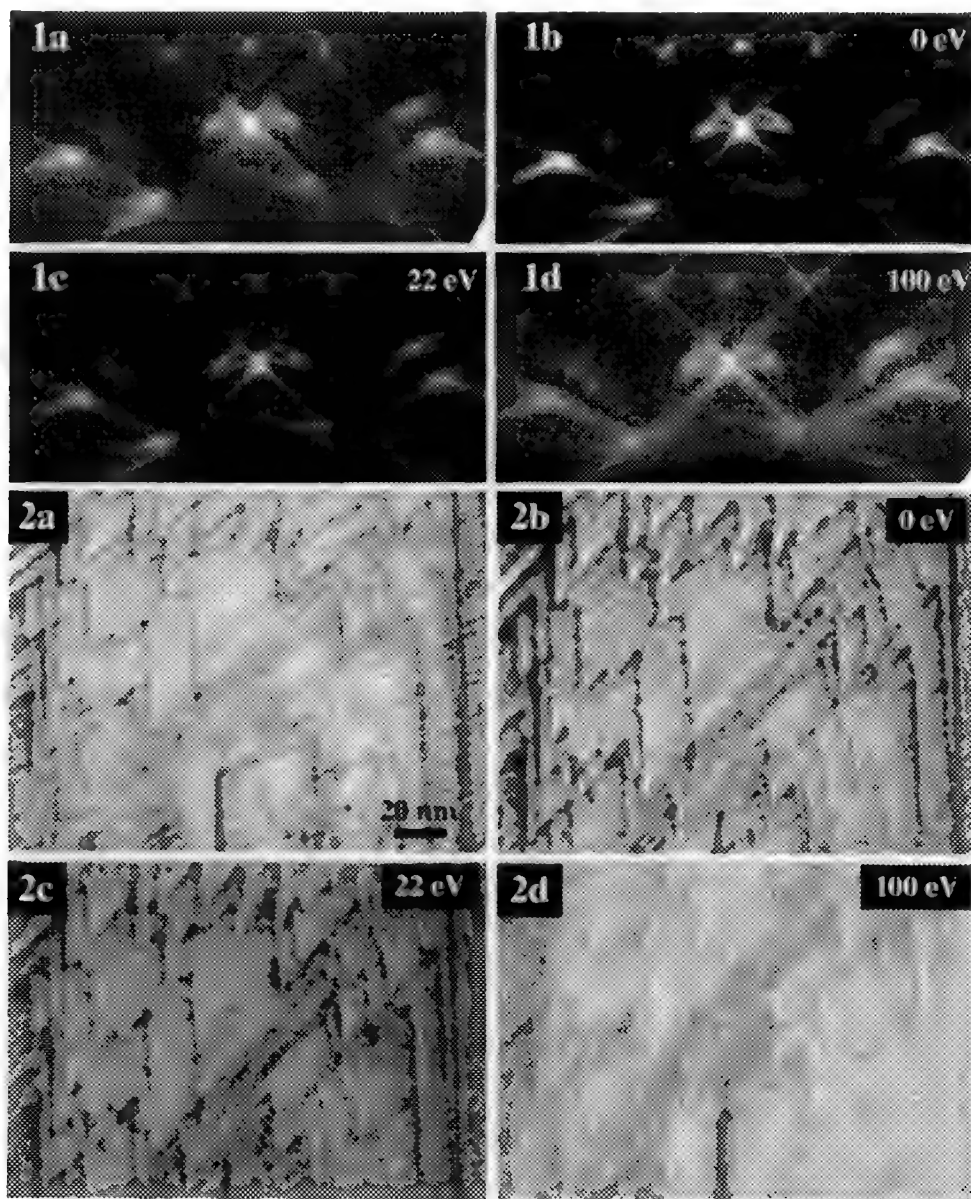
Fig.1--RHEED patterns of cleaved MgO (001) surface obtained with (a) all electrons, (b) 0 eV loss electrons, (c) 22 eV loss electrons and (d) 100 eV loss electrons.

Fig.2--REM images of cleaved MgO (001) surface obtained with (a) all electrons , (b) 0 eV loss electrons, (c) 22 eV loss electrons and (d) 100 eV loss electrons.

A NEW METHOD FOR DETERMINING SAMPLE THICKNESS: A COMPARISON TO EXPERIMENTAL RESULTS

John Blackson* , Suichu Luo and David C Joy **

EM Facility, University of Tennessee, Knoxville, TN 37996-0810,
*Permanent address:Dow Chemical Co., Midland, MI 48667
**Oak Ridge National Laboratory, Oak Ridge, TN 37831

Sample thickness is an important parameter in quantitative electron microscopy, [1,2][3]. Several methods for determining sample thickness have been described previously.[4] A theoretical method presented here utilizes the low loss region of the electron energy loss spectrum to calculate sample thickness. The method avoids many of the limitations of other methods and is applicable to a wide variety of samples. The method is compared to film thicknesses determined experimentally as described below.

Chromium films were deposited simultaneously onto collodion supported TEM grids and cured epoxy blanks using a Denton Hi Res 100 coater equipped with a Syton quartz crystal monitor. The cured epoxy blanks were covered with a layer of unpolymerized epoxy that was then cured. The chromium sandwich was cross sectioned using ultramicrotomy techniques employing a diamond knife. Sections were produced which were as thin as possible (<50 nm) to minimize measurement errors. Chromium film thickness was determined directly using transmission electron microscopy (Fig. 1). A tilting stage was used to optimize the alignment of the film in the microscope. A diffraction grating replica was used to accurately calibrate microscope magnification. The current procedure involved high vacuum chromium sputtering although other metals could be sputtered or evaporated and examined using the same method. The collodion support on the TEM grids was dissolved away using acetone saturated filter paper leaving chromium films of known thickness. Parallel electron energy loss spectroscopy was performed on the calibrated chromium films using a Topcon 002B 200KeV TEM equipped with a Gatan parallel EELS. The spectrometer was controlled using Gatan EL/P Software.

The theoretical method was applied to the acquired spectra. The method incorporates a FFT convolution procedure to obtain the single scattering distribution by an iterative curve fitting process. The single scattering distribution Sig (E) was determined using Equation 1 where; Ang (E,β) is the angular distribution function, E is the energy loss and β is the collection semiangle.

$$Sig\ (E) = k\ Im(-1/\varepsilon\ )\ Ang(E,\beta) \qquad (1)$$

$$Im\{-1/\varepsilon\ \} = \frac{\omega\ \tau\ \omega_p^2}{(\omega^2-\omega_x^2)^2+\omega^2\tau^2} \qquad (2)$$

Im (-1/ε), is calculated using Equation 2 . M shell excitations are proportional to E^{-r} [1] ,which are saw tooth curves. The factor k in Equation 1 was determined by sum rule allowing the thickness of the sample to be obtained using Equation 3 where $E_T = 1/2\ mv^2$, I_o and ΔE are zero loss peak intensity and the energy loss increment per channel, respectively.

$$Thickness = 332.5\ k\ E_T\ /I_o/\Delta E \qquad (3)$$

Table 1 compares the experimental data to our theoretically calculated thicknesses and the thicknesses calculated using Egerton's deconvolution program.[1] Good agreement exists between theoretical values and experimentally measured thicknesses with the theoretical values being within 5% of the experimental. Figure 2 compares the theoretically modeled spectrum to the experimental PEELS spectrum.

Table 1 Comparison of experimental and calculated thicknesses

	Experimental data	calculated data	Egerton's method
#1	44 .0 nm	43.7 nm	45.6 nm
#2	112.0 nm	111.3 nm	112.6 nm
#3	200.0 nm	210.3 nm	189.5 nm

References

1. R. F. Egerton, Electron Energy-Loss Spectroscopy in the Electron Microscope, Plenum Press(1986)
2. P. A. Crozier, Phil. Mag. B (1990) 61,311.
3. P. A. Crozier and R. F. Egerton, Ultramicroscopy. (1989)27,9.
4. D.B. Williams, Practical Analytical Electron Microscopy in Materials Science, Philips Electronic Instruments, Inc. (1984) 77.
5. R. H. Ritchie and A. Howie, Phil. Mag. (1977)36,463.
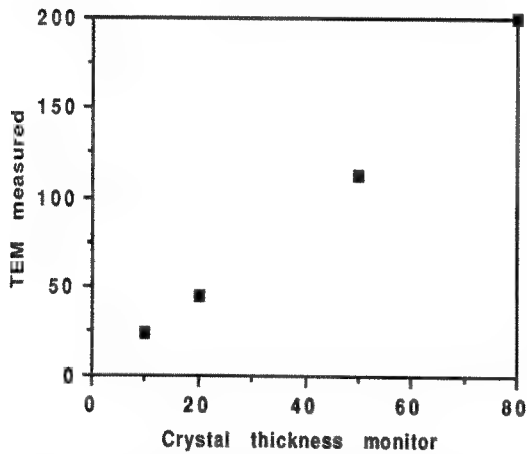
Fig.1 Comparison of experimentally measured thicknesses and quartz monitor thickness readings
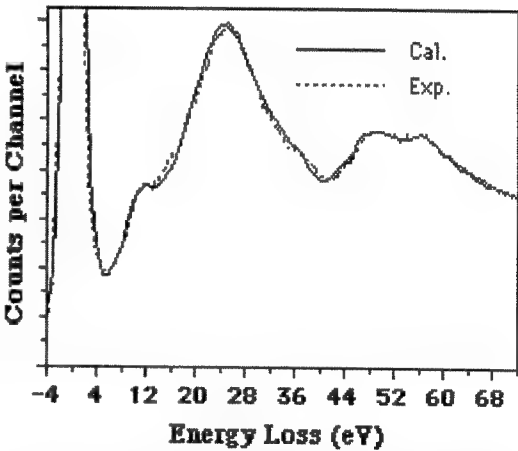
Fig.2 Comparison of simulated and experimental PEELS data for chromium. Recorded at 200keV, 5mrads collection semiangle

EXELFS REVISITED: AN IMPROVED DATA ANALYSIS TECHNIQUE

Maoxu Qian,[*] Mehmet Sarikaya,[*] and Edward A. Stern[+]

Materials Science and Engineering[*] and Physics[+], University of Washington, Seattle, WA 98195

EXELFS (extended energy loss fine structure) spectroscopy contains unique information of local atomic structure[1], same as XAFS[2] (X-ray fine structure), but has several advantages over XAFS, such as having high spatial resolution (nanoscale versus bulk), better low Z element sensitivity, parallel detectability, and no dependability on synchrotron-radiation-sources. Due to poor statistical total counts, however, EELS data quality is inferior and, therefore, EXELFS technique has not been well developed to its full advantages. The main limitations in EELS acquisition are channel-to-channel gain variations (CCGV) in the parallel detection system and low S/N ratio due to the instability of instrument that prevents long acquisition times. Techniques that circumvent CCGV, such as first or second difference, do not allow the retrieval of EXELFS signal from the spectra. Recently we have improved the EELS data acquisition technique[3] so that CCGV could effectively be corrected and statistical fluctuations could reach a level much lower than that in the fine structure. These improvements have opened up the possibility of deducing accurate atomic structure information from EELS spectrum at relatively high energy values (1000 to 2000 eV). In this paper, we describe the improved EXELFS data analysis technique and present preliminary results on Al, chosen as the calibration material as it is structurally well-known, resistant to electron radiation, has a K-edge at 1560 eV, quite high for EELS measurements and, hence, is a good test sample for the case discussed here.

The Al sample was prepared from a pure Al (99.999%) pellet that was rolled to a 0.2 mm-thin film, sealed in quartz tube in vacuum, and then annealed at 280 °C for 4 hours. A 3.0 mm disc was punched and electropolished for electron transparency. Measurements were performed with a low temperature holder in a Philips 430T TEM at 200kV in the image mode using a GATAN-666 EELS system with an acquisition software.[3,4] To avoid possible radiation damage or beam heating, the beam was only focused to a ~4 μm diameter and each spectrum was acquired with a 10 second-dwell time resulting in 100 counts/CH.

Since the statistics in data quality of EXELFS has already reached a level similar to that in a typical XAFS spectrum,[2] one could then apply the well-developed XAFS data analysis procedures[5,6] to the new EXELFS data. For this, both the XAFS software (developed in our laboratories)[5] and FEFF program[6] (a theoretical calculation prgram of XAFS) were used. Software used necessitates the deconvolution of plasmon scattering in EELS spectra even if the sample thickness is as small as 0.3 λ. The EL/P formatted[4] data of Al (Fig. 1) was then transferred to $x\mu$ format (x thickness and μ absorption). Also, the theoretical back-scattering data for each shell were calculated based on the known crystal structure. Both single and double scattering paths were included up to the third shell, thus altogether 6 paths (3 single scattering plus 3 double scattering paths) were used as shown in Table-I. Auto-background removal[5] was performed to deduce the χ data (Fig. 2). The k-range used is 2.4 - 8 Å^{-1} with k^3 weight. An r-space non-linear least-square-fit was performed with the FEFF calculated model.[6] The fitting r-range was 1-5 Å, which covered the first, second, and third shells. The variable parameters used were edge energy shift, ΔE_0; first shell distance shift, Δr; first, second, and third shell Debye-Waller (D-W) factors σ_1^2, σ_2^2, σ_3^2, and S_0^2. The number of variables (6) is much less than the number of independent data points (13). Figures 3 and 4 and Table-I show the fit results. The nearest-neighbor distance determined is 2.83±0.01 Å, and the first shell D-W factor is 0.0072 ± 0.0007 Å^2. We found that the structure information obtained from EXELFS has a good agreement with the known structure of Al with an accuracy of 0.01Å for first shell distance and ±10% for σ^2 with a reasonable E_0 shift of 3.5 eV. The S_0^2 of 0.66 is a bit too small probably due to the error in the deconvolution of plasmon scattering. In this work, we did not allow the coordinate number to vary because these numbers are strongly correlated to S_0^2. Therefore, we fixed the coordinate numbers at known values to evaluate the S_0^2 value, so that the coordination numbers in other cases can be determined.

1. R. D. Leapman and V. E. Cosslett, J. Phys. D (J. Appl. Phys.) **9**, 129 (1976).
2. D. E. Sayers et al., Phys. Rev. Lett. **27**, 1204 (1971); E. A. Stern, Optic, **61**, 45 (1982).
3. M. Qian, M. Sarikaya, and E. A. Stern, these proceedings.
4. M. Kundman, EL/P Software Instruction Manual, GATAN Inc. (1992).
5. XAFS Software (UWXAFS2.0) developed at University of Washington (contact the authors).
6. J. J. Rehr et al., J. Amer. Chem. Soc., **113**, 5135 (1991).
7. Research supported by NEDO, Japan, and University of Washington Royalty Research Fund.

Table-I: Fit Results of Al

Path #	Degen.	r (Å)	σ^2 (Å^2)	Comments
1	12	2.83 ± .01	0.0072 ± .0007	1st shell - ss
2	6	4.00 ± .02	0.0117 ± .0012	2nd shell - ss.
3	48	4.26 ± .02	same as path 1	1st shell - ds
4	48	4.84 ± .02	same as path 2	1st + 2nd shell -ds
5	24	4.84 ± .02	same as path 1	1st shell - ds
6	24	4.90 ± .02	0.0217 ± .0022	3rd shell - ss

ΔE_0 = -3.5 eV, $S_0{}^2$ = 0.66.

(ss: single scattering;
ds: double scattering)
Degen. = # of degeneracy
in each path.
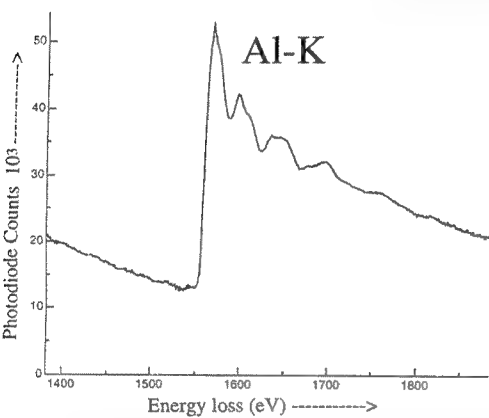
Fig. 1 - EELS spectrum exhibiting Al-K edge.
(thickness = 0.32 λ; E_0= 200 kV; EA = 2 mm
1 eV/CH; 10 secs/spectra; 400 spectra, IM)
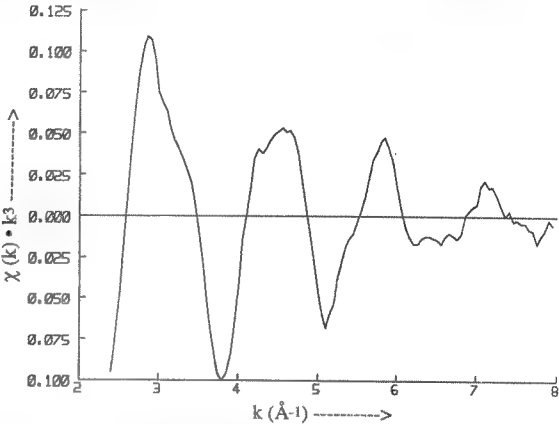
Fig. 2 - χ data corresponding to Fig. 1
with k^3 weight.
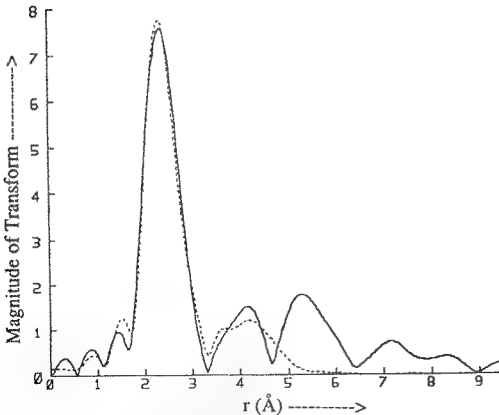
Fig. 3 - Fourier transform of the EXELFS of
Al versus **k** with the fit result (dashed).
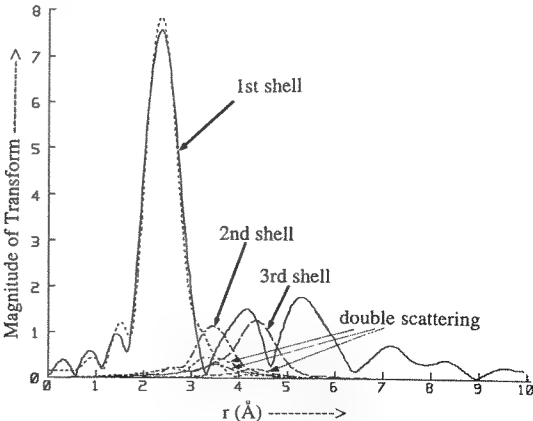
Fig. 4 - The same as Fig. 3, but shows
the fit results for each individual path.

585

ELEMENTAL MAPPING WITH AN ENERGY-SELECTING IMAGING FILTER

O.L. Krivanek, A.J. Gubbens, M.K. Kundmann and G.C. Carpenter[1]

Gatan Research and Development, 6678 Owens Drive, Pleasanton, CA 94588, USA
[1] CANMET Metals Technology Laboratories, 568 Booth St., Ottawa, Ont. K1A-0G1, Canada

Imaging filters produce energy-selected images in a few seconds, and chemical maps formed by processing of several images taken at different energy losses in typically less than one minute. On the other hand, imaging filters do not provide detailed spectra from each specimen point, and are vulnerable to artifacts due to variations in specimen thickness, and other effects influencing EELS background extrapolation and subtraction. These include diffraction contrast arising particularly in crystalline samples, edge overlap, and extended fine structures (EXELFS) in the pre-edge region caused by major edges at lower energies. We have therefore been exploring the practical usefulness of imaging filters on a range of specimens from materials science and biology. The results suggest that the imaging capability combined with full parallel-detection EELS performance delivers a very powerful experimental set-up.

Figure 1 shows an energy-filtered bright field image of a steel sample containing about 1 % Cu, obtained at 120 keV with the Gatan Imaging Filter[1,2] (GIF) attached to a Philips CM12ST microscope. The steel was aged at 500°C for 24 hours, and was suspected to contain small Cu precipitates. Fig. 2 shows a spectrum detected in parallel by the slow scan CCD camera of the filter from a specimen region about 200 nm in diameter near the specimen edge. There are strong oxygen K, chromium L, and iron L edges, but no Cu edge is visible. Fig. 3 shows the first difference spectrum in the vicinity of the expected Cu L edge location. The spectrum was produced by recording two spectra shifted by 10 eV, and subtracting them. Strong EXELFS structures due to the iron L edge are visible, but there is no readily recognizable feature at the copper L_3 threshold energy.

Figures 4 and 5 show images taken before and after the copper L edge with an energy window 20 eV wide. Small dark regions are present in the pre-edge image but not in the post-edge image. We therefore attempted to quantify this contrast into a Cu elemental map. Performing standard AE^{-r} background extrapolation and subtraction highlighted the regions as copper-rich, but it produced the unphysical result that the concentration was mostly negative. This was probably due to the weak Cu concentration, and the strong post-iron EXELFS structure which upset the quality of the fit. The background extrapolation also significantly increased the noise content of the images[2]. A better processing method was therefore to simply divide the post-edge image by the pre-edge one, which gave the result shown in Fig. 6. In the limit of small concentration of the element of interest, and an r-coefficient that does not vary across the image, the ratio method should simply show intensity variation corresponding to the Cu concentration, and be relatively free of artifacts associated with variations in specimen thickness, elastic (Bragg) scattering, and EXELFS structures. This is demonstrated by dividing the pre-edge image by one taken at a lower energy still (Fig. 7). The result shows mostly residual diffraction contrast, caused by thickness fringes moving between the two images.

Similar methodology applied to the chromium and oxygen edges also produced clear images of both elements. Chromium was present as an oxide contaminant due to the electropolishing, and was concentrated near the specimen edge (Fig. 8). Oxygen was present everywhere as a surface oxide film, and there was an increase of its concentration near the sample edge and in the chromium oxide particles (Fig. 9).

In summary, the distribution of elements present in concentrations of 1% and lower can be successfully imaged in a few seconds by an imaging filter, provided that the elements are segregated rather than spread throughout the sample. A simple processing method that divides a post-edge image by a pre-edge image produces "enhanced concentration" maps with minimum added noise, and is not greatly affected by many of the artifacts arising in elemental mapping of crystalline materials. Precise quantification will, however, be much more difficult, especially at concentrations below 1 %.

References

1. O.L. Krivanek et al., Microsc., Microanal. Microstruct. **3** (1992) 187.
2. A.J. Gubbens and O.L. Krivanek, Ultramicroscopy, in press.
3. M.K. Kundmann and O.L. Krivanek, Proceedings 1993 MAS meet., to be published.
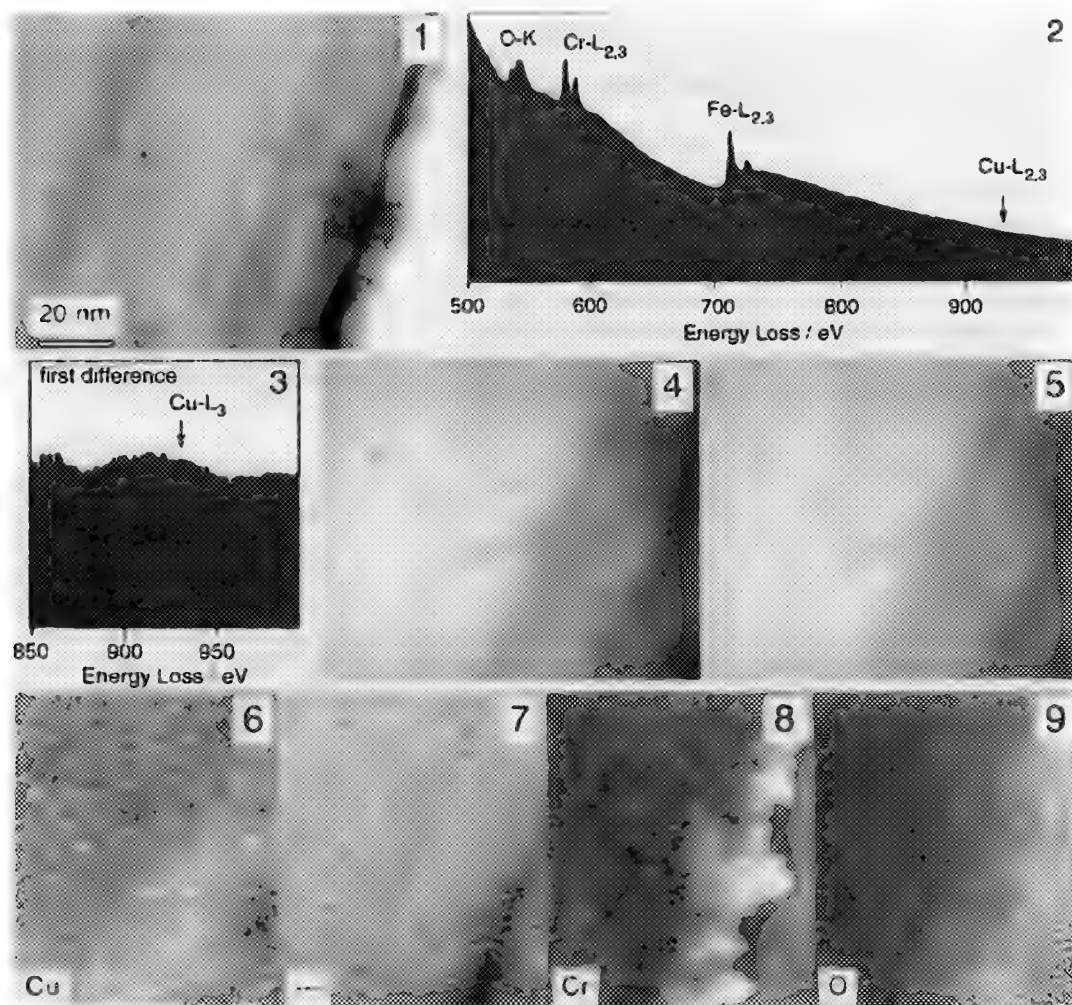
Fig. 1. Elastic bright field image of a copper-containing steel. Gatan Imaging Filter (GIF), Philips CM12ST TEM, 120 keV. Energy window 10 eV wide.
Fig. 2. Electron energy loss spectrum of the sample. Acceptance angle ~100 mrad, 8 sec acquisition.
Fig. 3. First difference spectrum of the copper L edge region. 16 sec total acquisition.
Fig. 4. Energy-selected image, pre-Cu $L_{2,3}$ (910±10 eV). 16 sec acquisition.
Fig. 5. Energy-selected image, post-Cu $L_{2,3}$ (1000±10 eV). 16 sec acquisition.
Fig. 6. Ratio image of post- and pre-Cu images (1000±10 eV / 910±10 eV).
Fig. 7. Ratio image of two pre-Cu images (910±10 eV / 850±10 eV).
Fig. 8. Ratio image of post- and pre-Cr $L_{2,3}$ images (580±5 eV / 550±5 eV).
Fig. 9. Ratio image of post- and pre-O K images (545±5 eV / 500±5 eV).

587

COMPOSITIONAL BIOLOGICAL MAPPING WITH X-RAYS IN THE ELECTRON MICROSCOPE

Ann LeFurgey*, D.A. Kopf, * and Peter Ingram**

*Duke University Medical Center, Durham, NC 27710 and **Research Triangle Institute, Research Triangle Park, N.C. 27709

New ideas in microprobe analysis over the last decade have refuted the notion that electron probe x-ray imaging is limited to multispectral data as qualitative maps. Electron microscopy is still the most widely used technique for high resolution imaging of biological materials. The acquisition and processing of digital quantitative elemental images of one to several cells in an electron microscope is now accomplished with advanced, commonly available microcomputers. A system developed in our laboratories uses a graphics-based microcomputer to acquire spectrally filtered x-ray data that is fitted to standards, to display the data and images on-line and in real time, and to correct the multispectral image with regard to specimen drift.[1] Statistics in the data acquisition is the limiting factor in both the image resolution and the ability to automatically recognize regions which need longer acquisition times.

Except in routine clinical or diagnostic situations, specimen preparation requires the tissues or cells to be rapidly frozen in a viable state in order to preserve their inherent elemental and anatomical integrity. Both high resolution quantitative x-ray images of freeze-dried cryosections and low electron dose bright field images can be acquired to obtain element and water contents from the same intracellular regions. This type of microchemical microscopy (microtopochemistry) facilitates direct correlation with parallel biochemical and (patho)physiological studies which focus on mechanisms of ionic homeostasis and compartmentation, i.e. structural biology at cellular and subcellular levels. It allows an unique method of investigation of intracellular concentration gradients and intracellular membrane potentials,[2,3] of the heterogeneity of cell responses to stimuli, of certain fast physiological events *in vivo* at ultrastructural resolution, and of events occurring with low frequency or involving cell-to-cell interactions.

Ideally the computer should analyze the data at each pixel, and in relation to the surrounding pixels, classify the pixel into a discrete value, e.g., the pixel is in mitochondria, cytoplasm, nucleus, or the pixel contains significantly more Ca, etc. In the presence of noisy pixel data, these discrete classes become statistical inferences with calculated probabilities.

In general, a multispectral classification scheme will create a set of images in which the brightness at each pixel corresponds to the correlation of the pixel's spectrum with a "basis" spectrum for each image. Prior knowledge of useful basis spectra can be used to generate images with a natural significance. In our case, the x ray spectra at each pixel are converted to images of elemental concentration through a multiple least square fit to reference spectra obtained from samples containing known amounts of each element. (The fitting parameters ultimately become the elemental concentrations, after a correction for the local sample thickness based on the continuum background, corrected to first order by the calculated elemental composition.)

If prior knowledge of the basis spectra is not available, or to avoid degradation of the data, a "principal component" analysis of the data will generate eigenspectra, and projection of each pixel spectrum onto these will generate a set of eigenimages.[4] The significance of these images will be given by the eigenvalue, and only as many images can be included as are significant at the desired level. In our case we allow for the seven known most frequently occurring physiological elements-- Na, Mg, P, S, Cl, K, Ca, plus three "unknowns" which might unexpectedly occur. If separate

eigenspectra analyses are performed in areas identified through morphological analysis, even better results can be expected. The best approach is a careful Bayesian approach using continuously refined *a priori* probabilities obtained from the data itself, as it is being scanned.

Noise limitation generally necessitates an experimental strategy which involves periodic rapid acquisition of several good signal-to-noise ratio images, which can be used for on-line and *post facto* drift correction, combined with static probes and relatively long multispectral images, as the essential interactive tools of investigation for biological x-ray microanalysis. A database keeps track of the image content from multiple regions which can be indexed to the images from whence they came, thus enabling similar regional information from many specimens to be collated. In addition the unified design of the software program provides for off-line processing and analysis by multiple investigators remote from the microscope.

The software developed has dramatically increased productivity in compositional data acquisition. The potential for growth and application of this once laborious technology is clearly unlimited, with new avenues of investigation emerging rapidly, e.g. forensic and environmental toxicology, biomedical diagnosis, trace element physiology and pathophysiology of organisms in both the plant and animal kingdoms, and geological, marine and earth sciences.

1. A. LeFurgey et al., J. Microscopy 165 (1992) 191.
2. M. Backus et al., Proc. 50th Ann. EMSA Mtg. (1992) 740.
3. M. Backus et al., Amer. J. Physiology (Cell Physiology) in press (1993).
4. R.C. Gonzalez and P. Wintz, <u>Digital Image Processing</u>, Addison-Wesley Publ. Co., Reading, MA. (1987), p. 122.
5. This work was supported by the National Science Foundation (NSF DIR9106607), National Institutes of Health (S10 RR06692), American Diabetes Association, North Carolina Biotechnology Center, and North Carolina Board of Science and Technology.

HIGH-SPATIAL-RESOLUTION X-RAY MICROANALYSIS: COMPARISON OF EXPERIMENT AND INCOHERENT SCATTERING CALCULATIONS

J. R. Michael and A. D. Romig, Jr.

Materials and Process Sciences Center, Sandia National Laboratories, Albuquerque, NM 87185

There have been many experimental efforts to measure the spatial resolution for x-ray microanalysis in the analytical electron microscope (AEM). [1-5] There have been three commonly utilized specimen geometries in these experiments: 1) segregant at a grain boundary, 2) interphase boundaries oriented parallel to the electron beam, and most recently 3) spherical particles embedded at various depths in thin foils. The results of many of these experiments have been analyzed with a number of models for the broadening of the electron beam as it traverses the thin foil. These models are typically based on incoherent electron scattering, typical of Monte Carlo simulations. [6] A vast majority of the published spatial resolution data support the incoherent scattering models as the best simulation of spatial resolution for x-ray microanalysis in the AEM. Recent experimental work using embedded particles to measure beam broadening has been used to support the coherent scattering model of beam broadening [5] The coherent scattering model considers the interaction of the wave nature of the electron and the periodic atomic structure of the specimen. [7] In this paper, the capability of the incoherent scattering model (Monte Carlo simulations) to describe the recent experimental measurements from embedded particles will be demonstrated.

There have been many excellent studies that have attempted to measure the x-ray spatial resolution for microanalysis in the AEM, but there are perhaps three that are most notable. [1,4,5] Each of these notable studies was conducted in an AEM equipped with a field emission electron gun operated at 100 kV. The earliest of these studies utilized the segregation of Fe to grain boundaries in MgO. [1] These authors observed that the widths of Fe concentration profiles measured across MgO grain boundaries did not vary significantly with specimen thickness, but that the concentration maximum of the measured Fe profile decreased with increasing specimen thickness. The experimental results were modeled by assuming: 1) a Gaussian intensity distribution in the electron source, and 2) that the width of the Gaussian distribution increased as the electron probe traversed the thin foil. Later, Monte Carlo simulations were also found to produce results which agreed with the experimental profiles. [8] The second study utilized the interphase interface technique to measure the x-ray spatial resolution in the AEM. [4] This study compared the experimental profiles with both the Gaussian broadening calculations and Monte Carlo simulations. An example of a profile from this study along with the results of a Monte Carlo simulation are shown in Figure 1. The incoherent scattering models adequately described the spatial resolution over a range of specimen thicknesses. The most recent study of spatial resolution in the AEM determined the extent of beam broadening in a thin foil by measuring concentration profiles across embedded spherical precipitates. [5] The authors of this study made no attempt to simulate the experimental results with any scattering model, but concluded that the extent of beam broadening was much smaller than predicted by the incoherent scattering models. On this basis, the authors state that the incoherent scattering model overestimates the extent of beam broadening and that coherent scattering of the electron probe better models the x-ray spatial resolution.

The present study utilized Monte Carlo simulations to calculate profiles from precipitates embedded at various depths in thin specimens and then compared the simulations with experimental data measured from embedded particles. The recent embedded particle study parameterized the experimental data by taking the ratio of the area under the experimental profile that fell outside the precipitate diameter to the total area of the profile, scaled by the precipitate diameter. [5] This parameterization scheme was an attempt to eliminate the effect of precipitate size on the measured broadening. The experimental results of this study along with the Monte Carlo simulation results are shown in Figure 2. The amount of scatter in the experimental results is quite large, but it is apparent that the beam broadening calculated by the Monte Carlo simulation, which assumes incoherent scattering, is consistent with the

experimental measurements. The Monte Carlo simulation does not overestimate the experimentally determined spatial resolution.

The data from the three studies of electron beam broadening in field emission gun equipped AEM's demonstrate that extremely high spatial resolutions can be achieved. The experimental results in all three studies can be adequately modeled by incoherent electron scattering (e.g. Monte Carlo simulations) with no need to invoke coherent electron scattering.

References

1. E. L. Hall et al., Phil Mag. A. (1981) 43, 1569.
2. T. A. Stephenson et al., Quantitative Microanalysis at High Spatial Resolution, London: The Metals Society (1981) 3.
3. A. D. Romig, J. Microsc. (1990) 135, 191.
4. J. R. Michael et al., J. Microsc. (1990) 160, 41.
5. W. A. Furdanowicz et al., Microbeam Analysis--1991 (1991) 463.
6. D. E. Newbury, Microbeam Analysis--1982 (1982) 79.
7. L. D. Marks, in J. B. Roberto et al., Eds., Advanced Photon and Particle Techniques for Characterizing Defects in Solids, MRS Proceedings (1985) 41, 247.
8. G. Cliff et al., Microbeam Analysis--1984 (1984) 37.
9. This work was supported by the U. S. Department of Energy under contract DE-AC04-76DP00789.
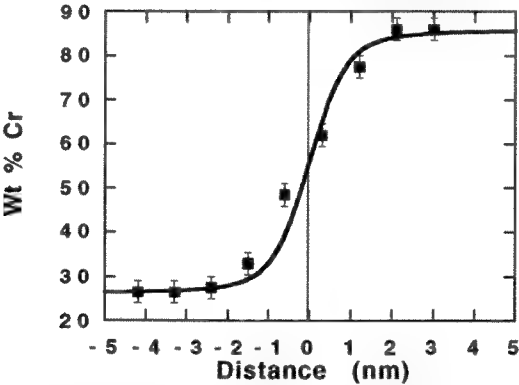
FIG. 1. Comparison of an experimental profile (from reference 4) and Monte Carlo calculations (solid curve) across an interphase interface in a 55 nm thick Ni-Fe-Cr alloy.
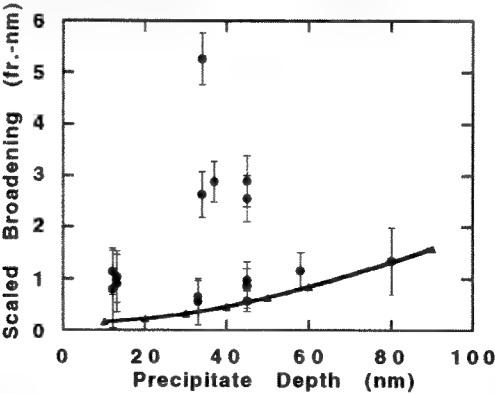
FIG. 2. Comparison of the experimental broadening measurements from embedded precipitates (from reference 5) with Monte Carlo electron trajectory simulations (solid curve) .

HOLE COUNT AND SECONDARY EXCITATION IN SEVERAL ANALYTICAL ELECTRON MICROSCOPES

E.A. Kenik, L.F. Allard, and J. Bentley

Metals and Ceramics Division, Oak Ridge National Laboratory, P.O. Box 2008, Oak Ridge, TN 37831

Hole count and secondary excitation are two concerns the analyst must address for energy dispersive X-ray spectrometry (EDXS) in the analytical electron microscope (AEM). Identification and minimization of the uncollimated radiation responsible for the hole count should be as important to the AEM manufacturer as it is to the microscopist, especially as "good" hole count performance can be a sales advantage. Secondary excitation (which we previously referred to as secondary fluorescence[1,2]) arises from excitation of the specimen by electrons or high energy x-rays generated by the interaction of the primary electron beam with the specimen. A test specimen (modified chromium thin film/molybdenum washer) described previously,[2] has been used to evaluate levels of both hole count and secondary excitation in a number of AEMs.

Hole count spectra from the test specimen have been measured for several Philips AEMs and have been compared to those produced by direct excitation of a thick region of the molybdenum support by the high energy electrons at reduced beam current. Fig. 1 compares spectra from a Philips CM12 AEM operating in the microprobe mode. The Mo L/K ratio, the Mo Kα peak/background ratio, and the shape of the background are very similar (Hole Count - L/K = 0.28, P/B = 49; thick Mo - L/K = 0.29, P/B = 49), indicating that electrons are the primary source of the hole count in this case. This conclusion is supported by the presence of a small chromium Kα peak in the hole count spectrum. The interaction of high energy x-rays with the ~35 nm thick chromium film should produce negligible chromium x-rays. Similar results were obtained for other Philips AEMs (EM400T/FEG and CM30).

The hole count and secondary excitation performance of several field emission gun (FEG) AEMs have been tested. The magnitudes of the hole count (HC) and the secondary excitation (SE) were estimated as:

$$HC = I_h(Mo)/[I_f(Cr)-I_h(Cr)] \qquad \text{and} \qquad SE = [I_f(Mo)-I_h(Mo)]/[I_f(Cr)-I_h(Cr)]$$

where I(A) is the integrated Kα peak intensity for element A and the subscripts refer to the positioning of the probe on the film (f) or in a hole (h).[2] For a Philips EM400T/FEG, SE = 0.04 near zero specimen tilt, but increased to SE = 0.4 at 45°, and HC = 0.03-0.05 for platinum "tophat" condenser (C2) apertures 50-150 µm in diameter. Since electrons were indicated as the primary source of the hole count, the possibility that electrons were being scattered from the aperture edge was checked. Hole count spectra were measured for a thin, molybdenum C2 aperture (100 µm-diam) where scattering from the aperture should be reduced. The Mo L/K and Kα P/B ratios were similar to those for the platinum apertures, indicating a primarily electron-induced hole count, even though the measured HC was much larger (HC = 0.65).

Tests were performed on a Philips CM20 FEG AEM using a beam-defining 30 µm-diam C1 aperture. The measured hole counts (HC = 0.017 for microprobe mode and HC = 0.014 for nanoprobe mode) were significantly lower than that for the EM400T/FEG; secondary excitation was similar (SE ~ 0.04). The hole count spectra exhibited low Mo L/K ratios (L/K <0.003) with a Mo Kα P/B of ~53. The low L/K ratio is consistent with a hole count generated by high energy x-rays;[3] however, further work is required to confirm this conclusion. Improved hole count performance in nanoprobe mode has been observed for several types of Philips AEMs (EM400, CM12, and CM30) along with slightly higher probe currents for constant aperture size and first condenser lens settings. A Hitachi HF2000 FEG AEM gave similar results (HC = 0.037, SE = 0.06) when only the 100 µm C1 beam-defining aperture was used. The hole count spectrum (Mo L/K = 0.22, Mo Kα P/B = 34) was similar to that produced by the incidence of high energy electrons on the molybdenum grid bars (Mo L/K = 0.16, Mo Kα P/B = 52). However, significant improvement in the hole count performance (HC = 0.003) was achieved when the so-called "hard X-ray" aperture (a non-beam-defining aperture between the second condenser and objective lenses) was inserted. The hole count rate under this condition was too low to collect a statistically significant spectrum in order to judge its origin. Only the largest diameter "hard X-ray" aperture reduced the hole count; two smaller apertures were beam-defining and resulted in high hole counts.

The originally proposed test specimen was a thin chromium film over a solid molybdenum washer.[4] However, because the chromium film tended to tear when placed on the washer, the film was first supported by a molybdenum grid, which was then attached to the washer.[2] During use of the modified test specimen, it was found that the values of HC and SE varied when measured in different grid holes. The values increased as the distance to the washer decreased. Reproducible values and comparative studies could be achieved, when the same grid hole was used. A second test specimen studied was a chromium film on a molybdenum grid, without a washer. Similar trends with specimen tilting and analysis mode were measured with this simpler test specimen on a Philips EM400T/FEG. When the measured values (HC = 0.014, SE = 0.017) were corrected for the difference in chromium film thickness (2.2×), the corrected values (HC = 0.032, SE = 0.037) are very close to those measured for the Cr/Mo grid/Mo washer test specimen and quoted above. Measurements on other AEMs are planned.[5]

1. P. Angelini and J. Bentley, Proc. Ann. EMSA Meeting 42 (1984) 582.
2. E.A. Kenik and J. Bentley, Microbeam Analysis - 1990, eds. J.R. Michael and P. Ingrams, San Francisco: San Francisco Press (1990):289.
3. J. Bentley et al., SEM/1979 II, AMF O'Hare: SEM Inc.(1979):581
4. N.J. Zaluzec, Microbeam Analysis - 1990, eds. J.R. Michael and P. Ingrams, San Francisco: San Francisco Press (1990):330.
5. Research sponsored by the Division of Materials Sciences and the Assistant Secretary for Conservation and Renewable Energy, High Temperature Materials Laboratory User Program, U.S. Department of Energy under contract DE-AC05-84OR21400 with Martin Marietta Energy Systems, Inc.
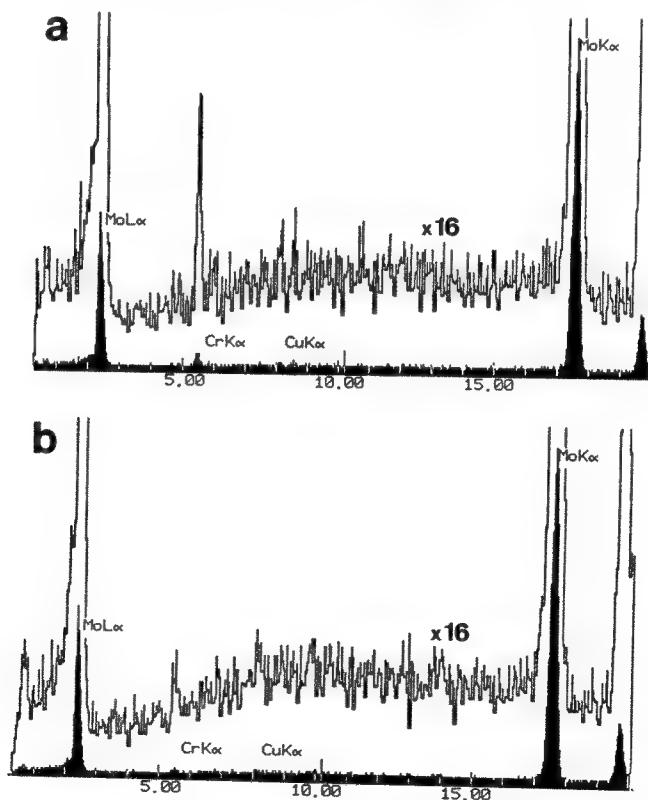
FIG. 1.--a) EDXS hole count spectrum (1200 s acquisition) and b) EDXS spectrum for direct excitation of molybdenum grid bar by 120 keV electrons at 400-fold lower probe current (100 s acquisition); Philips CM12, microprobe, 20° specimen tilt.

DETECTION LIMITS FOR ANALYTICAL ELECTRON MICROSCOPY WITH ELECTRON ENERGY LOSS SPECTROMETRY AND ENERGY-DISPERSIVE X-RAY SPECTROMETRY

Dale E. Newbury[1] and Richard D. Leapman[2]

[1]National Institute of Standards and Technology, Gaithersburg, MD 20899
[2]National Institutes of Health, Bethesda, MD 20892

The measurement of trace level constituents, arbitrarily defined for this study as concentration levels below 1 atom percent, has always been considered problematic for analytical electron microscopy (AEM) with energy dispersive x-ray spectrometry (EDS) and electron energy loss spectrometry (EELS). In a landmark study of various microanalysis techniques, Wittry evaluated the influence of various instrumental factors (source brightness, detection efficiency, accumulation time) and physical factors (cross section, peak-to-background) upon detection limits.[1] Although the ionization cross section, fluorescence yield, and collection efficiency favor EELS over EDS, the peak-to-background ratio of EELS spectra is much lower than that of EDS spectra, leading Wittry to suggest that the limit of detection should be 0.1 percent for EDS and 1 percent for EELS for practical measurement conditions. Recent developments in parallel detection EELS (PEELS) indicate that a re-evaluation of the situation for trace constituent determination is needed for those elements characterized by "white line" resonance structures at the ionization edge.[2,3] Leapman and Newbury have shown that numerous trace constituents (alkaline earth elements, transition metals, rare earth elements) below 100 parts per million (ppm) atomic can be detected by PEELS.[3] Leapman and Hunt have compared the limits of detection for PEELS and EDS on a theoretical basis and have made experimental measurements on high concentration systems.[4] In this work, comparison PEELS and EDS measurements have been made on dilute multi-component systems with minor (1-10%) and trace constituents (< 1%).

Two techniques were employed in combination to optimize trace sensitivity by PEELS: (1) The detective quantum efficiency (DQE) was maximized by increasing the beam current and adjusting the spectrum accumulation time so that the count rate reaches detector saturation for energy losses just below the range of interest. The saturated portion of the spectrum was then physically shifted off the detector array. For this work, a dedicated field emission gun scanning transmission electron microscope (FEG-STEM) was operated with beam currents in the range 5 - 15 nA, and a PEELS system equipped with a 1024 channel scintillator/photodiode detector was used with counting cycles of 0.1-2 seconds and spectrum accumulation times of 100 - 300 seconds. (2) PEELS spectra were collected under "second difference" conditions with an energy shift of ±6 eV to eliminate channel-to-channel gain variations and to extract "white line" features from the high spectral background. EDS spectra were collected for 500 s with the beam current and sample thickness selected to produce a deadtime of 30 - 40%. Samples tested included various trace element glasses produced as Standard Reference Materials, Research Materials, and candidate standards by NIST.[5] These materials were dry ground to form sub-micrometer sized particles and dispersed onto thin carbon films carried on copper grids. Table 1 shows a comparison of the elements detected in NIST glass 546 by EDS and PEELS where each technique was operated under optimized conditions. The EDS and PEELS results are highly complementary. All elements at 400 ppm atomic and above were readily detectable, and only trace Th and U at a level of ~ 100 ppm atomic were undetected by either technique. For the three serious peak interference situations found in the EDS analyses (B K and C K; P K and Zr L; Ti K and Ba L) the PEELS spectrum provides a particular advantage in spectral separation. The energy separation of the edges and the resolution of the PEELS spectrometer are sufficient for separating B K and C K, while alternative detection strategies can be used in other cases (e. g., Ti L and Ba M instead of Ti K and Ba L). Generally, detection is favored for PEELS for those elements with sharp white line features, such as Ba and Eu, whereas EDS is favored for elements with broad edge features, such has Ge. An example of the high PEELS sensitivity for Eu is illustrated in Figure 1, where the Eu M-edges are detected. Quantitative measurements of the peak-to-background in these spectra will permit comparison to theoretical calculations of the limit of detection.

References
1. Wittry, D. B., 9th Intl Conf. X-ray Optics and Microanalysis (European Congress on Electron Microscopy Foundation, Leiden), 3 (1980) 14.
2. Krivanek, O. L. and Kundmann, M. K., 49th Conf. Electron Microscopy Society America, ed., G. W. Bailey, San Francisco Press (1991) 724.
3. Leapman, R. D. and Newbury, D. E., 50th Conf. Electron Microscopy Society America, eds., G. W. Bailey, J. Bentley, and J. A. Small, San Francisco Press, (1992) 1250.
4. Leapman, R. D. and Hunt, J. A., Microscopy, Microanalysis, and Microstructures, 2 (1991) 231.
5. Catalog of Standard Reference Materials, National Institute of Standards and Technology, Gaithersburg, MD (1992-93).

Table 1 Detection of Constituents of NIST Glass K 546
(ND = not detected; interferences listed in parentheses)

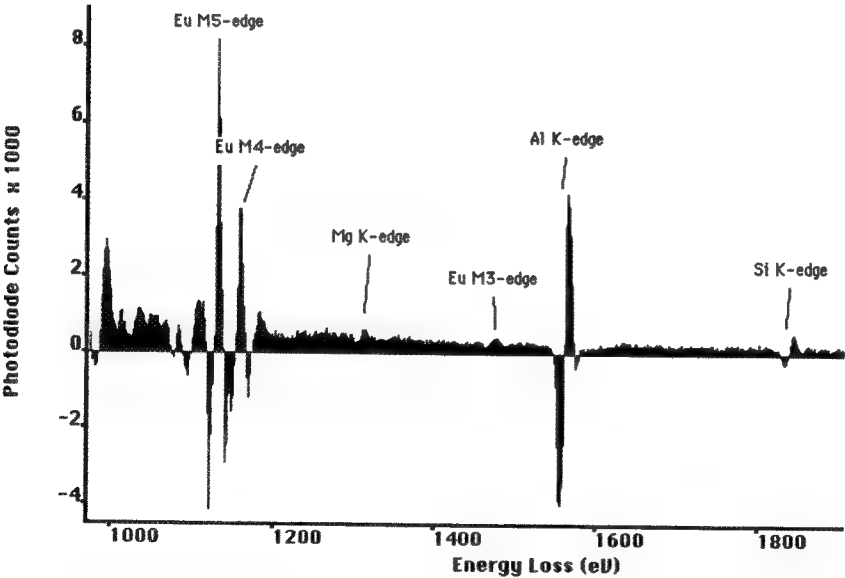| Element	Wt%	At%	EDS	PEELS
Li	2.16	4.73	ND	K
B	21.7	30.5	ND (C)	K
Mg	0.169	0.106	ND	K
Al	9.86	5.56	K	K
P	0.432	0.212	K (ZR L)	K
Ti	0.336	0.107	K (Ba L)	L
Cr	0.144	0.042	K	L
Ni	0.409	0.106	K	L
Ge	0.507	0.106	K	ND
Zr	0.637	0.106	K	L
Ba	0.958	0.106	L (Ti K)	M
Eu	1.06	0.106	L	M
Th	0.158	0.0104	ND	ND
U	0.204	0.0130	ND	ND

Figure 1 Portion of the PEELS spectrum showing detection of Eu, Mg, Al, and Si (contaminant).

REAL-SPACE DIFFERENCE SPECTROSCOPY AT INTERFACES

J. Bruley, H. Müllejans

Max-Planck-Institut für Metallforschung, 7000 Stuttgart 1, Germany

Parallel acquisition of spatially resolved electron energy-loss spectra (SREELS) enables the characterization of interfaces on a nanometer scale using the fairly weak but chemically specific core-absorption edges. A major hurdle for the routine qualitative and quantitative analysis is the very low signal-to-background ratio (and consequently low signal-to-noise ratio, SNR) of the absorption edge of a dilute element. In situations where the background is only slowly varying with energy, the weak edge may be exposed from the intense background either by empirically fitting a power-law curve prior to the edge and extrapolating, or by acquiring the spectrum in the 1st or 2nd energy difference modes (In the limit of small energy shifts such difference spectra are equivalent to derivatives with respect to energy loss). However, these techniques are unsuitable when: the background is strongly energy dependant, such as when the weak edge overlaps severely with the ELNES or EXELFS of a preceding edge; the region of interest is radiation sensitive; or there is specimen drift. For these cases the well established *"real-space" or spatial difference spectrum* provides clear advantages. The spatial difference spectrum is generated by evaluating the difference between two spectra. The first spectrum is recorded with the beam located on a region of interest such as an interface, defect or precipitate and a second reference spectrum is recorded in the neighboring matrix. The background in the first spectrum which is mostly due to the matrix can be matched almost perfectly by the second and removed. Equivalent counting statistics and reduced contamination is achieved with the region of interest being exposed to only half the irradiation dose necessary for the energy difference modes. Any slight change can be compensated for by normalization of the reference spectrum. In principle the reference can be recorded in several different locations and for longer times thus further reducing effects of damage, contamination and improving counting statistics. The real benefit of spatial difference is the ability to remove intense energy-dependant backgrounds which would otherwise obscure the interface sensitive component. In this report we compare the spatial difference mode directly with the more popular energy difference modes. As a model system, the detection of nitrogen in diamond has been chosen. The N-K edge at 400 eV lies on the EXELFS of the C-K.

Figure 1 compares 3 spectra recorded from a diamond specimen containing voidite defects. Such defects are about 2nm in dimension and are known to contain a high pressure phase of molecular nitrogen. The N-K edge is characterized by a 1.3eV fwhm white line at its threshold. This sharp feature is visible in the absorption spectrum (fig 1a). The spatial- (fig 1b) and 2nd- difference (fig 1c) spectra both expose the nitrogen signal with a significantly increased signal-to-background. The absorption data were recorded with one 30s readout with about 10k photodiode counts per channel. The 2nd difference spectra were recorded with three 20s readouts, so the total acquisition time was 60 seconds for both difference spectra. The energy displacement for the 2nd difference was 1.5 eV, chosen to match the width of the N edge at threshold. The SNR determines the detection sensitivity and accuracy in quantification. The experimentally determined SNR's for the two modes for different windows of integration are given in table 1. At 4 eV integration, the 2nd difference is slightly better, however over wide integration windows the spatial difference has the higher SNR. The improvement is due to the saw-tooth-like continuum absorption, which contributes intensity to the spatial difference spectrum but not to the 2nd difference.

A simple model has been used to numerically compare the different procedures. The N-edge was modelled by a Gaussian peak (1.2 eV fwhm), to match the white-line feature, and an extended saw-tooth edge, to match the continuum. The optimum displacement for the 2nd difference corresponds to about the full width of the white line feature. For integrations over 40 eV, the model clearly demonstrates the advantage of the spatial difference spectrum.

Platelet defects in diamond contain about 1/10 monolayer of nitrogen on a cube plane. The defect was oriented "edge-on". In this case, the N has no white line and so the spatial difference mode is evidently the better choice for optimum detection sensitivity, figure 3. The EXELFS structure of the diamond is dominant in the 2nd difference mode, obscuring the very weak signal. In the spatial difference spectrum the N-edge is superimposed on a smooth background making the step threshold at 406 eV visible.

596

Finally there are two further important advantages of spatial difference. The first relates to the ease of quantification, using standard cross-sections. The second, and in our opinion probably the most important, reason for performing spatial difference spectroscopy is the ability to reveal interface sensitive ELNES, containing elementally specific information concerning structure and bonding. Often information concerning changes in bonding and composition are of critical importance to the materials scientist. The automation of spatial difference could be easily achieved by computer control of the spectrometer and electron microscope and is a simple extension to the concept of spectrum imaging.
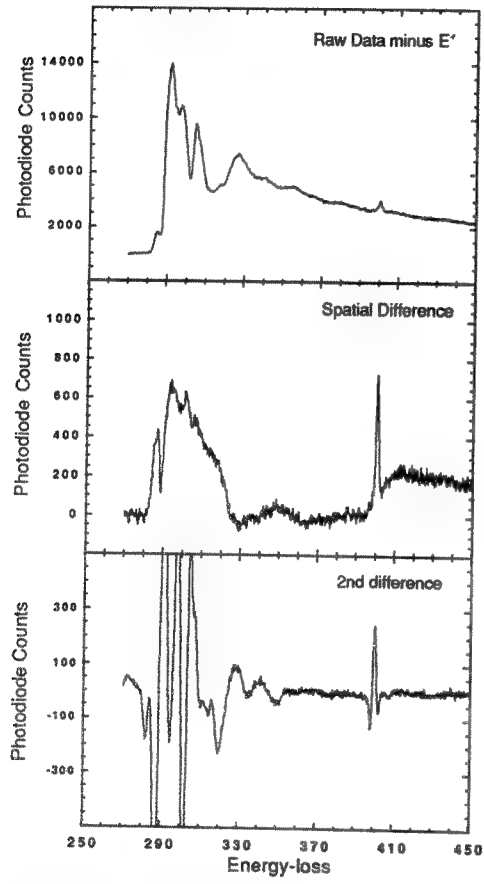
Figure 1. (a) Absorption spectrum of solid N_2 in diamond matrix (b) Spatial difference and (c) 2nd difference.

Figure 2. SNR as a function of energy displacement for 4 and 40 eV integration windows.

	SNR	
	$\Delta=4$ eV	$\Delta=40$ eV
Spatial Difference	44	82
2nd Difference	67	67

Table 1: Experimental SNR values for voidite spectra.
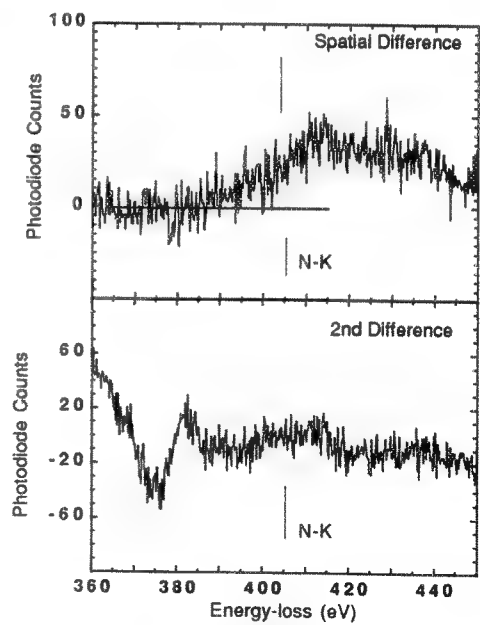
Figure 3. Comparison of spatial difference with 2nd difference for a weak saw tooth edge structure.

597

NANO-PROBE MICROANALYSIS OF GRAIN BOUNDARY CHEMISTRY IN $YBa_2Cu_4O_8$ AND ITS RELATIONSHIP TO WEAK-LINK BEHAVIOR

Z.L. Wang[1,5], J. Brynestad[2], D.M. Kroeger[1], Y.R. Sun[3], J.R. Thompson[3,4] and R.K. Williams[1]

[1] Metals and Ceramics Division / [2] Chemistry Division / [4] Solid State Division, Oak Ridge National Laboratory, P.O. Box 2008, Oak Ridge, TN 37831; [3] and Department of Physics / [5] and Department of Materials Science and Engineering, The University of Tennessee, Knoxville, TN 37996

Weak-link behavior in high temperature superconductors limits bulk applications of polycrystalline high T_c compounds. Possible sources of the effect include grain boundary (GB) disorder, microcracks and nonstoichiometric material at grain boundaries. Recently, electron energy-loss spectroscopy (EELS) studies of $YBa_2Cu_3O_{7-x}$ (Y123) have shown that grain boundary oxygen deficiency is correlated with the crystallographic misorientations of between the Y123 grains.[1] Studies of grain boundary chemistry in $YBa_2Cu_4O_8$ (Y124) by nano-probe energy dispersive X-ray spectroscopy (EDS) and EELS are reported in this paper. Transmission electron microscopy (TEM) studies were performed at 100 kV in a Philips EM400 TEM/STEM equipped with a field emission gun (FEG), which generates an electron probe smaller than 2 nm in diameter. The cation composition was determined by EDS and the O:Ba composition was determined using EELS. Kikuchi patterns were recorded from both sides of the grain boundaries to determine the misorientation of the two adjacent grains.

The observation of a pre-edge peak (Fig. 1) near the oxygen K ionization edge (O K) is related to the hole states produced by the O 2p state and Cu 3d states. The relative variation in intensity of the pre-edge peak indicates the change of hole concentration. In Y124 the pre-edge peak was observed for almost every grain and EDS did not show any significant cation compositional variation ($< 2\%$) between the grain boundary and the bulk. The grain boundaries are classified into three types: fully oxygenated (FO) boundaries, hole-deficient (HD) but not oxygen deficient boundaries, and oxygen deficient (OD) boundaries. Oxygen deficient boundaries are always hole deficient, but not vise versa. Fig. 2a shows the variation of O:Ba on GB and in the bulk for 26 pairs of grains. The first 22 boundaries are fully oxygenated and there is no hole deficiency. Boundaries #23-25 are also fully oxygenated but are hole deficient. Boundary #26, the only boundary which showed both oxygen deficiency and hole deficiency, was the interface between two different phases. The EDS analyses showed that cation compositions are the same within 3% for the adjacent grains forming boundaries #1 - 25.

To determine if there is any correlation between hole deficiency and grain boundary crystallography, the misorientation angle (or the rotation angle) was determined for each grain boundary, and the results are plotted in Fig. 2b. There is no obvious correlation between boundary misorientation angle, such as large or small, with oxygen concentration in Y124.

dc magnetization studies of the same Y124 material showed that the boundaries form weak links between the crystallites.[2] The data demonstrate that apparently stoichiometric grain boundaries can also form weak links between superconducting grains. Thus the weak-link behavior is probably an intrinsic phenomenon associated with high angle boundaries. Hole states (or the pre-edge peaks) were detected in Y124 at virtually every point analyzed, including the grain boundaries. This is different from Y123 in which only about 40-60% of the grain boundaries showed the pre-edge peak. Since the boundaries in polycrystalline Y124 are not very good at transmitting supercurrent, the connection between a lack of hole states at the boundary and weak-link behavior seems doubtful. It is also possible that a different mechanism may be responsible for the creation of the observed pre-edge peak at the O K edge in Y124 than in Y123.[3]

References:
1. Y. Zhu, Z. L. Wang and M. Suenaga, Phil. Mag. A, in press, 1993.
2. Z.L. Wang, J. Brynestad, D.M. Kroeger, Y.R. Sun, J.R. Thompson and R.K. Williams, submitted to Phys. Rev. B (1993).
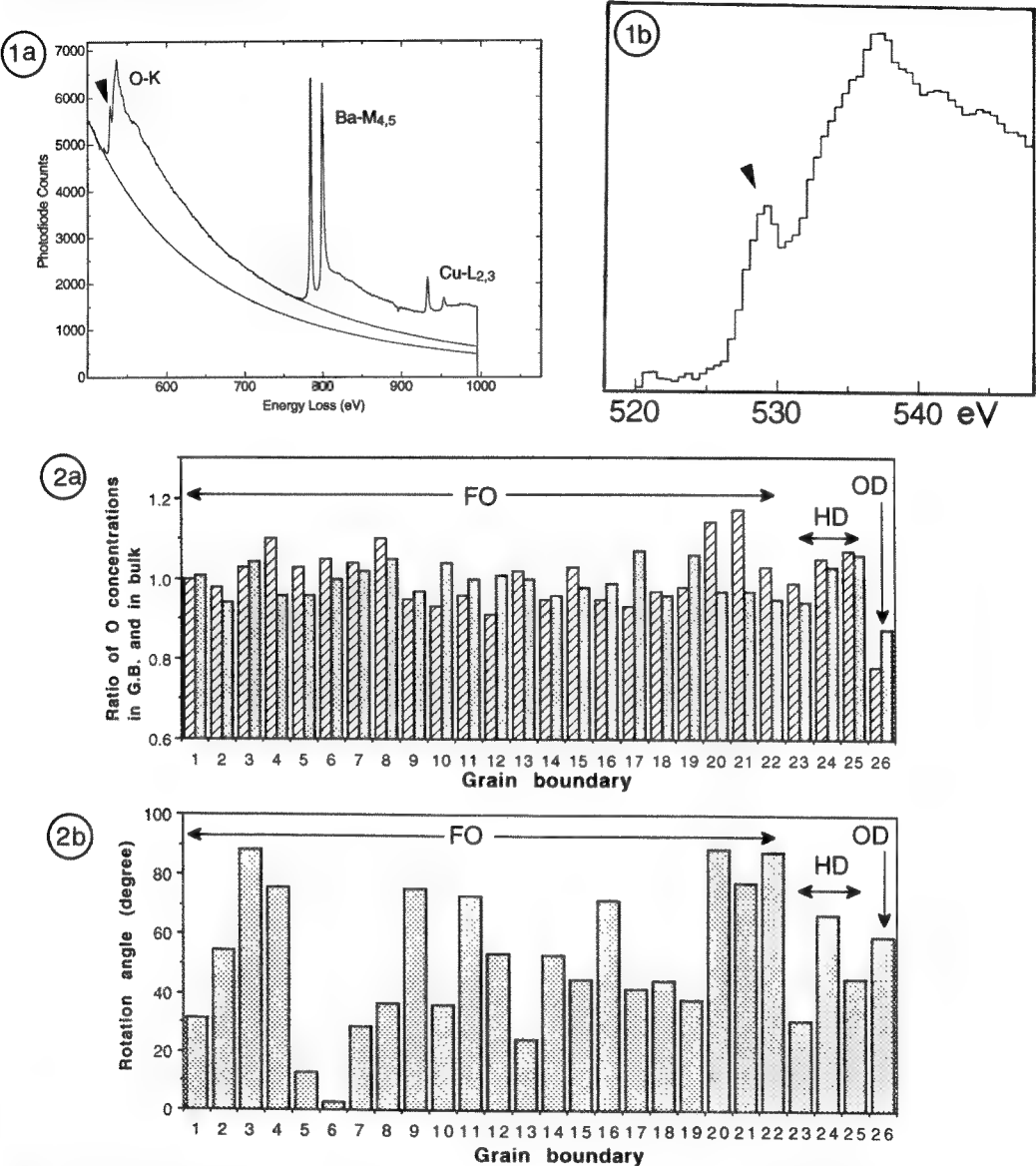
FIG. 1-- (a) EELS spectrum acquired from Y124 grain showing O K, Ba M$_{4,5}$ and Cu L$_{2,3}$ edges. The pre-edge peak is indicated by an arrowhead. (b) Pre-edge peak after subtraction of background.

FIG. 2-- (a) Ratios of oxygen concentrations on grain boundary and in bulk for adjacent grains of total 26 boundaries that have been examined by EELS and EDS, showing presence of fully oxygenated (FO), hole deficient (HD) and oxygen deficient (OD) boundaries. (b) is a plot of the misorientation angles for the corresponding boundaries shown in (a).

599

MICROANALYSIS OF BOUNDARIES BY AEM AT DIFFERENT VOLTAGES

Anthony J. Garratt-Reed

Center for Materials Science and Engineering, Massachusetts Institute of Technology, Cambridge, Ma. 02139, U. S. A.

It is well known that theory predicts a number of benefits for high-resolution analytical electron microscopy (AEM) in raising the electron energy. These benefits arise from three principal effects, namely, an anticipated linear decrease in the beam broadening in the foil with increasing energy, and an increase in the electron gun brightness with increasing energy, and an increase in the X-ray peak-to-background ratio as the electron energy is raised. In addition, the decrease in the electron wavelength with increasing energy can also lead to improvement in the image resolution, although generally not in the microanalytical resolution. To set off against these benefits is the disadvantage that the ionization cross-section decreases with increasing beam voltage. However, although for the case of non-relativistic electrons this can be a significant effect, in most cases, for relativistic electrons (those used for intermediate-voltage AEM, for example) this decrease is not severe. For example, fig. 1 plots the ionization cross-section for iron for electrons in the range 20-500kV, according to the relativistic equation of Chapman et. al.[1] A further area of interest is the effect of radiation damage in the sample, which may increase or decrease at higher voltages.

Garratt-Reed has discussed the analysis of boundaries by AEM, including the anticipated advantages of using intermediate voltages.[2,3] Verification of these advantages has not been possible until the advent of intermediate-voltage microscopes equipped with field-emission electron guns. Such an instrument, a VG Microscopes HB603, with a maximum operating voltage of 250kV, has recently been installed at the author's lab. It has been reported earlier that the anticipated improvement in X-ray peak-to-background ratio is achieved.[4] Evaluation of the instrument is continuing, but early experiments have involved the analysis of segregation on oxide grain boundaries.

In one series of experiments a sample of alumina scale, grown on an Fe-Cr-Al alloy doped with Zr, was analysed first in the HB603 at 200kV. The sample was then placed in an HB5 microscope, and the same areas were found and analysed at 100kV. Of interest was the Zr segregation. Figs 2 shows an expanded view of the region of the X-ray spectrum around the Zr K line, from analyses in the two microscopes of one particular point on a grain boundary. The areas of the Al lines have been normalised for the purposes of making these illustrations (the X-ray detector on the HB603 has significantly better resolution than that on the HB5, so simply matching the peaks heights is inappropriate). It can be seen that the Zr signal is far higher in the case of the 200kV spectrum. Specifically, the apparent Zr concentration is 0.86 wt% in the 200kV spectrum, and is 0.45 wt% in the 100kV spectrum. Significantly, while the HB5 is well characterized, and was operated in optimum conditions, the HB603 is not yet fully characterized, and may well not have been at an optimum microanalysis condition; it is not, therefore, yet appropriate to compare these results with theory. Interestingly, while no radiation damage was perceptible after the analysis at 200kV (which was performed first), there was significant visible damage present after the subsequent analysis at 100kV.

Judging from this initial work, it would appear that the benefits of increased voltage for microanalysis of boundaries are indeed real and achievable.[5]

600

References

1. J. Chapman et. al., *J. Microsc*, **136**, 179, 1984
2. A. J. Garratt-Reed, *SEM/85/I*, 21, 1985
3. A. J. Garratt-Reed, MRS symposium proceedings, **62**, 115, 1986
4. A. J. Garratt-Reed and S. von Harrach, Proc. 49th. Ann Mtg. EMSA, 348, 1991
5. Funding for this work was provided by the NSF under block grant number DMR90-22933
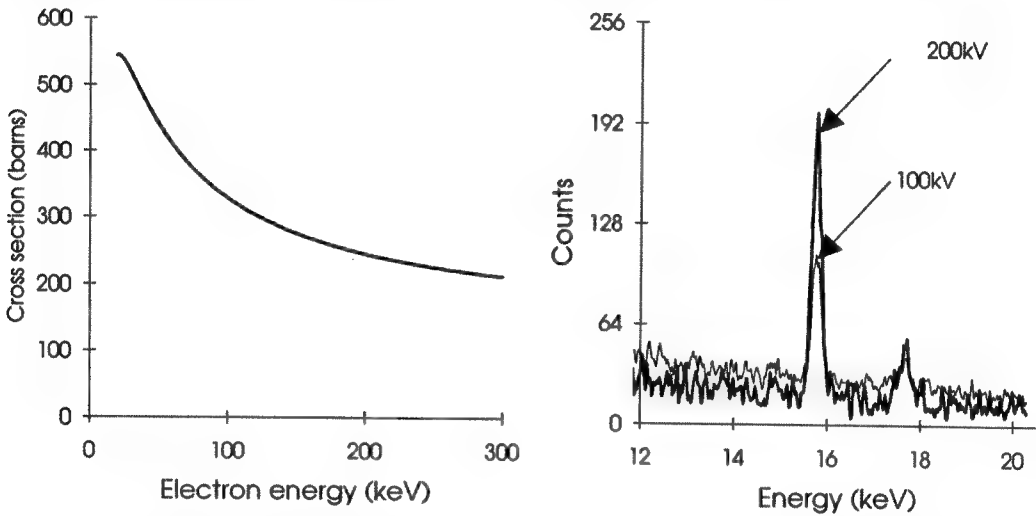
Fig 1: (Left, above) Plot of the ionization cross-section for iron as a function of electron energy in the range 20-300keV, according to the relativistic equation of Chapman et. al.[1] Fig 2: (Right, above) Plot of X-ray counts as a function of energy in the region of the zirconium K-line, for 100kV excitation (light line) and 200kV excitation (bold line), obtained from the same grain boundary in alumina scale formed on a Fe-Cr-Al alloy with Zr addition. The area of the aluminum peak in each spectrum was normalized for this plot.

CHARACTERIZATION OF ULTRAFINE COPPER OXIDE AEROSOLS FOR ANIMAL EXPOSURE STUDIES

John J. Godleski, G.G. Krishna Murthy, William Skornick, Victoria Hatch, Rebecca Stearns, and Marshall Katler

Respiratory Biology Program, Harvard School of Public Health, 665 Huntington Avenue, Boston, MA 02115

People are exposed to complex mixtures of air pollutants in the urban environment. The inhalation of acid-coated metal oxide fine particles is a well-recognized health effects problem, but the mechanisms of toxicity remain undefined. Ultrafine particles (<100 nm in diameter) are difficult to detect by conventional air sampling methodology. In order to characterize such particles, electron microscopy techniques are needed. In this abstract, we outline techniques to produce, characterize, and expose animals to ultrafine (1-30 nm) copper oxide aerosols.

The ultrafine copper oxide aerosols were generated using a high temperature tube furnace with molybdenum windings (0.93 m long), capable of operating at 1923° K. The temperature at the center of the furnace was maintained at 1709° K during the experiments. Copper metal shot of 99.99+ purity (Aldrich Chemical Co. Inc.) and 2-8 mm in size was used as the copper source. An alumina boat (30 x 8 x 3 mm) containing 2 g copper was placed at 0.187 m from the center of the furnace where the measured temperature was 1683° K. The copper vapors from the boat were carried by a pure argon stream and were oxidized by added oxygen. To determine the size distribution and concentration of the particles, copper oxide aerosols were passed through an electrostatic aerosol sampler (Model 3100, TSI Inc.) to collect the particles on carbon/formvar coated nickel grids (400 mesh). Airborne concentrations were confirmed by mass determination using teflon filters. Hamsters were exposed for 60 min to the ultrafine copper oxide aerosols. The animals were killed immediately after exposure. The lungs were fixed *in situ* by vascular perfusion with 2.5% glutaraldehyde, 1% osmium, and 0.5% uranyl acetate, embedded in araldite, and sectioned at 60 nm. Both the particle containing grids and the sections of the lung were studied with the Zeiss CEM902 energy filtering microscope using its electron energy loss spectroscopy (EELS), electron spectroscopic imaging (ESI), and image analysis capabilities.

The particles were characterized by sampling at random locations on a grid (at least 15 microscope field areas). Figure 1 shows a typical plot of particle size distribution sampling 10.017 μm^2 (total 18 field areas at 50,000 magnification). The size of the copper oxide aerosols ranged from 3-25 nm. The cumulative mean aerodynamic diameter determined from Figure 1 was 11.6 nm with a geometric standard deviation (σ g) of 1.56. The determined concentration of the ultrafine particles in the gas stream using the mean particle population obtained in a microscope field was 282.13 x 10^6 particles/cc. The particle concentration obtained from the mass determination was 302.69 x 10^6 particles/cc. The ultrafine copper oxide particles were nearly spherical as shown in Figure 2 which is a micrograph of particles collected on the grid. Figure 3 shows these particles in the airspace of the lung. Figure 4 is a typical EELS spectrum obtained from these ultrafine particles. The high concentrations of these ultrafine particles make their study by ESI and EELS a practical approach to establish their identity and determine their interactions with lung cells.

Fig. 1--Cumulative size distribution of copper oxide aerosol particles.
Fig. 2--Micrograph of copper oxide aerosol particles.
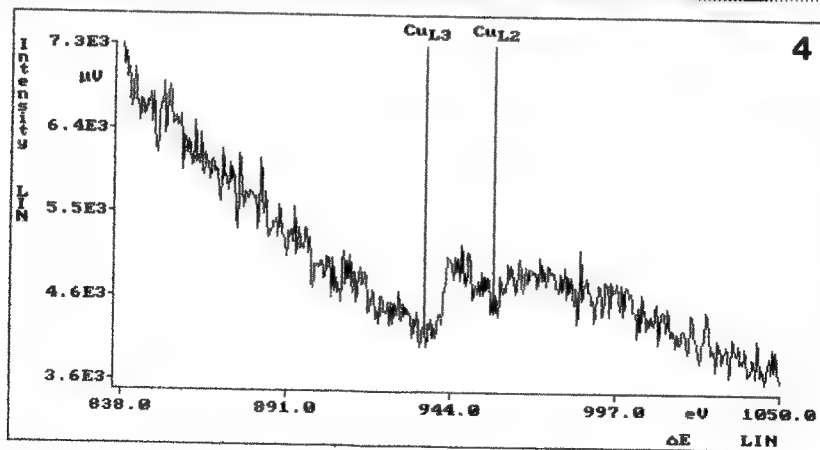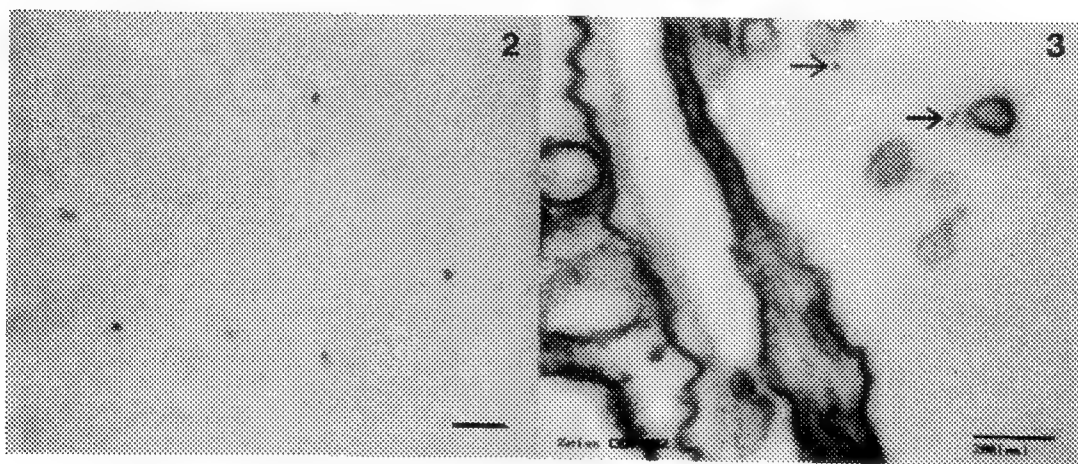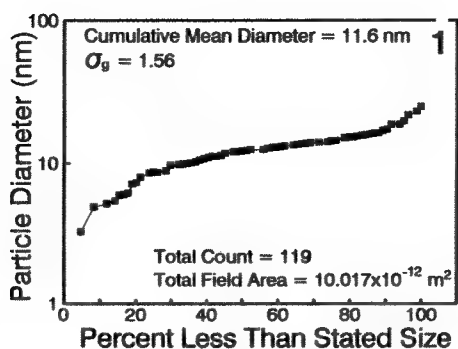Fig. 3--Identification of ultrafine copper oxide particles in the pulmonary airspace (arrows).
Fig. 4--EELS of an ultrafine copper oxide particle.

COMPOSITIONAL MAPPING OF BIOLOGICAL MATERIAL WITH THE SCANNING ION MICROPROBE

Riccardo Levi-Setti*, Jan M. Chabala*, and Sarah Smolik**

* Enrico Fermi Institute and Department of Physics, University of Chicago, Chicago, IL 60637
**Vollum Institute, Oregon Health Sciences University, Portland, OR 97201

The use of ion probes for microscopy and imaging microanalysis by secondary ion mass spectrometry (SIMS) is a destructive observational technique that can provide information inaccessible to the electron microscope. The damage to the sample caused by the ion-induced sputter erosion of its surface layers is exploited to identify and map the chemical and isotopic composition of the removed layers. Particularly good image resolution (20–70 nm) can be attained with heavy-ion focused probes, as with the University of Chicago 40 keV Ga^+ Scanning Ion Microprobe (UC SIM). The application of this instrument to biological research involving mineralized and soft tissue has been evaluated on several occasions, together with the requirements of specimen preparation for SIMS analysis.[1] In a review recently presented, [2] studies of mineralized tissues (bone, teeth) were discussed. We concentrate here on recent directions of our SIMS studies of soft biological material.

The sensitivity of SIMS to isotopes of any mass paves the way for the profitable use of tagged, tracer molecules in a host of biological applications as a preferable alternative to the use of radioisotopes and autoradiography.[4] This powerful technique, which can be applied to physiological studies of both mineralized and soft tissue, is particularly advantageous in cytogenetics in conjunction with the labeling of DNA by tagged nucleosides such as ^{14}C–thymidine or the nucleoside-analog bromodeoxyuridine (BrDU). The detection and mapping of these tracers in human chromosomes with the UC SIM has been previously reported.[3] It has been shown that the irreversible structural binding of the labels to the complex molecule of interest, DNA, bypasses the need for the exacting specimen preparation commonly followed for the microanalysis of soft tissue, and that standard techniques for optical microscope observations are adequate for SIMS analysis. Highlights of these experiments include the discovery of banding patterns in the distribution of the labels along the chromatids (SIMS bands), apparently mimicking the corresponding trypsin–Giemsa (G–bands) and fluorescent quinacrine mustard staining (Q–bands), and the detection of sister chromatid exchange activated by BrDU. The direct mapping of the distribution of a particular nucleoside in chromosomes is of value also in the interpretation of the origin of the banding patterns obtained by conventional staining methods. It was determined that our apparatus detects one out of about 12,000 BrDU molecules present in the chromosomes, and about one out of 70,000 U–^{14}C–thymidine molecules, revealed via the detection of $^{28}CN^-$.

We have now extended the above approach to the study of polytene chromosomes of *Drosophila melanogaster*, labeled with BrDU. 100 µg/ml BrDU (1:1 with ethanol) was added to the fly's food. Wild type Canton S *Drosophila* were allowed to lay eggs for 3-5 days on labelled food (chronic feed) at 18 °C. Salivary glands were removed from 3d instar, fixed in acetic:lactic:water, 3:1:2, and squashed with cover slips on silicon chips. The sandwiches were left flat at 4 °C for 16 hrs, then frozen in dry ice to remove the cover slip. The specimens were then washed in cooled ethanol and air dried. For SIMS analysis, the samples were then lightly coated with gold. SIMS maps of polytene chromosomes are shown in the accompanying figures, for CN⁻ (Figs. 1a and 2a), and $^{81}Br^-$ (Figs. 2a and 2b). The abundant CN⁻ signal provides good image resolution maps of the distribution of combined DNA and proteins. In contrast to the featureless CN⁻ maps of the highly condensed human chromosomes, the CN⁻ maps of Figs. 1a and 2a show a well defined banding pattern. From the similarity of these density bands with those known from optical microscopy, it is possible to recognize the end portion of the 2L chromosome in Fig. 2a. Submicrometer-wide bands are resolved in this image. The resolution of the corresponding images for the label $^{81}Br^-$ of Figs. 1b and 2b is not as good as for the CN⁻ images, due to the limited signal statistics. However, concentration of BrDU in the heterochromatic regions is evident. It is also apparent that chromosome puffs exhibit a much reduced label intensity, as the puff at midheight of Figs.
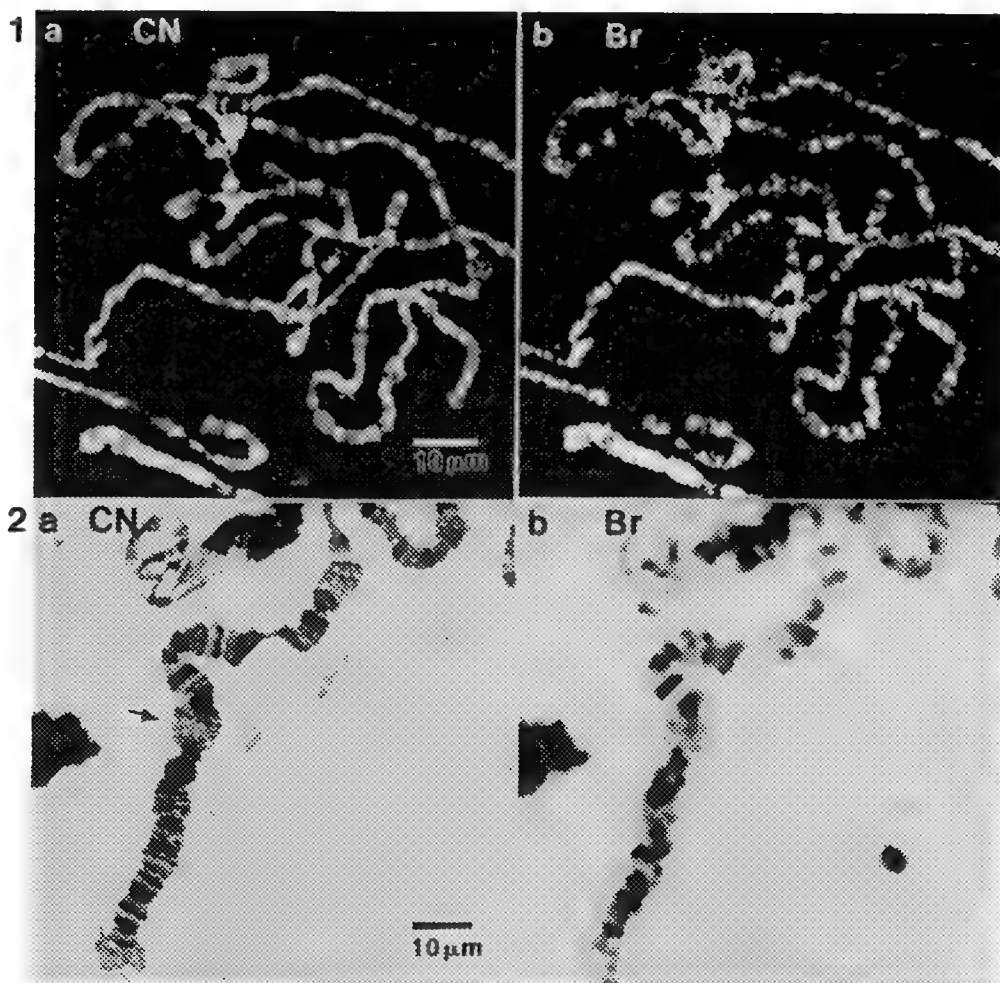
FIG. 1. (a) CN⁻ SIMS map of BrDU–labelled polytene chromosomes of *Drosophila melanogaster*.
(b) ⁸¹Br⁻ map showing the distribution of BrDU in the above chromosome spread.
FIG. 2. (a) CN- SIMS map of the terminal region of polytene chromosome 2L. Inverted contrast.
(b) Corresponding ⁸¹Br⁻ map, showing reduced label concentration in the puff at midheight.

2a (arrow) and 2b clearly indicates. This observation is consistent with the notion that puffs are regions of enhanced RNA transcription where the active chromatin is less condensed than the dense chromatin packing in the heterochromatic bands. [5]

1. J. Chabala and R. Levi-Setti, Analytical Elect. Microscopy–1987, D.C. Joy, ed. San Francisco: San Francisco Press (1987) 203; R. Levi-Setti, Ann. Rev. Biophys. Biophys. Chem. (1988) 17, 325.
2. J. M. Chabala and R. Levi-Setti, Proc. MAS'93, R. Linton, ed. VCH Publishers , in press.
3. R. Levi-Setti and M. Le Beau, Biol. Cell (1992) 74, 51; R. Levi-Setti, et al. SIMS VIII, A. Benninghoven et al. eds. Chicester: Wiley (1992) 669.
4. E. Hindie, et al. Scanning Microscopy (1988) 2, 1821.
5. This report is based on work supported by NSF Grant DIR 9017112.

QUANTITATIVE SINGLE-CELL FLUORESCENCE IMAGING OF INDICATOR DYES

David J. Gross, Mỹ G. Mahoney and Linda L. Slakey

Program in Molecular and Cellular Biology and Department of Biochemistry and Molecular Biology, University of Massachusetts, Amherst, MA 01003

The use of fluorescent molecular probes in combination with quantitative optical microscopy has burgeoned in the past few years due to dramatic advances in both fluorophore design and imaging instrumentation. A number of probes that exhibit fluorescence spectral shifts with ligand binding have been synthesized. Among them is fura-2, which has a high binding affinity for calcium ion and which shows an excitation spectral shift between the calcium-bound and calcium-unbound states. This talk will focus on fura-2-loaded arterial smooth muscle cells (SMC) stimulated to produce temporally and spatially dynamic changes in free cytosolic calcium ion concentration ($[Ca^{2+}]_i$) as measured by a charge-coupled device imaging system.

Intracellular Ca^{2+} is known to play a critical role in the regulation of the contractile state of vascular SMCs[1]. A variety of extracellular agonists have been shown to stimulate transient $[Ca^{2+}]_i$ elevation in vascular SMCs; among them are nucleotides that activate specific cell surface receptors[2]. ATP, which can activate several different receptors, is co-released with neurotransmitters[3] and may reach vascular SMCs at high micromolar concentrations[4]. Extracellular ATP stimulus of SMCs produces a $[Ca^{2+}]_i$ initial transient rise followed by periodic oscillations (Fig. 1). The initial transient appears to be nearly synchronous among individual cells, but the oscillations are asynchronous[5]. Both phases of the $[Ca^{2+}]_i$ response are all-or-none; the initial transient is activated in 50% of the cells at $[ATP] = 0.11 \pm 0.04\ \mu M$ while oscillations are activated at $2.6 \pm 1.4\ \mu M$[6].

$[Ca^{2+}]_i$ oscillations stimulated by nucleotide receptor activation propagate through arterial SMCs as waves and gradients even though the stimulus is applied homogeneously across the cell surface[7]. The gradients propagate relatively uniformly across the cell (Fig. 2), suggesting that the flux of Ca^{2+} ions at the gradient front is relatively constant. $[Ca^{2+}]_i$ oscillations originate from separate loci within an individual cell, suggesting that the mechanism of control of the oscillations is spatially inhomogeneous. Waves and gradients of $[Ca^{2+}]_i$ that originate from separate regions in a cell appear to arise via separate control mechanisms — Fig. 3 demonstrates that both propagating global and non-propagating local $[Ca^{2+}]_i$ gradients exist in single cells and that these gradients do not desensitize each other.

References

1. A.P. Somlyo and B. Himpens, FASEB J. (1989) 3, 2266.
2. J.L. Gordon, Biochem. J. (1986) 233, 309.
3. G. Burnstock and C. Kennedy, Circ. Res. (1986) 58, 319.
4. L.L. Slakey, in Biochemistry of Arachidonic Acid Metabolism, W. Lands, ed., Martinus Nijhoff, Boston (1985), 323.
5. J.J. Linderman, L.J. Harris, L.L. Slakey and D.J. Gross, Cell Calcium (1990) 11, 131.
6. M.G. Mahoney, C.J. Randall, J.J. Linderman, D.J. Gross and L.L. Slakey, Molec. Biol. Cell (1992) 3, 493.
7. M.G. Mahoney, L.L. Slakey, P.K. Hepler and D.J. Gross, J. Cell Sci. (1993) in press.
8. Supported by NSF DCB-9105429 and NIH HL 31854.
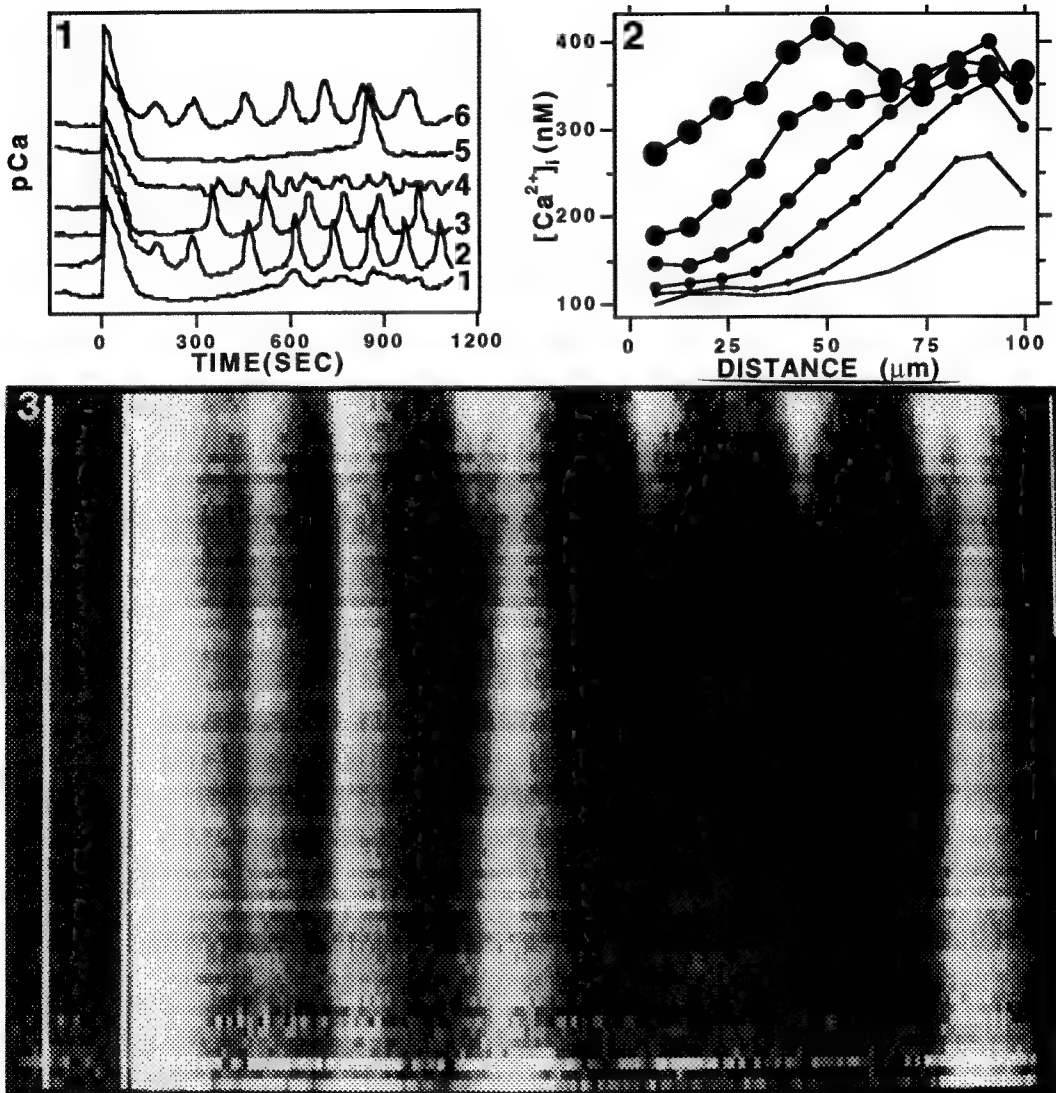
Fig. 1. Six SMCs on one coverslip respond to 50 μM ATP addition to the extracellular medium at t = 0. Each cell responds with an initial [Ca^{2+}]$_i$ rise followed by asynchronous oscillations.

Fig. 2. The [Ca^{2+}]$_i$ gradient in a single SMC during the rising phase of an oscillation/wave. Position in the cell is shown on the abscissa. Each curve shows the gradient in successive images collected at t = 443, 445, 448, 450, 452 and 454 sec after stimulus. Increasing time is indicated by increasingly large ● symbols.

Fig. 3. Independent global and local [Ca^{2+}]$_i$ oscillators in a single SMC are seen in this synthetic position vs. time image. The vertical axis shows position within the cell (bar = 50 μm) along a row of pixels in the cell image while the horizontal axis represents time, increasing from left (0 sec) to right (540 sec). [Ca^{2+}]$_i$ increases with increasing brightness of the image. The vertical white lines at the left indicate buffer wash and 50 μM ATP stimulation, respectively. Note that four global oscillations are produced in the whole cell and six local oscillations are seen at one end (top) of the cell.

SIMULTANEOUS HIGH-RESOLUTION SEM AND STEM OF ORGANIC COMPOUNDS AND BIOLOGICAL MACROMOLECULES

R.P. Apkarian,[*] K.A. Robinson,[1] Y. Yamasaki[2] and F.M. Menger[2]

Yerkes Regional Primate Research Center[*,] Div. of Cardiology[1], Department of Chemistry[2]. Emory University, Atlanta GA 30322

A simple spray mounting preparation of hydrocarbon based macromolecules onto coated grids or Si chips was employed for secondary electron (HRSEM) or in tandem with scanning transmission electron (STEM) imaging. The grid specimens were staged in the lens of a Topcon DS-130 SEM equipped with a Schottky field emission (SFE) source. A 1 nm probe, created at 25 kV, elicited low radiation damage to the molecules on the formvar support. Molecules on grids were stabilized with heavy metal stains and contrast enhanced by a 1 nm fine-grain Cr film. The strategy was to generate sufficient SE-I electrons for above-lens detection simultaneous with the collection of transmitted electrons by the below specimen STEM detector.

The bromine salt of a synthetic amphiphile, N-tetracosanyl-tetraethylenepentaammonium pentabromide was produced as a preliminary micelle solution of [10mM]. After vigorous sonication the solution was diluted to [1mM] with dH_2O, filtered through $0.65\mu m$ polycarbonate membrane, and mixed vol./vol. with 2% uranyl acetate (freshly prepared and filtered through $0.2\mu m$ PC membrane).[1] Very low density lipoproteins (VLDL) were ultracentrifuged from human plasma and fixed by dialysis against cacodylate buffered 1% OsO_4 for 2hrs then exhaustively dialyzed against dH_2O. Suspensions were drawn into capillary tubes and spray mounted onto the Si chips and grids using an EFFA spray mounter (E.F. Fullam, Inc.). Specimens were predegassed prior to loading into a Denton DV-602 turbopumped sputter system. The system was degassed to 8×10^{-8} torr and specimens were sputter coated with a 1 nm continuous fine-grain Cr film at 5×10^{-3} torr. Images were recorded on Polaroid 55 film in a 16 sec. scan either as a SEM/STEM split screen or in tandem.

The morphology of the amphiphile displayed mixed globular and rodlike aggregates seen in both HRSEM and STEM images (Fig. 1). Ten nm particles and larger 30 nm spheres displayed a threaded aggregation. Low voltage (25 kV) STEM at high magnification resolved the attachment of a 10 nm wide rod to a globular aggregate. VLDLs are triglyceride rich (55%) lipoprotein that range 30-80 nm in diameter. Osmium dialyzed and spray-mounted VLDLs displayed 40-50 nm spheres either as individual entities or attached to one another (Fig. 2). SE-I edge brightness contrast delineated their profiles in HRSEM images while high contrast regions suggest thickness variation in STEM images.

Spray mounting hydrocarbons impregnated with heavy metal stains followed by Cr coating provides quick and easy assessment, using an in-lens SFE-SEM equipped with a STEM detector and operated at 25 kV . Simultaneous or tandem recordings of specimens made in 16 sec photo scans at high magnifications provide quality contrasts. Reasonable resolution of these hydrocarbon samples was obtained due to clean Cr

coatings while brief dwell time of the 25 kV scanning probe minimized specimen damage. Digital recordings are being planned to enhance image quality.

References

1. T. Kunitake, et al. Am. Chem. Soc. (1981)103,5401.
2. J.A. Glomset, et al. J. Lipid Res. (1980)21,1116.
3. This research was supported by NIH grant RR-00165 from the National Center for Research Resources to the Yerkes Primate Center.
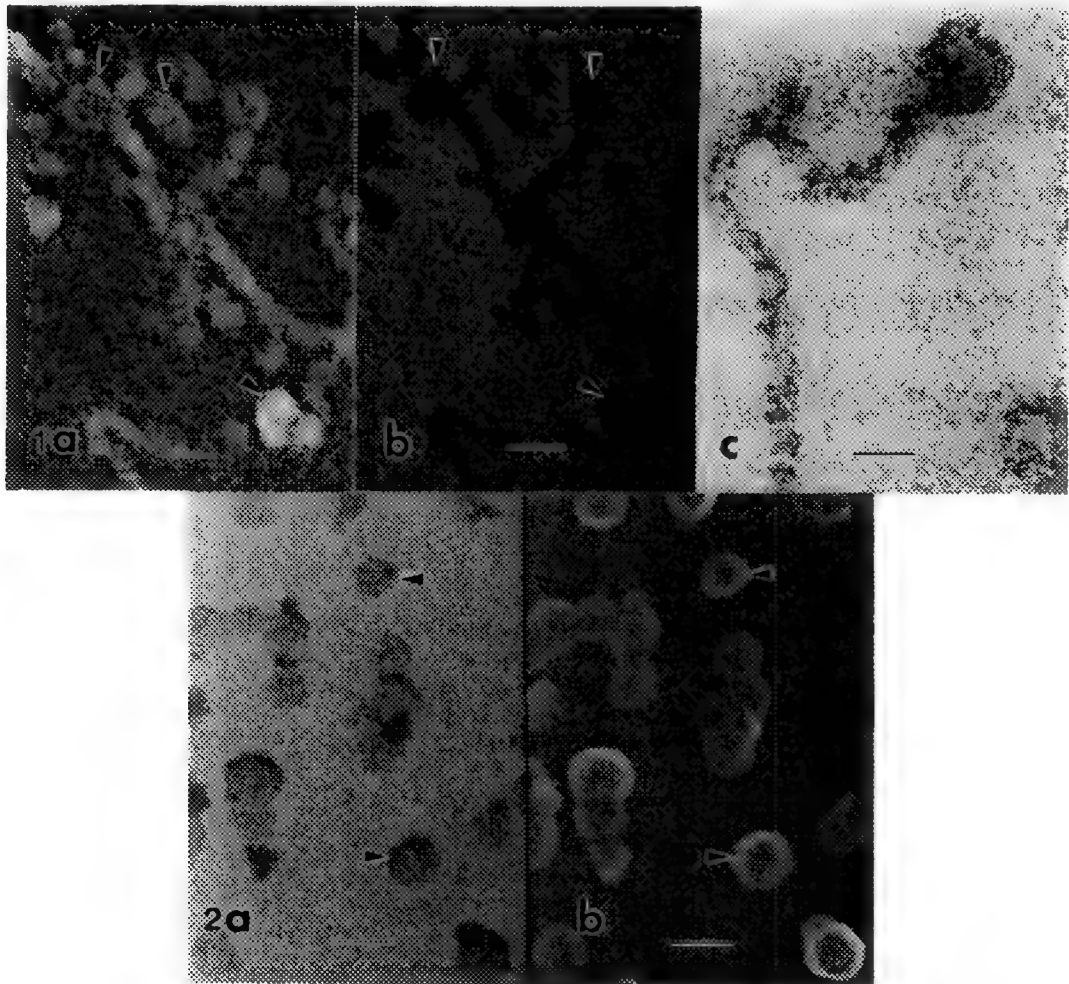
FIG. 1a.--HRSEM of synthetic amphiphile containing globular (arrows) and rod-like profiles. Bar = 50 nm.
FIG. 1b.--STEM of exact area as Fig. 1a. Bar = 50 nm.
FIG. 1c.--Higher-magnification STEM of rod attached to globular profile. Bar = 20 nm.
FIG. 2--(a) STEM (b) HRSEM split screen of VLDLs. Single 50 nm spheres (arrows) seen along with fused spheres. Bar = 50 nm.

HIGH-RESOLUTION SEM AND STEM OF ADRENOCORTICAL ENDOTHELIUM: MOLECULAR RESOLUTION OF MEMBRANE COMPLEXES

Robert P. Apkarian

Integrated SEM & Microanalytical Facility/Yerkes Research Center
Emory University, Atlanta GA 30322

A multitude of complex ultrastructural features are involved in endothelial cell (EC) gating and sorting of lipid through capillaries and into steroidogenic cells of the adrenal cortex. Correlative microscopy is necessary to distinguish the structural identity of features involved in specific cellular pathways.[1] In addition to diaphragmed fenestrae that frequently appear in clusters, other 60-80 nm openings; plasmalemma vesicles (PV), channels and pockets fitted with diaphragms of the same dimension, coexist on the thin EC surface.[2] Non-diaphragmed coated pits (CP) (100-120 nm) involved in receptor mediated endocytosis were also present on the EC membrane. The present study employed HRSEM of cryofractured and chromium coated specimens and low voltage HR-STEM of 80 nm thick LX-112 embedded sections stained with 2.0% uranyl acetate. Both preparations were imaged at 25 kV with a Topcon DS-130 FESEM equipped with in-lens stage and STEM detector.

HRSEM images of the capillary lumen coated with a 1nm continuous fine grain Cr film, provided the ability to scan many openings and resolve (SE-I contrast) the fine structure of diaphragm spokes and central densities (Fig. 1). Surface particles between openings represent ectodomains of the EC lumenal plasmamembrane. Plastic sections were prepared for conventional TEM, then imaged with the STEM detector of the DS-130 FESEM (Fig. 2). The membrane bilayer of interdigitating EC processes were observed along with diaphragmed vesicles and larger nondiaphragmed coated pits. ECs displayed diaphragmed fenestrae which contained a central density and was of the same dimension as those seen with HRSEM in Fig. 1a. STEM images of coated pits (Fig. 2b,d) displayed added relief contrast to the clathrin coat. Conventional TEM (Topcon 002B) of the same sections has provided a comparative image of a coated pit in order to appreciate the unit bilayer and clathrin coat. The DS-130 FESEM provided quality low voltage STEM and in tandem, in-lens SE imaging produced fine particle contrasts of molecular features.

References

1. R.P. Apkarian and N. L'Hernault. Scanning Microsc. 1990 4:125.
2. N. Simionescu and M. Simionescu. Targeted Diag. Ther 1991.5:45.
3. This research was supported by NIH grant RR-00165 from the National Center for Research Resources to Yerkes Primate Center.
4. Thanks to Dr. K.A. Robinson for adrenal perfusion.

FIG. 1-- HRSEM of Cr coated EC lumenal surface. a) Clusters of 60nm (*) and 120nm openings (arrows). b) Diaphragmmed openings with central density (D). a) Bar = 200nm. b) Bar = 50nm.
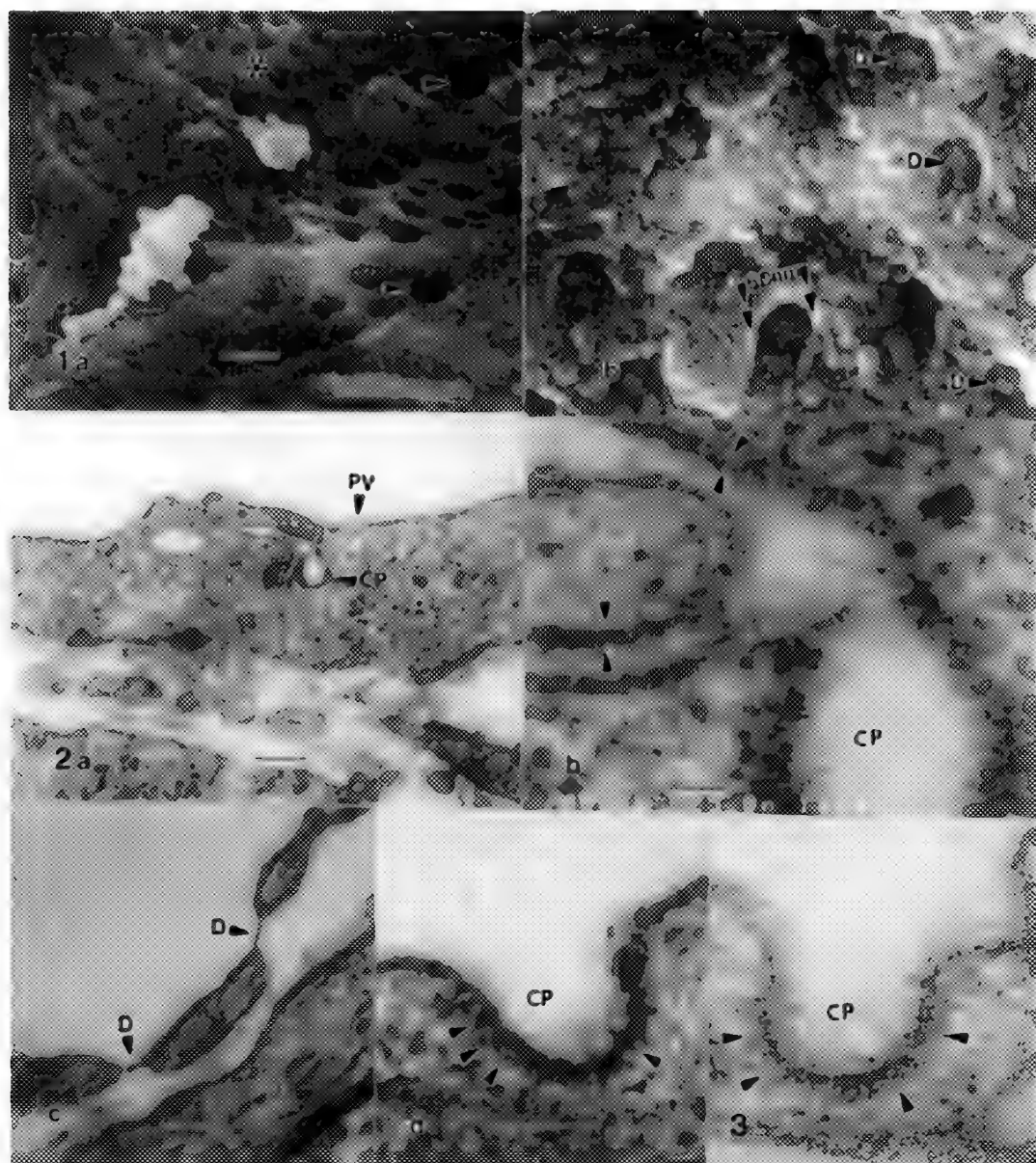
FIG. 2.-- a) HRSTEM of interdigitated EC (*). Note vesicle (PV) and
pit (CP) at base of surface digit. b) Higher magnification reveals
bilayer (arrows) of subsurface digit and CP. c) Thin EC expanse
contained fenestral diaphragm with central density (D). d) STEM
contrasts display clathrin on CP (arrows). a) Bar = 200nm.
b) Bar = 25nm. c-d) Bar = 100nm.
FIG. 3.-- TEM comparison of coated pit. Membrane bilayer is
resolved yet contrast of clathrin coat (arrows) is low. Bar = 100nm.

QUANTITATIVE MAGNETIC IMAGING IN STEM USING DPC

Ian R. McFadyen

IBM Research Division, Almaden Research Center, 650 Harry Road, San Jose CA 95120-6099

Magnetic domains can be imaged by a number of techniques in the transmission electron microscope. These techniques rely on the Lorentz force and are thus known collectively as Lorentz microscopy. More accurately the interaction of a fast electron with the magnetic induction of a sample can be described as a change in the phase of the electron wave where the phase gradient is given by:

$$\nabla\phi = 2\pi \frac{e}{h} \int_{-\infty}^{\infty} \vec{B} \times \vec{k} \, dz \qquad (1)$$

where e is the electron charge, h is Plank's constant, $\vec{B}$ is the magnetic induction and $\vec{k}$ is the unit vector along the electron trajectory. The integration from $-\infty$ to ∞ takes into account the magnetic stray fields in addition to the magnetic induction within the sample itself.

Magnetic samples can therefore be regarded as phase objects and the magnetic structure can be revealed by phase contrast techniques and at best one could hope to get a map of the phase gradient which is linearly related to the integrated induction. The two most commonly used phase contrast techniques are the Fresnel (defocus) and the Foucault (displaced aperture) techniques which reveal the domain walls and domains respectively[1]. Both of these techniques can be carried out in the TEM or the STEM (the TEM being far more efficient in this case) but neither provides a direct map of the integrated magnetic induction. Two techniques which can provide a map of the phase gradient, and therefore the integrated magnetic induction, are electron holography[2] and differential phase contrast (DPC); this talk will concentrate on DPC.

DPC requires the use of a STEM equipped with a detector with an antisymmetric response function[3], the antisymmetric response produces a signal which is proportional to the phase gradient of the electron beam. (In terms of the Lorentz force the detector response is proportional to the angle through which the electrons are deflected by the sample, which in turn is proportional to the integrated in-plane magnetic induction.) In general the detector used is a quadrant semiconductor photodiode which, by using difference signals between opposite quadrants or, alternatively, opposite halves, can provide two orthogonal components of the phase gradient and, therefore, of the integrated in-plane magnetic induction. By scanning the electron beam across the sample the integrated induction at every point in an image can be mapped out. This provides the direction and relative magnitude of the integrated induction at each point in the image. In many cases the absolute magnitude can be obtained by normalising the difference signal by the sum of the signals on the 4 quadrants. This removes the effects of the system gain, any beam current variations and the reduction in intensity hitting the detector due to Bragg scattering. For a significant number of cases non-magnetic phase contrast is superimposed on the magnetic contrast. In fact equation (1) should more properly be written:

$$\nabla\phi = 2\pi \frac{e}{h} \int_{-\infty}^{\infty} \vec{B} \times \vec{k} \, dz + \pi \frac{\nabla(Vt)}{\lambda E} \qquad (2)$$

where V is the electrostatic potential of the sample, t is the sample thickness, E is the electron energy and λ is the electron wavelength.

This non-magnetic contrast is normally at much higher spatial frequency than the magnetic contrast and can be removed by frequency filtering. This filtering can either be carried out after the image has been acquired or during image acquisition by modifying the detector response function, for example by replacing the solid quadrant detector with an annular quadrant detector[4]. The latter technique has the advantage of increasing the magnetic contrast signal to noise since it reduces the number of electrons acquired without reducing the difference signal (which is derived from the edges of the probe). This makes it easier to identify regions of interest during the microscope session. One disadvantage of the annular quadrant

612

detector is that the structural image produced by summing the signals from the 4 quadrants is very poor, this can be overcome by using an 8 segment detector consisting of a solid quadrant detector surrounded by an annular quadrant detector. This detector can provide a standard DPC image, high and low past filtered DPC images and a bright field image.

Since DPC is carried out on a STEM the images can easily be acquired by a computer and analysed to produce a variety of images of the in-plane induction: separate x and y component images; direction and magnitude images; vector maps; 2 dimensional histograms of x-component vrs y-component. The last of these provides a map of the overall magnetic distribution within the image region and is analogues to a low angle electron diffraction pattern in the TEM.

The DPC technique is a very powerful technique for imaging magnetic domain structures that provides quantitative information on the integrated magnetic induction due to the sample. Since it requires a STEM it is amenable to computer acquisition and analysis and can be correlated with both structural and chemical information available in that machine.

References

1. I. R. McFadyen and J. N. Chapman, EMSA Bulletin 22.2 (1992) 64-75
2. A. Tonomura, Proc. XIth Int. Cong. Electron Microscopy, Kyoto 1986 9-14
3. G. R. Morrison and J. N. Chapman, Optik 64 (1983) 1-12
4. J. N. Chapman et al. IEEE Trans. Magn., MAG-26 (1990) 1506-1511

CHARACTERIZATION OF EPITAXIAL DIAMOND ON
NATURAL DIAMOND SUBSTRATES BY CATHODOLUMINESCENCE

D.P. Malta, E.A.Fitzgerald[*], J.B. Posthill, R.A. Rudder, G.C. Hudson, R.J. Markunas

Research Triangle Institute, Research Triangle Park, NC 27709-2194

*AT&T Bell Laboratories, Murray Hill, NJ 07974

A large effort continues in the development of diamond growth technologies for the production of electronic-grade diamond epitaxy[e.g.1]. Diamond has several properties such as a wide band gap (5.48 eV) and high thermal conductivity (2000 W m^{-1}K^{-1}) that make it desirable for electronic applications. Characterization of diamond with cathodoluminescence (CL) spectroscopy yields information on impurity and defect distributions with both spatial and energy resolution, providing insight into the growth process.

Diamond films were grown by plasma-enhanced chemical vapor deposition (PECVD) on natural type Ia 1mm×1mm×0.25mm diamond substrates. The results of microstructural studies on this type substrate are discussed elsewhere in these proceedings[2]. Two films were selected for CL analysis based on their strikingly different surface morphologies but similar growth conditions. Both were grown for 6 hours at a substrate temperature of ∼750°C and a pressure of 5 Torr. The gas mixtures were varied: $CO/CH_4/H_2$ was used in one case and CH_4/H_2 in the other. Growth rates for both processes were estimated at 0.5μm/hr thus giving film thicknesses of ∼3μm. Films were examined topographically by field emission scanning electron microscopy (FESEM). Wavelength-resolved CL spectroscopy was performed in another SEM using a 15keV electron beam and a sample temperature of 6°K.

The CL spectrum from the film grown with the CO-containing gas mixture (Fig. 1a) showed a major peak at 432nm with a shoulder at 472nm and minor peaks at 575nm and 602nm. The film grown with CH_4/H_2 (Fig. 1b) showed major peaks at 444nm and 478nm with a shoulder at 384nm. In both spectra, appearance of the large peaks in the 800-900nm range was attributed to second harmonics due to the unavailability of appropriate filters; their large size is due to the increased sensitivity of the detector in that range. Corresponding surface morphologies are presented in Figs. 1c and 1d. The $CO/CH_4/H_2$-grown film appeared very smooth with a speckled contrast. The CH_4/H_2-grown film contained pyramid-like protrusions and scattered crystalline diamond particles.

Emissions at 384nm and 575nm have been attributed to N-vacancy complexes[3]. Emissions at 472nm and 478nm are unknown, however, they have been observed in polycrystalline diamond[4]. An emission at 737nm attributed[5] to di-Si interstitials and possibly N was not observed in either case but could have been obscured by the second harmonic peaks. Emissions at 432nm and 444nm are termed "band A" emissions and have been associated with closely spaced donor-acceptor (D-A) pairs likely due to nitrogen and boron impurities segregated at defects[6]. Emission at 602nm has also been observed previously[4] in CVD diamond and is thought to be due to band A emission from more widely spaced D-A pairs. Monochromatic CL images (not shown) from the $CO/CH_4/H_2$-grown film using the 432nm peak revealed a cellular structure similar to that observed in natural diamonds[7]. TEM on those natural diamonds indicated the cellular structure was composed of dislocations. Images from the CH_4/H_2-grown film using the 444nm and 478nm peaks independently indicated non-radiative sites corresponding with the pyramid-like features shown in Fig. 1d on a uniform background. In studying individual diamond grains using CL in the TEM, Graham[6] has determined that grains containing moderate densities of defects emit band A CL strongly and those with very high or low defect densities emit very weakly. By analogy, our observations appear to indicate that the pyramid-like features on the CH_4 H_2-grown film have a different defect density than the surrounding epitaxial film. Independent of whether the defect density in the hillock regions is higher or lower, these features are undesirable.

The fact that pyramid-like defects are not observed in the $CO/CH_4/H_2$-grown film and spatial uniformity is observed with respect to band A luminescence, suggests the potential superiority of CO-containing growth chemistries over the more widely used CH_4/H_2 mixtures for homoepitaxial diamond growth[8].

References

1. R.A. Rudder et al., Appl. Phys. Lett. **60**, 329, (1992)

2. J.B. Posthill et al., This proceedings

3. L.H. Robins et al. Phys. Rev. B **39**, 13367 (1989)

4. R.J. Graham et al., Appl. Phys. Lett. **59**, 2463 (1991)

5. A.T. Collins et al., J. Mat. Res. **5** 2507 (1990)

6. R.J. Graham et al., J. Appl. Phys. **69**, 3212 (1991)

7. Unpublished results obtained in our laboratory

8. The authors gratefully acknowledge the support of this work by the SDIO/IST through ONR (Contract No. N00014-92-C-0081)
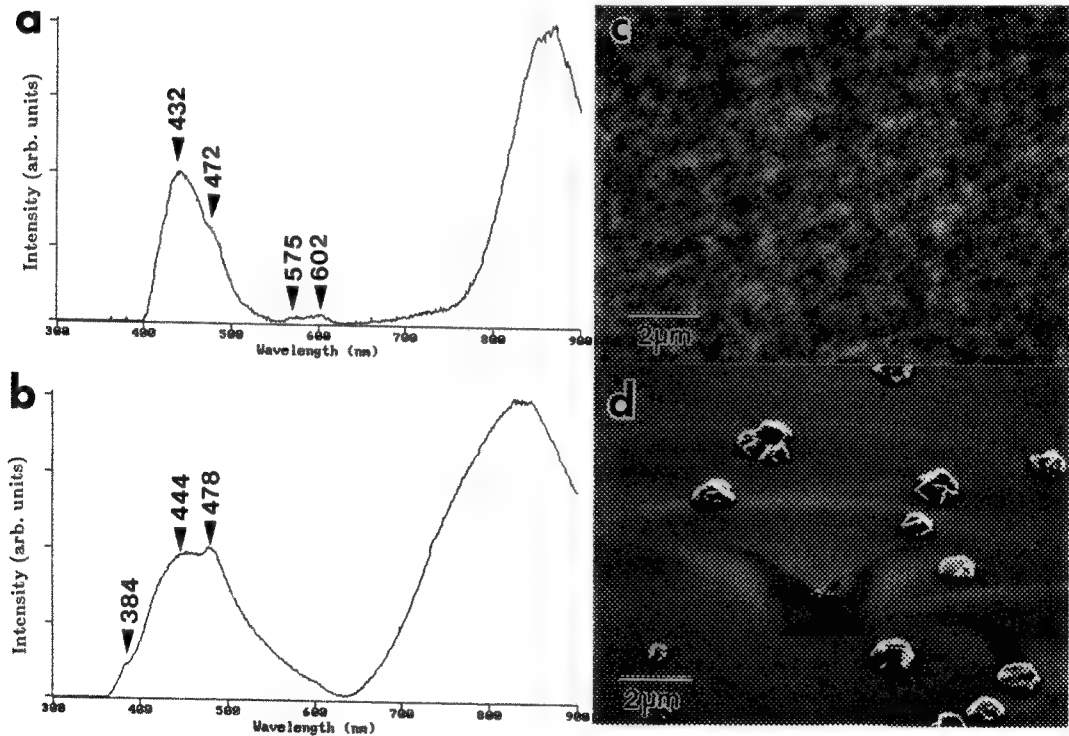
FIGURE 1: CL spectra and SEM topographical images of epitaxial diamond films grown by PECVD using gas mixtures of $CO/CH_4/H_2$ (a and c) and CH_4/H_2 (b and d)

DETECTION AND RESOLUTION IN INFRARED MICROPROBE ANALYSIS

John A. Reffner and Pamela A. Martoglio

Spectra-Tech, Inc.; 652 Glenbrook Rd.; Stamford, CT 06906

Detection and resolution are terms commonly used when describing infrared microprobe (IRM) analysis. However, the clear definitions of each are not always understood completely. It is the purpose of this work to define these terms as they apply to IRM analysis.

It is a well-known fact that, for optical imaging, the ability to resolve two separate points is dependent upon both the wavelength of radiation and the numerical aperture of the optical system. The implications of this law were first described in terms relevant to IRM analysis in 1987.[1] In order to be visually resolved, the Rayleigh criterion states that two points must be separated by 0.61l/NA (the radius of the central maximum of the Airy disk; see Figure 1). Since an IRM detects energy outside the central maximum, this criterion is not valid for spectral resolution.[2] With a 15X objective (NA = 0.58) over the spectral range of 600 - 4000 cm^{-1} (16.7 - 2.5 μm), the diffraction-resolution limit (DRL) ranges from 2.5 - 15 μm. In other words, two particles must be separated by at least 15 μm in order to be spectrally resolved over this wavelength range. This equation has been misused to imply that a single particle must be larger than the DRL to be detected in spectroscopic analyses. While the DRL is a necessary factor in establishing the IRM's detection limits, isolated particles below this limit can be detected and analyzed.

The use of confocal dual-image-plane apertures to define the sampling area improves edge resolution, significantly reduces the amount of diffracted radiation reaching the detector, and lowers the detection limit. Figure 2 illustrates the theoretical improvement in resolution and sample definition produced by confocal dual-image masks. These calculations also show that reducing the masked areas below the DRL does not reduce the analytical area but only reduces the total photon flux, and decreases spectral signal-to-noise.

Even if a particle is smaller than theoretically allowed, it can still be detected. The signal-to-noise performance of the IRM is the major limitation to detecting isolated, sub-resolution particles. While sub-resolution particles can be detected, photometric errors occur because these particles do not fill the entire sampling area and because the size of the sampling area is wavelength-dependent; these errors affect the spectral results. The spectrum of a 6-μm kaolin particle is shown in Figure 3. When this spectrum is compared with a large sample (see Figure 4), the distortion of absorption intensities is apparent. Instrumental factors that may improve detection are high-intensity sources, improved optical design, and more-sensitive detectors.

1. *Messerschmidt, R. G.; in The Design, Sample Handling, and Applications of Infrared Microscopes (P. B. Roush, ed.). Ann Arbor, MI: American Society for Testing and Materials (1987), 12.*

2. *Sommer, A. J.; and Katon, J. E.; Appl. Spec. (1991) **45**, 1633.*
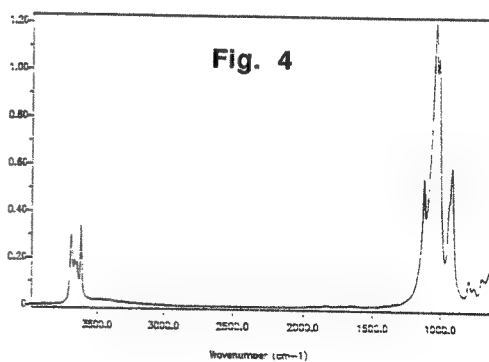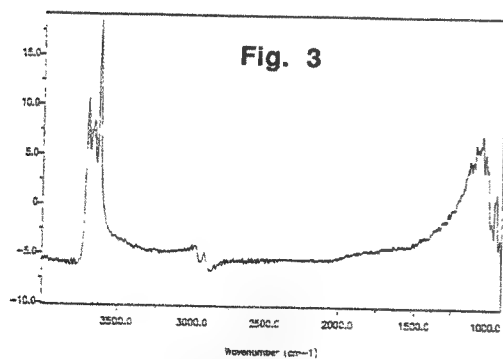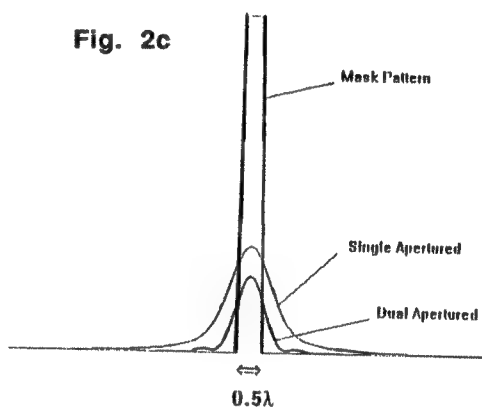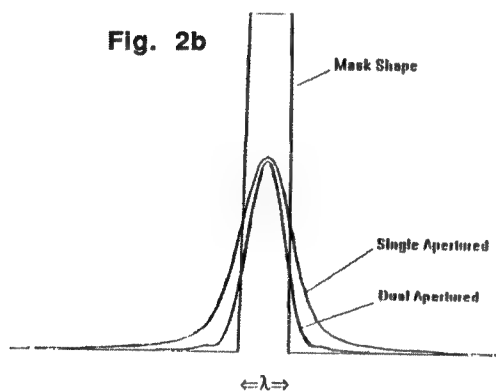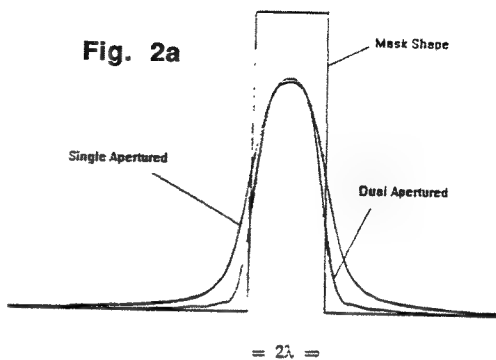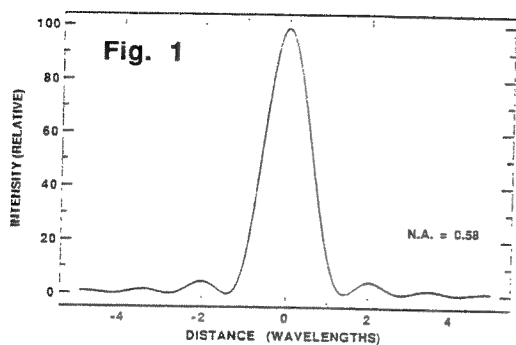
FIG. 1. -- Point diffraction pattern.

FIG. 2. -- Detection and resolution in FT-IR microscopy (a = 2λ, b = λ, and c = 0.5λ).

FIG. 3. -- Detection and resolution of Kaolin in Nujol after Nujol subtraction (6 x 6 μm particle in 12 x 12 μm dual aperture; 1024 scans at 8 cm^{-1}).

FIG. 4. -- Detection and resolution of Kaolin (256 scans at 8 cm^{-1}).

AN ELECTRON MICROSCOPY STUDY OF HIGH–THERMAL–CONDUCTIVITY RIBBON-SHAPE CARBON FIBERS

Kerry E. Robinson

Department of Chemical Engineering, Clemson University, Clemson, South Carolina 29634, USA

In an effort to develop a low-cost high thermal conductivity carbon fiber, ribbon-shaped fibers were melt-spun from a liquid crystalline, mesophase pitch precursor. Initial tests indicated that the ribbon-shaped fibers could be processed more easily and exhibited improved thermal conductivities when compared to commercial round fibers.[1] Evidently, it is the more linear, polycrystalline structure within these fibers that accounts for their improved thermal conductivities.[2] Thus, studies using scanning electron microscopy (SEM) and transmission electron microscopy (TEM) were conducted to fully analyze the transverse and longitudinal structure of these high thermal conductivity fibers.

Ribbon-shaped fibers, melt-spun from a synthetic mesophase pitch and then heat treated, were tested to determine their tensile strengths, tensile moduli and thermal conductivities. A Jeol JSM-I C848 SEM at an accelerating voltage of 20 kV was used to obtain general structural information, such as extent and texture of lamellar organization of the graphitic layers within the fibers, and the microstructure of the fibers was studied by TEM. The preparation of samples for TEM analysis was identical to that described previously.[2] All samples were examined by bright field imaging, 002 dark field imaging,[3] and selected-area electron diffraction (SAED) using a Hitachi H-600 TEM, operated at an accelerating voltage of 100 kV and using a condensor aperture of 200 μm.

The physical testing results showed that the ribbon-shaped fibers had mechanical and transport properties compatible to the best, commercially available high thermal conductivity fibers. Figures 1 and 2, SEM and TEM images of a ribbon-shaped fiber illustrate the typical disrupted, line-origin transverse structure which was common to most of the fibers studied. Bright field TEM images of longitudinal sections indicate that the crystallite layers are aligned along the fiber axis. As previously reported,[2] the crystallites appeared needle-like with definite alignment parallel to the fiber axis. SAED patterns similar to Figure 3, taken from longitudinal sections, indicate the conventional structure of carbon fibers, with the 002 carbon layers arranged parallel to the fiber axis, hence the 002 dots in the pattern. Further examination of this pattern showed that the 100 line is separated into two lines, the 100 and 101 lines. A 112 diffraction line is present, indicating the fiber is composed of large graphite-like crystallites with three dimensional ordering. Basal inter-layer spacings calculated from different selected areas within longitudinal sections indicated a range of d_{002} spacings across the fiber. 002 Dark-field images (Figure 4) of longitudinal sections provide an explaination for the different d-spacings. Dark-field imaging, specifically, allows one to observe the extent of folding of the crystallites aligned along the fiber axis.[3] Figure 4, indicates that fairly uniform regions of folded crystallites (indicated by arrows) are separated by planar regions of approximately the same width, aligned along the fiber axis. Preliminary measurements taken from these folded and planar regions indicate that 002 interlayer spacings of 0.3365 nm and 0.3410 nm (graphite d_{002} = 0.335 nm) exist for the planar and folded regions, respectively. This suggests that the fiber is more graphitic in the planar regions than the folded regions. This could be due to the fact the folding of crystallites causes structural constraints, inhibiting shrinkage during graphitization. These findings indicate that the microstructure of the synthetic pitch-based ribbon fibers is conducive to both high thermal conductivity and high strength, as the physical testing results indicate. The folded regions should prevent crack propagation in the fiber, and since these regions have a limited effect on the overall orientation of the 002 layer planes, the fibers should also have high thermal conductivities.[4]

1. K. E. Robinson , et al., Proc. of the 5th International Carbon Conference (1992) 816-818.
2. K. E. Robinson, Newsletter of The SouthEastern Electron Microscopy Society 8 (2) (1992) 7-11.
3. M. Endo, J. Material Science, 23 (2) (1988) 598-605.
4. This research was sponsored by the U.S. Department of the Navy, Office of the Assistant Secretary of the Navy, Manufacturing Technology, through contract # TDL No. 92 09.
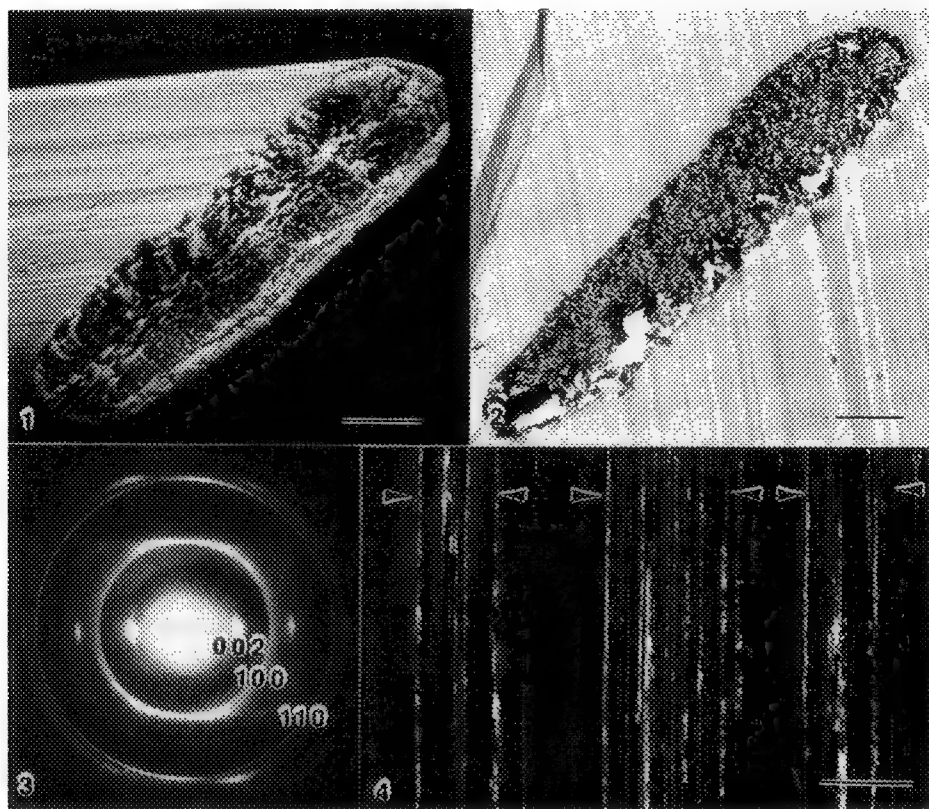
FIG. 1. SEM micrograph of a synthetic pitch-based, ribbon-shaped carbon fiber. Note the disrupted, line-origin texture. Bar = 5 μm.

FIG. 2. TEM bright-field image of a transverse section taken from a synthetic pitch-based, ribbon-shaped fiber. Bar = 5 μm.

FIG. 3. SAED pattern of a longitudinal section taken from a synthetic pitch-based, ribbon-shaped fiber. The 002, 100 and 110 diffraction lines are indicated.

FIG. 4. TEM 002 dark-field image of a longitudinal section taken from a synthetic pitch-based ribbon fiber. The folded regions are indicated by arrows. Bar = 1 μm.

AN INEXPENSIVE, EASY TO USE VIDEO IMAGING SYSTEM FOR INTRACELLULAR Ca^{2+} AND QUANTITATIVE FLUORESCENCE MICROSCOPY

Eric Gruenstein & Jesus Luna

Department of Molecular Genetics, Biochemistry, & Microbiology and the Center for Image Analysis, University of Cincinnati, College of Medicine, 231 Bethesda Ave., Cincinnati, OH 45267-0524

Fura-2 is the most commonly used member of a family of calcium sensitive flourescent dyes that allows the measurement of intracellular free calcium (Ca$_i$) by dual excitation fluorimetry. The use of this dye in conjunction with video imaging microscopy permits visualization of changes in Ca$_i$ with a high degree of spatial resolution. This resolution in turn allows the detection of Ca$_i$ gradients, waves, and other localized cellular responses not easily detected by photometric techniques. Despite these advantages, most published reports have utilized photometry rather than imaging, due largely to the higher cost and greater complexity of use of the latter technique. With these problems in mind, we have developed a turnkey calcium imaging system that is both inexpensive and simple enough to use that it can be mastered in 2-3 hours.

The specifications of the system are as follows:

Resolution	512 x 512 pixels
Speed	1 to 5 seconds/ratioed image pair, depending on fluorescence intensity
Regions of Interest	40 User definable areas of arbitrary shape
Operating System	Windows 3.1
Data Collection	Calculate ratios and graph data during experiment
	OR
	Save images and ratio after experiment
Wavelength Control	Computer controlled filter changer with shuttering to reduce bleaching
Other Applications	Densitometry and General Purpose Image Analysis/Morphometry

Data showing the distribution of free Ca^{2+} in the cytoplasm of a quiescent human fibroblast and the kinetics of stimulation of these cells with mitogens are illustrated on the next page.

Although this system is currently available only to members of the University of Cincinnati community, we are exploring the possibility of making it available extramurally. If it does become available to other researchers, we expect that it will be at a cost less than one third that of currently available calcium imaging systems.
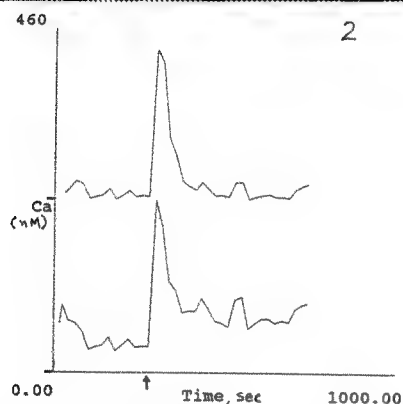
Fig 1. Spatial analysis of intracellular free calcium in normal
human fibroblasts. (A) Fluorescent image at 340 nm excitation; (B)
Fluorescent image at 380 nm excitation; (C) Intracellular free
calcium calculated from the 340/380 nm ratios at each pixel. Cells
were serum deprived for 2 days and loaded for 45 min with 3 uM
Fura-2AM followed by a 45 min post-incubation to insure the
complete hydrolysis of the internalized dye. Note the presence of
standing gradients of free calcium under these steady state
conditions with low levels in the nuclei and higher levels in an
asymmetric distribution in the perinuclear space, as previously
described.[1] Gray scale for calcium concentrations runs linearly
from 0 (black) to 200 nM (bright white).
Fig 2. Kinetic analysis of changes in intracellular free calcium
following stimulation of serum deprived cells with 10% fetal bovine
serum (arrow), as previously described.[2]

References

1. M. Wahl and E. Gruenstein, Molec Biol Cell 4(1993):293.
2. M. Wahl, R. Sleight, and E. Gruenstein, J. Cell Physiol.
150(1991):593.

DATA ACQUISITION AS A DESIGN PARAMETER IN THE MODERN AEM

Nestor J. Zaluzec

Electron Microscopy Center for Materials Research, Materials Science Division, Argonne National Laboratory, Argonne, Illinois 60439 , USA

Data is the essential component of all scientific investigations. From this information we, as experimentalists, formulate ideas, test theories, derive conclusions and design new experiments to continue our explorations of materials both in the physical and life sciences. Clearly without it we would be left with literally nothing to do. With that thought in mind it should be intuitively obvious that there are two essential aspects of all studies. The first is a well formulated experiment whose results will provide relevant data and second that the methodology/instrument we choose to utilize to collect the data has the ability to acquire the information we need to obtain about an object or phenomenon. By extension one would assume that having chosen an instrument that it was designed with the thought in mind to maximize the amount and quality of information for which it is being employed.

We can break down any experimental system into the following areas: the environment and manipulation of the specimen in the instrument, the probe used to investigate the specimen, the detectors used to measure information, and finally the transfer of data from the experiment to the outside world. It is essential that any experiment be considered to be a system composed of mutually complementary parts all of which should be working in concert to provide the maximum amount of data with a reasonable effort. The bane of the analyst, especially in the field of microscopy, is the fact that, more often than not, the configuration of the analytical equipment which we use for our experiment(s) is not that of a complete system but rather a collection of subsystems which have not been optimized. Optimizing each of these is not a trivial endeavor and if one considers the task of integrating each into an operating system then the job can become a nightmare. This is particularly true when the various components have been manufactured by different individuals/organizations who may not have been closely coordinated together. This is notably relevant in the modern analytical electron microscope (AEM). At the risk of alienating most every manufacturer let us present a pessimistic view of an AEM system.

Microscope manufacturers tend to concentrate their considerations to electron optics and seek to maximize their capabilities in imaging and probe forming systems. A few give some extra consideration to the specimen area, but most favor speed of specimen exchange and ease of operation over the optimization of the environment. This is a direct consequence of the fact that the primary data to be generated is an electron scattering experiment resulting in an image and/or diffraction pattern. Data output is generally recorded on film with high spatial resolution, but relatively small linear dynamic range and data transfer rates are extremely slow (< 1 kHz). Some attempts are being made to implement digital image acquisition using electron sensitive camera systems however, a good fraction of the work is being done by accessory manufacturers. Control of the electron dose in the basic instrument is visual, and absolute measurements of the incident and scattered electrons are seldom conducted. Ancillary detector manufacturers (XEDS, EELS, AES, CCD's....) while attempting to maximize the performance of their respective spectroscopic systems are usually limited by the constraints (in the positioning and size of their respective detectors) placed upon them by the instrument manufacturer. But then again few of these have these have tried to suggest other than minor changes to the basic system. Data throughputs from the detector to the analyzer vary wildly ranging from < 1 kHz on XEDS systems to > 10 MHz on electron counting systems. Furthermore, once the data is measured in a given acquisition system transfer of this information to an alternate analysis system can vary in speed by orders of magnitude. Control of some instruments ranges from almost Babalonic in nature: antiquated, confused and atrociously slow (<1 kHz); to some of the newer

systems that are so tightly integrated with flashy workstations that it is nearly impossible to modify them. Finally inter-system communication between the various data acquisition, control and analysis systems is almost nonexistent when the subsystems come from different sources.

Many of the above pessimistic viewpoints/compromises are based upon the driving forces in the market place as the majority of analysts do not need to deal with pushing the frontiers of analysis. State-of-the-art may mean the latest commercial product, and if the product generates the appropriate data and answers the questions posed then it was a suitable instrument and the most cost effective solution to our first question posed.

On the other hand the answers needed may require experimental configurations which push the limits of data collection. In this scenario, given the time (and money) one can attempt to optimize an analytical system by first considering the fact that data collection is of prime importance and it should dictate the design of an instrument. Such an instrument is then a resource for the community as a whole and serves to define the next generation of instrument available to the average user. The question then to ask is: as a system how do we design the "instrument" to generate, acquire, store and transmit the current generation of microanalytical data and in addition keep sufficient versatility to expand to experimental configurations yet to be implemented. The points to consider are:

- Maximize the available space about the specimen to allow multiple detector configurations and reasonable expansion for future developments yet to be "discovered" within the lifetime of the instrument (~ 10-15 years).
- Configure the specimen manipulation systems to allow maximal manipulation of the sample and the design of new stages.
- Achieve an environment which is free of contamination during the course of an experiment.
- Develop (spectroscopic) detector systems with data input rates which can keep up with the generation rates created by the all probes being employed and free of "system peaks" from the immediate surroundings. (This is a major obstacle particularly in XEDS!).
- Establishment of well defined, controlled and stable high intensity probes with measurement systems capable of characterizing the absolute probe characteristics to better than 0.1%.
- Implement high speed digital control of instrument with average I/O rates > 500 kbyte/sec, over all system parameters/functions. Digital counting systems with data depths of at least 24 bits and digital scanning systems capable of up to 4Kx4K area scans. Configurations should implement multiple microprocessors with local data storage to direct different tasks and have multiple I/O links including high speed serial, SCSI and DMA buses for instrument-to-instrument communication. Basic instrument interface controls must be developed to allow interactive control of the entire system by ancillary equipment using a standard command line interface.
- High speed data transfer (>10Mb/sec) from the primary instrument to ancillary systems using established international protocols (TCP/IP) and data formats (MSA/MAS file formats, TIFF imaging.....).
- Local data storage (>0.5-2 Gb) on data acquisition systems for short term analytical imaging.
- Remote workstations for data analysis.

Most of these items can be implemented today as they within the technological reach of present day instrumentation. It only remains for the community as a whole to demand this of the manufacturers.

INSTRUMENTAL DEVELOPMENTS FOR ELECTRON MICROSCOPES :
A STEM DETECTOR AND CORRECTORS FOR A LVSEM AND A 200 kV TEM

Max Haider

European Molecular Biology Laboratory, Postfach 10.2209, D-6900 Heidelberg, FRG

One advantage of scanning transmission electron microscopy (STEM) over conventional TEM which is often cited is the capability to simultaneously record the various scattered electrons with properly designed detectors. So far, this advantage has only been utilized to record bright-field or inelastic and dark-field (low and high angle)[1] images in parallel. However, it has not been used to record all transmitted electrons separately according to their scattering angle. We developed a flexible multichannel detector system based on a silicon chip which has been fabricated to our specifications. This detector consists of 30 rings which are split into 4 quadrants (see Fig. 1), and is operated in an electron counting mode. The rings can be used to separate the electrons according to their scattering angle for low and high angle dark-field images, to obtain the various phase-contrast images[2] and to normalize the signals by the sum of all detectors. The system records the signals of the 120 channels in parallel and the counts of each channel can be combined in an integer processing unit in order to form 8 different images[3]. The detector configuration for each image can be preselected by software[4] and the images are acquired with a time per pixel $t_p \geq 4$ μsec. Images can be obtained with a detector acceptance angle from zero up to a maximum of between 100 and 200 mrad depending on the excitation of the objective lens. The measured counting efficiency agrees well with an assumed dead-time of 90 nsec of the whole detector chain. The maximum recording frequency of the incoming electron flux is 12 MHz. Due to the low noise levels of the preamplifiers and the discriminators false counts are reduced to a negligible value of about 10 pixels, which shows only one counted electron when recording a 1024 x 1024 image with $t_p = 8$ μsec, all 120 channels summed up and without electron beam.

The observation of uncoated non conductive surfaces of thick specimens with a scanning electron microscope (SEM) is limited with respect to resolution by the penetration depth and the charging of the object. In order to overcome these two problems, the primary energy of the electron probe has to be reduced to a value, where the SE-yield of the material under observation is approximately unity. However, at low energies ($400 \leq E \leq 2000$ eV) the correction of the chromatic and the spherical aberration has to be considered in order to be able to focus the electron probe into a spot suitable for high resolution ($d \leq 2$ nm). We are currently developing such a corrected high resolution LVSEM[5], for which calculations showed that the attainable probe diameter is 1 nm at an energy of 500 eV[6].

The theoretically achievable resolving power of TEMs can be obtained on a routine basis with modern microscopes. However, even with these microscopes, the resolution is still limited by the two well known aberrations: the chromatic and the spherical aberration.

The correction of the chromatic aberration can be avoided when a field emission source and an acceleration voltage of U ≥ 200 kV are used. We started a project in order to investigate the feasibility of compensating only the spherical aberration by means of two hexapole fields and two transfer-dubletts as proposed by Rose[7]. For this purpose, a correction system has been developed and tested in an electron optical test bench. This system will be incorporated into a Philips CM 20 in order to test the correction under high resolution imaging conditions and to develop an appropriate alignment procedure. Presently, the CM 20 is equipped with a conventional tungsten filament which will be replaced by a field emission source when the correction of the spherical aberration can be demonstrated. The final goal of this project is a 200 kV TEM with a point resolution below 1 Å[8].

References :
1   J. S. Wall and J. F. Hainfeld, Ann. Rev. Biophys. Chem. (1986) 15, 355
2   H. Rose, Optik (1974) 39, 416
3   A. Epstein, Rev. Sci. Instrum. (1988), 59, 11
4   T. Bastian et. al., Open Bus Systems, Zuerich (1992) 179
5   H. Rose, Optik (1971) 33, 1
6   J. Zach, Optik (1989) 83, 30
7   H. Rose, Optik (1990) 85, 19
8   Part of this work (correction of the spherical aberration in a TEM) is supported by a grant of the Volkswagen Stiftung, Hannover, FRG.
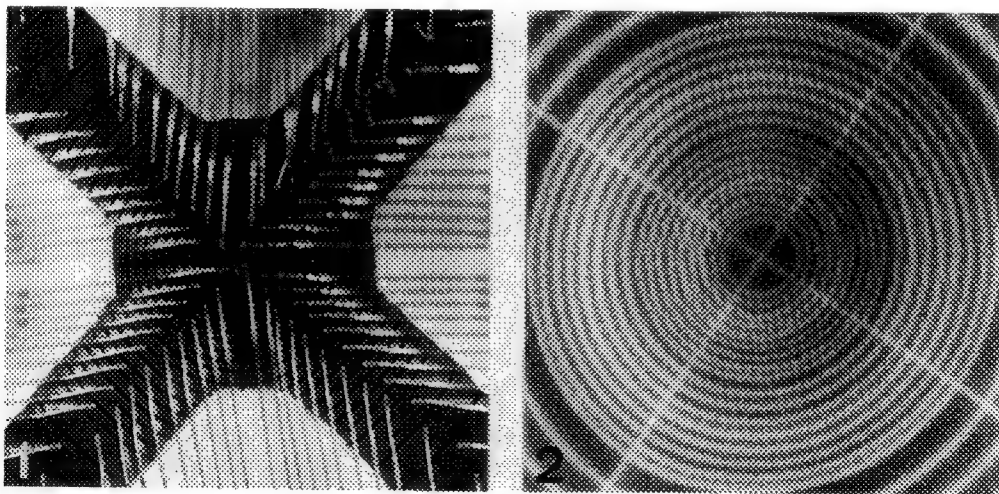
Fig. 1 - Photograph showing the inner part of the rear side of the multichannel detector. The shape of the individual rings can be seen as well as the bonding wires to feed the pulse, generated by a single electron to the preamplifier. The electrons are hitting the detector from below. The diameter of the silicon detector is 10 mm.
Fig. 2 - Structure of the detector obtained with a focused electron probe scanned across the detector and a beam current of 1 pA. The threshold voltage of the discriminator was reduced in order to show the individual channels. The bright lines are representing the gaps between adjacent channels because electrons are counted twice at these areas.

ELECTRON BEAM DAMAGE OF Ni3Al

David A. Muller*, John Silcox+

*Physics Department, Cornell University, Ithaca NY 14853
+Department of Applied and Engineering Physics, Cornell University, Ithaca NY 14853

In recent years, the effect of radiation induced sputtering in electron microscopy at voltages as low as 100 kV has been identified[1] and has emerged as a significant factor in microanalysis. The inhibiting effect of some surface layers has also been noted.[1] More generally, the use of focused electron probes (as in STEM) as a tool for materials modification on the nanoscale has also been developed.[2] We report here observations of electron radiation effects in Ni_3Al, a proto-typical high temperature, high strength intermetallic of some considerable interest.[3] This work is comparable to the study of electron radiation damage in aluminium reported by Bullough et.al.[4]

Fig. 1 illustrates the formation of holes in a Ni_3Al specimen and the associated nickel rich patches formed after irradiation at 100kV in the Cornell UHV HB501A STEM in spot mode with an estimated 10Å FWHM beam size at a beam current of 0.12 nA for a period of 20 minutes. The somewhat dramatic radiation damage is readily seen. (In a TEM the effects are more insidious as a large, uniform area is irradiated. The mass loss is not always apparent in bright field and can be easily mistaken for contamination or ion milling damage.) Microanalysis of the region in figure 1 has been undertaken by EELS and EDX and the primary result is shown in Fig. 2. Initially aluminium primarily is removed from the sample but after five minutes a significant rate of nickel loss also occurs. Fig. 3 shows the measured aluminium concentration as a function of time. Aluminium is steadily removed until the concentration reaches ~ 15% at which level it appears to remain constant. If prior to inserting a freshly jet-polished sample directly into the clean environment of the UHV-STEM, a specimen is viewed in a conventional instrument then a 50Å (estimated from EELS) carbon layer is deposited. Such a sacrificial layer protects the Ni_3Al sample for a period of up to an hour. These observations are consistent with the interpretation that the aluminium in the alloy is preferentially sputtered from the surface leaving behind a nickel rich layer. Studies of changes in the L_3 and L_2 nickel edge fine structure in the alloy and in the pure metal are consistent with these results. In Fig. 4 the Ni $L_{2,3}$ edge is shown in the alloy (top) and after irradiation for a period of 5 minutes with a 3Å FWHM beam and 0.1 nA. The critical point to note is the appearance in the irradiated sample of a white line on the L_2 edge that is characteristic of nickel enrichment.

A model for the radiation damage processes can be understood in terms of the work of Medlin et. al.[5] The beam energy of 100 kV is below the threshold for Frenkel pair production of vacancies and interstitials in the bulk although atoms can be displaced into existing vacancies. These vacancy-enhanced displacements provides a transport mechanism of vacancies away from the surface and atoms to the surface but there is no net mass loss from the film. At 100 kV the calculated cross section for surface sputtering of aluminium is 454 barns and is zero for nickel.[6] This would suggest that surface layers of Al would be lost at a rate of a monolayer per second while Ni would remain behind. Even as surface atoms are replenished by vacancy enhanced displacements, the surface would become progressively nickel rich, inhibiting further Al sputtering. If no nickel diffusion occured, the process would become self-limiting and the erosion would be halted. As shown in Fig. 1 some nickel surface diffusion does occur and once the initial Al is lost from the surface, it is the nickel migration rate that controls the mass loss in the sample. With a carbon overlayer in place, no surface sputtering of Al is possible and a 100 kV electron beam is not sufficiently energetic to displace Al atoms into carbon. At higher beam voltages (certainly by 300 kV) this is no longer the case and preferential sputtering of aluminium cannot be avoided.[7]

626

References

1. N.J. Zaluzec, J.F. Mansfield, Proc. 44th Ann. Meet. EMSA (1986) 708.
2. E. Kratschmer and M. Isaacson, J.Vac.Sci. Technol B,**5**(1) (1977) 369.
3. For a recent review see Viewpoint Set No. 17 of Scripta Metall. 25 Apr. (1991)
4. T.J. Bullough, et. al. EMAG-MICRO 89, Institute of Physics Conference Series 98 (1990) 267.
5. D.L. Medlin, D.G. Howitt, Phil. Mag. Lett. 64(3) (1991) 133.
6. C.R. Bradley, Argonne National Laboratory Report ANL-88-48.
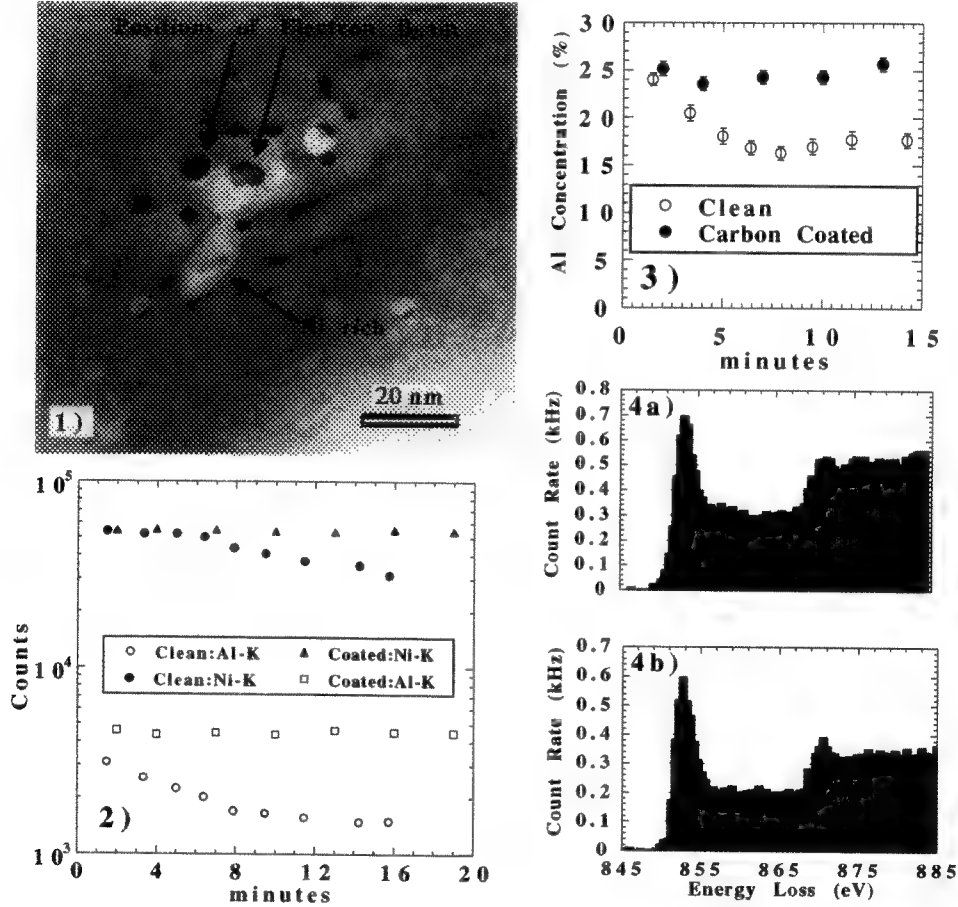
Fig. 1. Mass thickness image (plasmon intensity/zero loss signal) showing the holes formed by the electron beam after 10 min. exposure, and the "puddle" of nickel around the holes.
Fig. 2. EDX counts of the nickel and aluminium K edges for clean and coated specimens vs. time.
Fig. 3. Aluminium concentration vs. time as calculated from Fig 2.
Fig. 4. a) The Ni L2,3 EELS edge before beam damage has occurred and b) after 10 minutes exposure to the electron beam. The sharp peak at 870 eV is characteristic of nickel enrichment.

627

SCANNING FARFIELD AND SCANNING NEARFIELD PROBE MICROSCOPY OF CATALASE PLATELETS

Helmut F. Knapp, Frank A. Schabert and Andreas Engel

M.E. Müller Institute for High Resolution Electron Microscopy at the Biocenter, University of Basel, Klingelbergstrasse 70, CH-4056 Basel

High resolution (sub nm) and direct height information obtained through scanning probe microscopy (SPM) (such as from the STM and AFM) establishes SPM as a valuable tool for the investigation of biological samples. Unfortunately SPM allows only regions of a few µm to be scanned at high speed. For biological applications this is a disadvantage, because most samples will be only of the µm size and scattered across the much larger substrate. To make SPM investigation of biological samples less tedious, we combined a STM (or alternatively an AFM [1]) with an inverted confocal scanning laser microscope (CSLM), with a lateral and axial resolution of 200 nm and 400 nm, respectively. This enables to locate areas of interest on the substrate and position the tip of the STM. STM tips used are electro-chemically etched from Au to routinely attain tip radii in the 5 nm range. Catalase platelets were chosen as a sample, because of their established two different lattice repeats (17.5 nm and 6.8 nm [2]).

The catalase crystals where prepared according to the method of Wrigley [3] without glutaraldehyde. Shortly before use the crystals were centrifuged lightly, resuspended in distilled H_2O and a drop of the suspension deposited on carbon coated and glow discharged glass cover slips or formvar and carbon coated, glow discharged EM grids. The samples were then freeze dried and rotary shadowed with 1 nm Pt/Ir/C, yielding a fine grain coating stable in air [4]. The EM grid samples were viewed in the TEM to ensure fine grain coating and to control the lattice structure of the catalase platelets (Fig.1). The glass cover slip samples were viewed in the SEM to control proper adsorption of the catalase platelets (Fig.2). A more detailed analysis of the platelets can be done in the AFM (Fig.3) This however does not reach the resolution achieved with the STM, because even E-beam deposited contamination tips for AFM only yield tip radii of at best 12 nm. The sample is finally viewed through a home built [1] inverted CSLM (Fig.4) to position the STM tip (inset of Fig.4) to a catalase platelet. The resulting STM scan is shown in Fig.5.

FIG. 1:--TEM image of catalase crystal platelet adsorbed on formvar and carbon coated EM grid, freeze dried and rotary shadowed with 1 nm Pt/Ir/C at 45°. Scale bar represents 200 nm.
FIG. 2:--SEM image of catalase crystal platelet prepared analogous to preparation in figure 1, but on carbon coated glass cover slip. Sample is viewed at 45° electron beam incidence. Scale bar represents 1µm.
FIG. 3:--AFM image of same preparation as in figure 2. Full gray scale corresponds to 200 nm. Scale bar represents 5 µm.
FIG. 4:--CSLM image of area where STM image of figure 5 was taken (viewed from opposite side through glass cover slip. Scale bar represents 10 µm. Inset shows 13 µm x 13 µm CSLM scan taken separately of marked area. Arrow points to STM tip (start position of STM image).

[1] F.A.Schabert et al, submitted to Rev. Sci. Instr.
[2] P.N.T.Unwin, J.Mol.Biol. 98, (1975) 235-242
[3] N.G.Wrigley, J. Ultrastructure Res. 24, (1968) 454-464
[4] R.Wepf et al, J Microscopy 163 I, (1991) 51-54
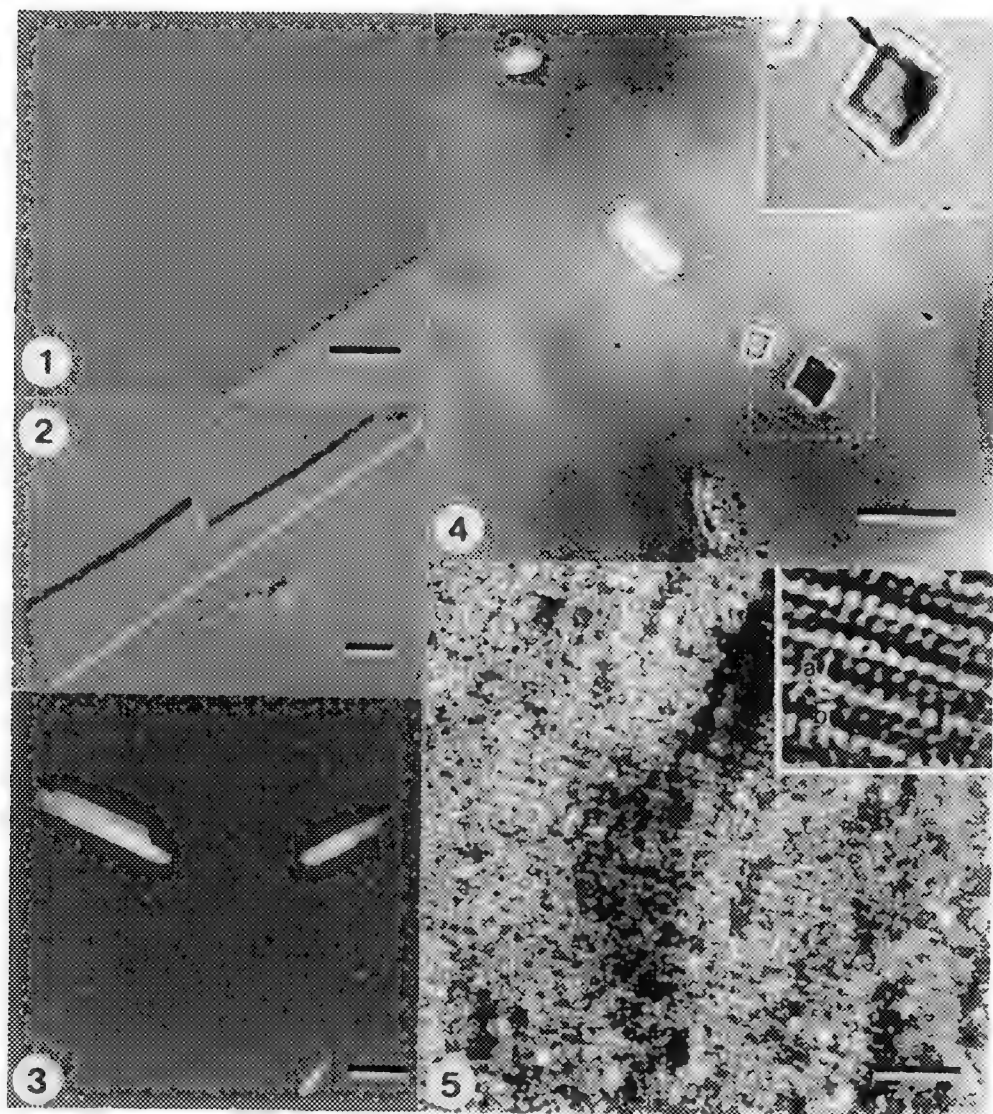
FIG. 5:--STM image of catalase preparation of figure 2. Scale bar represents 100 nm. Large lattice repeat of platelet is distinct on high pass filtered main image, while small repeat becomes visible after correlation averaging (85 nm x 85 nm inset, showing typical catalase crystal structure [(100) orientation]). Lattice vectors a and b are 17.4 nm and 7.1 nm in length respectively.

A FIELD-EMISSION SEM OPTIMIZED FOR OPERATION AT LOW BEAM VOLTAGE

JB Pawley, J Ximen*, PS-D Lin** and M. Schippert[§]
IMR, 1675 Observatory Dr. Madison, WI 53706: *Physics Dept. NJIT, Newark NJ,**Bellcore, NJ,
[§]AMRay Corp. Bedford, MA

The advantages of operating the SEM at low beam voltage (V_0) have been recognized for some time[1]. They include: less specimen charging, greater contrast in the fine topographic component of the secondary electron (SE) signal and reduced radiation damage[2]. Although initially it was difficult to obtain high resolution images when using low V_0, this limitation can be essentially overcome by employing both a FE source and an immersion objective lens[3]. In an instrument employing both of these features it is possible to produce a beam diameter of about 3 nm @ 1.5 kV. When insulating specimens are viewed under these conditions, the resolution in the image is limited more by the structure of the coating material than by the beam diameter, while on conductors, small structural features produce useful contrast only at low V_0.

The remaining obstacle to more widespread use of LVSEM for high resolution topographic imaging is the high cost of the equipment. At present, all commercial SEMs employing both a FE gun and an immersion objective are designed to operate at up-to 30kV and have complex and expensive vacuum systems[4]. As a result they sell in the range of $400-500k. We believed that by optimizing the design of an SEM for operation only at low V_0 and by simplifying the vacuum system we could develop an instrument that would sell for about $200k.

As a first step, we decided to build a new lens-stage-detector system around the eucentric, side-entry stage from a Philips 430 TEM and to operate it in conjunction with an FE gun and electronics console of conventional design. The vacuum system consists of a molecular drag pump and 3 ion pumps of 20, 60 and 220 l/s. As the extraction field of the Koiké-type SE detector used with an immersion objective is transverse and asymmetrical,it tends to degrade the optical performance of the lens, particularly at low V_0 [4].

We used simulation programs by E. Munro and J. Ximen to optimize the electron optical performance and to evaluate the effect of the collection field of the two lenses we designed.

The first, XM-5, design[5], was relatively conventional (UB = 5 mm, G = 7.5 mm, LB = 10 mm, C_s = 1.35mm, C_c = 1.55 mm, working distance (WD) =3mm, Fig 1). Because of the stage design, the upper polepiece had a long narrow bore between the gap and the detector chamber above. Although SE images showing 3 nm features were obtained at 1.5 kV with this lens and a Schottky FE source, (Fig. 2) the long upper bore complicated SE collection and meant that the lower scan coils had to be mounted more than 70 mm above the object-side back focal plane, a condition that compromised low magnification performance.

The second SL-8 design (Fig. 3) has similar gap dimensions (UB = 3 mm, G = 8 mm, LB = 5 mm, C_s = 1.2 mm, C_c = 1.33 mm, WD =3mm), but the upper part of the upper bore has been enlarged to permit the scan coils and microchannel plate backscattered electron (BSE) detector to be lowered while preserving an effective SE collection field. The resolution of the SL-8 design is at least as good as that of the XM-5 but the low magnification performance now extends down to 1000x without excessive distortion. (Magnification down to 50x is provided by a Low-mag Mode in which only one scan coil is used and the objective is only partially excited.) We are currently optimizing the geometry of the lower scan coils and the SE detector and are measuring the performance of the BSE detector mounted below the lower scan-coil .

For WD = 3, 4, 5mm, we have calculated SE- and BSE- trajectories for a variety of V_0. For SE initial energies of 5-10 eV, 86-93% of SE trajectories strike,the E-T collector in the SL-8 lens. For BSE initial energies of 100 - 1000 eV and divergence angles of 10^0- to 60^0 and azimuthal angles of 15^0 to 30^0, 30 to 60% of BSE trajectories strike the MCP collector depending on its position[6].

References:
1. J.B.Pawley, Low Voltage SEM, in Adv. Electr. & Electr. Phys. (ed P Hawkes), Academic Press, 83(1992) 203-73; P. Walther, et al. High Resolution LVSEM of frozen-hydrated cells, J.Microsc. (1992) 168, 169-80, 169-180 and H. Ris, Inst.Phys.Conf.Ser.98(1989) 657-62
2. D.C.Joy &J.B.Pawley, High Resolution SEM, Ultramicroscopy 47(1992) 80-100
3. T. Nagatani,et al, Development of ultra-high resolution LVSEM, Proc.XIIth ICEM Mtg.(1990) 388-389
4. J.B.Pawley, Practical Aspects of High Resolution LVSEM, Scanning(1990),12, 247–252.
5. Ximen,J.et.al.Electron optical design of a High Resolution LVSEM objective lens,EMSA,(1992)950-1.
6. This work supported by a grant from the Division of Instrument Resources, NSF and by AMRay Inc.
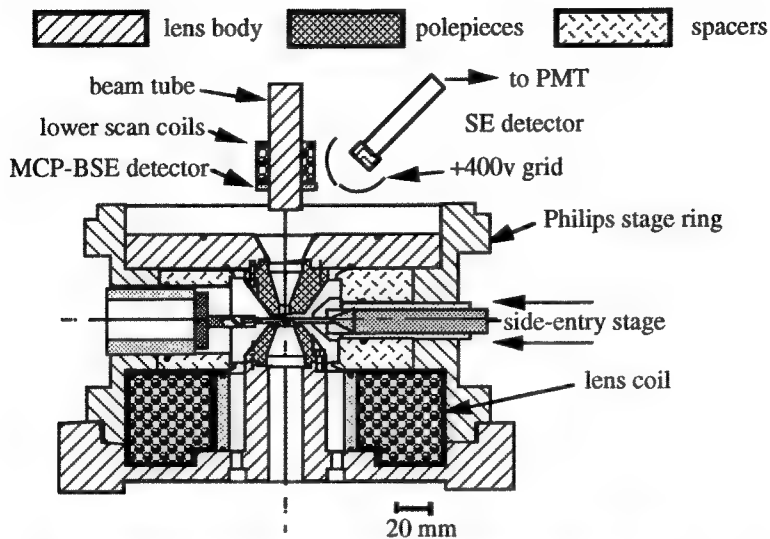
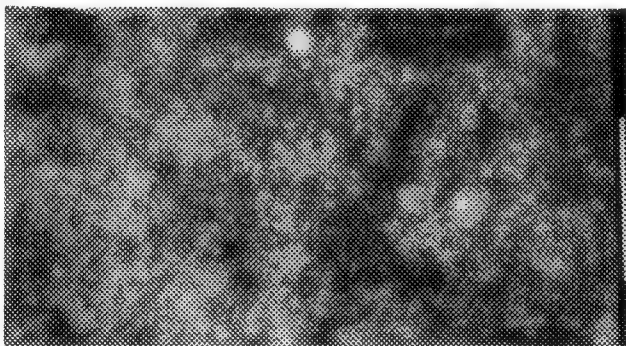Figure 1: XM-5 lens built around the side-entry stage from a Philips 430.

Figure 2: Secondary electron image of Pt particles on carbon imaged with XM-5 lens at 1.5kv, WD = 3 mm, 400kx original mag. Scale bar = 50 nm.
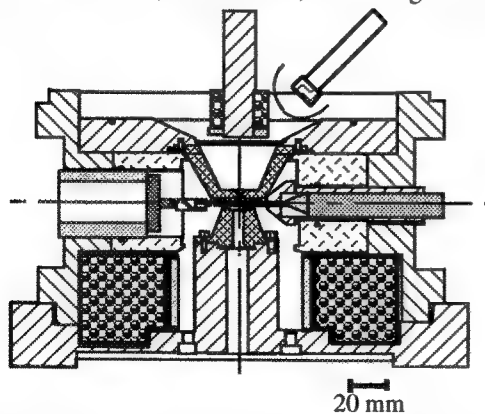

Figure 2: SL-8 lens. The larger bore in the region above the upper pole-piece improves the efficiency of SE collection and reduces scanning problems at lower magnification.

BRIGHTNESS MEASUREMENTS OF NANOMETER-SIZED FIELD-EMISSION TIPS

M.R. Scheinfein, W. Qian and J.C.H. Spence

Department of Physics and Astronomy, Arizona State University, Tempe, AZ 85287-1504

It has recently been suggested that the brightness of electron field-emitters of atomic dimensions may greatly exceed that of conventional field-emission sources [1,2]. We have therefore measured the brightness of tungsten nanotip field emitters. Brightness is defined as the current density per unit solid angle at a point for limitingly small angles and areas. The axial brightness, $B = \partial^2 I / \partial W \partial A$, when divided by the relativistically corrected acceleration potential V^*, the reduced brightness, $b = B/V^*$, is invariant at all points along the axis of a symmetric electron-optical system. For a given emission mechanism, the brightness at a point on a flat source is, by definition, independent of source size. Recently, there have been suggestions that new mechanisms come into play for cold field-emission sources of atomic dimensions, leading perhaps to higher brightness[1,2]. These include reported departures from Fowler-Nordheim behaviour[3], and quantum-mechanical focussing effects [4,5]. The attainment of the theoretical brightness limit is often prevented by space charge effects.

We therefore consider it worthwhile to report our measurements of the average brightness of such a nanotip field emitter. In order to assess the electron-optical properties of nanotips, a dedicated UHV chamber was constructed with *in situ* tip preparation capabilities.   A 0.006" diameter (111) single-crystal tungsten wire was spot-welded onto a 0.01" diameter tungsten heating loop. The tip was chemically etched by immersion in a 10% KOH solution. 3 V DC was applied between the tip and the remote electrode in solution (tip positive). The tip was further sharpened in 5% KOH with a pulsed DC voltage applied between the tip and a gold loop containing the etchant. We then rinsed the tip with deionized water and introduced it immediately into the UHV chamber. The tip was mounted a distance L = 3.5 cm from a micro-channel plate (MCP) assembly, on which field-emission microscopy (FEM) images could be viewed. By reversing the tip polarity and introducing in imaging gas, field-ion microscopy (FIM) images could be used to monitor the tip formation process [6]. Images were recorded using a liquid nitrogen cooled CCD camera system. The tips were cleaned *in-situ* by resistance heating to about 1800 ^{0}C. Initial tip radii were about 600Å, as estimated from Fowler-Nordheim plots. The tip was biased negatively during sputtering[7] causing field emitted electrons to ionize Neon atoms, which subsequently collide with and further sharpen rough regions of the tip where the field is strongest. Sputtering conditions required a voltage of a few hundred volts and a current of a few microamps at a Ne pressure of 10^{-5} Torr. The voltage was slowly reduced to maintain constant sputtering current as the tip was sharpened, thus maintaining an approximately constant electric field at the tip. The sharpening process, monitored using FIM images, which takes about 20 mins is stopped when the tip is terminated by a few atoms.

The current emitted by a single atom terminated nanotip was measured to be 2.15 mA at a tip voltage of 470 Volts. The magnification of the FEM images (hence the size of the effective source), was determined[15] and an upper limit on the protrusion radius of 10 Å was found. The over-all tip radius (the combination of the small protrusion and the supporting base) was determined from the Fowler-Nordheim plot shown in figure 1. The change in slope at voltages above 470 volts results from the turn on potential of the supporting base tip, and subsequent screening and space charge limited emission from the tip protrusion. The electron current distribution observed on the screen showed an approximately gaussian profile. Using the field emission intensity within 1/e of its maximum value gives the average source brightness at 470 V as $<B>$ = 3.3 x 10^8 A cm^{-2}.s r^{-1}.

Although the tip was physically terminated by only one or three atoms, at a voltage of 470 Volts, the fields are strong enough for other atoms near the tip apex to participate in field emission. At 470 Volts, the average current density on the tip surface is then 5.4×10^7 A/cm^2, well below the maximum current density for W. Figure 2 shows the average brightness measured using the above method plotted as a function of tip voltage, and the brightness normalized to 100 keV beam energy. $< B > = 7.7 \times 10^{10}$ A cm^{-2} sr^{-1} at $V_0 = 100$ kV for our nanotip operated in conjuction with such an ideal accelerator. This value may be compared with $< B > = 5 \times 10^8$ A cm^{-2} sr^{-1} for current cold field-emission (and zirconiated tungsten) sources, and $<B> = 10^6$ A cm^{-2} sr^{-1} for thermal tungsten filaments (both at 100 kV). An improvement of 2 orders of magnitude is apparent.

References:
1. H.W. Fink, IBM J. Res. Develop. **30**(5), 460 (1986); H. Fink,Physica Scripta **38**,260 (1988).
2. N. S. Garcia, J.J. Saenz, H.D. Raedt, J. Phys.: Condens. Matter **1**, 9931 (1989).
3. J. J. Saenz, N. Garcia, V. T. Binh, H. De Raedt, in Scanning Tunneling Microscopy and Related Methods, (Plenum Press, New York, 1990).
4. N. D. Lang, A. Yacoby, Y. Imry, Phys. Rev. Letts. **63**,1499 (1989).
5. E. Tekman, S. Ciraci, A. Baratoff, Phys. Rev. **42**, 9221 (1990).
6. M. K. Miller, D. A. Smith, Atom Probe Microanalysis , (Materials Research Society, Pittsburgh,1989).
7. A.P. Janssen, J.P. Jones, J. Phys. D: Appl. Phys., **4**, 118 (1971).
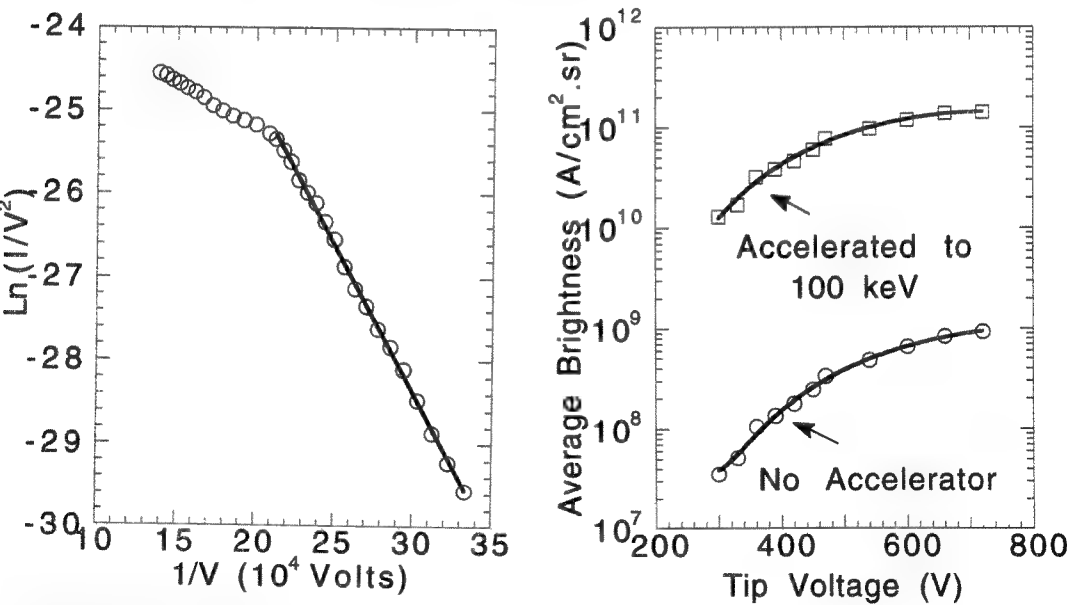8. M.R. Scheinfein, W. Qian, J.C.H. Spence, J. Appl. Phys. (in press, 1993).

Figure 1. Fowler-Nordheim plot of the nanotip (left).
Figure 2. Nanotip brightness measured as a function of tip voltage (right).

APPLICATIONS OF VIRTUAL OBJECTIVE APERTURE IN TEM

G.Y. Fan, T. Deerinck, C.C. Ahn†, J. Price, S.J. Young and M.H. Ellisman

San Diego Microscopy and Imaging Resource, U.C. San Diego, La Jolla, CA 92093
†Division of Engineering and Applied Sciences, Caltech, Pasadena, CA 91125

In a special imaging mode (B mode) available on a customized JEM-4000EX microscope[1], the objective mini lens (OM) is strongly excited so that the back focal plane of the objective lens (OL) is imaged onto the plane of the selected-area aperture (SA), Fig. 1, with a magnification of 3.2x. Thus the SA functions as a virtual objective aperture, the applications of which are summarized below.

1. Improving contrast in imaging thick sections of biological specimens.
The increased inelastic scattering in thick specimens results in image blur due to chromatic aberration present in the magnetic lenses. Such blur degrades image resolution and contrast. The energy loss spectrum in Fig. 2 (curve 1), from a 1 µm section of frog spinal ganglion, suggests that the inelastic contribution to images of this type of specimen is substantial. The use of an objective aperture (OA) can reduce some of the unwanted contributions (curve 2), but the SA in B mode is much more effective, as suggested by Fig. 1 and demonstrated by curved 3. The longitudinal magnification, which is the square of the lateral magnification, of the OM is the key to achieving this effect. Image contrast enhancement, due to both the energy filtering effect and the effectively smaller aperture size is particularly pronounced for samples thicker than 0.5 µm. Contrast improvement of up to 100%, as compared to that obtained with a same sized OA, has been achieved on some 2 µm sections.

2. Optical sectioning for thick (>1 µm) biological sections.
We are investigating the possibility of using a hollow-cone illumination device (HCID) to reduce the depth of field in electron microscopy. Due to the large semi-cone angle (>4°) required to achieve the kind of z resolution needed for optical sectioning, the OA must be removed so that the bright beam can pass through. In the B mode, the function of the OA can be assumed by the SA with the help of the image-shift coils working in synchronization with tilting coils to "de-scan" the beam, i.e., to bring the bright beam back to the optical axis. The images in Fig. 3, of a highly tilted (55°) holey carbon film, are acquired with and without the HCID switched on. The drastically reduced depth of field in Fig. 3b, acquired with a semi-cone angle of 4°, suggests that the HCID approach is promising.

3. Live stereo display with beam tilt.
The tilting angle achievable (>5°) with the strengthened tilting coils is enough to produced stereopairs with good 3-d effect. Again by using the B mode, the bright beam can be brought back to the optic axis with the image-shift coils and the SA used as virtual objective aperture to enhance contras. However, image aberrations, particularly astigmatism, introduced by such large beam tilts are serious. Preliminary tests indicate that astigmatism can be effectively compensated for with the current stigmators on this microscope for beam tilt up to ~±2.5°. Appreciable stereo effect can be achieved at these tilting angles. Fig. 4 shows a stereopair acquired with a beam tilt of ~±2.5°. Since beam tilt can be accomplished much faster than stage tilt, this opens up the possibility of on-line 3-d observation in electron microscopy. Due to the large number of deflectors (including the stigmators) that need be set for each beam tilt, switching between the two tilts by sending these values through the serial port from an external computer is possible but not practical due to the serial transmission speed (4800 baud). Our approach is to store the deflector settings in two User Memory channels (standard feature of the JEM-4000EX) and to switch between the two settings via external control. Initial tests indicate that because of the time required by the microprocessor to load the values and for beam settling, a rate of 1 Hz is practical. Faster rates should be achievable by direct analog control of the deflectors [2].

1. Neil Rowland et at, Proc. Ann. MESA Meeting (1992) 1040.
2. Supported by NIH National Center for Research Resources grant RR04050 to MHE.
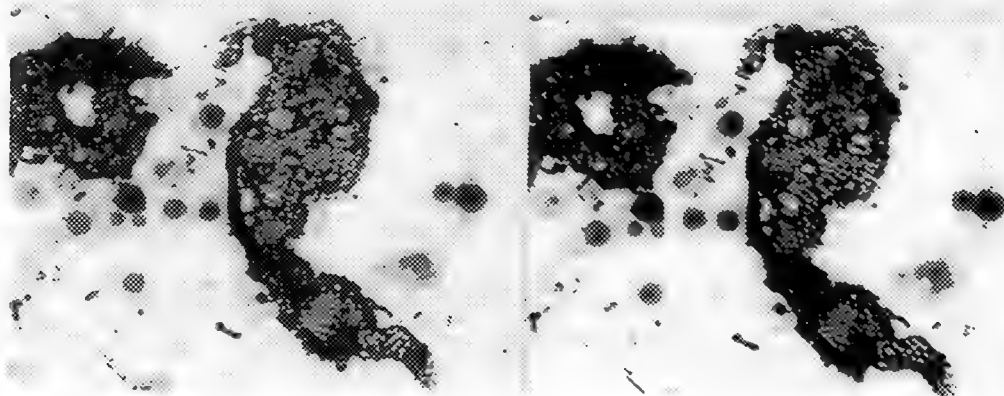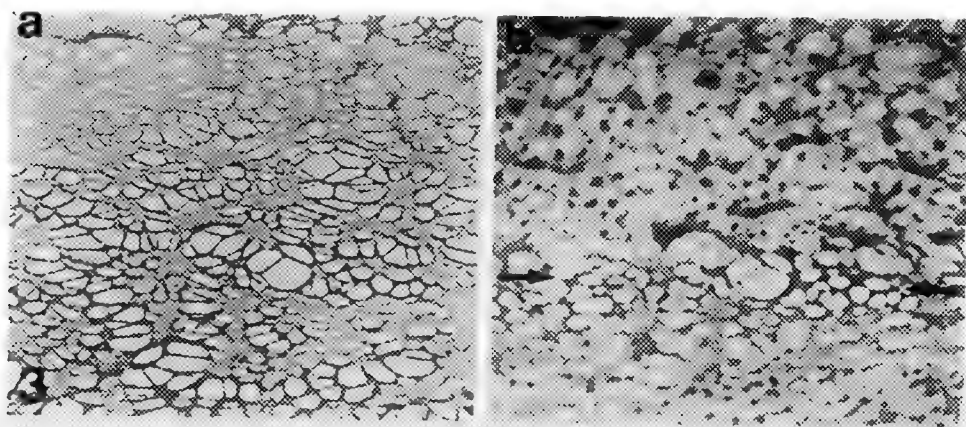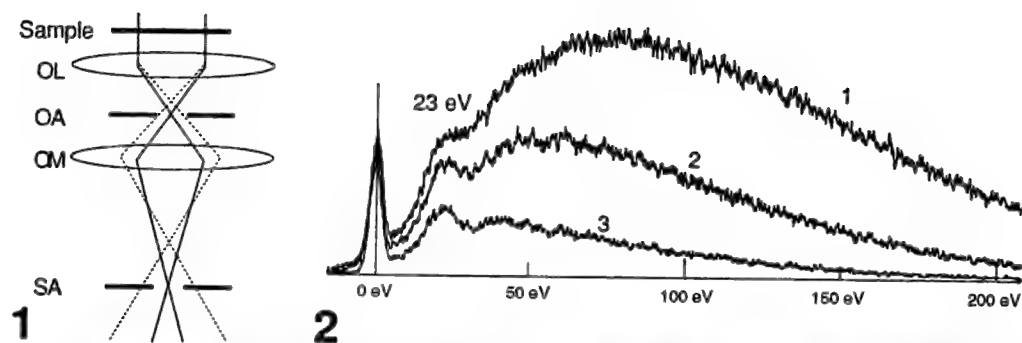
FIG. 1.--Schematic illustration of the energy filtering effect of SA in B mode. Solid and dotted lines indicate the optical path of elastically and inelastically scattered electron, respectively.
FIG. 2.--Energy loss spectra of a 1 μm section of frog spinal ganglion, B mode. (1) without any aperture, (2) with a 10 μm OA only and (3) 10 μm SA only, 200 kV, Gatan serial EELS.
FIG. 3.--Images of a holey carbon film tilted 55°, (a) without and (b) with a hollow-cone illumination.
FIG. 4.--Stereopair of the frog spinal ganglion Golgi apparatus, acquired with a beam tilt of ~±2.5°.

635

THE NSLS X-1AL SCANNING X-RAY MICROSCOPE

Chris Jacobsen[1], Janos Kirz[1], Steve Lindaas [1], Sue Wirick[1], Xiaodong Zhang[1], Shawn Williams[2], Erik Anderson[3], Dieter Kern[4], and Harald Ade[5]

[1]Department of Physics, SUNY at Stony Brook, Stony Brook NY 11794-3800; [2]Biology Department, Brookhaven National Laboratory, Upton NY 11973; [3]Center for X-ray Optics, Lawrence Berkeley Laboratory, Berkeley, CA 94720; [4]IBM T.J. Watson Research Center, Yorktown Heights, NY 10598; [5]North Carolina State University, Raleigh, North Carolina 26795

Soft x rays are well suited to the study of low-Z elements in 0.1–10 μm thick specimens. A variety of soft x-ray microscopes are now under operation[1], several of which achieve image resolutions[2] of 0.03–0.1 μm. Scanning x-ray microscopes offer some desirable charactistics: they are able to operate in a variety of imaging modes, including transmission, luminescence, dark field, and photoemission, and they enable minimum dose imaging by utilizing highly efficient photon counting detectors and placing moderate efficiency optics between the source and specimen rather than between specimen and detector.

The NSLS X-1AL scanning x-ray microscope uses an undulator at the National Synchrotron Light Source at Brookhaven National Laboratory as a tunable, high-brightness soft x-ray source. Monochromatized, spatially coherent illumination is focussed by a Fresnel zone plate fabricated using electron beam lithography. The sample is scanned through the 0.055 μm Rayleigh resolution focal spot using stepping motors (for large scans) and linearized piezos. Transmission images of e-beam-fabricated test patterns show that the microscope performance is at the diffraction limit of the optics used (Fig. 1).

Because of the high intrinsic contrast of organic materials relative to water at photon energies between the carbon and oxygen K-edges, the microscope is able to image wet, thick biological specimens at high resolution (fixation and staining are not required but may be advantageous for certain studies). These capabilities allow for studies of subcellular structure and for quantitative mass mapping[3]. By taking images at photon energies in the vicinity of an absorption edge, one can map the elemental concentration of mineralized calcium and the chemical bonding of carbon in both biological[4] and materials science[5] samples. Photoluminescence can be used to locate dye-loaded latex spheres, and efforts to use other dye-tagging methods are underway. These and other applications of the instrument will be described, as will anticipated future capabilities.

1. A. Michette et al., eds., **X-ray Microscopy III** (Springer-Verlag, Berlin, 1992).

2. C. Jacobsen et al., *Ultramicroscopy* **47**, 55–79 (1992).

3. S. Williams et al., these procedings.

4. X. Zhang et al., these procedings.

5. H. Ade et al., these procedings.

6. Supported by the NSF under grants DIR-9005893 and BIR-9112062, and the Office of Health and Energy Research, Department of Energy, under contract DE-FG02-89ER60858.
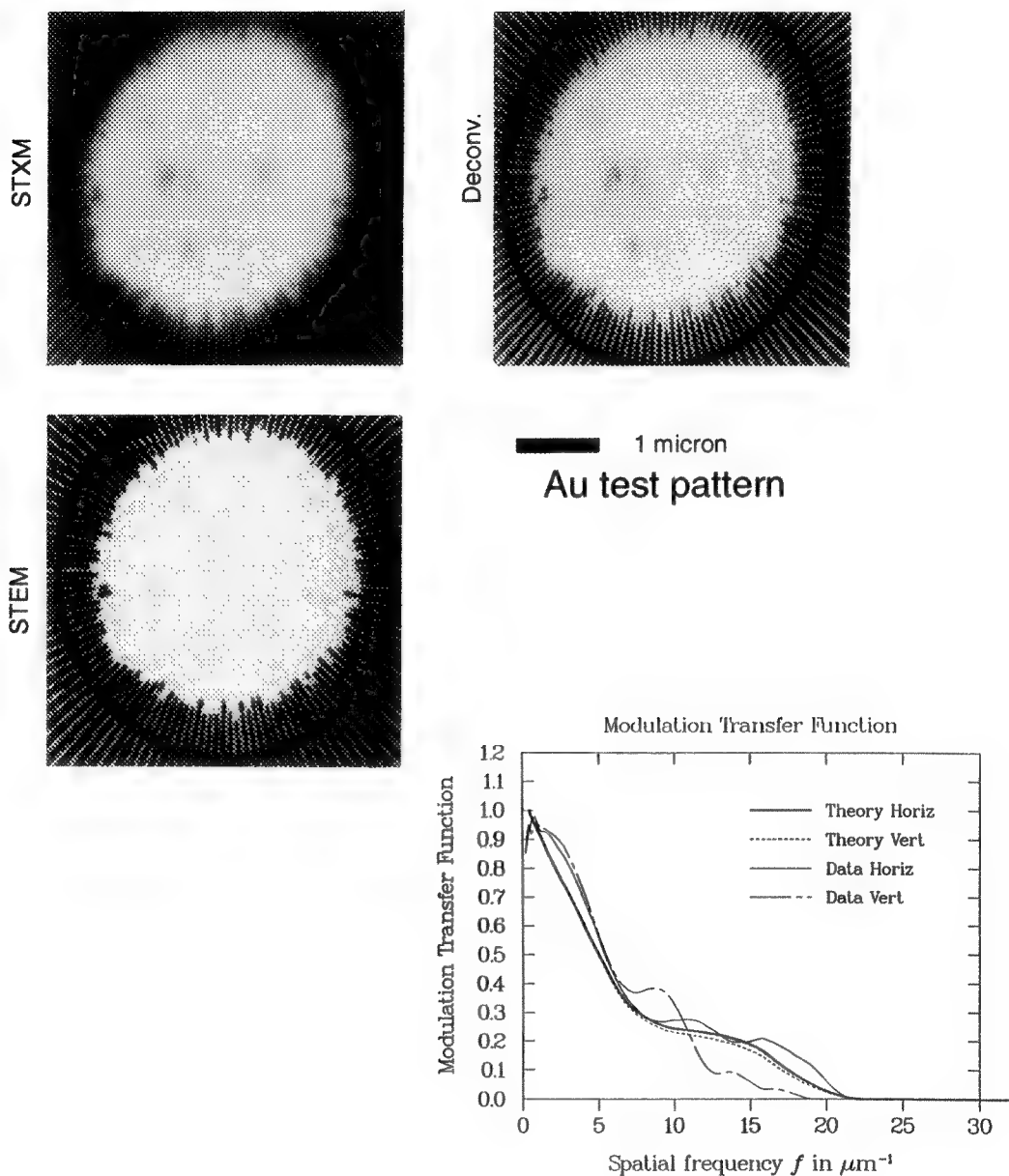
FIG. 1. Scanning transmission x-ray microscope (STXM) image of a electron-beam-fabricated Au test pattern with 36 nm minimum feature size. At upper left is shown the raw STXM image, at lower left is shown an STEM image of the test pattern, and at upper right is shown the result of deconvolving the theoretical point spread function from the image. The figure at bottom shows a comparison between the theoretical and measured modulation transfer functions, showing good contrast to spatial frequencies of 15 μm^{-1} or for features of size 33 nm.

A LINEAR-FIELD SCANNING-FORCE MICROSCOPE: APPLICATION TO X-RAY GABOR HOLOGRAPHY

Steve Lindaas[1], Chris Jacobsen[1] and Malcolm Howells[2]

(1.) Physics Department, State Univ of New York at Stony Brook, Stony Brook, NY 11794-3800.
(2.) Advanced Light Source, Lawrence Berkeley Laboratory, Berkeley, CA 94720

We have built a linear field Scanning Force Microscope to readout x-ray Gabor holograms recorded in photoresist. A field linearity yielding one half or less pixel registration error (for $10-50$ nm pixel sizes) across the scanned hologram is needed so that the resulting reconstruction is not significantly degraded. The desire for a large $(75\,\mu m)^2$ and linear scanning field necessitated designing our own stage since these conditions could not be met commercially.

Gabor holography is well positioned to exploit flash x-ray sources, such as x-ray lasers and free electron lasers, as well as ultra-bright third generation synchrotron sources as a sub-50 nm resolution imaging technique for biological samples. Gabor holography requires no optics (except for a monochromator with $\lambda/\Delta\lambda \sim 500$) and no sample prefocusing since the image is focused in the reconstruction process. Furthermore, sample alignment is eased since the area of illumination can be quite large. In fact, Gabor holography can be used to image large fields with multimode sources with the resulting numerical aperture, and hence resolution, being limited by the size of a single mode. However, Gabor holography is not a real time technique so there is no rapid feedback to improve the immediate experiment. In addition, the resolution has been limited by limitations in the reconstruction methods[1,2]. Our previous work had a resolution limit imposed by the method used to extract the hologram information from the photoresist recording medium. Figure 1 is a reconstructed hologram of zymogen granules which was read out using a Transmission Electron Microscope. Spiral distortions in low-magnification images with a commercial TEM, cause aberations in the reconstructed hologram[2] limiting the resolution to 56 nm.

To overcome this limitation we have built a Scanning Force Microscope with a linear scanning stage offering < 20 nm resolution over a $(70\,\mu m \times 70\,\mu m)$ field and a goal of field linearity of 1 part in 10,000. At present we operate the Scanning Force Microscope in contact mode though we ultimately plan to operate in noncontact mode. To test the stage linearity we scanned a holographic grating. Figure 2 is a picture of the grating with straight lines plotted on top. Visual inspection of this picture indicates good linearity. We are continuing to characterize the stage as well as obtain new hologram reconstructions. We will describe the design of the Scanning Force Microscope and discuss results obtained using it.

[1] D. Joyeux and F. Pollack, **OSA Proceedings on Short Wavelength Coherent Radiation: Generation and Applications**, R.W. Falcone and J. Kirz, eds. (Optical Society of America, Washington DC), Vol. **2**, (1988), pp. 295-302.

[2] C. Jacobsen, M. Howells, J. Kirz, and S. Rothman, "X-ray holographic microscopy using photoresists", *J. Opt. Soc. Am. A* **7**, No. 10, (1990), pp. 1847-1861.
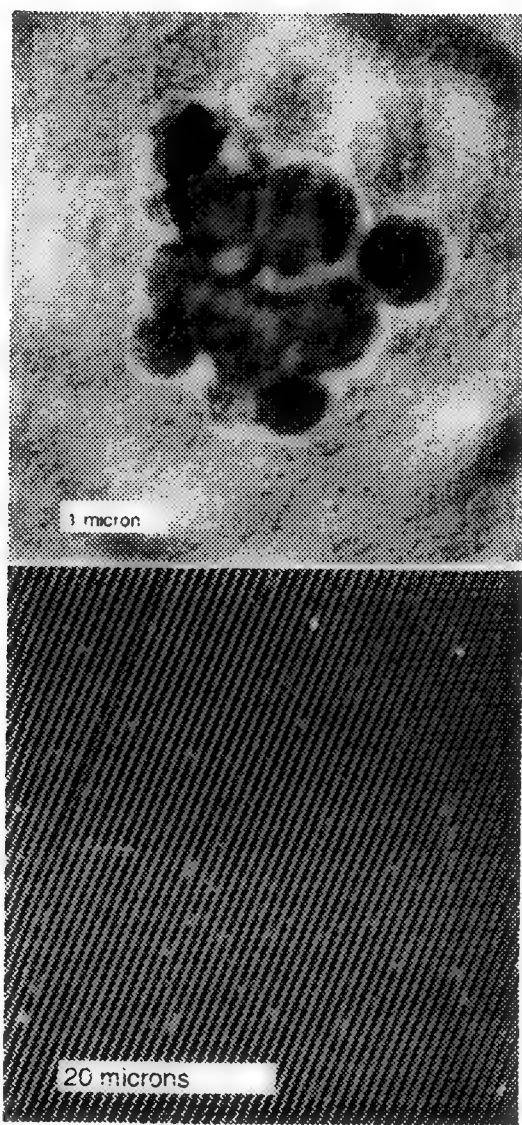
Figure 1. X-ray Gabor hologram of zymongen granules recorded at a wavelength of 1.8 nm. The hologram was recorded in photoresist (PMMA) and read out using a TEM which limits resolution to 56 nm.

Figure 2. Holographic grating scanned with a $(50\,\text{nm})^2$ pixel size and 1024×1024 pixels. Straight lines are plotted over the picture to determine the stage linearity. No deviation from the straight lines is visible indicating good linearity.

639

MODIFICATIONS OF A JEOL 2000EX TEM FOR IN SITU SURFACE STUDIES

Michael T. Marshall, Xianghong Tong, and J. Murray Gibson

Materials Research Laboratory, University of Illinois,
104 South Goodwin Avenue, Urbana, IL 61801

We have modified a JEOL 2000EX Transmission Electron Microscope (TEM) to allow in-situ ultra-high vacuum (UHV) surface science experiments as well as transmission electron diffraction and imaging. Our goal is to support research in the areas of in-situ film growth, oxidation, and etching on semiconducter surfaces and, hence, gain fundamental insight of the structural components involved with these processes. The large volume chamber needed for such experiments limits the resolution to about 30 Å, primarily due to electron optics . Figure 1 shows the standard JEOL 2000EX TEM. The UHV chamber in figure 2 replaces the specimen area of the TEM, as shown in figure 3. The chamber is outfitted with Low Energy Electron Diffraction (LEED), Auger Electron Spectroscopy (AES) , Residual Gas Analyzer (RGA), gas dosing, and evaporation sources. Reflection Electron Microscopy (REM) is also possible. This instrument is referred to as SHEBA (Surface High-energy Electron Beam Apparatus).

The UHV chamber measures 800 mm in diameter and 400 mm in height. JEOL provided adapter flanges for the column. The UHV chamber provides a clean environment for surface studies via a 200 l/s Thermionics ion getter pump with a 2000 l/s titanium sublimator pump. Differential pumping separates the chamber from the microscope to obtain a base pressure of 5×10^{-10} τ , after baking. The chamber is supported by heavy stainless steel rods mounted on the chassis of the TEM. Pneumatic vibration isolation pads are used in parallel with the manufacturers isolation system. Lead sheet was formed onto the chamber and peripheral areas to protect the user from x-rays generated by the 200 keV electron beam.

The sample manipulator shown in figure 4 allows x,y, and z, motion as well as two directions of tilt, therefore accommodating the various detector geometries. To remove surface contaminants, sample heating by direct current to about 2000 °C is possible. The temperature is reported by a thermocouple. To maintain UHV conditions, samples are loaded through an airlock system. The sample is mounted onto a cartridge which is delivered to the manipulator via a long transfer rod. The airlock uses a sizable chamber that can be set up for "dirty" depositions. The sample may then enter the UHV atmosphere without removal from the vacuum system.

The introduction of the chamber required other significant modifications to the TEM. The electron gun and upper column are now pumped by a 60 l/s Varian ion pump. The lower column is pumped with the original JEOL ion pump that was previously responsible for the entire microscope. The camera is diffusion pumped as before. A Leybold 150 l/s turbomolecular pump (TMP) is used for prepumping. Figure 5 shows the pumping network. As a consequence to adding the chamber, we were not able to use the pneumatic gun lift, so another mechanism for removing the gun for filament changes was required. The pneumatic gun lift also applies several hundred pounds of force that must be maintained for gun stability. The fixture shown in figure 6 creates this force through the reaction of a spring against the column and may be used to lift the gun as well.
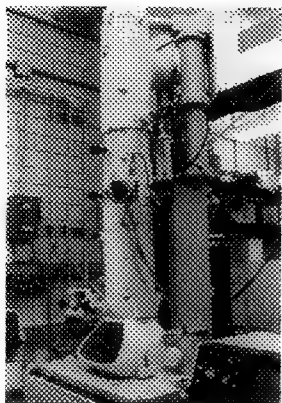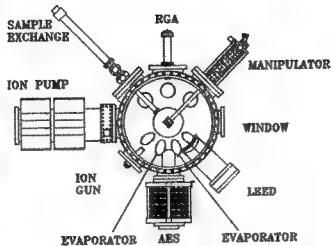
Fig. 1. Unmodified JEOL 2000EX TEM.

(top view)

Fig. 2. UHV Chamber with typical detector placement.
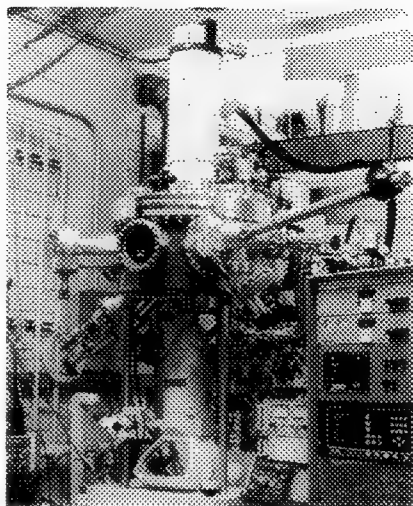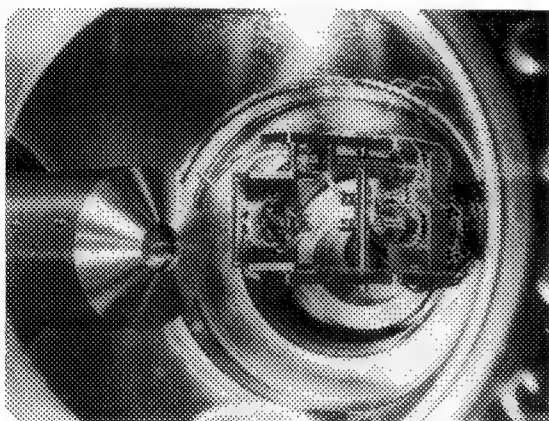

Fig. 3. Surface science UHV chamber installed.

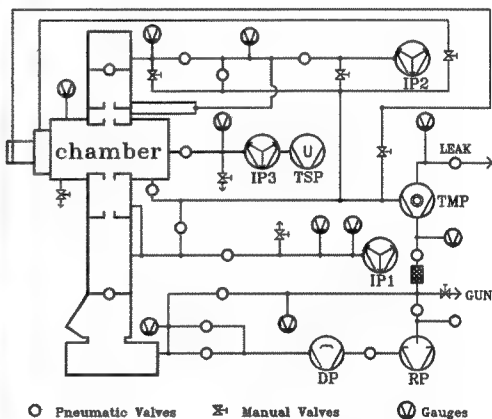Fig. 4. Specimen manipulator seen with retractable Auger detector.

Fig. 5. Pumping network.

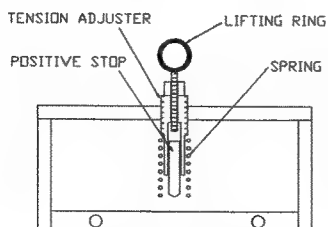

Fig. 6. Gun lifting/pressure device.

641

SINGLE-ELECTRON SENSITIVITY WITH A LENS-COUPLED CCD CAMERA

G.Y. Fan, Bruce Mrosko[*] and Mark H. Ellisman

San Diego Microscopy and Imaging Resource and [*]OLR Machine Shop
Dept. of Neurosciences, University of California at San Diego, La Jolla, CA, 92093-0608, USA

A lens coupled CCD camera showing single electron sensitivity has been built for TEM applications.[1] The design is illustrated in Fig. 1. The bottom flange of a JEM-4000EX microscope is replaced by a special flange which carries a large rectangular leaded glass window, 22 mm thick. A 20 μm thick layer of red phosphor is coated on the window, and the entire window is sputter-coated with a thin layer of Au/Pt. A two-lens relay system is used to provide efficient coupling between the image on the phosphor scintillator and the CCD imager. An f1.0 lens (Goerz optical) with front focal length 71.6 mm is used as the collector. A mirror prism, of the Amici type, is used to "bend" the optical path by 90° to prevent X-rays which may penetrate the leaded glass from hitting the CCD detector. Images may be relayed directly to the camera (1:1) or demagnified by a factor of up to 3:1 by moving the lens assembly. The CCD is a thinned, back-side illuminated, enhanced and AR coated 1kx1k Tektronix chip, with pixel size of 24 x 24 μm^2 and a quantum efficiency of ~80% at 600-650 nm wavelength range. This sensitivity is more than double that of the standard front-side illuminated CCD devices (<40%, Tektronix CCD data sheet). The particular grade 1 chip used in this camera was hand-selected by Tektronix, and has no defects. The CCD chip was packaged by Photometrics in a vacuum-sealed CH250 camera head with a 14-bit A/D converter running at 200 kHz (CE200A). The full well capacity of this chip was measured by both Tektronix and Photometrics to be 576 k CCD electrons.

Fig. 2 shows a high resolution image of phosphate collected using this camera system. The geometric distortion of the lens coupling system is very small (~1%), as demonstrated by the image in Fig. 3, of a square-grid graph paper taken before the system was installed on the microscope. Fig. 4 shows a set of images of a 0.25 μm section of a myelinated axon acquired with a high gain mode. The image in Fig. 4a has a dose of 0.45 e$^-$/pixel on the CCD. The fact that a faint image is visible with an average of less than one electron per pixel indicates that single electron sensitive is achieved with this lens configuration.

Lens coupling affords many advantages over the fiber-optical (FO) coupling currently endorsed by the commercial slow scan CCD camera systems,[2] as summarized below: (1) Effective shielding of X-rays due to the optical path bending and the lead baffle; (2) No chicken-wire patterns or Newton rings, as these are inherent problems of FO bundles and imperfect refraction index matching to the CCD chip; (3) Easier to shutter, since a shutter can be installed easily in the lens assembly, while in FO coupling the only choice is to shutter the elelcrton beam; (4) No interference with the microscope vacuum system, as the assembly is entirely outside of the microscope vacuum, whereas in FO coupling the entire CCD-fiber-optic coupling unit is cooled and is inside the microscope vacuum, and must be protected from ice formation when venting the microscope, and (5) Expandability, for exmaple lens or CCD components may be replaced to better suit a particular type of microscopy. This is not case in coupling rigid FO to the fragile and expensive CCD chips. The drawbacks of lens coupling are its bulkier size and a lower collection efficiency. But as has been shown, the latter does not represent a fundamental limitation, as it can be compensated by using more sensitive back-thinned devices and by careful matching of the scintillator emission to the peak efficiency of the CCD detector.[3]

References

1. G.Y. Fan and M.H. Ellisman, submitted to Ultramicroscopy (1993).
2. P.E.Mooney, G.Y.Fan and O.L.Krivanek. *Proc. ICEM* (1990) 164.
3. Supported by NIH grant RR04050 and a grant from the Human Frontiers of Science to M.H.E..
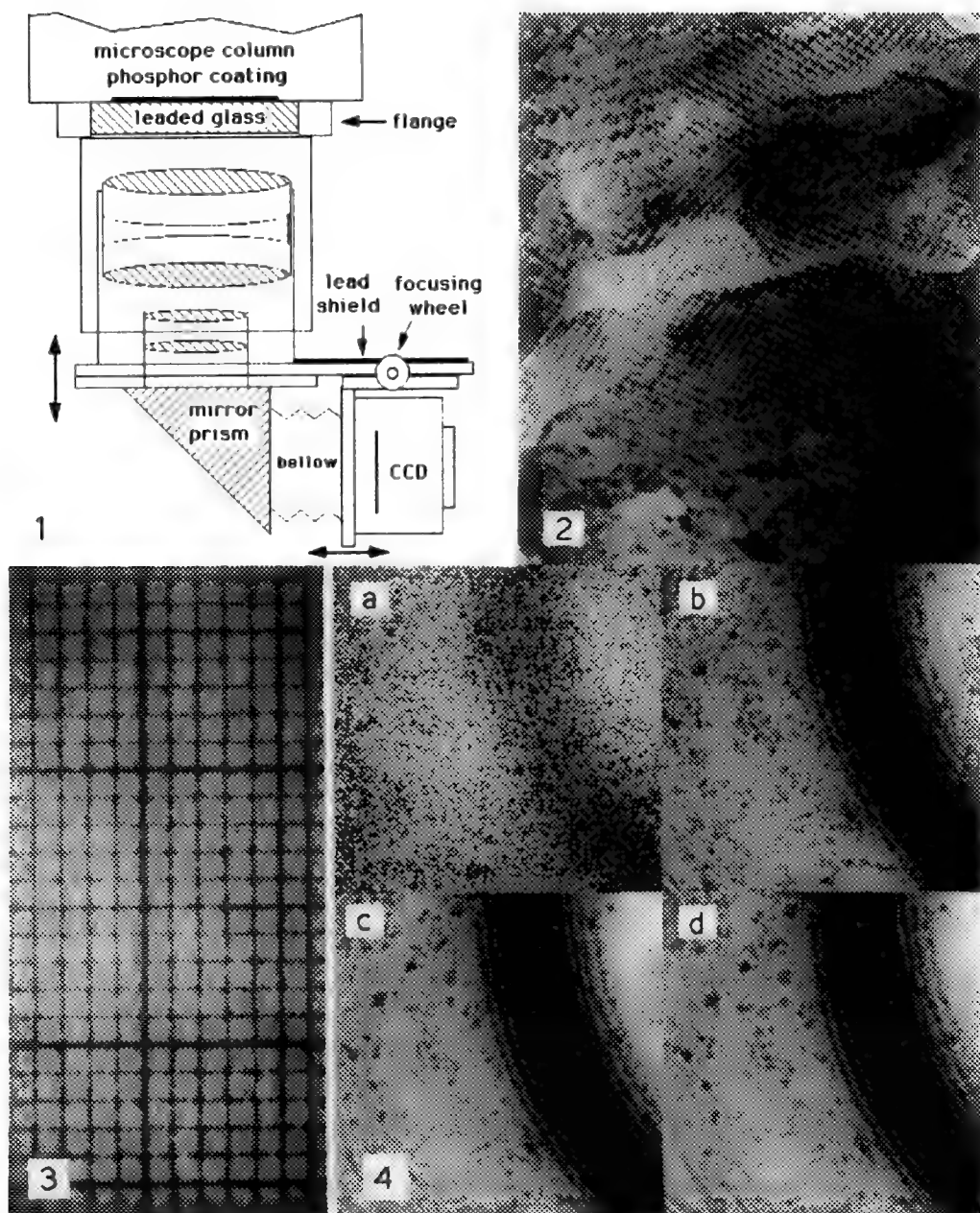
FIG. 1.--Design of a lens-coupled slow scan CCD camera for TEM applications. The entire assembly is enclosed in a lead-lined box for 400kV applications.

FIG. 2.--High resolution image of phosphate taken using this camera. Fringe spacing = 4.8Å.

FIG. 3.--Distortion test. Object : 1 mm square grid graph paper. Image size: 512x1024, half field.

FIG. 4.--Images of a 0.25 μm section of myelin. Exposures are 0.1, 1, 10 and 100 seconds for (a), (b), (c) and (d), corresponding to a dose of 0.45, 4.5, 45 and 450 e⁻/pixel on CCD, respectively.

643

OPTIMIZATION AND TESTING OF AN IMAGING ENERGY SPECTROMETER FOR HIGH-RESOLUTION ELECTRON-ENERGY-LOSS MICROANALYSIS

X.G. Jiang

Ontario Cancer Institute and Department of Medical Biophysics, University of Toronto,
500 Sherbourne Street, Toronto, Canada, M4X 1K9

Electron energy loss (EEL) microanalysis is a powerful technique for studying the chemical composition of a specimen and the distribution of each constituent.[1] The energy loss spectrum of the post-specimen electron beam, on which the technique is based, is obtained by the use of an energy spectrometer. In transmission electron microscopy, the most prevalent type of imaging energy spectrometer is the Prism-Mirror-Prism (PMP) design (Fig. 1).[2] It is compact in size and easy to align. For an acceptance half angle (β in Fig. 1) of 10 mradian, which corresponds to the full field of view of a modified Siemens 102 microscope of our laboratory, an experimental PMP spectrometer with a straight-faced magnetic prism has an energy resolution of 25 eV at the microscope operating voltage of 80 kV. This resolution has permitted ionization energies of different elements to be resolved, thus making the elemental microanalysis possible. However, a resolution of 25 eV is inadequate for resolving and possibly imaging with characteristic molecular energy losses, that are located in the 1.5-10 eV region of the electron energy loss spectrum. The present work has been to optimize the design, and hence the energy resolution of the PMP spectrometer, so that it can be used to study the feasibility of molecular microanalysis.

At a given acceptance half angle β, the resolution of a PMP spectrometer is mainly limited by the aperture aberrations of the magnetic prism on the level of the energy selecting slit. Previous studies have shown that in principle these aberrations can be minimized by appropriately curving the boundary faces.[3,4] To find the optimal facial curvatures of the magnetic prism, an iterative numerical procedure is used in the present study. First the magnetic field of the prism is calculated for a given combination of facial radii, then the focusing properties and the aperture aberrations are determined by tracing the incident electron rays through the spectrometer system. This routine is repeated systematically for different curvature combinations until the minimum in aberrations is reached.

Magnetic shunts are employed in the study to limit the fringing fields of the prism. As a result, the field around each circularly curved face can be considered to be rotationally symmetric, and the boundary element method developed by Kasper is then applied to the field determination.[5] The calculated fringing field on the median plane of the prism is given Fig. 2, together with the experimental data using a sensitive magnetometer of vibrating-loop type, especially designed for the measurements. The two sets of results agree with each other within 1% of the maximum field B_0.

The Bulirsch-Stoer extrapolation method is used for electron-ray tracing.[6] Steps are taken to reduce the computing time and to search for the optimal curvatures in a systematic fashion. It has been found that an energy resolution of 1.3 eV can be achieved for an acceptance half angle of 10 mradian, a factor of 18 improvement over that of an equivalent system with a straight-faced prism (Fig. 3).

Such an optimized spectrometer has been built. The cross sections of the electron beam after the first pass through the magnetic prism at equally spaced positions are in good agreement with computer simulated images (Fig. 4). Complete characterization of the system is now in progress.

References

1. F.P. Ottensmeyer, J. Ultrastructure Research (1984)88, 121.
2. R. Castaing et al, C. R. Acad. Sci. Paris (1962)255, 78.
3. H. Rose, Optik (1978)51, 305.
4. K.M. Adamson-Sharp, M.Sc Thesis (1980), University of Toronto.
5. E. Kasper, Optik (1987)77, 3.
6. J. Stoer et al, Introduction to Numerical Analysis, pp 458-460. Springer Verlag, New York 1980.

Fig. 1

Fig. 2

Fig. 3

Fig. 4
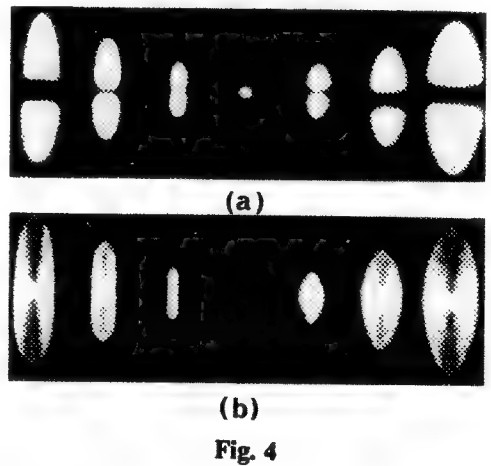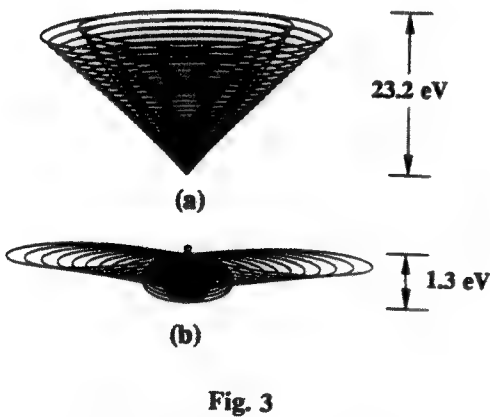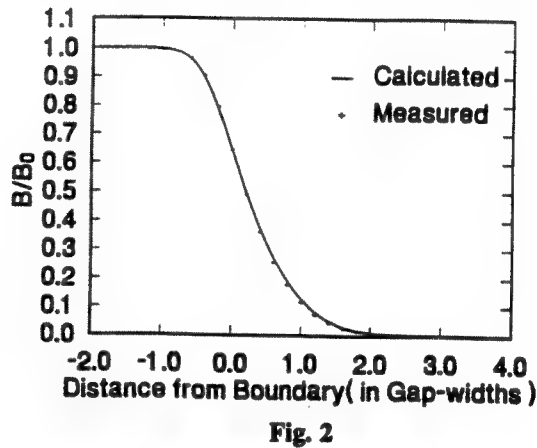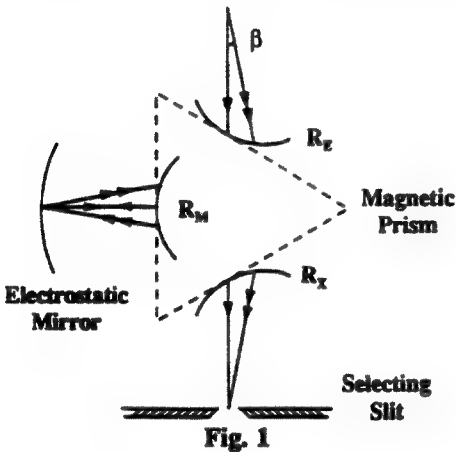
Fig. 1. Schematic diagram of PMP imaging energy spectrometer.
Fig. 2. Fringing field on median plane of magnetic prism.
Fig. 3. Computer simulated aberration figures for PMP spectrometer with (a) straight-faced prism or (b) optimally curved prism. (b) is enlarged by 6 relative to (a).
Fig. 4. (a) Experimentally recorded cross sections of electron beam after first pass through magnetic prism at evenly spaced positions. Size of central image is limited by resolution of florescent screen used. (b) Computer simulated cross sections at same locations.

645

COHERENT SOFT X-RAY SINGLE UNIT-CELL DIFFRACTION

Henry N. Chapman* and Rod Balhorn**

*Department of Physics, SUNY at Stony Brook, Stony Brook, NY 11794-3800
***Lawrence Livermore National Laboratory, Livermore, CA 94550

Following the basic ideas of x-ray structure analysis of single unit-cell specimens by Sayre it should be possible to determine the structure of weakly-scattering non-crystalline material from the radiation scattered from it, at a maximum resolution equal to half the wavelength of the radiation.[1,2] Therefore, in principle, it should be possible to determine structures to 1 nm resolution by soft x-ray diffraction at 2 nm wavelength. An imaging method based solely on diffraction should be an extremely powerful x-ray microscopy tool.

In order to determine the structure of the diffracting object however, the incident beam must be completely temporally and spatially coherent and the complex wave-field must be sampled across some surface at spatial frequency intervals of $1 / (2 * \Delta)$, where Δ is the resolution. Thus, a three-dimensional data set (a two-dimensional complex field) must be recorded to obtain the three-dimensional structure of the scatterer. In most cases, an area detector is used to determine the intensity of the wave-field, losing the phase information[3]. One general method of determining the phase of the wave-field is to use inversion procedures based on the Born approximation that the object scatters weakly. In this case, the far-field diffraction pattern is given by the Fourier transform of the object function, yet it is the squared modulus of the transform which is detected. In the absence of noise, and with the use of *a priori* information about the object, such as its support (the area in which the object is non-zero), it has been shown that the object function can be uniquely determined.[4,5] Methods used in macromolecular crystallography structure determination can also be employed.

Previous work has shown that it is possible to record diffraction patterns from microscopic non-crystalline objects, using a coherent high-intensity synchrotron x-ray source.[2,6] In particular, diffraction patterns of individual cells of Minutocellus polymorphus have been recorded with 1.8 nm x rays, showing spatial frequencies corresponding to a resolution of 7.0 nm in certain cases.[6] This technique has been developed further and has been used to study individual sonicated bull-sperm cells. (The sonication removes the tail and membrane from each sperm head.) Experiments have been performed at the beam-line X-1AS of the National Synchrotron Light Source at Brookhaven National Laboratory. This beam-line uses an undulator as a tuneable, high-brightness soft x-ray source, which is monochromatised with a grating. Spatial coherence was provided by a 15 μm diameter pinhole placed approximately 70 mm from the sample. Samples were mounted on thin silicon nitride windows, coated with a radiachromic nylon film which would record the position of the x-ray illumination on the sample. The diffraction patterns were recorded on soft x-ray photographic film, at a distance of 25 mm from the sample.

In addition, scanning x-ray micrographs, at a wavelength of 3.9 nm, were taken of the same regions of the samples that were exposed in the diffraction experiments. The NSLS X-1AL scanning transmission x-ray microscope (STXM) was used for this.[7] These micrographs could be used to determine the support function of the cell, which could then be used as information for a phase-retrieving algorithm. Shown in Fig. 1 is the STXM image of a sperm head and some non-organic fragments. In Fig. 2 are diffraction patterns obtained from two regions labelled on Fig. 1, with each region centred approximately 10 μm apart. Fig. 2(b) shows diffraction from an area which contains, as far as we can ascertain, a sperm head only. This pattern shows a rectangular lattice of points, suggesting some regularity of the internal structure of the sperm head. The maximum spatial frequency recorded in the pattern corresponds to a resolution of 80 nm. We are still uncertain as to the exact origin of the diffraction, but we have clearly shown that it is possible to record soft x-ray diffraction patterns from microscopic objects in accordance with previous work.

As yet we have not attempted to phase a diffraction pattern to reconstruct the object function. We do plan to do this, utilising high-resolution STXM images to give as much *a priori* information as possible, and employing direct detection by a CCD chip, which has the advantages of extreme sensitivity, linearity, high-dynamic range, and provides digital output.[8]

References

1. D. Sayre, Acta Cryst., **5**, 843 (1952).
2. D. Sayre, in *Proceedings of the 1990 Erice School on Direct Methods in Solving Crystal Structures*, ed. H. Schenk, Plenum 1991, p. 353.
3. In holography, where the scattered wave is interfered with a reference wave, the phase can be measured, but again this is done with a two-dimensional detector. Although some three-dimensional imaging is achieved longitudinal resolution is traded off against transverse resolution.
4. J. R. Fienup, J. Opt. Soc. Am. A, **4**, 118 (1987).
5. M. H. Maleki *et al.*, J. Opt. Soc. Am. A, **9**, 1356 (1992).
6. D. Sayre *et al.*, in *X-Ray Microscopy II*, Springer Series in Optical Sciences Vol 56 (1988).
7. C. Jacobsen *et al.*, these proceedings.
8. Supported by the Office of Health and Energy Research, Department of Energy, under contract DE-FG02-89ER60858. We gratefully acknowledge the expert help of David Sayre in performing these experiments and discussions with Janos Kirz.
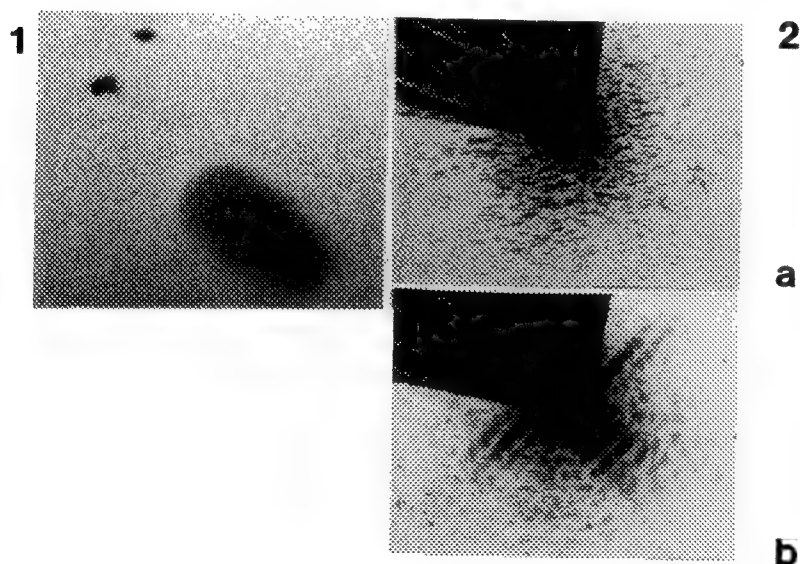
FIG 1: STXM image of a sonicated sperm-head and some non-organic debris, recorded with 3.9 nm x rays. Scale-bar = 5 μm.

FIG 2: Diffraction patterns recorded by illuminating regions of the sample shown in Fig. 1 with coherent 2.3 nm x rays: *(a)* shows the diffraction of a non-organic fragment (region *a* on Fig. 1) and *(b)* shows the diffraction of a sonicated sperm head (region *b* on Fig. 1). The top-left quadrant of each diffraction pattern is superimposed with strong scattering from the spatial-filter pinhole and from the frame of the silicon nitride window. Scale-bar = 400 μm.

CHEMICAL CONTRAST IN SCANNING TRANSMISSION X-RAY MICROSCOPE

X.Zhang,[1][*] H.Ade,[3] C.Jacobsen,[1] J.Kirz,[1] S.Lindaas,[1] V.Oehler,[1] S.Williams,[2] and S.Wirick [1]

1 Physics Dept., SUNY @ Stony Brook, Stony Brook, NY 11794
2 Biology department, Brookhaven National Lab, Upton, NY 11973
3 Physics Dept., North Carolina State University, Box 8202, Raleigh, NC 27695

The Scanning Transmission X-ray Microscope (STXM) on the X1A undulator beamline, at the National Synchrotron Light Source, BNL, has been used for imaging various wet, unstained biological samples at 55 nm Rayleigh resolution.[2] The microscope's Modulation Transfer Function was measured and agrees well with theoretical calculations, confirming the performance of the microscope as designed.[1,2] The microscope is operated mainly in direct imaging mode where x-rays of fixed energy are diffractively focused to a microprobe and the sample is scanned in two dimensions. By varying the x-ray energy while keeping the beam focused to one spot on the sample enables us to get localized chemical composition of the sample from the absorption spectra in an area smaller than 0.2 by 0.2 micron at present. The spatial distribution of the chemical compositions can be obtained with a spacial resolution of 55 nm by imaging at absorption maxima of specific chemical bonds.

The chemical sensitivity of the X-ray Absorption Near Edge Structure (XANES) provides a new contrast mechanism for organic system imaging.[3] The well-known shifts between π^* resonance from different chemical states have been used to distinguish different components.[3] Proteins and DNA, which are important components of biological samples, have different concentration of C=C, C=N and C=O bonds that give rise to different intensity of the π^* resonance in XANES. The different environment in protein and DNA of the same chemical bonds shifts the π^* resonance positions to different energies. The expected difference between the XANES spectra of bovine serum albumin (BSA), and DNA near the carbon absorption edge taken by the STXM has been observed (figure 1(a)). we have applied this difference to image chromosomes at different energies to obtain the absorption contrast dominated either by DNA or by protein, as illustrated in Figure 1(b). Quantitative mapping of DNA and Protein within biological samples is under development.

Since XANES spectra are chemical sensitive, they can be used to study chemical reactions. As an initial experiment, we have monitored changes on PMMA(polymethyl methacrylate) structure caused by x-ray damage using Carbon edge XANES. PMMA has been widely used as an x-ray or electron resist by breaking chains to reduce the molecular weight of the polymer, leading to higher solubility. It is well known that besides the chain scission process, there is also the process of cross linking which increases the molecular weight. The net development rate of exposed PMMA will depend on the competition of the two processes. Quantitative studies of the two processes can be done using XANES since the chain scission results in a decrease of C=O bond concentration while the cross linking increases the concentration of the C=C bonds. Both bonds have strong signals at the C edge, and the two processes can be studied quantitatively. Figure 2 shows chain scission process and the cross linking process with soft x-ray doses.

In summary, the chemical sensitivity of the XANES and the high resolution of the microscope allow us to obtain quantitative information of different chemical states and to distinguish systems with similar elemental compositions. It also provides capabilities to study changes in biological samples and other systems.[4]

References
1. C.Jacobsen et al, Diffraction-limited imaging in a scanning transmission x-ray microscope. Optics Communications 86(1991) 351-364.
2. C.Jacobsen et al, These proceedings.

3. H.Ade et al, *Chemical contrast in x-ray microscopy and spatially resolved XANES spectroscopy of organic specimens. Science, 6 November 1992, Volume 258, pp. 972-975.*
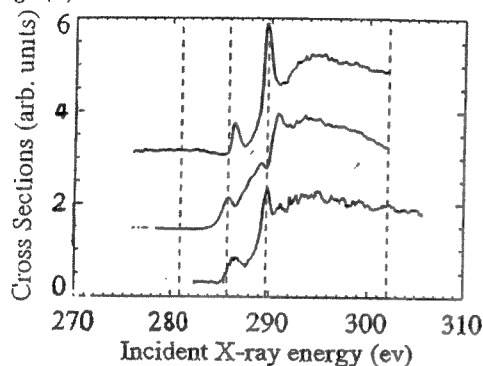
Fig.1(a)   Fig. 2
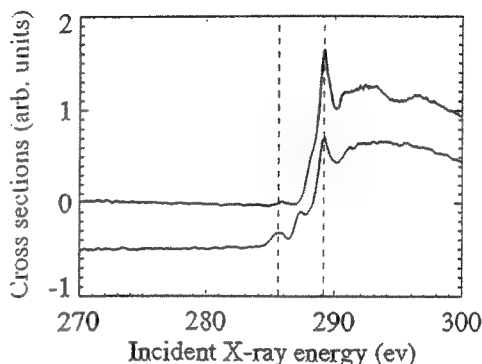
Fig.1(a) top: spectrum of bovine serum albumin (BSA), center: Spectrum of DNA, bottom: spectrum of V.faba chromosome.

Fig.2. top: the C-XANES spectrum of PMMA before x-rays exposure where the peak coming from C=O (289.2 ev) is strong and there is no obvious peak from C=C (285.6 ev) bond. bottom: C-XANES spectrum of PMMA after 560 MRad 302.0 ev x-ray dose. The peak from C=O bond is reduced which characterizes the chain scission while the peak from C=C bond is stronger, showing substantial cross linking.

Fig.1(b)
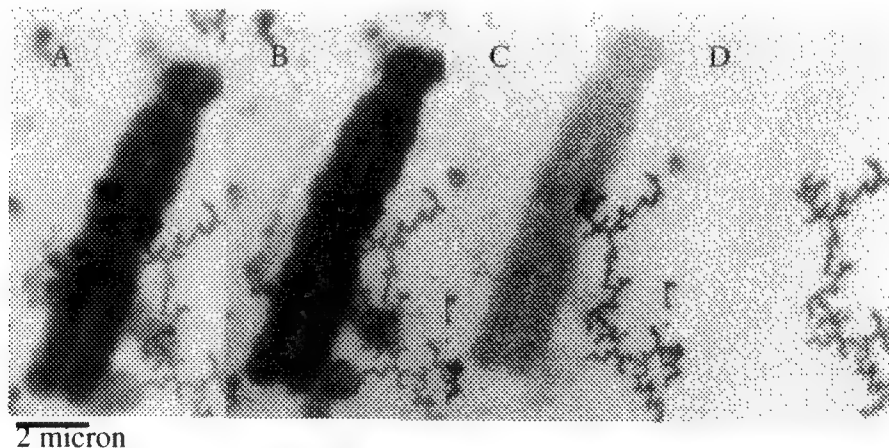
Fig.1(b) images of the same V.faba chromosome taken at different energies corresponding to different absorption peaks, image A is taken at above the absorption edge of carbon(302.0 ev), image B is taken at the absorption peak of protein(289.8 ev), image C is taken at the DNA absorption peak(285.9 ev), Image D is taken below the C-edge(281.0 ev) where the contrast between water and biological sample is poor.

SECOND-GENERATION SCANNING PHOTOEMISSION MICROSCOPE AT THE NATIONAL SYNCHROTRON LIGHT SOURCE

Cheng-Hao Ko,[*] Janos Kirz,[*] Harald Ade,[**] Erik Johnson,[***] Steven Hulbert,[***] Erik Anderson,[****] and Dieter Kern[*****]

[*] Department of Physics, SUNY, Stony Brook, NY 11794
[**] Department of Physics, NCSU, Rayleigh, NC 27695
[***] National Synchrotron Light Source, Brookhaven National Laboratory, Upton, NY 11973
[****] Center for X-ray Optics, Lawrence Berkeley Laboratory, CA 94720
[*****] IBM T. J. Watson Research Center, NY 10598

We are commissioning a new generation scanning photoemission microscope (X1-SPEM II) at beamline X1A of the National Synchrotron Light Source (NSLS). Our first generation scanning photoemission microscope (X1-SPEM I) was the first to achieve submicron resolution.[1] One of the major improvements is the replacement of the home-made single pass cylindrical mirror analyzer with a high energy resolution, multi-channel Hemispherical Sector Analyzer (HSA). The alignment scheme for the optical elements has also been redesigned. The advantages of these two major improvements will be discussed.

A photoemission microscope requires a high brightness source and a good focusing scheme. In most cases, a monochromator is placed between the photon source and the focusing optical elements. Our X1-SPEM uses the soft x-ray undulator at the NSLS as a high brightness source. A Fresnel zone plate is coherently illuminated by the monochromatic beam selected by the spherical grating monochromator (250-800 eV range) to form a microprobe, less then 0.2 μm in size.[2] An order sorting aperture between the zone plate and the specimen is used to stop the unwanted diffraction orders and transmit only the first order of focused beam. The flux in the focal spot is in the 5×10^8 to 5×10^9 photons/sec range. The electron energy analyzer is used to take photoelectron spectra within the focused spot. Chemical imaging is accomplished by a two dimensional scan with the energy window of the analyzer tuned to a photopeak in the spectrum. Sample current (total electron yield) and transmitted flux (for samples less then a few μm thick) can also be used to form images.[3]

One of the major applications of X1-SPEM is to generate XPS elemental and chemical state maps. This technique can be used to map chemical core-level shifts. To discern a chemical shift using the first generation system, multiple scans corresponding to different features in the spectrum have to be taken. By using a multi-channel HSA, the new instrument (X1-SPEM II) is able to simultaneously acquire multiple XPS images by collecting a photoelectron spectrum at each pixel of the image (Fig. 1). Sixteen images are formed in one scan with each image equally separated in photoelectron energy. This not only eliminates image registration problems but also greatly reduces the time required to form maps of chemical shifts. Energy resolution as well as count-rate are significantly improved.

X1-SPEM II is also designed to acquire near edge x-ray absorption spectra (NEXAFS) with a spatial resolution less then 0.2 μm over a 400 eV photon range without switching zone plates for different photon energies. Since the focal length of the zone plate is proportional to the photon energy, the focusing adjustment must be appropriately synchronized with the energy scan to keep the beam focused on the same location. The use of a phase zone plate (200 nm thick Ni) will increase the efficiency to 15%-18% in the 400-700 eV photon range as compared to 10% for an amplitude zone plate.[4]

References

1. H. Ade et al., Journal of Vacuum Science and Technology A 9 (1991)1902
2. A. G. Michette, Optical System for Soft X-rays, New York: Plenum Press (1986) Chap. 6
3. H. Ade et al., Appl. Phys. Lett. 56 (19), 7 May 1990
4. This work is supported in part by the National Science Foundation under grant DIR-9005893. Work at the NSLS is supported in part by the US Department of Energy under contract DE-AC02-76CH00016. The Center of X-Ray Optics is supported by the US Department of Energy under contract DE-AC-03-76SF00098.
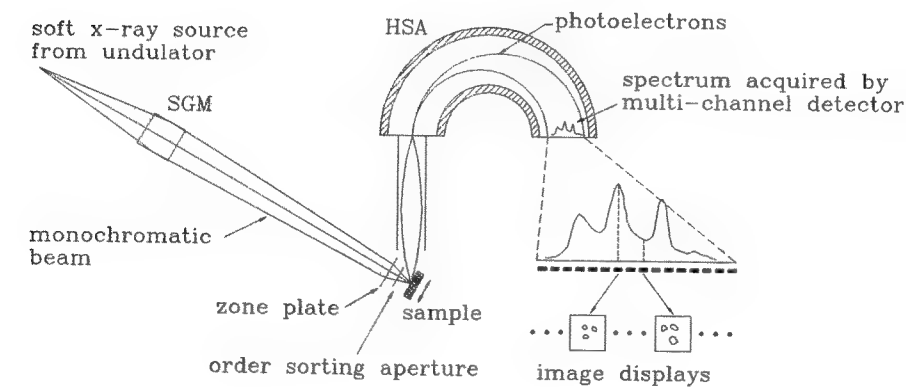
FIG. 1. - Schematic of X1-SPEM II using multi-channel HSA to collect photoelectron spectrum at each pixel of image.

3D MICROANALYSIS OF TISSUE VOLUMES
USING DUAL-ENERGY CONEBEAM X-RAY MICROTOMOGRAPHY

Roger H. Johnson

Center for Bioengineering, WD-12, University of Washington, Seattle, WA 98195

Using a modified SEM as a microfocus x-ray source and stimulable phosphor plates as detectors, we have built a conebeam microtomograph for 3D imaging of 1-10mm biological samples (Figure 1).[1,2] For individual projections, the resolution and exposure time are about three microns and two minutes, respectively, with the same parameters in the reconstruction depending on the number of views.

In conventional computed tomography (CT) each detector element integrates the energy incident upon it from all transmitted photons regardless of their wavelength. All spectral information is lost. It can be beneficial to acquire two sets of projections: one using a higher peak x-ray source energy than the other.[3] Figure 2 illustrates that tissue and bone will attenuate the two spectra differentially producing different contrast relationships in the high- and low-energy images. We have previously clinically applied post-processing dual-energy CT to analyze the mineral and fat content of lumbar vertebrae in perimenopausal, osteoporotic women.[4,5] The purpose of our current work is to apply a preprocessing dual-energy method, in which calculations are performed upon the detected projections prior to reconstruction, to the microscopic analysis of the soft tissue and bone phases in the guinea pig cochlea.

For most materials, the attenuation coefficient, μ, as a function of energy, E, can be quite accurately represented as:[6]

$$(1) \qquad \mu(E) = a_1 \frac{1}{E^3} + a_2 f_{KN}(E) \, , \quad \text{where the coefficient} \quad a_1 = K_1 \frac{\rho}{A} Z^4 \quad \text{and} \quad a_2 = K_2 \frac{\rho}{A} Z \, ,$$

$f_{KN}(E)$ is the Klein-Nishina equation,[7] K_1 and K_2 are constants, ρ is mass density, A is the atomic weight and Z the atomic number of the material. The first term or basis function on the right embodies the photoelectric interaction and the second accounts for Compton scattering.

Conceptually, CT detectors measure the integral of the attenuation coefficient along the source-detector trajectory, s:

$$(2) \qquad \int \mu(x,y,E)ds = A_1 \frac{1}{E^3} + A_2 f_{KN}(E), \quad \text{where} \quad A_1 = \int a_1(x,y)ds \quad \text{and} \quad A_2 = \int a_2(x,y)ds \, .$$

The dual-energy approach provides the two independent measurements required for every point in the projections in order to reconstruct the functions a_1 and a_2 in object space. The two measurements are:

$$(3) \qquad \left(\frac{I}{I_0} \right)_{kV_{peak}} = \int S_{kV_{peak}}(E)\exp[-A_1 \frac{1}{E^3} - A_2 f_{KN}(E)]dE \, , \quad \text{where } kV_{peak} \text{ is either high or low.}$$

If the system is well-determined (achievable by maximizing the difference between the source spectra) and the spectra, S, were known, these equations could be solved for A_1 and A_2 allowing the reconstruction of the a_1 (photoelectric) and a_2 (Compton) image volumes. Since in practice the spectra cannot be accurately known, the system is approximated with the power series:

$$(4) \qquad \ln\left(\frac{I}{I_0} \right)_{low} = b_0 + b_1 A_1 + b_2 A_2 + b_3 A_1^2 + b_4 A_2^2 + b_5 A_1 A_2 + b_6 A_1^3 + b_7 A_2^3$$

$$\text{and} \qquad \ln\left(\frac{I}{I_0} \right)_{high} = c_0 + c_1 A_1 + c_2 A_2 + c_3 A_1^2 + c_4 A_2^2 + c_5 A_1 A_2 + c_6 A_1^3 + c_7 A_2^3 \, .$$

The coefficients b_i and c_i are determined by obtaining projection images of a series of phantoms in which the "thicknesses" A_1 and A_2 are known. For an unknown sample, after obtaining the high- and low-energy intensities for each pixel, A_1 and A_2 are calculated from Equation (4) using the Newton-Raphson iterative method.

Our phantom system, designed to mimic the composition of the cochlea, is shown in Figure 3. Dimension X pertains to a layer of hydroxyapatite (HA)[8] and Y to lucite, each with well-characterized structure, chemistry and thickness. Dimension X ranges in steps from 100um to 1mm, with X+Y=3mm (the diameter of the guinea pig cochlea). Figure 4 shows the results of modeling the system. The spectra were obtained using Kramer's equation[9] and by curve-fitting Equation (1) to published values of μ for Pt (target foil), Be (window), Al (filter)[10], tissue and bone[11] to obtain the constants. Figure 4b shows clearly that I/I_0 is significantly different between high- and low-energy images of a given combination of the two layers. This enables the reconstruction of the contrast-enhanced a_1 and a_2 image functions and permits estimation of the bone and tissue concentration in each voxel.[12]

FIGURE 1: Schematic of x-ray microtomograph.

FIGURE 2: High and low energy spectra and mu's for tissue and bone.

References:

1. R.H. Johnson et al., Proc. Int. Congress for Electron Microscopy 12(1990)518.
2. R.H. Johnson et al., Proc. Ann. MSA Meeting 50(1992)584.
3. R.E. Alvarez and A. Macovski, Physics in Medicine and Biology 21(1976)733.
4. M.M. Goodsitt and R.H. Johnson, Medical Physics 19(1992)1025.
5. M.M. Goodsitt et al., Journal of Bone and Mineral Research 13(1991)217.
6. J. Hale, The Fundamentals of Radiological Science, Springfield: C. Thomas(1974).
7. W. Heitler, The Quantum Theory of Radiation, New York: Oxford University Press(1954).
8. Norian Corporation, 1025 Terra Bella Avenue, Mountain View, CA 94043.
9. H.A. Kramers, Phil. Mag. 46(1923)836.
10. E.F. Plechaty, Lawrence Livermore Pub. UCRL-50400(1975).
11. H.E. Johns and J.R. Cunningham, The Physics of Radiology, Springfield: Charles Thomas(1983).
12. Supported by the W.M. Keck Foundation.
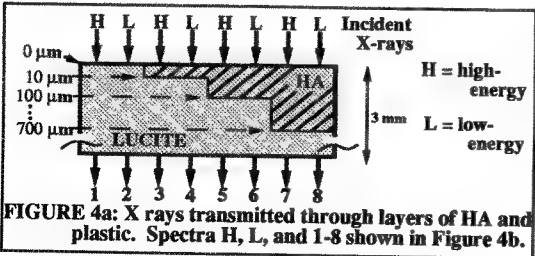
FIGURE 3: Cross-section of phantom disk.

FIGURE 4a: X rays transmitted through layers of HA and plastic. Spectra H, L, and 1-8 shown in Figure 4b.

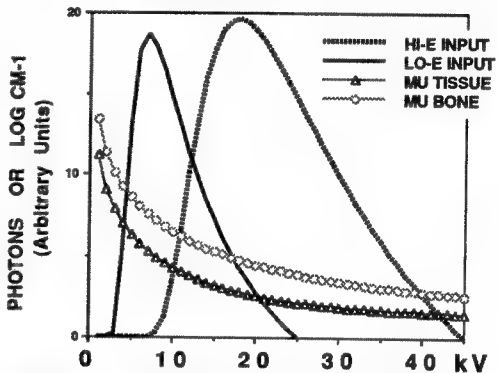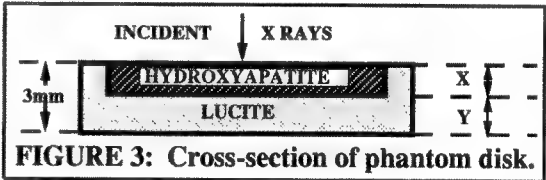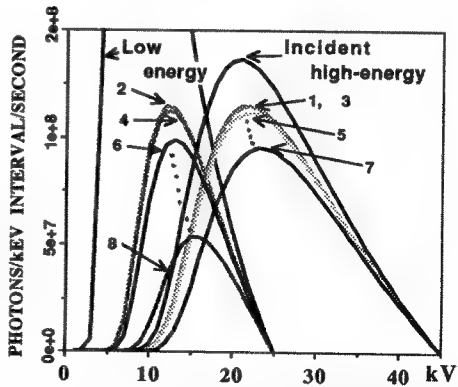FIGURE 4b: Incident and emergent high and low-energy spectra from sample of Fig. 4a.

653

CONE-BEAM 3D IMAGE RECONSTRUCTION IN X-RAY MICROTOMOGRAPHY

G. Wang*, P. C. Cheng, T. H. Lin, D. M. Shinozaki[1] and H. Kim[2]

AMIL-ARTS, Dept. of Electrical and Computer Engineering, State Univ. of New York, Buffalo, NY 14260, USA; [1]Dept. of Materials Engineering, Univ. of Western Ontario, London, Ontario, Canada N6A 5B7; [2]Laboratory for Laser Energetics, University of Rochester, Rochester, NY 14623

An X-ray shadow projection microscope system using a scannable point source of X-rays is under development at AMIL-ARTS, SUNY at Buffalo, USA. The point source is generated by a focussed electron beam, which can be steered electromagnetically in a plane perpendicular to the optical axis of the microscope. A specimen is mounted on a rotatable mechanical stage for microtomography. Considering the hardware characteristics of this system and the limitations of current cone-beam reconstruction algorithms, a generalized Feldkamp's cone-beam image reconstruction algorithm has been developed at our laboratories. In our cone-beam reconstruction, there are mainly two kinds of scanning scanning modes: planar and helix-like. A planar scanning locus is used to handle spherical or plate-like specimens. A typical case of planar scanning loci is a circle, which is used in Feldkamp's cone-beam reconstruction. A helix-like scanning locus is used to deal with rod-shaped specimens. Without loss of generality, a locus turn of the X-ray source can be defined in cylindrical coordinates by the following equation:

$$\rho = \rho(\beta), \ h = h(\beta), \ \beta \in [0, 2\pi] \tag{1}$$

In the planar scanning mode, $h(\beta) = 0, \beta \in [0, 2\pi]$. In the helix-like mode, $h(\beta) \in [z - \frac{h_p}{2}, z + \frac{h_p}{2}], \beta \in [0, 2\pi]$, where z is the vertical axis coordinate of a specimen horizontal slice, and h_p is the pitch of the helix-like scanning locus. We define the midplane to be the x-y plane in the planar scanning mode and be the plane with a longitudinal coordinate z in the helix-like mode. Our generalized cone-beam reconstruction formula is given as follows:

$$g(x, y, z) = \frac{1}{2} \int_{-\pi}^{\pi} \frac{\rho^2(\beta)}{(\rho(\beta) - s)^2} \int_{-\infty}^{\infty} R_\beta(p, \zeta) f(\frac{\rho(\beta)t}{\rho(\beta) - s} - p) \frac{\rho(\beta)}{\sqrt{\rho^2(\beta) + p^2 + \zeta^2}} dp d\beta \tag{2}$$

where $f(\cdot)$ is the reconstruction filter, and $\zeta = \frac{\rho(\beta)z'(\beta)}{\rho(\beta) - s}$. In the above formula, the local coordinate system $(x, y, z'(\beta))$ associated with the angle β is defined by $z'(\beta) = z - h(\beta)$. In the planar scanning mode, $z'(\beta) = z, \beta \in [0, 2\pi]$. In the helix-like scanning mode, $z'(\beta) \in [-\frac{h_p}{2}, \frac{h_p}{2}], \beta \in [0, 2\pi]$. The specimen is assumed to be centered at the origin of the coordinate system.

Because the variation of rotation axis position of the mechanical stage is one of the main error sources in microtomography, an elaborate feed-back system is being implemented to correct this. However, experiments have shown that the calibration process of the rotation axis position is both time-consuming and complicated. On the other hand, the X-ray source of our X-ray microscope can be precisely moved along a straight line by steering the e-beam electromagnetically. Therefore, to minimize the number of recalibrations of the mechanical axis position, our generalized algorithm can be used in a polygonal scanning mode to become a polygonal cone-beam algorithm. The straight line portions of the polygon are achieved by the X-ray source movement, and the

number of the polygon sides determines the number of the stage rotations. Consequently, the number of the stage rotations is greatly reduced.

In the case of microtomography, many specimens are not spherical but rather cylindrical. A dashed-line cone-beam algorithm is then proposed to handle rod-shaped specimens. The scanning locus required by the dashed-line cone-beam algorithm is a sequence of horizontal straight line pieces which approximately segments a helix, similar to "winding stairs". To achieve this scanning mode, two kinds of movements must be combined. First, the X-ray source is steered horizontally. Second, the mechanical stage is rotated and shifted mechanically with specified steps. The dashed-line algorithm is valuable in reducing the number of angular rotations and vertical shiftings of the mechanical stage. This means a much less number of the recalibrations of the stage position. Note that while reconstructing each horizontal slice of the specimen, it is required that $\beta = \pi$ corresponds to the horizontal scanning line segment closest to the slice and projection data collected from the upper and lower halves of the scanning locus turn are used to reconstruct the slice, so that the reconstruction error is minimized.

In order to reconstruct plate-like specimens (or thick films), the planar scanning mode is used. A plate-like specimen is placed parallel to the plane of the locus. Arrange the relative position so that the perpendicular passing through the center of the locus passes through the center of the specimen area of interest. This perpendicular is labeled the principal axis. A specific locus used is made to be similar to the shape of the area of interest, and substantially larger than that area. The detector plane is placed behind the specimen, parallel to the specimen, and the two-dimensional projection data recorded for each X-ray source position. After each frame of these projection data is mapped onto the plane facing the X-ray source and passing through the principal axis, our generalized cone-beam algorithm is applied to the modified projection data. In this way the problems associated with the standard limited angle approaches are avoided.

When the generalized cone-beam algorithm is applied in two-dimensions, a derivative-free noncircular fan-beam reconstruction formula is obtained. Assume that the scanning locus be symmetric with respect to the origin of the reconstruction coordinate system and the direction tangent to the locus stay outside of the fan delimited by the object support, the new fan-beam formula is proved. This means that the reconstruction is exact on the mid-plane in the planar scanning mode. The generalized cone-beam reconstruction algorithm can be regarded as a linear system. The spatially variant PSF of the generalized cone-beam reconstruction algorithm is derived. It is shown that the vertical integral of the PSF is an ideal *delta* funtion, provided that the horizontally projected scanning locus meet the above conditions required by the new fan-beam formula. it is then proved that the vertical integral of a reconstructed three-dimensional image is equal to that of the actual image, Furthermore, if an actual image is independent of the vertical axis, the reconstruction is exact. Our generalized algorithm was also validated in numerical experiments with Shepp and Logan's 3D head phantom. In the experiments, the generalized cone-beam algorithm consistently resulted in satisfactory reconstructed images.

G. Wang, T. H. Lin, P. C. Cheng and D. M. Shinozaki, J. Scanning Microscopy, (1992)14, 187
G. Wang, T. H. Lin, P. C. Cheng and D. M. Shinozaki, J. Scanning Microscopy, (1992)14, 350
G. Wang, T. H. Lin, P. C. Cheng and D. M. Shinozaki, IEEE Trans. Medical Imaging (In Press)
G. Wang, T. H. Lin and P. C. Cheng, IEEE Trans. Image Processing (In Press)
* Dr. G. Wang is currently with Mallinckrodt Institute of Radiology, Washington University, St. Louis, MO 63110, USA

STRUCTURE AND PROPERTIES OF ORGANIC LIQUID CRYSTALS

I.G. Voigt-Martin
Institut für Physikalische Chemie der Universität Mainz, 6500 Mainz, Germany

Organic liquid crystals (LCs), both in the monomeric and polymeric state, are capable of self organisation because of the anisotropic shape of their molecules. [1,2] By suitable molecular engineering it is thus possible to induce interesting physical properties like ferroelectricity, second harmonic generation (SHG) and photoconductivity. [3,4] For a deeper understanding it is necessary to gain insight into the relationship between molecular characteristics (electronic charge distribution, dipole moments, hyperpolarisabilities, molecular conformation), structural relations (symmetry relations, space groups, defects) and the above physical properties

For structure analysis electron diffraction patterns from different crystallographic zones with many higher orders of diffraction are required. Unfortunately a characteristic feature of LCs is their loss of all higher order reflections and a change in symmetry. Furthermore, LCs give rise to specific defects, which give important information about the elastic energy density of the system. These can only be characterised by a phase contrast imaging method in which the small angle spatial frequencies are transferred by the electron microscope phase transfer function. This requires the use of an unusually large defocus value, as we have described previously. [5-8]

Our approach, therefore, was to learn from diffraction how the transition from crystal to LC takes place and then to characterise the defects which occur in the crystals and LCs by medium-high resolution imaging. For both diffraction and imaging, kinematic and dynamical scattering effects were calculated using molecular modelling. Three molecules with specific physical properties were chosen:

(a) Triphenylene ether, forming a discotic mesophase (Photoconductivity) [8]

(b) Nitrobenzenebiphenylenester, forming a smectic C* mesophase (Ferroelectricity) [7]

(c) Phenylalkylaminodione, forming a smectic A mesophase (SHG) [9]

A typical example comparing crystal and liquid crystal is shown in the high resolution images of Figs 1(a) and 1(b) with appropriate diffraction patterns in the respective insets. Structure analysis then proceeded as follows:

I. Electron diffraction

I(a) The molecule is built up using semi-empirical quantum mechanical methods and its molecular conformation, its dipole moment and hyperpolarisability calculated.

I(b) This molecule is placed in the unit cell obtained from the experimental diffraction patterns in different orientations. At this stage it is necessary to take account of crystal field effects on the molecular conformation (Fig 2). The molecule is rotated and shifted until a best-fit is obtained between calculated (Fig 3) and experimental (Fig 1(a)) diffraction pattern.

I(c) The unit cell and atomic distribution obtained from above were compered with the potential maps from maximum entropy calculations, using the electron diffraction data. [9]

I(d) Both kinematic and dynamical scattering patterns were calculated and compared with experiment. [6-8]

I(e) The electron diffraction patterns from the LC mesophase were compared with their crystalline analogs. In this way the molecular significance of specific intensity losses (reduction in translational correlations) or arcing (reduction in orientational correlation) could be assessed.

II. High resolution imaging

II(a) By using suitable low dose, cryo techniques combined with computer-controlled imaging facilities to predetermine the most suitable electron microscope transferfunction, it was possible to obtain medium to high resolution images of all samples discussed in the introduction both in the crystalline and LC phases. [5-10]

II(b) Using the atomic co-ordinates from I(a) and the unit cell from I(b), the image was calculated as a function of sample thickness and defocus value, using dynamical scattering theory. [7-9]

II(c) The observed defects were characterised using a cross-correlation technique. [8]

Literature:
(1) R.Bryce, L.C.Murphy Nature 309, 19 (1984)
(2) H.Ringsdorf, B.Schlarb, J.Vezmer Angew. Chemie 101, (1988) 934
(3) E.Zerta, M.Ebert Angew. Chemie 101, (1989) 934
(4) H.Finkelmann Angew. Chemie 99, (1987) 840
(5) I.G.Voigt-Martin, H.Durst Macromolecules 22, (1989) 168
(6) I.G.Voigt-Martin, H.Krug, D.Van Dyck J.Physique 51, (1990) 2347
(7) I.G.Voigt-Martin, R.W.Garbella, S.U.Vallerian J.Physique II 2, (1992) 345
(8) I.G.Voigt-Martin, M.Schumacher, R.W.Garbella Macromolecules 25, (1992) 961
(9) I.G.Voigt-Martin, D.H Yan, C.Gilmore Phys.Rev. (submitted)
(10) I.G.Voigt-Martin, E.Zhou, P.Simon, R.W.Garbella, D.H Yan, W.Paulus, H.Ringsdorf
J.Chem.Phys (submitted).
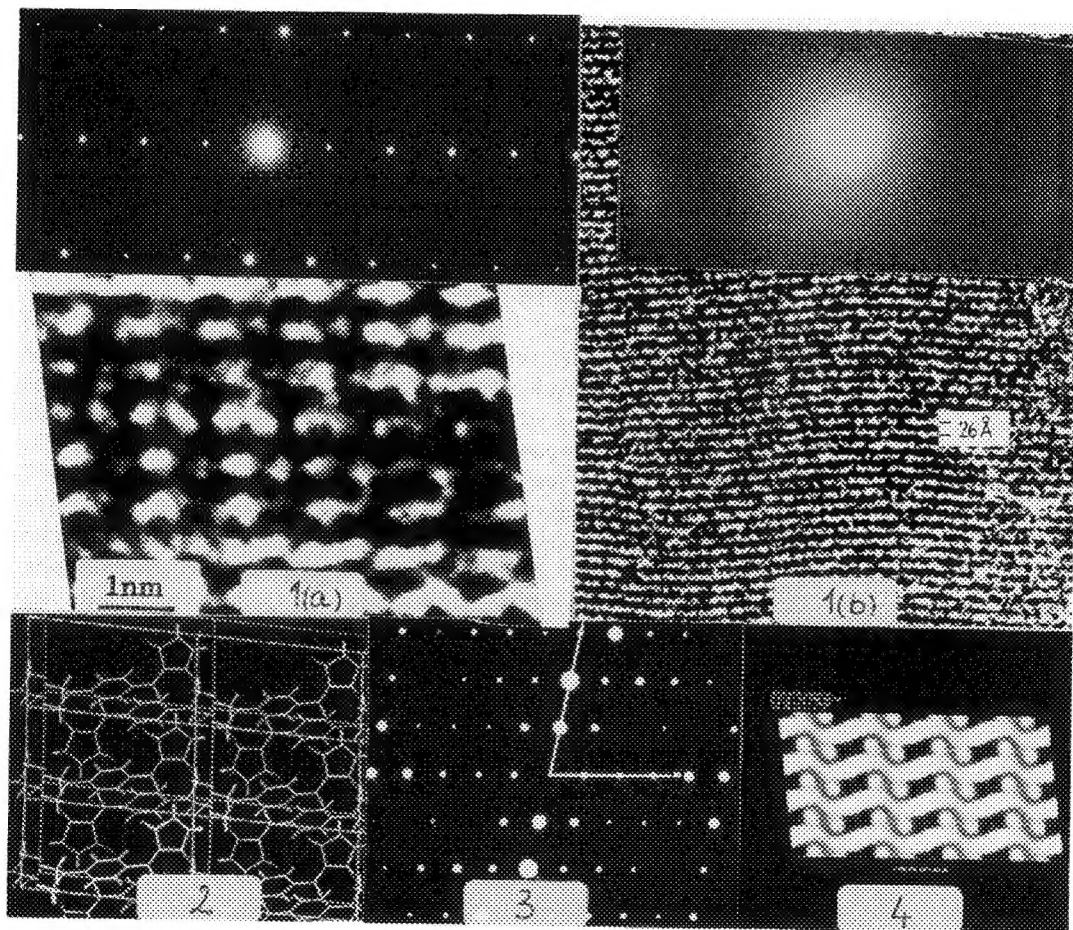
DIRECT PHASE DETERMINATION FROM EM IMAGES

Sven Hovmöller[1]*, Xiaodong Zou[1], Lars Eriksson[1], and Gunnar Svensson[2]

Structural[1] and Inorganic[2] Chemistry, Stockholm University, S-106 91 Stockholm, Sweden

EM images contain phase information, in contrast to X-ray and electron diffraction patterns. The phases are extracted from the Fourier transform (FT) of the EM image. However, there has been doubts as to what exactly this phase information is. Are the EM phases the same as those of the crystallographic structure factors F(hkl) as defined in x ray crystallography? Or are the phases so distorted by dynamical scattering that very sophisticated procedures are needed for phase retrieval, as has been suggested.[1]

We have investigated this question, by comparing phases obtained from EM-images with those of the x ray structure factors from two accurately refined barium niobium oxide crystals.

EM images of $Ba_4Nb_{14}O_{23}$ (orthorhombic *Cmmm*, a=20.782, b=12.448, c=4.148 Å) and $Ba_3Nb_{16}O_{23}$ (orthorhombic *Cmmm*, a=20.930, b=12.478, c=4.162 Å) were taken with a Philips CM 30 300kV and a JEOL 200CX 200kV electron microscope. Thin areas near the edge were analyzed by our newly developed image processing system, CRISP.[2] These structures had already been solved by single crystal and powder x-ray diffraction respectively, and refined to R-values of 3.1% and 5.1%.[3,4]

Four different micrographs of $Ba_4Nb_{14}O_{23}$ were digitized. Three of these had thin areas near the crystal edges, but one was considerably thicker. The FT of each image was calculated and phases for all reflections within 2.0 Å resolution were extracted with CRISP. The three thin crystals all had very good phases, with phase residuals of only 10 to 12 degrees for cmm symmetry, compared to 25 for the thicker crystal. There were 18 unique reflections within 2.5 Å resolution. In a centrosymmetric crystal like this one, there are only two possible phase values for each reflection; 0 or 180 degrees. This still leaves us with as many as 2^{18} (=262 144) different possible combinations of phases for each image. The three thin areas had 18, 17 and 16 phases correct, respectively. This proves that the phases from the FT of an EM image of a metal oxide crystal are in fact the same as those of x ray crystallography. The thicker crystal had 9 phases correct and 9 wrong. Until methods are derived to restore correct phases from such thick areas, these phases are useless and may be considered as no better than random phases. Outside 2.5 Å resolution the amplitudes fell dramatically, which leaves weaker reflections with less accurate phases. There is also the contrast transfer function cross-over in this region. As a consequence we have not yet been able to assign phases in the region outside 2.5 Å resolution.

Similar results were obtained with crystals of the other barium niobium oxide $Ba_3Nb_{16}O_{23}$. One severely tilted crystal had only one phase wrong among the 31 reflections within 1.9 Å resolution.

References
1. W. Coene, A.F. de Jong, H. Lichte, H. Tietz and D. van Dyck, Proc. 10th European Congress Electron Microscopy, Vol.I, 499-500, Granada 1992.
2. S. Hovmöller, Ultramicroscopy 41 (1992) 121-135
3. G. Svensson et al. Z. anorg. allg. Chem. 619 (1993) 133-137.
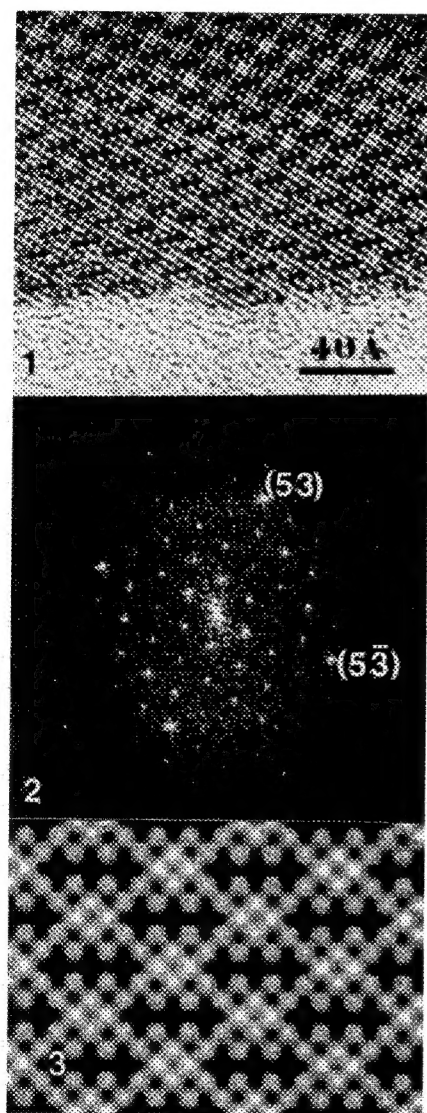4. V.G. Zubkov et al. to be published.

Amplitudes and phases of $Ba_4Nb_{14}O_{23}$

H	K	AMP	sAMP	PHA	sPHA	ERR
0	2	1647	1647	166	180	
0	4	981	981	187	180	
1	-3	710	772	180	180	
1	3	834	772	180	180	
1	-1	2587	2548	194	180	
1	1	2509	2548	200	180	
2	-4	44	63	351	0	
2	4	83	63	78	0	P
2	-2	703	718	339	0	
2	2	734	718	338	0	
2	0	1050	1050	345	0	
3	-3	169	239	352	0	
3	3	310	239	356	0	
3	-1	241	280	325	0	
3	1	320	280	350	0	
4	-4	80	185	130	180	P
4	4	291	185	212	180	
4	-2	631	869	166	180	
4	2	1108	869	180	180	
4	0	805	805	178	180	
5	-3	1532	2451	358	0	
5	3	3370	2451	1	0	
5	-1	1052	1199	189	180	
5	1	1347	1199	170	180	
6	-2	163	284	146	180	
6	2	405	284	193	180	
6	0	489	489	178	180	
7	-1	96	145	358	0	
7	1	195	145	27	0	
8	0	60	60	238	180	P

Fig. 1. A crystal of $Ba_4Nb_{14}O_{23}$

Fig. 2. The FT of Fig. 1

Fig. 3. The projected potential map calculated from the symmetrized structure factors in the Table.

Table. H K are the crystal indices, AMP amplitudes and PHA phases, as they have been extracted from the Fourier transform of the scanned crystal shown in Fig. 1. After the projected symmetry was found to be cmm, this symmetry was imposed on the data, giving the columns sAMP and sPHA (s for symmetrized). ERR denotes possible errors. In this case 3 reflections are marked with a P, indicating that these phases are uncertain, since they deviate more than 45 degrees from 0 or 180 degrees. Note that the phases are of higher quality than the amplitudes.

659

ELECTRON DIFFRACTION OF COPPER PHTHALOCYANINE ON THE HVEM

W. F. Tivol, J. N. Turner, M. P. McCourt,* D. L. Dorset *

Wadsworth Center for Laboratories and Research, Albany NY 12201-0509 and School of Public Health, the University at Albany, Albany NY 12201-0509, USA
* Electron Diffraction Department, Medical Foundation of Buffalo, Inc., Buffalo NY 14203-1196, USA

The use of high-energy (1200 kV) electrons has been shown to be advantageous in the *ab initio* structure analysis from electron diffraction of organic compounds.[1,2,3] Previous studies showed that *ab initio* analysis of copper perchlorophthalocyanine could be accomplished at accelerating voltages at or above 1000 kV, but not at 400 kV for crystals which are about 10 nm thick.[1,2] Copper perbromophthalocyanine could also be analyzed *ab initio* at 1200 kV, but the presence of severe dynamical scattering precluded such analysis at lower voltages.[3] A study of copper perchlorophthalocyanine at accelerating voltages from 200 kV to 1200 kV showed that dynamical scattering accounted for the differences among the diffraction patterns which lead to the failure of *ab initio* analysis at the lower voltages.[2]

The series of phthalocyanines offers a good model for the study of dynamical scattering and direct phasing methods, since it consists of relatively radiation-resistant compounds for which high-resolution diffraction patterns can be obtained. Furthermore, the symmetry of the molecule and the flatness of the unit cell simplify both the analysis and the multi-slice calculations used to investigate the effects of dynamical scattering. This allows studies at both the high voltages and the intermediate voltages (300 to 400 kV) used in modern electron microscopes.

Copper phthalocyanine was grown epitaxially from the vapor phase onto a clean KCl crystal face.[4] Electron diffraction patterns were obtained from crystals of the metastable α-form tilted at 32° and oriented so that the electron beam was parallel to the c-axis.[4]

Electron doses were kept to a minimum by the use of a 30 μm condenser aperture and a highly excited first condenser lens. The newly-installed video system allows scanning the specimen to find a crystal suitable for the correct orientation of the grid by rotating it within its own plane (See Fig. 1a.), following the crystal as the grid is rotated (See Fig. 1b.) and focusing the objective lens all at an illumination level below that necessary to distinguish anything by eye on the HVEM's phosphor screen.

The AEI EM7 high-voltage electron microscope was used at a voltage of 1000 kV in diffraction mode with a 10 μm selected area aperture. The data were recorded on DuPont Lodose Mammography film. Diffraction spots are seen out to a resolution of 0.07 nm (See Fig. 2). Intensities were measured on a Perkin-Elmer 1010A flat bed microdensitometer and processed on a VAX 6210 computer and a 3100 workstation using the diffraction-analysis package[5] of the SPIDER image processing software.[6]

The pattern obtained corresponds to a unit cell with lattice constants half those usually quoted, since in this projection the space group C2/c reduces to plane group p2.[4] Analysis of the data is in progress.[7,8]

References

1. Dorset, D.L., et al., *Ultramicroscopy* 38 (1991) 41.